

A 2 GSps 8 bit Folding & Interpolation ADC in 90 nm CMOS Technology

Yi Zhang^{1,2}, Qiao Meng³, Debo Wang^{1,2}, Changchun Zhang^{1,2}, and Yufeng Guo^{1,2}

¹Jiangsu Provincial Engineering Laboratory of RF Integration & Micropackaging, Nanjing, China

²College of Electronics Science and Engineering

Nanjing University of Posts and Telecommunications, Nanjing, China

³Institute of RF- & OE-ICs, Southeast University, Nanjing, China

Abstract— A single channel 2 GSps, 8 bit folding and interpolation (F&I) analog-to-digital converter (ADC) designed in TSMC 90 nm CMOS technology was presented in this paper. The ADC utilized cascaded folding architecture, which incorporated an additional inter-stage sample-and-hold amplifier between the two stages of folding circuits to enhance the quantization time. A pipelined track-and-hold amplifier (THA) with bootstrapped switch was taken as the front-end THA to improve its performance. The foreground digital assisted calibration was also employed in this design to correct the error of zero-crossing point caused by the circuit offset, thus to improve the linearity of the ADC. Chip area of the whole ADC including pads is $930\ \mu\text{m} \times 930\ \mu\text{m}$. Post simulation results demonstrate that under a single supply of 1.2 Volts, the ADC consumes 210 mW. For the clock of 2 GHz, the signal to noise and distortion ratio (SNDR) is 45.93 dB for Nyquist input signal frequency.

1. INTRODUCTION

Ultra-high-speed (GSps), medium resolution Analog-to-digital converters (ADCs) are the key element in many electronic systems, such as communication system, test equipment radar and radio astronomy system. With the development of technology, in many of these systems, signal has a bandwidth of over 1 GHz, such as the ultra-wide-band (UWB) technology. So, research of ADCs which has a sampling rate over 2 GSps is of great significance. Flash and Folding ADC are the primary candidates for GSps applications due to their high conversion speed and low latency. Although the flash architecture has been used in the highest speed ADCs, it has the severe disadvantage that it requires 2^N comparators for N bits of resolution, which results in a substantial area and power penalty starting at the 8 bit level. As a result, pipelined Folding and Interpolation (F&I) was adopted in this design of 2 GSps, 8 bit ADC.

In this design, cascaded folding architecture was taken to enhance the quantization time. Folding and interpolation factors were selected to be 3×3 and 2×8 to balance system area and performance. Foreground digital assisted calibration was adopted to eliminate device mismatch, the impact of gain error and the mismatch error of the channel.

In Part 2, key circuits and digital calibration will be presented. Part 3 gives layout and system simulation results. Part 4 is the conclusion and Part 5 is the acknowledgement.

2. CIRCUIT OF THE PROPOSED ADC

From Fig. 1 it can be seen that the proposed ADC is a single channel circuit. The upper part is the main circuit and the under part is the calibration circuit. For the main circuit, the coarse and the fine channel quantify the signal from the front-end track-and-hold amplifier (THA) respectively and deliver the quantization signal to the 8 D Flip-Flop (DFFs) to get the final results. The Fine channel is much more complicated than the coarse channel. It is composed of 19 preamps (1 for redundancy), two F&I stages (6 for the first stage with folding factor = 3 and interpolation factor = 2; 4 for the second stage with folding factor = 3 and interpolation factor = 8) and 12 inter-stage sample and hold amplifier (SHA) to enhance the quantization time, 32 comparators, 32 spark code elimination circuit and fine coding circuit. The coarse channel is composed of 6 preamps, 6 comparators, 1 synchronization circuit to make sure the result is right and coarse coding circuit.

The under part is the calibration circuit and it includes logic control, counter, DFF array and digital-to-analog converter (DACs). It will be explained more in Chapter 2.3.

2.1. The Front-end THA

For gigahertz sampling rate operation, it is far better to have a front-end THA as it can improve the dynamic performance of an ADC [1]. By holding the analog sample static during digitization,

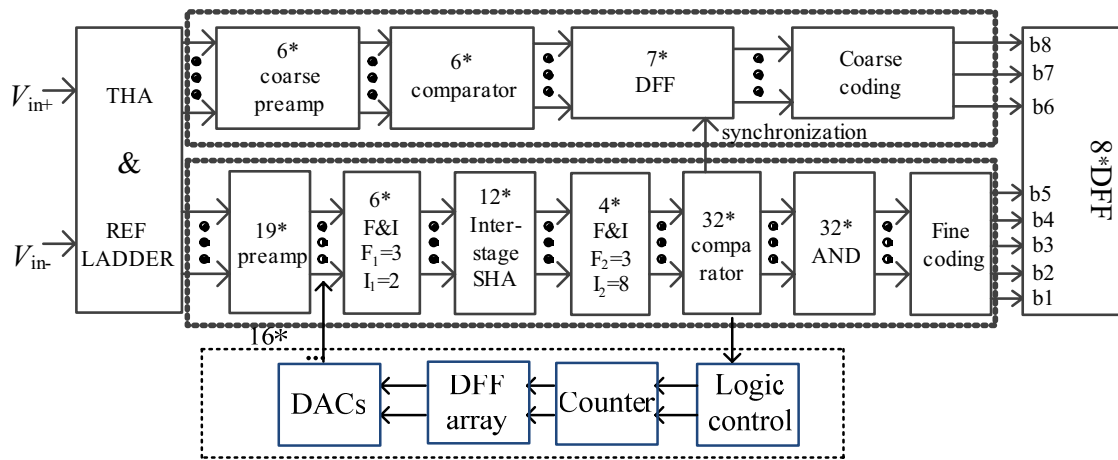


Figure 1: Diagram of the proposed ADC.

the THA largely removes errors due to skews in clock delivery to a large number of comparators, signal-dependent nonlinearity, and aperture jitter.

The THA designed takes the open-looped architecture, presented in Fig. 2. The bootstrapped switch is adopted as its equalized resistance has less to do with the input voltage, thus to improve THA’s linearity. Also, its over-drive voltage is larger than the normal MOS switch, so the equalized resistance is smaller, and the sampling rate is improved.

As the designed THA should be working at 2 GSps while having a resolution of over 8 bit, a second stage THA was designed after the regular THA, thus making a novel pipelined THA, shown in Fig. 2. The second stage THA tracks and holds the signal of the first stage THA. As the second stage THA’s input signal is less varying as the original input signal, the linearity requirement of the second stage is much easier to realize than the first stage. To gain a large bandwidth for the THA, the second stage also takes the bootstrapped switch, but much easier than the first one.

The simulation results demonstrate that the pipelined THA has a good performance. For clock of 2 GHz, input signal of 1 GHz, its 128 point Fast Fourier Transform (FFT) spectrum was shown in Fig. 3. It can be seen that the THA’s Signal to Noise and Distortion Ratio (SNDR) is 61.5 dB, suited for the ADC.

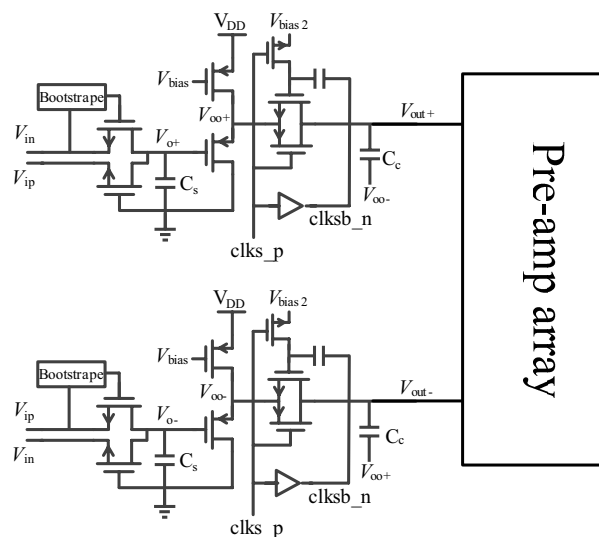


Figure 2: The designed pipelined THA.

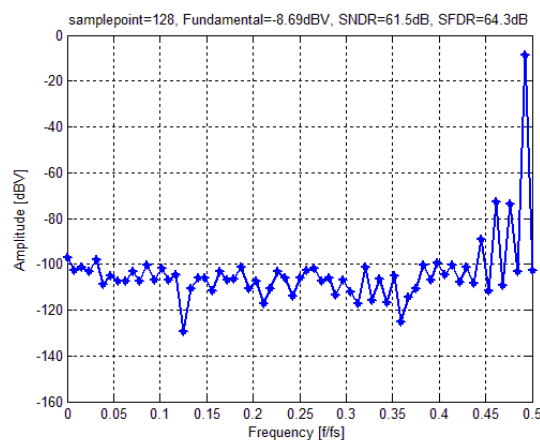


Figure 3: Output spectrum (Nyquist input@2 GSps).

2.2. Folding and Interpolation Network

With the analog pre-processing, the F&I architecture can better balance ADC's area, power and performance. The pre-amplifier array generates the original zero-crossing points, but never enough or it will be the flash architecture. As can be seen in Fig. 1, the two-stage cascaded F&I was taken in this design with inter-stage SHA circuit in between. These two stages are similar so it can be discussed together. With the help of F&I network, enough zero-crossing point will be generated while the system area and power is much smaller than its flash counterpart.

The first key element in designing the folding circuit is that it should have enough bandwidth to make sure signal can be settled within the limited time especially for ultra-high-speed ADCs. Second, it should have a certain gain to suppress the offset of next stage. Third, its offset should be controlled within a limited amount.

Figure 4 is the proposed F&I network. M1–M6 is the input differential pair as the folding factor is 3. M7 and M8 have two roles, first to insulate the signal from the input. Second, as the drain of three MOSFET is connected, its output capacitance is very large. With small sized M7 and M8, the bandwidth of the folding circuit can be increased. The AC simulation of the folding circuit is shown in Fig. 5. The gain is 5.38 dB and its -3 dB bandwidth is 4.9 GHz, suited for the ADC.

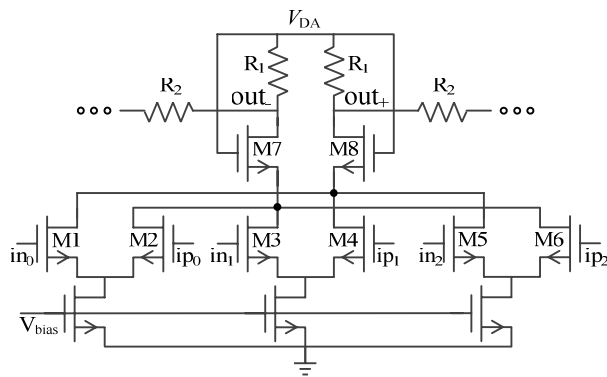


Figure 4: The designed F&I circuit.

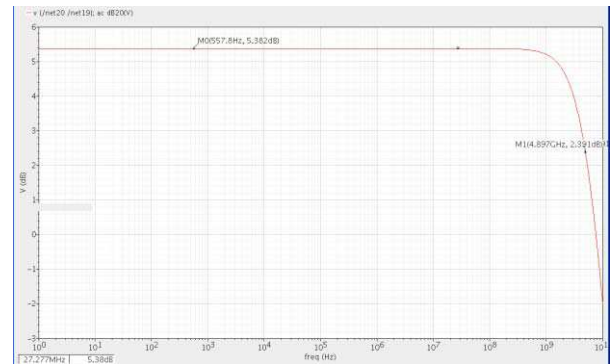


Figure 5: AC simulation result of folding circuit.

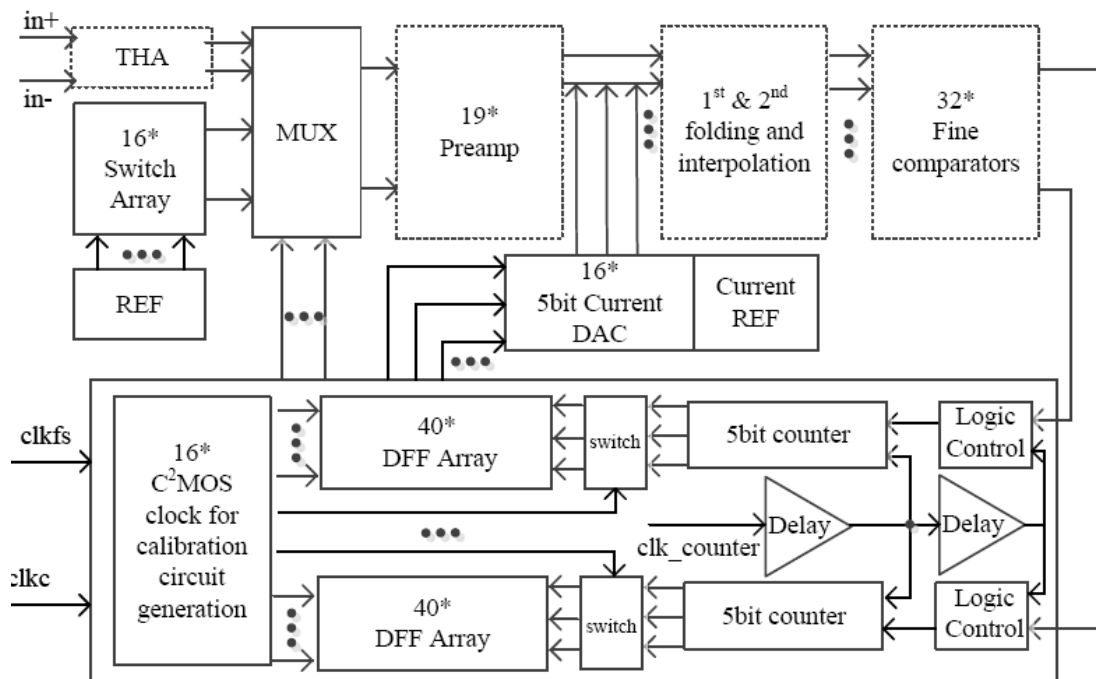


Figure 6: Diagram of digital assisted calibration.

2.3. Foreground Digital Assisted Calibration

As the main error in folding and interpolation architecture is the offset, and it will hardly change according to the temperature and external circumstance. Once the ADC is made, the offset is fixed. So, the foreground digital assisted calibration was adopted in this design. The actual offset can be measured and stored in the DFF array. When the ADC is working, the offset stored will be used to compensate for the real offset of the circuit, thus the offset is eliminated and the linearity is improved.

Figure 6 presents the diagram of the digital assisted calibration. From this figure, it can be seen that the offset of all the analog processing blocks, including pre-amplifier, inter-stage SHA, two stages of folding and interpolation circuit can be measured and stored. The calibration circuit contains three key sub-circuits as (1) the clock generation circuit for calibration. Here, the C²MOS circuit is adopted as it can generate 16 ways of calibration clock without overlapping. (2) The DFF array can be used to store the measured offset in the calibration phase. (3) The current DAC convert the stored digital offset to analog current and directly inject it to the output of pre-amplifier. In this way, it achieves the subtraction between the offset voltage and the stored offset voltage, thus the compensation is done and the linearity is improved.

3. LAYOUT AND SIMULATION RESULTS

To avoid the interference between analog and digital parts and obtain better performance, the power and ground patterns in analog and digital modules are separated. Fig. 7 is the layout of the ADC. Chip area is $930 \mu\text{m} \times 930 \mu\text{m}$ with pads.

Figure 8 shows the post simulation result of 128-point FFT output spectrum. From the figure,

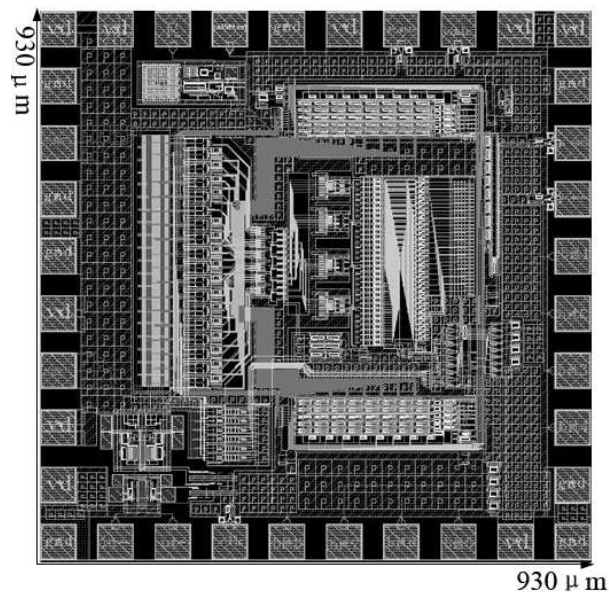


Figure 7: Layout of the ADC.

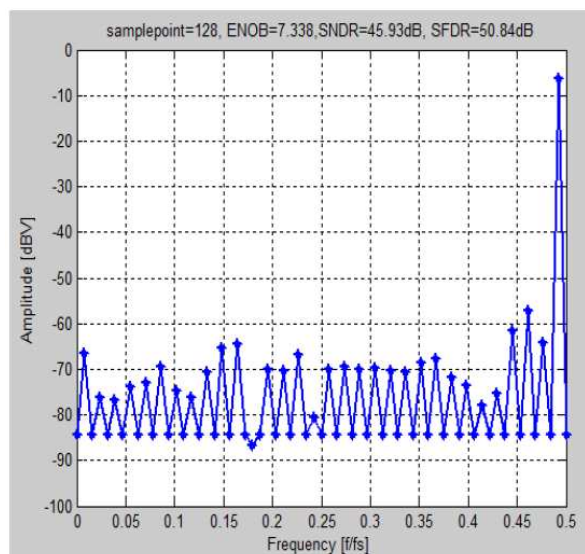


Figure 8: Output spectrum (Nyquist input @2 GSps).

Table 1: Post simulation results of F&I ADC and comparison with others.

Performance	[2]	[3]	[4]	[5]	This work
Technology	0.18 μm CMOS	0.18 μm CMOS	90 nm CMOS	90 nm CMOS	90 nm CMOS
Supply (V)	1.8	1.8	1	1.2	1.2
Clock (GHz)	1.6	1	2.7	1	2
SFDR (dB)	56	68.6		28.87	50.84
SNDR (dB)	46	56.5	33.6	27.35	45.93
Power (mW)	774	1260/channel	50	7.65	210
Area (mm^2)	3.6	49 (dual ADC)	0.36	0.063	0.865

it can be seen for Nyquist input signal ($f_{in} = 1$ GHz) @2 GSps, the Spurious Free Dynamic range (SFDR) is 50.84 dB and the SNDR is 45.93 dB, so the Effective Number Of Bit (ENOB) is calculated to be 7.338 bit. The result demonstrates that the ADC has a good dynamic performance.

The performance of the designed F&I ADC and the comparison with other published ones (SNDR and SFDR for Nyquist sampling in [2–4], 260 MHz@1 GSps in [5]) are listed in Table 1.

4. CONCLUSION

In this paper, a 2 GSps, 8 bit cascaded folding and interpolation ADC with foreground digital assisted calibration in TSMC 90 nm CMOS technology is presented. The ADC consumes an area of $930 \mu\text{m} \times 930 \mu\text{m}$ with pads and achieves a 7.338 bit of ENOB at Nyquist input frequency with a power consumption of 210 mW from a single supply voltage of 1.2 Volts. The simulation results demonstrate that the designed ADC is suitable for ultra-high-speed, medium resolution signal processing systems.

ACKNOWLEDGMENT

The research was sponsored by NUPTSF (Grant No. NY213076). Natural Science Foundation of Jiangsu Province under BK20140890&BK20141431. Jiangsu province science and technology support program — industrial part under BE2013130 and Doctoral Fund of Ministry of Education under 20133223110003.

REFERENCES

1. Razzaghi, A., “A single-channel 10 b 1 GS/s ADC with 2-cycle latency using pipelined cascaded folding architecture,” PhD Thesis, UCLA, 2008.
2. Taft, R. C., C. A. Menkus, M. R. Tursi, et al., “A 1.8-V 1.6 GSsample/s 8-b self-calibrating folding ADC with 7.26 ENOB at Nyquist frequency,” *IEEE Journal of Solid-State Circuits*, Vol. 39, No. 12, 2107–2115, 2004.
3. Taft, R. C., P. A. Francese, M. R. Tursi, et al., “A 1.8 V 1.0 GS/s 10 b self-calibrating unified-folding-interpolation ADC with 9.1 ENOB at Nyquist frequency,” *IEEE Journal of Solid-State Circuits*, Vol. 44, No. 12, 3294–3304, 2009.
4. Nakajima, Y., A. Saaguchi, T. Ohkido, et al., “A background self-calibrated 6 b 2.7 GS/s ADC with cascade-calibrated folding-interpolating architecture,” *IEEE Journal of Solid-State Circuits*, Vol. 45, No. 4, 707–718, 2010.
5. D’Amico, S., G. Cocciolo, A. Spagnolo, et al., “A 7.65-mW 5-bit 90-nm 1 Gs/s folded interpolated ADC without calibration,” *IEEE Transactions on Instrumentation and Measurement*, Vol. 63, No. 2, 295–303, 2014.

10 bit 100 MS/s SAR ADC with Reduced Loop Delay

Dong Li¹, Qiao Meng¹, Linfeng Wang¹, Yi Zhang², and Wenwei He¹

¹Institute of RF- & OE-ICs, Southeast University, Nanjing, China

²College of Electronics Science and Engineering

Nanjing University of Posts and Telecommunications, Nanjing, China

Abstract— A 10 bit 100 MS/s successive approximation register (SAR) analog-to-digital converter (ADC) is realized in 90 nm CMOS process. With the proposed logic control scheme and novel switch-driving register (SDR), the proposed SAR ADC achieves high conversion rate, low power, leading to SNDR of 59 dB and SFDR of 72.6 dB at 100 MS/s with 49.7 MHz input. The figure-of-merit (FoM) is 39.1 fJ/conversion-rate at 100 MS/s with a power consumption of 2.87 mW.

1. INTRODUCTION

With the feature size of CMOS devices scaled, design techniques for high speed SAR ADCs are being actively researched today in efforts to extend the advantages of a low-power characteristic to high speed applications. An effective design technique for high speed SAR ADC is the use of time-interleaving [1], but it suffers from matching problems between channels such as offset, gain, and sample-time skew often require complicated calibration. Another approach uses dynamic registers with asynchronous operation to reduce clock power and increase the conversion speed [2, 3].

Compared to synchronous processing, asynchronous processing technique optimizes the internal comparison time between subsequent bits. Therefore, it substantially shortens the conversion time. Nevertheless, the propagation delay in the successive approximation (SA) loop is also one of the dominant speed limiting factors, it can be reduced by optimizing the implementation of the SA logic [4].

This paper proposes a novel logic control scheme to reduce SA loop delay resulting in fast conversion operation. The remainder of the paper is organized as follows: Section 2 discusses the architecture analysis of the SAR ADC in order to obtain optimum performance. Section 3 introduces the circuits and implementation of building blocks of the proposed ADC. Layout of the proposed SAR ADC and simulation results are presented in Section 4 and conclusions are made in Section 5.

2. ADC ARCHITECTURE

The architecture of conventional SAR ADC is illustrated in Fig. 1(a) with the key blocks of capacitor network, comparator, SA control and the basic processing loop. As show in Fig. 1(a), the pulse generator generates the comparator control clock (CLKC) to trigger the comparator to regenerate and reset. After completing the comparison, a valid signal is generated to trigger the shift register to generate multi-phase clocks for switch-driving register (SDR). Then the comparison results are transmitted to switch-driving register and the outputs of the SDR are used to determine charging or discharging the DAC capacitor array before the next comparison. The key timing path is from the start of the comparison to the completely settlement of the DAC, the propagation delay in the critical path is one of the dominant speed limiting facts. In order to reduce the SA cycling time in SAR ADC, the timing path should be shortened. The proposed SAR ADC applies optimized

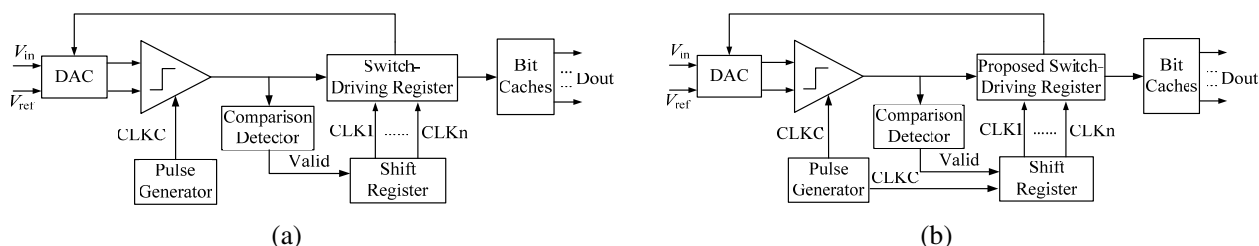


Figure 1: Block diagram of (a) conventional SAR ADC architecture; (b) SAR ADC architecture utilizing proposed logic control scheme.

logic control schemes to enhance the conversion speed, the block diagram of SAR ADC utilizing proposed circuit techniques is shown as Fig. 1(b).

3. CIRCUIT IMPLEMENTATION

3.1. Reference DAC

Figure 2 shows the detail schematic of the reference DAC. The DAC serves two purposes in a SAR converter: 1) it samples the input signal; 2) it generates a residue voltage between the input and current digital estimate. In the past few years, several power-efficient switching sequences for the capacitive DAC have been proposed such as the energy-saving, monotonic, and V_{cm} -based switching sequences [5–7].

A monotonic capacitor switching procedure is implanted during bit cycling in order to decrease the power consumption. In the first comparison, all bottom plates of these capacitances are connected to V_{refn} . The capacitors use the top plates to sample input signal and the MSB is determined by comparing the top plate's voltages directly without any change in the reference DAC. The MSB will be set to 1, if V_{DACP} is higher than V_{DACN} . Otherwise, the MSB is 0. Then the MSB triggers the SAR logic to control the reference switching of the DAC. If the MSB is 1, the capacitance C_{N1} is switched to V_{refp} . Otherwise, the capacitance C_{P1} is switched to V_{refp} .

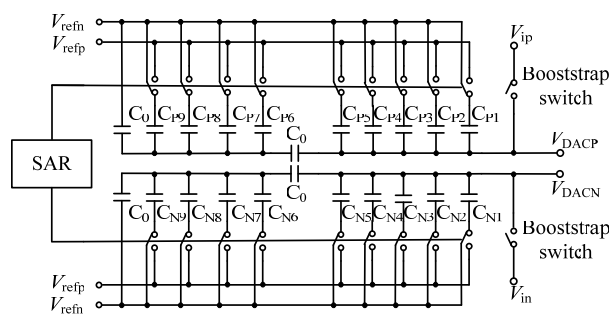


Figure 2: Schematic of the reference DAC.

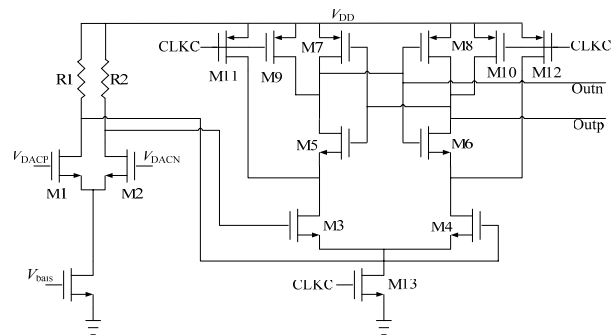


Figure 3: The schematic of the comparator.

3.2. Comparator

The schematic of the comparator is shown in Fig. 3, which consists of a pre-amplifier and a dynamic latched comparator. The pre-amplifier is used to block the kickback noise and enhance the comparison speed. During the conversion phase, the input voltage of the comparator approach V_{refp} . For optimum speed and yield of dynamic comparator, the input common-mode voltage is about 70% of the supply voltage [8]. Therefore, the comparator uses an N-type input pair rather than a P-type one. When CLKC goes low, the comparator is at the reset state and the outputs of the comparator are reset to high. When CLKC goes high, the input pair compares the two input voltages. According to the comparison result, the latch regeneration forces one output to high and the other to low. The dimensions of those MOSFETs in the comparator are carefully designed to satisfy the speed requirement.

3.3. Proposed Logic Control Scheme

In the proposed SAR ADC, the regeneration of the comparator and the operation of the shift register and the SDR are simultaneous. The timing diagram of the proposed SAR ADC is shown in Fig. 4(a). When CLKC goes high, the comparator goes in the regenerate state and conversion phase is beginning. It also triggers the shift register to generate multi-phase clocks for SDR. Then the SDR is enabled. Thus, the comparison results are direct transmitted to determine charging or discharging the DAC capacitor array before the next comparison without waiting for the completion of the comparison. The valid signal is only used to disable the corresponding-phase clock and is not in the key timing path. So the key path of the SA loop is shortened in the proposed SAR ADC. In addition, a novel SDR is proposed to further improve the conversion speed as shown in Fig. 4(b). RST is the reset signal. During the sample phase of the DAC, the output of the SDR is reset to low. The input of SDR is the output of the comparator. The outputs of SDR are connected to a serial of inverters used to drive the corresponding capacitors in the reference DAC. As a result, the

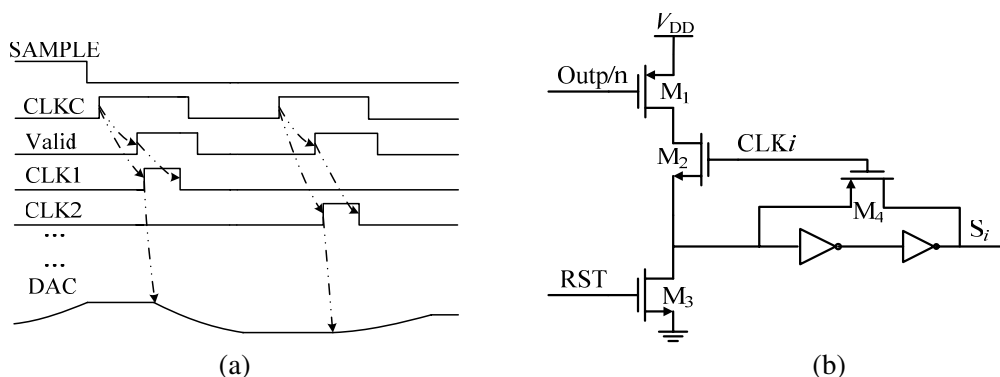


Figure 4: (a) The timing diagram of the proposed SAR ADC; (b) the proposed switch-driving register.

dynamic latch transfers comparator’s output to DAC directly when the comparator starts to latch. This eliminates the time delay from the comparator to generating a valid signal.

4. LAYOUT AND SIMULATION RESULTS

The prototype ADC is realized in 90 nm CMOS process. Fig. 5(a) shows the layout of the proposed SAR ADC. At 100 MS/s operation under a 1.2 V supply, the total power consumption is 2.87 mW. Unit capacitance of the DAC is 20 fF, and the total input capacitance is about 640 fF. Fig. 5(b)

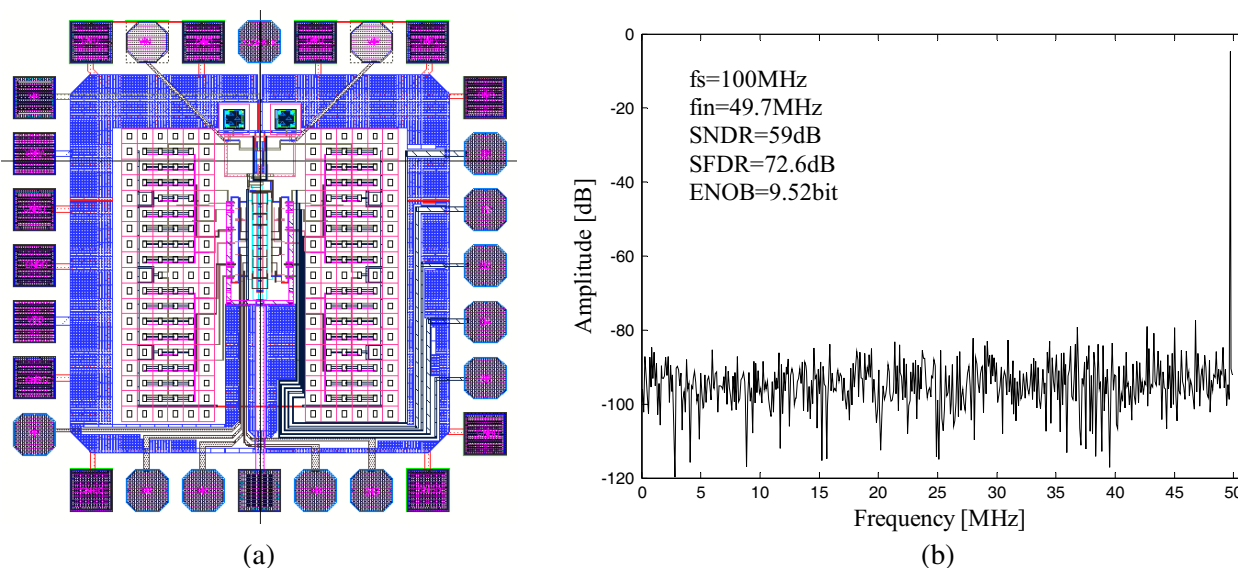


Figure 5: (a) Layout of the proposed ADC; (b) simulation results at 49.7 MHz (0.9 full-scale sine) input and 100 MS/s.

Table 1: Summary of this design and comparison with the others.

Ref	[3] TVLS	[6] JSSCC	[7] JSSCC	This work
Architecture	SAR	SAR	SAR	SAR
Technology	90 nm	0.13 μ m	90 nm	90 nm
Resolution (bit)	10	10	10	10
Sample Rate (MS/s)	30	50	100	100
Supply Voltage (v)	1	1.2	1.2	1.2
Power (mw)	0.98	0.826	3	2.87
SNDR (dB)	56.89	57	56.6	59
SFDR (dB)	68.65	65.9	71	72.6
ENOB (bit)	9.16	9.18	9.1	9.52
FoM (fJ/step)	57	29	55	39.1

shows the ADC dynamic performance. The SNDR and SFDR at 49.7 MHz input are 59 dB and 72.6 dB. To evaluate the overall performance of the ADC, we use a FoM equation defined as

$$\text{FoM} = \text{Power}/(2\text{ENOB} * fs) \quad (1)$$

where fs is the sampling frequency and ENOB is the effective number of bits. The resultant FoM is 39.1 fJ/conversion-step.

5. CONCLUSION

This paper presents a 10-bit 100 MS/s SAR ADC. The propagation delay of the SA loop is reduced by the proposed logic control method, which enhances the conversion speed of the SAR ADC. A new switch-driving register is proposed to further improve the conversion speed. The performance summary and comparison with state-of-the-art ADCs are shown in Table 1.

REFERENCES

1. Doris, K., E. Janssen, C. Nani, A. Zanicopoulos, and G. V. Weide, "A 480 mW 2.6 GS/s 10 b 65 nm CMOS time-interleaved ADC with 48.5 dB SNDR up to nyquist," *IEEE ISSCC Dig. of Tech. Papers*, 180–181, 2011.
2. Chen, S. W. M. and R. W. Brodersen, "A 6 b 600 MS/s 5.3 mW asynchronous ADC in 0.13 μm CMOS," *IEEE ISSCC Dig. of Tech. Papers*, 574–575, 2006.
3. Huang, G. Y., S. J. Chang, C. C. Liu, and Y. Z. Lin, "10-bit 30-MS/s SAR ADC using a switch-back switching method," *IEEE Transactions on Very Large Scale Integration (VLSI) Systems*, Vol. 21, No. 3, 584–588, 2013.
4. Chio, U.-F., H.-G. Wei, Y. Zhu, S.-W. Sin, S.-P. U, and R. P. Martins, "A self-timing switch-driving register by precharge-evaluate logic for high-speed SAR ADCs," *IEEE Asia Pacific Conference on Circuits and Systems (APCCAS)*, 1164–1167, 2008.
5. Pang, W. Y., C. S. Wang, Y. K. Chang, N. K. Chou, and C. K. Wang, "A 10-bit 500-KS/s low power SAR ADC with splitting capacitor for biomedical applications," *Proc. IEEE ASSCC Tech. Papers*, 149–152, Nov. 2009.
6. Liu, C. C., S. J. Chang, G. Y. Huang, and Y. Z. Lin, "A 10-bit 50-MS/s SAR ADC with a monotonic capacitor switching procedure," *IEEE J. Solid-State Circuits*, Vol. 45, No. 4, 731–740, Apr. 2010.
7. Zhu, Y., C. H. Chan, U. F. Chio, S. W. Sin, S. P. U. R. P. Martins, and F. Maloberti, "A 10-bit 100-MS/s reference-free SAR ADC in 90 nm CMOS," *IEEE J. Solid-State Circuits*, Vol. 45, No. 6, 1111–1121, Jun. 2010.
8. Wicht, B., T. Nirschl, and D. Schmitt-Landsiedel, "Yield and speed optimization of a latch-type voltage sense amplifier," *IEEE J. Solid-State Circuits*, Vol. 39, No. 7, 1148–1158, Jul. 2004.

High Speed Pipelined ADC Uses Loading-balanced Architecture

Linfeng Wang¹, Qiao Meng¹, Dong Li¹, Yi Zhang², and Wenwei He¹

¹Institute of RF- & OE-ICs, Southeast University, Nanjing, China

²College of Electronics Science and Engineering
Nanjing University of Posts and Telecommunications, Nanjing, China

Abstract— A 10-bit 200 MS/s Pipelined analog to digital converter (ADC) is realized using operational amplifier (op-amp) and capacitor sharing. A novel loading-balanced architecture is proposed to equal the capacitor load of the two adjacent stages which sharing one amplifier and reduce the load capacitor. Low power consumption is achieved by using loading-balanced architecture. The ADC is implemented in TSMC 0.18 μm 1P6M CMOS process. The supply voltage is 1.8 V. The simulation results show 57.7 dB SNDR and 61.13 dB SFDR with a 98 MHz input operating at a 200 MS/s sampling rate. The area is 1.2 mm \times 1.2 mm.

1. INTRODUCTION

Applications such as wireless sensor networks, image recognition and medical instrumentation require high-speed high-resolution and low power consumption analog to digital converters (ADCs). Pipelined ADC has been widely used in these fields because it achieves a good compromise between speed, accuracy and power consumption. Meanwhile many circuit techniques such as sample-and-hold Amplifier (SHA)-less front end [1], op-amp sharing [2], capacitor sharing [3] and scaling down capacitor values through the pipeline [4] has been developed to reduce the power consumption.

In this work, a prototype of 10 bit 200 MS/s pipelined ADC with loading-balanced architecture is developed, Fig. 1 is the architecture of the ADC. The circuit consists of eight 1.5 bit/stage and a 2 bit back end flash ADC. It uses one op-amp less than the traditional ADC for using SHA-less architecture. the number of op-amp is reduced from 8 to 4 for op-amp sharing technique is used, the load capacitor of the first stage is reduced equal to the second stage for capacitor sharing technique, the non-standard inter-stage gain makes the feedback factor of the first stage increased equal to the second stage. So the load of op-amp shared by the first two stages is balanced. The capacitor load and feedback factor of the third and fourth stage are the same. The fifth to eight stage is the same as the third and fourth stage. From the system view, all the loads of the OTAs shared are balanced. The design power optimized.

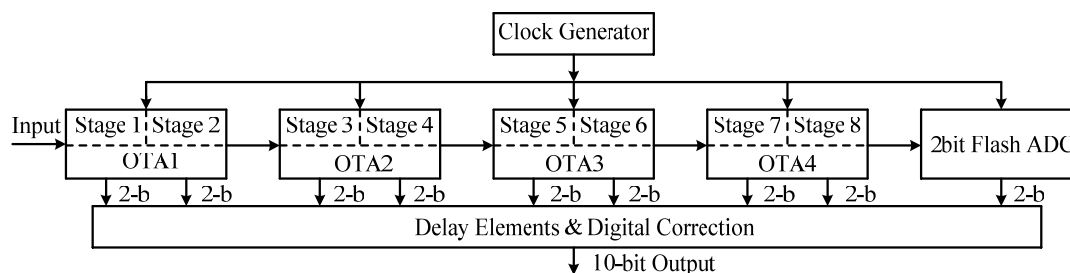


Figure 1: Architecture of the 12 bit loading-balance Pipelined ADC.

2. CIRCUIT DESIGN

2.1. The First and Second Stage with Loading-balanced Architecture

Figure 2 is the architecture of the first and second stage (the first unit), in order to lower the power consumption, noise contribution and reduce the die area. The loading-balanced pipelined ADC removes the first-end SHA, the input signal is sampled by the bootstrapped switch in directly. The ADC scaling down the capacitor value through the pipeline by the factor of 0.5, so when the first stage is settling in closed loop, the load capacitor is larger then the second stage. The shared op-amp is designed in accordance with the requirement of the first stage. So when the second stage is settling, a part of power will be wasted. The loading-balanced pipelined ADC using capacitor

sharing technique and non-standard inter-stage gain scaling down the load to the same with the second stage in settling, realizes the load balance between the two stages.

Figure 3 is the architecture of the first unit during four different phases. The Op-amp has two input pairs and works alternately to cancel the memory effect. The two pairs of the capacitors are working alternately controlled by the four non-overlapping clock phases which is shown in Figure 4. During the clock phase Φ_1 , the schematic of the first unit shown in Figure 3(a), the first stage is sampling the input signal, the second stage is settling in closed-loop. The lower input pair of the op-amp and the top pair of the capacitors are resetting, removing the residual charge. During the clock phase Φ_2 , the schematic of the first unit shown in Figure 3(b), the first stage is settling in closed-loop and producing the residue which is stored on the top pair of capacitors, the top input pair of the op-amp and the lower pair of the capacitors are resetting. During the clock phase Φ_3 , the schematic of the first unit shown in Figure 3(c), the first stage of the unit is sampling the input signal, and the second stage is settling, the lower input pair of the op-amp and the lower pair of capacitors are resetting. Produce the residue which is utilized by the third stage. During the clock phase Φ_4 , the schematic of the first unit shown in Figure 3(d), the second stage is settling in closed-loop and producing the residue which is stored on the lower pair of capacitors, the top input

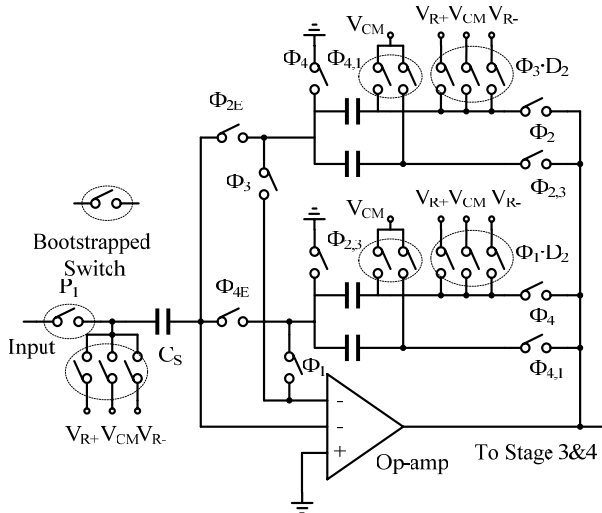


Figure 2: Schematic of the first unit.

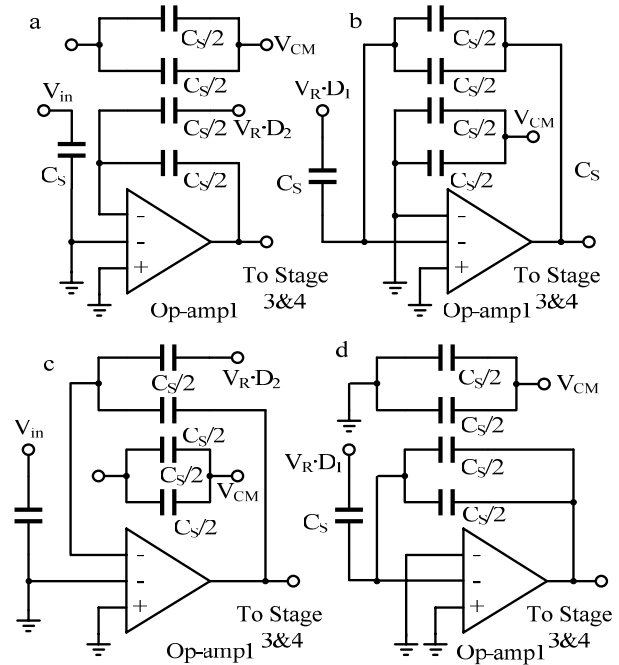


Figure 3: Architecture of the first unit in four phases.

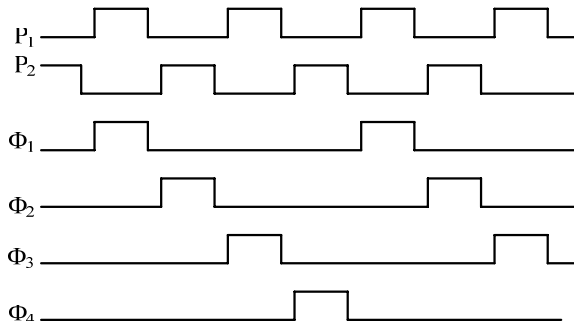


Figure 4: The clock signal used in Pipelined ADC.

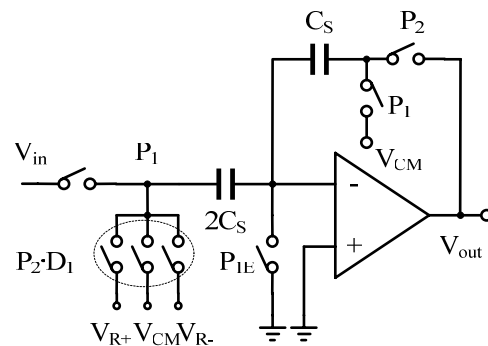


Figure 5: The conventional 1.5 bit/stage architecture.

pair of the op-amp and the top pair of the capacitors are resettling.

2.2. The Non-standard Inter-stage Gain Architecture

In conventional 1.5 bit/stage architecture, the gain of the multiplying digital-to-analog converter (MDAC) is two, the feedback factor is 0.5, all the stages have the same input and output range, the value is $\pm V_R$. Because the first stage using SHA-Less architecture, mismatch between sampling paths of comparator and MDAC leads to aperture error [5]. The conventional MDAC shown in Fig. 5 remove the mismatch successfully, but the feedback factor is 1/3, it wastes a part of power, and the load capacitor value between the first and second stage are different.

In this design, a novel non-standard inter-stage gain architecture is proposed, the architecture is shown in Fig. 6, it reduces the value of sample capacitor from $2C_S$ to C_S . The gain of the MDAC reduces from 2 to 1 [6], then the input range increase to $\pm 2V_R$, and the feedback factor increases to 0.5, the threshold of the comparators in first Sub-ADC increase from $\pm 1/4V_R$ to $\pm 1/2V_R$. The transfer functions of the two MDACs are shown in Fig. 7. The equivalent load capacitor values of the first and stage are the same, the value is $C_S/2$, it realizes the loading balanced and reduced the consumption.

The third and fourth stage (the second unit) use conventional 1.5 bit/stage which is shown in Fig. 8. The shared Op-amp has two input pairs to cancel the memory effect [7]. This unit uses capacitor sharing technique to realize the loading balance between the two stages, the sample capacitors of the second unit scaling down to $C_S/8$, the total value of the third stage is $C_S/4$. The sample capacitors of the fourth stage are not scale down further. Because the value of sample capacitor is near to parasitic capacitor. The load capacitor is not scales down substantially.

But the feedback factor will reduced evidently. So the value of the sample capacitors between the third and fourth stage is same. The five to eight stages are same to the third and fourth stage, so the value of the equivalent load capacitors is same.

3. SIMULATION RESULTS

The ADC is designed in TSMC 0.18 μm 1P6M CMOS process. The layout of the ADC is shown in Fig. 9. The Section A is the first and second stage, Section B is the third and fourth stage,

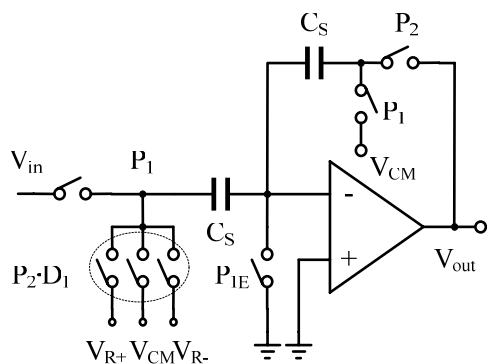


Figure 6: The non-standard inter-stage gain architecture.

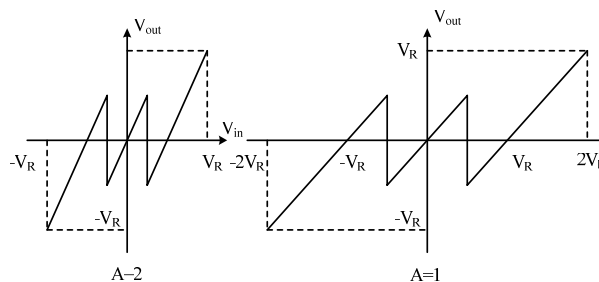


Figure 7: The two transfer functions.

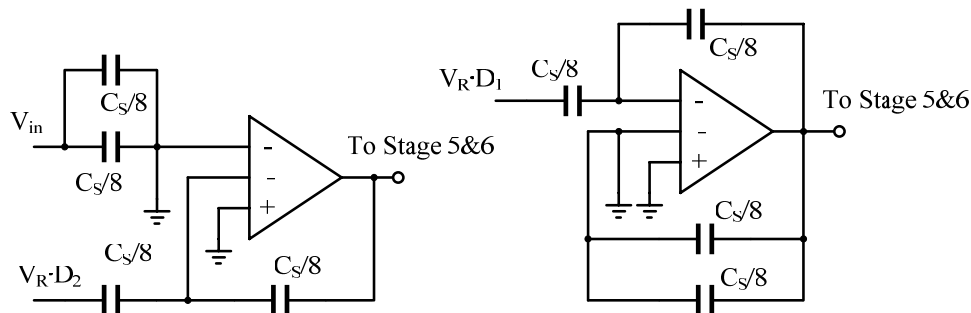


Figure 8: The conventional 1.5 bit/stage architecture.

Section C is the five and six stage, Section D is the seven and eight stage, Section E is the digital logical circuit, Section F is the output buffer circuit. The area is $1.2\text{mm} \times 1.2\text{mm}$. The ADC operates under supply of 1.8V . The single-end input swing is 1.2V . The simulation output FFT spectrum with 98.4MHz input frequency at 200MS/s is shown in Fig. 10, which exhibits SNDR of 57.68dB and SFDR of 61.13dB . Fig. 11 reveals the SNDR and SFDR of the ADC for an input frequency sweep at 200MS/s .

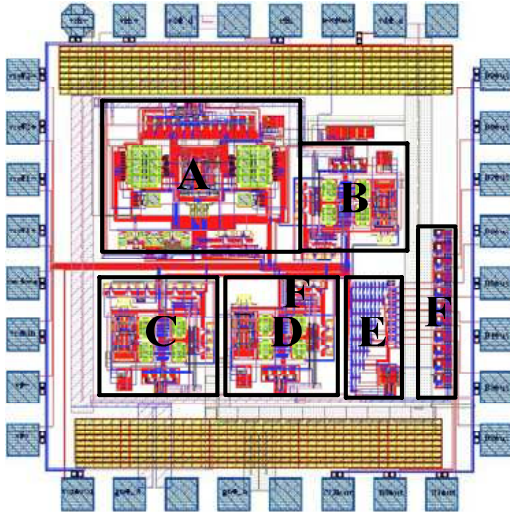


Figure 9: The layout of the ADC.

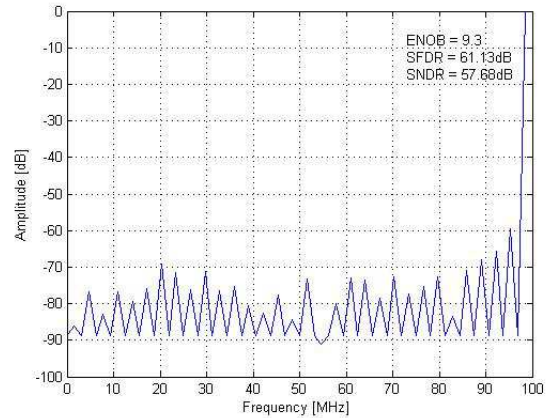


Figure 10: ADC output spectrum.

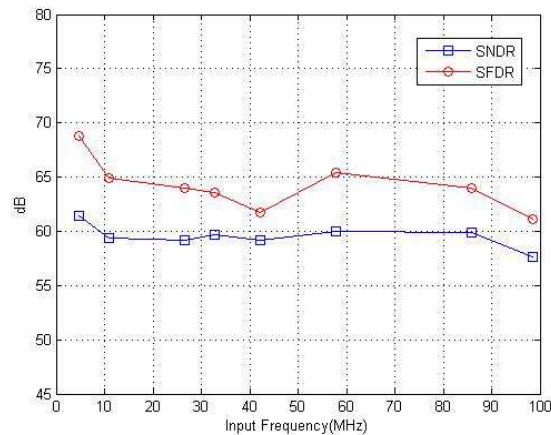


Figure 11: Dynamic performance versus input frequency.

4. CONCLUSION

This paper presents a 10 bit 200MS/s pipelined ADC with 1.8V supply. A novel loading-balanced architecture is proposed to equal the load capacitor of the two adjacent stages which sharing one amplifier. A non-standard inter-stage gain architecture is proposed to equate the load capacitor value between the first and second stage. reduce the load capacitor and power consumption. The third to eight stages are the same, so the equivalent load capacitors are the same, so the entire system realizes loading balance and reduces the power consumption. The method is verified by the experimental chip's simulation results, and showing SNDR of 57.68dB and SFDR of 61.13dB at 98.4MHz input frequency, the power is 115mW at 200MHz sample frequency.

REFERENCES

1. Min, B.-M., P. Kim, F. W. Bowman, D. M. Boisvert, et al., "A 69-mW 10-bit 80 MSample/s Pipelined CMOS ADC," *IEEE J. Solid-State Circuits*, Vol. 38, 2031–2039, Dec. 2003.

2. Nagaraj, K., H. Fetterman, J. Anidjar, S. Lewis, and R. Renninger, "A 250-mW, 8-b, 52-Msamples/s parallel-Pipelined A/D converter with reduced number of amplifier," *IEEE J. Solid-Stage Circuits*, Vol. 32, No. 3, 312–320, 1997.
3. Wu, P. Y., V. S. L. Cheng, and H. C. Luong, "A 1-V 100-MS/s 8-bit CMOS switched-Op-amp Pipelined ADC using loading-free architecture," *IEEE J. Solid-Stage Circuits*, Vol. 42, No. 4, 7320–7380, 2007.
4. Cho, T. B. and P. R. Gray, "A 10 b, 20 Msample/s, 35 mW Pipeline A/D converter," *IEEE J. Solid-Stage Circuits*, Vol. 30, No. 3, 3180–3205, 1995.
5. Lee, B., "Low-power techniques for high-performance pipelined Analog to digital converter," The University of Texas at Austin, Texas, 2007.
6. Devarajan, S., L. Singer, A. Kamath, et al., "A 16 bit, 125 MS/s, 385 Mw, 78.7 dB SNDR CMOS Pipeline ADC," *IEEE J. Solid-Stage Circuits*, Vol. 44, No. 12, 3305–3313, Dec. 2009.
7. Lee, K.-H., K.-S. Kim, S.-H. Lee, et al., "A 12 b 50 MS/s 21.6 Mw 0.18 μm CMOS ADC maximally sharing capacitors and Op-amps," Vol. 58, No. 9, 2127–2136, Sep. 2011.

A 30-GHz Low Phase Noise LC VCO and Frequency Divider in 90-nm CMOS Technology

Junliang Wang, Zhigong Wang, Jian Xu, and Yan Wen

Institute of RF- & OE-ICs, Southeast University, Sipailou 2, Nanjing 210096, China

Abstract— This paper presents the design of a 30-GHz low phase noise LC-tank voltage control oscillator (VCO) and a high speed frequency divided-by-two module in a 90-nm CMOS technology. A single cross-coupled PMOS transistor pair with drain resistors is adopted to suppress the flicker noise up-conversion. To improve the linearity, two sets of varactors with different DC biasing are implemented. The simulated tuning range of the VCO covers from 28.7 to 32.4 GHz in four tuning curves. The simulated output phase noise at offsets of 10 kHz, 100 kHz and 1 MHz are -50 , -78 , and -104 dBc/Hz, respectively. The power consumption of the VCO is 9 mW under a 1.2-V power supply. A current mode logic (CML) divided-by-two module is designed to operate at 28 to 40 GHz. The divider core draws 3.3 mA from a 1.2-V supply.

1. INTRODUCTION

In the fast-booming wireless communication market, more and more millimeter wave frequency bands are up-coming and pose the challenges of microwave CMOS chips. In China, the 59 ~ 64-GHz frequency band has been assigned for these applications, and recently a 45-GHz band of Q-band has been developed to support both long-range and short range high data rate wireless communications.

In a typical double-conversion low intermediate frequency receiver architecture for the 45-GHz applications, considering a first intermediate frequency (IF) of 15 GHz and a low second intermediate frequency, two local oscillator (LO) signals can be generated by a 30-GHz LC voltage control oscillator (LC-VCO) and its divided-by-two frequency divider. This paper presents the design of a 30-GHz narrow-band VCO and its high speed divider using a standard 90-nm CMOS process. Two drain resistors are adopted in the VCO to suppress the flicker noise up-conversion.

The paper is organized as follows: Section 1 is the introduction of the recent development of microwave wireless communications. Section 2 presents the VCO architecture and the phase noise enhanced technology. The current mode logic (CML) based divider structure and its operation are described in Section 3. Simulation results and conclusion are provided in Sections 4 and 5, along with a comparison of the presented work with other recent works.

2. VCO DESIGN

The schematic of the proposed VCO is shown in Fig. 1(a). It is an LC difference VCO with single NMOS cross-coupled devices. Two resistors R_D are inserted in series to the drain of the cross-coupled MOSFETs.

In practice, other suppression techniques have been used such as adopting a resonant network at the drain of the current source or inserting resistors in series to cross-coupled transistor sources. The former solution requires an LC resonant filter tuned to the $2f_0$ where f_0 is the oscillation frequency of the VCO. In wide band applications, a tuning mechanism needs to be added. The second solution reduces the harmonic generation at expenses of excess gain and start-up margin [1].

By inserting the resistors at the drain of the transistors, the excess gain of a single PMOS can be expressed as

$$G_X \approx g_{mp}R_D, \quad (1)$$

where g_{mp} is the transconductance of the PMOS transistor. The added delay causes by R_D can be estimated by

$$\tau_D \approx \omega_0 R_D C_D, \quad (2)$$

where C_D is the parallel capacitor at the drain of PM_{1,2}. The ideal suppression condition could be achieved when the following formula is met [2].

$$\left[\frac{G_X - 1}{4Q} - \omega_0 R_D C_D \right] + \left[\frac{(G_X - 1)^2}{8Q} - \frac{1}{2} \omega_0 R_D C_D \right] = 0 \quad (3)$$

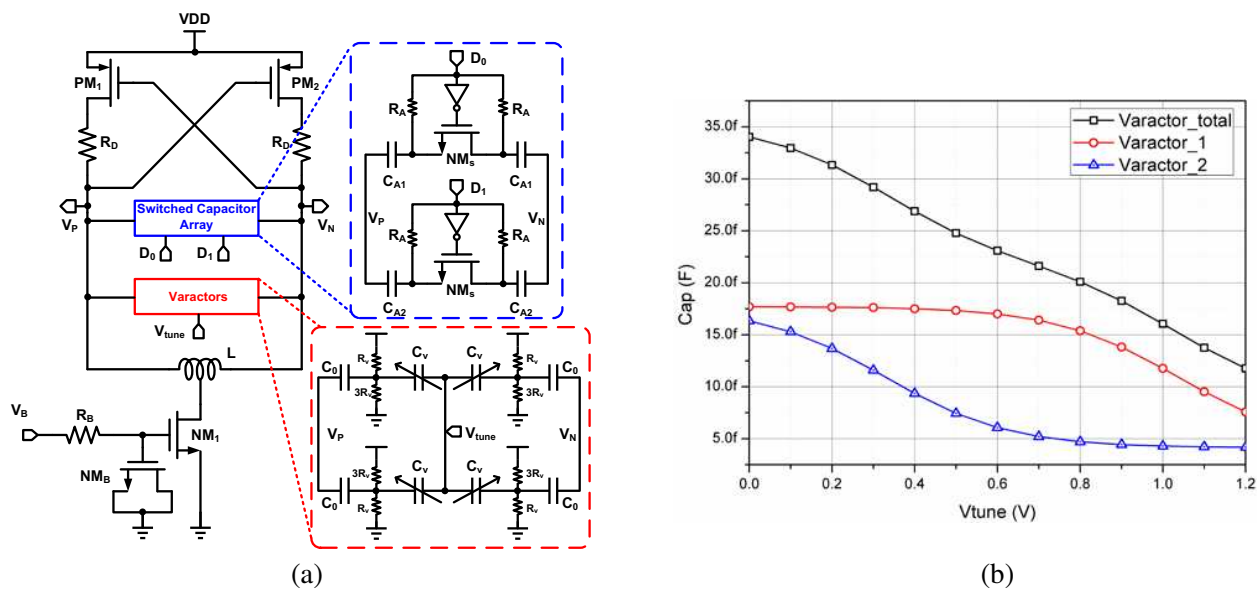


Figure 1: (a) LC-VCO topology with drain resistors. (b) Simulated varactor C-V curves.

Thus the optimum value of the drain resistor to suppress the flicker noise up-conversion is

$$R_D \approx \frac{G_X^2 - 1}{12Q\omega_0 C_D} \quad (4)$$

For the designed VCO, the quality factor of the inductor at 30 GHz can be as high as 40, and the g_m is designed to be large to ensure the start-up margin. To achieve a required output amplitude of the oscillator, a large current is usually needed. While a large resistance results a large voltage drop across the resistor, the output power of the VCO will be reduced, so the resistor size should be chosen wisely. G_X is usually set between 2 and 4 also to ensure the start-up.

Two varactor units are used as the voltage controlled module. Because of the poor linearity of a single varactor, two units are biased in different DC operating points. The simulated C-V curve is shown in Fig. 1(b). The VCO has a tuning range of about 3.7 GHz from 28.7 to 32.4 GHz, which covers the desired frequency bands. Based on the parameter we calculated above, the VCO gain is about 1 GHz/V on average.

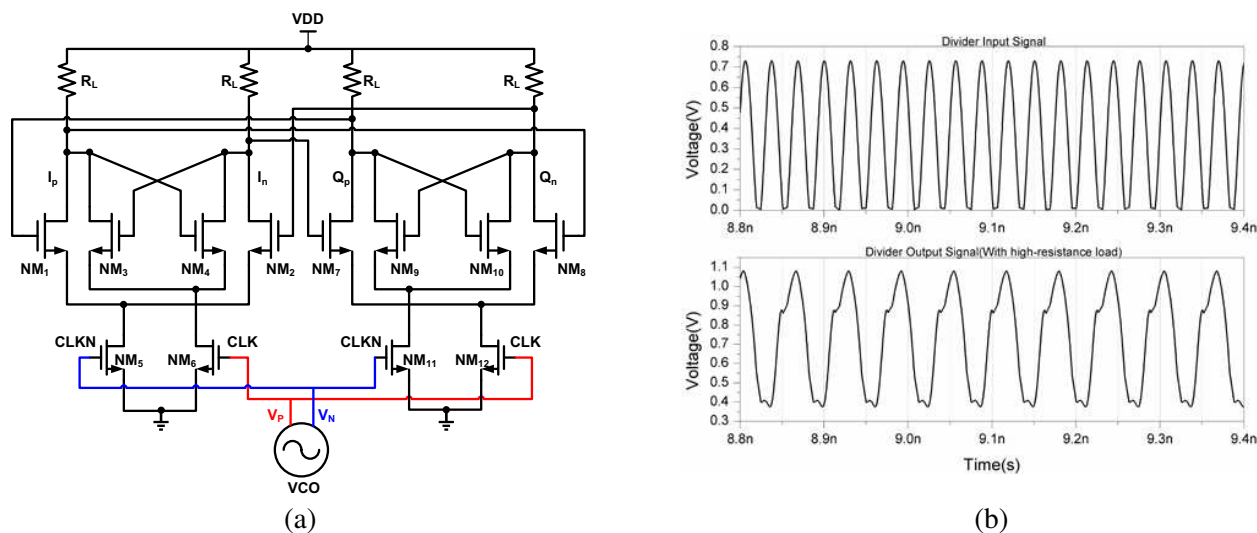


Figure 2: (a) The schematic of divided-by-2 CML divider. (b) Simulated transient waves of the divider.

3. DIVIDER DESIGN

In order to generate quadrature LO signals, two identical CML latches are used to build up a master-slave configuration. The input clock signals are coming from the 30-GHz LC-VCO, which is directly coupled to the clock transistors' gate. Thus, the gate capacitors should be considered while designing the VCO. In order to operate under a 1.2-V power supply voltage, the tail current sources have been removed. The schematic of the proposed divider is shown in Fig. 2(a).

The self-oscillation frequency has been set to 32 GHz. In each latch, the most of the current should be made flow through the sample pairs and the hold pairs only need about 1/3 of the total current. The sample pairs and hold pairs serve as analog mixers in each latch. Two latches, notified as latch I and Q, connected in a negative feedback loop. The whole CML divider can be seen as a ring oscillator. According to Barkhausen criterion, the locking range of the divider is restricted by the loop phase and loop gain. To reach the maximum locking range, the condition $g_{mh} \cdot R_L = 1$ should be satisfied, where g_{mh} is the transconductance of the hold pair. The simulated transient waves are shown in Fig. 2(b).

4. SIMULATION RESULTS

The 30-GHz LC-VCO and divided-by-2 CML frequency divider are designed in a standard 90-nm CMOS technology. The layout of the proposed schematics is shown in Fig. 3 with an area of

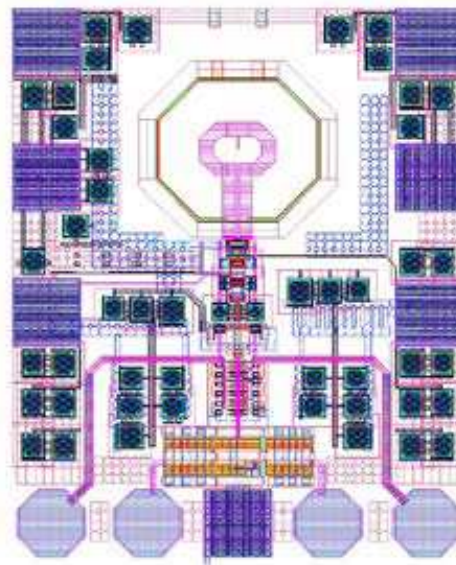


Figure 3: Layout of the proposed VCO and divider.

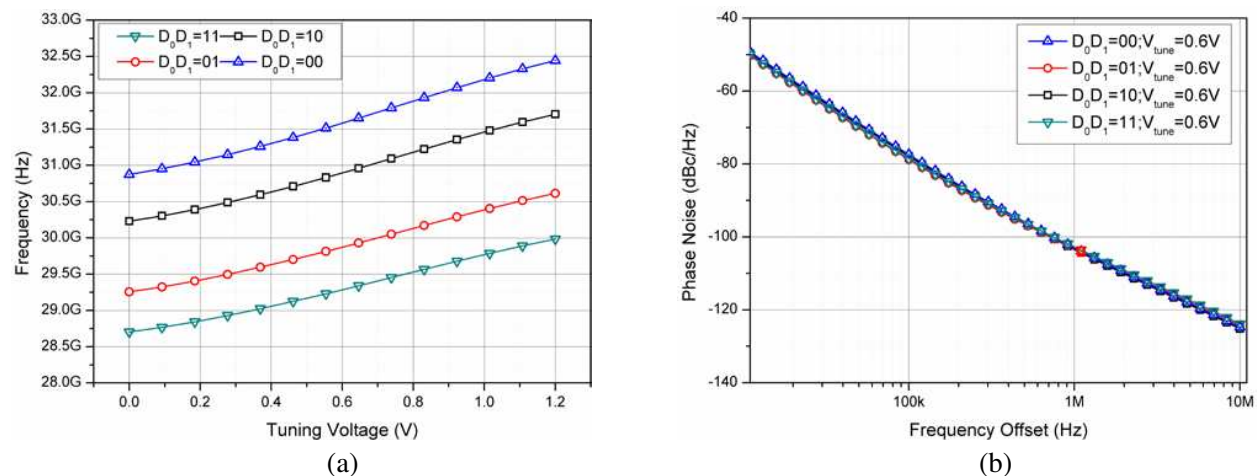


Figure 4: (a) Simulated tuning curves of the VCO. (b) Simulated phase noise of the VCO.

Table 1: Summary of the performance and comparison with SOA.

Ref.	Frequency Range (GHz)	Power Supply (V)	Phase Noise (dBc/Hz)	Power Consumption (mW)	Technology
3	53.2–58.4	0.7/0.43	−90.08, @1 MHz	1.2	90 nm CMOS
4	12.72–12.93	1.2	−105.25, @1 MHz	3	90 nm CMOS
5	38–43	1.2	−86.46, @1 MHz	5.9	90 nm CMOS
6	55.5–61.5	1	−90, @1 MHz	3.9	0.13 μ m CMOS
This work	28.7–32.4	1.2	-50, @10 kHz -78, @100 kHz -104, @MHz	9	90 nm CMOS

$609 \times 497 \mu\text{m}^2$. The VCO operates at the supply voltage of 1.2 V and draws an average current of 7.5 mA, and the divider consumes an average current of 3.3 mA under the same supply voltage.

The simulated tuning curves are plotted in Fig. 4(a). The simulated tuning range of the VCO covers from 28.7 to 32.4 GHz in four tuning curves. By adding the drain resistors, the phase noise of the VCO has a promotion in the closed-in frequency offsets. Fig. 4(b) shows that the output phase noise at an offset of 10 kHz, 100 kHz, and 1 MHz is −50, −78, and −104 dBc/Hz, respectively. Furthermore, different phase noise in different working frequency shows a small variation due to the delay brought in by the drain resistor.

5. CONCLUSION

In this work, a low phase noise 30-GHz LC-VCO with drain resistors and its divided-by-2 module are designed in a standard 90-nm technology. By adopting the drain resistors, the phase noise of the VCO has promoted phase noise performance at its closed-in frequency offsets. The CML divider operates within the frequency range of 22 to 40 GHz and generate quadrature LO signals.

REFERENCES

1. Bonfanti, A., F. Pepe, C. Samori, et al., “Flicker noise up-conversion due to harmonic distortion in Van der Pol CMOS oscillators,” *IEEE Transactions on Circuits and Systems I: Regular Papers*, Vol. 59, No. 7, 1418–1430, 2012.
2. Levantino, S., M. Zanuso, C. Samori, et al., “Suppression of flicker noise upconversion in a 65 nm CMOS VCO in the 3.0-to-3.6 GHz band,” *2010 IEEE International IEEE Solid-State Circuits Conference Digest of Technical Papers (ISSCC)*, 50–51, 2010.
3. Li, L., P. Reynaert, and M. Steyaert, “A 90 nm CMOS mm-wave VCO using an LC tank with inductive division,” *34th European IEEE Solid-State Circuits Conference, 2008, ESSCIRC 2008*, 238–241, 2008.
4. Zito, D. and D. Pepe, “Ku band LC-active 90 nm CMOS VCO,” *IET Active RF Devices, Circuits and Systems Seminar*, 17–26, 2011.
5. Ellinger, F. and H. Jackel, “38–43 GHz quadrature VCO on 90 nm VLSI CMOS with feedback frequency tuning,” *2005 IEEE MTT-S International Microwave Symposium Digest*, 3, 2005.
6. Borremans, J., M. Dehan, K. Scheir, et al., “VCO design for 60 GHz applications using differential shielded inductors in 0.13 μ m CMOS,” *IEEE Radio Frequency Integrated Circuits Symposium, 2008, RFIC 2008*, 135–138, 2008.

A 45-GHz CMOS Low-power LNA Using Active Feedback

Li Ma, Zhigong Wang, Jian Xu, and Xixi Chen

Institution of RF-&OE-ICs, Southeast University, Sipailou 2, Nanjing 210096, China

Abstract— A 45 GHz low power millimeter-wave (MMW) low noise amplifier (LNA) using 40 nm CMOS process is presented in this paper. The LNA comprises three stages. The first stage adopts the active feedback structure for good input matching. The output matching employs an L-type matching network. Simulation results show that both S_{11} and S_{22} are less than -18 dB at 45 GHz. A cascode structure is adopted in the third stage for better reverse isolation. The LNA consumes 18.7 mW under a 1.1-V voltage supply, achieving a maximum S_{21} of 17.9 dB. The minimum NF is 5.7 dB at 42.5 GHz. The simulation results show that the proposed LNA is promising for the 45-GHz application.

1. INTRODUCTION

In recent years, MMW circuits have been studied widely for its capability of high data rate communication. For example, the frequency band of 76 ~ 81 GHz is for automotive radar and 60 GHz is a promising band for high speed wireless communication [1, 2]. Q-LINKPAN which has been included in IEEE 802.11aj (45 GHz) Task Group is a newly proposed communication standard working within the 40–50 GHz [3].

An LNA that provides a good noise performance, excellent matching and enough gain is necessary in an MMW receiver. The development of deep submicrometer CMOS process makes it possible to implement a CMOS MMW LNA. Some MMW LNAs have been reported recently [4–6]. However, their power consumptions are relatively high and the matching is not satisfactory. In [6], for example, a 3-stage 79-GHz LNA is presented. Though a low NF 4.9 dB and a variable gain are achieved, the power consumption of 30.6 mW and $S_{22} < -10$ dB was not good enough. In this paper, a 45 GHz low power 3-stage LNA with excellent matching is designed in 40 nm CMOS process. An active feedback is adopted for the input matching.

2. CIRCUIT DESIGN

Considering the high transition frequency of the 40 nm CMOS process, excellent input matching is possible to achieve by feedback. The resistive feedback LNA in Fig. 1(a) and active feedback LNA in Fig. 1(b) are widely used in wideband LNA [7]. Ignoring the parasitic capacitors, the input impedance of the resistive feedback LNA is,

$$R_{in} \approx \frac{1}{g_{m1}} \quad (1)$$

where g_{m1} is the transconductance of M_1 .

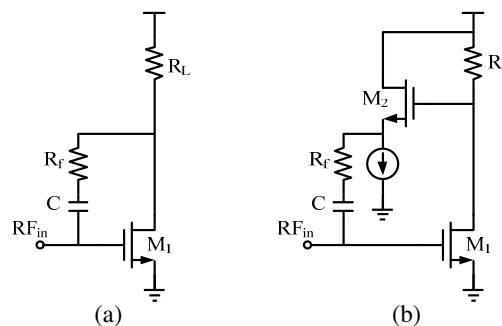


Figure 1: (a) Resistive feedback LNA; (b) Active feedback LNA.

Assuming that M_2 performs as an ideal buffer, the input impedance of the active feedback LNA is,

$$R_{in} = \frac{R_f}{1 + g_{m1}R_L} \quad (2)$$

Figure 5 shows the LNA's S-parameter and NF. The simulation results in Fig. 5(a) shows that $S_{11} < -10$ dB through the whole band of 40–50 GHz, and it achieves an S_{11} of -18.8 dB and an S_{22} of -25 dB at 45 GHz. The frequency band of $S_{22} < -10$ dB is 42 ~ 48.5 GHz. The maximum S_{21} is 17.9 dB at 42 GHz. The NF is less than 7 dB in the frequency band concerned. Table. 1 shows the simulation results summary and comparison with published works.

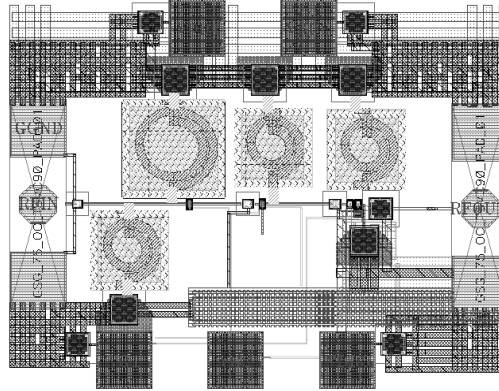


Figure 4: Layout of LNA.

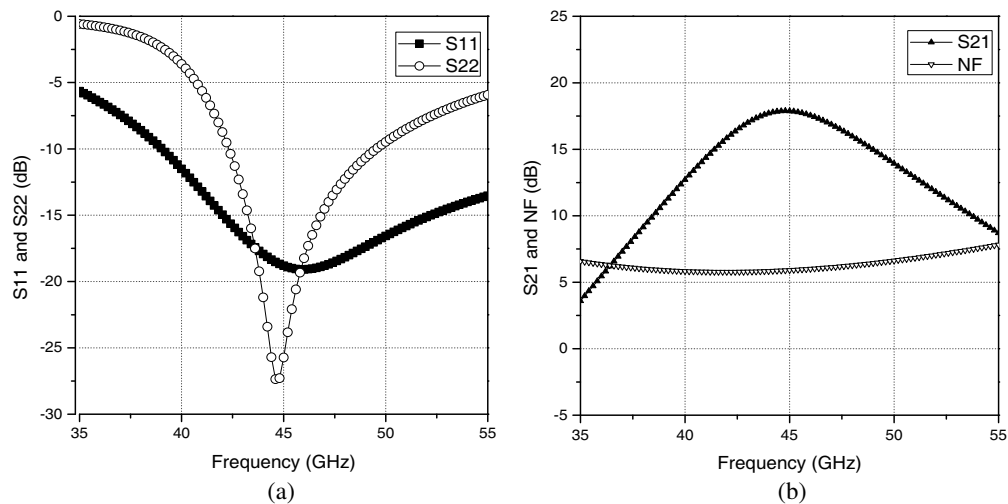


Figure 5: (a) Simulated S_{11} and S_{22} ; (b) Simulated S_{21} and NF.

Table 1: Simulation results summary and comparison.

	This Work	[1]	[5]	[6]
Process (nm)/VDD (V)	40/1.1	90/NA	65/1.5	28/0.9
3 dB BW (GHz)	41.5 ~ 49	77 ~ 81	2.1 ~ 39	74 ~ 84
NF _{min} (dB)	5.7	6.2	4.5	4.9
$S_{21\max}$ (dB)	17.9	13.5	11.5	23.8
IIP ₃ (dB)	-9	-11	NA	NA
Power (mW)	18.7	21.1	25.5	30.6

4. CONCLUSIONS

In this work, we demonstrate a low-power MMW LNA in a 40-nm CMOS process. The first stage of the LNA adopts the active feedback structure for a better input matching. A cascode structure is employed in the last stage for better reverse isolation. The LNA consumes 18.7 mW under a

1.1 V voltage supply. Compared to the published MMW LNAs, this work achieves the minimum power. The maximum S_{21} is 17.9 dB at 45 GHz. The LNA achieves a minimum NF of 5.7 dB at 42.5 GHz. The simulation results shows that the proposed LNA is promising for the Q-LINKPAN application.

REFERENCES

1. Lin, Y. S., G. L. Lee, C. C. Wang, et al., "A 21.1 mW 6.2 dB NF 77~ 81 GHz CMOS low-noise amplifier with 13.5 ± 0.5 dB S_{21} and excellent input and output matching for automotive radars," *IEEE Radio and Wireless Symposium (RWS)*, 73–75, 2014.
2. Hsieh, C. A., Y. H. Lin, Y. H. Hsiao, et al., "A 60 GHz low noise amplifier with built-in linearizer," *IEEE Microwave Symposium Digest (IMS)*, 1–3, 2013.
3. Zhu, F., W. Hong, J. X. Chen, et al., "A broadband low-power millimeter-wave CMOS down-conversion mixer with improved linearity," *IEEE Transactions on Circuits and Systems — II: Express Briefs*, Vol. 3, 138–142, 2014.
4. Kawai, S., T. Wang, T. Mitomo, et al., "A temperature variation tolerant 60 GHz Low Noise Amplifier with current compensated bias circuit," *IEEE Asian Solid-State Circuits Conference (A-SSCC)*, 429–432, 2013.
5. Feng, C., X. P. Yu, W. M. Lim, et al., "A compact 2.1–39 GHz self-biased low-noise amplifier in 65 nm CMOS technology," *IEEE Microwave and Wireless Components Letters*, Vol. 12, 662–664, 2013.
6. Medra, A., V. Giannini, D. Guermandi, et al., "A 79 GHz variable gain low-noise amplifier and power amplifier in 28 nm CMOS operating up to 125°C," *IEEE European Solid State Circuits Conference (ESSCIRC)*, 183–186, 2014.
7. Popuri, S., X. Xiang, and J. Sturm, "A wideband resistive feedback balun LNA in 65 nm CMOS technology," *IEEE 22nd Austrian Workshop on Microelectronics (Austrochip)*, 1–4, 2014.

A Varactor-based Tunable Microstrip Band Pass Filter

M. Y. Abou Shahine¹, M. Al-Husseini², Y. Nasser¹, and K. Y. Kabalan¹

¹American University of Beirut, Beirut 1107 2020, Lebanon

²Lebanese Center for Studies and Research, Beirut 2030 8303, Lebanon

Abstract— This paper presents a novel design of a varactor-based tunable microstrip band pass filter suitable for several applications such as LTE, UMTS, WiFi and others. The proposed filter is designed on a Rogers RO3203 substrate over a full ground plane. The filter is based on a $\text{PI}(\pi)$ -shaped slot incorporated in a microstrip line between a pair of gaps. The designed filter operates in the frequency band from 1.8 to 3 GHz. Frequency tunability is obtained by inserting a varactor in the design and modifying its capacitance using DC bias lines.

1. INTRODUCTION

TV Broadband wireless access communication systems are undergoing a rapid expanding growth. Such RF systems employ RF filters which are important components in their transceivers. Therefore, there is an increasing demand for low cost, compact size and high performance filters [1]. These filters are widely studied and different kinds have been proposed via different methods and structures in recent years. Future mobile communication systems will require wideband transmission in order to support high-speed and high-capacity data transmission. This has led to an increasing demand for dual-band band pass filters and tri-band band pass filters. However, tunability of these filters is a better solution.

In recent years, the demands of the multi-standard wireless communication industry have forced filters to be increasingly adaptable due to various constraints, such as size, geometry, impedance bandwidth and operating frequency. Such design constraints have forced filter designers to consider tunable filters, so that their behavior can adapt with changing system requirements or environmental conditions, and they can tune to several frequencies and operate for different applications. Therefore, tunability is a required feature in these wireless communication systems.

Due to the significant increase in the demand of tunable filters in modern multiband communication systems, several tunable band pass filters have been recently proposed with good tuning characteristics. There are many strategies and technologies to achieve tuning, including the use of microelectromechanical systems (MEMS), ferroelectric components, liquid crystals and split ring resonators and complementary split ring resonators among others [2–8]. Some of these strategies have been applied to the design of tunable filters by implementing varactor diodes [9]. The RFMEMS switched capacitor array reported in [2] as a RF component to achieve various kinds of tunable RF filters consists of RFMEMS direct contact switches and metal-insulator-metal capacitors. In [3], a band-pass tunable filter within frequency ranges of 13–20 GHz showing good stop rejection and sharp roll off frequency is designed using a novel design to turn the resonant frequency by micro-electromechanical systems (MEMS) switch and coplanar-waveguide (CPW) structures. A tunable filter in the Ku-band, which is realized in multilayer ferrite LTCC substrate with embedded bias windings and negating the need of a large electromagnet, is presented in [4]. In [5], a band-pass filter using ferrite nanoparticles as the active element in microstrip geometry is designed. The filter is based on ferromagnetic resonance and it is very compact and has wide frequency tunability. In [6], an MMIC active band-pass filter is designed for the implementation of a tunable RF filter in a $0.35\ \mu\text{m}$ SiGe BiCMOS technology. This filter structure is proposed for operation in the S-band applications and BiCMOS MMICs applications for wireless personal communication. The authors in [7] show that open split ring resonators (OSRRs) and open complementary split ring resonators (OCSRrs) can be used to implement tunable filters in coplanar waveguide (CPW) technology. By loading a CPW with shunt-connected varactor-loaded OSRRs, a band-stop filter with tunable central frequency results. A compact tunable band pass filter using a vertical stepped-impedance resonator (SIR) based on the conventional multi-layer printed circuit board (PCB), exhibiting high unloaded quality factor, compact size and low electromagnetic coupling to nearby RF circuits is reported in [8]. In [9], a compact electrical tunable microstrip band pass filter, realized by coupling two Hairpin-DGS resonators, is proposed. The tunability is achieved by embedding varactor diodes to the Hairpin-DGS resonators.

In this paper, a simpler and a highly effective tuning approach is introduced. A simple varactor-based tunable microstrip band pass filter based on a $\text{PI}(\pi)$ -shaped slot integrated in a microstrip line between a pair of gaps, is presented. Frequency tunability is achieved through inserting a varactor in the design and modifying its capacitance using DC bias lines. The designed filter operates in the frequency band from 1.8 to 3 GHz. The geometry and the design guidelines of the proposed antenna structures are presented in Section 2. The results are presented in Section 3. In Section 4 a brief conclusion is given.

2. FILTER STRUCTURE AND DESIGN

The configuration of the proposed tunable filter is shown in Fig. 1. A simple microstrip line is designed on a $40\text{ mm} \times 20\text{ mm}$ Rogers RO3203 substrate with dielectric constant of 3.02 and thickness $h = 1.6\text{ mm}$ over a full ground plane. The filter is based on a PI -shaped slot with two arms incorporated in the microstrip line between a pair of gaps. The detailed dimensions of the PI -slot, its arms and the gaps in the microstrip line are shown in Fig. 1.

The slot itself has bandstop characteristics since it changes the part of the microstrip line around it into an open loop resonator which is known for its bandstop action. The two gaps act as capacitors and transform the bandstop into a bandpass operation.

Frequency tunability is obtained by inserting a varactor (SMV1212) on the microstrip line as shown in Fig. 1 (red color) and modifying its capacitance using the shown DC bias lines. The size of the varactor is compatible with the design and its capacitance ranges between 0.6 and 71 pF. The dimensions of the slot and the gaps are optimized to achieve wider channel bandwidth and better tunability. The filter is designed and simulated using Ansoft HFSS.

3. RESULTS AND DISCUSSION

The simulated reflection coefficient plots of the tunable filter are given in Fig. 2 for the indicated capacitance values of the varactor. It is clear that frequency tunability has been achieved in the frequency band from 1.8 to 3 GHz. Considering several values for the capacitance of the varactor,

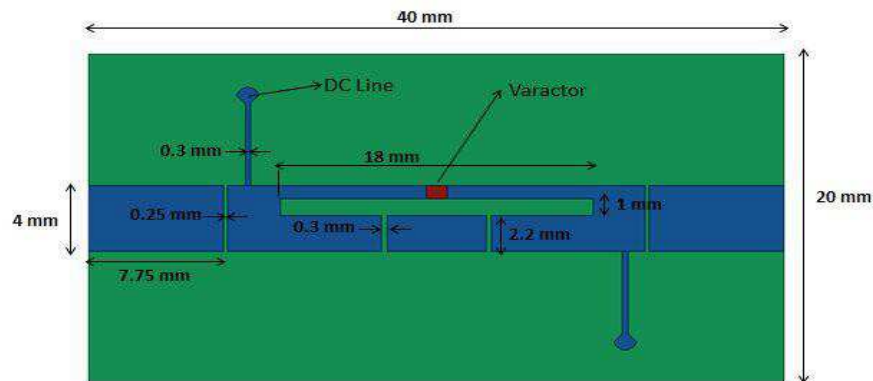


Figure 1: Configuration and dimensions of the proposed microstrip filter.

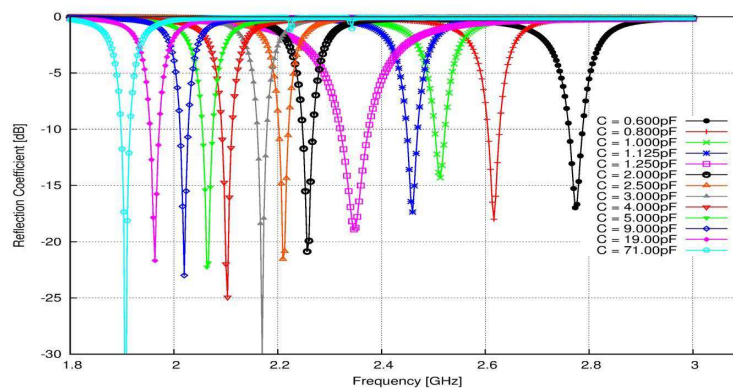


Figure 2: Reflection coefficients for different capacitance values.

the filter can operate on different frequencies in the 1.8–3 GHz band corresponding to different applications such as LTE, UMTS, WiFi, and others.

4. CONCLUSION

A novel design of a varactor-based tunable microstrip band pass filter is proposed in this paper. The designed tunable filter operates in the frequency band from 1.8 to 3 GHz and is suitable for several applications such as LTE, UMTS, WiFi and others. Frequency tunability is attained through inserting a varactor in the design and modifying its capacitance using DC bias lines. The operating bandwidth, the small size, and the frequency tunability make this filter a practical one that can be used for cognitive radio applications.

ACKNOWLEDGMENT

The authors would like to thank the Lebanese National Council for Scientific Research for supporting this research work.

REFERENCES

1. Pozar, D. M., *Microwave Engineering*, 291–373, John Wiley, 2000.
2. Lee, S.-S., H. Uchida, S. Soda, T. Nishino, H. Inoue, S. Izuo, Y. Yoshida, and M. Miyazaki, “An RFMEMS switched capacitor array for a tunable band pass filter,” *Solid-State Sensors, Actuators and Microsystems Conference*, 157–160, 2007.
3. Zhang, N.-B., Z. L. Deng, and J.-M. Huang, “A novel tunable band-pass filter using MEMS technology,” *2010 IEEE International Conference on Information and Automation (ICIA)*, 1510–1515, 2010.
4. Arabi, E., F. A. Ghaffar, and A. Shamim, “Tunable band pass filter based on partially magnetized ferrite LTCC with embedded windings for SoP applications,” *IEEE Microwave and Wireless Components Letters*, Vol. 25, No. 1, 16–18, January 2015.
5. Kuanr, B. K., V. Veerakumar, K. Lingam, S. R. Mishra, A. V. Kuanr, R. E. Camley, and Z. Celinski, “Microstrip tunable band-pass filter using ferrite (nanoparticles) coupled lines,” *IEEE Transaction on Magnetics*, Vol. 25, No. 10, 4226–4229, October 2009.
6. Dousti, M., M. Yazdizadeh, and F. Eshghabadi, “A 2.4-GHz SiGe BiCMOS MMIC active tunable band-pass filter design using artificial neural network,” *International Conference on Application of Information and Communication Technologies 2009 (AICT 2009)*, 1–4, 2009.
7. Vélez, A., F. Aznar, M. Durán-Sindreu, J. Bonache, and F. Martín, “Tunable coplanar waveguide band-stop and band-pass filters based on open split ring resonators and open complementary split ring resonators,” *IET Microwaves, Antennas & Propagation*, Vol. 5, No. 3, 277–281, July 2010.
8. Yang, T. and G. M. Rebeiz, “Compact tunable 2.1–2.9 GHz band-pass filter using a novel vertical stepped-impedance resonator,” *2014 IEEE MTT-S International Microwave Symposium (IMS)*, 1–4, 2014.
9. Boutejdar, A., A. Omar, M. Senst, E. P. Burte, A. Batmanov, and R. Mikuta, “A new design of a tunable WLAN-band pass filter using a combination of varactor device, RF-choke and hairpin-defected ground structure,” *2011 European Microwave Integrated Circuits Conference (EuMIC)*, 506–509, 2011.

An Optimized Opamp-sharing in 2nd Order $\Delta\Sigma$ Modulator Based on Changing the Stages Output Capacitance Timing Strategy

M. Sabaghi¹, M. Dashtbayazi², and S. Marjani^{1,2}

¹Laser and Optics Research School

Nuclear Science and Technology Research Institute (NSTRI), Tehran, Iran

²Department of Electrical Engineering, Ferdowsi University of Mashhad, Mashhad, Iran

Abstract— In this paper a new approach to OPAMP sharing was proposed. In this way, the pulse-width dedicated is proportional to output capacitance. Consequently, the created harmonic distortion is minimized and the power efficiency is maximized.

1. INTRODUCTION

Delta-sigma modulators are very used in the Control loop of the DC-DC Switching Converters that tabernacle with PWM generators and decreases the ripple and noise of the DC-DC converters [1]. In fact these modulators covert analog input signal $U(z)$ to a digital representation $Y(z)$. The difference between output digital signal and input analog signal of modulators is so called quantization error $E(z)$. Quantization error is known as noise which limits analog to digital modulators accuracy. In this type of modulators, the quantization noise is fed back to the input of the modulator and being attenuated while passing through loop filters. In addition, any other noise sources which are located in the forward path of the modulator could be attenuated by this technique of fed back the noise signals to the input. Attenuating quantization noise causes an increase in accuracy of the modulator Concept of a conventional delta sigma modulator is shown in Figure 1.

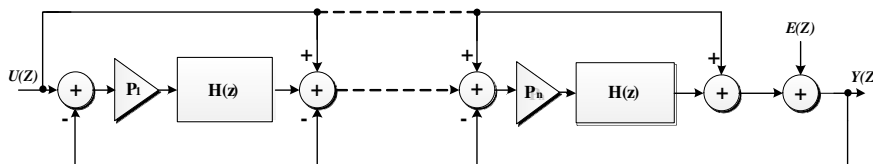


Figure 1: The conventional n th order delta sigma modulator.

The signal transfer function $S_{TF}(z)$ and noise transfer function $N_{TF}(z)$ of the delta sigma modulator is as the following:

$$Y(Z) = (1 - Z^{-1})^n E(Z) + U(Z) \quad (1)$$

$$\begin{cases} S_{TF}(Z) = \frac{Y(Z)}{U(Z)} = 1 \\ N_{TF}(Z) = \frac{Y(Z)}{E(Z)} = (1 - Z^{-1})^n \end{cases} \quad (2)$$

In the conventional delta sigma modulators, increasing forward path filters more than 3 usually leads to instability [2]. There has been introduced many techniques which provide the same noise transfer function and signal transfer function as the conventional has for the high order noise shaping by mathematical techniques [3–5].

In this paper, a new approach to opamp-sharing has been introduced in which provides a second order noise shaping by moving opamp between two stages.

The paper has been organized as the following. Next section describes the conventional noise shaping method and it has been followed by the proposed noise shaping method. Finally the paper presents the second order modulator simulation results.

2. CONVENTIONAL NOISE SHAPING METHOD

An important of ideas for decreases of the power consumption and area is opamp-sharing. In this technique, opamp moved from stage1 to stage2 and conversely. In conventional idea, two phases are used that the pulse width dedicated to phases are the same. But the stage output capacitance (i.e., equal the whole capacitances in one integrator in a stage) in stage1 is more than stage2, because

the stage1 once shaped the noises while the stage2 twice shaped the noises. Therefore the stage2 needed to pulse-width (i.e., phase pulse-width) less than stage1. Pulse-width dedicated to phases in conventional noise shaping method shown in Figure 2.

If the pulse-width dedicated to stages of delta-sigma modulator has been the same while the output capacitances of the stages are different, with moving the opamp between the stages, the harmonic distortions are increases and resultant the SNDR is decreases Therefore with this technique, for struggle the harmonic distortions should be increase the sampling frequency that the phase1 pulse-width increases. Therefore power consumption and chip area are increases.

3. PROPOSED NOISE SHAPING METHOD

According to discussion in Section 2 for opamp-sharing technique should be the pulse-width dedicated to stages is designed according to stages output capacitance.

In this design, we effort that the pulse-width dedicated to stages have been based on stages output capacitance. Timing diagram for the proposed noise shaping method seen in Figure 3.

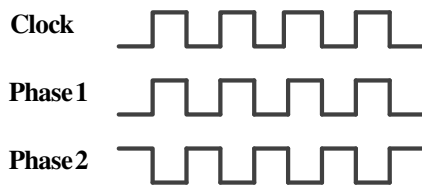


Figure 2: Timing diagram for conventional noise shaping method.

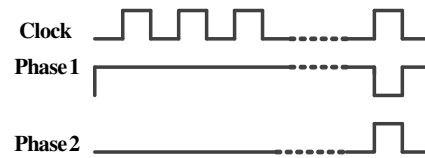


Figure 3: Proposed noise shaping method timing diagram.

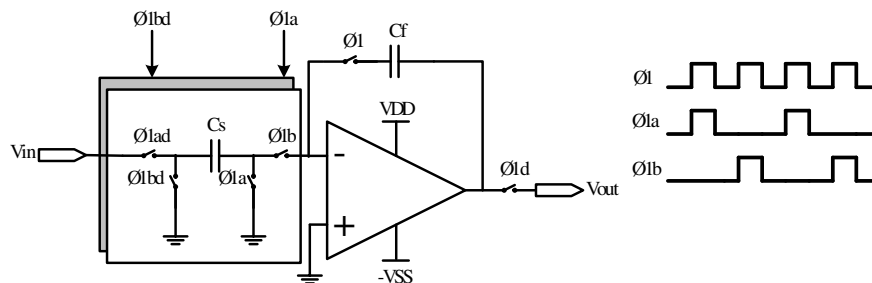


Figure 4: Proposed Switch-Capacitor Integrator in phase1 (Φ_1).

According to Figure 3, the pulse-width dedicated to stage2 is less than stage1 and the phases are madding from the clock signal with very high frequency rather than two phases. With this technique, the power dissipation and chip area minimized by factor about two.

The proposed integrator structure shown in Figure 4. In this structure, the opamp only required in one phase and it can move to other stages. According to Figure 4 based on [6], in the phase Φ_{1a} , the integrator sampled the input signal on the sampling capacitor (C_S) and in the phase Φ_{1b} , the integrator transfer the electric load from sampling capacitor to integrator capacitor (C_f) and conversely. Therefore, the opamp not require been in the integrator structure at phase2 and moved to other integrator.

4. SIMULATION RESULTS

In this paper, the proposed block diagram in Figure 5 is simulated. According to Figure 5, the opamp has been in stage1 at phase1 (Φ_1) and the opamp has been in the other stage at phase2 (Φ_2). The output capacitance of the stage1 is about six times than stage2. Therefore, the pulse-width for stage1 is about six times other stage.

The proposed idea simulated at the 130 nm CMOS model and the comparison between State-of-the-Art Works between the proposed paper results and some other papers presented at the Table 1. According to this table, the proposed SNDR and power consumption are 80.7 dB and 69.2 μ w respectively, resultant FoM equal 392.2 fJ/step-conv that higher than other papers.

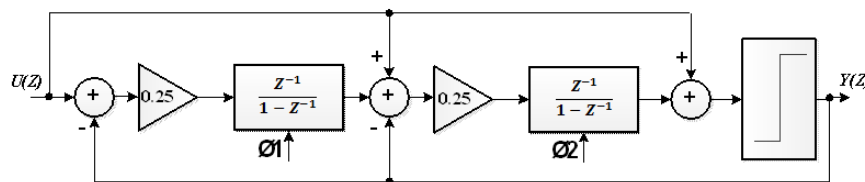


Figure 5: Proposed 2nd order delta-sigma modulator block diagram.

Also, Table 2 shows the simulation results in the process corners. According to this table, the tolerance between T.T corner and other corners for the SNDR is less than 10%, that an appropriate error of engineering.

Table 1: Comparison to State-of-the-Art works.

Parameters	[7]	[8]	[9]	[10]	This Work
V_{DD} (v)	0.9	1.4	1.2	0.9	1.2
CMOS Technology (nm)	180	180	130	65	130
f_{BW} (Hz)	10 k	256	10 k	500	10 k
Order	2	2	2	2	2
SNDR (dB)	80.1	72	87.8	76	80.7
Power (μw)	200	13.3	148	2.1	69.2
FoM (fJ/step-conv)	1210	7980	369	407	392.2

Table 2: Simulation results for the proposed 2nd order $\Delta\Sigma$ at different process corners.

Parameters	T.T	S.S	S.F	F.S	F.F
f_{BW} (Hz)	10 k				
SNDR (dB)	80.66	81.85	78.70	80.21	78.23
ENOB (bit)	13.11	13.30	12.78	13.03	12.70
FoM (fJ/s-c)	392.25	295.79	540.16	385.39	648.44

5. CONCLUSION

In this paper, a new approach to OPAMP sharing was proposed. In this way, the pulse-width dedicated is proportional to output capacitance. Consequently, the created harmonic distortion is minimized and the power efficiency is maximized. In this design, in one 2nd stage delta-sigma modulator with 10 kHz of bandwidth, the power dissipation equal of $69.2 \mu\text{w}$, resultant the FOM is 392.2 fJ/step.

REFERENCES

- Alghamdi, M. K. and A. A. Hamoui, "A spurious-free switching buck converter using a delta-sigma modulation controller with a scalable sampling frequency," *IEEE J. Solid-State Circuits*, Vol. 47, 841–851, Feb. 2012.
- Johns, D. and K. Martin, *Analog Integrated Circuit Design*, Wiley, New York, 1997.
- Malcovati, P., et al., "Behavioral modeling of switched-capacitor sigma-delta modulators," *IEEE Trans. Circuits Syst. I*, Vol. 50, 352–364, Mar. 2003.
- Cannillo, F., et al., "1.4 V 13 W83dBDRCT-modulator with dual-slope quantizer and PWM DAC for biopotential signal acquisition," *Proc. ESSCIRC*, 267–270, Sep. 2011.
- Nilchi, A. and D. A. Johns, "A low-power Delta-Sigma modulator is using a charge-pump integrator," *IEEE Trans. Circuits Syst. I*, Vol. 60, 1310–1321, May 2013.

6. Yao, L., M. S. J. Steyaert, and W. Sansen, “A 1-V 140- μ W 88-dB audio sigma-delta modulator in 90-nm CMOS,” *IEEE J. Solid-State Circuits*, Vol. 39, 1809–1818, Nov. 2004.
7. Goes, J., B. Vaz, R. Monteiro, and Paulino, “A 0.9 V modulator with 80 dB SNDR and 83 dB DR using a single-phase technique,” *IEEE Int. Solid-State Circuits Conf. Dig. Tech. Papers*, 74–75, Feb. 2006.
8. Cannillo, F., et al., “1.4 V 13 W83dBDRCT-modulator with dual-slope quantizer and PWM DAC for biopotential signal acquisition,” *Proc. ESSCIRC*, 267–270, Sep. 2011.
9. Nilchi, A. and D. A. Johns, “A low-power Delta-Sigma modulator is using a charge-pump integrator,” *IEEE Trans. Circuits Syst. I*, Vol. 60, 1310–1321, May 2013.
10. Yeknami, A. F., et al., “Low-power DT $\Delta\Sigma$ modulators using SC passive filters in 65 nm CMOS,” *IEEE Trans. Circuits Syst. I*, Vol. 61, 358–370, Feb. 2014.

A 4 MHz-10-GHz, 10-ps/dec Dynamic Comparator Using Negative Resistance Combined with CMOS Input Pair

M. Dashtbayazi¹, S. Marjani^{1,2}, and M. Sabaghi²

¹Department of Electrical Engineering, Ferdowsi University of Mashhad, Mashhad, Iran

²Laser and Optics Research School

Nuclear Science and Technology Research Institute (NSTRI), Tehran, Iran

Abstract— A high speed, low delay/log (ΔV_{in}) dynamic comparator using negative resistance combined with CMOS input differential pair is proposed and designed in IBM 180 nm CMOS process technology.

1. INTRODUCTION

Comparators are very used in the Control loop of the DC-DC Switching Converters. In the loop of DC-DC Switching Converters, PWM generators uses comparator that compare Triangular wave with the difference DC-DC output voltage and reference voltage. Due to limited accuracy, comparison speed and power consumption, comparison of the input data is regarded as one of the limiting factor of the high speed VLSI data conversion system. There is a growing need for the development of low power, low voltage and high speed circuit techniques and system building blocks because of increasing demand for portable and hand held high speed devices. On the one hand, low voltage operation is required to use as few batteries as possible for low weight and small size. On the other hand at the high frequency of operation, Low power consumption is demanded to prolong battery lifetime as much as possible [1, 2]. In the recent decade, due to the rapid advancement in Analog-to-Digital conversion devices, the rapid advancement of VLSI technology causes the evolution of digital integrated circuit technologies for signal processing systems that operate on a wide variety of continuous-time signals including DC-DC switching converters, speech, medical imaging, sonar, radar, consumer electronics and telecommunications.

Already with voltage scaling, sub-threshold voltage region demands require technology for new architecture and innovative circuits. Previous advances in MOS technologies meet it for higher speed applications, however due to MOS device mismatches, it is difficult to achieve a high speed and accuracy at the same time [3].

One of the key components in PWM generators as the fundamental block for the A/D conversion, are the comparators. In fact they are the link between analog domain and digital domain for compare a set of variable or unknown values against that of a constant or known reference value [4]. Many DC-DC switching converters in the control loop demands high-speed, low-power comparators with small chip area. For low-voltage operation, developing new circuit structures is preferable in order to avoid stacking too many transistors between the supply rails [5].

The organization of this paper is as follows. Section 2 described the proposed dynamic comparator. Section 3 illustrates the simulation results. A comparison to the conventional comparators is also presented, followed by the conclusions in Section 4.

2. PROPOSED DYNAMIC COMPARATOR

2.1. Structure

The comparators are consists of two parts namely pre-amplifier and latch that these parts operate in the same phase. Therefore, comparator can pull the latch. In the second phase, the pre-amplifier output nodes up to the power supply voltage level. Also, the comparator offset can be cancelled in this phase [6, 7]. Consequently, the comparator offset effect has not been considered in this paper. Fig. 1 shows the circuit diagram has been used in simulations that has been obtained from [8] with adding Q2 and Q4 that a dual rail pre-amplifier is achieved. For decreasing the loading effect on the comparator output, two CMOS inverters have been used to supply capacitive loads. The comparator consumes dynamic power because the comparator consists of dynamic latch and pre-amplifier [9].

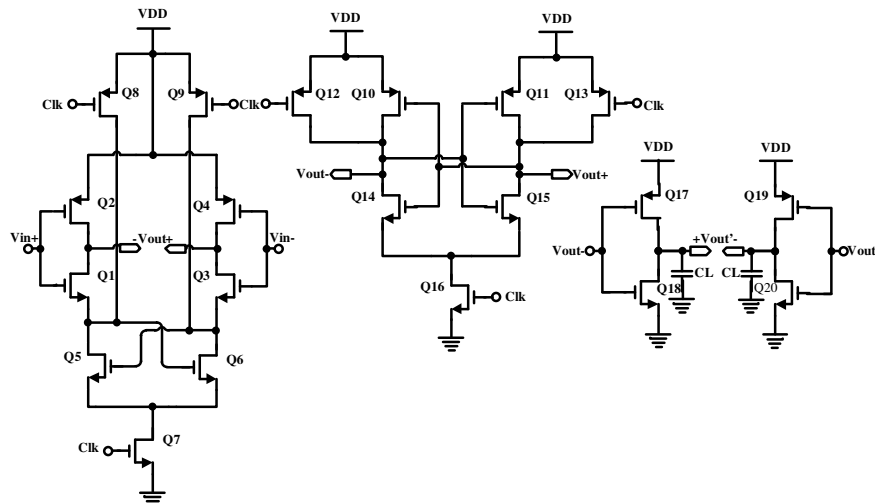


Figure 1: Schematics of the dynamic comparator and CMOS inverters.

2.2. Transient Behavior

Figure 2 shows the sketch map of the transient behavior of the dynamic comparator in the comparison phase. By the switching transistors Q8, Q9, Q12, and Q13 during the reset phase, the output terminals and the drain side voltages of Q5 and Q6 are all pulled high to VDD, respectively. By turning on the two tail transistors Q7 and Q16, the comparison phase begins. Therefore, the CMOS input stage transfers the differential small signal to the cross coupled stage. Q2, Q4 are activating when the input common mode is lower than the Q1 or Q3 threshold voltage. Therefore, the dual-rail differential input obtain since they are supplies the preamplifier output. Based on [10], the comparison transition can be divided into three phases (from phase 1 to phase 3). The output terminals are pulled down by two tail transistors Q7 and Q16 during the phase 1. Until one of the two output terminal voltages decreases to $(V_{DD} - V_{thp})$, the p-channel transistors Q10 and Q11 remain cut-off. The Q2 and Q4 activate when the cross-coupled stage composed from Q1, Q3, Q5 and Q6 cannot start. Therefore, the speed of proposed idea is more than paper [8]. In order to enhance the voltage difference between the output terminals, the cross-coupled inverters provide strong positive feedback in the phase 2. The transition state changes from phase 2 into phase 3 when one of the transistors Q14 and Q15 is cut-off. There is no static power dissipation since the current flows through these n-channel MOSFETs stop automatically after the transition. Fig. 3 shows transient behavior of the proposed dynamic comparator at 1 GHz. As seen, both of the output terminals are pulled low in the beginning of the compare operation. One of the output terminals charge through the p-channel transistor when the transition goes from phase 1 into phase 2.

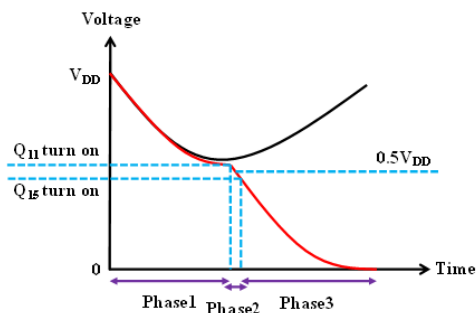


Figure 2: The sketch map for the transition behavior of the dynamic comparator.

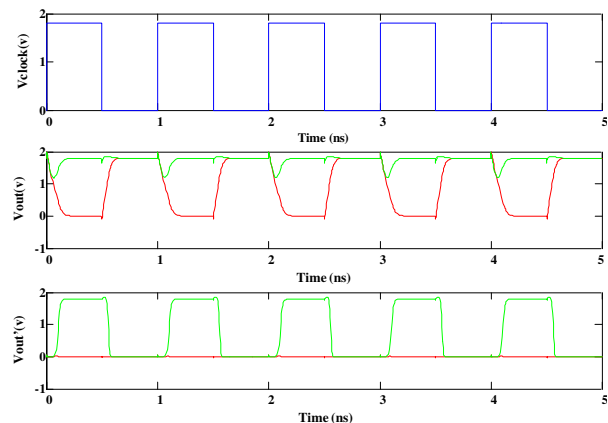


Figure 3: Simulated transient behavior of the proposed comparator structure.

Therefore, the strong positive feedback provided by these two cross-coupled inverters separates the output voltages. Against paper [8], this design aren't use from p-wells, thus the cost of comparator chip is lower.

3. SIMULATION RESULTS

In this paper for increase the simulation reliability, the post-layout simulation is done. The layout of proposed comparator shown in Fig. 4.

According to Fig. 4, layout size of proposed comparator is equal to $31.3 \mu\text{m} \times 18.5 \mu\text{m}$. For increase of the comparator sampling frequency to 10 GHz, the transistor layout designed based on multi-finger transistors. With this technique, the nodes capacitance of transistors is minimum; therefore the sampling frequency was minimized and the layout size was maximized. The av_extracted view of proposed comparator shown in Fig. 5.

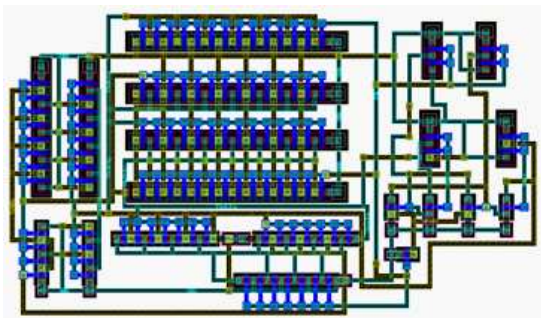


Figure 4: Layouts of the dynamic comparator and CMOS inverters.

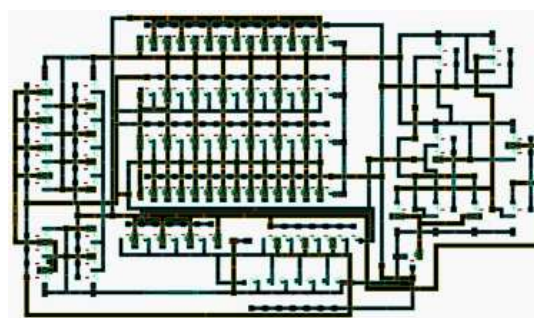


Figure 5: Av_extracted view of the dynamic comparator and CMOS inverters.

The Proposed idea simulated at the 180 nm CMOS model. The post-layout simulation results versus Sampling Frequency presented at the Table 1.

Table 1: Post-layout simulation results of the proposed comparator versus sampling frequency.

Sampling Frequency (GHz)	0.004	0.01	0.1	1	5	10
Resolution (mv)*	27	24	25	27	700	700
Power Supply (v)**	0.4	0.45	0.55	0.8	1.05	1.8
Power Consumption (μw)***	0.835	2.07	20.7	204.6	795.6	964

*Resolution calculated at 1.8 V DC power supply.

**Power supply calculated for maximum resolution.

***Power consumption calculated at maximum resolution and 1.8 V DC power supply.

For playing features of the proposed paper, we simulating the circuits at 180 nm CMOS that is a lower technology than recent reported papers but in this paper, the sampling frequency received to 10 GHz. The comparison State-of-the-Art Works between the proposed paper results and some other papers presented at the Table 2.

Table 2: Comparison to State-of-the-Art works.

Specifications	[8]	[10]	[11]	[12]	This Work
CMOS Process (nm)	90	Scaled to 90	90	65	180
Sampling Rate (GHz)	3	3	3	7	10
Supply/ICMV	1.2/1	1.2/1	1.2/1	1.2/1	1.8/0.9
Energy/decision (fJ)	71	88	90	185	50.6

The energy/decision for the proposed comparator is equal to 50.6 fJ that is highest value between papers at Table 2.

4. CONCLUSION

The proposed dynamic comparator structure has an added degree of freedom that enables higher input transconductance stage using negative resistance technique to get better delay/log (ΔV_{in}) performance at low power consumption. Moreover, the structure is very suitable for advanced deep sub-micron CMOS process with lower threshold voltage to achieve higher operation speed for multi-giga Hz optical and data conversion systems. In this paper, we received to Energy/decision equal 50.6fJ at 10GHz.

REFERENCES

1. Peluso, V., P. Vancorenland, A. M. Marques, M. S. J. Steyaert, and W. Sansen, "A 900-mV low-power $\Sigma\Delta$ A/D converter with 77-dB dynamic range," *IEEE Journal of Solid-State Circuits*, Vol. 33, 1887–1897, Aug. 2002.
2. Roh, H., Y. Choi, and J. Roh, "A 89-dB DR 457-W 20-kHz bandwidth Delta-Sigma modulator with gain-boosting OTAs," *Analog Integrated Circuits and Signals Processing*, Vol. 64, 173–182, 2010.
3. Yin, G. M., F. Op't Eynde, and W. Sansen, "A high-speed CMOS comparator with 8-b resolution," *IEEE Journal of Solid-State Circuits*, Vol. 27, 208–211, Aug. 2002.
4. Yu, L., J. Y. Zhang, L. Wang, and J. G. Lu, "A 12-bit fully differential SAR ADC with dynamic latch comparator for portable physiological monitoring applications," *4th International Conference on Biomedical Engineering and Informatics*, Vol. 1, 576–579, Oct. 2011.
5. Balasubramanian, K., "A flash ADC with reduced complexity," *IEEE Transactions on Industrial Electronics*, Vol. 42, 106–108, Aug. 2002.
6. Chan, C. H., et al., "A voltage-controlled capacitance offset calibration technique for high resolution dynamic comparator," *International SoC Des. Conf*, 392–395, Nov. 2009.
7. Xu, Y., et al, "Offset-corrected 5 GHz CMOS dynamic comparator using bulk voltage trimming: Design and analysis," *IEEE New Circuits Syst. Conf*, 277–280, Jun. 2011.
8. Chen, B. W., et al., "A 3-GHz, 22-ps/dec dynamic comparator using negative resistance combined with input pair," *IEEE Asia-Pacific Conf. Circuits Syst*, 648–51, Dec. 2010.
9. Liu, C. C., et al., "A 10-bit 50-MS/s SAR ADC with a monotonic capacitor switching procedure?," *IEEE J. Solid-State Circuits*, Vol. 45, 731–740, Mar. 2010.
10. Wicht, B., T. Nirschl, and D. Schmitt-Landsiedel, "Yield and speed optimization of a latch-type voltage sense amplifier," *IEEE J. Solid-State Circuits*, Vol. 39, 1148–1158, Jun. 2004.
11. Schinkel, D., E. Mensink, E. Klumperink, E. van Tuijl, and B. Nauta, "A double-tail latch-type voltage sense amplifier with 18ps setup+hold time," *IEEE ISSCC Digest of Technical Papers*, 314–315, Feb. 2007.
12. Goll, B. and H. Zimmermann, "A 65 nm CMOS comparator with modified latch to achieve 7 GHz/1.3 mW at 1.2 V and 700 MHz/47 μ W at 0.6 V," *IEEE ISSCC Digest of Technical Papers*, 328–329, Feb. 2009.

Binary Mixtures of Chiral Gases

C. Presilla^{1,2} and G. Jona-Lasinio^{1,2}

¹Sapienza Università di Roma, Italy

²Istituto Nazionale di Fisica Nucleare, Italy

Abstract— A possible solution of the well known paradox of chiral molecules is based on the idea of spontaneous symmetry breaking. At low pressure the molecules are delocalized between the two minima of a given molecular potential while at higher pressure they become localized in one minimum due to the intermolecular dipole-dipole interactions. Evidence for such a phase transition is provided by measurements of the inversion spectrum of ammonia and deuterated ammonia at different pressures. In particular, at pressure greater than a critical value no inversion line is observed. These data are well accounted for by a model previously developed and recently extended to mixtures. In the present paper, we discuss the variation of the critical pressure in binary mixtures as a function of the fractions of the constituents.

1. INTRODUCTION

According to quantum mechanics chiral molecules, that is, molecules which are not superimposable on their mirror image, should not exist as stable stationary states. Consider ammonia NH_3 . The two possible positions of the N atom with respect to the plane of the H atoms are separated by a potential barrier and can be connected via tunneling. This gives rise to stationary wave functions delocalized over the two minima of the potential and of definite parity. In particular, the ground state is expected to be even under parity. Tunneling induces a doublet structure of the energy levels.

On the other hand, the existence of chiral molecules can be interpreted as a phase transition. In fact, isolated molecules do not exist in nature and the effect of the environing molecules must be taken into account to explain phenomena characterized by instabilities. This interpretation underlies a simple mean-field model developed in [1] to describe the transition of a gas of NH_3 molecules from a nonpolar phase to a polar one through a localization phenomenon which gives rise to the appearance of an electric dipole moment. Even if ammonia molecules are only pre-chiral [2], the mechanism, as emphasized in [1], provides the key to understand the origin of chirality.

A quantitative discussion of the collective effects induced by coupling a molecule to the environment constituted by the other molecules of the gas was made in [3]. In this work it was shown that, due to the instability of tunneling under weak perturbations, the order of magnitude of the molecular dipole-dipole interaction may account for localized ground states. This suggested that a transition to localized states should happen when the interaction among the molecules is increased.

Evidence for such a transition was provided by measurements of the dependence of the doublet frequency under increasing pressure: the frequency vanishes for a critical pressure P_{cr} different for NH_3 and ND_3 . The measurements were taken at the end of the 1940s and beginning of the 1950s [4–6] but, as far as we know, no quantitative universally accepted theoretical explanation exists in spite of many attempts. The model [1] gives a satisfactory account of the empirical results. A remarkable feature of the model is that there are no free parameters. In particular, it describes quantitatively the shift to zero-frequency of the inversion line of NH_3 and ND_3 on increasing the pressure.

Recently, we extended the model [1] to gas mixtures [7]. This case may be of interest, among other things, for the interpretation of the astronomical data such as those from Galileo spacecraft [8] which measured the absorption spectrum of NH_3 in the Jovian atmosphere. Formulas for the critical pressure of a general mixture have been provided.

In the present paper, we investigate the behavior of the critical pressure in binary mixtures. We show that the critical pressure of a chiral species can be increased or decreased by several orders of magnitude by mixing it with a proper fraction of a proper species, chiral or non polar.

2. CHIRAL GAS

We model a gas of all equal chiral molecules as a set of two-level quantum systems, that mimic the inversion degree of freedom of an isolated molecule, mutually interacting via the dipole-dipole

electric force. At moderate density, we approximate the behavior of the $N \gg 1$ molecules of the gas with the mean-field Hamiltonian

$$h(\psi) = -\frac{\Delta E}{2}\sigma^x - G\frac{\langle\psi, \sigma^z \psi\rangle}{N}\sigma^z, \quad (1)$$

where σ^x and σ^z are the Pauli matrices and ψ is the Pauli spinor representing the mean-field molecular state with normalization $\langle\psi, \psi\rangle = N$. The scalar product between two Pauli spinors is defined in terms of their two components in the standard way. The parameter ΔE is the inversion energy-splitting measured by spectroscopic methods in the rarefied gas. The parameter G accounts for the effective dipole interaction energy of a single molecule with the rest of the gas. It can be estimated in two different but equivalent ways [7].

The first way to estimate G is based on the so called Keesom energy, namely, G is identified with the effective dipole-dipole interaction obtained after averaging over all possible molecular distances and all possible dipole orientations. These averages are calculated assuming that, concerning the translational, vibrational, and rotational degrees of freedom, the N molecules behave as an ideal gas at thermal equilibrium at temperature T . This assumption relies on a sharp separation (decoupling) between these degrees of freedom and the inversion motion. The result is

$$G = \frac{4\pi}{9} \frac{\mu^4 P}{(4\pi\epsilon_0 k_B T)^2 d^3}, \quad (2)$$

where P is the pressure of the gas, μ the electric-dipole moment of the molecules and d the minimal distance between two molecules, namely, the so called molecular collision diameter. At fixed temperature, the effective interaction constant G increases linearly with the gas pressure P .

The second way to estimate G is based on the reaction field mechanism [9]. Let us consider a spherical cavity of radius a in a homogeneous dielectric medium characterized by a relative dielectric constant ϵ_r . An electric dipole $\boldsymbol{\mu}$ placed at the center of the cavity polarizes the dielectric medium inducing inside the sphere a reaction field \mathbf{R} proportional to $\boldsymbol{\mu}$. As a result, the dipole acquires an energy

$$\mathcal{E} = -\frac{1}{2}\boldsymbol{\mu} \cdot \mathbf{R} = -\frac{\epsilon_r - 1}{2\epsilon_r + 1} \frac{\mu^2}{4\pi\epsilon_0 a^3}. \quad (3)$$

Since $\epsilon_r \simeq 1$, we can approximate the first fraction in Eq. (3) by the Clausius-Mossotti relation

$$\frac{\epsilon_r - 1}{\epsilon_r + 2} = \frac{1}{3}\rho(\alpha + \alpha^D), \quad (4)$$

where α is the molecular polarizability and $\alpha^D = \mu^2/(3\epsilon_0 k_B T)$ is the Debye (orientation) polarizability. Observing that for a chiral gas $\alpha^D \gg \alpha$ (for instance, in the case of NH_3 we have $\alpha \simeq 2 \text{ \AA}^3$ whereas $\alpha^D \simeq 217 \text{ \AA}^3$ at $T = 300 \text{ K}$), we get

$$\mathcal{E} = -\frac{4\pi}{9} \frac{\mu^4 P}{(4\pi\epsilon_0 k_B T)^2 a^3}. \quad (5)$$

Microscopic arguments [10, 11] show that the radius of the spherical cavity a is not arbitrary but must be identified with the the minimum distance between two interacting molecules, namely, the molecular collision diameter d introduced in Eq. (2). We thus have $\mathcal{E} = -G$.

The state ψ collectively describing the inversion degree of freedom of the gas of N chiral molecules is determined as the minimal-energy stationary state of the Hamiltonian of Eq. (1). This corresponds to find the lowest-energy eigenstate of the nonlinear eigenvalue problem $h(\psi)\psi = \lambda\psi$, with the constraint $\langle\psi, \psi\rangle = N$. We refer the reader to [1, 7] for the mathematical details, here we just state the main results.

There exists a critical value of the interaction strength, $G_{\text{cr}} = \Delta E/2$, such that for $G < G_{\text{cr}}$ the mean-field eigenstate with minimal energy is $\psi = \sqrt{N}\varphi_+$, where φ_+ is the eigenstate of σ^x with eigenvalue $+1$, i.e., the molecules are delocalized. For $G > G_{\text{cr}}$ there are two degenerate solutions of minimal energy which can be termed chiral states, in the sense they are transformed into each other by the parity operator σ^x . For $G \gg G_{\text{cr}}$, these solutions become the localized states

$\sqrt{N}\varphi_L, \sqrt{N}\varphi_R$, where φ_L, φ_R are the eigenstates of σ^z . The energy associated with the state ψ is a continuous function of G with a discontinuous derivative at $G = G_{\text{cr}}$. We thus have a quantum phase transition between a delocalized (or achiral, or nonpolar) phase and a localized (or chiral, or polar) phase. In view of the dependence of G on P , we can define a critical pressure at which the phase transition takes place

$$P_{\text{cr}} = \frac{9}{8\pi} \frac{\Delta E d^3 (4\pi\epsilon_0 k_B T)^2}{\mu^4}. \quad (6)$$

Note that the value of P_{cr} is completely determined in terms of the microscopic parameters ΔE , μ and d and the temperature T .

In [1] we have also shown that in the delocalized phase the inversion angular frequency of the interacting molecules depends on the pressure as $\hbar\bar{\omega}(P) = \Delta E \sqrt{1 - P/P_{\text{cr}}}$. This formula is interesting as it expresses the ratio of two microscopic quantities, $\hbar\bar{\omega}$ and ΔE , as a universal function of the ratio of the macroscopic variables P and P_{cr} . Furthermore, it is in very good agreement with some spectroscopic data showing the shift to zero frequency of the inversion line of NH_3 or ND_3 at increasing pressures [4–6].

3. BINARY MIXTURES

Consider a gas mixture of two species labeled 1 and 2. In this case, the Clausius-Mossotti relation reads as

$$\frac{\epsilon_r - 1}{\epsilon_r + 2} = \frac{1}{3} (\rho_1 (\alpha_1 + \alpha_1^{\text{D}}) + \rho_2 (\alpha_2 + \alpha_2^{\text{D}})), \quad (7)$$

where the Debye polarization $\alpha_i^{\text{D}} = \mu_i^2 / (3\epsilon_0 k_B T)$ is given in terms of the molecular electric-dipole moment μ_i of the species $i = 1, 2$. According to the reaction field arguments discussed above, a chiral molecule, let us say of species i , having dipole moment μ_i , acquires, due to the interaction with all the other molecules of the mixture, the energy

$$\mathcal{E}_i = -\frac{1}{3} (\rho_1 (\alpha_1 + \alpha_1^{\text{D}}) + \rho_2 (\alpha_2 + \alpha_2^{\text{D}})) \frac{\mu_i^2}{4\pi\epsilon_0 d_i^3}, \quad (8)$$

where d_i is the molecular collision diameter of the i -th species. We now specialize the discussion in the following two cases.

3.1. Mixtures of a Chiral Gas with a Non Polar Gas

For a mixture of chiral and non polar molecules, the mean-field molecular state of the chiral species, assumed as species 1, is determined similarly to the case of a single chiral gas. The only degree of freedom of the non polar molecules is the deformation which, in turn, is proportional to the electric dipole moment of the chiral molecules. We may thus describe the mixture by a single mean-field molecular state, ψ_1 , normalized to the number of molecules of the species 1, $\langle \psi_1, \psi_1 \rangle = N_1$. As before, we assume that this state is determined as the lowest-energy eigenstate of the eigenvalue problem associated with the mean-field Hamiltonian

$$h_1(\psi_1) = -\frac{\Delta E_1}{2} \sigma_1^x - G_1 \frac{\langle \psi_1, \sigma_1^z \psi_1 \rangle}{N_1} \sigma_1^z. \quad (9)$$

In this Hamiltonian $-G_1$ represents the effective dipole interaction energy of a single chiral molecule with all the other molecules, chiral and non polar, of the mixture. Thus we can identify $-G_1 = \mathcal{E}_1$, where \mathcal{E}_1 is given by Eq. (8) with $i = 1$, $\alpha_1 \ll \alpha_1^{\text{D}}$, and $\alpha_2^{\text{D}} = 0$, namely,

$$G_1 = (\gamma_{11} P_1 + \gamma_{12} P_2), \quad (10)$$

$$\gamma_{11} = \frac{4\pi}{9} \frac{\mu_1^4}{(4\pi\epsilon_0 k_B T)^2 d_1^3}, \quad \gamma_{12} = \frac{1}{3} \frac{\alpha_2 \mu_1^2}{4\pi\epsilon_0 k_B T d_1^3}. \quad (11)$$

As usual we used the ideal gas relations $\rho_1 = P_1/k_B T$ and $\rho_2 = P_2/k_B T$, where P_1 and P_2 are the partial pressures of the two species.

The analysis of the nonlinear eigenvalue problem $h(\psi_1)\psi_1 = \lambda_1\psi_1$, with the constraint $\langle \psi_1, \psi_1 \rangle = N_1$, is identical to the case of a single chiral gas. We have a localization phase transition when

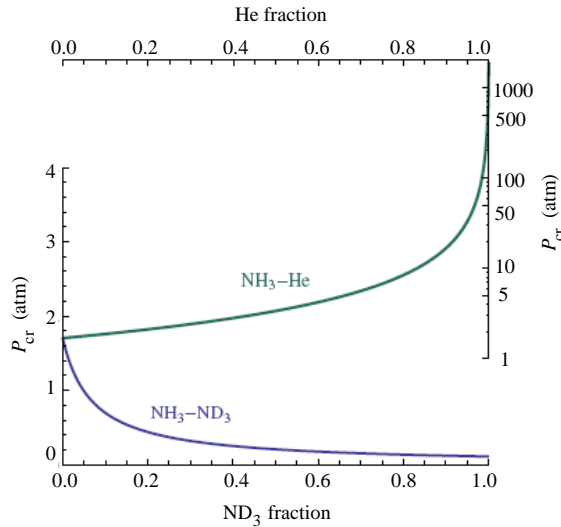


Figure 1: Critical pressure of the localization phase transition in a binary mixture of NH_3 as a function of the fraction of the second constituent chosen as ND_3 (bottom-left axes) or He (top-right axes).

$G_1 = \Delta E_1/2$. The transition can be considered as a function of the total pressure $P = P_1 + P_2$ of the mixture and of the fractions of the two species $x_1 = P_1/P$ and $x_2 = P_2/P$. In this case, instead of a unique critical pressure, we have a critical line parametrized by x_1 or $x_2 = 1 - x_1$, e.g.,

$$P_{\text{cr}} = \frac{\Delta E_1}{2x_1\gamma_{11} + 2x_2\gamma_{12}}. \quad (12)$$

In Fig. 1, we show the variation of the critical pressure in a NH_3 -He mixture as a function of the He fraction. The value of P_{cr} increases from the critical pressure of pure NH_3 to a maximum reached for a vanishing NH_3 fraction. The value of this maximum depends on the nature of the non polar species, it is greater the smaller is the molecular polarizability α_2 .

3.2. Mixtures of Two Chiral Gases

For a mixture of two chiral gases, we describe the inversion degrees of freedom of the two species by mean-field molecular states ψ_1, ψ_2 normalized to the number of molecules of the corresponding species. These states are obtained as the lowest-energy eigenstates of the eigenvalue problem associated with the coupled mean-field Hamiltonians

$$h_1(\psi_1, \psi_2) = -\frac{\Delta E_1}{2}\sigma_1^x - \sum_{j=1}^2 G_{1j} \frac{\langle \psi_j, \sigma_j^z \psi_j \rangle}{N_j} \sigma_1^z, \quad (13a)$$

$$h_2(\psi_1, \psi_2) = -\frac{\Delta E_2}{2}\sigma_2^x - \sum_{j=1}^2 G_{2j} \frac{\langle \psi_j, \sigma_j^z \psi_j \rangle}{N_j} \sigma_2^z. \quad (13b)$$

Pauli operators now have a label $i = 1, 2$ relative to the species they refer to. Each term $-G_{ij}$ represents the effective dipole interaction energy of a single molecule of species i with all the other molecules of species j . By matching $-G_{i1} - G_{i2} = \mathcal{E}_i$, where \mathcal{E}_i is given by Eq. (8) with $\alpha_1 \ll \alpha_1^{\text{D}}$ and $\alpha_2 \ll \alpha_2^{\text{D}}$, we get

$$G_{ij} = \gamma_{ij}x_jP, \quad \gamma_{ij} = \frac{4\pi}{9} \frac{\mu_i^2 \mu_j^2}{(4\pi\epsilon_0 k_B T)^2 d_i^3}, \quad (14)$$

where P is the total pressure of the mixture and x_1, x_2 the fractions of the components.

The solution of the coupled nonlinear eigenvalue problem $h_1(\psi_1\psi_2)\psi_1 = \lambda_1\psi_1$ and $h_2(\psi_1\psi_2)\psi_2 = \lambda_2\psi_2$, with the constraints $\langle \psi_1, \psi_1 \rangle = N_1$ and $\langle \psi_2, \psi_2 \rangle = N_2$, is discussed in [7]. As in the case of a single chiral gas, the mixture undergoes a localization phase transition at a critical pressure P_{cr} . For $0 < P < P_{\text{cr}}$, the lowest-energy molecular state of the mixture corresponds to molecules of

both species in a delocalized symmetric configuration. For $P > P_{\text{cr}}$, new minimal-energy molecular states appear with twofold degeneracy. These states correspond to molecules of both species in a chiral configuration of type L or R . We have a particularly simple formula for P_{cr} ,

$$\frac{1}{P_{\text{cr}}} = \sum_{i=1}^2 x_i \frac{1}{P_{\text{cr}}^{(i)}}, \quad P_{\text{cr}}^{(i)} = \frac{\Delta E_i}{2\gamma_{ii}} = \frac{9}{8\pi} \frac{\Delta E_i d_i^3 (4\pi\epsilon_0 k_B T)^2}{\mu_i^4}, \quad (15)$$

the inverse critical pressure of the mixture is the fraction-weighted average of the inverse critical pressures of its components. In Fig. 1, we show the variation of the critical pressure in a NH_3 - ND_3 mixture as a function of the ND_3 fraction. The value of P_{cr} ranges from the critical pressure of pure NH_3 to that of pure ND_3 , namely, from 1.69 atm to 0.11 atm. By changing ND_3 with, for instance, D_2S_2 , the minimal value of P_{cr} can be extended down to 4.3×10^{-9} atm, the critical pressure of deuterated disulfane.

4. CONCLUSION

Our approach to the existence of chiral molecules is based on ideas of equilibrium statistical mechanics. One may be surprised by the presence of a quantum phase transition at room temperatures. We emphasize that the transition takes place only in the inversion degrees of freedom. The dynamics of these degrees of freedom is affected by temperature only through the values of the coupling constants.

We have shown that with the addition of a proper fraction of a second species, non polar or chiral, the critical pressure of an ammonia mixture can vary in a range of several orders of magnitude. As a consequence, the inversion line of ammonia, as well as, possibly, that of the second chiral constituent, should undergo a frequency shift rather different from that measured for pure gases, see [7]. An experimental verification of these predictions is well within the reach of present technology and would represent a critical test of our theory.

REFERENCES

1. Jona-Lasinio, G., C. Presilla, and C. Toninelli, "Interaction induced localization in a gas of pyramidal molecules," *Phys. Rev. Lett.*, Vol. 88, 123001, 2002.
2. Ammonia is a potentially chiral molecule, it becomes chiral only under substitution of two of the hydrogens with different atoms like deuterium and tritium. We refer to potentially chiral molecules like ammonia as pre-chiral or, for simplicity, chiral.
3. Claverie, P. and G. Jona-Lasinio, "Instability of tunneling and the concept of molecular structure in quantum mechanics: The case of pyramidal molecules and the enantiomer problem," *Phys. Rev. A*, Vol. 33, 2245–2253, 1986.
4. Bleaney, B. and J. H. Loubster, "Collision broadening of the ammonia inversion spectrum at high pressures," *Nature*, Vol. 161, 522–523, London, 1948.
5. Bleaney, B. and J. H. Loubster, "The inversion spectra of NH_3 , CH_3Cl and CH_3Br at high pressures," *Proc. Phys. Soc., Sec. A*, Vol. 63, 483–493, London, 1950.
6. Birnbaum, G. and A. Maryott, "Change in the inversion spectrum of ND_3 from resonant to nonresonant absorption," *Phys. Rev.*, Vol. 92, 270–273, 1953.
7. Presilla, C. and G. Jona-Lasinio, "Spontaneous symmetry breaking and inversion-line spectroscopy in gas mixtures," *Phys. Rev. A*, Vol. 91, 022709, 2015.
8. Hanley, T. R., P. G. Steffes, and B. M. Karpowicz, "A new model of the hydrogen and helium-broadened microwave opacity of ammonia based on extensive laboratory measurements," *Icarus*, Vol. 202, 316–335, 2009.
9. Böttcher, C. T. F., *Theory of Electric Polarization*, Elsevier, Amsterdam, 1973.
10. Linder, B. and D. Hoernschemeyer, "Cavity concept in dielectric theory," *J. Chem. Phys.*, Vol. 46, 784–790, 1966.
11. Hynne, F. and R. K. Bullough, "The Onsager reaction field as a screened self-interaction in refractive index theory," *J. Phys. A*, Vol. 5, 1272–1295, 1972.

A Novel Ka-band Spatial Combiner Amplifier: Global Design and Modeling

Alberto Leggieri¹, Davide Passi¹, Franco Di Paolo¹, Marco Bartocci²,
Antonio Tafuto², and Antonio Manna²

¹Department of Electronic Engineering, University of Rome Tor Vergata, Rome, Italy

²Eltronica SpA, Via Tiburtina Valeria Km. 13, Rome 7-00100, Italy

Abstract— This article describes the complete design of high performances Ka-Band small size Spatial Power Combiner (SPC) Amplifier. Several multiple physics aspects are treated in the proposed study as electromagnetic behavior and thermo-mechanical features. The combiner consists of quadruple Fin lines to microstrip (FLuS) transitions inserted into a WR28 waveguide T-junction. In this structure, 16 Monolithic Microwave Integrated Circuit (MMIC) Solid State Power Amplifiers (SSPA's) are integrated. In order to drive the active devices at full power, thermal exposition has been controlled by an opportune heat-sinker subjected to a cooling air flow. A main design has been followed by FEM simulation using Ansys-Ansoft HFSS and Comsol Multiphysics. Scattering parameters, stresses and strains have been computed together with the temperature and airflow distributions. A mean insertion loss of 2 dB is achieved with a return loss better the 10 dB in the 31–37 GHz bandwidth while operating at maximum power. In such condition, the transistors present a maximum displacement of 28.7 μm caused by the thermal expansion of the material due to a channel temperature of 125°C, and special techniques have to be applied to avoid the MMIC's breakage.

1. INTRODUCTION

Spatial Power Combiner (SPC) Technology [1–7] is actually knowing an increasing interest as a suitable alternative to high power Vacuum Tubes (VT's) microwave amplification. A single VT has higher power output than a single transistor but the reliability and low voltage operation [8, 9] of the Solid State (SS) technology may give a notable benefit. Of course, in the range of millimeter waves and signal power levels greater than kilowatt only VT's like Gyrotrons or Free Electron Lasers can be employed [10–13], and no competition exists between SSPA's and VT's. The traditional approach to obtain a significant power output using SSPA's is the binary combining of many transistors through microstrip Transmission Lines [14, 15]. This solution is limited to the losses which each printed transmission line (TL) combiner and to the limited number of devices to a power of two. The Spatial Power Combining approach shows evident advantages over the classical binary technique. This technique is employed to design the Spatial Power Amplifier (SPA), in which power dividing and combining is performed in a parallel way, rather than in a serial way, and losses are little dependent with the number of used PA's [16]. Furthermore, SPA loss is rather constant with the number of amplifiers. In this work, the design and simulation a novel high performance and small size SPC working in Ka Band is presented, interfacing with standard WR28 waveguides. It employs an innovative matched quadruple antipodal Fin Line transition. Such innovative SPC allows the in-phase combination of 16 MMIC PA's achieving a high combining efficiency. Several circuitual and technological solutions have been adopted [17]. In order to reduce the combining loss and size and to reach wideband matching, exponential Finline-to-microstrips (FLuS) transitions have been considered. In order to improve the operative band, a parasitic void has been implemented by inserting an anti-resonance metal in the antipodal FLuS transition profile [18]. Together with the electromagnetic (EM) design of the SPA, the whole structure has been developed for the corrected thermo-mechanical operation which ensures the desired electromagnetic behavior, and avoids undesired alteration due to the thermo-mechanical effects related to the operative condition of the devices.

When high power levels are manipulated, heat sinking systems are especially important in order to avoid performance degradation and even device failure [19]. The power dissipation of the active devices produces a considerable temperature increase of both the PA's and the connected structure. If the SSPA's temperature exceeds the maximum allowed value (specified by the SSPA's vendor), an amplification failure or device damage may occur. The computation of the temperature is performed when the heat generated by the MMIC's power dissipation has been diffused on all the reachable SPA components which have been cooled by the opportune heat sinkers connected to the

device body cooled by an incident air flow. The calculation is performed through a stationary analysis when the system is thermally stable. A fixed external temperature has been assumed for the inlet air particles. The heat exchange occurs over all the SPA outer surfaces but is maximized on the heat sinker structure. A Finite Element Method (FEM) based simulation using Ansys-Ansoft HFSS has been employed to predict the Electromagnetic behavior of the structure and a Multi-physics modeling based design using COMSOL has been employed to perform Thermodynamics and Fluid-Dynamics analysis coupled to structural mechanics computation. Stresses and strains have been computed together with the temperature and airflow distributions. In order to decrease computational time and resources while maintaining accuracy and a nice grade of reliability, the device model is organized by using several architectural strategies shown in this paper. Since the device has two symmetry planes, only a quarter of the SPC structure has been employed for the modeling by introducing opportune symmetry boundary conditions.

2. ELECTROMAGNETIC DESIGN

The amplifier reported in this paper uses a WR28 rectangular waveguide at input and output. In order to deliver power to MMICs, four Al_2O_3 cards were employed, each one containing quadruple (quad) FLuS transitions (Figure 1). The Fin Line taper in each FLuS can be used as a broad-band impedance transformer between the waveguide and MMIC amplifier. To reduce the combining loss, an exponential FL taper has been chosen in antipodal configuration [20]:

$$w(z) = w_0 \exp \left[\frac{z}{l} \ln(w_f) \right], \quad (1)$$

where w_0 stands for initial taper width, w_f for the final one and l is the total length of the transition. It can be demonstrated that the impedance vary with the same behavior of (1) [21]. Microstrip Lines were designed following Hammerstad formulas reported in [22]. To improve the return loss at the waveguide when loaded by the Fin Lines and to symmetrise currents on the substrate, dielectric Parallel Quarter Wave Transformers (P-QWT's) have been designed, starting by the general design philosophy for single QWT given in [20].

The selection of the simulated geometry has been carefully determined, to avoid undesired lack of software convergence or bad results [23]. The 3D simulated structure is shown in Figure 2, from which we recognize that one quarter of the structure shown in Figure 2 can be analyzed with the software. The wave equation in the frequency domain (2) has been solved by HFSS Driven Modal

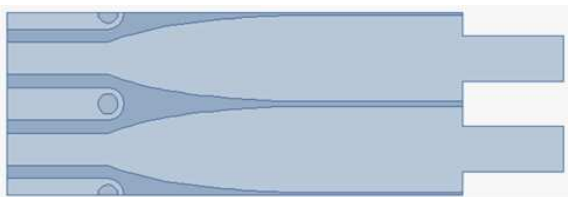


Figure 1: Quadruple FLuS employing the innovative dielectric parallel QWT.

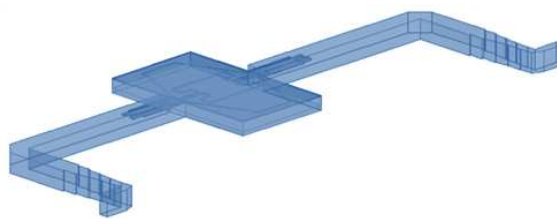


Figure 2: 3D quarter section of the WR28 SPC EM model.

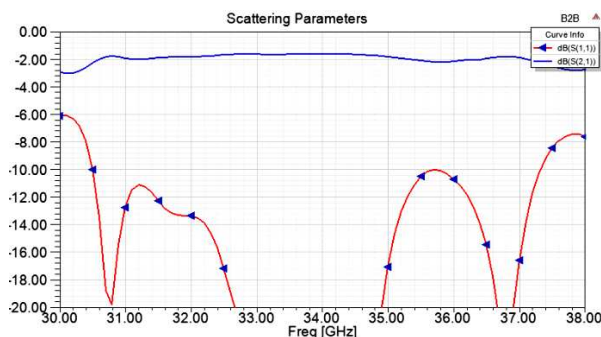


Figure 3: SPC simulation results: insertion loss and return loss in dB, in the operating bandwidth.

computation [19].

$$\nabla \times \mu_r^{-1} (\nabla \times \bar{E}) - k_0^2 \left(\varepsilon_r - \frac{j\sigma}{\omega\varepsilon_0} \right) \bar{E} = 0 \quad (2)$$

where μ_r is the permeability, ε_r the permittivity and σ the conductivity of the material; ε_0 is the permittivity of the vacuum, k_0 the wave number in free space, ω the wave angular frequency and \bar{E} the electric field. The simulated S -parameters are given in Figure 3. By observing such images we note that the proposed WR28 SPC passive structure ensures a maximum insertion loss of 2.2 dB and a minimum Return Loss of 10 dB in the whole 31–37 GHz band.

3. THERMO-MECHANICAL DESIGN

The heat generated by power dissipation on the MMIC's channel cause carriers and shell warming. If no cooling system is provided the SPA's temperature increase until the active devices breakdown. For this reason, an oportune cooling system has been designed formed by heat sinks and cooling fan. The analyzed structure is realized in a WR28 waveguide, whose central part allows for the insertion of two metal carrier which holds up the antipodal FLuS's and MMIC SSPA's. The material to use for the carrier has been investigated in this work, in order to improve the heat conduction. An Aluminum shell contains two 2 mm copper carriers. The carriers are placed at the center of the waveguide and each face of the carrier holds 8 active devices and 2 FLuS's printed on an Alumina substrate. The model used for the analysis is shown in Figure 4. The heat sources are 16 parallelepipeds, one per MMIC, with size of $5.4 \times 0.2 \times 0.01$ mm; they represent the FET's channel and each source dissipate 21 W on GaAs. The analysis is based on the complete coupling of the COMSOL Laminar Flow, Heat Transfer and Structural Mechanics modules. No mechanical movements are allowed on the external walls, since has been assumed that the air can't move any part of the structure, including the heat-sinker wings. This condition avoids any normal force on the surfaces and any rotation, allowing for the computation of the sole heat exchange.

The Thermodynamics and fluid dynamics study has been solved by adopting a fully coupled stationary calculation in order to evaluate the temperature distribution, when the maximum temperature is reached by the active devices and all the structure is subjected to an oportune air flow.

Heat Transfer has been computed by solving the Heat Equation in the steady state (3) [24].

$$-\nabla \cdot (k\nabla T) = Q \quad (3)$$

where T is the temperature (K), k the thermal conductivity ($\text{W}\cdot\text{m}^{-1}\cdot\text{K}^{-1}$) of the material and Q is the heat power density ($\text{W}\cdot\text{m}^{-3}$). The air motion is modeled with a single phase laminar flow and computed by solving the system of (4) and (5) in a stationary analysis.

$$\rho(u \cdot \nabla)u = \nabla \cdot \left[-pI + \mu \left(\nabla u + (\nabla u)^T \right) - \frac{2}{3}\mu (\nabla \cdot u) I \right] + F \quad (4)$$

$$\nabla \cdot (\rho u) = 0 \quad (5)$$

where p is the pressure, u is the velocity field ($\text{m}\cdot\text{s}^{-1}$), ρ the material density ($\text{kg}\cdot\text{m}^{-3}$), μ the dynamic viscosity ($\text{Pa}\cdot\text{s}$) of the material (the air) and F is the volume force ($\text{N}\cdot\text{m}^{-3}$). The symbol I stand for the identity matrix and T for the transposing operation.

The Structural Mechanics analysis shares the computation variables with the thermodynamic and fluid dynamics calculation, consisting in a large computation system. The thermal expansion calculated by the structural analysis has been employed to estimate the deformation of the material induced by the heat generated by the SSPA's power dissipation during the operation at the maximum power rating. Surfaces are intended as in a stationary temperature regime, cooled by the external environment condition as shown by the Thermo-Fluid Dynamics analysis. The analysis has solved the system of stress steady state Equation (6) fully coupled with the computation of the (3), (4) and (5) by computing the thermal expansion of the materials [19].

$$-\nabla \cdot \sigma = \bar{F}_V \quad (6)$$

where σ is the stress (Nm^{-2}) and \bar{F}_V is the force per unit volume (Nm^{-3}). The mechanical boundary conditions have been chosen in order to leave waveguide external walls free from any constriction, ensuring the ability to swell. This condition avoids any normal force on such walls

and any rotation, allowing to compute the complete deformation of the transistors. The solid model is intended as isotropic and the structural transient behavior as quasi-static. The thermal expansion induced forces have symmetric application points, due to the geometric symmetry. The surfaces which lie on the back plane of Figure 4 are modeled as symmetry boundary condition. The mechanical analysis has been performed by considering the nominal operative ratings of the SPC, while operating at maximum power of 21 W per transistor and cooling the SPC by an air laminar flux with a velocity of 10 ms and initial temperature of 0°C. This is a value obtainable with a liquid chiller or much easier when the SPC is employed on Airplanes. In the following images, black color outlines represent the original conformation, and the stained volumes represent the deformed structure. Furthermore, the scale factor of the deformation has been magnified, in order to better view the displacements. In Fig. 4 the airflow streamline is reported including the temperature distribution of the air flowing around the SPC structure. By the heat transfer with the warmed SPA, the air flux reaches a maximum temperature of 54.5°C. In such condition, the channels of the transistors reach a maximum temperature of 125°C shown in Fig. 5. In Fig. 6 is represented the maximum stress on the carrier and MMIC devices: it is located near the inner angles of the carrier and locally reaches 0.26 GNm⁻². MMIC devices need to be carefully held to the carrier since the different thermal expansion coefficients of the materials may induce a mismatch which can damage the crystal. A deep description of the physical principle governing these effects is reported in [26–29]. According to such studies and basing on our heritage by considering the stress to which the MMIC devices are subjected, a typical acceptable value for the displacement of a GaAs crystal of the dimensions of the employed MMIC, exactly the type TGA2575 produced by Triquint [30], needs to not exceed 5 μm on the narrow side. A maximum displacement of 56.3 μm is located on the cooling wings of the heat sinker and near the interface between the outermost SSPA’s and the external surface of the SPC, is located a displacement of 28.7 μm (shown in Fig. 7), enough negligible from the EM guiding properties of the structure but critical for the GaAs MMIC survivability. In order to allow for the heat dissipation without mismatch between coefficients of thermal expansion (CTE) for GaAs and conductors, MMIC’s are brazed onto CuMo heat spreader and the whole assembly is brazed onto copper carriers. Hence, at each temperature value obtained

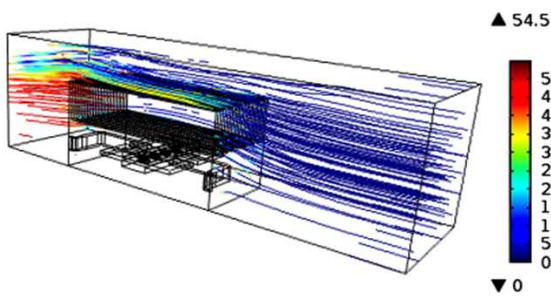


Figure 4: Airflow streamlines with temperature distribution on a quarter section of the SPC.

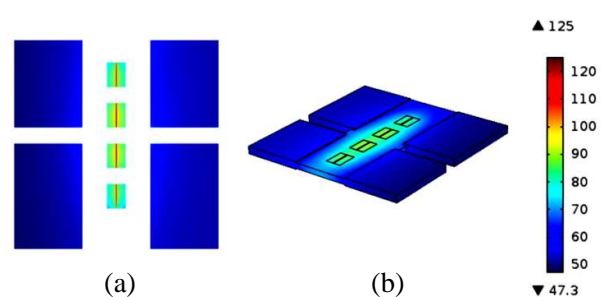


Figure 5: (a) Temperature distribution (°C) on carrier and MMIC in plane section and (b) 3D view.

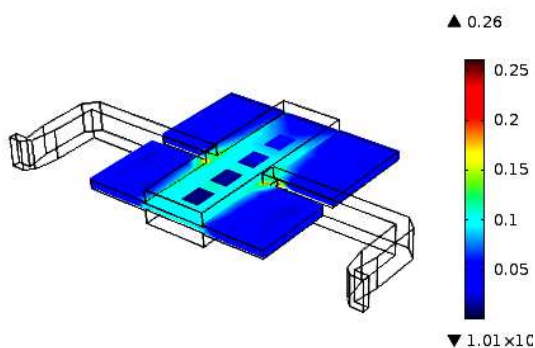


Figure 6: Maximum stress on carrier and MMIC (GNm⁻²).

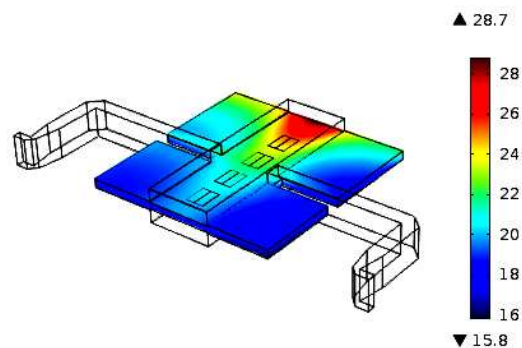


Figure 7: Maximum displacement on MMIC (μm).

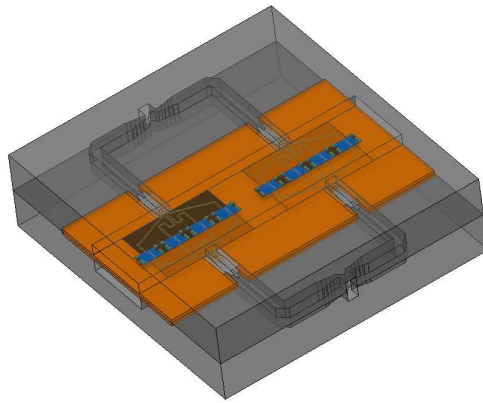


Figure 8: The whole structure of the Ka-band SPC amplifier.

we need to add about 4°C, by our heritage, to consider the CuMo effect in thermal conduction.

The mechanical design considers the compactness of the final SPA, the maximum possible heat transfer and the simplicity of the assembling. This SPA has been designed to use standard WR28 flanges and to employ 16 MMIC Triquint TGA2575 HPA's operating at these WG frequencies. At the amplifier input, a Waveguide T-junctions in E -plane is used to split the signals in two WR28 arms. The branches of T-junction have designed with four-step Chebyshev transformer in order to obtain small reflections to the input port in Ka band. In Figure 8 we report the complete CAD drawing of the Ka-band SPC amplifier, including 16 SSPA MMIC's: heat sinker is removed for a better view. From such image we recognize the bulk of the SPC made of Aluminum, the innovative quadruple fin lines with the innovative P-QWT, the copper carriers, the equalization lines and the MMIC's with their DC feed capacitors placed on CuMo heat spreader. The size of this SPC is $90 \times 92 \times 25$ mm, but size can be still reduced.

4. CONCLUSIONS

This study describes a novel SPC Ka Band Power Amplifier based on the spatial combination of 16 SSPA MMIC's. Several multiple physics aspects are treated in the proposed study as the electromagnetic behavior and thermo-mechanical features in order to drive the active devices at full power. A reliable computational electromagnetic model have shown an operating bandwidth from 31 GHz to 37 GHz, with a mean insertion loss of 2 dB for the passive SPC and minimum return loss of 10 dB in the whole bandwidth. MMICs fault and undesired thermal expansion with related stresses and displacements have been prevented. A maximum channel temperature of 125°C is expected while the device operates at full power and cooled by an opportune airflow. Maximum stress on the carriers, MMIC devices and cooling wings has been computed. Such a study has allowed for the selection of the proper materials for carriers and interfaces between them and MMIC's. Due to the proposed thermo-mechanical design, each MMIC device can be driven at full power reaching its maximum power output $P_{out} = 35.5$ dBm. Since the average Insertion Losses are 2.0 dB, the proposed SPA (employing 16 MMIC amplifiers) can provide a maximum power output of about 45.8 dBm occupying $90 \times 92 \times 25$ mm.

REFERENCES

1. Leggieri, A., G. Orenco, D. Passi, and F. Di Paolo, "The squarax spatial power combiner," *Progress In Electromagnetics Research C*, Vol. 45, 43–55, 2013.
2. Russo, I., L. Boccia, G. Amendola, and G. Di Massa, "Parametric analysis of grid amplifiers," *Proceedings of European Microwave Week*, 1326–1329, Amsterdam, 2008.
3. An, D., X. Li, J. Mou, and X. Liv, "A new type of Ka-band waveguide-based power combining structures," *Proceedings of ICMMT 2008*, 1–4, Nanjing, China, Apr. 21–24, 2008.
4. Russo, I., L. Boccia, G. Amendola, and H. Shumacher, "Compact hybrid coaxial achitecture for 3–10 GHz UWB quasi-optical power combiner," *Progress In Electromagnetics Research*, Vol. 122, 77–92, 2012.
5. Lopz, D., L. Bortoli, J-P Fraysse, D. Langrez, J. F. Villemazet, J. L. Cazaux, G. Soubercaze-Pun, and L. Lapierre, "HPA module for active antenna applications," *Proceedings of 5th European Microwave Integrated Circuit Conference*, 404–407, Paris, Sep. 27–28, 2010.

6. Jia, P., L. Y. Chen, A. Alexanian, and R. A. York, "Multioctave spatial power combining in oversized coaxial waveguide," *IEEE Trans. on MTT*, Vol. 50, No. 5, 1355–1360, May 2002.
7. Cheng, N.-S., P. Jia, D. B. Rensch, and R. A. York, "A 120-W X-band spatially combined solid-state amplifier," *IEEE Trans. on MTT*, Vol. 47, No. 12, 2557–2561, Dec. 1999.
8. Symons, R. S., "Tubes: Still vital after all these years," *IEEE Spectrum*, 52–63, Apr. 1998.
9. Barbour, E., "The cool sound of tubes," *IEEE Spectrum*, 24–35, Aug. 1998.
10. Levush, B., D. K. Abe, J. P. Calame, B. G. Danly, K. T. Nguyen, E. J. Dutkowski, R. H. Abrams, and R. K. Parker, "Vacuum electronics: Status and trends," *IEEE Radar Conference*, 971–976, 2007.
11. Armstrong, C. M., "The vitality of vacuum electronics," *IEEE 14th International Vacuum Electronics Conference (IVEC)*, 1–3, 2013.
12. Booske, J. H., R. J. Dobbs, C. D. Joye, C. L. Kory, G. R. Neil, G.-S. Park, J. Park, and R. J. Temkin, "Vacuum electronic high power terahertz sources," *IEEE Transactions on Terahertz Science and Technology*, Vol. 1, No. 1, 54–75, 2011.
13. Qiu, J. X., B. Levush, J. Pasour, A. Katz, C. M. Armstrong, D. R. Whaley, J. Tucek, K. Kreischer, and D. Gallagher, "Vacuum tube amplifiers," *IEEE Microwave Magazine*, Vol. 10, No. 7, 38–51, 2009.
14. Russel, K. J., "Microwave power combining techniques," *IEEE Trans. on MTT*, Vol. 27, No. 5, 472–478, May 1979.
15. Chang, K. and C. Sun, "Millimeter-wave power combining techniques," *IEEE Trans. on MTT*, Vol. 31, No. 2, 91–107, Feb. 1983.
16. DeLisio, M. P. and R. A. York, "Quasi-optical and spatial power combining," *IEEE Trans. on MTT*, Vol. 50, No. 3, Mar. 2002.
17. Passi, D., A. Leggieri, F. Di Paolo, M. Bartocci, A. Tafuto, and A. Manna, "High efficiency Ka-band spatial combiner," *Advanced Electromagnetics*, Vol. 3, No. 2, 10–15, 2014.
18. Ponchak, G. E. and A. N. Downey, "A new model for broadband waveguide to microstrip transition design," NASA Technical Memorandum 88905, Lewis Research Center Cleveland, Ohio, Dec. 1986.
19. Leggieri, A., D. Passi, F. Di Paolo, and G. Saggio, "Multiphysics design of a spatial combiner predisposed for thermo-mechanically affected operation," *Journal of Electromagnetic Waves and Applications*, Vol. 28, No. 17, 2153–2168, 2014.
20. Bhat, B. and S. K. Koul, *Analysis, Design and Applications of Fin Lines*, Artech House, 1987.
21. Collin, R. E., *Foundations for Microwave Engineering*, McGraw-Hill International Editions, 1992, ISBN 0-07-011811-6.
22. Di Paolo, F., *Networks and Devices Using Planar Transmission Lines*, CRC Press LLC, 2000, ISBN 0-8493-1835-1.
23. Passi, D., A. Leggieri, and F. Di Paolo, "Computational electromagnetic design of the squarax spatial power combiner," *Ansys UGM 2014*, Milano, Italy, 2014.
24. COMSOL "Heat transfer module user's guide," 75–99, 184–224, COMSOL AB, Stockholm, 2012,
25. COMSOL "Heat transfer module user's guide," 69–72; 111–212, COMSOL AB, Stockholm, 2012.
26. Chen, C. P., "Fracture MEchanics evaluation of GaAs," *JPL Report*, Oct. 15, 1984.
27. Vidano, R. P., D. W. Paananen, T. H. Miers, J. M. Krause-Singh, K. R. Agricola, and R. L. Hauser, "Mechanical stress reliability factors for packaging GaAs MMIC and LSIC components," *IEEE Trans. on Components, Hybrids, and Manufacturing Tech.*, No. 4, 612–617, Dec. 1987.
28. Pavio, J. and D. Hyde, "Effects of coefficient of thermal expansion mismatch on solder attached GaAs MMICs," *IEEE MTT-S International Microwave Symposium Digest*, Vol. 3, 1075–1078, 1991.
29. Jin, M., J. Xu, and Y. Fang, "Investigation on mechanical characteristics of semi-insulating GaAs crystal under different load," *International Conference on Materials for Renewable Energy & Environment (ICMREE)*, Vol. 1, 100–103, 2011.
30. Tryquint Semiconductor Inc., "TGA2575 Ka-band 3 watt power amplifier," Product Datasheet, 2012.

Formation of One-dimensional Image by Pulsed Light Diffraction on Running Sound Wave

Victor Petrov¹ and Roman Kijan²

¹St.-Petersburg Politechnical University, St.-Petersburg, Russia

²Laser Zentrum Hannover e.V., Hannover, Germany

Abstract— The advanced systems for formation of a TV image on a projection screen is an acoustooptic system that relies on the principle of exposure of the entire TV 1D image by one laser pulse and further deflection of 1D images across the frame. The case of a diffracted field for wide-band anisotropic light diffraction by a slow shear elastic wave near the optical axis of an acoustooptic modulator made from a crystal of paratellurite TeO₂ was considered. We rely on the solution for the diffracted field and consider the problem of formation of the image of an amplitude-modulated 1D image that fills the acoustooptic modulator aperture on the projection screen. As a light source, a copper-vapor laser with wavelength $\lambda_0 = 0.5106 \mu\text{m}$ and generation pulse duration $\tau_0 = 10 \text{ ns}$ was used.

1. THE CASE OF A LOW EFFICIENCY OF ACOUSTOOPTIC INTERACTION FOR CONVERGING LIGHT BEAM

Let us consider the system for formation of a 1D image (Figure 1) that includes an acoustooptic modulator (AOM), input cylindrical lens L₁, and an objective consisting of lenses L₂ and L₃. The X'OZ' and Y'OZ' planes of the system are chosen so that in one of them (X'OZ') light diffraction in the AOM and formation of the 1D image on the screen Sc occur, and in the other plane (Y'OZ') formation of the spatial distribution of the 1D image and its deflection in the screen plane takes place. The medium for the acoustooptic interaction is a TeO₂ crystal.

Our consideration refers to the interaction geometry which is employed in a real device (Figure 2) and which corresponds to the case of wide-band anisotropic light diffraction by a slow shear elastic wave [1, 2].

We assume that an ultrasonic wave with the polarization vector directed along the [110] axis coinciding with the Y' axis propagates along the $[\bar{1} 10]$ direction of the crystal coinciding with the X' axis of the optical system. The wave vector of the light wave \mathbf{k} makes angle θ with its projection on the (110) plane, and the projection of this vector on the (110) plane is at angle α to the Z' axis.

Angles α and θ are assumed to be small, and we have

$$\begin{aligned} k'_x, k'_y &\ll k; k'_x = k_x = -k \sin \theta \approx -k\theta; \\ k'_y &= k \cos \theta \sin \alpha \approx -k\alpha \end{aligned} \quad (1)$$

where $k = 2\pi/\lambda_0$ is the amplitude of the wave vector of the light wave for a free space.

Then, following by a formalism, developed in [2], using the same notations, and by assuming that the light pulse shape corresponds to the Gaussian distribution law and also that the light source coherence time $\tau_{\text{coh}} = l_{\text{coh}}/c$ (l_{coh} is the longitudinal coherence length) is much shorter than the radiation pulse duration (this is fulfilled, for example, for the copper-vapor laser), we get the time-average distribution of light intensity in the 1D image on the screen

$$\begin{aligned} I(x'_1, y'_1) &= \frac{1}{T} \int_{-\infty}^{+\infty} \exp \left\{ -\frac{t^2}{\tau_0^2} 4 \ln 2 \right\} I_1(x'_1, y'_1, t_1) dt \\ &= \Gamma_0 \left\{ D_0 + m_0 \exp \left\{ -\frac{\pi f_0 \tau_0}{2\sqrt{\ln 2}} \right\}^2 \sqrt{D_1^2 + D_2^2} \sin \left(\frac{2\pi f_0}{\nu} x' + \Delta_1 \right) \right. \\ &\quad \left. + \frac{m_0}{2} \exp \left\{ -\frac{\pi f_0 \tau_0}{2\sqrt{\ln 2}} \right\}^2 \sqrt{D_3^2 + D_4^2} \sin \left(\frac{4\pi f_0}{\nu} x' + \Delta_2 \right) \right\} \end{aligned} \quad (2)$$

where T is the period over which time integration is performed; and τ_0 is the light pulse duration at the 0.5 light intensity level. The first term in Expression (2) defines the constant component

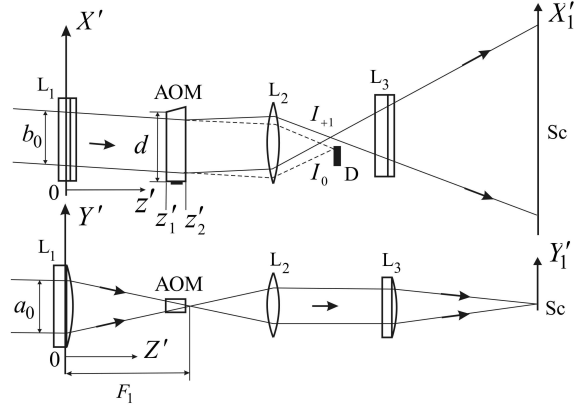


Figure 1: Optical scheme of the system for formation of a 1D image in two mutually perpendicular planes: AOM — acousto-optic modulator; L_1 — input cylindrical lens; L_2, L_3 — lenses of the objective; Sc — screen; D — diaphragm; I_0, I_{+1} — intensities of the incident and diffracted light beams; a_0, b_0 — light beam sizes along two coordinates; F_1 — focal distance of L_1 ; d — acousto-optic modulator size along the X' axis.

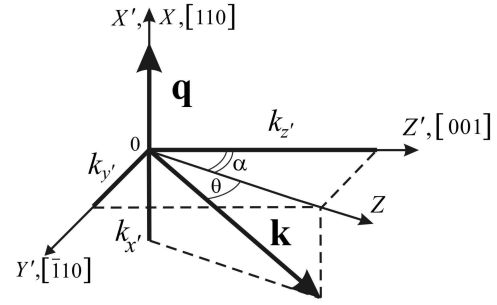


Figure 2: Geometry of acousto-optic interaction: \mathbf{k}, \mathbf{k}_s — wave vectors of light and sound waves; $k_{x'}, k_{y'}, k_{z'}$ — projections of vector \mathbf{k} on the coordinate axes; θ — angle between wave vector \mathbf{k} and its projection on the (110) plane; α — angle between the Z' axis and projection of vector \mathbf{k} on the (110) plane.

in the signal of the image, the second term gives modulation with the input signal frequency, and the third term describes nonlinear distortions in the image at a doubled signal frequency. Coefficient Γ_0 characterizes changes in the average light intensity in the 1D image on the screen due to transformation of the light beam sizes.

2. MODULATION-TRANSFER FUNCTION OF THE SYSTEM

The Expression (2) corresponds to the case of a low diffraction efficiency. Let us use this expression to find the modulation-transfer function (MTF) of the system. To this end, we consider the cross section of this distribution by the plane $y = y_0$ for which $I(y_0) = I_{\max}$. We define the contrast transfer function versus modulation frequency f_0 as

$$M(f_0) = I_{\max}(f_0) - I_{\min}(f_0) / I_{\max}(f_0) + I_{\min}(f_0) \quad (3)$$

Function (3) was calculated for different light pulse durations τ_0 and cones of angles of light incidence on the sound beam $2\tilde{\alpha}$ which corresponded to the choice of different focal distances F_1 for different central frequencies of ultrasound f and Bragg angles $\theta_0^{(0)}, \theta_0^{(1)}$ corresponding to these frequencies, and also for different acousto-optic interaction lengths L . The medium for the acousto-optic interaction was the TeO_2 crystal. The light radiation wavelength in the calculations was taken to be 510.6 nm, which corresponded to the green line of the copper-vapor laser, and the ultrasonic wave modulation depth was $m_0 = 1$.

Calculations showed that $M(f_0)$ was nearly independent of the cone of the angles of incidence $2\tilde{\alpha}$ in the plane orthogonal to the scattering plane. Its shape was mainly determined by the choice of the carrier frequency of ultrasound f , ultrasonic beam with L , and light pulse duration τ_0 . Figure 3 shows calculated MTF families for different parameters. It can be seen that as the light pulse duration becomes smaller, the decrease in the MTF slows down. As ultrasonic beam sizes reduce (interaction length L , Figure 3(b)) the MTF decrease becomes slower which can be explained by an increase in the spatial-frequency region of acousto-optic interaction due to broadening of the directional diagram of the elastic wave emitter. In all the cases a decrease in length L leads to an increase in the contrast in the image transfer.

Figure 4 shows the dependence of coefficient N on modulation frequency f_0 plotted for the same functions $I(f_0)$ as in Figure 3(a).

$$N(f_0) = \ln \{I_{\max}(f_0) / I_{\min}(f_0)\} \quad (4)$$

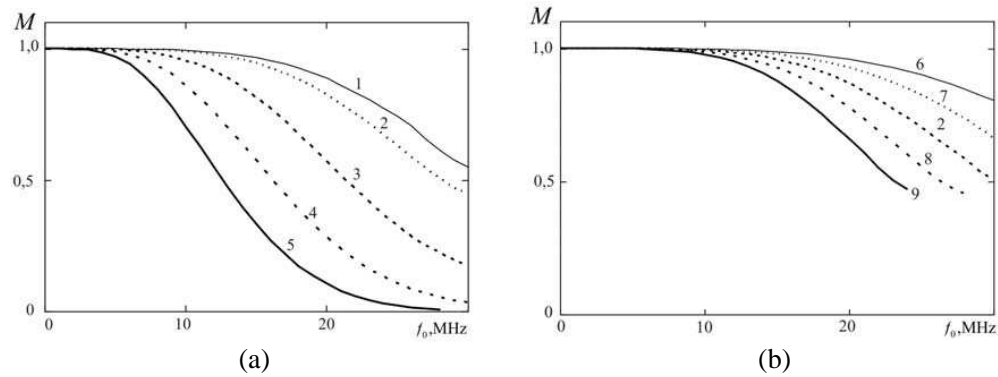


Figure 3: (a) MTF of the system as a function of light pulse duration τ_0 , (b) interaction length L , basic set of parameters: $f = 80$ MHz; $L = 4$ mm; $\tau_0 = 10$ ns (curves 2); τ_0 , ns: 5 (1), 10 (2), 20 (3), 30 (4), 40 (5); L , mm: 2 (6); 3 (7), 4 (2), 5 (8), 6 (9).

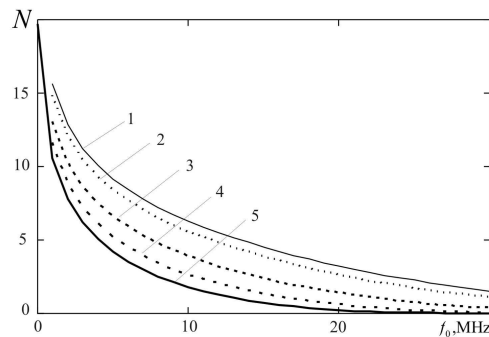


Figure 4: Logarithmic contrast transfer function for different pulse durations τ_0 , ns: 5 (1), 10 (2), 20 (3), 30 (4), 40 (5).

The number of tone levels the eye can perceive is taken to be

$$N(f_0) = \frac{1}{\sigma} \ln \{I_{\max}/I_{\min}\} \quad (5)$$

where σ is the threshold contrast; $\sigma = 0.02$ – 0.05 . The dependences in Figure 4 can be useful for estimation of the number of tone levels (gray levels) and highest frequency of the image the eye can perceive. If we assume that the highest MTF frequency is the frequency $f_0 = f_h$ at which $N(f_h) = \sigma$ and solve the relevant equations, we obtain that at $\tau_0 = 40$ ns the highest frequency is $f_h \cong 25$ MHz, at $\tau_0 = 30$ ns $f_h \cong 31$ MHz, and at $\tau_0 = 20$ ns $f_h \cong 50$ MHz.

3. RESULTS AND CONCLUSIONS

In the approximation of a low diffraction efficiency, a two-dimensional field distribution in the (+1)st diffraction order in the focal plane of the input cylindrical lens and a time-average distribution of intensity of light from a pulsed coherent source in the image plane have been calculated. Calculations of the modulation-transfer function of the acoustooptic system for the 1D image formation including a pulsed copper-vapor laser and AOM from a paratellurite crystal (TeO_2) for different light pulse durations, carrier frequencies of ultrasound, acoustooptic interaction lengths, and also angles of light incidence on the AOM in the plane orthogonal to the scattering plane have been carried out.

Numerical calculations have shown that an increase in the light pulse duration leads to a decrease in the contrast in transfer of amplitude-modulated signals at high frequencies. An increase in the contrast at high frequencies results from a decrease in the piezotransducer width and decrease in the carrier frequency of ultrasound. It approaches the frequency of two-phonon interaction.

Requirements to the choice of the focal distance of the input cylindrical lens and cone of angles of light incidence on the AOM in the plane orthogonal to the plane of diffraction at which no noticeable decrease in the average intensity of diffracted light occurs have been formulated.

REFERENCES

1. Petrov, V., "Digital holography for bulk image acoustooptical reconstruction," *Digital Holography and Three-dimensional Displays: Principles and Applications*, 73–99, 430, by Ting-Chung Poon, Ed., Springer, 2006.
2. Korikov, C., Y. Mokrushin, and R. Kiyan, "Transmitting of a full-TV image by a pulsed one-dimensional serial optical frames: A non-linear approach," *Internet of Things, Smart Spaces, and Next Generation Network and Systems*, 662–675, 716, S. Balandin, et al., Eds., Springer, 2014.

RF Design of Input Cavity Structure of a Low Frequency, High Average Power IOT

Meenu Kaushik^{1,2} and L. M. Joshi^{1,2}

¹CSIR-Central Electronics Engineering Research Institute (CEERI), Pilani, Rajasthan, India

²Academy of Scientific and Innovative Research (AcSIR), New Delhi, India

Abstract— Inductive Output Tube (IOT) is a vacuum electron tube capable of amplifying RF power with very good efficiency. IOT has been extensively used in TV services as UHF transmitters to amplify both audio and video signals. Its moderate power gain, high efficiency and long life make it suitable for this application. Besides that, this tube has been proving its capability and reliability in scientific areas like in high energy particle accelerators and fusion plasma heating purposes. The paper will present the RF design of input cavity of a low frequency (~ 350 MHz) IOT carried out at CSIR-CEERI. It is an important component of the device. The simulation of the cavity has been carried out in CST and MAGIC2D codes. The CAD drawings have been prepared and the cavity structure has been fabricated. The details of design approach using CAD tools shall be presented in this paper.

1. INTRODUCTION

The IOT was invented in 1938 by AV Haeff but it took long time to recognize the ability and potential of this device. The tube came in prominence when it was used in UHF transmitters where its performance impressed the microwave researchers [1]. The structure of the device is similar to any other linear beam tube, like klystron, having some major differences in its operation. The input RF cavity, being an important part of the device, has to be designed with many technical constraints. The velocity modulation occurs in the interaction gap of the cavity which is placed onto the gun part.

The major components of IOT are electron gun, input/output cavities, input/output couplers, focussing magnet and collector, as shown in Figure 1. Pierce's type gridded electron gun is used for electron beam generation. The RF input signal is applied between cathode and a grid which is positioned close to and in front of the cathode.

The inner wall of the cavity is connected between the cathode and grid — the two electrodes both of which are at a large negative potentials. Further, it is necessary to maintain the outer wall of the cavity and its tuning mechanism at ground potential. The method used to form bunches is somewhat different from the conventional linear beam tubes. The modulated beam passes into the RF output interaction region of the IOT. The device has no intermediate cavities. An output coupler connects the cavity to the output feeder system. The electron beam is focused using a suitable magnetic focussing system. The spent electron beam is dissipated in a copper collector either air cooled or liquid cooled depending on the power level involved [2–4].

IOTs are widely used in TV services as UHF transmitters to amplify both audio and video signals. It has average power gain, very high efficiency and sufficient long life which make it suitable for this application. Apart from this, IOT's significance has now being recognized for scientific applications too. They are used as RF source in a number of international high energy particle accelerators such as Diamond, CERN and LANSCE [5].

2. DESIGN APPROACH AND RESULTS

IOT has only two resonant cavities- one input and one output cavity. The velocity modulation will occur in the input cavity where the nose cone gap is the distance between the cathode and grid. The cavity should be smartly positioned so that the cathode-grid gap plays the role of cavity drift gap and contributes to the interaction between electron beam (emitting from the electron gun) and the input RF signal (applied at the cathode-grid gap). As the cathode-grid distance is very small in the range of 0.3 mm, the design of the cavity should be such that the required field pattern (E and H) could be obtained within the cavity for proper modulation. One key issue is that the cavity operates in grounded mode and in this case, the inner wall of the cavity is connected to the cathode and grid, having high negative potential, hence proper isolation of the input circuit is mandatory for its successful operation.

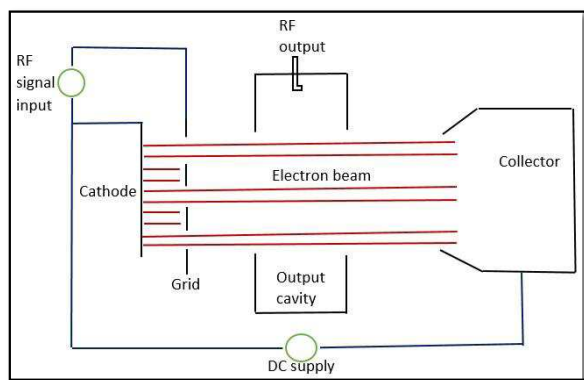


Figure 1: Schematic of IOT.

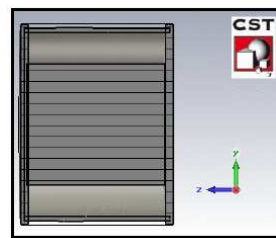


Figure 2: Structure of input cavity.

The paper presents the simulation results of a 350 MHz input cavity carried out in CST and MAGIC PIC software. The cavity structure shown in Figure 2 is chosen for properly placing the cavity onto the cathode-grid gap. The inner conductor, shorted at one end and open at other end (which makes the cathode-grid gap), acts as cathode which is emitting electron beam from its face and the outer conductor dimensions (diameter and length) are the deciding factor of the desired resonance of input RF signal in the cavity. The design is so chosen because in this structure, E field peaks at the gap and B field maximises at the short end which is the desirable field profiles for coupling the input power to this cavity.

For choosing the initial dimensions of the cavity, there are some limitations and considerations. Within the inner conductor of the cavity, in actual, cathode has to be placed. Therefore, the inner conductor has to be of sufficient diameter so that the cathode will be inserted in it properly. Hence, the inner conductor's diameter's estimation is taken from the cathode diameter (which is already simulated according to the beam parameters). The outer conductor's diameter is optimized through various iterations to get the resonance of the desired frequency in the cavity. The critical dimension is the cathode-grid gap. The gap is taken so small (~ 0.3 mm) to have only 1–2 percent of the RF cycle being interacted with the electron beam so that proper and efficient velocity modulation takes place for sufficient bunching of the electrons. On the other hand, decreasing the gap distance below the specified value will cause breakdown issues. Therefore, this gap is chosen within safe limits to properly serve its purpose of modulation in the cavity.

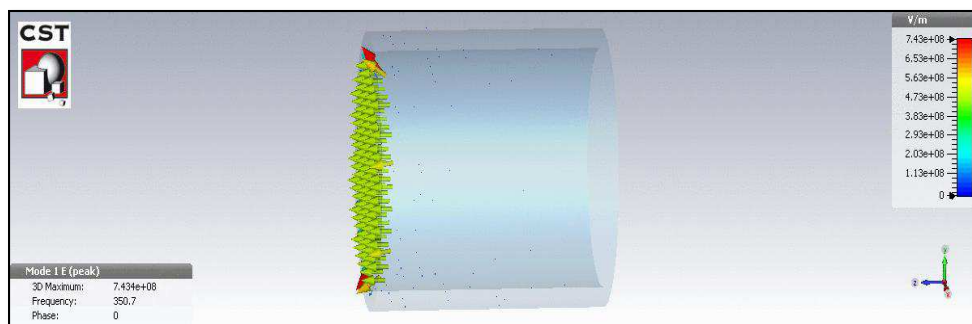


Figure 3: Resonant frequency @ 0.3 mm gap.

The cavity structure is similar to a radial cavity whose inductance, capacitance and resonant

frequency can be estimated from the following equations [6]

$$L = \frac{\mu l}{2\pi} \ln(b/a) \quad (1)$$

$$C = \epsilon_0 \left[\frac{\pi a^2}{d} - 4a \ln \left(0.765 / \sqrt{\{l^2 + (b-a)^2\}} \right) \right] \quad (2)$$

$$f_r = \frac{c}{2\pi \sqrt{\epsilon_r} \sqrt{\left\{ al \left[\frac{a}{2d} - \frac{2}{l} \ln \left(\frac{0.765}{\sqrt{\{l^2 + (b-a)^2\}}} \right) \right] \ln \left(\frac{b}{a} \right) \right\}}} \quad (3)$$

where L is the inductance produced in the cavity wall, μ is the permeability, C is the capacitance in the cavity gap, ϵ_0 is the permittivity of free space, f_r is the resonant frequency, ϵ_r is the relative permittivity of the material of the cavity, a and b are radius of inner and outer conductor respectively, d is the cathode-grid gap, l is the height of the cavity and $c = 3 \times 10^8$ m/s is the velocity of light in vacuum.

Figures 3 and 4 provide the information about the resonant frequency and E field pattern obtained in CST and MAGIC respectively. Based on the results obtained, the input cavity has been fabricated as shown in Figure 5. The cold test measurements are planned for validating the simulation results. The experimental results will also be presented in the talk.

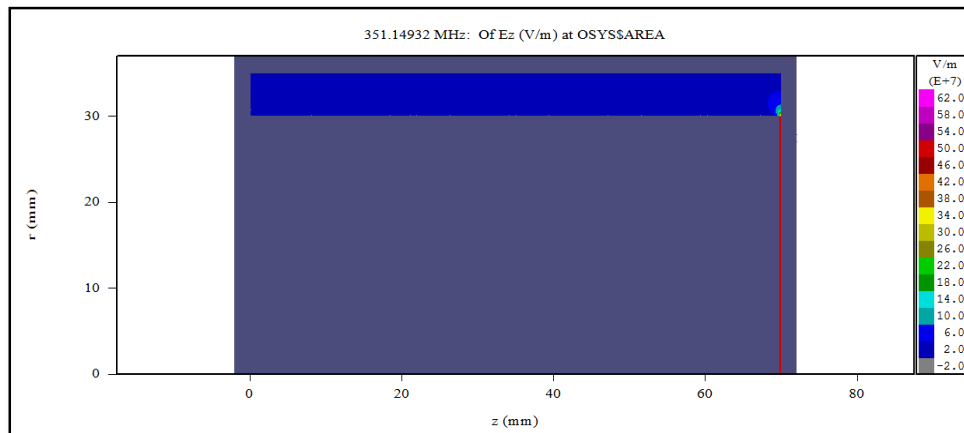


Figure 4: Resonant frequency in MAGIC code.



Figure 5: Fabricated input cavity.

3. CONCLUSION

IOTs are now widely recognized as a useful vacuum tube for various microwave applications. The results of input cavity of an IOT under development at CSIR-CEERI are presented in this paper. The eigen-mode analysis of the cavity has been done in CST as well as MAGIC codes and is

fabricated in the CEERI workshop. From simulations, it can be concluded that the cavity structure presented in the paper will be suitable for generating resonance of the RF input signal in an IOT. The design adopted is also suitable for putting it onto the electron gun structure which is necessary for the velocity modulation of the electron beam.

ACKNOWLEDGMENT

The authors are thankful to Dr. Chandra Shekhar, Director, CSIR-CEERI, for allowing us to present the paper.

REFERENCES

1. Preist, D. H. and M. B. Shrader, "The Klystrode-An unusual transmitting tube with potential for UHF-TV," *Proceedings IEEE*, Vol. 70, No. 11, Invited Paper, November 1982.
2. Carter, R. G., "Simple model of an inductive output tube," *IEEE Transactions on Electron Devices*, Vol. 57, No. 3, March 2010.
3. Kowalczyk, R. D., "Input circuit for a wideband IOT," *IEEE-IVEC*, 15–17, Kitakyushu, May 2007.
4. Shrader, M. B. and D. H. Preist, "Klystrode update," *IEDM*, Vol. 30, 1984.
5. McGinnis, D. and M. Lindroos, "The European spallation source," *2013 IEEE 14th International Vacuum Electronics Conference (IVEC)*, Paris, May 21–23, 2013.
6. Liao, S. Y., *Microwave Devices and Circuits*, 3rd Edition, Pearson Education, 1990.

Polarization Sensitivity Mitigation for AM-CO-OFDMA PON Uplink Transmission

S. M. Jung, K. H. Mun, and S. K. Han

Department of Electrical and Electronic Engineering, Yonsei University
50 Yonsei-ro, Seodaemun-Gu, Seoul, Korea

Abstract— A novel technique for mitigating the polarization sensitivity between the uplink multiple access signals was proposed in the AM-CO-OFDMA PON uplink transmission. To provide uplink multiple access on the orthogonal frequency division multiplexing (OFDM) based optical access network, the polarization difference between the uplink optical signals are unavoidable issue which degrades a transmission performance severely. By using symple digital signal processing with Pythagorean identity, we experimentally demonstrated stable transmission performance of various polarization states of uplink multiple access signals.

1. INTRODUCTION

In recent years, coherent optical transmission is moved down to the area of optical access network with its attractable advantages likes high receiver sensitivity, fineness of its spectral selectivity and dense spectral efficiency [1, 2]. Especially, with orthogonal frequency division multiplexing, the coherent orthogonal frequency division multiple access passive optical network (CO-OFDMA PON) has tremendous attention because of its easy of multiple access with dynamic bandwidth allocation (DBA) on the same nominal wavelength and high spectral efficiency with the adaptive modulation on the individual subcarriers of OFDM signal frame [3]. But, to realize OFDMA based PON system, there are some critical issues which come from the de-correlation of the uplink optical fields which transmitted from each optical network unit (ONU). Because the uplinks signals are carried on the same nominal wavelength, it generates optical beating interference (OBI) effects which related with the optical phase difference of uplink optical fields when it detected at the photo diode [4]. We already solved the OBI problems with the balanced detection of coherent receiver [5]. But, there is another issue in the practical system, the received uplink optical fields couldn't have same polarization states each other because of its different transmission path and responses of the devices in the link. These variously polarized optical fields lead to the signal fluctuation after photo-detection and crosstalk between the multiple access user signals.

In this paper, we proposed polarization sensitivity mitigation technique in CO-OFDMA uplink multiple access and experimentally demonstrated it. By using Pythagorean identity with the intensity modulation for uplink multiple access, we eliminated unwanted phase fluctuations of received optical fields of uplink multiple access signals.

2. SCHEMATICS

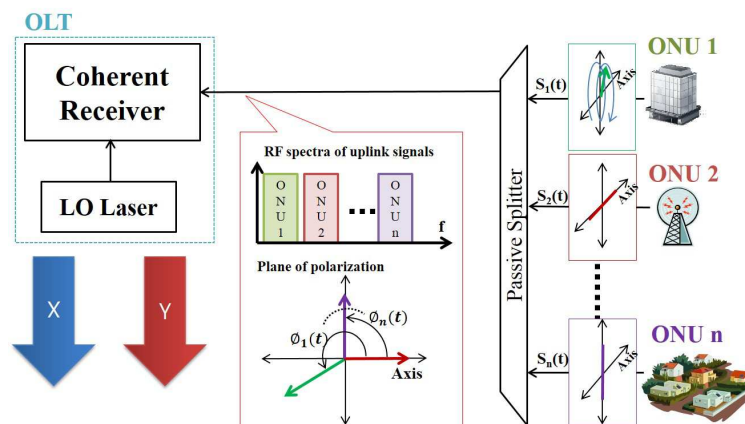


Figure 1: CO-OFDMA uplink transmission.

Figure 1 shows the CO-OFDMA uplink transmission link conceptually in view of RF spectrum and the plane of polarization. In the OFDMA PON, the multiple access can be easily provided by allocating subcarrier sub-bands of OFDM signal frames to each users. In this scheme, especially in uplink transmission, uplink multiple access signals are carried on the optical fields with same nominal wavelength but different transmission paths. These different transmission paths which has different birefringence and channel response in the link cause different polarization responses for each arrived optical fields at the receiver. Because coherent detection uses the optical beating between received signals with local oscillator laser (LO), the polarization mismatch between optical fields of received signals with optical field of LO laser cause unwanted signal fluctuations and signal crosstalk between each polarization output of the coherent receiver. As a result, the received signals at each polarization output of coherent receiver can be described as

$$X(t) = S_1(t) \cos(\phi_1(t)) + S_2(t) \cos(\phi_2(t)) + \dots + S_n(t) \cos(\phi_n(t)). \quad (1)$$

$$Y(t) = S_1(t) \sin(\phi_1(t)) + S_2(t) \sin(\phi_2(t)) + \dots + S_n(t) \sin(\phi_n(t)). \quad (2)$$

where $X(t)$ and $Y(t)$ are two orthogoanl polarization componenets, the parallel with reference polarization axis 'X-polarization' and orthogonal polarization componenets with it 'Y-polarization', respectively, and $S_n(t)$ and $\phi_n(t)$ are the n -th uplink signal and polarization angle with respect to the reference polarization axis in each detection moment. We note here, even though the uplink optical fields are arbitrary polarized, at the received moment, it can be considered as linear polarization with each polarization angles. To eliminate the effect of the polarization mismatch, we use trigonometric features of the sinusoidal function which called Pythagorean identity with additional DC bias because the signals have bipolar amplitude.

$$U(t) = \sqrt{X'^2(t) + X''^2 + Y'^2(t) + Y''^2}$$

$$= \sqrt{DCs + 2 \sum_{k=1}^{n-1} \sum_{j=k+1}^n S_k(t)S_j(t) \cos \{\phi_k(t) - \phi_n(t)\} + 2 \{S_1^2(t) + S_2^2(t) + \dots + S_n^2(t)\}} \quad (3)$$

where $X'(t) = DC + X(t)$, $X''(t) = DC - X(t)$, $Y'(t) = DC + Y(t)$ and $Y''(t) = DC - Y(t)$. By using the Pythagorean process, it generates unwanted DC components and the beating components between the ONU signals. But, because the ONU signals basically have orthogonality each other, during the FFT process of the OFDM demodulation process, the beating components are vanished and the DC components could not have influence on the subcarriers.

3. EXPERIMENTS AND RESULTS

Figure 2 shows the experimental setup for the proposed scheme. In this experiment, we used self-homodyne detection to avoid carrier frequency offset (CFO). An external cavity laser (ECL) with a center wavelength of 1550.223 nm and linewidth of 50 kHz was used as an optical source. And we used 3 dB coupler to split the launched optical source to the signal carrier and the LO source. And there were additional 3 dB coupler to modulate different user signals by using mach-zehnder modulator (MZM) which droved by arbitrary waveform generator. We used polarization controllers (PCs) before the MZM to maximize the modulation efficiency. Between the uplink signal modulators, we used additional polarization controller and polarization scrambler to generate all the possible polarization state between the uplink optical fields. Before the coherent receiver, additional PCs were used to control the optical field to maximize receiver performance. In the experiments, we used DMT as a modulation format. The calculated DMT signal was loaded into an 8 Gs/s arbitrary waveform generator. The number of FFT size was 512 with Hermitian symmetry. So, the number of effective subcarriers was 256 ranging from DC to 4 GHz and each subcarrier were mapped with 4 QAM. Between each ONU subcarrier subbands, we gave the guard band of 8 subcarriers to reduce the inter-user-interference. As a result, the usable subcarriers for ONU 1 were ranging from 5 to 124 and ONU 2 were ranging from 133 to 252, total transmission throughput was 7.38 Gb/s. The received DMT signal was captured by a digital phosphor oscilloscope with sampling rate of 25 Gsample/s and evaluated by offline processing.

Figure 3 shows the RF spectra of the received signal in each experiment. To analyze the effect of the Pythagorean process to the polarization mismatch in the OFDMA PON uplink transmission, we compare the BER for each case. Without the Pythagorean process, the received signal for uplink ONU signals go through the serious fluctuation because of the polarization mismatch between

ACKNOWLEDGMENT

This work was supported by the ICT R&D program of MSIP/IITP, Republic of Korea. [2014-044-012-001]

REFERENCES

1. Lavery, D., R. Maher, D. Millar, B. Thomsen, and S. Savory, "Digital coherent receivers for long-reach optical access networks," *J. Lightwave Technol.*, Vol. 31, No. 4, 609–620, 2012.
2. Straullu, S., F. Forghieri, V. Ferrero, and R. Gaudino, "Optimization of self-coherent reflective PON to achieve a new record 42 dB ODN power budget after 100 km at 1.25 Gbps," *Opt. Express*, Vol. 20, No. 28, 29590–29598, 2012.
3. Cvijetic, N., "OFDM for next-generation optical access networks," *J. Lightwave Technol.*, Vol. 30, No. 4, 384–398, 2012.
4. Banat, M. M. and M. Kavehrad, "Reduction of optical beat interference in SCM/WDMA networks using pseudorandom phase modulation," *J. Lightwave Technol.*, Vol. 12, No. 10, 1863–1868, 1994.
5. Won, Y.-Y., S.-M. Jung, and S.-K. Han, "Suppression of optical beat interference-noise in orthogonal frequency division multiple access-passive optical network link using self-homodyne balanced detection," *Opt. Fiber Technol.*, Vol. 20, No. 4, 309–313, 2014.

Optically Controlled Triple Notched UWB Antenna

Heba Zakaria¹, Moataza Hindy², and Adel El-Henawi¹

¹Faculty of Engineering, Ain Shams University, Cairo, Egypt

²Electronics Research Institute, Cairo, Egypt

Abstract— This paper presents a new optically controlled reconfigurable ultra-wideband antenna (UWBA). The coplanar fed microstrip antenna can work at eight modes using optically controlled switches. This design proposes triple narrow notched bands at center frequencies 3.5 GHz “WIMAX”, 5.5 GHz “WLAN” and 8.4 GHz. The proposed antenna satisfies the voltage standing wave ratio (VSWR) requirement of less than 2 in the frequency band between 2.8 to 11.8 GHz except for the three rejected bands. The proposed antenna provides high gain, and high efficiency all over the frequency band excluding the rejected bands.

1. INTRODUCTION

The ultra-wideband (UWB) planar antennas play an increasingly important role in current UWB systems due to its attractive merits, such as small size, low cost and ease of fabrication. Over the commercial frequency band from 3.1 to 10.6 GHz approved by FCC [1] there are some other existing narrowband systems, such as Bluetooth application at center frequency of 2.45 GHz, WiMAX system (3.4–3.7 GHz), C-band satellite (3.7 to 4.2 GHz) and Wireless Local Area Network (WLAN) communication systems (5.15–5.35 GHz) and (5.725–5.825 GHz), WPAN and 7.15–9 GHz [1]. To avoid possible interference between UWB system and these bands it is desirable to design UWB antennas with notched bands. Electronic switches were mounted across or along the resonators to activate the corresponding band notches. Simple microwave switches have been applied in designs to control antennas, filters, phase shifters, and couplers [2–7]. The research of optically controlled microstrip switches started in 1970s and is continuing throughout to today. Advantage of optically controlled microwave circuits is high level of isolation between the controlling electronic circuit and the microwave circuit [6]. Optical switches were introduced in the designs for achieving frequency and beam reconfigurable antennas [7–10].

2. ANTENNA DESIGN

Coplanar fed microstrip UWB antenna was designed on a 35×28 mm FR4 substrate with relative dielectric constant of 4.6 and thickness of 1.5 mm. This design proposes triple narrow notched bands at center frequencies 3.5 GHz “WIMAX”, 5.5 GHz “WLAN” and 8.4 GHz. The notched bands can be achieved by adjusting the dimensions of the microstrip structure and by inserting inverted C, L and U shaped slots. The coplanar fed microstrip UWB antenna is shown in Fig. 1(a) while Fig. 1(b) illustrates the inserted optically controlled switches. The proposed UWBA can work at eight modes using controlling switches ON and OFF. The optical switches are made by placing $0.5 \text{ mm} \times 0.5 \text{ mm}$ silicon wafers over the slots of the resonator. When laser is applied to all switches (ON state) the notches disappear and the antenna operates in full ultra wideband frequency range from 2.8 to 11.8 GHz. In case, all switches are OFF, all the three notches are activated. Table 1 explains the eight modes of operation of the proposed antenna.

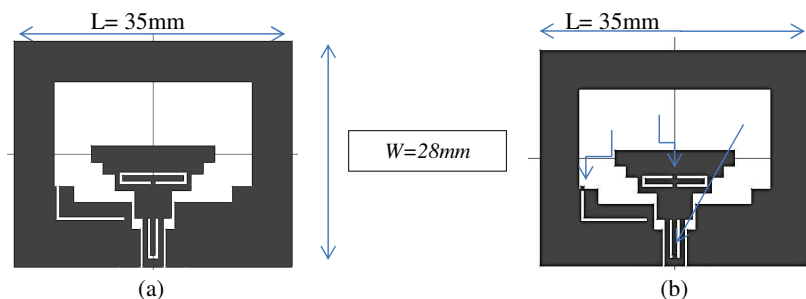


Figure 1. The geometry of the proposed ultra wideband antenna (a) the origin design (b) UWBA without 3 switches.

3. SIMULATION AND EXPERIMENTAL RESULTS

Figure 2 shows the simulated VSWR in two cases, when all switches are either ON (state 1) or OFF (state 2) as shown in Table 1. The bands with center frequencies 3.5, 5.5, and 8.5 GHz are rejected when all switches (S_1 , S_2 and S_3) are OFF. When all switches are ON we obtain the UWB range from 2.8 to 11.8 GHz with return losses less than -10 dB. Fig. 3 shows the fabricated antenna while Fig. 4 presents comparison between measured and simulated return loss (S_{11}). Measurements of the antenna was performed in the anechoic chamber and it fits fairly well with IE3D simulations. Moreover, the average gain of this antenna is 4.5 dBi (Fig. 5).

case	Notched Band	S_1	S_2	S_3
1	3.5 & 5.5 & 8.5 GHz	OFF	OFF	OFF
2	None	ON	ON	ON
3	3.5 GHz	ON	OFF	ON
4	5.5 GHz	OFF	ON	ON
5	8.5 GHz	ON	ON	OFF
6	3.5 & 5.5 GHz	OFF	OFF	ON
7	3.5 & 8.5 GHz	ON	OFF	OFF
8	5.5 & 8.5 GHz	OFF	ON	OFF

Table 1.

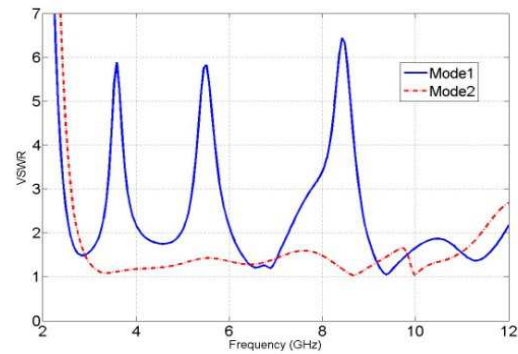


Figure 2. VSWR of UWBA model1 “state 1” mode2 “state 2” UWB from 2.8 to 11.8 GHz.



Figure 3. Fabricated antenna.

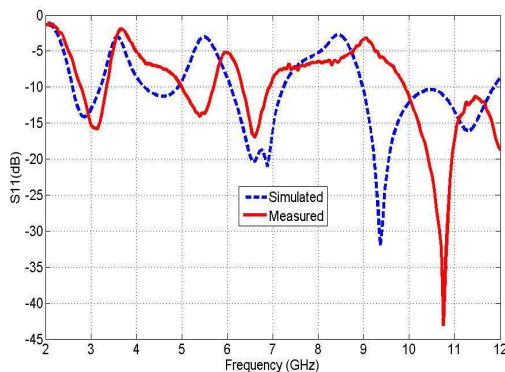


Figure 4. Measured and simulated S_{11} for state 1 of the UWBA.

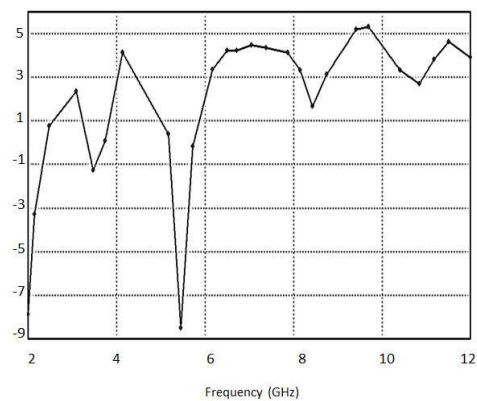


Figure 5. Antenna gain at state 1.

4. RADIATION PATTERNS

The simulated E -plane- and H -plane normalized radiation patterns at 3.475, 5.455, 8.425 GHz and 9.69 GHz for state 1 are plotted in Fig. 6. Radiation patterns are semi omni-directional.

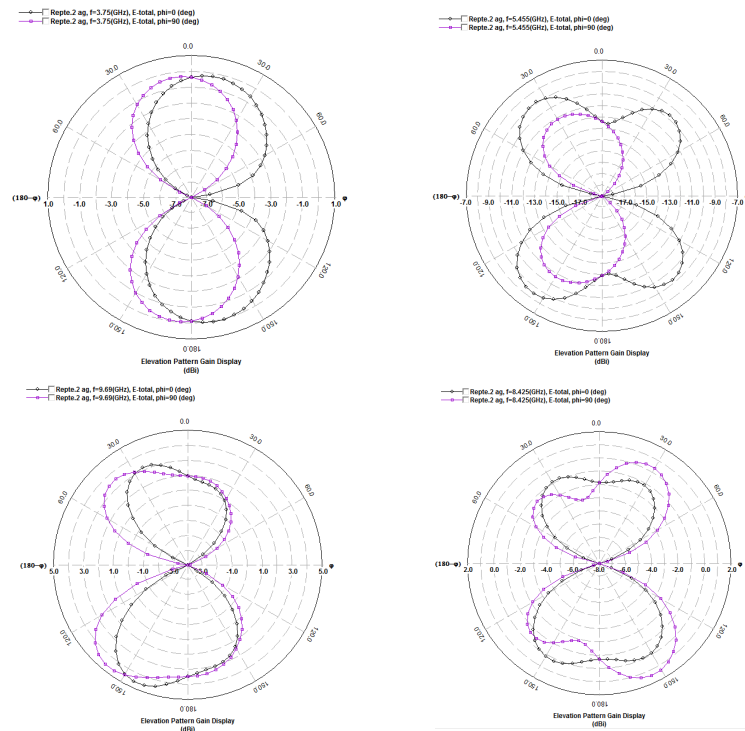


Figure 6.

REFERENCES

1. First Report and order, "Revision of part 15 of the commission's rule regarding ultra-wideband transmission system FCC 02-48," Federal Communications Commission, 2002.
2. Flemish, J. R. and R. L. Haupt, "Optimization of a photonicly controlled microwave switch and attenuator," *IEEE Transactions on Microwave Theory and Techniques*, Vol. 58, No. 10, 2582–2588, 2010.
3. Hindy, M. A., "Wave guide tapers, attenuates and switches using laser control," *Proceedings of the IEEE Midwest Symposium on Circuits and Systems*, 700–703, USA, 1988.
4. Hindy, M. A., "High speed microstrip switching," *The Proceedings of the Midwest Symposium on Circuits and Systems*, 708–711, USA, 1989.
5. Hindy, M. A., "MM-wave filter with laser control in waveguide," *Journal of Applied Optics (OSA)*, Vol. 34, No. 36, 8294–8297, Dec. 1995.
6. Al-Ruwaihi, K. M. and M. A. Hindy, "Analysis of a digital microstrip optical switch: A novel method," *Journal of Applied Optics, OSA*, Vol. 36, No. 6, Feb. 1997.
7. Draskovic, D., C. Panagamuwa, J. C. Vardaxoglou, and D. Budimir, "Frequency reconfigurable RF circuits using photoconducting switches," *International Journal of RF and Microwave Computer-Aided Engineering*, Vol. 20, No. 1, 15–21, 2010.
8. Mehranpour, M., J. Nourinia, C. Ghobadi, and M. Ojaroudi, "Dual band-notched square monopole antenna for ultra-wideband applications," *IEEE Antennas Wireless Propag. Lett.*, Vol. 11, 172–175, 2012.
9. Panagamuwa, C. J., A. Chauraya, and J. C. Vardaxoglou, "Frequency and beam reconfigurable antenna using photoconducting switches," *IEEE Transactions on Antennas and Propagation*, Vol. 54, No. 2, 449–454, 2006.
10. Tawk, Y., A. R. Albrecht, S. Hemmady, G. Balkrishnan, and C. G. Christodoulou, "Optically pumped frequency reconfigurable antenna design," *IEEE Antennas and Wireless Propagation Letters*, Vol. 9, 280–283, 2010.

Multicomponent Rogue Waves

A. B. Aceves¹, F. Baronio², M. Conforti³, A. Degasperis⁴, B. Frisquet⁵,
B. Kibler⁵, S. Lombardo⁶, G. Millot⁵, Ph. Morin⁵, and S. Wabnitz²

¹Southern Methodist University, USA

²University of Brescia, Italy

³Lille University, France

⁴University of Rome I, Italy

⁵University of Bourgogne, France

⁶Northumbria University, UK

Abstract— We overview theoretical and experimental advances in the field of rogue wave solutions of multi-component optical wave systems. In these systems, the transfer of energy among the coupled waves may lead to novel and complex extreme wave phenomena. We focus our attention on the case of vector field co-propagation in randomly birefringent optical fibers, and on the coupling among counter-propagating waves in a periodic nonlinear waveguide.

1. INTRODUCTION

Rogue and extreme waves occur in many scientific and social contexts, ranging from hydrodynamics and oceanography to geophysics, plasma physics, Bose-Einstein condensates, financial markets and nonlinear optics. A typical example of rogue wave is given by the sudden appearance in the open sea of an isolated giant wave, whose height and steepness are much larger than the average sea values, that subsequently disappears without a trace. A universal model for the dynamics of rogue waves is provided by the one-dimensional nonlinear Schrödinger (NLS) equation in the self-focusing regime [1, 2]. Here the mechanism that leads to the generation of rogue waves is nonlinear wave mixing, that generates modulation instability (MI) of the continuous wave (CW) background. The nonlinear development of MI past the initial stage of exponential sideband amplification is described by families of exact solutions such as the Akhmediev breathers. A special member of this solution family is the Peregrine soliton [3], which represents a wave that is localized both in its space and time dimensions. The Peregrine soliton was only recently experimentally observed in optical fibers [4].

A new frontier in the study of rogue waves is provided by multi-component wave systems, where the transfer of energy among the coupled modes may lead to novel and unexpected complex phenomena: consider for example parametric three-wave interactions in quadratic media [5]. Here we provide an overview of our recent advances in the theory and experiments on multi-component rogue waves, involving either the co-propagation of two orthogonal polarization modes in randomly birefringent optical fibers [6, 7], or the counter-propagation of two linearly polarized waves in a periodic nonlinear Bragg grating [8]. Polarization coupling in randomly birefringent telecommunication fibers is described by the vector NLS equation (VNLSE) or Manakov system. In both the anomalous and in the normal dispersion regime of the fiber, we found a new class of coupled wave rogue wave solutions. In the normal dispersion regime, where MI is absent for scalar waves, we experimentally demonstrated the generation of black vector rogue waves by means of standard telecom components. On the other hand, pulse propagation in periodic fiber Bragg gratings is described by a variant of the massive Thirring model. We found the rational rogue wave solution of the massive Thirring model, which opens the way for the observation of rogue waves in periodic optical media.

2. POLARIZATION ROGUE WAVES

Let us consider first the VNLSE (also known as Manakov system), that we write in a dimensionless form as

$$\begin{cases} iu_t^{(1)} + u_{xx}^{(1)} - 2s \left(|u^{(1)}|^2 + |u^{(2)}|^2 \right) u^{(1)} = 0 \\ iu_t^{(2)} + u_{xx}^{(2)} - 2s \left(|u^{(1)}|^2 + |u^{(2)}|^2 \right) u^{(2)} = 0, \end{cases} \quad (1)$$

where $u^{(1)}(x, t)$, $u^{(2)}(x, t)$ represent field envelopes and x , t are the transverse and longitudinal coordinates, respectively. Subscripted variables in Eq. (1) stand for partial differentiation. Here,

we have normalized the equations in a way such that $s = \pm 1$. Note that in the case $s = -1$, Eq. (1) refer to the focusing (or anomalous dispersion) regime; in the case $s = 1$, Eq. (1) refer to the defocusing (or normal dispersion) regime.

As shown in [6, 7], both semi-rational and rational solutions of the VNLSE exist, with the property of representing amplitude peaks that are localized in both x and t coordinates. These solutions are constructed by means of the standard Darboux dressing method and, for Eq. (1) with $s = -1$ (anomalous dispersion regime), semi-rational solutions be expressed as [6]

$$\begin{pmatrix} u^{(1)}(x, t) \\ u^{(2)}(x, t) \end{pmatrix} = e^{2i\omega t} \left[\frac{L}{B} \begin{pmatrix} a_1 \\ a_2 \end{pmatrix} + \frac{M}{B} \begin{pmatrix} a_2 \\ -a_1 \end{pmatrix} \right], \tag{2}$$

with the following notation: $L = \frac{3}{2} - 8\omega^2 t^2 - 2a^2 x^2 + 8i\omega t + |f|^2 e^{2ax}$, $M = 4f(ax - 2i\omega t - \frac{1}{2})e^{(ax+i\omega t)}$, and $B = \frac{1}{2} + 8\omega^2 t^2 + 2a^2 x^2 + |f|^2 e^{2ax}$, where f is a complex arbitrary constant. The dressing construction of the vector rogue wave (2) leads to the arbitrary complex parameter f , and two real parameters a_1, a_2 associated with the background plane wave. We note also that the dependence of L, M and B (see (2)) on x, t is both polynomial and exponential only through the dimensionless variables ax and $\omega t = a^2 t$. Moreover the vector solution (2) turns out to be a combination of the two constant orthogonal vectors $(a_1, a_2)^T$ and $(a_2, -a_1)^T$ [6].

The superposition of the dark and bright contributions in each of the two wave components $|u^{(j)}|$ may lead to complicated breather — like pulses. The single contributions of the dark shape L/B and bright shape M/B are better displayed when f.i. $a_2 = 0$. In this case typical distributions $|u^{(1)}(x, t)|, |u^{(2)}(x, t)|$ are displayed in Fig. 1. Here we show a vector dark-bright soliton together with a single Peregrine soliton. By decreasing the value of $|f|$, Peregrine and dark-bright solitons separate. By increasing $|f|$, Peregrine and dark-bright solitons merge and the Peregrine bump cannot be identified while the resulting dark–bright pulse appears as a boomeron-type soliton, i.e., a soliton solution with a time-dependent velocity.

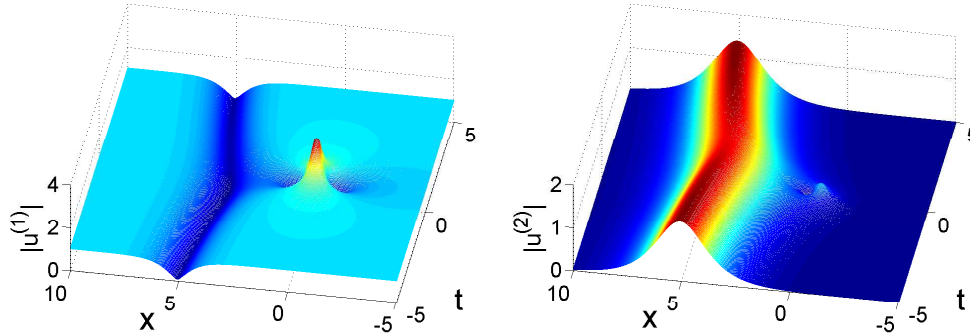


Figure 1: Deterministic vector freak wave envelope distributions $|u^{(1)}(x, t)|$ and $|u^{(2)}(x, t)|$ of (2). Here, $f = 0.1, a_1 = 1, a_2 = 0$.

On the other hand, in the normal dispersion or self-defocusing regime Eq. (1) with $s = 1$ have the rational solutions [7]

$$u^{(j)} = u_0^{(j)} \left[\frac{p^2 x^2 + p^4 t^2 + px(\alpha_j + \beta\theta_j) - i\alpha_j p^2 t + \beta\theta_j}{p^2 x^2 + p^4 t^2 + \beta(px + 1)} \right] \tag{3}$$

where

$$u_0^{(j)} = a_j e^{i(q_j x - \nu_j t)}, \quad \nu_j = q_j^2 + 2(a_1^2 + a_2^2), \quad j = 1, 2; \tag{4}$$

represent the backgrounds of expressions (3),

$$\begin{aligned} \alpha_j &= 4p^2 / (p^2 + 4q_j^2), \quad \theta_j = (2q_j + ip) / (2q_j - ip), \quad j = 1, 2; \\ \beta &= p^3 / \chi (p^2 + 4q_1 q_2), \quad p = 2\text{Im}(\lambda + k), \\ q_1 + q_2 &= 2\text{Re}(\lambda + k), \quad q_1 - q_2 = 2q, \quad \chi = \text{Im}k. \end{aligned}$$

As for the computation of the complex value of k and λ , k is either one of the complex solutions of a fourth order polynomial, and λ is the double solution of a cubic polynomial [7].

Figure 2 shows a typical dark-dark solution (3), that will be the object of the experimental study reported in the last section of this article. The family of solutions (3) in the defocusing regime, exhibits a novel feature with respect to the focusing regime solutions. In fact, here threshold conditions for the parameters a_1 , a_2 , q exist, due to the requirement that the parameter k be strictly complex, and that λ be a double solution of its polynomial equation. Quite remarkably, these rogue wave existence conditions are the same conditions that also lead to the presence of baseband modulation instability (MI), that is, to MI gain for arbitrarily small frequency shifts of the sidebands from the orthogonally polarized pumps [7].

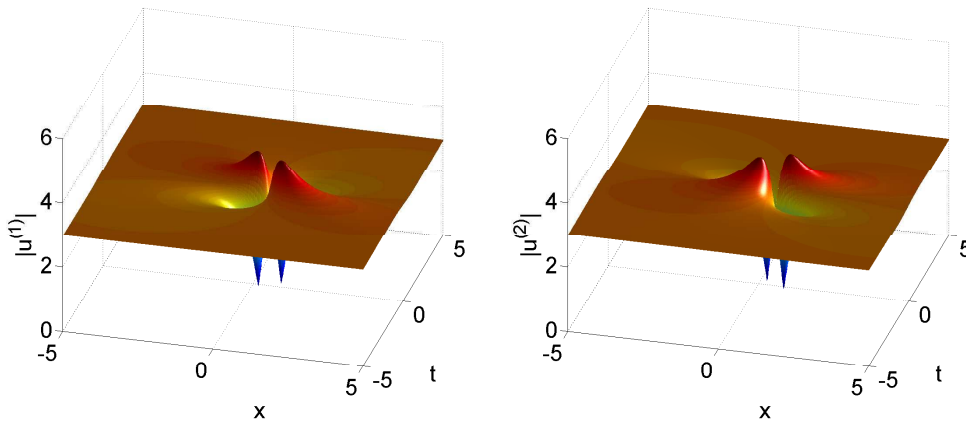


Figure 2: Rogue waves envelope distributions $|u^{(1)}(x,t)|$ and $|u^{(2)}(x,t)|$ of (3). Here, $a_1 = 3$, $a_2 = 3$, $q = 1$. $k = 4.02518i$ and $\lambda = -4.92887i$.

3. ROGUE WAVES IN PERIODIC MEDIA

We discuss now the rogue wave solution of the so-called classical massive Thirring model (MTM), a two-component nonlinear wave evolution equation that is completely integrable by the inverse scattering transform technique [9]. The MTM is a particular case of the coupled mode equations (CMEs) that describe pulse propagation in periodic or Bragg nonlinear optical media [10]. Note that soliton solutions of the MTM can be mapped into Bragg or gap solitons, that enable pulse reshaping and dispersion-less slow light generation in nonlinear Bragg gratings [11].

Let us express the MTM equations for the forward and backward waves with envelopes U and V , respectively, as

$$\begin{aligned} U_\xi &= -i\nu V - \frac{i}{\nu}|V|^2 U \\ V_\eta &= -i\nu U - \frac{i}{\nu}|U|^2 V. \end{aligned} \quad (5)$$

Here the light-cone coordinates ξ , η are related to the space coordinate z and time variable t by the relations $\partial_\xi = \partial_t + c\partial_z$ and $\partial_\eta = \partial_t - c\partial_z$, where $c > 0$ is the linear group velocity. By developing a novel form of the Darboux transform method [12], we obtained the MTM rogue soliton solution

$$U = ae^{-i\omega t} \frac{\mu^*}{\mu} \left[1 - \frac{4}{\mu^*} q^*(q+i) \right], \quad V = -ae^{-i\omega t} \frac{\mu}{\mu^*} \left[1 - \frac{4}{\mu} q^*(q+i) \right] \quad (6)$$

where: $\omega = -\nu(1 - \frac{a^2}{\nu^2})$, $q = -\frac{a^2}{\nu c}(ip(z - z_0) - c(t - t_0))$, $p = \sqrt{\frac{\nu^2}{a^2} - 1}$, $\mu = 2|q|^2 - iq + iq^* + 1 - \frac{1}{p}(q - q^* + i)$, and z_0 and t_0 are arbitrary space and time shifts.

Figure 3 shows an example of the analytical rogue wave solution (6). Here we have set $\nu = -1$, $c = 1$, $a = 0.9$, $t_0 = 2$ and $z_0 = 3.5$. As can be seen, the initial spatial modulation at $t = 0$ evolves into an isolated peak with a maximum intensity of about *nine times* larger than the CW background intensity. We numerically confirm the stability of the analytical solution (6), and show that it may also be applied to describe the generation of extreme waves in the more general context of nonlinear grating propagation as described by the CMEs. Finally, we discuss the physical implementation

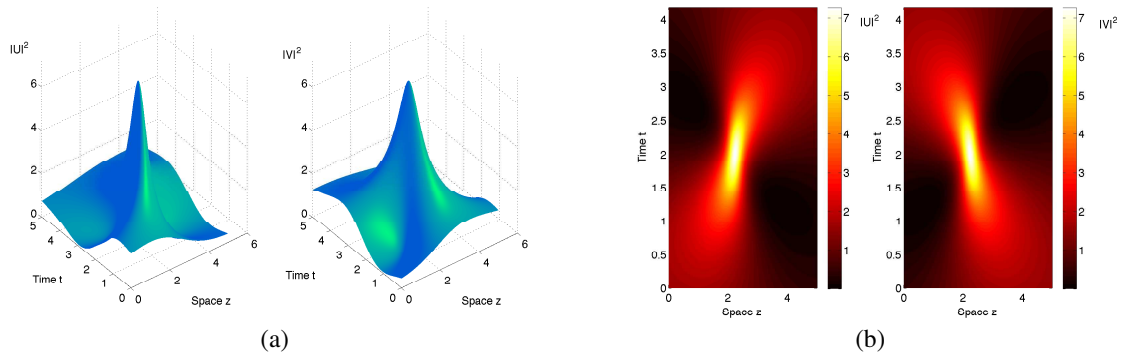


Figure 3: Space-time evolution of intensities in forward and backward rogue components: (a) surface or (b) contour plots.

of MTM rogue waves by using electromagnetically induced transparency, which leads to giant enhancement of cross-phase modulation, and suppression of self-phase modulation [13].

4. EXPERIMENTAL RESULTS

Let us finally discuss the experimental observation of vector dark-dark rogue wave solution of the VNLSE (3), resulting from the nonlinear coupling of two orthogonally polarized pump waves, propagating at different carrier frequencies in the normal dispersion regime of the randomly birefringent optical fiber. Thanks to cross-phase modulation and dispersive group-velocity walk-off, the two coupled pumps experience baseband MI [7]. Next, the nonlinear evolution of MI leads to the generation of spatio-temporal localized black rogue waves, exhibiting a hole of the optical intensity in each of the waves. In our experiments, MI was induced by the initial intensity modulation of the two orthogonal pumps with the frequency shift Ω . Nonlinear propagation happens in a reverse True Wave fiber, with relatively large normal chromatic dispersion of $-14 \text{ ps nm}^{-1} \text{ km}^{-1}$, the nonlinear coefficient $\gamma = 2.4 \text{ W}^{-1} \text{ km}^{-1}$ and the linear loss coefficient of 0.25 dB/km at $\lambda_0 = 1554.7 \text{ nm}$. This fiber has a very low PMD value ($0.017 \text{ ps km}^{-1/2}$). Panels (e), (f) of Fig. 4 compare the experimentally observed output intensity after propagation in 3 km of fiber (red curves), with the intensity

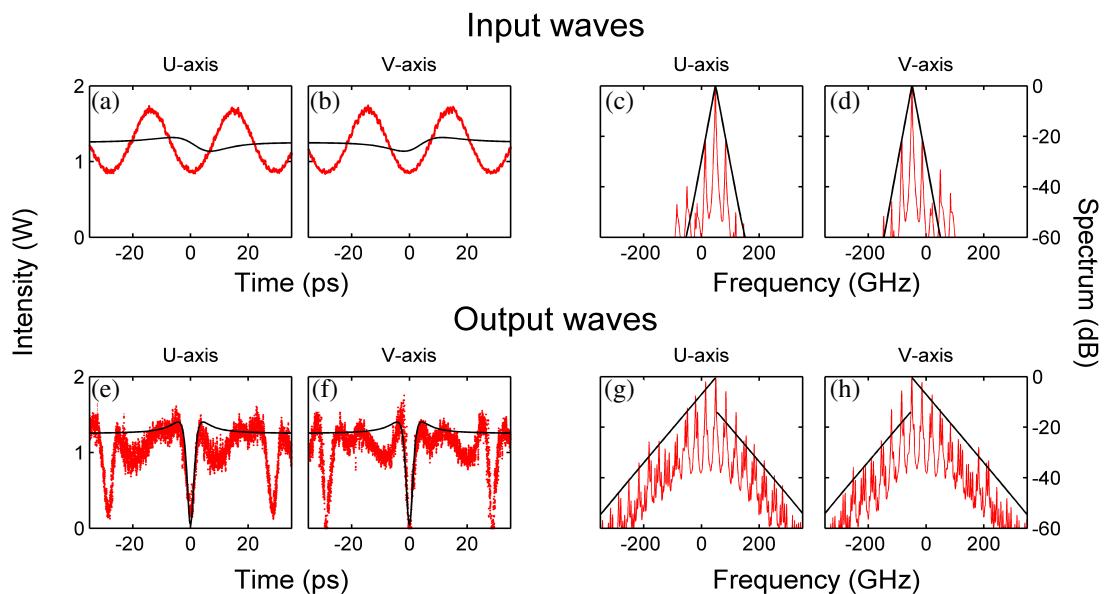


Figure 4: Observation of black vector rogue wave. (a), (b) temporal profile of power in the U and V polarization modes at the fiber input; (c), (d) power spectra at the fiber input; (e), (f) output intensities after 3 km of optical fiber; (g), (h) power spectra at the fiber output. Red solid traces are experimental results and black solid curves represent the analytical black vector rogue wave.

profile of the analytical dark-dark rogue solution (black curves). As can be seen, an excellent agreement is achieved, which is surprising since the experimentally imposed initial modulation is much deeper than the exact solution (see Figs. 4(a), (b)). Note that a temporal periodic experimental waveform (and not a single dark dip) is obtained, because of practical experimental constraints: in principle, an isolated rogue dip could be observed by indefinitely decreasing the initial modulation frequency Ω . Note that the signature of the rogue dip in the frequency domain is the development of a significant spectral asymmetry (see Figs. 4(g), (h)).

5. CONCLUSION

We presented an overview of our recent theoretical and experimental progress on rogue wave solutions of multi-component optical wave systems. In particular, we described rogue waves in both the anomalous and the normal dispersion regime for the co-propagation of two orthogonally polarized modes in a randomly birefringent optical fiber. We further obtained the space-time localized rogue wave solution resulting from the coupling of counter-propagating waves in a periodic nonlinear medium. We have also report the first experimental observation of a multi-component rogue wave, in the form of a dark-dark vector rogue light hole in a telecommunication optical fiber.

ACKNOWLEDGMENT

The present research was supported by the Italian Ministry of University and Research (MIUR, Project Nb. 2012BFNWZ2), the Italian Institute for Nuclear Physics (INFN Project Nb. RM41), and by the Agence Nationale de la Recherche (ANR NoAWE).

REFERENCES

1. Solli, D. R., C. Ropers, P. Koonath, and B. Jalali, "Optical rogue waves," *Nature*, Vol. 450, 1054–1057, 2007.
2. Dudley, J. M., F. Dias, M. Erkintalo, and G. Genty, "Instabilities, breathers and rogue waves in optics," *Nat. Photon.*, Vol. 8, 755, 2014.
3. Peregrine, D. H., "Water waves, nonlinear Schrödinger equations and their solutions," *J. Australian Math. Soc. Ser. B*, Vol. 25, 16, 1983.
4. Kibler, B., J. Fatome, C. Finot, G. Millot, F. Dias, G. Genty, N. Akhmediev, and J. M. Dudley, "The Peregrine soliton in nonlinear fibre optics," *Nat. Phys.*, Vol. 6, 790, 2010.
5. Baronio, F., M. Conforti, A. Degasperis, and S. Lombardo, "Rogue waves emerging from the resonant interaction of three waves," *Phys. Rev. Lett.*, Vol. 111, 114101, 2013.
6. Baronio, F., M. Degasperis, M. Conforti, and S. Wabnitz, "Solutions of the vector nonlinear Schrödinger equations: Evidence for deterministic rogue waves," *Phys. Rev. Lett.*, Vol. 109, 044102, 2012.
7. Baronio, F., M. Conforti, A. Degasperis, S. Lombardo, M. Onorato, and S. Wabnitz, "Vector rogue waves and baseband modulation instability in the defocusing regime," *Phys. Rev. Lett.*, Vol. 113, 034101, 2014.
8. Degasperis, A., A. B. Aceves, and S. Wabnitz, "Bragg grating rogue wave," *Phys. Lett. A*, Vol. 379, 1067, 2015.
9. Kuznetsov, E. A. and A. V. Mikhailov, "On the complete integrability of the two-dimensional classical Thirring model," *Teor. Mat. Fiz.*, Vol. 30, 193, 1977.
10. Aceves, A. B. and S. Wabnitz, "Self-induced transparency solitons in nonlinear refractive periodic media," *Phys. Lett. A*, Vol. 141, 37, 1989.
11. Eggleton, J. B., R. E. Slusher, C. M. de Sterke, P. A. Krug, and J. E. Sipe, "Bragg grating solitons," *Phys. Rev. Lett.*, Vol. 76, 1627, 1996.
12. Degasperis, A., "Darboux polynomial matrices: The classical massive Thirring model as study case," *Journal of Physics A: Mathematical and Theoretical*, arXiv:1411.7965v1, 2014.
13. Schmidt, H. and A. Imamoglu, "Giant Kerr nonlinearities obtained by electromagnetically induced transparency," *Opt. Lett.*, Vol. 21, 1936, 1996.

F-band Millimeter-wave Signal Generation for Wireless Link Data Transmission Using On-chip Photonic Integrated Dual-wavelength Sources

Robinson Guzman¹, Guillermo Carpintero¹, Carlos Gordon¹,
Katarzyna Lawniczak², and Xaveer Leijtens²

¹Tecnología Electrónica, Universidad Carlos III de Madrid, Leganés, Madrid, Spain

²Photonic Integration, Technical University of Eindhoven, Eindhoven, The Netherlands

Abstract— Millimeter-waves (30–300 GHz) have interest due to the wide bandwidths available for carrying information, enabling broadband wireless communications. Photonics is a key technology for millimeter wave signal generation, recently demonstrating the use of photonic integration to reduce size and cost. In this paper, we present two dual-wavelength Photonic Integrated Circuit (PIC) structures designed for signal generation using the optical heterodyne technique. We demonstrate a 1 Gbps data rate wireless link that does not require any stabilization scheme to lock the two wavelengths. Both integrated dual-wavelength sources are based on an Arrayed Waveguide Grating element. A novel building block -Multimode Interference Reflectors (MIRs) — is used to integrate on-chip one of these structures, without need of cleaved facets to define the laser cavity. This fact enables us to locate any of these structures at any location within the photonic chip.

1. INTRODUCTION

Generation of signals with frequencies in the upper millimeter-wave (mmW) band (> 60 GHz) has recently become attractive. This frequency band has a wide range of potential applications from broadband wireless communications, Radio-over-Fiber (RoF) to spectroscopy [1]. In broadband wireless communications, the use of higher mmW carrier frequencies is a cost-effective method that allows increasing the data rate using simple modulation formats as ON-OFF Keying (OOK) or Amplitude Shift Keying (ASK). This avoids costly computational coding schemes. The broad available bandwidth gives these ranges the potential to become key in the convergence between wired (fiber optic networks) and wireless (backhauling 5G) services. Among the obstacles to develop millimeter wave applications is the lack of signal sources [2]. The generation of signals above 100 GHz is challenging using full-electronic techniques [3]. Photonic techniques are considered to be superior providing wide bandwidth, broad tuning range and superior stability.

There are several photonic techniques that are available for mmW generation. Among the different optical signal generation techniques, optical heterodyning is the most promising. This method requires an optical signal source generating two different wavelengths that are mixed into a photodiode or photoconductor (used as photomixer) [4]. The generated signal is an electrical beat-note at a frequency given by the difference between the wavelengths. Photonic integration advances have already been reported in this line [5]. Photonic Integrated Circuits (PIC) have key advantages enabling the integration of multiple photonic building blocks within a single chip, increasing compactness, functionality and performance [5]. Integration reduces fiber coupling interfaces having a huge impact on the cost and component footprint, allowing compact and cost efficient mmW transmitters.

In this work we present a photonic-based millimeter-wave signal source using monolithically integrated dual-wavelength sources based on arrayed waveguide grating (AWG) using a new building block, Multimode Interference reflectors (MIR) [7]. The main advantage of this approach is that we do not require the chip facets for the laser resonator, enabling on-chip post-processing of the dual wavelength signal. In addition, samples were fabricated using a multi-project wafer (MPW) run under a generic technology foundry, which further addresses cost issues. Furthermore, this paper presents our progress in F-band wireless link system technologies that contribute to extending the transmission distance of the wireless links.

2. DUAL-WAVELENGTH LASER SOURCES

Two different structures of monolithically integrated dual-wavelength laser sources (DWLS) have been developed which are suitable for fabrication in a Generic InP-based technology platform

through a Multi-Project Wafer (MPW) run. The first DWLS consists of a set of sixteen SOAs, one per channel, labeled CH N (with $N = 1$ to 16), as shown in Fig. 1(a). All the SOAs used for the channel selection are $600\ \mu\text{m}$ long. An additional SOA is located at the AWG's common output in order to boost the output optical power of the two wavelengths generated by two separated channel biased simultaneously. The length of the Boost amplifier is $750\ \mu\text{m}$. The AWG central wavelength is $\lambda = 1550\ \text{nm}$, the channel spacing $\Delta\lambda = 0.8\ \text{nm}$ (100 GHz) and the FSR is $7.2\ \text{nm}$ (900 GHz). The frequency spacing between the two generated wavelengths is an integer multiple of the AWG channel spacing ($\Delta\lambda$). A drawback of this structure is that the wavelength spacing is not tunable since it is fixed by the AWG.

The novelty of our design is that is an on-chip solution through the use of novel multimode interference reflectors (MIR), shown in Fig. 1(c) to create the required Fabry-Perot cavity of the AWG laser without requiring the facets of the chip which has been implemented and developed on the second DWLS. This device consists of an AWG with 4 channels, one SOA per channel labeled SOA N (with $N = 1$ to 4) and one common output, as shown in Fig. 1(b). Two of the channels implement EOPMs. The designed AWG has a $\Delta\lambda$ and a FSR of $0.961\ \text{nm}$ (120 GHz) and $5.61\ \text{nm}$ (700 GHz), respectively. All the SOAs used both for the channel selection and for the common output are $400\ \mu\text{m}$ long. The lengths of the EOPMs are $1000\ \mu\text{m}$. MIR reflector structures implemented in this design derive from a standard multimode interference (MMI) coupler, in which deeply etched 45 mirrors at suitable locations reflect back the light by total internal reflection.

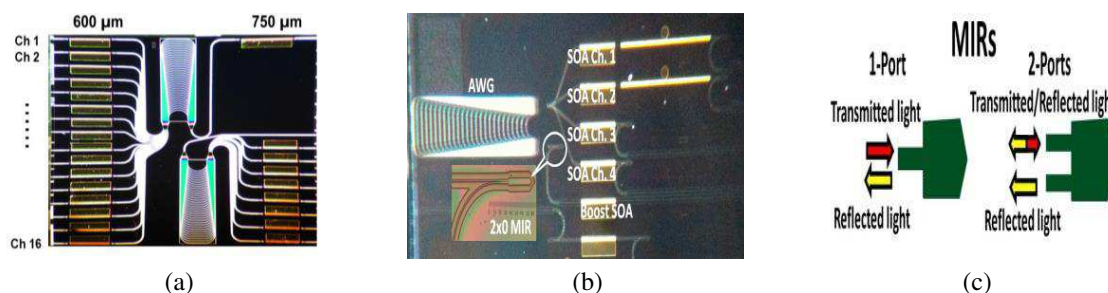


Figure 1: (a) Microscope photograph of cleaved facet structure 16-channels AWGL. The cleaved facets of the chip use as mirror a partially reflective (PR) coated with a reflection value of 32% approximately. (b) Microscope photograph of on-chip structure 4-channels AWG, two of them with EOPM and two other without. MIRs are used to define the FP cavity, and one Boost amplifier at the CO. MIRs' reflectivity has a value about 60%. (c) 1-port (left) and 2-ports (right) MIRs.

3. PHOTONIC WIRELESS LINK DATA TRANSMISSION SYSTEM

This section describes an F-Band (90–140 GHz) wireless data transmission link using the PICs described above as signal sources at the transmitter, with on-off keying (OOK) modulation format and envelope detection at the receiver. In Fig. 2(a), a schematic diagram of the experimental setup where the photonic technique of optical heterodyning is employed for the generation and modulation of mmW signals is shown. A photograph of the photonic wireless link data transmission system measurement setup is shown in Fig. 2(b). A guide rail with a length about 30 cm is used for moving the SBD away from the transmitter, from 0 cm to 24 cm. For evaluating the bit error rate measurement at different distances between the transmitter and receiver, the average output power generated by the U2T PIN photodiode (PD) is set at $2.4 \pm 0.35\ \text{mW}$ for 101 GHz and $0.87 \pm 0.15\ \text{mW}$ for 114 GHz carrier frequency, respectively. The average input optical power of the PIN-PD is set at 10.5 dBm. A difference of 5 dBm between 101 GHz and 114 GHz carrier frequency at the PIN-PD's output is obtained due to the fact that the $-3\ \text{dB}$ cutoff frequency of the PIN-PD is about 95 GHz, thus take this value into account is very important for the analysis of the BER measurement of the wireless link.

In Fig. 3(a) and Fig. 4(a) are shown eye pattern demodulated, amplified and filtered by the receiver module with a wireless carrier frequency of 101 GHz and 114 GHz, respectively. Likewise, in Fig. 3(b) and Fig. 4(b) are shown the bit error rate (BER) characteristics at 1 Gbps for each wireless carrier frequency, respectively. Two different word length, $n = 23$ and $n = 31$ are chosen to measure the quality and performance of the wireless link system at different distances.

The eye patterns are measured using a BERTWave MP2100. As can be seen in Fig. 3(a), the

eye of the received signal is clearly open, even at the maximum distance allowed by the guide rail system. The time variation at zero crossing is below 188 ps and the eye opening 752 ps. This can also be observed by the BER measurement, achieving an error free transmission with a BER $< 10^{-11}$ (both for $2^{23}-1$ and $2^{31}-1$) at 1 Gbps and a distance less than 15 cm, as shown in Fig. 3(b). However, for distances between 15 cm and 24 cm, we have obtained a BER $< 10^{-9}$ (both for $2^{23}-1$ and $2^{31}-1$), being still a good result of the performance of the wireless link system at 101 GHz carrier frequency. For distances in the meter or even kilometer range, additional RF amplifiers would be required as the system performance gets noise limited for such distances. In this receiver scheme, SNR of the system is mostly determined by the noise figure (NF) of set of amplifiers connected after the SBD detector. From Fig. 4(a) and Fig. 4(b), we can observe that the eye pattern at distances larger than 9 cm begin to contract vertically becoming smaller in the center of the eye and as result the BER measurement value is increased. However, the Bit Error Rate (BER) was below 10^{-9} measured using a $2^{23}-1$ and $2^{31}-1$ PRBS sequence at 1 Gbps and ≈ 9 cm distance between Tx and Rx using an 114 GHz carrier frequency.

The wireless link system is limited by the UTC-PD's bandwidth and the responsivity of the whole antenna-integrated SBD including the silicon lens. Therefore, it gives as result a great difference between Fig. 3(b) and Fig. 4(b). The BER measurement can be improved adding a trans-impedance amplifier in order to saturate the received signal from the output of the second LNA.

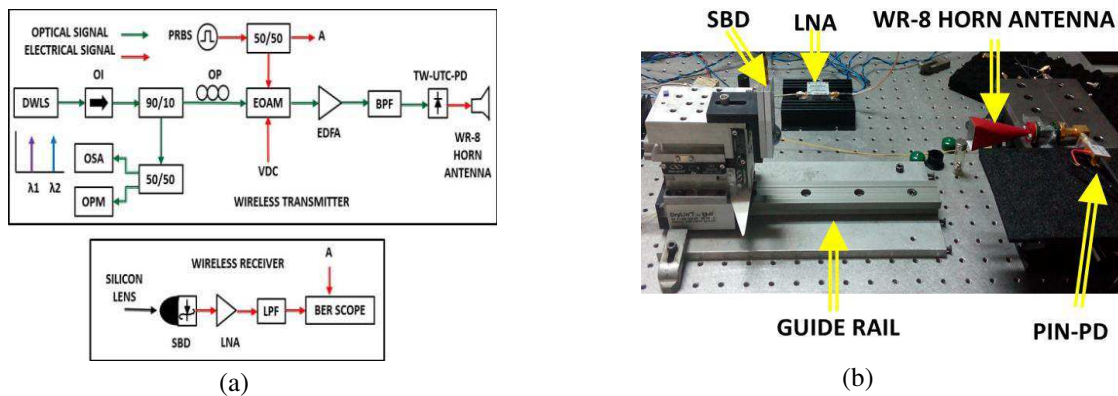


Figure 2: (a) Block diagram of experimental setup used for F-Band (90–140 GHz) Wireless Link Communication System based on OOK modulation and direct data detection. Data is modulated using an amplitude modulator (EOAM) and amplified using Erbium-doped fiber amplifiers (EDFA). A high speed photodiode launches the electric signal. (b) Photograph of the wireless link measurement setup. A guide rail system is used for moving the receiver away from the transmitter, from 0 cm to 24 cm.

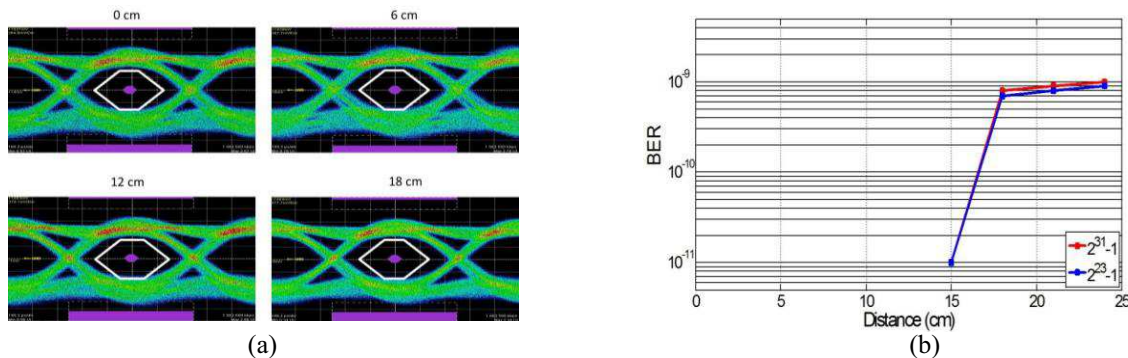


Figure 3: (a) Eye-Pattern of the received PRBS data, $n = 31$, at 1 Gbps after the transmission of the wireless link. The wireless receiver is placed at different distance from the transmitter, as shown in Fig. 2(b). The carrier frequency is about 101 GHz using a non-return zero digital (NRZ) signal. (b) Bit Error Rate (BER) against distance between the transmitter and the receiver. Two different word length, $n = 23$ and $n = 31$ are selected in order to measure the quality and performance of the wireless link system at different distances.

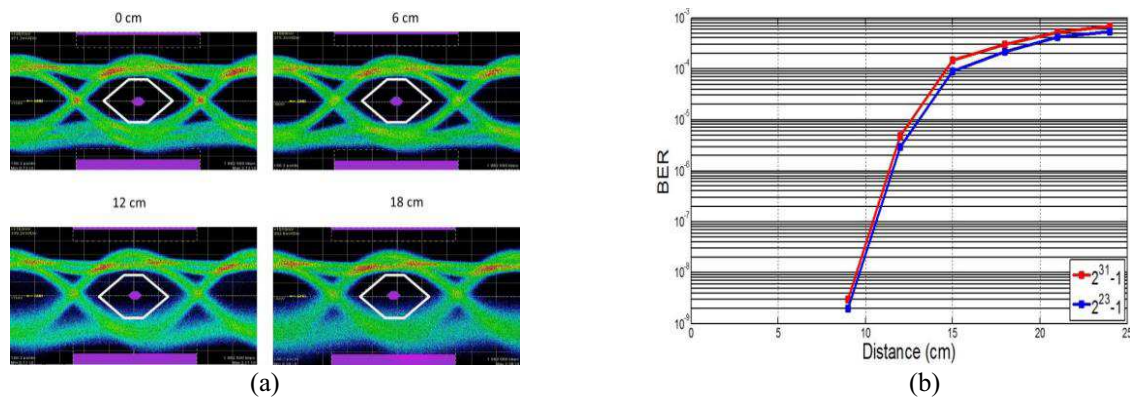


Figure 4: (a) Eye-Pattern of the received PRBS data, $n = 31$, at 1 Gbps after the transmission of the wireless link. The wireless receiver is placed at different distance from the transmitter, as shown in Fig. 2(b). The carrier frequency is about 114 GHz using a non-return zero digital (NRZ) signal. (b) Bit Error Rate (BER) against distance between the transmitter and the receiver. Two different word length, $n = 23$ and $n = 31$ are selected in order to measure the quality and performance of the wireless link system at different distance.

4. CONCLUSIONS

We have also demonstrated ‘error-free’ transmission over a photonic enabled wireless link at a data rate of 1 Gbps with $\text{BER} < 10^{-11}$ and 10^{-9} over 15 cm and 9 cm distance without observing an error floor (i.e., distance can be extended if RF amplification is provided) using carrier frequencies of 101 GHz and 114 GHz, respectively. The system uses two key components, a PIN-PD and a zero-bias Schottky barrier diode receiver. Both have a great potential to realise compact transmitter and receiver modules. These devices was produced on an InP-based technology multi-project wafer run, with great potential to develop low-cost and compact sources and with the possibility to integrate further functionality.

ACKNOWLEDGMENT

This work was supported by Spanish Ministerio de Economía y Competitividad DiDACTIC project (TEC2013-47753-C3-3-R) and Consejera de Educacin, Juventud y Deporte of Comunidad de Madrid DIFRAGEOS project (P2013/ICE-3004).

REFERENCES

1. Kukutsu, N. and Y. Kado, “Overview of millimeter and terahertz wave application research,” *NTT Technical Review*, Vol. 7, No. 3, March 2009.
2. Nagatsuma, T. and H. Ito, “High-power RF uni-traveling-carrier photodiodes (UTC-PDs) and their applications,” *Advances in Photodiodes*, Prof. Gian Franco Dalla Betta (Ed.), ISBN: 978-953-307-163-3, InTech, DOI: 10.5772/14800, 2011.
3. Nagatsuma, T., et al., “Photonic generation of millimeter and terahertz waves and its applications,” *Applied Electromagnetics and Communications*, Vol. 1, No. 4, 24–26, 2007.
4. Seed, A. J., H. Shams, M. J. Fice, and C. C. Renaud, “TeraHertz photonics for wireless communications,” *Journal of Lightwave Technology*, Vol. 33, No. 3, 579–587, 2015.
5. Carpintero, G., K. Balakier, Z. Yang, R.C. Guzmán, A. Corradi, A. Jimenez, G. Kervella, M. J. Fice, M. Lamponi, M. Chitoui, F. van Dijk, C. C. Renaud, A. Wonfor, E. A. J. M. Bente, R. V. Penty, I. H. White, and A. J. Seeds, “Microwave photonic integrated circuits for millimeter-wave wireless communications,” *Journal of Lightwave Technology*, Vol. 32, No. 20, 3495–3501, 2014.
6. Smit, M., X. Leijtens, E. Bente, J. Van der Tol, H. Ambrosius, D. Robbins, M. Wale, N. Grote, and M. Schell, “Generic foundry model for InP-based photonics,” *IET Optoelectronics*, Vol. 187, 2011.
7. Xu, L., X. J. M. Leijtens, et al., “MMI-reflector: A novel on-chip reflector for photonic integrated circuits,” *ECOC Proceedings Vienna '09*, September 2009.

Design and Simulation of Ultra-compact 25-Gbit/s Directly-modulated V-cavity Tunable Laser at 1310-nm Band

Lingxuan Lan, Lin Wu, and Jian-Jun He

Center for Integrated Optoelectronics

State Key Laboratory of Modern Optical Instrumentation

Department of Optical Engineering, Zhejiang University, Hangzhou 310027, China

Abstract— We design and investigate a high-speed directly-modulated tunable V-cavity laser working in the 1310-nm band. The laser is ultra-compact with a device size of only $300\ \mu\text{m} \times 200\ \mu\text{m}$. The simulation results show that $21 \times 200\ \text{GHz}$ tuning with $\sim 40\ \text{dB}$ side-mode suppression ratio is achieved. And the simulated 3-dB bandwidth of small signal response can reach 29.9 GHz. Moreover, 10 Gbit/s and 25 Gbit/s direct modulations are demonstrated with clear eye-opening. Error-free 10-km single-mode fiber transmission is also obtained.

1. INTRODUCTION

In recent years, the spectacular increase of the traffic in both local area and access networks has led to the introduction of high-speed transmission in the 1310-nm band [1, 2]. Tunable semiconductor lasers working in this band have attracted great attention and interest. Besides their use for source sparing with the advantages of reduced inventory and cost, they are also the key components for next-generation wavelength-agile optical networks.

A variety of tunable lasers have been developed with excellent performance, such as sampled grating distributed Bragg reflector (SGDBR) lasers [3, 4], superstructure grating (SSG) DBR lasers [5, 6], digital supermode (DS) DBR lasers [7] and MEMS based lasers [8]. However, in addition to the fabrication complexities involving non-uniform gratings and multiple epitaxial regrowth, tunable lasers based on grating or MEMS structure often need many electrodes and complicated electronic circuits with multi-dimensional current control algorithms and look-up tables for wavelength tuning. Such complexities reduce the fabrication yield and operational reliability, and increase the cost as well.

To mitigate the problem, a V-cavity tunable laser structure has recently been proposed and demonstrated. It has the advantages of fabrication simplicity and compactness, and can achieve good single-mode selectivity while allowing the lasing wavelength to be tuned over a wide range. By employing this V-cavity laser structure, we have designed and investigated a high-speed directly-modulated tunable laser working in the 1310-nm band.

2. DEVICE STRUCTURE

Figure 1(a) shows the schematic diagram of the designed V-coupled cavity laser. It consists of a channel selector cavity and a reference cavity with slightly different optical path lengths, which are coupled by a reflective 2×2 half-wave coupler. The two coupled cavities are defined by deep trench and three electrodes are deposited within them. The gain electrode which covers the active waveguide part of the two cavities and the coupler region is used for providing optical gain and direct modulation signal. And the channel selector electrode works with the reference electrode in tuning the lasing wavelength through the Vernier effect. The detailed theory of this structure has been described in [9].

The active waveguide is based on AlGaInAs/InP multiple quantum wells (MQW) structure with five compressively strained 5.5 nm $\text{Al}_{0.172}\text{Ga}_{0.15}\text{In}_{0.678}\text{As}$ QWs sandwiched between tensilely strained 10 nm $\text{Al}_{0.295}\text{Ga}_{0.22}\text{In}_{0.485}\text{As}$ barriers. And the photoluminescence peak wavelength is about 1295 nm. By carefully designing the graded index (GRIN) layer and reducing the width of ridge waveguide to $2.5\ \mu\text{m}$, the optical field can be well confined in MQW layer while maintaining single transverse mode. In this way, the layer and waveguide structure are optimized to obtain a mode confinement factor of 0.16 for better performance. For passive waveguide, quantum well intermixing technology is used for blue shifting the bandgap, which can reduce the adverse influence of thermal-optic effect on carrier plasma-induced wavelength tuning.

The free spectral ranges of the channel selector cavity and the reference cavity are designed to be 190 GHz (i.e., $220\ \mu\text{m}$ cavity length) and 220 GHz (i.e., $210\ \mu\text{m}$ cavity length), respectively. By optimizing the normalized cross-coupling coefficient $\chi = |C_{12}|^2 \cdot (|C_{12}|^2 + |C_{22}|^2)^{-1}$ to 0.025, a

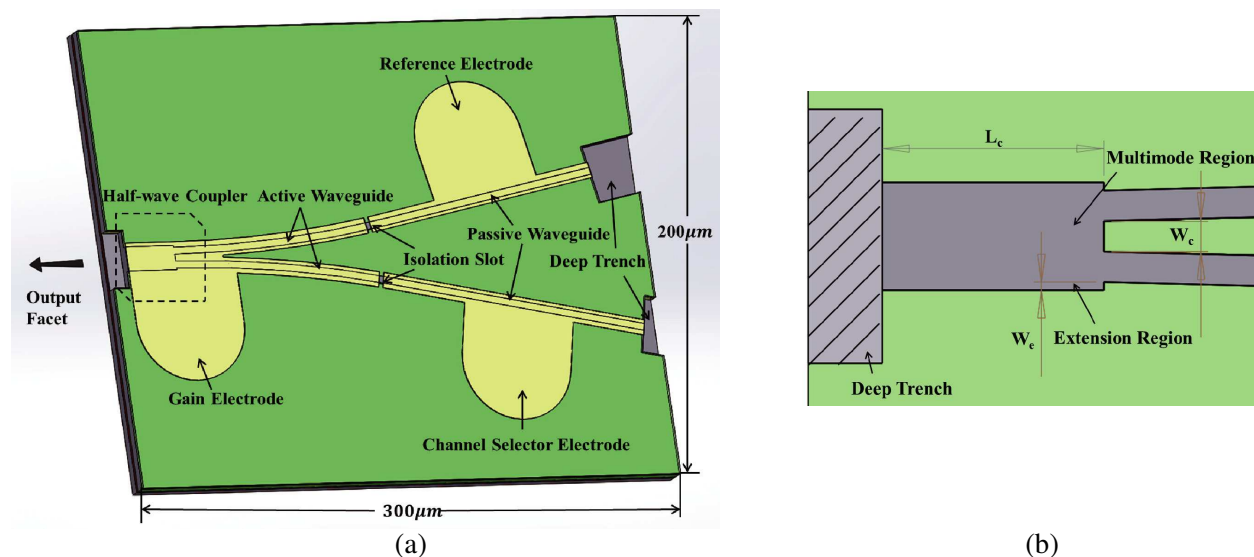


Figure 1: Schematic diagram of (a) the V-cavity laser and (b) the half-wave coupler.

large threshold gain difference of 6.95 cm^{-1} is obtained. To achieve this target χ with a relative phase $\phi = m\pi$ ($m = 0, \pm 1, \pm 2, \dots$) as well as reduce excess loss which can be calculated as $\varepsilon = -10 \log_{10}(|C_{11}|^2 + |C_{12}|^2 + 2|C_{11}||C_{12}|\cos(\varphi))$, two extension regions are added to the half-wave coupler, as shown in Figure 1(b). Through 3D parameters scanning of the width of the extension regions W_e , the width of the gap W_c and the length of the multimode coupling region L_c , the optimal parameters can be found, which are $W_e = 0.5 \mu\text{m}$, $W_c = 2.75 \mu\text{m}$ and $L_c = 26.5 \mu\text{m}$. From the overall structure perspective, the V-cavity laser is ultra-compact with a device size of only $300 \mu\text{m} \times 200 \mu\text{m}$.

3. STATIC AND DYNAMIC CHARACTERISTICS

Static and dynamic simulations for tunable lasers are important for reducing the R&D costs and improving the performance efficiently. The time-domain traveling-wave (TDTW) method is commonly used to model various characteristics of tunable lasers [10, 11]. In this paper, an advanced TDTW implementation called PICWave is used to perform simulations of our device. The details of the theoretical model can be found in [12].

We first calculate the output power emitted from the channel selector cavity facet and the junction voltage as a function of the injected current on the gain electrode while the channel selector electrode and the reference electrode are biased at 9.7 and 26 mA, respectively. As shown in Figure 2, turn-on voltage is about 1 V and threshold current is 23.6 mA. No kinks are observed on the L-I-V curves.

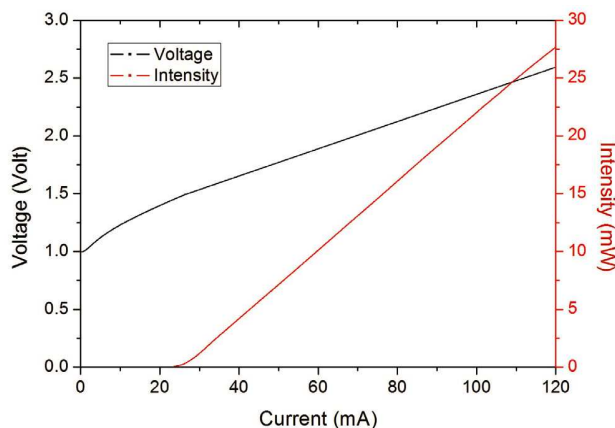


Figure 2: The output power and the voltage as a function of injection current.

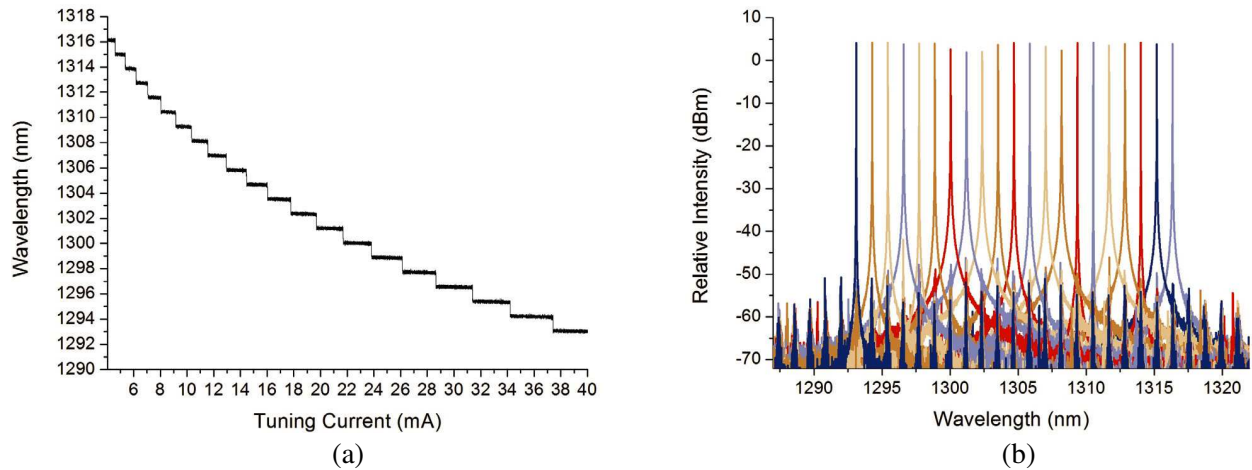


Figure 3: (a) Simulated tuning characteristics and (b) superimposed 21 channels laser spectra.

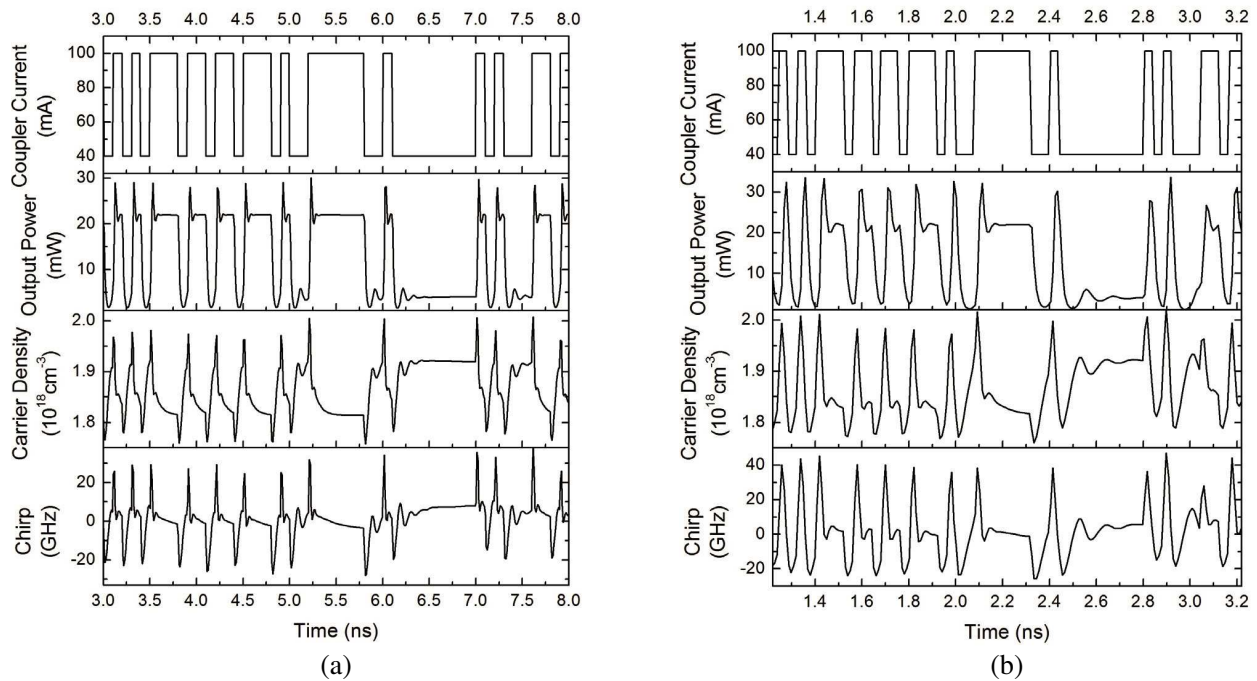


Figure 4: Time response of large signal (a) 10 Gbit/s and (b) 25 Gbit/s direct intensity modulation.

To simulate the single electrode controlled discrete tuning characteristics of the V-cavity laser, we set the current on the gain electrode and the reference electrode fixed at 70 and 26 mA, respectively. As shown in Figure 3(a), when the current on the channel selector electrode increase from 4 mA to 40 mA, wavelength switching of 21 consecutive channels with 200 GHz channel spacing from 1293 to 1316.2 nm is achieved. The corresponding superimposed spectra are shown in Figure 3(b), with about 40 dB side-mode suppression ratio.

Small signal response simulation is carried out by injecting a current impulse to the gain electrode, and then using the FFT algorithm to analyze the frequency spectrum of the received electrical power. The simulated 3-dB bandwidth is 29.9 GHz when the gain electrode is biased at 70 mA, showing good modulation characteristic.

In order to achieve large extinction ratio in direct intensity modulation, large bias current and modulation depth of the RF signal are needed. However, this would increase the wavelength chirp in return. Thus, a compromise between the extinction ratio and the chirp is made. Bias current and modulation depth on the gain electrode are set to 70 and 30 mA, which corresponds to 40 mA for “0” and 100 mA for “1”. Then, 10 Gbit/s and 25 Gbit/s pseudo-random NRZ current signals

are injected into the gain electrode, the time response of output power, the carrier density, and the chirp are simulated through the TDTW model, as shown in Figure 4. From this figure, we can see that as the injected current increases, the output power increases with an obvious overshoot while this overshoot can be suppressed by a low-pass filter in practice. Even though the transient chirp of 25 Gbit/s operation at the rising edge increases about 16 GHz in contrast to 10 Gbit/s operation, the transient chirp at the falling edge and adiabatic chirp don't show any degradation.

A 0.5- μ s-long 10 Gbit/s and a 0.3- μ s-long 25 Gbit/s 32-bit pseudorandom NRZ sequences are used to generate the eye diagrams of the direct intensity modulations, which are shown in Figure 5. Both eyes are clearly open with an extinction ratio of over 8 dB. Then we use OptiSystem Software to simulate the bit error rate (BER) performance for 25 Gbit/s operation after 10-km single-mode fiber transmission. When received power is -10.97 dBm, the BER of received signal is about 3.1×10^{-14} , which shows error-free ($\text{BER} < 10^{-12}$) operation is possible.

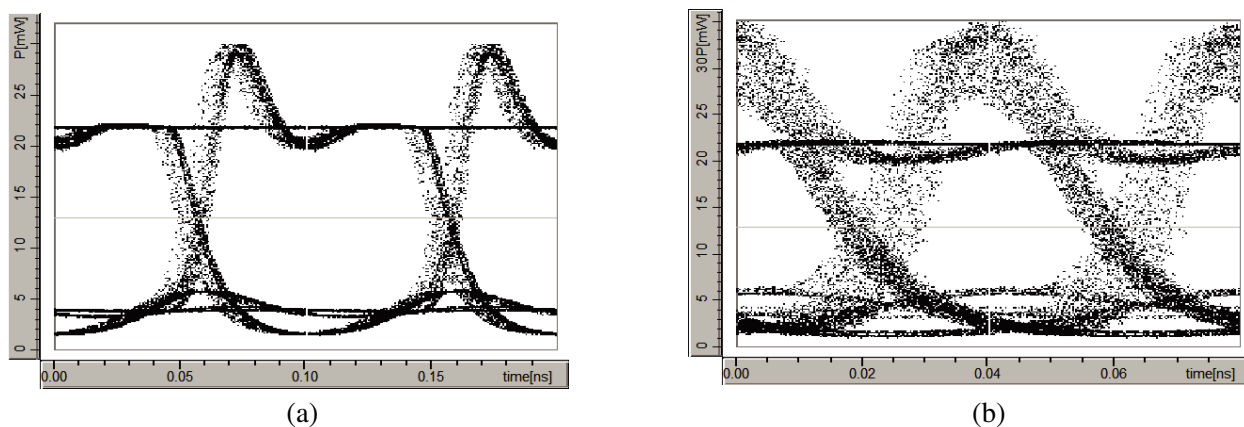


Figure 5: Eye diagram of (a) 10 Gbit/s and (b) 25 Gbit/s direct intensity modulation.

4. CONCLUSION

We have presented the design and simulations of a high-speed directly-modulated tunable V-cavity laser working in the 1310-nm band with an ultra-compact size of $300 \mu\text{m} \times 200 \mu\text{m}$. The time-domain traveling-wave model is employed to investigate the static and dynamic characteristics. 21×200 GHz tuning with ~ 40 dB side-mode suppression ratio is achieved. The simulated 3-dB bandwidth is 29.9 GHz when the gain electrode is biased at 70 mA and extinction ratio of 10 Gbit/s and 25 Gbit/s direct modulations are both over 8 dB. Error-free 10-km single-mode fiber transmission is also obtained. The proposed device is a promising candidate for light source of wavelength-agile access and data center networks.

ACKNOWLEDGMENT

This work was supported by the National High-Tech R&D Program of China (grant 2013AA014401) and the National Natural Science Foundation of China (grant 61377038).

REFERENCES

1. Kapon, E. and A. Sirbu, "Long-wavelength VCSELs: Power-efficient answer," *Nature Photonics*, Vol. 3, No. 1, 27–29, 2009.
2. Ingham, J. D., M. Webster, A. Wonfor, et al., "Wide-frequency-range operation of a high-linearity uncooled DFB laser for next-generation radio-over-fiber," *Optical Fiber Communication Conference*, Optical Society of America, FO3, 2003.
3. Mason, B., G. A. Fish, S. P. Den Baars, et al., "Widely tunable sampled grating DBR laser with integrated electroabsorption modulator," *IEEE Photonics Technology Letters*, Vol. 11, No. 6, 638–640, 1999.
4. Coldren, L. A., "Monolithic tunable diode lasers," *IEEE Journal of Selected Topics in Quantum Electronics*, Vol. 6, No. 6, 988–999, 2000.
5. Tohmori, Y., Y. Yoshikuni, H. Ishii, et al., "Broad-range wavelength-tunable superstructure grating (SSG) DBR lasers," *IEEE Journal of Quantum Electronics*, Vol. 29, No. 6, 1817–1823, 1993.

6. Ishii, H., F. Kano, Y. Tohmori, et al., “Narrow spectral linewidth under wavelength tuning in thermally tunable super-structure-grating (SSG) DBR lasers,” *IEEE Journal of Selected Topics in Quantum Electronics*, Vol. 1, No. 2, 401–407, 1995.
7. Ward, A. J., D. J. Robbins, G. Busico, et al., “Widely tunable DS-DBR laser with monolithically integrated SOA: design and performance,” *IEEE Journal of Selected Topics in Quantum Electronics*, Vol. 11, No. 1, 149–156, 2005.
8. Berger, J. D., Y. Zhang, J. D. Grade, et al., “Widely tunable external cavity diode laser using a MEMS electrostatic rotary actuator,” *IEEE Advanced Semiconductor Lasers and Applications, Digest of the LEOS Summer Topica*, 2, 2001.
9. He, J. J. and D. Liu, “Wavelength switchable semiconductor laser using half-wave V-coupled cavities,” *Optics Express*, Vol. 16, No. 6, 3896–3911, 2008.
10. Dong, L., R. Zhang, D. Wang, et al., “Modeling widely tunable sampled-grating DBR lasers using traveling-wave model with digital filter approach,” *Journal of Lightwave Technology*, Vol. 27, No. 15, 3181–3188, 2009.
11. Zhi, J., H. Zhu, D. Liu, et al., “Travelling wave analysis on high-speed performance of Q-modulated distributed feedback laser,” *Optics Express*, Vol. 20, No. 3, 2277–2289, 2012.
12. Wu, L., J. J. He, and D. Gallagher, “Modeling of widely tunable V-cavity semiconductor laser using time-domain traveling-wave method,” *JOSA B*, Vol. 32, No. 2, 309–317, 2015.

Self-homodyne Detection in Optical Coherent Transmission Using Extracted Carrier as the Local Oscillator by Saturated SOA

K. H. Mun, S. M. Jung, and S. K. Han

Department of Electrical and Electronic Engineering
Yonsei University, 50 Yonsei-ro, Seodaemun-Gu, Seoul, Korea

Abstract— We proposed a self-homodyne coherent detection technique in coherent optical transmission using extracted carrier from the received optical signal by saturated semiconductor optical amplifier (SOA) as LO. Saturated SOA has data erasing characteristic, so LO light can be extracted from the received optical signal by erasing modulated data of the optical signal. In the proposed scheme, there is no CFO because LO light originating from the received signal has a totally same wavelength with the signal. Thus, expensive OFLL or complex CFO compensate algorithm can be avoided; also, colorless operation is possible, and there is no additional requirement of optical fiber for LO light transmission, so it is cost efficient. The test bed has been set up, and the feasibility was experimentally demonstrated.

1. INTRODUCTION

Coherent optical network is one of the possible candidates for next generation optical network because it fits for long-reach transmission in terms of power sensitivity and applicable to single carrier based high order modulation as well as multicarrier modulation: mQAM, OFDM, et cetera. In coherent optical transmission system, the signal is detected by optical mixing it with local oscillator (LO) light; therefore, an unstable relation of these phase and frequency causes phase noise and carrier frequency offset (CFO). In order to realize coherent system, the techniques to mitigate the problems are essential; thus, in coherent communication research area, it is considered for a key technology. Fundamentally, there are two kinds of techniques of solving the problems. It is one of the solution to trace the phase and frequency of the signal, and then match it with that of LO [1, 2]; another solution is using digital signal processing (DSP) which estimates, and compensates phase noise and CFO [3]. However, the first one is inefficient in terms of cost; also, the second one has a disadvantage concerning system latency and complexity.

Self-coherent system, in which LO light is transmitted from the source at transmitter, is a promising alternative in comparison with the aforementioned system [4]. This system is cost efficient because a laser used as LO is not required at the receiver. In addition, CFO compensation algorithm is not needed in the DSP and phase noise occurs less than conventional coherent system because LO light originates from the source; thus, it has an advantage in terms of the system complexity. Especially, self-coherent system is possible to do colorless operation, and the property is a big advantage in case of WDM system expansion. By the way, transmitting LO light at the transmitter through an independent single-mode fiber (SMF) is not efficient; therefore, in self-coherent system, it is one of the main researching issues how transmitting LO light efficiently. There is a scheme using multi-core fiber (MCF) for transmitting LO light through another core with the signal [5]; however, in order to realize the scheme, installation of new MCFs is required. The other technique is using polarization division multiplexing (PDM). In this system, LO light is transmitted through orthogonal polarization with the signal [6]. Using this technique, the transmission capacity increasing by PDM is impossible. Carrier extraction technique, also, can be exploited in self-coherent system. Particularly, in optical OFDM system, dozens of subcarriers around DC is padded with zeros at the transmitter, and then LO light is extracted by Fabry-Perot tunable filter (FP-TF) from the transmitted OFDM signal [7]; also, using injection locked laser, LO light can be enhanced [8]. In case of using FP-TF, its bandwidth should be narrow as laser linewidth ($<$ hundreds of kHz). In addition, the center wavelength of FP-TF should be aligned with that of the carrier; thus, external FP-TF controller is required because of the laser wavelength drift [7].

In this paper, self-homodyne detection scheme using extracted carrier by saturated SOA as LO is proposed. The proposed scheme, in the same manner as the above-mentioned self-coherent system, does not require the laser used as LO and CFO compensation algorithm in the DSP because the LO light is extracted from the transmitted optical signal; therefore, this is comparatively cost efficient and less complex than conventional coherent system. In addition, the high optical power of LO light is gained by SOA. Basically, the receive sensitivity of coherent detection increases in proportion to

the optical power of LO light, so typically, about 10 dBm is required as the optical power of LO. In the proposed system, the LO power requirement can sufficiently be satisfied. Meanwhile, there is no additional requirement of SMF or MCF for LO light transmission; thus, it has an advantage in terms of system realization. In the following Section 1, the concept of the proposed scheme which uses extracted carrier by saturated SOA as LO light is discussed. And then, the experimental set-up is explained; also, the demonstration result is discussed in Section 2. Lastly, the conclusion is following.

2. SELF HOMODYNE DETECTION USING SATURATED SOA

When SOA is operated in the deep saturation region, it acts as an optical data eraser because saturated SOA has a property that a low level signal is given more gain than a high level signal [9]. In the deep saturation region, the saturation property much more enhanced. In other words, the high level signal scarcely has gain; whereas, the low level signal has almost whole gain. Consequently, the extinction ratio of the signal extremely decreases, and the optical signal is erased. Meanwhile, according to [10], saturated SOA has high pass filter property caused by carrier-density depletion and fast phenomena such as carrier transport in multiple layers and fast phenomena. Therefore, carrier extraction can be found filtering the baseband signal. The concept is shown in Figure 1. First of all, the modulated optical signal which has frequency f_0 is separated at the ONU input by the optical power splitter; then, a part of signal is entered SOA1 which acts an optical amplifier providing the enough optical input power of SOA2. This is because the input optical power of SOA2 should be big enough so as to operate in the deep saturation region. Subsequently, Saturated SOA erases the modulated optical signal, and extracts the optical carrier using as LO light. The extracted carrier has frequency f_0 which is totally same as the transmitted signal. Lastly, another part of signal separated at the ONU input is entered to coherent receiver, and then the signal is detected by mixing the optical signal with the extracted optical carrier.

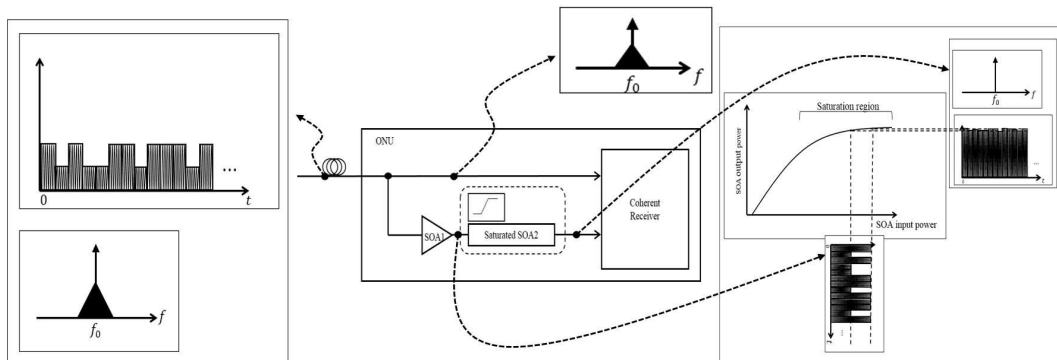


Figure 1: The schematic diagram of self-homodyne detection using extracted optical carrier by saturated SOA as LO light.

3. EXPERIMENT AND RESULTS

Figure 2 presents the experimental set-up. An external cavity laser (ECL) which has 50 kHz linewidth and 1550.223 nm center wavelength was used as the optical source. The electrical QPSK signal was generated by arbitrary waveform generator (AWG), and it was modulated to the optical signal using optical IQ modulator which consists of one mother-Mach zehnder modulator (MZM) and two sub-MZMs. The optical IQ modulator was followed by polarization controller (PC) in order to maximize the MZM output power because it is a polarization dependent component. The transmitted optical signal was divided by 3 dB coupler, and one of them was entered to the input port of coherent receiver and another was entered to the LO port after passing through the carrier extraction part which is consisted of two SOAs. The first SOA acted as an optical amplifier to retain the enough input power of SOA2 for the gain saturation and SOA2 functioned as the optical data eraser. The Each SOA was followed by PC for its polarization dependency, and led by optical tunable filter which has 0.25 nm bandwidth in order to cut out amplified spontaneous emission (ASE) noise. As shown in Figure 2, the input power of SOA2, which is amplified by SOA1, was 8.7 dBm and the output was 9.2 dBm; therefore, in accordance with the fact that SOA2 gain decreased to 0.5 dB, SOA2 was in the deep saturation region. This is because, according to the

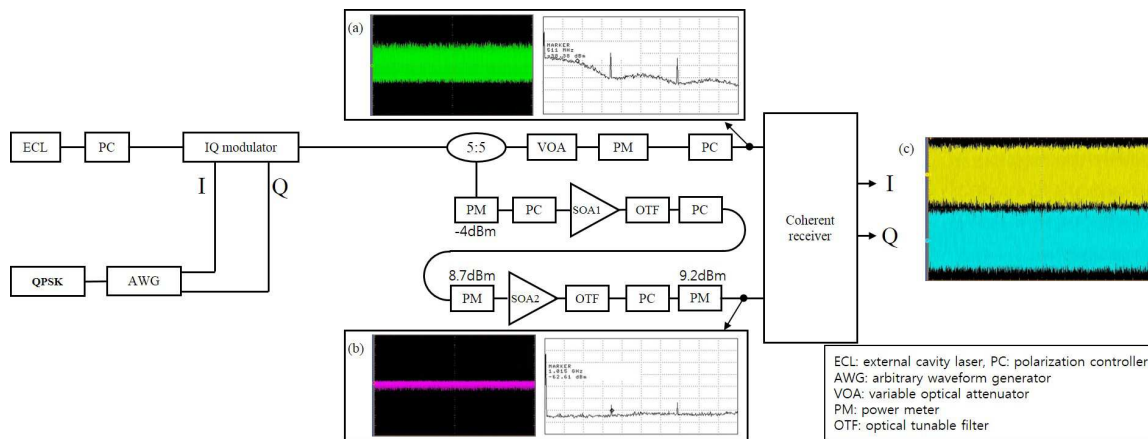


Figure 2: The experimental setup diagram.

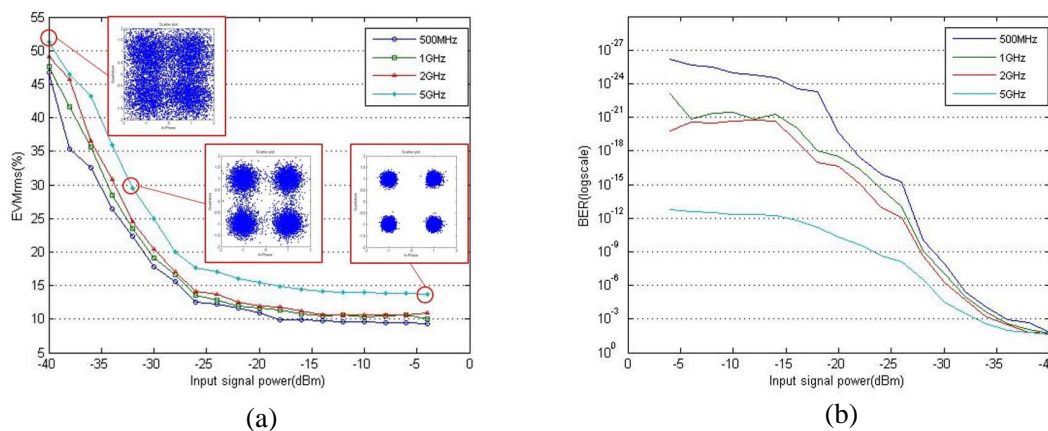


Figure 3: (a) The optical input power vs. EVMrms (%), (b) the optical input power vs. BER.

definition, the output power when SOA gain decreases from typical gain by 3 dB is the saturated output power. The polarization of the optical signal and LO light had to be carefully tuned by PC because the polarization states affects optical mixing process in the coherent receiver.

Figure 2(a) shows the 1 GHz bandwidth QPSK signal which was directly detected in front of the signal input of the coherent receiver in time domain and frequency domain, and erasing the QPSK signal by the saturated SOA is presented in Figure 2(b). After coherent detection using the extracted carrier, each *I* and *Q* signal was separately gotten, and each signal in time domain is presented in Figure 2(c).

To evaluate the system performance, EVMrms was measured according to the input signal power in each case of 500 MHz, 1 GHz and 5 GHz. In Figure 3(a), EVMrms of 500 MHz, 1 GHz and 2 GHz was about 10%, and in case of 5 GHz, it was about 14%. EVMrms increased as the input signal power decreased. Also, along with increasing the signal bandwidth, EVMrms increased because of the high pass filter property of the saturated SOA. Figure 3(b) shows the BER performance according to the input signal power, and as the input power decreased, the BER performance got worse. In case of 500 MHz, 1 GHz and 2 GHz, BER of less than 10^{-12} was obtained by -20 dBm and for the 5 GHz case, it was achieved at -15 dBm. Assuming Reed-Solomon Forward error correction (FEC) limit 10^{-3} for error-free operation, the input power margin was achieved at about -33 dBm in case of 5 GHz and it was achieved about -35 dBm in the others.

4. CONCLUSION

Self-homodyne detection using carrier extraction technique by saturated SOA was proposed, and have been discussed in this paper. In brief, the extracted carrier by saturated SOA can be used as LO light of coherent receiver, and this concept was experimentally demonstrated in order to evaluate the system performance. Assuming Reed-Solomon FEC limit 10^{-3} , the power margin

of -33 dBm was achieved within 5 GHz QPSK transmission. The proposed technique does not need an additional laser for LO, and there is no CFO because the LO light originates from the transmitted optical signal. In addition, without additional installation of SMF or MCF, system realization is possible. For the reasons, the proposed system is cost efficient and has low system complexity. Particularly, it is possible to operate colorless system; therefore, in case of expansion to WDM, it would be very useful.

ACKNOWLEDGMENT

This work was supported by the ICT R&D program of MSIP/IITP, Republic of Korea. [2014-044-012-011].

REFERENCES

1. Camatel, S. and V. Ferrero, "Homodyne coherent detection of ASK and PSK signals performed by a subcarrier optical phase-locked loop," *IEEE Photon. Technol. Lett.*, Vol. 18, No. 1, 142–144, 2006.
2. Chochol, M. and J. M. Fabrega, "Frequency offset compensation loop for 16-QAM optical coherent systems," *ICTON 2011*, 1–4, Stockholm, Sweden, Jun. 2011.
3. Seimetz, M., *High-order Modulation*, 99–115, Springer-Verlag, Berlin, Heidelberg, New York, 2009.
4. Adhikari, S., S. L. Jansen, M. Alfiad, B. Inan, V. A. J. M. Sleiffer, A. Lobato, P. Leoni, and W. Rosenkranz, "Self-coherent optical OFDM: An interesting alternative to direct or coherent detection," *ICTON 2011*, 1–4, Stockholm, Sweden, Jun. 2011.
5. Puttnam, B. J., J. Sakaguchi, W. Klaus, Y. Awaji, J. M. D. Mendinueta, N. Wada, A. Kanno, and T. Kawanishi, "Investigating self-homodyne coherent detection in a 19-core spatial-division-multiplexed transmission link," *Opt. Express*, Vol. 21, No. 2, 1561–1566, 2013.
6. Shinada, S., M. Nakamura, Y. Kamio, and N. Wada, "16-QAM optical packet switching with real-time self-homodyne detection using polarization-multiplexed pilot-carrier," *Proc. ECOC 2012*, 1–3, Amsterdam, Netherlands, Sep. 2012.
7. Adhikari, S., S. L. Jansen, M. Alfiad, B. Inan, A. Lobato, V. A. J. M. Sleiffer, and W. Rosenkranz, "Experimental investigation of self coherent optical OFDM systems using Fabry-Perot filters for carrier extraction," *Proc. ECOC 2010*, 1–3, Munich, Germany, Jun. 2010.
8. Adhikari, S., S. Sygetos, A. D. Eliss, B. Inan, S. L. Jansen, and W. Rosenkranz, "Stabilization of self-coherent OFDM with injection locked laser," *Proc. ICTON 2012*, 1–4, Coventry, England, Jul. 2012.
9. Conforti, E., C. M. Gallep, S. H. Ho, A. C. Bordonalli, and S. M. S. Kang, "Carrier reuse with gain compression and feed-forward semiconductor optical amplifiers," *IEEE Trans. Microwave Theory Tech.*, Vol. 50, No. 1, 77–81, 2002.
10. Kenji, S. and H. Toba, "Reduction of mode partition noise by using semiconductor optical amplifiers," *IEEE J. Quantum Electr.*, Vol. 7, No. 2, 328–333, 2000.

THz Oscillations in DNA Monomers, Dimers and Trimers

K. Lambropoulos, K. Kaklamanis, G. Georgiadis, M. Theodorakou,
M. Chatzieftheriou, A. Morphis, M. Tassi, and C. Simserides

Faculty of Physics, Department of Solid State Physics
National and Kapodistrian University of Athens
Panepistimiopolis, GR-15784 Zografos, Athens, Greece

Abstract— We call *monomer* a B-DNA base-pair and study electron or hole oscillations in *monomers*, *dimers* and *trimers*. We employ two Tight Binding (TB) approaches: (I) at the base-pair level, using the on-site energies of the base-pairs and the hopping parameters between successive base-pairs and (II) at the single-base level, using the on-site energies of the bases and the hopping parameters between neighboring bases. With (II), for monomers, we predict oscillations with frequency $f \approx 50$ –550 THz. With (I), for dimers, we predict oscillations with $f \approx 0.25$ –100 THz, for trimers made of identical monomers $f \approx 0.5$ –33 THz. In other cases, the oscillations may be not strictly periodic, but Fourier analysis shows similar frequency content. For dimers, we compare approaches (I) and (II). Finally, we present calculations with (III) Real-Time Time-Dependent Density Functional Theory (RT-TDDFT) for the adenine-thymine (A-T) and the guanine-cytosine (G-C) base-pairs. It seems that a non conventional source or receiver of electromagnetic radiation with f from fractions to THz to just below PHz could be envisaged.

1. INTRODUCTIONCARRIER

oscillations within “molecular” systems have been sporadically presented in the literature. Real-Time Time-Dependent Density Functional Theory (RT-TDDFT) [1] simulations predicted oscillations (≈ 0.1 -10 PHz) within p-nitroaniline and FTC chromophore [2], zinc porphyrin, green fluorescent protein chromophores and adenine-thymine base-pair [3]. In a simplified single-stranded helix of 101 bases, a collinear uniform electric field induces THz Bloch oscillations [4]. Single and multiple charge transfer within a typical DNA dimer in connection to a bosonic bath, where each base-pair is a single site, has been studied [5], too.

Here we call *monomer* a B-DNA base-pair and study carrier oscillations in *monomers*, *dimers* and *trimers*. We assume that isolation of a few consecutive B-DNA base-pairs is possible, e.g. by connecting at the boundaries moieties with very small transfer integrals with our segment. We employ two Tight-Binding (TB) approaches: (I) at the base-pair level using the on-site energies of the base-pairs and the hopping parameters between successive base-pairs [6, 7] and (II) at the single-base level using the on-site energies of the bases and the hopping parameters between neighboring bases. The TB parameters can be found in Refs. [6–9]. We solve the system of (I) N or (II) $2N$ coupled differential equations to determine the spatiotemporal evolution of an extra carrier (electron or hole) along a N base-pair DNA segment. Carriers move either between the HOMOs or between the LUMOs of the relevant sites [(I) base-pairs, (II) bases]. The resulting oscillations are \approx in the THz domain, a region of intense research [10]. We also perform calculations with (III) RT-TDDFT for the adenine-thymine (A-T) and the guanine-cytosine (G-C) base-pairs. In Section 2 we outline our TB [(I) and (II)] and RT-TDDFT [(III)] approaches. Our results for monomers, dimers and trimers are presented in Sections 3, 4 and 5, respectively. In Section 6 we state our conclusions.

2. THREE APPROACHESACCORDING

to TB approach (I) [description at the base-pair level] the HOMO or LUMO wave function of a given DNA segment, made of N base-pairs, $\Psi_{DNA}(\mathbf{r}, t)$, is considered as a linear combination of the base-pair wave functions $\Psi_{bp}^{\mu}(\mathbf{r})$ with time-dependent coefficients

$$\Psi_{DNA}(\mathbf{r}, t) = \sum_{\mu=1}^N A_{\mu}(t) \Psi_{bp}^{\mu}(\mathbf{r}). \quad (1)$$

$|A_{\mu}(t)|^2$ gives the probability of finding the carrier (hole for HOMO, electron for LUMO) at base-pair μ . The time evolution of the coefficients $A_{\mu}(t)$ obeys the system of equations [8]

$$i\hbar \frac{dA_{\mu}}{dt} = E^{\mu} A_{\mu} + t^{\mu, \mu-1} A_{\mu-1} + t^{\mu, \mu+1} A_{\mu+1}, \quad (2)$$

where E^μ , $\mu = 1, 2, \dots, N$ are the HOMO or LUMO on-site energies of the base-pairs, and $t^{\mu,\mu'}$ are the HOMO or LUMO hopping integrals between two nearest neighboring base-pairs.

According to TB approach (II) [description at the single-base level] $\Psi_{DNA}(\mathbf{r}, t)$ is derived from the single-base wave functions, according to the expression

$$\Psi_{DNA}(\mathbf{r}) = \sum_{\mu=1}^N [A_\mu(t)\Psi_b^{\mu,1}(\mathbf{r}) + B_\mu(t)\Psi_b^{\mu,2}(\mathbf{r})] \quad (3)$$

where $\Psi_b^{\mu,i}$, $i = 1, 2$ and $\mu = 1, 2, \dots, N$, is the wave function of the base at the μ -th base-pair and in the i -th strand. $|A_\mu(t)|^2$, $|B_\mu(t)|^2$ give the probability to find the carrier at the base of strand 1 and 2, respectively, of the μ -th base-pair. In this case, the system of equations is [8]

$$i\hbar \frac{dA_\mu}{dt} = E^{\mu,1}A_\mu + t^{\mu,1;\mu,2}B_\mu + t^{\mu,1;\mu-1,1}A_{\mu-1} + t^{\mu,1;\mu+1,1}A_{\mu+1} + t^{\mu,1;\mu-1,2}B_{\mu-1} + t^{\mu,1;\mu+1,2}B_{\mu+1}, \quad (4)$$

$$i\hbar \frac{dB_\mu}{dt} = E^{\mu,2}B_\mu + t^{\mu,2;\mu,1}A_\mu + t^{\mu,2;\mu-1,2}B_{\mu-1} + t^{\mu,2;\mu+1,2}B_{\mu+1} + t^{\mu,2;\mu-1,1}A_{\mu-1} + t^{\mu,2;\mu+1,1}A_{\mu+1}. \quad (5)$$

$E^{\mu,i}$ are the HOMO or LUMO on-site energies of the base at the μ -th base-pair and in the i -th strand, and $t^{\mu,i;\mu',i'}$ are the HOMO or LUMO hopping parameters between neighboring bases, i.e., between (a) two successive bases in the same strand, (b) complementary bases that define a base-pair, and (c) diagonally located bases of successive base-pairs. To determine the temporal and spatial evolution of electrons or holes along a N base-pair DNA segment, we solve the system of (I) N or (II) $2N$ coupled differential equations with the eigenvalue method [6, 7, 11].

RT-TDDFT is a DFT-based approach for the explicit propagation of the coupled effective single-particle time-dependent Kohn-Sham (TDKS) equations in time. Real-time simulations can be used to compute not only spectroscopic properties (e.g., absorption spectra), but also the time and space-resolved electronic response to arbitrary external fields. Within NWChem computational chemistry package [1], the calculation starts with the computation of the ground state single-particle reduced density matrix \mathbf{P} , whose time evolution is governed by the von Neumann equation (in atomic units)

$$i \frac{\partial \mathbf{P}}{\partial t} = [\mathbf{F}(t), \mathbf{P}(t)]. \quad (6)$$

\mathbf{F} is the time-dependent Fock matrix. The Magnus propagator with a two-step predictor-corrector scheme for the Fock matrix is used for the integration of Eq. (6), which is stable and conserves the density matrix idempotency. At the end of each time step the resulting time-dependent observables (e.g., fragment charge, dipole moment) are computed from the calculated density matrix.

3. MONOMERSWE

used Approach (II), supposing that initially we place the carrier at one of the bases. We can prove that an extra hole or electron oscillates between the bases with frequencies (or periods)

$$f = \frac{1}{T} = \frac{\sqrt{(2t)^2 + \Delta^2}}{h}. \quad (7)$$

t is the hopping integral between the complementary bases and Δ is the energy gap between the on-site energies of the complementary bases. Our results for A-T and G-C, both for holes and electrons, are shown in Fig. 1, with parameters from Ref. [8] (“HKS parametrization”) and from Ref. [9] (“MA parametrization”). For HKS parametrization, $f \approx 50$ – 200 THz ($T \approx 5$ – 20 fs), for MA parametrization, $f \approx 250$ – 550 THz ($T \approx 2$ – 4 fs). These ranges correspond to wavelength $\lambda \approx 545$ nm– 6000 nm, i.e., from visible to near-infrared and mid-infrared. The maximum transfer percentage p [$\max(|B_1(t)|^2)$ for initial conditions $A_1(0) = 1, B_1(0) = 0$] is very small in all cases: the carrier is not very likely to be transferred between the monomer bases. The pure maximum transfer rate pf is also very small in all cases.

We also performed semi-ab initio simulations [12]. Initially, for each (neutral) base-pair, we optimized geometry with Cs symmetry constraint at BNL ($\mu = 0.3$)/6-31G* level of theory. Then, we obtained the initial state through a Constrained DFT calculation [13], with the constraint of an extra carrier at a specific base. Finally, RT-TDDFT computed the time evolution from this initial

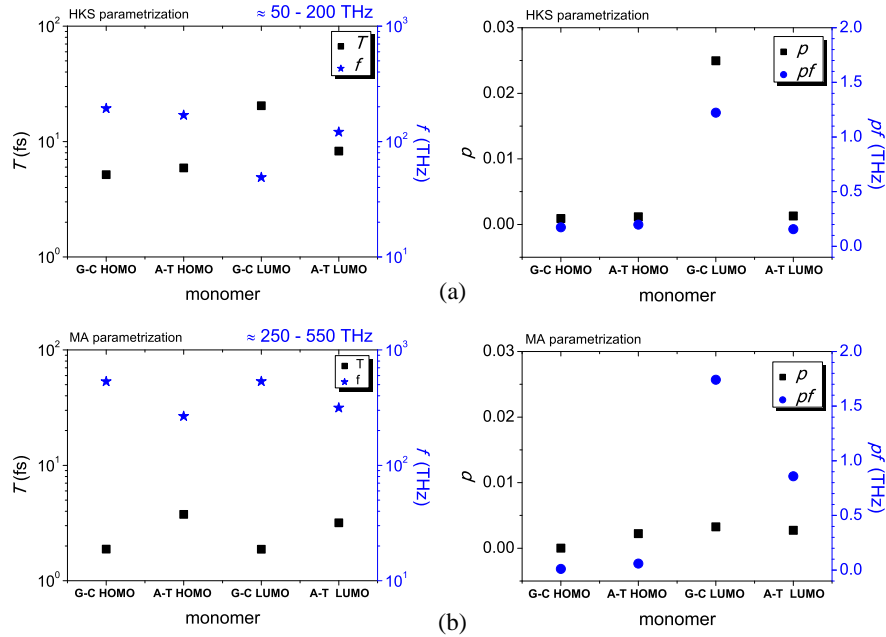


Figure 1: Charge oscillations in A-T and G-C according to the single-base approach (II). (a) TB parameters from Ref. [8] (HKS parametrization). (b) TB parameters from Ref. [9] (MA parametrization).

state, for $t = 1500$ a.u., of fragment charge and total (base-pair) dipole moment at each direction. We extracted oscillation frequencies by FFT analysis from the component of dipole moment parallel to the inter-base axis. Preliminary results indicate one or two major frequencies in the THz range (25–70 THz, 175–740 THz) and one narrow band at the PHz range (2.5–3.5 PHz). THz oscillations are generally predominant, with the exception of G-C monomer when the extra electron (hole) is initially placed on Cytosine (Guanine). The ultrafast oscillations in the PHz range appear to be slightly above the absorption peak of the neutral A-T base pair [3].

4. DIMERSLET

we denote by X_{compl} (Y_{compl}) the complementary base of X (Y). The notation YX means that the bases Y and X of two successive base-pairs are located at the same strand in the direction $5' - 3'$. $X-X_{\text{compl}}$ is the one base-pair and $Y-Y_{\text{compl}}$ is the other base-pair, separated and twisted by 3.4 \AA and 36° , respectively, relatively to the first base-pair. Y and X can be either guanine (G), adenine (A), cytosine (C), or thymine (T).

With approach (I) we proved that the carrier movement in all dimers is strictly periodic [6, 7, 11] and the frequencies (or periods) are given by Eq. (7), where, now t is the hopping integral between the base-pairs and Δ is the energy gap between the on-site energies of the base-pairs. Using the TB parameters from Ref. [6], we found that $f \approx 0.25\text{--}100$ THz ($T \approx 10\text{--}4000$ fs). The maximum transfer percentage $p = 1$ for dimers made of identical monomers; $p < 1$ for dimers made of different monomers. Using approach (II), one cannot strictly determine periodicity in the carrier movement between the four bases. Hence, f , T , p , and pf cannot be defined, but Fourier analysis shows similar frequency content in the THz domain. Approaches (I) and (II) allow us to determine the mean probability to find the carrier at a site [base-pair for (I), base for (II)]. Specifically: (a) Carrier transfer is large in dimers made of identical monomers; it is very small in dimers made of different monomers. (b) For dimers made of identical monomers, if purines are crosswise to purines, the carrier changes strand (from strand 1 to strand 2 or vice versa), while if purines are on the same strand, the carrier is transferred through the strand it was initially placed at. (c) For dimers made of different monomers, the carrier is transferred (albeit in small percentage) through the strand it was initially placed at. A comparison between the mean probabilities found with approaches (I) and (II) is shown in Fig. 2, using the HKS parametrization [8]. Single and multiple charge transfer within a typical DNA dimer in connection to a bosonic bath, where each base-pair is approximated by a single site, as in our TB approach (I), has been studied in Ref. [5]. In the subspace of single charge transfer between base-pairs the authors obtain a period slightly greater than 10 fs, having used a “typical hopping matrix element” 0.2 eV . If we use our Eq. (7), with $t = 0.2 \text{ eV}$ for

the “typical hopping matrix element” and identical dimers, i.e., difference of the on-site energies $\Delta = 0$, we obtain a period $T \approx 10.34$ fs in accordance with the dotted line in Fig. 4 of Ref. [5].

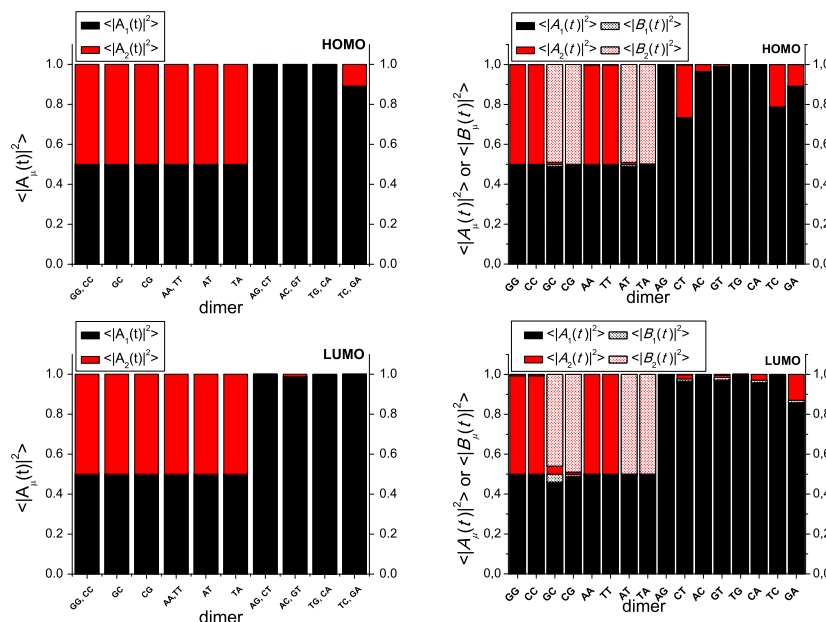


Figure 2: The mean probabilities to find an extra carrier [hole (1st row) or electron (2nd row)] at each site of a DNA dimer, as determined with (I) the base-pair approach (left column) and (II) the single-base approach (right column). For (I), the carrier is initially placed at the 1st monomer, while, for (II), it is initially placed at the base of the 1st monomer that belongs to the 1st strand. We used the HKS parametrization [8].

5. TRIMERSUSING

approach (I), we proved [6, 7] that for trimers made of identical monomers an extra carrier oscillates periodically, according to the expression

$$f = \frac{1}{T} = \frac{\sqrt{t^2 + t'^2}}{h}, \quad (8)$$

where t, t' are the hopping integrals between the base-pairs. For such trimers, when all purines are on the same strand, $t = t'$. Using the TB parameters from Ref. [6], we find that the frequencies of these oscillations are in the range $f \approx 0.5\text{--}33$ THz ($T \approx 30\text{--}2000$ fs) [7], which is narrower than for dimers. For 0 times crosswise purines, the maximum transfer percentage $p = 1$, while for 1 or 2 times crosswise purines $p < 1$ [6, 7]. For trimers made of different monomers, no periodicity can be determined, since the frequencies depend on the specific parameter values used. Hence, carrier movement may be non-periodic [6, 7]. Generally, increasing the number of monomers above three, the system becomes more complex and periodicity is lost [7]; even in the simplest cases, e.g., tetramers made of identical monomers with all the purines on the same strand, there is no periodicity [11]. Approach (II) does not allow one to strictly determine any periodicity, hence T, f, p , and pf cannot be defined. However, Fourier analysis shows similar frequency content.

6. CONCLUSIONWITH

TB approach (II), we predicted electron or hole oscillations in DNA monomers with $f \approx 50\text{--}550$ THz ($T \approx 2\text{--}20$ fs), i.e., $\lambda \approx 0.545\ \mu\text{m}\text{--}6\ \mu\text{m}$, from visible to near- and mid-infrared. For monomers the maximum transfer percentage p and the pure maximum transfer rate pf between the bases are very small. With TB approach (I), we predicted electron or hole oscillations in DNA dimers with $f \approx 0.25\text{--}100$ THz ($T \approx 10\text{--}4000$ fs), i.e., $\lambda \approx 3\text{--}1200\ \mu\text{m}$, in the mid- and far-infrared. For dimers made of identical monomers $p = 1$, but for dimers made of different monomers $p < 1$. With approach (II), the carrier oscillations are not strictly periodic but the frequency content is similar to that predicted with approach (I). For the mean probabilities to find the carrier at a particular site, the two approaches give similar, complementary results. For trimers made of identical monomers the

carrier oscillates periodically with $f \approx 0.5\text{--}33\text{ THz}$ ($T \approx 30\text{--}2000\text{ fs}$) for 0 times crosswise purines $p = 1$, for 1 or 2 times crosswise purines $p < 1$. For trimers made of different monomers the carrier movement may be non-periodic but the frequency content is similar. Finally, calculations based on (III) RT-TDDFT for DNA monomers indicate one or two major frequencies in the THz range (25–70 THz, 175–740 THz) and one narrow band at the PHz range (2.5–3.5 PHz).

ACKNOWLEDGMENT

A. Morphis thanks the State Scholarships Foundation-IKY for a Ph.D. research scholarship via “IKY Fellowships of Excellence”, Hellenic Republic-Siemens Settlement Agreement. M. Tassi thanks the State Scholarships Foundation-IKY for a post-doctoral research fellowship via “IKY Fellowships of Excellence”, Hellenic Republic-Siemens Settlement Agreement. We thank the University Computer Center and Cy-Tera Project (Cyprus) for computer resources.

REFERENCES

1. <http://www.nwchem-sw.org/index.php/Release62:RT-TDDFT>.
2. Takimoto, Y., F. D. Vila, and J. J. Rehr, “Real-time time-dependent density functional theory approach for frequency-dependent nonlinear optical response in photonic molecules,” *J. Chem. Phys.*, Vol. 127, 154114, 2007.
3. Lopata, K. and N. Govind, “Modeling fast electron dynamics with real-time time-dependent density functional theory: Application to small molecules and chromophores,” *J. Chem. Theory Comput.*, Vol. 7, 1344–1355, 2011.
4. Malyshev, A. V., V. A. Malyshev, and F. Domínguez-Adame, “DNA-based tunable THz oscillator,” *Journal of Luminescence*, Vol. 129, 1779–1781, 2009.
5. Tornow, S., R. Bulla, F. B. Anders, and G. Zwicknagl, “Multiple-charge transfer and trapping in DNA dimers,” *Phys. Rev. B*, Vol. 82, 195106, 2010.
6. Simserides, C., “A systematic study of electron or hole transfer along DNA dimers, trimers and polymers,” *Chem. Phys.*, Vol. 440, 31–41, 2014.
7. Lambropoulos, K., K. Kaklamanis, G. Georgiadis, and C. Simserides, “THz and above THz electron or hole oscillations in DNA dimers and trimers,” *Ann. Phys. (Berlin)*, Vol. 526, 249–258, 2014.
8. Hawke, L. G. D., G. Kalosakas, and C. Simserides, “Electronic parameters for charge transfer along DNA,” *Eur. Phys. J. E*, Vol. 32, 291–305, 2010.
9. Mehrez, H. and M. P. Anantram, “Interbase electronic coupling for transport through DNA,” *Phys. Rev. B*, Vol. 71, 115405, 2005.
10. Yin, X., B. W.-H Ng, and D. Abbott, *Terahertz Sources and Detectors, in Terahertz Imaging for Biomedical Applications*, Chapter 2, Springer Science+Business Media, LLC, Springer New York Dordrecht Heidelberg London, <http://www.springer.com/978-1-4614-1820-7>, ISBN 978-1-4614-1820-7 e-ISBN 978-1-4614-1821-4, 2012.
11. Lambropoulos, K., “Charge transfer in small DNA segments: Description at the base-pair level,” Diploma thesis, National and Kapodistrian University of Athens, Greece, 2014.
12. Valiev, M., E. J. Bylaska, N. Govind, K. Kowalski, T. P. Straatsma, H. J. J. van Dam, D. Wang, J. Nieplocha, E. Apra, T. L. Windus, and W. A. de Jong, “NWChem: A comprehensive and scalable open-source solution for large scale molecular simulations,” *Comput. Phys. Commun.*, Vol. 181, 1477–1489, 2010.
13. Wu, Q. and T. Van Voorhis, “Direct optimization method to study constrained systems within density-functional theory,” *Phys. Rev. A*, Vol. 72, 024502, 2005.

Formation of Caustics by Refraction of Structured Laser Radiation in the Diffusive Layer of Liquid

A. V. Vedyashkina, I. L. Raskovskaya, and I. N. Pavlov
 V. A. Fabrikant Physics Department, National Research University
 “Moscow Power Engineering Institute”, Moscow 111250, Russia

Abstract— One of actual and promising method of researching optically inhomogeneous media by using electromagnetic radiation is the method of the laser refractography. It is based on the phenomenon of refraction of structured laser radiation in optically inhomogeneous media and registration of its form deviations with the digital video camera. The case when inhomogeneity in liquid is created by diffusion. It was researched conditions for the occurrence of caustics in longitudinal probing of optical stratified inhomogeneous media by plane and cylindrical laser beams were researched in this work. Experimental setup for caustics visualization was shown. The method was shown for solving the inverse task of finding properties of the medium by analyzing caustics’ location.

1. INTRODUCTION

Nowadays researching of optically inhomogeneous media represents great scientific interest. The refractive index is not the same in any point in such media and light passes due to refraction not rectilinearly. It is often important to know what occurs when two or more mediums with different physical characteristics contact each other, how the refractive index of liquid changes by heating or cooling objects inside it.

One method of researching optically inhomogeneous media is the method of the laser refractography. It is based on the phenomenon of refraction of structured laser radiation (SLR) in optically inhomogeneous media and registration of its form deviations with the digital video camera [1, 2]. This method is essentially different from the methods of researching of optically inhomogeneity that were known previously such as schlieren and shadowgraph techniques [3].

Application of laser techniques for the reconstruction of physical characteristics of medium, causing inhomogeneity of the refractive index it is advisable to probe medium by structured laser beams formed by diffractive optical elements (DOE).

Light lines with a fanciful form appear on the table, when a glass of water is located on it. Similar moving curves can be seen at the bottom of a shallow pond, water surface of which is roughness. These curves are caustics. Caustic is the envelope of light rays reflected or refracted by the curved surface or object [4]. Nevertheless, in this method caustics are special lines and special surfaces, and beside them the intensity of the light field increases sharply [5]. When probing inhomogeneity by SLR caustics appears, its location can be determined by using refractogram processing program with high precision, it is possible to solve the inverse task of finding properties of the inhomogeneous medium. Theory of caustics is directly related with one of mathematical section — the theory of catastrophes [6].

2. DIFFUSIVE LAYER OF LIQUID

Diffusive layer of liquid is a special type of inhomogeneity, which appears near interface of two liquid media with various physical characteristics. Liquids with various refraction indexes are considered in this work. Refraction index of optically denser liquid is n_1 , less dense — n_2 ($n_1 > n_2$) (Fig. 1). Distribution of the refraction index in diffusive layer can be described by different function such as linear or hyperbolic tangent, in this paper exponential model is used [7]:

$$n(x) = n_2 + \frac{n_1 - n_2}{1 + \exp\left(\frac{x-x_s}{h}\right)}, \quad (1)$$

where h — characteristic half-width of layer, x_s — middle of layer.

Let layered-inhomogeneous medium in which there is the diffusive layer has following parameters: $n_1 = 1.3410$, $n_2 = 1.3310$, $x_s = 50$ mm, $h = 1.1$ mm. Distribution of the refraction index is presented in Fig. 2.

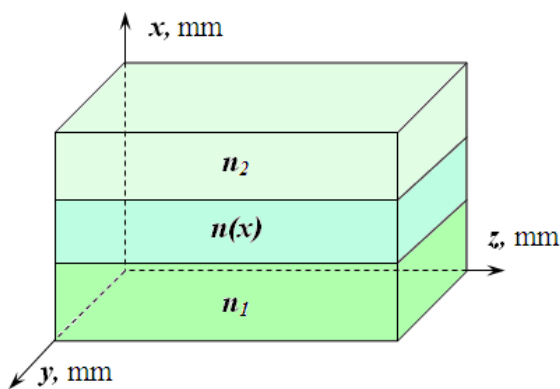


Figure 1: Diffusive layer's model.

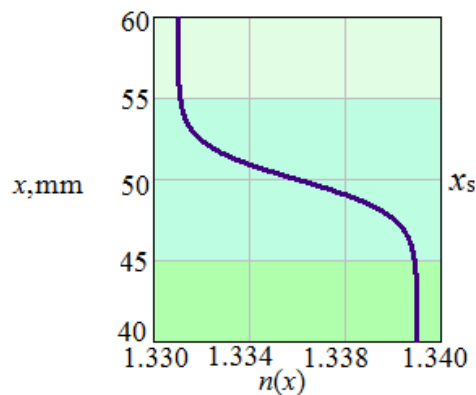


Figure 2: Distribution of refraction index in diffusive layer of liquid.

Relation (2) is the equation of the ray trajectory in a plane-layered medium, given the refractive index distribution $n(x)$ and the initial conditions $z_0 = z(0)$, α_0 — the angle at which the ray enters the medium, n_0 — refraction index in entry point of the ray in medium.

$$z(x) = z_0 + \int_0^x \frac{n_0 \sin \alpha_0 dx}{\pm \sqrt{n^2(x) - n_0^2 \sin^2 \alpha_0}}. \tag{2}$$

Using this expression it is possible to simulate on a propagation of a plane laser beam in diffusion layer of liquid by approximating it with a set of infinitely thin rays. Fig. 3 shows formation and confluence of two caustic surfaces. With the help of this refractogram we can model and determine the location, shape of caustics and the point of confluence it will be possible to solve the inverse task of finding properties of the medium in comparison with the experimental results [8].

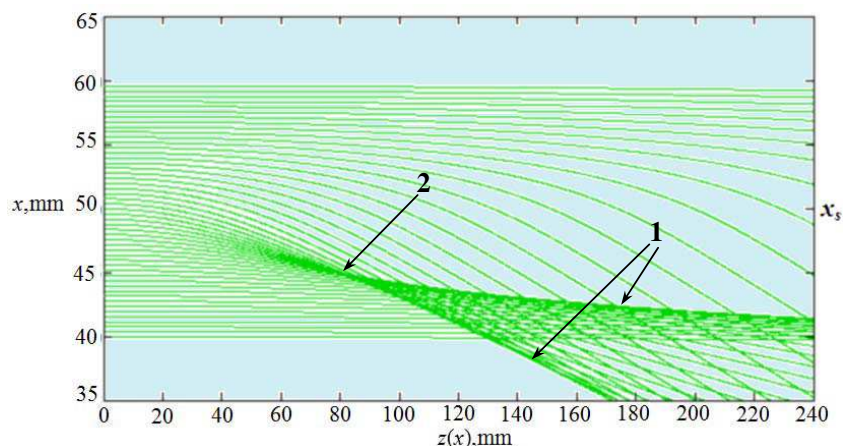


Figure 3: Formation of caustics (1) and point of their confluence (2) in the propagation of a plane laser beam in diffusive layer.

3. CAUSTICS' FORMATION IN EXPERIMENT

In order to observe and register refractogram of plane laser beam propagation in inhomogeneous media it is possible to use setup, which is presented in Fig. 4. Laser 1 and built-in optical system 2 form plane laser beam, which probes cuvette 3 with created diffusive layer 4 in it. 2D-refractogram 6 is registered by digital camera 5 and processed by using special algorithm on personal computer 7.

For creation of diffusive layer of liquid we used distilled water and water-NaCl mixture. Refractogram storing was made by recording the scattered radiation on special particles added in water. Parameters of medium: refractive indexes of saline water $n_1 = 1.3410$ and distilled water $n_2 = 1.3310$. Photo, which was received during experiment is presented in Fig. 5.

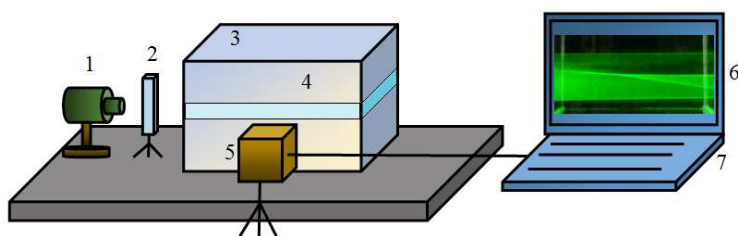


Figure 4: Setup for experiment with the diffusive layer of liquid and probing plane laser beam: 1 — laser, 2 — optical system, 3 — transparent cuvette, 4 — diffusive layer, 5 — digital camera, 6 — 2D-refractogram, 7 — PC.

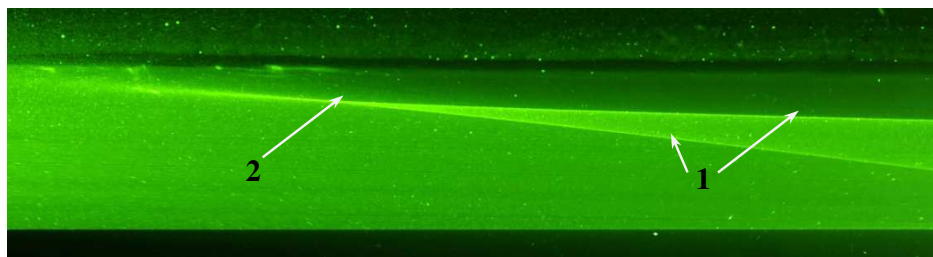


Figure 5: Experimental 2D-refractogram with presence of caustics (1) and point of their confluence (2) in diffusive layer of liquid with probing plane laser beam.

Using a specially devised algorithm for refractogram processing it is possible to separate caustic surfaces. By comparing their position and coordinating of their confluence with the calculated ones we can get distribution of the refractive index or the value h . By registering refractograms at variable moments of time at constant interval we can determine the dependence of the refractive index distribution on time, that gives an indication on how liquids diffuse each other.

4. 3D-VISUALIZATION OF CYLINDRICAL BEAM'S REFRACTION

Experimental setup is presented in Fig. 6.

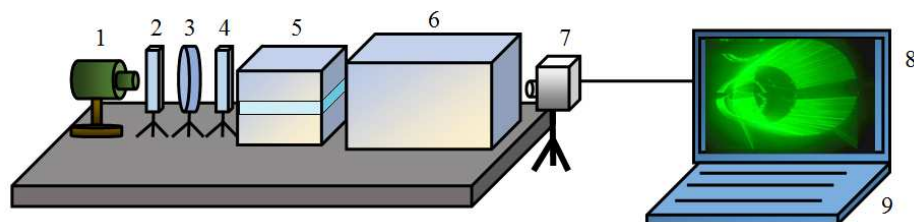


Figure 6: Experimental setup: 1 — laser, 2, 4 — lenses, 3 — DOE, 5 — cuvette with diffusive layer of liquid, 6 — cuvette with scattering particles in water, 7 — digital camera, 8 — 3D-refractogram, 9 — PC.

To form cylindrical laser beam it was created optical system, which consists of laser 1, lens 2 for focusing beam in registration area, DOE 3 and lens 4 for making beam parallel. In order to observe and register 3D-refractogram of cylindrical laser beam spreading in inhomogeneous mediums it is possible to use two cuvetts [9]. Creation of diffusive layer is taking place in cuvette 5 but 3D-refractogram's registration is not possible there because of distortion presence. That is why registration of refractogram realizes in the second cuvette 6. Registration of 3D-refractogram 8 was made by digital camera 7 and processed by personal computer 9.

3D-refractogram of the laser beam propagating in a homogeneous medium is shown in Fig. 7. During the experiment it was changing position of laser beam's center. There are three characteristic main positions: laser beam's center lies in the planes of the upper, lower boundaries layer and in the plane of middle of layer. The third case is presented in Fig. 8.

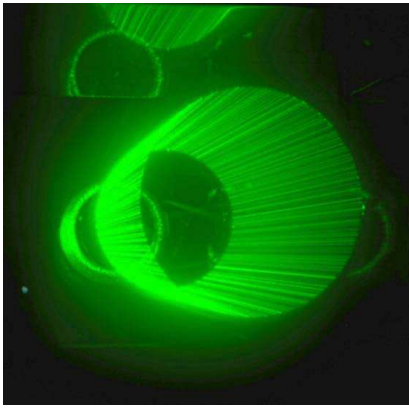


Figure 7: 3D-visualization of cylindrical laser beam propagation in homogeneous medium.

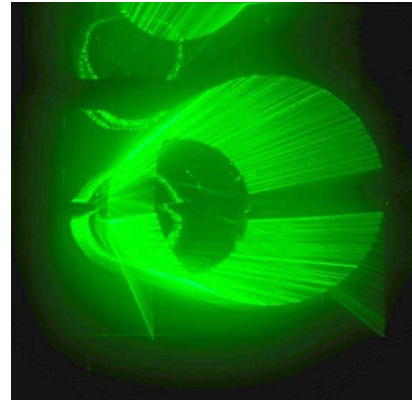


Figure 8: 3D-visualization of cylindrical laser beam propagation in diffusive layer of liquid.

5. CONCLUSION

Modeling of laser beams' caustics and researching of their shape give possibility to foresee laser beam actions in inhomogeneous media. It is very important to know the area of caustics' occurrence that allows optimizing experiments. At the consideration experimental refractogram, which was made in diffusive layer, it is possible to analyze how mediums can diffuse each other and estimate distribution of refraction index.

ACKNOWLEDGMENT

This work was supported by Russian Foundation for Basic Research (grant No. 14-08-00948-a).

REFERENCES

1. Rinkevichyus, B. S., O. A. Evtikhieva, and I. L. Raskovskaya, *Laser Refractography*, 189, Springer, New York, 2011.
2. Raskovskaya, I. L., B. S. Rinkevichyus, and A. V. Tolkachev, "Structured beams in laser refractography applications," *Laser Beams Theory Properties and Applications*, 399–414, Nova Science Publishers, Inc., NY, 2011.
3. Settles, G. S., "Schlieren and shadowgraph techniques," *Visualizing Phenomena in Transparent Media*, 387, Springer, New York, 2001.
4. Born, M. and E. Wolf, *Principles of Optics*, 952, Cambridge University Press, 1999.
5. Vedyashkina, A. V., "Computer modeling of optical rays' refraction in inhomogeneous mediums," *Journal of Beijing Institute of Technology*, Vol. 22, Suppl. 1, 71–76, 2013.
6. Arnold, V. I., S. M. Gusein-Zade, and A. N. Varchenko, *Singularities of Differentiable Maps*, Vol. 1, 393, Springer, New York, 2012.
7. Vedyashkina, A. V., I. N. Pavlov, I. L. Raskovskaya, and B. S. Rinkevichyus, "Experimental and computer 3D-visualization's dynamics of optical caustics in inhomogeneous mediums," *Proceedings of 16 International Symposium on Flow Visualization*, report ISFV16-1178.
8. Raskovskaya, I. L., "Refractometry of optical inhomogeneous media by registration of caustics position with used of structured laser radiation," *Avtometriya*, Vol. 50, No. 5, 92–98, 2014.
9. Yesin, M. V., I. L. Raskovskaya, B. S. Rinkevichyus, and A. V. Tolkachev, "Three-dimensional refractograms and its applications for diagnosis of gradient inhomogeneities," *Radiotechnics and Electronics*, Vol. 57, No. 4, 485–491, 2012.

Self-organizing And Filamentary Behaviour in Broad-area Lasers

A. V. Pakhomov^{1,2}, A. A. Krents^{1,2}, D. A. Anchikov¹, and N. E. Molevich^{1,2}

¹Department of Physics, Samara State Aerospace University, Samara, Russia

²Theoretical Sector, Lebedev Physical Institute of Russian Academy of Sciences
Samara Branch, Samara, Russia

Abstract— Presented work is concerned with analytical and numerical investigation of broad-area lasers dynamical regimes resulting from the stability loss of the steady lasing. It is shown that depending on the type of spatio-temporal instability filamentary and pattern forming behaviour may be observed in the system. Main principles and formation concepts of these dynamical regimes in the transverse section of the broad-area laser emission were considered and elaborated.

1. INTRODUCTION

Broad-area lasers are often necessary for high-power laser applications since increasing of transverse sizes of pumping region entails increasing the output power. However, for pumping levels well above the lasing threshold broad-area lasers exhibit complicated spatio-temporal dynamics. This is caused by the development of steady lasing instabilities that turn to be especially complex in broad-area lasers as transverse space-coupling processes and corresponding nonlinearities become involved. As a result related laser operation leads to degradation of brightness of these devices and coherence reduction of emitted beam. That is why these dynamical regimes deserve more detailed investigation.

On the other hand, complex spatio-temporal dynamics makes broad-area laser an interesting object to explore the general aspects of behaviour in nonlinear spatially-extended systems. Such systems are known to exhibit spontaneous pattern formation, chaotic and turbulent regimes that turns out to be very similar regardless the particular model under investigation. Thanks to laser being a very practically relevant device experimental observation of different nonlinear spatio-temporal regimes seems to be most feasible just in the laser systems.

In presented paper we report on detailed investigation of spatio-temporal instabilities emergence for steady stationary operation in broad-area lasers. We have shown that free-running broad-area laser can demonstrate both filamentary behaviour accompanied by nonregular pulsations of optical field and self-organization phenomena when different regular patterns can be observed. We found the bifurcation mechanisms responsible for each dynamical regime and model parameters regions for their implementing.

2. THEORETICAL MODEL

Our analysis was based on Maxwell-Bloch equations for frequency detuned cavity along with transversely distributed two-level lasing media [1, 2]:

$$\begin{cases} \frac{\partial E}{\partial t} = \sigma (P - E (1 - i\delta)) + ia\Delta_{\perp} E \\ \frac{\partial P}{\partial t} = -(1 + i\delta) P + DE \\ \frac{\partial D}{\partial t} = -\gamma [D - r + \frac{1}{2} (E^* P + EP^*)] \end{cases}, \quad (1)$$

where E , P , D are slowly varying dimensionless envelopes of electric field, polarization and population inversion; $\gamma = \gamma_{II}/\gamma_{\perp}$, $\sigma = k/\gamma_{\perp}$, where γ_{\perp} , γ_{II} and k are the decay rates of polarization, population inversion and electric field respectively. r is the pump parameter, $\delta = (\omega_0 - \omega_{cav})/(\gamma_{\perp} + k)$ stands for the normalized frequency detuning between the centre of gain line ω_0 and cavity frequency ω_{cav} scaled to the line half-width. Diffraction of the field is described by Laplace operator Δ_{\perp} acting in the transverse directions with Δ_{\perp} as the diffraction parameter. Electric field in model (1) is scaled to the amplitude of the transparency field and population inversion is scaled to the threshold value. Time is normalized to the coherence time.

This model considers a single-longitudinal-mode operation thus neglecting the nonlinear effects in longitudinal dimension in favor of the transverse dynamics. We restricted our analysis to the case of $\delta \leq 0$ when laser naturally selects spatially homogeneous steady operation as the first lasing solution [3]:

$$D_{st} = 1 + \delta^2; \quad |E_{st}|^2 = r - D_{st}; \quad P_{st} = (1 - i\delta) E_{st}. \quad (2)$$

Since pump r and frequency detuning δ are variable control parameters in system (1) principal importance is related to the ratios between the intracavity field and active medium decay rates described by parameters σ and γ . Stability analysis of solution (2) together with numerical modeling demonstrated several separable dynamical regimes depending on the latter ratios. Principally, it allowed distinguishing filamentary instability from pattern forming instability.

3. FILAMENTARY DYNAMICS

Filamentary behaviour is shown to emerge for incoherent light-media interaction when medium polarization instantaneously follows the intracavity field. It corresponds to the ratios $\gamma \ll \sigma \ll 1$. Such values are typical, for example, for solid-state and semiconductor laser systems. This filamentary dynamical regime is found to be induced by modulation-type instability as steady lasing (2) loses its stability against small perturbation with finite wavelength. Steady lasing is preserved for non-detuned cavity but inclusion of nonzero detuning results in its breakup.

Figure 1 shows typical image for this regime. Intensity profile (Fig. 1(a)) has very nonregular view with the temporal series (Fig. 1(b)) in the form of complex sustained oscillations.

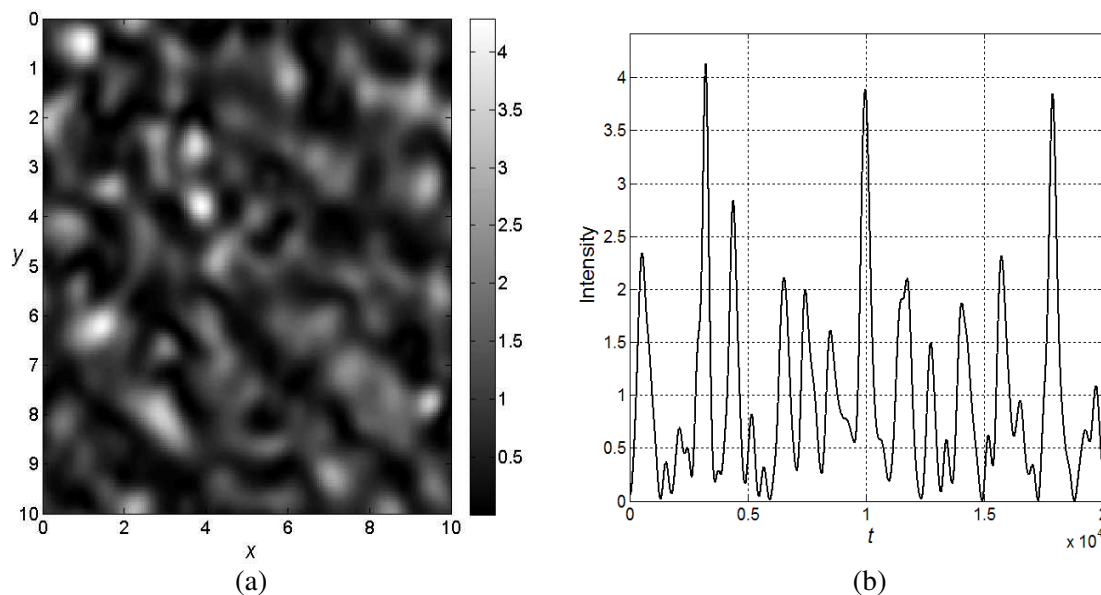


Figure 1: Filamentary pattern for $\sigma = 0.05$, $\gamma = 0.0001$, $\delta = -0.5$, $r = 2$; (a) instantaneous intensity profile; (b) intensity time series.

A number of mechanisms that can contribute to filamentation are known. First of all according to the seminal paper [4] the influence of Kerr self-focusing nonlinearity is defining in the case of strongly nonlinear light-matter interaction that is relevant for both passive and active systems. Another important mechanism is concerned with the strong gain-index coupling in semiconductor materials [5].

Our results show possibility of such dynamics in active system without gain-index coupling for even low electromagnetic field intensity just above the threshold. Indeed, when the instability is fully developed, the observed dynamics are similar to filamentary behaviour what is accompanied with both temporal and spatial nonregular dynamics although our model does not explicitly include gain-index coupling. Hence we expect this instability to be one of the possible routes to filamentation and light threads formation in numerous active optical systems when extending the transverse section like semiconductor and solid-state lasers and amplifiers.

4. SELF-ORGANIZING BEHAVIOUR

Some aspects of self-organization in broad-area lasers were reported earlier [6–8] and described the generation of tilted waves, localized solitons and optical vortices.

In our problem statement pattern formation is found to evolve for coherent light-media interaction that is usually realized in some atomic and molecular gas active mediums and implies comparable values for the material and field decay rates ($\gamma \leq \sigma \sim 1$).

A careful analytic treatment revealed a distinct scenario for the subsequent dynamics. Steady lasing becomes unstable in favor of self-oscillating homogeneous operation when the definite threshold for pumping value is exceeded. This type of dynamics doesn't reach however a steady behaviour since it is in turn destabilizes owing to instability against small perturbations with finite wavelength. The latter instability then governs the spatio-temporal evolution of the system giving rise to diverse processes.

Numerical simulations showed that the development of spatial inhomogeneties can follow several ways leading to a number of spontaneously forming regular patterns.

In some cases the creation of phase singularities is observed each of them containing a zero of the electric field. Then the spiral waves eventually appear, consisting of time-periodic phase distribution with rotating movement around the spiral cores together with a stationary intensity

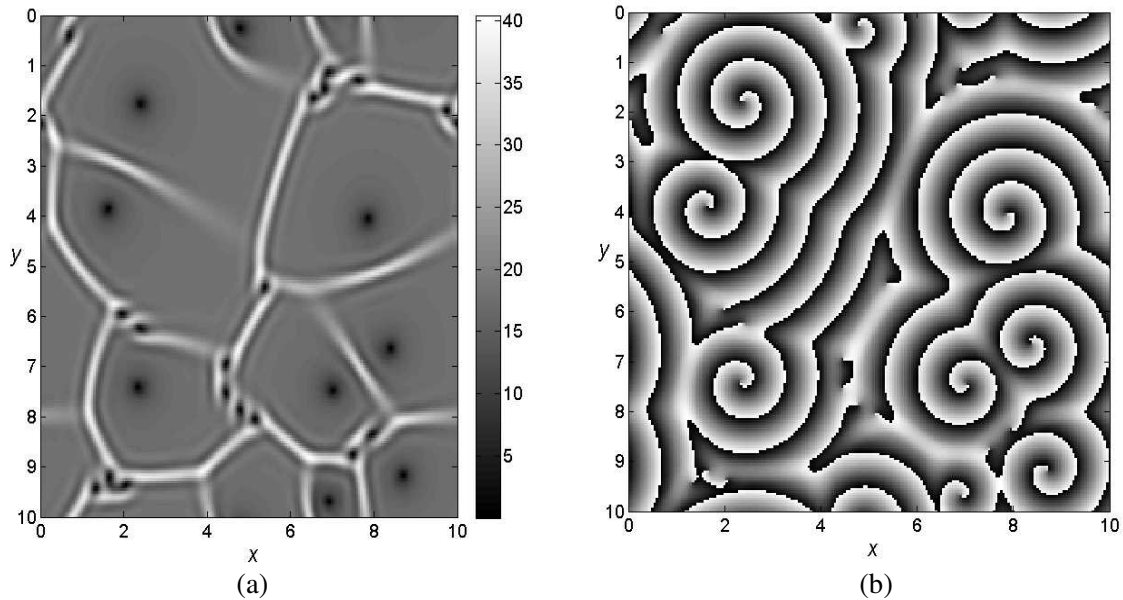


Figure 2: Spiral pattern for $\sigma = 4$, $\gamma = 0.7$, $\delta = -0.1$, $r = 20$; (a) stationary intensity profile; (b) rotating electric field phase profile.

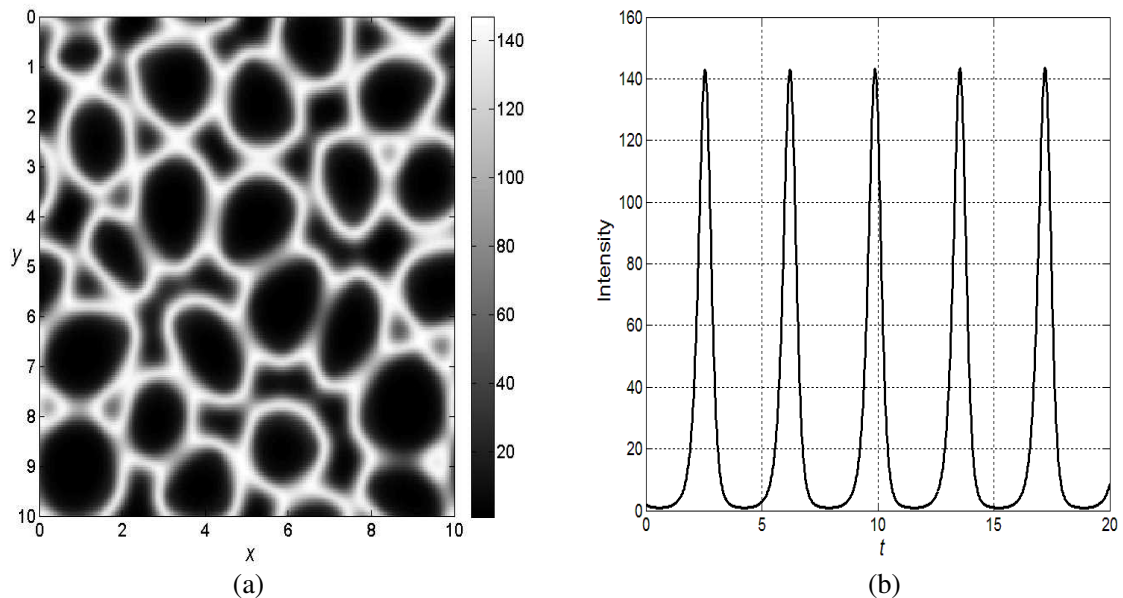


Figure 3: Standing wave pattern for $\sigma = 5$, $\gamma = 0.1$, $\delta = -0.3$, $r = 30$; (a) instantaneous intensity profile; (b) intensity time series.

profile where each spiral core occupies some area separated from each other by the sharp shock walls. All these aspects are clearly visible in Figs. 2(a)–(b) obtained for an appropriate set of model parameters.

Otherwise the formation of oscillating inhomogeneous intensity profile was found. In this instance self-organizing processes lead to spatially modulated standing autowaves. Specific shape of intensity profile is regular enough but it doesn't demonstrate any symmetry properties (see example on Fig. 3(a)). Temporal evolution for the field intensity is the periodic one though it exhibits a definite phase shift for each pair of points in the transverse laser section (Fig. 3(b)).

Described above scenarios of pattern formation seems to be specific for nonlinear optics only as the complex character of the optical field turns out to be the defining factor. Though main aspects of the self-organizing behaviour are general regardless the physical origin of particular system broad-area laser being an active nonlinear optical system shows a peculiar variety of optical patterns.

5. CONCLUSION

To conclude, we performed stability analysis for steady stationary operation of broad-area free-running lasers. We revealed that either filamentary or self-organizing dynamics may be observed depending on character of light-medium interaction. Basically filamentation is found to evolve for the coherent interaction while otherwise more complicated pattern forming is obtained. Main principles and bifurcation mechanisms responsible for the definite transverse spatio-temporal dynamics were studied. We hope our findings to contribute to the general understanding of nonlinear dynamical regimes in broad-area lasers and to allow controlling and optimization of the characteristics of laser emission.

ACKNOWLEDGMENT

Authors acknowledge financial support from the Ministry of Education and Science of Russian Federation (project 1451), under the Program for Improving Competitiveness of SSAU for 2013–2020 and from Russian Foundation for Basic Research (project 14-03-31419 mol.a).

REFERENCES

1. Lugiato, L. A., G.-L. Oppo, J. R. Tredicce, L. M. Narducci, and M. A. Pernigo, "Instabilities and spatial complexity in a laser," *J. Opt. Soc. Am. B*, Vol. 7, No. 6, 1019–1033, 1990.
2. Khanin, Ya. I., *Fundamentals of Laser Dynamics*, International Science Publishing, Cambridge, 2006.
3. Jacobsen, P. K., J. V. Moloney, A. C. Newell, and R. Indik, "Space-time dynamics of wide-gain-section lasers," *Phys. Rev. A*, Vol. 45, No. 11, 8129–8137, 1992.
4. Bespalov, V. I. and V. I. Talanov, *JETP Letters*, Vol. 3, 307, 1966.
5. Marciante, J. R. and G. P. Agrawal, "Spatio-temporal characteristics of filamentation in broad-area semiconductor lasers," *IEEE J. Quant. Electronics*, Vol. 33, No. 7, 1174–1179, 1997.
6. Weiss, C. O. and Ye. Larionova, "Pattern formation in optical resonators," *Rep. Progr. Phys.*, Vol. 70, 255–335, 2007.
7. Arecchi, F. T., S. Boccaletti, and P. Ramazza, "Pattern formation and competition in nonlinear optics," *Physics Reports*, Vol. 318, No. 1, 1–83, 1999.
8. Staliunas, K. and V. J. Sanchez-Morsillo, *Transverse Patterns in Nonlinear Optical Resonators*, Springer Verlag, Berlin, 2003.

Hydrogen and Humidity Sensing Based on WGMs of Elastic Polymer Optical Microresonators

M. Eryürek¹, Y. Karadag², S. Anand¹, N. Kılınc³, A. Kiraz¹

¹Department of Physics, Koç University, Rumelifeneri Yolu, Sarıyer, İstanbul 34450, Turkey

²Department of Physics, Marmara University, Göztepe, İstanbul 34722, Turkey

³Department of Mechatronics Engineering, Niğde University, Niğde 51245, Turkey

Abstract— We report hydrogen and humidity sensor employing elastic polymer (SU-8) optical microresonators. The sensing mechanism relies on the optical whispering gallery mode (WGM) resonance shifts in the transmission spectra of these microresonators. WGMs are excited through SU-8 waveguides in which a tunable laser light is coupled from an optical fiber. Relative humidity between 0 and 65% is detected at room temperature. For hydrogen sensing, the microresonators are coated with a thin layer of palladium (Pd) metal layer to increase the sensing performance. Hydrogen gas is detected reversibly between 0.3 and 1.5%. Hydrogen gas concentrations higher than 1.5% result irreversible degradation of the devices because of a phase transition occurring in the Pd layer.

1. INTRODUCTION

Hydrogen gas attracts a lot of attention as energy source courtesy of high efficiency in energy conversion and non-toxic side products [1, 2]. However, low flammable limit (4%), small molecular volume and high diffusion coefficient of hydrogen gas (H_2) introduce difficulties in hydrogen storage. Different sensing mechanisms, such as thermal [3], electrical [4], mechanical [5], acoustic [6] and optical methods [7] are used for H_2 detection. Optical sensors are generally more suitable for reversible detection of H_2 at low concentrations. First reported optical H_2 sensor relies on interferometric changes of a laser light in a Pd-coated optical fiber [8]. Afterwards, optical H_2 sensors are demonstrated utilizing reflection spectroscopy [9], reflectivity [10] or surface plasmon resonance changes [11].

In this paper, we report H_2 detection using whispering gallery mode (WGM) resonance shifts of optical microresonators fabricated by standard UV photolithography. WGM resonances of the microresonators are very sensitive to the size of the microresonator. In order to employ this phenomenon, a thin layer of palladium (Pd) is coated on the microresonators, since the lattice constant of Pd lattice increases when H_2 is adsorbed in Pd [12]. SU-8 polymer is used as the photoresist for the material of the microresonators since SU-8 is elastic and its refractive index is high enough to confine the laser light. In the literature, elastic nature of SU-8 is used for strain sensing [13], photoacoustic microscopy [14] and opto-mechanically tunable lasing [15]. Similar microresonator-based detection of H_2 down to 0.7% employs WGM shifts due to a local temperature increase because of the combustion of H_2 [16]. In another work, vertical cavity lasers are used for H_2 detection, in which the change in the complex refractive index of Pd results a shift in the lasing wavelength [17]. As compared to these previous studies, our system provides lower detection limit of 0.3% H_2 using a relatively simple fabrication technique.

2. MICROFABRICATION

Fabrication of sensor devices consists of a two-step UV photolithography procedure. In the first step, SU-8 microresonator and waveguide structures are fabricated on a thick-oxide wafer. Extra thick oxide layer provides smaller refractive index (1.445) than SU-8 (1.573) so that the light can be confined in the SU-8 layer [18]. Then in the second step Pd microdisks are deposited on these microresonators using lift-off technique. The optical power circulates at the outermost edge of the microresonator. Therefore the diameters of Pd microdisks are designed smaller than the diameters of the corresponding microresonators to avoid optical loss due to Pd metal.

3. MEASUREMENTS

Tunable laser light is coupled from an optical fiber to SU-8 waveguide using butt-coupling method [19] (See Figure 1). As the wavelength of the laser is changed in a controlled manner, the transmission spectrum is collected using another optical fiber butt-coupled to the other end of the SU-8 waveguide. Before H_2 sensing experiments, the humidity in the sample chamber is removed with dry

nitrogen gas and during that time blue-shift is observed [20]. Then H_2 concentration is changed in the sample chamber using gas flow controllers and the WGM resonances are monitored. Detection signal obtained from Pd-coated and uncoated devices are given in Figure 2. 10% H_2 results about 15 pm of resonance shift in the case of uncoated microresonator. On the other hand, 15 pm resonance shift is achieved under 0.5% H_2 when Pd-coated microresonator is used. Therefore Pd coating improves the sensitivity of the device 20-fold.

H_2 detection performance of the devices are tested in the humid environment. The humidity of

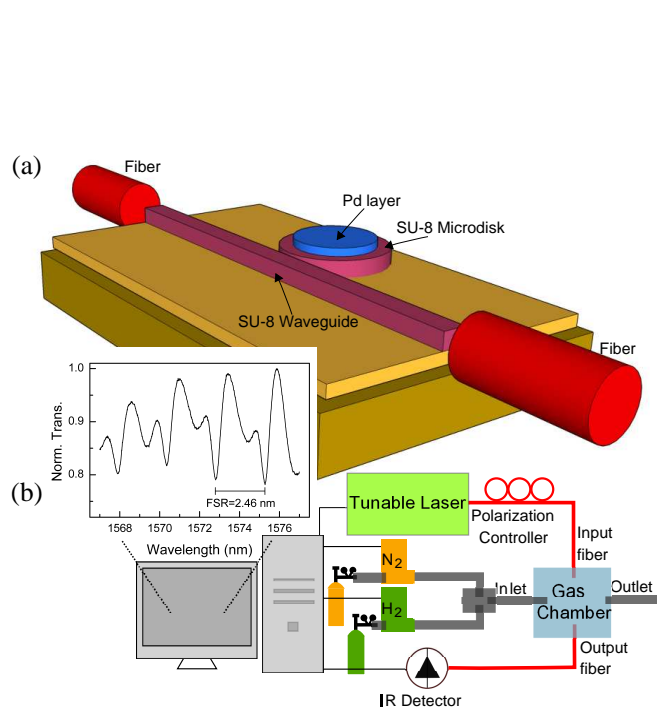


Figure 1: H_2 sensing results obtained from (a) sketch of the sample area. Tunable laser light is coupled from an optical fiber to the SU-8 waveguide. Then the optical WGMs of the Pd-coated SU-8 microresonator are excited from the SU-8 waveguide, (b) the whole experimental setup. The sample is put into a gas chamber in which the H_2 concentration and relative humidity can be changed in a controlled manner. The inset shows an exemplary spectrum obtained from a Pd-coated microresonator.

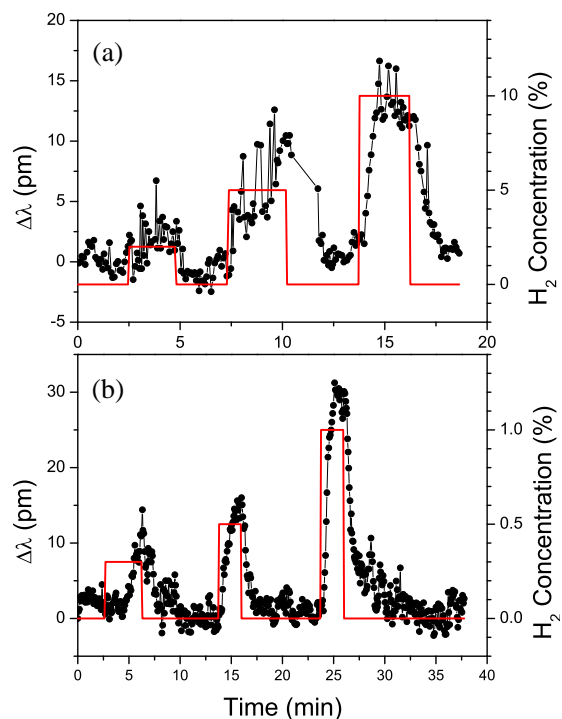


Figure 2: H_2 sensing results obtained from (a) Uncoated SU-8 microresonator and (b) Pd-coated SU-8 microresonator. Red lines indicate the H_2 concentration in the sample chamber and black dots indicate the resonance shifts.

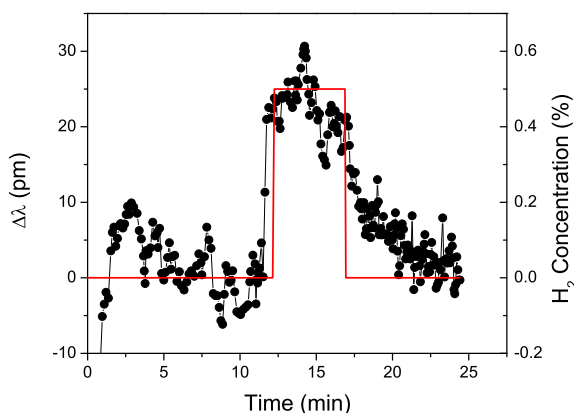


Figure 3: H_2 detection signal obtained from Pd-coated SU-8 microresonator in the presence of 51% RH.

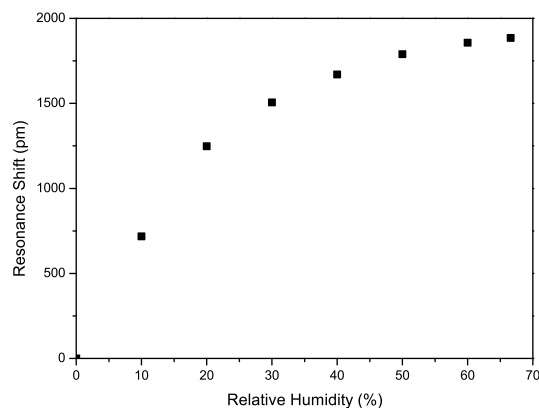


Figure 4: Humidity detection using uncoated SU-8 microresonator. Resonance shift increases as the RH increases up to 65%.

the sample chamber is kept constant at 51% relative humidity (RH) at room temperature during the sensing experiment. 0.5% H_2 is detected under humid conditions (See Figure 3). Ability to detect H_2 under humidity may lead to practical applications.

Sensing performance of the uncoated resonators are tested for humidity. In general, polymers are good absorbers of humidity [20]. Therefore there is no need to coat the SU-8 polymer microresonator with an extra active layer. This makes the fabrication procedure a lot easier. At room temperature, RH between 0 and 65% is successfully detected using transmission spectra of uncoated microresonators (See Figure 4).

4. CONCLUSION

In conclusion, H_2 sensing under dry environment and humid environment are presented as well as the humidity sensing using optical WGM resonance shifts. It is possible to reversibly detect less than 1% H_2 with or without the humidity in the environment. Pd is used as an active layer for H_2 detection to improve the sensitivity. On the other hand, humidity sensing does not require any extra coating because the material of the microresonator itself is polymer which has high absorption of humidity. At room temperature, RH between 0 and 65% is detected using uncoated microresonators.

ACKNOWLEDGMENT

This work is supported by Türkiye Bilimsel ve Teknolojik Araştırma Kurumu (TÜBİTAK) Grant No. 110T803. One of the authors, SA, thanks Co-founded Brain Circulation Scheme of TÜBİTAK for support.

REFERENCES

1. Christofides, C. and A. Mandelis, "Solid-state sensors for trace hydrogen gas detection," *Journal of Applied Physics*, Vol. 68, No. 6, R1–R30, 1990.
2. Hübert, T., L. Boon-Brett, G. Black, and U. Banach, "Hydrogen sensors — A review," *Sensors and Actuators B*, Vol. 157, 329–352, 2011.
3. Lee, E.-B., I.-S. Swang, J.-H. Cha, H.-J. Lee, W.-B. Lee, J. J. Pak, J.-H. Lee, and B.-K. Ju, "Micromachined catalytic combustible hydrogen gas sensor," *Sensors and Actuators B*, Vol. 153, 392–397, 2011.
4. Favier, F., E. C. Walter, M. P. Zach, T. Benter, and R. M. Penner, "Hydrogen sensors and switches from electrodeposited palladium mesowire arrays," *Science*, Vol. 293, 2227–2231, 2001.
5. Chou, Y.-I., H.-C. Chiang, and C. C. Wang, "Study on Pd functionalization of microcantilever for hydrogen detection promotion," *Sensors and Actuators B*, Vol. 129, 72–78, 2008.
6. Dong, S., F. Bai, J. Li, and D. Viehland, "Sound-resonance hydrogen sensor," *Applied Physics Letters*, Vol. 82, 4590–4592, 2003.
7. Silva, S. F., L. Coelho, O. Frazao, J. L. Santos, and F. X. Malcata, "A review of palladium-based fiber-optic sensors for molecular hydrogen detection," *IEEE Sensors Journal*, Vol. 12, 93–102, 2012.
8. Butler, M. A., "Optical fiber hydrogen sensor," *Applied Physics Letters*, Vol. 45, No. 10, 1007–1009, 1984.
9. Maciak, E. and Z. Opilski, "Transition metal oxides covered Pd film for optical H_2 gas detection," *Thin Solid Films*, Vol. 515, 8351–8355, 2007.
10. Bévenot, X., A. Trouillet, C. Veillas, H. Gagnaire, and M. Clément, "Hydrogen leak detection using an optical fiber sensor for aerospace applications," *Sensors and Actuators B*, Vol. 67, 57–67, 2000.
11. Bévenot, X., A. Trouillet, C. Veillas, H. Gagnaire, and M. Clément, "Surface plasmon resonance hydrogen sensor using an optical fibre," *Measurement Science and Technology*, Vol. 13, 118–124, 2002.
12. Noh, J.-S., J. M. Lee, and W. Lee, "Low-dimensional palladium nanostructures for fast and reliable hydrogen gas detection," *Sensors*, Vol. 11, 825–851, 2011.
13. Bholá, B., H.-C. Song, H. Tazawa, and W. H. Steier, "Polymer microresonator strain sensors," *IEEE Photonics Technology Letters*, Vol. 4, 4496, 2014.
14. Li, H., B. Dong, Z. Zhang, H. F. Zhang, and C. Sun, "A transparent broadband ultrasonic detector based on an optical micro-ring resonator for photoacoustic microscopy," *Scientific Reports*, Vol. 17, No. 4, 867–869, 2005.

15. Flatae, A. M., M. Buresi, H. Zeng, S. Nocentini, S. Wiegele, D. Wiersma, and H. Kalt, "Optomechanically tunable polymeric microlasers," *CLEO*, 2014.
16. Yebo, N. A., D. Taillaert, J. Roels, D. Lahem, M. Debligny, D. Van Thourhout, and R. Baets, "Silicon-on-insulator (SOI) ring resonator-based integrated optical hydrogen sensor," *IEEE Photonics Technology Letters*, Vol. 21, No. 14, 960–962, 2009.
17. Griffin, B. G., A. Arbabi, A. M. Kasten, K. D. Choquette, and L. L. Goddard, "Hydrogen detection using a functionalized photonic crystal vertical cavity laser," *IEEE Journal of Quantum Electronics*, Vol. 48, No. 2, 160–168, 2012.
18. Dai, D., L. Yang, Z. Sheng, B. Yang, and S. He, "Compact microring resonator with 2×2 tapered multimode interference couplers," *Journal of Lightwave Technology*, Vol. 27, No. 21, 4878–4883, 2009.
19. Bellini, B., A. d'Alessandro, and R. Beccherelli, "A method for butt-coupling optical fibres to liquid crystal planar waveguides," *Optical Materials*, Vol. 29, 1019–1022, 2007.
20. Schmid, S., S. Kühne, and C. Hierold, "Influence of air humidity on polymeric microresonators," *Journal of Micromechanics and Microengineering*, Vol. 19, 1–9, 2009.

Electron Beam Detection by Induced Resonance in Cylindrical Cavity

Alberto Leggieri^{1,2}, Davide Passi¹, Franco Di Paolo¹, Giuseppe Felici²,
Alessia Ciccotelli², Silvia De Stefano², and Filippo Marangoni²

¹Dipartimento di Ingegneria Elettronica, Università degli Studi di Roma “Tor Vergata”, Roma, Italy

²S.I.T., Sordina IORT Technologies S.p.A., Aprilia, Italy

Abstract— An investigation on the power energy injection in a resonator by electron stream is reported in this paper, by documenting the power transfer from an electron beam to a resonant cavity, coupled to an external circuitry. The proposed system has been employed to measure the radiation dose deposited by a medical electron linear accelerator. A prototype has been fabricated and tested through VNA cold measurements and dose deposition measurements. A microcontroller system has been employed to obtain a digital output, the Monitor Units. The linearity of the Monitor Units for different values of accumulated dose, have allowed to employ this system for the real time dose measurements.

1. INTRODUCTION

Real time radiation detectors are employed to control the output of artificial radiation sources. In particular, medical linear accelerators (LINAC's) design, production and operation are subjected to strict regulations mostly regarding the control of the emitted radiations. Beam current measurements of a medical mobile electron LINAC, dedicated to Intra Operative Radiation Therapy (IORT) have been performed through a particular detector and discussed in this paper. In medical accelerator field, beam monitoring system are required by the main technical standards for the real time measurement of the dose delivered to the target while the beam is crossing them [1, 2]. Beam current monitoring for the dose measurement is typically performed by employing ionization chambers connected to suitable electronic circuitry and digital data processing [3]. Traditional beam current monitoring systems are based on ionization chambers and requires high voltage biases [3, 4]. This study investigates on the electron beam current emitted by a medical electron linear accelerator using the power exchange of the beam current with a passive resonant cavity [5] placed at the output interface of the accelerator. In this paper, experimental evidence is presented showing the complete equivalency, in terms of global performance, of the current revelation performed by exploiting the cavity-beam interaction principle with the classical technology, based on ionization chambers, however without the need of high voltage.

2. DETECTION ARCHITECTURE

The proposed radiation detector is based on the power exchange of the beam current with a passive resonant cavity [5] placed at the output interface of the accelerator. The beam current, crossing the resonant cavity provides a magnetic field fluxing through a magnetic loop inserted in the cavity volume. As consequence of the beam to cavity interaction, a voltage is induced at the loop terminals. This voltage, representative of the real time beam current is then elaborated by a microcontroller based elaboration system. The information on the beam current are processed to manage the dose delivered by the accelerating machine. This device allows the measurement of a physical observable quantity directly related with the dose deposited by the beam. Furthermore, no high voltage is needed as happens for the ionization chambers, since the proposed radiation detector does not need any bias. In order to manipulate the information on the current, a frequency down conversion is performed by revealing the signal envelope. For this aim, the pickup voltage, which falls on the matched impedance, is rectified by a RF detector diode. The detector diode output is forwarded to a voltage integrator. The voltage representative of the beam current is integrated during the time duration of the macro-bunch. Since the electric charge is the time integral of the current, the voltage output of the integrator is, at this point, representative of the charge. The main block diagram representative of the operating principle is depicted in Figure 1.

The bunched current produced by the LINAC have an amplitude of $I_{beam} = 1.11$ mA. Such current have the alternate form of charge bunches, modulated at the operating normal mode frequency $f = 2998$ MHz of the accelerator. Hence, quasi-Gaussian micro-bunches are separated by

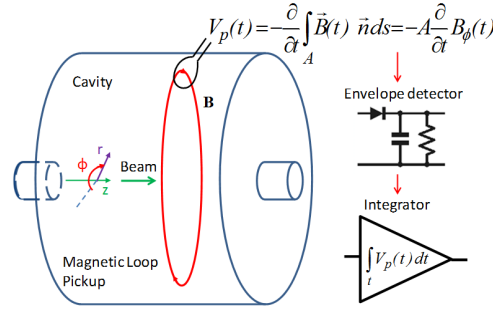


Figure 1: Operating principles — block diagram.

the period of $T = 1/f \approx 0.33$ ns. As the bunches follow each other periodically in time, the spectral content of the current beam is a line at the accelerating pulsation $\omega_0 = 2\pi f$ and whole-number harmonics [4]:

$$I_{beam}(t) = \sum_{n=1}^{\infty} I_n \sin(n\omega_0 t) \quad (1)$$

A simplified approach can be adopted by treating the bunched current as a square wave, whose first harmonic is given by:

$$I_1(t) = I_1 \sin(\omega_0 t) \quad (2)$$

where

$$I_1 = I_{beam} \frac{2}{\pi} \sin\left(\pi \frac{t_{on}}{T}\right) \quad (3)$$

where I_{beam} is the amplitude of the bunched beam current.

In the approximation of a square wave beam current, the duration of the high level of the current, t_{on} , corresponds to the time duration of the bunch t_{bunch} . By considering the (3), neglecting the superior harmonics, the amplitude of the injected first harmonic beam current of the analyzed LINAC is $I_1 = 0.66$ mA. This harmonic content has been employed to induce oscillations in an opportune resonant cylindrical cavity operating in the TM_{010} mode at the accelerator normal mode frequency f . Since the minimum energy of the beam is greater than 4 MeV, no holes are required on the cavity base surface, but an opportune aluminum window (transparent to these energetic charges) is employed for allowing the beam crossing and entering the cavity. The window thickness is chosen to limit the surface scattering. The beam current cross the window and enter the cavity where exchange power with it inducing a current I_0 on the cavity walls and energy is stored. In order to extract information on the amplitude of the beam current, a magnetic loop is inserted into the cavity. Inserting a pickup on the amplitude of the beam current, the output power derived from such device must come from the work done by the beam against the fields which it itself generates [6].

The voltage induced between the loop terminals V_p can be derived starting from the second Maxwell's equation applied to B_ϕ [7]. The positioning of the loop in the cavity is chosen making the loop encloses a surface A perfectly normal to the azimuthal direction. In such conditions the $V_p(t)$ can be given by:

$$V_p(t) = -\frac{\partial}{\partial t} \int_A \vec{B}(t) \cdot \vec{n} ds = -A \frac{\partial}{\partial t} B_\phi(t) \quad (4)$$

The cavity behaves as though its shunt impedance were similarly located in the beam tube wall; hence when either type of device is connected to an external electric circuit, it behaves as though its electrical impedance were identical with its shunt impedance. A consequence of the latter result is that for such a device to behave as a matched load, it must be connected to the external circuit via an impedance matching device such as a transformer [6]. For this reason it's of vital importance for the consistence of this dissertation that the cavity shows a critical coupling, identifiable by a coupling factor $k = 1$, observable with the frequency behavior of the impedance shown to the loop terminals. This means that all the power per cycle is extracted by the loop without reflections [8]. Another vital constraint of the model regards the operating frequency of the LINAC and the cavity used as detector. The cavity needs to operate in the TM_{010} mode at the normal mode pulsation ω_0 . If the frequency of the LINAC changes without the frequency of the cavity detector changing in the

same manner, the output signal will be attenuated, as regulated by the filtering effects of the cavity over the harmonics induced by the beam current crossing. The attenuation can be identified by deriving the modulus of the 3 dB transfer function of the standard parallel RLC resonator described in [9]. In absence of frequency shift, the maximum voltage is obtained and its value coincides with V_p . The voltage attenuation is regulated by the unloaded quality factor of the cavity Q_0 [8].

By considering the definition of the current as the variation of charges in the time unit [7], the charge emitted by the LINAC per bunch is given by:

$$Q_{bunch} = - \int_{t_{bunch}} I_{beam}(t) dt = - \int_0^{t_{bunch}} I_{beam} \sin(\omega_0 t) dt = I_{beam} \frac{\cos(\omega_0 t_{bunch}) - 1}{\omega_0} \quad (5)$$

While knowing the energy $W_{beam}(\omega_0 t)$ of the charges e crossing the detector, the value of the deposited dose per micro bunch pulse can be obtained by the energy ratio per unit of effective mass $m(E)^*$ of the matter where the dose D_{bunch} is deposited from each bunch, as expressed by (6):

$$D_{bunch} = \frac{\partial W_{beam}(\omega_0 t)}{\partial m(E)^*} \cong \frac{\int_0^{t_{bunch}} W_{beam}(\omega_0, t) \cdot I_{beam}(\omega_0, t) dt}{em(E)^*} \quad (6)$$

The amount of dose deposited by a macro-bunch pulse of duration t_{pulse} can be found by multiplying D_{bunch} for the number of micro-bunches per macro-bunch pulse. This value can be obtained by multiplying the LINAC normal mode frequency for the duration of the macro-bunch pulse, linearly approximated by:

$$D_{pulse} = D_{bunch} t_{pulse} f \quad (7)$$

The direct relation between the dose deposited by the beam and the beam current can be noted.

3. SYSTEM DESIGN

One of the principal requirements for the proposed detector is the small thickness, needed to insert the system at the end of the LINAC radiant head. Moreover, the cavity needs to be integrated with another cavity to compose a redundant system composed by two cavities disposed along the same axis. This requirement will further reduce the available space. Hence, in order to reduce the size as much as possible, a length of $\lambda/16$, corresponding to $L_{gap} = 6.25$ mm has been chosen for the initial pillbox cavity length. A tradeoff between the power losses and the operative bandwidth of the cavity was performed, yielding to the selection of the brass as the material for the realization of the device. This choice was led by the fact that the device is subjected to thermal effects due to the variability of the external environment conditions. A lower quality factor can make the system more robust to such variation. The trade off originates by the fact that lowering Q increases the losses reducing the voltage output. After the analytical design a computational electromagnetic modeling using the finite elements method has been implemented. In order to realize the system of two integrated cavity avoiding normal mode coupling between them, a cylindrical section has been added to the cavity to allow the beam current exiting from the first cavity to enter in another identical cavity without inserting a metallic shield. The radial aperture of such cylindrical section is enough large to allow the beam crossing without increasing the electrical coupling between the two cavities. Basing on the specification of the drift tube, a reasonably larger aperture has been chosen. A reentrant cavity shape has been individuated by employing POISSON SUPERFISH to find the desired profile ensuring good values of quality factor and shunt resistance, while maintaining the presence of the drift tube. The cavity radius has been increased in order to make the cavity tunable by inserting opportune tuning screws. For this reason the design frequency has been decreased to $f = 2997.5$ MHz. This cavity presents a shunt impedance of $Z_s = 12.8$ M Ω m $^{-1}$ and a quality factor of $Q_0 = 3.4 \cdot 10^3$ while the transit time factor is $T = 0.766$. A complete electromagnetic modeling has been performed on HFSS version 15 of ANSYS. A rectangular magnetic loop have been employed for the power extraction. The profile of the loop, as well as the distance from the cavity lateral walls, have been chosen to obtain the critical coupling between the cavity and the load, with the minimum reflections [8]. In order to allow for the connection of an SMA, a tapered coaxial line has been added as impedance transformer from the section the magnetic loop to the SMA. The 3D simulated structure of the whole system is shown in Figure 2, where the magnetic loops and the coaxial lines are highlighted for a better view.

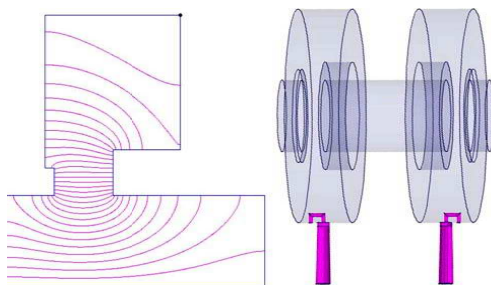


Figure 2: Field profile of a quarter of the re-entrant cavity modelled in POISSON SUPERFISH (a) and the whole cavity-loop system in ANSYS-ANSOFT HFSS (b) model.

This condition has allowed for the maximum available power transfer and ensured the applicability of the theory formulated in this paper. The simulated S -parameters are given in Figure 3, S_{11} , and 4, S_{21} . The proposed cavity to magnetic loop system ensures a maximum cross talk between the two channels of -32 dB and a return loss of 20.7 dB at the designed resonance.

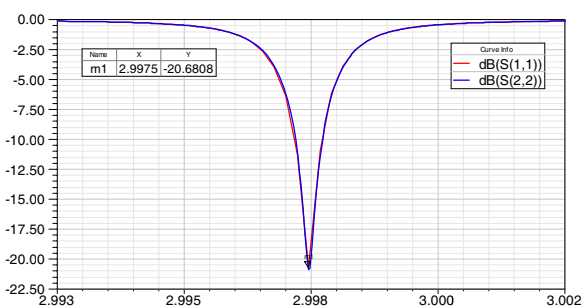


Figure 3: Simulated S_{11} amplitude in dB.

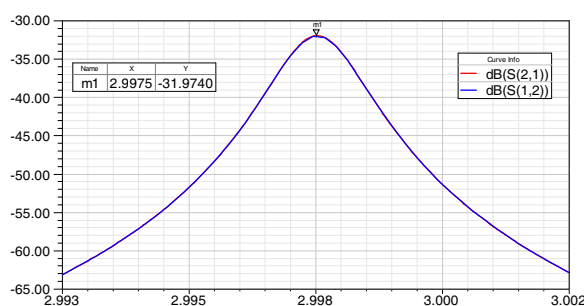


Figure 4: Simulated S_{21} amplitude in dB.

4. FABRICATION AND MEASUREMENTS

Cold measurements of scattering parameters and hot measurements of the dose deposition have been performed on the detector prototype. Since the detector output can be influenced by the temperature exposition, the cavity shares the thermostatisation circuit of the LINAC where flowing controlled temperature water. The detector prototype is depicted in Figure 5 where tuning screws, SMA connectors and thermostatisation pipes can be noted.

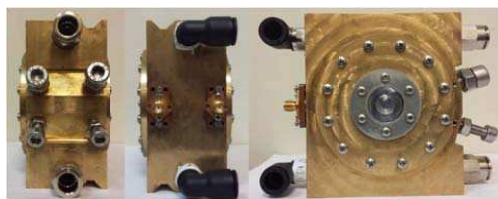


Figure 5: Radiation detector prototype.

Table 1.

Energy Setting	Mean Energy [MeV]	Beam Current [mA]	Voltage Output [mV]	MU/pulse
<i>A</i>	5.5	0,74	84.5	0.797
<i>B</i>	7.1	0,90	164.0	1.570
<i>C</i>	9.0	1.03	253.5	2.695
<i>D</i>	10.5	1.11	300.0	3.534

Measured reflection parameters in the frequency bandwidth have been exported from a Rohde and Schwarz ZVL 12 VNA and elaborated through a custom MATLAB code, computing the quality factor and the coupling factor by the detuned short position technique [8]. The device have shown a quality factor $Q_0 = 2.25 \cdot 10^3$, a return loss $RL = 23$ dB a cross talk between the two integrated cavities of $IL = -34$ dB and a Coupling Factor $k = 1.02$, as described in Figures 6, 7 and 8. In order to asses quantitatively the results achieved, a direct measurement of the accelerated beam has been performed. The output current of the LINAC has been forwarded into the cavity observing the output voltage of the envelope detector. Radiation measurements have been performed on the LIAC-S[®] accelerating structure, by varying the LINAC energy settings [10]. The machine has been set with the parameters described in Table 1. The pulse duration of the macro-bunch is $\tau = 3.5 \mu\text{s}$ and the pulse repetition frequency is $f_{PRF} = 10$ Hz. Mean electron beam energy has been measured according to IAEA TRS 398 protocol [11] at the application point of the ionizing radiation. Percentage Depth Dose (PDD) curves have been measured using PTW MP3 XS water-phantom with suitable detectors and PTW Mephysto mc² processing software [12] and reported in Figure 9. The output measurements have shown a $R_{50} = 4.5$ cm, corresponding to an average energy of about 10.5 MeV, as shown by the curve reported in Figure 9.

The detector voltage output has been integrated by an operational amplifier during the macro bunch pulse time. The integral output has been elaborated through a microcontroller system,

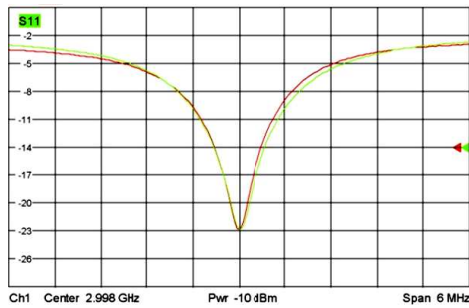


Figure 6: Measured S_{11} amplitude in dB.

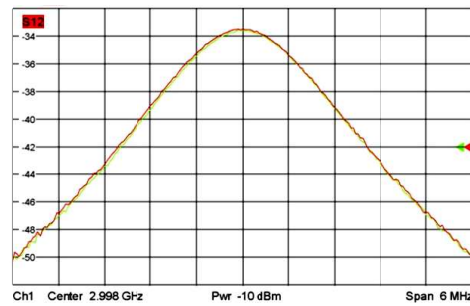


Figure 7: Measured S_{21} amplitude in dB.

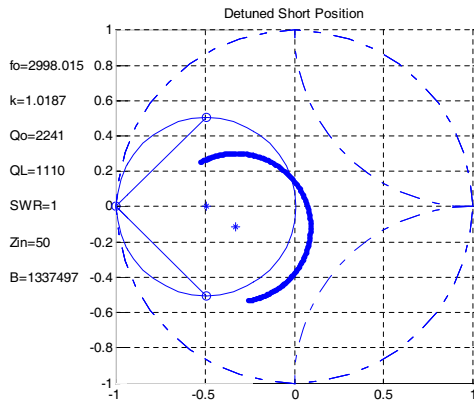


Figure 8: Coupling analysis computation.

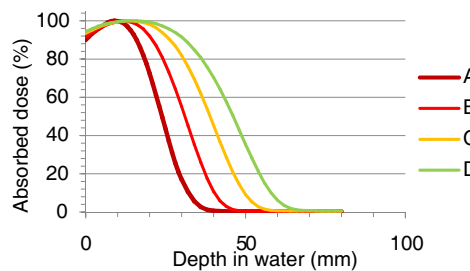


Figure 9: Percentage Depth Dose measurements.

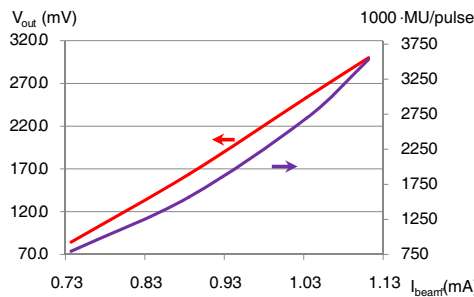


Figure 10. Voltage output and 10^3 MU/pulse vs I_{beam} .

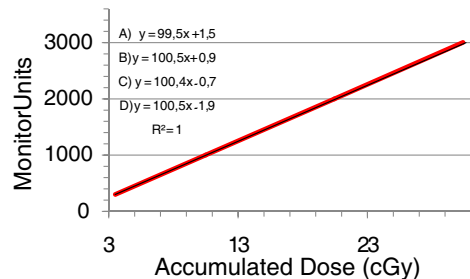


Figure 11. Linearity: Accumulated Dose, MU vs Gy.

obtaining a digitalized value representative of the dose emission, the monitor units per pulse (MU/pulse) [1]. The system has been calibrated to yield the precise measurement of the deposited dose also yielding the secondary interactions. Each monitor unit has been calibrated to 1 cGy. The relation between the injected beam current and the output of the detector diode is reported in Figure 10. The linearizable behavior of the peak voltage output (V_{out}) and dose digital representation (MU/pulse) against the beam current can be noted.

The measurements shown in Figure 11 report the linearity of the accumulated monitor units for different values of total emitted dose. This results allows for the employment of the proposed system in a medical electron LINAC for controlling dose delivered to the patient.

5. CONCLUSIONS

This paper proposes an investigation on the power energy injection in a resonator by electron stream. A novel approach for beam monitoring of a medical electron accelerator is proposed. This kind of device requires strong reliability monitoring system for the real time measurement of the dose delivered to the patient. In this paper, the complete applicability of the proposed principle to such requirements has been shown. The proposed technology is based on the power exchange of the LINAC beam current with a passive resonant cavity placed at the output interface of the accelerator. This detector can operate without high voltage biases, required by the traditional beam monitors based on ionization chambers. Several prototype measurements have shown the complete equivalency of the proposed device with the traditional ionization-based systems but presenting several advantages, as the absence of high voltages and the fact that the proposed system measures the physical observable quantity directly related with the dose, the beam current.

REFERENCES

1. International Standard EN 60601-2-1, *Medical Electrical Equipment — Part 2-1: Particular Requirements for the Basic Safety and Essential Performance of Electron Accelerators in the Range 1 MeV to 50 MeV*, 3rd Edition, International Electrotechnical Commission, 2009.
2. Turner, A. P., “Regulations, standards and guidelines for the use of medical electron linear accelerators,” *IEEE Transactions on Nuclear Science*, Vol. 26, No. 1, 1979.
3. Uvarov, V. L., et al., “A beam monitoring and calibration system for high-power electron LINACs,” *Proceedings of the Particle Accelerator Conference*, Vancouver, BC, 1997.
4. Ruf, M., S. Muller, S. Setzer, and L. P. Schmidt, “Beam position and energy monitoring in compact linear accelerators for radiotherapy,” *IEEE Transactions on Biomedical Engineering*, Vol. 61, No. 2, 2014.
5. Rosenzweig, J. B., *Accelerator Technology II: Waveguides and Cavities*, 183–193, Fundamentals of Beam Physics, Oxford University Press, Oxford, 2003.
6. Goldberg, D. A. and G. R. Lambertson, “Dynamic devices a primer on pickups and kickers,” 540–561.
7. Ramo, S., J. R. Whinnery, and T. Van Duzer, “Resonant cavities,” *Fields and Waves in Communication Electronics*, 3rd Edition, 303–310, 699–701, 719–723, New York, John Wiley & Sons, 1994.
8. Leggieri, A., D. Passi, G. Felici, S. De Stefano, and F. Di Paolo, “Magnetron high power system design,” *International Journal of Simulation System Science and Technology*, Vol. 16, 2015.
9. Di Paolo, F., “Resonant elements,” *Networks and Devices Using Planar Transmission Lines*, 505–512, CRC Press LLC, 2000.
10. S.I.T. S.p.A., LIAC-S product description, Italy, 2013, Available: <http://soiort.com>.
11. IAEA TRS 398, “Absorbed dose determination in external beam radiotherapy: An international code of practice for dosimetry based on standards of absorbed dose to water,” Vienna, December 2000.
12. PTW Freiburg GmbH, Mephysto Software Suite product description, Germany, 2012, Available: <http://www.ptw.de/2082.html>.

Low-loss Millimeter-wave Phase Shifters Based on Mechanical Reconfiguration

P. Romano¹, O. Araromi², S. Rosset²,
J. Perruisseau-Carrier³, H. Shea², and J. R. Mosig¹

¹Laboratory of Electromagnetics and Acoustics (LEMA)
École Polytechnique Fédérale de Lausanne (EPFL), Switzerland

²Microsystems for Space Technologies Laboratory
École Polytechnique Fédérale de Lausanne (EPFL), Switzerland

³Deceased. Adaptive MicroNano Wave Systems
École Polytechnique Fédérale de Lausanne (EPFL), Switzerland

Abstract— We propose different concepts of mechanically reconfigurable true-time-delay phase shifters using micro-actuators at millimeter-waves (MMW). The mechanical reconfiguration allows to achieve phase shift reconfiguration with very low losses. One of the proposed concepts has been fully implemented and tested, demonstrating state-of-the-art performance in terms of phase-shift/loss ratio.

1. INTRODUCTION

Reconfigurable phase shifters are critical components in modern communications and remote sensing systems at millimetre-wave (MMW). In general, advanced reconfiguration capabilities are increasingly required to dynamically update antenna characteristics, such as coverage, polarization or operating frequency [1, 2]. Different technologies are currently available for the implementation of tunable phase shifters, including semiconductors, RF-MEMS, Liquid Crystal and ferroelectrics [3]. However, a common feature to all these technologies is the significant increased loss, complexity and cost with regard to non-reconfigurable devices. In this context, low-loss reconfigurability, complexity and cost are driving factors in the choice of a given technology and can constitute major limitations to future development of MMW antenna devices [1].

Here we propose the analysis, design, and implementation of mechanically reconfigurable MMW phase shifters using micro-fabricated actuators. The desired phase shift tuning is obtained modifying the physical geometry of the device in order to affect the propagation constant. Such an approach allows to completely isolate the actuation part from the electromagnetic (EM) active area, thereby achieving reconfiguration with losses comparable to the device fixed counterpart. In particular, the preliminary design and performance of three different reconfigurable concepts are presented in Section 2. The design of one concept has been further optimized to be manufactured and tested, and is described in Section 3.

2. PHASE SHIFTERS BASED ON MECHANICAL RECONFIGURATION

We propose the design of reconfigurable true-time delay (TTD) phase shifters, which are key building blocks in many array antenna systems, including wideband beamsquint-free scanning arrays. The basic idea is to affect the propagation constant of a transmission line (TL) section, thereby providing TTD. Using micro-actuators, this can be done by changing the geometry of the device, in order to modify the effective permittivity of the equivalent TL. The proposed concept can potentially be implemented using different technologies for mechanical reconfiguration. For instance electrostatic (e.g., [4, 5]), magnetic (e.g., [6, 7]), piezoelectric (e.g., [8, 9]) or electroactive polymers (e.g., [10–13]) actuators could be integrated to implement the final device. Here dielectric electroactive polymer (DEAP) actuators are used to reconfigure the fabricated phase shifter presented in Section 3.

The devices presented here consist of a fixed TL, that is microstrip, coplanar waveguide (CPW) or rectangular waveguide (RWG) loaded by a movable part (dielectric or metallic), which induces a change in the TL propagation constant β . Thus, the differential phase shift between two different states A and B is given by:

$$\Delta\phi_{AB} = -(\beta_B - \beta_A) L_{PS} \quad (1)$$

where L_{PS} is the active length of the device, that is the section directly affected by reconfiguration. When quasi-TEM TLs (e.g., microstrip or CPW) are considered, the propagation constant can be

written as $\beta = \omega\sqrt{\mu_0\varepsilon_0}\sqrt{\varepsilon_{r,eff}}$. Therefore, a given phase reconfiguration is achieved modifying the effective relative permittivity $\varepsilon_{r,eff}$.

However, the dynamic control of β (i.e., of the phase) via the mechanical reconfiguration of the TL geometry necessarily comes with a simultaneous variation of the TL characteristic impedance, which will affect the matching of the phase shifter. Therefore, a “minimum mismatch” design approach [13] is applied to the presented concepts. That is, the dimensions of the fixed TL and of the loading parts in the active area are optimized to maximize the phase shift to loss figure, while simultaneously minimizing the mismatch. In particular, the optimization process is based on the maximization of two figures of merit (FoMs): the maximum differential phase shift per unit length expressed by (2) and the maximum differential phase shift per unit length per mismatch given by (3) [13]:

$$\text{FoM}_1 = \frac{\phi_B - \phi_A}{L_{PS}} \quad (2)$$

$$\text{FoM}_2 = \frac{\phi_B - \phi_A}{L_{PS} |\Gamma_{\max}|} \quad (3)$$

Both FoMs are normalized by the length of the active section L_{PS} , which allows to compare performance of different devices independently from their length. Moreover, all simulated results presented in Table 1 in terms of propagation constant and differential phase shift are obtained normalizing scattering parameters to the “optimal” reference impedance Z_{opt} that assures the mismatch minimization [13]. All proposed phase shifter concepts (shown in Fig. 1) are optimized to operate at Ka-band (25–40 GHz), which is of increasing interest, e.g., for commercial satellite communications.

Table 1: Performance comparison for the proposed phase shifter concepts at 35 GHz.

Concept	Actuation	$\Delta\beta_{\max}$ [rad/m]	FoM ₁	FoM ₂
Fig. 1(a)	In-plane	560.4	32.1	581.9
Fig. 1(b)	Out-of-plane	61.9	3.5	34.3
Fig. 1(c)	In-plane	308.5	21.5	140.6

The concept of Fig. 1(a) is based on a microstrip TL (quasi-TEM) and in-plane actuation (e.g., [10, 13]). The horizontal displacement of the central strip induces a change in $\varepsilon_{r,eff}$ due to the particular shape of the bottom dielectric: when the strip is moved in the $-\Delta x$ direction, the portion of dielectric below increases ($\varepsilon_{r,eff}$ increases), while it reduces with a displacement in the $+\Delta x$ (the air portion below the strip increases, decreasing $\varepsilon_{r,eff}$). It is clear that this effect is magnified increasing the substrate permittivity ($\varepsilon_r = 10$ is chosen for our design). The “trapezoidal” cut of the dielectric is introduced to improve the matching (impedance tapering) between the feeding (fixed) microstrip and the movable section. The compliant connections shown in Fig. 1(a) can be realized using flexible metallizations (e.g., [14]) or alternatively replaced by a capacitive coupling between fixed and movable strips. Preliminary performance reported in Table 1 assume a total displacement of 400 μm ($\Delta x = \pm 200 \mu\text{m}$), which corresponds to only 0.04λ at the design central frequency $f_0 = 30$ GHz. Simulated scattering parameters are shown in Fig. 2(a). Insertion loss is always lower than 1.5 dB and return loss better than 10 dB, with a phase shift/loss ratio of around 350 deg/dB at 35 GHz.

The basic idea characterizing the concept depicted in Fig. 1(b) is the variable loading of a WR-28 RWG. A metallic rod is vertically moved inside the active area by one or more out-of-plane actuators (e.g., [9, 11]), modifying the capacitance per unit length (and thus the propagation constant) of the equivalent TL. More specifically, the propagation constant increases if the metallic load is “pushed” inside the RWG (Δh increases). The loading part is properly shaped to improve the matching between the fixed and reconfigurable sections. This device has the advantage to be a “closed” structure, which is very appealing for high power applications and could be easily manufactured using standard micromachining techniques. Moreover, it does not comprise any dielectric in the EM active area. Simulated performance of Table 1 refer to a total vertical displacement $\Delta h = 1$ mm. Simulated results of Fig. 2(b) predict an insertion loss lower than 0.6 dB and a return loss better than 15 dB. The mean phase shift/loss ratio is around 180 deg/dB at 35 GHz.

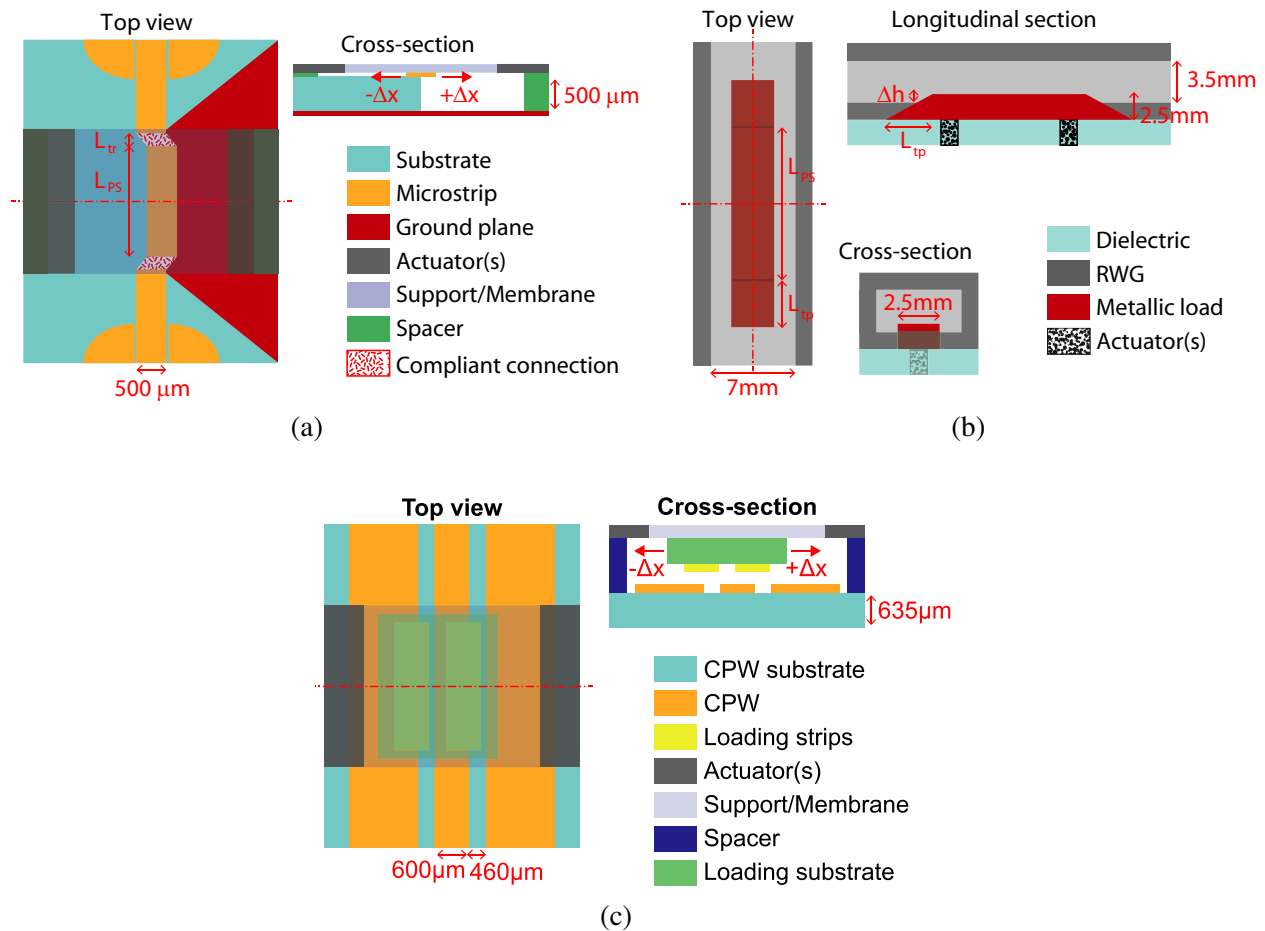


Figure 1: Simplified drawing of the proposed phase shifter concepts. (a) Reconfigurable phase shifter based on a microstrip TL: the central section can be reconfigured modifying the effective relative permittivity. (b) Rectangular waveguide loaded by a metallic rod that can be displaced in the vertical direction affecting the capacitance per unit length of the equivalent TL. (c) Reconfigurable concept based on a conventional CPW loaded by two suspended metallic strips, which are horizontally displaced by in-plane actuators.

The phase shifter concept illustrated in Fig. 1(c) consists of a conventional coplanar waveguide (CPW) loaded by two suspended metallic strips (their spacing is constant), which are supported and horizontally displaced in the $\pm\Delta x$ direction by in-plane actuators. The actuation part also assures that the vertical spacing between the CPW and the strips keeps constant. Simulated performance of Table 1 assume a total horizontal displacement of $530\ \mu\text{m}$ ($\Delta x = \pm 265\ \mu\text{m}$) [13].

The results presented in Table 1 and Fig. 2 highlight very good performance for the microstrip-based concept of Fig. 1(a) that exhibits a phase shift per unit length of $32.1^\circ/\text{mm}$ with very low losses. The RWG concept (Fig. 1(b)) presents lower phase shift performance with extremely low losses (only ohmic), but can be suitable for high power applications. However, the achievable phase shift can be increased replacing the metallic load with a high permittivity dielectric (adding dielectric losses). The device of Fig. 1(c) exhibits the best trade-off between performance and low-cost/low-complexity fabrication process. In fact, it does not require any flexible/compliant connection between the movable and fixed part (in contrast with the concept shown in Fig. 1(a)), and can be easily prototyped (and tested) using standard manufacturing techniques and in-house available technology. Thus, it was selected to be fabricated and tested. A detailed description of the manufacturing and test of the proposed reconfigurable phase shifter is given in Section 3.

3. IMPLEMENTATION AND MEASUREMENTS

3.1. Reconfiguration Approach

Dielectric electroactive polymer (DEAP) actuators are selected to implement the proposed phase shifter reconfiguration (Fig. 1(c)) [13]. DEAPs, also known as artificial muscles, consist of an elas-

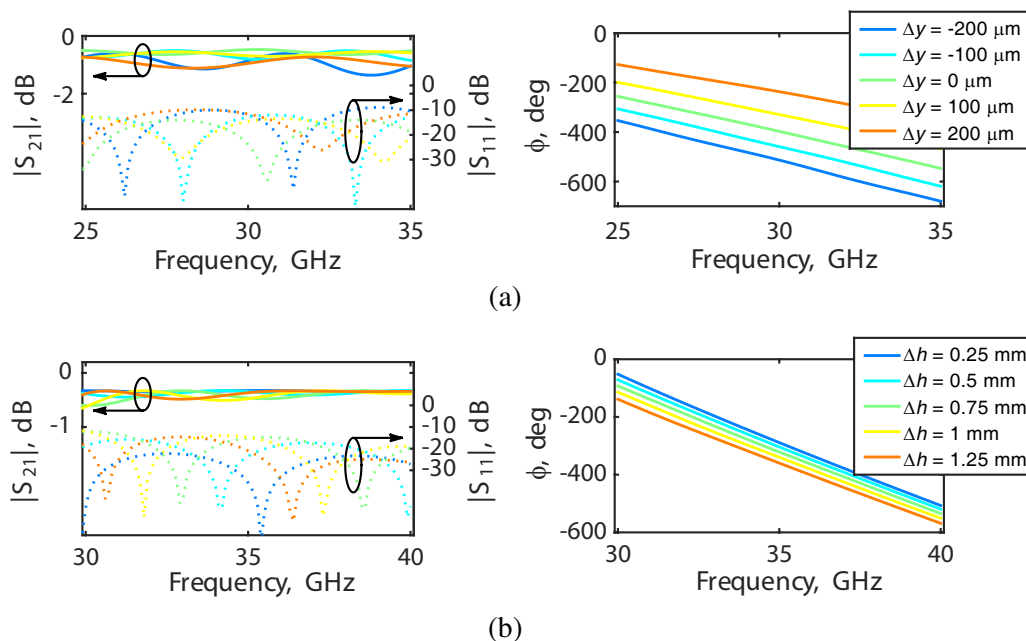


Figure 2: Simulated scattering parameters for different states of reconfiguration. (a) Concept of Fig. 1(a): $L_{PS} = 10$ mm, $L_{tr} = 200$ μ m, substrate with $\epsilon_r = 9.8$ and $\tan \delta = 0.002$ (e.g., Rogers TMM10i). The compliant connections are modeled as a resistive sheet with $R_S = 30 \Omega/\square$ [14]. (b) Concept of Fig. 1(b): $L_{PS} = 20$ mm, $L_{tp} = 5$ mm. A conductivity $\sigma = 2.9 \times 10^7$ S/m is considered for all metallic parts, and actuators are completely shielded from the EM active area.

tommer membrane sandwiched between two compliant electrodes. The subsequent application of a voltage bias across the electrodes results in thickness compression and large (over 200%, [10]) in-plane area expansion. In addition, DEAPs provides mechanical actuation with low cost materials and fabrication, low device complexity, large strain, reduced size and bulkiness and analogue operation. DEAPs currently typically require high actuation voltage (in the kilovolt range) to achieve large strain expansion. This high voltage is considered an acceptable drawback given the advantages brought by the DEAP technology. The required voltages can be readily obtained using commercial DC-DC converters fitting in less than 2 cm². Moreover, it is worth noting that currents are very small and power is only required to change the device configuration (and not to hold a constant position), hence providing very low power actuation.

A detailed drawing of the phase shifter cross section is shown in Fig. 3(a). The needed horizontal displacement of the loading strips is realized by two antagonist planar DEAP actuators, which are integrated in the polydimethylsiloxane (PDMS) membrane. They are composed of carbon black

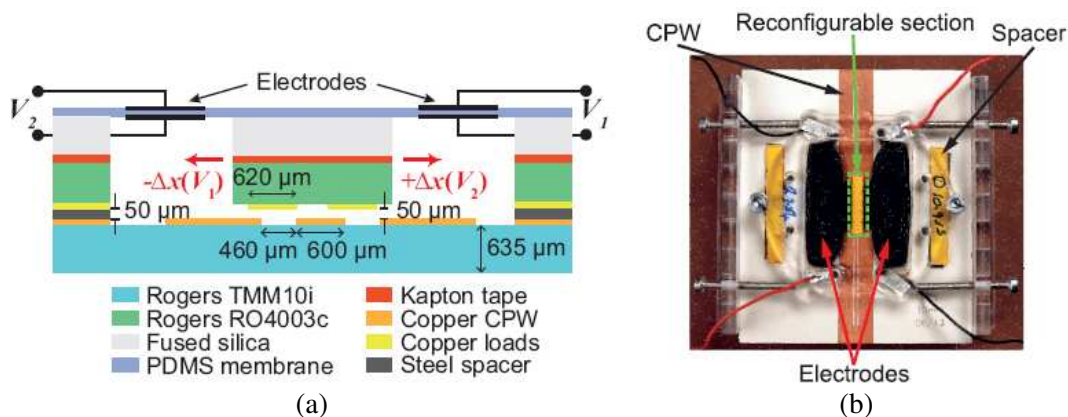


Figure 3: Manufactured reconfigurable phase shifter. (a) Simplified cross-section drawing of the proposed phase shifter concept. (b) Picture (top view) of the fabricated prototype.

particles in a PDMS matrix and are applied using a stamping method. As a result of the actuation, the loading part, fixed to a passive region in the center of the membrane, is displaced linearly in-plane. In particular, a voltage V_1 induces a movement $-\Delta x$ (towards minimum phase shift), while a voltage V_2 generates a movement of $+\Delta x$ (towards maximum phase shift) in the opposite direction (Fig. 3). Such an approach allows to completely isolate the actuator part from the EM active area (Fig. 3), providing phase shift reconfiguration with very low losses (only ohmic and dielectric losses), as it is demonstrated by the experimental characterization of the manufactured prototype presented in 3.2.

3.2. Design, Fabrication and Test

The design process is optimized to comply with all the constraints imposed by the EAP technology and the manufacturing techniques available in our laboratory. The device assembly (cross-section) with the materials used and relevant dimensions of the reconfigurable section are shown in Fig. 3(a). The length of the reconfigurable section is fixed to 10 mm for the presented prototype, but can be subsequently selected according to the phase shift requirement for a given application, since these two quantities are directly proportional (TTD phase shifter).

The final prototype is designed to be modular and manually assembled; this allows us to use the same CPW TL with different reconfigurable parts (for testing purposes) and to replace single pieces in case of local failure. Therefore, the different components are fabricated separately using commercial materials (Fig. 3(a)) and standard printed circuit board (PCB) fabrication processes (avoiding cleanroom activities), thus reducing manufacturing complexity and obtaining a very low-cost prototype. The fabricated phase shifter based on DEAP reconfiguration is shown in Fig. 3(b).

Probe-based 2-port scattering parameters measurements are used to characterize the fabricated prototype of Fig. 3(b) in the range 25–35 GHz. A thru-reflect-line (TRL) calibration is used to remove the effect of the transitions between the coaxial-based network analyzer and the CPW-based device and to place the measurement reference planes at the edges of the reconfigurable section. Measured scattering parameters in the full frequency range are reported in Fig. 4. The fabricated phase shifter provides a maximum analog phase range (i.e., between maximum and minimum displacement) of around 180° at 30 GHz with extremely low losses. The insertion loss is in fact always lower than 1.6 dB with an average value of 0.83 dB over the total frequency range. The return loss is always better than 11 dB, which means good matching for all the phase shifting states in the whole 10 GHz bandwidth. The low-loss phase shift reconfiguration demonstrated by experimental results, allows state-of-the-art performance in terms of the most important figure of merit for TTD phase shifters, namely, the phase-shift/loss ratio. Indeed, a mean value of $235^\circ/\text{dB}$ is achieved at 35 GHz, considerably outperforming semiconductor phase shifters at similar frequencies (e.g., [15]). Moreover, it also compares well to lower-loss state-of-the-art MEMS reconfigurable phase shifters (e.g., [16]). In addition, the device proposed here offers a large analog tuning range, which represents an advantage over the digital behavior of its MEMS and MMIC counterparts. It is worth noting that the total phase range can be increased using longer loading lines (TTD principle, Eq. (1)).

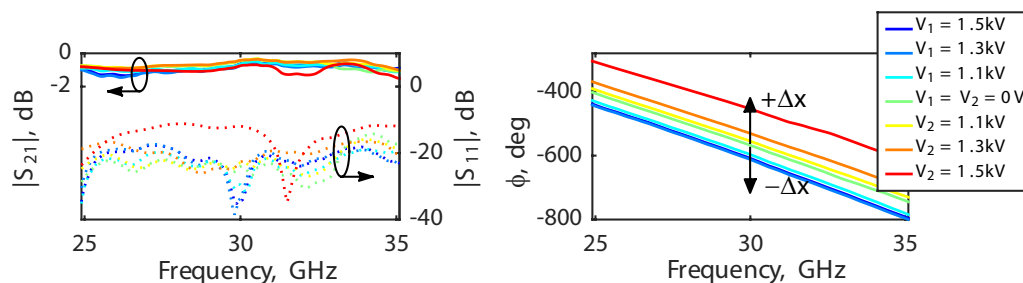


Figure 4: Measured scattering parameters in the range 25–35 GHz for the fabricated phase shifter of Fig. 3(b). Different reconfiguration states are shown, i.e., $V_1 = V_2 = 0$ kV, $V_1 = 1.1, 1.3, 1.5$ kV, $V_2 = 1.1, 1.3, 1.5$ kV.

4. CONCLUSION

The phase shift performance of three different mechanically reconfigurable concepts operating at Ka-band have been presented. All the proposed phase shifters are based on a fixed TL perturbed by loading elements, which are displaced using micro-actuators. The optimized design, fabrication and

experimental characterization of a CPW-based concept have been reported, highlighting excellent phase shift to loss figure of merit ($235^\circ/\text{dB}$ at 35 GHz).

ACKNOWLEDGMENT

This work was supported by the European Space Agency (NPI project REACT) and the Swiss National Science Foundation (SNSF) under Grant No. 133583. The authors would like to thank Jean-Christophe Angevain (Antenna and Sub-Millimeter Wave Section, ESA ESTEC) for stimulating discussion.

REFERENCES

1. Mangenot, C. and G. Toso, "European space technology harmonisation technical dossier on array antennas european space agency," *ESTEC, TEC-EEA*, Noordwijk, 2012.
2. Arrebola, M., J. A. Encinar, R. Cahill, and G. Toso, "Dual-reflector antenna with a reflectarray subreflector for wide beam scanning range at 120 GHz," *2012 Int. Conf. Electromagn. Adv. Appl.*, 848–851, 2012.
3. Hum, S. V. and J. Perruisseau-Carrier, "Reconfigurable reflectarrays and array lenses for dynamic antenna beam control: A review," *IEEE Trans. on Antennas Propag.*, Vol. 62, No. 1, 183–198, 2014.
4. Legtenberg, R., A. W. Groeneveld, and M. Elwenspoek, "COMB-drive actuators for large displacements," *J. Micromech. Microeng.*, Vol. 6, 320–329, 1996.
5. Chen, C., C. Lee, Y.-J. Lai, and W. Chen, "Development and application of lateral COMB-drive actuator," *Jpn. J. Appl. Phys.*, Vol. 42, 4059–4062, 2003.
6. Cugat, O., J. Delamare, and G. Reyne, "Magnetic micro-actuators and systems (MAGMAS)," *IEEE Trans. Magn.*, Vol. 39, No. 6, 3607–3612, 2003.
7. Hage-Ali, S., Y. Orlic, N. Tiercelin, R. Sauleau, P. Pernod, V. Preobrazhensky, and P. Coquet, "A millimeter-wave elastomeric microstrip phase shifter," *2012 IEEE MTT-S*, Jun. 17–22, 2012.
8. Kim, S.-G., T.-Y. Yun, and K. Chang, "Time-delay phase shifter controlled by piezoelectric transducer on coplanar waveguide," *IEEE Microw. Wireless Compon. Lett.*, Vol. 13, No. 1, 19–20, Jan. 2003.
9. Wu, J., J. Lou, M. Li, G. Yang, X. Yang, J. Adams, and N. X. Sun, "Compact, low-loss, wide-band, and high-power handling phase shifters with piezoelectric transducer-controlled metallic perturber," *IEEE Trans. Microw. Theory Techn.*, Vol. 60, No. 6, 1587–1594, 2012.
10. Pelrine, R., R. Kornbluh, Q. Pei, and J. Joseph, "High-speed electrically actuated elastomers with strain greater than 100%," *Science*, Vol. 287, No. 5454, 836–839, 2000.
11. Carpi, F., G. Frediani, and D. De Rossi, "Hydrostatically coupled dielectric elastomer actuators," *IEEE-ASME Trans. Mechatron.*, Vol. 15, No. 2, 308–315, 2010.
12. Shea, H., "Miniaturized EAPs with compliant electrodes fabricated by ion implantation," *Electroactive Polymer Actuators and Devices (EAPAD) 2011*, Vol. 7976, May 2011.
13. Romano, P., O. Araromi, O., S. Rosset, H. Shea, and J. Perruisseau-Carrier, "Tunable millimeter-wave phase shifter based on dielectric elastomer actuation," *Appl. Phys. Lett.*, Vol. 104, No. 5, 024104, 2014.
14. Romano, P., S. Rosset, L. Maffi, H. Shea, and J. Perruisseau-Carrier, "Electromagnetic characterisation of flexible conductive membranes at millimetre-waves," *Electron. Lett.*, Vol. 49, No. 5, 353–354, 2013.
15. Yang, J. G. and K. Yang, "Ka-band 5-bit MMIC phase shifter using InGaAs PIN switching diodes," *IEEE Microw. Wireless Compon. Lett.*, Vol. 21, No. 3, 151–153, 2011.
16. Hayden, J. S. and G. M. Rebeiz, "Very low-loss distributed X-band and Ka-band MEMS phase shifters using metal-air-metal capacitors," *IEEE Trans. Microw. Theory Techn.*, Vol. 51, No. 1, 309–314, 2003.

Tunable Periodic Deflector Structure Based on Ferroelectric Materials

R. A. Platonov¹, A. G. Altyinnikov¹, I. V. Kotelnikov¹,
A. B. Kozyrev¹, V. N. Osadchy¹, and A. G. Chernokalov²

¹Saint Petersburg Electrotechnical University “LETI”, Russian Federation

²Limited Liability Company Samsung Research Center, Russia Federation

Abstract— The electrically tunable lens based on nonlinear ferroelectric materials ($\text{Ba}_{0.4}\text{Sr}_{0.6}\text{TiO}_3$) for deflecting of the microwave (MW) beam is presented. The distinctive feature of the deflector is the use of multilayer periodic structure FE/LD/FE/LD/.../FE (FE-ferroelectric, LD-linear dielectric) with transparent for MW signal electrodes. Simulation and experiments demonstrate that periodic structure provides the slow wave propagation effect, that in turn results in the increase of effectiveness of lens operation. At frequency ~ 30 GHz the lens provides scan angle $\alpha \sim \pm 20$ deg.

1. INTRODUCTION

The electrically scanning antennas are actively developing devices for telecommunication and radar system. Traditional solution of the beam antenna scan is the phased array antenna (PAA), which application in present time is becoming very actual in anti-collision car radars, in/out door communication systems, in space radars and etc. [1, 2]. One of the main disadvantages of mm wave PAA is a rather large MW losses in dividers and intrinsic feeders for the strip-line technology and very complicated and expensive construction in a case of the metal waveguide technology. In recent years electrically tunable lenses (ETL) becomes powerful beam-forming platform that can be used instead of phase array antennas. This approach allows the radical decrease of MW losses and greatly simplified design due to absent of dividers and intrinsic feeder lines. In a set of works the ferroelectric materials are proposed to be used as a base of tunable distributed elements of lenses [3–6]. According our knowledge there are no publications devoted to multilayer structure periodic in longitudinal plane (along direction of wave propagation). The use of periodicity in longitudinal plane allows to decrease of control voltages value and increase of scan angle in comparison with nonperiodic and transverse periodic analogues. The main parameters of the periodic lens were obtained by modelling and were confirmed by experimental testing of prototype lens at frequency ~ 30 GHz.

2. THEORETICAL PART

Basic concept and simulation results. The basic concept of ferroelectric ETL is described in [3, 6]. It consists of ferroelectric plate covered by high resistive electrodes, which are transparent for the microwave signal (Fig. 1(a)). ETL deflects the microwave beam in one plane for realization of 1D scan regime. The principle of operation of the device is as follows: application of different control voltages between ends of the top high resistive electrode leads to different E -field values between top and bottom electrodes along the FE plate, that in turn, results in the corresponding variation of the permittivity along the plate (see color density variation in Fig. 1(a)). The value of deflection angle α is determined by the difference of the signal phase shift values at opposite edges of the ferroelectric layer $\Delta\phi$ [4]:

$$\alpha = \arctan \frac{\lambda \Delta\phi}{l \cdot 2\pi} = \arctan \frac{d}{l} (\sqrt{\epsilon(0)} - \sqrt{\epsilon(E_{\max})}), \quad (1)$$

where λ — the wavelength in free space; l — the deflectors aperture size; d — the thickness of the ferroelectric layer; $\epsilon(E)$ — the permittivity as a function of control electric field.

Thereby, the higher deflection angle, for ETL with fixed aperture, can be achieved due to the increase of the lens thickness and/or the ferroelectric nonlinearity. However, both of these options lead to the increase of MW losses and values of the control voltage. Furthermore, in order to maintain any angle of beam propagation (except for $\alpha = 0$) the control current continuously flowing through high resistive electrodes is needed, that inevitably leads to the heating phenomena in FE plates.

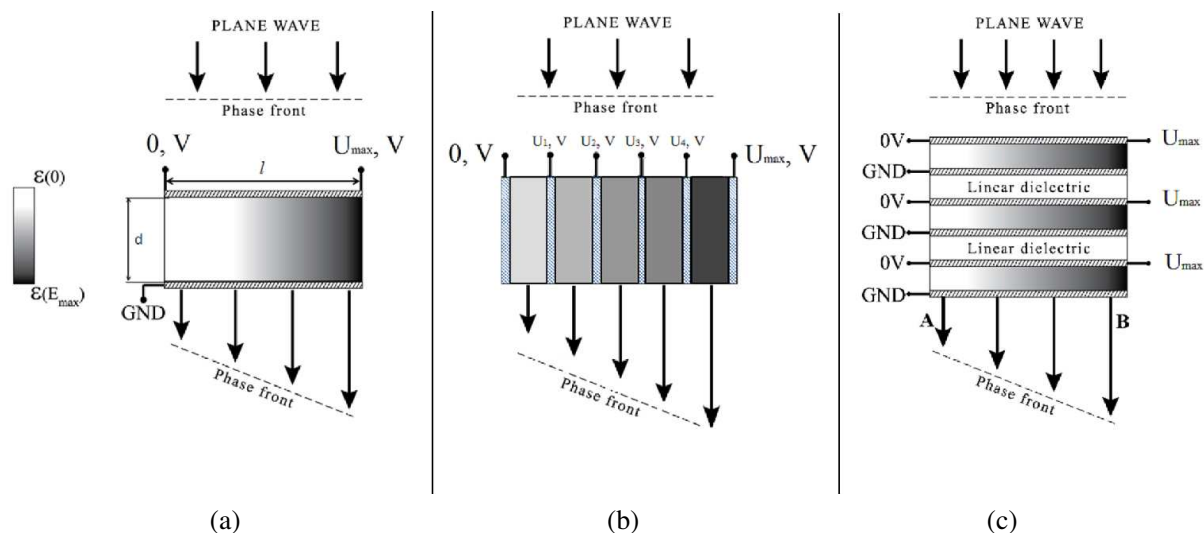


Figure 1: (a) One-layer and (b) multilayer ETL periodic in transverse and (c) longitudinal plane based on ferroelectric materials.

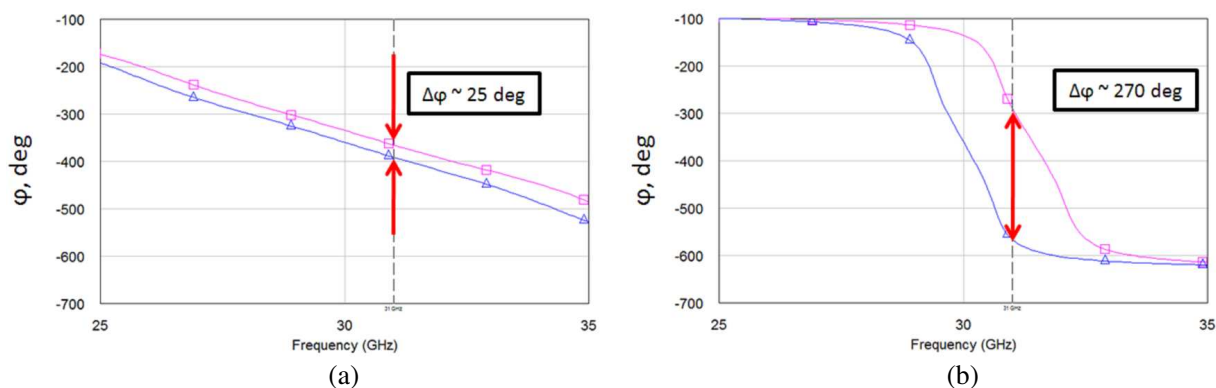


Figure 2: (a) Phase shift of one-layer and transverse periodic (classical) ETLs; (b) phase shift of periodic ETL.

To solve the problems mentioned above the more complex designs of ferroelectric lenses were elaborated (Fig. 1(b)) [4, 5]. The main difference of ETLs proposed in [4, 5] in comparison with construction of Fig. 1(b) is the periodicity of their structure in the transverse plane relative to the direction of the wave propagation (Fig. 1(b)). However these constructions provide the possibility to decrease the control voltages, but do not result to the increase of the scan angle at the same sizes.

In present work the construction based on periodic in longitudinal plane structure is proposed (Fig. 1(c)). In contrast to the lenses presented earlier, the periodic structure of this lens provides the slow-wave propagation and has a passband characteristic. These properties allow to achieve the higher value of $\Delta\phi$ in comparison with classical approach described above. The distinctive feature of the deflector is the use of multilayer periodic structure FE/LD/FE/LD/.../FE (FE-ferroelectric, LD-linear dielectric) with transparent for MW signal electrodes.

The thickness of each ferroelectric layer is equal to $\lambda_{FE}/2$ (λ_{FE} — the wavelengths in a ferroelectric material), while the thickness of the linear dielectric layer is $\lambda_{LD}/4$ (λ_{LD} — wavelengths in a linear dielectric). Thus ferroelectric layers can be considered as half-wave tunable resonators coupled by quarter-wave transformers. Ferroelectric layers are covered by electrodes transparent for microwave. Application of the same control voltages to ferroelectric layers leads to change of their permittivity, that results in tuning of structures passband to higher frequencies. The effectiveness of the proposed periodic structure is illustrated in Fig. 2, where the simulation results of

the phase shift for periodic (Fig. 1(c)) and structures that shown in Figs. 1(a), (b). Note that the permittivity and the total thickness of FE layers of both structures are identical.

The tunability of ferroelectric material is $k = 1.1 (k = \epsilon(0)/\epsilon(E_{\max}))$. It is clear that for the our periodic structure the value of $\Delta\phi$ is an order of magnitude more in comparison with nonperiodic one. In accordance with (1) for lens with $l = 30$ mm that results to the radical increase of the scan angle from $\alpha \approx 1.3$ deg. (nonperiodic structures — Figs. 1(a), (b)) to $\alpha \approx 14$ deg. (periodic one — Fig. 1(c)). Thereby the use of the ferroelectric lens with proposed periodic structure allows to obtain higher performance of ETL at relatively low control voltages and ferroelectric nonlinearity in comparison with existed analogues.

The object for full wave analysis of lens in Ka frequency band is presented in Fig. 3(a). Lens consists of three FE layers and air gaps between them with the plane area of the structure of 30×30 mm². The step-like approximation to describe the distribution of the permittivity along the FE layers (x -axis) was used (Fig. 3(b)). In the experimental prototype the required distribution is provided by application of control voltages between the strips and continuous ground electrodes on top and bottom surfaces of each FE layer. Note that open-ended for control currents strip electrodes provide the non-heating regime.

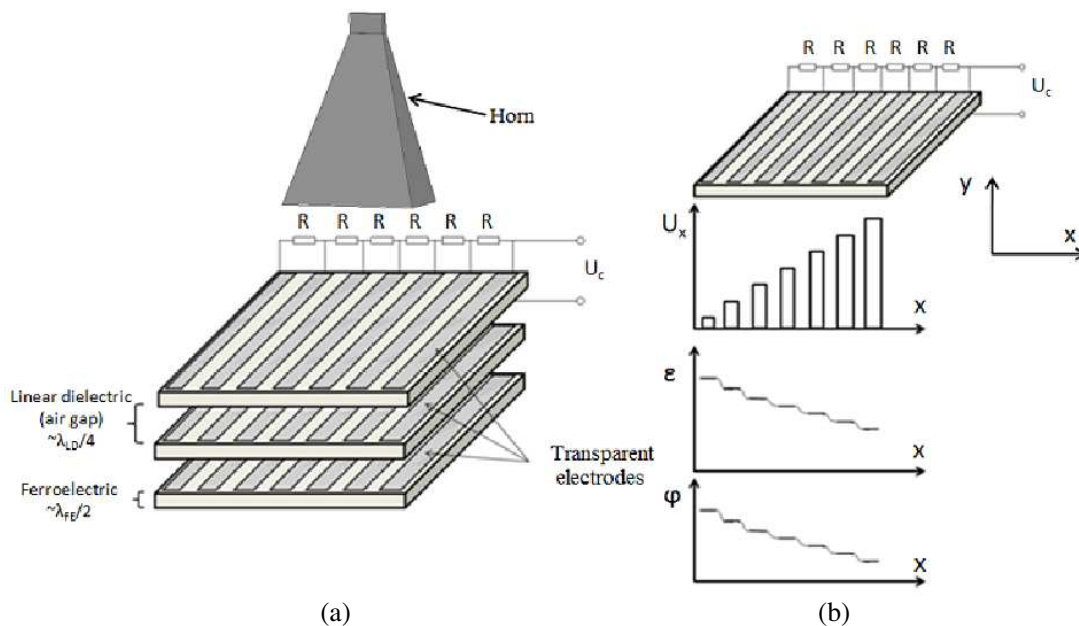


Figure 3: (a) Construction of electrically tunable lens based on periodic structure of ferroelectric layers; (b) single ferroelectric layer with corresponding step-like distribution of dielectric constant (ϵ) and phase shift (ϕ) under control voltage (U_x).

Values of electrical lengths for FE ceramic plates and air gaps are $\lambda_{FE}/2$ and $\lambda/4$, for each media respectively. In accordance with theory of periodic structures and principles of the filter design these electrical lengths are the most effective to obtain required amplitude and phase parameters of scattering coefficients (S_{11} and S_{21}) for such structures [7]. The horn with aperture size equal to cross sizes of lens (30×30 mm²) is used as a source of the microwave plane wave.

Simulation results show that 9% change of dielectric constant (from $\epsilon_1 = 100$ down to $\epsilon_2 = 91$) of all ferroelectric layers leads to the tune of central passband frequency on the half of the bandwidth (Fig. 4(a)) that in practice has to characterize the bandwidth of lens as $\Delta f \approx 1$ GHz. Variation of ETLs beam pattern in condition of different distribution of ϵ along its plane (x -axis) is shown in Fig. 4(b). The step variations of ϵ_{FE} from 100 down to 91 (tunability $k = 1.1$) and from 100 down to 78 ($k = 1.28$) correspond to 10.5 and 22.5 degrees scan angle respectively in comparison with pattern for system with no variation of $\epsilon_{FE} = 100$. The inset in Fig. 5(b) demonstrates the weak dependence of radiation pattern on frequency in operation passband. Note that simulation is done for lossless electrodes and dielectrics elements of structure.

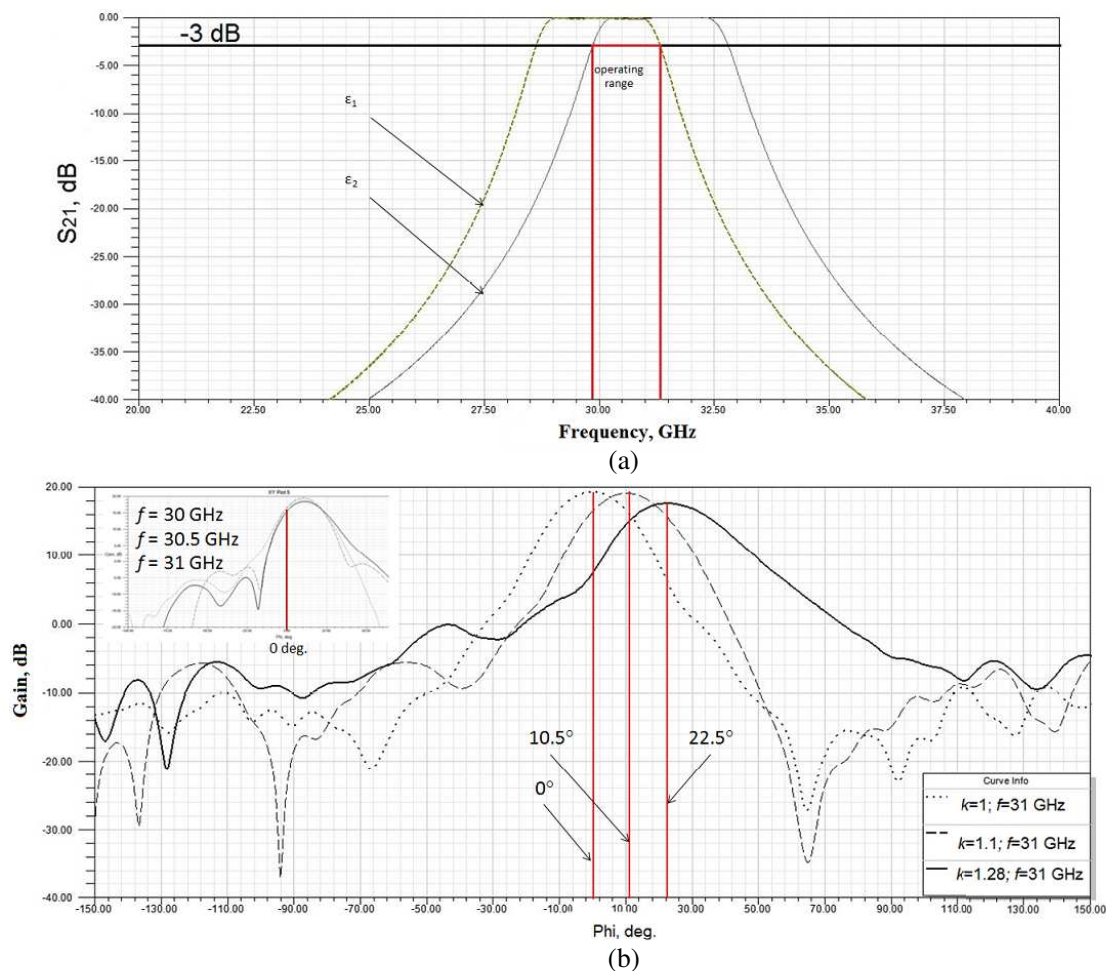


Figure 4: Characteristic of three ferroelectric layers periodic structure: (a) frequency dependence of transmission coefficient; (b) scan of lens pattern at different tunabilities of ceramic; variation of pattern at different operating frequencies (insert).

3. EXPERIMENTAL RESULTS

As a material for ETLs ferroelectric layers the ceramic of solid solution of barium-strontium titanate $\text{Ba}_x\text{Sr}_{1-x}\text{TiO}_3$ with composition $x = 0.4$ was used. The permittivity of the ceramic is about 400. The thickness of each ferroelectric layer is 0.25 mm that corresponds to $\sim \lambda_{\text{FE}}/2$ electrical length at operating frequency 30 GHz. The tunability of material is about 2 ($k = 1.8$ at 10 V/ μm). The microwave losses of ceramic in 30 ÷ 60 GHz frequency range corresponds to $\tan \delta = 0.01 \div 0.02$. These values were estimated on the base of direct measurement of insertion losses (S_{21}) for 30 and 60 GHz signal passing through the single 0.25 mm ferroelectric plate without electrodes. The time-tuning response of the dielectric constant under unipolar pulse control E -field was not more than 1 μs [8] that is suitable for application of scan antennas.

To be a transparent for microwaves the lens electrodes has to be made from high resistive material. As a rule for similar applications the ZnO and Si-Ti-Ce composition with surface resistance up to 10 MOhm/square are used [9]. The value of insertion losses for one electrode layer of these materials with thickness ~ 10 nm is less than 0.2 dB at 30 GHz operating frequency. But in our proof of art experiments the simplest spray graphite technology is used. In accordance with our experimental data the graphite films with thickness ~ 10 μm demonstrate the surface resistance of 1 ÷ 2 kOhm/square and at $f = 30$ GHz their additional microwave losses are about of 1.5 dB per graphite layer.

In Fig. 5(a) the photo of lens prototype installed in holder is presented. The lens with area of 30 × 40 mm² consists of the periodic structure FE/Air/FE/Air/FE with graphite electrodes on the surfaces of FE plates. To fixate the ferroelectric ceramic plates in a space and to provide their correct separation by air gaps the special textolite holder with conductive traces for application of

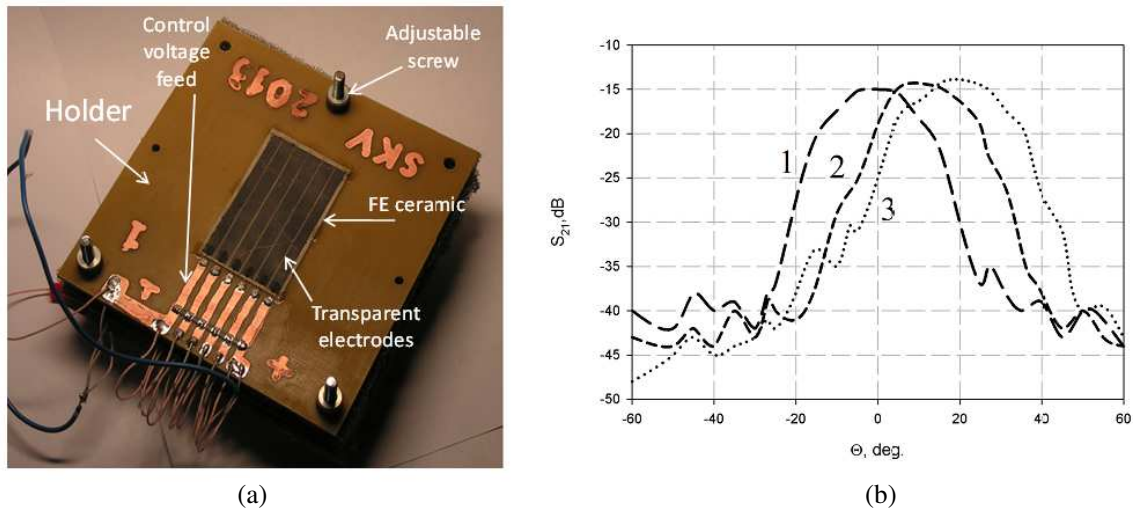


Figure 5: (a) Prototype of lens installed in adjustable holder; (b) scan of the radiation pattern at different gradients of the voltage distribution along the plate: (1) — zero voltage; (2) — $(0(\div)400)$ V; (3) — $(0(\div)800)$ V.

control voltages was designed. The horn with aperture diameter of 30 mm is used as a source of ~ 30 GHz quasi-plane wave for lens irradiation. The results of measurements of far-field radiation patterns at different control voltages are presented in Fig. 5(b). Experimentally observed scan angle $\alpha \approx 20$ deg. is in a good agreement with simulation one $\alpha \approx 22$ deg. (see Fig. 4(b)). Measured MW insertion losses of lens prototype is rather high (~ 15 dB) and is mainly determined by losses in graphite electrodes (~ 10 dB) and reflective losses (~ 2 dB) due to mismatching between horn and lens.

4. CONCLUSION

Simulation and experimental testing of the new construction of microwave (~ 30 GHz) electrically tunable deflector based on the ferroelectric periodic structure were done. The simplest three layer deflector prototype demonstrates the experimental scan angle $\alpha = \pm 20$ degrees. Taking into account no frequency dispersion of the dielectric permittivity of ferroelectric BSTO materials up to 100 GHz the tunable lenses on their base can be considered as not expensive, fast acting beam steer devices of mm and sub mm wavelengths.

REFERENCES

1. Wehling, J. H., "Multifunction millimeter-wave systems for armored vehicle application," *IEEE Trans. Microw. Theory Tech.*, Vol. 53, No. 3, 1021–1025, 2005.
2. Yeary, M., G. Crain, R. Kelley, et al., "Phased array weather/multipurpose radar," *IEEE Aerosp. Electron. Syst. Mag.*, Vol. 26, No. 10, 12–15, 2011.
3. Wames, R. E., W. F. Hall, W. W. Hall, and T. C. Lim, "Monolithic, voltage controlled, phased array," US Patent 4323901, 1982.
4. Jaganmohan, B. L., D. P. Patel, and V. Krichevsky, "Voltage-controlled ferroelectric lens phased arrays," *IEEE Trans. Antennas Propag.*, Vol. 47, No. 3, 458–468, 1999.
5. Cherman, V., P. Fihol, S. Gevorgian, et al., "Ferroelectric lens," US Patent 0237322, 2009.
6. Kozyrev, A. B., A. Chernokalov, V. Osadchy, A. Altynnikov, and I. Kotelnikov, "Deflecting device for electromagnetic radiation," US Patent 0343009, 2013.
7. Pozar, D. M., *Microwave Engineering*, 3rd Edition, Wiley, New York, 2005.
8. Altynnikov, A. G., A. G. Gagarin, M. M. Gaidukov, A. V. Tumarkin, et al., "Suppression of slow capacitance relaxation phenomenon in Pt/Ba_{0.3}Sr_{0.7}TiO₃/Pt thin film ferroelectric structures by annealing in oxygen atmosphere," *AIP Appl. Phys. Lett.*, Vol. 104, No. 4, 042903-1–042903-3, 2014.
9. Minami, T., "Present status of transparent conducting oxide thin-film development for Indium-Tin-Oxide (ITO) substitutes," *Thin Solid Films*, Vol. 516, No. 17, 5822–5828, 2008.

Point-to-point Radio Link Variation at E-band and Its Effect on Antenna Design

A. N. H. Al-Rawi, A. Dubok, M. H. A. J. Herben, and A. B. Smolders

Electromagnetics Group, Department of Electrical Engineering
Eindhoven University of Technology, The Netherlands

Abstract— Radio propagation will strongly influence the design of the antenna and front-end components of E-band point-to-point communication systems. Based on the ITU rain model, the rain attenuation is estimated in a statistical sense and it is concluded that for backhaul links of 1–10 km, antennas with a gain of 49.5 dBi are required. Moreover, depolarization can be a limiting factor for backhaul systems that are employing orthogonal polarization in order to improve capacity. Antenna mast movement becomes a relevant problem due to the narrow beamwidth of the high gain antennas, which is around 0.7° . We propose to implement a focal plane array as feed for the parabolic reflector antenna. This is to tackle the mast movement by electronic beam steering and to increase EIRP by increasing the number of active antenna elements, and to assist the mechanical alignment during installation.

1. INTRODUCTION

The network architectures of LTE and LTE-advanced promise the mobile users a wired experience in their wireless network. This puts high demands on the capacity (bits/sec) of the backhaul of these cellular systems. Fiber optics can due to its virtually unlimited capacity (10s of Gbps) fulfill these demands. However laying optical fibers in an urban and rural area is very expensive, and therefore a wideband point-to-point radio link can be a good alternative. Millimeter-wave wireless systems operating in E-band (71–76, 81–86, 92–95 GHz), offer a bandwidth of 13 GHz which is sufficient to produce a bit rate of 1 Gbps with simple modulation schemes such as QPSK. This makes these systems a good option for the backhaul. There is an increasing demand on extending the E-band backhaul range. This is to reduce the construction and maintenance cost. It relies on increasing the antenna gain. As a consequence, the unwanted movement of the antenna mast becomes very relevant at this band because it causes a drop in the SNR. In addition, the antenna alignment during installation becomes cumbersome.

2. POINT-TO-POINT LINK VARIATION

The atmospheric window at E-band shows very low attenuation whereas it is significantly high at the neighboring 60 GHz band due to oxygen absorption [1]. Therefore, the 60 GHz band is limited to indoor and short range applications. The free-space and rain attenuation is high at E-band and they become very significant on the extended range of 10 km. These effects have been considered in [2].

Based on the ITU rain model [3] and data [4, 5] we analyzed the effect of rain in a statistical sense (see Fig. 1). For a backhaul length of 5 km, with rain attenuation of 0.01% of the time (i.e., 99.99% system availability); the total attenuation will be [$A_{tot} = \text{free-space } 143.4 \text{ dB} + \text{rain attenuation } 15.2 \text{ dB} + \text{atmosphere attenuation } 4 \text{ dB} = 162.6 \text{ dB}$]. A large antenna gain is required to compensate for such large attenuation. At an antenna gain of 41 dBi, a SNR at the receiver input of 40.4 dB, and with the assumption that the receiver has a noise figure of 10 dB, the SNR_d at the detector input is 30.4 dB. This is quite sufficient for QPSK with a bit error rate of 10^{-6} , that usually requires an SNR around 10 dB. For the longer path length of 10 km, the total attenuation is 179.5 dB, and SNR_d at the detector input is 16.5 dB. This is still adequate for the demodulator to accurately perform. Exceeding the rain attenuation of 0.01% to 0.001% of the time (i.e., 99.999% system availability) to increase the reliability of the point-to-point wireless communication, the total attenuation for 5 and 10 km path length is 175 dB and 195 dB, respectively. The SNR_d for the 5 km path length is 21 dB whereas for the 10 km path length it is 1 dB. The latter can be improved by increasing the receiver antenna gain to 49.5 dBi. This brings SNR_d to 9.5 dB, which is sufficient for QPSK with a bit error rate of 10^{-6} . This also can be further improved by reducing the receiver noise.

In addition, and due to the anisotropic nature of the rain medium, a pure vertically-polarized wave will arrive at the receiver with a small horizontally-polarized field component. This effect

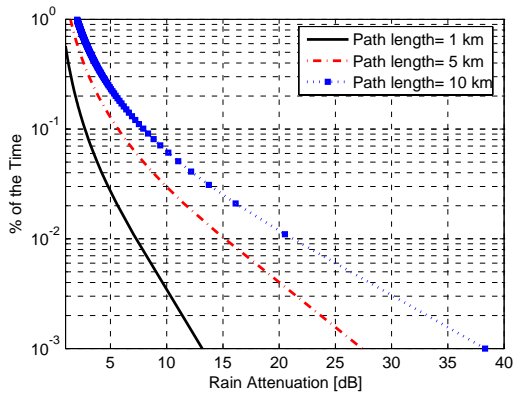


Figure 1: Fraction of the time versus the rain attenuation.

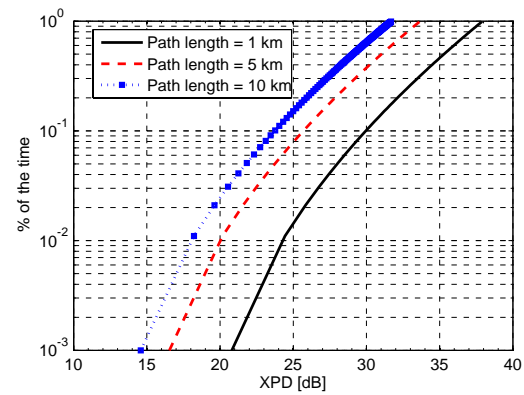


Figure 2: Fraction of the time versus cross polar discrimination.

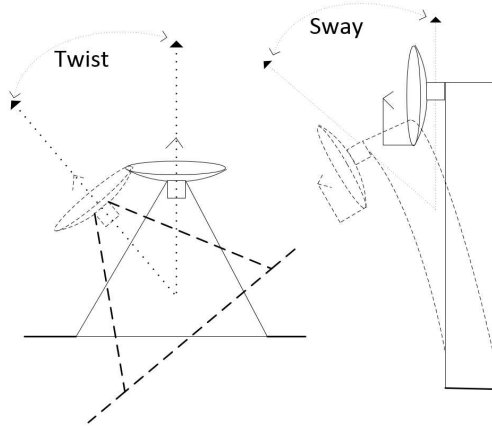


Figure 3: The motion of the antenna mast as twist and sway.

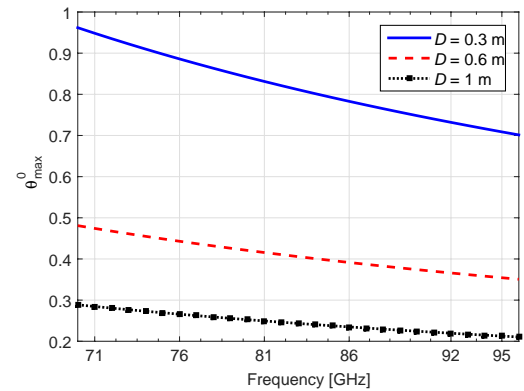


Figure 4: Maximum allowed twist/sway.

causes co-channel interference and due to that the channel capacity of wireless communication systems employing orthogonal polarization in order to double the capacity will be reduced. The depolarization is commonly quantified by the reduction in the cross-polar discrimination (XPD). The minimum XPD occurring during 0.01% of the time is related to the rain attenuation exceeded during 0.01% of the time. Most models and the standard ITU model [3] use this fact to estimate the XPD. As shown in Fig. 2, a shorter path length, i.e., 1 km has larger cross-polarization discrimination as compared to the longer ones. Moreover, reducing 0.01% of the time to 0.001% will reduce the cross-polarization discrimination. At 0.001% of the time the XPD can drop to 15 dB at a path length of 10 km.

The vertical gradient of the atmosphere refractive index can cause variation on the angle-of-departure and -arrival. However, based on the ITU model and data [6], these variations are not so significant for a path length of 1 or 10 km. For instance, the variation for 0.001% of the time is 0.09 degree for a 10 km path length. This is quite small as compared to the beamwidth of a typical high-gain E-band antenna (0.7° – 1.2°).

The movement of the antenna mast is very relevant because high-gain antennas with small beamwidths are used for E-band backhaul systems. This motion is best described as twist and sway of the antenna mast, and illustrated in Fig. 3. This is mainly happening when the wind blows. Due to mast movement the propagating wave will no longer leave/enter the transmit/receive antenna at the maximum of its radiation pattern. This leads to an additional attenuation. The radiation pattern of the parabolic reflector antenna is used to estimate the -3 dB beamwidth. This estimation is repeated for three reflector diameters. The -3 dB point will set the specification on the maximum allowed twist and sway. Sway and twist exceeding the corresponding values in Fig. 4 will cause a significant degradation of the communication link. The wind forces can cause twist or sway up to 1 degree.

3. E-BAND ANTENNA DESIGN

The proposed configuration consists of a symmetrical reflector antenna and a focal plane array (FPA) as the feed antenna. This configuration is depicted in Fig. 5. The selected diameter is 95λ (i.e., 0.4 m) and delivers a maximum gain of 49.5 dBi at 71 GHz. The selected diameter is needed in order to compensate the total attenuation for the extended range of 10 km. The antenna gain is limited by the FCC regulation for E-band [7]. The configuration is modeled by using physical optics (PO) and a plane wave incident to the reflector antenna [8, 9]. The encircled power analysis [10, 11] is then applied in the focal plane to estimate the FPA size as a function of F/D , scan angle, and antenna efficiency. The efficiency here is the available power on the surface of the FPA disk normalized by the power captured by the reflector. The required scan angle is ± 5 degree, this is to track the mast movement and to assist the mechanical alignment. Due to the mast motion (twist and sway), the main beam is moving within a cone, therefore the topology of the FPA is chosen to be a circular disk.

In Fig. 6 the efficiency as function of FPA size is plotted for practical F/D ratios, and at the maximum required scan angle of 5° . An efficiency criterion of 80% criterion is used to select an appropriate F/D ratio and the FPA size. This criterion is to ensure high efficiency for the extended range of 10 km. $F/D = 0.6$ yields the smallest FPA size and this is important to minimise feed blockage. This means that the FPA has a 30 mm radius.

The trade-off is that the main beam in the focal plane is concentrated in a small region around the focal point (see Fig. 7). With the assumption that the antenna element spacing is equal to $\lambda = 2$. Practically, this limits the number of antennas to about 28 elements per scan angle (see Fig. 8). Therefore the EIRP can not be improved by exciting more array elements to create the beam. However, this can be improved by axially displacing the FPA in order to broaden the field

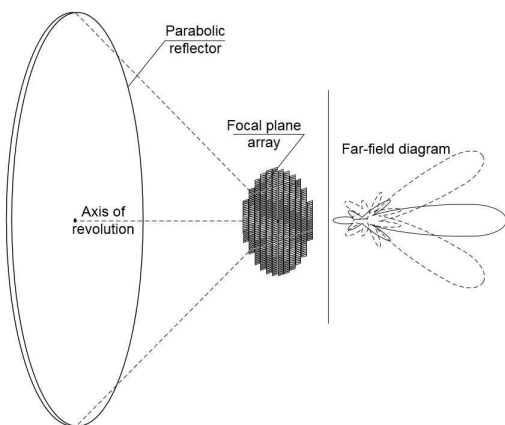


Figure 5: Artist impression of the FPA and reflector for point-to-point E-band wireless communications.

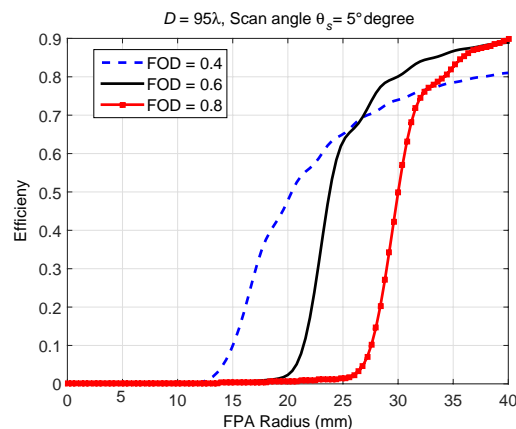


Figure 6: Encircled power analysis is applied in order to estimate the FPA size versus efficiency.

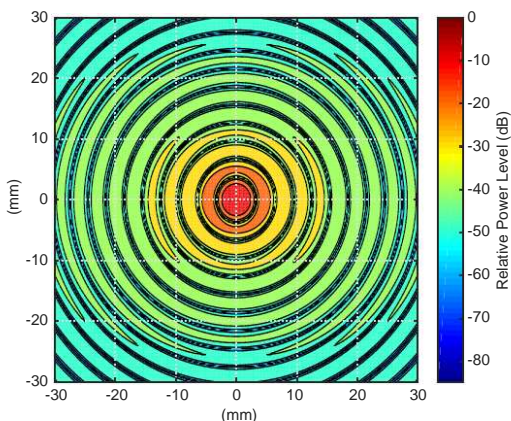


Figure 7: The field distribution image in the focal plane.

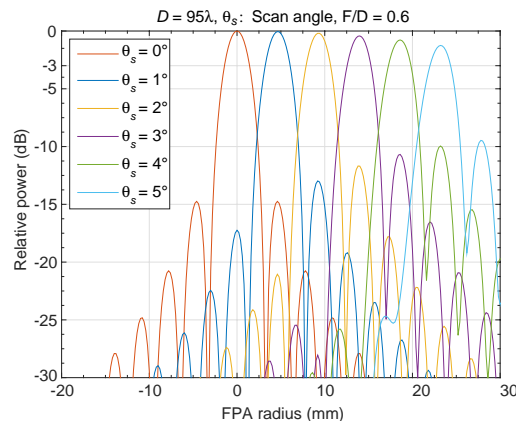


Figure 8: Cuts of the field distribution along the beam scan.

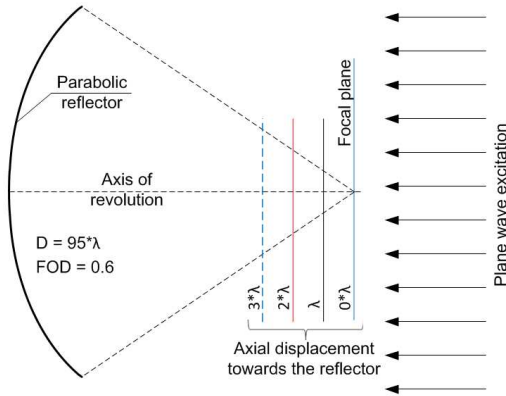


Figure 9: Axial displacement of the focal plane Model.

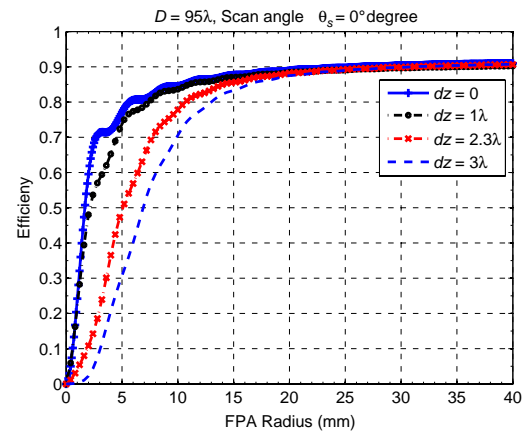


Figure 10: Efficiency versus FPA size for a range of axial displacements (dz). ($F/D = 0.6$).

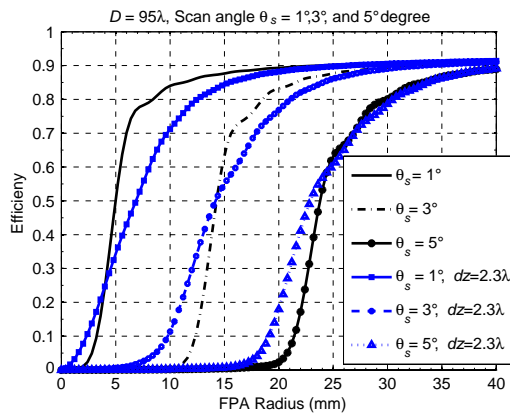


Figure 11: Efficiency of the axially displaced focal plane as a function of scan angle.

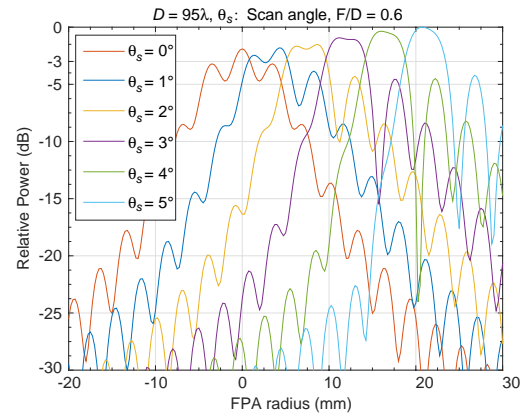


Figure 12: Cuts of the field distribution along the beam scan of the axially displaced plane.

distribution. The axial displacement (dz) is with λ steps towards the reflector as depicted in Fig. 9. 2.3λ is chosen as the optimum axially displaced focal plane. By exceeding it, the main beam of the focal plane pattern is going to be bifurcated. The efficiency curve of it is less steep and indicates the effects of broadening. Moreover, the 80% efficiency criterion still gives a small enough size of the FPA (see Fig. 10). In Fig. 12 the efficiency curves of the scan beam scenario, show a beam broadening up to 3° . Increasing the angle of incidence the effect of broadening is decreased because the scanned beam is getting narrower. We believe this is happening because of some focusing effect by the reflector. The beam broadening as shown in Fig. 12 indicates that the number of antenna elements can be increased significantly. About 78 elements will be involved up to 3° and to a less extent at 4° and 5° . Hence, EIRP can be improved and because of the overlap of the beams, array element reuse is possible.

4. CONCLUSION

High gain antennas at both the transmit and receiver site of the backhaul communication link are necessary to deliver acceptable levels of SNR. This is due to the rain attenuation and the large freespace attenuation. As a consequence of the high gain antenna requirement, the radiation pattern has a very narrow beamwidth. Due to this, the mast movement is very relevant. This problem has to be tackled, otherwise, additional attenuation will occur, resulting an outage. With the proposed antenna configuration of the FPA these issues can be overcome. The selected values of the reflector antenna diameter, F/D ratio, and FPA size are a good starting point for an optimized antenna design.

ACKNOWLEDGMENT

This work is supported by the Netherlands Foundation of Technical Sciences (STW).

REFERENCES

1. Rec. ITU-R P.676-6, "Attenuation by atmospheric gases," 2005.
2. Dyadyuk, V., J. D. Bunton, and Y. J. Guo, "Study on high rate long range wireless communications in the 71–76 and 81–86 GHz bands," *Proceedings of the 39th European Microwave Conference*, 2009.
3. Rec. ITU-R P.530-15, "Propagation data and prediction methods required for the design of terrestrial line-of-sight systems," 2013.
4. Rec. ITU-R P.838-03, "Specific attenuation model for rain for use in prediction methods," 2005.
5. Rec. ITU-R P.837-06, "Characteristics of precipitation for propagation modelling," 2012.
6. Rec. ITU-R P.453-10, "The radio refractive index: Its formula and refractivity data," 2012.
7. Federal Communications Commissions, "Allocation and service rules for the 71–76 GHz, 81–86 GHz, and 92–95 GHz bands," 2005.
8. Minnett, H. C., B. Mac, and A. Thomas, "Fields in the image space of symmetrical focusing reflectors," *Proceedings of the IEE*, Vol. 115, 1419–1430, 1968.
9. Ng Mou Keha, N. and L. Shafai, "Characterization of dense focal plane array feed for parabolic reflectors in achieving closely overlapping or widely separated multiple beams," *Radio Sci.*, Vol. 44, 2009.
10. Ivashina, M. V. and C. G. M. van't Klooster, "Focal field analyses for front-fed and offset reflector antenna," *2003 IEEE Antennas and Propagation Society International Symposium*, Vol. 2, 750–753, 2013.
11. Hayman, D. B., T. S. Bird, K. P. Esselle, and P. Hall, "Encircled power study of focal field for estimating focal plane array size," *2005 IEEE Antennas and Propagation Society International Symposium*, Vol. 3A, 371–374, 2015.

60 GHz Antenna on Metallic Nanowired Membrane Substrate

L. G. Gomes¹, M. V. Pelegrini¹, P. Ferrari², G. P. Rehder¹, and A. L. C. Serrano¹

¹Laboratory of Microelectronics, University of São Paulo, Brazil

²IMEP-LAHC, Grenoble University, France

Abstract— This work presents the analysis of the novel metallic nanowired membrane (MnM) substrate for designing antennas at the 60 GHz frequency band. The fabrication process of a rectangular patch antenna on the MnM-substrate is presented in detail. The antenna is fed through a modified microstrip line with slow-wave effect in order to reduce the feed line width. The fabrication is done in two phases, first the microstrip circuits are fabricated on a 50- μm -thick membrane; then it is assembled on a mechanical base to accommodate the two different substrate thicknesses used for the antenna and the slow-wave transmission line. The structure is simulated using a 3D EM software and the results indicate this substrate is a viable choice for antenna design, however gain increasing techniques must be used because of the high dielectric constant of the substrate.

1. INTRODUCTION

Given the need for gigabit data transfer rates and the fact that the microwave spectrum is already saturated with a great number of protocols and applications, the mm-wave frequency range, which comprises frequencies from 30 GHz to 300 GHz, is getting more and more attention since early 2000s. Among these, the 60 GHz frequency has been the focus of several researches for household and short-range wireless data transfer applications [1].

Despite of the reduction in size of lambda-based passive circuits at mm-waves, there is still an issue regarding low-cost integration, especially for antennas, which always occupy a large area. Antennas operating at mm-waves present sizes ranging from hundreds of micrometers up to a few millimeters [2], which enables the integration of planar antennas with transceivers either as a System-on-Chip-(SoC) [3] or as a System-in-Package (SiP). SiP avoids the complications of using semiconductor substrates and IC manufacturing processes, which are not entirely optimized for mm-wave passive components. Antennas manufactured using the SiP technique can employ alternative substrates, such as low temperature cofired ceramic (LTCC) [4], fused silica [5], liquid crystal polymer (LCP) [6], and Teflon [7]. They can also make use of gain increasing techniques, such as arrays and beam steering, to compensate loss caused by the abrupt signal attenuation at 60 GHz, and avoid fading issues. In order to reduce passive circuit elements even further, circuits based on slow wave concepts have been presented using different techniques and materials to reduce the phase velocity [8]. However, having the antenna fabricated in a different substrate often leads to extra interconnections using vias, which tend to be lossy, bulky, costly and hard to fabricate at mm-waves.

The metallic nanowired membrane substrate (MnM) allows an easy hybrid integration of slow-wave and classical, non-slow-wave, passive circuit elements on the same low-cost substrate [9]. This great advantage associated to a high substrate dielectric constant ($\epsilon_r = 9.8$), motivated this work. We present the design and fabrication of a rectangular patch antenna on the MnM-substrate in order to determine whether it is a viable choice in high efficiency mm-wave antenna designs.

2. DESIGN

The MnM-substrate, as explained in [9], consists of a nanoporous alumina membrane with a thickness of 50 μm filled with copper nanowires in specific regions, a copper ground plane on its underside, and a silicon dioxide layer on its upper side. The advantage of this substrate is to allow hybrid integration of slow-wave structures with non-slow-wave structures. The MnM-substrate provides two different dielectric constants: 9.8, which is the porous alumina without nanowires, and an effective dielectric constant, $\epsilon_{r\text{eff}}$, of about 30 in the regions with nanowires. These nanowires yields the slow-wave effect, which increases $\epsilon_{r\text{eff}}$ that leads to miniaturization by trapping the electric field in the thin oxide region.

Given the novel nature of this substrate and the need to investigate whether it is viable as an antenna substrate, the authors chose a rectangular patch antenna structure since it is very well

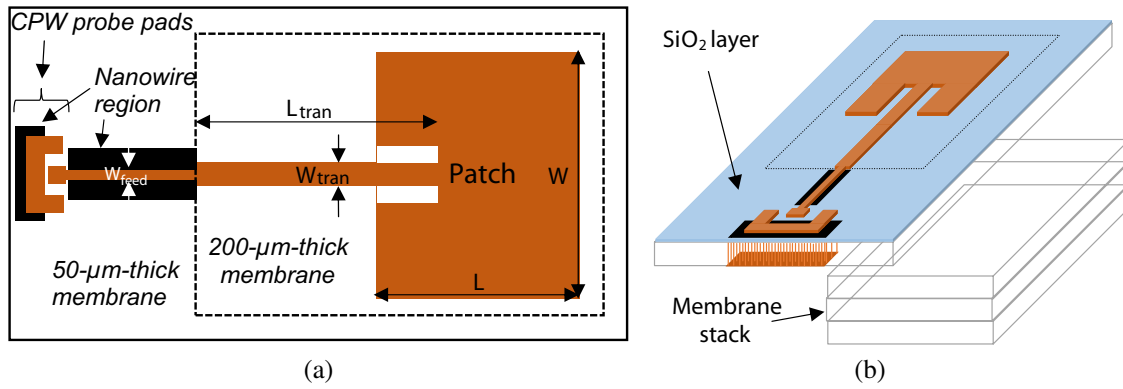


Figure 1: Patch antenna structure, being (a) a top view and (b) a perspective view of the antenna structure and its substrate.

modeled and understood and widely available in technical literature. Fig. 1 illustrates the proposed antenna.

For an antenna to irradiate efficiently, the substrate should be thick and its ϵ_r close to 1, so the value chosen for ϵ_r was the smallest one, 9.8. On the other hand, there is a limit for the substrate thickness, beyond which loss due to surface waves has to be accounted for. (1) gives the maximum substrate thickness h before surface wave propagation can exist [10]:

$$h = \frac{n * c}{4 * f_r * \sqrt{\epsilon_r - 1}} \quad (1)$$

where c is the speed of light. If the resonant frequency f_r of the proposed antenna is 60 GHz and $n = 1$ for the first excited surface wave mode TE_1 , h results in $\sim 421 \mu\text{m}$. A compromise is required for the substrate thickness, since thicker substrates means more efficient antennas, but wider transmission lines will be required to connect to the antenna. At 60 GHz, the dimensions of a transmission line can become comparable to the dimensions of the antenna, degrading its performance.

The thickness of 2000 μm was chosen for this antenna. This thickness was obtained with the stacking of three 50- μm -thick membranes below the membrane on which the antenna was fabricated.

Once ϵ_r and h are defined, the patch width W and length L were theoretically defined to be $W = 1200 \mu\text{m}$ (2), and $L = 800 \mu\text{m}$ (3).

$$W = \frac{c}{2 * f_r} * \sqrt{\frac{2}{\epsilon_r - 1}} \quad (2)$$

$$L = 0.5 * \frac{c}{f_r * \sqrt{\epsilon_r}} \quad (3)$$

Those initial values were optimized in order to obtain a resonance frequency at 60 GHz and to shift a higher order resonance mode above 80 GHz. Further, the antenna feed needs closer attention. The antenna is fed by a 50- Ω transmission line, but in such substrate with thickness of 200 μm and $\epsilon_r = 9.8$, its width is almost as wide as the patch, and will reduce the overall antenna efficiency. Moreover, if we choose to feed the antenna by just connecting a 50- Ω transmission line to the border of the patch, an impedance transformer would be necessary to match these impedances. The impedance at the border of the patch is about 400 Ω , thus the transformer line impedance would be around 140 Ω and its width would be close to the minimum dimension that the fabrication process could accurately produce. Therefore, a traditional quarter wavelength transformer is also not feasible. To overcome these issues, a slow-wave 50- Ω feed line was designed on a 50- μm nanowire-filled region of the MnM-substrate, which reduces considerably the width of this feeding line. In addition, a solution comprising an impedance transformer and inset feed was used, which reduces the impedance of the traditional line, enlarging its width to acceptable dimensions within the fabrication limits. The design was optimized using the EM simulator HFSS and the final dimensions, shown in Fig. 1 are: $W = 750 \mu\text{m}$, $L = 730 \mu\text{m}$, $W_{feed} = 15 \mu\text{m}$, $W_{tran} = 30 \mu\text{m}$, $L_{tran} = 800 \mu\text{m}$.

3. MANUFACTURING

Since the feeding line should be fabricated on a 50- μm MnM-substrate and the antenna on a 200- μm stack of four membranes, the antenna assembly consists of two parts: the MnM-substrate and a metallized silicon cavity. Nanowires were also used to connect the ground of the coplanar pads used for the measurement probes to the microstrip ground.

A single 50- μm -thick alumina porous membrane was used to fabricate the microstrip circuits: the patch antenna, the impedance transformer and the slow wave feeding line. The process sequence is described as follows, illustrated in Fig. 2. **1-** A porous membrane with 25 mm in diameter acquired from Synkera with 55-nm pores, spaced 150 nm apart, was boiled in trichloroethylene, then acetone and last isopropyl alcohol, for 5 minutes on each solvent, for cleaning. **2-** 1- μm silicon dioxide (SiO_2) was deposited by PECVD to be used as a mask. **3-** The SiO_2 was patterned by photolithography in the regions where the nanowires will grow and SiO_2 etch on BOE (buffered oxide etch). **4-** A copper (Cu) seed layer was deposited by sputtering. **5-** The nanowires were grown by Cu electrodeposition. **6-** SiO_2 and Cu seed were removed by mechanical polishing. **7-** 1- μm of SiO_2 was deposited by PECVD. **8-** The nanowire region for the ground pad was patterned. **9-** 50-nm Cu seed was sputtered and thickened by electrodeposition up to 3 μm . **10-** The circuit elements were patterned by photolithography and Cu etch with a solution of ceric ammonium nitrate and acetic acid.

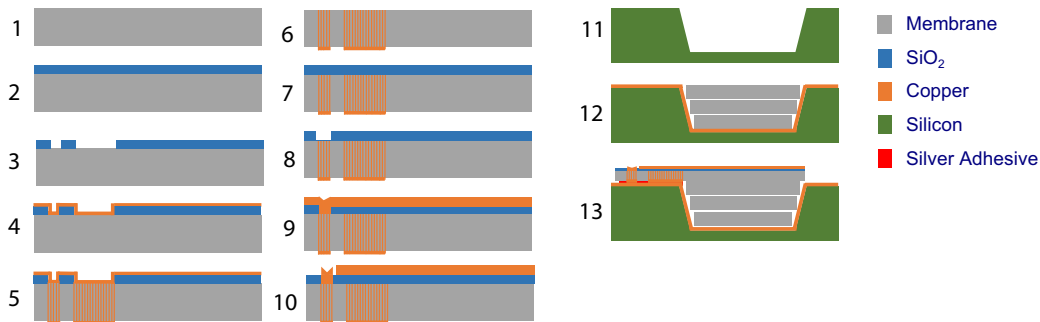


Figure 2: View of a transversal cut of the antenna presented in Fig. 1 with its fabrication process: (1–10) Steps of the microstrip devices. (11–13) Steps of the mechanical silicon substrate assembly.

11- A 150- μm deep cavity was etched in the silicon wafer with a potassium hydroxide solution (30% at 60°C) and covered by a Cu layer of 3 μm to act as the ground plane for the whole antenna. **12-** A bare membrane was cut using a LPKF laser system, and stacked into the cavity. **13-** A single patch antenna, also cut with laser, was aligned above the cavity. A silver conductive adherent was used to assure electrical contact between grounds (ground pad, slow wave 50- Ω feeding line, and antenna).

4. DISCUSSION AND RESULTS

The designed antenna structure was simulated and the results of return loss (S_{11}), gain, and radiation pattern are shown in Fig. 3. The simulated antenna presented 5.4 dBi of gain with 2.4% of 10-dB bandwidth.

Since the antenna gain is reduced with the increase of ϵ_r , any antenna fabricated on this substrate will present a lower gain compared to a similar structure fabricated on a substrate with lower ϵ_r . However, since passive elements size is also reduced by an increase of ϵ_r , any antenna fabricated over this substrate will also occupy a smaller area compared to a similar structure fabricated on a substrate with lower ϵ_r . The further miniaturization provided by the slow-wave effect present on the MnM-substrate means that a compact antenna array can be easily designed to increase the system gain. Beam steering techniques may also be achieved using integrated slow-wave phase shifters.

The loss tangent, $\text{tg}(\delta)$, of the alumina and the SiO_2 is low enough to not affect the gain drastically. Simulations assuming a hypothetical worst-case scenario, assuming $\text{tg}(\delta) = 0.001$ for both alumina and silicon dioxide, barely changed the gain. It is worth to note that optimization for losses and gain was not the focus of this work, but the antenna fabrication viability on the MnM-substrate.

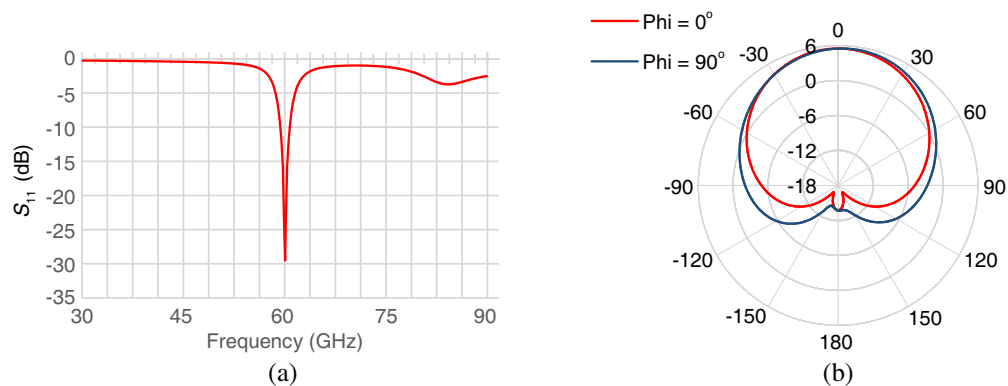


Figure 3: Simulation results for the designed antenna. (a) shows the frequency response of the return loss (S_{11}). (b) shows its radiation pattern at 60 GHz.

A simple improvement in this design would be to remove the alumina membrane from inside the cavity to reduce ϵ_r , which would increase the antenna gain, although its dimensions would also increase.

The fabrication process was successful and the fabricated antenna is shown in Fig. 4. This figure shows the silicon wafer on which the metallized cavities were etched. The detail in yellow shows the final antenna assembly, where a 50- μm -thick membrane bearing the antenna structure was aligned over the cavity filled with the three membranes-stack. The detail in blue shows the antenna structure with the patch, the impedance transformer, the slow-wave feed and the CPW pad.

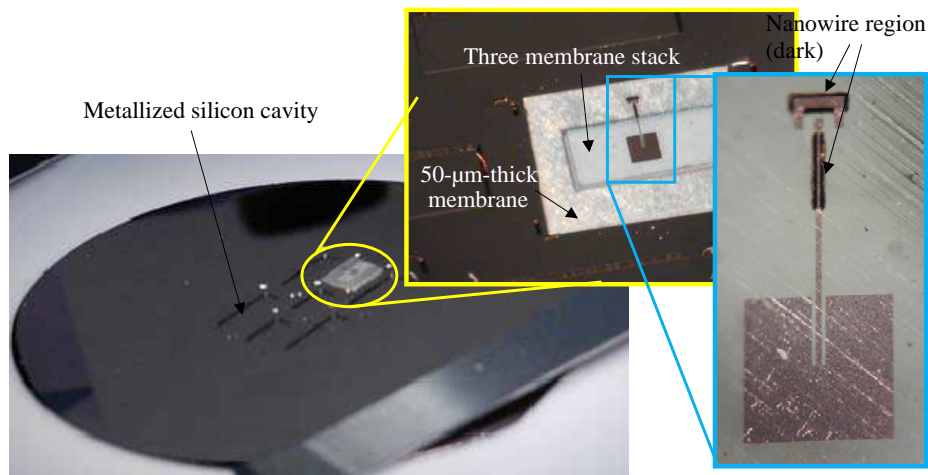


Figure 4: The fabricated 60 GHz antenna on the Mnm-substrate.

5. CONCLUSION

This work presented the analysis of the novel MnM-substrate for designing antennas at 60 GHz. The fabrication process of the rectangular patch antenna on the MnM-substrate was validated. The fabricated antenna was fed through a modified microstrip line with slow-wave effect, and the results indicated that this substrate is a viable choice for antenna design in mm-wave frequencies. However gain increasing techniques should be used because of the high dielectric constant of the substrate.

ACKNOWLEDGMENT

This work is funded by the São Paulo Research Foundation (FAPESP).

REFERENCES

1. Daniels, R. C., et al., “60 GHz wireless: Up close and personal,” *IEEE Microwave Magazine*, 544–550, 2010.
2. Peters, F. D., et al., “77 GHz millimeter wave antenna array with Wilkinson divider feeding network,” *Progress In Electromagnetics Research B*, Vol. 9, 193–199, 2009.
3. Gutierrez, F., et al., “On-chip integrated antenna structures in CMOS for 60 GHz WPAN systems,” *IEEE Journal on Selected Areas in Communications*, 1367–1378, 2009.
4. Lamminen, A. E., et al., “60-GHz patch antennas and arrays on LTCC with embedded-cavity substrates,” *IEEE Transactions on Antennas and Propagation*, Vol. 56, No. 9, 2865–2874, 2009.
5. Manzillo, F. F., et al., “A 60-GHz passive broadband multibeam antenna system in fused silica technology,” *IEEE Antennas and Wireless Propagation Letters*, Vol. 12, 1376–1379, 2013.
6. Nejad, M. B., et al., “Chip package and antenna co-design of a tunable UWB transmitter in system-on-package with on-chip versus off-chip passives,” *Electronics System Integration Technology Conference*, Vol. 1, 291–298, 2006.
7. Enayati, A., et al., “Millimeter wave horn antenna in package solution fabricated in a Teflon-based multilayer PCB technology,” *IEEE Transactions on Antennas and Propagation*, Vol. 61, No. 4, 1581–1590, 2013.
8. Ke, P.-Y., et al., “Characterization of compact V-band GaAs CMRC filter using slow wave CPW transmission line technology,” *Progress In Electromagnetics Research B*, Vol. 43, 355–372, 2012.
9. Serrano, A. L., et al., “Modeling and characterization of slow-wave microstrip lines on metallic nanowire-filled-membrane substrate,” *IEEE Transactions on Microwave Theory and Techniques*, Vol. 62, No. 12, Part 2, 3249–3254, 2014.
10. Pozar, D. M., et al., “Considerations for millimeter wave printed antennas,” *IEEE Transactions on Antennas and Propagation*, Vol. 31, No. 5, 740–747, 1983.

Analysis of Sampling Grids for Spherical Near-field Antenna Measurements

R. Cornelius and D. Heberling

Institute of High Frequency Technology, RWTH Aachen University, Germany

Abstract— Modern spherical near-field to far-field transformation algorithms, in contrast to Fourier based ones, offer arbitrary sampling grids without inherent oversampling. This raises the question how the measurement samples should be distributed on the sphere. In this paper different sampling grids for spherical near-field antenna measurements are presented and evaluated. It is shown that the spherical transformation problem is in general well-conditioned and can be solved accurately. Measurement results emphasize the possible measurement time reduction due to the reduction of oversampling. However, positioning hardware has to be included in the analysis, because complex measurement trajectories might increase the measurement time.

1. INTRODUCTION

Spherical near-field antenna measurement is a popular, well-known and accurate method to characterize an antenna under test (AUT). The electromagnetic field is measured on a closed surface around the antenna and transformed to the far-field by a near-field to far-field transformation. A commonly used transformation algorithm first calculates a spherical mode spectrum using Fourier transforms [1]. From this mode spectrum the far-field is derived. Due to the Fourier transform the transformation algorithm is very fast and efficient but requires equiangular sampling in spherical coordinates which causes oversampling. In order to improve the measurement speed more efficient sampling grids may be used at the expense of different and/or more complex transformation algorithms. Reformulating the transmission formula in [1] in matrix form as used for truncation error reduction in [2] is a very simple and straightforward approach which will be used in this paper. Alternatively, algorithms not restricted to equiangular sampling [3, 4] could be used. Furthermore, near-field interpolation methods could be utilized to determine the near-field on an equiangular grid [5]. Besides the larger sampling flexibility new algorithms provide additional features like higher order probe correction, the possibility of different measurement distances and position correction. Due to the technical progress in computer technology the transformation time is usually negligible compared to the measurement time and therefore a less important factor. Although new algorithms have been successfully tested by simulations and measurements [3, 4, 6], a comprehensive investigation of different sampling grids is still missing. So far only little attention has been paid to the minimal number of required near-field samples and their distribution over the sphere. This distribution is also a very important factor for the measurement time due to different capabilities of different positioning systems (e.g., roll-over-azimuth, robot arm). In this paper we will present different sampling grids and besides the location of the sampling points the polarization will be investigated. The near-field to far-field transformation algorithm used is based on calculation of the spherical modes by matrix inversion. Therefore the condition number of the grids will be evaluated and compared. Simulations and measurements will be performed for all grids. Finally the required relative measurement time and accuracy will be analyzed for the different sampling grids. It will be highlighted that the measurement speed can be increased compared to equiangular sampling.

2. NF-FF TRANSFORMATION USING MATRIX INVERSION

The well-known spherical near-field transmission formula [1]

$$w(A, \chi, \theta, \phi) = \sum_{\substack{smn \\ \mu}} Q_{smn} e^{im\phi} d_{\mu m}^n(\theta) e^{i\mu\chi} P_{s\mu n}(kA) \quad (1)$$

can be directly interpreted as a linear equation system

$$\mathbf{w} = \Psi \mathbf{Q} \quad (2)$$

where \mathbf{w} is the measured signal, Q_{smn} are the spherical mode coefficients, $e^{im\phi} d_{\mu m}^n(\theta) e^{i\mu\chi}$ represents the spherical mode rotation and $P_{s\mu n}$ are the probe coefficients. Spherical modes are orthogonal

solutions of Maxwell's equations in spherical coordinates. Their complex amplitudes are denoted as Q_{smn} and have three indices: degree n , order $m \leq n$ and $s \in [1, 2]$ associated to the field components of TE- and TM-waves. In antenna measurements the modes are band limited in $m \in [1, M]$ and $n \in [1, N]$ according to:

$$M \leq N = kr_0 + n_1 \quad (3)$$

k is the wavenumber, r_0 is the radius of a sphere containing the antenna and n_1 is a constant which influences the accuracy (usually 10, [1]). Thus the highest mode excited by an AUT is limited by its size in relation to frequency. Higher order modes are highly attenuated and do not contribute significantly to the far-field characteristic. The total number of modes ($M = N$), equal to the number of unknowns, can be calculated from its band limitation by

$$\#_{Modes} = P_{\min} = 2N(N + 2) = 2N^2 + 4N \quad (4)$$

The linear equation system (2) can be solved with different methods as for example least squares [6] and does in general not require any specific sampling grid. Methods based on matrix inversion require of course more computational power but are affordable for antenna measurement applications with several thousands of measurement points.

3. POINT DISTRIBUTION ON SPHERE

In general, infinitely many possibilities exist to distribute P points on a sphere and as stated above no specific sampling criterion has to be fulfilled. However, in antenna measurement applications covering the whole sphere is required in order to avoid truncation errors [2]. Therefore the measurement points need to cover the whole sphere. Equal distribution is an intuitive choice but not compulsory. The investigated schemes are:

3.1. Equiangular

The required equiangular sampling steps are calculated from the band limitation by

$$\Delta\theta = \frac{2\pi}{(2N + 1)}; \quad \Delta\varphi = \frac{2\pi}{(2M + 1)} \leq \frac{2\pi}{(2N + 1)}; \quad \chi = \left[0, \frac{\pi}{2}\right]; \quad (5)$$

$$P = P_\theta P_\varphi P_\chi = (N + 1)(2N + 1) \cdot 2 = 4N^2 + 6N + 2 \quad (6)$$

The samples are concentrated near the poles and the sphere is therefore highly oversampled (roughly by factor of 2).

3.2. Thinned Equiangular

A sampling strategy to reduce the oversampling at the poles is the reduction of measurement points in φ depending on the value θ taking into account the fact that the latitude circles have different radii ($\propto \sin(\theta)$).

$$\Delta\theta = \frac{2\pi}{(2N + 1)}; \quad \Delta\varphi = \frac{2\pi}{\lceil(2M + 1) \sin(\theta)\rceil} \leq \frac{2\pi}{\lceil(2N + 1) \sin(\theta)\rceil}; \quad \chi = \left[0, \frac{\pi}{2}\right] \quad (7)$$

3.3. Platonic

Platonic solids are an exact solution to the distribution problem for $P = (4, 6, 8, 12, 20)$. If more samples are required tessellation of the platonic solid can be used but is restricted to fixed numbers which makes it very inflexible. For this reason they are not very useful in measurement practice but are included in the analysis for reference.

3.4. Spiral

Spiral scanning schemes on the sphere are appropriate to distribute points equally on the sphere [6, 7]. The spiral scanning scheme used for our analysis is based on [7], where the slope is fixed:

$$\varphi = \alpha\theta \quad (8)$$

The slope is determined so that the distance between two spiral lines is equal to the distance Δs between two neighboring points equally placed along the spiral path.

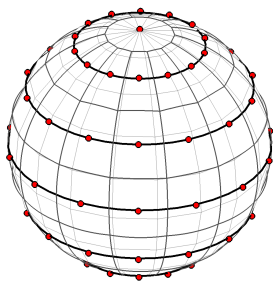


Figure 1: Equiangular sampling.

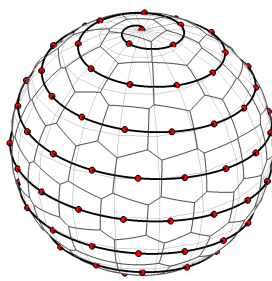


Figure 2: Spiral sampling.

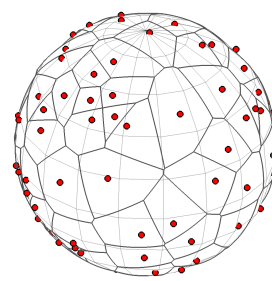


Figure 3: Random sampling.

Table 1: Sampling point distribution analysis.

Sampling	P	ΔA_{area}	$\Delta d_{\text{distance}}$
Equiangular	2664	39.0%	25.9%
Thinned equiangular	2698	0.4%	1.7%
Platonic (Dodecahedron)	1922	2.0%	1.0%
Platonic (Icosahedron)	2562	6.4%	2.9%
Spiral	2664	0.3%	1.2%
Random	2664	41.5%	23.5%

3.5. Random

Although deterministic sampling schemes provide advantageous features as deterministic uncertainty analysis and well defined trajectories, random point distributions are also suitable. The random sampling scheme is included in the analysis to emphasize the bandwidth of sampling possibilities.

3.6. Geometric Comparison of Sampling Grids

Figure 1 to Figure 3 show selected sampling grids including Voronoi cells for a low number of sampling points. The different sampling grids are evaluated by two measures

1. Mean of the relative Voronoi cell area difference to the mean cell area (ΔA_{area}).
2. Mean of the relative distance variation of neighboring samples ($\Delta d_{\text{distance}}$).

which are shown in Table 1. As expected the variation of the Voronoi cell area is very large for equiangular sampling. The variations are reduced for all other deterministic sampling methods which perform very well. It is important to note that the number of samples $P \geq P_{\text{min}}$ can only be defined arbitrarily for spiral and random sampling. Furthermore, random sampling does also not generate well distributed points.

4. POLARIZATION ANALYSIS

So far only the location of the sampling point has been considered. The polarization of the probe at each sampling position is an additional parameter which has to be included in the analysis. Three major possibilities will be considered for further analysis:

1. Randomly chosen polarization ($\chi \in [0, 2\pi]$) at each sampling point.
2. Two orthogonal polarizations at each sampling point.
3. Randomly chosen fixed polarization ($\chi = 0$ or $\chi = \frac{\pi}{2}$) at each sampling point.

Measurements with only one fixed polarization are, as expected, not possible and due to missing information the matrix always gets singular. To study different selections of the polarization, the condition number of the matrix Ψ is calculated for various oversampling ratios. Figure 4 shows the condition number for polarization case 1. Equiangular and thinned equiangular are well-conditioned but always oversampled. A reduction of the oversampling is not possible and leads to singular matrices - these points are excluded from the plot. For spiral and random sampling the oversampling can be reduced by the cost of a worse condition number. However, even for the determined system the matrix is not singular. The behavior changes slightly if at each point

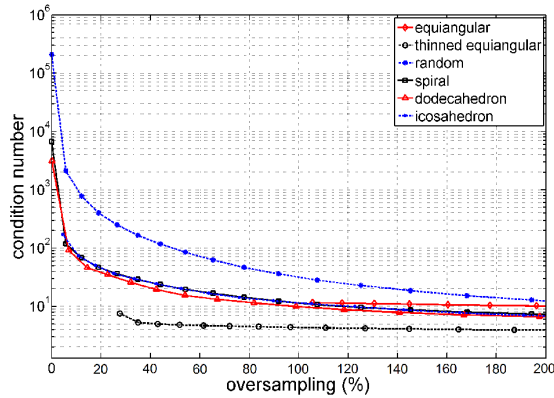


Figure 4: Condition number for case 1.

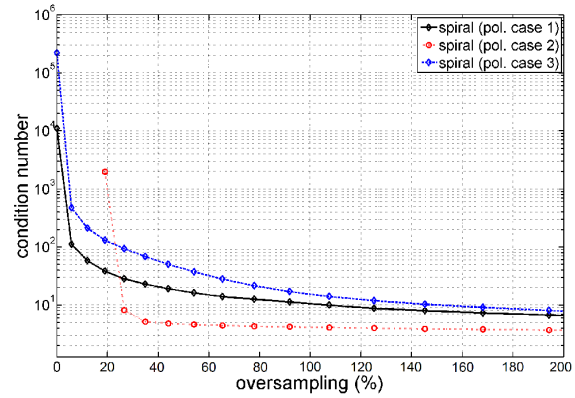


Figure 5: Condition number for spiral sampling.

Table 2: Simulation mode differences compared to FT based results.

Sampling	P	Over.	cond.	Noiseless		Noisy (SNR = 70 dB)	
				ΔQ_{mean}	ΔQ_{max}	ΔQ_{mean}	ΔQ_{max}
Equiangular	2660	108%	9	-318 dB	-291 dB	-82.1 dB	-72.5 dB
Thinned equiangular	1588	27%	6	-319 dB	-296 dB	-81.1 dB	-70.7 dB
Platonic (Dodecahedron)	1922	54%	15	-316 dB	-295 dB	-79.5 dB	-70.0 dB
Platonic (Icosahedron)	1284	3%	173	-314 dB	-290 dB	-76.4 dB	-55.8 dB
Spiral	1498	20%	35	-314 dB	-293 dB	-75.0 dB	-65.8 dB
Random	1498	20%	160	-306 dB	-294 dB	-65.2 dB	-54.8 dB

two orthogonal polarizations (case 2) or randomly chosen fixed polarizations (case 3, Figure 5) are measured. For spiral scanning the matrix gets singular for case 2 if the oversampling ratio tends towards zero. This linear dependencies are assumed to result from the fact that the number of locations (θ, φ) is halved compared to the other cases in order to keep the total number of samples constant. Further analysis showed that the condition number increases slightly with the number of unknowns. In conclusion, the polarization measurement method is not a crucial parameter as long as the condition number, which can be calculated in advance, is still acceptable. Therefore it can be selected mainly according to system possibilities.

5. SIMULATION RESULTS

A simulated 64 element dipole array is used to investigate the effect on the spherical mode calculation. The electric near-field of the dipole array is simulated for the different sampling grids. Next, the absolute linear differences in the mode spectrum are calculated for evaluation.

$$\Delta Q = |Q_{FT} - Q_{iSampling}| \quad (9)$$

Although the matrix solution of the transmission formula does not differ significantly from the Fourier transform (FT) based solution [6], the calculated modes are compared to the FT based algorithm, because this is a well accepted method. The results are summarized in Table 2 and show that in the noiseless and noisy case all sampling grids are suitable to achieve accurate results compared to the Fourier transform algorithm. The differences for equiangular sampling are the differences between the Fourier transform and least squares algorithm. Due to the higher condition number, icosahedron and random sampling have larger errors.

6. MEASUREMENT RESULTS

Measurements in the spherical near-field measurement chamber of the Institute of High Frequency Technology were performed with an double ridged horn SAS-571 from AH-System as test object. The measurement results are summarized in Table 3. The relative measurement time t_{rel} is improved by one third with thinned equiangular and spiral scanning compared to equiangular. However platonic and random sampling takes more time, even when having less samples, because of sub-optimal measurement trajectories. Optimization of these is a complex task and is out of the

Table 3: Measurement mode differences compared to FT based results.

Sampling	P	t_{rel}	t_{point}	cond.	ΔQ_{mean}	ΔQ_{max}
Equiangular LS (same data as FT)	2400	100%	5.0 s	9	-103.9 dB	-68.8 dB
Equiangular LS (rep. meas.)	2400	100%	5.0 s	9	-71.2 dB	-38.3 dB
Thinned equiangular	1464	66%	5.5 s	6	-74.2 dB	-42.0 dB
Platonic (Dodecahedron)	1922	228%	14.4 s	13	-68.0 dB	-40.4 dB
Platonic (Icosahedron)	1284	142%	13.5 s	6	-70.9 dB	-41.8 dB
Spiral	1380	63%	5.6 s	29	-66.3 dB	-43.4 dB
Random	1380	136%	12.2 s	146	-59.4 dB	-36.1 dB

scope of this paper. For equiangular sampling the difference between both algorithm (first row) and two successive measurements (reproducibility, second row) are shown. According to these values all measurement grids perform good and the mean difference for thinned equiangular is the smallest. Higher condition numbers increase especially the maximum error and are a good uncertainty parameter.

7. CONCLUSION

In this paper a set of sampling schemes for spherical near-field antenna measurements was investigated. The main advantage of non-equiaangular sampling grids is the reduction of oversampling. It was shown by simulation that the new sampling grids provide a well-conditioned linear equation system which can be solved accurately. Furthermore measurements were performed to investigate the realized accuracy and measurement speed. The main result is that the total measurement time can be reduced, but depends on the positioning system. In addition, it has been found that the transformation error is closely linked to the condition number and is thus well suited for uncertainty estimation.

REFERENCES

1. Hansen, J. E., *Spherical Near-field Antenna Measurements*, Peter Peregrinus Ltd., United Kingdom, 1988.
2. Wittmann, R. C., C. F. Stubenrauch, and M. H. Francis, "Spherical scanning measurements using truncated data sets," *Proceedings of the 24th AMTA Annual Meeting & Symposium*, Nov. 2002.
3. Sarkar, T. and A. Taaghoul, "Near-field to near/far-field transformation for arbitrary near-field geometry utilizing an equivalent current and MoM," *IEEE Trans. Antennas Propag.*, Vol. 47, No. 3, 566-573, 1999.
4. Schmidt, C., M. Leibfritz, and T. Eibert, "Fully probe-corrected nearfield far-field transformation employing plane wave expansion and diagonal translation operators," *IEEE Trans. Antennas Propag.*, Vol. 56, No. 3, 737-746, 2008.
5. Bucci, O. M., C. Gennarelli, and F. D'Agostino, "A new and efficient NF-FF transformation with spherical spiral scanning," *Proceedings of IEEE Antennas and Propagation Society International Symposium*, Jul. 2001.
6. Cornelius, R., M. Dirix, H. Shakhmourad, and D. Heberling, "Investigation of different matrix solver for spherical near-field to far-field transformation," *Proceedings of the 9th European Conference on Antennas and Propagation (EuCAP 2015)*, Apr. 2015.
7. Saff, E. and A. Kuijlaars, "Distributing many points on a sphere," *The Mathematical Intelligencer*, 1997.
8. Koay, C. G., "Analytically exact spiral scheme for generating uniformly distributed points on the unit sphere," *Journal of Computational Science*, 2011.

A Dual V-band Push-push VCO Using the 0.18 μm CMOS Process Technology

Yu-Hsin Chang and Yen-Chung Chiang
National Chung Hsing University, Taiwan

Abstract— In this paper, a dual-band push-push voltage-controlled oscillator implemented in the 0.18- μm CMOS process for V-band applications is presented. By using a fourth order resonance network composed of symmetric inductors and varactors and a push-push topology, the oscillation frequencies of the proposed circuit can be switched with only one control signal between two bands. And the second order harmonic is extracted from the central taps of inductors to achieve the frequencies of two V-band operations. The tuning ranges of the proposed voltage-controlled oscillator are from 67.78 to 69.42 GHz and from 52.2 to 54.7 GHz, respectively. The measured phase noise at 1 MHz frequency offset are -86.4 dBc/Hz and -90.5 dBc/Hz for 69.42 GHz and 54.7 GHz output frequencies, while the corresponding phase noises at 10 MHz frequency offset are -108.4 dBc/Hz and -112 dBc/Hz, respectively. The core circuit consumes a 12.96 mW dc power from a 1.8-V supply.

1. INTRODUCTION

Wireless communication systems operated in the millimeter-wave bands have been developed in recent studies [1–7]. In the transceiver front end, the voltage-controlled oscillator (VCO) is an essential building block of the frequency synthesizer which generates a local oscillator (LO) signal to perform modulation and demodulation functions. Adopting the CMOS process technology to implement VCO designs is popular due to its low cost and high integration. V-band VCOs implemented by using the CMOS process technologies have also been proposed [1–4] successfully. However, these previous works were only designed for single band and they were not suitable for multiband applications [5]. Although the VCO proposed in [6] has two resonant modes by using the fourth order LC tank, it was designed at lower frequencies and not for V-band applications. Because of the limitation of the CMOS devices, it is a difficult task to design a dual-band VCO in the 0.18- μm CMOS process technology for V-band applications.

The purpose of this paper is to present a dual band VCO with a fourth order LC tank with the push-push topology that operates in the V band to overcome above limitation by utilizing the TSMC 0.18- μm CMOS process technology. This paper is organized as follows. In Section 2, circuit design of the proposed dual V-band push-push VCO is discussed. The measured results of the fabricated chip are shown in Section 3. And a short conclusion is given in Section 4.

2. CIRCUIT DESIGN

Figure 1 shows a simplified diagram of the RF front end for a dual V-band receiver. Signals from the antennas are firstly fed in the band pass filters (BPFs) to filter out the out-of-band interferences. The desired signals from the BPFs are selected by a switch and the received RF signals are amplified by using a dual band low-noise amplifier (LNA). A wide band mixer named as 1st Mixer is used to convert the RF signals to the IF band by mixing with the V-band local oscillation (LO) signals. The dual V-band VCO is utilized to provide the required V-band LO signals in such a receiver.

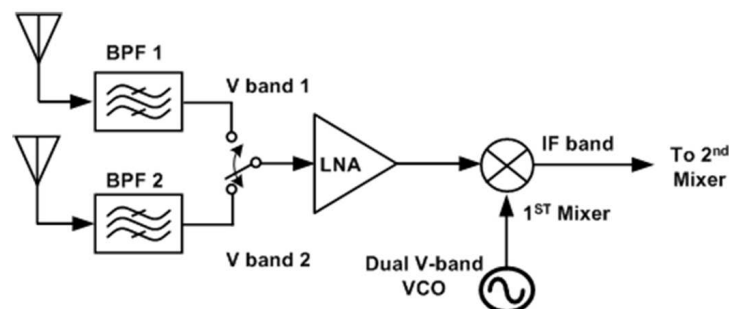


Figure 1: Simplified diagram of the RF front end with a dual V-band receiver.

As indicated in the previous section, it is difficult to design a dual-band VCO for the V band applications by adopting the 0.18- μm CMOS process. One possible method to extend the operation frequency of a VCO is the push-push technique [3]. To generate the V-band LO signals for a dual V-band operation, the proposed VCO utilizes a fourth order LC tank with only one controlled voltage. Compared with using two VCOs for each band, the proposed circuit topology has the advantage on design and cost. Figure 2 shows the schematic of the proposed dual V-band VCO in which the tank formed by varactors $C_{\text{VAR}1}$, $C_{\text{VAR}2}$, inductors L_1 , L_2 , L_3 , and parasitic capacitance (C_P ; not shown explicitly in Figure 2) is for output frequency selections of the V band 1 and V band 2 via the controlled voltage V_C and a cross-coupled transistors pair (M_1 – M_2) is used for compensating the losses of the tank including other parasitic effects. The current source (I_B) provides the required dc bias current for the VCO core. We design the proposed dual V-band VCO by deriving the impedance of the fourth order network. Due to the symmetry, the impedance of the half circuit of the fourth order LC tank neglecting losses in the tank can be derived as

$$Z(s) = \frac{s^3 L L'_3 C_{\text{VAR}} + s L'_3}{s^4 L L'_3 C_{\text{VAR}} C_P + s^2 (L C_{\text{VAR}} + L'_3 C_{\text{VAR}} + L'_3 C_P) + 1}, \quad (1)$$

where L and C_{VAR} represent the corresponding quantities with subscript 1 or 2, and L'_3 indicates the single-end inductance of L_3 in the half circuit. The oscillation occurs if the denominator in (1) becomes 0 with $s = j2\pi f_{\text{osc}}$ which leads to two possible solutions expressed as

$$f_{\text{osc}} = \frac{1}{2\pi} \left(\frac{B \pm \sqrt{B^2 - 4A}}{2A} \right)^{\frac{1}{2}} \quad (2)$$

where $A = L L'_3 C_{\text{VAR}} C_P$ and $B = L C_{\text{VAR}} + L'_3 C_{\text{VAR}} + L'_3 C_P$.

Output oscillation signal with a second order harmonic ($2f_{\text{osc}}$) is extracted from the middle terminal of the center-tap inductors (L_2 – L_3) connected commonly and an open-drain output buffer amplifier is adopted via buffer capacitance (C_B) for the chip measurements.

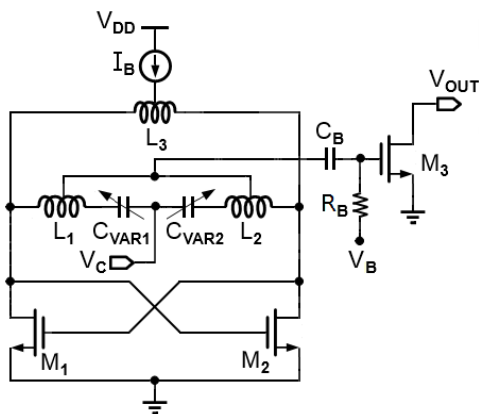


Figure 2: Schematic of the proposed VCO.

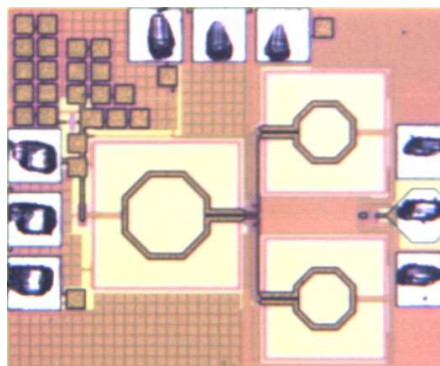


Figure 3: Micrograph of the proposed VCO.

3. MEASURED RESULTS

The proposed VCO is fabricated in the TSMC 0.18 μm CMOS process technology. The micrograph of the chip is as shown in Figure 3. And the chip area is $0.695 \times 0.565 \text{ mm}^2$. The core circuit and the output buffer of the proposed VCO consume 12.96 mW and 8.1 mW dc power, respectively from a 1.8-V power supply. The cable loss was not calibrated in the following measured results.

Figures 4(a) and 4(b) show the measured output spectrums of the proposed VCO for V band 1 that is the lower band and V band 2 that is the upper band. Their output frequencies can be seen are 54.7 GHz with a measured power of -41.84 dBm without calibrating the 10 dB line loss and 69.42 GHz with a measured power of -47.22 dBm without calibrating 16 dB line loss, respectively. Figure 5(a) shows the measured phase noises of the proposed VCO for V band 1 and it reads -90.5 dBc/Hz and -112 dBc/Hz at 1 MHz and 10 MHz frequency offsets, respectively, under 54.7 GHz output frequency. And Figure 5(b) shows the measured phase noises of the proposed

VCO for V band 2 and it reads -86.4 and -108.4 dBc/Hz at 1 MHz and 10 MHz frequency offsets, respectively under 69.42 GHz output frequency. Figures 6(a) and 6(b) show the measured tuning ranges of the proposed VCO for V band 1 and V band 2, respectively, and the tuning range for V band 1 is from 52.2 GHz to 54.7 GHz with the controlled voltage V_C swept from 1.1 V to 1.8 V while the tuning range for V band 2 is from 67.78 GHz to 69.42 GHz with the controlled voltage V_C swept from 0 V to 1 V.

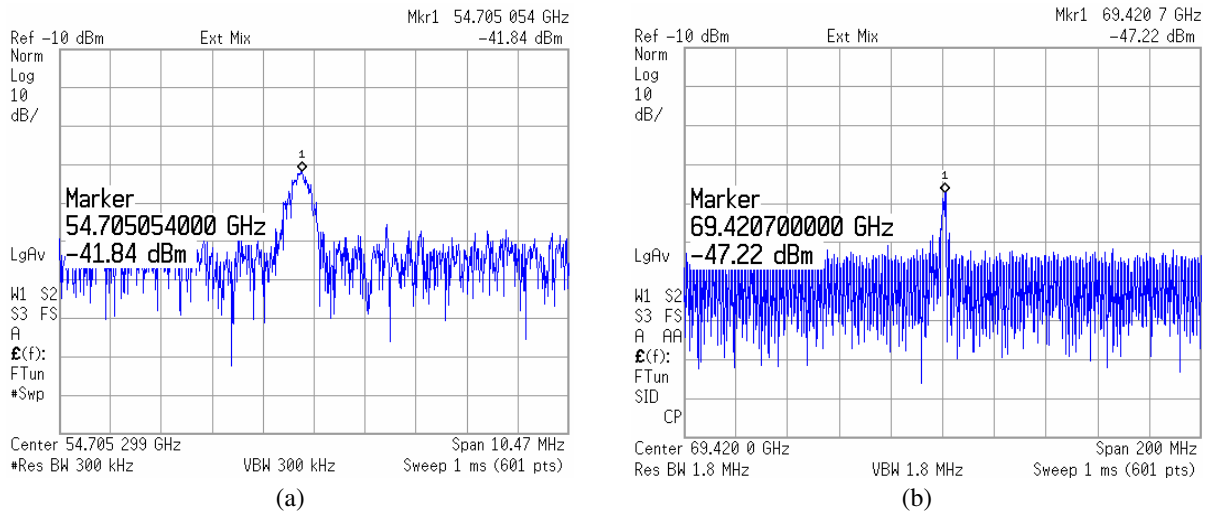


Figure 4: Measured output spectrums for (a) V band 1 and (b) V band 2.

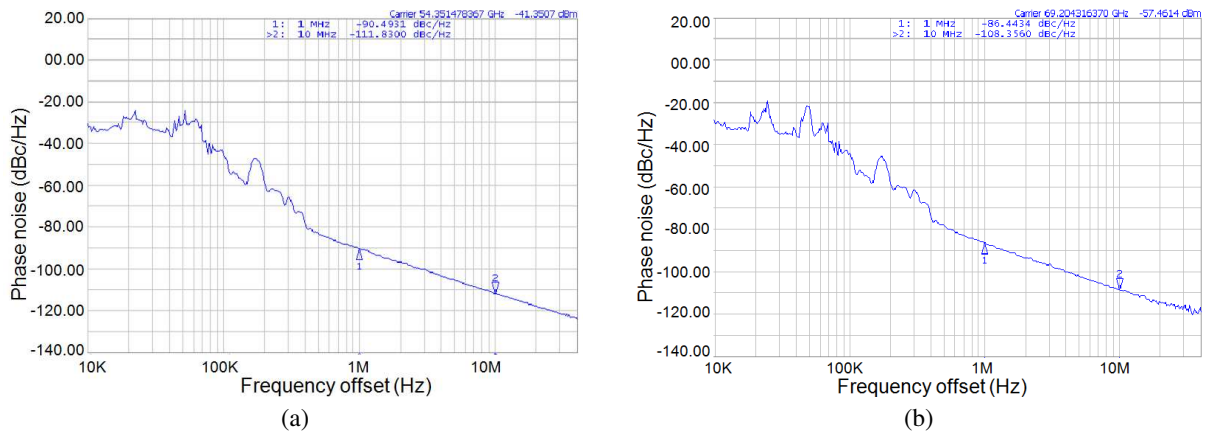


Figure 5: Measured phase noises for (a) V band 1 and (b) V band 2.

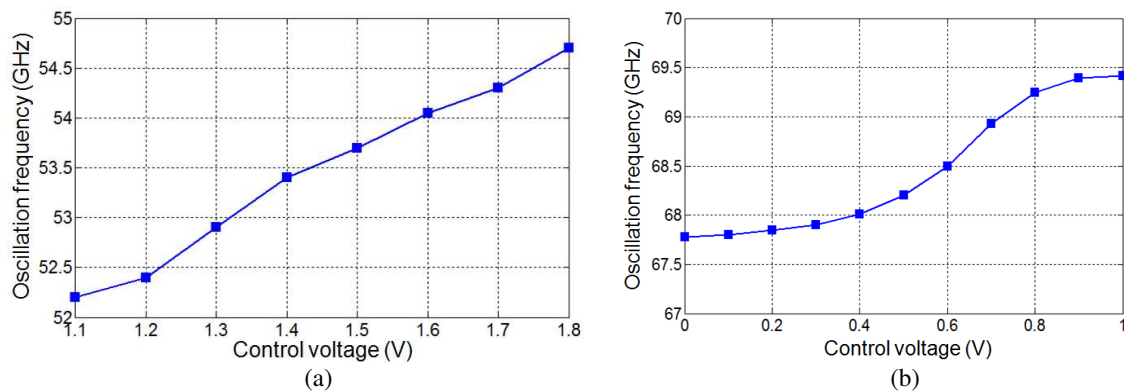


Figure 6: Measured output tuning ranges for (a) V band 1 and (b) V band 2.

4. CONCLUSIONS

In this paper, we have proposed a dual-band push-push VCO implemented in the TSMC 0.18- μm CMOS process for V-band applications. The proposed VCO adopts a fourth order resonant network to generate two oscillations for V band 1 and V band 2 switched by only one controlled voltage. The measured phase noises at 1 MHz frequency offset are -86.4 dBc/Hz and -90.5 dBc/Hz, respectively, around 68.5 and 53.3 GHz of the output frequencies. And the measured tuning ranges of the proposed VCO are 2.4% and 4.65% for the upper band and the lower band, respectively. The core circuit of the proposed VCO consumes a 12.96 mW dc power under a 1.8-V supply.

ACKNOWLEDGMENT

This work was supported in part by the Ministry of Education, Taiwan, R. O. C. under the ATU plan and by the Ministry of Science and Technology, Taiwan, R. O. C. under Grant NSC101/102-2220-E-005-010 and MOST103-220-E-005-002. The authors would like to thank the National Chip Implementation Center (CIC) in Hsinchu, Taiwan for the chip fabrication, measurement and other technical supports.

REFERENCES

1. Shigematsu, H., T. Hirose, F. Brewer, and M. Rodwell, "Millimeter-wave CMOS circuit design," *IEEE Trans. Microw. Theory Tech.*, Vol. 53, No. 2, 472–477, 2005.
2. Hsieh, H. H. and L. H. Lu, "A V-band CMOS VCO with an admittance-transforming cross-coupled pair," *IEEE J. Solid-State Circuits*, Vol. 44, No. 6, 1689–1696, 2009.
3. Chiu, H. C. and C. P. Kao, "A wide-tuning-range 69 GHz push-push VCO using 0.18 μm CMOS technology," *IEEE Microw. Wireless Compon. Lett.*, Vol. 20, No. 2, 97–99, 2010.
4. Li, L., P. Reynaert, and M. Steyaert, "A 60 GHz CMOS VCO using capacitance-splitting and gate-drain impedance-balancing technique," *IEEE Trans. Microw. Theory Tech.*, Vol. 59, No. 2, 406–413, 2011.
5. Li, Z. and K. K. O, "A low-phase-noise and low-power multiband CMOS voltage-controlled oscillator," *IEEE J. Solid-State Circuits*, Vol. 40, No. 6, 1296–1302, 2005.
6. Jang, S. L., Y. K. Wu, C. C. Liu, and J. F. Huang, "A dual-band CMOS voltage-controlled oscillator implemented with dual-resonance LC tank," *IEEE Microw. Wireless Compon. Lett.*, Vol. 19, No. 12, 816–818, 2009.
7. Yi, X., C. C. Boon, J. Sun, N. Huang, and W. M. Lim, "A low phase noise 24/77 GHz dual-band sub-sampling PLL for automotive radar applications in 65 nm CMOS technology," *IEEE Asian Solid-State Circuits Conference (A-SSCC)*, 417–420, Nov. 11–13, 2013.

Spatial Power Combiner Technology

Davide Passi¹, Alberto Leggieri¹, Franco Di Paolo¹, Antonio Tafuto², and Marco Bartocci²

¹University of Roma “Tor Vergata”, Via del Politecnico 1, Roma 00133, Italy

²Electronica SpA, Via Tiburtina Valeria Km 13.7, Roma 00100, Italy

Abstract— This article describes the spatial power combining techniques dealing with the state of the art of Spatial Power Combiners (SPC) considering recent developments. A brand-new splitting scheme is proposed where different types of SPC are grouped according to the space where power combining and splitting occur. This paper should provide compendium knowledge for SPC design and selection of the opportune SPC basing on the target application.

1. INTRODUCTION

In airborne and space applications, characteristics like reliability, size, efficiency and weight of the Power Amplifiers (PA) assume a very important role in the selection of the proper PA to be employed. High RF power levels are demanded to vacuum tubes amplifiers like TWTA, Klystron or Gyrotrons but those have the main disadvantage to use heated wires and bulky magnets or electromagnets that give greater size and weight and reduce efficiency [1]. So, combined Solid State PA (SSPA) would be greatly appreciated if they could give at least the same order of magnitude in RF power levels, since in this case graceful degradation is increased. Spatial power combining technique is an alternative one to combine many SSPA reducing to a minimum extent the combining losses [2–4].

This article deals with the state of the art of Spatial Power Combiners (SPC) and their characteristics [14]. In addition, it is proposed a new splitting scheme for the SPC family, grouped respect to the ambient where combining and splitting take place, as shown in Figure 1. The fundamental SPC Amplifier’s concept is to provide a large power value with minimum losses. In SPC the electromagnetic energy coming from input is divided as much as possible in the space, without using transmission lines, and it is sent to many SSPA’s. After amplified energy is collected, it is sent to output port with the lowest possible number of transmission lines.

SPC employees probes, antennas or transitions to take the spatial RF energy and send it to a two wires transmission line: the use of connectors at the amplifiers ports exclude the combiner to belong to the class of SPC. The system’s quality is usually determined from its efficiency. SPC efficiency can be defined as how much power is sent to amplifiers respect to how much power is provided to input port, such as it quantifies the capability of the combiner to intercept incoming energy P_I and distribute it to N energy dividing/combining internal ports, that is

$$\eta = \frac{\sum_{k=1}^{k=N} P_{O,k}}{P_I}$$

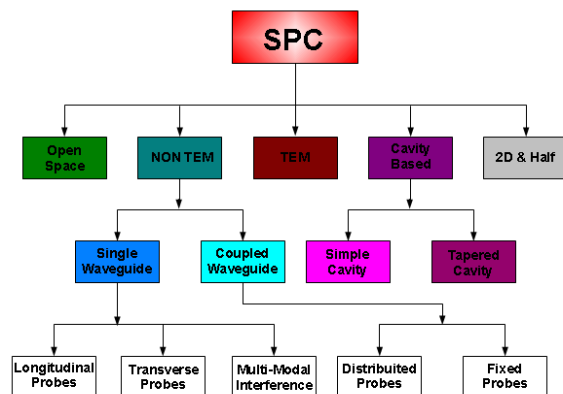


Figure 1: SPC’s family.

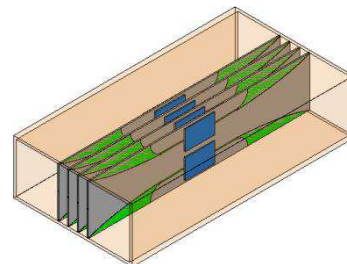


Figure 2: Single waveguide SPC with fin lines.

where $P_{O,k}$ is the input power at the k -th amplifier. Referring to scheme in Figure 1, the distinction between different types of SPC is done considering the propagation modes in the medium. Thus, there are TEM and Non TEM spatial combiners, cavity based, open space and 2D&Half ones.

2. NON TEM SPATIAL POWER COMBINERS

Non TEM SPC use waveguides to confine RF electromagnetic energy and it is composed by three families: the single waveguide family, with longitudinal probes and transverse probes, the coupled waveguides and the multimodal interference families.

RF probes can be directly realized on amplifier, usually a MMIC, or out of them. RF probes can be realized in many ways, as monopoles, dipoles, patches or slots or combinations among them. In many other cases Fin Line transition are realized, especially when wide band applications are needed.

2.1. Single Waveguide

The Single Waveguide SPC (SW-SPC) is the most common amplifiers among all Non TEM SPC. Single waveguides with longitudinal probes (SW-LP-SPC), uses transitions placed along the direction of energy propagation to couple energy with amplifying devices: the most used transitions are the Fin Lines [5]. The general assembly of these kind of SPC's is shown in Figure 2. There are several Fin Lines tapers such as linear, exponential and sine-square taper (and many others one) and they can be printed on single or double face of a substrate, called card. Furthermore to meet the power requirements many stacked cards can be employed into a single waveguide. The cards more distant by the waveguide's center are less excited than closest ones. This effect is due to the electric field distribution. An Electromagnetic Band Gap (EBG) [6] can be inserted in the waveguide to improve the probes feeding. In this way electric field distribution (TE_{10}) is made different from half sine shape and the uniform probes exciting and the system balance is increased allowing to utilize more cards. Due to the use of EBG, the operative band is considerably decreased.

Fin Lines are also distinguished by transition's type, usually to micro-strip; thus, a slot line to micro-strip transition and an antipodal one exist, where the electric field rotates from its initial polarization to the orthogonal one. After quasi-TEM mode is allowed inside a two wire transmission line, usually a microstrip, waveguide can be made wider to stack more amplifiers: This result in a sort of oversized waveguide is used. Now, we show an example taken by our experience: a Ka band SPC [3]. This SPC contains a Quad Fin transition type, but only two cards are inserted inside the WR28 waveguide, due to small size of this waveguide; so this combiner would hold only 8 MMIC's. To overcome this limit, we used Tee-Junctions at input and output so that our SPC can now combine 16 MMICs. A sketch of the combiner and its performance are shown in the Figures 3 and 4 below.

Single waveguide with Transverse Probes (SW-TP-SPC), uses these last placed orthogonally to the direction of energy propagation to catch and send the amplified energy.

The whole set of the amplifiers elements and probes are named Grid Amplifier [7]. The basic concept in SPC Grid Amplifiers is to intercept the incoming signal with a defined polarization, amplify it with the active device and then send the amplified signal using the orthogonal polarization respect the incoming one. In Transmission Type Grid Amplifiers (TT-GA) two polarizers are adopted to allow the electric field to pass through with a specified polarization and they are useful to decouple somehow input and output waveguide ports reflections, thus increasing the stability of

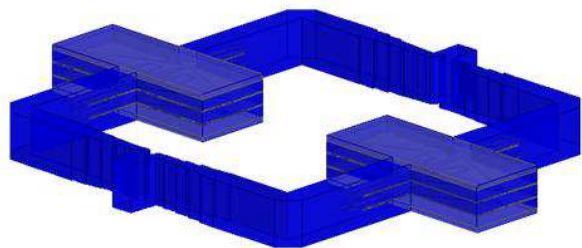


Figure 3: Ka band SPC: sketch of the microwave side.

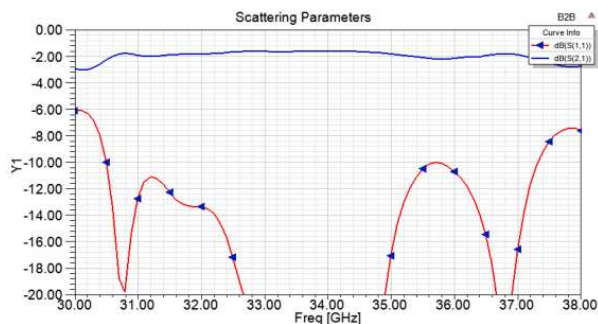


Figure 4: Ka band SPC performance.

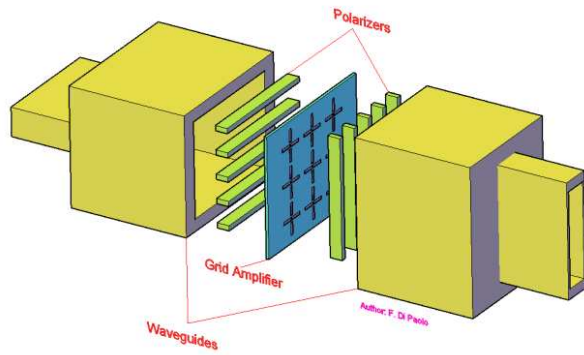


Figure 5: Transmission type grid amplifier.

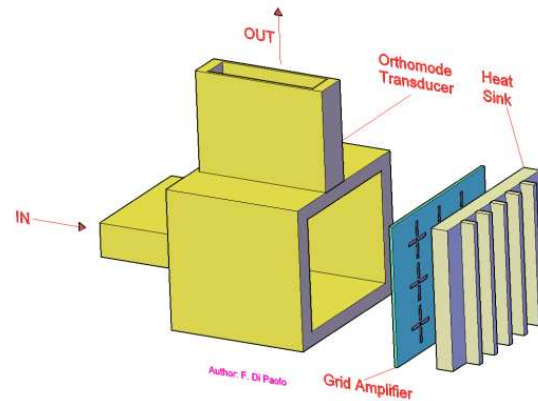


Figure 6: Reflection type grid amplifier.

the amplifier from oscillations. In Reflection Type Grid Amplifiers (RT-GA) the same MMIC is employed in reception and transmission so a short circuit can be placed back of it. MMIC amplifies and rotates the electric field while an ortho-mode transducer, or a couple cross polarized horn antennas, discriminates the polarizations. Examples of TT-GA and RT-GA are given in Figures 5 and 6. The reflection type has more heat removal capacities than the transmission type because the second one spreads the heat through the metal of the waveguide while the first one has heat sink placed just back the MMIC.

2.2. Multimodal Interference Combiners

A different type of SPC is the Multimodal Interference SPC (MMI-SPC), uses the interferences among many propagating modes in an overmoded waveguide. The resulting effect is the same found in optics, and first discovered by the English physicist William Henry Fox Talbot through experiments in optics. He discovered that in an overmoded waveguide the exciting field at incoming port replicates N times at given distance depending by operating frequency and waveguide dimensions. A picture of this phenomenon is reported in Figure 7.

This multimodal interference effect is also named “Talbot’s effect” and it is selective in frequency due to its nature. The field of SPC’s based on Talbot’s effect is actually under analysis [8], and the effective utility as an amplifiers has to be still proved with some experiment.

2.3. Coupled Waveguides

The Coupled Waveguides SPC (CW-SPC) use two waveguides connected between them through two wires transmission lines [9]. These SPC use amplifying devices that are outside the probing and combining area, that is they fail the implicit concept of all SPC, but they are anyway “spatial” when probing and combining energy.

Two examples of Distributed Probes Coupled Waveguide SPA are shown in Figures 8 and 9.

A common characteristic of all coupled waveguide SPC is that they use short circuits at one extreme of the waveguides, so a stationary wave regime is generated. Two kinds of electromagnetic coupling between the waveguides and the two transmission lines are used, which can be defined as E-coupling, using E-probe, and H-coupling, using H-probe. This kind of amplifiers reduce a lot the

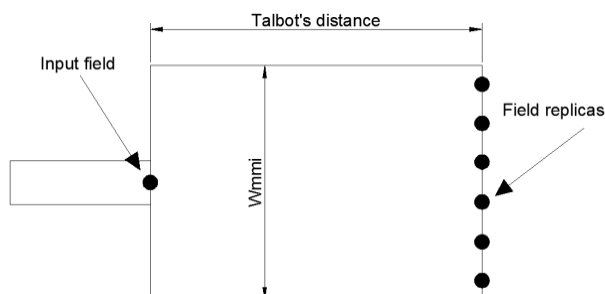


Figure 7: The concept of MMI in overmoded waveguide.

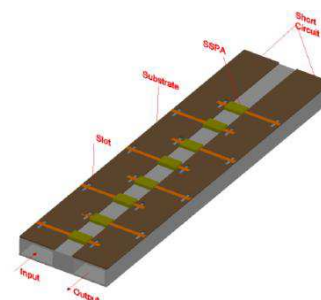


Figure 8: Distributed probes H-coupled waveguide SPA (DPHCW-SPA).

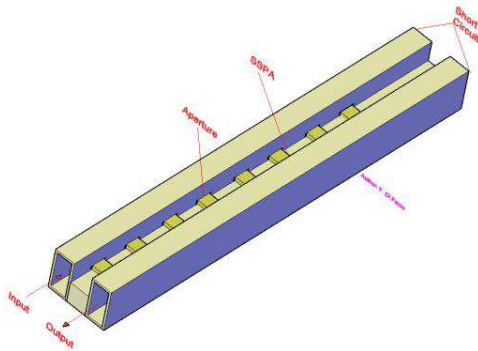


Figure 9: Distributed probes E-coupled waveguide SPA (DPECW-SPA).

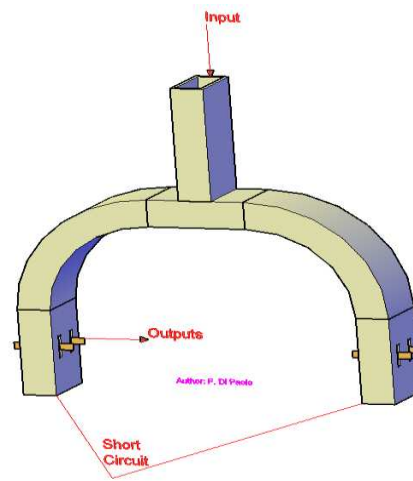


Figure 10: Fixed probes E-coupled waveguide SPC, with 8 E-probes.

risk of unwanted oscillations due to input-output coupling. Coupled Waveguides SPC are divided in two subgroups, the distributed probes group and fixed probes group. In the first case, probes are located along the waveguide, while in the second case probes are located just near the shorting wall of the waveguide.

The operating bandwidth of this kind of SPC using distributed probes is usually around 10–15%, evidently much smaller than the operating bandwidth of the used waveguide. This is due to the fact that in addition to use short circuits at one extreme of the coupled waveguides, that creates a regime of stationary waves inside the waveguides where positions of maxima and minima are highly frequency dependent, the multiple reflections at the distributed probes interacts between them causing an additional bandwidth reduction. Often, sliding shorts are used instead of fixed position shorts, to allow some kind of tuning so that maximum energy transfer is reachable, and consequently a maximum efficiency for this kind of amplifier is obtainable.

Fixed Probes Coupled Waveguides SPC (FPCW-SPC) has probes placed inside waveguide in a way that there is not a distributed coupling. An example is shown in the Figure 10, for the case of E-coupling. The operating bandwidth of Fixed Probes Coupled Waveguide SPC (FPCW-SPC) is wider than Distributed ones. This is due to the fact that the monopoles used to capture the energy inside the waveguide can be tuned to proper matching the frequency dependent reflections at the waveguide short circuit and it is possible to cover the full TE_{10} mode operating bandwidth.

H-coupling probes, that are slots, are realized at the waveguide widest side, and microstrips are used to connect the slots between the two waveguides. Slots are placed near the waveguide narrowest side, at the top, where the electric field is at its minimum value, and the magnetic field is used to couple energy to the top microstrip. The incoming energy, at the input waveguide, is captured by microstrips probes placed on these slots and sent to other slots realized on the output waveguide. To make an amplifier, SSPA's are placed between the microstrips.

The E-coupled mechanism between the waveguide and microstrip is realized making an aperture at the center of the waveguide widest side, and letting a microstrip to enter inside the aperture to capture energy inside the waveguide. Since such apertures are made at the center of the waveguide, here the electric field is at its maximum value and just this field is used to couple energy to the microstrip. The incoming energy at the input waveguide is captured by such microstrips E-probes placed inside the apertures and sent to other apertures realized on the output waveguide. To make an amplifier, SSPA's are placed between the microstrips. E-probes inside the waveguide are less radiative than H-probes so they present a good combining efficiency, in addition E-probes have a 5% useful bandwidth wider than H-ones thanks their non resonant aperture.

3. TEM SPATIAL POWER COMBINERS

TEM SPC use TEM transmission lines to confine RF electromagnetic energy [10]. The simplest and well known TEM structure is the coaxial transmission line. In this section are going to illustrate two versions, the classic circular and the square one. Another peculiarity of this kind of SPC is to present an ultra-wide operating band, this is due to the fact that TEM transmission line allows the

RF to propagate from DC to the first high order mode cutoff frequency (depends on its geometric size). A linear relationship exists between frequency and wavelength so no dispersion arises and pulsed signal can pass without distortion. To full cover the operating bandwidth a Fin Line is employed to capture the incoming TEM. EM power density has a dependence along the radius r as $1/r^2$ and Fin lines have to be designed to compensate this effect, thus Fin Line nearest the external radius need to have a wider aperture of the Fin Line nearest the inner one. Metallic carrier of the circular coaxial SPC, where Fin Lines will be placed on, have a wedge profile to form all together the cylindrical transmission line. This fact comply the making process because each carrier have to perfectly overlap with closed ones. In addition an ad-hoc heat sink is applied due to its no standard shape.

To solve this problem a square coaxial (Squarax) SPC can be employed [2].

Due to its symmetric nature it has not mechanical problem and its performances are similar to the circular coaxial SPC.

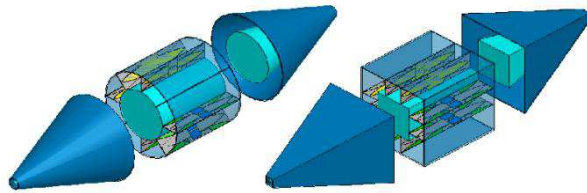


Figure 11: Circular and square coaxial TEM SPC's.

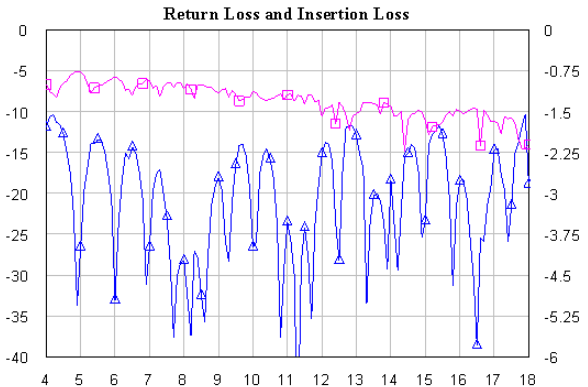


Figure 12: SQUARAX coaxial SPC performance.

In the whole cases a coaxial taper is employed to join the wider and the standard sized coaxial transmission line together. The performance of the Squarax SPC is reported in the Figure 12. As mentioned before, TEM SPC's are the best choice when wide operating bandwidth is required, greater than what can be reached for a waveguide.

4. CAVITY BASED, OPEN SPACE AND 2D&HALF SPATIAL POWER COMBINERS

Cavity Based SPC (CB-SPC) use a closed cavity excited by an input port, and the output ports are realized inserting probes inside such cavity [11]. Two different groups exist in this family and differ from how the input port couples with the cavity: if the coupling is made through a conical transmission line the SPC is named in literature as Conical Transmission Line SPC or Tapered Cavity SPC, otherwise it is named in many ways like Radial SPC, Coaxial SPC or Simple Cavity SPC. In CB-SPC's even if no probes, transitions and active devices are used the structure cannot work an ordinary transmission line, since such CB-SPC's use cavities to realize the SPC function. Two different ways exist to couple the ports to the cavity: It is possible to couple the cavity magnetically or electrically. Magnetic coupling are usually preferred in high power SPC's, to decrease somewhat the problem of electric field discharge when using electric coupling. This combiner family has not been accepted in the great family of SPC due to the external place of the amplifying devices that are joined with cavities through connectors. Tapered Cavity SPC, usually, has a central coaxial connector and many peripheral ones where the external PA's are connected. The central connector excites the cavity after a proper impedance matching realized through a conical transmission line. Different from previous SPC Cavity based, Simple Cavity SPC doesn't use tapering at the central connector. Their efficiency is very high due to the fact that they use closed cavities and thus energy is well confined inside it.

Open Space SPC (OSS) use amplifiers connected to probes placed in an open space environment [12]. The type of the used probes are dependent to the frequency and operating bandwidth of the system, but in general dipoles or wideband tapered antennas are the most employed ones, respectively for narrowband and wideband applications. In addition, input probes are placed in orthogonally polarization to the output ones to avoid the raise of unwanted oscillations due to

coupling between input and output. The probes used in single waveguide SPC are also employed in the open space family. Usually lenses are used to focus the beam to and from grid amplifier. The lens is a Gaussian beam former and gives an excellent phase and amplitude distribution due to the necessity to an uniform feed of the grid amplifier. Two horn antennas can be employed to increase the field uniformity and to avoid to use bulky lens. This is shown in the Figure 14.

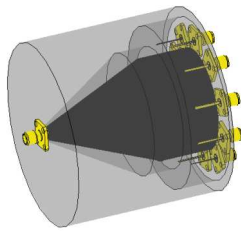


Figure 13: Tapered cavity SPC.

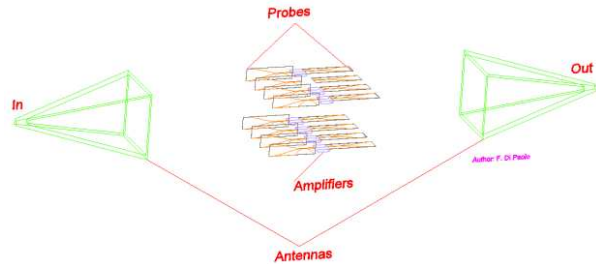


Figure 14: Open space spatial power amplifiers with horn antennas.

2D&Half SPC, that are two dimensions and half SPC, are named in that way due its little vertical dimension respect the other [13]. Probing and summing energy is made the TE surface wave. This family remembers SIW technology (Substrate Integrated Waveguide) or micro open space SPC. In general, with 2D&Half SPC's it is quite difficult to have good heat management for the active devices, and eventual application to high power SPC must be well investigated. This is because heat sink can disturb the surface wave propagation.

5. COMMON TECHNOLOGICAL AND OPERATIVE ASPECTS IN SPC DESIGN

SPC, grouped in any ways, as shown in Figure 1, share some problems related to the employment of different technologies in the same device and the use of electromagnetic bounded space. Common technological and operative aspects are discussed in this section.

A considerable problem regards the High Order Modes (HOM) excitation. Unless such excitation is desired, as in MMI-SPC's or SPC in oversized waveguides, in all the other cases it is an unwanted situation. SW-LP-SPC's should be carefully loaded by Fin Lines to reduce the risk of HOM. SW-TP-SPC's are less prone to excite HOM, at least when they are used as TT-GA; in RT-GA, the design should be oriented with attention to avoid HOM excitation. Coax-SPC's use wider dimension of what strictly necessary, to allow the use of as many amplifiers as possible between the inner and outer coaxial conductor, and this oversizing is cause of possible HOM excitation.

Another problem regards the uncollected power. It is the power that it is not captured by the probes, but travels through the transmission line or/and is reflected back at the origin. This uncollected power is cause of decrease in efficiency, since it is not used by probes and consequently it is not combined at the output. Uncollected power is present in almost all SPC's we have reported in this document, with an exception: the CB-SPC's. These last SPC's use in fact cavities for power dividing and combining process, and in a good design all of the cavity energy participates to this process. It is for this reason that CB-SPC's have the highest combining efficiency.

The available area for active devices represents a notable topic: Whenever a transmission line based SPC is used, when the frequency increases there is a reduced available space for MMIC's. This is true for non-TEM SPC and particularly for TEM-SPC. For a Coax-SPC it is not so simple to enlarge the area to place MMIC's, since in this case it is also necessary to realize the necessary place inside the coaxial internal conductor. In general, any type of SPC which employ oversized waveguide resolve in some way the problem of limited space for MMIC's.

Power Supply Routing (PSR) is an important aspect of SPC design: It is strongly dependent to the technology used to realize the SPC. In general the PSR complexity increases with the number of active elements inside in the SPC Amplifier, but it is less critical when amplifiers are placed outside the SPC.

In design of SPC, particular attention needs to be given to the thermal management: SPC's using Fin Lines, regardless if they are purely passive or active, have a peculiar thermal problem: The possible bending of the Fin Line vs. temperature. If a bending occurs, the Fin Lines does not intercept the maximum possible field, but only a port of it. Substrate bending vs. temperature can be reduced a lot if hard substrates are used, as Alumina or Aluminum Nitride. The drawback

to use hard substrates for Fin Lines is that they load dielectrically the air inside the transmission line. First of all, brazing the MMIC PA's is necessary, rather than die attach with epoxy. For high power SPC's is the heat removal capacity that limits the reachable power from such amplifiers, and a compromise between output power, available space for the SPC and thermal removal capacity must be found.

Mechanical considerations during the design are mandatory when several technologies are combined, as happens with SPC approach. SPC's using probes with soft substrates should be carefully mechanically designed to respects the system, requirements to vibration survivability. The tolerance to vibration is dependent to the mechanical methods used to assembly the SPC. Sealing is another issue. We have seen that the most used SPC Amplifiers employ cards to compose the structure. In such cases, it is difficult to have a hermetic SPC so it is better to use hermetic packages for the PA's.

6. CONCLUSIONS

In this work we have described the spatial power combining techniques, dealing with the state of the art of the spatial power combiners. An innovative SPC family tree has been introduced, based on propagation media and type of probes, longitudinal or transversal. All the branches of this tree have been analyzed and a comparison among them has been discussed. Finally, common problems in every SPC have been analyzed: these are HOM excitation, Uncollected Power, available area for active devices, power supply routing, thermal management and mechanical considerations.

REFERENCES

1. Armstrong, C. M., "The vitality of vacuum electronics," *IEEE 14th International Vacuum Electronics Conference (IVEC)*, 1–3, 2013.
2. Leggieri, A., D. Passi, and F. Di Paolo, "The Squarax amplifier: An electromagnetic and thermo-mechanical innovation," *PIERS Proceedings*, 2273–2280, Guangzhou, Aug. 25–28, 2014.
3. Passi, D., A. Leggieri, F. Di Paolo, M. Bartocci, A. Tafuto, and A. Manna, "High efficiency ka-band spatial combiner," *Advanced Electromagnetics*, Vol. 3, No. 2, 10–15, Dec. 2014.
4. Leggieri, A., D. Passi, G. Saggio, and F. Di Paolo, "Multiphysics design of a spatial combiner predisposed for thermomechanically affected operation," *Journal of Electromagnetic Waves and Applications*, Vol. 28, No. 17, 2153–2168, 2014.
5. Bhat, B. and S. K. Koul, *Analysis, Design and Optimization of Fin Lines*, Artech House, 1987.
6. Belaid, M. and K. Wu, "Spatial power amplifier using a passive and active TEM waveguide concept," *IEEE Trans. on MTT*, Vol. 51, No. 3, 684–689, Mar. 2003.
7. Chung, Y., C. T. Cheung, M. P. DeLisio, and D. B. Rutledge, "W-band waveguide-packaged InP HEMT reflection grid amplifier," *IEEE Microwave and Wireless Components Letters*, Vol. 16, No. 6, 324–326, Jun. 2006.
8. Yang, N., C. Caloz, and K. Wu, "Substrate integrated waveguide power divider based on multimode interference imaging," *IEEE MTT-S IMS Digest*, 883–886, 2008.
9. Jiang, X., L. Liu, S. C. Ortiz, and A. Mortazawi, "A Ka-band power amplifier based on a traveling-wave power-dividing/combining slotted waveguide circuit," *IEEE Trans. on MTT*, Vol. 52, No. 2, 633–639, Feb. 2004.
10. Casto, M., M. Lampenfeld, P. Jia, P. Courtney, S. Behan, P. Daughenbaugh, and R. Worley, "100W X-band GaN SSPA for medium power TWTA replacement," *IEEE MTT-S IMS Digest*, 1–4, 2011.
11. Shan, X. and Z. Shen, "A suspended-substrate Ku-band symmetric radial power combiner," *IEEE Microwave and Wireless Components Letters*, Vol. 21, No. 12, 652–654, Dec. 2011.
12. Pickens, W. S., L. W. Epp, and D. J. Hoppe, "Hard horn design for quasi-optical power combining using solid-state power amplifiers," *IPN Progress Report*, 1–21, 42–156, Feb. 15, 2004.
13. Perkons, A. R. and T. Itoh, "TE surface wave power combining by a planar 10-element active lens amplifier," *IEEE MTT-S IMS Digest*, Vol. 2, 691–694, 1997.
14. Passi, D., A. Leggieri, F. Di Paolo, M. Bartocci, and A. Tafuto, "State of the art of spatial power combining," Under Submission in PIER.

Using Microwave Radiation for Porcelain Tableware Sintering

T. Santos^{1,4}, L. Hennetier², V. A. F. Costa³, and L. C. Costa¹

¹Department of Physics and I3N, University of Aveiro, Aveiro 3810-193, Portugal

²Technological Center for Ceramic and Glass Industries, Coimbra 3025-307, Portugal

³Department of Mechanical Engineering, University of Aveiro, Aveiro 3810-193, Portugal

⁴CICECO, University of Aveiro, Aveiro 3810-193, Portugal

Abstract— This work presents an improved microwave multimode cavity for porcelain tableware sintering. It includes 6 magnetrons, each one with a nominal power of 1 kW at 2.45 GHz. The distribution of the electromagnetic field inside the cavity is calculated using the COMSOL Multiphysics software. The improved automated control system comprises the use of a pyrometer that allows the analysis of the thermal delay between the temperature given by a thermocouple and the real temperature in the porcelain material. Results exclude the existence of the so-called non-thermal microwave effect, recognized in some literature. Physical properties, such as density, rupture energy and impact resistance, are compared with those of tableware obtained by conventional methods. The improved microwave oven allows a better temperature measurement, with a faster sintering with the same quality standards than the conventional sintered porcelain.

1. INTRODUCTION

Microwave processing of materials has been increasingly used in different areas such as ceramics sintering [1–3], ceramics drying [4], metal powders heating [3], oil products [5], lime and concrete [6], wood [7], pyrolysis [8], chemistry [11], etc..

To avoid overheating, uniform electromagnetic field inside the cavities is required [3, 10]. However, the local electromagnetic field can be used to join materials with better heating control than with conventional convective heating methods [11]. The way how the radiation interacts with the material depends on a high number of parameters such as the radiation frequency, position of the microwave generators, geometric form of the load, dielectric properties, thermal conductivity, specific heat, density and electromagnetic and thermal behavior of the materials during the heating process [12]. To overcome the inhomogeneous heating some techniques like the use of turntables, mode stirrers, and others much more complex [1, 2] can be implemented. The absorbed power density of the microwave radiation can be expressed by

$$P = \frac{1}{2} [(\sigma_{dc} + \omega\varepsilon_r'') E^2 + \omega\mu_r'' H^2] \quad (1)$$

where σ_{dc} is the dc electrical conductivity, ε_r'' and μ_r'' are the imaginary parts of the permittivity and permeability, respectively and E and H are the electric and magnetic fields. The simplified unsteady heat transfer equation is given by

$$\rho C \frac{\partial T}{\partial t} = k \nabla^2 T + P \quad (2)$$

where ρ , C and k are the density, the specific heat and the thermal conductivity of the material, respectively.

Our study aims the understanding of the heating process of ceramic materials by microwave radiation in multimode ovens, its applications, limitations, as well as the optimization and opportunities of this heating method.

2. ELECTROMAGNETIC FIELD SIMULATIONS

Simulation studies are essential to understand the intrinsic heterogeneity of the electromagnetic field that leads to inhomogeneous heating of the material to be sintered. Specific technical solutions such as the orientation of the waveguides, and the locations where they are positioned, as well as the samples position inside the oven, were studied.

The analysis of the electromagnetic field at a macroscopic level implies the modeling of the Maxwell's equations, subject to the boundary conditions. The COMSOL Multiphysics software

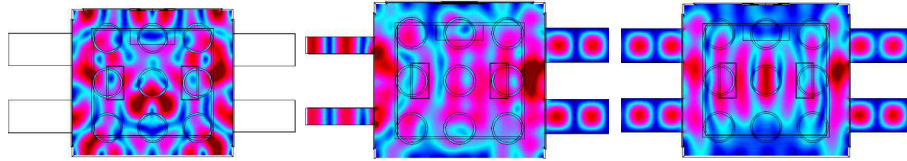


Figure 1: Simulated electric field, for different magnetron configurations.

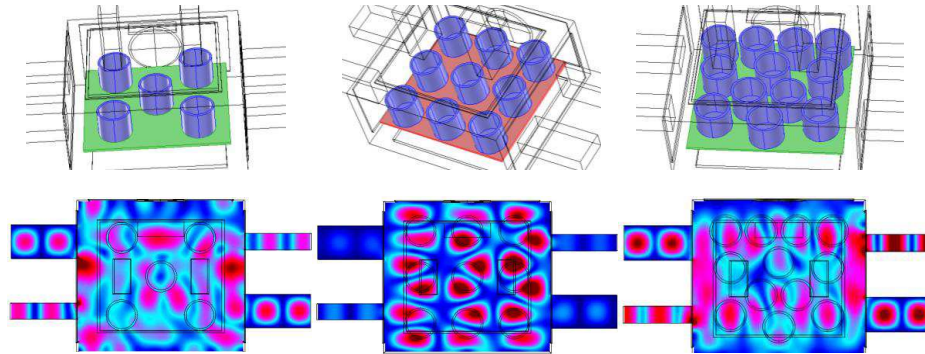


Figure 2: Load schedules and simulation results for different numbers and positions of the porcelain cups inside the cavity.

incorporates the differential equations that the finite element method can handle. The microwave radiation is fed by rectangular ports, and its electric field vector is determined by,

$$\vec{\nabla} \times \left(\mu^{-1} \vec{\nabla} \times \vec{E} \right) - k_0^2 \left(\epsilon' - \frac{i\sigma}{\omega\epsilon_0} \right) \vec{E} = 0 \quad (3)$$

The losses in the conductive walls are sufficiently small to not significantly affect the distribution of the electromagnetic field, and so the boundary conditions of the cavity are approximated as perfect conductors, $\vec{n} \times \vec{E} = 0$. The electromagnetic field simulations of the cavity loaded with porcelain cups ($\epsilon^* = 2.2 - i5 \cdot 10^{-4}$) and a SiC plate ($\epsilon^* = 18.2 - 1.78i$), for a total power of 6 kW, are shown in Figures 1 and 2. The measurement of the complex permittivity, at 2.45 GHz, was made using the small perturbation theory [13, 14], with a cavity operating in the TE₀₁₅ mode, using a HP 8753D network analyser.

The uniformity characteristics are higher when the number of pieces inside the oven cavity is increased; observed experimentally. Figure 2 shows three schemes for different porcelain positions and number of cups.

3. MULTIMODE CAVITY DESIGN

For the monitoring and the temperature control inside the 6 magnetrons (6M) oven, and consequently the energy applied to the sample, a LabView code was developed that uses a *power-time-indirect temperature control* that comprises a set of combinations of a number of magnetrons that are active (*power*) during a particular time interval (*time*) which will act in a range of a predetermined temperature (*temperature*). This combination ensures a higher uniformity of the electromagnetic field inside the cavity and so a quicker sintering of the porcelain, with lower power consumption. To avoid electromagnetic interference in the readings of the thermocouple, and even its damage, it is shielded with a platinum foil. Biscuit and glazed porcelain pieces were tested.

In the oven floor, a immediately above the thermal insulation, a silicon carbide (SiC) plate that works as a base for the porcelain and as microwave susceptor was placed immediately above the thermal insulation, absorbing part of the electromagnetic radiation and transferring heat to the surroundings materials.

4. PHYSICAL CHARACTERIZATION

We do not present a results' color analysis, but we can see by naked eye that the sintering of tableware in a microwave oven is incomplete not due to its physical characteristics but because it is not possible to obtain the white porcelain unless a reactive gas that bonds chemically to the iron

oxides that exist in the porcelain raw material is introduced. We tested in a nitrogen atmosphere, although the porcelain obtained under those conditions was whiter, it does not meet the industrial standards.

Table 1 shows the physical characterization of samples MW1-7 (Biscuit) and MWG (Glazed). CVG and CVB are the glazed and biscuit conventional sintered cups. MWx are the cups sintered with microwave radiation. MW5, 6, 7 have a dwell time of 5, 10 and 20 min. 12 cups were sintered in each set.

From Table 1 we observe that the glazed porcelain sintered with microwave radiation (MWG) at 1358°C shows physical characteristics very close to those of the glazed porcelain conventionally

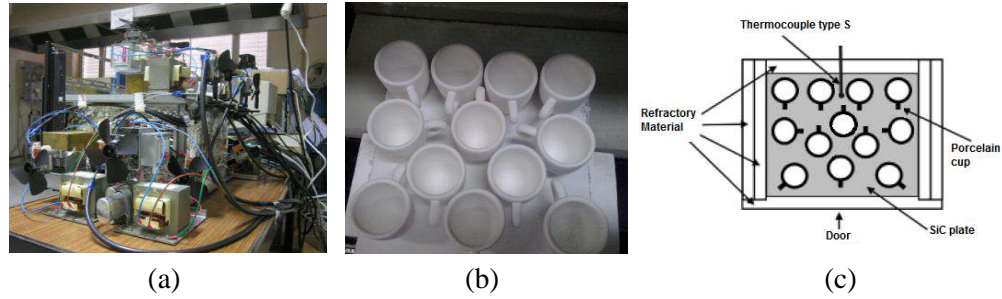


Figure 3: Photographs of (a) the 6M oven, (b) of the SiC plate and the relative porcelain positions, and (c) interior layout of the furnace.

Table 1: Physical properties of some sintered porcelains. T_P and T_T are the temperature measure by the pyrometer and by the thermocouple, respectively.

Sample	CVG	CVB	MW0	MW1	MW2	MW3
Impact resistance ($\text{J}\cdot\text{cm}^{-2}$)	0.89 ± 0.28	1.05 ± 0.21	0.90 ± 0.14	1.03 ± 0.25	1.00 ± 0.15	0.81 ± 0.15
Rupture energy (J)	0.18 ± 0.03	0.17 ± 0.05	0.18 ± 0.03	0.19 ± 0.03	0.19 ± 0.03	0.17 ± 0.03
Apparent density ($\text{g}\cdot\text{cm}^{-3}$)	2.408 ± 0.005	2.443 ± 0.002	2.452 ± 0.013	2.439 ± 0.027	2.439 ± 0.029	2.398 ± 0.083
Open porosity (%)	0.30 ± 0.15	0.51 ± 0.29	2.34 ± 2.02	0.43 ± 0.15	0.41 ± 0.17	1.75 ± 2.05
T_P ($^{\circ}\text{C}$)	—		1315	1350	1365	1380
T_T ($^{\circ}\text{C}$)	1380		1268	1313	1322	1349
Time (min)	200		64	70	68	70

Sample	MW4	MW5	MW6	MW7	MWG
Impact resistance ($\text{J}\cdot\text{cm}^{-2}$)	0.67 ± 0.15	1.05 ± 0.27	0.78 ± 0.13	0.89 ± 0.14	0.86 ± 0.26
Rupture energy (J)	0.15 ± 0.02	0.20 ± 0.05	0.14 ± 0.03	0.16 ± 0.03	0.17 ± 0.05
Apparent density ($\text{g}\cdot\text{cm}^{-3}$)	2.331 ± 0.047	2.438 ± 0.029	2.436 ± 0.047	2.428 ± 0.047	2.410 ± 0.027
Open porosity (%)	3.70 ± 5.65	0.56 ± 0.027	0.36 ± 0.15	0.29 ± 0.07	0.31 ± 0.18
T_P ($^{\circ}\text{C}$)	1400	~ 1365			1358
T_T ($^{\circ}\text{C}$)	1372	~ 1325			1315
Time (min)	70	70 + 5	70 + 10	70 + 20	66

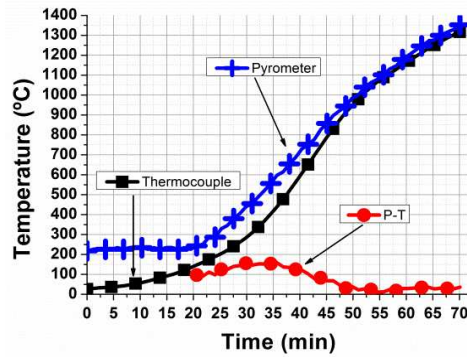


Figure 4: Sintering cycle for the MW1 sample.

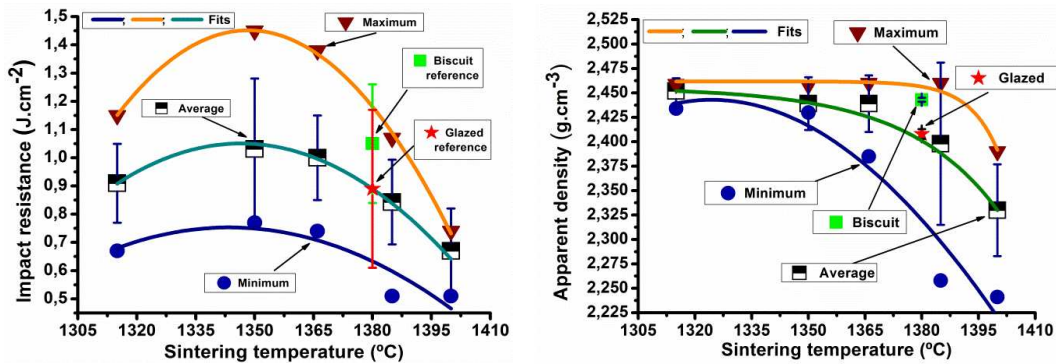


Figure 5: Impact resistance and apparent density as function of the sintering temperature. (read with the pyrometer).

sintered (CVG — 1380°C). Figure 4 presents the sintering cycle for the samples MW1 and Figure 5 the average, minimum and maximum impact resistance and apparent density for some samples as function of sintering temperature. References (conventionally sintered) of biscuit and glazed porcelain cups are also presented.

From Figure 5 we conclude that the best sintering temperature for the biscuit samples is around 1350–1365°C. Although in industrial conventional heating the maximum sintering temperature is close to 1380°C, this temperature is measured with thermocouples whose tips are measuring the air temperature. Industrial practice gives that the effective porcelain temperature is lower, normally between 1350°C and 1360°C. Comparing with the temperature (measured with the pyrometer) of the samples sintered with microwave radiation, these temperatures are in accordance with the temperatures of our best samples, MW1&2, for the biscuit and MWG for the Glazed sample.

The thermal delay between the temperature given by the thermocouple and the real temperature in the porcelain material at the minute 35 it is about 160°C. This difference decreases for values close to 35°C for higher temperatures. This difference is not very high, but it can be significant enough to produce the bloating phenomenon (bubbles formation) [15, 16]. Nevertheless, it must be taken into account that the measurements reported from compared measuring instruments were obtained from different spots.

5. CONCLUSION

The number of samples and their positions are very important in the heat homogenization.

The relationship between the porcelain density and the sintering dwell time duration is not conclusive, but results indicate that the dwell time can be eliminated. The tip of the thermocouple lies fairly close to the material sample, approximately 1 cm from its surface, and for the maximum temperature its reading is nearly 35°C lower than the temperature measured by the pyrometer. This difference is not very high, but it can be significant enough to produce the bloating phenomenon. The best results are for the samples MW1 & MW2, with sintering temperatures close to 1355°C. With the adequate control of a few microwave generators, it is possible to create a uniform electromagnetic field and therefore a more uniform heating, even at high heating rates. It

is shown the viability of microwave radiation sintering of utilitarian porcelain. This technology is a good alternative to the conventional heating, allowing shorter sintering times. It is also shown the relevance of accurate temperature measurements. As consequence, we exclude the existence of a non-thermal microwave effect in the microwave sintering of porcelain tableware.

ACKNOWLEDGMENT

This work is funded by FEDER funds through the COMPETE 2020 Programme and National Funds through FCT — Portuguese Foundation for Science and Technology under the project UID/CTM/50025/2013. The authors are grateful to the company “Porcelanas da Costa Verde” for providing the samples for this study.

REFERENCES

1. Bykov, Y. V., K. I. Rybakov, and V. E. Semenov, “High-temperature microwave processing of materials,” *J. Phys. D: Appl. Phys.*, Vol. 34, 55–75, 2001.
2. Oghbaei, M. and O. Mirzaee, “Microwave versus conventional sintering: A review of fundamentals, advantages and applications,” *Journal of Alloys and Compounds*, Vol. 494, 175–189, 2010.
3. Santos, T., L. C. Costa, L. Henrietier, M. A. Valente, J. Monteiro, and J. Sousa, “Microwave processing of porcelain tableware using a multiple generator configuration,” *Applied Thermal Engineering*, Vol. 50, 677–682, 2013.
4. Itaya, Y., S. Uchiyama, and S. Mori, “Internal heating effect and enhancement of drying of ceramics by microwave heating with dynamic control,” *Transport in Porous Media*, Vol. 66, 29–42, 2007.
5. Liu, C. H., L. B. Zhanga, C. Srinivasakannan, J. H. Peng, B. G. Liu, and H. Y. Xia, “Dielectric properties and optimization of parameters for microwave drying of petroleum coke using response surface methodology,” *Drying Technology*, Vol. 32, 328–338, 2014.
6. Fall, M. L., V. Yakovlev, C. Sahi, I. Baranova, J. G. Bowers, and G. L. Esquenazi, “Energy efficient microwave hybrid processing of lime for cement,” *Steel, and Glass Industries*, 2012, Doi: 10.2172/1034621.
7. Torgovnikov, G. and P. Vinden, “Method of microwave treatment of wood,” US Patent No. 20040178193 A1, Sep. 16, 2004.
8. Lam, S. S., A. D. Russell, C. L. Lee, and H. A. Chase, “Microwave-heated pyrolysis of waste automotive engine oil: Influence of operation parameters on the yield, composition, and fuel properties of pyrolysis oil,” *Fuel*, Vol. 92, 327–339, 2012.
9. Herrero, M. A., J. M. Kremsner, and C. O. Kappe, “Nonthermal microwave effects revisited: On the importance of internal temperature monitoring and agitation in microwave chemistry,” *J. Org. Chem.*, Vol. 73, 36–47, 2008.
10. Whipple, Jr., R. Z., “Microwave delivery system with multiple magnetrons for a cooking appliance,” US Patent No. 6,680,467 B1, Jan. 20, 2004.
11. Olofinjana, A., P. K. D. V. Yarlagadda, and A. Oloyede, “Microwave processing of adhesive joints using a temperature controlled feedback system,” *Int. J. Mach. Tools Man.*, Vol. 41, 209–225, 2001.
12. Santos, T., L. C. Costa, M. A. Valente, J. Monteiro, and J. Sousa, “Electromagnetic and thermal history during microwave heating,” *Appl. Therm. Eng.*, Vol. 31, 3255–3261, 2011.
13. Henry, F. and A. J. Berteaud, “New measurement technique for the dielectric study of solutions and suspensions,” *J. Micr. Power*, Vol. 15, 235–242, 1980.
14. Costa, L. C., S. Devesa, and F. Henry, “Microwave dielectric properties of polybutylene terephthalate (PBT) with carbon black particles,” *Micr. Opt. Tech. Lett.*, Vol. 46, 61–63, 2005.
15. Bragança, S. R. and C. P. Bergmann, “A view of whitewares mechanical strength and microstructure,” *Ceramics International*, Vol. 29, 801–806, 2003.
16. Iqbal, Y. and W. E. Lee, “Microstructural evolution in triaxial porcelain,” *J. Am. Ceram. Soc.*, Vol. 82, 3121–3127, 2000.

Design of Complex Metal-dielectric Diffraction Gratings

Alexander Lerer¹, Stepan Vyhlička^{2,3}, Galina Kalinchenko²,
Daniel Kramer², and Bedrich Rus²

¹Physics Department of Southern Federal University
Zorge St. 5, Rostov-na-Donu 344090, Russia

²ELI Beamlines, Fyzikální Ústav AV ČR, v.v.i.
Na Slovance 2, 182 21 Praha 8, Czech Republic

³Faculty of Mathematics and Physics, Charles University, Ke Karlovu 3, Prague 2, 121 16, Czech Republic

Abstract— A Volume Integral Equation (VIE) Method was developed to simulate optical wave diffraction on metal-dielectric one and two dimensional diffraction gratings based on flat multilayered structures with regular inhomogeneity in each layer. Exact solution of the equation is obtained with the Galerkin method, taking into account complex dielectric permittivity of metals and semiconductors in optical range. The Method is applicable for s and p polarized waves. As objects to investigate we chose metal-dielectric photonic crystals and multilayer reflective dielectric-semiconductor diffraction gratings. Dispersion characteristics with windows of opacity are found out. The results are compared to the simulations done by commercial numerical software.

1. INTRODUCTION

Mathematical and computational methods in electromagnetic theory have been attracting an increasing attention of scientific community because of recent hi-tech progress. Implementation of photonic and plasmonic nanostructures significantly expands horizons of signal processing. The unique capabilities of plasmonic waveguides to manipulate light signals in volumes less than diffraction limit will allow us to increase device densities in integrated photonic circuits. Plasmonic based sensors and detectors have already been used in biomedicine and optical communications [1]. High power laser systems recently reached PetaWatt power [2], and their progress led to the development of multilayer dielectric (MLD) diffraction gratings. Nowadays MLD gratings with impressive performances and size have been designed and manufactured by several companies [3, 4]. Better understanding of light diffraction and propagation ensures effective design of nanolayered diffraction gratings and photonic crystals. To proof a design accuracy, the same object needs to be simulated by different methods.

The majority of mathematical methods for calculation of electromagnetic fields can be split in two groups. The first group, the methods based on direct solution of wave equations with defined boundary conditions, includes finite-difference time-domain, the finite element method, and the finite integration technique. In the second group of methods the boundary problem is reduced to the solution of integrals, the integra-differential, pairs of integrals, and pairs of sum equations. The advantage of the first group of methods is their versatility. Their disadvantages are high requirements for a computer processing power, long calculation time, the need to digitize not only the scattering object, but also the space around the scatterer, and difficulties with simulations of small-scale elements. In addition, there is a problem with satisfaction of boundary conditions for radiation to open space. For the second group of methods these problems do not exist. The choice of the integral equation (IE) type is defined by the structure of the object under investigation. Therefore, the methods based on the IE solution are not as universal as the methods in the first group, but computer programs based on them work several orders of magnitude faster.

The main goal of this paper is a development of new semi-analytical method to solve vector integral-differential equation, describing electromagnetic wave diffraction and propagation in twodimensional periodic all-dielectric and metal-dielectric structures. As the subjects of investigation we chose plane wave propagation in photonics crystals and laser pulse diffraction on multilayer dielectric diffraction gratings. Both objects are planar multilayer structures formatted of dielectric or metallic layers (number of layers is N_l) in N_s layers there are insertions. The insertions are periodical with period — d . Dielectric layers are parallel to the plane $z = 0$. The number of layers in a structure is arbitrary, top and bottom layers are half infinite and the layer numeration is from top to bottom. Plane electromagnetic wave of arbitrary polarization $\vec{E}^e(x, y, z)$ is incident on the first layer. Horizontal cross-section of the insertion has an elliptical shape, and the size of

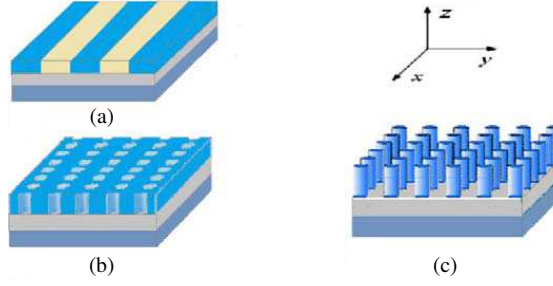


Figure 1: Structures under consideration.

the ellipse depends on the vertical coordinate z . The vertical cross-section is a trapezium. Because the number of insertions and their locations are arbitrary, we can simulate structures of absolutely arbitrary cross-section. Dielectric constants of the layers are complex, which gives us a possibility to simulate metal layers in optical wavelength range. The grating is periodical in x direction, and fields can be described by function $\exp(-ik_x x)$ where $(k_{1,x}, k_{1,y}, k_{1,z})$ are wave vector components of incident wave.

2. VOLUME INTEGRAL METHOD

In Lerer's paper [5] the problem of diffraction on a multilayer two-dimensional dielectric diffraction grating was reduced to the solution of a volume integral-differential equation (VIDE). VIDEs have several advantages: they are simpler than surface ones [6]; inhomogeneity and nonlinearity do not make simulations more complicated as it happens in the case of surface equations and also the method gives an electrical field inside of insertions as the equation solution.

One embodiment of this method was implemented in paper [7]. In this paper we propose another implementation of the method for more complex DR and an arbitrary direction of external electromagnetic wave propagation. Since the structure is periodic, the equation is solved only inside of the volume of one insertion with cross section S :

$$\frac{D_r(y, z)}{\tau} = E_r^e(y, z) + \frac{1}{d} \sum_{q=-\infty}^{\infty} \sum_{s=1}^3 \int_S \exp[i\beta_q \bar{y}] \tilde{g}_{rs}(z, z') D_s(z') dy' dz', \quad r = 1, 2, 3, \quad yz \in S \quad (1)$$

where $\bar{y} = y - y'$, $D_r(y, z) = E_r(y, z) \tau(yz)$, $\tau(y, z) = \varepsilon_b(yz) / \varepsilon_2 - \varepsilon_n(z)$, $\beta_q = \frac{2q\pi}{d} + k_{1,x} k_{1,y} k_{1,z}$, are projections of incident wave vector, $\varepsilon_n(z)$, $\varepsilon_b(xyz)$ is dielectric permittivity of ambient layer at the point of observation and of insertion. The expressions for the elements of tensor Green function \tilde{g}_{rs} for external field $\vec{E}^e(yz)$ were developed in [8]. $\vec{E}^e(yz)$ is the incident field plus the field scattered by the multilayer structure without inhomogeneity. If the plane of incidence is $y = 0$ the Equation (1) splits into two equations which describe either TE or TM waves.

The Equation (1) is bi-singular [5] and effective numerical simulation methods supposed to take this fact into account. A method to simulate optical metallic nano-vibrators based on semi-analytical IE solution was presented in papers [5] and [8]. The method is based on integral representation of Green Function. The VIDE kernel singularity shows itself in slow convergence in matrix elements of the set of linear algebraic equations obtained by the Galerkin Method. It is simpler to improve the convergence than to make integral kernel singularity regularization. This approach was used in this work. We seek a solution in the form

$$D_r(y', z') = \sum_{\mu=0}^{N_y-1} \sum_{v=1}^{N_z} X_{\mu\nu}^r V_{\mu\nu}(y', z')$$

where $X_{\mu\nu}^r$ are unknown coefficients, $V_{\mu\nu}(y'z')$ are basis functions, where $V_{\mu\nu}(y, z) = Y_{\mu\nu}(y) \sigma_\nu^{(1)}(z)$, $Y_{\mu\nu}(y) = C_{\mu\nu} P_\mu(\frac{y-\bar{y}_v}{l_v})$, where P_μ are Legendre polynomials, \bar{y}_v are coordinates of inhomogeneity center, l_v is the inhomogeneity half-width at $z = z_v$, z_v is a knot of spline function $\sigma_\nu^{(1)}(z)$ and the constant $C_{\mu\nu}$ is chosen so that the Fourier transformation of $Y_{\mu\nu}(y)$ can be represented as $\tilde{Y}_{\mu\nu}(\beta_q) = (-i)^\mu \frac{J_{\mu+1/2}(\beta_q l_v)}{(\beta_q l_v)^{1/2}} \exp(-i\beta_q \bar{y}_v)$. For one dimensional grating the asymptotic series is summed analytically.

3. SIMULATION RESULTS

In this work we investigated two types of photonic crystals (PC). The first one is sieve-looking, made of several dielectric layers with round periodical holes in them. In particular, the structure consists of three layers of dielectric, placed on a dielectric substrate, as shown in the Fig. 2.

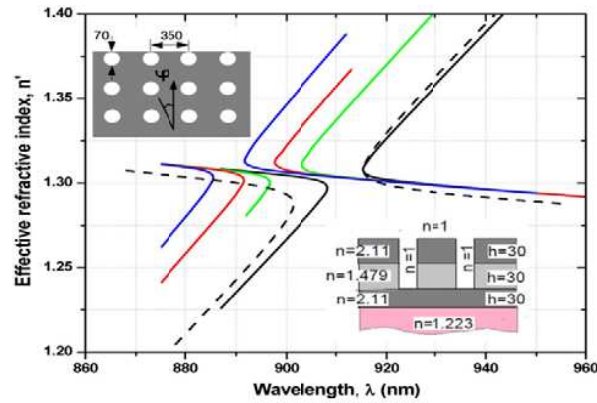


Figure 2: Dispersion characteristics of waves propagating at different angles to the axis x in all-dielectric PC [Fig. 1(b)]. Black solid curves correspond to $\varphi = 0^\circ$, green to $\varphi = 10^\circ$, red to $\varphi = 12^\circ$, and blue to $\varphi = 14^\circ$. The dashed curves depict the result for $\varphi = 0^\circ$ obtained by Ansoft HFSS commercial software. All dimensions are in nanometers.

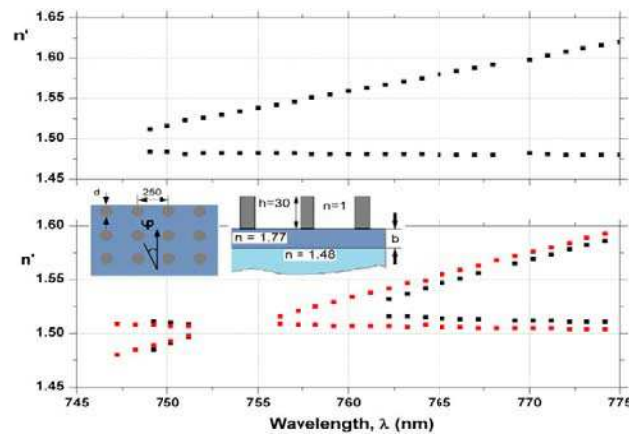


Figure 3: Dispersion characteristics for PC made of silver cylinders placed on a two-layer dielectric structure [Fig. 1(c)]. The dielectric layer thickness is $b = 100$ nm on the upper graph and $b = 150$ nm on the lower graph. The red symbols refer to cylinders of 70 nm diameter, black to 90 nm. A wave propagates at the angle $\varphi = 0^\circ$.

Two-dimensional grating is perforated in two upper layers. As can be seen from the Fig. 2, the PC has a window of opacity. In the opacity window area the phase velocity of zero harmonic with a normal dispersion ($p = q = 0$, p, q are the numbers of spatial harmonics on x and y axes, respectively) and minus first harmonic with anomalous dispersion ($p = -1, q = 0$) become equal, and dispersion curves for both harmonics merge and make one wedge-looking curve. From the equality of phase speeds for these spatial harmonics it follows that wavelength in the middle of opacity window satisfies the condition

$$\frac{dn}{\lambda} \cos \varphi = 0.5, \quad (2)$$

where d is PC period. At this wavelength, waves reflected from neighboring insertions interfere in phase, and wave propagation in the PC becomes impossible. In the Fig. 2 we can see that opacity window moves toward shorter wavelength when the angle of propagation changes from 0° to 14° , what is consistent with the Equation (2). Also, from our calculations, we found that waves with

grating than for lasers with central length 1053 nm. Here we present Littrow-mounted semiconductor-dielectric reflective diffraction grating with efficiency higher than 96% over 100 nm. The corrugated layer is made of fused silica and two top bi-layers are made of hafnia/silica. At the bottom of the multilayer stack we incorporate three silicon/fused silica bi-layers. The idea to use silicon/silica bi-layers is based on low light absorption by silicon for wavelengths longer than 900 nm and on relatively big difference in refraction coefficients of silicon and silica [11]. The grating design, electric field distribution and diffraction efficiency are presented on Fig. 5.

4. CONCLUSION

A Volume Integral Equation (VIE) Method was developed to simulate optical wave diffraction on metal-dielectric one and two dimensional diffraction gratings based on flat multilayered structures with regular inhomogeneity in each layer. Exact solution of the equation is obtained with the Galerkin method, taking into account the complex dielectric permittivity of metals and semiconductors in optical range. As examples of photonic crystals we simulated sieve-looking diffraction grating placed on multilayer dielectric substrate and metal forest-looking grating placed on multilayer dielectric substrate. The results are compared to the simulations done by commercial numerical software Ansoft HFSS. Also, VIE Method was applied for a design of broad-band multilayer reflective diffraction gratings for compression of high-energy ultra-short laser pulses. Electric field distribution inside of the gratings is also numerically studied. The results were compared to the simulations by numerical Fourier Modal Method in LightTrans Virtual Lab. The methods show excellent agreement.

ACKNOWLEDGMENT

The authors acknowledge the support of the following grants “CZ.1.05/1.1.00/02.0061”, “CZ.1.07/2.3.00/20.0091” and “SFU 2014-2016#201.01-07.2014/PPIG”.

REFERENCES

1. Stockman, M. I., “Nanoplasmonics: past, present, and glimpse into future,” *Opt. Express*, Vol. 19, 22029–22106, 2011.
2. <http://www.stfc.ac.uk/CLF/Facilities/Vulcan/12248.aspx>.
3. <http://www.plymouthgrating.com/Applications/Applications%20Page.htm>.
4. <https://lasers.llnl.gov/programs/psa/pdfs/gratings/multilayer.pdf>.
5. Lerer, A. M., “Theoretical investigation of 2D periodic nanoplasmon structures,” *J. Commun. Technol. Electron.*, Vol. 57, 1151–1159, 2012.
6. Kyurkchan, A. G. and S. A. Manenkov, “Analysis of diffraction of a plane wave on a grating consisting of impedance bodies of revolution,” *Journal of Quantitative Spectroscopy & Radiative Transfer*, Vol. 112, 1343–1352, 2011.
7. Kalinchenko, G. A. and A. M., “Lerer wideband all-dielectric diffraction grating on chirped mirror,” *IEEE/OSA J. of Lightwave Technology*, Vol. 28, No. 18, 2743–2749, 2010.
8. Golovacheva, E. V., A. M. Lerer, and N. G. Parkhomenko, “Diffraction of electromagnetic waves of optical range on a metallic nanovibrator,” *Moscow Univ. Phys. Bull.*, Vol. 66, 5–11, 2011.
9. Palik, E. D., *Handbook of Optical Constants of Solids*, Academic Press, Boston, 1985.

In Re Electric Switching Sense of Microwave Magnetic Field Rotation near Varactor-loaded Dipole Excited by a Plane Wave

Valery Butylkin^{1,2}, Galina Kraftmakher¹, and Yuri Kazantsev¹

¹Kotelnikov Institute of Radioengineering & Electronics RAS, Moscow, Russia

²Moscow Institute of Physics & Technology, State University, Dolgoprudnyi, Russia

Abstract— A movement of a microwave magnetic field near a dipole, which is excited by a plane electromagnetic wave, is investigated theoretically. The total microwave magnetic field \vec{H} being a superposition of fields of incident and scattered waves is under consideration. A varactor-loaded dipole is simulated by equivalent oscillator. It has been shown that projections of the field \vec{H} of electromagnetic wave near the dipole satisfy the canonical ellipse equation (in the general case). This ellipse' orientation and magnitudes of half-axes depend on electric parameters of the equivalent oscillator as well on the dipole length and distance from it. The total magnetic field \vec{H} rotates in one direction at frequencies above the frequency ω_0 of the dipole resonance (DR) and in the counter direction below ω_0 . Viz, left-handed \vec{H} -field takes place at frequencies $\omega > \omega_0$ while right-handed \vec{H} -field corresponds to $\omega < \omega_0$. When the dipole break is loaded with a varactor one can change the capacity C of the equivalent oscillator by application of bias voltage to the varactor. It results in tuning the DR. Electrically tunable DR can switch sense of rotating of the magnetic field. This effect in aggregate with the phenomenon of ferromagnetic resonance (FMR) in ferrite can provide electrically controlled nonreciprocity of transmission of microwaves. It can be useful in information technologies (IT) for development of fast-switched nonreciprocal devices.

1. INTRODUCTION

Dipoles are often used as elements of antennas and delay lines. At the last years there has been increasing interest in studies of metastructures based on resonant dipoles or other conductive elements (e.g., see [1, 2]). Usually, polarization of the electric field of these structures was subjecting to more detailed analysis. Now interesting effects have been observed in metastructures containing ferrite and chains or gratings of conducting elements [3–10]. These metastructures possess microwave nonreciprocity and are of interest for development of microwave devices such as nonreciprocal isolators and circulators. In these cases microwave nonreciprocity is due to different absorption of the wave whose sense of rotation of magnetic field \vec{H} coincides with sense of precession of the ferrite spins, and of the wave possessing the opposite sense of magnetic field rotation [11]. That is why it is important to study properties of microwave magnetic field on a neighborhood of dipoles. Such searches were undertaken in papers [6–8, 10, 12].

Traditional experimental techniques can only provide data about the electric field. In [12] method of measurements of properties of magnetic field of surface wave was proposed using the resonance excited in a single planar double split ring. It has been shown experimentally that near planar grating of parallel dipoles irradiated by a plane wave with electric field parallel to dipoles, the microwave magnetic field lies in the plane orthogonal to dipoles and has both transverse and longitudinal components.

apers [6–8, 10] are devoted to theoretical investigations of gratings of conducting resonant elements (dipoles, double split rings, spirals, etc.) which were simulated by bianisotropic (in the general case) layers. In accounts [7, 10] it was used effective parameters (effective permeability and refractive index) of bianisotropic media [13–15]. It has been shown that near a bianisotropic layer the microwave magnetic field is rotating, the rotation senses being opposite at the right and at the left of the layer. The connection between microwave nonreciprocity and the magnetic field rotation has been noted. It was also found that there is reversal sense of the wave magnetic field rotation under transposition of the bianisotropic layer and ferrite as well under re-tuning between ranges of forward and backward waves (if the metamaterial is “left-hande” in some frequency diapasons).

Recently, it has been found experimentally that using a single varactor-loaded dipole one can control the nonreciprocity via voltage change [16–19]. Because the time constants of electrical control devices is in orders less than the time of ferrites magnetization reversal which takes place under traditional magnetic handling (e.g., see [20–22]), such metastructure can be a basis of fast-switched nonreciprocal devices and therefore causes peculiar interest.

In the paper under presentation it is theoretically researched behavior of a microwave magnetic field near a single dipole which is excited by a plane electromagnetic wave.

Theoretical methods based on effective parameters are inapplicable to this case. Therefore we carry out direct computations.

2. ELLIPTIC POLARIZATION OF TOTAL MICROWAVE MAGNETIC FIELD

The task configuration is depicted in Figure 1.

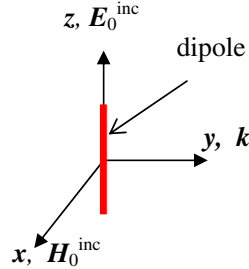


Figure 1: Disposition of dipole with respect to incident wave. \mathbf{k} , $\mathbf{E}_0^{\text{inc}}$, $\mathbf{H}_0^{\text{inc}}$ are wave, electric and magnetic vectors of incident wave.

A plane electromagnetic wave

$$\vec{E}^{\text{inc}} = \vec{e}_z \frac{1}{2} \{ E_{0z}^{\text{inc}} \exp[i(\omega t - ky)] + \text{c.c.} \}, \quad \vec{H}^{\text{inc}} = \vec{e}_x \frac{1}{2} \{ H_{0x}^{\text{inc}} \exp[i(\omega t - ky)] + \text{c.c.} \} \quad (1)$$

falls onto a dipole that is placed as it is pictured in Figure 1. Here \vec{e}_j are the coordinate orthonormal basis vectors, wave number $k = 2\pi/\lambda$, the dipole length $l \ll \lambda$. The ratio of electric and magnetic amplitudes is equal to the vacuum wave impedance $Z_0 = E_{0z}^{\text{inc}}/H_{0x}^{\text{inc}}$.

The scattered wave is characterized by complex amplitudes of projections of its magnetic field which in spherical coordinates are [23]

$$H_{\varphi}^{\text{scat}} = \frac{I_z l}{4\pi} \sin \theta \left(\frac{\exp(-ikr)}{r^2} + ik \frac{\exp(-ikr)}{r} \right), \quad H_{\theta}^{\text{scat}} = H_r^{\text{scat}} = 0. \quad (2)$$

Here θ , φ are zenith and azimuth angles, r is radial coordinate. I_z is complex amplitude of z -projection of the current that induced in dipole by electric field of the incident wave (1). To determine it let us simulate the dipole by equivalent oscillator possessing a capacity C , an inductance L and a resistance R . Introducing the oscillator impedance Z , current phase α and resonance frequency ω_0

$$Z = \sqrt{R^2 + (\omega L - 1/\omega C)^2}, \quad \alpha = \tan^{-1} [(1 - \omega^2/\omega_0^2)/\omega RC], \quad \omega_0 = (LC)^{-1/2}, \quad (3)$$

one can easily find that

$$I_z = H_{x0}^{\text{inc}} l (Z_0/Z) \exp(i\alpha). \quad (4)$$

Complex amplitudes of nonzero Cartesian projections of the scattered wave magnetic field are

$$H_x^{\text{scat}} = -H_{x0}^{\text{inc}} g \sin \theta \sin \varphi \exp(i\beta), \quad H_y^{\text{scat}} = H_{x0}^{\text{inc}} g \sin \theta \cos \varphi \exp(i\beta). \quad (5)$$

Here the notations are

$$g = \frac{Z_0 l^2}{4\pi Z r^2} \sqrt{1 + k^2 r^2}, \quad \beta = \alpha - kr + \tan^{-1} kr. \quad (6)$$

Figure 2 shows vectors of magnetic fields of incident and scattered waves and their projections. Magnetic fields of both incident and scattered waves are plane-polarized. Let us consider their superposition at points \mathcal{M}_0 ($r, \theta = \pi/2, \varphi = 0$) and \mathcal{M}_π ($r, \theta = \pi/2, \varphi = \pi$) that are placed in the entry plane ($y = 0$) symmetrically with respect to the dipole. Normalized total magnetic field in this points is equal to $\vec{h}(t) = \vec{H}/H_{x0}^{\text{inc}} = \vec{e}_x h_x(t) + \vec{e}_y h_y(t) = \vec{e}_x \cos \omega t + \vec{e}_y G \cos(\omega t + \beta)$. Magnitude $G = \pm g$, “+” and “−” refer correspondingly to points \mathcal{M}_0 and \mathcal{M}_π . Turning the coordinate system

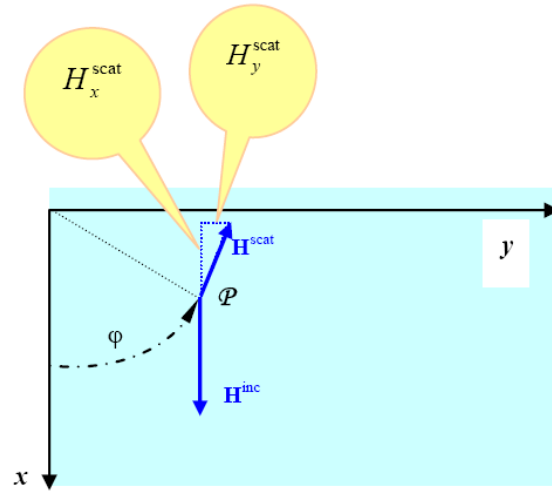


Figure 2: Magnetic fields of incident and scattered waves at an arbitrary point \mathcal{P} .

around z -axis on the angle $\Phi = 0.5 \tan^{-1} (2G \cos \beta / (1 - G^2))$ one can obtain that the magnetic field projections on new axes x' , y' satisfy the canonical ellipse equation

$$h_x^2 b_{x'}^{-2} + h_y^2 b_{y'}^{-2} = 1. \quad (7)$$

It confirms and extends the derived for $kr \ll 1$ proposition of [19] about elliptical polarization of microwave magnetic field near a dipole. Figure 3 shows rotating microwave magnetic field.

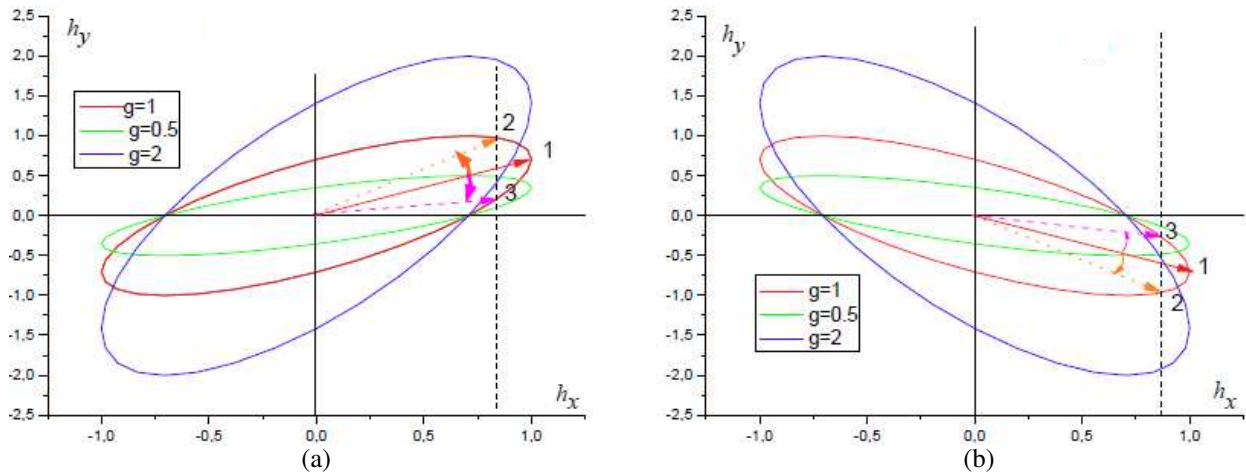


Figure 3: Movement of normalized total microwave magnetic field \mathbf{h} in points \mathcal{M}_0 (a) and \mathcal{M}_π (b) for various values of g . Straight arrows depicts field \mathbf{h} in instants of time $t=0$ (No. 1, red) and $t = \tau < \pi/2\omega$ (color) for $g = 1$. Bent arrows point sense of rotation of \mathbf{h} . Brown lines (No. 2) correspond to $\omega_0 < \omega$, magenta lines (No. 3) correspond to $\omega_0 > \omega$.

In (7) inverse squares of half-axes of the ellipse, along which the end of the vector $\vec{h}(t)$ moves, are equal to

$$b_{x',y'}^{-2} = \frac{1 + g^2}{2g^2 \sin^2 \beta} \left[1 \mp \text{sign}(\cos 2\Phi) \sqrt{1 - \left(\frac{2g \sin \beta}{1 + g^2} \right)^2} \right]. \quad (8)$$

Elliptical polarisation degrades into the plane one when $g \rightarrow 0$ or $\sin \beta \rightarrow 0$ as well under $g \rightarrow \infty$.

First condition takes place by sizeable moving from resonant frequency ω_0 , second one can be fulfilled near exact resonance under small kr . Curves of Fig. 3 have been calculated under the last condition for frequency detuning from the resonance on half-width of resonance curve for which $\alpha = \pm \pi/4$.

As follows from Fig. 3, re-tuning between these frequencies changes sense rotating of total magnetic field. Obviously, the same effect can be gotten by re-tuning of resonance frequency ω_0 . The last can be provided with varactor-loaded dipole by application of bias voltage to the varactor that changes the capacity C of the equivalent oscillator.

3. CONCLUSION

It has been developed unique features of microwave magnetic field \vec{H} near a dipole due to incident and scattered fields' superposition. Particularly, rotating of total microwave magnetic field nearby a dipole and possibility of change of this rotating sense have been revealed. Thereby the way to explanation of effect of the nonreciprocity electric control [17–19] has been found.

REFERENCES

1. *Nanostuctured Metamaterials*, European commission, Directorate-General for Research. Editors: Anne F. de Baas, Sergei Tretyakov, Philippe Barois, Toralf Scharf, Volodymyr Kruglyak and Iris Bergmair, Belgium, 2010.
2. Zheludev, N. I. and Y. S. Kivshar, "From metamaterials to metadevices," *Nature materials*, Vol. 11, No. 11, 917–924, 2012.
3. Butylkin, V. S. and G. A. Kraftmakher, Giant nonreciprocal effect under conditions of mutual influence of ferromagnetic and chiral resonance," *Tech. Phys. Letters.*, Vol. 32, No. 9, 775–778, 2006.
4. Butylkin, V. S. and G. A. Kraftmakher, "Nonreciprocal microwave transmission in metastructures with transversely magnetized ferrite plate and a grating of resonant elements," *Tech. Phys. Letters.*, Vol. 33, No. 10, 856–860, 2007.
5. Butylkin, V. S. and G. A. Kraftmakher, "Nonreciprocal transmission spectrum of a ferrite plate — resonant element grating metasandwich with split resonance," *Tech. Phys. Letters*, Vol. 35, No. 5, 397–400, 2009.
6. Butylkin, V. S. and G. A. Kraftmakher, "Nonreciprocal effects in propagation of microwaves along a waveguide structure formed from a ferrite plate and a lattice of resonant elements," *J. Commun. Technol. Electron.*, Vol. 54, No. 7, 775–782, 2009.
7. Butylkin, V. S., G. A. Kraftmakher and V. P. Mal'tsev, "Surface waves guided by a plate made from a bianisotropic resonance metamaterial," *J. Commun. Technol. Electron.*, Vol. 54, No. 10, 1124–1135, 2009.
8. Kraftmakher, G. A. and V. S. Butylkin, "Nonreciprocal amplitude-frequency resonant response of metasandwiches "ferrite plate-grating of resonant elements"," *European Physical Journal, Applied Physics*, Vol. 49, No. 3, 33004, 2010.
9. Cochet, G., A. Vallecchi, A. G. Schuchinsky, and P. Queffelec, "Entwined spiral arrays on ferrite substrate," *Proceedings of 6th International Congress on Advanced Electromagnetic Materials in Microwaves and Optics*, 215–217, Sankt-Peterburg, Russia, September 2012.
10. Butylkin, V. S., G. A. Kraftmakher, and V. P. Mal'tsev, "The nonreciprocity of microwave transmission along a bianisotropic-ferrite metastructure," *J. Commun. Technol. Electron.*, Vol. 58, No. 6, 543–550, 2013.
11. Lax, B. and K. J. Button, *Microwave Ferrites and Ferromagnetics*, McGraw-Hill, New York, 1962.
12. Butylkin, V. S., G. A. Kraftmakher, and S. L. Prosvirnin, "Method of surface polariton field structure measurement using resonance excited in a single planar double split ring," *Tech. Phys. Letters*, Vol. 38, No. 2, 147–150, 2012.
13. Butylkin, V. S. and G. A. Kraftmakher, "A left-handed composite medium based on waveguiding structures with a bianisotropic filling," *J. Commun. Technol. Electron.*, Vol. 51, No. 5, 484–497, 2006.
14. Butylkin, V. S. and G. A. Kraftmakher, "Passbands of bianisotropic and waveguide-bianisotropic metamaterials based on planar double split rings," *J. Commun. Technol. Electron.*, Vol. 53, No. 1, 1–14, 2008.
15. Butylkin, V. S. and G. A. Kraftmakher, "The effect of chirality on the existence of backward waves in metamaterials made from resonance planar chiral elements," *J. Commun. Technol. Electron.*, Vol. 53, No. 7, 758–766, 2008.
16. Kraftmakher, G. A., V. S. Butylkin, and Y. N. Kazantsev, "Electrically controlled frequency bands of nonreciprocal passage of microwaves in metastructures," *Tech. Phys. Letters*, Vol. 39, No. 6, 505–508, 2013.

17. Kraftmakher, G. A., V. S. Butylkin, and Y. N. Kazantsev, "Electrically tunable nonreciprocity of microwave transmission through "ferrite-varactor loaded resonant element" planar metas-structure," *Phys. Status Solidi C*, Vol. 11, No. 5-6, 1033–1038, 2014.
18. Kraftmakher, G., V. Butylkin, and Y. Kazantsev, "Sign reversal of the nonreciprocity of mi-crowave propagation on a "ferrite + varactor-loaded dipole" metastructure without reversal of the magnetization direction," *Book of Abstracts of 8th International Congress on Advanced Electromagnetic Materials in Microwaves and Optics (Metamaterials 2014)*, Copenhagen, Den-mark, August 2014, <http://congress2014.metamorphose-vi.org>.
19. Butylkin, V. S., G. A. Kraftmakher, and Y. N. Kazantsev, "About electric control of nonre-ciprocity of microwave transmission in metastructures," *Zhurnal radioelektroniki: elektronnyi zhurnal*, No. 12, 1-14, 2014. URL: <http://jre.cplire.ru/jre/dec14/22/text.html> [in Russian].
20. Oriental Magnetics Co. LTD., "Microwave Ferrite Products," URL: <http://www.magnet-china.com/microwave-ferrite-products.html>.
21. Future Electronics, URL: <http://www.futureelectronics.com/en/diodes/switching-diodes.aspx>.
22. Bodger, B., and T. Edridge, "Ferrite circulator switches and their applications," *Microwave J.*, November 1, 2003.
23. Neganov, V. A., O. V. Osipov, S. B. Raevskii, and G. P. Yarovoi, *Electrodynamics and Prop-agation of Radio Waves*, publishing house "Radiotekhnika," Moscow, 2007 (in Russian).

Analysis of EMG Waves from a Pulse Source

R. Kadlec, D. Nešpor, P. Fiala, and E. Gescheidtová

Department of Theoretical and Experimental Electrical Engineering
Brno University of Technology, Technická 3082/12, Brno 616 00, Czech Republic

Abstract— The authors report on an analysis of conditions on the boundary between layers having varied electromagnetic properties. The research is performed using consistent theoretical derivation of analytical formulas, and the underlying problem is considered also in view of multiple boundaries, including the effect of the propagation of electromagnetic waves exhibiting different instantaneous speed.

The paper includes a theoretical analysis and references to the generated algorithms. The main algorithm was assembled to enable simple evaluation of all components of the electromagnetic field in relation to the speed of the wave propagation in a heterogeneous environment. The proposed algorithms are compared by means of different numerical methods for the modelling of electromagnetic waves on the boundary between materials; moreover, electromagnetic field components in common points of the model are also subject to comparison.

The article describes the obstacles in comparison of different principles based analyses. Thus, analysis using numerical modelling performed via the wave equation in the ANSYS and the applied methods in the Matlab program.

When in conjunction with tools facilitating the analysis of material response to the source of a continuous signal, the algorithms constitute a supplementary instrument for the design of a layered material. Such design enables the realization of, for example, recoilless plane, recoilless transition between different types of environment, and filters for both optical and radio frequencies. This phenomenon occurs in metamaterials.

1. INTRODUCTION

Inhomogeneities and regions with different parameters generally appear even in the cleanest materials. During the passage of an electromagnetic wave through a material, we can observe amplitude decrease and wave phase shift. These phenomena are due to the concrete material characteristics, such as conductivity, permittivity, or permeability [1]. If a wave impinges on an inhomogeneity, there occurs a change in its propagation. The change manifests itself in two forms, namely in reflection and refraction. In addition to this process, polarisation and interference may appear in these waves [2].

In the Matlab program, algorithms were created that simulate reflection and refraction in a lossy environment on the boundary between two dielectrics. The reflection and refraction are in accordance with Snell's law for electromagnetic waves, as shown in Fig. 1(a).

The interpretation of the propagation of electromagnetic waves on a layered heterogeneous medium is expressed by the formula

$$\mathbf{E}_{rl} = \mathbf{E}_{il} \rho_{El} \cdot e^{-j \mathbf{k}_l \mathbf{u}_{nrl} \times \mathbf{r}_l}, \quad \mathbf{E}_{tl} = \mathbf{E}_{il} \tau_{El} \cdot e^{-j \mathbf{k}_l \mathbf{u}_{ntl} \times \mathbf{r}_l}, \quad (1)$$

where \mathbf{E}_{rl} a \mathbf{E}_{tl} are the reflection and refraction of the electromagnetic waves on the boundary line ($l = 1, \dots, \max$) according to Fig. 1(a), \mathbf{E}_{il} is the amplitude electric field strength on the boundary line l , ρ_{El} and τ_{El} are the reflection coefficient and transmission factor on the boundary line l , \mathbf{k}_l is the wave number of the layer, \mathbf{r}_l is the electromagnetic wave positional vector on the boundary line l , \mathbf{u}_{ntl} and \mathbf{u}_{nrl} are the unit vectors of the propagation direction.

2. OBLIQUE INCIDENT WAVE ON A LAYERED MEDIUM

The Matlab-based analysis using Equation (1) was performed in the planar layers. Fig. 2 show the response of the environment of 5 layers with the same thickness $d = 20$ mm. During the transmission, the wave at the frequency of 1.5 GHz passes through a material 1 with parameters $\varepsilon_{r1} = 1$, $\mu_{r1} = 1$ and $\gamma_1 = 1 \cdot 10^{-9}$ S/m, where the wave is reflected and refracted. Furthermore, the wave propagates through material 2 with parameters $\varepsilon_{r2} = 81.6$, $\mu_{r2} = 0.999991$, and $\gamma_2 = 4.405 \cdot 10^{-9}$ S/m. The incidence of the wave on boundary 1 is at the angle of θ_0 . The described configuration is according to Fig. 1(a). The selection of the material parameters is only of testing character, and thus it does not have any special meaning.

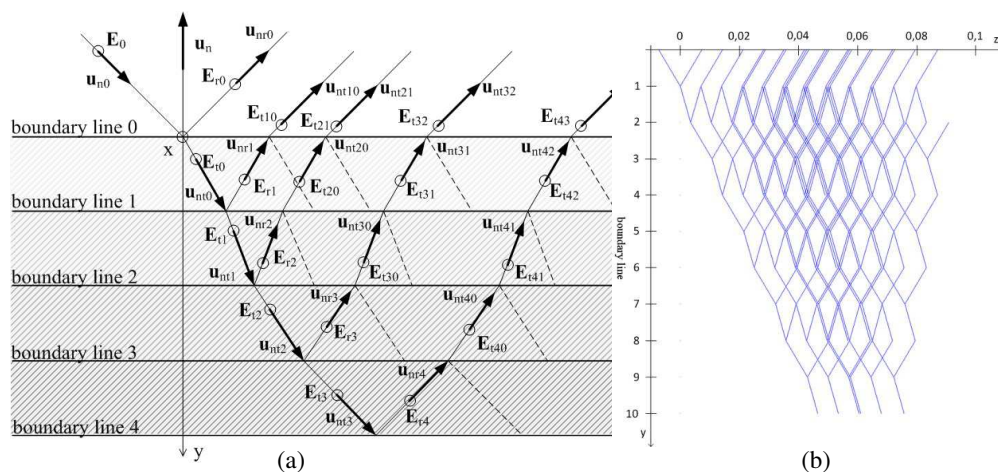


Figure 1: The reflection and refraction of the electric component of an electromagnetic wave on a layered medium: (a) layout, (b) Matlab for 2000 cycles.

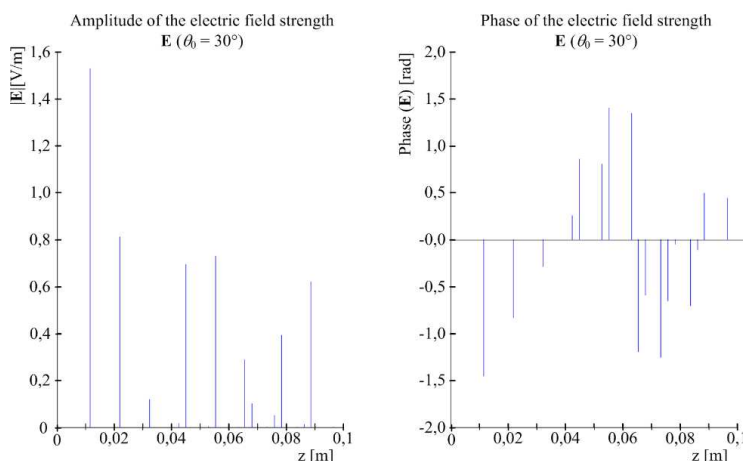


Figure 2: The strength of the electric component of the TE wave on a layered medium at the angle $\theta_0 = 30^\circ$.

The results of the analysis shown in the images consist in the modules of the electric field strength \mathbf{E} along the boundary between the first layer and the external environment. The analysis of the response to the incidence of an EMG wave on the surface of a multilayered environment within the given time interval is presented in Fig. 2; here, the module of the electric field strength \mathbf{E} is introduced depending on the plane leading from the centre of the model towards its edge. The distribution of the modules of the electric field strength \mathbf{E} on the surface of the material is obvious from the waveform of the EMG waves propagating through and reflecting from a multilayered material, as shown in Fig. 1(b).

3. COMPARISON WITH FEM MODEL

In order to verify the properties of the analytical model, we used numerical approach utilised the finite element method (FEM). As the mathematical expression, we applied the enhanced wave equation for a lossy environment:

$$\nabla^2 u + f \frac{\partial u}{\partial t} + g \frac{\partial^2 u}{\partial t^2} - f_c(x, y, z, t) = 0, \quad \forall g(x, y, z) \neq 0, \quad \forall f(x, y, z) \neq 0, \quad \text{in } \Omega \quad (2)$$

where u is the searched functional, f a function of the electromagnetic wave damping, g a function of the electromagnetic wave excitation, f_c a function of the lossy environment, Ω the defining domain of variables and functions.

Direct comparison of the different analysis results obtained via the applied methods can be performed only with substantial difficulty. For this reason, we designed algorithms to evaluate

the selected time intervals in the ray-tracing model. The evaluation of the module of the electric field strength \mathbf{E} on the surface of the material at these time intervals is indicated in Fig. 3. A continuous electromagnetic wave was generated by the source. A suitably selected time interval of the medium response expressed by the maximum values of the electromagnetic field strength facilitates verification by the instantaneous values obtained via the applied finite element method. Fig. 3 shows that the results acquired through both analyses are comparable.

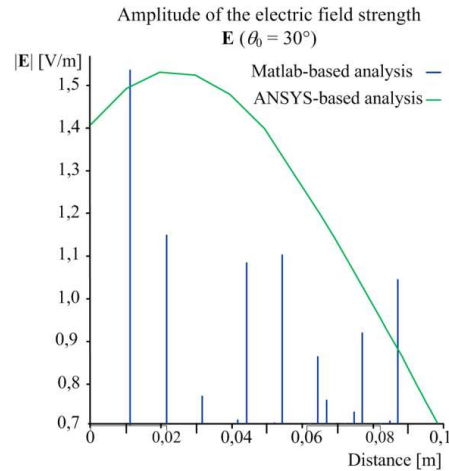


Figure 3: The diagram of the distribution of the electric field strength \mathbf{E} : for $\theta_0 = 30^\circ$, on the surface of the material, and in the plane of incidence.

4. VARIOUS PARAMETERS OF THE INCIDENT WAVE ON A LAYERED MEDIUM

Figure 4 compare the distribution of module of the electric field strength E , which is sent from the source in the form of one pulse and the continuous signal. Fig. 4(a) shows the distribution of the wave, which is propagate from the pulsed source in the form of one pulse of one period. Fig. 4(b) shows the distribution of the waves, which are propagate from the source during a time $t = 20 \cdot T$. The response of the material is represented by superposition of the reflected and transmitted electromagnetic waves.

The thickness of the layers in this analysis is $d = 100 \cdot \lambda$, where λ is the wavelength of the wave emitted from the source with a frequency $f = 700$ THz. This response is independent on the propagation time, as shown a comparison in Fig. 4. Results of the analysis are shown in this figures are for incident at the angle $\theta_0 = 30^\circ$.

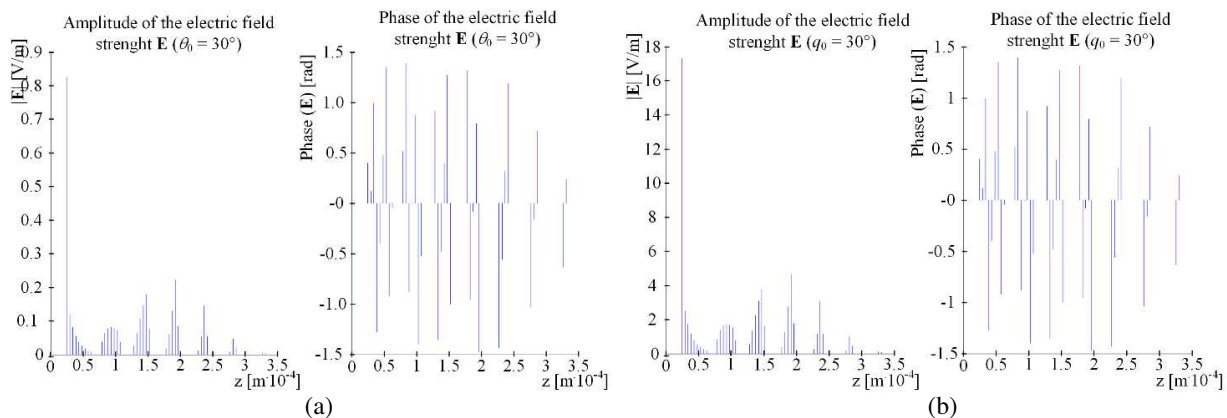


Figure 4: The strength of the electric component of the TE wave on a layered medium for $d = \lambda \cdot 100$ and (a) $t = T$, (b) $t = 20 \cdot T$ ($f = 700$ THz).

Following the interpretation of the analysis by changing the parameters of the model. Fig. 5 shows the same response as in the previous analysis, but with different material parameter $\epsilon_{r2} = 4$.

Fig. 5(a) and Fig. 5(b) compare the change in the layer thickness a change in the angel of incidence. From the analysis it can be determined that the response is different mainly due to the angle of incidence. The thickness of the layers are not reflected in changes in the shape analysis of modules and phases of the electric field strength.

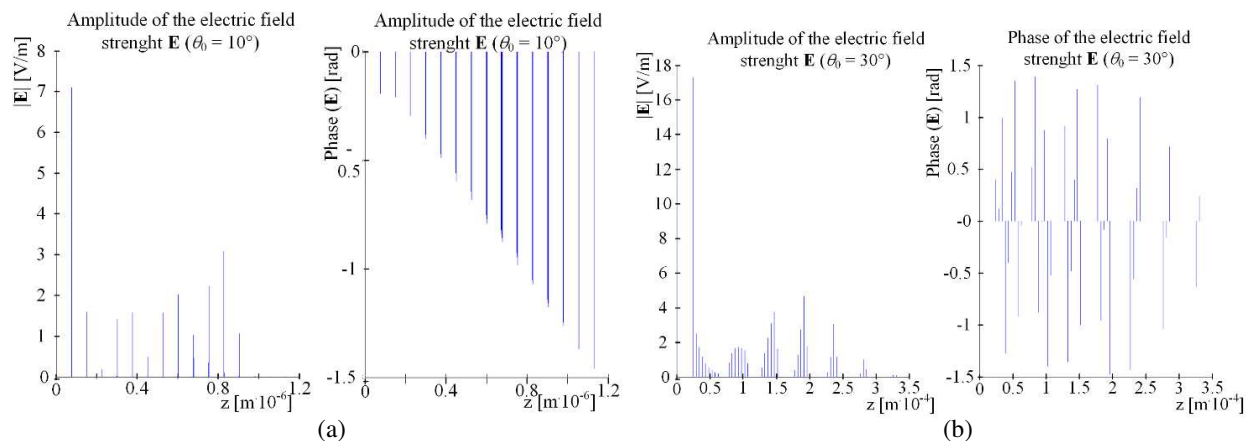


Figure 5: Oblique incidence on the layered medium for (a) $d = \lambda$ and $\theta_0 = 10^\circ$; (b) $d = \lambda/100$ and $\theta_0 = 70^\circ$ ($\varepsilon_{r2} = 4$, $t = 20 \cdot T$, $f = 700$ THz).

5. CONCLUSION

The article presents a comparison of two approaches to the analysis of wave propagation in a layered material structure. The first of these techniques is based on the propagation of electromagnetic waves as defined by analytical formulas (1) and was solved in the Matlab program. The second approach exploits the FEM applied to the wave equation. The FEM-based solution was conducted using the ANSYS system. The actual comparison of the results provided by both approaches cannot be performed directly.

Numerical modelling carried out by means of the wave equation and ANSYS produces a continuous source of electromagnetic waves. Interference effects between the reflected and refracted waves arise on the boundary between the layers. Moreover, the interference process is also entered by the time-delayed waves from the source and by interface reflections [4].

The results of the ANSYS-based analysis of the propagation of electromagnetic waves in a material in the time-domain corresponds to the resulting distribution of the superimposed field intensities on individual boundaries of the analytical model. The analytical solution and its algorithms process the time-varying phenomena of the pulsed source. The analytical solution includes the effect of time-dependent propagation of electromagnetic waves in a heterogeneous medium, and it results in the distribution of the electromagnetic field at the boundaries during certain moments of time.

The EMAG module of ANSYS is not a convenient tool for the evaluation of either the pulse process or the maximum values of an electromagnetic wave in a heterogeneous environment. This solution, despite being very robust in the time domain, is not suitable for multiple layers due to the method of the element mesh division. In FEM-based numerical models, the number of divisions of the discretised mesh can be determined only with difficulty (considering the wavelength of the propagating wave), and the solution of a large model by currently available means is almost impossible. Importantly, this drawback can be eliminated via the proposed method. The analysis of the pulsed source of the electromagnetic wave by means of an analytical model provides expectable results in heterogeneous structures since the behavior of phase change is uniform. The analytical solution allows us to analyse the response of the material in detail for the individual parts.

ACKNOWLEDGMENT

Research described in this paper was financed by the National Sustainability Program under grant LO1401, by the Czech Science Foundation under grant no. GA15-08803S, a project of the BUT science fund, No. FEKT-S-14-2545, and a project from the Education for Competitiveness Operative Programme, no. CZ.1.07.2.3.00.20.0175 (Electro-researcher). For the research, infrastructure

of the SIX Center was used.

REFERENCES

1. Schmidt, E. *Optické vlastnosti pevných látek*, 1. vyd. Praha: Státní pedagogické nakladatelství, 200, 1986.
2. Dedek, L. and J. Dedková, *Elektromagnetismus. 2*, 232, ISBN 80-214-1548-7, Brno, VUTIUM, 2000.
3. ROUBAL, Z. and T. Kříž, “A 3D magnetic measurement for $S/N < 0.01$,” *PIERS Proceedings*, 981–985, Suzhou, China, September 12–16, 2011.
4. Rroubal, Z. and V. Smejkal, “Determination of parameters in the Jiles-Atherton model for measured hysteresis loops,” *Proceeding Measurement*, 127–131, ISBN: 9788096967254, Smolenice, SAV, 2013.
5. Drexler, P. and R. Kubásek, “Pulsed magnetic field fiber optic sensor based on orthoconjugate retroreflector,” *Proceedings of SCS 2009 International Conference on Signals, Circuits and Systems*, ISBN: 978-1-4244-4398-7, Tunisia, 2009.

Propagation of Fluorescence Radiation through μ -capillary Holes of Glass Micro-channel Plate

Mikhail Mazuritskiy¹, Alexander Lerer¹, Alexander Ezovtsov¹, and Galina Kalinchenko²

¹Physics Department, Southern Federal University, Zorge St. 5, Rostov-na-Donu 344090, Russia

²ELI Beamlines, Fyzikální ústav AV ČR, v.v.i. Na Slovance 2, 182 21 Praha 8, Czech Republic

Abstract— The features of soft X-ray fluorescence spectra of radiation propagating inside micro-channel plates have been studied in the framework of wave approximation. X-ray and fluorescence yield due to the grazing incidence reflection phenomenon have been investigated with respect to the geometry of channel walls. We researched experimental spectra collected at the exit of micro-capillaries under total X-ray reflection condition and supported them with theoretical calculations taking into account a surface transition layer at waveguide surface. It was shown that the wave penetrating through cladding material substantially modifies the wave field near the waveguide surface. It results in a significant increase of total energy flux inside guiding layer and leads to additional spatial modulation of the electromagnetic field. Diffraction phenomena at the exit of a hollow X-ray waveguide (with real and imaginary parts of permittivity) were investigated using the model of Fraunhofer diffraction of waves at far zone.

1. INTRODUCTION

Capillary optics is one of the fastest growing X-ray optical technologies [1] because of its superior capacity of generating high flux density beam in the μm - and sub μm range. Properties and peculiarities of X-ray beams formed by polycapillary optics have been intensively studied in the past 25 years [2–6]. Investigations of X-ray waveguides and micro-capillary optics based on the phenomenon of multiple total external reflections are devoted to ultra focusing properties and partially coherent beams. Application of the wave optics methods allows the process of guided transmission of X-ray radiation to be described in details. In microchannels the propagation features are defined by the radiation interaction with a curved surface and characterized by the waves that propagate close to the capillary walls. Basic point of the X-ray beam transportation in capillary channel (as an X-ray waveguide) is the mode regime [2] associated in particular with a surface channeling of X-ray radiation.

Propagation of X-rays through micro-capillaries is of great interest due to the high efficiency of radiation transportation by holes of micro-capillaries, and, as a consequence, due to the possibility for creation of new optical elements conditioning the X-ray beams. In addition to the high practical importance, capillary optical systems represent a fine tool for studying fundamental features of radiation dispersion by a surface. The continuing investment in, and development of, new sources of intense and even coherent x-ray radiation as well as the refinement and extension of methods to probe matter with these sources attests to the continuing importance of this field.

The micro-channel plate (MCP) systems can be applied to focus and collimate X-rays. The optics can provide a highly effective low weight device and may be ideally suited for use in a lot of applications. Grazing-incidence X-ray methods based on the analysis of the secondary radiation (fluorescence) from a solid surface as a result of interaction with primary radiation have a great scientific and applied interest. If the grazing angle is less than the Fresnel one, and incident photons are capable to excite the atomic levels then both X-ray fluorescence and elastic scattering are observed. In the previous manuscripts were published [7–11] experimental results on the spectroscopy of X-ray fluorescence transportation through the MCP.

One of the goals of this work is to present the theoretical model on transmission of X-ray fluorescence radiation emitted by walls of the silicon glass micro-channels through microcapillary structures. Inelastic scattering and propagation of fluorescence radiation have been studied in anomalous dispersion region of the energy range near the SiL — absorption edge. Also, we have presented results on X-ray transmission through microcapillary structures, aimed at the Research&Development of dedicated optics working in “water window” spectral region (energy 100–600 eV).

2. METHOD

2.1. Basic Steps of Our Theoretical Model

- ▶ Calculation of propagation constants and constants of attenuation (excitation) too for wave modes of a single capillary;
- ▶ It was considered that wave parameters of the single capillary are correspond to the parameters of micro-channel plate (MCP) polycapillary structures;
- ▶ Mode amplitudes at the input of the polycapillary structures have been calculated with the help of Kirchhoff - Huygens method;
- ▶ Using attenuation (excitation) constants mode amplitudes was calculated at the output of the capillaries;
- ▶ Angular distribution of X-ray radiation at the exit of MCP was calculated on the base of Kirchhoff-Huygens method;
- ▶ Investigation of the X-ray diffraction (diffraction pattern) at a long distance from the MCP have been performed using the model of Fraunhofer diffraction of waves.

2.2. Calculation of Parameters of Waveguide Modes in a Single Capillary

X-ray radiation propagates through silicon glass plates in a vacuum inside the holey cylindrical waveguides (pores). According to our model transition layer was taken into account at the surface of inner shell microchannels. In this approximation the permittivity ($\varepsilon \approx 1 - \delta - i\beta$) varies smoothly between value of 1 to the value for substrate - dielectric constant of silicon glass (see Figure 1).

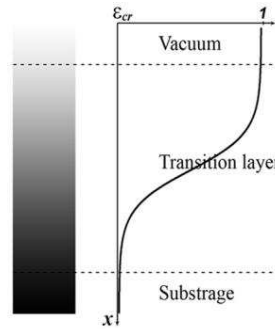


Figure 1: The model of transition layer for the waveguide channel surface.

In addition, we can taken into account an insignificant polarization of X-ray waves in the X-ray waveguide ($|\varepsilon| \cong 1$) and field was described with the help of scalar potential $\Psi(r, \varphi, z) = U(r) \cos m\varphi \exp(-i\gamma z)$, where γ — is a complex propagation constant. Function $\Psi(r, \varphi, z)$ satisfies to the Helmholtz equation

$$\Delta \Psi(r, \varphi, z) + k^2 \varepsilon(r) \Psi(r, \varphi, z) = 0$$

Δ — is the Laplace operator, $k = 2\pi/\lambda$, λ — is a radiation wavelength in vacuum.

In the frame of our approximation of transition layer the cylindrical transition layer (inner shell of the micro-channel) was deviated into N sub-layers (rings in the cross section). The permittivity of the each ring is a constant and it was determined by the dielectric constant corresponding to the radius of the middle of this ring. The dispersion equation for the complex value of the propagation constant γ can be solved numerically using the math method proposed in [12].

2.3. The Calculation of the Mode Amplitude at the Input of the Capillaries

We considered a propagation of plane waves and coordinates $z = 0$, $z = -h$ corresponded to the entrance and exit of waveguide ends respectively. The math expression below is present by a plane waves at the input of the capillaries

$$\Psi^{ext}(x, z) = \exp[i(k_x x + k_z z)], \quad (1)$$

where $k_x = k \sin \varphi$, $k_z = k \cos \varphi$, φ — grazing angle between the X-ray beam and wall of the microchannel wall. In the plane of $z = 0$ we have

$$\Psi^{ext}(x, 0) = \exp(ik_x x) = \exp(ik_x r \cos \varphi) = 2 \sum_{m=0}^{\infty} \nu_m i^m J_m(k_x r) \cos m\varphi \quad (2)$$

$$\nu_n = \begin{cases} \frac{1}{2}, & n = 0, \\ 1, & n \neq 0. \end{cases}$$

At the entrance of the capillary the wave amplitude $A_{mn}(0)$ can be calculated with the help of integral:

$$A_{mn}(0) = \int_0^R r dr \int_0^{2\pi} \Psi^{ext}(r \cos \varphi, 0) \Psi_{mn}(r, \varphi, 0) d\varphi \quad (3)$$

After substituting the Equations (1), (2) in the (3) was obtained the relations:

$$A_{mn} = 2\pi i^m I(m, \kappa_{mn}, k_x, R)$$

$$I(m, \kappa_{mn}, k_x, R) = \int_0^R r J_m(k_x r) J_m(\kappa_{mn} r) dr$$

$$= R \frac{\kappa_{mn} J_{m-1}(\kappa_{mn} R) J_m(k_x R) - k_x J_m(\kappa_{mn} R) J_{m-1}(k_x R)}{(\kappa_{mn})^2 - k_x^2}$$

κ_{mn} — transverse wave mode number which has index mn.

The amplitude at the exit of the capillary is equal:

$$A_{mn}(h) = A_{mn}(0) \exp(-\gamma''_{mn} h),$$

where $\gamma''_{mn} = \text{Im} \gamma_{mn}$ is the attenuation coefficient in the case of $\gamma''_{mn} > 0$, and excitation coefficient for $\gamma''_{mn} < 0$.

Summary field in the capillary was calculated in our model as:

$$U_{\Sigma}(r, \varphi, z) = \sum_{m=0}^{\infty} \sum_{n=1}^{\infty} A_{mn} U_{mn}(r, \varphi, z) = \sum_{m=0}^{\infty} \sum_{n=1}^{\infty} A_{mn} J_m(\kappa_{mn} r) \cos m\varphi \exp(i\gamma_{mn} z) \quad (4)$$

2.4. Angular Distribution of the X-ray Radiation Intensity Calculation Collected at the Output of the MCP

The radiation field at the output of the MCP was consider as a double row on spatial harmonics

$$V(x, y, z) = \sum_{p=-\infty}^{\infty} \sum_{q=-\infty}^{\infty} B_{pq} \exp[i\chi_{pq}(x, y, z)] \quad (5)$$

where B_{pq} — is the amplitudes of spatial harmonic and $\chi_{pq}(x, y, z)$ is the phases.

We have taken into account for X-ray condition of $z \gg \lambda$ to perform calculations only for waves $k > \rho_{pq}$.

The amplitudes of space harmonics can be estimated with the help of integral:

$$B_{pq} = \int_0^R r dr \int_0^{2\pi} V(x, y, h) U_{\Sigma}(r, \varphi, h) d\varphi \quad (6)$$

After substituting the Equations (4), (5) in the (6) was obtained the relations below:

$$B_{pq} = 2\pi \sum_{m=0}^{\infty} i^m \sum_{n=1}^{\infty} A_{mn} I(m, \kappa_{mn}, \rho_{pq}, R) \quad (7)$$

In the calculations in (7) in the sum over n considered only propagating waveguide modes, the upper limit of summation in the sum over m was selected numerical experiment, it usually does not exceed three. Each space harmonic — is a plane wave which projections of wave vector on the axis “ x , y ” are equal to α_p , β_{pq} , respectively. The angles of the diffraction peaks (in the spherical coordinates) are defined by

$$\begin{aligned} k_{x,pq} &= k \cos \varphi_{pq} \sin \theta_{pq} = \alpha_p, \quad k_{y,pq} = k \sin \varphi_{pq} \sin \theta_{pq} = \beta_{pq}, \\ k_{z,pq} &= k \cos \theta_{pq} = \gamma_{pq}. \end{aligned}$$

3. RESULT

In this work, we have studied the angular distribution of the X-ray field passed through microchannels whose energy corresponds to the anomalous dispersion region of the $\text{SiL}_{2,3}$ absorption edges. The transition layer was considered as a waveguide, where the total reflection effect occurs only at the interface with the material. Radiation leaves the transition layer at the interface with vacuum; as a result, the wave rapidly damps. The damping of the wave in the waveguide can be compensated in the presence of amplification owing to the excitation of X-ray SiL fluorescence inside this layer.

The experimental layout shown in Figure 2, describes the optical configuration available at the Polarimeter end-station of the UE52.SGM at the BESSY II synchrotron radiation facility. We used for the experiments ~ 0.3 mm thick MCPs with a hexagonal shape in the transverse cross-section, made with a lead silicate (PbSiO_3) composition, manufactured by the BASPIK [13]. Such compact optical devices contain regular holey channels with a diameter of $3.4 \mu\text{m}$ and with a pitch size of $4.2 \mu\text{m}$. As shown in Figure 2, the entrance surface of the MCP was illuminated by a primary monochromatic radiation. The radiation propagating inside the micro-channels was collected by a single photodiode placed on the other side of the polycapillary structure. In the transmission geometry, the grazing angle θ between the incident primary beam and MCP microchannel walls was set while rotating the device around the “ θ ” axis (see Figure 2).

The angular distribution of the radiation, i.e., the intensity vs. angle at the exit of a MCP, in the total external reflection condition for different grazing angles of the incident beam has been investigated. Performing the angular scan of the photodiode position sets at the exit of the MCP (angles “ ϕ ” of the photodiode), we may identify the positions where the maximum intensity of emitted radiation occurs. For any fixed value of the θ -angle between the incident monochromatic radiation and MCP microchannel walls, the intensity distribution between two maxima $\phi = \pm\theta$ in the angular range $-\phi \leq \phi \leq \theta$ has been measured. Finally, the spectra for different θ angles and for different positions of the photodiode: $\phi_1, \phi_2, \phi_3, \dots, \phi_n$, have been collected.

Figure 3 shows the angular distribution of the radiation intensity at the output of the micro-channel plate experimentally obtained at the Polarimeter experimental station at the BESSY II synchrotron center (1) and calculated distributions (2, 3) on the base of the theoretical model presented here. The performed calculation shows that radiation intensity maxima at $E = 120$ eV at the output of the micro-channel plate should be observed at the angles $\theta = \pm 5$ deg. and

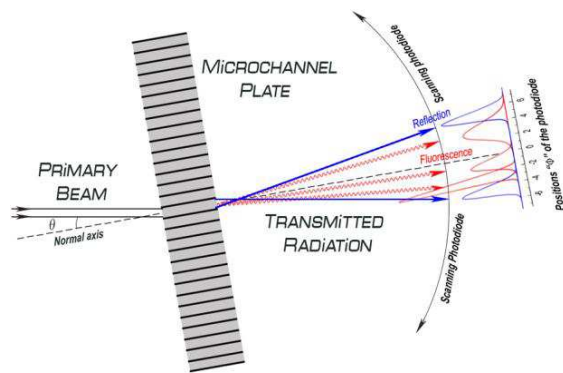


Figure 2: Experimental layout for transmission mode radiation through MCP.

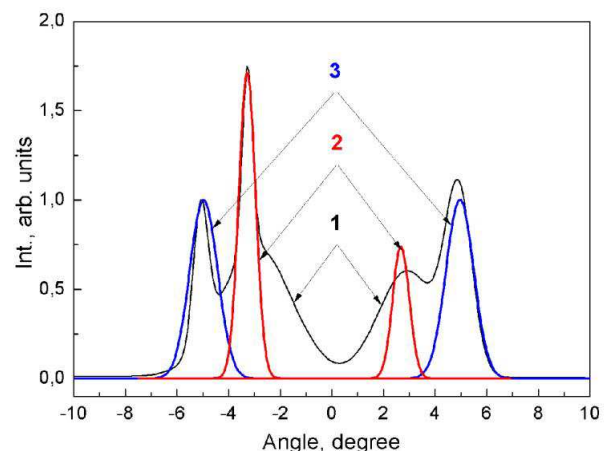


Figure 3: Angular distribution of the radiation intensity at the output of the micro-channel plate.

$\theta \approx \pm 3$ deg.. Two peaks marked by (2) in the figure are lines which have been calculated in the case of excitation radiation inside the microchannels. We have found that angle of output X-ray fluorescent radiation does not dependent on the angle of incidence radiation on the MCP.

Thus, the theoretical values are in good agreement with the experimentally observed values. We attribute the revealed maxima at $\theta = \pm 5$ deg. with reflection of primary radiation at the exit and $\theta \approx \pm 3$ deg. in the distribution of the intensity of X-rays at the output of micro-capillaries to the surface fluorescence waves propagating in the transition layer of microchannels. Experimental spectrum shows the additional maximum at the angle about $\theta \approx -2$ deg. which nature may be connected with X-ray fluorescence radiation according to the theoretical possibility yield fluorescence at small angles too.

4. CONCLUSIONS

The x-ray fine structures and the angular distribution of X-ray radiation propagating inside microchannels of MCPs have been interpreted in the energy range of the anomalous dispersion of the SiL_{2,3} absorption edges thanks to calculations performed within a model that takes into account a surface transition layer at the sample surface. In this work was revealed that transition layer where the total reflection of X-rays takes place acts as an effective waveguide. As a consequence, for a device whose channels are much longer than the radiation wavelength, the radiation at the exit of MCPs shows maxima at angles corresponding to theoretical calculations.

In the future it may be allowed to identify optimal transport conditions for the fluorescence radiation excited inside of microcapillary structures. The fluorescence transport conditions optimization is very important for improvement of X-ray focusing properties and, in principle, for delivery of high flux density on a sub-micrometer area of sample.

ACKNOWLEDGMENT

This work was partially supported by the Southern Federal University (project No. 213.01-07-2014/08) and Helmholtz Zentrum Berlin, BESSY II (project No. 14100626).

REFERENCES

1. Tsuji, K., J. Injuk, and R. Van Grieken, Eds., *X-ray Spectrometry: Recent Technological Advances*, Wiley, 2004.
2. Dabagov, S. B., *Phys. Usp.*, Vol. 46, 1053–1075, 2003.
3. Kumakhov, M. A. and F. F. Komarov, *Phys. Rep.*, Vol. 191, 289–350, 1990.
4. Bilderback, D. H., S. A. Hoffman, and D. J. Thiel, *Science*, Vol. 263, 201–203, 1994.
5. Pfeiffer, F., C. David, M. Burghammer, C. Riekel, and T. Salditt, *Science*, Vol. 297, 230–234, 2002.
6. Dabagov, S. B., M. A. Kumakhov, S. V. Nikitina, et al., *J. Synchrotron Rad.*, Vol. 2, 132–135, 1995.
7. Mazuritskiy, M. I., *JETP Letters*, Vol. 84, No. 7, 381–383, 2006.
8. Mazuritskiy, M. I. and J. Synchrotr, *Rad.*, Vol. 19, 129–131, 2012.
9. Mazuritskiy, M. I., S. B. Dabagov, K. Dziedzic-kocurek, and A. Marcelli, *NIM B*, Vol. 309, 240–243, 2013.
10. Mazuritskiy, M. I., A. M. Lerer, A. A. Novakovich, and R. V. Vedrinskii, *Jetp Lett.*, Vol. 98, 130–133, 2013.
11. Mazuritskiy, M. I., S. B. Dabagov, A. Marcelli, A. Lerer, et al., *J. Opt. Soc. Am. B*, Vol. 31, No. 9, 2182–2187, 2014.
12. Lerer, A. M., I. V. Donets, G. A. Kalinchenko, and P. V. Makhno, *Photon. Res.*, Vol. 2, 31–37, 2014.
13. Vladikavkaz Technological Center “BASPIK”, Microchannel Plates, <http://www.baspik.com/eng/products/nauka/>.

Diffraction by Arbitrary-angled Dielectric Wedges: Closed Form High-Frequency Solutions

M. Frongillo¹, G. Gennarelli², and G. Riccio¹

¹D.I.E.M., University of Salerno, Via Giovanni Paolo II 132, Fisciano (SA) 84084, Italy

²Institute for Electromagnetic Sensing of the Environment, National Research Council
Via Diocleziano 328, Naples 80124, Italy

Abstract— Diffraction inside and outside an arbitrary-angled lossless penetrable wedge is considered in this study. Closed form expressions are presented for the diffracted field in the inner region of the wedge and the surrounding space in the case of E -polarized incident plane waves. They are obtained by performing a uniform asymptotic evaluation of the radiation integrals arising from the use of a physical optics approximation for the equivalent electric and magnetic surface currents lying on the inner and outer wedge faces. Good accuracy in the evaluation of the total field, ease of use and implementation in a computer code are the advantages of the proposed solutions, which permit to compensate the geometrical optics discontinuities.

1. INTRODUCTION

Uniform Asymptotic Physical Optics (UAPO) solutions were proposed in explicit closed form by the authors in [1] and [2] for evaluating the field diffracted by right- and obtuse-angled lossless dielectric wedges in the inner and outer regions. In addition, the corresponding time domain diffraction coefficients were derived in [3] and [4] via an inverse Laplace transform. Their knowledge allows one to evaluate (via a convolution integral) the transient diffracted field originated by an arbitrary function plane wave impinging on the wedge. The UAPO-based approach in the frequency domain has been also applied to acute-angled wedges [5] considering a specific range of incidence directions. The UAPO solutions were able to compensate the Geometrical Optics (GO) discontinuities, accurate when compared with available numerical tools, and easy to handle since expressed in terms of the GO response of the structure and the transition function of the Uniform Theory of Diffraction (UTD) [6]. On the other hand, the use of a PO approximation implies inaccuracies in the case of grazing incidence and in correspondence of the dielectric interfaces.

This research contribution is devoted to extend the analysis in [5] to all possible cases of plane wave incidence and to provide generalized UAPO solutions, which can be applied to the diffraction by a wedge with arbitrary apex angle. Such solutions include those proposed in [1, 2, 5] as particular cases and are obtained accounting for the equivalent electric and magnetic PO current densities on the internal and external faces of the wedge. Multiple internal reflections and external transmissions are considered for their explicit evaluation by varying the direction of the incident plane wave. Numerical tests confirm the effectiveness of the proposed UAPO solutions for the field diffracted in the dielectric wedge-shaped region and the surrounding free-space.

2. UAPO DIFFRACTED FIELD

A lossless non-magnetic ($\mu_r = 1$) wedge-shaped region is considered with relative permittivity ε_r and propagation constant $k_d = k_0\sqrt{\varepsilon_r}$, k_0 being the free-space wavenumber. Its surfaces are S_0 and S_n , and the internal apex angle α is assumed less than $\pi/2$ (see Fig. 1). The incidence direction is perpendicular to the edge and defined by ϕ' , while the observation point is $P(\rho, \phi)$. The wedge is illuminated by the incident electric field $\underline{E}^i = E_0^i e^{-jk_0 \tau \hat{z}}$ (E -polarization).

The approach for obtaining the UAPO diffracted field is the same used in [1, 2, 5], and neglects the surface waves. Two separate diffraction problems are solved by formulating the corresponding radiation integrals in terms of electric and magnetic equivalent PO surface currents on the internal and external faces of the wedge.

2.1. $0 < \phi' < \pi/2$

If $\theta^i = \pi/2 - \phi'$ is the external incidence angle, the waves penetrate into the wedge through S_0 with the transmission angle $\theta_{0L}^t = \sin^{-1}(\sin \theta^i / \sqrt{\varepsilon_r})$, and travel toward the apex undergoing N reflections/transmissions before moving away from it. A crucial interaction point is that corresponding to the internal incidence angle $\theta_{N+1}^i = (N+1)\alpha - \theta_{0L}^t = \theta_{0R}^t$. Accordingly, the number of total internal reflections is $N + M + 1$, where $M = \text{Int}[(\pi/2 - \theta_{0R}^t)/\alpha]$. Transmitted waves through S_0 and S_n exist until the total reflection occurs inside the wedge.

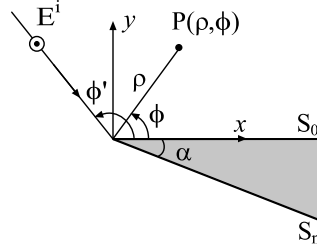


Figure 1: Geometry of the problem.

2.1.1. Internal Region

$$\underline{E}_{int}^d(P) = [D_L^{int} + D_R^{int}] \frac{e^{-jk_d \rho}}{\sqrt{\rho}} E_0^i \hat{z} = \left[(D_L^{int})_{S_0} + (D_L^{int})_{S_n} + (D_R^{int})_{S_0} + (D_R^{int})_{S_n} \right] \frac{e^{-jk_d \rho}}{\sqrt{\rho}} E_0^i \hat{z} \quad (1)$$

with

$$(D_L^{int})_{S_0} = \frac{e^{-j\pi/4}}{2\sqrt{2\pi k_d}} T_0 B(N, \theta_{0L}^t, \theta_n^i, \rho, \phi); \quad (D_R^{int})_{S_0} = \frac{e^{-j\pi/4}}{2\sqrt{2\pi k_d}} T_0 \Gamma(N) B(M, -\theta_{0R}^t, -\theta_m^i, \rho, \phi) \quad (2)$$

$$(D_L^{int})_{S_n} = \frac{e^{-j\pi/4}}{2\sqrt{2\pi k_d}} T_0 B'(N, \theta_n^i, \rho, \phi); \quad (D_R^{int})_{S_n} = \frac{e^{-j\pi/4}}{2\sqrt{2\pi k_d}} T_0 \Gamma(N) B'(M, -\theta_m^i, \rho, \phi) \quad (3)$$

where T_0 is the transmission coefficient at the free space/dielectric interaction, $\Gamma(N)$ represents the product of the internal reflection coefficients R , $\theta_n^i = \theta_{0L}^t - n\alpha$, $\theta_m^i = \theta_{0R}^t + m\alpha$. Moreover,

$$B(L, \theta_0^t, \theta_l^i, \rho, \phi) = (\sin \phi - \cos \theta_0^t) F\left(k_d, \rho, 2\pi - \phi, \frac{\pi}{2} - \theta_0^t\right) + \sum_{\substack{l=1 \\ \text{even}}}^L \left(\prod_{p=1}^{l-1} R_p \right) [(1 + R_l) \sin \phi + (1 - R_l) \cos \theta_l^i] F\left(k_d, \rho, 2\pi - \phi, \frac{\pi}{2} - \theta_l^i\right) \quad (4)$$

$$B'(L, \theta_l^i, \rho, \phi) = \sum_{\substack{m=1 \\ \text{odd}}}^L \left(\prod_{p=1}^{l-1} R_p \right) [(1 - R_l) \cos \theta_l^i - (1 + R_l) \sin(\phi + \alpha)] F\left(k_d, \rho, \phi - (2\pi - \alpha), \frac{\pi}{2} - \theta_l^i\right) \quad (5)$$

where

$$F(k, \rho, u, \pm v) = \frac{F_t\left(2k\rho \cos^2\left(\frac{u \pm v}{2}\right)\right)}{\cos u + \cos v} \quad (6)$$

and $F_t(\cdot)$ is the standard UTD transition function [6].

2.1.2. External Region

$$\underline{E}_{ext}^d(P) = \left[(D_L^{ext})_{S_0} + (D_L^{ext})_{S_n} + (D_R^{ext})_{S_0} + (D_R^{ext})_{S_n} + DI + DR \right] \frac{e^{-jk_0 \rho}}{\sqrt{\rho}} E_0^i \hat{z} \quad (7)$$

with

$$(D_L^{ext})_{S_0} = -\frac{e^{-j\pi/4}}{2\sqrt{2\pi k_0}} T_0 C(N+1, q\theta_n^t, \theta_n^i, \rho, \phi); \quad (D_R^{ext})_{S_0} = -\frac{e^{-j\pi/4}}{2\sqrt{2\pi k_0}} T_0 \Gamma(N) C(M, -\theta_m^t, \theta_m^i, \rho, \phi) \quad (8)$$

$$(D_L^{ext})_{S_n} = \frac{e^{-j\pi/4}}{2\sqrt{2\pi k_0}} T_0 C'(N+1, p\theta_n^t, \theta_n^i, \rho, \phi); \quad (D_R^{ext})_{S_n} = \frac{e^{-j\pi/4}}{2\sqrt{2\pi k_0}} T_0 \Gamma(N) C'(M, -\theta_m^t, \theta_m^i, \rho, \phi) \quad (9)$$

$$DI + DR = [(1 - R_0) \sin \phi' - (1 + R_0) \sin \phi] F(k_0, \rho, \phi, \pm \phi') \quad (10)$$

where

$$C(L, \theta_l^t, \theta_l^i, \rho, \phi) = \sum_{\substack{l=1 \\ \text{even}}}^L T_l \left(\prod_{p=1}^{l-1} R_p \right) \left[\sin \phi + \cos \theta_l^i \right] U(\theta_c - \theta_l^i) F\left(k_0, \rho, \phi, \pm \left(\frac{\pi}{2} - \theta_l^t\right)\right) \quad (11)$$

$$C'(L, \theta_l^t, \theta_l^i, \rho, \phi) = \sum_{\substack{l=1 \\ \text{odd}}}^L T_l \left(\prod_{p=1}^{l-1} R_p \right) \left[\sin(\phi + \alpha) - \cos \theta_l^t \right] U(\theta_c - \theta_l^i) F\left(k_0, \rho, (\phi + \alpha), \pm \left(\frac{\pi}{2} - \theta_l^t\right)\right) \quad (12)$$

in which θ_l^t is the transmission angle at the dielectric / free space interactions and $U(\theta) = 1$ if $\theta > 0$, 0 elsewhere.

2.2. $\pi/2 < \phi' < \pi - \alpha$

The external incidence angle is now $\theta^i = \phi' - \pi/2$. The waves penetrate into the wedge through S_0 with the transmission angle $\theta_{0R}^t = \sin^{-1}(\sin \theta^i / \sqrt{\epsilon_r})$.

2.2.1. Internal Region

$$\underline{E}_{int}^d(P) = \left[(D_R^{int})_{S_0} + (D_R^{int})_{S_n} \right] \frac{e^{-jk_d \rho}}{\sqrt{\rho}} E_0^i \hat{z} \quad (13)$$

with

$$(D_R^{int})_{S_0} = \frac{e^{-j\pi/4}}{2\sqrt{2\pi k_d}} T_0 B(M, -\theta_{0R}^t, -\theta_m^i, \rho, \phi); \quad (D_R^{int})_{S_n} = \frac{e^{-j\pi/4}}{2\sqrt{2\pi k_d}} T_0 B'(M, -\theta_m^i, \rho, \phi) \quad (14)$$

2.2.2. External Region

$$\underline{E}_{ext}^d(P) = \left[(D_R^{ext})_{S_0} + (D_R^{ext})_{S_n} + DI + DR \right] \frac{e^{-jk_0 \rho}}{\sqrt{\rho}} E_0^i \hat{z} \quad (15)$$

with

$$(D_R^{ext})_{S_0} = -\frac{e^{-j\pi/4}}{2\sqrt{2\pi k_0}} T_0 C(M, -\theta_m^t, \theta_m^i, \rho, \phi); \quad (D_R^{ext})_{S_n} = \frac{e^{-j\pi/4}}{2\sqrt{2\pi k_0}} T_0 C'(M, -\theta_m^t, \theta_m^i, \rho, \phi) \quad (16)$$

2.3. $\pi - \alpha < \phi' < \pi$

The waves penetrate into the wedge through S_0 and S_n , and travel outwards from the apex undergoing reflections/transmissions. Accordingly, the solutions proposed for the case B can be used for the waves penetrating each surface.

3. NUMERICAL RESULTS

Figure 2 shows the results concerning a wedge characterized by $\epsilon_r = 3$ and $\alpha = 20^\circ$ when illuminated by a plane wave impinging at $\phi' = 35^\circ$. The field magnitude is collected on a circular path with $\rho = 4\lambda_0$, λ_0 being the free-space wavelength. In addition to the boundaries related to the incident and specular reflection directions, three GO boundaries exist in the external region (see Fig. 2(a))

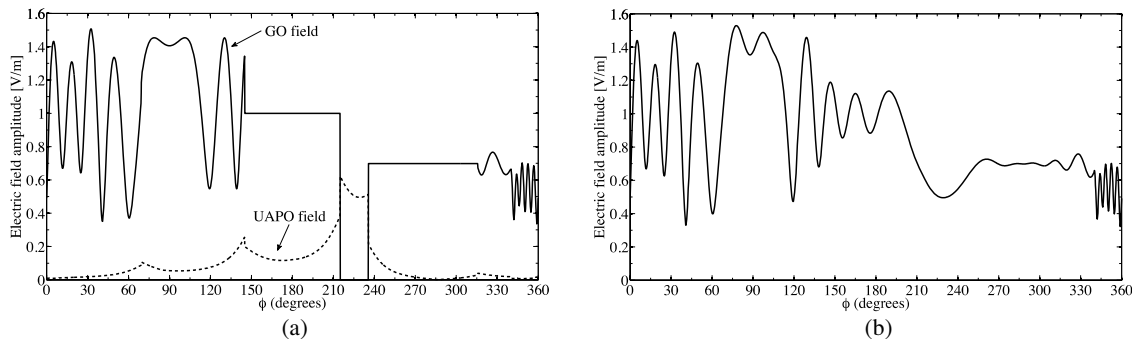


Figure 2: Electric field amplitude.

since the total internal reflection occurs at the fourth interaction. As can be seen in Fig. 2b, the total field is continuous, thus confirming that the UAPO diffracted field (see Fig. 2(a)) is able to compensate the GO discontinuities. Note that the use of a PO approximation implies inaccuracies at the dielectric interfaces.

REFERENCES

1. Gennarelli, G. and G. Riccio, "A uniform asymptotic solution for diffraction by a right-angled dielectric wedge," *IEEE Trans. Antennas Propagat.*, Vol. 59, 898–903, 2011.
2. Gennarelli, G. and G. Riccio, "Plane-wave diffraction by an obtuse-angled dielectric wedge," *J. Opt. Soc. Am. A*, Vol. 28, 627–632, 2011.
3. Gennarelli, G. and G. Riccio, "Time domain diffraction by a right-angled penetrable wedge," *IEEE Trans. Antennas Propagat.*, Vol. 60, 2829–2833, 2012.
4. Gennarelli, G. and G. Riccio, "Obtuse-angled penetrable wedges: a time domain solution for the diffraction coefficients," *Journal of Electromagnetic Waves and Applications*, Vol. 27, 2020–2028, 2013.
5. Gennarelli, G., M. Frongillo, G. Riccio, "High-frequency evaluation of the field inside and outside an acute-angled dielectric wedge," *IEEE Trans. Antennas Propagat.*, Vol. 63, No. 1, 374–378, 2015.
6. Kouyoumjian, R. G. and P. H. Pathak, "A uniform geometrical theory of diffraction for an edge in a perfectly conducting surface," *Proc. of IEEE*, Vol. 62, 1448–1461, 1974.

Analysis and Design of a Wideband Low Phase Noise LC VCO

Xuemei Lei, Jianxin Zhang, and Jing Shi

College of Electronic Information Engineering
Inner Mongolia University, Daxuexilu, Hohhot 010010, China

Abstract— In this paper, a LC voltage-controlled oscillator (LC-VCO) design optimization methodology based on switchable capacitor array is presented. The study of the compromises between phase noise and tuning range permits optimization of the design for given specifications. According to analytical phase noise models and tuning range, it allow to get a design space map where the design tradeoffs are easily identified. The proposed VCO is designed with the proposed methodology and implemented in SMIC's 0.18- μm RF CMOS technology and the chip area is $650\ \mu\text{m} \times 500\ \mu\text{m}$, including the test buffer circuit and the pads. Simulation results show that its tuning range is 36.4%, from 4.5 to 6.5 GHz. The simulating phase noise is $-112.8\ \text{dBc/Hz}$ at 1 MHz offset from the 6.5 GHz carrier. The maximum average power consumption of the core part is 6.47 mW at 1.8 V power supply.

1. INTRODUCTION

With the development of wireless communication technology, multi-standard portable terminals become a research focus. the RF front-end should be compatible with various wireless communication standards covering the frequency range from several hundred kHz to several GHz. Thus, the large tuning range and low phase noise wideband VCO becomes more and more important.

It is common that a CMOS VCO uses a varactor-tuned LC resonator and the ratio of the maximum to minimum capacitance of a typical varactor in CMOS technology is around 4–6, which in turn limits the frequency tuning range to a ratio of approximately 2–2.5 [1]. To extend the tuning range, the LC-tank VCO may employ a switchable capacitor array [2–8] or inductor array [9, 10]. Moreover, inductor array needs larger areas than the capacitor array and isn't suitable for the oscillating frequency below 10 GHz. Thus LC-VCO with a switchable capacitor array has been applied more widely.

The tuning range and phase noise of the LC-VCO, with switchable capacitor array, have been degraded by the switch parasitic capacitance and loss. In this paper, the relationship between phase noise and tuning range can be analyzed based on switchable capacitor array. The tradeoffs between phase noise and tuning range permits optimization of the design is discussed. A LC-VCO is implemented in SMIC's 0.18- μm RF CMOS technology. The theoretical analysis results have been verified by the simulation results.

2. CIRCUITS DESIGN

2.1. Analysis of Tuning Range

The oscillating frequency of LC-VCO is determined by LC tank. The equivalent circuit of the LC tank with a switchable capacitor array is shown in Fig. 1. Thus, the oscillation frequency of LC-VCO is given by

$$f_{osc} = \frac{1}{2\pi\sqrt{L\left(\frac{C_v}{2} + C_{array} + C_{para}\right)}} \quad (1)$$

where C_v and C_{array} are the capacitance of the varactor and switchable capacitor array, respectively; C_{para} is the parasitic capacitance. The change range of the LC-VCO oscillating frequency is controlled by the capacitance of the capacitor array and varactors. The capacitance of varactors, controlled by the controlled voltage (V_C), is so small that the change rate of the LC-VCO oscillating frequency is not enough large. Thus, the large tuning range mainly depends on the capacitor array. Under the general conditions, the cell of a switchable capacitor array consists of two switches and two capacitors. The schematic of the cell is shown in Fig. 2. Assuming the switch is ideal, the capacitance of the capacitor array is given by

$$C_{array} = \frac{D_0 C}{2} + D_1 C + 2D_2 C + 4D_3 C + \dots + 2^{n-1} D_n C \quad (2)$$

where, $D_0, D_1, D_2, D_3, \dots$ and D_n are the controlled words of the switch with values of 1 or 0.

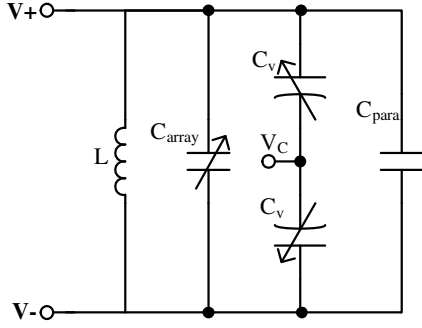


Figure 1: Equivalent circuit of the LC tank.

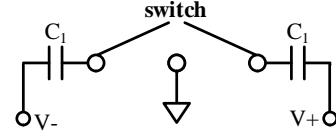


Figure 2: Schematic of the cell of switchable capacitor array.

The capacitance of the varactors depends on the value of V_c . Thus, the gain of proposed VCO is given:

$$K_{VCO} = \frac{\partial f_{osc}}{\partial V_c} = -\frac{1}{4\pi\sqrt{L} \left(\frac{C_v}{2} + C_{array} + C_{para}\right)^{1.5}} \frac{\partial C_v}{\partial V_c} \quad (3)$$

The tuning range (TR) of the proposed oscillation is given as:

$$TR = 2 \frac{\sqrt{\frac{C_{v,max}}{2} + C_{array,max} + C_{para}} - \sqrt{\frac{C_{v,min}}{2} + C_{para}}}{\sqrt{\frac{C_{v,max}}{2} + C_{array,max} + C_{para}} + \sqrt{\frac{C_{v,min}}{2} + C_{para}}} \quad (4)$$

The tuning range is determined by the capacitance ratio of the MOS varactors and the parallel switchable capacitor bank. In practice, the influence of the switch is important and shouldn't be neglected. The switch can be equivalent to a resistance R_{on} . The Equation (2) is changed and the equivalent admittance of the capacitor array is written as:

$$Y_{array} = \left(\frac{D_0}{2} + D_1 + 2D_2 + \dots + 2^{n-1}D_n\right) \cdot \left(\frac{j\omega_o C_1}{1 + (\omega_o C_1 R_{on})^2} + \frac{(\omega_o C_1)^2 R_{on}}{1 + (\omega_o C_1 R_{on})^2}\right) \quad (5)$$

Thus, the practical capacitance of the capacitor array is given by

$$C_{Parray} = \left(\frac{D_0}{2} + D_1 + 2D_2 + \dots + 2^{n-1}D_n\right) \frac{C_1}{1 + (\omega_o C R_{on})^2} \quad (6)$$

According to above, the conclusion could be drawn that the practical tuning range is smaller than Equation (4). Furthermore, maximum oscillation frequency is determined by inductor and varactors in LC tank and the extension of bandwidth is focus on the switchable capacitor array.

2.2. Analysis of Phase Noise

The phase noise of LC-tuned oscillator [11, 12] can be written as:

$$L(\Delta\omega) = 10 \log \left[\frac{kTR_{eff}(1+A)}{V_{max}^2/2} \left(\frac{\omega_0}{\Delta\omega}\right)^2 \right] \quad (7)$$

$$R_{eff} = R_L + R_C + \frac{1}{R_p(C\omega_o)^2} \quad (8)$$

Based on Equations (7) and (8), the phase noise of the LC-VCO depends on the equivalent resistance of LC tank and the amplitude of oscillation. The capacitor array of LC-VCO changes RC and C. Thus, Equation (8) can be written as:

$$R_{eff} = R_L + \frac{1}{\left(R_p \parallel R_{Parray} \parallel \frac{1+(\omega_o C R_C)^2}{(\omega_o C)^2 R_C}\right) \left[\left(\frac{\omega_o C}{1+(\omega_o C R_C)^2} + C_{Parray}\right) \omega_o\right]^2} \quad (9)$$

$$R_{Parray} = \frac{1 + (\omega_o C R_{on})^2}{\left(\frac{D_0}{2} + D_1 + 2D_2 + \dots + 2^{n-1}D_n\right) (\omega_o C)^2 R_{on}} \quad (10)$$

From the Equations (9) and (10), the conclusion can be drawn the capacitor array degrades the phase noise of LC-VCO.

According to Abidi model [13], the $1/f^2$ phase noise can be written as:

$$L(\Delta\omega) = \frac{8FkTR}{V_0^2} \left(\frac{\omega_0}{2Q\Delta\omega} \right)^2 \quad (11)$$

$$F = 1 + \frac{4RI\gamma}{\pi V_0} + \frac{4}{9}g_m R\gamma \quad (12)$$

And the structure of the LC-VCO, without tail current source, has better phase noise performance.

On the other hand, substrate noise and power noise are important sources of phase noise. In order to restrain substrate noise and power noise, LC filter network is inserted between a cross-coupled transconductance circuit and power. The resonant frequency of two LC filter networks can be written as

$$f \approx 2f_o \quad (13)$$

where f_o is the average of LC-VCO oscillation frequency.

2.3. Circuit Design

Based on the above analysis, the structure of the proposed wideband low phase noise LC-VCO is a double cross-coupled transconductance structure without tail current source, which is usually preferred in low-power and low phase noise applications. It consists of 4 parts, including a double cross-coupled transconductance circuit, an LC tank, two LC filter networks, and two isolation circuits for output nodes. The loss of the LC tank is canceled by the double cross-coupled transconductance circuit through generating a negative resistance. The LC tank consists of a spiral inductor, two MOS varactors, and a parallel switchable capacitor array. The parallel switchable capacitor array is a 4-bits coarse tuning element by changing the control codes and two MOS varactors are fine-tuning elements by changing the control voltages. It is shown in Fig. 3. And the cell of the parallel switchable capacitor array is shown in Fig. 2.

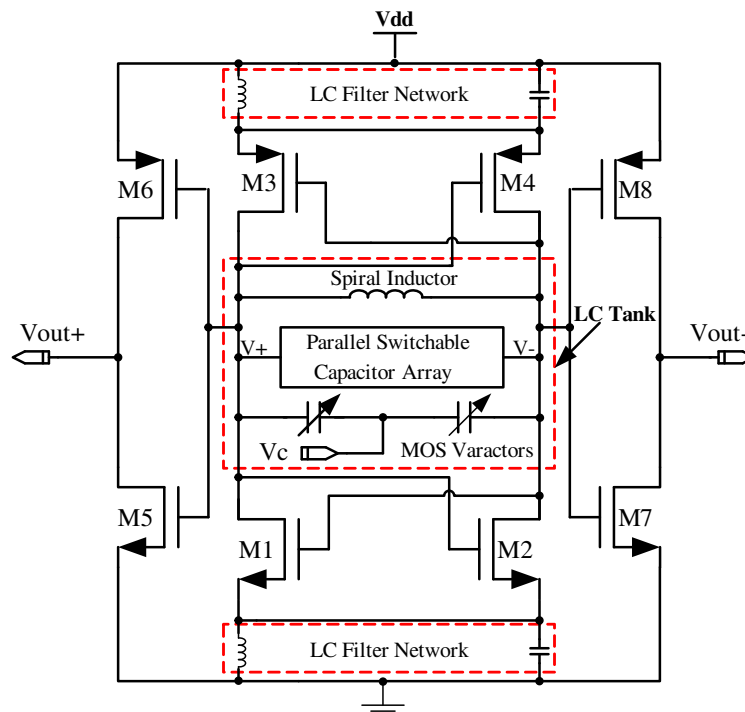


Figure 3: Schematic of the proposed VCO.

3. SIMULATION RESULTS

The wideband low-phase-noise VCO has been implemented in a SMIC's 0.18- μm RF CMOS technology. Fig. 4 shows the layout of the LC-VCO. The chip area is $650\ \mu\text{m} \times 500\ \mu\text{m}$, including the test buffer circuit and the pads.

The f - V curve of the proposed VCO is simulated as a function of the control codes of the parallel switchable capacitor bank. The simulated result is shown in Fig. 5. It decreases with the control codes changing from "0000" to "1111". This is consistent with Equations (1) and (6). And the tuning range is from 4.5 to 6.5 GHz and the average power consumption is 6.47 mW at 1.8 V power supply when the oscillating frequency is 6.5 GHz.

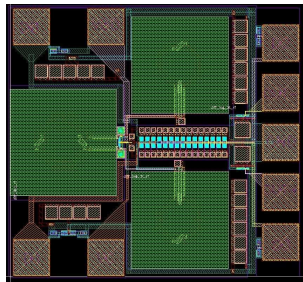


Figure 4: Layout of the proposed VCO.

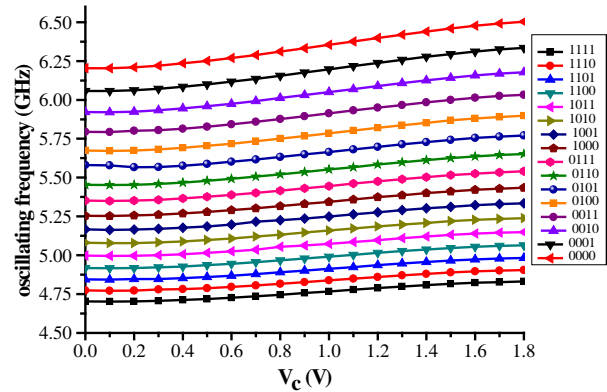


Figure 5: The simulated f - V curve of the proposed VCO.

To simulate the phase noise, the control voltage changes from 0 to 1.8 V with 0.1 V step and the control-code is from "0000" to "1111". In order to analyze and compare the phase noise in different controlled code and the different controlled voltage (V_c), the phase noise at 1 MHz offset is shown in the Fig. 6. The phase noise at 1 MHz offset is shown in the Fig. 7, which the controlled voltage (V_c) is 0 V. From the Figs. 6 and 7, it is seen that the different controlled code could lead to different phase noise. It is accordance with the Equations (7), (9) and (10).

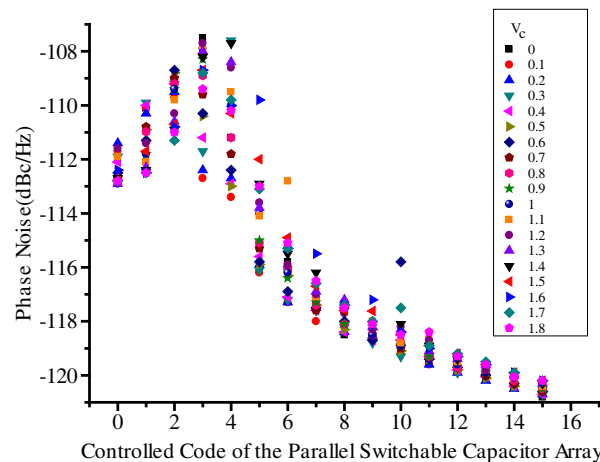


Figure 6: Simulated phase noise of the proposed VCO at 1 MHz offset.

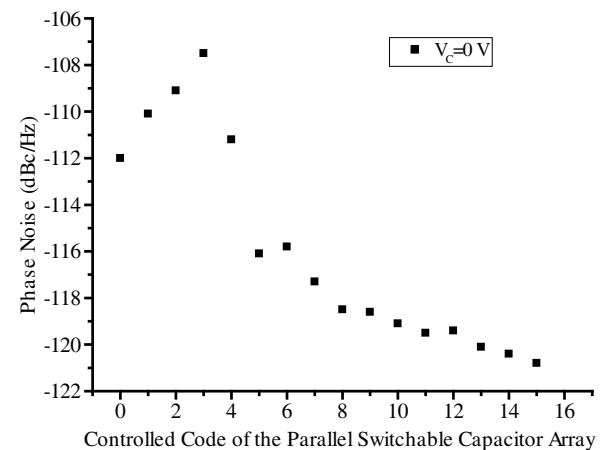


Figure 7: Simulated phase noise of the proposed VCO at 1 MHz offset.

4. CONCLUSION

The influence of the capacitor array is analyzed on tuning range and phase noise in LC-VCO. According to the analysis results, the wide band LC VCO with a low phase noise and low power consumption is designed. The simulated results show the tuning range of the proposed VCO is 36.4%. The simulating phase noise is $-112.8\ \text{dBc/Hz}$ at 1 MHz offset from the 6.5 GHz carrier.

The maximum average power consumption of the core part is 6.47 mW at 1.8 V power supply. On the other hand, the simulated results are in agreement with theories analysis.

REFERENCES

1. Safarian, Z. and H. Hashemi, "Wideband multi-mode CMOS VCO design using coupled inductors," *IEEE Transactions on Circuits and Systems — I: Regular Papers*, Vol. 56, No. 8, 1830–1843, 2009.
2. Lu, J., N.-Y. Wang, and M.-C. F. Chang, "14.6–22.2 GHz LC-VCO in 65 nm CMOS technology for wideband applications," *Electronics Letters*, Vol. 47, No. 6, 385–386, Mar. 17, 2011.
3. Wang, Y.-J., X.-N. Fan, and B. Li, "A 0.18 μm 1 V 5 GHz LC VCO designed for WSN applications," *IEEE 11th International Conference on Solid-State and Integrated Circuit Technology (ICSICT)*, 1–3, Xi'an, China, Oct. 29–Nov. 1, 2012.
4. Qi, X. and Z. Li, "A low power consumption, low phase noise, and wide tuning range LC VCO with ACC," *IEEE 13th International Conference on Communication Technology (ICCT)*, 1070–1073, Sep. 2011.
5. Tang, X., F. Huang, M. Shao, and Y. Zhang, "A wideband 0.13 μm CMOS LC-VCO for IMT-advanced and UWB applications," *IEEE MTT-S International Microwave Workshop Series on Millimeter Wave Wireless Technology and Applications (IMWS)*, 1–4, Nanjing, Sep. 2012.
6. Chun, C. H., H. S. Choi, Q. D. Bui, S. Y. Kang, J. Y. Jang, U. B. Lee, I. Y. Oh, and C. S. Park, "Compact wideband LC VCO with active inductor harmonic filtering technique," *Electronics Letters*, Vol. 47, No. 3, 190–191, Feb. 3, 2011.
7. Ponton, D., G. Knoblinger, A. Roithmeier, F. Cernoia, M. Tiebout, M. Fulde, and P. Palestri, "LC-VCO in the 3.3- to 4-GHz band implemented in 32-nm low-power CMOS technology," *IEEE Transactions on Circuits and Systems — II: Express Briefs*, Vol. 58, No. 8, 467–471, Aug. 2011.
8. Lei, X., Z. Wang, and K. Wang, "A wideband low phase noise LC VCO for DRMDAB frequency synthesizer," *Journal of Southeast University*, Vol. 26, No. 4, 528–531, 2010.
9. Liu, S.-L., K.-H. Chen, and A. Chin, "A Dual-resonant Mode 10/22-GHz VCO with a Novel Inductive Switching Approach," *IEEE Transactions on Microwave Theory and Techniques*, Vol. 60, No. 7, 2165–2177, Jul. 2012.
10. Italia, A., C. M. Ippolito, and G. Palmisano, "A 1-mW 1.13–1.9 GHz CMOS LC VCO using shunt-connected switched-coupled inductors," *IEEE Transactions on Circuits and Systems — I: Regular Papers*, Vol. 59, No. 6, 1145–1155, Jun. 2012.
11. Craninckx, J. and M. Steyaert, "Low-noise voltage controlled oscillators using enhanced LC-tanks," *IEEE Transactions on Circuits and Systems — II Analog and Digital Signal Processing*, Vol. 42, No. 12, 794–804, Dec. 1995.
12. Hajimiri, A. and T. H. Lee, "Phase noise in CMOS differential LC oscillators," *Symposium on VLSI Cirnrirr*, 48–51, Honolulu, HI, 1998.
13. Rael, J. J. and A. A. Abidi, "Physical processes of phase noise in differential LC oscillators," *IEEE Custom Integrated Circuits Conference*, 569–572, Orlando, FL, USA, 2000.

Adaptive Beam-forming Optimization Based Hybrid PSO-GSA Algorithm for Smart Antennas Systems

Ahmed Magdy¹, Osama M. El-Ghandour², and Hesham F. A. Hamed¹

¹Department of Electrical Engineering, Minia University, Minia, Egypt

²Department of Electronics, Communications, and Computer Engineering
Helwan University, Cairo, Egypt

Abstract— In this paper, a novel technique is presented to enhance the performance analysis of smart antennas systems with different geometries based on Hybrid Particle Swarm Optimization with Gravitational Search Algorithm (Hybrid PSO-GSA) algorithm. Complex excitations (phases) of the array radiation pattern are optimized based on Hybrid PSO-GSA algorithm using N elements for a Uniform Circular Array (UCA) geometry. The results are compared with those obtained using Uniform Linear Array (ULA) in the previous work. Simulation and discussion results prove enhancement in performance when using the proposed adaptive strategy based UCA smart antenna for different scenarios even for a big set of simultaneously incident signals in terms of normalized array factor.

1. INTRODUCTION

Adaptive beam-forming capabilities for smart antenna arrays are nowadays used in different applications such as suppression and reduction of interference in wireless mobile communication, besides its effects on the overall quality of service [1, 2]. There are different optimization techniques deal with Adaptive beam-forming for smart antennas. Particle Swarm Optimization (PSO), Central Force Optimization (CFO), and Bacterial Swarm Optimization (BSO) are well known Global optimization techniques that are based on a nature-inspired heuristic [3–5]. It was proven that CFO requires higher computational complexity but on the other hand it has better performance than PSO in [6].

Recently, Gravitational Search Algorithm (GSA) is considered as a new optimization technique [7]. Where a set of various standard benchmark functions, synthesis of thinned scanned concentric ring array antenna, and a fully digital controlled reconfigurable concentric ring array antenna problems were examined in [8, 9]. In most cases the GSA provided superior or at least comparable results with PSO and CFO. The GSA was proposed in [10, 11] for calculating the dimensions of a rectangular patch antenna, and for Direction of Arrival (DOA) estimation using a Uniform Circular Array (UCA) of 12 elements based on maximum likelihood (ML) criteria and showed better performance results over PSO and multiple signal classification (MUSIC) in terms of computational time for fitness function and RMSE. In [12], planar ultra-wide band (UWB) antennas with irregular radiator shapes are designed using GSA and compared with those obtained using CFO algorithm, it was found that, the GSA gives better performance than CFO. In [13], GSA was implemented using Open-MP and its results outperform the PSO by 65.09% in terms of normalized array factor. In [14], an algorithm is used for finding the best optimal excitation weights, and optimal uniform inter-element spacing for hyper beam-forming of linear antenna arrays. In [15], a new algorithm based on Hybrid Particle Swarm Optimization with Gravitational Search Algorithm (Hybrid PSO-GSA) technique was proposed and showed better performance than standard PSO and GSA in terms of computational speed.

In this paper, a novel algorithm that is based on the hybrid PSO-GSA technique is developed for optimal beam-forming using ULA and UCA. The goal is to maximize the beam of the radiation pattern towards the intended user or Signal of Interest (SOI) and minimize the beam of the radiation pattern towards Signal Not of Interest (SNOI) based on controlling the complex weights (phase) of ULA or UCA. The paper is organized as follows. In Section 2, the system model and problem formulation for adaptive beam-forming is explained. However hybrid PSO-GSA algorithm is proposed in Section 3. Simulation results and discussions for beam-forming are discussed in Section 4. Finally, Section 5 presents the conclusion.

2. PROBLEM FORMULATION

Smart antenna based on UCA topology by using N elements is showed in Figure 1. In this section, 12 elements in array structure are distributed uniformly along the circle of radius r , where θ is the

azimuth angle, λ is the wavelength, the angle between adjacent elements is θ_0 , and $d = 0.5\lambda$ is the space between two adjacent elements. In the synthesis of beam-forming, the complex excitation for each element must be optimized to minimize radiation power intensity at certain directions and maximize the main-lobes to other directions. The following fitness function must be minimized to maximize the total output power toward the desired signal at θ_i and minimize the total output power in the direction of the interfering signals at θ_j .

$$\text{fitness function} = - \sum_{i=1}^k a_i AF(\theta_i) + \sum_{j=1}^L b_j AF(\theta_j) \quad (1)$$

where the number of SOI users is represented in constant k , and L represents the number of SNOI hackers. $AF(\theta_i)$ is the array factor that will be maximized or minimized in specific directions for ULA and UCA using evolutionary algorithms.

$$AF(\theta_i) = \sum_{n=1}^N e^{j[\beta * r * \cos(\theta - \text{pos}_n) - \alpha_n]} \quad \text{for UCA} \quad (2)$$

$$AF(\theta_i) = \sum_{n=1}^N e^{j[\beta * (n-1) * d * \cos(\theta) - \alpha_n]} \quad \text{for ULA} \quad (3)$$

where α_n represents the complex excitation phase of the n -th element, pos_n is the angular position of the n -th element, and β is the phase shift constant.

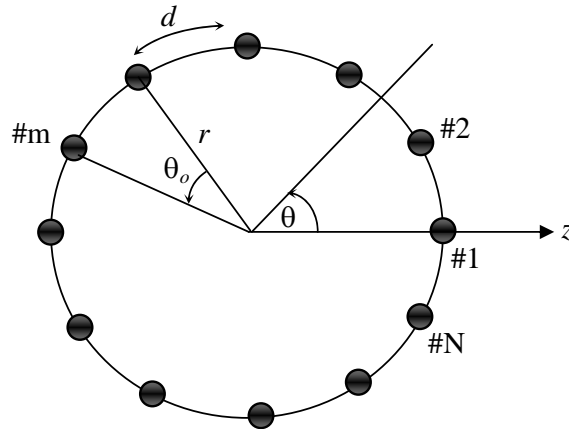


Figure 1: Geometry of the UCA with N elements.

In this paper, our model assumes user #2 as transmitter, desired user #1 as receiver at desired angle $\text{SOI} = \theta_d$ from user #2, and hacker at angle $\text{SNOI} = \theta_h$ from user #2. In this work, smart antennas array using linear and circular topology are obtained.

3. HYBRID PSOGSA ALGORITHM OPTIMIZATION TECHNIQUE

Several different hybridization methods for heuristic algorithms were presented in [16], when two different algorithms can be hybridized in high-level or low-level with relay or co-evolutionary method as homogeneous or heterogeneous. In this paper, PSO with GSA was hybridized using low-level co-evolutionary heterogeneous hybrid. The basic idea of hybrid PSOGSA is to combine the ability of social thinking (gbest) in PSO with the local search capability of GSA. In order to combine these algorithms, updating velocity is proposed as follow:

$$v_i(t+1) = w * v_i(t) + C1 * \text{rand} * a_i(t) + C2 * \text{rand} * (\text{gbest} - x_i(t)) \quad (4)$$

where $v_i(t)$ is the velocity of agent i at iteration t , w , rand , gbest , $C1$ and $C2$ are taken from PSO algorithm in [4]. On the other hand, from GSA in [7], $a_i(t)$ is the acceleration of agent i at iteration t can be calculated by,

$$a_i^d(t) = \frac{F_i^d(t)}{M_{ii}(t)} \quad (5)$$

where, inertia mass, active gravitational mass and passive gravitational $M_{ai} = M_{pi} = M_{ii} = M_i$; $i = 1, 2, \dots, K$, $F_i^d(t)$ is the total force acting on i th agent calculated as:

$$F_i^d(t) = \sum_{i=1, j \neq 1} \text{rand}_j F_{ij}^d(t) \quad (6)$$

where $F_{ij}^d(t)$ is the force acting on agent ' i ' from agent ' j ' at d th dimension and t th iteration is computed as below:

$$F_{ij}^d(t) = G(t) \frac{M_{pi}(t)M_{aj}(t)}{R_{ij}(t) + \epsilon} (x_j^d(t) - x_i^d(t)) \quad (7)$$

where, $R_{ij}(t)$ is the Euclidian distance between two agents ' i ' and ' j ' at iteration t , $G(t)$ is the computed gravitational constant at the same iteration, and ϵ is a small constant.

$$G(t) = G_0 e^{(\alpha t/T)}. \quad (8)$$

In this problem G_0 is set to 100, α is set to 20 and T is the total number of iterations. In each iteration, the positions of particles are updated as follow:

$$x_i(t+1) = x_i(t) + v_i(t+1) \quad (9)$$

In hybrid PSO-GSA [15], firstly, each agent is considered as a candidate solution. As can be seen in Figure 2, after initialization, evaluate the fitness function based on Equation (1). Gravitational force, gravitational constant, and resultant forces among agents are calculated using (6), (8) and (7) respectively, After that, the accelerations of particles are defined as (5). In each iteration, the best solution so far (gbest) must be updated. After calculating the accelerations and with updating the best solution so far, the velocities and the positions of all agents can be updated using (4) and (9) respectively. Finally, after agents are updated. The process of updating velocities and positions will be stopped by meeting an end criterion.

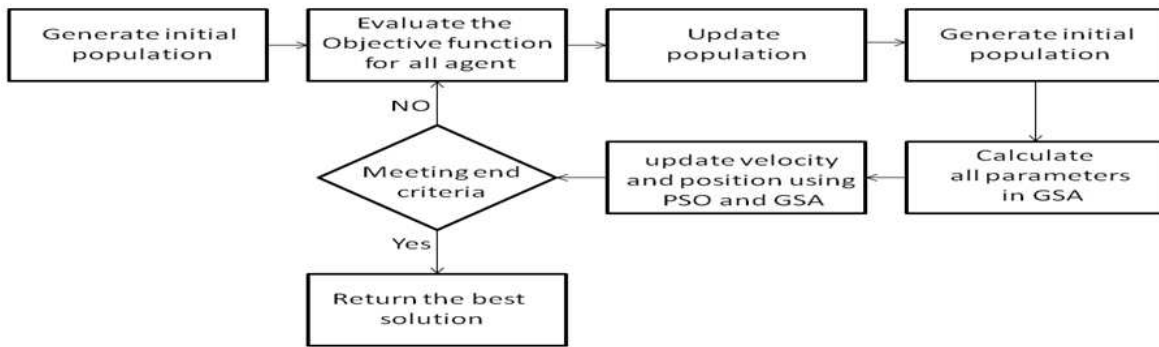


Figure 2: Flow chart for steps in hybrid PSO-GSA algorithm.

4. SIMULATION AND DISCUSSION RESULTS

In this section, the capability of hybrid PSO-GSA technique for adaptive beam-forming with a UCA and ULA is studied. In this section our model is discussed according to end of Section 2, the first scenario is SOI 30° and SNOI $-30^\circ = -330^\circ (360^\circ - \text{SOI}(\theta_h))$ (broadside direction)). Figure 3 is obtained for normalized array factor comparison using ULA and UCA by Hybrid PSO-GSA at SOI 30° and SNOI -30° in polar and rectangular representation. It is found that, only UCA topology has capability to direct the main beam toward user #1 (SOI) and null at hacker #1 (SNOI). It is clear that the directed power toward the intended direction (30°) using UCA is better than that obtained by ULA more than 6 dB (approximately 55%). On the other hand, the directed null (zero power) toward the intended direction (-30°) using UCA is better than that obtained by ULA by approximately 35 dB.

In the real applications user #2 in our model may not be located at certain 30° , for this reason the second scenario is proposed where SNOI changed around -30° . Figure 4(a) shows SOI at 30° and a changed value -40° for SNOI. Accordingly the results showed an improvement of more than

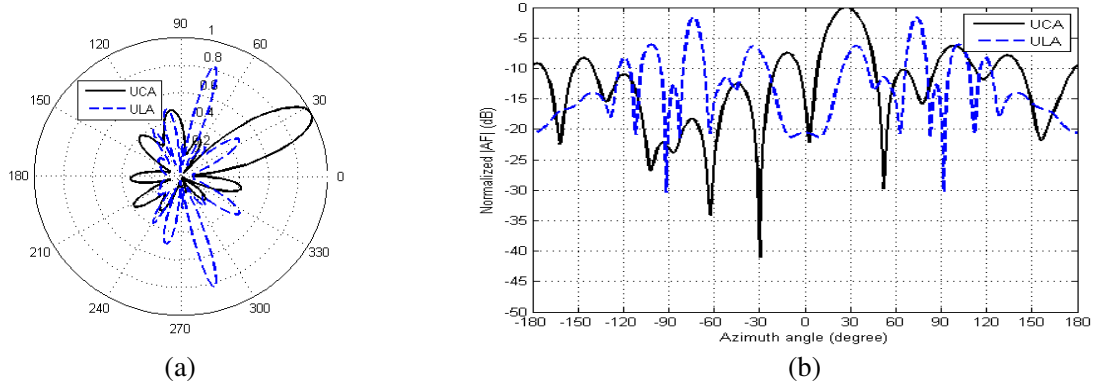


Figure 3: Normalized array factor comparison using ULA and UCA by Hybrid PSO GSA at SOI 30° and SNOI $-30^\circ = 330^\circ$, (a) polar representation and (b) rectangular representation.

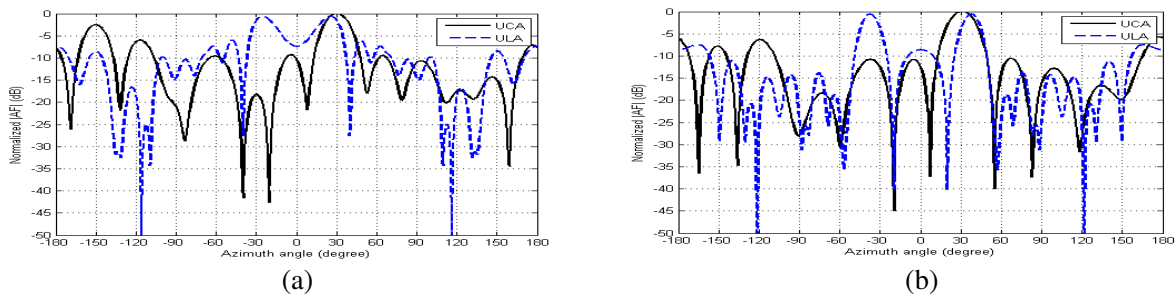


Figure 4: Normalized array factor comparison using ULA and UCA by hybrid PSO GSA at (a) SOI 30° and SNOI -40° , (b) SOI 30° and SNOI -20° .

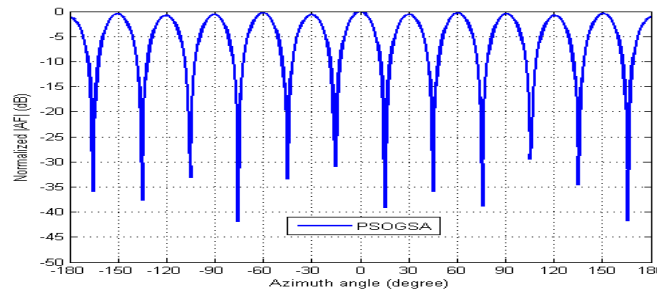


Figure 5: Normalized array factor using hybrid PSO GSA for UCA smart antenna.

1.5 dB and approximately 14 dB for SOI and SNOI respectively. Figure 4(b) shows SOI at 30° and a changed value -20° for SNOI. Accordingly the results showed an improvement of more than 3.5 dB and approximately 5 dB for SOI and SNOI respectively.

Also, it can be noticed that an extra undesired main beam in the broadside direction is obtained in the ULA geometry. Therefore, the first case is the worst case in ULA because $SNOI = \theta_h = (-30^\circ(330^\circ)) = 360 - SOI(\theta_h)$ (broadside direction). In general, the results obtained by UCA are better than those obtained from ULA which used in [14] for all directions in all scenarios. Finally, Figure 5 proves hybrid PSO GSA has great ability for optimization in beam-forming even for a big set of simultaneously incident signals (k in (1) = 11 desired angles where UCA has 12 elements). Algorithm is employed with a population size of 30 and 150 iterations. The hybrid PSO GSA is used to adjust the weights of phase shift of the excitation of each element of the UCA array for beam synthesis to maximize the output power toward the desired signals at SOI $\theta_i = [-150^\circ, -120^\circ, -90^\circ, -60^\circ, -30^\circ, 0^\circ, 30^\circ, 60^\circ, 90^\circ, 120^\circ, 150^\circ]$ where a_i in (1) at section #2 = [1.4, 1.5, 1.4, 1.4, 1.4, 1, 1.4, 1.4, 1.4, 1.5, 1.4] for previous angle respectively.

5. CONCLUSION

In this paper, a novel technique is proposed for smart antennas systems based on ULA and UCA to enhance the performance of adaptive beam-forming in wireless communications applications. As can be seen from our model that the directed power in terms of normalized array factor toward the intended direction (SOI) using UCA is better than ULA more than 6 dB (approximately 55%), more than 3.5 dB and more than 1.5 dB for different scenarios, on the other hand, directed null to SNOI better than ULA by approximately 35 dB, 5 dB and 14 dB for several scenarios. In addition, simulations of beam-forming showed ability on accurate results even for a big set of simultaneously incident signals. It is found that hybrid PSO-GSA is more attractive for beam-forming applications based on our fitness function.

REFERENCES

1. Lehne, P. H. and M. Pettersen, "An overview of smart antenna technology for mobile communications systems," *IEEE Commun. Surveys Tutorials*, Vol. 2, 2–13, 1999.
2. Chryssomallis, M., "Smart antennas," *IEEE Antennas Propag. Mag.*, Vol. 42, 129–136, 2000.
3. Kennedy, J. and R. Eberhart, "Particle swarm optimization," *IEEE International Conference on Neural Networks*, Vol. 4, 1942–1948, Perth, Australia, 1995.
4. Mahmoud, K. R., M. El-Adawy, R. Bansal, S. H. Zainud-Deen, and S. M. M. Ibrahim, "Analysis of uniform circular arrays for adaptive beamforming applications using particle swarm optimization algorithm," *Int. J. of RF and Microwave Computed Aided Eng.*, Vol. 18, 42–52, 2008.
5. Formato, R. A., "Central force optimization: A new metaheuristic with applications in applied electromagnetics," *Progress In Electromagnetics Research*, Vol. 77, 425–491, 2007.
6. Mahmoud, K. R., "Central force optimization: Nelder-Mead hybrid algorithm for rectangular microstrip antenna design," *Electromagnetics*, Vol. 31, 578–592, 2011.
7. Rashedi, E., H. Nezamabadi-Pour, and S. Saryazdi, "GSA: A gravitational search algorithm," *Information Sciences*, Vol. 179, No. 13, 2232–2248, 2009.
8. Chatterjee, A., G. K. Mahanti, and N. N. Pathak, "Comparative performance of gravitational search algorithm and modified particle swarm optimization algorithm for synthesis of thinned scanned concentric ring array antenna," *Progress In Electromagnetics Research B*, Vol. 25, 331–348, 2010.
9. Chatterjee, A., G. K. Mahanti, and P. R. S. Mahapatra, "Design of fully digital controlled reconfigurable dual-beam concentric ring array antenna using gravitational search algorithm," *Progress In Electromagnetics Research C*, Vol. 18, 59–72, 2011.
10. Altinoz, O. T. and A. E. Yilmaz, "Calculation of optimized parameters of rectangular patch antenna using gravitational search algorithm," *2011 International Symposium on Innovations in Intelligent Systems and Applications (INISTA)*, 349–353, Jun. 15–18, 2011.
11. Mohamed, A. M., K. R. Mahmoud, S. G. Abdel Gawad, and I. I. Ibrahim, "Direction of arrival estimation based on maximum likelihood criteria using gravitational search algorithm," *PIERS Proceedings*, 1162–1167, Taipei, Mar. 25–28, 2013.
12. Mahmoud, K. R., "UWB antenna using gravitational search algorithm," *Journal of Engineering Sciences*, Vol. 41, No. 5, Faculty of Engineering, Assiut University, Sep. 2013.
13. Mahmoud, K. R. and S. Hamad, "Parallel implementation of hybrid GSA-NM algorithm for adaptive beam-forming applications," *Progress In Electromagnetics Research B*, Vol. 58, 47–57, 2014.
14. Ram, G., D. Mandal, R. Kar, and S. P. Ghoshal, "Optimized hyper beamforming of linear antenna arrays using collective animal behaviour," *The Scientific World Journal*, Vol. 2013, 13 pages, Article ID 982017, 2013.
15. Mirjalili, S. and S. Z. Mohd Hashim, "A new hybrid PSO-GSA algorithm for function optimization," *IEEE International Conference on Computer and Information Application, ICCIA*, 2010.
16. Talbi, E. G., "A taxonomy of hybrid metaheuristic," *Journal of Heuristics*, Vol. 8, No. 5, 541–546, 2002.

Semiconductor Temperature Tunable Metamaterial for Terahertz Applications

K. L. Koshelev^{1,2,3} and A. A. Bogdanov^{2,3,4}

¹Saint-Petersburg State Polytechnical University, St. Petersburg 195251, Russian Federation

²ITMO University, St. Petersburg 197101, Russian Federation

³Ioffe Institute, St. Petersburg 194021, Russian Federation

⁴The Academic University, St. Petersburg 194021, Russian Federation

Abstract— We introduce a new model of homogeneous temperature tunable THz metamaterial with controllable frequency range of hyperbolic dispersion based on semiconductor superlattice with doped quantum wells. We develop a theory of quantum homogenization which is based on the Kubo formula for conductivity. The proposed approach takes into account the wave functions of the carriers, their distribution function and energy spectrum. We show that the components of the dielectric tensor of the semiconductor metamaterial can be efficiently manipulated by external temperature.

1. INTRODUCTION

Hyperbolic metamaterials (HMMs) are one of the fastest developing branches of modern optics [1–3]. The dielectric function of HMMs is described by a tensor with two different components corresponding to the directions along (ε_{\parallel}) and across (ε_{\perp}) the optical axis. Depending on the sign of these components, the crystal represents a dielectric medium ($\varepsilon_{\perp} > 0$, $\varepsilon_{\parallel} > 0$), a metal ($\varepsilon_{\perp} < 0$, $\varepsilon_{\parallel} < 0$) or a hyperbolic metamaterial ($\varepsilon_{\perp}\varepsilon_{\parallel} < 0$). For HMMs the shape of equal-frequency surface in \mathbf{k} -space represents a one- or two-sheet hyperboloid depending on the signature of permittivity tensor [3]. This results in a singularity of the photon density of states and explains the unique optical properties of HMMs [4].

Here we propose a new concept of an ultra homogeneous temperature tunable metamaterial based on a semiconductor superlattice for THz applications. Here, the term *ultra homogeneous* implies that the superlattice consists of coupled quantum wells separated by thin (~ 1 nm) tunnel-transparent barriers. Superlattices with barriers of such a thickness are widely used, for example, in quantum cascade lasers [5]. In this case, in contrast to a superlattice with thick barriers, quantum effects are particularly relevant and, therefore, it is incorrect to describe the dielectric function of each layer separately and then apply the homogenization procedure. Therefore, another approach, which takes into account the wave functions of the carriers, their energy spectrum modified by the superlattice potential and the carrier distribution function, should be used. We discuss the theory of proper approximation (quantum homogenization) further in Section 2.

The paper is organized as follows. In Section 2 we develop a quantum homogenization theory and derive the main equations for the effective permittivity tensor. In Sections 3 and 4, we analyze the band structure and effective dielectric function of a Te-doped GaAs/Al_{0.3}Ga_{0.7}As superlattice depending on the temperature and frequency of the electromagnetic field. Finally, in Section 5 we summarize our major results.

2. MODEL

2.1. Quantum Homogenization

Within the effective medium approximation, a multilayered structure with layer permittivities ε_i and layer thicknesses d_i can be considered as uniaxial optical crystal with permittivity tensor whose principle components are determined as

$$\frac{1}{\varepsilon_{\parallel}} = \frac{1}{d} \sum_i \frac{d_i}{\varepsilon_i}, \quad \varepsilon_{\perp} = \frac{1}{d} \sum_i d_i \varepsilon_i, \quad d = \sum_i d_i. \quad (1)$$

As we have mentioned in the introduction, these formulas are inapplicable when the thickness of the layers is comparable with electron wavelength and, therefore, quantum mechanics laws become relevant. We consider a more accurate approach based on the Kubo formula [6]. It takes into

account the distribution function of the carriers, their wave functions and spectrum modified by the superlattice potential:

$$\varepsilon_\alpha(\omega) = \varepsilon_\alpha^\infty \left(1 - \frac{\Omega_\alpha^2}{\omega(\omega + i\gamma)} \right) + \frac{4\pi i}{\omega} \sigma_\alpha(\omega). \quad (2)$$

Here and in what follows, the index $\alpha = \parallel, \perp$ corresponds to the directions along and across the optical axis of the metamaterial. Parameter $\varepsilon_\alpha^\infty$ is a permittivity of the lattice without free carriers, γ is inverse momentum relaxation time of the carriers which is supposed to be isotropic for simplicity.

The first term interprets classical Drude-Lorentz formula and the second term describes inter-band transitions. One can see that implementation of a superlattice in a semiconductor makes its plasma frequency anisotropic and we can distinguish plasma frequencies along (Ω_\parallel) and across (Ω_\perp) the optical axis:

$$\Omega_\alpha^2 = \frac{4\pi e^2}{\varepsilon^\infty} \frac{2}{(2\pi\hbar)^3} \sum_i \iiint f(E, \mu, T) \frac{\partial^2 E_i}{\partial p_\alpha^2} d^3p. \quad (3)$$

Here E_i is the carrier energy in the i -th miniband which depends on the momentum \mathbf{p} , $f(E, \mu, T)$ is the Fermi-Dirac distribution function, μ is the chemical potential, T is the temperature. The sum is over all the minibands. Here we neglect hole contribution into the plasma frequency because we will consider n -doped semiconductor structures. Eq. (3) is similar to the classical definition of plasma frequency:

$$\Omega^2 = \frac{4\pi n e^2}{\varepsilon^\infty m^*}. \quad (4)$$

Indeed, the difference between Eq. (3) and Eq. (4) is that in Eq. (3) we just average the inverse effective anisotropic mass $1/m^* = \partial^2 E / \partial p^2$ with distribution function $f(E, \mu, T)$.

In order to calculate Ω_\perp and Ω_\parallel we need to determine the energy spectrum $E_i(\mathbf{p})$ and the chemical potential μ .

2.2. Energy Spectrum of Carriers

Let us consider a periodic semiconductor superlattice with period d consisting of a quantum well with thickness d_1 and a barrier with thickness d_2 and height V [Fig. 1(a)]. Effective masses in the well and barrier we put equal to m_1 and m_2 , respectively.

Energy dispersion of electrons in i -th miniband can be found from the dispersion equation.

$$\cos(p_\parallel d / \hbar) = \cos(p_1 d_1 / \hbar) \cos(p_2 d_2 / \hbar) - \frac{1}{2} \sin(p_1 d_1 / \hbar) \sin(p_2 d_2 / \hbar) \left(\frac{p_1 m_2}{p_2 m_1} + \frac{p_2 m_1}{p_1 m_2} \right) \quad (5)$$

where $p_1 = \sqrt{2m_1 E(p_\parallel)}$, $p_2 = \sqrt{2m_2 (E(p_\parallel) - V)}$. This dispersion equation can be obtained from the Schrödinger equation using the Floquet's theorem.

2.3. Chemical Potential

We consider the case of doped semiconductor structures on the example of a superlattice with quantum wells uniformly doped with shallow donors.

In highly doped structures, wave functions of neighbour donors can overlap. This results in a shift of donor levels and formation of a donor band. In the case of a considerable shift, the donor band can overlap with the conduction band.

The chemical potential μ can be calculated from the electroneutrality condition [7]. It states that free carrier concentration is equal to the concentration of ionized donors:

$$\sum_i \int f(\mathbf{p}, \mu, T) \frac{2d^3p}{(2\pi\hbar)^3} = n_d \int \frac{g(E)dE}{2e^{(\mu-E)/(kT)} + 1} \quad (6)$$

Here n_d is the full donor concentration, $g(E)$ is a donor distribution function which can be approximated by a Gaussian with standard deviation Δ and maximum at E_d .

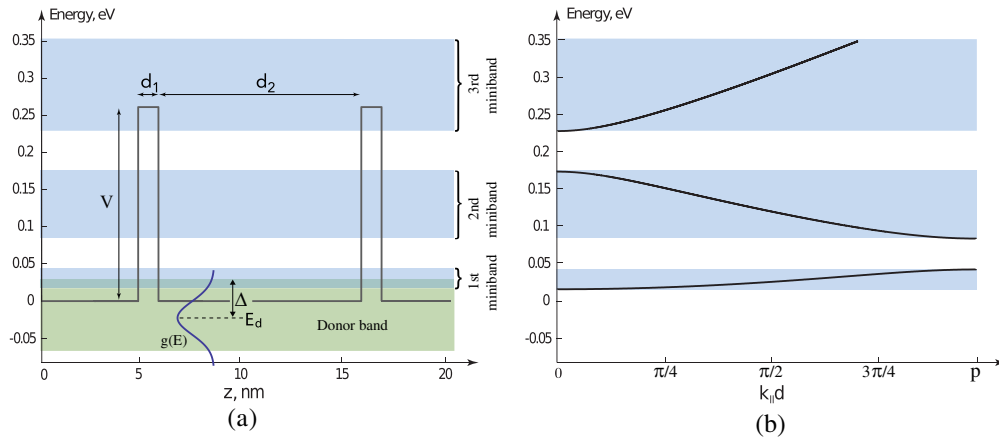


Figure 1: (a) Conduction band profile of n -doped superlattice. Blue shaded areas represent the energy of the minibands. Green shaded area corresponds to the donor band. Thicknesses of the well and the barrier are denoted as d_1 and d_2 , respectively, V is the height of the barrier, $g(E)$ is a donor distribution function with standard deviation Δ and a maximum at E_d . (b) Electron energy dispersion in GaAs/Al_{0.3}Ga_{0.7}As superlattice with following parameters: $d_1 = 10$ nm, $d_2 = 1$ nm, $V = 0.26$ eV.

3. BAND STRUCTURE OF THE SUPERLATTICE

The model described above is applicable for superlattices of various compounds and designs. As an example, let us consider a superlattice that consists of GaAs quantum wells and Al_{0.3}Ga_{0.7}As barriers. Thickness of the quantum well d_1 and the barrier d_2 we put equal to 10 and 1 nm, respectively. We consider the high frequency permittivity in Eq. (2) to be isotropic ($\varepsilon_{\parallel}^{\infty} = \varepsilon_{\perp}^{\infty}$) and put it equal to 11 [8]. The calculated band structure and electron dispersion are shown in Fig. 1(b). We consider that quantum wells are uniformly doped with Te donors with concentration $n_d = 1 \times 10^{18} \text{ cm}^{-3}$. The energies of Te donors in bulk GaAs and in the superlattice are slightly different due to quantum confinement that arises from the superlattice potential. We neglect this difference and put $E_d = 0.03$ eV as in a bulk material [7]. The standard deviation of the donor distribution function Δ for such a doping level is about several hundredths of an electron-volt. In the structure under consideration we put $\Delta = 0.03$ eV, which is in accordance with Refs. [9].

4. EFFECTIVE DIELECTRIC FUNCTION OF THE SUPERLATTICE

We calculate the frequency and temperature dependencies of the permittivity tensor components using the quantum homogenization approach [Eq. (3)]. The frequency dependence of ε_{\perp} and ε_{\parallel} at room temperature is shown in Fig. 2(a). The average energy between minibands and, therefore, frequencies of interband transitions are about 0.05 eV [Fig. 1(a)], which corresponds to a frequency of 10 THz. So, the contribution of interband transition into the dielectric function [second term in Eq. (2)] can be neglected at frequencies of 1 THz without any considerable precision losses. Thus, quantum homogenization predicts that, beyond the interband transition, the tensor components of a superlattice with thin layers can be described within the classical Drude-Lorentz formula with plasma frequency described by Eq. (3).

This results qualitatively differ from effective parameters obtained within the classical homogenization procedure which predicts a resonance behaviour of ε_{\parallel} at a nonzero frequency. There is no contradiction here. Classical homogenization implies that all layers are isolated from each other and that the carriers do not move from one layer into a neighbouring one. Qualitatively it is equivalent to the restoring force that obstructs the carrier transport. This force results in an appearance of the resonance in ε_{\parallel} . Quantum homogenization implies that the barriers are tunnel transparent and charges can move freely throughout the whole volume of the sample. Therefore, the dielectric function ε_{\parallel} is similar to that of a metal but takes into account interband transitions.

One can see from Fig. 2(a) that there are three frequency regions which correspond to different forms of the equal-frequency surfaces in k -space: (i) at frequencies $\omega/2\pi > 4.1$ THz the material behaves like a dielectric; (ii) at frequencies $2.2 \text{ THz} < \omega/2\pi < 4.1$ THz the form of the equal-frequency surface is a hyperboloid and the material exhibits optical properties of HMM; (iii) at $\omega/2\pi < 2.2$ THz electromagnetic waves decay exponentially into the medium, similar to the behaviour in a metal.

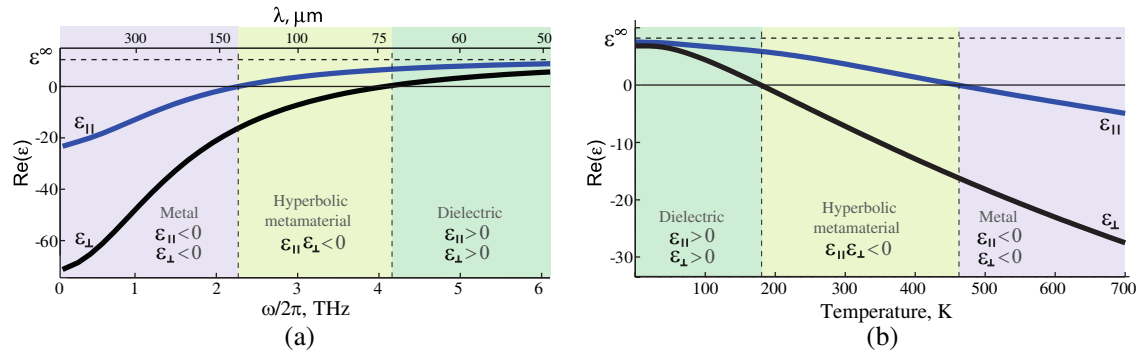


Figure 2: (a) Frequency dependence of real part of dielectric function along (blue line) and across (black line) the optical axis. Temperature $T = 300$ K. (b) Temperature dependence of real part of dielectric function along (blue line) and across (black line) the optical axis. Permittivity of the media without free carriers ϵ^{∞} is shown by the dashed line. Frequency $\omega/2\pi = 3$ THz.

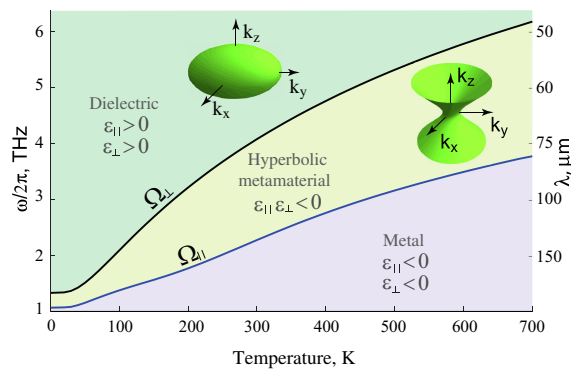


Figure 3: Temperature dependence of plasma frequency along the optical axis (blue line) and across the optical axis (black line). Insets show the shape of equal-frequency surfaces in the dielectric and hyperbolic regimes.

The temperature dependence of ϵ_{\perp} and ϵ_{\parallel} at a frequency of 3 THz is shown in Fig. 2(b). One can see that the material behaves as a dielectric, HMM or a metal depending on the temperature. Dielectric dispersion can be realized at the temperature of liquid nitrogen, the hyperbolic regime is achieved at room temperature.

Figure 3 represents a topological phase state diagram. Solid lines show the temperature dependence of the longitudinal Ω_{\parallel} and transversal Ω_{\perp} plasma frequencies. These lines divide the plane of the figure into three regions. It follows from Eq. (2) that every region corresponds to the one of the possible regimes: dielectric, metal or hyperbolic. The shapes of equal-frequency surfaces corresponding to each regimes are shown in the insets of Fig. 3.

5. CONCLUSION

In this work we proposed a new concept of an ultra homogeneous temperature-tunable metamaterial based on a doped semiconductor superlattice. We have shown that the classical homogenization procedure is inapplicable for the description of the metamaterial in terms of effective parameters because of the tunnel transparency of the barriers separating the quantum wells and that quantum homogenization should be used. We developed the theory of quantum homogenization applied to semiconductor nanostructured metamaterials. It is based on the Kubo formula for conductivity and takes into account wave functions of the carriers, their energy spectrum and distribution function.

We have shown that the components of the dielectric tensor the semiconductor metamaterial can be efficiently manipulated by external temperature. Efficient temperature tunability is a distinctive feature of semiconductors which is explained by the high sensitivity of free carrier concentration to the temperature.

A significant advantage of semiconductor metamaterials is the possibility of their direct integration into optoelectronic devices and optical integrated circuits. Moreover, semiconductor materials combine two important features. On one hand, the energy spectrum of the carriers in semiconduc-

tor nanostructures can be precisely tailored with quantum engineering technologies. On the other hand, there are many methods of dynamic control of the electron distribution function in semiconductors, which are well-developed and widely applied in nano- and optoelectronics. These are, for example, electrical injection, optical pumping, thermal excitation, electron heating by electric field, etc. The advantages mentioned earlier and the rich functionality of semiconductor metamaterials allow to consider them as important element of future optoelectronics.

ACKNOWLEDGMENT

All analytical results were obtained with a support of the Russian Foundation for Basic Research (project No. 13-02-0411) and the results of numerical simulations were obtained with a support the Russian Science Foundation (project No. 15-12-20028).

REFERENCES

1. Guo, Y., et al., “Applications of hyperbolic metamaterial substrates,” *Advances Optoelectron.*, Vol. 2012, 2012.
2. Cortes, C. L., et al., “Quantum nanophotonics using hyperbolic metamaterials,” *Journal of Optics*, Vol. 14, 063001, 2012.
3. Poddubny, A., et al., “Hyperbolic metamaterials,” *Nature Photonics*, Vol. 7, 948–957, 2013.
4. Jacob, Z., et al., “Broadband Purcell effect: Radiative decay engineering with metamaterials,” *Applied Physics Letters*, Vol. 100, 811051, 2012.
5. Gmachl, C., et al., “Recent progress in quantum cascade lasers and applications,” *Reports on Progress in Physics*, Vol. 64, 1533, 2001.
6. Murayama, Y., *Mesoscopic Systems: Fundamentals and Applications*, John Wiley and Sons., 2008.
7. Sze, S. M. and K. K. Ng, *Physics of Semiconductor Devices*, John Wiley and Sons., 2006.
8. Adachi, S., *GaAs and Related Materials*, World Scientific, 1994.
9. Brody, T. P., “Nature of the valley current in tunnel diodes,” *Journal of Applied Physics*, Vol. 33, 100–111, 1962.

Noise Spectroscopy Tests in the Analysis of Materials and Periodic Material Structures

Z. Szabo¹, P. Drexler¹, J. Seginak¹, D. Nešpor¹,
M. Steinbauer¹, P. Marcoň¹, and P. Fiala²

¹Department of Theoretical and Experimental Electrical Engineering
Technická 12, Brno 616 00, Czech Republic

²SIX VUT v Brně, Technická 12, Brno 616 00, Czech Republic

Abstract— The authors discuss the application of a broadband noise signal in the research of periodic structures and present the basic testing related to the described problem. Generally, noise spectroscopy tests are carried out to verify the behaviour of the response of periodic structures, and the related objective consists in recording the properties of microscopic structures in natural and artificial materials. The aim is to find a metrological method to investigate structures and materials in the frequency range between 100 MHz and 10 GHz; this paper therefore characterizes the design of a suitable measuring technique based on noise spectroscopy and introduces the first tests conducted on a periodic structure. In this context, the applied instrumentation is also shown to complement the underlying theoretical analysis.

1. INTRODUCTION

In general terms, spectrometry can be defined as a discipline analyzing the properties and origination of the spectra of harmonic signals or electromagnetic waves. The related research methods are based on the interaction between an electromagnetic wave and the measured sample of matter. The dependence of irradiation intensity changes on the wavelength is examined within electromagnetic spectroscopy; this discipline comprises, for example, Raman spectroscopy, which measures the spectrum of electromagnetic irradiation scattered on the basis of the Raman effect (non-elastic scattering). This effect causes the scattered irradiation to exhibit a wavelength slightly different from the incident radiation, mainly due to a part of the energy being transferred at vibrational junctions of a molecule. The discussed technique provides information on the structure and spatial arrangement of the quantum mechanical model of a molecule, and it is applicable for different materials, such as carbon [2, 3]. Another subregion of spectrometry consists in a method which utilizes the Fourier transform and is based on a mathematical transformation of the interferogram of the signal intensity dependence on the path difference of the beams; this difference is acquired via detecting the signal out of the interferometer. The interfering beams travel through the burette containing the sample. Fourier type spectrometers [1] are applied in, for example, infrared spectroscopy, UV/VIS spectroscopy, attenuated total reflection, atomic absorption spectroscopy, X-ray fluorescence, and weight spectroscopy to measure the proportion of weight to the ion charge. Weight spectrographs and spectrometers utilize the motion of a particle of the quantum mechanical model of matter in the electric and magnetic fields. We have the formula

$$m = \frac{p^2}{2 \cdot E_{\text{kin}}}, \quad (1)$$

where m is the weight, p are the dynamics of a moving particle, and E_{kin} is the kinetic energy of a specific particle. The weight can be determined from a comparison of the dynamics and the kinetic energy; this is performed via the passage of an ion having the charge Q through the “energy filter” and the “dynamics filter”, both of which are materialized by means of an electric and a magnetic field from the application of Faraday’s law of induction and Lorentz’s forces acting on the particles of mass:

$$\mathbf{F} = q(\mathbf{E} + \mathbf{v} \times \mathbf{B}), \quad (2)$$

where \mathbf{F} is the vector of the force acting on the particle with an electric charge q , \mathbf{E} is the electric intensity vector, \mathbf{v} is the vector of the instantaneous velocity of the motion of the electrically charged particle, and \mathbf{B} is the magnetic flux density vector. Other subareas comprise spectroscopy utilizing nuclear magnetic resonance, which is applied to determine the distribution of atoms in the vicinity of nuclei exhibiting non-zero nuclear spin (^1H , ^{13}C , ^{31}P , ...). In the given context, let us

note that nuclear magnetic resonance spectroscopy [4–6] is a physical-chemical method exploiting the interaction between atomic nuclei of the quantum mechanical model of matter and an external magnetic field. The technique examines the distribution of nuclear spin energies in the magnetic field and investigates the transition between individual spin states caused by radio frequency irradiation. Current methods within NMR spectroscopy are nevertheless fully applicable also in defining the spatial structure of smaller proteins, thus complementing the X-ray structural analysis. Another related technique utilizes electron paramagnetic resonance to measure particles containing non-pair electrons; this is a method enabling us to solve the problems of magnetic resonance spectroscopy. Other procedures involve nuclear quadrupole resonance and muon resonance [7]. Noise spectroscopy can be effectively practised via both harmonic analysis and statistics. To evaluate signals in continuous time, we can suitably use the Fourier transform [8], which can be further modified for other signal types. The evaluation of discrete signals is then feasible by means of the discrete Fourier transform [9] and the fast Fourier transform algorithm [10]. However, the Fourier transform is not applicable for the investigation of non-stationary signals; such signals can be examined more advantageously via wavelet transform and its modified algorithm, the discrete wavelet transform [11, 12]. Noise spectroscopy also utilizes wideband signals, for which we can suitably use the Burg algorithm method [13–15].

1.1. Ultrawideband Signals (Noise)

Noise can be generally characterized as a stochastic, random signal, whose description is deliverable via several approaches. Of these, the most prominent one consists in the amplitude area, where the signal is described by distributing the amplitudes, expressing the probability density, and specifying the distribution function. Another description technique is materialized via the autocorrelation function in the time region and by means of the power spectral density in the frequency area. Noise can be classified with “colours” assigned according to the frequency range; we then distinguish between white, grey, brown, red, pink, and other noise variants. These noise types are specific in their properties and sources. White noise, for example, consists of random samples exhibiting uniform and constant spectral power densities. Other properties of white noise include also infinity of the frequency spectrum; this is, however, a mere theoretical assumption because if the frequency spectrum were infinite, the total power of the signal would be infinite too. By extension, pink noise — also known as *1/f noise* or *oscillating noise* — is a signal or process having such frequency range that the power frequency density is directly proportional to the reverse value of the frequency. This condition occurs multiple times within the process and is therefore termed *transition between white and red noises*. Red noise is similar to the pink one but exhibits a power frequency density lowered by 6 dB per octave with increasing frequency [18].

1.2. Macroscopic Environment

The term *macroscopic material* generally denotes any material observable with the naked eye. The denomination is related to longitudinal dimensions, although it is also used to denote the effects and quantities connected with macroscopic objects. An isotropic environment constitutes a form of matter whose physical properties are identical or approximately identical in all directions of the coordinate system; an anisotropic environment is then one whose properties change in directions of the coordinate system. Then, for example, the relationship between the electric flux density $\mathbf{D}(t)$ and the electric intensity $\mathbf{E}(t)$ can be expressed by linear combination of the squared component of the vector $\mathbf{D}(t)$:

$$\begin{aligned} \begin{pmatrix} D_x \\ D_y \\ D_z \end{pmatrix} &= \begin{pmatrix} \varepsilon_{11} & \varepsilon_{12} & \varepsilon_{13} \\ \varepsilon_{21} & \varepsilon_{22} & \varepsilon_{23} \\ \varepsilon_{31} & \varepsilon_{32} & \varepsilon_{33} \end{pmatrix} \begin{pmatrix} E_x & E_y & E_z \end{pmatrix} \cdot \begin{pmatrix} B_x \\ B_y \\ B_z \end{pmatrix} \\ &= \begin{pmatrix} \mu_{11} & \mu_{12} & \mu_{13} \\ \mu_{21} & \mu_{22} & \mu_{23} \\ \mu_{31} & \mu_{32} & \mu_{33} \end{pmatrix} \begin{pmatrix} H_x & H_y & H_z \end{pmatrix} \begin{pmatrix} J_x \\ J_y \\ J_z \end{pmatrix} = \begin{pmatrix} \gamma_{11} & \gamma_{12} & \gamma_{13} \\ \gamma_{21} & \gamma_{22} & \gamma_{23} \\ \gamma_{31} & \gamma_{32} & \gamma_{33} \end{pmatrix} \begin{pmatrix} E_x & E_y & E_z \end{pmatrix}. \quad (3) \end{aligned}$$

The coefficients ε_{jk} of this linear transformation (3) are components of the symmetrical tensor of electric permittivities. A homogeneous environment is defined as one having constant properties in the space of the monitored material. Similarly, (3), it is possible to write the magnetic field properties, namely the magnetic permeability μ_{jk} with the magnetic field intensity vectors $H(t)$, the magnetic flux density $\mathbf{B}(t)$, and the current field with the specific conductance γ_{jk} (3) for vectors of the electric field intensity $\mathbf{E}(t)$ and the current density $\mathbf{J}(t)$.

1.3. Periodic Structures

From the perspective of description, a macroscopic material (MM) can be defined via a quantum mechanical (QM) model. The MM is then examined based on the incidence/irradiation of an electromagnetic wave, and from this interaction we then deduce the properties of the sample. The QM model of the sample comprises a high number of repeated structures, and it is thus possible to use the term *periodic material structure*. Depending on the result of the EMG wave interaction, we can deduce the basic and complementary properties of the sample (conductor; semiconductor; or insulator). Such utilization of similar effects is also typical of spectroscopy [2]. Research in the given area was already performed by Yablonovitch, whose experiments focused on an EMG wave in the spectrum of light [19]. The beginnings of research into the interaction between radiation and a periodic structure can be traced to the first years of the 20th century, a period when Bragg discovered by observation that, under certain conditions, atomic structure can behave like a mirror. This holds true, for example, in X-rays if the conditions are satisfied of a wavelength λ and a distance d between two neighbouring atoms at the angle of incidence Θ :

$$\lambda = 2d \cdot \sin(\Theta \pm \delta), \quad (4)$$

where δ is the angle deviation. Reflections of the incident EMG wave will occur, Fig. 1.

It is nevertheless obvious that the material and its atoms in themselves do not exhibit this property and that the periodicity of the structure must be ensured on the scale of wavelengths of the incident EMG wave. In periodic structures, the above-described effect can be used to determine the properties of the monitored sample of material. If an unknown sample of material, conceived according to the QM model, is irradiated with an EMG wave exhibiting a sufficient wavelength, we will find conditions that facilitate reflection of the selected EMG wave from the applied electromagnetic wave spectrum. The wave selection depends on the actual periodicity of the material. The ideal frequency range of the transmitted wave is infinite bandwidth; theoretically, this condition can be satisfied by white noise. When the reflected part of the EMG wave is captured, it is advantageous to have ready suitable evaluation tools, for example the Fourier transform, wavelet transform, or other techniques introduced above.

1.4. Periodic Structure Analysis

In order to be able to investigate the actual spectroscopic method working with a white noise signal, there has to be the possibility of mathematically describing periodic structures, and it is important to know their mathematical characteristics. The structure can then be analyzed. If we assume a periodic structure with finite dimensions, such analysis is performable with a finite method enabling basis approximation of the geometry and the function. In periodic structures exhibiting a low level of periodicity and large dimensions of the model, finite methods cannot be applied effectively, and a different mathematical model must be chosen. Artificial periodic structures include, for example, metamaterials [14] composed of elementary bound resonators.

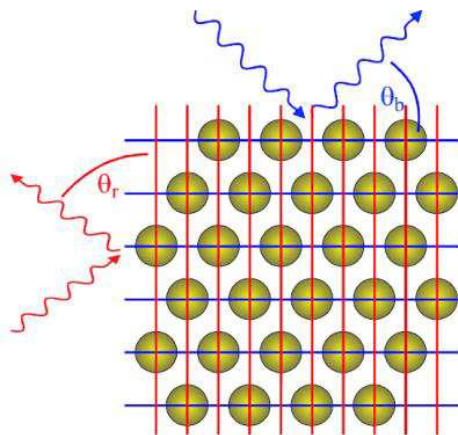


Figure 1: X-ray reflection from the periodic structure of atoms.



Figure 2: The applied noise generator and power amplifier. The image shows the tested noise generator, whose output power is 0 dBm in the frequency range of between 100 kHz and 10 GHz.

1.5. Benefit of Noise Spectroscopy

The contribution of noise spectroscopy consists in the use of an ultrawideband signal, which will enable us to acquire, within a single instant of time, a response to the entire spectrum of electromagnetic waves. However, the selective approach to signal sweep into the frequency spectrum carries with it the problem of time delay, and this drawback can be eliminated only with difficulty. Thus, the above-described effect of time-unshifted reflections from the periodic structures cannot be attained. In comprehensive investigation of material structures for the micro-wave application (tensor and composite), the properties of materials are studied by means of classic single-frequency methods, which bring about certain difficulties in the research process [20]. In boundary changes with a size close to the wave-length, wrong information concerning the examined objects can occur. One of the possible ways of suppressing negative sources of signals consists in the use of wide-band signals such as white noise, and this approach can be further reinforced by analyzing the problem of absorption in the examined material. The indicated methods require a source of noise, a receiving and a transmitting antenna, and A/D conversion featuring a large bandwidth; for our purposes, the bandwidth ranged between 50 MHz and 10 GHz. Until recently, it had not been possible to design an A/D converter of the described speed or materialize devices with the above-mentioned bandwidth. Currently, high-end oscilloscopes are available with a sampling frequency of hundreds of Gsa/s.

2. NOISE SOURCE

At present, the appropriate type of source is supplied by certain manufacturers in the given field. Importantly, for the noise spectroscopy application, we require a comparatively large output power of up to 0 dB/mW; the assumed bandwidth characteristics then range up to 10 GHz. At this point, it is also necessary to mention the fundamental problem of finding active devices able to perform signal amplification at such high frequencies. Our requirements are thus limited by the current status of technology used in the production of commercially available devices; the highest-ranking solution for the bandwidth of up to 10 GHz can be found only up to the maximum of 0 dB/mW. In the noise spectroscopy experiments, we utilized a generator and an amplifier (NC1128A), Fig. 2. In order to verify the applicability of the noise spectroscopy laboratory arrangement (Fig. 4), we tested a metamaterial (periodic structure) designed for the frequency of 199.9 MHz (Fig. 3).

3. METHOD

Repeated transmission and sensing of both the signal provided by the noise generator and the external signals were carried out at the initial stage of the research. The repetition was performed for each sampled frequency, and the incident power spectrum was summed. Thus, we obtained the frequency dependence of the transmitted signal energy distribution. Generally, if the transmitter/receiver set is not located in a room with a defined spectral absorbance, we can expect uniform energy distribution within the whole frequency range. The record is, at its end, transformed to the frequency dependence of the specific power. In the described manner, we acquired the characteristics of the spectrum measurement background. At this point, the examined sample was placed



Figure 3: The first tuned periodic structure tested to verify the noise spectroscopy measurement.



Figure 4: The arrangement of the noise spectroscopy station (free room).

in a support case (Figs. 4, 5(a), 5(b)); the sample for such application can be layered or periodic, and it is expected to provide the assumed frequency characteristic. Subsequently, repeated measurement was performed observing the above-outlined procedure. In the case of a markedly frequency-dependent background, the obtained characteristic can be corrected. Fig. 6 shows the frequency dependencies of the measurement setup and the multi-layer material.

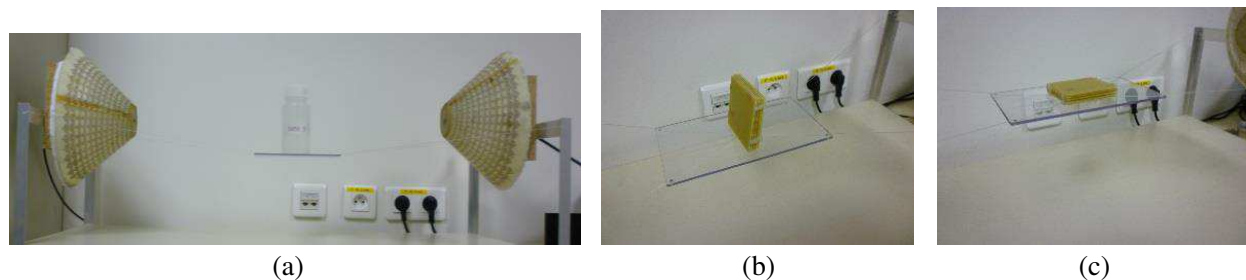


Figure 5: (a) The liquid and (b) solid samples arranged in a laboratory for the sensing and evaluation of the spectrum (no shielded chamber; free room).

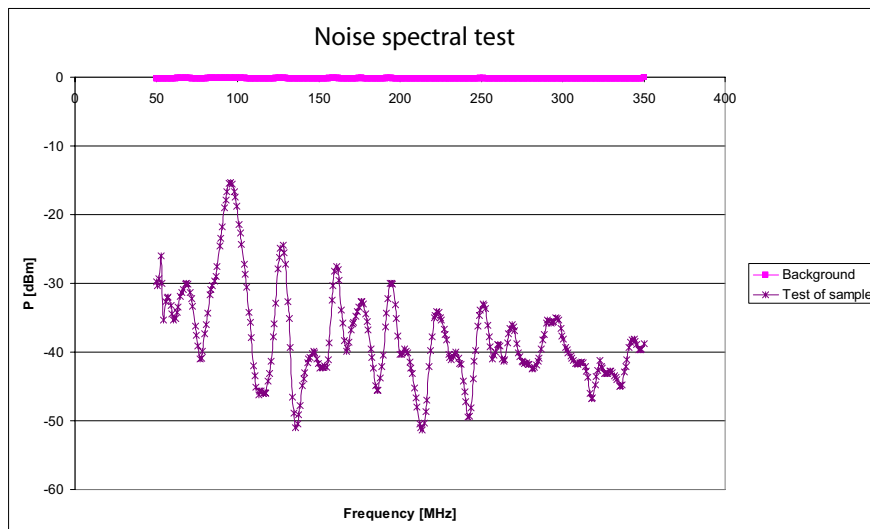


Figure 6: The waveform and spectrum of the noise generator output for the measured sample; $f = 50\text{--}350$ MHz.

4. CONCLUSION

The research paper provides an elementary overview and description of instrumentation for noise spectroscopy measurement and the related experiments. Noise spectroscopy operations within the frequency band of between 10 MHz and 10 GHz can be performed using currently available technologies. The noise source comprised a generator (NC1108A) and an amplifier (NC1128A).

ACKNOWLEDGMENT

The research described in this paper was financed by the National Sustainability Program under grant No. LO1401, for the actual analyses and experiments, infrastructure of the SIX Center was used.

REFERENCES

1. Hollas, J. M., *Modern Spectroscopy*, 1–482, Wiley, New York, 2004.
2. Ferraro, J. R., *Introductory Raman Spectroscopy*, 1–434, Academic Press, Waltham, 2002.
3. Adar, F., “Entering Raman’s realm,” *Spectroscopy*, Mar. 1, 2011, <http://www.spectroscopy-online.com/entering-ramans-realm>, Apr. 1, 2015.

4. Pitner, T. P., J. D. Glickson, J. Dadok, and G. R. Marshall, "Solvent exposure of specific nuclei of angiotensin. II. Determined by NMR solvent saturation method," *Nature*, Vol. 250, 467, 582–584, 1974.
5. Dadok, J. and R. F. Spencer, "Correlation NMR spectroscopy," *Journal of Magnetic Resonance*, Vol. 13, No. 2, 243–248, 1974.
6. Dadok, J., *High-field NMR Instrumentation*, 1–55, Wiley Online, New York, 2007.
7. Steinbauer, M., B. Král, I. Fiala, M. Staněk, M. Procházka, P. Fiala, J. Segiň'ak, and P. Drexler, "Detection of selected chemical substances by means of nuclear quadrupole resonance," *PIERS Proceedings*, 1036–1040, Aug. 25–28, Guangzhou, 2014.
8. Gujar, S. K., S. Maheshwari, I. Björkman-Burtscher, and P. C. Sundgren, "Magnetic resonance spectroscopy," *Journal of Neuro-Ophthalmology*, Vol. 25, No. 3, 217–226, 2005.
9. Kufner, A. and J. Kadlec, *Fourier Series*, 1–207, Academia, Praha, 1969.
10. Uhlíř, J. and P. Sovka, *Digital Signal Processing*, 1–100, ČVUT, Praha, 1995.
11. Misiti, M., Y. Misiti, G. Oppenheim, and J. M. Poggi, *Wavelet Toolbox, Users Guide*, The Mathworks Inc., 2006.
12. Addison, P. S., *The Illustrated Wavelet Transform Handbook*, 1–368, CRC Press, Boston, 2002.
13. Ferus, M., "High resolution FT spectroscopy," Laboratory of FT and Laser Spectroscopy, Jul. 15, 2013, <http://www.jh-inst.cas.cz/~ftirlab/bruker>, Apr. 1, 2015.
14. Měcháček, R., "Spectral impulse signal analysis," 1–110, Bachelor Work, Brno University of Technology, 2008.
15. Mallat, S., *A Wavelet Tour of Signal Processing*, 1–637, Academic Press, New York, 1999.
16. Šikula, J., B. Koktavý, P. Vašina, Z. Chobola, and V. Juránková, "Noise reliability indicators," *Proc. European Symposium on Reliability of Electron Devices*, 341–346, 1993.
17. Bertoni, H. L., L. H. Cheo, and T. Tamir, "Frequency-selective reflection and transmission by a periodic dielectric layer," *IEEE Transactions on Antennas and Propagation*, Vol. 37, No. 1, 78–83, 1989.
18. Casse, B. D. F., O. Wilhelmi, and B. T. Saw, "Singapore synchrotron light source," National University of Singapore Research Link, 2005.
19. Stanley, C. and S. A. Douglas, *Principles of Instrumental Analysis*, 1–1039, Thomson Brooks/Cole, Sydney, 2007.
20. Herrmann, R. and C. Onkelinx, "Quantities and units in clinical chemistry: Nebulizer and flame properties in flame emission and absorption spectrometry," *Pure and Applied Chemistry*, Vol. 58, No. 12, 1737–1742, 1986.

Supercontinuum Generation in a Silicon Nanowire Embedded Photonic Crystal Fiber

E. Gunasundari¹, Abdosllam M. Abobaker², K. Senthilnathan¹, S. Sivabalan³,
K. Nakkeeran⁴, and P. Ramesh Babu¹

¹Photonics, Nuclear and Medical Physics Division

School of Advanced Sciences, VIT University, Vellore 632 014, India

²Department of Communications Engineering, College of Electronic Technology, Bani Walid, Libya

³School of Electrical Engineering, VIT University, Vellore 632 014, India

⁴School of Engineering, University of Aberdeen, Aberdeen AB24 3UE, UK

Abstract— In this paper, we demonstrate the supercontinuum generation in a silicon nanowire embedded photonic crystal fiber (SN-PCF) using fully-vectorial finite element method. The variation of supercontinuum is investigated by changing the fiber length, pump peak power and pump wavelength. The proposed fiber exhibits broad spectrum of more than 2200 nm within 2 mm length of fiber for peak power of 500 W of input pulse.

1. INTRODUCTION

The photonic crystal fiber (PCF) is a good platform for manipulating tunable dispersion with high nonlinear properties by arranging the air-holes in the core-cladding geometry suitably. PCF has been an intense topic of research for supercontinuum generation (SCG) ever since the work by Ranka et al [1, 2]. Pumping near a zero dispersion wavelength (ZDW) with high nonlinearity facilitates less power requirement. SCG finds wide applications in different fields such as wavelength division multiplexing [3, 4], optical sensing [5], spectroscopy [6, 7], optical coherence tomography (OCT), etc..

There have been many theoretical and experimental reports of SCG in various guided-wave structures, such as single-mode fibers, PCF, silica nanowires, etc.. The previous results suggest that it is possible to achieve SCG at low optical power and over short propagation distances provided the guiding medium exhibits high nonlinear response and tunable dispersion properties. In a typical PCF based supercontinuum source, the effective mode area of the PCF is roughly $\sim 1 \mu\text{m}^2$ with several metres of PCF. Further, by reducing the core down to nm size and by tapering the micro-structured core, the effective optical nonlinearity can be increased [8]. Although these previous studies have demonstrated efficient generation of supercontinuum in on-chip integration, those sources demand a large propagation length for generating high spectral broadening.

A promising alternative solution is provided by silicon waveguide sources [9], which have the advantage of employing an emerging silicon-on-insulator (SOI) integrated-photonics platform. Silicon has excellent transmission properties compared to silica and does not require high power density to bring in nonlinearity owing to its huge nonlinear coefficient. Till date, many reports for SCG in silicon nanowire are available [8, 10, 11]. Recently, the possibility of SCG of 500 nm bandwidth at telecommunication wavelength has been demonstrated with various input peak powers for various SOI waveguide lengths. Such a dielectric silicon waveguide with a nanocore diameter could provide a remarkably strong field confinement, enhanced light-matter interactions and strong tunable dispersions when embedded into PCF. The resulting silicon photonic device known as silicon nanowire embedded photonic crystal fiber (SN-PCF) has been proposed very recently [12]. In this paper, we report the supercontinuum of bandwidth wider than 500 nm in SN-PCF with less input peak power.

The paper is laid out as follows. In Section 2, we discuss the design of a SN-PCF using a fully-vectorial finite element method. We study the optical properties of SN-PCF including group velocity dispersion (GVD), third order dispersion (TOD) and nonlinearity by varying the core diameter in Section 3. We investigate the evolution of supercontinuum by changing the fiber length, pump peak power and pump wavelength for 480 nm core diameter in Section 4. Finally, we summarize the findings in Section 5.

2. DESIGN OF THE PROPOSED SN-PCF

The schematic cross section and mode field distribution at $0.8 \mu\text{m}$ wavelength for 480 nm core diameter of the proposed SN-PCF as shown in Figs. 1(a) and (b). It is composed of circular air

holes in the cladding arranged in a triangular pattern and a circular nanosize core. Here, the air-hole diameter is 1120 nm. We analyze the optical properties by increasing the core diameter from 420 to 480 nm. We have already explored all the optical properties for the various core diameters ranging from 1000 to 300 nm [12]. In this work, we choose to vary the core diameter from 420 to 480 nm for analyzing the optical properties for a wavelength range from 0.8 to 1.7 μm for supercontinuum generation. The justification for this range of study is because of tight mode confinement within the core and nearly zero dispersion with high nonlinearity. In order to determine the dispersion of SN-PCF, it is necessary to compute the effective refractive index of the fundamental mode and the same is done by finite element method.

3. OPTICAL PROPERTIES

In this section, we explore the various linear and nonlinear optical properties. We study the impact of dispersions of fundamental mode for different core diameters. The variations of GVD and TOD with respect to wavelength for various core diameters are shown in Fig. 2(a). As is seen in Fig. 2(a), when the core diameter is reduced from 480 nm to 440 nm, the GVD decreases upon increasing the wavelength due to the increase in field distribution towards the core-cladding boundary. However, at 420 nm core diameter, the GVD decreases up to 1.65 μm wavelength beyond which, this dispersion switches to normal regime. From the Fig. 2(a), it is clear that the 480 nm core diameter exhibits a less anomalous GVD ($-0.4909 \text{ ps}^2/\text{m}$) at 0.8 μm wavelength. Further, we report a less TOD ($0.6595 \times 10^{-3} \text{ ps}^3/\text{m}$) at 0.8 μm wavelength for 480 nm core diameter and this is evident from Fig. 2(a).

Due to the small core diameter and high nonlinear index coefficient of silicon ($4 \times 10^{-18} \text{ m}^2/\text{W}$), the SN-PCF exhibits tight mode confinement compared to conventional PCF. But a significant fraction of the optical mode propagates in air as the evanescent field. Hence, an accurate estimation

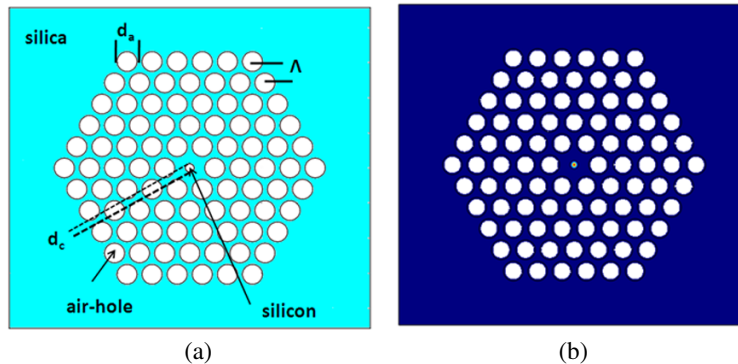


Figure 1: (a) Geometrical structure of the proposed fiber and (b) mode field distribution at 0.8 μm wavelength for 480 nm core diameter.

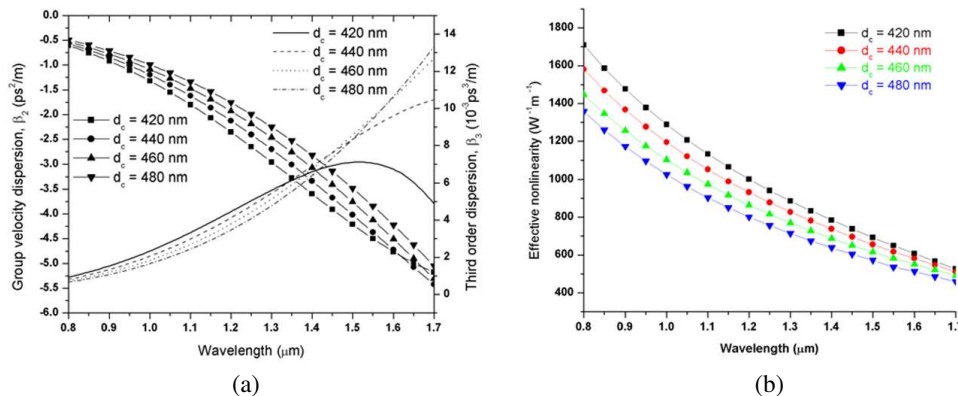


Figure 2: (a) Variations of GVD and TOD and (b) variations of nonlinearity of the proposed SN-PCF for different core diameters.

of the nonlinear coefficient γ^V is needed for small core diameter. It is known that the mode confinement determined by the effective mode area becomes much pronounced upon reducing the core diameter of the proposed fiber. Fig. 2(b) depicts the variation of effective nonlinearity with respect to wavelength for various core diameters. The results show a slowly decreasing nonlinearity with the increase in wavelength. The proposed structure possesses a maximum effective nonlinearity for lower wavelengths at 420 nm core diameter.

4. SIMULATION OF SUPERCONTINUUM GENERATION

We study the SCG using the generalized nonlinear Schrödinger equation with the effects of two photon absorption and free-carrier absorption using the proposed SN-PCF as follows [10],

$$\frac{\partial A}{\partial z} = -\frac{1}{2}(\alpha + \alpha^f)A - \frac{i}{2}\beta_2\frac{\partial^2 A}{\partial T^2} + \frac{\beta_3}{6}\frac{\partial^3 A}{\partial T^3} + i\gamma^V [1 + \omega/\omega_0] A \int_{-\infty}^{\infty} [R(T - \tau)|A|^2] d\tau \quad (1)$$

where, $A(z, T)$, α , α^f , β_2 , β_3 , γ^V and $R(T - \tau)$ represent the field envelope, linear loss, free-carrier contribution term, GVD, TOD, effective nonlinearity and Raman response function. In this simulation, we ignore the effects of free carrier absorption, two photon absorption and loss owing to their insignificant role in the interaction. The nonlinear response function $R(t)$ is defined by [10] $R(t) = \gamma(1 - f_R)\delta(t) + f_R h_R(t)$, includes both instantaneous electronic and delayed Raman contributions. The fractional Raman contribution is $f_R = 0.043$ and delayed Raman response $h_R(t)$ of silicon is expressed as: $h_R(t) = \Omega_R^2 \tau_1 \exp(\frac{-t}{\tau_2}) \sin(\frac{t}{\tau_1})$, where the parameters τ_1 ($= 10$ fs) and τ_2 ($= 3$ ps) correspond to the Raman shift and the bandwidth of the Raman gain spectrum,

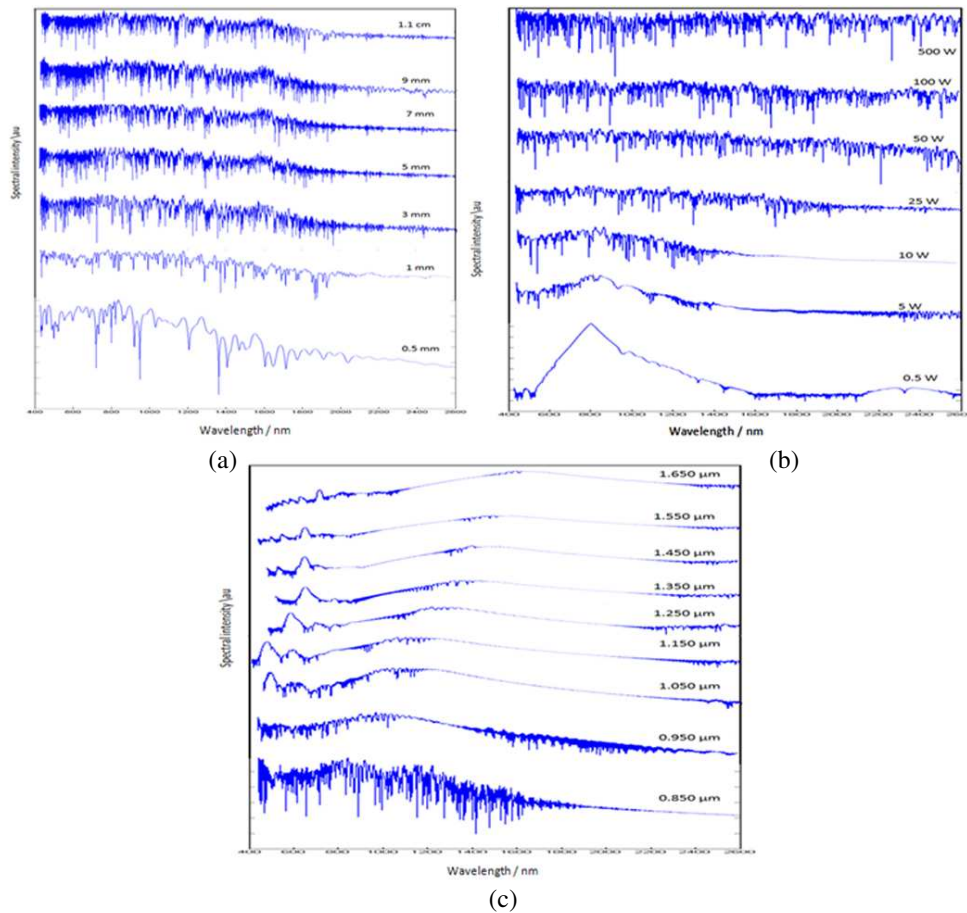


Figure 3: Measured supercontinua in the SN-PCF with (a) the different fiber lengths at the pump wavelength of $0.8 \mu\text{m}$ for the input peak power of 25 W and pulse duration of 50 fs, (b) the pump peak power increasing from 0.5 W to 500 W at the pump wavelength of $0.8 \mu\text{m}$ of 2 mm of SN-PCF and (c) different pump wavelengths from $0.850 \mu\text{m}$ to $1.650 \mu\text{m}$ for the input peak power of 25 W and width of the pulse is 50 fs.

respectively. We investigate the pulse propagation in SN-PCF by symmetrized split-step Fourier method [13]. We consider the input electric field with an input soliton order (N) is given by [14], $A(0, t) = N\sqrt{P_0} \operatorname{sech}[\frac{t}{T_0}]$, where P_0 is the peak power and T_0 is the input soliton duration defined as $T_{FWHM}/1.763$, where T_{FWHM} is the full width at half maximum (FWHM) of the input pulse. The soliton order of the input pulse is determined by both pulse and fiber parameters through $N^2 = \frac{L_D}{L_{NL}}$. Here, $L_D = \frac{T_0^2}{|\beta_2|}$ and $L_{NL} = \frac{1}{\gamma P_0}$ are the characteristic dispersive and nonlinear length scales, respectively.

5. RESULTS AND DISCUSSIONS

In this section, first, we investigate the evolution of supercontinuum by varying the length of the fiber using hyperbolic secant input pulse with pulse width of 50 fs. When pumping the pulse in the anomalous dispersion regime nearest to ZDW, the wider spectrum occurs due to the cumulative effect of dispersive waves, soliton fission and Raman soliton self-frequency shift. The spectra of supercontinuum in the SN-PCF with different length of fibers, i.e., $L = 0.5, 1, 3, 5, 7, 9$, and 11 mm for a less input peak power of 25 W are shown in Fig. 3(a).

Second, we study the supercontinuum evolutions by increasing the pump peak power from 0.5 to 500 W at 0.8 μm wavelength in an SN-PCF of 2 mm length as shown in Fig. 3(a). We note that L_D is much larger than L_{NL} when peak power is 0.5 W. At this juncture, SCG is initiated by the self-phase modulation (SPM) and the same is shown in Fig. 3(b). When the pump peak power further increases, the spectrum is broadened by the combined action of SPM, soliton fission and Raman effect. As a result, we obtain a broad spectrum of 1530 nm for a range of wavelengths from 420 to 1950 nm as shown in Fig. 3(b). Thus, the proposed SN-PCF exhibits a narrow spectrum of 300 nm when peak power is relatively less (0.5 W). On the other hand, a wider spectrum of 2100 nm is observed for a maximum peak power of 500 W.

Finally, we investigate the variations of supercontinuum for an input peak power of 25 W with 50 fs pulse width by varying the pump wavelengths from 0.850 to 1.650 μm in a 2 mm length of SN-PCF as shown in Fig. 3(c). We obtain a broad spectrum at shorter wavelength of 0.850 μm due to the effects of low anomalous GVD with high nonlinearity. Further, upon increasing the pump wavelength, we observe a narrow spectrum as order of the soliton is less.

6. CONCLUSION

We have demonstrated the supercontinuum using a silicon nanowire embedded photonic crystal fiber. Further, we have investigated the supercontinuum by varying the length of the fiber, peak power of the input pulse and operating wavelength. We have observed a wider bandwidth exceeding 1300 nm in a 11 mm length of SN-PCF. Further, we have obtained a broad spectrum of more than 2200 nm for a large input peak power of 500 W. Finally, we have obtained a broad spectrum exceeding 1500 nm at a shorter wavelength of 0.850 μm .

ACKNOWLEDGMENT

KSN wishes to thank CSIR [No. 03(1264)/12/EMR-II] and DST [No. SR/FTP/PS-66/2009], Government of India, for the financial support through the sponsored projects. SS wishes to thank DST [No. SR/S2/LOP-0014/2012], Government of India, for the financial support through the sponsored project.

REFERENCES

1. Ranka, J. K., R. S. Windeler, and A. J. Stentz, "Visible continuum generation in air silica microstructure optical fibers with anomalous dispersion at 800 nm," *Opt. Lett.*, Vol. 25, No. 1, 25–27, 2000.
2. Liao, M., X. Yan, G. Qin, C. Chaudhari, T. Suzuki, and Y. Ohishi, "A highly non-linear tellurite microstructure fiber with multi-ring holes for supercontinuum generation," *Opt. Express*, Vol. 17, No. 18, 15481–15490, 2009.
3. Morioka, T., H. Takara, S. Kawanishi, O. Kamatani, K. Takiguchi, K. Uchiyama, M. Saruwatari, H. Takahashi, M. Yamada, T. Kanamori, and H. Ono, "1 Tbit/s (100 Gbit/s10 channel) OTDM/WDM transmission using a single supercontinuum WDM source," *Electron. Lett.*, Vol. 32, No. 10, 906–907, 1996.

4. Nakasyotani, T., H. Toda, T. Kuri, and K. Kitayama, "Wavelength-division-multiplexed millimeter-waveband radio-on-fiber system using a supercontinuum light source," *J. Lightwave Technol.*, Vol. 24, No. 1, 404–410, 2006.
5. Kaminski, C. F., R. S. Watt, A. D. Elder, J. H. Frank, and J. Hult, "Supercontinuum radiation for applications in chemical sensing and microscopy," *Appl. Phys. B*, Vol. 92, 367–378, 2008.
6. Liu, Y., M. D. King, H. Tu, Y. Zhao, and S. A. Boppart, "Broadband nonlinear vibrational spectroscopy by shaping a coherent fiber supercontinuum," *Opt. Express*, Vol. 21, No. 7, 8269–8275, 2013.
7. Sanders, S. T., "Wavelength-agile fiber laser using group-velocity dispersion of pulsed supercontinua and application to broadband absorption spectroscopy," *Appl. Phys. B*, Vol. 75, No. 7, 799–802, 2002.
8. Foster, M., A. L. Gaeta, Q. Cao, and R. Trebino, "Soliton-effect compression of supercontinuum to few-cycle durations in photonic nanowires," *Opt. Express*, Vol. 13, No. 18, 6848–6855, 2005.
9. Boyraz, Ö., P. Koonath, V. Raghunathan, and B. Jalali, "All optical switching and continuum generation in silicon waveguides," *Opt. Express*, Vol. 12, No. 17, 4094–4102, 2004.
10. Yin, L., Q. Lin, and G. P. Agrawal, "Soliton fission and supercontinuum generation in silicon waveguides," *Opt. Lett.*, Vol. 32, No. 4, 391–393, 2007.
11. Driscoll, J. B., X. Liu, S. Yasserli, I. Hsieh, J. I. Dadap, and R. M. Jr. Osgood, "Large longitudinal electric fields (E_z) in silicon nanowire waveguides," *Opt. Exp.*, Vol. 17, No. 4, 2797–2804, 2009.
12. Gunasundari, E., K. Senthilnathan, S. Sivabalan, M. Abdosllam Abobaker, K. Nakkeeran, and P. Ramesh Babu, "Waveguiding properties of silicon nanowire embedded photonic crystal fiber," *Opt. Materials*, Vol. 36, No. 5, 958–964, 2014.
13. Dudley, J. M. and J. R. Taylor, *Supercontinuum Generation in Optical Fibers*, Cambridge University Press, 2010.
14. Agrawal, G. P., *Nonlinear Fiber Optics*, Academic Press, 2007.

Dispersion Characteristics of Zinc Oxide Nanorods Organized in Two-dimensional Uniform Arrays

A. M. Lerer¹, P. E. Timoshenko^{1,2}, G. A. Kalinchenko³,
E. M. Kaidashev², and A. S. Puzanov¹

¹Physics Department, Southern Federal University, Russia

²Laboratory of Nanomaterials, Southern Federal University, Russia

³ELI-Beamlines, Czech Republic

Abstract— The electromagnetic waves propagation in a two-dimensional periodic array of zinc oxide nanowaveguides covered with a thin metal film is solved by the separation of variables method in cylindrical coordinates. The numerical results obtained by our method are in good agreement with the ones computed by the commercial software COMSOL MultiphysicsTM over all optical range and have minor deviations for the wavelength range close to the critical wavelength. Resonances located at the amplitude-frequency characteristics of optical nanoantennas may be interpreted as resonances of circular bilayer nanowaveguide segments with the ZnO core covered with thin metal shell. The results may also be used to predict the resonant wavelength of two-dimensional periodic arrays of ZnO nanorods coated with a thin metal layer and grown on a dielectric substrate.

1. INTRODUCTION

The new design of optical antennas based on the ZnO nanorods coated with a thin metal film is discussed in the paper [1]. The diffraction of electromagnetic waves by a single metal-dielectric nanooscillator and array of ones placed at the interface between dielectric layers has been solved. The dependencies of electrodynamic characteristics of optical antennas on the geometrical parameters were compared with the experimental data. Resonances located at the amplitude-frequency characteristics of optical nanoantennas may be interpreted as resonances of circular bilayer nanowaveguide segments with the ZnO core covered with thin metal shell. In this regard it is of interest to investigate the range of the optical characteristics of similar waveguides.

The calculated dispersion characteristics of single waveguide and two-dimensional periodic arrays of ones are discussed in this paper. The dielectric constant dispersion of ZnO [2] and metal [3] were took into account. The metals are known to have a finite complex dielectric constant in the optical range.

2. STATEMENT OF THE PROBLEM

The Fig. 1 shows the geometry of optical waveguide composed of a core covered by a thin metal shell. The core has a radius R_1 and a dielectric constant ε_1 . The shell with a dielectric constant ε_2 has a radius R_2 . The thickness of the shell is $d = R_2 - R_1$. We assume that the dielectric constant ε_3 outside of the waveguide is equal to free space permittivity. The magnetic permeability

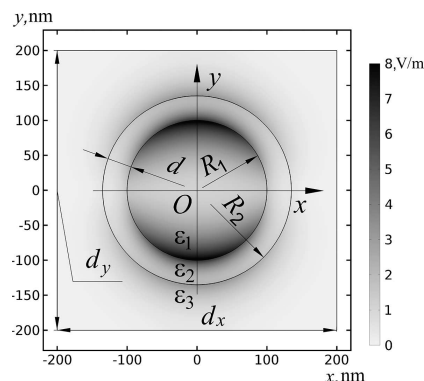


Figure 1: The electric field of the cylindrical nanowaveguide with $\lambda = 450$ nm, $R_1 = 100$ nm, $\varepsilon_1 = 4.0397 + 0.002i$ (ZnO), $R_2 = 135$ nm, $\varepsilon_2 = 6.0830 + 0.7462i$ (Ag), $\varepsilon_3 = 1$, $d_x = d_y = 400$ nm.

μ everywhere is equal to free-space permeability. The geometry shown in Fig. 1 of optical waveguide is described by Cartesian rectangular coordinate system. The x - and y -axis are the longitudinal coordinate. The z axis is directed along the waveguide being unlimited in this direction. The parameters d_x and d_y are periods of the array along x and y axes, respectively.

The method of separation variables in cylindrical coordinate system (r, ϕ, z) is applied to determine the frequency dependence of the complex propagation constant $\gamma(\omega)$ in the nanoantennas.

The electromagnetic field in the waveguide can be written by the longitudinal component of the electric $P^e(r, \phi) \exp(-i\gamma z)$ and magnetic $P^\mu(r, \phi) \exp(-i\gamma z)$ Hertz vector.

The solution of Helmholtz equation for waveguide arrays is assumed in the form:

$$P^e(r, \phi) = \sum_{m=1}^{\infty} \hat{P}_m^e(r) \sin m\phi, \quad P^\mu(r, \phi) = \sum_{m=1}^{\infty} \hat{P}_m^\mu(r) \cos m\phi \quad (1)$$

where m is the azimuthal wave mode number. The summing symbol in (1) should be omitted in case of a single waveguide. The function $\hat{P}_m^{e,\mu}(r)$ may be written:

- in the core of the waveguide ($r \leq R_1$):

$$\hat{P}_m^{e,\mu}(r) = A_m^{e,\mu} \frac{\hat{J}_m(r)}{\eta_1^2 \hat{J}_m(R_1)}, \quad (2)$$

- in the shell ($R_1 \leq r \leq R_2$):

$$\hat{P}_m^{e,\mu}(r) = \frac{1}{\eta_2^2 \Phi_m^{(2)}(R_1, R_2)} \left[A_m^{e,\mu} \Phi_m^{(2)}(r, R_2) - C_m^{e,\mu} \Phi_m^{(2)}(r, R_1) \right], \quad (3)$$

- in free space ($r \geq R_2$) in case of a single waveguide:

$$\hat{P}_m^{e,\mu}(r) = C_m^{e,\mu} \frac{\hat{K}_m(r)}{\eta_3^2 \hat{K}_m(R_2)}, \quad (4)$$

- in free space ($r \geq R_2$) in case of a periodic waveguide array:

$$\hat{P}_m^{e,\mu}(r) = \frac{1}{\eta_3^2 \Phi_m^{(2)}(R_2, R_3)} \left[C_m^{e,\mu} \Phi_m^{(2)}(r, R_3) - B_m^{e,\mu} \Phi_m^{(3)}(r, R_2) \right], \quad (5)$$

where R_3 is an arbitrary radius, satisfying the condition $R_3 > \sqrt{d_x^2 + d_y^2}/2$. In Eqs. (2)–(5) we use

$$\hat{J}_m(r) = \begin{cases} J_m(\eta_1 r), & \eta_1^2 \geq 0, \\ I_m(\eta_1 r), & \eta_1^2 < 0, \end{cases} \quad \hat{K}_m(r) = \begin{cases} N_m(\eta_3 r), & \eta_3^2 \geq 0, \\ K_m(\eta_3 r), & \eta_3^2 < 0, \end{cases}$$

$$\Phi_m^{(j)}(r, d) = \begin{cases} J_m(\eta_j r) N_m(\eta_j d) - N_m(\eta_j r) J_m(\eta_j d), & \eta_j^2 \geq 0, \\ I_m(\eta_j r) K_m(\eta_j d) - K_m(\eta_j r) I_m(\eta_j d), & \eta_j^2 < 0, \end{cases}$$

$A_m^{e,\mu} = \begin{Bmatrix} E_{z,m}(R_1) \\ H_{z,m}(R_1) \end{Bmatrix}$, $C_m^{e,\mu} = \begin{Bmatrix} E_{z,m}(R_2) \\ H_{z,m}(R_2) \end{Bmatrix}$, $B_m^{e,\mu} = \begin{Bmatrix} E_{z,m}(R_3) \\ H_{z,m}(R_3) \end{Bmatrix}$ are an unknown coefficients,

$E_{z,m}$ and $H_{z,m}$ are longitudinal components of the electromagnetic field, $\eta_j^2 = k^2 \varepsilon_j - \gamma^2$, k is a wavenumber, $J_m(z)$ is the Bessel function, $I_m(z)$ is the modified Bessel function, $N_m(z)$ is the Neumann function, $K_m(z)$ is the Macdonald function.

The solution is an ordinary in case of a single waveguide except the Hertz vector that can be written in form (2)–(5) satisfying the continuity condition of the longitudinal component of the electromagnetic field in boundaries $r = R_{1,2}$. The components $E_{\phi,m}(r)$, $H_{\phi,m}(r)$ should be found in each waveguide region considering boundary conditions. The solution may be written as system of linear algebraic equations (SLAE) for the four unknown coefficients. The dispersion relation is obtained by calculating the determinant of the SLAE being equated to zero.

In Eq. (5) we use an arbitrary radius R_3 and additional unknown coefficients $B_m^{e,\mu}$ in case of two-dimensional periodic array of zinc oxide nanowaveguides. The unknown coefficients $A_m^{e,\mu}$ and

$B_m^{e,\mu}$ may be omitted by using the continuity condition of azimuthal components $E_{\phi,m}(r)$, $H_{\phi,m}(r)$ on boundaries $r = R_{1,2}$. Lets sum in (1) for $m \leq M$, $M \gg 1$ values and require satisfaction the boundary conditions of $H_z(r, \phi) = 0$ in M values on the side of the cell $x = d_x/2$ and $E_z(r, \phi) = 0$ in M values on the top side of the cell $y = d_y/2$. These conditions are valid for waves in the array of waveguides excited by a normal incidence plane wave with polarization along the y -axis. The dispersion relation is also obtained by finding the determinant of the SLAE being equated to zero for unknown coefficients $C_m^{e,\mu}$.

The propagation constant in waveguides with complex permittivity has a complex value. It is very difficult to locate complex roots of a complex function at the complex plane. To solve this issue we use the Cauchy’s argument principle [7].

Only waves with low losses has a wide range of practical applications. In this case we may simplify the finding complex roots method [8,9]. The propagation constant may be assumed as $\gamma(\varepsilon' - i\varepsilon'')$. Lets expand it in a Taylor and take three terms of the series:

$$\gamma(\varepsilon' - i\varepsilon'') \approx \gamma(\varepsilon') - i\varepsilon''\gamma'(\varepsilon') - (\varepsilon'')^2\gamma''(\varepsilon')/2.$$

The derivatives don’t depend on the direction because the function $\gamma(\varepsilon)$ is an analytic. Therefore, we replace derivatives by finite differences:

$$\varepsilon''\gamma'(\varepsilon') \approx \gamma(\varepsilon') - \gamma(\varepsilon' - \varepsilon''), \quad (\varepsilon'')^2\gamma''(\varepsilon') \approx \gamma(\varepsilon' + \varepsilon'') + \gamma(\varepsilon' - \varepsilon'') - 2\gamma(\varepsilon').$$

Hence

$$\gamma(\varepsilon' - i\varepsilon'') \approx \gamma(\varepsilon') - i[\gamma(\varepsilon') - \gamma(\varepsilon' - \varepsilon'')] - [\gamma(\varepsilon' + \varepsilon'') + \gamma(\varepsilon' - \varepsilon'') - 2\gamma(\varepsilon')]. \quad (6)$$

Using this approach, the three real propagation constants of waveguide with a real permittivity should be found and applied the expression (6) to them to determine the complex propagation constant. The detailed analysis and verification of the numerical method described in this paper are shown in [8,9]. The calculation error increases sharply when $n''/n' > 0.1$ where $\gamma/k = n' - in''$. So, if we use the silver as a coating film, the fairly large errors are in the wavelength range 400–440 nm.

3. RESULTS AND DISCUSSIONS

The numerical results for EH_{11} mode of the waveguide with radius $R_1 = 100$ nm covered by silver thin film having different thicknesses close to 40 nm are presented in this paper. These geometrical parameters are typical for ZnO nanorods [1,4,5].

The Fig. 2 shows the dispersion curves of the wave mode EH_{11} of a single waveguide with the various shell thicknesses d . It also displays the refractive index ZnO n_{ZnO} (curve 5). The

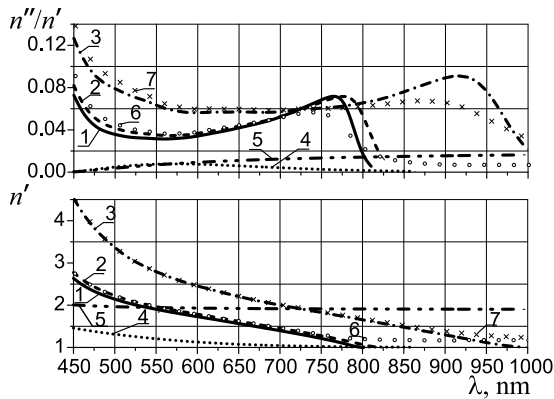


Figure 2: Dispersion curves of the optical waveguide with different shell thicknesses d : 1 — 45 nm, 2 — 35 nm, 3 — 15 nm, 4 — 0, 5 — ZnO, 6 — 35 nm (FEM), 7 — 15 nm (FEM).

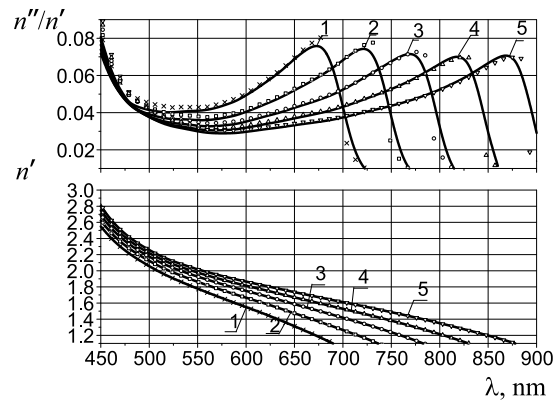


Figure 3: Dispersion curves of the waveguide with fixed shell thickness $d = 40$ nm and different core radii R_1 : 1 — 80 nm, 2 — 90 nm, 3 — 100 nm, 4 — 110 nm, 5 — 120 nm. The results obtained by FEM in COMSOL Multiphysics™ are marked by symbols.

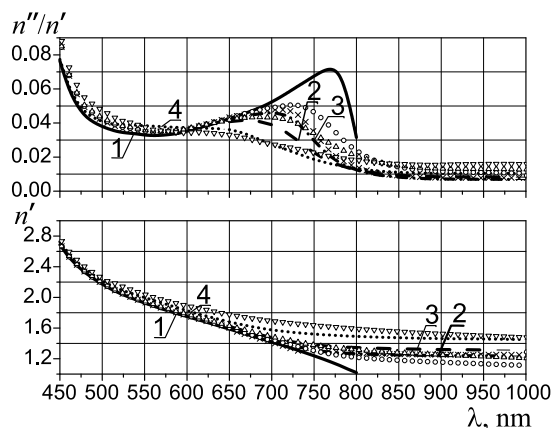


Figure 4: Dispersion curves of the array of waveguides with $R_1 = 100$ nm, $R_2 = 140$ nm and various unit cell size: 1 — single waveguide, 2 — array of waveguides with $d_x = d_y = 350$ nm, 3 — 325 nm, 4 — 300 nm. The results obtained by FEM are marked by symbols.

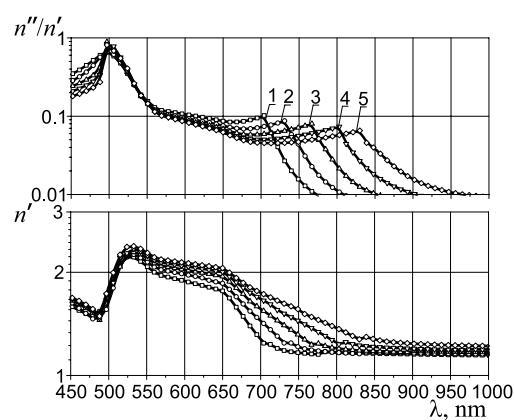


Figure 5: Dispersion curves of the mode EH_{11} of the waveguide calculated by FEM with gold shell thickness $d = 40$ nm and different core radii R_1 : 1 — 80 nm, 2 — 90 nm, 3 — 100 nm, 4 — 110 nm, 5 — 120 nm.

surface plasmon-polaritons (E -waves) localized near the boundary of ZnO-Ag can be excited in wavelength range where $n > n_{\text{ZnO}}$. When the refractive index $n < n_{\text{ZnO}}$, the volume wave localizes in the waveguide and decreases exponentially outside it. The waveguide properties don't depend on thickness of the silver shell d , when the thickness d is greater than 30 nm. The properties of the metal in optical waveband will close to microwave waveband when the wavelength increases. Therefore, the fundamental wave mode in the bilayered waveguide ZnO-Ag in contrast to a dielectric waveguide has a limited critical wavelength.

The dispersion curves in Fig. 2 with a shell thickness $d = 35$ nm (curve 6) and 15 nm (curve 7) are computed by COMSOL MultiphysicsTM platform of finite-element physics-based modeling and simulation. As the advantages of using the finite element method (FEM) for the numerical calculation of the optical layered structures properties [10], we may highlight the conservatism and high stability of the numerical method, the ability to solve problems with a complicated geometry and to reduce the mesh in those places where special care isn't required. Comparing the data of curves 2 and 3, 6 and 7, we can see that the results are in good agreement with the results of simulation in COMSOL MultiphysicsTM. Dispersion characteristics are calculated by FEM have minor differences in the waveband close to the critical wavelength.

If we increase waveguide radius as shown in Fig. 3, the wave retardation coefficient will increase too and the losses will become considerably lower.

The wave mode EH_{11} has a strong field localization in the waveguide in optical wavelength range, thus the dispersion properties of a periodic waveguide array as shown in Fig. 4 have a very weak dependence on the distance between nanorods.

The Fig. 5 shows the dispersion curves have significant differences compared with similar characteristics at Fig. 3 for waveguides with a silver shell, because the complex dielectric constant of gold and silver are essentially different.

4. CONCLUSION

For a quantitative estimate the resonant wavelengths of optical nanoantennas should be interpreted them as resonances of double-layer nanowaveguide segments composed of the ZnO core and the thin metal shell excited an integer number of half wavelengths of the waveguide.

The resonances of a periodic waveguide array with average distance between adjacent nanorods 700 nm were presented in paper [1] on wavelengths: 550 nm, 650 nm, 890 nm and 1340 nm. The quantitative estimate calculated by the method described in this paper and by the COMSOL MultiphysicsTM gives values of 500–550 nm, 600–670 nm, 780–800 nm and 1400–1420 nm.

The results discussed in this paper may be used to predict the resonant wavelengths of two-dimensional periodic array of ZnO nanorods grown on a dielectric substrate.

ACKNOWLEDGMENT

The authors acknowledge the support of the Ministry of Education and Science, provided by grant 16.219.2014/K, and the part of the Internal Grant project of Southern Federal University in 2014–2016y., provided by grant 213.01.-07.2014/08PCHVG, for carrying out this research study.

REFERENCES

1. Kaidashev, E. M., N. V. Lyanguzov, A. M. Lerer, and E. A. Raspopova, “Experimental and theoretical investigation of silver-coated ZnO nanorod arrays as antennas for the visible and near-IR spectral range,” *Technical Physics Letters*, Vol. 40, No. 7, 79–86, 2014.
2. Rakic, A. D., A. B. Djuricic, J. M. Elazar, and M. L. Majewski, “Optical properties of metallic films for vertical-cavity optoelectronic devices,” *Applied Optics*, Vol. 37, No. 22, 5271–5283, 1998.
3. Dai, Z. H., R. J. Zhang, J. Shao, Y. M. Chen, Y. X. Zheng, J. D. Wu, and L. Y. Chen, “Optical properties of zinc-oxide films determined using spectroscopic ellipsometry with various dispersion models,” *J. Korean Phys. Soc.*, Vol. 55, No. 3, 1227–1232, 2009.
4. Lorenz, M., A. Rahm, B. Cao, Z. P. Jesus, E. M. Kaidashev, N. Zhakarov, G. Wagner, T. Nobis, C. Czekalla, G. Zimmermann, and M. Grundmann, “Self-organized growth of ZnO-based nano- and microstructures,” *Phys. Status Solidi B*, Vol. 247, No. 6, 1265–1281, 2010.
5. Lyanguzov, N. V., V. E. Kaydashev, I. N. Zakharchenko, Y. A. Kuprina, O. A. Bunina, Y. I. Yuzyuk, A. P. Kiselev, and E. M. Kaidashev, “Use of various growth catalysts for laser sputtering of ZnO micro- and nanorods,” *Technical Physics*, Vol. 57, No. 4, 534–542, 2012.
6. Mayer, S. A., *Plasmonics: Fundamentals and Applications*, Springer, New York, 2007.
7. Lavrentiev, M. A. and B. V. Shabbat, *Methods of the Theory of Functions of a Complex Variable*, Nauka, Moscow, 1965.
8. Lerer, A. M., I. V. Donets, G. A. Kalinchenko, and P. V. Makhno, “Theoretical investigation of nanoplasmonic waveguide structures,” *Electromagnetic Waves and Electronic Systems*, Vol. 18, No. 9, 5–13, 2013.
9. Lerer, A. M., I. V. Donets, G. A. Kalinchenko, and P. V. Makhno, “Volume integral method for investigation of plasmonic nanowaveguide structures and photonic crystals,” *Photon. Res.*, Vol. 2, No. 1, 31–37, 2014.
10. Hoffmann, J., C. Hafner, P. Leidenberger, J. Hesselbarth, and S. Burger, “Comparison of electromagnetic field solvers for the 3D analysis of plasmonic nano antennas,” *Proceedings of SPIE7390, Modeling Aspects in Optical Metrology II*, Vol. 3790, 73900J-1–73900J-11, Munich, Germany, Jun. 2009.

Dynamical Evolution of the Laser Linewidth at Switch-on

G. P. Puccioni¹, N. Dokhane², and G. L. Lippi^{3,4}

¹Istituto dei Sistemi Complessi, CNR, Italy

²Department of Physics, Faculty of Science, University of M'Hamed Bougara, Algeria

³Institut Non Linéaire de Nice, Université de Nice-Sophia Antipolis, France

⁴UMR 7335 CNRS, France

Abstract— We investigate the dynamical evolution of the spectrum of a homogeneously broadened (semiconductor) laser switched from far below-threshold to above threshold. Four dynamical regimes are identified with spectral features which remain hidden in a standard detection based on the total laser output.

1. INTRODUCTION

Lasers have been studied for over fifty years and much work has been devoted to understanding and characterizing their main features: their narrow linewidth and threshold properties, thus also their efficiency. Although the first realization of a diode laser dates back to 1962 [1], semiconductor lasers have taken a leading role in the 1980's thanks to considerable technological advances and to their potential for telecommunications. These efforts have been well-rewarded and nowadays semiconductor lasers are ubiquitous both for their direct applications (e.g., telecommunications) and for their *support* role (e.g., pump lasers). Curiously, some of the questions we address in this paper do not seem to have received a large amount of attention, or have found only partial answers which can be tracked to separate papers published over the years.

Here, we present an overview of the questions pertaining the *average, macroscopic* evolution of the laser field intensity starting from below threshold until the equilibrium distribution of emission is reached above threshold, where equilibrium is to be intended as dynamically stationary both for the emitted power and for the spectral distribution. We achieve this goal by analyzing the growth of an ensemble of modes for a multimode laser, described by a standard rate-equation model [2], which are used to monitor at the same time the dynamics of the emitted power and its spectral distribution. Indeed, the analysis is carried out by considering a very large number of cavity modes, chosen to give a good sampling of the spontaneous linewidth (113 modes in the numerical simulations), and following their temporal evolution (and extinction for most of them) towards the above-threshold emission. In this paper, we present a physical discussion of the various aspects of the dynamics, leaving the laborious technical aspects of the analysis to papers already published or in progress.

2. FROM BELOW TO ABOVE THRESHOLD

We consider the transition from the average equilibrium distribution of radiation below threshold, which reflects the average spontaneous emission seeded into the lasing modes, to the equilibrium, above threshold emission — i.e., after all transients in the total emission and in the individual mode emission (thus, in the spectral distribution) have died out. As already mentioned, we use a dense and extended longitudinal cavity mode distribution to obtain a detailed picture of those components which eventually disappear when stable lasing occurs.

The transition is obtained by applying a sudden change (Heaviside function) to the pump rate in a standard rate-equation model [2]. Although some of the results we obtain may be somewhat model-dependent, it is well-established that rate equations provide a very robust underlying dynamical structure, thus reliable predictions. In the following, we will use interchangeably the concept of modal or spectral dynamics, since the former represents a discrete sampling of the latter and is the tool we use to efficiently follow the changes in the optical spectrum. However, here we will focus on the *spectral* aspects, while in the more technical papers we use the modal approach to quantitatively analyze the details of the dynamics.

To better place the problem into context, we are going to discuss the spectral evolution of the laser emission (curve a in Fig. 1(a)) compared to the standard picture of the transient, as provided by the output of a detector placed in front of the laser. Four different regimes of operation can be identified, as summarized in Fig. 1(a):

- I. below transparency, the evolution of the spectrum (i.e., represented by the growth of the individual modes) is characterized by a slight broadening, rather than narrowing, due to the reduced amount of absorption in the wings (Fig. 1(b), curve a). Thus, the spectral line slightly deforms given that the wing modes experience a somewhat larger differential growth (Fig. 6 in [3]).
- II. The differential gain (Fig. 6 in [3]) now privileges the central modes and the actual mode selection process *begins* to take place, however, in this region, the dynamics of the carrier density (i.e., population inversion in a generic laser) are decoupled from those of the modal intensity (i.e., the electromagnetic — e.m. — field emission) [4–8] and its evolution can be studied independently. The spectral emission (curve b in Fig. 1(b)) is slightly narrower than that of the spontaneous emission below threshold, but differs entirely from that of the true lasing action. What may appear counterintuitive, but can be numerically and analytically [3] proven to hold, is that this region extends to e.m. intensity values which are not negligible (Fig. 1(a)) and may amount to up to 10–20% of the peak value.
- III. This region is characterized by a very strong growth of the field intensity and by the interdependent oscillations which take place between the total e.m. field emission and the carrier density (relaxation oscillations, cf. curves a and b in Fig. 1(a)). What is hidden by the traditional outlook based on the description of the total intensity growth, is the fact that the spectral width in this regime is still very large. Further, the intermodal dynamics, i.e., the spectral features, display an unexpected behaviour [3].
- IV. When looking at the total emitted power, e.g., the signal coming from a detector, one concludes that the laser has reached steady state emission at the end of Region III and that this fourth region, which occupies a very considerable fraction of the transient evolution from below to above threshold (over 90% of the time interval) has no place in a dynamical description. This mistaken impression comes from the observation of the total intensity, rather than the modal intensities (or spectral features). Curve c in Fig. 1(a) shows the evolution of the central mode, i.e., the one which eventually dominates the emission. During the relaxation oscillations this mode carries a fraction of the modal power which is well below its equilibrium contribution (e.g., compare peak emission in Fig. 1(a), curves a and c or spectral contributions at line

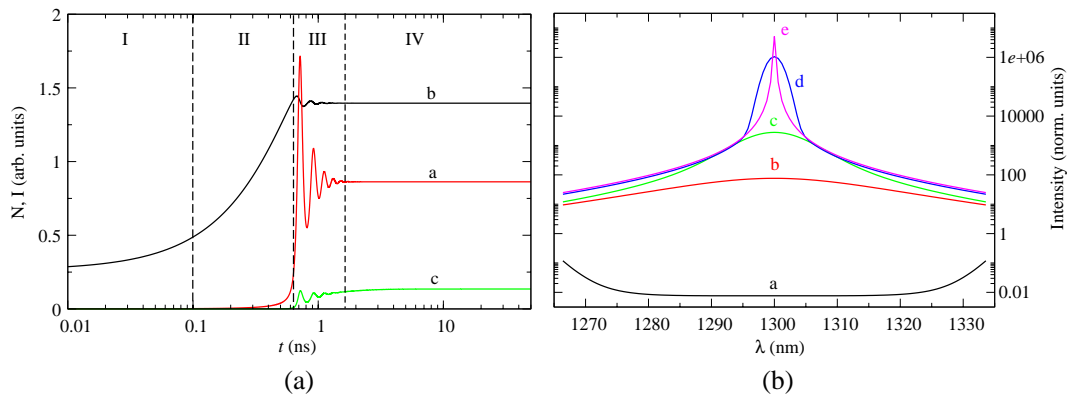


Figure 1: (a) Schematic representation of the four regimes which occur in the transition between the below-threshold and the above-threshold stationary spectral distributions when switching on a laser. Total intensity a, as measured by a detector placed in front of the laser, computed on the basis of a standard rate equation model [2]. A pump step is applied at time $t = 0$ to bring the laser from below to above threshold (parameters as in [9]). Curve b represents the carrier density (or population inversion), while curve c displays the temporal evolution of the central lasing mode. Notice the use of a logarithmic scale for time to better display the various regimes. For graphical purposes, both intensities a and c are divided by 10^5 , while the carrier number b is divided by 10^8 . (b) Evolution of the spectral distribution of the laser emission (representing the lineshape). Curve a is the initial, below threshold equilibrium distribution (lateral increase due to reduced off-resonance absorption in the modeling choice [2]). Spectrum b corresponds to the crossing of the stationary threshold (i.e., shortly before the end of Region II), while c is the spectrum at the intensity peak (curve a in (a)). Spectrum d corresponds to the end of Region III, i.e., at the end of the relaxation oscillations, while the stationary (narrow-line) spectrum e is attained only at the end of Region IV. For details cf. [3, 9].

center in Fig. 1(b), curves c and e). The evolution of the spectrum throughout Region IV is very slow but leads to a substantial change in lineshape (cf. curves d and e in Fig. 1(b)). This dynamical (apparent) *peculiarity* is thoroughly discussed in [9].

This description highlights the underlying complexity of the evolution which takes place between the initial, below threshold, equilibrium spectral distribution and the corresponding equilibrium state above threshold. The analysis is done using semiconductor laser parameters, but it qualitatively holds for any other kind of device with homogeneous emission linewidth.

Below, we offer some details about the physics characterizing each region. For Region I it suffices to realize that the, at first sight counterintuitive, broadening and deformation of the emission line is due to the (standard) modeling choices which give a larger differential increase of photons in the spectral wings of the intracavity laser field because of the reduced absorption below transparency.

3. REGION II

In the single-mode picture of any laser representation, one considers this region as the latency regime [10] of a Class B laser [11] where the carriers (or population inversion) accumulate at their own rate before attaining the threshold value. This simplified representation, although effective, does not provide information about the line reshaping. Direct numerical simulations, well supported by an analytical solution of the carrier density growth [3], show that the linewidth at the instant where the static threshold is crossed (i.e., when the carrier density dynamically crosses its asymptotic value for the first time) is still approximately half the initial linewidth (curve b in Fig. 1(b)). Thus, even though some linewidth reduction takes place due to the frequency-selective growth in the presence of the cavity feedback, its effect is largely insufficient to ensure the final spectral purity which is attained at steady state operation. This is not surprising, given that stimulated emission has not yet really taken hold. As already mentioned, the decoupled regime, where the stimulated emission follows the carrier density without appreciably influencing it, extends to e.m. field intensity values well in excess of what one would reasonably consider a negligible perturbation (cf. total intensity value a at the transition between Regions II and III, compared to its asymptotic value in Region IV).

4. REGION III

From the point of view of a global description (i.e., the output measured by the detector) this is the crucial region, since most of the field intensity growth and its relaxation to the asymptotic state take place here. The quadrature oscillations between the total intensity (curve a, Fig. 1(a)) and the carrier density b, damped within a few cycles are characteristic of the turn-on of any Class B laser.

However, the spectral evolution shows a much more complicated picture. First, a nonnegligible ensemble of cavity modes participates in the peak. This is a direct consequence of the residual linewidth, but its existence is entirely hidden in the internal dynamics, which is not normally visible. A hint of the complexity of the problem can be had by comparing the evolution of the total intracavity field b to that of the central mode c. In the oscillatory regime, the central mode's peak does not even reach its asymptotic value (at $t = 20$ ns), while the total intensity has a peak which is double as large. This implies that other modes play a dominant role in the dynamics, with peak intensities which overcome their stationary values by more than a factor 2 (to compensate for the central mode(s) for which we observe a power defect).

This is indeed the case, as shown in [3]. Lateral modes, symmetrically placed a few units from line center (≈ 4 nm far away) carry the largest peaks (Fig. 11 in [3]). The dynamics are therefore dominated by this set of modes which deform the transient spectral distribution of the e.m. radiation. This larger differential gain for the side modes is accompanied by a larger relaxation oscillation frequency and stronger damping (Fig. 12 in [3]).

Looking at the spectral distribution provides a complementary picture of the this discussion since a substantial amount of line reshaping takes place in this region. Curves b–d (Fig. 1(b)) show three different spectral distributions, at the beginning b, at the e.m. intensity peak c and at the end d of Region III, respectively. The emergence of the peak is clearly due to a differential growth of the central modes, without a strong domination of the centre one. Indeed, in the very short time interval between the start of Region III and the total intensity peak (a in Fig. 1(a)) the spectrum evolves from b to c (Fig. 1(b)) showing a wideband evolution of the intensity distribution. Interestingly, we notice that the spectral components located between 5 and 10 nm from linecenter

(i.e., between 8 and 17 modes away from the central one) reach their steady state value already at the total intensity peak occurrence! During the relaxation oscillation phase the group of modes closer to line center (i.e., ± 7 modes) substantially grow (a few order of magnitudes!), however without any strong mode selection. The line shape which pops out of the “background” — bearing the approximate features of a very wide gaussian — vaguely resembles a gaussian (in semilogarithmic scale) with spectral width in the nanometer range. Notice that during the relaxation oscillations the far wing-modes keep growing until they reach their steady state contribution.

5. REGION IV

The observation of the total laser output (curve a, Fig. 1(a)) states that the transition is completed at the end of Region III and that the laser has reached its equilibrium above-threshold state. Comparison with the computed dynamics of the carrier density (or population inversion, in a generic laser) confirms this assertion b. Observation of the side modes [3, 9], instead, contradicts this statement since the modal dynamics is not yet complete. Curve c in Fig. 1(a) clearly shows that the central mode is steadily growing in Region IV (reaching its steady state at the end of the figure). For quantitative comparison, the vertical scale in the figure has been chosen to be the same for the two intensities and thus does not allow for a clear view of the central mode’s growth. Notice also that, in order to better display the various regimes in a single figure, the time axis is plotted in logarithmic scale. Thus, the temporal dynamics appears compressed in its latter parts, while instead it occupies approximately 90% of the transient.

The deficit in power carried at line center, which amounts to saying that the line narrowing has not yet been completed at the beginning of Region IV, implies that the energy distribution is still far from its equilibrium value. Whence the existence of the residual dynamics which connects the *final* spectral distribution at the end of Region III to the asymptotic, equilibrium one typical of the laser lineshape. It is important to notice that, since the total intensity (curve a in Fig. 1(a)) shows a deficit, other modes must carry an excess of power at the beginning of the relaxation period, Region IV. This is indeed the case [9]. Inspection shows a close connection between the faster relaxation (cf. Figs. 11 and 12 of [3]), due to stronger growth and faster damping of selected side modes, and the amount of energy they carry at the end of the relaxation oscillations for the total intensity a. Thus, in Region IV. some modes decay away, while others (the central ones) grow towards their asymptotic value. The spectral picture, Fig. 1(b), confirms this analysis since it shows that strong line narrowing takes place in Region IV (compare curves d, at the beginning, and e at the end of the time interval), characterized by a substantial growth of the central mode and by a very strong decay of most of the modes which have contributed to the fast settling of the relaxation oscillations.

The slow growth, compared to the rest of the very fast dynamics, may appear at first to be quite puzzling, since it results from the laser response to the step-like increase of the pump rate to bring the laser from below to above threshold. One wonders why the laser should at first react fast and why the total e.m. energy settles to its equilibrium state in a time scale which is approximately one order of magnitude faster than the corresponding spectral content. After all, one would intuitively expect that, since the laser emission is dominated by one (or at most a few) mode(s), the temporal response of the ensemble should not differ too drastically from that of the individual mode(s) characterizing the laser performance above threshold.

An in-depth analysis shows that, within the framework of rate-equation models — giving in this context a rather accurate picture of reality —, the actual modal relaxation/growth rates structurally depend on the distance from line center through a combination of losses and gain (Section IV in [9] and Section III in [3]). This can be easily recognized by looking at the (approximate) structure of the dynamical equations for the modal intensities [3]:

$$\frac{dI_j}{dt} \approx [\alpha_j \mathcal{N}(t) - \mathcal{K}_j] I_j + B_j \mathcal{F}(\mathcal{N}(t)), \quad (1)$$

$$\mathcal{K}_j = \alpha_j N_0 + \frac{1}{\tau_p}; \quad B_j = \beta_j B; \quad \alpha_j = \Gamma g_p \left[1 - 2 \left(\frac{\lambda_j - \lambda_p}{\Delta \lambda_G} \right)^2 \right], \quad (2)$$

where I_j represents the intensity of the j -th mode, \mathcal{N} the carrier density, α_j is the modal gain, \mathcal{K}_j is the effective relaxation mode constant, B_j is the modal spontaneous emission coupling coefficient, $\mathcal{F}(\mathcal{N}(t))$ the (average) spontaneous emission factor, Γ the cavity confinement, g_p the gain, λ_j and λ_p represent the modal and peak wavelengths, respectively, $\Delta \lambda_G$ the linewidth, τ_p the cavity lifetime

and β_j the fraction of spontaneous emission coupled into the j -th mode. Since spontaneous emission is added to each mode but varies only very slowly, the equilibrium condition — corresponding to $\frac{dI_j}{dt} = 0$ — implies that the bracket for the central mode (always a negative number) is the least negative (Table I in [9]) — i.e., the smallest number if absolute value —. Thus the corresponding time scale is the slowest. Since the slowest mode dominates the evolution and acts as a Master Mode [12], the slow convergence of the spectrum is thus explained.

6. CONCLUSION

In conclusion, with the help of a detailed numerical analysis we have shown that the transient from the initial to the final equilibrium states in a laser is characterized by several regimes with a dynamics far more complex than the one monitored by the simple output power. Surprising spectral features are identified in the various transient regimes.

ACKNOWLEDGMENT

We are grateful to S. Balle, M. Brambilla, C. R. Mirasso, M. San Miguel, and J. R. Tredicce for helpful discussions.

REFERENCES

- Hall, R. N., G. E. Fenner, J. D. Kingsley, T. J. Soltys, and R. O. Carlson, “Coherent light emission from GaAs junctions,” *Phys. Rev. Lett.*, Vol. 9, No. 9, 366–368, 1962.
- Byrne, D. M., “Accurate simulation of multifrequency semiconductor laser dynamics under gigabits-per-second modulation,” *J. Lightwave Technol.*, Vol. 10, No. 8, 1086–1096, 1992.
- Puccioni, G. P. and G. L. Lippi, “Fast dynamics and spectral properties of a multilongitudinal-mode semiconductor laser: Evolution of an ensemble of driven, globally coupled nonlinear modes,” *Physics Optics*, arXiv: 1401.4947v1, Jan. 20, 2014.
- Zhang, X. X., W. Pan, J. G. Chen, and H. Zhang, “Theoretical calculation of turn-on delay time of VCSEL and effect of carriers recombination,” *Optics & Laser Technol.*, Vol. 39, 997–1001, 2007.
- Ab-Rahman, M. S. and M. R. Hassan, “Temperature dependence of turn-on time delay of semiconductor laser diode: Theoretical analysis,” *Opto-Electron. Rev.*, Vol. 18, No. 4, 458–466, 2010.
- Ab-Rahman, M. S. and M. R. Hassan, “Theory of shutdown of semiconductor laser source remotely,” *J. Opt. Soc. Am. B*, Vol. 27, No. 8, 1626–1633, 2010.
- Ab-Rahman, M. S. and M. R. Hassan, “The combined effect of temperature of operation and external optical feedback on the turn-on time delay of semiconductor laser diodes,” *Optik*, Vol. 122, No. 3, 266–272, 2011.
- Hisham, H. K., A. F. Abas, G. A. Mahdiraji, M. A. Mahdi, and A. S. Muhammad Noor, “Comment on: Theoretical calculation of turn-on delay time of VCSEL and effect of carriers recombination,” *Optics & Laser Technol.*, Vol. 44, No. 6, 1995–1998, 2012.
- Dokhane, N., G. P. Puccioni, and G. L. Lippi, “Slow dynamics in semiconductor multi-longitudinal-mode laser transients governed by a master mode,” *Phys. Rev. A*, Vol. 85, No. 4, 043823(1–9), 2012.
- Lippi, G. L., S. Barland, N. Dokhane, F. Monsieur, P. A. Porta, H. Grassi, and L. M. Hoffer, “Phase space techniques for steering laser transients,” *J. Opt. B: Quantum Semiclass. Opt.*, Vol. 2, No. 3, 375–381, 2000.
- Tredicce, J. R., F. T. Arecchi, G. L. Lippi, and G. P. Puccioni, “Instabilities in lasers with an injected signal,” *J. Opt. Soc. Am. B*, Vol. 2, No. 1, 173–183, 1985.
- Haken, H., *Synergetics: An Introduction*, Springer, Berlin, 1978.

Transmission Properties of THz Silicon Photonic Crystal Fiber

Abdosllam M. Abobaker¹, E. Gunasundari², K. Senthilnathan², S. Sivabalan³,
K. Nakkeeran⁴, and P. Ramesh Babu²

¹Department of Communications Engineering, College of Electronic Technology, Bani Walid, Libya

²Photonics, Nuclear and Medical Physics Division, School of Advanced Sciences
VIT University, Vellore 632 014, India

³School of Electrical Engineering, VIT University, Vellore 632 014, India

⁴School of Engineering, University of Aberdeen, Aberdeen AB24 3UE, UK

Abstract— In this paper, using finite element method, we design a novel photonic crystal fiber which acts as a terahertz (THz) silicon waveguide. We study the important transmission properties, namely, group velocity dispersion (GVD), absorption coefficient, effective mode area and effective nonlinearity by varying the core diameter and distance between two consecutive air-holes for a wide range of frequency from 0.5 to 10 THz. The proposed THz silicon PCF exhibits three zero dispersions at 1.75, 4.8 and 7.8 THz frequencies. Further, we report a low absorption coefficient of 10^{-4} cm^{-1} in a broad frequency region (2.5 to 10 THz). We obtain a large mode area of 325 mm^2 at 0.5 THz frequency for the core diameter of 0.9 mm and the pitch of 3 mm. These results show that the proposed THz silicon PCF (THz-SPCF) would turn out to be a good candidate for THz waveguide compared to other plastic THz waveguides.

1. INTRODUCTION

THz radiation lies between electronic and optical region in the electromagnetic spectrum with frequencies ranging from 300 GHz to 10 THz. In recent years, THz regime has gained impetus as it finds applications in various important fields such as imaging, astronomy, communications, pharmaceutical quality control, etc. [1–3]. For the successful implementation of THz systems, low loss and commercially viable waveguides are essential. To date, most of the THz systems rely on free space propagation due to the virtual absence of low-loss waveguides at THz frequencies. In general, plastic, metallic ribbon waveguides and polymer PCFs have demonstrated THz guidance and they are fabricated using the drill and draw, stack and fuse technology [4–8]. Very recently, there have been reports of using plastic PCFs as THz waveguides [9, 10]. PCFs consisting of a waveguiding core and a cladding layer with spatially periodic air holes are currently another subject of intensive research, because a number of unusual properties, such as endlessly single mode, tailorable dispersion, and controllable mode area, have been demonstrated with such fibers [11–13]. The reported PCFs for THz frequencies were based on high-density polyethylene or polytetrafluorethylene (Teflon) both of which have low loss in the THz regime [6, 9, 10]. Thus, reasonably long and low-loss terahertz photonic crystal fibers (TPCFs) have been realized. In view of the rapid progress in both the THz and the PCF fields, TPCFs with better-controlled properties can be envisaged.

In this paper, we analyze the transmission properties using a new kind of silicon triangular PCF with low loss teflon. Compared to the conventional optical fibers, our newly designed silicon triangular PCF has many advantages, namely, less absorption loss, larger nonlinear refractive index than that of silica and stronger light confinement. The paper is laid out as follows. In Section 2, we discuss the design of a THz-SPCF using a fully-vectorial finite element method. We study the transmission properties of THz-SPCF including GVD, absorption loss, effective mode area and nonlinearity by varying the core diameter and lattice constant between the two consecutive air-holes for a wide range of frequencies in Section 3. Finally, we summarize the findings in Section 4.

2. DESIGN OF THE PROPOSED THZ-SPCF

Figure 1(a) shows the geometrical cross-section of the proposed THz-SPCF. The PCF is an index guided one wherein the core material is of silicon with air holes distributed in the cladding. The core region can have a higher effective index than the cladding region, and by a modified total internal reflection principle, THz waves can be effectively confined in the core region as guiding modes. In this structure, the cladding of the PCF consists of five rings of air holes distributed in a triangular pattern around the core region. In general, the number of air hole rings in the cladding decides the confinement loss and in this work, we optimize the number of rings to five for ensuring better light confinement. In this design, as the air-filling fraction (d/Λ) is kept as 0.3. Here, we

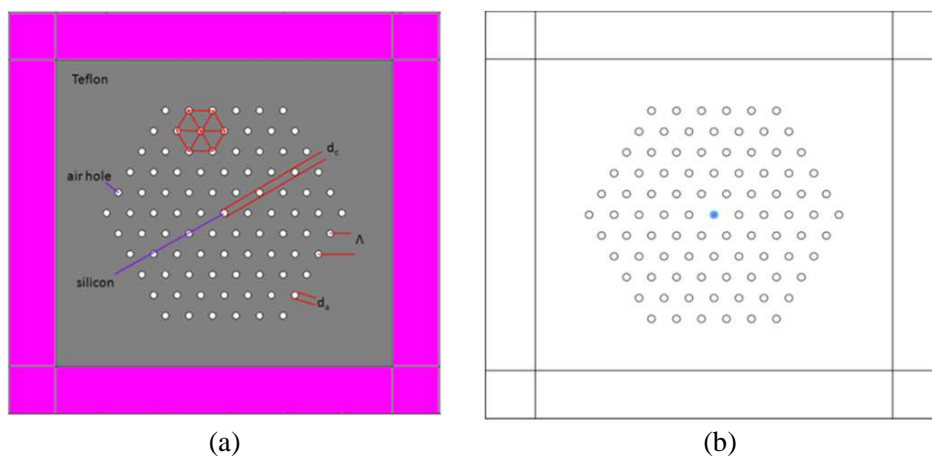


Figure 1: (a) Geometrical structure of the proposed fiber and (b) mode field distribution at 3 THz frequency for $d_c = 0.6$ mm and $\Lambda = 3$ mm.

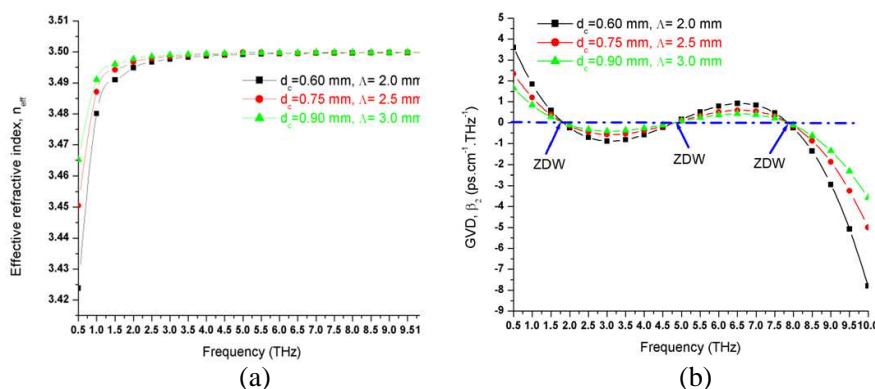


Figure 2: (a) Variations of effective refractive index and (b) GVD of the proposed THz-SPCF for different core diameters and air-hole distances.

study the transmission properties for the various air-hole diameters (0.6, 0.75 and 0.9 mm) with various pitch (2, 2.5 and 3 mm) for a wide range of frequency from 0.5 to 10 THz. A full-wave finite element method is used to systematically analyze the transmission properties of the THz-SPCF. In the calculation, perfectly matched layers are used as the absorbing boundary. The refractive indices of the dielectric material, core material and the air holes are 1.5, 3.5 and 1, respectively. To simplify the analysis, material dispersion is neglected. Figure 1(b) illustrates the mode field distribution in contour view at 3 THz frequency when the core diameter is 0.6 μ m. In order to determine the dispersion of THz-SPCF, it is necessary to compute the effective refractive index of the fundamental mode.

In Figure 2(a), we plot the effective index as a function of frequency for various core diameters and pitch. The effective index is calculated for a range of frequencies from 0.5 to 10 THz. From the Figure 2(a), as the frequency increases, the effective index of the fundamental mode increases slowly up to 3 THz due to small amount of light spreading towards the silicon core boundary. It may be noted here that the effective index of the fundamental mode is less than the silicon effective index. Further, with the increment in frequency, the effective index of the fundamental mode is almost equal to silicon refractive index due to tight confinement of light within the core. However, as the frequency is increased further, the modal field is tightly bounded within the center of the silicon core. So, the effective index becomes constant for a broad range of frequencies from 3 to 10 THz.

3. TRANSMISSION PROPERTIES OF THZ-SPCF

In general, the dispersion is the main reason for pulse broadening which restricts the transmission speed in communication systems. As mentioned above, the material used here has a negligible material dispersion, so a near-zero waveguide dispersion becomes essential. The waveguide dispersion depends on the geometry of the fiber, specifically the air hole pitch, Λ and the diameter of the core,

d_c . The GVD, β_2 (ps/THz.cm), is determined from the second derivative of the effective mode index as a function of the frequency. We use the following equation for determining the GVD [14],

$$\beta_2 = \frac{1}{c} \left[2 \frac{dn_{eff}}{d\omega} + \omega \frac{d^2 n_{eff}}{d\omega^2} \right], \quad (1)$$

where $\omega = 2\pi f$ and $n_{eff} = \text{Re}(\beta)c/\omega$ denotes the real part of the effective refractive index of the mode and c is the velocity of light in vacuum. Figure 2(b) shows the variations of dispersion parameter β_2 with frequency for different values of pitch, Λ by keeping d_c and the filling factor, d/Λ as constant. The proposed fiber exhibits three zero dispersion frequencies (ZDFs) and they are 1.75, 4.8 and 7.8 THz for different values of Λ . The loss is an important parameter due to the large size (mm) of the THz-SPCF. Since the propagation loss is the main reason for the power dissipation of the guided THz waves due to the material absorption. The confinement loss is very low compared to the material absorption. So, we ignore the confinement loss in this paper. According to perturbation theory, relative absorption loss for the fundamental modes of the proposed THz-SPCF can be expressed by [15],

$$L_{abs} = \frac{\alpha_{mod}}{\alpha_{mat}} = \sqrt{\frac{\epsilon_0}{\mu_0}} \frac{\int_{background} n_b |E|^2 dA}{\left| \int_{all} S_z dA \right|}, \quad (2)$$

where n_b is the refractive index of the background dielectric material, α_{mod} is the absorption coefficient for the fundamental polarization modes, and α_{mat} is the bulk material absorption coefficient

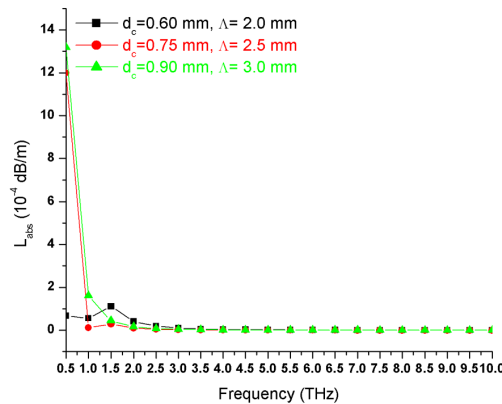


Figure 3: Variations of absorption loss of the proposed THz-SPCF for different core diameters and air-hole distances.

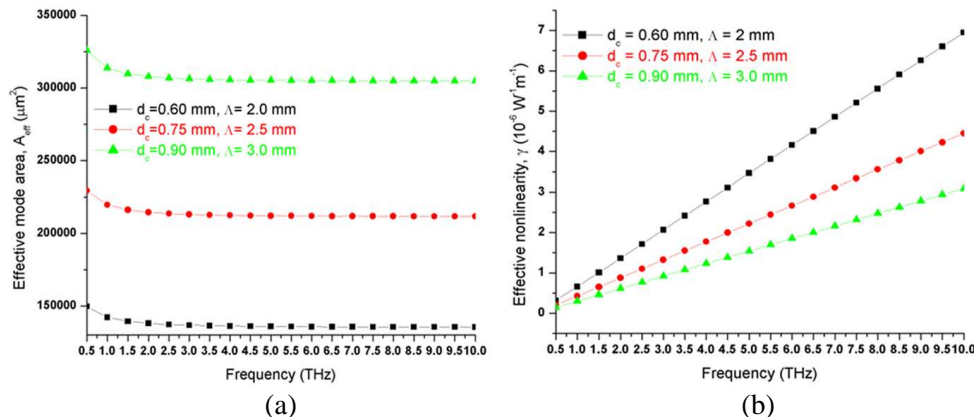


Figure 4: (a) Variations of effective mode area and (b) variations of effective nonlinearity for various core diameters and air-hole distances.

of the dielectric material. Although α_{mat} is related to the frequency dependent on the dielectric material, the relative absorption loss $\alpha_{mod}/\alpha_{mat}$ is dependent on the parameters of the fiber only. The variation of absorption loss for various fiber parameters is shown in Figure 3. The absorption loss is very high for lower frequency due to the fundamental mode residing mostly in the solid silicon core. The absorption loss is almost constant for various fiber diameters for a wider range of frequencies from 2 to 10 THz which is evident in Figure 3.

The nonlinear coefficient of a THz-SPCF can be calculated as follows:

$$\gamma = \frac{\omega n_2}{c A_{eff}} \quad (3)$$

where n_2 is the nonlinear index coefficient and the value of n_2 is $4 \times 10^{-18} \text{ m}^2/\text{W}$, c is the speed of light in vacuum, and A_{eff} is the effective mode area of the proposed fiber. As the air-hole diameter becomes larger, although more energy of the THz-wave could be confined in the core areas of this PCF, A_{eff} is larger, which leads to a low nonlinearity as shown in Figures 4(a) and (b).

4. CONCLUSION

In this paper, we have proposed a novel air-clad silicon photonic crystal fiber and studied the transmission properties for different core diameters using fully-vectorial finite element method. We have been able to achieve three zero dispersions at 1.75, 4.8 and 7.8 THz frequencies and also report a low absorption coefficient of 10^{-4} cm^{-1} in a broad frequency region (2.5 to 10 THz). We expect that these desired optical properties that have been investigated would be useful in photonic device applications.

ACKNOWLEDGMENT

KSN wishes to thank CSIR [No. 03(1264)/12/EMR-II] and DST [No. SR/FTP/PS-66/2009], Government of India, for the financial support through the sponsored projects. SS wishes to thank DST [No. SR/S2/LOP-0014/2012], Government of India, for the financial support through the sponsored project.

REFERENCES

1. Chan, W. L., J. Deibel, and D. M. Mittleman, "Imaging with terahertz radiation," *Rep. Prog. Phys.*, Vol. 70, 1325–1379, 2007.
2. Strachan, C. J., P. F. Taday, D. A. Newnham, K. C. Gordon, J. A. Zeitler, M. Pepper, and T. Rades, "Using terahertz pulsed spectroscopy to quantify pharmaceutical polymorphism and crystallinity," *J. Pharm. Sci.*, Vol. 94, No. 4, 837–846, 2005.
3. Abbott, D. and X. C. Zhang, "Scanning the issue: T-ray imaging, sensing, and retection," *Proc. IEEE*, Vol. 95, No. 8, 1509–1513, 2007.
4. Mendis, R. and D. Grischkowsky, "Plastic ribben THz waveguide," *J. Appl. Phys.*, Vol. 88, 4449–4451, 2000.
5. Wang, K. and D. M. Mittleman, "Metal wires for terahertz waveguiding," *Nature*, Vol. 432, 376–379, 2004.
6. Goto, M., A. Quema, H. Takahashi, S. Ono, and N. Sarukura, "Teflon photonic crystal fiber as terahertz waveguide," *Jpn. J. Appl. Phys.*, Vol. 43, L317–L319, 2004.
7. Nielsen, K., H. K. Rasmussen, A. J. L. Adam, P. C. Planken, O. Bang, and P. U. Jepsen, "Bendable, low-loss Topas fibers for the terahertz frequency range," *Opt. Express*, Vol. 17, No. 10, 8592–8601, 2009.
8. van Eijkelenborg, M. A., M. C. J. Large, A. Argyros, J. Zagari, S. Manos, N. A. Issa, I. Bassett, S. Fleming, R. C. McPhedran, C. Martijn de Sterke, and N. A. P. Nicorovici, "Microstructured polymer optical fiber," *Opt. Express*, Vol. 9, No. 7, 319–327, 2001.
9. Park, H., M. Cho, J. Kim, and H. Han, "Terahertz pulse transmission in plastic photonic crystal fibres," *Phys. Med. Biol.*, Vol. 47, No. 21, 3765–3769, 2002.
10. Han, H., H. Park, M. Cho, and J. Kim, "Terahertz pulse propagation in a plastic photonic crystal fiber," *Appl. Phys. Lett.*, Vol. 80, 2634–2636, 2002.
11. Birks, T. A., J. C. Knight, and P. S. Russell, "Endlessly single-mode photonic crystal fiber," *Opt. Lett.*, Vol. 22, No. 13, 961–963, 1997.

12. Knight, J. C., J. Arriaga, T. A. Birks, A. Ortigosa-Blanch, W. J. Wadsworth, and P. S. Russell, “Anomalous dispersion in photonic crystal fiber,” *IEEE Photon. Technol. Lett.*, Vol. 12, No. 7, 807–809, 2000.
13. Ferrando, A., E. Silvestre, J. J. Miret, and P. Andres, “Nearly zero ultraflattened dispersion in photonic crystal fibers,” *Opt. Lett.*, Vol. 25, No. 11, 790–892, 2000.
14. Agrawal, G. P., *Nonlinear Fiber Optics*, Academic Press, 2007.
15. Snyder, A. W. and J. D. Love, *Optical Waveguide Theory*, Chapman Hall, New York, 1983.

Collapse of Nonlinear Terahertz Pulses in n -InSb

C. Castrejon-Martinez, V. Grimalsky, S. Koshevaya, and J. Escobedo-Alatorre

CIICAp, Autonomous University of State Morelos (UAEM)

Av. Universidad 1001, Cuernavaca, ZP 62209, Mor., Mexico

Abstract— There are investigated nonlinear electrodynamic phenomena in volume narrow-gap semiconductors n -InSb, n -InAs at frequencies 1–5 THz. The nonlinearity of the electron gas due to the Kane dispersion law is dominating there. The equation for the amplitude, which is slowly varying with respect to time only, has been derived. The saturation of nonlinearity is taken into account. Under a propagation of THz transverse limited electromagnetic pulses through the structure intrinsic InSb- n -InSb-intrinsic InSb both the longitudinal and transverse focusing occurs. This leads to the wave collapse, or the concentration of the wave energy near one point. The optimum conditions for realizing wave collapse are obtained. A comparison is given with the structures that include the graphene sheets.

1. INTRODUCTION

The radiation of the terahertz (THz) range $f = 100 \text{ GHz} - 30 \text{ THz}$ is used in spectroscopy, medicine, scanning, and environmental science [1]. Nonlinear materials for THz range are: graphene and semimetals, paraelectrics, superlattices, and narrow gap semiconductors. The narrow-gap semiconductors like InSb, InAs, $\text{Cd}_x\text{Hg}_{1-x}\text{Te}$ possess high dynamic nonlinearity in THz range under the temperatures $T \geq 77 \text{ K}$ due to the nonparabolicity of the electron dispersion law [2, 3].

In this report the nonlinear electrodynamic phenomena in i -InSb- n -InSb- i -InSb structures are investigated, where the nonlinearity of the electric current due to the nonparabolicity of the dispersion law of conduction electrons is dominating. Generally this nonlinearity is not cubic and the general expression for the current density is used. Under a propagation of electromagnetic (EM) pulses through n -InSb both the longitudinal and transverse focusing occurs. This phenomenon results in the strong compression of the input pulses that leads to the wave collapse and concentration of the EM energy near one point.

2. BASIC EQUATIONS

Nonlinear propagation of transversely limited EM pulses in simple structures i -InSb- n -InSb- i -InSb is considered. The possibility of wave collapse of input pulses is of great interest. The structures have interfaces parallel to XY plane, while EM wave propagates in OZ direction. The almost linearly polarized EM wave $E = E_x$ is considered.

The n -InSb layer has the equilibrium electron concentration $n_0 \sim 10^{15} - 10^{16} \text{ cm}^{-3}$ under the temperatures $T \geq 77 \text{ K}$. The electrodynamic nonlinearity is due to the electron nonlinearity of the Kane dispersion law [2, 3]. The hydrodynamic equation of motion of the electron gas can be presented as [3]:

$$\frac{d}{dt} \left(\frac{m^* v}{(1 - (v/v_n)^2)^{1/2}} \right) = eE, \quad \text{where} \quad v_n = \left(\frac{E_g}{2m^*} \right)^{1/2}; \quad (1)$$

This equation of motion is analogous to the relativistic equation of motion of the particle, when the velocity of light c is replaced by the characteristic velocity $v_n \approx 1.2 \cdot 10^8 \text{ cm/s}$. Here v is the electron velocity, $m^* \approx 0.014 \cdot m_e$ is the electron effective mass, $E_g \approx 0.23 \text{ eV}$ is the forbidden gap for InSb [4, 5]. From Eq. (1) it is possible to get the following expression for the density of the electron current:

$$j \equiv en_0 v = \frac{e^2 n_0}{m^*} \frac{A}{(1 + (eA/m^* v_n)^2)^{1/2}}; \quad \text{where} \quad E \equiv \frac{\partial A}{\partial t} \quad (2)$$

Generally the electron nonlinearity is of the saturating type. For the electric field the wave equation is used:

$$c^2 \Delta E - \frac{\partial^2 D}{\partial t^2} - 4\pi \frac{\partial j}{\partial t} = 0 \quad (3)$$

Here D is the linear electric induction that includes the polarization of the crystalline lattice. The frequency-dependent linear dielectric permittivity of the semiconductor crystal is [4]:

$$\varepsilon(\omega) = \varepsilon(\infty) - \frac{\omega_T^2(\varepsilon(0) - \varepsilon(\infty))}{\omega(\omega - i\gamma) - \omega_T^2}; \quad (4)$$

Here $\varepsilon(0)$, $\varepsilon(\infty)$ are low- and high-frequency dielectric permittivities, ω_T is the frequency of transverse optical phonons, γ is the lattice dissipation [4].

The solution of Eq. (3) can be searched in the following form [6–9]:

$$E = \frac{1}{2}C(z, \rho, t) \exp(i\omega t) + c.c. \quad (5)$$

The amplitude C is slowly varying in time t , but the dependencies on z and the radial coordinate ρ are arbitrary. This is important for the nonlinear focusing of EM wave considered below.

From Eq. (5) it is possible to obtain the following expression for D [6, 9]:

$$D \approx \frac{1}{2} \left(\varepsilon C - i \frac{d\varepsilon}{d\omega} \frac{\partial C}{\partial t} - \frac{1}{2} \frac{d^2\varepsilon}{d\omega^2} \frac{\partial^2 C}{\partial t^2} \right) \exp(i\omega t) + c.c. \quad (6)$$

After substitution of Eqs. (6) and (2) into Eq. (3), the following nonlinear equation for the wave amplitude C has been derived:

$$\begin{aligned} \frac{\partial C}{\partial t} + \frac{ic^2}{2\omega\varepsilon^{(1)}} \left(\frac{\partial^2 C}{\partial z^2} + \Delta_{\perp} C \right) + \frac{i\omega\varepsilon}{2\varepsilon^{(1)}} \left(1 - \frac{\omega_p^2}{\omega^2\varepsilon} \left(1 + \frac{i\nu}{\omega} \right) \right) C \\ + \frac{i\omega_p^2\omega}{2\omega^2\varepsilon^{(1)}} \left[1 - Q^{-1/2} \left(1 - \frac{e^2|C|^2}{8(m^*v_n\omega)^2} Q^{-1} \right) \right] C = 0; \quad \text{where} \quad Q = 1 + \frac{e^2|C|^2}{2(m^*v_n\omega)^2}. \end{aligned} \quad (7)$$

Here $\varepsilon^{(1)} = \varepsilon + (\omega/2)(d\varepsilon/d\omega)$ is the correction of the permittivity due to the frequency dispersion, $\omega_p = (4\pi e^2 n_0/m^*)^{1/2}$ is the electron plasma frequency. The collision frequency ν of electrons is taken into account here. It is of about $\nu = 2 \times 10^{11} - 10^{12} \text{ s}^{-1}$ for InSb in the temperature $T = 77 \text{ K} - 300 \text{ K}$. It follows from Eq. (7) that the nonlinearity in n -InSb is focusing both in the longitudinal direction z and in transverse one ρ . The volume nonlinearity of n -InSb results in the wave collapse of the pulses, as our simulations are demonstrated.

Equation (7) is added by boundary conditions that are obtained from the continuity of the tangential components E_x and H_y at the boundaries i -InSb- n -InSb. At $z < 0$ both the incident and reflected waves are present, at $z > L_z$ only the transmitted wave exists. In the parabolic approximation the boundary conditions are:

$$\frac{\partial C}{\partial z} - ikC = -2ikE_i(\rho, t), \quad z = 0; \quad \frac{\partial C}{\partial z} + ikC = 0, \quad z = L_z; \quad \text{where} \quad k = \frac{\omega}{c}\varepsilon^{1/2} \quad (8)$$

Here $E_i(\rho, t)$ is the amplitude of the incident wave in the input.

3. RESULTS OF SIMULATIONS

The incident pulse is:

$$E_i(\rho, t) = E_{i0} \exp \left(- \left(\frac{t - t_1}{t_0} \right)^6 \right) \exp \left(- \left(\frac{\rho}{\rho_0} \right)^6 \right) \quad (9)$$

The shape of the input pulse is almost rectangular both for time t and for the transverse radial coordinate ρ .

It is investigated a simple structure that includes n -InSb layer of the thickness $L_z = 0.12 \text{ cm}$. At $z < 0$ and $z > L_z$ there is i -InSb. In n -InSb the equilibrium electron concentration is $n_0 = 10^{16} \text{ cm}^{-3}$, the electron collision frequency is $\nu = 6 \cdot 10^{11} - 10^{12} \text{ s}^{-1}$ ($T \geq 77 \text{ K}$), the low- and high-frequency permittivities are $\varepsilon(0) = 17.1$, $\varepsilon(\infty) = 15.15$; the frequency of transverse optical phonons is $\omega_T = 3.376 \cdot 10^{13} \text{ s}^{-1}$, the lattice dissipation is $\gamma = 0.01\omega_T$, see Eq. (4) [4, 5]. The THz pulses

with the carrier frequency $\omega = 2 \cdot 10^{13} \text{ s}^{-1} < \omega_T$ are considered. The half-widths of the input pulses vary within the limits $\rho_0 = 0.01\text{--}0.03 \text{ cm}$. The wave reflection at the input is small.

The results of simulations for n -InSb are presented in Figs. 1–3. The electric field is normalized to $E_n = 14.4 \text{ kV/cm}$ there. For all cases the parameter t_1 is $t_1 = 12 \text{ ps}$, see Eq. (9). The wave collapse occurs when the maximum amplitude of the input pulse exceeds some threshold that depends on the dissipation. Also the duration of the input pulse and the transverse width should be optimized, to produce the maximum compression.

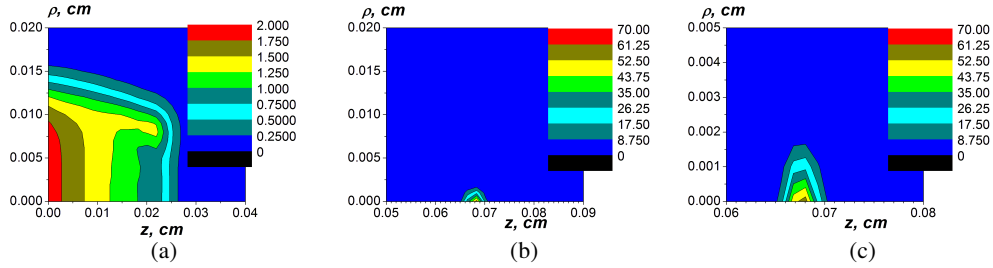


Figure 1: The collapse of the THz pulse in n -InSb with the maximum input amplitude $E_{i0} = 18.7 \text{ kV/cm}$. The transverse width of the input pulse is $2\rho_0 = 0.031 \text{ cm}$, the duration is $2t_0 = 11 \text{ ps}$. The part (a) is distribution of $|C(z, \rho)|^2$ at $t = t_1 = 12 \text{ ps}$, the parts (b) and (c) are $|C|^2$ for the maximum compression $t = 21.5 \text{ ps}$, general and detailed views. The electron dissipation is $\nu = 6 \cdot 10^{11} \text{ s}^{-1}$.

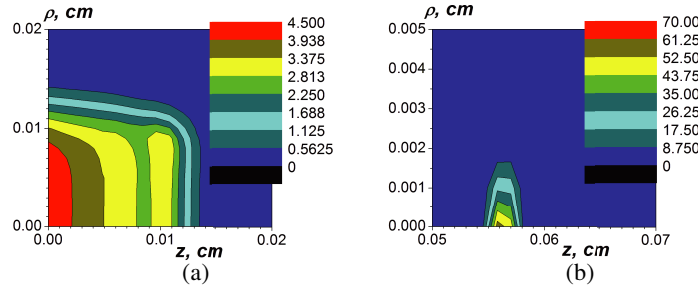


Figure 2: Spatial distribution $|C|^2$ of the pulse. The input amplitude is $E_{i0} = 28.8 \text{ kV/cm}$. The transverse width of the input pulse is $2\rho_0 = 0.028 \text{ cm}$, the duration is $2t_0 = 5.6 \text{ ps}$. Part (a) is for the time moment $t = t_1 = 12 \text{ ps}$, (b) is for $t = 23 \text{ ps}$. A higher dissipation $\nu = 10^{12} \text{ s}^{-1}$.

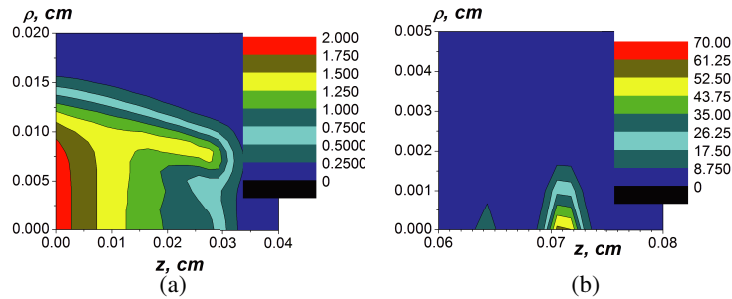


Figure 3: Spatial distribution $|C|^2$ of the pulse within the structure. The input amplitude is $E_{i0} = 18.7 \text{ kV/cm}$. The transverse width of the input pulse is $2\rho_0 = 0.031 \text{ cm}$, the duration is $2t_0 = 14 \text{ ps}$ (a longer pulse, compared with Fig. 1). Part (a) is for the time moment $t = t_1 = 12 \text{ ps}$, (b) is for $t = 22 \text{ ps}$.

When there is some deviation from the optimum input parameters, EM concentrates near several points, as seen in Fig. 3(b). The input pulse is longer, when compared with Fig. 1.

The wave collapse also can be realized in the narrow-gap semiconductor n -InAs, where the structures i -InAs- n -InAs- i -InAs are simulated. The electron concentration is $n_0 = 10^{16} \text{ cm}^{-3}$, the effective mass is $m^* \approx 0.023 \cdot m_e$, the forbidden gap is $E_g \approx 0.31 \text{ eV}$ [4, 5], $v_n \approx 1.1 \cdot 10^8 \text{ cm/s}$; the low- and high-frequency permittivities are $\varepsilon(0) = 15.15$, $\varepsilon(\infty) = 12.3$; the frequency of transverse

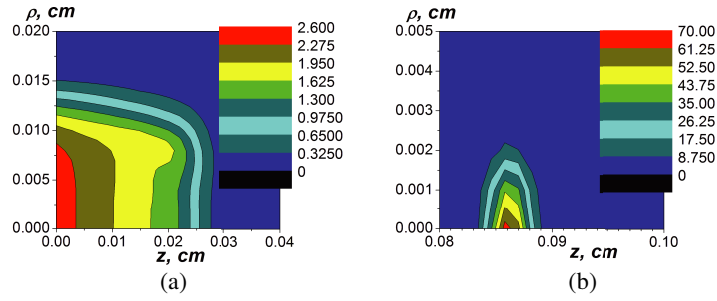


Figure 4: The wave collapse in n -InAs. The maximum input amplitude is $E_{i0} = 25$ kV/cm. The transverse width of the input pulse is $2\rho_0 = 0.03$ cm, the duration is $2t_0 = 9.6$ ps. Part (a) is for the time moment $t = 12$ ps, (b) is for $t = t_1 = 23.5$ ps. The electron dissipation is $\nu = 6 \cdot 10^{11} \text{ s}^{-1}$.

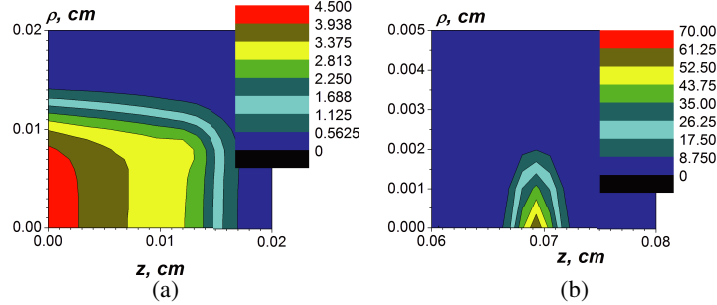


Figure 5: The wave collapse in n -InAs. The maximum input amplitude is $E_{i0} = 33.4$ kV/cm. The transverse width of the input pulse is $2\rho_0 = 0.025$ cm, the duration is $2t_0 = 6$ ps. Part (a) is for the time moment $t = t_1 = 12$ ps, (b) is for $t = 22$ ps. The higher dissipation $\nu = 10^{12} \text{ s}^{-1}$.

optical phonons is $\omega_T = 4.046 \cdot 10^{13} \text{ s}^{-1}$, the lattice dissipation is $\gamma = 0.01\omega_T$ [4, 5]. The results of simulations are given in Figs. 4, 5. Here the electric field is normalized to $E_n = 16.7$ kV/cm. The wave collapse occurs at higher input amplitudes of the pulses.

Therefore, the wave collapse of input THz pulses of the durations 5–20 ps and the transverse widths 0.02–0.04 cm in the structures that include n -InSb or n -InAs semiconductors can be used for the concentration of the electromagnetic energy near some point within the crystal. Because the electron dissipation is quite high $\nu > 5 \cdot 10^{11} \text{ s}^{-1}$, the realization of stable temporal or spatial solitons in THz range is doubtful, whereas the wave collapse can take place.

4. CONCLUSIONS

The principal effect reported in this paper is the nonlinear spatiotemporal focusing of THz pulses that leads to the wave collapse, or the concentration of EM energy near some point within the narrow-gap semiconductors n -InSb or n -InAs. The carrier frequency should be chosen below the frequency of transverse optical phonons. The shape of the input pulse should be optimized, to obtain the single nonlinear focus. The optimization should be realized for the input amplitudes of the pulses and on their durations and transverse widths.

In a distinction to the structures with n -InSb or n -InAs, in the structures with graphene layers [10] the wave collapse is absent [7, 8]. Other phenomena, like the transition to the transmission regime of short incident pulses due to nonlinearity and change of the transverse widths of the pulses [7, 8], can be realized both in the structures with the graphene layers and with the narrow-gap semiconductors. In THz range the nonlinearity manifests at similar levels of the input amplitudes both for the structures with graphene layers and with the n -InSb ones.

ACKNOWLEDGMENT

The authors are grateful to SEP-CONACyT (Mexico) for a partial support of our work.

REFERENCES

1. Perenzoni, M. and D. J. Paul (Eds.), *Physics and Applications of Terahertz Radiation*, Springer, N.Y., 2014.

2. Belyantsev, A. M., V. A. Valov, V. N. Genkin, A. M. Leonov, and B. A. Trifonov, "Dynamic mechanism of nonlinearity and frequency conversion of millimeter electromagnetic radiation in *n*-Type InSb," *Sov. Phys. JETP*, Vol. 34, No 3, 471–473, 1972.
3. Bass, F. G. and A. A. Bulgakov, *Kinetic and Electrodynamic Phenomena in Classical and Quantum Semiconductor Superlattices*, Nova Publ., N.Y., 1997.
4. Yu, P. Y., and M. Cardona, *Fundamentals of Semiconductors*, Springer, N.Y., 2010.
5. Levinshtein, M., S. Rumyantsev, and M. Shur, *Handbook Series on Semiconductor Parameters*, Vol. 1, World Scientific, Singapore, 1999.
6. Castrejon-M., C., V. Grimalsky, S. Koshevaya, and A. Zamudio-Lara, "Propagation of transversely bounded nonlinear electromagnetic pulses through periodic media," *Journal of Non-linear Optical Physics and Materials*, Vol. 21, No 2, paper 1250022 (13 pp.), 2012.
7. Rapoport, Y., V. Grimalsky, and I. Iorsh, "Nonlinear reshaping of THz pulses with graphene metamaterials," *Pis'ma v ZhETF*, Vol. 98, No. 8, 561–564, 2013.
8. Rapoport, Y. G., V. V. Grimalsky, and C. Castrejon-M., "Nonlinear spatiotemporal focusing of terahertz pulses in the structures with graphene layers," *Proc. 2014 IEEE 34th Intl. Conf. on Electronics and Nanotechnology, ELNANO 2014*, 31–34, Kyiv, Ukraine, 15–18 April 2014.
9. Kivshar Y. S. and G. P. Agrawal, *Optical Solitons*, Academic Press, N.Y., 2003.
10. Mikhailov, S. A., "Non-linear electromagnetic response of graphene," *Europhys. Lett.*, Vol. 79, No. 2, paper 27002 (4 pp.), 2007.

Resonant Antenna Design Employing Equivalent Circuit Mode

Cheng-Nan Hu, Siam-Chen Huang, Jhih-Neng Yang, and Jen-Kai Hong

School of Communication Engineering, Oriental Institute of Technology, New Taipei 22061, Taiwan

Abstract— Utilization of the equivalent circuit model has shown more time-effective for designing RF circuits and antennas rather than Electromagnetic fields analysis. This study investigates equivalent circuit perspective on designing the resonant antenna. An equivalent π -network circuit is firstly proposed to approach the electromagnetic fields coupling of a closely coupled two-element diversity antenna. Thus, the improvement on the isolation between antennae can be straightforward achieved by employing resonant method. Numerical and experimental study are presented herein.

1. INTRODUCTION

Antenna diversity provides superior spectrum efficiency in a narrow-band cellular reuse system to increase data rates by reducing the fading that occurs in mobile communications [1–3]. However, designing two or more antennas on a small mobile terminal with a higher isolation between the antennas remains a challenge to fulfill the improved aesthetic design, regarding the stringent volume requirement. Many studies have been conducted to improve the isolation between two antennas through the use of various approaches, including designs that incorporate reflectors [4, 5]; an additional ground plane [6]; band-notched slots [7, 8]; and electromagnetic band-gap structures on the ground plane [9].

In this study, an equivalent circuit model (Figure 1) is firstly proposed to simulate the frequency response of the electromagnetic fields coupling mechanism of a two-element inverted-L antenna array (Figure 1) such that the diversity antenna with very high isolation can be achieved by simply using a decoupling capacitor between two antennas. Numerical study is conducted by using ADS2009 and EM simulator to validate the proposed equivalent circuit model. AND a two-element inverted antenna array printed on a FR4 substrate with height of 0.8 mm is built for experimental validation, showing excellent performance in the measured results in the desired operating bands to prove the effectiveness of the proposed design method.

2. DESIGN AND RESULTS

Figure 1(a) shows the proposed layout and photos of diversity antenna configuration integrated by two inverted-L antennas in which the dimensions of the antennas are optimized using a general-purpose EM solver (GEMS) to obtain desirable antenna performance. Concerning the optimization antenna topology and position (Figure 1(a)), the design parameters are optimized using GEMS. The structure parameters of the experimental diversity antenna are as follows [Figure 1]: $L_1 = L_2 = 26.25$ mm, $d = 6$ mm, and $w = 1.17$ mm. However, as shown in Figure 1(b), the electromagnetic fields coupling through either radiated or conducted path will result in poor isolation (~ 8 dB) between antennas to degrade the system performance.

Although two inverted-L antennas are placed perpendicularly, the electromagnetic fields of two antennas are not totally orthogonal based on the simulated results using EM simulator. Meanwhile,

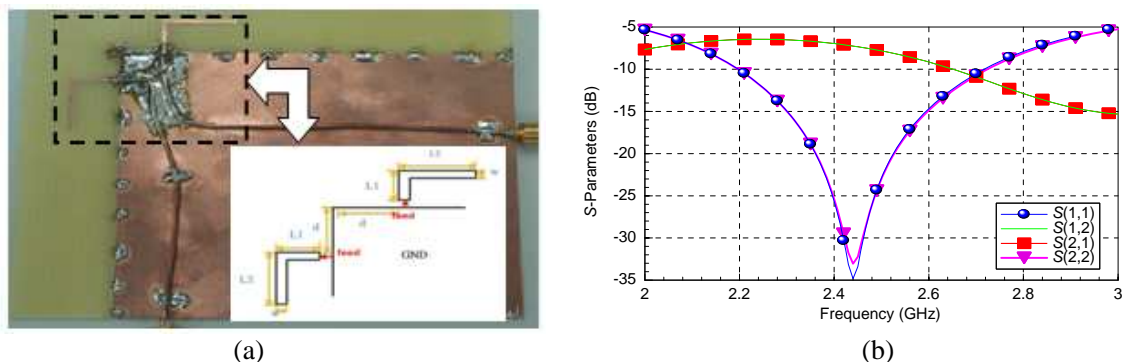


Figure 1: (a) Proposed layout/photos of diversity antenna; (b) simulated S -parameters using GEMS.

the proximate magnetic flux interaction caused by common-ground return signals of the nearby antenna feeds also yields the coupling power through conductive path. Consequently, it is very difficult to design a compact diversity antenna with high isolation by using EM simulation based on microscopic point of view.

To overcome this difficulty, in this study, the equivalent circuit model is firstly applied to approach the electromagnetic field coupling mechanism of two coupled printed inverted-L antennas. Since the use of the equivalent circuit approach can show physical-based perspective, the improvement on isolation performance of the coupled diversity antenna can be solved directly from macroscopic point of view. In this design example, two inverted-L antennas are present by two series RLC resonant circuits, respectively. As the well known fact that inductive impedance can be used to represent the frequency behavior of the magnetic flux interaction caused by the common-mode ground return signal and electric radiated current source. The parasitic capacitance is generally used to model the electric field coupling between ground metal and printed antenna. Thus, a π network (Figure 2(a)) is employed to simulate the mutual coupling of two antennas. The circuit parameters of the equivalent model can be obtained by applying the simulated two port S -parameter using GEMS to the ADS2009 optimization test bench of the ADS2009 and then a de-coupling capacitor ($C_d = 0.65$ pf in Figure 2(a)) can be simply calculated to form a parallel resonant circuit at the desired frequency band to trap the coupling signals between two antennas. Thus, diversity antenna with high isolation performance is achieved simply. Figure 2(b) shows the proposed layout/photos to implement decoupling capacitor.

Then, substituting computed decoupling capacitor, C_d , in to GEMS EM simulator for full-wave validation, we find the optimal C_d is about 0.27 pf to consider additional parasitic capacitance due to separation of ground. Final, the experimental diversity antenna is tested to compare with simulated results, showing the isolation can be improved from -8 dB to better than -20 dB at the frequencies of interest. The slight degradation can be attributed to the loading effect of addition de-coupling capacitor.

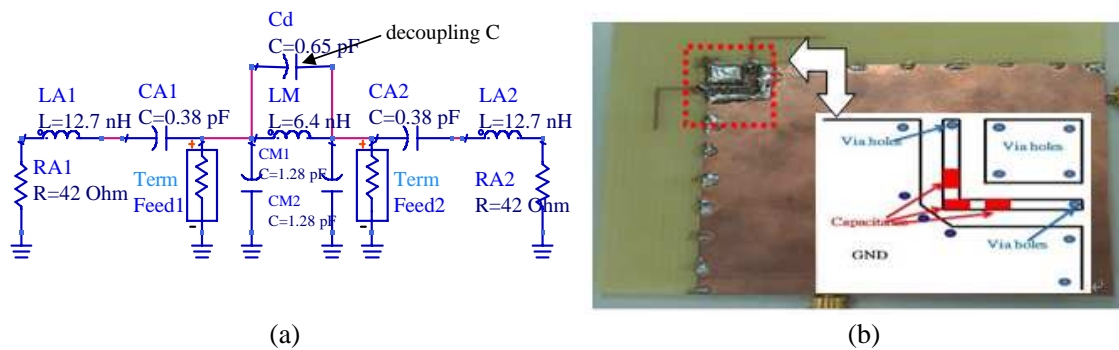


Figure 2: (a) Proposed equivalent circuit model and corresponding circuit parameters; (b) layout/photos of diversity antenna to implement decoupling capacitor (C_d) by using 31 pf in series.

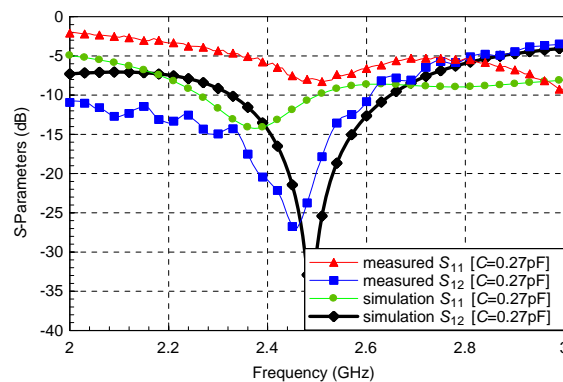


Figure 3: The comparison of the simulated (GEMS) and measured S -parameters.

3. CONCLUSION

Simulated results indicate that the use of the proposed method is useful to eliminate the loop ground surface current for isolation improvement. Experimental study of the proposed diversity antenna configuration shows that excellent isolation between two antennae is achievable in a highly compact size for terminal devices applications.

REFERENCES

1. Hu, C. N., B. Tai, and A. Yang, “Meander-line folded monopole design for UMTS/HSDPA-based data-card applications,” *IEEE Antennas and Wireless Propagation Letters*, Vol. 7, 279–282, 2008.
2. Hu, C.-N., “Diversity antenna design for use in UMTS/HSPA-based data-cards”, *IET Microwaves, Antennas & Propagation*, Vol. 4, No. 9, 1191–1198, 2010.
3. Vaughan, R. G. and J. Bach Andersen, “Antenna diversity in mobile communications,” *IEEE Trans. on Vehicular Tech.*, Vol. 36, No. 4, 149–172, Nov. 1987.
4. Wu, T.-Y., S.-T. Fang, and K.-L. Wong, “A printed diversity dual-band monopole antenna for WLAN operation in the 2.4 and 5.2 GHz band,” *Microwave and Optical Technology Letters*, Vol. 36, No. 6, Mar. 20, 2003.
5. Fhi, G., B. Li, and D. Qi, “Dual band printed diversity antenna for 2.4/5.2 GHz WLAN application,” *Microwave and Optical Technology Letters*, Vol. 45, No. 6, Jun. 20, 2005.
6. Gao, Y., C. C. Chiau, X. Chen, and C. G. Parini, “Modified PIFA and its array for MIMO terminals,” *IEE Proc. Microwaves, Antennas and Propagation*, Vol. 152, No. 4, 255–259, Aug. 2005.
7. Karaboikis, M., C. Soras, G. Tsachtsiris, and V. Makios, “Compact dual-printed inverted-F antenna diversity system for portable wireless devices,” *IEEE Antennas and Wireless Propagation Letters*, Vol.3, 9–14, 2004.
8. Kim, K.-J., W.-G. Lim, and J.-W. Yu, “High isolation internal dual-band planar inverted-F antenna diversity system with band-notched slots for MIMO terminals,” *36th European Microwave Conference*, 141–1417, Sep. 10–15, 2006.
9. Chiau, C. C., “Study of the diversity antenna array for the MIMO wireless communication systems,” Ph.D. Thesis, Department of Electric Engineering, University of London, Queen Mary, UK, Apr. 2006.

Flexible PIFA Antenna Design for Wireless Sensor Networks in Wearable Healthcare Applications

I. Gil and R. Fernández-García

Department of Electronic Engineering

Universitat Politècnica de Catalunya, 08222 Colom 1, Terrassa, Spain

Abstract— In this work a flexible wearable PIFA antenna has been designed in order to operate according to the Bluetooth v4 standard (2400–2483.5 MHz) in healthcare applications designed for wireless sensor networks. The substrate design includes the textile and human skin effects as well as the antenna flexible substrate (Pyradox). The return losses results show a strong detuning (36.8%) of the operation frequency of the antenna due to the outfit and human skin presence, instead of air, and therefore a redesign of the antenna dimensions has been done (42.2% of miniaturization of the antenna layer). Some antenna performance changes are observed in terms of the radiation pattern and gain reduction due to the body proximity.

1. INTRODUCTION

Narrowband flexible printed circuit board (F-PCB) antennas play an important role in the design of wearable electronics for applications such as body area networks (BAN), wireless personal area networks (WPANs) and medical sensor networks [1, 2]. Microstrip technology is typically used due to its low cost, planar conformability, small factor and ease manufacture. Concurrently, in recent years, the Wireless Sensor Networks (WSNs) [3] have emerged as a communication technology to address applications such as health care monitoring, environmental sensing, industrial monitoring, etc.. The WSNs consist of small communication nodes containing a sensing part, a microcontroller, communication components and a battery. Wearable WSN healthcare applications require compact size and optimized radiation patterns [4] and, therefore, the antenna design play a fundamental role in customized designs. The planar inverted-F antenna (PIFA) is a common antenna for portable devices because of its excellent balance between low-profile, low-cost and performance [5]. Obviously, since the human body is composed of a large variety of tissues types (with different dielectric properties) the substrate design of the wearable antennas must include their effects, specifically to take into account the overall dielectric constant of the device and losses.

In this work an optimized F-PCB PIFA including the textile and human skin effects has been designed and simulated for wearable WSN healthcare applications operating under the Bluetooth v4 standard. The return loss impact, radiation pattern and antenna gain have been analysed and compared. Section 2 addresses the PIFA design and final geometry, whereas Section 3 is focused on the antenna performance. Finally in Section 4, the main conclusions are summarized.

2. F-PCB PIFA DESIGN AND GEOMETRY

The proposed PIFA has been designed by means of the commercial *Keysight Advanced Design Systems and Momentum* software. Figure 1 shows the proposed substrate based on the implementation of the flexible PIFA in the commercial Pyralux (dielectric constant $\epsilon_{rP} = 4.6$, thickness $h_P = 50 \mu\text{m}$). A textile layer ($\epsilon_{rT} = 2$, $h_T = 1 \text{ mm}$) has also been considered to emulate the outfit impact on the antenna. Finally, the human skin has been included as the lowest layer in the substrate ($\epsilon_{rS} = 39$, $h_S = 1.5 \text{ mm}$) [6]. The antenna has been designed to operate under the Bluetooth v4 standard (2400–2483.5 MHz). The original F-PCB meandered antenna has been designed in a single Pyralux dielectric and it is illustrated in Figure 2(a). A rectangular inset fed at 2.45 GHz with 50Ω input impedance has been considered for matching condition. The final geometry corresponds to the following parameters: Original Antenna: $W_A = 0.6 \text{ mm}$; $L_{A1} = 16.6 \text{ mm}$; $S_{A1} = 1.4 \text{ mm}$; Ground plane: $W_G = 20.6 \text{ mm}$; $L_G = 14.6 \text{ mm}$; Via: $\Phi = 0.3 \text{ mm}$. The total dimensions of the PIFA correspond to $20.6 \times 26.0 \text{ mm}^2$. Since the impact of the textile and skin effect increases the effective dielectric constant of the substrate, a reduction in the original antenna frequency operation is expected. Therefore, a redesign of the F-PCB is required in order to guarantee the specifications. The optimized PIFA including textile and human skin impact is depicted in Figure 2(b), where most dimensions remain constant, except: $L_{A2} = 9.6 \text{ mm}$; $S_{A2} = 0.4 \text{ mm}$, which implies a PIFA area reduction of 42.2%.

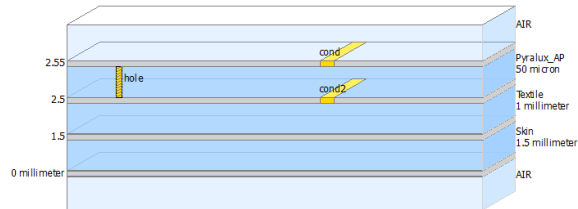


Figure 1: Substrate definition including F-PCB, textile and skin effects.

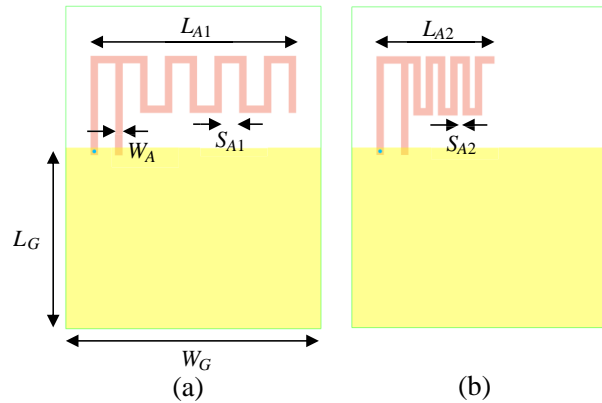


Figure 2: Geometry of the (a) original and (b) redesigned meandered PIFA antenna.

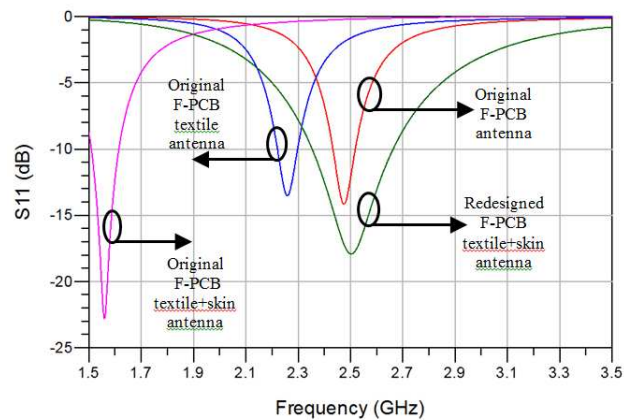


Figure 3: Return loss of the original and redesigned PIFA antennas.

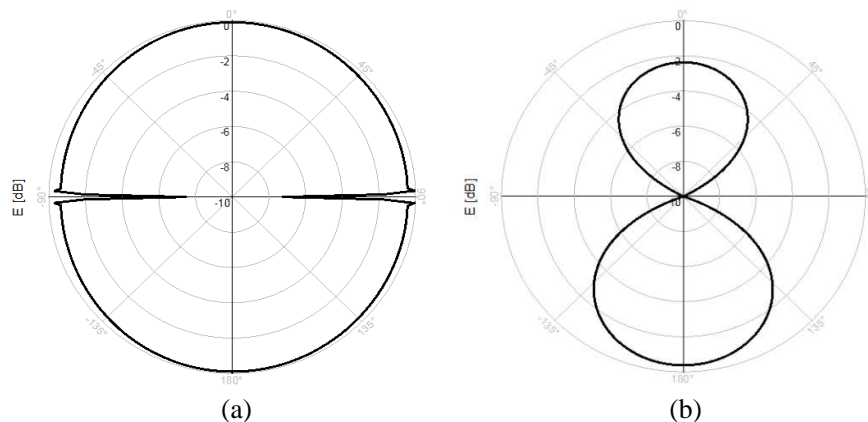


Figure 4: Normalized radiation pattern for the maximum radiation level case at 2.45 GHz for the (a) original ($\phi = 141^\circ$) and (b) redesigned meandered PIFA antenna ($\phi = 177^\circ$).

3. F-PCB PIFA PERFORMANCE

The antenna return losses (S_{11}) for several steps with regard to the optimization design process are depicted in Figure 3. An original PIFA meandered antenna has been designed at the operation frequency in Pyralux substrate. A $S_{11} = -14.2$ dB is obtained with a fractional bandwidth of $BW = 3.5\%$ (at $S_{11} = -10$ dB). The impact of the textile reduces the operation frequency of the original PIFA a 8.5%, with $S_{11} = -13.5$ dB and the fractional bandwidth remains almost constant ($BW = 3.3\%$). Finally, the combination of textile and skin effect implies a frequency detuning of

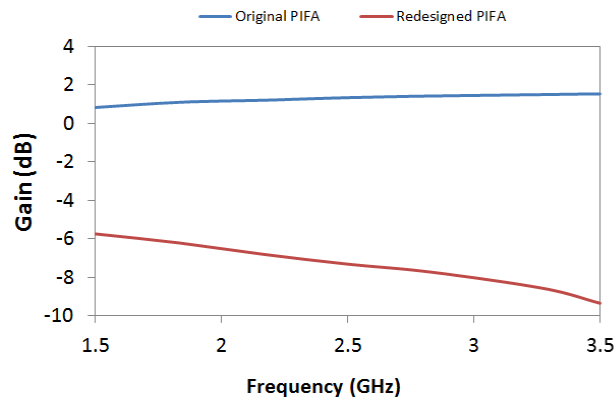


Figure 5: Antenna gain for the (a) original and (b) redesigned meandered PIFA antenna.

36.8%, with $S_{11} = -22.7$ dB and $BW = 6.8\%$. Obviously, the introduction of the textile and skin layers increases the overall dielectric constant and, therefore, a reduction in the radiation frequency is expected. The redesigned antenna (substrate described in Figure 1) performance correspond to 300 MHz bandwidth ($BW = 12.5\%$) and a maximum return losses of $S_{11} = -18$ dB. The original antenna designed with Pyralux and air substrate shows an excellent radiation pattern, as depicted in Figure 4(a). The redesigned antenna shows a radiation pattern reduced (2 dB in the maximum radiation direction), as expected due to the body proximity impact and attenuation. It is also observed that the angle of maximum radiation is also modified from $\phi = 141^\circ$ to $\phi = 177^\circ$. Moreover, the directivity of the wearable antenna is increased, whereas the gain is reduced from 1.5 dBi (original antenna) to -7 dBi.

4. CONCLUSIONS

A flexible wearable PIFA antenna developed for wireless sensor networks has been healthcare applications has been designed under Bluetooth v4 standard. Analytical results from method of moments simulation have been presented and discussed. The textile and human skin effects have been studied in terms of the antenna operation frequency, radiation pattern and gain. The human body proximity provokes certain degradation in the antenna performance (reduction of the efficiency and gain), as expected. Research is in progress in order to confirm experimentally the previous results, and to extend the analysis to other kind of F-PCB microstrip and coplanar antennas.

ACKNOWLEDGMENT

This work was supported by the Spanish Government-MINECO under Project TEC2013-41996-R and AGAUR 2014 SGR 375.

REFERENCES

1. Guha, D. and Y. M. M. Antar, *Microstrip and Printed Antenna*, John Wiley & Sons, 2011.
2. Shrestha, S., M. Agarwal, P. Ghane, and K. Varahramyan, "Flexible microstrip antenna for skin contact application," *International Journal of Antennas and Propagation*, Vol. 2012, 1–5, Jun. 2012.
3. Akyildiz, I. F., T. Melodia, and K. R. Chowdury, "Wireless multimedia sensor networks: A survey," *IEEE Wireless Communications*, Vol. 14, No. 6, 32–39, Dec. 2007.
4. Kan, Y.-C. and C.-K. Chen, "Analysis of the inverted-F antennas integrated on the displacement detector for wireless sensor network applications," *Asia Pacific Microwave Conference*, 1849–1851, 2009.
5. Wong, K. L., *Planar Antennas for Wireless Communications*, John Wiley & Sons Inc., 2003.
6. Gabriel, C., S. Gabriel, and E. Corthout, "The dielectric properties of biological tissues: I. Literature Survey," *Phys. Med. Biol.*, Vol. 41, 2231–2249, 1996.

Dual-band Printed Antenna for WLAN Applications

Lanchao Zhang, Tao Jiang, and Yingsong Li

College of Information and Communication Engineering, Harbin Engineering University
Harbin 150001, China

Abstract— A compact dual-band printed antenna is presented and discussed for wireless local area networks (WLAN) applications in this paper. The proposed antenna is printed on a FR4 substrate with a dielectric constant of 4.3 and an overall size of $40 \times 40 \times 1.6 \text{ mm}^3$. The antenna consists of two meandering strips which locate at the top and bottom sides of the substrate, respectively. The top strip aims to generate a resonance frequency operating at 5.8 GHz WLAN band, while the bottom strip can provide another resonance for 2.4 GHz WLAN applications. Simulated results show that the proposed antenna can provide two resonance frequencies and good omnidirectional radiation patterns, making it suitable for lower and upper WLAN applications.

1. INTRODUCTION

Nowadays, wireless communication systems have attracted much more attention in home and abroad. Since WLAN communication can work in both 2.4 GHz and 5.8 GHz bands, an antenna is required to operate in dual frequency bands simultaneously. However, it is a great challenge to design dual-band or multi-band antennas integrated into the inside of modem compact wireless devices.

Consequently, a great number of methods have been proposed to implement dual-band or multi-band antennas. Fractal geometries such as Koch snowflake, Minkowski-like pre-fractal patch and Peano fractal curve have been presented and investigated in detail [1–4]. However, these antennas are complex in structures. Several dual-band or multi-band antennas have been designed by using multi-branches [5–10]. Among these well designed antennas, each branch can produce a resonance frequency for multi-band applications. However, they are large in size, which limits their applications in practical engineering. Another effective method to design multi-band antenna is realized by using various slots such as U-shaped slot [11–13], which can control the current path and, hence, control the resonance frequency.

In this paper, a dual-band antenna with small size and simple structure is presented for lower and upper WLAN applications. The proposed antenna has two strips located at the top and bottom sides of a FR4 substrate whose dielectric constant is 4.3. The antenna with a small size of $40 \times 40 \times 1.6 \text{ mm}^3$ can operate in both 2.4 GHz and 5.8 GHz bands. Also, the proposed antenna can provide an omnidirectional radiation patterns, rendering it promising for portable WLAN terminals.

2. ANTENNA DESIGN

The configuration of the proposed dual-band antenna is shown in Fig. 1. The proposed antenna consists of a FR4 substrate with the dielectric constant of 4.3, a ground plane, two meandering strips which are printed on the top and bottom sides of the substrate, respectively. The top meandering strip is connected with a 50-Ohm coaxial line, while the bottom meandering strip is set under the top one. By using this structure, the impedance matching can be highly improved. The detailed configuration of the antenna is depicts in Figs. 1(b) and 1(c). The proposed antenna is optimized by using CST and the optimal parameters are listed in Table 1.

Table 1: Optimal parameters of the proposed antenna.

Parameters	$H1$	$H2$	$H3$	$H4$	L	$L1$	$L2$
Unit (mm)	16	5	14	12	40	16	7
Parameters	$L3$	$L4$	$L5$	$L6$	$W1$	$W2$	$W3$
Unit (mm)	8.7	11	10	2.7	3.5	2	1

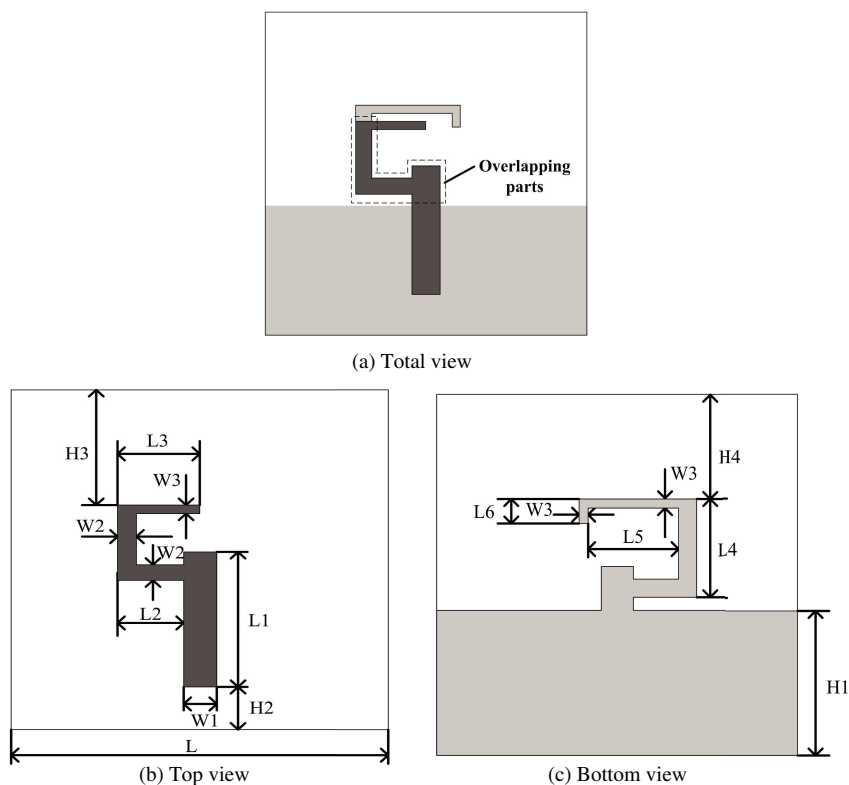


Figure 1: The configuration of the proposed antenna.

3. RESULTS AND DISCUSSION

In order to better understand the performance of the proposed antenna, the effects of the key parameters $L3$ and $L6$ are investigated and illustrated in Fig. 2 and Fig. 3. Fig. 2 shows the return loss of the proposed antenna with varying $L3$. It can be seen that the center frequency of the upper band shifts from 6 GHz to 5.6 GHz with an increase of $L3$ ranging from 8.3 mm to 9.1 mm, while the center frequency of the lower band moves from 2.5 GHz to 2.3 GHz with an increase of $L6$ ranging from 1.7 mm to 3.7 mm. The simulated result with varying $L6$ is given in Fig. 3. Thus, the upper and lower bands can be tuned by adjusting the dimensions of the top and bottom strips, respectively. The proposed antenna has been optimized by the use of CST and the optimal return loss of the antenna is demonstrated in Fig. 4. It can be seen that the antenna covers the bandwidths of WLAN 2.4 GHz (2.4–2.484 GHz) and WLAN 5.8 GHz (5.725–5.825 GHz) with respect to S_{11} less than -10 dB.

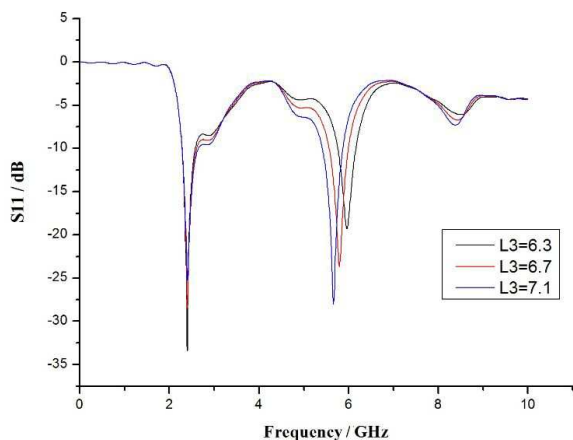


Figure 2: The return loss of the proposed antenna with varying $L3$.

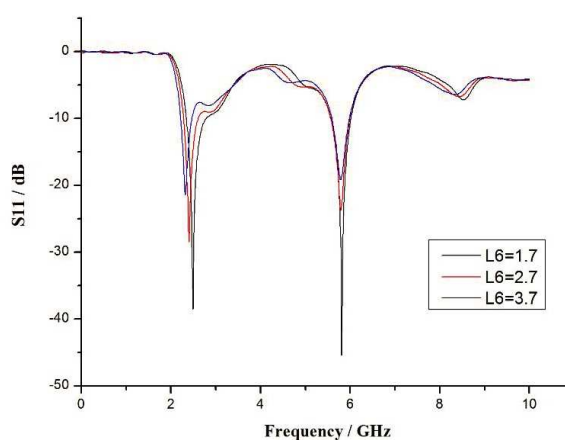


Figure 3: The return loss of the proposed antenna with varying $L6$.

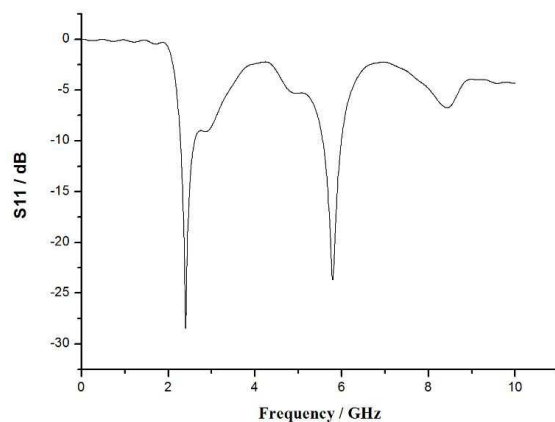


Figure 4: Optimal return loss of the proposed antenna.

The 3-D radiation patterns of the proposed antenna at 2.4 GHz and 5.8 GHz are displayed in Fig. 5. It is found that the proposed antenna has nearly omnidirectional radiation characteristics in the operating bands.

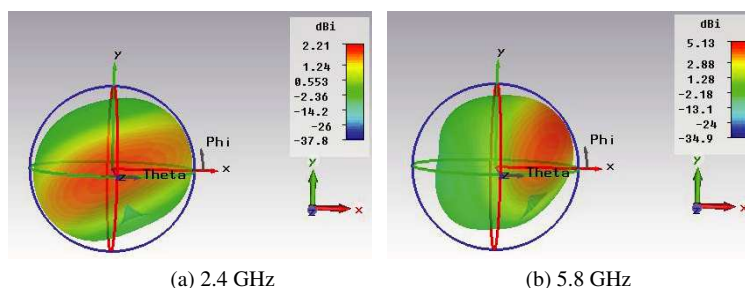


Figure 5: The 3-D radiation patterns of the proposed antenna at 2.4 GHz and 5.8 GHz.

4. CONCLUSION

A dual-band antenna has been proposed and well investigated for WLAN applications, which is small in size. By using an overlapping strip structure, the proposed antenna can achieve a good impedance bandwidth within the dual operating bands. Also, the proposed antenna has a tunable dual-band function at both 2.4 GHz and 5.8 GHz bands, and can provide nearly omnidirectional radiation patterns, which make it suitable for miniaturized WLAN devices.

ACKNOWLEDGMENT

This paper is funded by the International Exchange Program of Harbin Engineering University for Innovation-oriented Talents Cultivation. This work was also partially supported by the Navy Defense Foundation of China (4010403020102), the Science and Technology innovative Talents Foundation of Harbin (2013RFXXJ083), the Foundational Research Funds for the Central Universities (HEUCF131602, HEUCFD1433).

REFERENCES

1. Yadav, S., R. Choudhary, U. Soni, B. Peswani, and M. M. Sharma, "Koch curve fractal antenna for Wi-MAX and C-band wireless applications," *Proceedings of the Next Generation Information Technology*, 490–494, September 2014.
2. Ali, J. K. and A. S. A. Jalal, "A miniaturized multiband Minkowski-like pre-fractal patch antenna for GPS and 3g IMT-2000 handsets," *Asian Journal of Information Technology*, Vol. 6, No. 5, 584–588, 2007.
3. Choukiker, Y. K. and S. K. Behera, "ACS fed Koch fractal antenna for wide-band applications," *International Journal of Signal and Imaging Systems Engineering*, Vol. 6, No. 1, 9–15, 2013.

4. Abdulkarim, S. F., A. J. Salim, J. K. Ali, A. I. Hammoodi, M. T. Yassen, and M. R. Hassan, "A compact Peano-type fractal based printed slot antenna for dual-band wireless applications," *Proceedings of RF and Microwave Conference*, 329–332, Penang, Malaysia, December 2013.
5. Kuo, Y. L. and K. L. Wong, "Printed double-T monopole antenna for 2.4/5.2 GHz dual-band WLAN operations," *IEEE Transactions on Antennas and Propagation*, Vol. 51, No. 9, 2187–2192, 2003.
6. Thomas, K. G. and M. Sreenivasan, "A novel triple band printed antenna for WLAN/WiMAX applications," *Microwave and Optical Technology Letters*, Vol. 51, No. 10, 2481–2485, 2009.
7. Li, R. L., B. Pan, J. Laskar, and M. M. Tentzeris, "A novel low-profile broadband dual-frequency planar antenna for wireless handsets," *IEEE Transactions on Antennas and Propagation*, Vol. 56, No. 4, 1155–1162, 2008.
8. Li, Y., X. Yang, Y. Bai, and T. Jiang, "Dual-band antenna handles WLAN/WiMAX," *Microwaves & RF*, Vol. 50, No. 6, 80–88, 2011.
9. Li, Y., W. Li, and R. Mittra, "A compact ACS-fed dual-band meandered monopole antenna for WLAN and WiMAX applications," *Microwave and Optical Technology Letters*, Vol. 55, No. 10, 2370–2373, 2013.
10. Li, Y., W. Li, and Q. Ye, "A compact asymmetric coplanar strip-fed dual-band antenna for 2.4/5.8 GHz WLAN applications," *Microwave and Optical Technology Letters*, Vol. 55, No. 9, 2066–2070, 2013.
11. Su, C. M., H. T. Chen, and K. L. Wong, "Printed dual-band dipole antenna with U-slotted arms for 2.4/5.2 GHz WLAN operation," *Electronics Letters*, Vol. 38, No. 22, 1308–1309, 2002.
12. Kim, T. H. and D. C. Park, "Compact dual-band antenna with double L-slits for WLAN operations," *IEEE Antennas and Wireless Propagation Letters*, Vol. 4, 249–253, 2005.
13. Janapsatya, J., K. P. Esselle, and T. S. Bird, "A dual-band and wideband planar inverted-F antenna for WLAN applications," *Microwave and Optical Technology Letters*, Vol. 50, No. 1, 138–141, 2008.

Unequal Power Divider Using Series RC Circuit for Improved Isolation

Young Kim¹, Seok-Hyun Sim¹, and Young-Chul Yoon²

¹Kumoh National Institute of Technology, Republic of Korea

²Catholic Kwandong University, Republic of Korea

Abstract— This paper presents a high dividing ratio unequal power divider with improved isolation using a series RC circuit. To improve isolation, we used an isolation component composed of a series resistor and capacitor circuit. This circuit is placed at an arbitrary position in the quarter-wave transmission line to achieve power division. In addition, to achieve a high dividing ratio, the low impedance line is composed of a capacitive loaded transmission line with slow-wave characteristics. To validate the performance of the proposed unequal power divider, we simulated and fabricated the unequal power divider for an operating frequency of 1 GHz. The experimental results are in good agreement with the simulated results.

1. INTRODUCTION

A power divider is a fundamental component in RF and microwave systems, such as in feeding networks for array antenna systems [1], power amplifiers [2], and six-port reflectometers [3]. Conventional unequal power dividers have poor isolation and output port matching conditions because the quarter-wave transmission lines used for power division are nearby. To improve performance, many papers have examined design methods, such as using multi-stage, dual band, and parallel RLC isolation networks [4], 0° phase shifting isolation stages [5], multi-section transmission line and multi-layer techniques [6], isolation networks [7], exponentially tapered lines [8], and multi-layer slotlines with BPF responses [9].

To improve the isolation performance of a conventional power divider, most design methods employ multilayer or multi-section configurations to reduce the interference between dividing transmission lines. These methods have the drawbacks of large size and complex structure. Because the quarter-wave transmission lines for power dividing must be nearby to allow the connection of the isolation component, the isolation performance degrades between output ports. In addition, because the end point of the small-size isolation component is connected to the output port, it is difficult to add connections between output ports and other circuits.

In this paper, we present an unequal power divider with improved isolation based on a series RC circuit. The series RC isolation component is placed at an arbitrary position in the quarter-wave transmission line [10]. In addition, to design an unequal power divider with a high dividing ratio, the used low impedance line is a transmission line with a shunt open stub to achieve slow-wave characteristics [11]. The proposed unequal power divider is theoretically analyzed to derive equations for output port matching and isolation. For the validation of the proposed 10 : 1 unequal power divider, we simulated and fabricated the device for an operating frequency of 1 GHz.

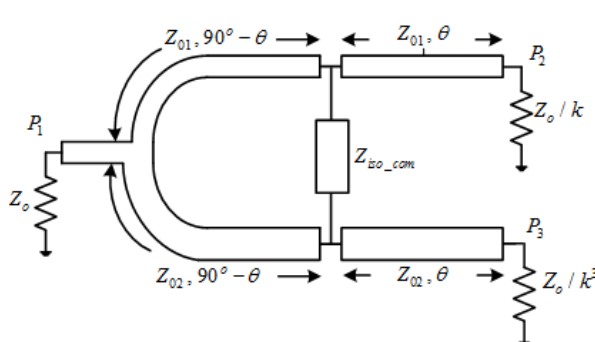


Figure 1: Configuration of the proposed unequal power divider.

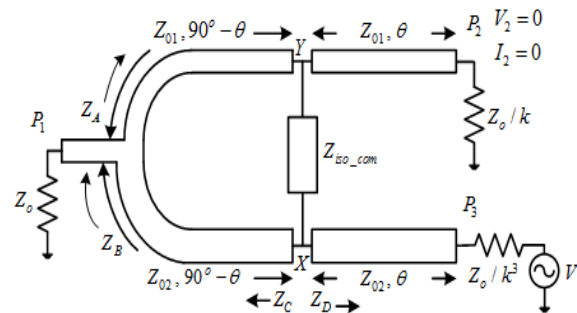


Figure 2: Equivalent circuit for matching and isolation.

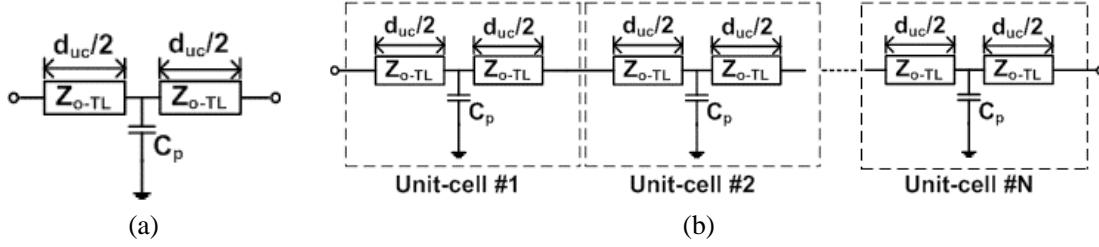


Figure 3: Transmission line with shunt open stub. (a) Equivalent circuit of unit-cell structure. (b) Cascade connection of unit-cells.

2. THEORY AND DESIGN

The configuration of the proposed unequal power divider is shown in Figure 1.

The power-dividing ratio of the divider is $k^2 (= P_3/P_2)$. The isolation components are placed at an arbitrary position in the quarter-wave transmission line. When the matching condition at port 1 is satisfied, the characteristic impedances are $Z_{01} = \sqrt{(1+k^2)/k}Z_o$ and, $Z_{02} = \sqrt{(1+k^2)/k^5}Z_o$. To find the optimum position θ of the isolation component to determine the matching and isolation conditions between output ports, the source is excited at port 3 in Figure 2. If the perfect isolation condition between output ports is satisfied, the voltage and current at port 2 are zero. Therefore, point Y is essentially shorted. In this condition, the impedances $Z_A \sim Z_D$ in Figure 2 are given by

$$Z_A = jZ_{o1} \tan(90^\circ - \theta), \quad Z_B = \frac{Z_A \cdot Z_o}{Z_A + Z_o} \quad (1)$$

$$Z_C = Z_{o2} \frac{Z_B + jZ_{o2} \tan(90^\circ - \theta)}{Z_{o2} + jZ_B \tan(90^\circ - \theta)}, \quad Z_D = Z_{o2} \frac{Z_o/k^3 + jZ_{o2} \tan \theta}{Z_{o2} + j(Z_o/k^3) \tan \theta} \quad (2)$$

To match the output port at position X , the following condition must be satisfied

$$\frac{1}{Z_C} + \frac{1}{Z_{iso.com}} = \frac{1}{Z_D^*} \quad (3)$$

From Equations (1)~(3), the isolation component $Z_{iso.com}$ can be defined as

$$Z_{iso.com} = R_{iso.com} + jX_{iso.com} \quad (4)$$

where $R_{iso.com}$ and $X_{iso.com}$ are the resistance and reactance of the isolation component, respectively.

According to Equation (4), the isolation component $Z_{iso.com}$ can be implemented using a series resistor and capacitor circuit.

To design the 10 : 1 unequal power divider, the impedance values of the transmission line are found. $Z_{01} = 93.25 \Omega$ and $Z_{02} = 9.33 \Omega$. In addition, the transformer impedance value of the P_3 output port is 8.89Ω . Because these impedance values are very low, corresponding structures are difficult to fabricate on a microstrip line because of their large widths. We designed the equivalent circuit of a unit-cell to overcome these problems, specifically, by using a short length transmission line with a shunt open stub, as shown in Figure 3. Because the unit-cell has slow-wave characteristics, the cascade connection transmission line of the unit-cell can be used to reduce the physical length of the transmission line and to create low impedance lines. To design a capacitive loaded transmission line (CLTL) with N unit-cells and electrical length θ_{CLTL} , we can calculate the transmission line length d_{uc} and capacitance C_p for a given transmission line (Z_{o-TL} and v_{o-TL}) and given values (Z_{o-CLTL} and v_{o-CLTL}) of the CLTL as follows:

$$d_{uc} = \frac{Z_{o-CLTL} \cdot \theta_{CLTL} \cdot v_{o-TL}}{2\pi \cdot f_o \cdot N \cdot Z_{o-TL}}, \quad C_p = \frac{\theta_{CLTL} \cdot (Z_{o-TL}^2 - Z_{o-CLTL}^2)}{2\pi \cdot f_o \cdot N \cdot Z_{o-TL}^2 \cdot Z_{o-CLTL}} \quad (5)$$

The capacitance C_p can be implemented using shunt open stubs

$$2\pi \cdot f_o \cdot C_p = \frac{1}{Z_{OP-ST}} \cdot \tan\left(\frac{2\pi f_o}{v_{OP-ST}} \cdot l_{OP-ST}\right) \quad (6)$$

where Z_{OP-ST} and v_{OP-ST} are the characteristic impedance and phase velocity of the open stub transmission lines, respectively, and l_{OP-ST} is the open stub length.

3. SIMULATED AND MEASURED RESULTS

In this section, the simulated and experimental results regarding the proposed unequal power divider are described. We designed an unequal power divider with a power ratio of $k^2 = 10$, an isolation component placed at the center position $\theta = 45^\circ$, and an operating frequency of 1 GHz. The isolation component is a series circuit composed of a $15\text{-}\Omega$ resistor and 1.8-pF capacitor. The Teflon substrate for the proposed unequal power divider had a dielectric constant of 2.2, a thickness of 0.787 mm , and a conductor thickness of 0.035 mm . The simulation was carried out using Microwave Office, which is a software developed by National Instruments.

Figure 4 shows the variation of isolation S -parameters as the isolation component position θ changes. In addition, Figure 5 shows the variation in resistor and capacitor values as θ changes. Figure 6 shows a photograph of the fabricated $10 : 1$ unequal power divider. To implement the low impedance lines, we used Equations (5), and (6). The transmission line width, length (W_{o-TL} , d_{uc}) and open stub width, length (W_{OP-ST} , l_{OP-ST}) of the CLTL are listed in Table 1. Figure 7 shows the S -parameter results for the proposed divider. The 50-MHz center frequency shift is caused by the fabrication inaccuracy of the microstrip line. The insertion loss of $|S_{21}|$ is 11.1 dB and $|S_{31}|$ is 1.3 dB . The return loss of $|S_{11}|$ is 17 dB , $|S_{22}|$ is 15 dB , and $|S_{33}|$ is 17 dB . In addition, the isolation of $|S_{23}|$ is 25 dB .

Table 1: CLTL microstrip line — element dimensions for low characteristic impedances.

	W_{o-TL} (mm)	d_{uc} (mm)	W_{OP-ST} (mm)	l_{OP-ST} (mm)	N
$Z_{o-CLTL} = 9.33\ \Omega$ (Z_{O2})	5.2	2.9	1.0	39	3
$Z_{o-CLTL} = 8.89\ \Omega$ (transformer)	5.2	3.2	1.0	43	5

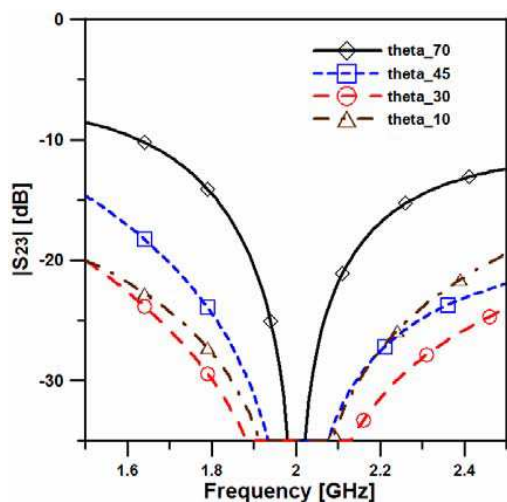


Figure 4: Simulation results for the isolation S -parameter variation of a $10 : 1$ power divider versus θ .

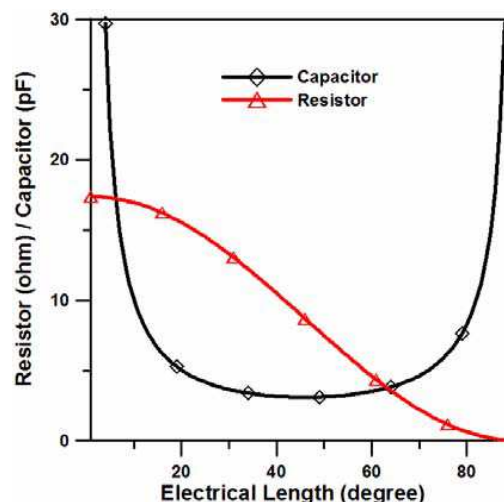


Figure 5: Variation of resistor and capacitor values versus θ .

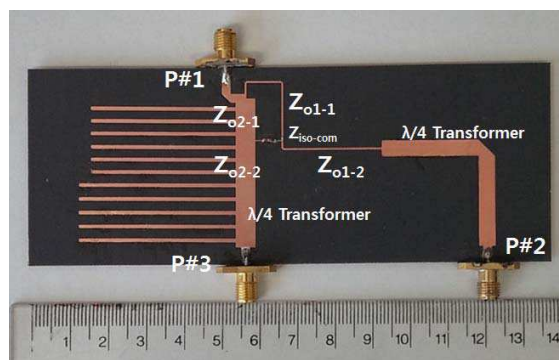


Figure 6: Photograph of fabricated $10 : 1$ unequal power divider.

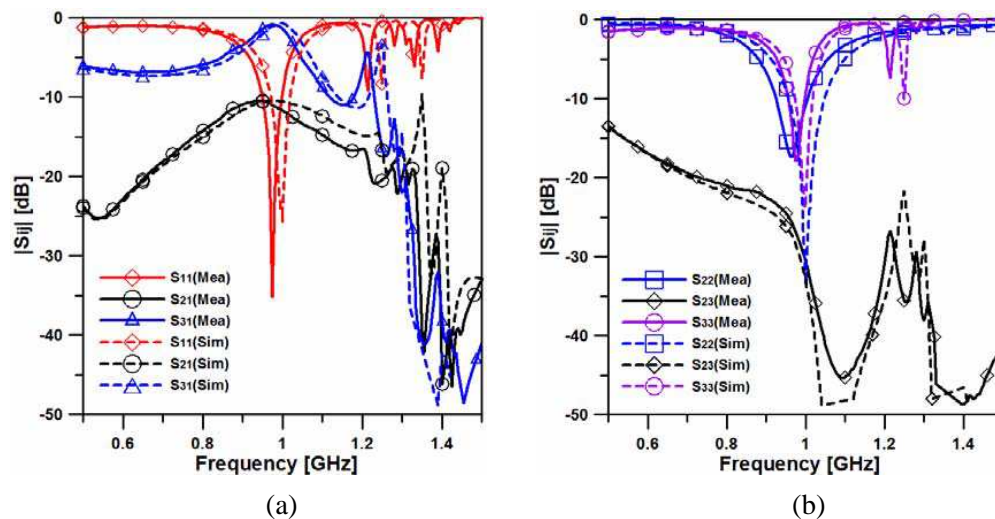


Figure 7: S -parameter results of proposed 10 : 1 unequal power divider, (a) $|S_{11}|$, $|S_{21}|$, $|S_{31}|$ and (b) $|S_{22}|$, $|S_{23}|$, $|S_{33}|$.

4. CONCLUSION

This paper presented a 10 : 1 unequal power divider with improved isolation. The series RC circuit of the isolation component is placed at the $\theta = 45^\circ$ position in the quarter-wave transmission line. Using a capacitive loaded transmission line of a small transmission line and a shunt open stub, the low impedance line of the 10 : 1 unequal power divider was realized. The proposed divider has good performance such as good port matching, low insertion loss and high isolation.

REFERENCES

- Kim, J. G., H. S. Lee, J. B. Yoon, and S. C. Hong, "60 GHz CPW-fed post-supported patch antenna using micromachining technology," *IEEE Microw. Wireless Compon. Letters*, Vol. 15, No. 1, 635–637, Oct. 2005.
- Kim, J. H., J. H. Cha, I. D. Kim, and B. M. Kim, "Optimum operation of asymmetrical-cells based linear Doherty power amplifiers uneven power drive and power matching," *IEEE Trans. Microw. Theory Tech.*, Vol. 53, No. 5, 1802–1809, May 2005.
- Ghannouchi, F. M. and A. Mohammadi, *The Six-port Technique with Microwave and Wireless Applications*, Artech House, Norwood, 2009.
- Wang, X., I. Sakagami, K. Takahashi, and S. Okamura, "A generalized dual-band Wilkinson power divider with parallel L, C, and R components," *IEEE Trans. Microw. Theory Tech.*, Vol. 60, No. 4, 952–964, Apr. 2012.
- Kim, S.-H., J.-H. Yoon, Y. Kim, and Y.-C. Yoon, "A modified Wilkinson divider using zero-degree phase shifting composite right/left-handed transmission line," *IEEE MTT-S Int. Microw. Symp. Dig.*, 1556–1559, May 2010.
- Liu, L., R. Jin, H. Yu, X. Liang, J. Geng, and X. Bai, "A compact ultra-wideband power divider with high isolation," *IEEE Antennas Propag. Int. Symp.*, 641–642, Jul. 2014.
- Kao, J.-C., Z.-M. Tsai, K.-Y. Lin, and H. Wang, "A modified Wilkinson power divider with isolation bandwidth improvement," *IEEE Trans. Microw. Theory Tech.*, Vol. 60, No. 9, 2768–2780, Sep. 2012.
- Chiang, C.-T., "Ultra wideband power divider using tapered line," *Progress In Electromagnetics Research*, Vol. 106, 61–73, 2010.
- Song, K. and Q. Xue, "Novel ultra-wideband (UWB) multilayer slotline power divider with bandpass response," *IEEE Microw. Wireless Compon. Letters*, Vol. 20, No. 1, 13–15, 2010.
- Kim, Y. and Y.-C. Yoon, "A modified unequal power divider with a complex isolation component for enhanced isolation," *Microw. Optical Tech. Letters*, Vol. 57, No. 2, 322–324, Feb. 2015.
- Eccleston, K. W. and S. H. Ong, "Compact planar microstrip line branch-line and rat-race couplers," *IEEE Trans. Microw. Theory Tech.*, Vol. 51, No. 10, 2119–2125, Oct. 2003.

Microwave Amplifier Design for Solid State Radar Transceivers at X-band

T. J. Korfiati¹, E. A. Karagianni², Ch. N. Vazouras²,
Ch. C. Lessi¹, and N. K. Uzunoglu³

¹Department of Informatics and Telecommunications
National and Kapodistrian University of Athens, Panepistimioupoli, Athens 15784, Greece

²Department of Naval Sciences, Hellenic Naval Academy
Hatzikyriakou Avenue, Piraeus 18539, Greece

³Department Division of Information Transmission Systems and Material Technology School of Electrical and Computer Engineering National Technical University of Athens
Zografou Campus Heroon Polytechniou 9, Zografou 15780, Greece

Abstract— A design approach to amplifier bias circuits using a discrete GaN on SiC HEMT is presented. Incorporating matching circuits to bias circuits, various simulations are carried out to minimize the effect of bias circuits on the overall behavior of the amplifier. Simulation results show good matching with $S_{11} = -12.2$ dB, $S_{22} = -14$ dB and a gain value at 15.4 dB. The resulting S parameter values correspond to $K = 1.3$ and $D < 1$, demonstrating stability of the circuit. Using this approach, a single stage X-band amplifier design with only one MMIC amplifier is presented, exhibiting an excellent performance at 10 GHz, which can be utilized in Solid State T/R module for advanced Phased Array Radar Systems.

1. INTRODUCTION

Distributed architectures employing solid state power amplifiers (SSPA) using gallium nitride (GaN) device technology promise to play an important role in the next generation of military, civilian, and commercial radar transmitters. These devices can support systems with higher sensitivity, increased detection range and improved reliability with lower cost and weight [1]. Use of GaN Monolithic Microwave Integrated Circuit (MMIC) in Transmit/Receive (T/R) modules enables improved resolution and DC power distribution efficiency [2, 3]. For solutions of this type, an important is fitting all the components in a package comprising a suitable amplifier.

The purpose of this paper is the analysis, the study and design of a single stage amplifier, with an operating frequency in X-band, band (or, with another terminology, in the I and the lower portion of J band); to demonstrate the proposed approach a typical design frequency is adopted at 10 GHz, around which a significant spectrum segment is usually allocated for radiolocation (on a primary or/and secondary basis). The final goal of the design is a reliable amplifier suitable for use in phase controlled arrays. A GaN transistor is selected to take advantage of several useful features [4], such as reduced heat sensitivity due to the high value of thermal conductivity [5], and hence elimination of cooling systems, reducing the weight and required board space of the overall circuit. Moreover, due to high impedance presented by GaN, fewer matching components are used, resulting in further cost and weight reduction.

2. ADVANCES OF GAN MICROWAVE AMPLIFIER TECHNOLOGY

The inherent power limitations of SSPA devices (as compared with traditional microwave tubes) may be circumvented, to some extent, by parallel module architectures based on parallel in-phase combination of several SSPA modules to achieve the desired output power level. High gain levels are achievable with this type of design (of the order of 70 dB or even higher). The parallel module concept may also be extended to the power supply, resulting in elimination of single points of failure in any active component within the SSPA; if one module fails, the SSPA can continue operation at reduced output power. This, of course, is made practical thanks to the low operating voltage required by SSPAs, as contrasted to extremely demanding voltage supply requirements of microwave tubes. In any case, higher power transistor designs enabling increased output power capability of an SSPA are highly desirable.

Recently, a range of high power wide band GaN amplifiers seem to gradually find their way into commercial availability. As the reliability of the devices improves, suppliers (see, e.g., [3, 8]) plan to push the advantages of GaN technology up in frequency to satisfy the need for improved

efficiency in the X, Ku & K-Band communications market. The high energy gap (3.4 eV) of the GaN compared with GaAs, as well as the high critical electric field (3.5 MV/cm), are the main properties that can support high voltage applications such as a high power amplifier. What is more, GaN is suitable for high current density applications because it has high charge density ($10^{13}/\text{cm}^2$) and high thermal conductivity (1.5 W/cm/K). High saturation velocity (2.7×10^7 cm/s) and medium mobility ($1500 \text{ cm}^2/\text{V/s}$) are properties that allow the use of GaN in high frequencies applications.

3. PHASED ARRAY RADARS

There are two types of phased arrays: Passive and Active (Figure 1). Passive phased arrays have a central transmitter and receiver, with phase shifters located at each radiating element or sub-array. The passive array is the least expensive phased array because of its low number and cost of components. Active arrays use T/R modules mounted directly on the antenna to provide the last stage of amplification for transmitted signals, the first stage of amplification for receive signals, and provide both amplitude and phase control at each radiating element. Use of T/R modules in active arrays provides advantages of amplitude control, low loss, and graceful degradation over passive arrays. Notwithstanding these advantages, high cost and low efficiency of the modules poses an obstacle to development of active phased array antennas. A typical T/R module [2, 7] for pulsed radar applications (Figure 2) comprises an electronically controlled attenuator and phase

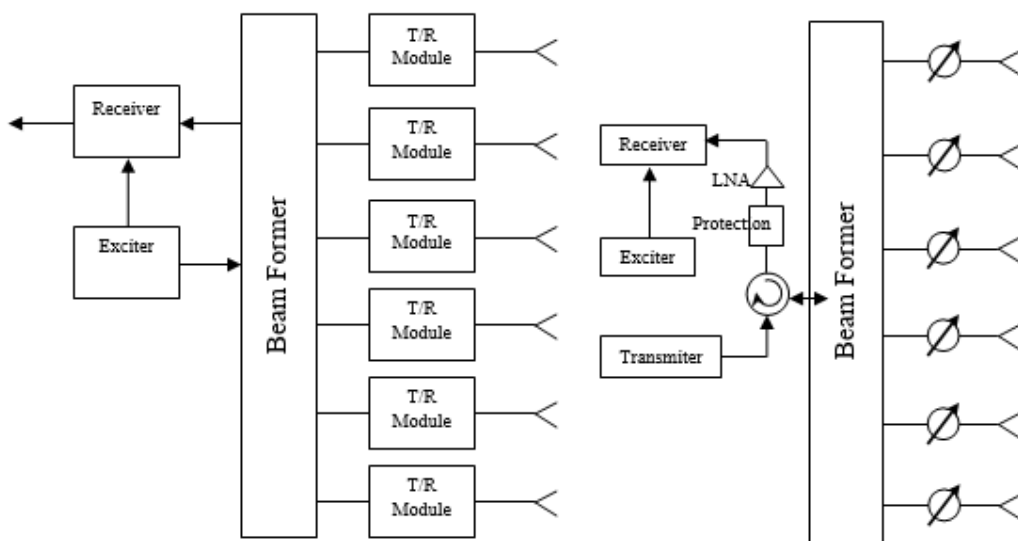


Figure 1: Block diagrams of active and passive phased arrays.

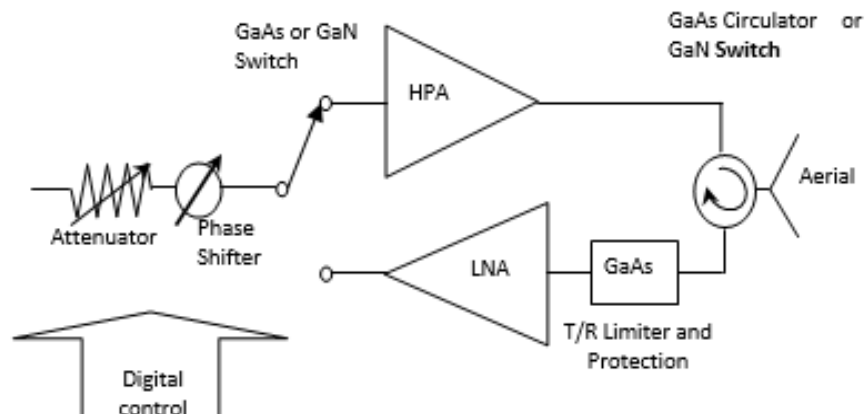


Figure 2: Typical T/R module components for both GaAs and GaN technologies.

shifter (used in both transmit and receive mode by means of appropriate switching), along with the high power amplifier (HPA) at the output branch and the low noise amplifier (LNA) at the input branch. A switch (probably combined with a circulator) acts as a duplexer for transmit and receive. A limiter is sometimes added before the LNA to reduce very strong incoming signals from jammers or unusually large targets too close to the radar. All components are assembled in one single T/R module.

4. MMIC DESIGN

The approach to design amplifier bias circuits is presented in this work. A discrete GaN on SiC HEMT was used [8]. Figure 3 depicts the simulation results for the bias circuit and Figure 4 the ones for the matching circuits of the amplifier. Incorporating matching circuits to bias circuits (Figure 5, Figure 6), various simulations are extracted to find what bias circuits do not affect the overall behavior of the amplifier [9].

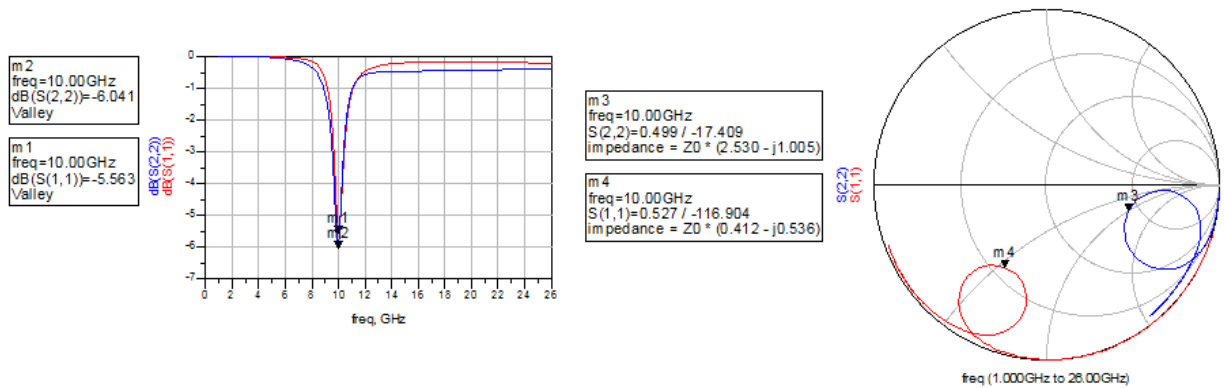


Figure 3: Simulation results — tuning circuit.

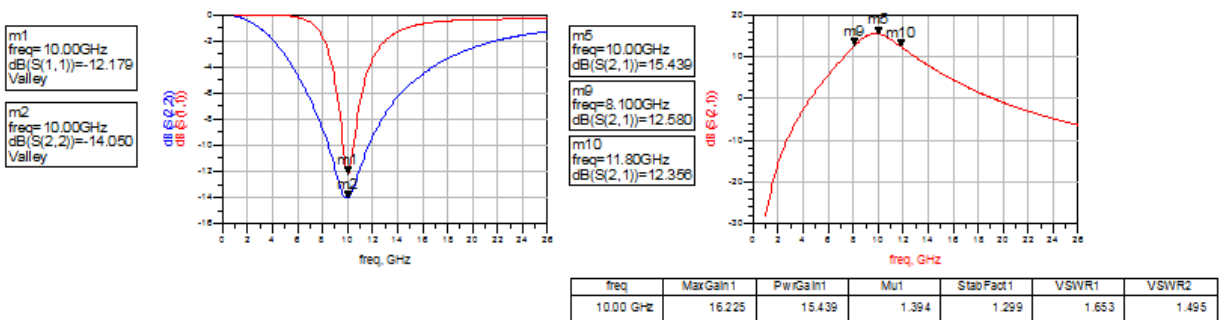


Figure 4: Simulation results — matching circuits.

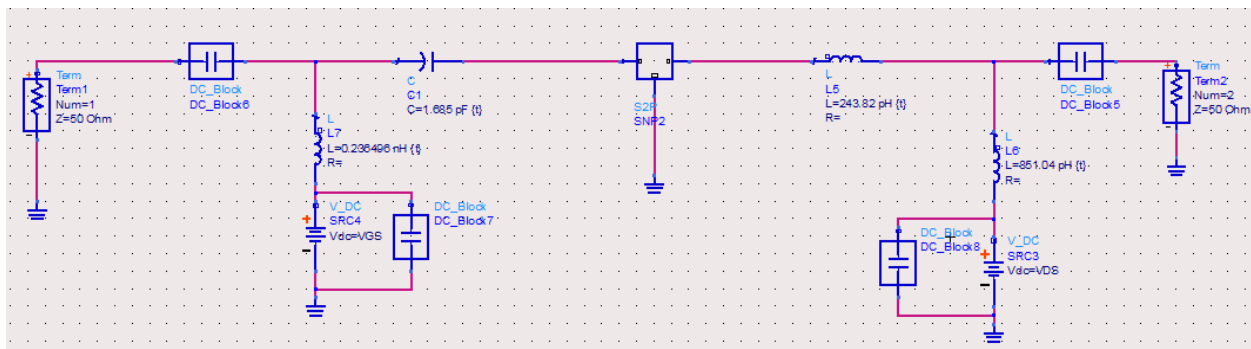


Figure 5: Final circuit.

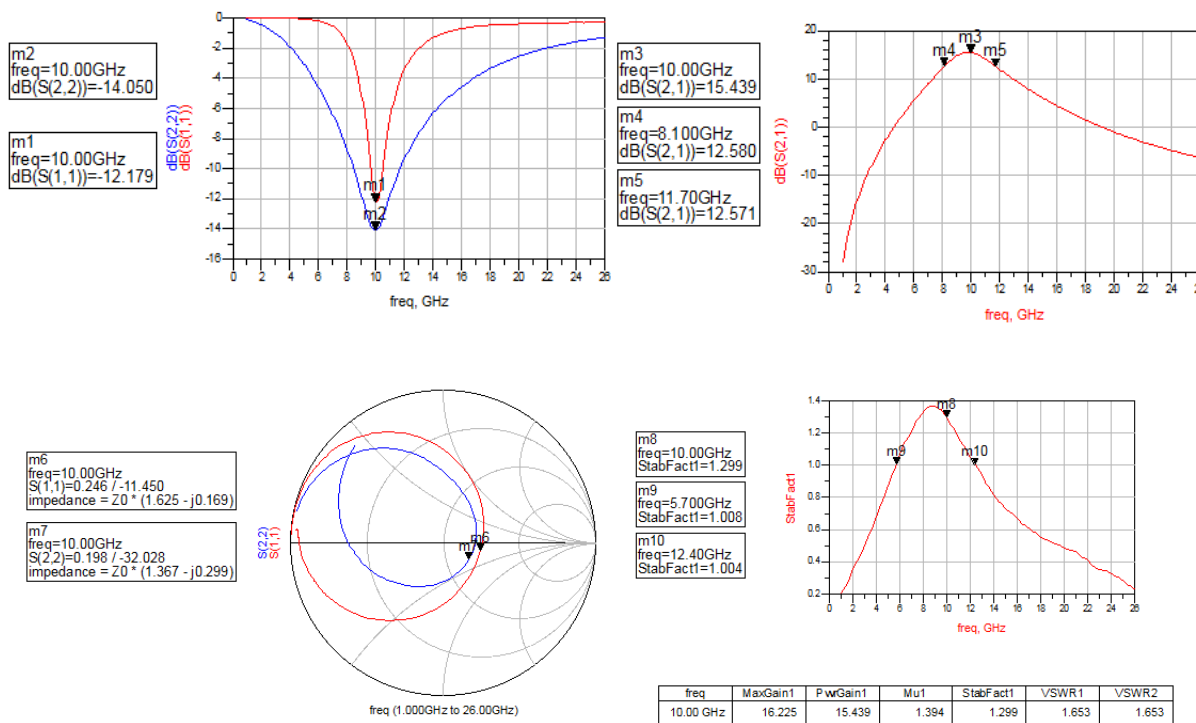


Figure 6: Simulation results — final circuit.

5. CONCLUSIONS

In this paper, a single stage X-band amplifier design which using only one MMIC amplifier has been shown to exhibit an excellent performance at 10 GHz for possible utilization in Solid State T/R modules for advanced Phased Array Radar Systems [9–11]. From simulation results we have a good matching, $S_{11} = -12.2$ dB, $S_{22} = -14$ dB and a gain value at 15,4 dB, almost the maximum supported. With the corresponding S parameter values S resulting from the design, we found $K = 1.3$ and $D < 1$ implying circuit stability. So in conclusion, we note two parameters. In view of the important need for lightweight and small sized amplifiers (one or two transistors) as an important factor in the structure of T/R modules, we may conclude that selection of the GaN technology as demonstrated above, positively contributes to amplifiers with low weight, size and cost, and with very good performance adjustment, gain, and bandwidth, presenting noteworthy application potential.

REFERENCES

1. Kopp, B. A., M. Borkowski, and G. Jerinic, “Transmit/receive modules,” *IEEE Trans. Microwave Theory and Tech.*, Vol. 50, 827–834, 2002.
2. Karagianni, E. A., Ch. C. Lessi, and C. Vazouras, “On-going GaN SSPA for naval radar transmitters: A MMIC amplifier design,” *9th International Conference on High-Performance Marine Vehicles*, 253–260, Athens, Greece, Dec. 2014.
3. Teledyne Microwave, www.teledynewireless.com/products/SSPA/SSPA.aspx, 2014.
4. Kopp, B. A., M. Borkowski, and G. Jerinic, “Transmit/receive modules,” *IEEE Trans. Microwave Theory and Tech.*, Vol. 50, 827–834, 2002.
5. Nuttinck, S., E. Gebara, J. Laskar, B. Wagner, and M. Harris, “RF performance and thermal analysis of AlGaIn/GaN power HEMTs in presence of self-heating effects,” *IEEE MTT-S Int. Microwave Symp. Dig.*, 921–924, 2002.
6. Zhang, A. P., L. B. Rowland, E. B. Kaminsky, J. W. Kretchmer, V. Tilak, A. F. Allen, and B. J. Edward, “Performance of AlGaIn/GaN HEMTs for 2.8 and 10 GHz power amplifier applications,” *IEEE MTT-S Int. Microwave Symp. Dig.*, 251–254, 2003.
7. Parker, D. and D. C. Zimmermann, “Phased arrays — Part I: Theory and architectures,” *IEEE Trans. Microwave Theory and Tech.*, Vol. 50, 678–687, 2002.

8. TriQuint Semiconductor, TGF2023-01, 6 Watt Discrete Power GaN on SiC HEMT datasheet, 2013.
9. Lessi, C. and E. Karagianni, “An X-band low noise amplifier design for marine navigation radars,” *Int. J. Communications, Network and System Sciences*, Vol. 7, 75–82, 2014.
10. DeTect Inc., “Advantages of a solid-state based radar system over a magnetron-based marine radar system,” r.ga.120903, 2009.
11. Turner, S. D., *Reliability Advantages of Modular Solid State Power Amplifiers compared to Traveling Wave Tube Amplifiers*, Paradise Datacom, Boalsburg, PA, USA, 2013.

THz Generation of Bloch Oscillators from SiC Structures due to Strong Electric Fields

V. I. Sankin, A. V. Andrianov, A. G. Petrov,
S. S. Nagalyuk, P. P. Shkrebiy, and A. O. Zachar'in
Ioffe Institute, 26 Politekhnicheskaya, St. Petersburg 194021, Russia

Abstract— We report on the observation and studies of the THz electroluminescence from 4H-SiC, 6H-SiC and 8H-SiC $n^+-n^-n^+$ structures with natural superlattice under electrical field applied along the natural superlattice axis (along the C-crystal axis). It is shown that there are two channels of the terahertz electroluminescence, which are responsible for the narrow emission lines at 5.3–12.7 meV and wider lines at 13 meV. The first emission channel can be well explained by the optical intraladder transitions in the Bloch oscillations regime. Presumably, the second emission channel is caused by optical interladder transitions between the states in different Wannier-Stark ladders.

1. INTRODUCTION

When electric field F is applied to an electron in periodic potential with period d , its translation motion can be transformed into oscillatory motion [1] with frequency ω given by

$$\omega = eFd/\hbar. \quad (1)$$

where e is an electron charge.

For one-dimensional periodic potential the dependence of the electron energy E on its wave vector k is also periodic. When electron, experiencing acceleration under applied electric field reaches the edge of Brillouin zone its group velocity changes the sign and electron starts to move back. Such oscillatory motion, named as Bloch oscillation (BO), and that defines the threshold values of electric field F_t [1]

$$W = eF_t l, \quad (2)$$

where W is a width of conduction band and l is the mean free path of electron.

Some evidence of BO and corresponding THz radiation were obtained by optical techniques in biased artificial superlattices under band-to-band excitation by femtosecond laser pulses [2]. In these experiments THz emission in the form of few cycles of rapidly damping THz electromagnetic oscillation has been observed. There is an alternative explanation of such emission as a quantum beating of the states in Wannier Stark ladders [3]. The damping of such oscillation takes place in 2–3 order faster than BO.

2. EXPERIMENT

The novel idea of the present work is that BO regime can be realized in the natural superlattice (NSL) of silicon carbide (SiC) polytypes with strong bias electric field. It should be noted that there is no heterointerfaces in the SiC NSLs. The superperiodical SiC polytypes is self-organized along the C -axis and this is absolutely stable phenomenon with precise crystalline parameters [4]. The period of SiC NSL, d , is equal to $c/2$ [5], where c is the size of unit cell along C -axis, and for 4H-, 6H-, 8H-polytypes the periods are 5, 7.5 and 10 Å, respectively. Experimental data testifying about minizone spectrum in SiC polytypes have been obtained previously [6]. The existence of minizone spectrum in SiC polytypes was supported theoretically in Refs. [7, 8]. In the Ref. [6] it was reported about the negative differential conductivity (NDC) caused by BO regime and Wannier-Stark localization. The Ref. [9] reported about the first experimental observation of the intense THz electroluminescence caused by BO regime in SiC NSL.

The current paper is aimed to study of the THz emission associated with the BO in NSL in different hexagonal polytypes of silicon carbide 4H-SiC, 8H-SiC and in 6H-SiC at largest field. The main goal of the current paper is to present the certain proof of the existence of BO using the comparative analysis of the THz EL in three NSLs.

It can be seen that, at low temperature concentration of free electron in SiC is negligible and for observation of BO electrons should be injected into active area from adjacent highly doped emitter.

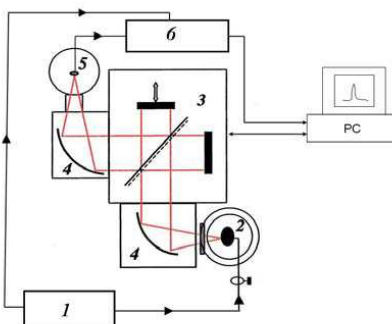


Figure 1: The schema of the measurement setup for investigation of THz electro-luminescence spectra from SiC NSLs. 1 — the generator of electrical pulses; 2 — helium optical cryostat, which was optimized for the THz spectral domain, with sample; 3 — Michelson interferometer; 4 — parabolic mirrors; 5 — silicon bolometer, 6 — lock-in amplifier.

The detailed description of the studied unipolar $n^{++}-n^{-}-n^{+}$ diode mesa-structures can be found in Ref. [9]. The setup for spectral measurements is shown on Fig. 1.

The structures fabricated on the n^{+} substrate was attached to the insulating heat-conducting p-SiC plate by the thin silver layer using a thermo compression. It allowed us to improve the thermal contact and to increase the applied electric power by 40% without any noticeable Joule heating of the active region of the $n^{++}-n^{-}-n^{+}$ and bipolar $n^{++}-\pi-n^{+}$ structures comparing with results of Ref. [9].

Impact ionization of nitrogen in $n^{++}-n^{-}-n^{+}$ 4H-SiC structures [10] occurs at electric fields up to 50 times smaller than threshold electric fields of Bloch oscillations obtained from (Eq. (2)). Therefore bipolar $n^{++}-\pi-n^{+}$ structure analogous to reported earlier [6] was used for observation of the THz BO emission from 4H-SiC.

As it was pointed out in Ref. [9] the sizable broadening of the THz emission line takes place at applied voltage 255 V as compared with that at 240 V. It was explained hypothetically by the lattice heating, but the occurrence of the weak high energy emission line with the maximum at 13.0 meV remains unexplained. For that reason we have not increased the current and voltage applied until the heat sink improvement mentioned above.

3. DISCUSSION

Figure 2(a) shows luminescence spectra of $n^{++}-n^{-}-n^{+}$ mesa structures for different applied voltage. These spectra consist of the single, symmetrical emission lines L1 with the maximum at 5.18–7.5 meV and the spectral width of 3.0-meV.

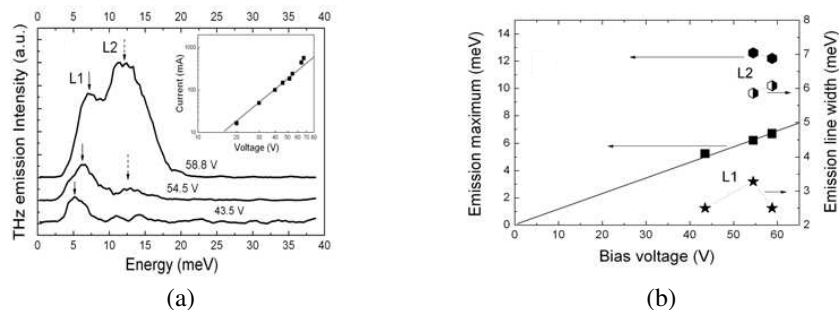


Figure 2: (a) Spectra of the THz emission from a $n^{++}-n^{-}-n^{+}$ 8H-SiC NSL at different bias voltages and at $T \sim 7$ K. The figure insert shows a typical I-V characteristic of the $n^{++}-n^{-}-n^{+}$ 8H-SiC NSL. Points are experimental data. The solid curve is the result of approximation of the data by a power law ($I = const \propto V^{2.5}$). (b) The result of decomposition of the experimental spectra by two Gaussian lines for different bias voltages. The solid line is a linear fit of the L1-line peak position versus the bias voltage.

The peak energy of 5.2 meV corresponds to electric field magnitude of 5.2×10^4 V/cm (Eq. (1)). The value of the electric field F shows also that only a part (about 35%) of the bias voltage drops

on the active region of the structure. It is worth to note also that the spectrally integrated THz emission peak power was about $3.5 \mu\text{W}$ and $10 \mu\text{W}$ at 9.1 W of peak pumping power for 8H- and 6H-SiC NSLs, respectively. Such a ratio of the emission powers in reasonable agreement with the theory of THz BO radiation from SiC NSLs [9].

It is worth to note that the electric field of the THz BO emission appearance of the order of $5.2 \times 10^4 \text{ V/cm}$ is 1.6 times less than that for 6H-SiC NSL. This difference in electric fields is caused by the difference in the width of the first minibands in 6H-SiC and 8H-SiC 260 and 140 meV respectively [6] and it is in accordance to (Eq. (2)).

The electric field F required for appearance of THz EL correlates with the threshold field F_t of NDC [6] taking into account the temperature difference of the BO threshold field. The width of the THz emission lines remains practically unchanged in the voltage range from 43.5 to 58.8 V (Fig. 2(b)). This indicates that the electric field is practically homogeneous in the active region of the structures. Increase of the voltage till 54.5 V (corresponding to electric field $6.2 \times 10^4 \text{ V/cm}$ Eq. (1)) leads to a shift of the emission lines L1 to higher energy (Fig. 2(b)) and to an appearance of the second emission line L2 centered at energy 12.9 meV. Further increase of the voltage, till the value 58.8 V is accompanied by sharp rise of electrical current and intensity of second line, which became dominant in the spectrum. The width of the second line at 58.8 V is about 7.0 meV and energy maximum lies near the 12.5 meV.

It was found that the THz EL from side face of the mesa structure is linearly polarized along the C-crystal axis (along the electric field) and the polarization degree is about 56%.

The current through the structure is proportional to voltage in the $5/2$ power in accordance with the theoretical result for the I-V characteristics in BO regime [9]. The dependence of the intensity of EL on the current is almost linear.

The low energy shift of the spectral peaks in the 8H-SiC NSL THz emission comparing with that for 6H-SiC NSL is the consequence of the quantitative differences in miniband widths of 8H-SiC and 6H-SiC. This is convincing proof of the realization of the BO regime in these NSLs

As a surprise in this study the strong electroluminescence line comes at $12.5 \pm 0.1 \text{ meV}$. The intensity of this line superlinearly increases with current as $P \sim I^{2.5}$.

As mentioned above, the relatively weak line at $13.0 \pm 0.1 \text{ meV}$ have been observed in 6H-SiC THz EL spectra too [9]. Fig. 3 demonstrates two spectra of the THz emission of 6H-SiC at 255 V (shown before in Ref. [9]) and the spectrum at 295 V obtained in the current work. It is clearly seen that the L2 lines with the maximum near 13.0 meV grows drastically with the pump power increase as $P \sim I^7$.

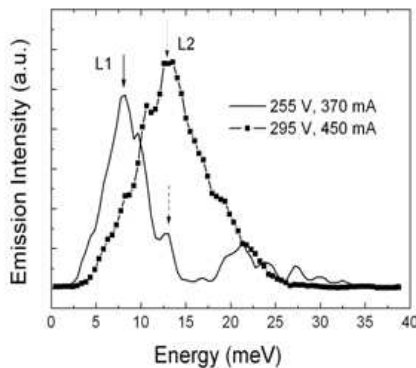


Figure 3: Spectra of the THz emission from the NSL 6H-SiC $n^{++}-n^{-}-n^{+}$ structures.

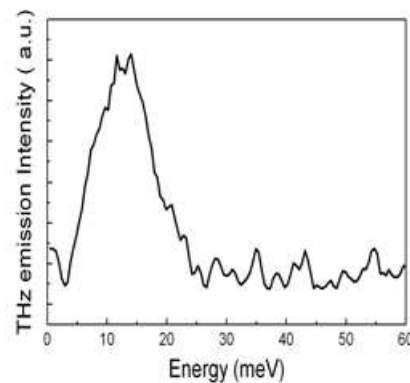


Figure 4: The THz emission for a 4H-SiC bipolar $n^{++}-\pi-n^{+}$ structure at the bias voltage of 30 V and the current of 1150 mA. $T \sim 7 \text{ K}$.

The full spectrum width increase at 295 V can be substantially explained by the superposition of two lines: at 9.5 meV (extrapolated transition energy of the L1 at 295 V) and 13.0 meV L2 rather than the line broadening due to the heating and field increase. Although it should be mentioned that L2 is 1.7 times wider than L1. It should be emphasized that the detection of L2 in the THz EL spectra of 6H-SiC NSL becomes possible after carrying out the investigations of 8H-SiC NSL, which has the well-resolved THz EL in the 7.5–12.9 meV range (Fig. 2(a)) and it has allowed us to

make a statement (see Fig. 2(b)) that the L2 line is not directly related to the THz BO emission. However, it can occur at the conditions of electron Wannier Stark localization in a degenerated states system of neighboring conduction band minimum in K point [8].

The total emission power of the THz emission at 295 V is about $P = 4 \times 10^{-5}$ W. It is in five orders more than the estimation of the black body emission power with the maximum at 13.0 meV ($T = 30$ K).

So, both in 6H-SiC and 8H-SiC NSLs we have revealed the strong emission lines, marked by L2 in this paper, which are very similar in their behavior.

Figure 4 shows the spectrum of THz emission from 4H-SiC bipolar $n^{++}-\pi-n^+$ structure. There is a single broad peak centered at 12.8 ± 0.5 meV ($F = 250$ kV/cm) with width 11 meV. The voltage applied between two n^+ — areas was 30 V, and the current reaches 1150 mA. The sample based on 4H-SiC has the highest threshold electric field required for observation of THz emission, and the highest current. Due to high level of current the sample demonstrated rapid degradation. For that reason only one spectrum has been obtained and the same analysis as for 6H-SiC and 8H-SiC was not possible. However, as is seen the spectrum shows a broad emission line centered at 12.8 meV with spectral width of 11 meV. It is quite possible that such a broad line is associated with the superposition of two lines having the same nature as it was mentioned above, which, however, for 4H-SiC are arranged substantially closer to each other than in 6H- and 8H-SiC.

It was experimentally established that the peak energy of EL in the 8H-SiC $n^{++}-\pi-n^+$ structures is 1.5 times greater than for $n^{++}-n^- -n^+$ structures. According to these arguments the spectrum peak in $n^{++}-n^- -n^+$ 4H-SiC structures will probably be near the 8.4 meV energy that would correspond to the $F = 168$ kV/cm electric field inside the NSL(see Eq. (1)).

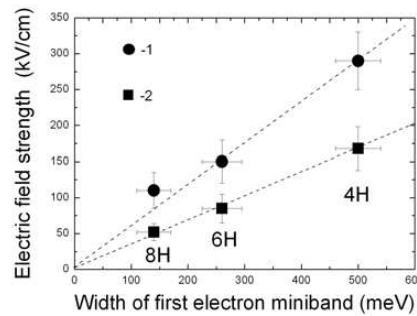


Figure 5: The dependence of the threshold field for the negative differential conductivity (1), obtained before at 300 K [6] and the minimal electric field required for the observation of the THz BO emission (2) at 7 K (Ref. [9] and present work) on the first miniband width in the 8H-, 6H- and 4H-SiC NSLs. The dashed lines are linear fits of the experimental data.

The threshold fields for the NDC and the THz emission correlate well for 4H-, 6H- and 8H-SiC NSLs. Fig. 5 shows the dependence of the threshold electric field for the observation of the NDC at 300 (Fig. 5, (1)) and electric field required, for the observation of THz emission at 7 K (Fig. 5, (2)) on the first minizone width in the 4H-, 6H- and 8H-SiC NSLs. The both dependencies are linear that is yet another proof of BO nature of these effects as far as it corresponds to Eq. (2) at practically the same mean free paths for electrons in 4H-, 6H- and 8H-SiC NSL. The experimental results indicate that for $l = 170\text{\AA}$ and 310\AA for 300 and 7 K, respectively.

4. SUMMARY

Thus, the BO regime was realized in the natural superlattices 4H, 6H and 8H-SiC on the U-line (M-L) parallel to the C -axis of the hexagonal Brillouin zone. It is established that intense THz emission can be attributed to the intraladder transitions between the Wannier-Stark states and has all characters of the BO effect.

As a result we can state that NSL SiC is a source of the electrically tunable terahertz emission in the 1.6–2.3 THz and in the 3.2 THz ranges.

Authors are thankful to Dr. A. M. Monakhov for fruitful discussion.

REFERENCES

1. Zener, C. and H. H. Wills, *Proc. R. Soc. London Ser. A*, Vol. 145, 523, 1934.

2. Washke, C., et al., *Phys. Rev.Lett.*, Vol. 70, 3319, 1993.
3. Voisin, P., *Ann. Phys. Fr.*, Vol. 22, 681, 1997.
4. Verma, A. R. and P. Krishna, *Polymorphism and Polytypism in Crystals*, Wiley, New York, 1966.
5. Choyke, W. J. and L. Patrick, *Phys. Rev.*, Vol. 127, 1868, 1962.
6. Sankin, V. I., *Semiconductors*, Vol. 36, 717, 2002.
7. Nilsson, H.-E., M. Hjelm, C. Frojdh, et al., *J. Appl. Phys.*, Vol. 86, 965, 1999.
8. Laref, A. and S. Laref , *Phys. Stat. Sol. (b)*, Vol. 245, No. 1, 89–100, 2008.
9. Sankin, V. I., A. V. Andrianov, A. G. Petrov, and A. O. Zakhar'in, *Appl. Phys. Lett.*, Vol. 100, 111109, 2012.
10. Sankin, V. I., A. Petrov, and M. A. Kaliteevski, *J. Appl. Phys.*, Vol. 114, 063704, 2013.

Electromagnetic Emission Analysis of a Multiband EMI Filter Based on Sub-wavelength Resonators

J. M. Ruiz¹, I. Gil², and M. Morata¹

¹Escuela Universitaria Salesiana de Sarriá, Psg. Sant Joan Bosco 74, Barcelona, E-08017, Spain

²Department of Electronics Engineering, UPC Barcelona Tech, Colom 1, Terrassa, E-08222, Spain

Abstract— In this paper the electromagnetic emission of sub-wavelength EMI filter based on SRR and CSRR resonator has been analysed by means of near E and H fields simulation with the FDTD SEMCAD® software. The target bands are 900 MHz (RFID UHF), 1.8 GHz (GSM) and 2.4 GHz (ISM, Instrumentation, Scientific and Medical). A 3-stages/5-stages rejection band filter was designed and fabricated in a PCB. The preliminary simulation results show that the more significant emissions take place at higher frequencies, the 1.8 GHz GSM band and ISM band (2.4 GHz), and are located at the resonators' surface.

1. INTRODUCTION

The increasing of the electromagnetic emissions in the last years requires the design of electronic systems which are immune to electromagnetic interferences (EMI). These new electronic systems must also fulfill the international regulations requirements for radiated emissions, in order to ensure the compatibility with other electronic devices. Since low cost and highly-integrated circuits and systems are required, new filtering techniques are necessary to reduce cost and dimensions of standard EMI filters. In this direction, new solutions have been developed based on Electromagnetic Band Gaps [1, 2], a type of metamaterials. Metamaterials are artificial fabricated materials based on periodic or quasi-periodic structures with electromagnetic controllable properties. Among them, we can find the sub-wavelength resonators named split-ring resonator (SRR) [3] and the complementary split-ring resonator (CSRR) [4, 5], which are used to reduce the EMI in printed circuit boards (PCB).

In this paper, the electromagnetic emissions of a multiband microstrip filter based on SRRs and CSRRs have been analyzed. The filter has been designed for the target frequency bands of RFID UHF, GSM and the 2.4 GHz industrial, scientific and medical (ISM) band. The electromagnetic radiated emissions have been evaluated by means of the commercial SEMCAD software [6]. Moreover, the insertion losses (S_{21}) and return losses (S_{11}) have been experimentally measured.

The paper is organized as follows: Section 2 is about the circuit design, Section 3 shows the experimental and simulated results and Section 4 summarizes the conclusions.

2. EMI FILTER DESIGN

A complete discussion for the design and preliminary results can be found at [5] and [7]. The starting point consists of a conventional microstrip line which can be potentially affected by RFI in the range of RFID UHF ($f_{o1} \sim 900$ MHz), GSM frequency uplink and downlink bands ($f_{o2} \sim 1.8$ GHz) and ISM ($f_{o3} \sim 2.45$ GHz).

The sub-wavelength particles considered in this work correspond to the original SRR and the dual counterpart of the SR, the CSR. Fig. 1 shows the implemented layout of the EMI filter. The design strategy is based on the implementation of the SRRs in order to develop the stop-band filter at the higher frequency band (ISM). These particles have been etched in the top side of the PCB, close to the host microstrip line. Specifically, a 5-stage SRR has been implemented (Fig. 2(a)) for the ISM band. Concerning the lower frequency bands (i.e., the corresponding with the higher dimensions required resonators), two arrays of 3-stage CSRs have been used in order to develop the stop-band responses at RFID UHF and GSM. They can be etched in the metal ground plane of the PCB and, therefore, no extra area is required (Fig. 2(d)).

The EMI filter was fabricated by using a *Rogers RO3010* substrate (dielectric permittivity, $\epsilon_r = 10.2$ and thickness, $h = 1.27$ mm). A $50\ \Omega$ microstrip line, with 1.18 mm width and 47 mm length was inserted. A square topology has been chosen for all the resonators in order to enhance the coupling to the host line. Since the distance of the SRRs to the host line is a key point, they have been placed as close as possible to the microstrip line (200 μm). Concerning CSRs, they have been etched underneath the microstrip line in order to maximize the electrical coupling to

it. Because the number of resonators stages determines the level of rejection of each stop-band filter response, a higher rejection level is expected in case of SRRs. The reduction in the number of stages of CSRs is due to the requirement to include two rejection bands. Finally, the distance between adjacent SRRs and CSRs has a direct impact in the rejection bandwidth. Therefore, it has been also considered as a significant parameter for the final implementation (200 μm).



Figure 1: Topology of the designed multiband microstrip EMI filter. (a) Top layer with microstrip line and the SRRs designed at 2.45 GHz. (b) Bottom layer with CSRs etched in the ground metal tuned at 900 MHz and 1.8 GHz, respectively. Metallization zones are depicted in grey.

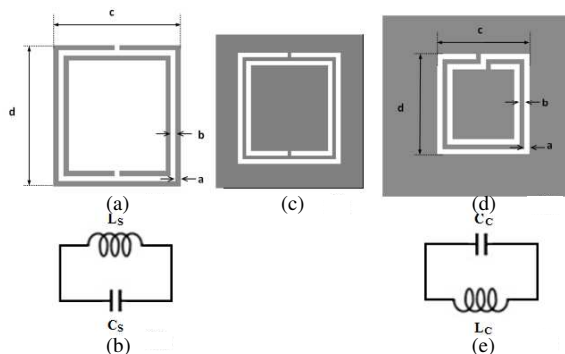


Figure 2: Sub-wavelength particles dimensions: $a = b = 0.2\text{ mm}$ for all the particles. ISM: $c = 5\text{ mm}$, $d = 5.5\text{--}5.8\text{ mm}$. GSM: $c = 3.7\text{ mm}$, $d = 4\text{ mm}$. RFID: $c = 5.5\text{--}5.9\text{ mm}$, $d = 7.5\text{ mm}$.

3. RESULTS

3.1. Measured S_{11} and S_{21} Parameters

Figure 3 shows the measured results of insertion losses (S_{21}) and return losses (S_{11}) [7]. Concerning the rejection level, a higher level is achieved at the ISM band by means of the SRRs, due to the larger number of implemented stages. This fact also implies a wider bandwidth in the stop-band frequency response. The losses of the allowed bands present an average value of 1.5 dB and are basically due to the presence of connectors and ohmic losses. Measured return losses show a low level at the allowed frequency bands (less than 10 dB).

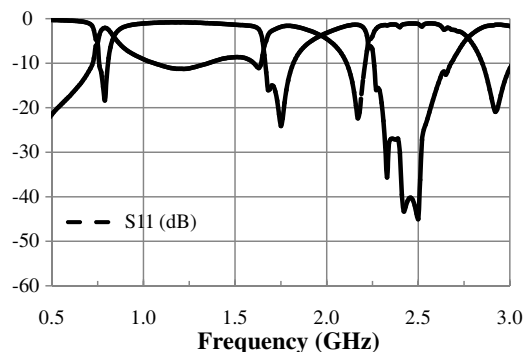


Figure 3: Experimentally measured frequency responses of the insertion losses (S_{21}) and return losses (S_{11}).

3.2. Simulated Radiation Pattern

The electromagnetic emissions simulation have been performed by using the Finite-Difference Time Domain (FDTD) *SEMCAD software*. To determine the most relevant radiation frequencies, an analysis of the previous results should be done. These frequencies correspond to those that have a higher value of the total power losses, obtained by means of the expression (1):

$$P_{\text{loss}} = 1 - |S_{11}|^2 - |S_{21}|^2 \tag{1}$$

In these cases, an important part of the incident power is neither transmitted nor absorbed; therefore it must be radiated [8]. Table 1 shows these frequencies and the corresponding value of expression (1).

Table 1: List of frequencies with higher values of power loss.

Freq. (GHz)	0.75	1.66	2.22	2.40	2.63
P_{loss}	0.48	0.62	0.45	0.35	0.37

As can be seen, these frequencies correspond to the stop-bands of the filter, except for 2.22 GHz. This one (2.22 GHz) appears due to the fact that the return losses (S_{11}) are very low, while insertion losses have a significant value. That happens because this frequency corresponds to the resonance frequency of a CSSR's subset, as we will see below.

The following figures show the simulated RMS values of the electric (E) near-field, dB normalized to the maximum, and the radiated electric field, E_{max} , calculated by taking into account the maximum electric field components in both ϕ and θ coordinates, E_ϕ and E_θ , according to expression (2).

$$E_{\text{max}} = \sqrt{(E_{\phi,\text{max}})^2 + (E_{\theta,\text{max}})^2} \quad (2)$$

The radiation pattern has been studied at the yz plane ($\phi = 90^\circ$), which allows to visualize the radiation impact.

As can be seen in Figs. 4–8, the emission takes place mainly at the corresponding resonators, except for the 2.22 GHz, which corresponds to the resonance frequency of a subset of the SRRs resonators and, for this reason, the S_{11} parameter is very low at this frequency, while the S_{21}

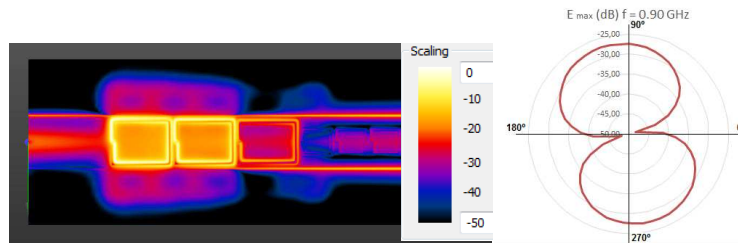


Figure 4: Simulated RMS values for E near-field and normalized radiation pattern at 0.90 GHz.

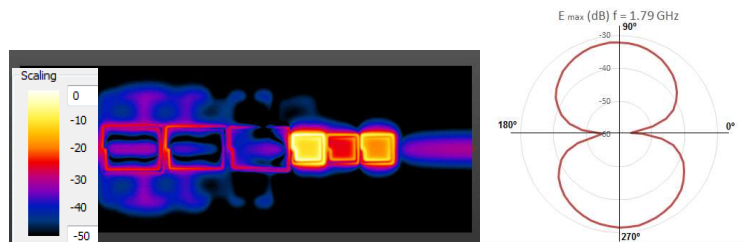


Figure 5: Simulated RMS values for E near-field and normalized radiation pattern at 1.79 GHz.

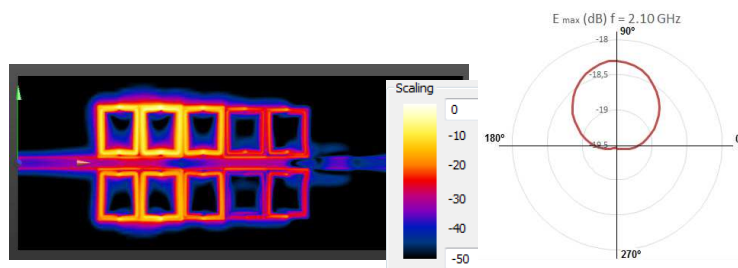


Figure 6: Simulated RMS values for E near-field and normalized radiation pattern at 2.10 GHz.



Figure 7: Simulated RMS values for E near-field and normalized radiation pattern at 2.43 GHz.

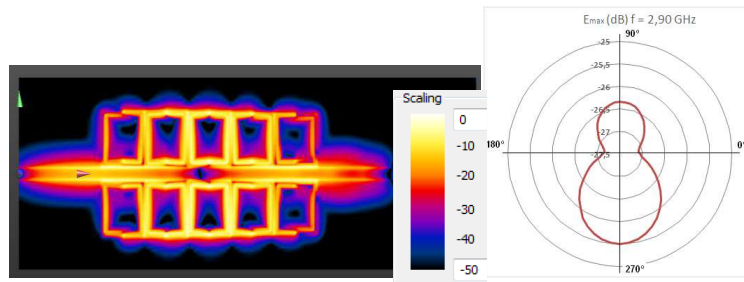


Figure 8: Simulated RMS values for E near-field and normalized radiation pattern at 2.90 GHz.

indicates that there are not significant insertion losses. In this case, the emission is directed only to z-positive (perpendicular to the top board layer) values.

It is also remarkable, that the main emissions occur at the base frequency 0.90 GHz and its harmonic: 1.79 GHz ($\approx 2 \cdot 0.90$) and 2.90 GHz ($\approx 3 \cdot 0.90$).

4. CONCLUSIONS

A multiband filter, designed by SRR's and CSR's, was tested and simulated. The experimental data show a good response, with rejections levels up to 20 dB/40 dB. The simulations of both near and far-field were done and the results are shown, further measurements shall be done to assure that the device can satisfy the conventional electromagnetic normative.

ACKNOWLEDGMENT

This work has been partially supported by Generalitat de Catalunya (SGR2009-1425) and the Spanish Government (TEC2010-18550).

REFERENCES

1. Shahparnia, S. and O.M. Ramahi, "Electromagnetic interference (EMI) reduction from printed circuit boards (PCB) using electromagnetic bandgap structures," *IEEE Transactions on Electromagnetic Compatibility*, Vol. 46, 292-303, November 2004.
2. Irvani, B. M. and O. M. Ramahi, "Design, implementation and testing of miniaturized electromagnetic bandgap structures for broadband switching noise mitigation in high-speed PCBs," *IEEE Transactions on Advanced Packaging*, Vol. 30, 171-179, May 2007.
3. Pendry, J. B., A.J. Holden, D. J. Robbins, and W. J. Stewart, "Magnetism from conductors and enhanced nonlinear phenomena," *IEEE Trans. Microwave Theory and Techniques*, Vol. 47, 2075-2084, November 1999.
4. Baena, J. D., J. Bonache, F. Martin, R. Marqués, F. Falcone, T. Lopetegui, M. A. G. Laso, J. García-García, I. Gil, M. F. Portillo, and M. Sorolla, "Equivalent-circuit models for SRRs and CSRRs coupled to planar transmission lines," *IEEE Transactions on Microwave Theory and Techniques*, Vol. 53, 1451-1461, April 2005.
5. Pérez, D., I. Gil, J. Gago, R. Fernández-García, J. Balcells, S. Member, D. González, N. Berbel, and J. Mon, "Reduction of electromagnetic interference susceptibility in small-signal analog circuits using complementary split-ring resonators," *IEEE Trans. on Comp., Pack. and Manuf. Tech.*, Vol. 2, No. 2, 240-247, October 2012.
6. "SEMCAD," Schmid & Partner Engineering AG (SPEAG).

7. Gil, I., R. Fernández, J. Gago, and J. Balcells, “Multiband EMI filter based on metamaterials,” *IEICE Electron. Express*, Vol. 7, No. 9, 563–568, May 2010.
8. Bait-Suwailam, M. M. and O. M. Ramahi, “Ultrawideband mitigation of simultaneous switching noise and EMI reduction in high-speed PCBs using CSRR,” *IEEE Transactions on Electromagnetic Compatibility*, Vol. 54, No. 2, April 2012.

Overhead and Cable Transmission Lines Magnetic Fields: Standardization, Estimation, and Design

N. B. Rubtsova and A. Yu. Tokarskiy

FSBSI “Research Institute of Occupational Health”, Moscow, Russian Federation

Abstract— Overhead and cable power transmission lines magnetic field strength estimation algorithm is presented. Example of 500 kV overhead transmission line power frequency MF strength distribution is presented in comparison with 500 kV cable transmission line MF distributions. According with the problem of general public electromagnetic safety maintenance is suggested the optimal circuits’ arrangement with changed order of the phases that allow reducing the 50 Hz MF values to maximal permissible levels (hygienic standards of general public exposure).

It is shown that multiphase sources create the field of elliptic polarization, which most root-mean square strength value is on the ellipse major axis, whereas result values calculation by components with Pythagorean Theorem use lead to errors with the increase of real value to 41%. By the example of 500 kV lines is shown the differences between results of the applied calculation methods. For 500 kV cable lines the ways of MF value decrease to permissible levels under different kinds of it lying are examined.

There is shown that socket joint use with cables and its locations in the corners of equilateral triangle under correctly changed order of the phases as well as slight increase of cable depth gives the possibility to avoid the ferromagnetic screens arrangement, and to cut costs.

1. INTRODUCTION

Power frequency (PF) electromagnetic field (EMF) general public electromagnetic safety ensuring is a significant problem, especially in terms of magnetic field (MF) exposure, in connection with increased risk of health loss. The main sources of PF EMF are the current facilities involved in power generation, transmission and utilization. The most important are overhead and cable power transmission lines (OTL and CL).

PF EMF human health hazard effects safety system three principle includes: safety by time, safety by distance, and safety by protective means.

Safety by time is realized in Russian occupational and general public PF EMF hygienic standards, that are partially different from international and some national standards. Russian PF electric (EF) and magnetic field maximal permissible levels are one of the strictest in the world. In addition, in order to general public protect from PF EF on both sides of the OTL: from 20 m for 330 kV OTL to 55 m for 1150 kV OTL. Sanitary protection zone are established according to PF EF permissible value 1 kV/m, and not take into account PF MF hygienic standard (8 A/m).

For CL sanitary protection zone is not defined, and 1 m security zone is only. This problem is of particular relevance due to the fact that CLs are the source of PF MF mainly, that were classified by International Agency for research on cancer (IARC) in 2002 as potential carcinogens (2b”) on leukemia for children, which led to WHO recommendations for “precautionary principle” introduction in general public hygienic regulation.

Urgent necessity not only overhead transmission line, but cable line (110–500 kV) electromagnetic safety problem adequate solutions, design stage including it follows.

2. OTL AND CL MF STRENGTH CALCULATION METHOD

OTL single phase has current \dot{I} , with wire at h distance from the earth (for underground CL h has negative value) on the Y axis and at Y distance from the origin along the X axis creates MF in point D of surrounding space, the intensity of which is determined by Ampere’s circuital law:

$$\dot{H} = \dot{I} / (2\pi r), \quad \text{where } r^2 = (a - x)^2 + (y - h)^2.$$

MF strength components along the X and Y axes are determined by the expressions:

$$H_X = H (y - h) / r \quad \text{and} \quad H_Y = H (a - x) / r.$$

If the line consists not one but i wires having \dot{I}_i currents, created by every wire i MF intensity vector components module $\dot{\mathbf{H}}_{X_i}$ and $\dot{\mathbf{H}}_{Y_i}$ are determined by formula:

$$\dot{H}_{X_i} = \frac{\dot{I}_i}{2\pi} \frac{y - h_i}{(a_i - ?)^2 + (y - h_i)^2}, \quad \dot{H}_{Y_i} = \frac{\dot{I}_i}{2\pi} \frac{a_i - ?}{(a_i - ?)^2 + (y - h_i)^2}.$$

MF intensity components full values in D point are determined by the addition of similar components:

$$\dot{H}_{XD} = \sum_{i=1}^N \dot{H}_{X_i}; \quad \dot{H}_{YD} = \sum_{i=1}^N \dot{H}_{Y_i}.$$

If all of \dot{I}_i currents have the same argument (initial phase angle), MF intensity polarization will be linear, and $\dot{\mathbf{H}}_D$ full vector module is determined by expression of Pythagorean Theorem $H_D = \sqrt{H_{XD}^2 + H_{YD}^2}$. In case of \dot{I}_i currents arguments are not equally, MF polarization is elliptical.

MF strength components effective values changes in time for D arbitrary point are described by equation:

$$H_{XD}(t) = H_{XD} \sin(\omega t + \varphi_{XD}) \quad H_{YD}(t) = H_{YD} \sin(\omega t + \varphi_{YD}).$$

Under $\varphi_{XD} - \varphi_{YD} = \pm n\pi/2$, where n — even integer, or 0, MF polarization is linear, under $\varphi_{XD} \neq \varphi_{YD}$ — is elliptical, and under $H_{XD} = H_{YD}$, and $\varphi_{XD} - \varphi_{YD} = \pm n\pi/2$, where n — integer is an odd number, — is circular. Under elliptical polarization [1, 2] $\mathbf{H}_D(t)$ resulting vector rotates in the space by ellipse (Figure 1) with variable angular velocity ω_0 :

$$\omega_0 = \frac{H_{XD}H_{YD} \sin(\varphi_{YD} - \varphi_{XD})}{H_{XD}^2 \sin^2(\omega t + \varphi_{XD}) + H_{YD}^2 \sin^2(\omega t + \varphi_{YD})}.$$

Passing $\mathbf{H}_D(t)$ vector of extrema, i.e., \mathbf{H}_{\max} and \mathbf{H}_{\min} positions occurs at time point t_{ex} :

$$t_{ex} = \frac{1}{2\omega} \operatorname{arctg} \left[(-1) \frac{H_{XD}^2 \sin(2\varphi_{XD}) + H_{YD}^2 \sin(2\varphi_{YD})}{H_{XD}^2 \cos(2\varphi_{XD}) + H_{YD}^2 \cos(2\varphi_{YD})} \right],$$

At that between \mathbf{H}_{\max} under t_{ex}^{\max} and \mathbf{H}_{\min} under t_{ex}^{\min} for $f = 50$ Hz frequency and $\omega = 2\pi f$ time distance is 0,005 c. MF polarization elliptical form factor $\mathcal{K}_e = H_{\min}/H_{\max}$.

If, neglecting the changes in time, to determine MF strength current value by Pythagorean Theorem expression $H = \sqrt{H_{XD}^2 + H_{YD}^2}$, we will get H value that will always be greater than H_{\max} (Figure 1).

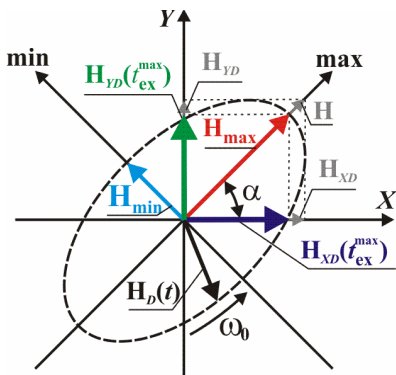


Figure 1: MF elliptical polarization in point D .

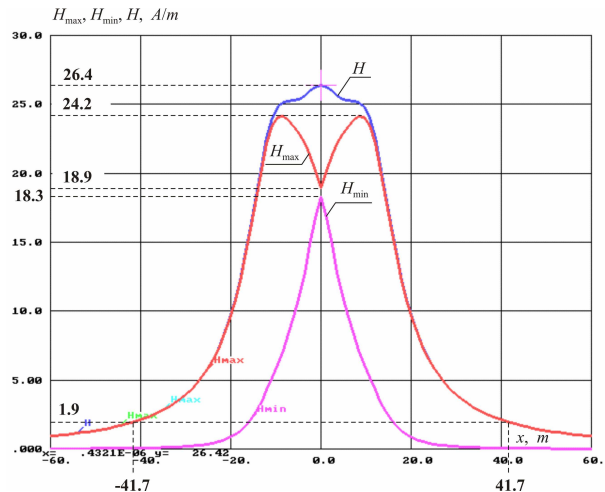


Figure 2: Distribution of MF strength created by 500 kV OTL currents at 1.8 m high for $h_{\Gamma} = 8$ m conductors distance to the ground.

H_{\max} and H_{\min} values can be determined by expression [2]:

$$H_{\min}^{\max} = \sqrt{\frac{1}{2} (H_{XD}^2 + H_{YD}^2) \pm \frac{1}{2} \sqrt{(H_{XD}^2 + H_{YD}^2)^2 - 4H_{XD}^2 H_{YD}^2 \sin^2(\varphi_{YD} - \varphi_{XD})}}, \quad (1)$$

???, ?? [2]??? [3].

3. OVERHEAD TRANSMISSION LINES MAGNETIC FIELDS

Overhead transmission line MF are reviewed by 500 kV OTL posted on intermediate tower with horizontal phases disposition example. OTL phase are made three wires AC-400/51 brand with $d = 0.4$ m bundle conductors step ($R_P = 0.231$ m bundle conductors radius). Distance between middle and extreme phases centers $-b = 11.5$ m. Minimal distance to the ground is $h_\Gamma = 8$ m. Phase current values are: $\dot{I}_A = 1$ kA, $\dot{I}_B = 1e^{-j120^\circ}$ kA, and $\dot{I}_C = 1e^{-j240^\circ}$ kA.

Figure 2 show MF H_{\max} , H_{\min} and H values distribution, created by the same 500 kV TL the same currents at 1.8 m above the ground. On the OTL axis under $x = 0$ m $H_{\max} = 18.9$ A/m, $H_{\min} = 18.3$ A/m, $\mathcal{K}_e = 0.97$ and $H = 26.4$ A/m. H more H_{\max} on 7.5 A/m or on 39.7%. Maximal value $H_{\max} = 24.2$ A/m is achieved under $x = \pm 8.5$ m. At the border of sanitary protection zone under $x = \pm 41.7$ m $H_{\max} = 1.9$ A/m.

Maximal excess of MF strength real value ?????? in computing by expression of Pythagorean Theorem is in case of field circular polarization, when $H_{\max} = H_{\min}$ and $\mathcal{K}_e = 1.0$. In this case $H = \sqrt{2}H_{\max}$ excess H above H_{\max} is 41.4%.

4. POWER CABLE LINE MAGNETIC FIELDS

CL cables due to the presence of the current carrying conductor insulation can be located in close proximity to each other. Underground CL cables are located either in the horizontal or vertical plane, or a triangle. At the intersection of communications and roadways each cable is placed in a plastic tube (PT). Each phase cables are connected along CL by means of socket joint. As a rule cables and socket joint in places of cable connections are located horizontal. CL depth of lying is 1.5–2.5 m. CL are places in security zone, where hygienic standard is 16 A/m. Outside the border of security zone (at 1 m distance from extreme cable), MF value should not be more 8 A/m (hygienic standard for territory of housing estate). Examine MF values at 2 m distance from extreme cable too.

CL MF are reviewed by 500 kV CL two parallel circuit connected to the same busline as at its beginning and end example. It means that currents in the same named phases of even circuit are equal (same values). 500 kV CL made by Suedkabel cable 2XS(FL)2Y 1×2500 RMS/300 290/500 kV make-up with 150 mm outside diameter, in places of socket joint are used Suedkabel electrically-operated clutch SEHDVCB 362/420/550 make-up with c 510 mm outside diameter. When crossing with communications 500 kV CL each cable is laid inside PT 280 mm diameter with 20.6 mm wall thickness. 500 kV CL phase current module is 1 kA for each circuit. CL load is symmetric.

Review 500 kV CL part laid in tube, placed in a triangle at 2.0 m depth with 1.0 m distance between the centers of circuits. Figure 3(a) shows MF H_{\max} calculative values distribution; Figure 3(b) shows MF H calculative values distribution at 0 m, 0.5 m, 1.5 m and 1.8 m above the ground.

H_{\max} value at the earth surface is over than 16 A/m above the CL and over than 8 A/m at the border of security zone (1 m) (Figure 3(a), 0 m line), but in 2 m distance from CL extreme cable PF level is lower than hygienic standard. At 0.5 m above the ground H_{\max} is lower 16 A/m inside the security zone and 8 A/m in 2 m distance from CL, but is above 8 A/m in 1 m distance. At 1.5 m and 1.8 m above the ground PF MF levels not exceed hygienic standards.

MF calculation by H expression shows exceeding of permissible values in 1 m and 2 m distance from CL at ground and 0.5 m above the ground level, and standard compliance at 1.5 m and 1.8 m above the ground only (Figure 3(b)). H values are much more H_{\max} strength.

MF H_{\max} value decrease above 500 kV CL two circuits is possible by deepening of line laying as well as by increase the distance between b circuits centers.

To achieve 16 A/m and 8 A/m permissible levels compliance without increase $b = 1.0$ m and $h = 2.0$ m distances for 500 kV CL two circuits is possible by one of circuit cable order of the phase change. Still considered a symmetric version of the alternation of 500 kV CL two circuits cables phases: $\begin{matrix} A_1 \\ C_1 B_1 \end{matrix}$ of left circuit and $\begin{matrix} A_2 \\ C_2 B_2 \end{matrix}$ of right circuit. If you leave CL left circuit order

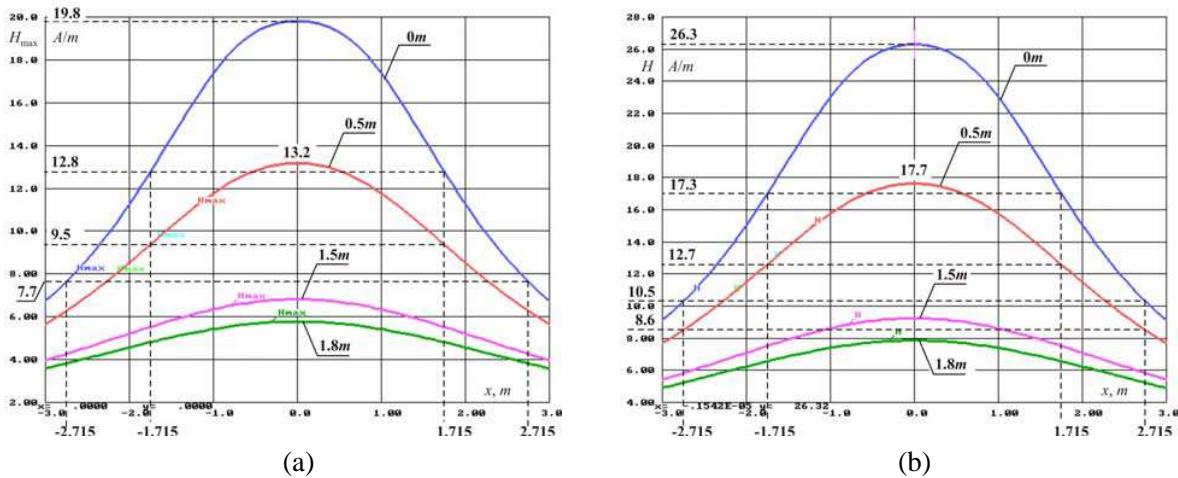


Figure 3: Distribution of (a) H_{max} and (b) H , created by 500 kV CL, laid triangle.

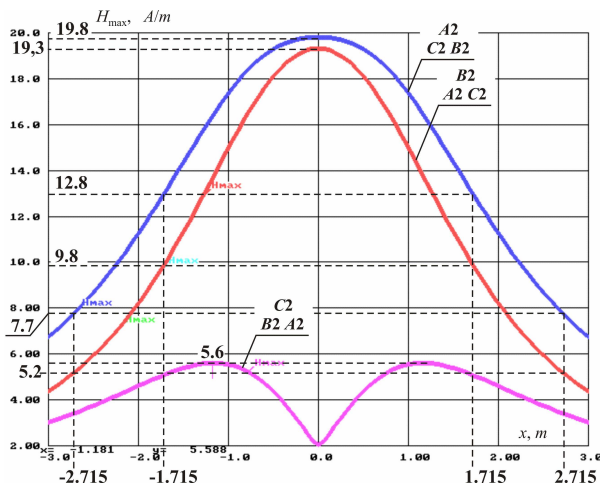


Figure 4: Distribution of created by 500 kV CL MF H_{max} values at ground surface under laying in tubes with $b = 1.0$ m and $h = 2.0$ m, and right circuit cables order of the phase A_2 , B_2 and C_2 .

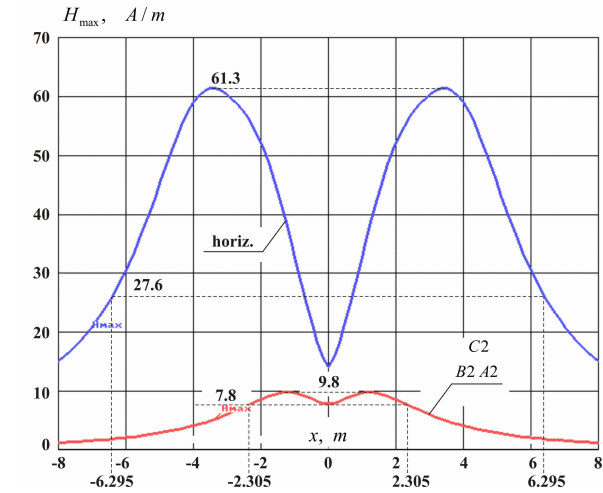


Figure 5: Distribution of MF value H_{max} , created at ground surface by socket joint with horizontal cables (“horiz.” line) and triangle with changed C_2 order of phase socket joint of 500 kV double-circuit CL.

of the phase without change, and right circuit order of the phase change to $B_2 A_2$, MF strength sharply reduced. Figure 4 shows created at ground surface by 500 kV CL currents MF H_{max} value distribution, under left circuit order of the phase $A_1 C_1 B_1$, and right circuit order of the phase $A_2 C_2 B_2$,

$$B_2 A_2 C_2, \text{ and } B_2 A_2.$$

Under right circuit cables order of the phase $B_2 A_2$ MF strength at ground surface is lower than $H_{max} = 5.6$ A/m inside and outside of security zone. However, the design can not prevent the error in order of the phase because under and right phase cables order of the phase $A_2 C_2 B_2$ the effect of MF compensation is practically absent.

The maximal MF values are observed places of cable with horizontal cables and couplings socket joint. To socket joint place cables are suitable triangle in the ground or in the tubes, and connections are transferred to the horizontal position. Cable and socket axis are located in the ground at $h_s = 1.925$ m depth. The distance between same circuits nearby cables is 1.32 m, and between first and second circuits nearby cables is 2.4 m.

Figure 5 shows the distribution of MF level, created at ground surface by socket joint with horizontal cables and couplings (“horiz.” line). MF value inside of 1 m security zone is very high (61.3 A/m), and at its border MF value is 27.6 A/m (substantial higher permissible levels 16 A/m, and 8 A/mm). Traditionally MF level decrease is achieved by socket joint covering by means of expensive ferromagnetic screen.

Under cables and sockets arrangement at equilateral triangles vertexes with 0.6 m side, and left circuit cables order of the phase $C_1^{A_1} B_1$, and right circuit cables order of the phase $B_2^{C_2} A_2$, and under arrangement of cable (socket) axis of top triangle vertex at 1.905 m depth, and lower vertexes — at 2.425 m depth MF value at ground surface will reduce to 9.8 A/m inside of 1 m zone and — to 7.8 A/m at its border (Figure 5, $B_2^{C_2} A_2$ line). Deepening of socket joint only 0.5 m more horizontal leads to significant reduce of MF levels up to accepted standards without expensive ferromagnetic screen placing.

5. CONCLUSION

Some optimal ways of occupational and environmental OTL and CL electromagnetic safety maintenance are presented. Adequate methods of PF MF values calculation let even at the design stage to solve this problem. The particular importance is played by light of MF elliptical polarization when the calculation without regard to its temporal parameters leads to errors upwards from true MF value to 41.4%.

Presented data substantiate the necessity of 110–500 kV CL sanitary protection zone organization. To ensure PF MF permissible levels for residential construction compliance (8 A/m in Russia) at 1 m distance is possible only at CL laying considerable depth, which is expensive, laborious and adversely affects CL operation and maintenance. This determines the size of sanitary protection zone must be not less than 2 m from CL.

Socket joints with cable and coupling arrangement at equilateral triangles vertexes with properly modified phase sequence under slight increase of their laying depth application allows to PF MF hygienic standards maintenance without ferromagnetic screen installation.

REFERENCES

1. Dikoi, V. P., A. Y. Tokarskiy, Y. A. Iostson, and M. S. Misrikhanov, “Power frequency ellipsoid magnetic field calculation and measurement methods,” *Proceeding of Ivanov’ Power University, Issue. IV. M., Energoatomizdat*, 215–223, 2001 (in Russian)
2. Misrikhanov, M. S., N. B. Rubtsova, and A. Y. Tokarskiy, “Power network objects electromagnetic safety maintenance,” *Science (Nauka)*, 868, 2010 (in Russian).
3. Misrikhanov, M. S., Y. A. Iostson, N. B. Rubtsova, and A. Y. Tokarskiy, “Computer program ‘electromagnetic parameters of overhead transmission lines’,” No. 2006613744, Oct. 27, 2006 (in Russian).

Electromagnetic Compatibility of Contactless Power Transfer Modeled in FEM Analysis Software

R. Fajtl and K. Buhr

Department of Electric Drives and Traction, Faculty of Electrical Engineering
Czech Technical University in Prague, Technická 2, 166 27 Prague 6, Czech Republic

Abstract— This paper deals with basic parameters of contactless power transfer (CPT) and modelling of CPT in FEM analysis software. There are described basic equations for computing parameters of CPT components. The main part of this paper refers about creating CPT transformer model in multiphysics software Maxwell Ansys to determine basic CPT parameters such as induction and impedance of CPT transformer, its electromagnetic field and its effect on surroundings. CPT operates at high frequencies so its electromagnetic compatibility with other electric devices is very important because it may cause serious risks of fail of devices such as pacemakers or communication devices.

1. INTRODUCTION OF CONTACTLESS POWER TRANSFER (CPT)

Contactless power transfer is action when electric energy is transferred between two physically unconnected electric devices. Electromagnetic induction is used to transfer energy between galvanically isolated electric devices. This solution of energy transfer is very useful in environment of applications where conventional electricity wire transfer would be impractical or even dangerous. CPT is used in many applications such as toothbrushes, mobile phones and public transportation for charging electric devices.

Figure 1 shows basic CPT component blocks which are used for contactless power transfer.

2. CPT ANALYSIS

As shown in Figure 1. CPT consists of many functional blocks. The main part is CPT transformer which is formed by two large gap air coils. To achieve high efficiency of energy transfer CPT transformer has to operate at high frequencies. But high operational frequencies cause high impedance of CPT transformer and increase reactive power transferred by CPT. There the primary and secondary capacity compensations are used on both sides of CPT transformer to reduce reactive power values.

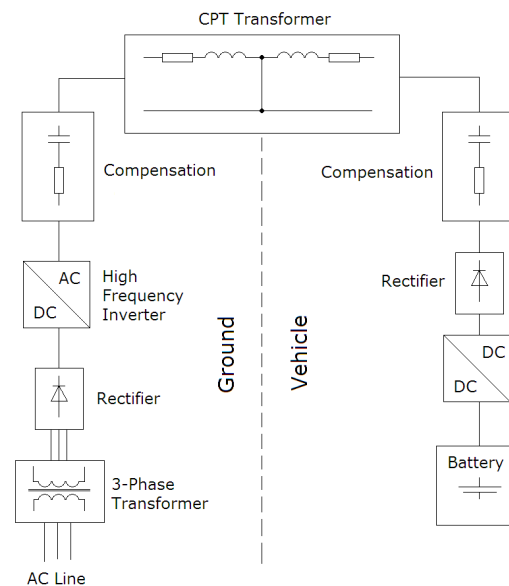


Figure 1: Scheme of basic CPT components.

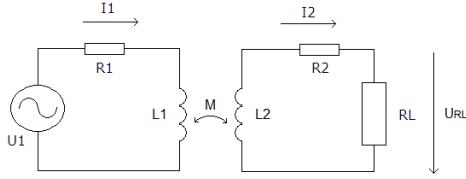


Figure 2: CPT transformer equivalent scheme.



Figure 3: Spiral plate coil parameters.

2.1. CPT Transformer Parameters

CPT transformer consists of two air coils with large gap. Magnetic flux in CPT is transferred in air and doesn't need magnetic core thus CPT transformer is lighter and has nearly no-load losses (magnetization losses are just in wires). Figure 2 shows the CPT transformer equivalent scheme.

Basic CPT transformer parameters are primary R_1 [Ω] and secondary R_2 [Ω] resistances, primary L_1 [H] and secondary L_2 [H] self inductances and mutual inductance M [H].

This article deals with CPT transformer created by two spiral plate coils which are used for induction heating. The spiral plate coil parameters are shown in Figure 3.

The spiral coil self inductance L is given by Equation (1):

$$L = \frac{(aN)^2}{8a + 11b} * 10^{-6} \text{ [H]} \quad (1)$$

where N is turns of coil, a [cm] is coil mean diameter and b [cm] is layer thickness.

The spiral coil mutual inductance M is given by Equation (2):

$$M = k_V \sqrt{L_1 L_2} \text{ [H]} \quad (2)$$

where k_V [-] is mutual bond factor.

CPT transformer resistance is given by Equation (3):

$$R = \frac{\rho N a}{\pi b^2} \text{ [\Omega]} \quad (3)$$

where ρ [Ω/m] is resistivity of coil wire.

Active power transferred by CPT is given by Equation (4):

$$P_2 = \frac{\omega_0 M^2 Q_S}{L_2} I_2 \text{ [W]} \quad (4)$$

where ω_0 is resonant operational frequency (angle velocity).

Impedance Z of CPT transformer is given by Equation (5):

$$Z = \frac{(\omega M)^2 + (R_1 + j\omega L_1)(R_L + R_2 + j\omega L_2)}{R_L + R_2 + j\omega L_2} \text{ [\Omega]} \quad (5)$$

CPT efficiency η is given by Equation (6):

$$\eta = \frac{R_L}{(R_L + R_2) \left(1 + \frac{R_1(R_L + R_2)}{(\omega M)^2}\right) + R_1 \left(\frac{L_2}{M}\right)^2} \text{ [-]} \quad (6)$$

If condition given by Equation (7) is fulfilled the maximal efficiency η_{\max} is given by Equation (8).

$$\frac{R_1(R_L + R_2)}{(\omega M)^2} \Rightarrow 0 \quad (7)$$

$$\eta_{\max} = \frac{R_L}{R_L + R_2 + R_1 \left(\frac{L_2}{M}\right)^2} \text{ [-]} \quad (8)$$

2.2. CPT Capacity Compensation Parameters

From Equation (4) is evident that transferred active power depends not only on CPT transformer parameters but also on operational frequency and transformer quality Q_S . Reactive power has to be compensated to increase transferred active power value. There are four basic connection scheme of compensation used in CPT. They differ in capacitors connections. Most used capacity compensation is series-series (SS) shown in Figure 4. It can operate as a current source (first stage of battery charging) and a voltage source (second stage of battery charging).

The secondary capacity compensation value for compensated reactive power is given by Equation (9):

$$C_2 = \frac{1}{\omega_0^2 L_2} \text{ [F]} \tag{9}$$

The primary capacity compensation is given by Equation (10):

$$C_1 = \frac{C_2}{L_1 L_2} \text{ [F]} \tag{10}$$

3. CPT MODEL IN MAXWELL ANSYS

Equations mentioned in previous text are very simplistic and they don't conclude many factors that affect CPT operational parameters. These factors are for example electric vehicle construction parts, transformer coils misalignment and others.

CPT components arrangement in an electric vehicle is shown in Figure 5, which are 1 — Power supply, 2 and 5 — capacity compensation, 3 and 4 — CPT transformer air coils, 6 — DC Buck, 7 — Batteries, 8 — Driver, 9 — Electric motor.

All vehicle components have to be included in computing to achieve correct CPT operational parameters.

Maxwell Ansys is FEM analysis software that is able to compute electromagnetic field distribution in electric devices and display it. It is also able to compute basic electromagnetic and

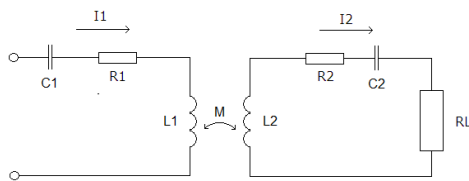


Figure 4: Scheme of SS capacity compensation.

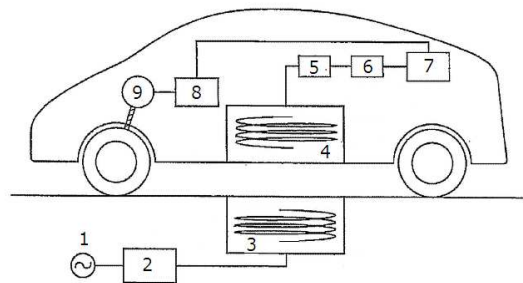


Figure 5: CPT components arrangement in an electromobile.

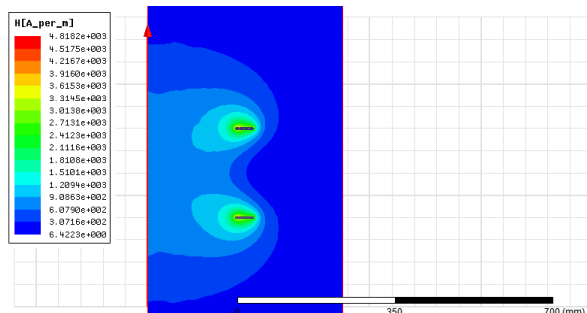


Figure 6: Two air coils CPT transformer magnetic field.

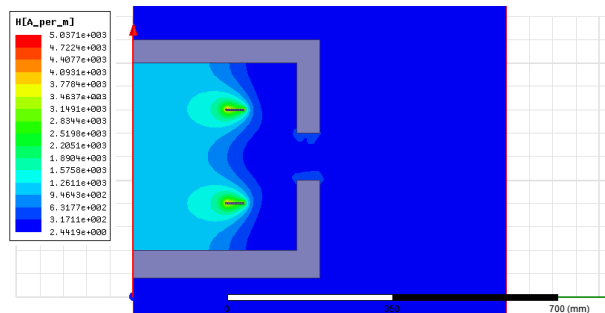


Figure 7: Shielded CPT transformer magnetic field.

mechanical parameters of electric devices. Some simulations of contactless power transfer was made in this software and obtained basic CPT parameters.

Figure 6 displays magnetic field in CPT transformer formed by two large gap air coils. This model is cylindrical around Z axis and current density value in wires is 2 A/mm^2 .

Magnetic field of shielded CPT transformer is shown in Figure 7.

These simulations and their results can be used for computing real CPT transformer parameters and its operational behavior.

4. COMPARISON OF CPT PARAMETERS OBTAIN FROM ANALYTIC EQUATIONS AND MODEL SIMULATIONS

Table 1 shows differences between CPT parameters computed by analytic equations described in first part of this paper and CPT parameters obtained by FEM analysis software Maxwell Ansys. It's calculated for two spiral coils with same physical parameters with air gap 20 cm. The CPT transformer operates at frequency 100 kHz.

Table 1: Calculated CPT parameters.

Parameter	Analytical computed	Maxwell Ansys
L_1 [μH]	246.6	147.1
L_2 [μH]	246.6	147.1
R_1 [Ω]	0.017	0.023
R_2 [Ω]	0.017	0.023
M [μH]	49.32	29.42

Spiral coils parameters are — number of turns 10, mean coil radius 20 cm, layer thickness 0.2 cm, air gap 20 cm and material copper and mutual bond factor $k_V = 0.2$.

5. CONCLUSIONS

In the previous paragraphs are described basic CPT operational parameters and how they can be computed by FEM analysis software. Data of CPT model simulations in this software are very useful for creating real CPT device for electric vehicle battery charging. It's possible to obtain basic CPT parameters such as inductances, impedances, operational frequency, capacitance of capacity compensation, magnetic field layout and others. Parameters obtained from basic analytic circuit equations don't include other construction parts in CPT environment. But CPT model simulations in FEM analysis software are able to obtain precious data. Maxwell Ansys is multiphysics software and is able to compute CPT electromagnetic compatibility and how it can affect its surroundings.

ACKNOWLEDGMENT

Research described in this article was supported by the Czech Grant Agency under SGS research program No. SGS13/196/OHK3/3T/13.

REFERENCES

1. Sallan, J., J. L. Villa, A. Llombart, and J. F. Sanz, "Optimal design of CPT systems applied to electric vehicle battery charge," *IEEE Transactions on Industrial Electronics*, Vol. 56, No. 6, 2140–2149, Jun. 2009.
2. Wang, C.-S., O. H. Stielau, and G. A. Covic, "Load models and their application in the design of loosely coupled inductive power transfer systems," *International Conference on Power System Technology, Proceedings, PowerCon 2000*, Vol. 2, 1053–1058, 2000.
3. Wang, C.-S., O. H. Stielau, and G. A. Covic, "Design considerations for a contactless electric vehicle battery charger," *IEEE Transactions on Industrial Electronics*, Vol. 52, No. 5, 1308–1314, Oct. 2005.
4. Van der Pijl, F. F. A., J. A. Ferreira, P. Bauer, and H. Polinder, "Design of an inductive contactless power system for multiple users," *Conference Record of the 2006 IEEE Industry Applications Conference, 41st IAS Annual Meeting*, Vol. 4, 1876–1883, Oct. 8–12, 2006.
5. Schinji, I., T. Jidosha, and K. Kaisha, "Noncontact electric power receiving device, noncontact electric power transmitting device, noncontact electric power feeding system, and electrically powered vehicle," Patent, AH01F3814FI, 20110148351, Japan, Jun. 23, 2011.

6. Sample, A. P., D. A. Meyer, and J. R. Smith, “Analysis, experimental results and range adaptation of magnetically coupled resonators for wireless power transfer,” *IEEE Transactions on Industrial Electronics*, Vol. 58, No. 2, 544–554, Feb. 2010.
7. Lee, R., L. Wilson, and C. Carter, *Electronic Transformers and Circuits*, A Wiley-Interscience Publication, New York, 1988.

Parallel Imaging Based on Multicore DSP for FMCW SAR

Chengfei Gu, Wenge Chang, and Xiangyang Li

College of Electronic Science and Engineering

National University of Defense Technology, Changsha, Hunan 410073, China

Abstract— A Ku-band FMCW SAR system is demonstrated which has the capability of real-time processing with the application of single high-performance multi-core DSP. The navigational data of platform movement, which particularly used for high precision motion compensation, is accurately measured by GPS and accelerometer. Furthermore, to realize the real-time processing, the parallel processing approach based on multicore DSP is presented in detail, also the time consumptions of key steps are minutely listed. To verify the capability of real-time processing, several automobile experiments are campaigned with the FMCW SAR sensor on the top of the car. The obtained results of real-time processing and post-processing are presented and compared, processed with 35 cm and 25 cm resolution, respectively.

1. INTRODUCTION

The combination of frequency modulated continuous wave (FMCW) and synthetic aperture radar (SAR) leads to a compact and high-resolution imaging sensor, and this makes FMCW SAR be a hot spot in recent SAR research [1, 2]. FMCW SAR not only has the characteristics of day-or-night and adverse-weather operation, but also holds the advantages of lightweight and low power consumption. Predictably, FMCW SAR will have enormous potential application in remote sensing and mapping. However the main challenge of this compact and high-resolution sensor is the realization of real-time imaging.

Because of the finite board load and rigid time requirement, the real-time processing of FMCW SAR has been a bottleneck. In this paper, only a highly integrated multicore digital signal processor (DSP) is chosen as the processing kernel [3]. It is known that the automobile based SAR experiment is flexible and essential for FMCW SAR system debug before the airborne based experiment [4, 5]. In order to validate the performance of real-time SAR imaging, several automobile experiments have been successfully performed. At the end of this paper, the real-time processing and post-processing imageries are shown and compared, processed with 35 cm and 25 cm resolution, respectively.

The remainder of this paper is briefly organized as follows. In Section 2, the imaging algorithm for FMCW SAR is reviewed. Section 3 depicts the parallel processing flow of real-time imaging, also the time consumptions are minutely listed. In Section 4, the results of real-time processing and post processing are presented and compared, also the qualities of corner reflects are analyzed in detail. Finally, Section 5 gives the conclusion of this paper.

2. IMAGING ALGORITHM FOR FMCW SAR

It is known that, for SAR imaging algorithms, the time-domain algorithm is not suitable for the real-time processing. The frequency-domain algorithm includes Range-Doppler Algorithm (RDA), Range Migration Algorithm (RMA), Chirp-Scaling Algorithm (CSA), Frequency-Scaling Algorithm (FSA), etc. [1, 2]. However RMA is not suitable for real-time processing because of its time-consuming interpolation. CSA can't process the deramped signal of FMCW SAR. RDA can only deal with the narrow swath width and low resolution SAR imaging. Hence, in this paper, the extended FSA [1, 2] is chosen as the real-time processing algorithm. The imaging geometry of automobile experiment is shown in Fig. 1.

The expression of the transmitted FMCW signal is [1, 2]

$$s_t(\hat{t}, t_m) = \text{rect}\left(\frac{\hat{t}}{T_p}\right) \cdot \exp\left[j2\pi\left(f_c t + \frac{1}{2}\gamma\hat{t}^2\right)\right] \quad (1)$$

in which \hat{t} is the fast time, T_p is the signal time width. f_c and γ are the carrier frequency and the chirp rate of transmitted signal, respectively. The deramped signal is simplified as [1,2]

$$s_{if}(\hat{t}, t_m) = A \cdot \text{rect}\left(\frac{\hat{t} - 2R'/c}{T_p}\right) \cdot \exp\left[-j\frac{4\pi}{\lambda}R_B\right] \cdot \exp\left[-j\frac{4\pi\gamma\hat{t}}{c}R'\right] \cdot \exp(-j2\pi f_d\hat{t}) \cdot \exp\left[j4\pi\gamma\left(\frac{R'}{c}\right)^2\right] \quad (2)$$

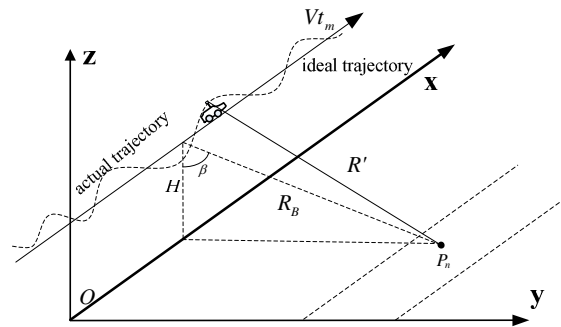


Figure 1: Automobile based imaging geometry.

where the variable R' and R_B are the instantaneous range and the zero-doppler slant range from sensor to point P_n . t_m is the slow time, f_d is the doppler frequency in azimuth. c and λ stand for the light velocity and the wavelength, respectively. The first exponential term and the second one represent the doppler modulation in azimuth and the signal in range. The third exponential term is the range migration introduced by the platform movement within a sweep. The last one is the residual video phase (RVP), and the frequency scaling algorithm is based on the RVP term [1, 2].

3. REAL-TIME PROCESSING FLOW

3.1. Signal Processing Flow

The data flow of real-time processing is shown in Fig. 2.

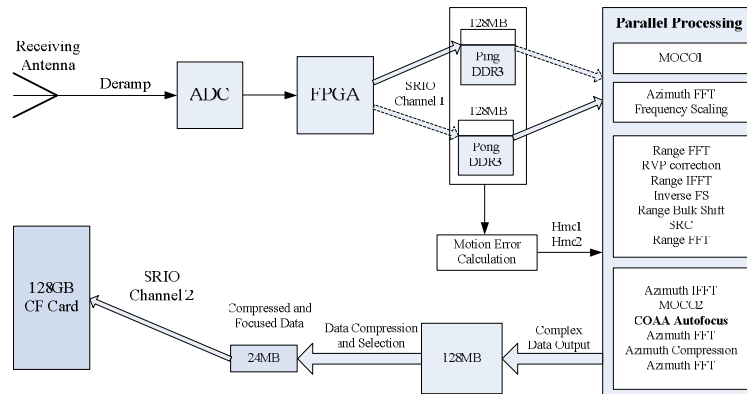


Figure 2: Data flow of real-time processing.

As shown in Fig. 2, the received signal is digitally recorded after the ADC. And FPGA buffers the raw data into DDR3 SDRAM through the SRIO channel 1. The motion error of Ping or Pong data matrix is accurately measured based the GPS and accelerometer data. After the motion error calculation, the data matrix is under parallel processing by multicore DSP [6]. The parallel processing contains basic FS processing, two-order motion compensation and COAA autofocus. The output of the parallel processing is the complex float data with a size of 128MB. The following process is data compression and selection. After the compression and selection of processed data, the focused imaging data is stored into CF card using the SRIO channel 2.

3.2. Automobile Experiment and the Time-consuming

The proposed parallel imaging flow has been validated on a compact FMCW SAR sensor, which carries an eight-core DSP. The compact FMCW SAR sensor is mounted on the top of a sport utility vehicle (SUV), and the recorded raw data undergo real-time processing onboard. The signal bandwidth is 600 MHz, and the velocity of SUV is about 16.2 m/s. The swath width and the center slant range are 800 m and 1 km, respectively. The time consumptions of real-time processing are listed in Table 1.

As listed in Table 1, the motion error calculation of data matrix is about 0.0168 s. The parallel processing time of FS algorithm is 1.405 s and the COAA autofocus costs 0.7739 s. Considering

Table 1: Summarizes of real-time processing time-consuming.

Operations	Value (s)
Motion Error Calculation	0.0168
Parallel FS Processing	1.4050
Parallel COAA Autofocus	0.7739
Data Compression	0.0684
Overlapped Data Transmission	0.0119
Focused Data Storage	0.3030
Total Processing Time	2.579

the throughput of CF card, the storage time of focused data is about 0.303s. The total time consumption of the parallel processing flow is about 2.579s, which satisfies 3.072s real-time limit.

4. RESULTS AND QUALITY ANALYSIS

4.1. Images of Real-time and Post Processing

After times of automobile experiments, some beneficial real-time processing results are gained. Fig. 3 shows one of these real-time processed images.

In Fig. 3, the imagery covers areas of $350\text{ m} \times 400\text{ m}$ (azimuth \times range) island and the central slant range is about 1 km. Target 2 is a stone arch bridge and the target 1 is a waterside terrace close to the Xiangjiang River. The optical photographs in Fig. 3 are two targets on the island. Comparing the imaging result with the optical photograph, we can say that the real-time processing result gains well geologic matching. Moreover, the characteristic targets, such as the waterside terrace and the stone arch bridge, are well focused. The real-time processing and post-processing results of the same scene are shown in Fig. 4.

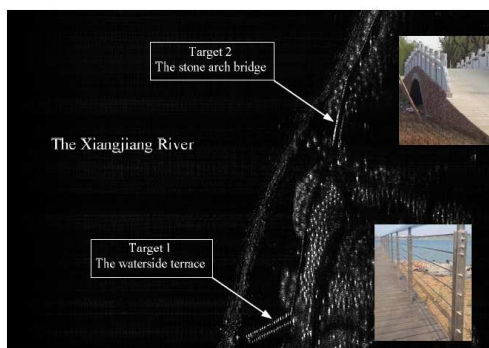


Figure 3: The automobile real-time imaging result.

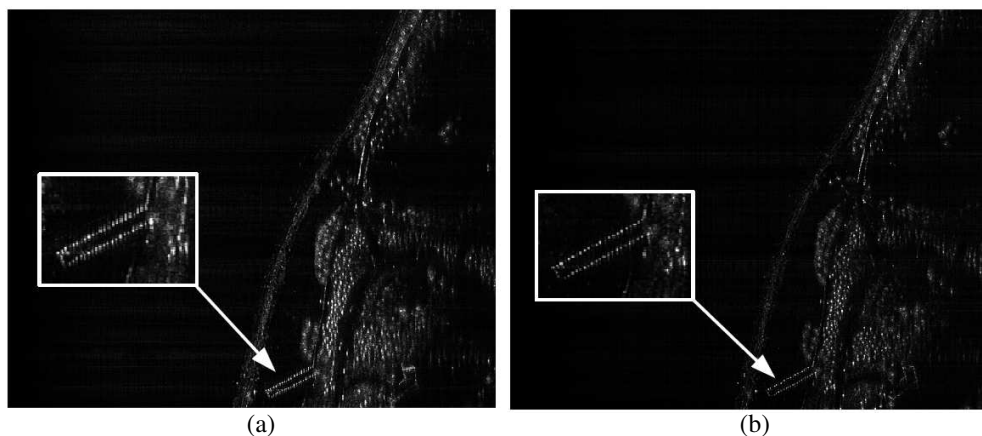


Figure 4: Comparison of (a) real-time processed and (b) post-processed images.

In Fig. 4, the sub-image (a) is the real-time processed result, and the sub-image (b) is the result of post processing. Comparing Fig. 4(a) with Fig. 4(b), the overall effect of two images are close to each other, and the result verifies the efficiency of the real-time processing flow. Besides the two-order motion compensation and COAA autofocus, the post-processing has also implied the PGA processing. Hence, the focused result of post-processing is better than the real-time one. The analysis result shows that the resolution of post-processed image is about 25 cm.

Table 2: Point targets analysis.

Parameters		$T1$	$T2$	$T3$	$T4$
Range	IRW(m)	0.364	0.334	0.322	0.388
	PSLR(dB)	-25.19	-26.72	-31.38	-25.58
	ISLR(dB)	-16.13	-15.55	-16.21	-14.74
Azimuth	IRW(m)	0.341	0.361	0.352	0.364
	PSLR(dB)	-29.31	-36.17	-31.34	-25.73
	ISLR(dB)	-16.06	-18.67	-15.44	-13.39

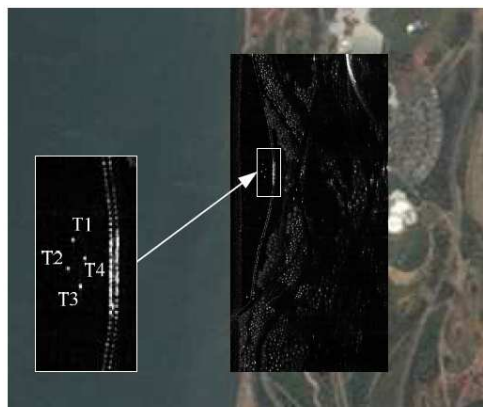
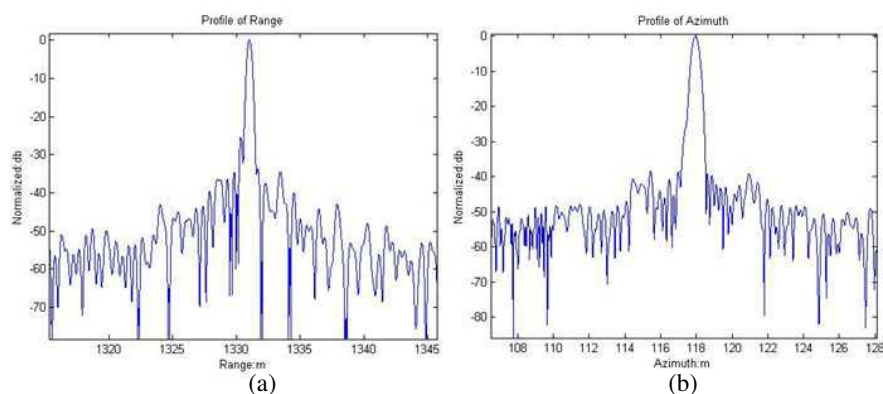


Figure 5: Real-time processing result with corner reflectors.

Figure 6: Profiles of $T1$ in (a) range and (b) azimuth.

4.2. Quality Analysis

To assess the quality of real-time processed image, four corner reflectors are specifically scattered on the test field. The real-time imagery with corner reflectors is shown in Fig. 5.

As shown in Fig. 5, the imaging scene is an island with size of $800\text{ m} \times 350\text{ m}$ (azimuth \times range) in the Xiangjiang River with about 1 km central slant range. Targets 1 to 4 in Fig. 5 are

four corner reflectors to be analyzed. Two dimensional impulse response width (IRW), peak-to-side lobe ratios (PSLR) of four corner reflectors are listed in Table 2.

The azimuth and range profiles of $T1$ in Fig. 5 are shown in Fig. 6(a) and Fig. 6(b), respectively.

With the application of hamming window, the obtained mean range resolution is about 0.35 cm. Also the average result in azimuth shows a good resolution of 0.35 cm. The PSLR and ISLR results are both good. In a word, the analysis results demonstrate a high focusing quality. The efficiency of proposed real-time processing flow is also validated.

5. CONCLUSION

A compact real-time processing SAR sensor is presented in this paper. On the foundation of this compact SAR system, the FSA which also contains two-order motion compensation and time-consuming COAA autofocus processing is efficiently realized in parallel with a single eight-core DSP. Furthermore, both the real-time processing result and the post-processing result of automobile experiment are presented and compared, also the quality of SAR images are analyzed in detail.

REFERENCES

1. Meta, A., P. Hoogeboom, and L. P. Ligthart, "Signal processing for FMCW SAR," *IEEE Trans. Geosci. Remote Sens.*, Vol. 45, No. 11, 3519–3532, 2007.
2. Jia, G. W., M. Buchroithner, W. G. Chang, and X. Y. Li, "Simplified real-time imaging flow for high-resolution FMCW SAR," *IEEE Geosci. Remote Sens. Lett.*, Vol. 12, No. 5, 973–977, 2015.
3. "TMS320C6678 multicore fixed and floating-point digital signal processor data manual," Texas Instruments Incorporated, Texas, United States, 2011.
4. Wang, R., Y. H. Luo, Y. K. Deng, and Z. M. Zhang, "Motion compensation for high-resolution automobile FMCW SAR," *IEEE Geosci. Remote Sens. Lett.*, Vol. 10, No. 5, 1157–1161, 2013.
5. Cho, B. L., Y. K. Kong, H. G. Park, and Y. S. Kim, "Automobile-based SAR/InSAR system for ground experiments," *IEEE Geosci. Remote Sens. Lett.*, Vol. 3, No. 3, 401–405, 2006.
6. Gu, C. F., X. Y. Li, W. G. Chang, G. W. Jia, and H. S. Tian, "Matrix transposition based on TMS320C6678," *Proceedings of GSMM*, 29–32, Harbin, China, May 2012.

Monitoring of Buoyancy Effects to Structures by Tsunami Water after Heavy Seismic Shocks

Shigehisa Nakamura
Kyoto University, Japan

Abstract— This work concerns on monitoring of structures under heavy seismic shocks. The author concentrates his interest to introduce some typical problems of structures. Specific references are found in the coastal zones at the event of the 2011 Earthquake in the northwestern Pacific. It is discussed what could be the key in order to realizing the hazardous damages of the structures especially in the coastal zones.

1. INTRODUCTION

This work concerns on monitoring of structures under heavy seismic shocks. The author concentrates his interest to introduce some typical problems of structures. Specific references are found in the coastal zones at the event of the 2011 Earthquake in the northwestern Pacific. It is discussed what could be the key in order to realizing the hazardous damages of the structures especially in the coastal zones.

2. A BASIC NOTE

It must be well understood that structure engineering is noted on the bases of the elastic properties of the members as a parts which forming a structure.

As for a structural construction, there should be considered a systematic combination for the purpose to complete the aim of construction for purpose.

In any case to note about a structural construction, it should be considered to take into account of physical and dynamical parameters at considering to construct a structure to be complete at any conditions of external forcing.

As far as we concern about a structural construction, it should be essential to take the structural construction as a structure systematically constructed by the members of elastic materials.

Then, the structure should be a system structure which could be also an elastic body so that it is necessary to consider a formulation for an equivalent elastic material.

As for any elastic body, dynamics of a structural construction, a formulation should be in need for forcing to the elastic body by using several physical and dynamical parameters.

Essentially, strain-stress relation should be considered (not only pressure). In this case, it should be considered a tensor for elastic body, for example, in a Cartesian coordinate, i.e.,

$$F = \begin{vmatrix} F_{xx} & F_{xy} & F_{xz} \\ F_{yx} & F_{yy} & F_{yz} \\ F_{zx} & F_{zy} & F_{zz} \end{vmatrix}, \quad (1)$$

or, in a simple form as follows;

$$F = |F_{ijk}|, \quad (2)$$

where the notations “ i, j, k ” are notifying the x, y, z components.

In this work, the author notes some typical cases of tsunami tragedies in relation to a buoyancy effect of tsunami waters after a destructive earthquake.

Some of the typical cases were found at the 2011 earthquake in the northwest Pacific.

The interested cases can be seen to be possible when buoyancy effect of tsunami water after the seismic shock at the earthquake, for example, at 2011 earthquake.

3. BUCKLING OF BUILDINGS AFTER TWISTING AND SWINGING

One of the seismic effect is an impulsive impact to the tall buildings.

Since the 1995 Kobe earthquake, the earthquake engineers have had to concentrate their interests to the vertical forcing of seismic action to the public structure.

Nevertheless, the 2011 Tohoku earthquake in the northwest Pacific were a specific case for demonstrating what effects could be appeared to the tall buildings in the urban areas.

In the case of the 2011 earthquake, it was found that a typical buckling pattern above the first floor but the ground floor of the tall buildings.

There must be a guideline for construction of tall building, then, it was trusted that all of the buildings are stiff to any external impacts even in nature nevertheless buckling pattern was found even a building ready to any seismic shock.

An example of the buckling patterns at the corner-footing of the tall buildings above the first floor but at the ground floor. This fact tells the burden-loading, and forcing to the steel members for the interested structure.

The author unfortunately would not to describe to the details about this buckling.

It must be taken to be in fact that the seismic action was beyond the critical condition in the guideline for tall building construction.

Adding to the above, the author has his question about the buckling pattern found even in the case of tall building arranged a anti-seismic device in order to protect the structure of the building. It is in need to see whether critical criteria in the guideline are properly set for the purpose of safety.

Anti-seismic devise has been introduced after the 1995 earthquake hit the urban area in Kobe, which was noticed by an leading advisor in earthquake engineering.

The anti-seismic devise had a chance for having the first actual test at 2011 earthquake.

4. BUOYANCY EFFECT OF TSUNAMI WATERS

It can be considered simply that the buoyancy effect of tsunami waters can be related to a balance of power between the gravity and buoyancy.

Then, what is important to consider is the vertical component of the forcing in F noted above. This means that it is enough to consider only F_{zz} and the other components can be taken to be zero.

5. BUILDING LIFT UP

After the seismic shock of an interested earthquake, tsunami waters hit the structures on the coastal zones.

Strong seismic shock affects as an impulsive force to the arranged piles supporting the building to be suffered.

Seismic waves force to make arranged and loosed piles which fail support any building against the vertical forcing of the gravity.

Then, tsunami waters easily make the building in a floating state because the weight of the building is less than the water mass removal corresponding to the buoyancy effect of the tsunami water to float the building in the tsunami water.

When the tsunami water depth beyond the height of the building, the piles never work as supporting function for the building. Then, the building must be easily lifted up to float in the tsunami waters.

When the sea level becomes higher after increasing the tsunami water than the height of the building, then, the tsunami forcing to the building horizontally to pull down on the ground surface after filling up the water into the vacant space of the building, or to force drifting in the tsunami waters.

Now, action of the drifting building should be a problem of a water wave motion in the afield of hydrodynamics. Nevertheless, the author, here, has to be in wondering whether the designed the building never considering with any possibility of up-lift of the structure. In addition, the author is anxious in mind considering the building was constructed under some consideration about strain-stress relation in the building with the piles arranged for an effective support to the structure in safe.

It is pity that the author has to leave his mind leaving to ask some complete procedure must be required at starting to design and to construct the structure.

6. TOPPING BOAT ON A BUILDING

An unexpected tsunami high water shed out almost all of the wooden houses to destroy one block of the residents.

The tsunami high water brings a drifting boats and tankers on the water surface though the tsunami waters kindly put a drifting boat on a roofing flat of building submerged building. Oc-

asionally, a traffic system must be blocked by a tsunami water sitting of a big tanker crossing a route of the life line.

The tanker on the sea had left on land at the top of the building suffered by the flood of the tsunamis generated by the earthquake on 11 March 2011 in the coastal zone in the northwest Pacific.

This happening should be considered as a result caused by a buoyancy effect of tsunami water accompanied by the earthquake on that day.

7. CONTAINER DRIFT IN COASTAL ZONE

In the coastal zones and harbors, there are located many of the tanks and containers for fossil fuel tanks. Those should be called as a base location where the fuel containers were put on the ground surface of the coastal zone at the head of the bay facing the ocean. There are various kinds of containers in size and in shape for fitting to the surrounding coastal configurations.

Some of them are cylindrical shape with a circular bottom in an isolated state from the ground surface and with a circular top cover for roofing of every one of the containers.

Then, the containers can be easily to lift up by the buoyant effect of the tsunami water flow raising the water level beyond the designed tsunami protection level around the coast at a hazardous earthquake under sea. The containers surely start to flow on the water surface after the effect of the tsunami water in a horizontal motion out of the ocean across the bay mouth to hit the land area facing the sea waters on the coastal zone.

The containers' design is under an assumed condition only for put on the land surface, so that the floating containers on the tsunami water are in drifting and rolling under on the way to the land area of the coastal zones. Some one of the drifting containers get a crack at the top or bottom, then, the contained materials of fossil fuel flow out of the container to the water surface to spread on. During the containers drifting, their cracks appeared to break the containers' structure, and, some shocks of metallic collapses must be act easily as trigger for firing and burning of the fossil fuel. Then, the burning fuel and containers float and hit the coastal area where some communities and industries are located for active social services. It is unfortunate that landing of the fired containers make to fire most of the functions in service for the colonies and industries.

Adding to the above, the buildings for the buoyant local governments are forced to burn and to be suffered by the tsunami water up-lift as well as that of the containers.

These are in drift after the buoyant effect at a horizontal flow of the tsunami water motion rather than that caused by the seismic effects at the earthquake under sea.

In fact, what noted above was seen in the coastal zones at 2011 earthquake in the north-west Pacific.

8. CONCLUSION

This work concerns on buoyant effects of the tsunamis generated by the offshore earthquake to the structures and hazardous damages in the coastal zones. There are the other patterns of the destructive processes at the actions of the tsunamis induced by the strong earthquakes undersea. Then, the author has to close his notices in a restricted dynamic processes in the costal zones. As for the other related problems, the author might be able to describe in the other chance.

This work was accepted just after the Nepal eathquake on 25 April 2015.

Monitoring of Orographic Patterns in Relation to Tsunami Earthquake

Shigehisa Nakamura
Kyoto University, Japan

Abstract— This work is a note to problems on monitoring of orographic processes. In relation to tsunami earthquake found on the planet earth, orographic patterns are selected as references. In a scope of any electromagnetics scope, it has been hard to consider any application can be effective for orographic process found on the earth in the past. Now, the author has to notice about application.

1. INTRODUCTION

The author introduces his note to problems on monitoring of orographic processes in relation to tsunami earthquake found on the planet earth. In a scope of any electromagnetics scope, it has been taken to be hard to consider any application can be effective for orographic process found on the earth in the past.

For the purpose, the author has intended to apply some techniques using electromagnetic functions though there had been various kinds of barriers not only in the scope of electromagnetics but the other related field.

Especially, the orographic process under the sea surface is hard to find even using any functions of electromagnetics.

Recently, advanced technologies help us to introduce them to produce a more convenient tool for the purpose of monitoring the orographic process.

2. GEOLOGICAL SURVEYS

In his work, the author tends to refer to the geological data, even though there is left to be solved about some problems about accuracy and definitions of the related factors.

In this work, the unit defined and used as the universal unit is taken as reference. Then, any problem can be described well to be seen well.

A glimpse of the orographic processes can be seen above the sea surface. Then, it is more possible to see the orographic processes in a global scale.

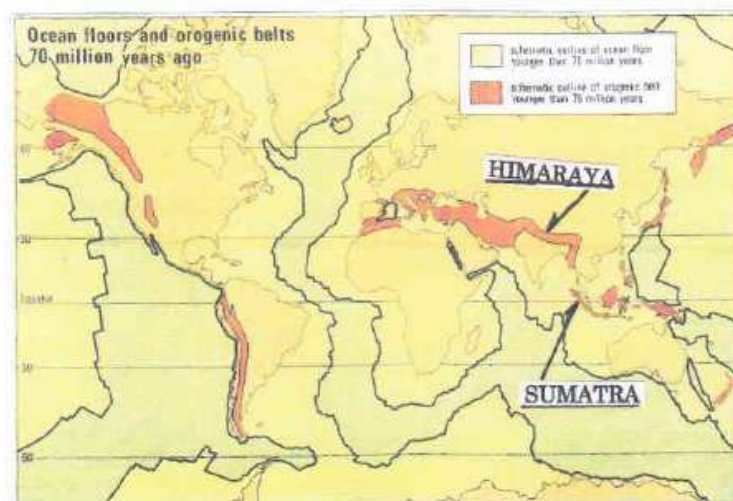


Figure 1: Patterns of ocean floors and orographic belts (70 million years ago).

3. OCEANFLOORS AND OROGENIC BELTS

In the geological time scale, it has been taken to be more realistic to consider the scientific survey in a global scale, for example, as is shown in Figure 1.

In this Figure 1, it is shown that the ocean floors and orographic belts 70 million years ago. The author had ever seen many local maps for the local orographic patterns.

This figure must be the first time to introduced the oceanfloors and orographic belts in a global scale.

In this Figure 1, it can be seen a glance of the orographic belt younger than 70 million years and of the oceanfloors younger than 70 million years.

4. TSUNAMI EARTHQUAKES

In 11 March 2011, one of the tsunami earthquakes hit the coast to destroy the human activities. The geodetic survey has shown that the crust displacement pattern was a pattern indicating as if the epicenter of seismic normal fault was the point of convergent of the horizontal displacement.

It was said that a similar pattern must be seen if the monitored data was obtained when the 2004 Banda Ace tsunami earthquake.

These seismic events were evaluated as very severe hazardous events.

5. YOUNGER OCEAN FLOOR

As a local problem, the author would give his notice to the scientists in seismology.

The 2011 earthquake in the northwestern Pacific had given to an impact to their vision of the tsunami earthquake.

The scientists in local seismic prediction must have had some mistaken at defining a set of so called “seismic parameters”. This parameters has had been introduced to specify the past significant earthquakes in the land area on the bases of the directly measured indices closely related to the interested seismic event. They have never had any equivalent indices directly measured for the tsunami earthquakes generated undersea even now in 2015. If so, several discrete data must be exist to fail some missing at their seismic prediction. They had extensively assumed that the seismic parameters for specifying the tsunami earthquake without any understanding of its dynamical meaning. In addition, the data for that purpose was not enough to actively support any one of the past tsunami earthquakes. There has had to refer to a convenient set derived on the bases of the historical documentations.

Now, some of the scientists must be anxious to consider the tsunami earthquake hitting the south Japan. Nevertheless, the author has to point out that the coasts of the south Japan is just neighbor the Philippine Plate which includes a younger ocean floor younger than 70 million years. This means that the expected tsunami earthquake to hit the coast of the south Japan must be completely different from the tsunami to hit the coast of the east Japan where the Fukushima Nuclear Power Station was located.

It is necessary to take into consideration on what is known on orographic process on the earth.

6. OROGRAPHIC PROCESS

Each of the two hazardous tsunami earthquakes was located at a point just neighbor the cost. The location of each seismic events is understood to generated by the interaction of the two tectonic plates where the two plates are convergent to form an interface each other.

It is said that the widely discussed to the details by the seismologists though the author knows that they were extended their model on the bases of no dynamics.

Then, they have to start for their model renewal.

However, the author has to note that the orographic pattern between Himaraya and Sumatra in Asian area is quite similar to the pattern between the mountain range in the south island and the volcanic range in the north island in New Zealand of the southern Pacific.

It is unfortunate that the data is limited so that the author has to note with his bold assumption.

In the southern hemisphere, the number of the data must be small so that it is hard to consider an orographic process in any geological scale.

Now, the author reminds to the satellite monitoring of the earth surface, and, he is expecting to hear about a more advanced research must be appeared.

Unfortunately, the author has only limited number of the data in orology, though it can be noted the data shown as (referring to the description on the published geographic map).

The peak height of Manaslu was 8156 m in 1980 though it is 8163 m in 2012, and, the peak of Annapurna was 8071 m in 1980 though it is 8091 in 2012.

The above two peaks are located in the west of Himarayan mountain range at the west of the peak of Everest though the 2004 Indonesian tsunami earthquake left a lowered land areas along the coastal zones.

The above fact is showing a twist of the crustal front between the Indian crust and the Eurasian crust in the Southeast area. A quite similar twist case must be seen on minor front passing the South Island and the North Island formed between the Australian plate and the Pacific plate.

7. SATELLITE MONITORING

As the scientists already aware of that, the satellite monitoring was contributive to inform three dimensional pattern of the land surface undulations time to time at the tsunami earthquake occurred on 11 March 2011. The monitored data was processed and distributed soon by the Geographic Research Institute, located just neighbor the epicenter of the tsunami earthquake.

At a sudden happening, a quick response is effective. Nevertheless, we have had seen many cases of severe hazards to destroy a quiet life and to wash out on the coastal land surface.

Now, we have to live with nature.

8. CONCLUSIONS

The author noted about orographic process in relation to tsunami earthquake with his bold assumption. For a more advanced research, satellite monitoring would be effective.

This work was accepted just after the Nepal destructive earthquake on 25 April 2015.

An Efficient Approach of Lengthening Battery Age and Working Hours through Redistributing Battery Packs

L. Chen¹, X. H. Feng¹, G. C. Wan², and M. S. Tong²

¹School of Electrical and Electronic Engineering, Shanghai Institute of Technology, Shanghai, China

²Department of Electronic Science and Technology, Tongji University, Shanghai, China

Abstract— As electric vehicles and energy storage systems continue to develop and popularize, how to maximize the working time of batteries has become a major concern. For the sake of facilitating battery management, individual batteries are generally grouped to form battery packs by serial and parallel connections and a complete power supply system consists of those packs either in series or in parallel. However, the inconsistency of performances between different battery packs will seriously aggravates in the usage of batteries, resulting in a sharp reduction on the working time of batteries. In this paper, we propose a novel scheme of redistributing battery packs and design an appropriate system of managing the charging and discharging process of batteries, so that the lifetime of batteries can be greatly extended.

1. INTRODUCTION

The smart power management devices have wide applications in electric vehicles (EV) and energy storage systems. For the sake of facilitating battery management, individual batteries are generally grouped to form battery packs by serial and parallel connections and a complete power supply system consists of the battery packs in serial and parallel connections. Initially, the performance of each individual battery which constitutes battery packs is different and the difference between individual batteries will be gradually enlarged during the use of batteries, resulting in a significant degradation of the battery packs' performance [1, 2]. Because the released maximum power by a power supply system is determined by the minimum-power battery pack and the minimum-power battery pack will be seriously harmed if it continuously discharges and we must stop its discharging process. Similarly, if the maximum-power battery pack has a full charge, we must stop its further charge to prevent it from being harmed. When the difference of performance between battery packs is magnified, the working hours of power supply system will sharply reduce and the age of batteries will also be shortened greatly.

In this paper, we fully investigate a set of lithium-iron-phosphate batteries and propose an efficient approach for lengthening the working hours and age of the batteries by redistributing battery packs. The approach analyzes the data about the state of charge (SOC) and voltage of battery packs and then quantifies the level of their inconsistency between battery packs. The redistribution of battery packs will be automatically managed according to the level of inconsistency and we have designed a smart electronic device for controlling the process. The experimental tests show that the approach can significantly lengthen the working hours and age of batteries and we will show the details of design and testing results.

2. FACTORS IMPACTING THE REDISTRIBUTION OF BATTERY PACKS

Because of the advantages of high energy density, low cost, and safety, LiFePO₄ battery has become the first choice of mobile battery. From the point of usage, the performance parameters of LiFePO₄ battery include the capacity, battery voltage, internal resistance, charge-discharge scale, depth of discharge, and circular working life [3], etc.. The battery capacity includes the theoretical capacity, actual capacity, and SOC. The theoretical capacity is the capacity that allows all active substances in the interior of battery to take part in a chemical reaction and the total energy is calculated using Faraday's law. The battery capacity represents the maximum value of theoretical capacity and the battery discharge capacity is only a part of theoretical capacity. The actual capacity is defined as the electricity that allows the battery to be fully charged or reach the maximum capacity that can be given. The SOC is defined as the used battery's discharge in the rate of C/30 and in the temperature of 25 degree before the cut-off voltage can get the battery capacity.

The battery voltage includes the open-circuit voltage and operating voltage. The open-circuit voltage (OCV) of a battery is defined as the potential difference between two balanced electrodes of thermodynamics when the circuit is in an open-circuit state. The OCV is affected mainly by its

material properties such as polarity and electrolyte materials [4]. The operating voltage (OV) is defined as the potential difference between two electrodes of the battery in a working state, which is also called terminal voltage. When the battery is in charging, the OV is bigger than the OCV. When the battery is in discharge, the OV is inferior to the OCV [5]. Because the internal resistance is difficult to measure, the cut-off voltage and SOC of charging and discharging in the battery packs are used as reference variables so that the redistribution of battery pack model can be simplified.

3. EXPERIMENTS AND RESULTS

3.1. Method of Redistributing Battery Packs

The redistribution of battery packs is determined according to the cut-off voltage and cut-off SOC of charge and discharge in a battery pack. The battery pack is formed by serial and parallel connections of individual batteries and its internal structure is shown in Figure 1.

If the cutoff voltage of charge in a batter pack is higher or closer to the voltage limit, then it means that individual batteries in a battery pack have a better performance and have a better consistency between different individual batteries because the individual battery has a higher voltage when its performance is better. However, as the usage of individual batteries increases and their aging aggravates, their performance will drop significantly and the voltage drop on the internal resistance of the batteries also increases. If the cut-off voltage of discharge in a battery is lower or it gets closer to the limit of discharge voltage, it simply reflects that the consistency of individual batteries in the battery pack is better. The SOC of battery packs is determined by the individual battery which has the least SOC.

We define the maximum cut-off voltage of charging as V_i and the maximum cut-off SOC of charging as SOC_j in a battery pack. We take an energy system which is shown in Figure 2 as an example. The system consists of four series-connect battery packs and three parallel-connection battery packs.

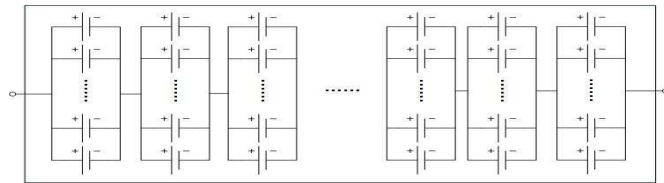


Figure 1: The internal structure of a battery pack.

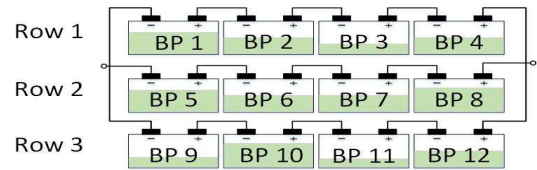


Figure 2: No redistribution of battery packs.

A low-voltage battery is charged by a high-voltage battery when they are connected in parallel and it will cause an energy assumption by the internal resistance of the battery. We define V_{L1} , V_{L2} and V_{L3} as follows.

$$V_{L1} = V_1 + V_2 + V_3 + V_4 \quad (1)$$

$$V_{L2} = V_5 + V_6 + V_7 + V_8 \quad (2)$$

$$V_{L3} = V_9 + V_{10} + V_{11} + V_{12} \quad (3)$$

In order to ensure that the battery pack will not charge each other, resulting in a waste of energy, we must ensure that V_{s1} , V_{s2} and V_{s3} are similar or equal to each other. Additionally, in order to ensure a maximum efficiency for the battery, we need to have a similar or equal maximum SOC in the battery pack of each row by the method of time-sharing work. The meaning of time-sharing work denotes that the battery pack of one row which has a large capacity will be charged by a switch when the EV needs a less power so that the battery pack's capacity in each row can be approached. All battery packs work when the EV needs an adequate power. So, the conditions of redistributing battery packs can be listed as follows.

- 1) V_{L1} , V_{L2} , and V_{L3} are similar or equal to each other;
- 2) SOC_1 , SOC_2 , SOC_3 , and SOC_4 are similar or equal to each other;
- 3) SOC_5 , SOC_6 , SOC_7 , and SOC_8 are similar or equal to each other;
- 4) SOC_9 , SOC_{10} , SOC_{11} , and SOC_{12} are similar or equal to each other;

In order to decide the time of redistributing battery packs, we need to define the level of inconsistency in the battery packs and redistributing battery packs will happen when the level is exceeded. Table 1 shows the parameters of battery packs used for simulations.

Table 1: Parameters of battery packs.

Battery pack	SOC	Voltage	Battery pack	SOC	Voltage
Battery pack 1	82%	30 V	Battery pack 7	79%	24 V
Battery pack 2	74%	22 V	Battery pack 8	78%	22 V
Battery pack 3	77%	22 V	Battery pack 9	78%	25 V
Battery pack 4	77%	23 V	Battery pack 10	79%	29 V
Battery pack 5	80%	28 V	Battery pack 11	75%	23 V
Battery pack 6	74%	24 V	Battery pack 12	79%	22 V

3.2. Simulation Test and Analysis of Results

In order to complete the experiment and verify the method, we should first build a simulation test platform. The platform is set up through the object-oriented language — C sharp and it can simulate the discharge characteristics of the battery pack. Discharge rate is C/5 when the battery pack is discharging and the battery's working time is 11.15 h when the battery pack is not in a redistribution. The results are shown in Figure 3. According to the condition about the redistribution of battery packs, the battery's working time is 11.45 h when the battery pack is of redistribution. The results are shown in Figure 4.

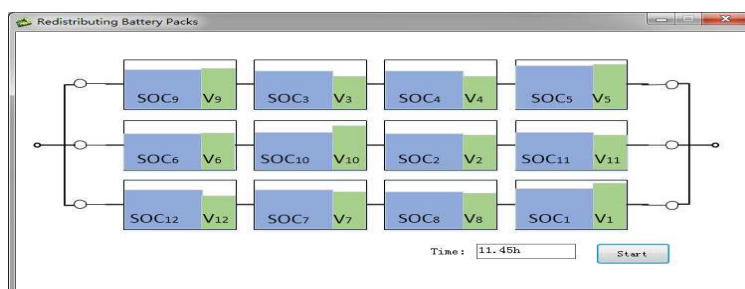


Figure 3: No redistribution of battery packs.

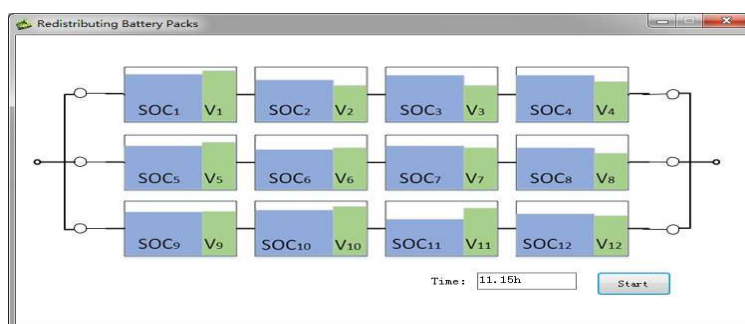


Figure 4: Redistribution of battery packs.

According to the results in Table 2, we can see that the prolonged working time of battery changes with different discharge rates when the battery pack status is the same and the prolonged working time is longer when the discharge rate is smaller. Therefore, the battery's working time is lengthened when the redistribution of battery packs happens.

Table 2: The simulation results.

Discharge Rate	No Redistribution (unit: hour)	Redistribution (unit: hour)
C/15	33.45 h	34.35 h
C/5	11.15 h	11.45 h
C/3	6.69 h	6.87 h

4. CONCLUSION

In this paper, a redistribution scheme for battery packs has been presented based on the relationship between the battery pack voltage and SOC. The scheme is verified through a simulation test bench. Also, the experimental results show that the proposed scheme is effective and feasible.

REFERENCES

1. Xue, J.-H., J.-L. Ye, et al., "Battery group technology and application of energy storage system," *Power Technology*, Vol. 37, No. 20, 1945–1946, 2013.
2. Teng, L., C.-T. Lin, and Q.-S. Chen, "Inconsistency analysis of LiFePO₄ battery packing," *Trans. Tsinghua Univ. (Sci & Tech.)*, Vol. 52, No. 7, 1001–1002, 2012.
3. Shi, W., J.-C. Jiang, et al., "Research on SOC estimation for LiFePO₄ Li-ion batteries," *Journal of Electronic Measurement and Instrument*, Vol. 24, No. 8, 769–770, 2012.
4. Wang, L.-Z., M. Xiang, S.-H. Gu, and H.-J. Wang, "Open circuit voltage and its effect factors," *Battery*, Vol. 29, No. 4, 157–159, 1999.
5. Xia, C.-Y., S. Zhang, and H.-T. Sun, "A strategy of estimating state of charge based on extended Kalman filter," *Power Technology*, Vol. 31, No. 5, 414–415, 2013.

An Accurate Estimation for the State of Health of Lithium-ion Batteries by Using Fuzzy Logic System

L. Chen¹, F. Q. Xiong¹, G. C. Wan², and M. S. Tong²

¹School of Electrical and Electronic Engineering, Shanghai Institute of Technology, Shanghai, China

²Department of Electronic Science and Technology, Tongji University, Shanghai, China

Abstract— Lithium-ion batteries have been widely used as a power source for electric vehicles and the lack of accurate estimation for the state of health (SOH) has seriously affected the practical applications of lithium-ion battery packs, so it is very imperative to find a good solution. In this paper, we propose an accurate estimation method for the SOH by using a fuzzy logic system. We first perform charging and discharging experiments for the lithium-ion batteries to obtain the residual capacitance and equivalent DC resistance under different SOHs. Then a fuzzy logic system is figured out according to the relationship between the equivalent DC resistance and the SOH. The SOH of the batteries is estimated online through inputting the calculated equivalent DC resistance into the fuzzy logic system. Experimental results show that this method is very effective to calculate the SOH of lithium-ion batteries.

1. INTRODUCTION

Recently, energy crisis and environmental pollution has become increasingly serious and the development of lithium-ion batteries as a power source has been very essential. One of the most important applications of the lithium-ion batteries is to be the power source of electric vehicles and whether electric vehicles will be widely used or not mainly depends on the performance of the batteries. Thus we must properly monitor and evaluate the state of health (SOH) of batteries to ensure that electric vehicles can operate safely and reliably [1].

The SOH and state of charge (SOC) are the two important indexes reflecting the state of batteries. In recent years, many attentions have been paid to the estimation methods of SOC such as Coulomb counting or Ah counting, adaptive Kalman filtering, extended Kalman filter [2], artificial intelligent methods and impedance spectroscopy. In contrast, the study on the SOH has not received a sufficient attention [3]. The SOH estimation belongs to a nonlinear problem which requires a highly accurate solution and the traditional linear estimation methods cannot meet the estimation requirements. As there has not been a mature estimation method for the SOH so far, it is imperative to find a solution for the lithium-ion batteries.

The SOH is a figure of merit for the condition of a battery (or a battery pack) compared to its ideal conditions. Typically, a battery's SOH will be greater than or equal to 100% at the time of manufacturing and then will decrease over time and use. IEEE standard 1188-2005 specifies that when the battery's capacitance decreases to 80%, the battery should be replaced. In fact, the degradation of lithium-ion batteries can be attributed to its change of internal chemical composition [4]. During the charging and discharging process, the lithium-ion batteries will also produce some irreversible side effects in addition to have a specific oxidation and reduction reaction. The side effects often generate lithium salt which adheres to the electrode and increase the equivalent DC resistance of the battery [5]. The lithium in the lithium salts will no longer take part in the charge and discharge reaction in the form of li-ion. That is to say, the maximum capacitance of a battery is reduced from a macroscopic view. In addition, in the initial stage of charging and discharging process, the battery's materials will react with electrolytes on the interface between a solid and liquid phase and form a passivation layer, called solid electrolyte interface (SEI), covering the surface of the electrode's materials. Li-ion will encounter some obstacles when getting through the SEI. These obstacles are the so-called internal resistance of the battery. The thicker the SEI film is, the bigger the equivalent DC resistance of the battery is. Thus the maximum capacitance of the battery is relatively reduced and its SOH can be obtained by measuring the equivalent DC resistance in its different life stages.

In this paper, we propose an appropriate method to accurately estimate the SOH for lithium-ion batteries. The charging and discharging experiments are performed first and the corresponding fuzzy rule table can then be defined according to the relationship between the equivalent DC resistance and the SOH. Also, the static estimation and dynamic estimation are combined together so that the system reliability and the estimation accuracy can be improved. The simulated results

show that the method can remarkably enhance the estimation accuracy for the SOH of lithium-ion batteries and it could be very useful in electric vehicles.

2. CALCULATION OF EQUIVALENT DC RESISTANCE

Lithium-ion batteries usually adopt a constant current at the beginning and then take a constant voltage to charge. When the terminal voltage of the battery does not reach 3.65 V, the constant-current charging method is adopted. When the terminal voltage reaches 3.65 V, the constant-voltage charging method with 3.65 V is used. During the constant-current charging process, the equivalent DC resistance can be obtained by periodically shutting off the charging current in a short time (less than 1%). The equivalent DC resistance can be calculated by

$$r_n = \frac{U_{cn} - U_{ocvcn}}{I_c} \quad (1)$$

where r_n is the equivalent DC resistance of the n th ($n = 1, 2, 3, \dots$) sample point, U_{cn} is the last charging voltage before cutting off the current of the n th charging cycle, U_{ocvcn} is the last terminal voltage during the process of cutting off the current in the n th charging cycle, and I_c is the charging current. The advantage of this method is that during the constant-current charging process, the equivalent DC resistance can be obtained simply by measuring the battery's terminal voltage at different times. Figure 1 shows the changes of the equivalent DC resistance at different SOHs during the constant-current charging process.

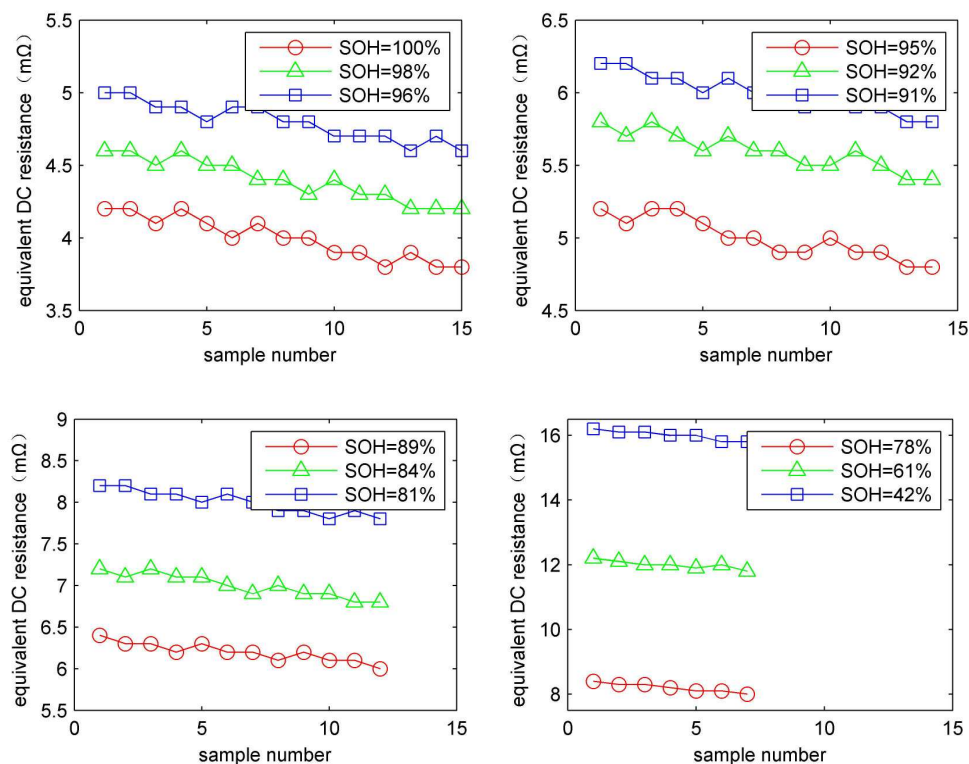


Figure 1: Equivalent DC resistance at different SOHs during the constant-current stage.

3. RELATIONSHIP BETWEEN EQUIVALENT RESISTANCE AND SOH

The battery used in this paper is a lithium-iron-phosphate power battery with 3.2 V and 100 Ah. The discharge cut-off voltage of the battery is 2.5 V, the charge cut-off voltage is 3.65 V, the charging current is 0.2C, and the discharge current is 0.5C. The charging and discharging experiment is conducted under different SOHs. In the constant-current charging stage, the current is shut off for 5 seconds every 15 minutes, and the U_{cn} and U_{ocvcn} are then recorded, respectively. The equivalent DC resistance of each sample point can be calculated and the average value of all points is regarded as the equivalent DC resistance of the battery. Figure 2 shows the relationship between the equivalent DC resistance of a lithium battery and its SOH.

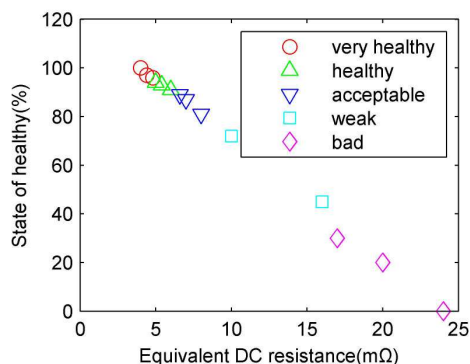


Figure 2: Relationship between the equivalent DC resistance and SOH of a lithium battery.

4. SOH ESTIMATION

The fuzzy logic method is an effective way to estimate the SOH of a lithium battery by using the equivalent DC resistance [6]. The parameters about the equivalent DC resistance and SOH of lithium-ion batteries mentioned in Figure 1 can be used as the samples of establishing the fuzzy system and the fuzzy system can serve to online estimate the batteries under other health conditions. The input to the fuzzy logic system is the average value of equivalent DC resistances during the constant-current charging phase and the output is the estimated SOH. The fuzzy rules, which are defined based on the data given in Figure 2, are shown in Table 1. The output of the fuzzy logic system is in the range of [0, 1.2] and the fuzzy membership functions in shown in Figure 3. The fuzzy logic system is constructed by using the singleton fuzzifier, the centroid defuzzifier, and the Mamdani product inference engine [7]. All the aforementioned procedures for constructing the proposed SOH estimator are performed offline.

Table 1: Fuzzy rules for estimating the SOH.

FUZZY RULES	
1	IF equivalent DC resistance is very small, THEN SOH is very healthy
2	IF equivalent DC resistance is small, THEN SOH is healthy
3	IF equivalent DC resistance is medium, THEN SOH is acceptable
4	IF equivalent DC resistance is large, THEN SOH is weak
5	IF equivalent DC resistance is very large, THEN SOH is bad

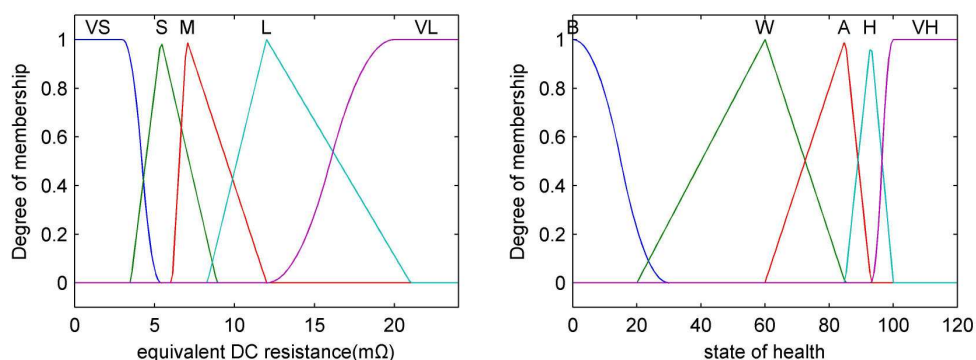


Figure 3: Fuzzy membership functions for the input and output variables of the fuzzy logic system.

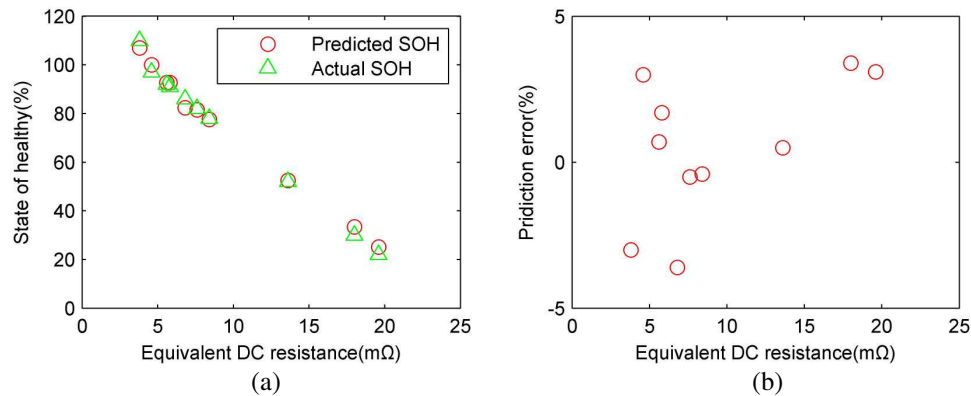


Figure 4: A comparison of the estimated SOH with the actual SOH and the prediction error.

5. EXPERIMENTAL RESULTS

In the above section, we have introduced the method of using the fuzzy logic to estimate the SOH of a lithium-ion battery. However, all these steps are achieved offline. In this section, we propose an online estimation method by using the previously-established systems. During the constant-current charging stage, the current is shut off for 5 seconds every 15 minutes, and U_{cn} and U_{ocvcn} are recorded respectively. Then the equivalent DC resistance of each sample point and the average value of all points can be calculated. The SOH of a battery can be obtained online through inputting the calculated average value of equivalent DC resistance into the fuzzy inference engine. The experiment results and prediction error are shown in Figure 4. It can be seen from Figure 4(b) that the estimation error of this method is less than 5%, meaning that it is a good method to accurately estimate the SOH of a battery.

6. CONCLUSION

In this paper, a new method for estimating the SOH of lithium-ion batteries has been investigated. By taking the calculated equivalent DC resistance of lithium-ion batteries during the charging process as the input of the pre-established fuzzy logic system, the estimation of SOHs will be online. The experimental results show that the error of using this method to estimate the SOH is not more than 5%, which can well satisfy the requirement of electric vehicles. Moreover, we can effectively extend the service life of a battery pack by replacing the individual battery cell whose health condition declines to its critical value. This method can greatly reduce the cost and show a high economic value. Meanwhile, it can also provide the necessary reference for estimating the SOC of lithium-ion batteries, equalizing and fault diagnosis of electric vehicles.

REFERENCES

1. Zheng, N., Z. Wu, M. Lin, and L. T. Yang, "Health-monitoring systems based on electronic textiles," *IEEE Trans. Inf. Technol. Biomed.*, Vol. 14, No. 2, 350–359, Mar. 2010.
2. Kim, J. and B. H. Cho, "State-of-charge estimation and state-of-health prediction of a Li-ion degraded battery based on an EKF combined with a preunit system," *IEEE Trans. Veh. Technol.*, Vol. 60, No. 9, 4249–4260, Nov. 2011.
3. Tsang, K. M. and W. L. Chan, "State of health detection for Lithium ion batteries in photovoltaic system," *Energy Conversion Management*, Vol. 65, No. 7, 2013.
4. Kassem, M., J. Bernard, and R. Revel, "Calendar aging of a Graphite/LiFePO₄ cell," *J. Power Sources*, Vol. 20, No. 8, 296–305, 2012.
5. Liu, P., J. Wang, and J. Hicks-Garner, "Aging mechanisms of LiFePO₄ batteries deduced by electrochemical and structural analyses," *Electrochem. Soc.*, Vol. 157, No. 4, 499–507, 2010.
6. Shahriari, M. and M. Farrokhi, "Online state-of-health estimation of VRLA batteries using state of charge," *IEEE Transactions on Industrial Electronics*, Vol. 60, No. 1, 191–202, 2013.
7. Zenati, A., Ph. Desprez, and H. Razik, "Estimation of the SOC and the SOH Li-ion batteries by combining impedance measurements with the fuzzy logic inference," *Proc. 36th IEEE IECON*, 1773–1778, Glendale, AZ, 2010.

Estimation of Equivalent Model Parameters for LiFeO₄ Batteries Based on Particle Swarm Optimization

L. Chen¹, T. Geng¹, Q. Zhang¹, G. C. Wan², C. H. Jiang², and M. S. Tong²

¹School of Electrical and Electronic Engineering, Shanghai Institute of Technology, Shanghai, China

²Department of Electronic Science and Technology, Tongji University, Shanghai, China

Abstract— State of charge (SOC) is an important parameter of battery management system (BMS) which reflects the reliability, safety, and lifetime of batteries. However, SOC cannot be measured directly and we have to estimate it via analyzing some other parameters such as voltage, current, and temperature. An accurate estimation strategy of SOC is necessary for the BMS and we propose a novel model based on particle swarm optimization (PSO) in this paper. The PSO is an optimization method which originated from artificial intelligence and evolutionary computation. It is a simple, effective, and universal theory which solves problems by seeking their individually best and globally best solutions. We apply this theory to optimally estimate the SOC parameters for LiFeO₄ Batteries and the simulated and experimental results have demonstrated its effectiveness.

1. INTRODUCTION

Power batteries are very important components in electric vehicles and they have a significant impact on the performance and security of a whole vehicle. To ensure the safe and reliable operation of batteries, designing an optimal battery management system (BMS) is very essential. The BMS manages the batteries based on their states and instructions from a vehicle management system (VMS). The voltage, current, and temperature of batteries can be measured directly by sensors while other parameters such as the state of charge (SOC) has to be estimated indirectly by certain algorithms which usually rely on the battery model and its parameters. The battery model and parameters are essential because they form the basis of loop simulations for hardware and SOC estimation, and also provide a reference for the control of BMS.

In this paper, we propose a unified form of equivalent circuit model for LiFeO₄ batteries based on the analysis of similarity between the internal mechanism and external characteristic of a chemical power source. A two-order equivalent circuit [1] of LiFeO₄ batteries is built and their resistance and capacity are estimated with a least square method (LSM) [2] and particle swarm optimization (PSO) [3]. By comparing the results from different estimation methods, we find that the relationship between the SOC and the electric motive force (EMF) or EMF-SOC can be significantly affected by the temperature. We also build a backward-propagation (BP) neural network [4] in which the EMF and temperature are taken as inputs while the SOC works as an output and the results are used to estimate the SOC. The simulated and experimental results show that the proposed estimation method can accurately estimate the SOC for LiFeO₄ batteries.

2. PARTICLE SWARM OPTIMIZATION (PSO)

The PSO was first proposed by Kennedy and Eberhart in 1995 [5]. It is an optimized computational method based on a swarm intelligence and simulates the internal action between individuals, group, and environment. Nowadays, the PSO is widely used in process optimization, parameter estimation, and system control. In the PSO theory, the position of a particle represents a solution of optimization problem. Each particle has a position and velocity that decide its direction and speed. The state of particles depends on adaptive values that are determined by objective function. Suppose in a D -dimension objective search space, a group is formed by m particles which are randomly initialized. Then the position and flying velocity of the i th particle can be represented by $X_i = (x_{i1}, x_{i2}, \dots, x_{iD})^T$ and $V_i = (v_{i1}, v_{i2}, \dots, v_{iD})^T$, respectively. Particles will track two extremum values in a solution space. On each iteration, the individual extremum $Pb_i = (pb_{i1}, pb_{i2}, \dots, pb_{iD})^T$ represents the best position of the particle while the global extremum $Gb = (gb_1, gb_2, \dots, gb_D)^T$ represents the best position of the group. The velocity and position are updated each time according to the following formulas:

$$v_{id}^{k+1} = v_{id}^k + c_1 r_1^k (p_{id}^k - x_{id}^k) + c_2 r_2^k (gb_d^k - x_{id}^k) \quad (1)$$

$$x_{id}^{k+1} = x_{id}^k + v_{id}^{k+1} \quad (2)$$

where v_{id}^k represents the velocity of the i th particle in the D th dimension in the k th iteration and x_{id}^k represents its current position. Also, c_1 and c_2 are the acceleration factors or learning factors which adjust the maximum step size of the flight to the globally best particle and individually best particle. The adaptive values of c_1 and c_2 can accelerate the convergence and help the particles to avoid falling into a local optimum. In addition, r_1 and r_2 are the random numbers in the range $[0, 1]$, p_{id} represents the position or coordinate of the individual extremum point of the i th particle in the D th dimension, and g_d represents the position of the global extremum point in the D th dimension [6].

3. PSO PARAMETER IDENTIFICATION BASED ON SECOND-ORDER RC EQUIVALENT

3.1. LSM

Mathematical model of a battery should reflect and take into account its self-discharge phenomenon, capacity, and resistance over potential and environmental temperature. In this paper, a second-order RC equivalent circuit model is used to simulate the battery. In this model, E represents the battery's voltage which is affected by the SOC and R_0 refers to its ohmic internal resistance. Also, R_1 and C_1 denote its electrochemical polarization resistance and capacitance, respectively, and they constitute a RC parallel circuit, while R_2 and C_2 indicate its consistent polarization resistance and capacitance, respectively, and they constitute another RC parallel circuit. The test data of a study on a 60AH-LiFePO₄ battery by means of a constant discharge is shown in Figure 2. The battery starts a discharge after 100s, and stops the discharge when reaching the point B. The RC network is in a zero input response from the point A to point B and the voltage rebounds rapidly as soon as the circuit is broken. In the circuit, the loop current is zero and the ohmic internal resistance drop is also zero.

$$R_0 = \frac{U_D - U_B}{I} \tag{3}$$

At the same time, the RC network is in a zero input response. The voltage from the point B to point C is

$$U_B(t) = E_C(t) - I \times R_1 \times e^{-\frac{t}{R_1 \times C_1}} - I \times R_2 \times e^{-\frac{t}{R_2 \times C_2}} \tag{4}$$

where $E_C(t)$ refers to the voltage at the point C. We utilize the test data and LSM [7] to figure out the parameters including R_1 , R_2 , C_1 , and C_2 . The result is shown in Figure 3.

3.2. Battery's Parameter Identification Based on the PSO

We initialize 10 particles and each particle's position is $X_i = (R_{1i}, R_{2i}, \frac{1}{C_{1i}}, \frac{1}{C_{2i}})^T$ while its velocity is $V_i = (v_{i1}, v_{i2}, v_{i3}, v_{i4})^T$. All initial values are randomly chosen in the range of $[0, 1]$. On each iteration, the parameter

$$Y_1(t) = E_C(t) - I \times R_1 \times e^{-\frac{t}{R_1 \times C_1}} - I \times R_2 \times e^{-\frac{t}{R_2 \times C_2}} \tag{5}$$

is calculated while $Y_2(t)$ is its counterpart obtained by an experiment. The fitness function is

$$f = \sum_t \frac{|Y_2(t) - Y_1(t)|}{Y_2(t)} \tag{6}$$

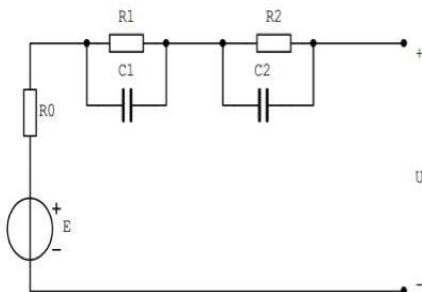


Figure 1: A model for an FeLiPO₄ battery.

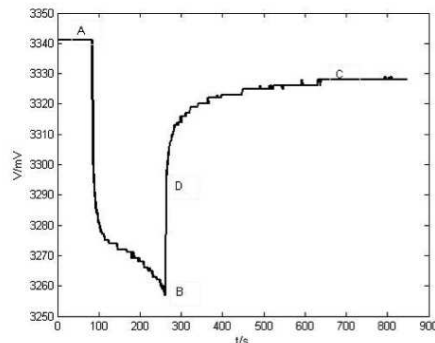


Figure 2: Discharge curve of an FeLiPO₄ battery.

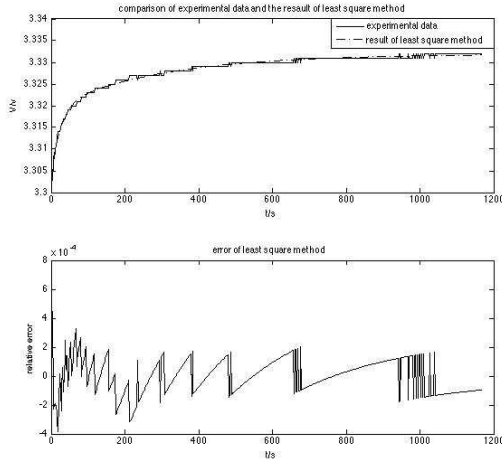


Figure 3: Parameters figured out by a LSM.

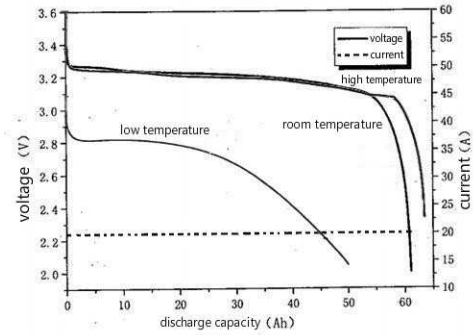


Figure 4: EMF-SOC relationship in different temperatures.

and the iteration is performed by the following steps:

Step 1: When $g = 1$, the position X_i^1 and velocity V_i^1 of the searched points are initialized with the random numbers in the range of $[0, 1]$, and $P_i^1 = X_i^1$. Then we calculate the individual extremum values and the global extremum value is the best one among the individual extremum points. Record the index of the best particle and set G as the position of that particle.

Step 2: Update the new position X_i^2 and velocity V_i^2 for each particle by Equations (1) and (2) and calculate the particle's new fitness value. If the new value is better than the previous value, then let $P_i = X_i^2$. If there is an individual value that is better than the current global value, the position of that particle will be set as G and the index of that particle will be recorded. The global extremum value is then updated correspondingly.

Step 3: If the number of iterations reaches the maximum value that is set in advance, then the iteration will stop and the best solution will be output. Otherwise, go back to Step 2.

3.3. EMF-SOC Model of LiFePO_4 Battery Based on BP Neural Network

The initial capacitance should have been known before an ampere-hour method is used to calculate the residual capacitance of a battery. Currently, the relation of $\text{SOC} = f(\text{SOC})$ is mostly used to get the initial SOC. If the battery has rested for a long time, its terminal voltage can be regarded as the EMF. For different temperatures, the same EMF corresponds to different SOC as shown in Figure 4. The BP network is a one-way-communication and multilayer-feed-forward neural network and the BP means the backward propagation of errors whose main idea is the gradient descent. Using the gradient search techniques can make the actual output value of network have an expected error of square minimum value. The initial capacitance is affected by terminal voltage and temperature. The EMF-SOC BP neural network can be obtained by setting the EMF and temperature of the battery as an input while setting the SOC as an output.

3.4. Construction of State Space for Battery

We can get the state space for a battery according to the following equations

$$\begin{bmatrix} \text{SOC}_k \\ U_k^0 \\ U_k^1 \\ U_k^2 \end{bmatrix} = \begin{bmatrix} 1 & & & \\ & 0 & & \\ & & e^{-\frac{\Delta t}{R_1 \times C_1}} & \\ & & & e^{-\frac{\Delta t}{R_1 \times C_1}} \end{bmatrix} \times \begin{bmatrix} \text{SOC}_{k-1} \\ U_{k-1}^0 \\ U_{k-1}^1 \\ U_{k-1}^2 \end{bmatrix} + \begin{bmatrix} -\frac{\eta \Delta t}{Q} \\ R_0 \\ R_1 \left(1 - e^{-\frac{\Delta t}{R_1 \times C_1}}\right) \\ R_2 \left(1 - e^{-\frac{\Delta t}{R_2 \times C_2}}\right) \end{bmatrix} \times i_{k-1} + w_{k-1} \quad (7)$$

$$U_{k-1} = \text{OCV}(\text{SOC}_{k-1}) - i_{k-1} \times R_0 - U_{k-1}^1 - U_{k-1}^2 + V_{k-1}. \quad (8)$$

In the equations, SOC_k is the value of the SOC at the k th moment, U_k^0 is the terminal voltage of ohmic internal resistance, U_k^1 and U_k^2 are the terminal voltages of polarization resistance, Δt is the sampling time, η is the coulomb coefficient, Q is the nominal capacitance of the battery, i is the current, and U_{k-1} is the voltage of the battery. The random signal w_{k-1} and v_{k-1} refer to an incentive noise and observation noise, respectively. We assume that they are white noises which are independent of each other and follow a normal distribution.

4. SIMULATION RESULTS

We present the simulation results for the battery parameter identification based on the PSO method. Assuming that $c_1 = c_2 = 2$ and r_1 and r_2 are the random numbers in the range of $[0, 1]$. The dimensional speed v_d is clamped between $[v_{d\min}, v_{d\max}]$ to prevent particles from moving away from the search space. The number of iterations is selected as 10 and the identification results with corresponding errors are shown in Figure 5. On the other hand, if the number of hidden layers of the neural is selected as 5, the output of hidden layers of the neuron is selected as a “tansig” function, the transfer function of the output is a “purelin” function, and the training function is a “trainlm” function, then the EMF-SOC BP neural network can be established by setting the EMF and temperature of the battery as an input while setting the SOC as an output. The result is shown in Figure 6.

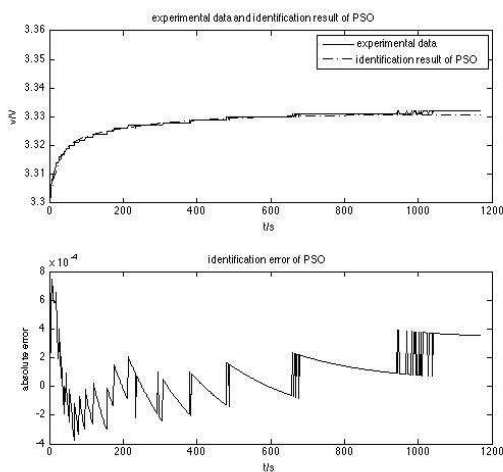


Figure 5: Result of the PSO.

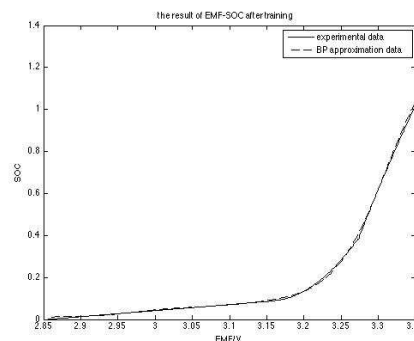


Figure 6: Result of the EMF-SOC based on the BP network.

5. CONCLUSION

We use the LSM to identify the parameters of battery model. We also establish a second-order RC network model for the LiFePO_4 battery and figure out the values of some parameters such as capacitances and resistances by the LSM and the PSO. Comparing these two algorithms, we find that the PSO can reach the same accuracy as the LSM. The structure of EMF-SOC neural network based on the BP neural network can be obtained via setting the EMF and temperature as an input and the SOC as an output. The accuracy of calculating the SOC can be enhanced by considering the influence of temperature. We present some simulated and experimental data to demonstrate the estimation method and good results have been observed.

REFERENCES

1. Salameh, Z. M., M. A. Casacca, and W. A. Lynch, “A mathematical model for lead-acid batteries,” *IEEE Transactions on Energy Conversion*, Vol. 7, No. 1, 93–98, 1992.
2. Chen, K., Y. Su, T. Li, and Z. Sun, “Modeling and remaining capacity estimation of lithium-ion battery for electric vehicles,” *Automotive Engineering*, Vol. 36, No. 4, 404–408, 2014.
3. Liu, R., X. Wang, and C. Tang, “Identification for hole transporting properties of NPB based on particle swarm optimization algorithm,” *Acta Physica Sinica*, Vol. 36, No. 2, 1–7, 2014.

4. Wei, D., G. Cao, and X. Zhu, “Modeling proton exchange membrane fuel cell (PEMFC) based on neural networks identification,” *Journal of System Simulation*, Vol. 15, No. 6, 817–819, 2003.
5. Kennedy, J. and R. Eberhart, “Particle swarm optimization,” *Proceedings of IEEE International Conference on Neural Networks*, 1942–1948, Perth, Western Australia, 1995.
6. Yang, W. and Q. Li, “Survey on particle swarm optimization algorithm,” *Engineering Science*, Vol. 6, No. 5, 87–94, 2004.
7. Xu, O., Y. Fu, H. Su, and L. Li, “A selective moving window partial least squares method and its application in process modeling,” *Chinese Journal of Chemical Engineering*, Vol. 22, No. 7, 799–804, 2014.

Noncoherent Detection for Multi-hop Amplify-and-forward-based Multi-branch Cooperative Diversity Systems

Minghe Mao¹, Ning Cao¹, Yunfei Chen^{1,2}, and Haobing Chu³

¹School of Computer and Information, Hohai University, Nanjing 210098, China

²School of Engineering, University of Warwick, Coventry CV4 7AL, UK

³School of Engineering, UBC Okanagan, Kelowna, BC V1V 1V7, Canada

Abstract— Since the actual distribution of the received signals in multi-hop amplify-and-forward (AF) relaying transmission is no longer Gaussian, which is caused by the multiplication of fading gains and noise, a new fitted distribution named as logistic distribution is used to derive a novel noncoherent detector based on the maximum likelihood (ML) method. In order to get better performance of the receiver, one or more multi-hop AF links are added to form a multi-branch cooperative diversity system. Therefore, at the destination, combining method is applied to combine several signals together to obtain better diversity gains. Numerical results show that the new detector based on the logistic distribution outperforms the conventional energy detector. Also, it is shown that the performance of receiver is significantly improved when combining method is applied in the multi-branch cooperative diversity system especially when the number of branches increases.

1. INTRODUCTION

Since the demand of wireless applications, such as mobile phones, wireless sensing networks, smart home applications, is growing broadly, the research of mobile communications technology develops rapidly. In wireless communications, one of the main problems that impact signal performances is fading [1]. In order to overcome this problem, many different technologies have been developed. Cooperative diversity [2] with multi-hop relaying is a good candidate which stands out of them.

Space Diversity technology is a receiver technique that can improve the signal performance by adding wireless link at a low cost [1]. At the receiver, more than one transmission paths are received. If one path undergoes a deep fade, another path may have a robust signal. Therefore, selecting the robust paths or combining different paths with different weight factors can improve the signal to noise ratio (SNR) of the receiver, thus the signal quality is improved. In cooperative wireless communications, signals can be transmitted from a source to its destination through different cooperative links and combined in the receiver. In general, there are three combining methods which are selection combining (SC), equal-gain combining (EGC) and maximum-ratio combining (MRC). Only focusing on the performance point of view, MRC is the best, EGC is at the middle and SC is the worst. But SC is the easiest one for implement. In this work, MRC and SC are investigated for comparison.

Each cooperative link may consist of several relays in order to reduce the signal dispersion loss and the performance degradation [3]. There are two main relaying techniques that can be used in the multi-hop relaying transmission. One is the amplify-and-forward (AF) technique and the other is the decode-and-forward (DF) technique [4–6]. In this work, we consider using AF in each multi-hop relaying link due to its simplicity [7, 8]. Without any further processing, the AF relay amplifies its received signal and retransmits the amplified signal to the next relaying node until the signal arrives at the destination. Where fixed relaying is assumed due to its simplicity and no requirement of acknowledge in network layer [9]. Thus, each relay amplifies the noise at the same time when it amplifies the retransmitting signal.

In a multi-hop and multi-branch cooperative diversity system, estimating the fading gains which is required in coherent detection causes a huge amount of overhead. Thus, noncoherent detection is preferred for simplicity in the applications with limited system resources [10]. Energy detection is a widely used noncoherent detection technique [11, 12]. In energy detection, the energy of the received signal is calculated and compared with a threshold, which is based on the Gaussian assumption of the received sample [13]. However, in multi-hop AF relaying systems, due to the multiplication of fading gains and noise the overall noise in the received signal is no longer Gaussian after several relays, such that the received sample is not Gaussian either. Thus, new distribution should be proposed, and the performance of the conventional energy detector for noncoherent detection can be further improved by using the new distribution of the received signal.

In this work, the actual distribution of the received signal is first introduced based on the distribution fitting techniques. The derivation is based on the assumption of independent and identically distributed Rayleigh fading and Rician fading hops. Based on these distributions, the maximum likelihood (ML) method is used to generate the new noncoherent detector. Then the performance of the new detector is investigated and compared with the conventional energy detector. The performance of two combining methods with different number of branches are compared with the original performance in single hop Rayleigh channel. Numerical results show that the new detector based on the proposed distribution outperforms the energy detector and that the performance gain increases when the number of branches increases and the number of hops decreases.

2. SYSTEM MODEL

Cooperative diversity is composed of multi-hop diversity and multi-branch diversity. Multi-hop diversity allows a long distance signal transmission and multi-branch diversity combines multiple received signals together to get better received performance. A multi-branch multi-hop cooperative diversity system [2] is shown in Fig. 1. An information source S transmits signal x through M independent branches to its destination D . Each branch is a link that includes $N - 1$ relays R_{ji} ($j = 1, 2, \dots, M; i = 1, 2, \dots, N$) with N hops over the fading channel. Where x is considered as an on-off keying (0-1) signal. For simplicity, the on-off keying signal is suitable for noncoherent energy detection. Each relay node incurs an additive white Gaussian noise n_{ji} . The fading coefficients for each hop of fading channel is h_{ji} . Thus, the received signal of the j th-branch is given by

$$y_{jN} = h_{j1}h_{j2} \dots h_{jN}x + h_{j2}h_{j3} \dots h_{jN}n_{j1} + h_{j3}h_{j4} \dots h_{jN}n_{j2} + \dots + h_{jN}n_{jN-1} + n_{jN}, \quad (1)$$

when $x = 1$, the received signal of the j -th branch at the destination is

$$y_{jN}^1 = P_{sj} + P_{nj}, \quad (2)$$

where the signal part $P_{sj} = \prod_{i=1}^N h_{ji}$, and the noise part $P_{nj} = \sum_{i=1}^N (\prod_{k=i+1}^N h_{jk})n_{ji}$. When $x = 0$, the received signal of the j -th branch at the destination becomes

$$y_{jN}^0 = P_{nj}. \quad (3)$$

In conventional researches, the noise part P_{nj} is assumed to follow Gaussian distribution [14]. But for the noncoherent detection in this work, since h_{ji} is unknown, P_{nj} is not Gaussian anymore. In particular, the number of terms in P_{nj} increases when the number of hops increases and P_{nj} becomes less Gaussian. Finding the exact distribution for the noise part is an entry point of this work.

Due to the variable number of hops, it is difficult to derive the theoretical distribution of y_{jN}^0 and y_{jN}^1 , if not impossible. Therefore, the distribution fitting is performed. Tests show that the logistic distribution has the smallest fitting errors when SNR is large enough for the AF relaying

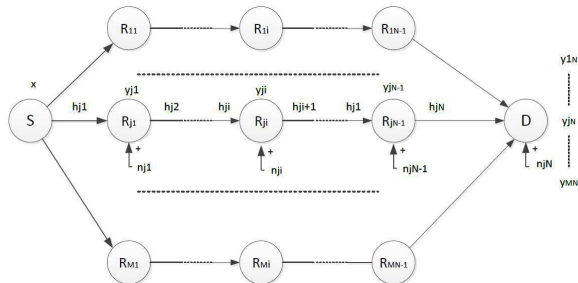


Figure 1: System model.

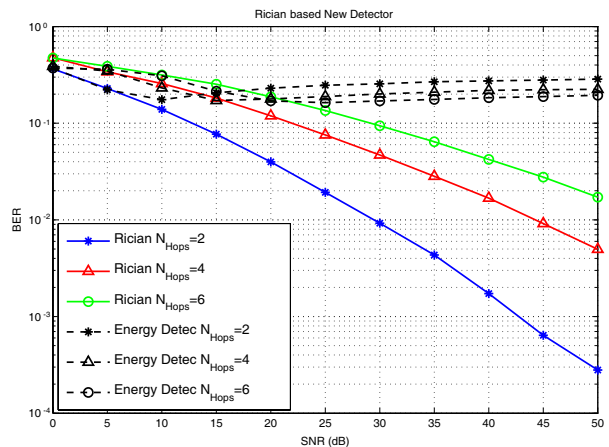


Figure 2: Performance comparison with Rician factor $K = 1$.

multi-hop transmission. The probability density function (PDF) of the logistic distribution is given by

$$f(x) = \frac{e^{-\frac{x-\mu}{\sigma}}}{\sigma \left(1 + e^{-\frac{x-\mu}{\sigma}}\right)^2}, \quad (4)$$

where μ is the mean and σ is the standard deviation. These two parameters can be calculated in the fitting. Based on the numerical calculation results for each branch, the relationships between these distribution parameters and the values of SNR and N_{Hops} can be derived. Since the mean μ can be approximated as 0. Using curve fitting, one has

$$\sigma_{0j} = 0.02497 - 0.01882 \cdot \sin(0.6969 \cdot \pi \cdot N_{\text{Hops}} \cdot \text{SNR}_j) + 0.428 \cdot e^{-(0.1103 \cdot \text{SNR}_j)^2}, \quad (5)$$

where $j = 1, 2, \dots, M$,

$$\sigma_{1j} = 0.001402 \cdot N_{\text{Hops}}^2 - 0.04206 \cdot N_{\text{Hops}} + 0.4462. \quad (6)$$

Then the PDFs of the received signal can be approximated as: when $x = 0$,

$$f(y_{jN}|x=0) = \frac{e^{-\frac{y_{jN}}{\sigma_{0j}}}}{\sigma_{0j} \left(1 + e^{-\frac{y_{jN}}{\sigma_{0j}}}\right)^2}, \quad (7)$$

when $x = 1$,

$$f(y_{jN}|x=1) = \frac{e^{-\frac{y_{jN}}{\sigma_{1j}}}}{\sigma_{1j} \left(1 + e^{-\frac{y_{jN}}{\sigma_{1j}}}\right)^2}. \quad (8)$$

3. RECEIVER FOR SINGLE BRANCH

Using the derived PDFs in the previous section, new noncoherent detectors can be proposed. Based on the ML principle [13], assume that the probabilities for the source transmitting "0" and "1" are the same, or $P(x=0) = P(x=1)$, the detector can be derived as

$$\mathcal{D}(y_N) = \prod_{j=1}^M \frac{f(y_{jN}|x=1)}{f(y_{jN}|x=0)} \underset{0}{\overset{1}{\geq}} \frac{P(x=0)}{P(x=1)} = 1. \quad (9)$$

Substitute (7) and (8) into (9), one has

$$\mathcal{D}(y_N) = \prod_{j=1}^M \frac{\sigma_{0j}}{\sigma_{1j}} e^{\frac{\sigma_{1j} - \sigma_{0j}}{\sigma_{0j} \sigma_{1j}} y_{jN}} \left(\frac{1 + e^{-\frac{y_{jN}}{\sigma_{0j}}}}{1 + e^{-\frac{y_{jN}}{\sigma_{1j}}}} \right)^2 \underset{0}{\overset{1}{\geq}} 1. \quad (10)$$

4. COMBINING METHODS

In this paper, MRC and SC combining methods are considered. For SC, as shown in the system model Fig. 1, the destination D receives M copies of the transmitted source signal. The signal of the branch with the highest instantaneous SNR is chosen by the combiner and used for demodulation. The choice of the instantaneous SNR γ_c can be obtained by

$$\gamma_{c, \text{SC}} = \max(\gamma_1, \gamma_2, \dots, \gamma_M), \quad (11)$$

where $\gamma_1, \gamma_2, \dots, \gamma_M$ represent the instantaneous SNRs of the received signals at the first, the second, \dots , and the M -th branches. Since each branch is independent, assume that there is a SNR threshold γ below which the received signal of the corresponding branch should be eliminated.

Since a SNR which is always guaranteed to be above the threshold is selected in SC, the diversity improves signal performance and reduces outage probability without additional transmit power. But it is not the best diversity technique due to its not using all of the branches.

For MRC, the combiner weights all the received signals according to their own qualities. Thus the instantaneous SNR at the output of the combiner is

$$\gamma_{c,\text{MRC}} = \sum_{i=1}^M \gamma_i, \quad i = 1, 2, \dots, M. \quad (12)$$

Intuitively, MRC can be applied to any diversity application and provide a great performance improvement at the expense of high implementation complexity and high cost of time and money.

5. NUMERICAL RESULTS

This section presents numerical results to evaluate the BER of the new detector for single branch and multi branches with combining methods when different hop numbers are implemented. A number of 10^5 data symbols are used in the simulation. Fig. 2 shows the BER vs. SNR for different numbers of hops using the new detector based on the logistic distribution compared with the conventional energy detector in Rician fading channel, where the parameter K of Rician fading channel is assumed to be 1. One find that the energy detector based on the three hops numbers all have BER floors. Notably, the BER of energy detector decreases when the hops number increases if the SNR is larger than 20 dB. The reason may be that the Gaussian distribution parameters estimated by the distribution fitting tool is not so accurate when the fading channel is Rician. The new detector makes significant performance improvement. Obviously, when the number of hops increases the BER increases.

To check the effect when assumption does not match reality, Fig. 3 shows the effect when Rayleigh fading channel is used to do distribution fitting but the actual channel is Rician and the received signals are Rician signals. One sees that the BER curves of the non-matched new detector based on Rayleigh channel parameters but using Rician samples are higher than the matched new detector. The non-matched BER performance will degradate even worse when the number of hops and SNR increase. One should also note that, compared with Fig. 2, the novel detector still have better performance than energy detector even when the channel condition is non-matched.

Figure 4 shows the comparison of the BER using different combining methods with different number of hops and the original BER of single branch and single hop. One sees that, to achieve the same performance of the original BER more than two branches with two hops should be combined when SC combining method is implemented, while more than one branch is needed when MRC is implemented. Based on the same transmission condition, the MRC method outperforms the SC method. And the more the number of branches is combined, the better the BER performance will be. This indicates the advantage of the implementation of diversity combining methods in the multi-hop multi-branch cooperative systems.

Figure 5 compares the conventional energy detection on single branch with the new detector based on logistic distribution using MRC methods with different branches when the source signal is transmitted by 5 AF relaying hops. One sees that, all the MRC combining curves based on the new detector outperforms the conventional energy detector. And the BER of the new detector can further decrease when the branche number increases and the MRC method is applied.

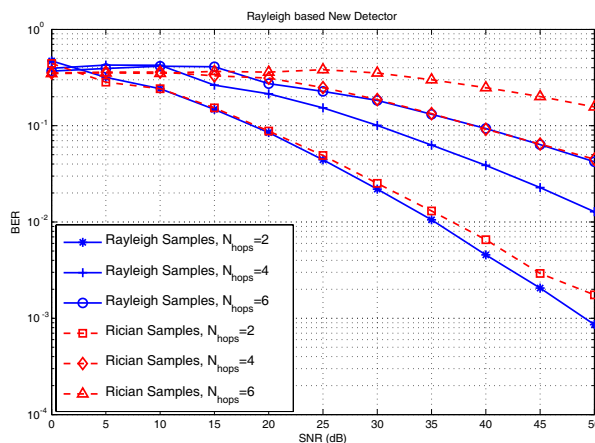


Figure 3: Assumption not matching reality.

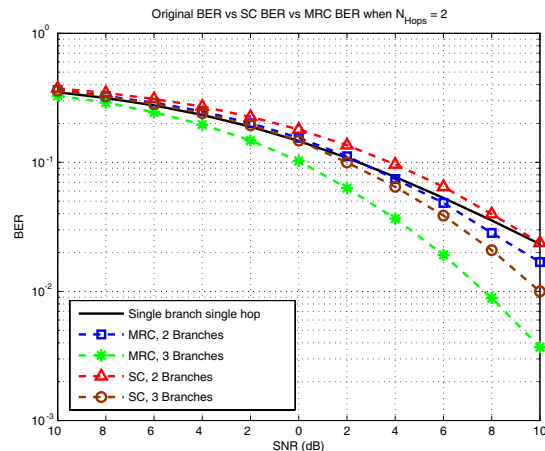


Figure 4: Different combining methods.

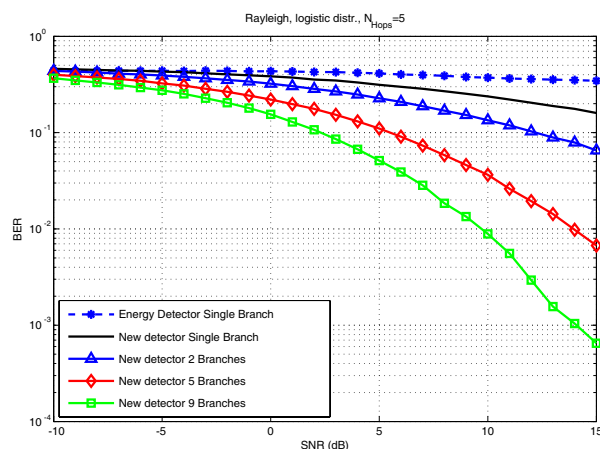


Figure 5: Different branch numbers with 5 hops.

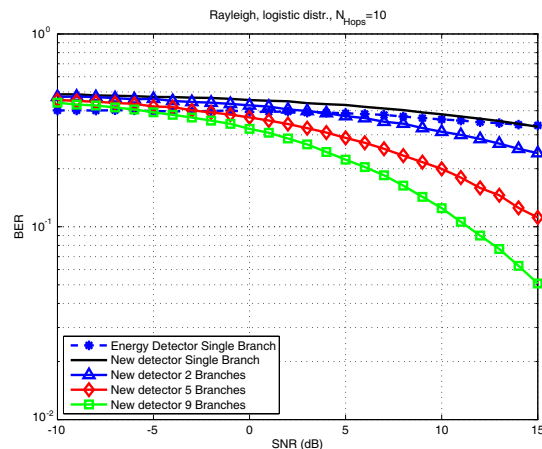


Figure 6: Different branch numbers with 10 hops.

Figure 6 shows the different results from Fig. 5 when the number of hops is changed into 10. Comparing with Fig. 5 one sees that, the performance of new detector combining different numbers of branches all degrades when the number of hops increases, while the performance of energy detection almost does not change. Notably, as the number of hops increases the new detector with single branch does not outperform the energy detector. This indicates the importance of the diversity combining in multi-branch systems. One observes that more branches can provide higher performance. However, the increasing number of branches is at the expense of the increasing complexity and cost. Thus, there is a trade off between performance and the cost of complexity and money.

6. CONCLUSIONS

In multi-hop AF relaying channel, the actual distribution of the received signals is not Gaussian any more, while the Gaussian distribution is always assumed to be the distribution in conventional researches. In this paper, novel detector using ML principle for the multi-hop AF multi-branch cooperative diversity system has been proposed based on the new fitted logistic distribution of received signals. Numerical results have shown that the new detector outperforms the conventional energy detector when the number of hops is low especially when use combining methods to combine multi branches. To investigate the case when the channel assumption does not match reality, the effect when Rayleigh fading channel is used to do distribution fitting but the actual channel is Rician and the received signals are Rician signals has been shown to indicate that the new detector can even outperform the conventional energy detector. The performance gain increases when the SNR increases or when the branch number increases and the hop number decreases.

REFERENCES

1. Rappaport, T. S., *Wireless Communications: Principles and Practice*, 2nd Edition, Pearson Education, Inc., India, 2002.
2. Ribeiro, A., X. Cai, and G. B. Giannakis, "Symbol error probabilities for general cooperative links," *IEEE Trans. Wireless Commun.*, Vol. 4, No. 3, 1264–1273, May 2005.
3. Laneman, J. N., D. N. C. Tse, and G. W. Wornell, "Cooperative diversity in wireless networks: Efficient protocols and outage behavior," *IEEE Trans. Information Theory*, Vol. 50, No. 12, 3062–3080, Dec. 2004.
4. Farhadi, G. and N. C. Beaulieu, "Capacity of amplify-and-forward multi-hop relaying under adaptive transmission," *IEEE Trans. Commun.*, Vol. 58, No. 3, 758–763, Mar. 2010.
5. Zhao, Y., R. Adve, and T. J. Lim, "Symbol error rate of selection amplify-and-forward relay systems," *IEEE Commun. Lett.*, Vol. 10, No. 11, 757–759, Nov. 2006.
6. Farhadi, G. and N. C. Beaulieu, "On the performance of amplify-and-forward cooperative links with fixed gain relays," *IEEE Trans. Wireless Commun.*, Vol. 7, No. 5, 1851–1856, May 2008.
7. Yu, M. and J. Li, "Is amplify-and-forward practical better than decode-and-forward or vice versa," *Proc. IEEE Int. Conf. Acoustics, Speech, and Signal Processing (ICASSP)*, Vol. 3, 365–368, Mar. 2005.

8. Souryal, M. R. and B. R. Vojcic, “Performance of amplify-and-forward and decode-and-forward relaying in rayleigh fading with turbo codes,” *Proc. ICASSP 2006*, Vol. 4, 681–684, 2006.
9. Farhadi, G. and N. C. Beaulieu, “Fixed relaying versus selective relaying in multi-hop diversity transmission systems,” *IEEE Trans. Commun.*, Vol. 58, No. 3, 956–965, Mar. 2010.
10. Chen, D. and J. N. Laneman, “Noncoherent demodulation for cooperative diversity in wireless systems,” *Proc. IEEE Global Comm. Conf.*, Vol. 53, 31–35, Dallas, TX, Nov. 2004.
11. Chen, Y., “Analytical performance of collaborative spectrum sensing using censored energy detection,” *IEEE Trans. Commun.*, Vol. 7, No. 4, 1326–1337, Apr. 2008.
12. Visser, F. E., G. J. M. Janssen, and P. Pawelczak, “Multinode spectrum sensing based on energy detection for dynamic spectrum access,” *Proc. IEEE Veh. Technol. Conf.*, 1394–1398, Singapore, 2008.
13. Kay, S. M., *Fundamentals of Statistical Signal Processing: Detection Theory*, Prentice-Hall, Upper Saddle River, NJ, 1993.
14. Lu, H., Y. Chen, and N. Cao, “Accurate approximation to the PDF of the product of independent Rayleigh random variables,” *IEEE Antennas Woreless Propag. Lett.*, Vol. 10, 1019–1022, Oct. 2011.

A New Design of High-speed Decimal Direct Digital Frequency Synthesizer

Guochun Wan, Gui Zhu Yin, Jie Zhang, and Mei Song Tong

Department of Electronic Science and Technology
Tongji University, 4800 Cao'an Road, Shanghai 201804, China

Abstract— The conventional direct digital frequency synthesizer (DDS) adopts a binary algorithm which limits the output frequency resolution in some applications and cannot switch frequency and phase quickly. To solve the problem, high-speed decimal DDS was proposed to improve the conventional DDS algorithm by using decimal and binary mixed algorithm and pipelined segments accumulator to realize the phase accumulation. In addition, the look-up-table (LUT) method is also adopted to achieve fast waveform output and it has shown high-speed and high-resolution performances. The new DDS is designed with VHDL language and its timing simulation results is also presented.

1. INTRODUCTION

Direct digital synthesizer (DDS) has been widely used in wireless communications due to its convenience and high frequency resolution. Although the resolution of the current design has been high, the binary operation phase accumulation restricts the minimum resolution of the DDS which is only 2^{-M} , where M is the number of accumulator bits, and this cannot meet a special output frequency requirement. In some applications, for example, in the terminal of very long baseline interferometry (VLBI) technology, more precise frequency signal is needed to adjust the received microwave signal. To satisfy this demand, the mixture of decimal and binary operation is used to enhance the DDS minimum frequency resolution to $2^{-M} \times 10^{-N}$, where M is the number of binary bits and N is the number of decimal bits.

The conventional DDS adopts a binary algorithm which limits the output frequency resolution in some cases and cannot switch the frequency and phase quickly. To solve this problem, the high-speed decimal DDS was proposed to replace the conventional DDS algorithm by using the mixture of decimal and binary algorithms and pipelined segment accumulator to realize the phase accumulation. It also uses a look-up table (LUT) to achieve a fast waveform output so that a high-speed and high-resolution performance can be achieved. We implement the new DDS design with VHDL language and its good performance has been demonstrated by simulations.

2. MAIN STRUCTURE OF DDS

. THE OVERALL STRUCTURE OF DDS

The basic block diagram of the DDS is shown in Figure 1. It consists of phase accumulator, waveform memory, D/A converter (DAC), and low pass filter (LPF). Here, the first three parts constitute a NC frequency synthesizer. Phase accumulator is the core part of DDS, and it begins to accumulate based on the phase offset and uses the frequency control word as a step. Once the output of accumulator overflows, it completes a cycle. Here the frequency control word and phase offset are set as the DDS input. The accumulator output in one cycle represents the phase of sinusoidal signal. Firstly, we divide the sinusoidal signal into M parts and store them in a ROM after quantification. Secondly, we use the look-up-table (LUT) method for the phase accumulator output data to output a corresponding amplitude data, and then obtain the corresponding step waveform through D/A converter. Finally, we use a low-pass filter to smoothen the step waveform and output a continuous sine wave.

The expression of sinusoidal signal is given by the following equation:

$$S_{out} = A \sin(w \cdot t) = A \sin(2\pi \cdot f_{out} \cdot t) \quad (1)$$

When expressing this Equation in digital logic, we have to transform it into a discrete time of one CLK cycle and $\Delta\theta$ represents the increased angle value.

$$\Delta\theta = 2\pi \cdot f_{out} \cdot T_{CLK} = \frac{2\pi \cdot f_{out}}{F_{CLK}} \quad (2)$$

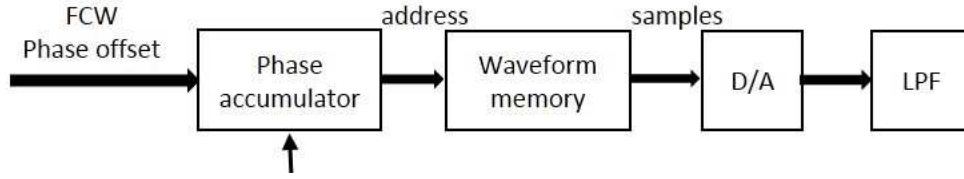


Figure 1: The basic block diagram of DDS.

To quantify the value of $\Delta\theta$, we divide 2π into $2^M \times 10^N$ parts and then express the phase increment in each CLK cycle in terms of $\beta_{\Delta\theta}$:

$$\beta_{\Delta\theta} = \frac{\Delta\theta}{2\pi} \times 2^M \times 10^N \tag{3}$$

Hence, the equation of sinusoidal signal in digital will be shown in the following equation in which θ_{K-1} represents the previous phase value:

$$S_{out} = A \sin(\theta_{K-1} + \Delta\theta) = A \sin \left[\frac{1}{2\pi \times 2^M \times 10^N} (\beta_{\theta_{K-1}} + \beta_{\Delta\theta}) \right] \tag{4}$$

Finally, we can get a conclusion based on Equation (1) to Equation (4), i.e., the phase increment $\beta_{\Delta\theta}$ (it is also called FCW) determines the signal output frequency. According to Equation (2) and Equation (3), the output frequency can be written as [1]:

$$f_{out} = \frac{K}{2^M \times 10^N} \cdot F_{CLK} \tag{5}$$

. THE MIXED PHASE ACCUMULATOR

In DDS circuit, phase accumulator is a crucial part to determine the performance of DDS. Considering the internal structure of FPGA, we design a phase accumulator which not only meets the requirement of frequency resolution but also improves the system speed. Its structure is showed in

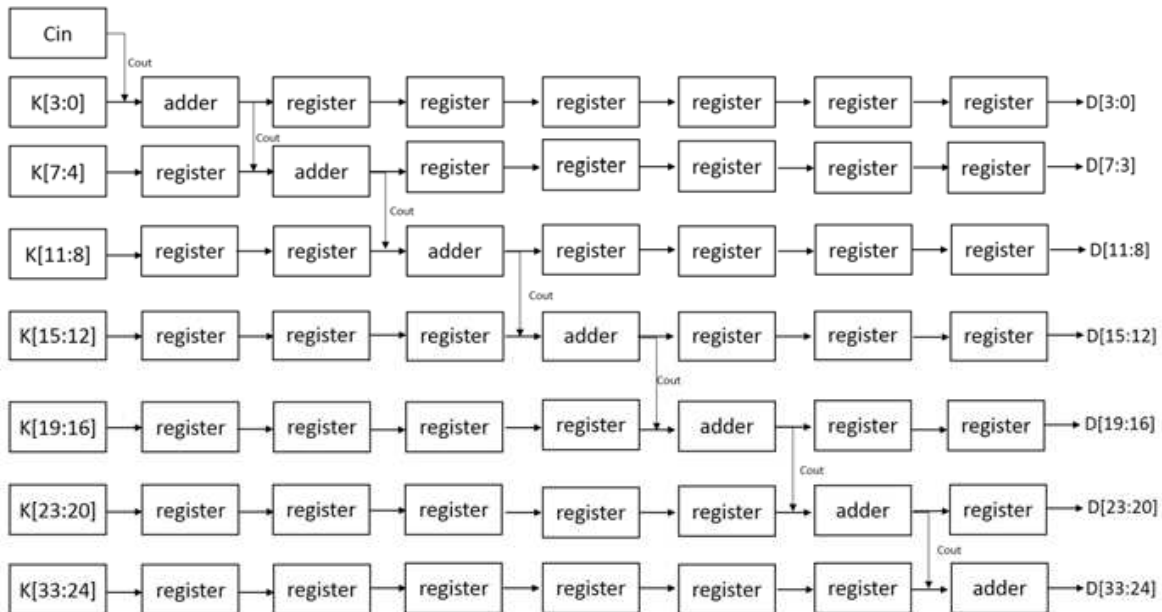


Figure 2: The structure of pipelined segment accumulator.

Figure 2. Here we design a 34-bits accumulator in which 10 bits are used for binary accumulation and 24 bits are used for decimal accumulation. The 24 bits are divided into 6 parts, and each part has 4 bits for transforming BCD-code operation. A pipelined-segments-accumulation algorithm is applied because if we use a very wide bits adder to constitute the accumulator directly. The adder delay will limit the accumulator's operating speed greatly [2]. Segment accumulator makes each part add their relevant bits in one stage, and then transmit the carry bit to next stage for further accumulation. Since each part operates in one stage and at the same time, the total delay just exists between the stages, the system speed will be improved greatly [3].

. PHASE TO AMPLITUDE CONVERSION

Phase-to-amplitude conversion is another important part of DDS circuit. In this system, we use the ROM look-up table to achieve the conversion. We divide the 2π section into several parts and quantify them by using phase accumulator outputs as addresses to look up their corresponding amplitude and finally output the amplitude. Due to the symmetry of sine wave, it is oddly symmetric in the sections of $[0 : \pi]$ and $[\pi : 2\pi]$ while it is evenly symmetric in the sections of $[0 : 0.5\pi]$, $[0.5\pi : \pi]$, $[\pi : 1.5\pi]$, and $[1.5\pi : 2\pi]$. Therefore, we can use one-fourth cycle of sine wave to get the whole cycle amplitude. We take the highest bit of phase accumulator outputs (MSB) to judge the positive or negative signal and use the second highest bit (MSB-1) to judge whether its address is reversed or not. The remaining bits are initial addresses which we use the phase to represent.

As shown in Figure 3, when MSB-1 is 0, meaning that the point is in two or four, the effective address is equal to phase. However, when MSB-1 is 1, which means that the point is in one or three, the effective address is $2^{\text{MSB}-1}$ -phase. When MSB is 0, it means that the amplitude is positive and the other is negative.

MSB	MSB-1	quadrant	Positive /negative	Address direction
0	0	One	+	normal
0	1	two	+	reverse
1	0	three	-	normal
1	1	four	-	reverse

Figure 3: Phase-to-amplitude conversion.

3. DESIGN EXAMPLE AND SIMULATION RESULTS

We design a DDS whose system clock (F_{CLK}) is 512 MHz and output value is 14 bits. We use 34-bits phase accumulator to ensure that the frequency resolution is sufficient and phase accumulator is of a 7-stage pipeline structure. The first part uses 10 bits to accumulate and the remaining 6 parts use 4 bits for each (BCD code) to accumulate. The phase-to-amplitude conversion is 14 bits and the last 20 bits of phase accumulator output are cut down. We set the input data $\text{pinc} = \text{"0000110000"} \&X \text{"000000"}$ and $\text{poff} = \text{"0011000000"} \&X \text{"111111"}$, then its ISim simulation result is shown in Figure 4. Here, pinc is the frequency control word (FCW) and poff means the phase offset.

The output sine waveform in time domain is shown in Figure 5(a) and Figure 5(b) illustrates the output phase continuity. Figure 6(a) and Figure 6(b) depict the simulation output in frequency domain after an FFT transformation and the abscissa of the pulse in Figure 6(a) is the desired design frequency. We enlarge the figure in Figure 6(b) to have a clear view and it can be seen that the output value is 24 MHz. To verify the correctness of the simulation, we set $\text{pinc} = \text{"0000110000"} \&X \text{"000000"}$, which is 48×10^6 in decimal system based on Equation (5).

$$f_{\text{out}} = \frac{48 \times 10^6}{2^{10} \times 10^6} \times 512 \text{ MHz} = 24 \text{ MHz} \quad (6)$$

This result is mapped with Figure 6(b), demonstrating that this design is successful.

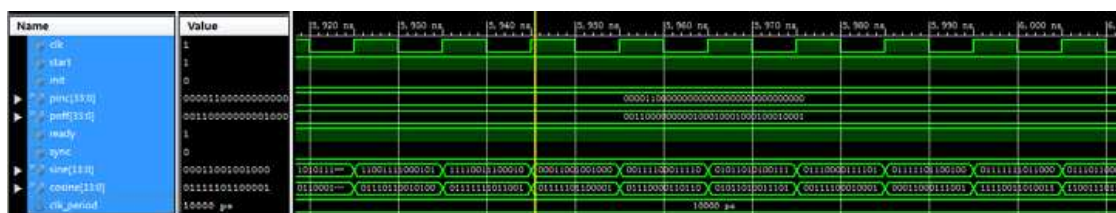


Figure 4: ISim simulation result.

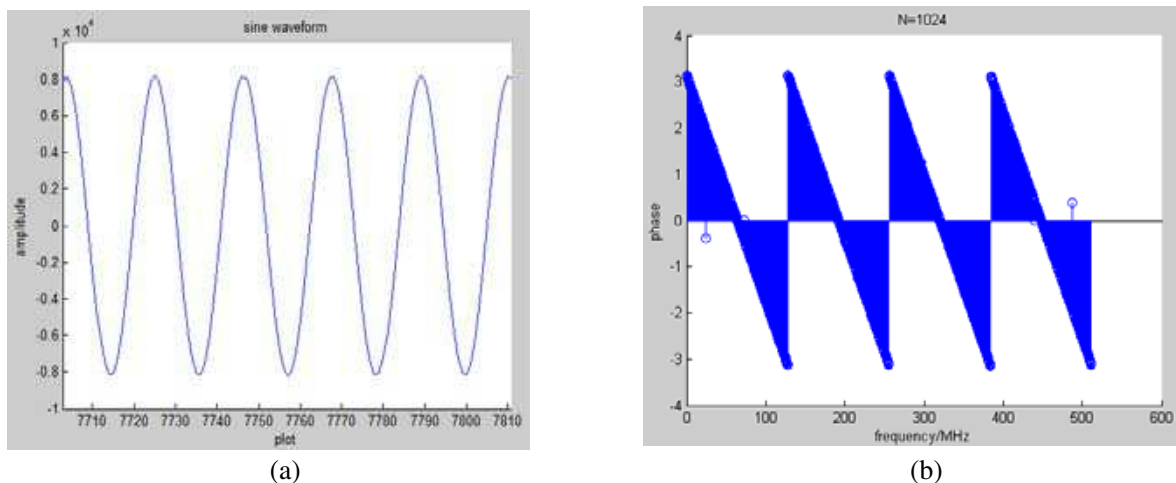


Figure 5: Output sine waveform and phase spectrum.

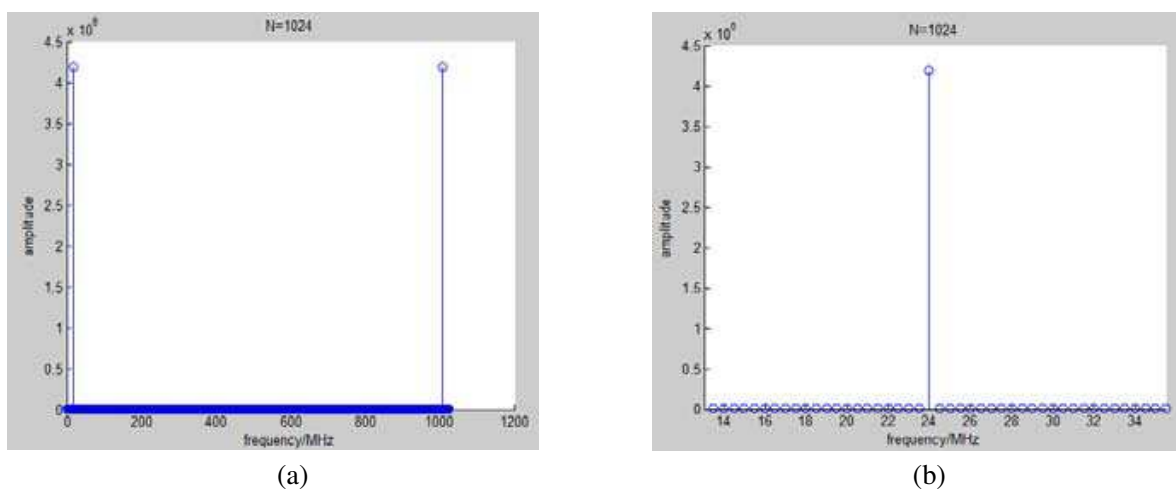


Figure 6: Output sine frequency spectrum.

4. CONCLUSION

This paper introduces a mixed phase accumulator algorithm to meet frequency resolution and a pipelined-segments accumulation algorithm to improve the system's operating speed. Also, the simulation result is given to verify the realization of the idea. In the practical design, more details will be modified but the essential part will keep the same as in this paper.

REFERENCES

1. Liu, C. and S.-Z. Wang, "Design of DDS and implementation with FPGA," *Microelectronics and Computer*, Vol. 21, No. 5, 63–65, 2004.
2. Liu, W. and J. Lin, "DDS waveform generator implemented with microcontroller and FPGA," *Foreign Electronic Measurement Technology*, Vol. 26, No. 12, 26–29, 2007.
3. Wu, Y. J., "Several key design and implementation with IP core in china VLBI data acquisition system," *Technical Report*, Shanghai Astronomical Observatory, 2009.

Coverage Impact for Data Traffic Profiling in WCDMA Networks

Karolis Žvinys, Darius Guršnys, and Evaldas Stankevičius

Department of Telecommunication Engineering
Vilnius Gediminas Technical University, Lithuania

Abstract— Nowadays UTRAN is a key data carrier in mobile communications. Serving a majority of customers and processing an enormous traffic quantity it must ensure a sufficient quality of service (QoS) level. QoS reflects how satisfied the users are with the received services. The goal of this research is to ascertain a benefit of QoS for differently profiled UEs. This study investigates HSPA service dependence on uneven radio network conditions for separate users. Users belong to background traffic class and use a data service as other conventional network users. To draw an impact of radio conditions variation, radio signal strength was decreased gradually for a user with a higher priority. The research is performed on heavily loaded commercial network WCDMA cells. The performance of the user experience is analyzed by the metrics — data rate and channel quality, which are provided graphically and reflect the user received gain based on radio environment changes. Customers' prioritization drawbacks in cellular networks are introduced in study also.

1. INTRODUCTION

With rapid development of mobile networks, operators need to continuously ensure the high quality services. Quality of service is a comprehensive reflection of the service capability of a WCDMA system [1,2]. The goal of study is to discover an impact for user received data services with individual QoS based on uneven network conditions. Therefore study investigates three differently profiled customers which belong to background 3G traffic class [3]. Main focus is paid for evaluation of customers achieved uplink and downlink throughput regarding to variable signal strength. Data rate measurements are carried out in a commercial mobile network. On this study user profile QoS management over core and UTRAN networks has been applied only. It means that QoS profiling over Iub/Iur links was not involved into consideration. Further investigation process consists of analysis of related works on Section 2. Section 3 provides a determination of user profiles and NodeB selection. The rest part of research presents the obtained results and conclusions on Sections 4, 5 and 6.

2. RELATED WORKS

To ensure the end-to-end QoS for each class a bearer service with explicit attributes must be set up. Only when the appropriate core, UTRAN and transport network QoS parameters are determined, a reasonable quality of services can be ensured respectively. Main characteristics of expected QoS are jitter, delay, throughput and signal strength [5]. Usually mean throughput demonstrates an influence for prioritized service of separate traffic class. Many of researches are conducted about non real time services quality assurance in mobile networks. The achievements of better performance and user's satisfaction are obtained by improving resource sharing and utilization [6]. Different QoS management algorithms are implemented in networks for priority based service efficiency improvement [4]. Proposed models comprise sophisticated quality management techniques related to packet scheduling, power allocation and network coordination [7]. Latter management strategy covers multi-domain QoS control between UMTS and WLAN networks. This becomes a relevant topic for majority of Telco, because an increasing data flow force them to introduce small cells and hotspots to carry user plane data with an appropriate QoS [8]. Certainly the investigation of QoS dependence on dynamic radio conditions is relevant.

3. USER PROFILE AND NODEB SELECTION

The QoS is defined during subscription and when a user sends a service request, the CN negotiates with the 3G network in order to provide proper QoS. For ensuring required QoS allocation/retention priority (ARP) and scheduling priority indicator (SPI) parameters are used. Combining the values of these two parameters and setting up other required information users can be classified into three different categories: gold, silver and copper. The priorities of these user categories are organized as follows: gold user has higher priority than silver user twice and the silver is also twice better

than copper. This study examines differently profiled customers which use FTP UL/DL services belonging to background traffic class. This class is not very sensitive for delay, but high values of data rate are preferred. The scenario of data collection involves only heavy loaded cells. Analyzed priority users camp on the same cell as other conventional network users and use the services at the same time. Daily load statistics of a typical NodeB which was used in the research are shown in the graphs.

Figure 1 shows the number of served UEs per day. It is observed that the NodeB serve the number of users between 4000–5000 each day. The dotted line indicates the average number of UEs camped on base station for each 15 minutes period over twenty-four hours. Accordingly Figure 2 demonstrates transferred traffic volume of uplink and downlink data which is close to 40 GB for DL and 8 GB for UL. Such a WCDMA base station is held as a heavy loaded and this requires of resources to be scheduled differently for camped UEs. In many cases NodeB's operate with several or more carriers per cell in order to be able to handle the incoming traffic.

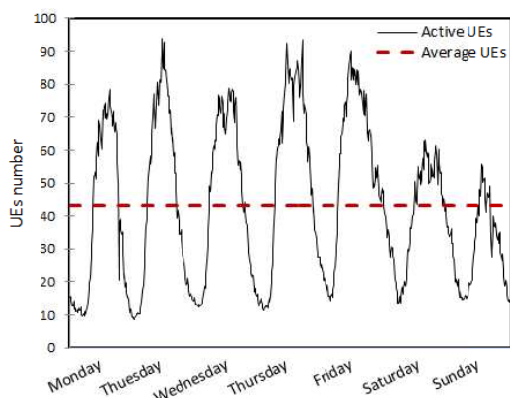


Figure 1: Number of active packet switch UEs per NodeB.

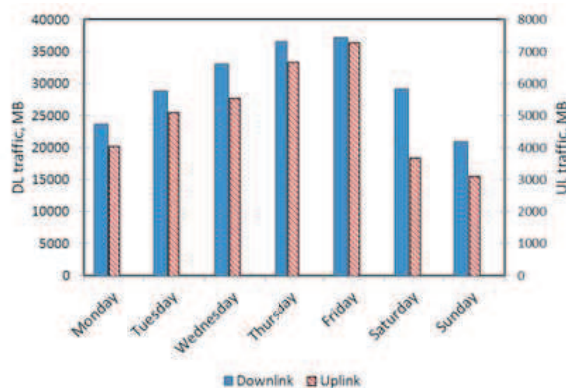


Figure 2: Daily traffic volume of uplink and downlink in heavy loaded NodeB.

4. HSDPA USERS PROFILING

The basic results obtained over the research are provided in this section. First we will discuss the data related with HSDPA QoS profiling. Results presented below cover differently profiled users experience based on received data rate when radio signal is uneven. To draw an impact of radio conditions variation, a radio signal strength changes for a user with a higher priority gradually.

In Figure 3(a) it is seen that UE with higher priority achieves better DL rate when radio signal is more less equal. Scheduled transmission time is frequent compared with copper user. The difference amongst attained throughput is close to double. However when a channel quality begins to deteriorate and the signal strength starts to fade the NodeB scheduling algorithm reassess the scheduling of resources for next TTI. In this way a resources are reallocated to UEs that are able to take advantage of them. This means that channel quality evaluation is an important part of ensuring best QoS. Figure 3(b) shows the user obtained throughput rate when CQI decreases. Despite the superior priority of gold user the received service quality is getting worse depending on RSCP. The same trend is observed when gold versus silver or silver versus copper users are investigated.

What can be highlighted is that the gap of throughput between the G vs S or S vs C users is lower compared to G vs C. This is due to combination of ARP and SPI parameters which weight is significant when radio signal fluctuates approximately at the same level. Otherwise the data rate is mostly dependent on CQI value and reallocation of scheduling. This is also confirmed by the fact that data rate of UE with a poor radio signal remains low even when other UE stops downloading. Consequently a higher priority against the other consumers does not guarantee better quality services in any case.

5. HSUPA USERS PROFILING

In the uplink a pure time division scheduling does not provide a comparable benefit as in downlink. It is limited by the power of UE which means that full uplink channel capacity can't be utilized

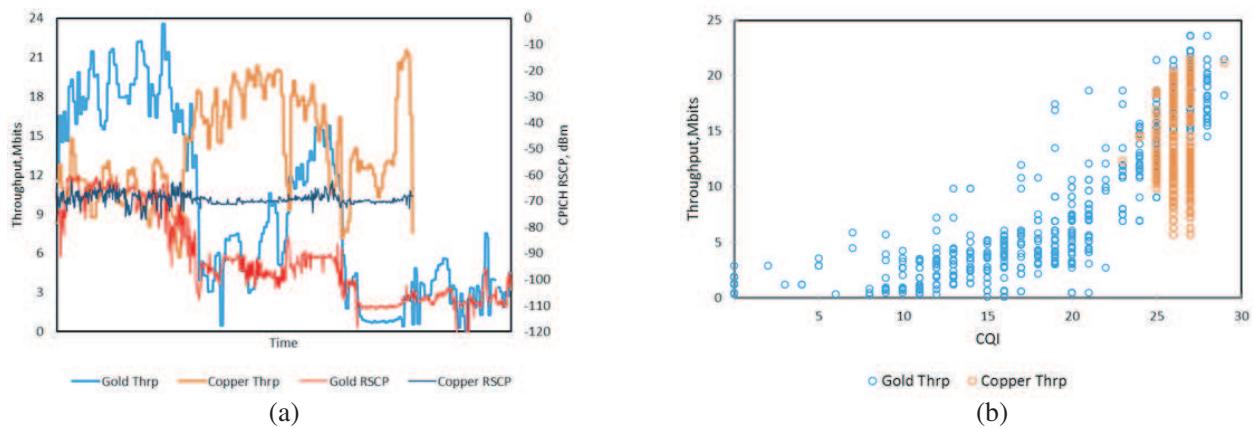


Figure 3: (a) Gold versus Copper user HSDPA throughput related to radio signal changes. (b) CQI corresponding throughput distribution.

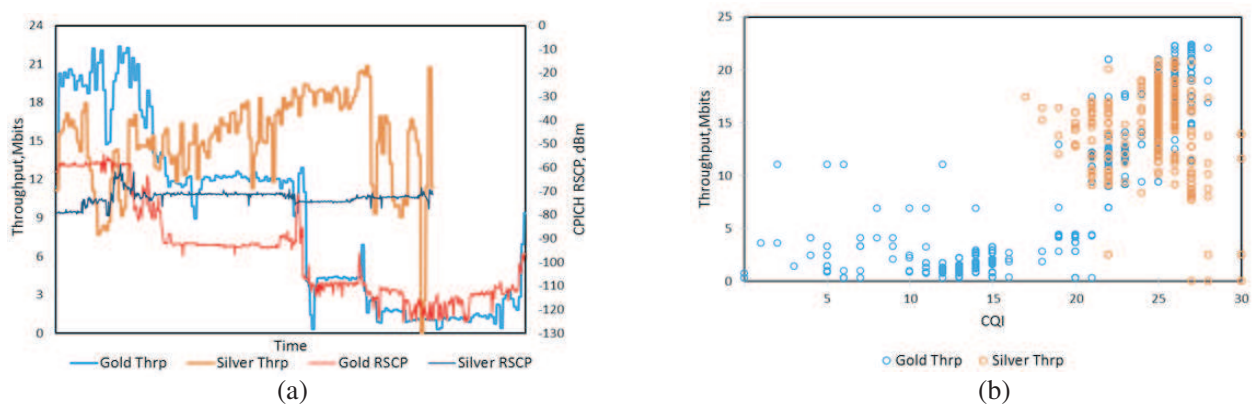


Figure 4: (a) Gold versus Silver user HSDPA throughput related to radio signal changes. (b) CQI corresponding throughput distribution.

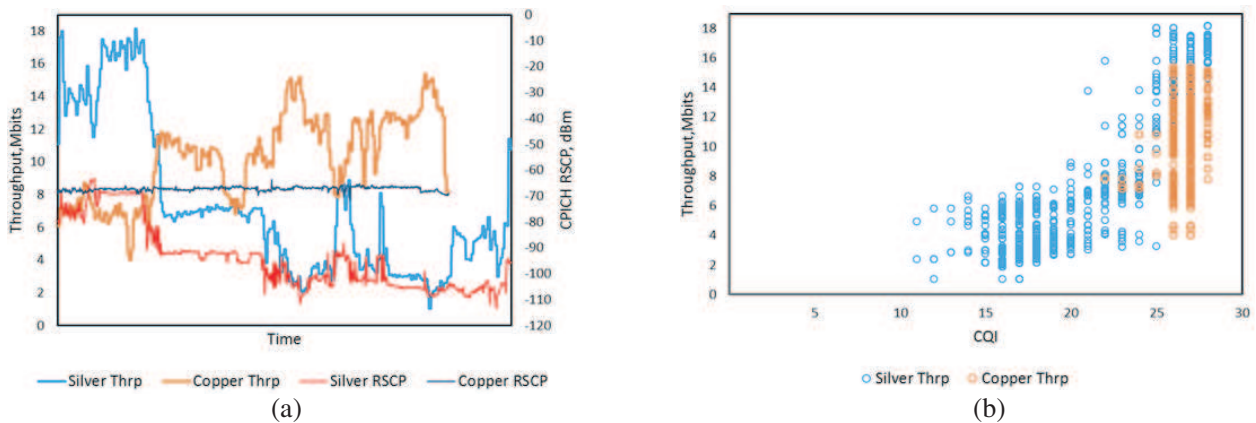


Figure 5: (a) Silver versus Copper user HSDPA throughput related to radio signal changes. (b) CQI corresponding throughput distribution.

efficiently by single transmitting UE. The obtained results of HSUPA performance over this research confirmed a limited availability to serve prioritized services on uplink channel. It can be seen from the graphs below.

Charts named as (a) contain the results of data throughput related to signal strength for uplink transmitting UE. Practically it does not matter which pair of profiled UE's would be compared. Because as it can be seen data rate is more less equal mutually and a given profile is irrelevant. Nevertheless when the RSCP decreases to the bound of -90 dBm of one the UE, data rate diminishes

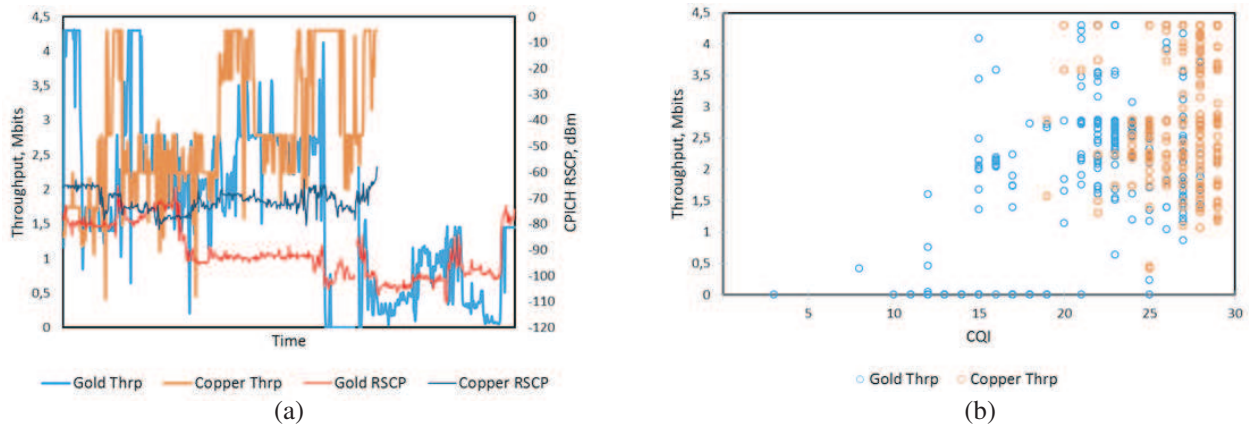


Figure 6: (a) Gold versus Copper user HSUPA throughput related to radio signal changes. (b) CQI corresponding throughput distribution.

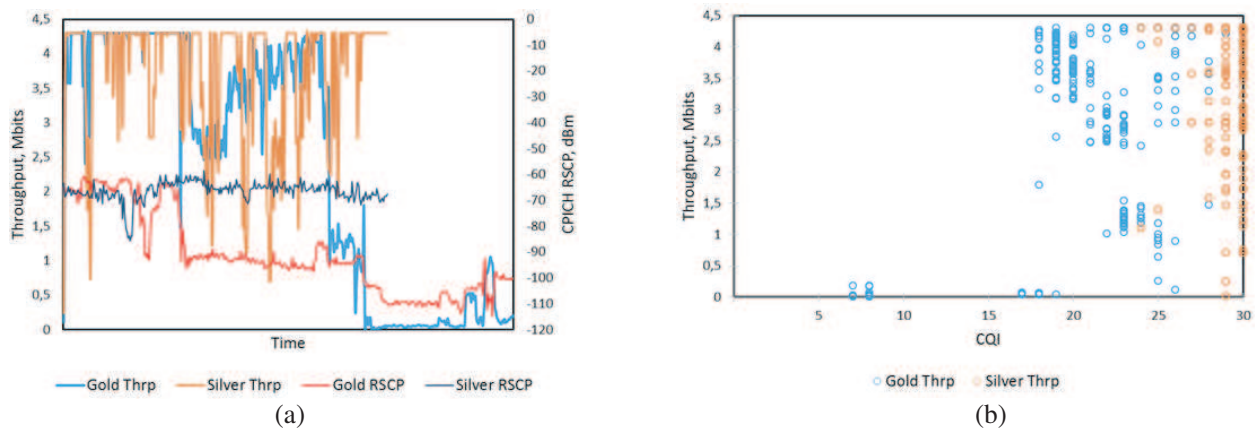


Figure 7: (a) Gold versus Silver user HSUPA throughput related to radio signal changes. (b) CQI corresponding throughput distribution.

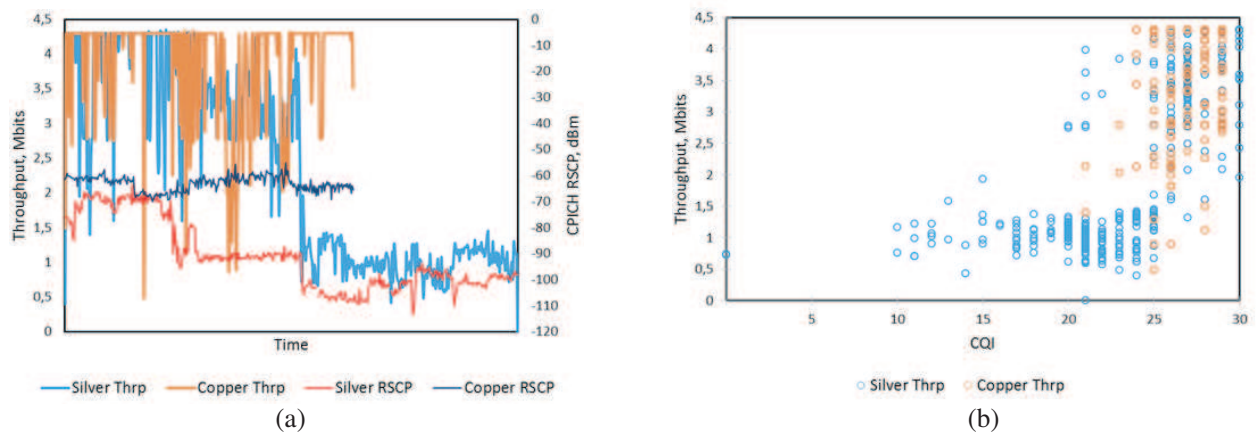


Figure 8: (a) Silver versus Copper user HSUPA throughput related to radio signal changes. (b) CQI corresponding throughput distribution.

suddenly. This is mainly dependent on the change of the channel coding and its quality. Very low data rate measurements can be noted in the CQI charts.

The fact of minor importance of higher priority in uplink transfer was also verified under the identical radio conditions for both UE's. Collected results are provided below in the graphs.

Provided charts represent S vs C UE's data rates distributions when radio environment is same for both handsets. As it can be seen from the results no gain for a highly prioritized UE is determined. This trend is common for both poor and good radio environments. Also it does not

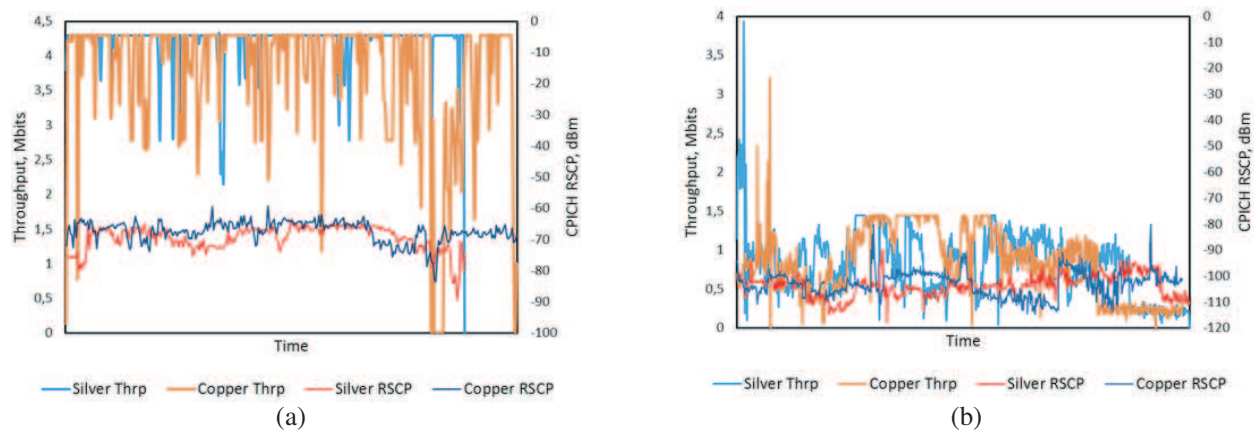


Figure 9: (a) Silver versus Copper user HSUPA throughput at good radio signal for both. (b) Silver versus Copper user HSUPA throughput at poor radio signal for both.

matter which pair would be under investigation.

6. CONCLUSIONS

The basis of UTRAN QoS management allows to ensure the QoS for each user and to provide DiffServ for different users, thereby meeting the requirements of more users. Prioritization grants a higher user quality of experience and gives the ability to control data users in WCDMA networks. This research revealed the benefit gained from a given priority. HSDPA gold user can enjoy a better data rate instead of silver or copper users, but this is valid until the radio signal strength is mutually equal and strong. Otherwise the results showed that the decreasing pilot signal strength affects data rate and it becomes mostly dependent on channel quality. In this case the given priority loses a sense and the available channel resources are allocated to the UE which is able to use them. On uplink channel data transfer prioritization is not very efficient way, because of limited UE power. Obtained results demonstrate that the users sending data to the base station are more or less equal despite their priority. Only when RSCP decreases to weak level HSUPA throughput becomes very low. Consequently QoS management is an efficient way to provide superior level services, but certainly it will not be possible for all cases.

REFERENCES

1. Soldani, D., M. Li, and R. Cuny, *QoS and QoE Management in UMTS Cellular Systems*, John Wiley & Sons, Ltd., 2006, ISBN: 0-470-01639-6.
2. Li, S. and C. Tsao, "QoS issues in GPRS/UMTS networks," Computer & Communications Research Laboratories, Industrial Technology Research Institute, Hsinchu, Taiwan, Online Available: <http://kom.aau.dk/group/04gr995/Share/3GQoS.pdf>, Dec. 28, 2014.
3. "Quality of Service (QoS) concept and architecture," 3GPP TS 23.107, V12.0.0 (2014-09), Online Available: http://www.3gpp.org/ftp/specs/archive/23_series/23.107/, Jan. 4, 2015.
4. Balasubramanian, D., "QoS in cellular networks," Washington University, Online Available: http://www.cs.wustl.edu/jain/cse574-06/ftp/cellular_qos/index.html, Jan. 14, 2015.
5. Thethi, A. S. and R. S. Sawhney, "Performance evaluation of QoS parameters in UMTS network using qualnet," *International Journal of Distributed and Parallel Systems (IJDPs)*, Vol. 1, No. 2, 57–66, Nov. 2010.
6. Leong, C. W., W. Zhuang, Y. Cheng, and L. Wang, "Optimal resource allocation and adaptive call admission control for voice/data integrated cellular networks," *IEEE Transactions on Vehicular Technology*, Vol. 55, No. 2, Mar. 2006, ISSN: 0018-9545.
7. Gómez, G., J. P. González, M. C. Aguayo-Torres, J. F. Paris, and J. T. Entrambasaguas, "QoS modeling for performance evaluation over evolved 3G networks," *Q2SWinet'07 Proceedings of the 3rd ACM Workshop on QoS and Security for Wireless and Mobile Networks*, New York, 2007.
8. Ericsson Mobility Report, "On the pulse of the networked society," 2014, Online Available: <http://www.ericsson.com/mobility-report>, Jan. 25, 2015.

A Nyström-based Approach for Solving Time-domain Magnetic Field Integral Equation

W. J. Chen, G. C. Wan, J. Zhang, and M. S. Tong

Department of Electronic Science and Technology
Tongji University, 4800 Cao'an Road, Shanghai 201804, China

Abstract— Transient electromagnetic (EM) scattering by conducting objects is formulated by time-domain magnetic field integral equation (TDMFIE). Traditionally, the TDMFIE is solved by combining the method of moments (MoM) in spatial domain and a march-on in time (MOT) scheme in temporal domain. We propose a different scheme in which the Nyström method is used in spatial domain while the MoM with Laguerre function as basis and testing functions is employed in temporal domain. The Nyström method is simple in implementation and does not require a basis or testing function and conforming meshes. The time-domain MoM can naturally enforce the causality and fully eliminate the numerical instability. A numerical example for EM scattering by a conducting cylinder is presented to demonstrate the approach and its merits can be observed.

1. INTRODUCTION

Transient electromagnetic (EM) problems can be formulated by a time-domain integral equation approach. For conducting or homogeneously penetrable objects, the time-domain surface integral equations (TDSIEs) including the time-domain electric field integral equation (TDEFIE), time-domain magnetic field integral equation (TDMFIE), or their combination can be applied. Traditionally, the TDSIEs are solved by combining the method of moments (MoM) in spatial domain and a march-on in time (MOT) scheme in temporal domain [1]. The MoM requires a well-designed basis function like the Rao-Wilton-Glisson (RWG) basis function [2] which needs conforming triangular meshes in geometric discretization and double surface integrations in evaluating matrix elements. The MOT scheme, on the other hand, suffers from a late-time instability problem although some improved versions have been proposed in recent years [3]. The instability and accuracy are still dependent upon the choice of time step [4].

In this work, we propose a different scheme to solve the TDMFIE for transient scattering problems by conducting objects. Compared with the TDEFIE, the TDMFIE is thought of little more difficult to solve due to the nature of its integral kernel. We use the Nyström method [5] to discretize the spatial domain while employ the MoM with Laguerre basis and testing functions to discretize the temporal domain for the TDMFIE [6]. The merits of Nyström method in spatial domain includes the simple mechanism of implementation, removal of basis and testing functions, and allowance of using nonconforming meshes. The Nyström method requires an efficient treatment for singular integrals, but we have developed a robust technique to handle them [7] and it can be applied to the TDSIEs by a minor revision. The time-domain MoM (TDMoM) with Laguerre basis and testing functions may be superior to the MOT because the Laguerre function can naturally enforce the causality and also the Galerkin's testing scheme can fully eliminate the numerical instability with a march-on-in-degree (MOD) procedure [8]. A numerical example for EM scattering by a conducting cylinder is presented to illustrate the scheme and its robustness has been verified.

2. TIME-DOMAIN MAGNETIC FIELD INTEGRAL EQUATION (TDMFIE)

Consider the scattering of transient EM wave by a conducting object with a surface S in free space. The problem can be formulated by the TDMFIE, i.e.,

$$\hat{n} \times [\mathbf{H}^{inc}(\mathbf{r}, t) + \mathbf{H}^{sca}(\mathbf{r}, t)] = \mathbf{J}(\mathbf{r}, t), \quad \mathbf{r} \in S \quad (1)$$

where $\mathbf{H}^{inc}(\mathbf{r}, t)$ and $\mathbf{H}^{sca}(\mathbf{r}, t)$ are the incident magnetic field and scattered magnetic field, respectively, \hat{n} is the unit normal vector at an observation point \mathbf{r} , and $\mathbf{J}(\mathbf{r}, t)$ is the induced electric current density on the object. The scattered magnetic field is related to the vector potential $\mathbf{A}(\mathbf{r}, t)$ by

$$\mathbf{H}^{sca}(\mathbf{r}, t) = \frac{1}{\mu_0} \nabla \times \mathbf{A}(\mathbf{r}, t) \quad (2)$$

and the tangential component of the magnetic field can be written as

$$\hat{n} \times \mathbf{H}^{sca}(\mathbf{r}, t) = \frac{1}{4\pi} \nabla \times \int_S \frac{\mathbf{J}(\mathbf{r}', \tau)}{R} dS' = \frac{1}{2} \mathbf{J}(\mathbf{r}, t) + \hat{n} \times \frac{1}{4\pi} \int_S \nabla \times \frac{\mathbf{J}(\mathbf{r}', \tau)}{R} dS' \quad (3)$$

where the integral with a dash indicates that it is a Cauchy-principal-value (CPV) integral. With the above derivation, the MFIE can be formulated as follows

$$\frac{1}{2} \mathbf{J}(\mathbf{r}, t) - \hat{n} \times \frac{1}{4\pi} \int_S \nabla \times \frac{\mathbf{J}(\mathbf{r}', \tau)}{R} dS' = \hat{n} \times \mathbf{H}^{inc}(\mathbf{r}, t) \quad (4)$$

from which the unknown current density can be solved.

3. NYSTRÖM-BASED APPROACH FOR SOLVING THE TDMFIE

We mesh a conductor surface into N small triangular patches and ΔS_n is the area of the n th patch. We introduce the unknown source vector $\mathbf{e}(\mathbf{r}', t)$ which is related to the unknown current density by

$$\mathbf{J}(\mathbf{r}', t) = \frac{\partial}{\partial t} \mathbf{e}(\mathbf{r}', t) \quad (5)$$

and it can be expanded as

$$\mathbf{e}(\mathbf{r}', t) = \sum_{n=1}^N e_n(t) \mathbf{J}_n(\mathbf{r}'). \quad (6)$$

The unknown current density can then be expanded as

$$\mathbf{J}(\mathbf{r}', t) = \sum_{n=1}^N \mathbf{J}_n(\mathbf{r}') \frac{\partial}{\partial t} e_n(t). \quad (7)$$

If we apply the Nyström method in spatial domain, i.e., the integration over a small triangular patch is replaced with a summation under a quadrature rule provided that the integrand is regular, then we have

$$\begin{aligned} & \frac{1}{2} \frac{\partial}{\partial t} e_m(t) \hat{t}_{mp}^{(l)} \cdot \mathbf{J}_{mp} - \frac{1}{4\pi} \hat{t}_{mp}^{(l)} \cdot \hat{n}_{mp} \times \sum_{n=1}^N \sum_{q=1}^Q w_q \left[\frac{1}{c} \frac{\partial^2 e_n(\tau_{mpnq})}{\partial t^2} \mathbf{J}_{nq} \times \frac{\hat{R}_{mpnq}}{R_{mpnq}} \right. \\ & \left. + \frac{\partial e_n(\tau_{mpnq})}{\partial t} \mathbf{J}_{nq} \times \frac{\hat{R}_{mpnq}}{R_{mpnq}^2} \right] = V_{mp}^{(l)}(t), \quad m = 1, 2, \dots, N; \quad p = 1, 2, \dots, Q \end{aligned} \quad (8)$$

where $\mathbf{J}_{nq} = \mathbf{J}(\mathbf{r}'_{nq}) = J_{nq}^u \hat{u} + J_{nq}^v \hat{v}$ is the value of spatial component of unknown current density at the source point \mathbf{r}'_{nq} or the q th quadrature point in the n th patch and it only has two independent components J_{nq}^u and J_{nq}^v in a local coordinate system $\{u, v, w\}$ established over the patch plane because it is a surface current density. Also, $\mathbf{J}_{mp} = \mathbf{J}(\mathbf{r}_{mp}) = J_{mp}^u \hat{u} + J_{mp}^v \hat{v}$ has an analogous meaning but for the observation point \mathbf{r}_{mp} located at the p th quadrature point in the m th patch. These spatial components of current densities should be transformed into the components in the global coordinate system $\{x, y, z\}$ in the implementation. We have chosen two orthogonal unit tangential vectors $\hat{t}_{mp}^{(l)} = \hat{t}^{(l)}(\mathbf{r}_{mp}) = t_{mp}^{x(l)} \hat{x} + t_{mp}^{y(l)} \hat{y} + t_{mp}^{z(l)} \hat{z}$ at the observation point ($l = 1, 2$) to test the above equation so that the TDMFIE can be transformed into a matrix equation in space domain. The right-hand side of the equation is given by

$$V_{mp}^{(l)}(t) = \hat{t}_{mp}^{(l)} \cdot \hat{n}_{mp} \times \mathbf{H}^{inc}(\mathbf{r}_{mp}, t) \quad (9)$$

and \hat{n}_{mp} is the unit normal vector at the observation point. The above procedure can only be used for a far interaction between the observation point and a source patch or $m \neq n$ which allows the direct application of a quadrature rule. If the observation point is inside the source patch or $m = n$, we have a singularity problem and we have to employ a singularity treatment technique to handle it [7].

In the temporal domain, we use the Laguerre function $\phi_j(t) = e^{-t/2}L_j(t)$ as a basis function to expand $e_n(t)$ [6], i.e.,

$$e_n(t) = \sum_{j=0}^{\infty} e_{nj}\phi_j(st) \tag{10}$$

where s is the scaling factor to control the support of expansion. Substituting this representation to Eq. (8) and using $\phi_i(st)$ as a testing function to test Eq. (8), we can obtain

$$\begin{aligned} \hat{t}_{mp}^{(l)} \cdot \frac{s}{2} \sum_{j=0}^i \left(\frac{1}{2}e_{mj} + \sum_{k=0}^{j-1} e_{mk} \right) - \sum_{n=1}^N \sum_{q=1}^Q \left\{ \frac{s^2}{c} I_{1nq}^{(l)} \sum_{j=0}^i \left[\frac{1}{4}e_{nj} + \sum_{k=0}^{j-1} (j-k)e_{nk} \right] I_{ij}(sR_{mpnq}/c) \right. \\ \left. + s I_{2nq}^{(l)} \sum_{j=0}^i \left(\frac{1}{2}e_{nj} + \sum_{k=0}^{j-1} e_{nk} \right) I_{ij}(sR_{mpnq}/c) \right\} = V_{mpi}^{(l)}, \quad i = 0, 1, \dots, \infty \end{aligned} \tag{11}$$

where

$$I_{1nq}^{(l)} = \frac{w_q}{4\pi} \hat{t}_{mp}^{(l)} \cdot \hat{n}_{mp} \times \mathbf{J}_{nq} \times \frac{\hat{R}_{mpnq}}{R_{mpnq}} \tag{12}$$

$$I_{2nq}^{(l)} = \frac{I_{1nq}^{(l)}}{R_{mpnq}} \tag{13}$$

$$I_{ij}(sR_{mpnq}/c) = \int_0^\infty \phi_i(st)\phi_j(st - sR_{mpnq}/c) d(st) \tag{14}$$

$$V_{mpi}^{(l)} = \int_0^\infty \phi_i(st)V_{mp}^{(l)}(t) d(st) \tag{15}$$

and $I_{ij}(sR_{mpnq}/c)$ and $V_{mpi}^{(l)}$ can be calculated according to the formulations in the appendix in [6]. Note that there are two spatial-domain coefficients in $I_{1nq}^{(l)}$ and $I_{2nq}^{(l)}$ which are the two independent components J_{nq}^u and J_{nq}^v of \mathbf{J}_{nq} and they should be combined with the time-domain coefficient e_{nj} together to form two new unknown coefficients which can be determined by two groups of Eq. (11) when $l = 1, 2$.

4. NUMERICAL EXAMPLE

We consider the transient EM scattering by a conducting cylinder to demonstrate the approach. The cylinder is centered at the origin of a rectangular coordinate system and it has a cross-section

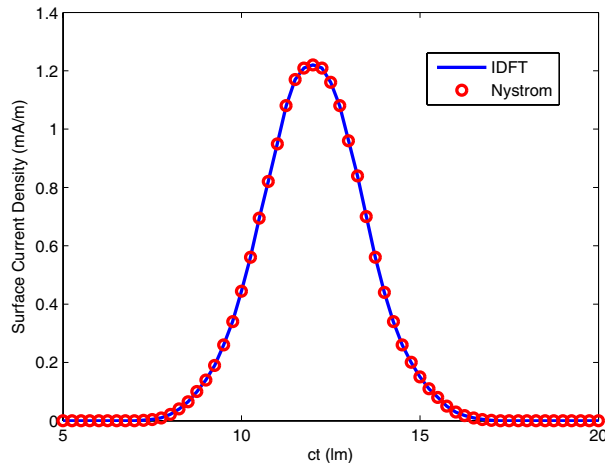


Figure 1: Solution of z -directed current density at $z = 0$ on a cylinder surface for transient scattering by a conducting cylinder.

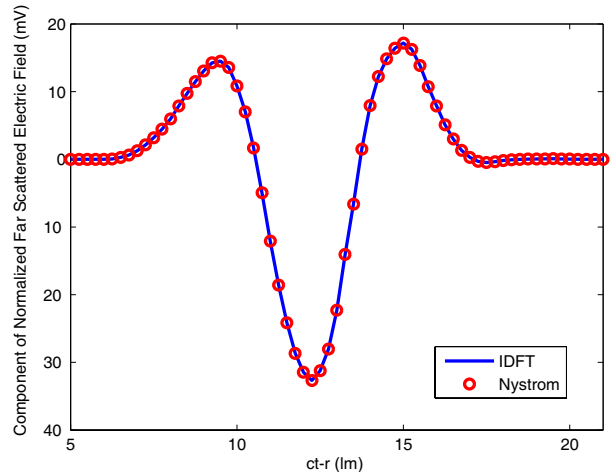


Figure 2: Solution of θ -component of normalized far-zone scattered electric field for transient scattering by a conducting cylinder.

radius $a = 0.5$ m and a height $h = 1.0$ m. The surface of the cylinder is discretized into 826 triangular patches. A Gaussian plane wave is illuminating the scatterer along the $-z$ direction and the electric field and magnetic field are defined by

$$\mathbf{E}^{inc}(\mathbf{r}, t) = \hat{x} \frac{4e^{-\gamma^2}}{\sqrt{\pi}T}, \quad \mathbf{H}^{inc}(\mathbf{r}, t) = -\frac{1}{\eta} \hat{z} \times \mathbf{E}^{inc}(\mathbf{r}', t) \quad (16)$$

where $\gamma = 4(ct - ct_0 + \mathbf{r} \cdot \hat{z})/T$, T is the width of Gaussian impulse, and t_0 is the time delay denoting the time when the pulse peaks at the origin. We choose a Gaussian pulse with $T = 8.0$ lm (light meter) and $ct_0 = 12.0$ lm as an incident wave. Figure 1 shows the solution of z -directed current density at $z = 0$ on the cylinder surface while Figure 2 plots the solution of the θ -component of normalized far-zone scattered electric field observed along the backward direction. The results agree well with the solutions obtained from the inverse discrete Fourier transform (IDFT) of frequency-domain solutions.

5. CONCLUSION

In this work, the transient EM scattering by conducting objects is formulated through the TDM-FIE. We develop a different scheme to solve the TDMFIE by combining the Nyström method in spatial domain and the MoM with the Laguerre basis and testing functions in temporal domain. The benefits of the new scheme include the simple mechanism of implementation with a use of non-conforming and low-quality meshes in spatial domain and the natural satisfaction of causality with a full elimination of instability in temporal domain. A numerical example for EM scattering by a conducting cylinder is presented to demonstrate the scheme and good results have been observed.

ACKNOWLEDGMENT

This work was supported by the National Natural Science Foundation of China with the Project No. 61271097.

REFERENCES

1. Rao, S. M., *Time Domain Electromagnetics*, Academic Press, San Diego, 1999.
2. Rao, S. M., D. R. Wilton, and A. W. Glisson, "Electromagnetic scattering by surfaces of arbitrary shape," *IEEE Trans. Antennas Propagat.*, Vol. 30, No. 3, 409–418, May 1982.
3. Weile, D. S., G. Pisharody, N.-W. Chen, B. Shanker, and E. Michielssen, "A novel scheme for the solution of the time-domain integral equations of electromagnetics" *IEEE Trans. Antennas Propagat.*, Vol. 52, No. 1, 283–294, Jan. 2004.
4. Shi, Y. and J.-M. Jin, "A time-domain volume integral equation and its marching-on-in-degree solution for analysis of dispersive dielectric objects," *IEEE Trans. Antennas Propagat.*, Vol. 59, No. 3, 969–978, Mar. 2011.
5. Canino, L. S., J. J. Ottusch, M. A. Stalzer, J. L. Visher, and S. Wandzura, "Numerical solution of the Helmholtz equation in 2D and 3D using a high-order Nyström discretization," *J. Comput. Phys.*, Vol. 146, 627–663, 1998.
6. Jung, B. H., Y.-S. Chung, and T. K. Sarkar, "Time-domain EFIE, MFIE, and CFIE formulations using Laguerre polynomials as temporal basis functions for the analysis of transient scattering from arbitrary shaped conducting structures," *Progress In Electromagnetics Research*, Vol. 39, 1–45, 2003.
7. Tong, M. S. and W. C. Chew, "A novel approach for evaluating hypersingular and strongly singular surface integrals in electromagnetics," *IEEE Trans. Antennas Propagat.*, Vol. 58, No. 11, 3593–3601, Nov. 2010.
8. Jung, B.-H., Z. Ji, T. K. Sarkar, M. Salazar-Palma, and M. Yuan, "A comparison of marching-on in time method with marching-on in degree method for the TDIE solver," *Progress In Electromagnetics Research*, Vol. 70, 281–296, 2007.

A Hybrid Scheme for Solving Transient Electromagnetic Problems with Conductors

W. J. Chen, G. C. Wan, J. Zhang, and M. S. Tong

Department of Electronic Science and Technology
Tongji University, 4800 Cao'an Road, Shanghai 201804, China

Abstract— Transient electromagnetic (EM) scattering by conducting objects is formulated by time-domain electric field integral equation (TDEFIE). Conventionally, the TDSIE is solved by combining the method of moments (MoM) in spatial domain and a march-on in time (MOT) scheme in temporal domain. We propose a hybrid scheme in which the Nyström method is used in spatial domain while the MoM with Laguerre function as basis and testing functions is employed in temporal domain. A numerical example for EM scattering by a conducting cube is presented to demonstrate the approach and its merits can be observed.

1. INTRODUCTION

Solving transient electromagnetic (EM) problems is essential in many applications such as the design of radar cross section of aircrafts and design of some antennas or microwave circuits. The problems are usually of broadband, nonlinear, and time-varying characteristics and can only be described by time-domain governing equations. Although time-domain differential equations can be used to solve the problems, the time-domain integral equations (TDIEs) may be preferred in many situations due to their unique merits [1]. The TDIEs could be in different forms and they are electric field integral equation (EFIE), magnetic field integral equation (MFIE), and combined field integral equation (CFIE), in a time-domain form, if objects are conducting or homogeneously penetrable.

Those TDIEs are usually solved by combining the method of moments (MoM) in spatial domain and a march-on-in-time (MoT) scheme in temporal domain. The MoM requires a well-designed basis function like the divergence-conforming Rao-Wilton-Glisson (RWG) basis function [2] or curl-conforming edge basis function [3], resulting in an inconvenient implementation. On the other hand, the MoT scheme is conventionally inefficient and inherently unstable due to the low- and high-frequency modes of creeping into the solution [4]. The late-time instability of MoT has not been fully solved albeit many improved versions have been developed in recent years [5].

We propose a novel hybrid scheme to efficiently solve the time-domain EFIE for transient EM problems with conductors. The Nyström method instead of the traditional MoM is used in spatial domain while the MoM instead of the conventional MoT is employed in temporal domain. The benefits of Nyström method in spatial domain include the simple mechanism of implementation, removal of basis and testing functions, and allowance of using nonconforming and low-quality meshes [6]. In time domain, we use the MoM with Laguerre basis and testing functions which was proposed by Jung et al. [7] and it is superior to the MoT scheme because the Laguerre function can naturally enforce the causality. Using a Galerkin's testing, we can eliminate the numerical instability through a march-on-in-degree (MoD) procedure. We present a numerical example to demonstrate the hybrid scheme and its robustness has been observed.

2. FORMULATIONS

Consider the scattering of transient EM wave by a conducting object with a surface S in free space. The problem can be formulated by the TDEFIE, or the tangential component of total electric field vanishes on the object surface. The scattered electric field $\mathbf{E}^{sca}(\mathbf{r}, t)$ is related to the magnetic vector potential $\mathbf{A}(\mathbf{r}, t)$ and electric scalar potential $\Phi(\mathbf{r}, t)$ by

$$\mathbf{E}^{sca}(\mathbf{r}, t) = -\frac{\partial}{\partial t}\mathbf{A}(\mathbf{r}, t) - \nabla\Phi(\mathbf{r}, t) = -\frac{\mu_0}{4\pi} \int_S \frac{1}{R} \frac{\partial}{\partial t} \mathbf{J}(\mathbf{r}', \tau) dS' - \frac{1}{4\pi\epsilon_0} \nabla \int_S \frac{1}{R} q(\mathbf{r}', \tau). \quad (1)$$

In the above, ϵ_0 and μ_0 are the permittivity and permeability of free space, respectively, $\mathbf{J}(\mathbf{r}, t)$ and $q(\mathbf{r}', t)$ is the current density and charge density induced on the conductor surface, respectively, $R = |\mathbf{r} - \mathbf{r}'|$ is the distance between an observation point \mathbf{r} and a source point \mathbf{r}' , and $\tau = t - R/c$ is the retarded time with c being the speed of light in free space. By using the continuity equation and

introducing a new source vector $\mathbf{e}(\mathbf{r}, t)$ which is related to the charge density by $q(\mathbf{r}, t) = -\nabla \cdot \mathbf{e}(\mathbf{r}, t)$, we can write the TDEFIE as

$$\left[\mu_0 \int_S \frac{1}{R} \frac{\partial^2 \mathbf{e}(\mathbf{r}', \tau)}{\partial t^2} dS' - \frac{1}{\epsilon_0} \nabla \int_S \frac{1}{R} \nabla' \cdot \mathbf{e}(\mathbf{r}', \tau) dS' \right]_{tan} = 4\pi \mathbf{E}^{inc}(\mathbf{r}, t)|_{tan}, \quad \mathbf{r} \in S \quad (2)$$

or

$$\left[\mu_0 \int_S \frac{1}{R} \frac{\partial^2 \mathbf{e}(\mathbf{r}', \tau)}{\partial t^2} dS' + \frac{1}{\epsilon_0} \int_S \nabla \nabla \left(\frac{1}{R} \right) \cdot \mathbf{e}(\mathbf{r}', \tau) dS' \right]_{tan} = 4\pi \mathbf{E}^{inc}(\mathbf{r}, t)|_{tan}, \quad \mathbf{r} \in S. \quad (3)$$

3. HYBRID SCHEME OF SOLVING THE TDEFIE

We mesh a conductor surface into N small triangular patches and ΔS_n is the area of the n th patch. The unknown source vector $\mathbf{e}(\mathbf{r}', t)$ can then be expanded as

$$\mathbf{e}(\mathbf{r}', t) = \sum_{n=1}^N e_n(t) \mathbf{e}_n(\mathbf{r}'). \quad (4)$$

If we apply the Nyström method in spatial domain, i.e., the integration over a small triangular patch is replaced with a summation under a quadrature rule provided that the integrand is regular, then we have

$$\left[\mu_0 \sum_{n=1}^N \sum_{q=1}^Q \frac{w_q}{R} \frac{\partial^2 e_n(\tau)}{\partial t^2} \mathbf{e}(\mathbf{r}'_{nq}) + \frac{1}{\epsilon_0} \sum_{n=1}^N \sum_{q=1}^Q w_q \nabla \nabla \left(\frac{1}{R} \right) \cdot \mathbf{e}(\mathbf{r}'_{nq}) e_n(\tau) \right]_{tan} = 4\pi \mathbf{E}^{inc}(\mathbf{r}, t)|_{tan} \quad (5)$$

where $\mathbf{e}(\mathbf{r}'_{nq}) = \mathbf{e}_{nq} = e_{nq}^u \hat{u} + e_{nq}^v \hat{v}$ is the value of unknown source vector at the q th quadrature point in the n th patch and it has two independent components e_{nq}^u and e_{nq}^v in a local coordinate system $\{u, v, w\}$ established over the patch plane. If we choose two orthogonal unit tangential vectors $\mathbf{t}^{(l)}(\mathbf{r}_{mp}) = \mathbf{t}_{mp}^{(l)} = t_{ump}^{(l)} \hat{u} + t_{vmp}^{(l)} \hat{v} + t_{wmp}^{(l)} \hat{w}$ at the p th quadrature point in the m th observation patch ($l = 1, 2$) to test the above equation, then we have

$$\sum_{n=1}^N \sum_{q=1}^Q \left[\frac{\mu_0}{4\pi} \frac{\partial^2 e_n(\tau)}{\partial t^2} a_{mpnq}^{(l)} + \frac{e_n(\tau)}{4\pi\epsilon_0} b_{mpnq}^{(l)} \right] = \mathbf{t}_{mp}^{(l)} \cdot \mathbf{E}^{inc}(\mathbf{r}, t) \quad (6)$$

where

$$a_{mpnq}^{(l)} = \frac{w_{nq} \mu_0}{R_{mpnq}} \mathbf{t}_{mp}^{(l)} \cdot \mathbf{e}_{nq}, \quad b_{mpnq}^{(l)} = \frac{w_{nq}}{\epsilon_0} \mathbf{t}_{mp}^{(l)} \cdot \nabla \nabla \left(\frac{1}{R} \right) \cdot \mathbf{e}_{nq}. \quad (7)$$

The above procedure could have a singularity problem which occurs when $m = n$ but we have developed a robust treatment technique [8].

In the temporal domain, we use the Laguerre function $\phi_j(t) = e^{-t/2} L_j(t)$ as a basis function to expand $e_n(t)$ [7], i.e.,

$$e_n(t) = \sum_{j=0}^{\infty} e_{n,j} \phi_j(st) \quad (8)$$

where s is the scaling factor to control the support of expansion. Substituting this representation to Eq. (6) and using the relevant formulations in the appendix in [7], we can obtain

$$\begin{aligned} & \sum_{n=1}^N \sum_{q=1}^Q \left[\left(0.25s^2 a_{mpnq}^{(l)} + b_{mpnq}^{(l)} \right) e_{n,j} I_{ii}(sR_{mpnq}/c) \right. \\ & = V_{mpi} - \sum_{n=1}^N \sum_{q=1}^Q \sum_{j=0}^{i-1} \left(0.25s^2 a_{mpnq}^{(l)} + b_{mpnq}^{(l)} \right) e_{n,j} I_{ij}(sR_{mpnq}/c) \\ & \quad \left. - \sum_{n=1}^N \sum_{q=1}^Q \sum_{j=0}^i s^2 a_{mpnq}^{(l)} \sum_{k=0}^{j-1} (j-k) e_{n,k} I_{ij}(sR_{mpnq}/c) \right] \quad (9) \end{aligned}$$

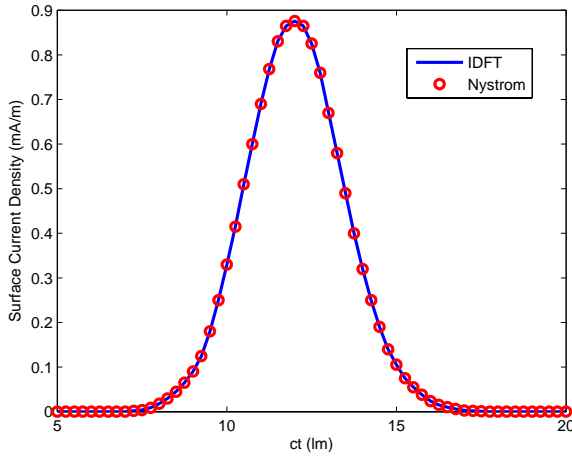


Figure 1: Solution of z -directed current density at $z = 0$ on a cube surface for transient scattering by a conducting cube.

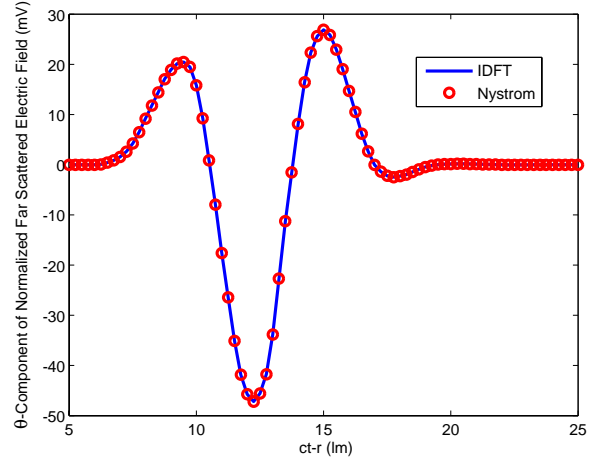


Figure 2: Solution of θ -component of normalized far-zone scattered electric field for transient scattering by a conducting cube.

where $I_{ij}(sR_{mpnq}/c)$ and V_{mpi} can be calculated according to the formulations in the appendix in [7]. Note that there are two spatial-domain coefficients in $a_{mpnq}^{(l)}$ and $a_{mpnq}^{(l)}$ which are the two independent components e_{nq}^u and e_{nq}^v of \mathbf{e}_{nq} and they should be combined with the time-domain coefficient e_{ni} together to form two new unknown coefficients which can be determined by two groups of Eq. (9) when $l = 1, 2$.

4. NUMERICAL EXAMPLE

We consider the transient EM scattering by a conducting cube to demonstrate the approach. The cube is centered at the origin of a rectangular coordinate system and has a side length $s = 1.0$ m whose surface is discretized into 826 triangular patches. A Gaussian plane wave is illuminating the scatterer along the $-z$ direction and the electric field and magnetic field are defined by

$$\mathbf{E}^{inc}(\mathbf{r}, t) = \hat{x} \frac{4e^{-\gamma^2}}{\sqrt{\pi T}}, \quad \mathbf{H}^{inc}(\mathbf{r}, t) = -\frac{1}{\eta} \hat{z} \times \mathbf{E}^{inc}(\mathbf{r}', t) \quad (10)$$

where $\gamma = 4(ct - ct_0 + \mathbf{r} \cdot \hat{z})/T$, T is the width of Gaussian impulse, and t_0 is the time delay denoting the time when the pulse peaks at the origin. We choose a Gaussian pulse with $T = 8.0$ lm (light meter) and $ct_0 = 12.0$ lm as an incident wave. Figure 1 shows the solution of z -directed current density at $z = 0$ on the cube surface while Figure 2 plots the solution of the θ -component of normalized far-zone scattered electric field observed along the backward direction. The results agree well with the solutions obtained from the inverse discrete Fourier transform (IDFT) of frequency-domain solutions.

5. CONCLUSION

In this work, the transient EM scattering by conducting objects is solved by the TDEFIE. We develop a hybrid scheme by combining the Nyström method in spatial domain and the MoM with the Laguerre basis and testing functions in temporal domain. The benefits of the new scheme include the simple mechanism of implementation with a use of nonconforming meshes in spatial domain and the natural satisfaction of causality with a full elimination of instability in temporal domain. A numerical example for EM scattering by a conducting cube is presented to demonstrate the scheme and good results have been observed.

ACKNOWLEDGMENT

This work was supported by the Specialized Research Fund for the Doctoral Program of Higher Education of China (Project No. 20120072110044).

REFERENCES

1. Rao, S. M., *Time Domain Electromagnetics*, Academic Press, San Diego, 1999.

2. Rao, S. M., D. R. Wilton, and A. W. Glisson, "Electromagnetic scattering by surfaces of arbitrary shape," *IEEE Trans. Antennas Propagat.*, Vol. 30, No. 3, 409–418, May 1982.
3. Sun, L. E. and W. C. Chew, "A novel formulation of the volume integral equation for electromagnetic scattering," *Waves Random Complex Media*, Vol. 19, No. 1, 162–180, Feb. 2009.
4. Weile, D. S., G. Pisharody, N.-W. Chen, B. Shanker, and E. Michielssen, "A novel scheme for the solution of the time-domain integral equations of electromagnetics," *IEEE Trans. Antennas Propagat.*, Vol. 52, No. 1, 283–294, Jan. 2004.
5. Shi, Y. and J.-M. Jin, "A time-domain volume integral equation and its marching-on-in-degree solution for analysis of dispersive dielectric objects," *IEEE Trans. Antennas Propagat.*, Vol. 59, No. 3, 969–978, Mar. 2011.
6. Canino, L. S., J. J. Ottusch, M. A. Stalzer, J. L. Visher, and S. Wandzura, "Numerical solution of the Helmholtz equation in 2D and 3D using a high-order Nyström discretization," *J. Comput. Phys.*, Vol. 146, 627–663, 1998.
7. Jung, B. H., Y. S. Chung, and T. K. Sarkar, "Time-domain EFIE, MFIE, and CFIE formulations using Laguerre polynomials as temporal basis functions for the analysis of transient scattering from arbitrary shaped conducting structures," *Progress In Electromagnetics Research*, Vol. 39, 1–45, 2003.
8. Tong, M. S. and W. C. Chew, "A novel approach for evaluating hypersingular and strongly singular surface integrals in electromagnetics," *IEEE Trans. Antennas Propagat.*, Vol. 58, No. 11, 3593–3601, Nov. 2010.

Influences of High Relative Humidity on Extremely Low Frequency Electric Field Measurements

Leena Korpinen¹, Hiroo Tarao^{1,2}, Rauno Pääkkönen¹,
Oleksandr Okun^{3,4}, and Lauri Sydänheimo¹

¹Tampere University of Technology, Tampere, Finland

²Department of Electrical and Computer Engineering

Kagawa National College of Technology, Kagawa, Japan

³LLC Soyuzenergooproekt, Kharkiv, Ukraine

⁴Department of Electrical Energy

National Technical University “Kharkiv Polytechnic Institute”, Kharkiv, Ukraine

Abstract— The paper presents a study of extremely low frequency (ELF) electric field (EF) measurements in a climate room when the electric field meters were in a high-humidity environment before the measurements. We employed two methods: (1) the sensor was placed on a tripod; and (2) the sensor was fixed using a plastic clamp and was suspended by three fishing lines. We evaluated only two sensor types. However, we noted that a high-humidity environment before the measurement period influenced the results. In the future, it is important to take pre-measurement humidity into account.

1. INTRODUCTION

An earlier study [3, 4] indicated that humidity can influence electric field measurement results; thus, it is important to take into account when these results will be compared to the values given in different exposure safety guidelines (e.g., the International Commission on Non-Ionizing Radiation Protection (ICNIRP) [2] or Directive 2013/35/EU of the European Parliament and of the Council on the minimum health and safety requirements regarding the exposure of workers to the risks arising from physical agents (electromagnetic fields) [1].

The aim of the study was to investigate extremely low frequency (ELF) electric field measurements in a climate room when the electric field meters were in a high-humidity environment before the measurements.

2. MATERIALS AND METHODS

We used the commercial three-axis meters EFA-3 and EFA-300, which contained a bandwidth ranging from 5 Hz to 2 kHz. We employed two methods: (1) the sensor was placed on a tripod (Fig. 1.); and (2) the sensor was fixed using a plastic clamp and was suspended by three fishing lines (Fig. 2).



Figure 1: Method 1 — the sensor placed on tripod.



Figure 2: Method 2 — sensor fixed using plastic clamp and three fishing lines.

With Method 1 (with both meters), the first experiment period included 7 measurements, when the relative humidity was 75%, the temperature was 15°C and the electric fields varied from 1 kV/m

to 25 kV/m. Then, the meter measurements took over 3 hours, exposing them to humidity varying from 79% to 95%. Then, the second measurement period began. With Method 2, the protocol was similar; however, the meters endured high humidity for over 5 hours and temperature varied.

3. RESULTS AND DISCUSSION

Tables 1–8 show the measured results with Methods 1 and 2 using two meters EFA-3 and EFA-300.

Table 1: Measured results with Method 1 (first period) using meter EFA-3 (planned relative humidity 75% and planned temperature 15°C).

Measured temperature°C	Relative humidity, %	Voltage, kV	Calculated EF, kV/m	Measured EF, kV/,m	Error $(E_m - E)/E\%$
15.3	75.1	0.78	1.04	1.06	1.6
15.4	74.8	3.81	5.08	5.24	3
15.4	74.7	5.25	7	7.23	3.3
15.4	74.6	7.58	10.11	10.41	3
15.5	74.6	11.22	14.96	15.36	2.7
15.5	74.4	15.05	20.07	20.63	2.8
15.5	74.3	18.73	24.97	25.69	2.9

Table 2: Measured results with Method 1 (second period) using meter EFA-3 (planned relative humidity 75% and planned temperature 15–25°C).

Measured temperature°C	Relative humidity, %	Voltage, kV	Calculated EF, kV/m	Measured EF, kV/,m	Error $(E_m - E)/E\%$
25	74.9	0.76	1.013	1.08	6.8
25	75.4	3.66	4.88	5.4	10.6
25	75.4	5.21	6.95	7.69	10.7
24.9	75.5	7.45	9.93	11.2	12.8
24.8	75.8	11.33	15.11	17.12	13.3
24.8	76.1	15.06	20.08	22.93	14.2
24.7	76.2	18.76	25.01	28.65	14.5
19.4	79.7	0.77	1.03	1.06	3.6
19.5	79.4	3.77	5.03	5.44	8.3
19.6	79.1	5.22	6.96	7.62	9.4
19.6	78.9	7.54	10.05	10.95	8.9
19.6	78.7	11.26	15.01	16.45	9.6
19.6	78.6	15.09	20.12	22.23	10.5
19.7	78.6	18.83	25.11	27.81	10.8
19.8	74	0.77	1.03	1.02	-1.1
19.7	74.6	3.72	4.96	5.05	1.8
19.7	74.7	5.22	6.96	7.11	2.2
19.7	74.7	7.47	9.96	10.29	3.4
19.7	74.4	11.27	15.03	15.57	3.6
19.7	74.2	15.01	20.01	20.77	3.8
19.7	74.3	18.77	25.03	26.05	4.1
14.7	75.7	0.77	1.03	1.02	-1
14.6	76	3.74	4.99	5.01	0.4
14.6	76.2	5.25	7	7.1	1.5
14.6	76	7.49	9.99	10.22	2.3
14.7	75.8	11.31	15.08	15.35	1.8
14.8	75.6	14.89	19.85	20.29	2.2

In the first periods of Method 1, the maximum percentage error was 5.6%, and in Method 2, it was 11.9%. In the second period, the maximum percentage errors were 14.5% (Method 1) and 24.4% (Method 2).

Table 3: Measured results with Method 2 (first period) using meter EFA-3 (planned relative humidity 75% and planned temperature 15°C).

Measured temperature°C	Relative humidity, %	Voltage, kV	Calculated EF, kV/m	Measured EF, kV/m	Error $(E_m - E)/E$ %
15	75.2	0.78	1.04	1.16	11.9
14.9	75.4	3.78	5.04	5.6	11.2
14.9	75.3	5.24	6.99	7.78	11.3
15	75.3	7.43	9.91	11.01	11.1
15	75.2	11.33	15.11	16.67	10.4
15.1	74.9	14.96	19.95	21.8	9.3
15.1	74.9	18.8	25.07	27.2	8.5

Table 4: Measured results with Method 2 (second period) using meter EFA-3 (planned relative humidity 75% and planned temperature 25°C).

Measured temperature°C	Relative humidity, %	Voltage, kV	Calculated EF, kV/m	Measured EF, kV/m	Error $(E_m - E)/E$ %
25	74.7	0.78	1.04	1.27	22.5
25.1	74.8	3.65	4.87	6.05	24.4
25	75	5.21	6.95	8.59	23.7
25	75	7.45	9.93	12.27	23.5
24.9	74.9	11.25	15	18.38	22.5
24.8	75.4	14.97	19.96	24.43	22.4
24.8	75.4	18.71	24.95	30.5	22.2

Table 5: Measured results with Method 1 (first period) using meter EFA-300 (planned relative humidity 75% and planned temperature 15°C).

Measured temperature°C	Relative humidity, %	Voltage, kV	Calculated EF, kV/m	Measured EF, kV/m	Error $(E_m - E)/E$ %
14.7	74.5	0.76	1.01	1.07	5.6
14.7	74.2	3.73	4.97	5.18	4.2
14.8	74.1	5.24	6.99	7.32	4.8
14.8	74.1	7.49	9.99	10.46	4.7
14.8	74	11.22	14.96	15.69	4.9
14.9	74.1	15.02	20.03	21	4.9
14.9	74.1	18.74	24.99	26.18	4.8

Table 6: Measured results with Method 1 (second period) using meter EFA-300 (planned relative humidity 75% and planned temperature 25°C).

Measured temperature°C	Relative humidity %	Voltage, kV	Calculated EF, kV/m	Measured EF, kV/m	Error $(E_m - E)/E$ %
25	74.9	9.76	1.01	0.98	-2.9
24.9	75.1	3.77	5.03	5.06	0.7
24.9	74.9	5.22	6.96	7.1	2.1
24.9	75.4	7.54	10.05	10.18	1.3
24.9	75.3	11.25	15	15.26	1.7
24.9	75.5	14.99	19.99	20.38	2
24.8	75.1	18.75	25	25.55	2.2

The error was always positive in our tests (0–25%), and this means that when the meters give higher values than calculated values, then the relative humidity is high. There are inaccuracies in our tests, but it is also interesting to note that the accuracy of the meters is reported to be ± 3 – ± 5 %. When the relative humidity is high, it can influence measurement results such that scores fall below the reported accuracy range of the meters. In practice, it is also good to calculate the electric field exposure, when possible, and compare the measurement results to the calculation results.

Table 7: Measured results with Method 2 (first period) using meter EFA-300 (planned relative humidity 75% and planned temperature 15°C).

Measured temperature °C	Relative humidity %	Voltage, kV	Calculated EF, kV/m	Measured EF, kV/m	Error $(E_m - E)/E$ %
15	75.4	0.76	1.01	1.1	8.1
15.1	75.6	3.75	5	5.43	8.7
15.1	75.6	5.26	7.01	7.67	9.4
15.1	75.7	7.49	9.99	10.93	9.4
15.1	75.6	11.23	14.97	16.33	9.1
15.1	75.6	14.97	19.96	21.76	9
15.2	75.5	18.75	25	27.2	8.8

Table 8: Measured results with Method 2 (second period) using meter EFA-300 (planned relative humidity 75% and planned temperature 25°C).

Measured temperature °C	Relative humidity %	Voltage, kV	Calculated EF, kV/m	Measured EF, kV/m	Error $(E_m - E)/E$ %
25	75	0.75	1	1.05	5
25	75	3.77	5.03	5.25	4.5
25	75	5.22	6.96	7.37	5.8
25	75	7.54	10.05	10.87	8.1
25	75	11.26	15.01	15.99	6.5
25	75.1	14.98	19.97	21.3	6.6
25	75.1	18.78	25.04	26.8	7

4. CONCLUSION

We evaluated only two sensor types because there are a limited number of commercial sensors available for electric field measurements. Therefore, our material is quite limited. In conclusion, it can be stated that in the future, it is important to also take humidity into account in the pre-measurement period and not only during electric field measurements.

ACKNOWLEDGMENT

The assistance of the staff of the Group of Environmental Health, Tampere University of Technology (Markus Wirta and Tero Haapala) is gratefully acknowledged. Special thanks go to Kari Lahti (Tampere University of Technology, Department of Electrical Engineering) for his advice and support on working in the climate room.

REFERENCES

1. European Parliament and Council of the European Union, "Directive 2013/35/EU of the european parliament and of the council on the minimum health and safety requirements regarding the exposure of workers to the risks arising from physical agents (Electromagnetic Fields) (20th individual directive within the meaning of article 16(1) of directive 89/391/EEC) and repealing directive 2004/40/EC," 21, Official Journal of the European Union, 2013.
2. ICNIRP, "Guidelines for limiting exposure to time varying electric and magnetic fields (1 Hz–100 kHz)," *Health Phys.*, Vol. 99, 818–836, 2010.
3. Korpinen, L. H., J. Kuisti, H. Tarao, and J. Elovaara, "Influence of relative humidity on analyzing electric field exposure using ELF electric field measurements," *Bioelectromagnetics*, Vol. 34, No. 5, 414–418, 2013.
4. Korpinen, L., H. Kuisti, H. Tarao, R. Pääkkönen, and J. Elovaara, "Comparison of electric field exposure measurement methods under power lines," *Radiation Protection Dosimetry*, Vol. 158, No. 2, 221–223, 2014.

Examples of Variation in Measured ELF Electric Fields under 400 kV Power Lines

Leena Korpinen¹, Rauno Pääkkönen¹, Hiroo Tarao^{1,2},
Oleksandr Okun^{3,4}, and Lauri Sydänheimo¹

¹Tampere University of Technology, Tampere, Finland

²Department of Electrical and Computer Engineering
Kagawa National College of Technology, Kagawa, Japan

³LLC Soyuzenergooproekt, Kharkiv, Ukraine

⁴Department of Electrical Energy

National Technical University “Kharkiv Polytechnic Institute”, Kharkiv, Ukraine

Abstract— The paper presents how the measured extremely low frequency (ELF) electric fields (EFs) fluctuate in the same measurement place when the humidity varies. EF measurements were performed at three places near 400 kV power lines. In Place A (nine measurements), the EFs varied from 6.8 to 12.5 kV/m when relative humidity was from 70.5% to 86%. In Place B (five measurements), the EFs were 5.1–8.2 kV/m when relative humidity ranged from 67% to 76%, and in Place C (two measurements), the EFs were 0.90–0.92 kV/m when humidity was 68–76%. The measured EFs varied significantly.

1. INTRODUCTION

The physiological effects and public exposures of electromagnetic fields have been studied at Tampere University of Technology (TUT). Parts of the earlier projects have also measured the electric fields in the same place under 400 kV power lines [4, 5].

Humidity is not expected to significantly influence the electric field (EF). However, laboratory tests have demonstrated that it can influence EF measurement systems when humidity is sufficient to cause condensation on the sensor and on the supporting structure (tripod) [1]. It has been found during these laboratory tests that EFs measured in high humidity conditions are always higher than the correct values. According to the previous considerations, accurate EF measurements cannot be performed under rainy conditions [1].

The aim of the work was to investigate how the measured ELF electric fields fluctuate in the same measurement place when humidity varied. When we compare the measured values to the recommendations (e.g., guidelines of the International Commission on Non-Ionizing Radiation Protection (ICNIRP) [3] or Directive 2013/35/EU [2]), it is important to know how humidity influences the measured results.

2. MATERIALS AND METHODS

During three days, the EF measurements were performed at three places near 400 kV power lines in Finland. Figures 1–3 show the measurement places.



Figure 1: Measurement Place A, near 400 kV power line.



Figure 2: Measurement Place B, near 400 kV power line.



Figure 3: Measurement Place C, near 400 kV power line.

Table 1: Electric field measurement results at different places.

Date and time	Meter	Measurement place	Electric field strength	Relative humidity (Measurement time)
12.08 08:39	EFA-300	A	12.5 kV/m	86.0% (08:42)
12.08 08:58	EFA-3	A	10.5 kV/m and 10.9 kV/m	79.0% (09:00)
12.08 20:20	EFA-300	A	7.5 kV/m	70.5% (20:21)
12.08 20:24	EFA-3	A	6.8 kV/m and 7.2 kV/m	70.5% (20:21)
27.08 13:05	EFA-300	B	5.05 kV/m	67.0% (12:59)
27.08 13:13	EFA-300	C	0.92 kV/m	68.0% (13:20)
28.08 10:32	EFA-300	C	0.9 kV/m	76.0% (10:31)
28.08 11:01	EFA-300	B	7.3 kV/m and 7.8 kV/m	76.0% (11:04)
28.08 11:05	EFA-300	A	10.2 kV/m	76.0% (11:04)
28.08 11:09	EFA-3	A	10.8 kV/m and 11.0 kV/m	76.0% (11:04)
28.08 11:12	EFA-3	B	8.0 kV/m and 8.2 kV/m	76.0% (11:04)

Details of the measurement places have been published earlier [3,4]. The EF strength was measured with two 3-axis commercial electric meters: EFA-3 meter (accuracy $\pm 5\%$, RMS) and EFA-300 meter (accuracy $\pm 3\%$, RMS).

In Place A, nine electric field measurements were performed, in Place B, five measurements, and in Place C, two measurements.

3. RESULTS AND DISCUSSION

Table 1 shows the EF measurement results at Places A, B, and C.

In Place A, the EFs varied from 6.8 to 12.5 kV/m when relative humidity was from 70.5% to 86%. In Place B, the EFs were 5.1–8.2 kV/m when relative humidity ranged from 67% to 76%, and in Place C, the EFs ranged from 0.90–0.92 kV/m when humidity was 68–76%.

In Place A, the EFs varied from 6.8 to 12.5 kV/m when relative humidity was from 70.5% to 86%. In Place B, the EFs were 5.1–8.2 kV/m when relative humidity ranged from 67% to 76%, and in Place C, the EFs were 0.90–0.92 kV/m when humidity spanned 68–76%. The measured EFs varied significantly. For example, in Place A, the lowest EF (6.8 kV/m, relative humidity 70.5%) was only 54% of the maximum value (12.5 kV/m, relative humidity 86.0%). In the example, the difference in relative humidity was 15.5%. In Finland the voltage is always same on 400 kV power lines. Therefore, the changes of the voltage cannot explain our results.

4. CONCLUSION

The measurement material is quite limited; however, it is possible to find examples where the measured EFs were quite different when the humidity also varied. In the future, humidity is

important to take account in EF measurements.

REFERENCES

1. CIGRE (International Council on Large Electric Systems), “Technical guide for measurement of low frequency electric and magnetic fields near overhead power lines,” Working Group C4.203, CIGRE, Paris, France, 2009.
2. European Parliament and Council of the European Union, “Directive 2013/35/EU of the European Parliament and of the council on the minimum health and safety requirements regarding the exposure of workers to the risks arising from physical agents (electromagnetic fields),” *Official Journal of the European Union*, 21, 20th Individual Directive within the Meaning of Article 16(1) of Directive 89/391/EEC) and Repealing Directive 2004/40/EC, 2013.
3. ICNIRP, “Guidelines for limiting exposure to time varying electric and magnetic fields (1 Hz–100 kHz),” *Health Phys.*, Vol. 99, 818–836, 2010.
4. Korpinen, L., H. Kuisti, J. Elovaara, and V. Virtanen, “Cardiac pacemakers in electric and magnetic fields of 400-kV power lines,” *Pacing Clin. Electrophysiol.*, Vol. 135, 422–430, 2012.
5. Korpinen, L., H. Kuisti, J. Elovaara, and V. Virtanen, “Implantable cardioverter defibrillators in electric and magnetic fields of 400 kV power lines,” *Pacing Clin. Electrophysiol.*, Vol. 37, 297–303, 2014.

Possible Methods for Limiting Exposure to the Electric Fields of High Voltage Power Lines on Active Implantable Medical Devices in the Human Body

Oleksandr Okun^{1,2}, Leena Korpinen³, and Lauri Sydänheimo³

¹LLC Soyuzenergooproekt, Kharkiv, Ukraine

²Department of Electrical Energy

National Technical University “Kharkiv Polytechnic Institute”, Kharkiv, Ukraine

³Department of Electronics and Communications Engineering

Tampere University of Technology, Tampere, Finland

Abstract— The aim of the study is to consider the effect of additional shielding objects (with and without voltage) to reduce the electric field intensity under high voltage power lines. Results from electric field calculations generated by a 400 kV power line with a horizontal phase arrangement, additional shielding wires, and a row of trees are presented. It is concluded that plantings near the power lines can be used as a means of limiting exposure to electric fields on active implantable medical devices in the human body.

1. INTRODUCTION

According to earlier studies [1, 2], the electric fields (EFs) under a 400 kV power line (PL) in some conditions may disturb active implantable medical devices (cardiac pacemakers, implantable cardioverter defibrillator, and others) in the human body and affect their functioning. Therefore, it is reasonable to consider possible ways to limit the impact of EFs, generated by PLs, on medical devices.

One of the known methods of limiting EF intensity under PLs without changing the design of lines is to plant trees and shrubs under the power lines. The second simplest method of limiting the field intensity of PLs is to install grounded wires (shields) under lines' wires. It is economically feasible to connect shields under the line wires to a voltage source and thus ensure effective utilization of the cross section. In all these cases, the induced charges on grounded wires partially compensate for the EF produced by line wires and restrain the field intensity.

The aim of the study is to examine the shielding effect of additional objects (with and without voltage) to reduce the EF intensity under high voltage PLs as well as estimate the shielding effectiveness and the possibility of its application.

2. MATERIALS AND METHODS

The field intensity under power lines at the height h above the ground level in cases with shield wires (Figure 1) can be calculated utilizing a two-dimension formula similar to [3], but taking into account the presence of shields. The charges on shield and line conductors are determined by solving the system of Maxwell's potential equations, where voltages on grounded shields (passive

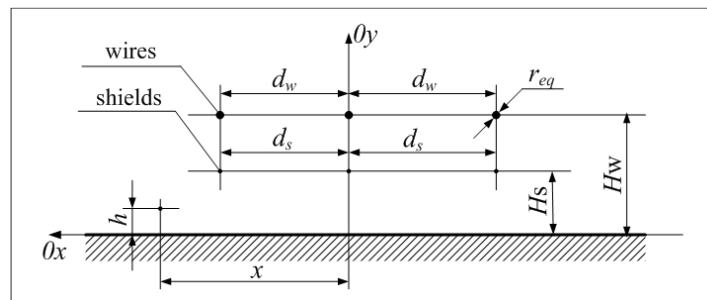


Figure 1: Scheme of PL wires and shield locations (H_w is the suspension height of the wires; H_s is the suspension height of the shields; d_w is the distance between the wires; d_s is the distance between the shields; r_{eq} is the equivalent radius of the wires; and x is the distance from the observation point).

shielding) are equaled to 0 or have the opposite sign to the voltages on the corresponding line wires (active shielding).

In cases with tree and shrub plantings, EFs can be calculated using the method above, assuming a row of trees or shrubs to be conductive cylinders with zero voltage. The geometrical parameters of these cylinders (the radius r and the height of the center of the cylinder above the ground surface H_{tr}) are approximately defined from equality of perimeters for the cross-section of the crown and cylinder.

3. RESULTS AND DISCUSSION

To consider the shielding effect of additional objects, a 400 kV PL with horizontal phase wires was chosen. The phase parameters were $a = 45$ cm, $n = 3$, $r_0 = 0.0165$ m, and $r_{eq} = 0.149$ m. The distance between the wires was 9 m. The distance from the wires to the ground was equal to 10 m. The height of the observation point above the ground surface was 1.8 m.

Table 1 presents the results of the EF calculations, generated by a PL of 400 kV, under grounded shield wires of different suspension heights.

It is seen from Figure 1 and Table 1 that the charges on grounded wires are induced, and the sign of these charges has the opposite sign to the charge on the corresponding wire. Therefore, the field intensity under the PL is reduced. Under an increase of suspension height of the shield wires, located under the PL, maximum values of the EFs in proximity to the PL decrease, but at the same time, the field values far from the system of wires remain almost unchanged in magnitude.

Table 2 shows the results of the EF calculations generated by a PL of 400 kV and shield wires with different voltage values U_s based on the phase voltage of the PL U_{PL} .

In the case of active shielding, as with the grounded wires, the charge on the lower wire has the opposite sign to the charge on the corresponding wire. However, the presence of potential on the lower shield wire increases the charge and, consequently, the shielding effect.

As it is seen from Table 2, when we increase voltages on shield wires, maximum EF intensity in proximity to the PL is decreased until it reaches a critical value. This value for the considered PL with horizontal phase wires is $0.25U_{PL}$. After this value, EF intensity begins to increase. It is

Table 1: EF intensity distribution under 400 kV PL and three passive shields with different H_s and $d_s = 9$ m.

Parameters of shields	Maximum EF intensity	EF intensity at distance 20 m from middle wire	EF intensity at distance 30 m from middle wire
without shields	7.51	3.31	1.16
$H_s = 2.5$ m	6.12	3.19	1.13
$H_s = 3$ m	5.91	3.16	1.13
$H_s = 4$ m	5.64	3.09	1.11
$H_s = 5$ m	5.48	3.02	1.09
$H_s = 6$ m	5.42	2.94	1.07

Table 2: EF intensity distribution under 400 kV PL and three active shields with $H_s = 4$ m, $d_s = 9$ m under different voltage U_s .

Parameters of shields	Maximum EF intensity	EF intensity at distance 20 m from middle wire	EF intensity at distance 30 m from middle wire
without shields	7.51	3.31	1.16
$U_s = 0$	5.64	3.09	1.11
$U_s = 0.1 U_{PL}$	4.87	2.95	1.08
$U_s = 0.15 U_{PL}$	4.55	2.88	1.06
$U_s = 0.2 U_{PL}$	4.26	2.80	1.05
$U_s = 0.25 U_{PL}$	4.00	2.73	1.03
$U_s = 0.3 U_{PL}$	4.46	2.66	1.01
$U_s = 0.35 U_{PL}$	5.61	2.59	1.00
$U_s = 0.4 U_{PL}$	6.78	2.51	0.98

most likely caused by prevalence of the field produced by the shields over the field generated by the PL wires. The behavior of the field values far from the PL are the same for all voltages, i.e., under an increase of shield voltages, the EF intensity decreases.

Furthermore, calculations show that the most shielding effect for the investigated PL is obtained under 25% from U_{PL} (i.e., under 38 kV of phase-to-earth or 66 kV of phase-to-phase voltages). The shielding efficiency for this voltage is 47%, significantly more than 25%, which is obtained in the case of the grounded shields.

Since the maximum field intensity values for the PL with horizontal phase wires are observed directly under the outside wires and EF under the middle conductor field is much smaller than under the outside wires (Figure 2), it is possible to achieve a more rational construction with using one or two grounded shields, placing them under the outside wires, instead of three.

Therefore, the results of the EF calculations, produced by a PL of 400 kV and one or two shield wires, are presented in Tables 3 and 4, respectively.

From Tables 3–4, the calculated EF values generated by the PL with one or two passive shields are almost the same as in Table 1 for the case of three shield wires. Further, a shield wire decreases EF intensity in its vicinity, but EF far from it is quite similar. Therefore, if it is necessary to reduce EF under PLs as well as near an object to be protected, an additional shield can be arranged near

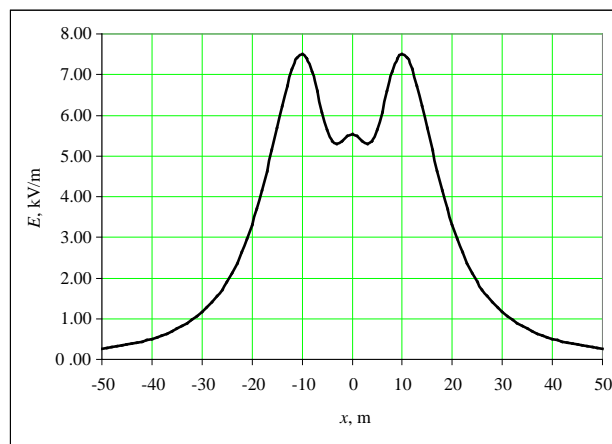


Figure 2: EF distribution under 400 kV PL without additional shielding objects.

Table 3: EF intensity distribution under 400 kV PL and one passive shield, located under an outside wire, with different H_s and d_s .

Parameters of shield	Maximum EF intensity (from shield's side)	EF intensity at distance 20 m from middle wire	EF intensity at distance 30 m from middle wire
without shields	7.51	3.31	1.16
$H_s = 4$ m; $d_s = 9$ m	5.70	3.10	1.11
$H_s = 4$ m; $d_s = 12$ m	6.06	2.88	1.07
$H_s = 4$ m; $d_s = 18$ m	7.30	2.02	1.02
$H_s = 4$ m; $d_s = 30$ m	7.50	3.26	0.59

Table 4: EF intensity distribution under 400 kV PL and two passive shields, located under the outside wires, with different H_s and d_s .

Parameters of shields	Maximum EF intensity	EF intensity at distance 30 m from middle wire	EF intensity at distance 30 m from middle wire
without shields	7.51	3.31	1.16
$H_s = 4$ m; $d_s = 9$ m	5.65	3.09	1.11
$H_s = 4$ m; $d_s = 12$ m	6.04	2.87	1.07
$H_s = 4$ m; $d_s = 18$ m	7.30	2.00	1.02
$H_s = 4$ m; $d_s = 30$ m	7.50	3.26	0.58

Table 5: EF intensity distribution under 400 kV PL and one row of trees located under an outside wire, with $H_{tr} = 4$ m, $r_{tr} = 1$ m and different d_{tr} .

Parameters of cylinder, representing a row of trees	Maximum EF intensity	EF intensity at distance 20 m from middle wire	EF intensity at distance 30 m from middle wire
without shields	7.51	3.31	1.16
$d_{tr} = 9$ m	5.61	2.64	1.00
$d_{tr} = 12$ m	5.58	1.97	0.89
$d_{tr} = 18$ m	6.91	1.08	0.74
$d_{tr} = 30$ m	7.51	3.31	0.64

this object.

In general, the presence of additional wires leads to an appreciable increase in the cost of a PL. Maintenance of double-circuit PL with different systems of voltages facilitates operational difficulties caused by the mutual electromagnetic influence between the circuits and a significant change in the parameters of both circuits in comparison with a single-circuit PL, especially for the lower circuit. Therefore, limiting EF intensity under PLs without changing the design of lines can be achieved by using trees and shrubs, which have a height of 4–5 m and relatively high conductivity during the whole year [4].

Table 5 shows the results of the EF calculations generated by a PL of 400 kV with a row of trees planted under an outside wire.

It is gathered from Table 5 that a row of trees, similar to the grounded wire, reduces EF intensity under the PL. EF distribution has more complex behavior than the case with the single grounded shield due to a larger radius and induced charge. For example, EF intensity close to a place where a row of trees is located jumps in magnitude. Moreover, it is obtained that the shielding effect at a distance from this place (at distances 20 and 30 m for $d_{tr} = 9, 12$ and 18 m) is greater than that achieved by the grounded shield.

4. CONCLUSION

Based on the received results, it can be concluded that installing additional grounded or energized wires and planting trees and shrubs generally reduce EF intensity under PLs significantly by using a number of objects or rows. On the contrary, the possibility of a practical application of the considered additional wires is not always economically feasible because it leads to an increase in cost or maintenance problems. Therefore, it is better to use trees and shrubs for the purpose of limiting EFs. In the presence of planting areas with a height of 4–5 m under PLs, the electromagnetic environment, including the safety of people with active implantable medical devices, can be improved.

In the future, to obtain more realistic results, it is necessary to conduct experimental studies and develop a detailed model of tree and shrubs plantings (with seasonal changes) based on numerical methods as a means of limiting EFs in proximity to PLs.

REFERENCES

1. Korpinen, L., H. Kuusti, J. Elovaara, and V. Virtanen, "Cardiac pacemakers in electric and magnetic fields of 400-kV power lines," *Pacing Clin. Electrophysiol.*, Vol. 135, 422–430, 2012.
2. Korpinen, L., H. Kuusti, J. Elovaara, and V. Virtanen, "Implantable cardioverter defibrillators in electric and magnetic fields of 400 kV power lines," *Pacing Clin. Electrophysiol.*, Vol. 37, 297–303, 2014.
3. Okun, O. and L. Korpinen, "Comparison of methods to define power line and substation's busbar wire capacitances in electric field calculation task," *8th International Workshop on Biological Effects of Electromagnetic Fields*, Varna, Bulgaria, Sep. 21–26, 2014.
4. Aleksandrov, G. N., *EHV Installation and Environmental Protection*, 134–138, Energoatomizdat, Leningrad, 1989 (in Russian).

Programmable Fiber-based in-band OSNR Monitoring for Flexgrid Coherent Optical Communication System

Ruoxu Wang¹, Liangjun Zhang¹, Ming Tang¹, Zhenhua Feng¹,
Rui Lin², Songnian Fu¹, and Perry Ping Shum³

¹Next Generation Internet Access National Engineering Lab (NGIA)
School of Optical and Electronic Information

Huazhong University of Science and Technology, Wuhan 430074, China

²School of Information and Communication Technology

The Royal Institute of Technology (KTH), Electrum 229, Kista 164 40, Sweden

³Photonics Centre of Excellence, School of Electrical and Electronic Engineering
Nanyang Technological University, Singapore 637553, Singapore

Abstract— With the rapid development of ultra-dense large capacity coherent WDM optical communication networks, the monitoring of in-band optical signal-to-noise ratio (OSNR) plays an essential role to ensure signal qualities. Different from the classic polarization-nulling method, we proposed and experimentally demonstrated a novel fiber-based programmable in-band OSNR monitoring method for flexgrid coherent transmission system, the OSNR monitor is based on linearly chirped fiber Bragg grating (LCFBG) and commercial thermal print head (TPH). For the coherent communication system, when the output power of the pre-amplifier at the receiving terminal is constant, degraded OSNR leads to decreased signal power and elevated ASE noise. Therefore, if the central spectrum (signal and in-band noise) is filtered by an ultra-narrow bandwidth optical filter, the output optical power is in proportional to the OSNR value, the influence of the filtered in-band ASE noise will be negligible with relatively high OSNR and the ultra-narrow bandpass filter is the key element for this technique. Based on the thermo-optic effect of the LCFBG, we used the in-house developed driver circuits and a LabVIEW based software to implement a programmable ultra-narrow passband optical filter for OSNR monitoring. Linear monitoring range of 9–27 dB OSNR values with wavelength ranging from 1530.6 to 1538 nm is achieved. The OSNR monitor has advantages of low cost, low insertion loss, large wavelength tunability and compatible with current optical fiber communication system.

1. INTRODUCTION

With the rapid development of ultra-dense large capacity coherent WDM optical communication networks, the monitoring of in-band optical signal-to-noise ratio (OSNR) plays an essential role to ensure signal qualities [1]. Except the classic polarization-nulling method [2], a novel method based on the integrated silicon microring/microdisk resonator based narrow passband optical filter was proposed [3] to monitor the OSNR recently [1, 4]. However, this method suffers from pretty large insertion loss due to the coupling difficulty between chips and fibers, and the operating wavelength range is limited.

In this work, we proposed and experimentally demonstrated an OSNR monitoring technology based on an all-fiber structured programmable ultra-narrow bandpass optical filter [5]. When the output power of the pre-amplifier at the receiving terminal is constant, degraded OSNR leads to decreased signal power and elevated ASE noise. Therefore, if the central spectrum (signal and in-band noise) is filtered by an ultra-narrow bandwidth optical filter, the output optical power is in proportional to the OSNR value, the influence of the filtered in-band ASE noise will be negligible with relatively high OSNR and the ultra-narrow bandpass filter is the key element for this technique.

2. SYSTEM CONFIGURATION AND EXPERIMENTAL RESULTS

The experimental setup is shown as Figure 1. A tunable laser is set as the optical source, the 16 QAM OFDM signal was generated from an offline DSP and fed into the I/Q modulator through the AWG (Arbitrary Waveform Generator, 10 GSam/s) to generate 16 QAM-OFDM optical signal with 20 Gb/s bit rate. A variable optical attenuator (VOA1) is used to adjust the optical signal power and an ASE noise after 1nm bandwidth tunable optical filter (TOF) is coupled with the signal by a 50 : 50 coupler for accurately setting the OSNR level. After transmission through 100km single mode fibers (SMFs), the optical signal with ASE noise are amplified by an EDFA operating under constant power mode thus the received optical power (ROP) is constant. After the

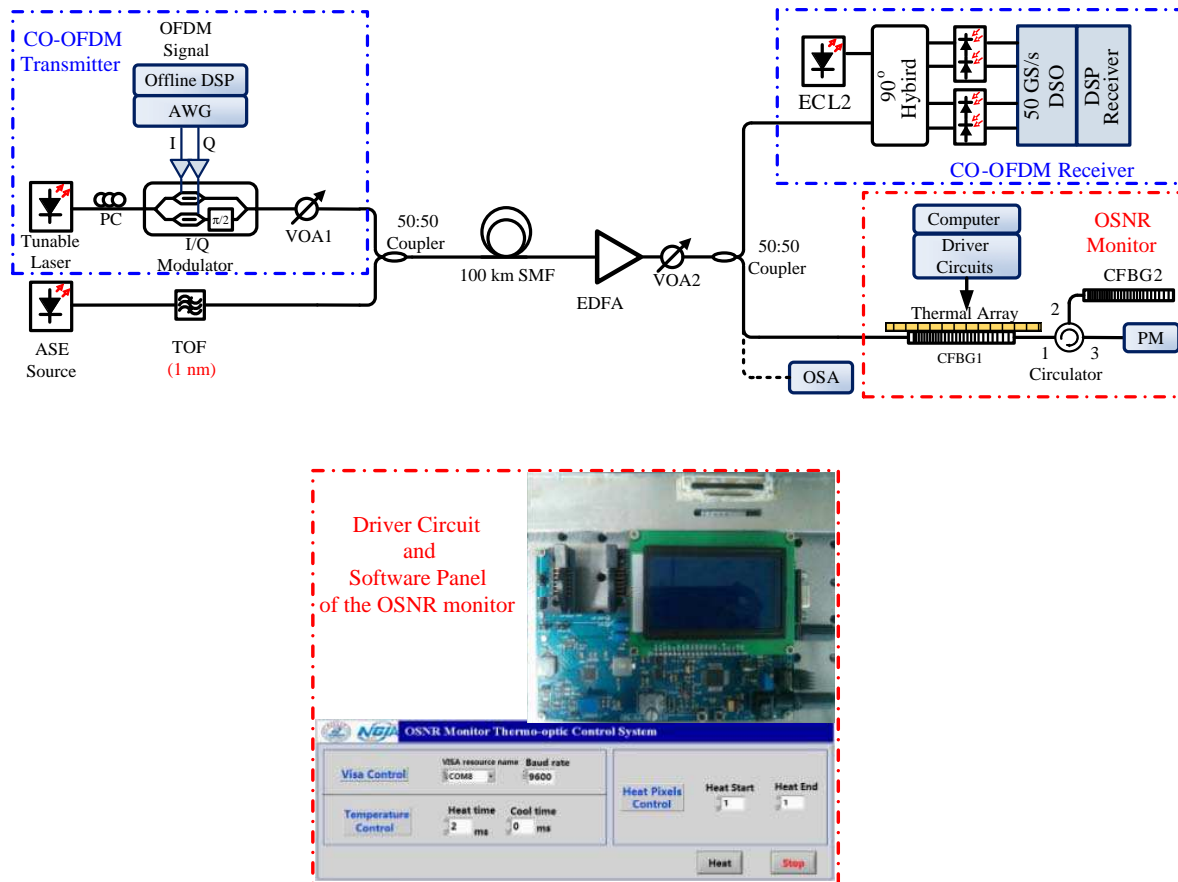


Figure 1: Experimental setup, driver circuits and computer software of the OSNR monitor.

EDFA, the VOA2 adjusts the ROP fed into the coherent optical OFDM receiver. A digital signal oscilloscope (DSO) with 50 GS/s sampling rate is used for data acquisition and the received signals are processed offline for data recovering. Meanwhile, 50% of the signal is coupled into our OSNR monitor. An Optical Spectrum Analyzer (OSA) is used for OSNR calibration.

The heart of our OSNR monitoring system is the all-fiber structured wavelength-variable optical filter based on a linearly chirped fiber Bragg grating (LCFBG) and a thermal print head (TPH), as shown in the right corner of Figure 1. TPH consists of 586 independent thermal pixels with spacing of $125\ \mu\text{m}$ and is fixed tightly with CFBG1. We can control the on/off status and heating temperature of each pixel respectively by computer software through in-house developed driver circuits. Utilizing the thermo-optic effect, we can introduce a temporary phase shift into the stopband of the LCFBG's transmission spectrum, thus an ultra-narrow transmission peak will appear at the stopband, as shows in the red box in Figure 2(a). The 3 dB bandwidth is less than 0.02 nm (limited by the OSA). Since the passband of the optical filter is much less than the transmission signal, a linear relationship between filtered optical power and OSNR is anticipated. In order to eliminate the unwanted ASE light beyond the stopband, CFBG2 is used together with the circulator to ensure that only the filtered optical power can reach the powermeter (PM). An advantage of our programmable optical filter is that the central wavelength can be easily reconfigured to meet the OSNR monitoring requirements for coherent communication systems at arbitrary wavelength. Figure 2(b) shows the superimposed transmission spectrum when we heat different position of the TPH. The filter's center wavelength can be accurately adjusted across the stopband of the LCFBG transmission spectrum. Therefore our technique will be ideal for the OSNR monitoring of flex-grid transmission system with the wavelength ranging from 1530.6 nm to 1538 nm. The operating wavelength range can be further increased by using optimized LCFBG and TPH.

We fixed the monitor's operation wavelength at 1535.82 nm (one of the DWDM channel center wavelength according to the standard of the ITU-T G.692), and adjusting the attenuation of the VOA1, we can alter the received OSNR value. The ROP after VOA2 is adjusted to several values and the relationship between monitor optical power after optical filter and the OSNR is

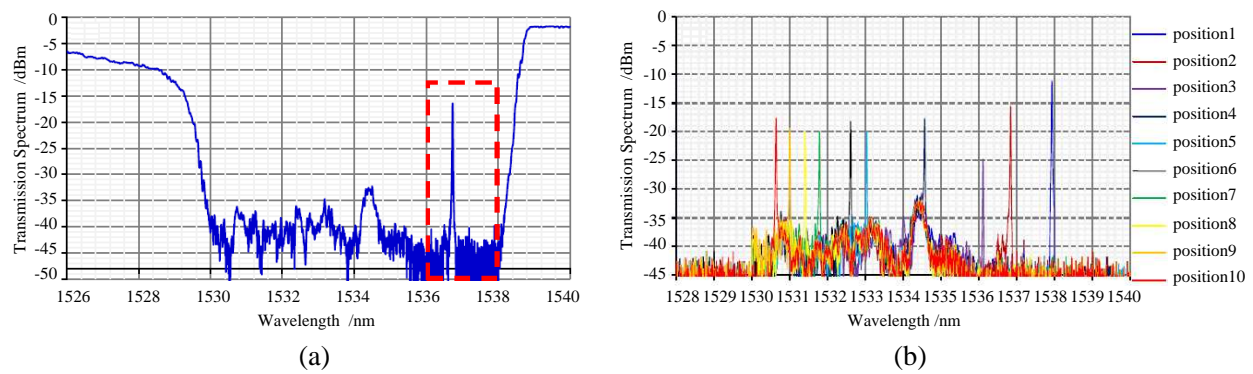


Figure 2: (a) Transmission spectrum of CFBG1 after heated specific pixels, the red box is the ultra-narrow optical filter introduced by thermal phase shift. (b) The transmission spectrum of the monitor with wavelength tunable range from 1530.6 to 1538 nm.

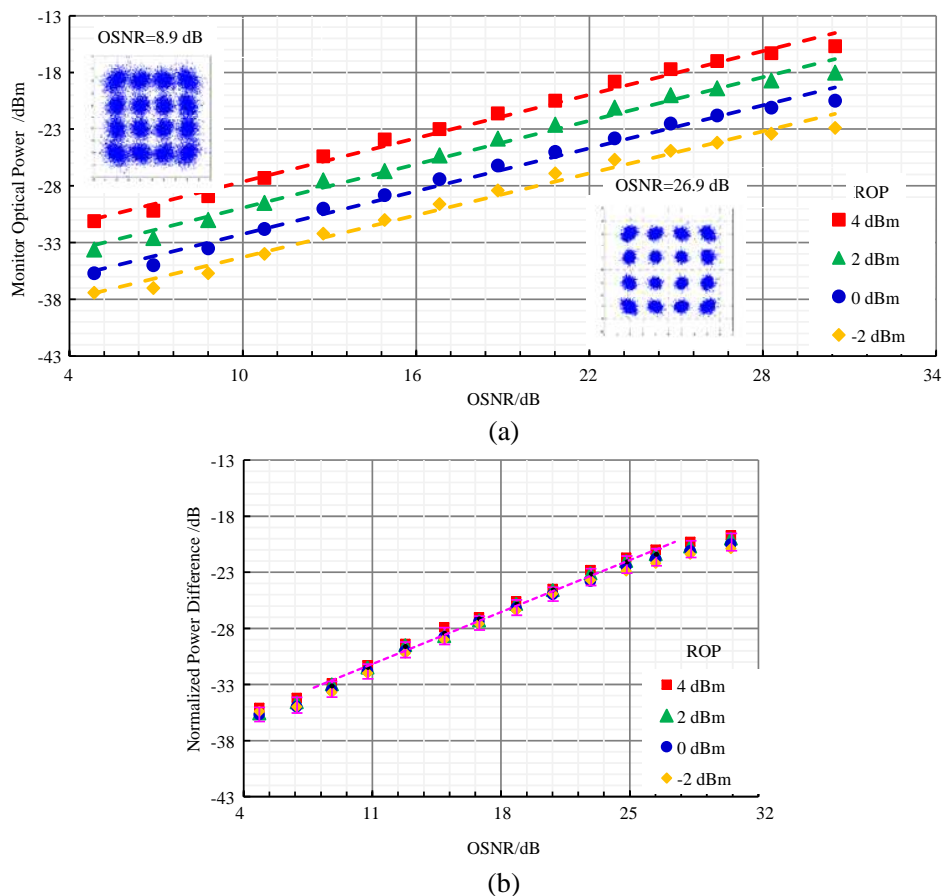


Figure 3: (a) Measured monitor power as a function of OSNR at different ROP. Insert: constellation of the 16 QAM-OFDM at ROP = 0 dBm. (b) Relationship between normalized power difference and OSNR, pink lines: error bars, pink dashed line: linearly working range.

demonstrated in Figure 3(a) at different ROPs. It can be clearly found that at all ROP values, the filtered output optical power shows a linear function of OSNR and the linear fitting curve matches the data very well. The inset diagrams in Figure 3(a) present the constellation of the 16 QAM OFDM signal at the best and worst OSNR situation when the ROP is 0 dBm after offline DSP processing. By comparing the filtered optical power and the ROP, the normalized power difference after the programmable optical ultra-narrow filter versus OSNR is plotted in Figure 3(b). It can be observed that, although the ROP is different, the normalized power difference data converges at the corresponding OSNR level and it can be regarded as a transfer function of OSNR monitoring. The error bars are calculated and are shown in the same figure. It can be seen that the linear

working range with negligible error (standard deviation < 0.5 dB) can be achieved when the OSNR varies from 9 to 27 dB, respectively.

3. CONCLUSION

We demonstrated an in-band OSNR monitoring with programmable ultra-narrow passband optical fiber filter for coherent transmission system. Linear monitoring range of 9–27 dB OSNR with wavelength ranging from 1530.6 to 1538 nm is achieved. The programmable ultra-narrow optical filter is based on linearly chirped fiber Bragg grating (LCFBG) and thermal print head (TPH), and we experimentally demonstrated the OSNR monitor for 16 QAM-OFDM transmission system. The scheme can be extended to monitor signal with other modulation formats and this technique is promising for practical deployment because it is fully compatible with the fiber transmission system.

ACKNOWLEDGMENT

This work is supported by the National 863 High-tech R&D Program of China (Grant No. 2013AA0-13402), the National Natural Science Foundation of China (Grant No. 61331010) the Fundamental Research Funds for the Central Universities, HUST: 2013TS052, and the Program for New Century Excellent Talents in University (NCET-13-0235).

REFERENCES

1. Xu, K., et al., “An ultracompact OSNR monitor based on an integrated silicon microdisk resonator,” *IEEE Photo. J.*, Vol. 4, 1365–1371, 2012.
2. Lee, J. H., et al., “OSNR monitoring technique using polarization-nulling method,” *IEEE Photonic. Tech. L.*, Vol. 13, 88–90, 2001.
3. Yang, J. Y., et al., “Optical signal-to-noise ratio monitoring of an 80 Gbits/s polarization-multiplexed return-to-zero differential phase-shift keying channel,” *Opt. Lett.*, Vol. 34, 1006–1008, 2009.
4. Li, Q., et al., “A fully-integrated in-band OSNR monitor using a wavelength-tunable silicon microring resonator and photodiode,” *Optical Fiber Communication Conference*, W3E.5, 2014.
5. Zhang, H., M. Tang, et al., “Programmable all-fiber structured waveshaper based on linearly chirped fiber Bragg grating and digital thermal controller,” *Appl Phys B — Lasers O*, Vol. 112, 479–484, 2013.

Dual Source Railway Vehicles

T. Lelek, V. Schejbal, and O. Sadilek

Department of Electrical and Electronic Engineering and Signaling in Transport Jan Perner Transport Faculty, Studentska 95, Pardubice 532 10, Czech Republic

Abstract— The paper deals with research activities about technical aspects of dual source railway vehicles on the Czech railway traffic system. The thought vehicle uses for powered traction equipment the catenary and traction battery system. The battery system design is based on the traction and vehicular simulations.

1. INTRODUCTION

The multisource railway vehicles are solving at Department of Electrical and Electronic Engineering and Signaling in Transport. Research activities are focused on the traction and propulsion computer simulations and on the real measurement of the experimental vehicle. The paper discusses a design of dual source railway vehicle (DSRV) with the trolley collector and the battery. It is expected that this vehicle will be operating in the Czech district.

The designed vehicle has a lot of advantages unlike conventional one. Among these advantages we might include operation in a short section without an electric line, elimination of combustion engine, using a principle of regenerative braking and recharging battery under catenary. Recharging in a station is not necessary. This realities lead to more effective vehicle using [5–7].

2. CONCEPTION OF DSRV

This research goes by way of the battery position analyses in the vehicle powered by catenary. In this case it is talking about DSRV, because there are the collector and the battery. This vehicle can be operating in short sections without catenary that are ordinary in the Czech Republic.

The electric equipment described by Fig. 1 was designed on base of a metropolitan railway vehicle. For this vehicle is 750 V a typical value of voltage in DC link. This is very advantageous because there is the battery inside DC link. The battery has to be connected to the DC link by converter and the isolating transformer when the voltage will be higher than 1000 V. Furthermore, the electric equipment must be constructed for a high voltage. This solution is more expensive and more complicated in comparison with the 750 V DC link technologies. If the battery would get high

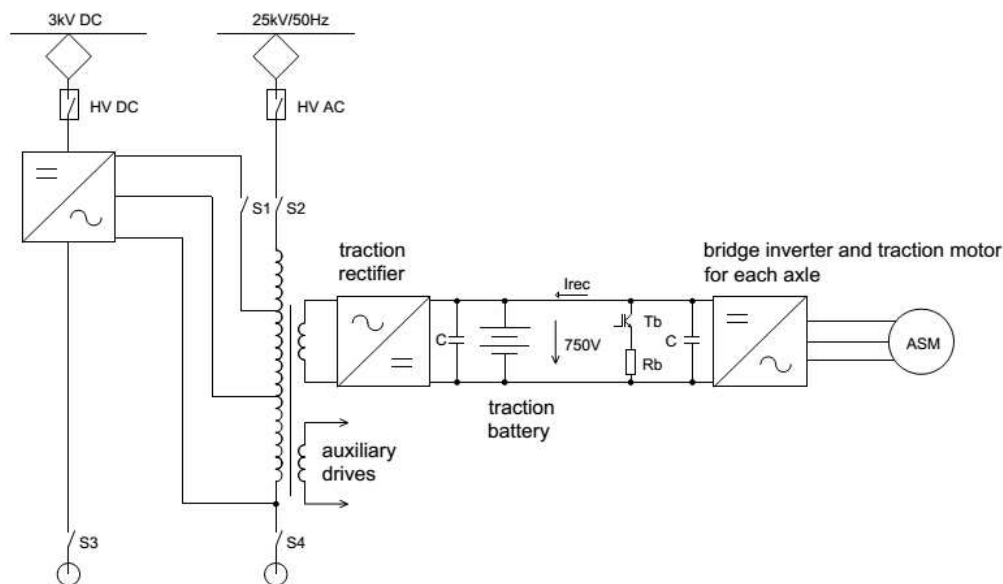


Figure 1: Two power supplies railway vehicle.

voltage on the ports she will be destroyed. It would be very dangerous situation for the passengers and staff. Furthermore, the conception that is in Fig. 1 has higher efficiency. The vehicle that is described above is powered from the catenary with 25 kV 50 Hz and 3 kV DC. The value of an alternate voltage is changed by a transformer and rectified by a rectifier. The DC voltage is led to the transformer through an inverter that creates an alternate voltage. The accumulator can be charged in the same time when traction inverters are consuming an electric energy from the DC link in case of intelligent control. The energy from regenerative braking can be saving to the accumulator or returning to the trolley wire. Energy storing to the battery is naturally preferable because the vehicle works with a higher efficiency [8, 9].

3. DESIGN AND DIMENSIONING OF THE BATTERY SYSTEM

The most restrictive equipment of DSRV is the accumulator of energy — the battery. This element determines the main parameters of non-electrified track — DSRV output power and range. It is necessary to design a battery for this track which will comply with these parameters: energy, power, safety and life time.

It seems that the best way for DSRV is to use electrochemical battery based on lithium (Li-ion). Li-ion batteries are the most modern one, because they have a lot of benefits in comparison with other batteries (Lead acid, NiMH, etc.). The main benefits are for mobile applications higher volumetric and mass energy density. Another benefit is relatively high nominal voltage around 3.2 V/cell because of the big potential difference between negative carbon electrode and positive lithium electrode. The disadvantages of Li-ion batteries are higher price and necessity of supervisor management system (BMS — battery management system). The Li-ion technology based on LiFePO₄ was selected for the proposal of traction calculations. This is the most used and safe technology nowadays [4, 9].

3.1. Ideological Proposal Design of Battery System

The battery system design is based on the knowledge of required energy for non-electrified section, required circumference wheel power and required converter DC link voltage. To achieve the needed voltage it is necessary to calculate the number of cells connected in series:

$$n_{\text{cells}} = U_{\text{dclink_nom}}/U_{\text{a_nom}}[-, V, V] \quad (1)$$

where n_{cells} is the number of cells in battery, $U_{\text{dclink_nom}}$ is the voltage of converter DC link and $U_{\text{a_nom}}$ is the nominal cell voltage. The next step is to determine the battery capacity in connection with track energy intensity and required power.

The traction drive chain consists of: traction converter, traction motors, transmissions and wheels. The battery contains internal resistance and the supply of electro motoric voltage. If the required circumference wheel power is known, the power from the battery (battery ports) is calculated as:

$$P_{bp} = P_{\text{wheel}}/\eta_{\text{drive}}[W, W, \%] \quad (2)$$

where P_{ab} is the required power on the battery ports, P_{wheel} is the required circumference wheel power and η_{drive} is the total drive efficiency. Next step is to calculate the current from the battery ports:

$$I_{bp} = P_{bp}/U_{\text{dclink_nom}}[A, W, V] \quad (3)$$

where I_{bp} is the current from the battery ports. Every traction battery contains internal parasite resistance which becomes energy loss. The energy loss depends on value of charging and discharging current. The efficiency of charging and discharging is reduced. During research activities it was determined on battery TS-LFP40AHA 40 Ah that internal resistance of LiFePO₄ technology is not dependent on depth of discharge (DOD) and also the value of charging/discharging current. The nominal battery capacity should be measured by standard CSN EN 62660-1 at discharging current of magnitude 0.3 C (current corresponding to 0.3 multiple of battery capacity). It means that if the battery is discharging by the current 0.3 C, the measured capacity of this current is equal to the catalog capacity. It is not possible to declare the compliance of this standard nowadays. For this reason it is necessary to determine the methodology which would make energetic safe solution. The model of DSRV uses for the simulation the capacity from catalogue which is used as internal capacity. It means that the energy from the battery is used for energy losses on internal battery resistance and traction work. Dependence of charging and discharging on current from battery with capacity 1000 Ah (WB-LYP1000AHA) was described in [16]. The defining is based on available

parameters from manufacturer. After approximations is possible to express equation for efficiency as:

$$\eta_{\text{char_dischar}} = -0.0094 \cdot I_{bp} + 100[\%, A] \quad (4)$$

where $\eta_{\text{char_dischar}}$ is the efficiency of charging and discharging. For the required battery capacity is possible to use this equation:

$$C_{\text{acu_nom}} = A_{\text{wheel}} / (U_{\text{dclink_nom}} \cdot \eta_{\text{drive}} \cdot \eta_{\text{char_dischar}}) [Ah, Wh, V, \%, \%] \quad (5)$$

where $C_{\text{acu_nom}}$ is the required battery capacity and A_{wheel} is the required circumference wheel energy. For the increasing of energy and power reserve is necessary to increase energy capacity by at least 25%.

$$C_{\text{acu_real}} = C_{\text{acu_nom}} / 0.8 = C_{\text{acu_nom}} \cdot 1.25 [Ah, Ah] \quad (6)$$

where $A_{\text{acu_real}}$ is the total battery capacity. Battery capacity meets energy requirements now. Now it is necessary to check if it is possible to give the battery a full traction load. In general this condition must be met:

$$I_{bp} \leq 3C [A, Ah] \quad (7)$$

where $3C$ is triple capacity — it is the current maximal allowed for LiFePO4 technology. If the condition is not met, the capacity has to be increased.

3.2. Design Validation in the Context of DSRV

The design of vehicle battery system needs the detailed knowledge of driving cycle — energy claims and work part of traction characteristics. The next premise for sophisticated battery system design is represented by the comprehensive set of technical parameters about exact type of battery. If is not possible to find out or measure the required parameters, the calculations must be done with a big reserve of energy and power.

4. SIMULATION OF DSRV AND OPERATING

The primary problem of DSRV design is a calculation necessary battery capacity. The valid capacity value is obtained if the numeric simulation for the required tracks is used. All simulations were done by Matlab.

The ground of simulation model was calculated the train motion equation. All the tractions calculations are solved with 20 ms period that was verified during testing of simulation model. At first the model loads parameters of the track and rail vehicle. The main parameters of the track are locations of gradient changes, speed changes and stations. The vehicle is characterized by the traction characteristic and the braking characteristic. In the next step model needs dates about a propulsion system for solving energetics calculations. The valid information about propulsion system is obtained after analyses of energy flows inside a propulsion chain. For the valid value of the accumulator capacity and the power dimensioning simulation model needs dates about auxiliary consumption. The air-conditioning and the heating are the significant components of the total auxiliary consumption.

After loading important parameters the program will calculate the traction force. In the next step the program compares the traction force Ft [N] with speed of the train v [kph] and computes the actual power ($P_{\text{wheel_act}} = v \cdot Ft$) on circumferences of wheels. The consumed energy E [kWh] can be determined by integration of infinitesimal elements of the power. The mathematical operation of the integration is transformed to the summation in the simulation model. The energy increments are calculated by multiplication an actual power $P_{\text{wheel_act}}$ with a period of the simulation T [ms]. The mentioned principle describes the Equation (12).

$$E_n = E_{n-1} + P_{\text{wheel_act}} \cdot T \quad (8)$$

The results are graphically presented as progresses after the simulation. The graphs describe the changing values during the vehicular ride. The energy in the battery is calculated from the traction energy and the efficiency of the propulsion system. Fig. 2 and Fig. 3 demonstrate the interpretations which come up from the simulation algorithms.

For a better transparency, simulation results were given to the average of 15 tracks that were passed by eight axels DSRV vehicle. The vehicle weight was 110t with included 115 passengers. The capacity of the battery was specified to the value 750 kWh. Than weight of lithium cells is 8t. With this battery the vehicle should be able to pass 50 to 80 km ride. Note that the battery is

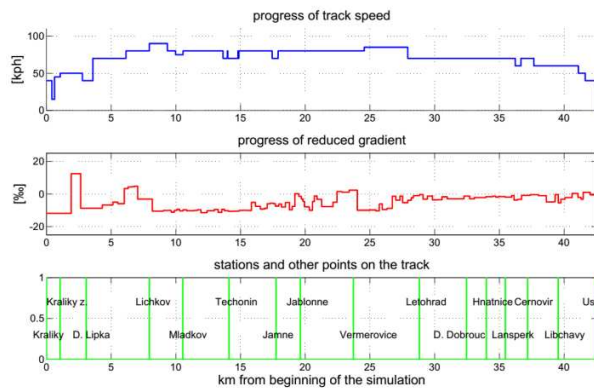


Figure 2: Examples of input quantities.

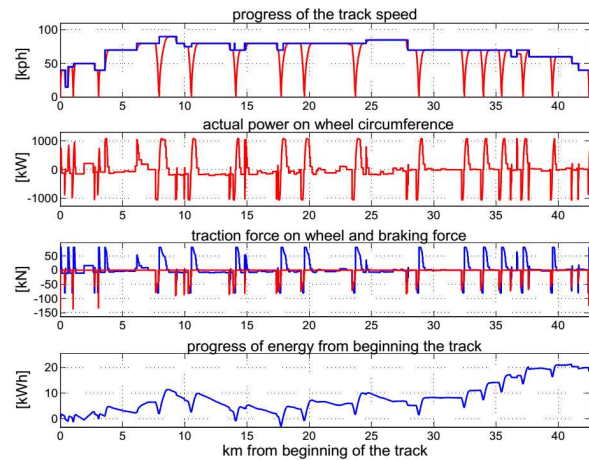


Figure 3: Examples of output quantities.

designed with 50% DOD. Note that the length of the ride depends mainly on the gradient. These same simulations were repeated for the dielectric railway vehicle, the clearly electric railway vehicle, the battery railway vehicle and the dielectric railway vehicle with a catenary collector.

It was followed that the vehicle of the DSRV type is more effective for an operation than other vehicles designed for the nonelectric section operation. Furthermore, the DSRV might be suitable for a clearly electricity operation after an irreversible death of the battery.

5. CONCLUSION

During the research activities it has noticed many contributions of the collector/battery DSRV against the conventional collector/combustion engine vehicle. In the comparison of the cost of electric energy and the fuel wins the electric energy. Therefore, the clearly electric operating vehicle is cheapest. On the second hand the operation of a vehicle powered by the combustion engine is the most expensive. The average way is to use DSRV with a battery. Therefore, the maintaining vehicle with the battery is cheaper than the maintaining vehicle with the combustion engine. Furthermore the energy from braking can be partly returned to the battery. Next an advantage is covered in more effective traffic flows. DSRV goes on the track with and without catenary. Consequently the people cannot change the train. The electric buses get more and more popularity around the world. The railway has to respond fast on this trend for keeping customers.

ACKNOWLEDGMENT

The research was supported by the TACR grant “Competence Centre of Railway Vehicles” No. TE0-1020038.

REFERENCES

1. Smil, V., “Energy myths and realities: Bringing science to the energy policy debate,” xiv+213, American Enterprise Institute, Washington, DC, 2010.
2. Kono, Y., N. Shiraki, H. Yokoyama, and R. Furuta, “Catenary and storage battery hybrid system for electric railcar series EV-E30,” *The 2014 International Power Electronics Conference*, 2014.
3. Hirose, H., K. Yoshida, and K. Shibamura, “Development of catenary and storage battery hybrid train system,” *ESARS*, 2012.
4. Dolecek, R., O. Cerny, L. Mlynarik, and P. Sykora, “Passenger accumulator fed railcars in regional railway traffic,” *Transport Problems 2014*, Silesian University of Technology, Katowice, 2014.
5. Bauer, J. and J. Lettl, “Solar power station output inverter control design,” *Radioengineering*, Vol. 20, No. 1, 258–262, Apr. 2011.
6. Lettl, J., J. Bauer, and L. Linhart, “Comparison of different filter types for grid connected inverter,” *PIERS Proceedings*, 1426–1429, Marrakesh, Morocco, Mar. 20–23, 2011.

7. Doleček, R., J. Novák, O. Černý, and M. Bartłomiejczyk, "Interference in power system for traction drive with PMSM," *Przegląd Elektrotechniczny*, Vol. 4, 204–207, R. 88 NR 9a/2012, ISSN 0033-2097, 2012.
8. Brown, S., "Diagnosis of lifetime performance degradation of lithium-ion batteries: Focus on power-assist hybrid electric vehicle and low-earth-orbit satellite applications," Doctoral Thesis, Applied Electrochemistry, School of Chemical Science and Engineering, Stockholm, 2008.
9. Marcicki, J., "Modeling, parametrization, and diagnostics for lithium-ion batteries with automotive applications," Dissertation, The Ohio State University, Ohio, 2012.
10. Doleček, R., J. Novák, and O. Černý, "Traction permanent magnet synchronous motor torque control with flux weakening," *Radioengineering*, Vol. 18, No. 4, ISSN 1210-2512, 2009.
11. Lelek, T., O. Sadilek, R. Dolecek, L. Mlynarik, and P. Sykora, "Dual source railway vehicles: MAREW," 5, 2015.

Design of Slot Planar Applicator for Local Thermotherapy

Jaroslav Vorlicek¹, Ladislav Oppl², and Jan Vrba²

¹Faculty of Biomedical Engineering, Department of Biomedical Technology
Czech Technical University in Prague, Technicka 2, Prague, Czech Republic

²Faculty of Electrical Engineering, Department of Electromagnetic Field
Czech Technical University in Prague, Technicka 2, Prague, Czech Republic

Abstract— This paper deals with the design construction and evaluation of the slot planar applicator of the square type. In fact composition of four applicators of this type is used for heating a large area under treatment. Matrix composition of applicators has total dimensions of 106 mm × 106 mm and operates at 434 MHz. From the measurement of impedance matching and final evaluation on agarose phantom using thermo-camera we can say that applicator is suitable for use in clinical practice.

1. MICROWAVE HYPERTHERMIA IN GENERAL

Term “microwave hyperthermia” [1] is used for artificial heating of biological tissue with microwave energy. The increase of temperature is caused by dissipation of electromagnetic energy in tissue, which behaves as a dielectric. The electromagnetic field causes polarization of the molecules and changes their rotation in the direction of electric vector of intensity field E . So if we let alternate current power to take effect on the molecule its field would lead to the alternating polarization from one direction to another. With increasing frequency, the molecule loses its ability to track the rapid changes, the effective dielectric constant decreases, loss angle increases and the energy field is converted to heat. Designated frequencies ISM (industrial, scientific, medical) for microwave applications are 435 MHz, 915 MHz and 2450 MHz. There is no practical use for frequencies above or under the higher resp. lower limit. As higher frequencies have very limited penetration and lower frequencies despite their deep penetration are very difficult to focus their power. Penetration is usually determined by equivalent penetration depth that is depth in which intensity of electromagnetic field decreases to cca 37% as of surface value.

What is the main purpose of heating biological tissue? One reason for doing this is to accelerate body’s natural healing processes or to augment conventional cancer therapy. It was observed already by ancient physicians, that increased temperature in tissue induces and speed up healing process, as we can read on prescriptions by Hippocrates of Cos. It’s known, that increased temperature induces better blood perfusion in heated tissue which causes better oxygenation and flushes waste products of metabolism out of the heated tissue. If we intentionally heat healthy tissue, we just increase its cellular metabolism to point, when even tremendously increased blood flow can’t cool down cells, and temperature in tissue reaches point, where cellular proteins are damaged. Without proteins and enzymes cell dies. We profit from this in cancer thermotherapy, when thanks to cancer poor and chaotic blood supply stream can’t cool down effectively cancer cells, while surrounding healthy tissue is easily cooled and remains undamaged. Sole hyperthermia is used rarely, as tissue cells by time develop certain resistance to heat. So the main potential is in combination with conventional cancer therapy to reach better results in treatment [2].

Limit for this form of therapy is water content in target tissue, as microwave is especially absorbed in water molecules. So primarily high-water content tissue like muscles are heated at most and we can poorly heat another structures like tendons or bones. This is both limitation but also advantage, as we can target quite precisely for example cancerous tissue against surrounding layers, due to its vast blood vessel interaction and thus very high water level content.

2. APPLICATORS FOR MICROWAVE HYPERTHERMIA

Microwave antennas for biomedical use, are usually called applicators. We can use both planar antennas and waveguides. Both types have different limitations and advantages, so it’s up to physician and biomedical engineer to decide which use in certain situations. The main differences are in energy transfer efficiency and versatility.

2.1. Waveguide Applicators

Basically we can describe waveguide applicator [3] as conductive tube with any shape of cross-section. Main advantage of this type of applicator is in fact, that it allows highest broadband power transfer and also has lowest loss of electromagnetic energy among all kinds of applicators.

Electromagnetic field is by the format of tube shaped to mods. Heat profile in treated tissue depends on used mod. Every mod has its critical frequency. For excitation of chosen mod in waveguide, we have to use higher than its critical frequency. On the contrary when we use lower than critical frequency, the transmitted energy is exponentially dampened through the waveguide, these mods are called evanescent. Common shapes of waveguides are rectangle and cylinder. Thickness of waveguide tube material has to be at least quintuple as its effective penetration depth.

$$k_{c,mn} = \sqrt{\left(\frac{m\pi}{2}\right)^2 + \left(\frac{n\pi}{2}\right)^2}.$$

Constant of cross-section of rectangle waveguide for mod TE_{mn} can be calculated as where a is longer side of waveguide, b is shorter side and m, n are indexes of mod.

2.2. Planar Applicators

Planar applicators [4] are versatile group of different shaped antennas realized as printed circuit board, so they are cheap to manufacture and could be even made of elastic materials. Most common shapes of such applicators are Archimedean double spiral and rectangle slot applicators. This type of applicator can be used both superficially and also intracavitary, as it can be realized as quite tiny spot antennas. Despite its lower transmission, compared to waveguides, is planar applicator with its flexibility and easy adhering to treated areas considerable choice.

Spiral applicator behaves as broadband antenna and is more resistant to dependence of working frequency on permittivity than slot applicator. On the other hand, slot applicator as a resonant structure allow us transfer more electromagnetic energy to target tissue Wavelength of this applicators can be calculated

$$\lambda = \frac{c}{f\sqrt{\varepsilon_{eff}}},$$

where c is speed of light, f is frequency and ε_{eff} is effective permittivity. We consider value of ε_{eff} higher than relative permittivity of used dielectric and lower than relative permittivity of treated tissue.

3. DESIGN AND EVALUATION OF APPLICATOR

To ensure optimal heat distribution in treated area we decided to design composition of four square slot applicators. To allow applicator operate in unshielded room, we chose operational frequency 434 MHz. To ensure maximum energy transfer to treated tissue, we had to find optimal impedance matching between applicator itself and treated tissue, so minimum of radiated energy is reflected back to antenna aperture. To design and simulate optimal solution for our applicator, we used CST MICROWAVE STUDIO 2011 software suite. This software is capable of entering variables as dimension parameters of individual geometric primitives and that allows easy modification of model parameters. After modeling geometry of applicator and stating its material dielectric parameters, we for it defined power source type “edge source” producing transversal electromagnetic wave. Simulations showed up, that no parasitic mode is transmitted in our antenna solution. Main goal of simulations was to find ideal impedance match between applicator and biological tissue (agarose model) with given parameters — permittivity $\varepsilon_r = 54$ and conductivity $\sigma = 0.8$ S/m. Agarose model was in simulation from applicator separated by water bolus of thickness $t = 30$ mm, as it would be separated in any biomedical application to prevent creating hotspots and to improve impedance matching of applicator and biological tissue. On Figure 1 is shown final impedance matching that we reached.

After finding an optimal solution for impedance matching for this applicator we ran couple of simulations to evaluate the field distribution. Field distribution can be found on the Figure 2, which is showing SAR distribution in all three cutting planes, from sagittal, frontal to transversal respectively.

After optimal design was found whole structure was realized and its properties evaluated on agarose model. Agarose phantom was chosen for its close nature like a high-water content biological structures, such as muscles. To ensure optimal dielectric properties, 3 g of salt (NaCl) was added

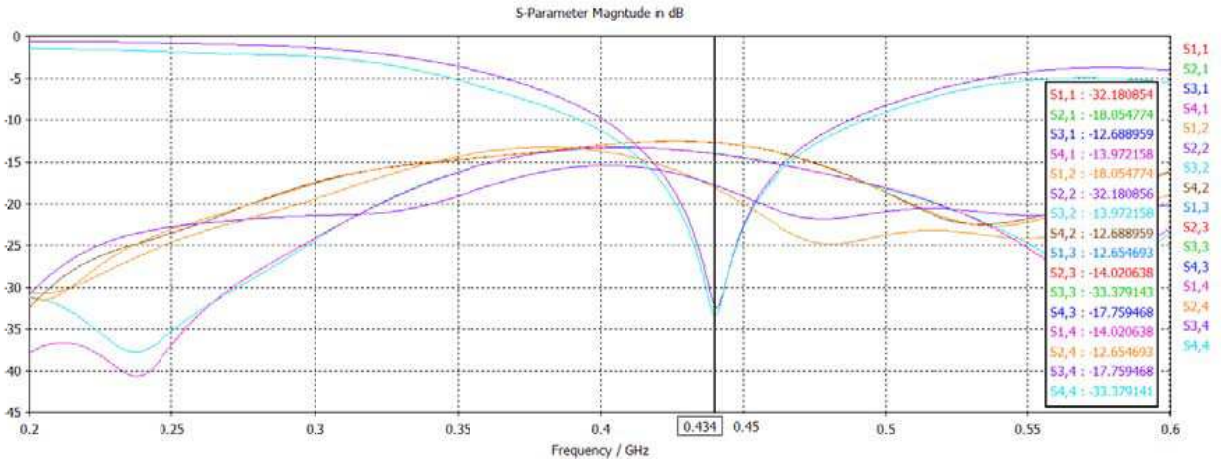
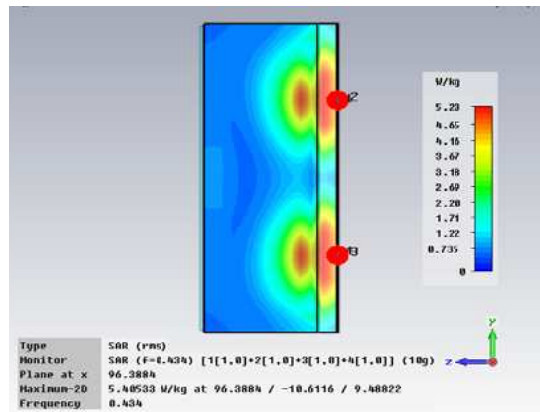
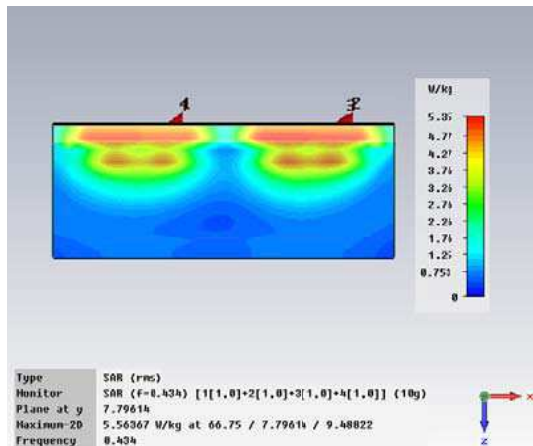


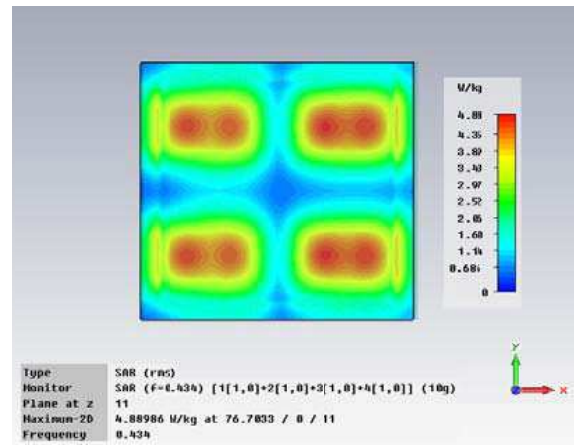
Figure 1: Impedance matching of the composition of four slot applicators all S -parameters (S_{11} , S_{22} , S_{33} and S_{44} were less than -30 dB).



(a)



(b)



(c)

Figure 2: (a) SAR distribution of composition of four applicators in sagittal cut plane. (b) SAR distribution of composition of four applicators in frontal cut plane. (c) SAR distribution of composition of four applicators in transversal cut plane.

to 1.25l agarose phantom. Heat profile in model was observed with thermo-camera FLIR P25 Figure 3. Power delivered to applicator was 50 W and time of exposure model was 2 minutes.

As resonant structure this type of applicator is strongly dependent on good impedance matching

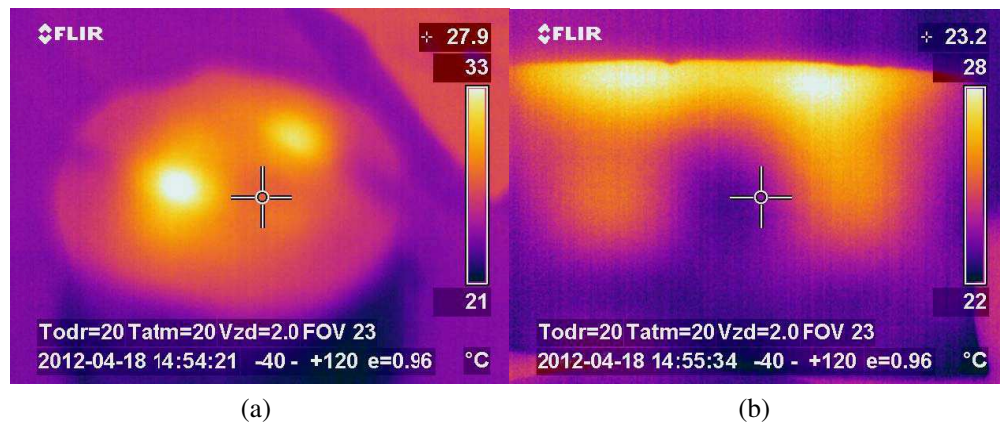


Figure 3: (a) Transversal view of irradiated agar phantom. (b) Sagittal view of irradiated agar phantom.

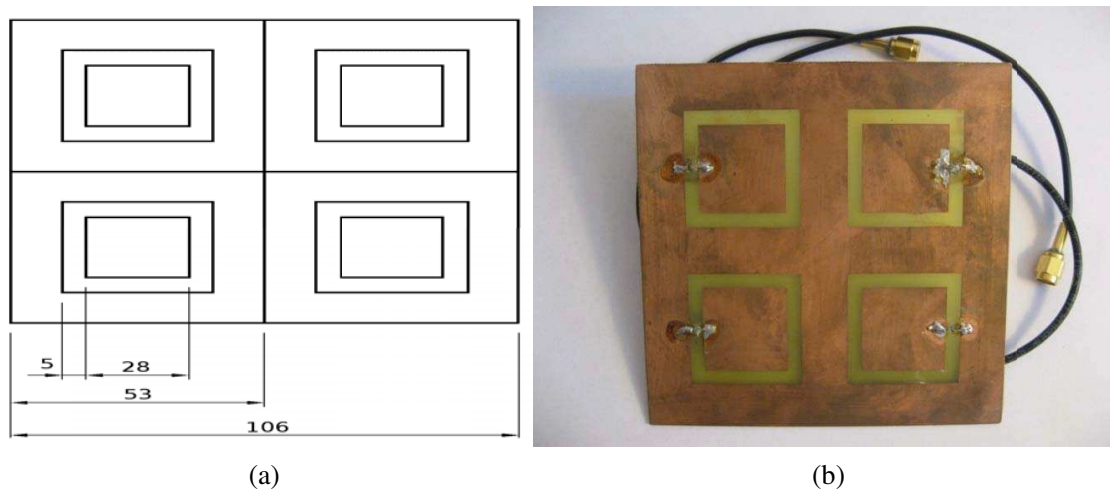


Figure 4: Composition of (a) four rectangular shaped slot planar applicators scheme, (b) final designed model.

to prevent creating hotspots and to ensure maximum energy is radiated from applicator aperture to target tissue, which was successful. For final design of the applicator see Figure 4.

4. RESULTS

Our applicator is suitable for superficial use in hyperthermia treatment. Limit for this form of therapy is water content in target tissue, as microwave is especially absorbed in water molecules. So primarily high-water content tissue like muscles are heated at most and we can poorly heat another structures like tendons or bones. This is both limitation but also advantage, as we can target quite precisely for example cancerous tissue against surrounding layers, due to its vast blood vessel interaction and thus very high water level content.

REFERENCES

1. Falk, H. M. and R. D. Issels, "Hyperthermia in oncology," *International Journal of Hyperthermia*, Vol. 17, No. 1, 1–18, 2001.
2. Kleef, R., D. E. Hager, and G. F. Baronzio, "Hyperthermia in cancer treatment: A primer," *Fever, Pyrogens and Cancer*, 276–337, Springer, US, ISBN 978-0-387-33441-7, 2006.
3. Vrba, J., *Lékařskéaplikacemikrovlńnétechniky*, skriptum CVUT, Praha 2003,1.vydání, ISBN 80-01-02705-8, 2003.
4. Safarik, J. and O. Rychlik, "Planar applicators for local hyperthermia," *19th International Conference Radioelektronika, 2009*, 349–352, Apr. 22–23, 2009.

Array of Spiral Applicators for Local Thermotherapy

Jaroslav Vorlicek¹, Ladislav Oppl², and Jan Vrba³

¹Faculty of Biomedical Engineering, Department of Biomedical Technology
Czech Technical University in Prague, Technicka 2, Prague, Czech Republic

²Faculty of Electrical Engineering, Department of Electromagnetic Field
Czech Technical University in Prague, Technicka 2, Prague, Czech Republic

Abstract— This article deals with the design and testing of planar microwave two-wire Archimedean spiral applicator. Applicator is designed to work on the frequency $f = 434$ MHz, aperture has a size of $35 \text{ mm} \times 35 \text{ mm}$ and its matrix composition consists of the five applicator of the same type. In this case, aperture has a size of $100 \text{ mm} \times 100 \text{ mm}$. Design simulation and the simulations of Specific Absorption Rate distribution are created in program CST MICROWAVE STUDIO 2009. Final evaluation of construction solution is established on SIXPORT for S_{11} coefficient and evaluation of SAR distribution is evaluated by infrared camera FLIR P25.

1. INTRODUCTION

Nowadays the use of microwave thermotherapy is a common part of the clinical hyperthermia oncology treatment. Thus, the paper deals with the prospective type of microwave planar applicator for thermotherapy. The discussed applicator is Archimedean two-wire spiral applicator. We are mainly interested in the shape of radiated power from the aperture and the depth of effective penetration of the biological tissue. This two main parameters have the crucial impact on the process of hyperthermia oncology treatment. Thus, we want to irradiate the cancerous tissues with the predictable dose of microwave radiation. This is reason why we are running the simulations of this above mentioned microwave thermo therapeutic applicator not only for the impedance matching to the biological tissue, but also for the shape of radiated power from applicator aperture together with the determining the depth of effective penetration. Numeric verification of SAR distribution is calculated in homogenous plane phantom having electrically the same parameters as the biological tissue.

2. THERMAL EFFECTS ON TISSUE

Hyperthermic effects on living organism are not that simple matter [1] as it can be seen but here comes a variety of factors to deal with. We can divide them into two major groups; effects caused by blood flow in the tissue and effects of the heat shock proteins (HSP). On cellular level we can describe the heat shock proteins as agents which are protecting the cells and the whole organism from lethal hyperthermia expositions.

In mammals the effects of higher temperatures (up to 43°C) cause cellular damage caused by a denaturation of proteins. When this happens the cell protein synthesis is terminated and apoptosis is induced.

Physiologically the thermal exposition in mammals happens together with fever when heat shock proteins come to action, this supports the hypothesis that the heat shock proteins are protecting the cells against high temperatures. In fact we still know very little about heat shock proteins as the fever sicknesses are as old as the humankind.

Other very important physiological parameter influencing tissue response to heat is the blood flow. At higher temperatures blood perfusion increases in many tumors and this effect is dependent on heating time, temperature and also tumor structure. Blood flow increases to improve tumor oxygenation, but in most cases it is not sufficient because the increased consumption of oxygen in heated tissue. When heating is terminated, blood perfusion and oxygenation slowly recover and how quickly this occurs appears to be tumor-specific. Similar physiological effects occur in normal tissues, but normal tissue has more sophisticated vascular structures to help the tissue deal with the higher temperatures. Heating tumors to higher temperatures typically causes a increase in perfusion during heating which is followed by vascular collapse and if sufficient, this will lead the tumor to necrosis. The speed and degree of vascular collapse depends on heating time, temperature and, of course, on the tumor.

The tumor vascular supply can also be exploited to improve the response to heat. Decreasing blood flow, using physiological modifiers or longer acting vascular disrupting agents prior to the

initiation of heating can both increase the accumulation of physical heat in the tumor, as well as increase the heat sensitivity of the tumor.

3. HYPERTHERMIA ONCOLOGY

Hyperthermia, also called thermotherapy, is a type of cancer treatment [2] in which body tissue is exposed to high temperatures (up to 43°C). It has been shown that high temperatures can damage and kill cancer cells, usually with lower injury to normal tissues. Damaging proteins and structures within cells is causing death of cancer cells by damaging proteins and their inner structures.

Hyperthermia is often used with other forms of cancer therapy, such as chemotherapy and radiation therapy. Hyperthermia may make some cancer cells more sensitive to radiation or harm other cancer cells that radiation cannot damage and it can also enhance the effects of certain cytostatics.

There are two main streams in hyperthermia thermotherapy depending on the area of the human body where the heat was applied. Thus, we have a local hyperthermia application and a whole body application.

In local hyperthermia, heat is applied to a small area, such as a tumor, using techniques that deliver energy to heat the tumor. Different types of energy may be used in this case including radio frequency, microwave, or ultrasound.

Depending on the tumor location, there are several approaches to local hyperthermia: External approaches are used to treat tumors in superficial area, which means that the tumors are not more than 30 mm below the skin. External applicators are often positioned around or near the appropriate region, and energy is focused on the tumor.

The internal method may be used to treat tumors close or near body cavities, such as the esophagus or rectum. Intracavitary applicators are placed inside the cavity and inserted into the tumor to deliver energy which dissipates into heat in the desired area.

Interstitial techniques are used to treat tumors deep within the body, such as brain tumors. This technique allows the tumor to be heated to higher temperatures than external techniques. Under anesthesia, intracavitary applicators are inserted into the tumor. Imaging techniques, such as ultrasound, may be used to make sure the probe is properly positioned within the tumor.

To ensure that the desired temperature is reached, but not exceeded, the temperature of the tumor and surrounding tissue is monitored throughout hyperthermia treatment. Using local anesthesia, the doctor inserts small needles with tiny thermometers into the treatment area to monitor the temperature. Imaging techniques, such as computer tomography, may be used to make sure the probes are properly positioned.

4. PLANAR APPLICATOR

Two-wire Archimedean spiral applicator configurations shown in Fig. 1, when properly excited, have been shown to be circularly polarized radiators with wide broadband characteristic with respect not only to input impedance but also to radiation pattern. In practice, the configuration is excited from a transmission line connected to the center terminals of the configuration.

Such energized two-wire Archimedean spiral radiates a broad circularly polarized beam to each side of the spiral. Each radiated beam is normal to the plane of the spiral. Accordingly, the radiated beams are identical except that the rotational sense of polarization of the radiated field on one side is the opposite of that on the other.

In most applications it is desirable that the spiral radiate to one side this is accomplished by appropriately backing the spiral on one side by a ground plane.

The matrix composition (see Fig. 2) of the two-wire Archimedean spiral applicators is a very useful when we want to irradiate the larger area, which can be useful for example treating the tumors in thoracic region.

5. SIMULATIONS

There has not been any rigorous theory to explain the spiral applicator. However, the following explanation of the radiating mechanism of the two-wire Archimedean spiral is offered through the experimental observations. The point of view taken is that the two-wire spiral applicator behaves as though it were a two-wire transmission line which gradually, by virtue of its spiral geometry, transforms itself into a radiating structure or antenna.

It is well known that a two-wire transmission line, of narrow spacing relative to wavelength of any length, yields a negligible amount of radiation when excited at its terminals. This is due

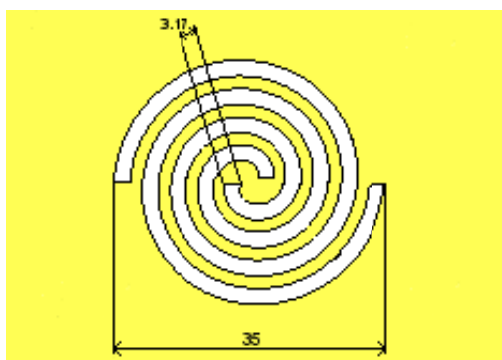


Figure 1: The scheme of the two-wire Archimedean spiral applicator.

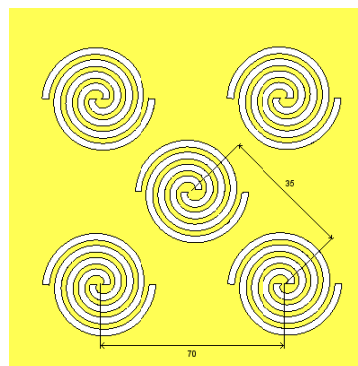


Figure 2: Matrix composition of five Archimedean spiral applicators.

to the fact that the currents in the two wires of the line at normal cross section are always 180° out-of-phase so that radiation from one line is effectively cancelled by the radiation from the other.

Simulations for this applicator have been done in the simulator of electromagnetic field CST MICROWAVE STUDIO 2009. This simulator uses a FDTD method to solve problems related to the electromagnetic field.

The one of the main objectives of the simulations was to find an impedance matching the thermo therapeutic applicator to the biological tissue with the required parameter $S_{11} < -15$ dB. As shows the Fig. 3, the best impedance matching the applicator was found with the width of the applicators arms 3.17 mm. Impedance matching in this case was $S_{11} = -24.8$ dB.

To sum up, after modeling the first shape of the applicator's body and setting the parameters of transient analysis with the proper field monitors, the first results have been obtained. When setting the cells mesh we have to be very careful and add sufficient discretization density of cells when it's needed; otherwise the results will not be so good. As the lowest discretization with sufficient outcome we can assume the density of 35 discretization lines per wavelength.

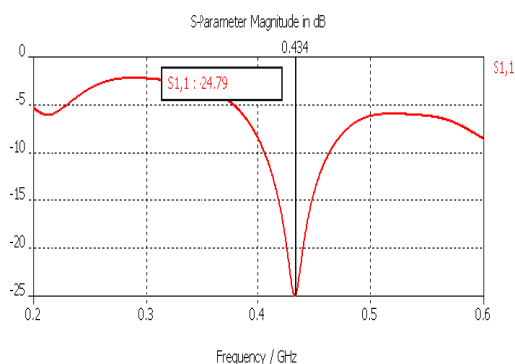


Figure 3: Impedance matching of two-wire Archimedean spiral applicator in wide range of frequencies.

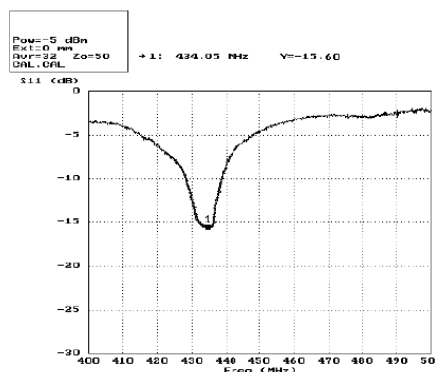


Figure 4: Impedance matching of two-wire Archimedean spiral applicator determined by measurement on SIXPORT.

The depth of effective penetration of the biological tissue is determined using the simulator of electromagnetic field SEMCAD BERNINA 13.4 and the depth is $d = 17$ mm.

6. RESULTS

Our main aim was to discuss the matrix composition of the two-wire Archimedean spiral applicators. From the results based on the simulations in simulator of electromagnetic field CST MICROWAVE STUDIO 2009, assume that this setup is the most suitable applicator for the superficial thermotherapy covering the largest area of tissue. Effective field size of the single applicator is 63% [3]. The measured impedance matching to the biological tissue is presented in Fig. 4. When

composed together in the shape of five spiral applicators, this setup is capable of effectively heating the superficially located tumors.

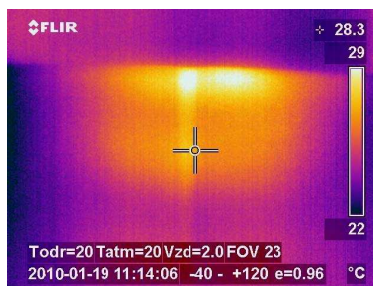


Figure 5: The thermal image of the SAR distribution in the agar phantom of the biological tissue, determined using the thermo camera FLIR P25.

7. CONCLUSIONS

As shown on previously presented results, the applicator is suitable for clinical practice where it can be used as a part of local superficial hyperthermia treatment. For a brief revision, the basic parameters of this applicator are: effective area of the aperture 63%, depth of effective penetration $d_{1/2} = 17$ mm and, naturally, the value of reflection coefficient $S_{11} = -15.6$ dB.

From the thermal image as shown on Fig. 5 we can assume that the constructed applicator is capable of heating superficially located tissues.

REFERENCES

1. Horsman, R. M., "Tissue physiology and the response to heat," *International Journal of Hyperthermia*, Vol. 22, No. 3, 197–203, 2006.
2. Falk, H. M. and R. D. Issels, "Hyperthermia in oncology," *International Journal of Hyperthermia*, Vol. 17, No. 1, 1–18, 2001.
3. Vorlicek, J. and J. Ruzs, "Useful Matlab tool for radio frequency designer," *Technical Computing Prague 2009, Full paper CD-ROM Proceedings*, P. Byron Ed., Humusofts.r.o. & Institute of Chemical Technology, Prague, 2009.

Simulation on Power Handling Enhancement for the Ohmic Contact RF MEMS Switch with Micro-spring Structure

Zhuhao Gong, Huiliang Liu, and Zewen Liu

Institute of Microelectronics, Tsinghua University, Beijing 100084, China

Abstract— This paper presents a RF MEMS (Radio Frequency Microelectromechanical System) switch which is capable of handling high power. By optimizing the design of its contact configuration and cantilever structure, the RF current distribution becomes more uniform through each contact of the multi-contact switch. The novel design of micro-spring cantilever structure also ensures a good contact between the contacts and top electrode when the switch is in the “on” state. The simulation results demonstrate the RF MEMS switch has excellent microwave performance: insertion loss < 0.15 dB, return loss > 31.6 dB and isolation > 14.5 dB from DC to 40 GHz as well as the ability of handling 3.1 W RF power which means a 300% improvement in power handling capability compared with traditional cantilever switch.

1. INTRODUCTION

The past 20 years has witnessed a booming development of the RF MEMS switch. Owing to their low insertion loss, low power consumption, wide frequency bandwidth, high isolation and high linearity, RF MEMS switches are believed to be the promising alternative to the conventional counterparts such as PIN diodes, field effect transistors (FETs) [1] and macro electromagnetic relays [2], which suffer from their disadvantages in high frequency performance, power consumption and linearity. However, the shortcomings of low power handling capability greatly prevent RF MEMS ohmic contact switches from being widely used in defense, industry and other fields of power applications.

The power handling capability of a switch can be defined as the maximum input power before the failure takes place. When the RF current gets through the ohmic contact switch increases, the temperature of the region near the contact will rise rapidly due to the small size of the whole structure and the larger contact resistance compared with the other parts. If the input power continues to grow, it will result in the micromelting and stiction at metal contact interface which causes failure of the switch, which is considered as the main factor of restricting the maximum power that a RF MEMS contact switch can handle.

The diverse range of approaches emerged in recent years to improve RF power handling capability of ohmic contact RF MEMS switch can be generally divided into two categories. One is to choose hard metals such as Platinum (Pt), Ruthenium (Ru) as the material of contact instead of Au-to-Au contact which would easily fail at high temperature [3]. A good example of this solution is the commercial contact RF MEMS switch from Radant MEMS Incorporation [4]. The other approach to improve power performance is by the application of novel switch structure design. The structure of multi-contact or multi-switch is proposed to realize the reduction of current through each contact [5–7], while additional hold electrode (pull-up electrode [8] and push-up electrode [9]) is proposed to avoid the self-actuation and adhesion of the RF MEMS switch under high power conditions. In addition, there are some unconventional structures like the 3D power switch based on springs and latches [10].

2. DEVICE OVERVIEW

The top view and cross section of the proposed ohmic contact switch are shown in Fig. 1. The structure is based on a cantilever with non-uniform thickness [11] which changes from $4\ \mu\text{m}$ to $1\ \mu\text{m}$ at its tip. This fixed-free cantilever topology is chosen because it has smaller size and lower pull-in voltage than fixed-fixed beam design. The thinner part at the tip of the cantilever, acting as a micro-spring which results in a larger deformation under the same actuation voltage, makes it easier to realize a stable contact without degrading the spring constant of the whole cantilever much. This advantage is especially important in multi-contact switch with thick top electrode for power application. Due to electromagnetic effect (skin effect and proximity effect) at high frequency, RF currents concentrate on the edges of transmission lines and tend to pass mostly by the outer contact dimples when the switch is in the “on” state. Thus, the contacts are configured in a 2×2 array to get more even current distribution instead of the traditional parallel contacts

configuration. The 4 contacts on the signal line, with a size of $8\ \mu\text{m} \times 8\ \mu\text{m}$ and a height of $0.4\ \mu\text{m}$, form Au-to-Au contact with the cantilever together. The holes on the top electrode are applied to improve the speed of releasing sacrificial layer and reduce the influence of the squeeze film damping.

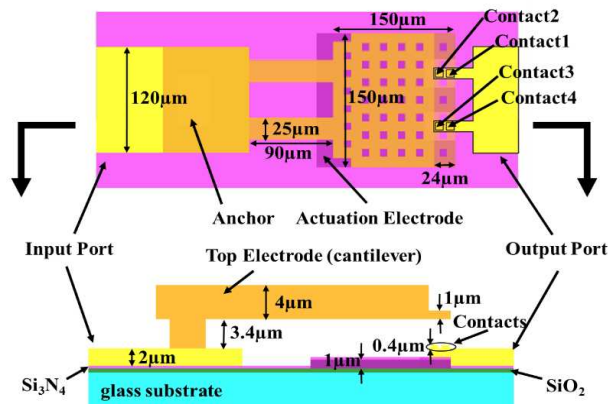


Figure 1: Top view and cross section of the ohmic contact switch.

3. DESIGN AND SIMULATION

3.1. Mechanical Design

The switch for power applications is often proposed with thick top electrode of high spring constant which could offer large restoring force in order to lower down the possibility of failure caused by adhesion. But it's hard for thick cantilever and beam to make a stable contact especially when there are more than two contacts unless a large actuation voltage is supplied at the risk of breaking down. Furthermore, process variation and residual stress induces distortion of movable parts so that the contact area may not be reproducible from device to device. While thinner metal film, with its low spring constant, deforms more easily and is more likely to get a good contact with multiple contact dimples even when the voltage applied is low. A good solution to comprise contact with power performance is to come up with a geometry that its movable part can be constituted of parts with different rigidities. Consequently, a switch based on micro-spring structure cantilever of non-uniform thickness is proposed so that the switch could have large restoring force as well as a good contact in the "on" state.

Mechanical and Electromechanical simulations were performed using CoventorWare to compare the uniform cantilever (with the constant thickness of $4\ \mu\text{m}$) switch with the proposed micro-spring cantilever (with thickness sharply changed from $4\ \mu\text{m}$ from to $1\ \mu\text{m}$) switch in 2×2 contact configuration. Their mechanical properties are summarized in Table 1.

According to the contact force data at $70\ \text{V}$ actuation voltage in Table 1, two contacts in the uniform cantilever switch don't form contact with the cantilever while all of four contacts in the

Table 1: Summary of mechanical properties.

Mechanical properties	uniform cantilever switch	micro-spring cantilever switch
Resonant frequency (Hz)	1.08×10^4	1.23×10^4
Generalized mass (kg)	6.60×10^{-10}	5.03×10^{-10}
Pull-in voltage (V)	33.1	32.8
Release voltage (V)	30.3	30
Contact force of each contact at 70 V actuation voltage (μN)	Contact1	24.07
	Contact2	-
	Contact3	-
	Contact4	23.24

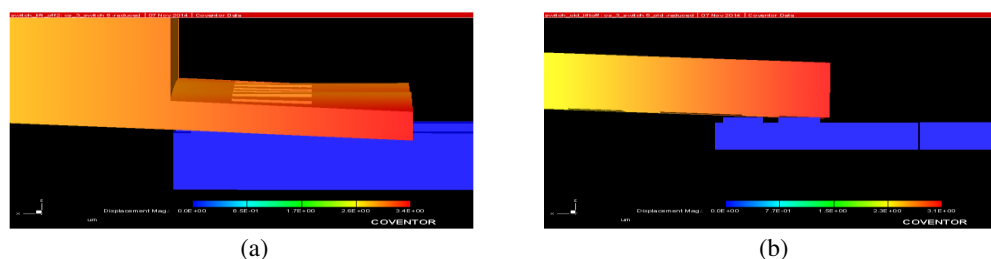


Figure 2: Simulation of the contacts condition by CoventorWare when the actuation voltage is 70 V, (a) uniform cantilever switch, (b) micro-spring cantilever switch.

micro-spring switch are in the contact state. Moreover, it can be seen from Fig. 2 that the thinner part of the micro-spring cantilever switch deflects a lot thus making a good contact with the four contacts, nevertheless, the tip of the uniform cantilever switch has little deformation so that the top electrode can only come into contact with front row of contacts. Therefore, the use of micro-spring cantilever structure has a significant effect in providing a good contact interface for high power multi-contact switches.

3.2. Microwave Performance Simulation

The size of CPW (Coplanar Waveguide) transmission line is optimized to guarantee a good impedance match at the Input and Output port. The finger structure used in signal line region under the cantilever reduces their overlap area as well as coupling capacitances, thereby resulting in an improvement in the isolation.

Figure 3 shows the simulated S -parameters of the uniform cantilever (with the constant thickness of $2\ \mu\text{m}$) switch and the proposed micro-spring cantilever switch through full-wave EM simulator-Ansoft HFSS as well as the measured S -parameters of this uniform cantilever switch [5] which implies a good consistence with the simulated results. The scanning electron micrograph of the uniform cantilever switch with two contacts in parallel is given in Fig. 4. The difference between the theoretical model and fabricated object, caused by process variation and bending upwards of the cantilever in the “off” state, leads to the difference between the simulated and measured results. From DC to 40 GHz, the simulation of the proposed RF MEMS switch exhibits outstanding microwave performance: insertion loss $< 0.15\ \text{dB}$, return loss $> 31.6\ \text{dB}$ (not shown in the figure) and isolation $> 14.5\ \text{dB}$.

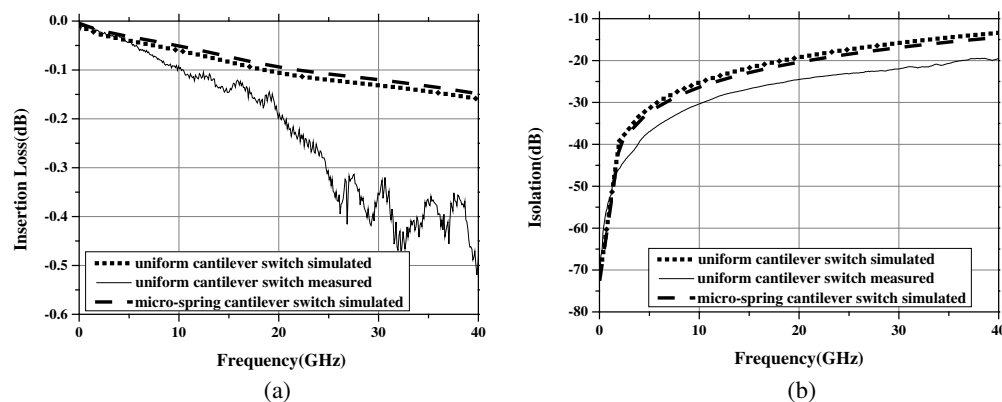


Figure 3: Simulated and measured S -parameters of the uniform cantilever switch and the proposed micro-spring cantilever switch, (a) insertion loss in the “on” state, (b) isolation in the “off” state.

3.3. Power Handling Enhancement Simulation

For ohmic contact RF MEMS switches, the RF power handling capability is typically limited by a localized temperature rise in the contact dimple owing to joule heating of the contact. The relationship among the temperature of the contact T_C , incident power P_{in} and contact resistance

R_C is as Equation (1).

$$T_C = \sqrt{\frac{R_C^2 P_{in}}{4L Z_0} + T_0^2} \tag{1}$$

where T_0 is the ambient temperature, L is the Lorenz number and Z_0 is the transmission line impedance ($50\ \Omega$). It can be seen from the equation that the contact temperature is in proportion to the contact resistance. In order to improve power handling capability of the RF MEMS switch, multiple contacts or multiple switches in parallel configuration are employed to reduce the total contact resistance and contact temperature. However, it is a big challenge to maintain even current distribution across multiple contacts (> 2) in high frequency.

To analyze the RF current distribution across each contact, simulations of the maximum RF current density through each contact in different contact configurations are done with the help of the EM simulator-Ansoft HFSS. The contact resistance in the HFSS switch model is set to be $0.2\ \Omega$ with a RLC module, which is extracted from the measured insertion loss. The simulation results indicate the current in the original switch (Fig. 5(a)) distributes equally between the two contacts with a maximum current density of $1.17 \times 10^4\ \text{A/m}$ at 10 GHz. As the original switch has been

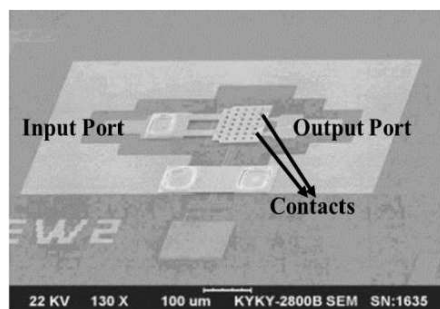


Figure 4: SEM micrograph of the uniform cantilever switch.

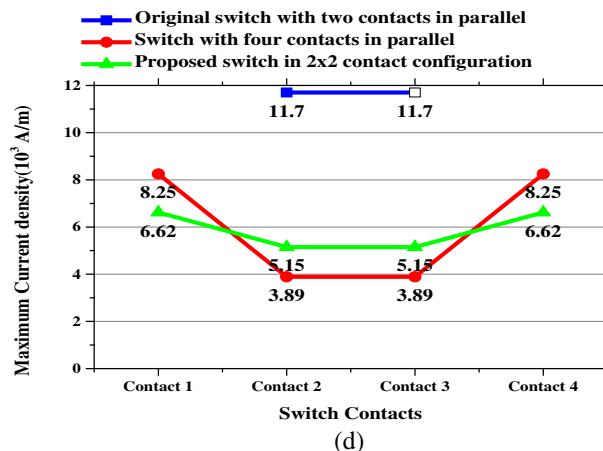
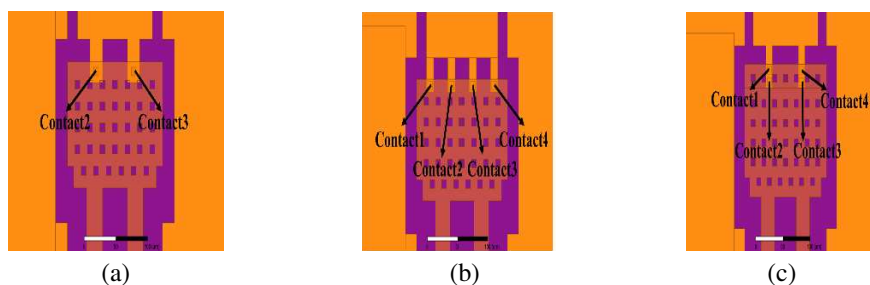


Figure 5: Current distribution in different contact configurations, (a) original switch with two contacts in parallel, (b) switch with four contacts in parallel, (c) proposed switch in 2×2 contact configuration, (d) HFSS simulations of current distribution for different switches with 1 W input signal at 10 GHz.

tested to possess the ability of handling 1 W RF power without failure at the same frequency [5], 1.17×10^4 A/m is set as a critical figure which limits the maximum current density that this kind of switch can operate properly at 10 GHz [12]. In other words, if the current density passes by one contact rises beyond the critical figure (1.17×10^4 A/m), the corresponding joule heat may cause the micromelting and stiction of the contact, eventually leading to the failure of the switch. In the optimized contact configuration, 4 contacts are arranged in 2×2 array (Fig. 5(c)) rather than parallel in a single row (Fig. 5(b)), which shows an improvement in the uniformity of current distribution across each contact as is shown in Fig. 5(d). The maximum current of the switch in 2×2 contact configuration doesn't reach the critical figure until the incident power increases to 3.1 W which implies that the proposed switch can at least deal with 3.1 W RF power at 10 GHz. Compared with the original switch, the power-handling capability of the designed switch improves over 300%.

4. CONCLUSION

A RF MEMS Switch with enhanced power handling capability based on the 2×2 contact array and micro-spring cantilever is proposed in this paper. Simulation results show that the adoption of optimized contact array ensures a more even current distribution between each contact in high frequency and therefore greatly improves its power-handling capability. While micro-spring cantilever structure exhibits a better performance than normal cantilever switch when dealing with the contact of multi-contact configuration for high power application. In addition, the microwave performance of the switch is analyzed and simulated.

ACKNOWLEDGMENT

The authors wish to acknowledge the support from NSFC with project No. 61273061 and Tsinghua University Funds.

REFERENCES

1. Rebeiz, G. M. and J. B. Muldavin "RF MEMS switches and switch circuits," *IEEE Microwave Magazine*, Vol. 2, No. 4, 59–71, 2001.
2. Patel, C. D., and G. M. Rebeiz "An RF-MEMS switch for high-power applications," *2012 IEEE MTT-S International Microwave Symposium Digest (MTT)*, 1–3, Montreal, Canada, June 2012.
3. Kwon, H., et al., "Contact materials and reliability for high power RF-MEMS switches," *IEEE 20th International Conference on Micro Electro Mechanical Systems, 2007. MEMS*, 231–234, Hyogo, Japan, January 2007.
4. Radant MEMS Inc., <http://www.radantmems.com>.
5. Liu, Z., Z. Hou, and Z. Li, "Study on RF MEMS switch with four parallel Ohm contacts for power handling enhancement," *Microwave and Optical Technology Letters*, Vol. 52, No. 3, 665–667, 2010.
6. Nishijima, N., J.-J. Hung, and G. M. Rebeiz, "Parallel-contact metal-contact RF-MEMS switches for high power applications," *17th IEEE International Conference on Micro Electro Mechanical Systems, 2004. MEMS*, 781–784, Maastricht, Netherlands, 2004.
7. Chow, L. L.-W., et al., "Lifetime extension of RF MEMS direct contact switches in hot switching operations by ball grid array dimple design," *IEEE Electron Device Letters*, Vol. 28, No. 6, 479–481, 2007.
8. Peroulis, D., S. P. Pacheco, and L. P. B. Katehi, "RF MEMS switches with enhanced power-handling capabilities," *IEEE Transactions on Microwave Theory and Techniques*, Vol. 52, No. 1, 59–68, 2004.
9. Simon, W., et al, "Designing a novel RF MEMS switch for broadband power applications," *32nd European Microwave Conference, 2002*, 1–4, Milan, Italy, September 2002.
10. Choi, J.-Y., et al, "Three-dimensional RF MEMS switch for power applications," *IEEE Transactions on Industrial Electronics*, Vol. 56, No. 4, 1031–1039, 2009.
11. DiNardo, S., et al., "Broadband rf-mems based spdt," *The 1st European Microwave Integrated Circuits Conference, 2006*, 501–504, Manchester, UK, September 2006.
12. Zhao, C. X., et al, "Power handling capability improvement of metal-contact RF MEMS switches by optimized array configuration design of contact dimples," *Key Engineering Materials*, Vol. 609, 1417–1421, 2014.

Evaluation of Electromagnetic Interference Emitted from Compact Fluorescent Lamps According to CISPR-15

A. Kocakusak¹, M. Cakır^{1,2}, S. Yalcın³, S. Ozen¹, and S. Helhel¹

¹Electrical & Electronics Engineering Department, Akdeniz University, Antalya 07058, Turkey

²Electrical & Electronics Engineering Department, Bayburt University, Bayburt, Turkey

³Electrical & Electronics Engineering Department, Suleyman Demirel University, Isparta, Turkey

Abstract— In this study, Electromagnetic interference (EMI) emitted by the compact fluorescent lamps (CFL) having biggest pie in the market has been investigated according to CISPR-15. Emissions of CFLs vary depending on trademark, since some cannot provide the requirements of CISPR-15 standards such that they act as contaminants in the electric supply system. Conducted analysis considering the limits of CISPR-15 at 150–500 kHz frequency brings out that the effect of CFL produced by Company A at 181.298 kHz is 83.94 dB μ V, whereas the effect of CFL produced by Company D at 173.593 kHz frequency is 49,92 dB μ V, respectively. Obtained results are out of CISPR-15 limits of 66–56 dB μ V.

1. INTRODUCTION

Today, EMC has become more precise issue with the increase of high speed/high frequency electronic devices available commercially at market for daily usage. The CLF lamps were recommended in the 1970s with minimizing the control circuit to be integrated into the cap of a standard lamp [1]. Use of CFL has become widespread in structures such as shopping malls, offices, factories, hotels, houses, schools, hospitals and so on in order to provide more efficient lighting and conserve electrical energy [2]. There are many commercial brands on the market, and some producers do not obey CISPR-15 standards. This irregular production mechanism has forced scientists to focus on EMI problems induced by CFLs present in the market in recent years.

The CFLs emit harmful ultraviolet radiations and the electromagnetic disturbances' fields. According to CISPR 15 F/399/CDV [3], the principal responsible for disturbance emissions is the common mode current, which generates conducted radiations transmitted in the power supply network.

2. COMPACT FLUORESCENT LAMPS AND ELECTROMAGNETICS INTERFERENCE

CFL consists of two separate components named electronic ballast and fluorescent tubes. Ignition of the lamp filaments requires high frequency sources such that those high frequency components are generated in two stages; 50/60 Hz AC to DC conversion is followed by DC to high frequency (20 kHz–40 kHz) AC conversion, and this conversion is basically known as high speed switching. This switching results in EMI emissions that need to be controlled and suppressed by using any standard methods.

2.1. Common Mode Noise and Difference Mode Noise

There are two types of noises throughout any electronics. The first type is differential mode (DM) noise conducted on the signal (VCC) line and GND line in the opposite direction to each other. Differential-mode interference causes the potential of one side of a signal transmission path to be changed with respect to another side. With this type of interference, the interference current path is wholly in the signal transmission path [4]. The second type is common mode (CM) noise conducted on all lines in the same direction. With an AC power supply line, for example, noise is conducted on both lines in the same direction. With a signal cable, noise is conducted on all the lines in the cable in the same direction. Differential mode noise is the current that results from the difference between phase and neutral voltages. Origin of differential mode is an interaction between circuit components. The noise voltage that is developed is the same in both transmission paths [4]. It is shown at Figure 1.

Voltages and currents are calculated for common mode noise as indicated in Eq. (1) and Eq. (2).

$$v_{cm} = \frac{v_p + v_n}{2} \quad (1)$$

$$i_{cm} = i_p + i_n \quad (2)$$

Voltages and currents of differential mode noise described as in Eq. (3) and Eq. (4).

$$v_{dm} = v_p - v_n \tag{3}$$

$$i_{dm} = \frac{i_p - i_n}{2} \tag{4}$$

50 Ω loads of line impedance stabilization network (LISN) are parallel during common mode and serial during differential mode. Thus Eq. (1) and (3) produce Eq. (5), Eq. (2) and (4) produce Eq. (6) [4].

$$v_{cm} = \frac{v_p + v_n}{2} = \frac{50 \Omega \cdot i_p + 50 \Omega \cdot i_n}{2} = \frac{50 \Omega}{2} \cdot (i_p + i_n) = 25 \Omega \cdot i_{cm} \tag{5}$$

$$v_{dm} = v_p - v_n = 50 \Omega \cdot i_p - 50 \Omega \cdot i_n = 2 \cdot 50 \Omega \cdot (i_p - i_n) = 100 \Omega \cdot i_{dm} \tag{6}$$

Conducted emission is assayed by military or civil standards. If the noise exceeds the limits it will have to be separated noise components by current probes or separation methods. The importance of noise separation is underlined by literature to achieve an appropriate filter design [5–7]. Obtained noise components allow us to determine EMI filter components both for common and differential mode.

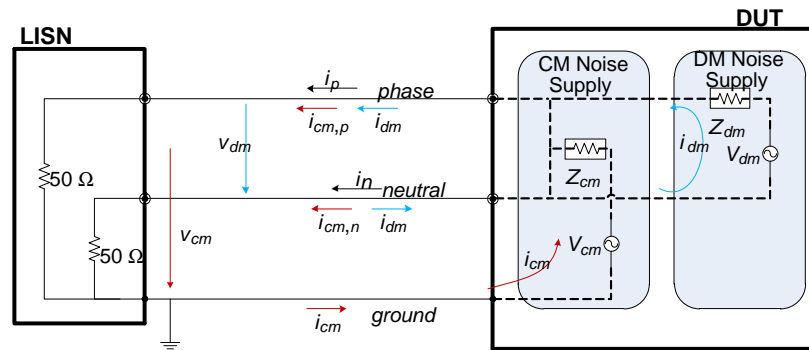


Figure 1: Common mode noise and difference mode noise.

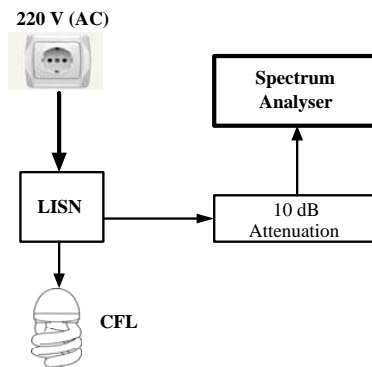


Figure 2: Measurement method of CFL

Table 1: The CISPR-15 limits.

Frequency Range (kHz)	Method	
	Quasi-peak (dBμV)	Average (dBμV)
9–50	110	-
50–150	90–80	-
150–500	66–56	56–46
500–5,000	56	46
5,000–30,000	60	50

3. CONDUCTED INTERFERENCE MEASUREMENTS

Conducted emission (CE) measurements were hold at 3m standard anechoic chamber at EMC Pre-Compliance Test Laboratory at Akdeniz University Industrial Based Microwave Research and Application Center (EMUMAM) [8]. The conducted interferences were measured using a Line Impedance Stabilization Network (LISN), while the levels of perturbations were recorded using an spectrum analyzer. Then the results were compared to CISRP 15 standard limits. Table 1 indicates the CISPR-15 standards' limits, and Figure 2 demonstrates the layout for CFL caused measurements.

4. RESULTS AND CONCLUSIONS

Some trademarks were observed that they are producing noises above the CISPR-15 values in the network, and measured values and limit values are presented in Table 2. Brand A predicts 83.94 dB μ V at 181,298 kHz which is about 18 dB above the permitted limit, Brand B predicts 79.67 dB μ V at 165 kHz which is about 14 dB above the limit and Brand C predicts 80.75 dB μ V at 168,5 kHz about 15 dB above the limit. However, Brand D predicts almost 50 dB μ V at 173,5 kHz which is about 6 dB below the limit. There is only one brand presents below CISPR-15 limits. Due to commercial and economic concerns, it looks that some companies having about 60% total market share are not obey EMC limits of CISPR 15.

Table 2: Measurement results.

Brand	Power (W)	Frequency (kHz)	Measured (dB μ V)	Limit (dB μ V)
A	22	181,298	83,94	66–56
B	20	164,908	79,67	66–56
C	18	168,528	80,75	66–56
D	20	173,593	49,92	66–56

Governments should increase the number of controls to save network, network components and connected devices for harmonics. Those controls will also regulate the market for standard products.

ACKNOWLEDGMENT

This study was supported by Akdeniz University Scientific Research Supporting Unit (BAP), and measurements were carried out at EMC Pre-Compliance Test Laboratory at Akdeniz University Industrial Based Microwave Research and Application Center (EMUMAM) [8] granted by State Planning Organization (2007K120530-DPT).

REFERENCES

1. Letertre, T., A. Azoulay, A. Destrez, F. Gaudaire, and C. Martinsons, "Characterization of compact fluorescent lights RF emissions in the perspective of human exposure," *EMC'09*, 22S3-3, Kyoto, 2009.
2. Ferreira, P. I. L., G. Fontgalland, G. F. Aragao, A. R. Z. Nascimento, R. C. S. Freire, and S. E. Barbin, "Conducted interference reduction from compact fluorescents lamps," *2010 Asia-Pacific International Symposium on Electromagnetic Compatibility*, Beijing, China, Apr. 12–16, 2010.
3. Istok, R., "Relation between disturbance radiation of CFL and resonant frequency of power supply cable," *Advances in Electrical and Computer Engineering*, Vol. 7, No. 1, 23–25, 2007, ISSN: 1582-7445, e-ISSN: 1844-7600.
4. Bockelman, D. E. and W. R. Eisenstadt, "Combined differential and common-mode scattering parameters: Theory and simulation," *IEEE Transactions on Microwave Theory and Techniques*, Vol. 43, No. 7, Jul. 1995.
5. Guo, T., D.-Y. Chen, and F.-C. Lee, "Separation of the common mode and differential mode conducted EMI noise," *IEEE Transactions on Power Electronics*, Vol. 11, No. 3, 480–488, 1996.
6. Paul, C. R., "A comparison of the contributions of common-mode and differential-mode currents in radiated emissions," *IEEE Transactions on Electromagnetic Compatibility*, Vol. 31, No. 2, 0018–9375, 1989.

7. Chiado-Caponet, M. and F. Profumo, “Devices for the separation of the common and differential mode noise: Design and realization,” *IEEE APEC’ 02*, 100–105, Dallas, USA, 2012.
8. <http://emumuam.akdeniz.edu.tr/tr>.

Analysis of the SMOS, MODIS and GCOM-W1 Data during the Growing Season in the Southern Part of the Western Siberia

P. P. Bobrov, A. S. Lapina, and A. S. Yashchenko

Omsk State Pedagogical University, Omsk, Russia

Abstract— A vegetation layer on soil surface makes significant contribution to the surface radiothermal emission. The SMOS Soil Moisture Retrieval Algorithm estimates vegetation attenuation (optical depth) to the soil emission at L-band by LAI data using semi-empirical equations. There are several vegetation indexes calculated by another satellite data. This paper presents the analysis of the SMOS level 2 optical depth data, normalized microwave polarization difference index (MPDI), microwave vegetation index (MVI) derived from GCOM-W1 data and optical vegetation indexes (LAI and NDVI).

1. INTRODUCTION

Soil moisture, as the fundamental parameter for the water resource formation on the land surface, plays an important role in climate changing. At this moment, there are two functioning satellites on orbit suitable for the determination of soil moisture with acceptable accuracy in global scale. The first is the Advanced Microwave Scanning Radiometer (AMSR2) on the GCOM-W1 satellite was launched on May 17, 2012. The second is the Soil Moisture and Ocean Salinity Mission (SMOS) launched on November 2, 2009. A distinguishing feature of SMOS radiometer (MIRAS) is its multi angular measurement capability at L-band (1.4 GHz) on full polarization [1]. The AMSR2 instrument measures radiation at six frequencies in the range of 6.9–89 GHz on dual polarization by conical scan at a fixed incidence angle of 55° [2].

The vegetation layer over the soil surface attenuates soil emission and adds its own contribution to the emitted radiation. These effects at low frequencies can be approximated by a simple model (τ - ω model). Emission from the two-layer medium consists of three terms: 1) the vegetation emission; 2) the vegetation emission reflected by the soil surface; 3) soil emission attenuated by the vegetation canopy. In this case radio brightness temperature is calculated by equation:

$$T_B = (1 - \omega) \cdot (1 - \gamma) \cdot (1 + \gamma R) \cdot T_V + (1 - R) \cdot \gamma T_S, \quad (1)$$

where ω is the single scattering albedo of the canopy; T_S , T_V is temperatures of the soil surface and canopy, respectively, R is the soil reflectivity, $\gamma = \exp(-\tau/\cos\theta)$ is the transmissivity of the vegetation layer, τ is the optical depth.

The vegetation attenuation factor can be computed from the optical depth related to the total vegetation water content (VWC) [3]. However, estimation of VWC at global scale is very difficult. The SMOS Level 2 algorithm uses optical depth data parameterized as a function of the LAI [4]. However, there are other indexes describing the state of vegetation. In this paper we study their relationship for territory of the Southern Part of the Western Siberia.

2. RESULT OF STUDIES

We used SMOS Level 2, AMSR2 Level 1R and MODIS (LAI and NDVI) data during analysis. The SMOS Level 2 data have fixed coordinates of the center pixel (discrete global grid — DGG) in contrast to AMSR2 1R data. We selected the AMSR2-1R pixel with coordinates not to differ from the coordinates of the SMOS Level 1C pixel more than 0.03 degrees on latitude and 0.06 on longitude. The MODIS NDVI data with higher spatial resolution were averaged within a SMOS Level 2 pixel. The GCOM-W1 and MODIS data available in HDF format are in contrast to the SMOS data available in binary XML format. The software for simultaneous processing of flow data in these formats wasn't found. The authors were carried out processing data from different satellites using program created by themselves in MATLAB.

The earliest studies for using satellite microwave radiometer data to assess the state of vegetation has been in [5]. Later microwave vegetation indexes calculated by AMSR-E data with equations [6]

has been proposed

$$\text{MDPI}(f_1) = \frac{T_{BV}(f_1) - T_{BH}(f_1)}{T_{BV}(f_1) + T_{BH}(f_1)}; \quad (2)$$

$$B(f_1 f_2) = \frac{T_{BV}(f_2) - T_{BH}(f_2)}{T_{BV}(f_1) - T_{BH}(f_1)}; \quad (3)$$

$$A(f_1 f_2) = \frac{T_{BV}(f_2) + T_{BH}(f_2) - B \cdot (T_{BV}(f_2) + T_{BH}(f_2))}{2}; \quad (4)$$

where T_{BP} is radio brightness temperature on p -polarization and n -frequency; A and B are microwave vegetation index.

The relationship between MVI, MPDI and SMOS Level 2 optical depth was very weak at the any type of surface (Fig. 1(a)). Moreover, correlation coefficient has a small value and his sign varies from one pixel to another. The relationship between SMOS Level 2 and NDVI was slightly better (Fig. 1(b)).

MODIS 16-day composite NDVI data including MOD and MYD products shifted in time at 8 days. We collected this data into an 8-day composite NDVI product. The AMSR2 data in the time interval of 8 days were averaged. The correlation relation between microwave vegetation index calculated according to Equations (2), (3), (4) by GCOM-W1 data and NDVI was better than it is shown in Figs. 1(a), 1(b) but depends on the type of surface (Figs. 2(a), 2(b)). Among them,

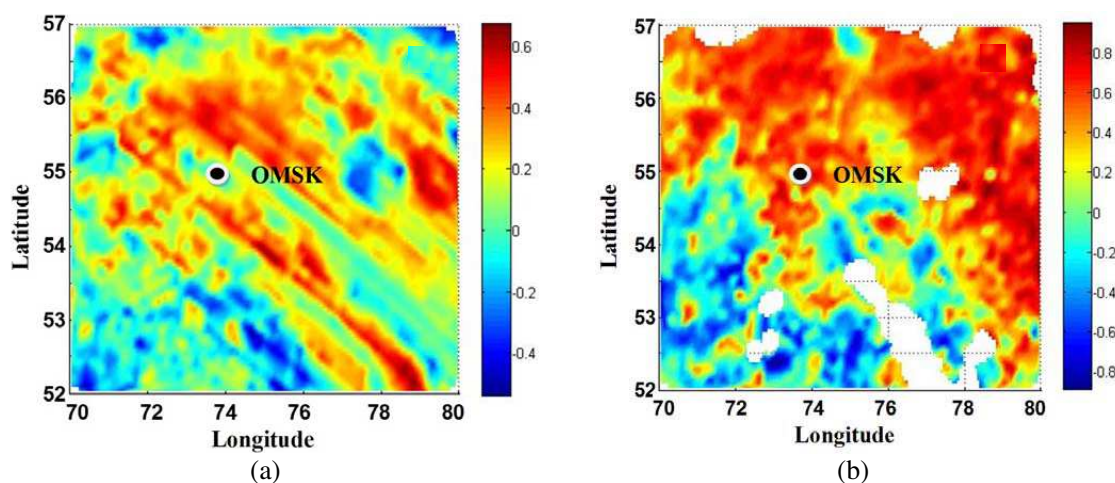


Figure 1: Map of correlation coefficient between (a) MVI_LA (6.9, 10.7 GHz) and SMOS Level 2 optical depth; (b) SMOS Level 2 optical depth and NDVI during the growing season 2013.

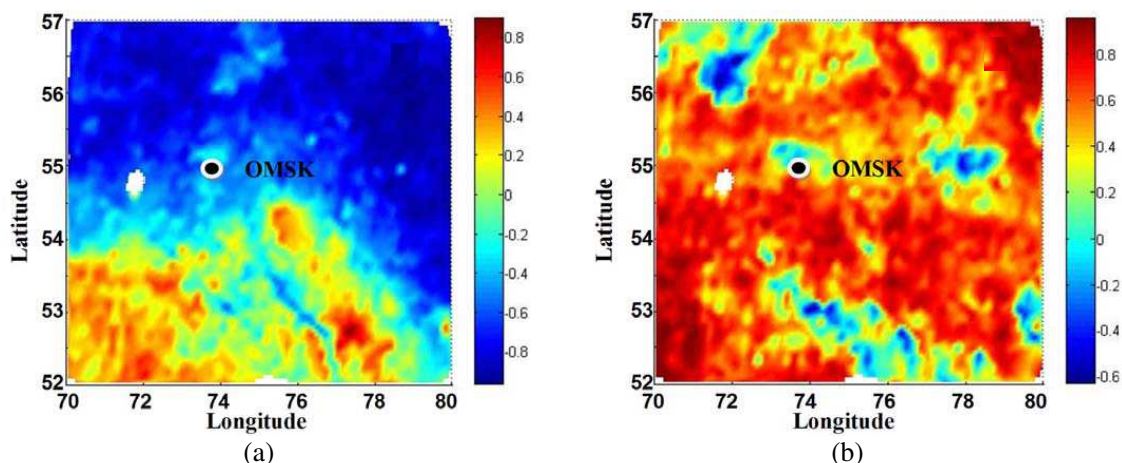


Figure 2: Map of correlation coefficient between (a) MPDI (6.9 GHz) and NDVI; (b) MVI_LA (6.9, 10.7 GHz) and NDVI during the growing season 2013.

the best dependence was observed for indexes MVI and MDPI calculated according to the data at $f_1 = 6.9$ and $f_2 = 10.7$ GHz. As well, on the map shown in Fig. 2(a) the dependence of the sign of the correlation coefficient on the type of surface is observed. This can be explained by the different changes of brightness temperature and NDVI during the growing season for different types of vegetation (Figs. 3(a), (b)). Such dependence between the MDPI and NDVI suggests a possibility of developing an algorithm of quantitative assessment of the vegetation state. The correlation relation between MVI.A (6.9, 10.7 GHz) and NDVI is weakly dependent on the type of vegetation on the surface and mainly determined by the lakes or urban territory in the pixel (Fig. 2(b)).

We also compared LAI (MODIS) and NDVI (MODIS) with ground-based measurements of the vegetation water content (VWC) taken from the southern part of forest-steppe and steppe zone. VWC was determined by thermogravimetric-weight contact method several times during the

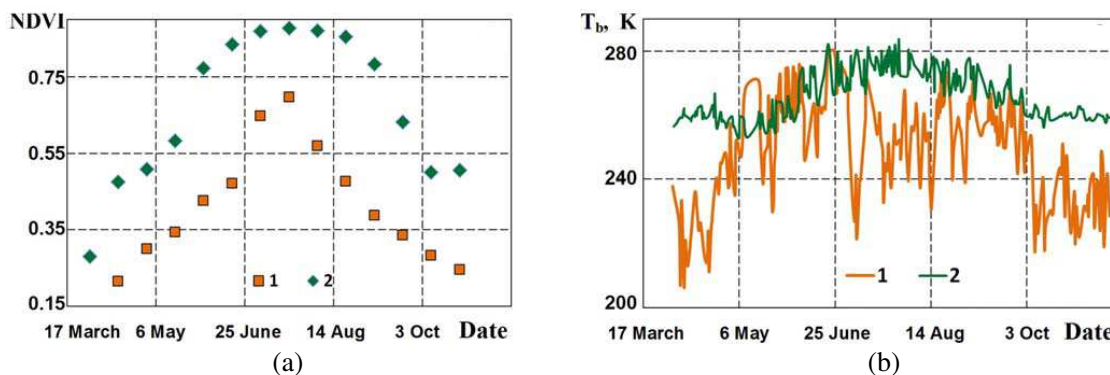


Figure 3: The time dependence of the (a) NDVI and (b) radiobrightness temperature at 6.9 GHz during the growing season 2013 for steppe (1) and *s* southern taiga (2) zone.

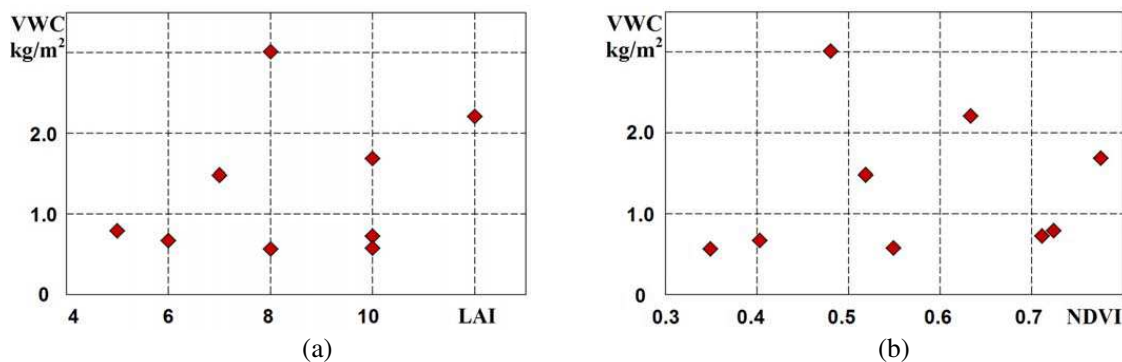


Figure 4: The relationship between (a) VWC and LAI; (b) VWC and NDVI.

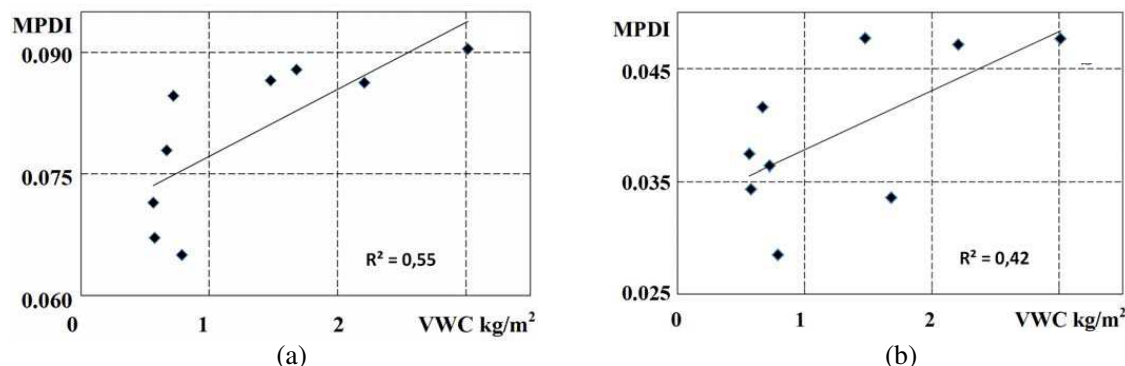


Figure 5: The relationship between VWC and MDPI at (a) 18 GHz; (b) 23 GHz. R^2 is accuracy of approximation, continuous line is trend.

season. Sample was carried out on agricultural fields and meadows near the center of SMOS Level 2 pixel. The correlation relation between LAI, NDVI and VWC was extremely low (Fig. 4). As it can be seen from the data the dependence between them is extremely low. However, for the final conclusions it must be a greater number of ground-based measurements.

The correlation relation between VWC and MDPI at frequencies of 18 GHz 23 GHz was better (Fig. 5). This dependence is observed despite the fact the ground measurements were carried out at a small number of points and a very large size of GCOM pixel in comparison with NDVI and LAI.

3. CONCLUSION

At this moment, a number of vegetation indexes describing the state of vegetation layer was proposed. All of them are qualitatively in good agreement with the processes occurring during the growing season. However, the relationship between the coefficients is extremely ambiguous. To the Southern Part of Western Siberia the best relationship is observed between MVI (6.9, 10.7 GHz), MPDI (6.9, 10.7 GHz) and NDVI. Preliminary data suggest about the perspective of methods of assessing state of vegetation using GCOM-W1 microwave data. The main problem appearing in the choosing of an index to assess the state of vegetation is the data validation.

ACKNOWLEDGMENT

This work was supported by Ministry of Education and Science of the Russian Federation through project 2014/336/1744.

REFERENCES

1. ESA EO Missions: SMOS//URL:<https://earth.esa.int/web/guest/missions/esa-operational-eo-missions/smos>.
2. SHIZUKU (GCOM-W1) to Provide Geophysical Quantity Product//URL: http://global.jaxa.jp/press/2013/05/20130517_shizuku_e.html.
3. Jackson T. J. and T. J. Schmugge, "Vegetation effects on the microwave emission of soils," *Remote Sens. Environ.*, Vol. 36, No. 3, 203–212, 1991.
4. Kerr, Y. H., P. Waldteufel, P. Richaume, J.-P. Wigneron, et al., "The SMOS soil moisture retrieval algorithm," *IEEE Trans. Geosci. Remote Sens.*, Vol. 50, No. 5, 1384–1403, 2012.
5. Choudhury, B. J. and C. J. Tucker, "Monitoring global vegetation using Nimbus-7 37 GHz data: Some empirical relations," *International Journal of Remote Sensing*, Vol. 8, No. 7, 1085–1090, 1987.
6. Shi, J., T. Jackson, J. Tao, J. Du, R. Bindlish, L. Lu, and K. S. Chen, "Microwave vegetation indices for short vegetation covers from satellite passivemicrowave sensor AMSR-E," *Remote Sensing of Environment*, Vol. 112, No. 12, 4285–4300, 2008.

A Spread Spectrum Clock Generator Using Discontinuous Modulation Technique for Reduction of Time Interval Errors

Taiming Piao, Jae-Kyung Wee, Inchaee Song, and Boo-Gyoun Kim
School of Electronic Engineering, Soongsil University, Seoul, Korea

Abstract— In this paper, we propose a novel discontinuous spread spectrum clock generator with a low maximum time interval error (MTIE) and low electromagnetic interference (EMI). The proposed circuitry was fabricated with 0.35 μm CMOS process and operated with 3.3 V supply voltage at the average center frequency of 100 MHz. The measured results showed the MTIE of 11.59 ns with the EMI reduction of 14.57 dBm.

1. INTRODUCTION

Nowadays, faster operating speed of automotive electronic units brings about such serious problems as functional failures due to electromagnetic interference at high frequency [1, 2]. An effective solution to diminish EMI is to modulate system clock frequency, which is known as a spread spectrum clock (SSC). This method reduces EMI by spreading energy of discrete frequency harmonics over a wide range of frequencies. However, asynchronous serial data protocols in vehicle networks require a strict time interval error (TIE) range because receivers in asynchronous CAN circuitry may detect wrong data when the TIE is out of range [2].

Several methods have been reported to find efficient solutions considering trade-offs between the TIE and EMI reduction. One method solving the TIE issue is to reduce a modulation index. While this approach reduces the MTIE, it degrades the EMI reduction [3]. Another method reported in [2, 4] can reduce the MTIE without sacrifice of EMI performance. However, its implementation needs complex and large additional circuitry. In this paper, we propose novel SSC technique which satisfies requirement on the MTIE and reduces EMI effectively in asynchronous vehicle networks.

2. DESIGN DESCRIPTIONS

2.1. EMI Reduction and MTIE

When a conventional triangular modulation profile is adopted for SSC, the reduction of EMI peaks can be estimated by Equation (1) [5]. In Equation (1), f_c , A_{mo} and F_{mo} are center spread frequency, modulation depth, and modulation frequency, respectively. In the center-spread method, the TIE is varied from 0 to MTIE within one modulation cycle. The MTIE level is also given in Equation (1) as a function of A_{mo} and F_{mo} [2, 5].

$$\text{EMI Peak Reduction} = 10 \times \log \left[\frac{A_{mo} \times f_c}{F_{mo}} \right], \quad \text{MTIE} = \frac{A_{mo}}{8 \times F_{mo}} \quad (1)$$

$$\text{EMI Peak Reduction} = 10 \times \log [8 \times \text{MTIE} \times f_c] \quad (2)$$

Equation (2) shows EMI peak reduction expressed with MTIE and f_c . In general, the higher MTIE gives rise to the higher EMI peak reduction as shown in Equation (2). However, requirement on the MTIE limits the use of SSC for asynchronous interfaces. Therefore, a new method to effectively reduce MTIE becomes indispensable in automotive networks requiring low EMI generation.

2.2. Proposed Discontinuous Modulation Technique

Figure 1 shows concepts of the conventional SSC and the proposed discontinuous spread spectrum clock (DSSC). Figure 1 also shows comparison between theoretical TIE plots. The proposed method is based on up-spread spectrums while the conventional SSC uses the center-spread spectrums with respect to the center frequency (Non-SSC frequency). In the conventional method, the modulation index (A_{mo}/F_{mo}) should be properly reduced to comply with the allowed MTIE. On the other hand, the proposed method can control TIE within the allowed MTIE by resetting TIE with selection of its half-frequency clock whenever the TIE runs over one clock cycle. Therefore, the proposed modulation depth A_{mo-p} can be larger than A_{mo-c} of the conventional SSC. The proposed DSSC technique with high modulation depth can reduce EMI effectively while maintaining the targeted MTIE.

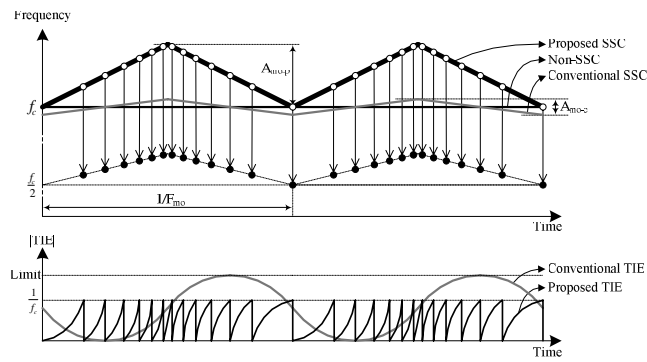


Figure 1: Comparison between the conventional SSC and the proposed DSSC.

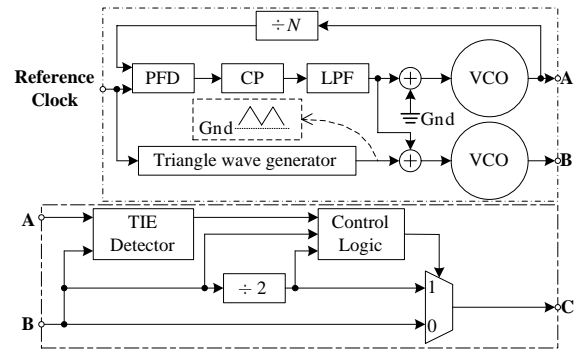


Figure 2: Block diagram of the proposed discontinuous modulation SSC (signal A: Non-SSC, signal B: Up-SSC, signal C: DSSC).

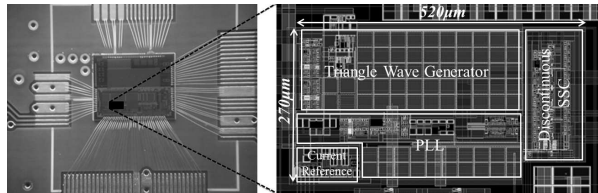


Figure 3: Test chip photograph and layout.

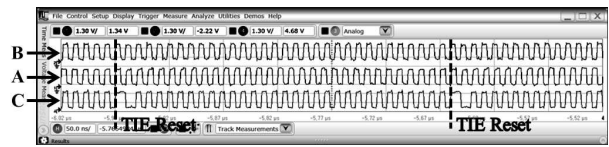


Figure 4: Measured discontinuous modulation SSC (signal A: Non-SSC, signal B: Up-SSC, signal C: DSSC).

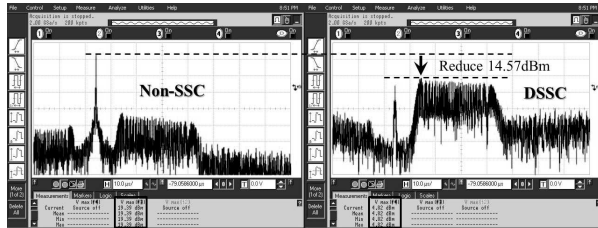


Figure 5: Measured spectrums of the output signals (DSSC and Non-SSC).

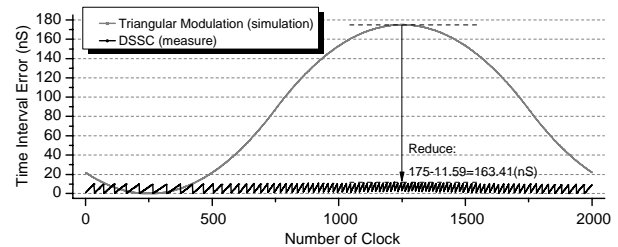


Figure 6: Measured time interval error.

2.3. Circuit Descriptions

Figure 2 shows the block diagram of the proposed discontinuous modulation SSC which consists of a PLL (Non-SSC) block, an up-spread spectrum clock (Up-SSC) block, a TIE detector, and a tiny control logic block. The Non-SSC clock is generated at the node A and the Up-SSC is simultaneously generated at the node B. In the next stage, the TIE detector compares the signal B with the signal A. It checks out whether the accumulated TIE is within one clock cycle. The detected signal is transferred into the Control Logic. The Control Logic and MUX select Up-SSC clock or its half-frequency clock generated through the $1/2$ divider. If the accumulative TIE reaches one clock cycle, the TIE is reset to zero by selection of the half-frequency clock. The repeating reset sequence can always keep the MTIE within one clock cycle. The photograph of the test module and the chip layout are shown in Figure 3. The designed chip size is $520\ \mu\text{m} \times 270\ \mu\text{m}$. The chip was fabricated with $0.35\ \mu\text{m}$ CMOS process and operated with $3.3\ \text{V}$ supply voltage.

3. MEASUREMENT RESULTS

The fabricated chip was tested with the modulation frequency (F_{mo}) of $50\ \text{kHz}$ and the modulation depth (A_{mo}) of 7% with respect to the center frequency (Non-SSC frequency) of $100\ \text{MHz}$. Figure 4 shows the measured clocks of Up-SSC (B), Non-SSC (A), and DSSC (C). It shows that the measured DSSC (C) resets the TIE to be zero whenever the TIE of Up-SSC is accumulated over one period of Non-SSC clock. Figure 5 shows the measured EMIs of the Non-SSC and the DSSC. The EMI characteristic of the DSSC was reduced by $14.57\ \text{dBm}$. Figure 6 shows comparison between the

simulated TIE of the conventional SSC and the measured TIE of the DSSC under the same EMI performance. The MTIE of the proposed DSSC is improved from 175 ns to 11.59 ns; i.e., by MTIE reduction of 163.4 ns.

4. CONCLUSION

The proposed SSC with discontinuous modulation technique can reduce EMI peaks while maintaining very low TIEs compared with the conventional SSC. Therefore, this scheme is very useful to apply to asynchronous interfaces where a strict MTIE and relatively low EMI are required. The measured results show that the EMI level is reduced by 14.57 dBm compared with the Non-SSC and the MTIE is 11.6 ns at the target frequency of 100 MHz.

ACKNOWLEDGMENT

This research was supported by a grant “High efficient heat rejection and supply technologies for zero emission vehicle (10035530)” from the Korea Evaluation Institute of Industrial Technology.

REFERENCES

1. Chang, H., et al., “A spread-spectrum clock generator with triangular modulation,” *IEEE Journal of Solid-State Circuits*, Vol. 38, No. 4, 673–676, Apr. 2003.
2. Steinecke, T., “Low-jitter frequency-modulated PLL,” *Asia-Pacific Symposium on Electromagnetic Compatibility*, 329–332, May 2012.
3. Zhou, J. and W. Dehaene, “A synchronization-free spread spectrum clock generation technique for automotive applications,” *IEEE Trans. Electromagn. Comp.*, Vol. 53, No. 1, 169–177, Feb. 2011.
4. Da Dalt, N., et al., “An all-digital PLL using random modulation for SSC generation in 65 nm CMOS,” *Solid-State Circuits Conference Digest of Technical Papers (ISSCC)*, 252–253, Feb. 2013.
5. Komatsu, Y., et al., “Bi-directional AC coupled interface with adaptive spread spectrum clock generator,” *Proceedings of IEEE Asian Solid-State Circuits Conference*, 71–74, Nov. 2007.

Effect of Neutral Grounding Methods on the Earth Fault Characteristics

Abdallah R. Al-Zyoud¹, A. Alwadie², A. Elmitwally², and Abdallah Basheer³

¹Electrical Engineering Department, Albalqa Applied University, Jordan

²Electrical Engineering Department, Najran University, Saudi Arabia

³National Electrical Power Company, Jordan

Abstract— Medium voltage (MV) distribution systems use different methods for grounding the neutral point. Influences of these grounding methods on the single line to ground (SLG) fault characteristics are discussed in this paper. Jordanian MV network is used as a case study. The network has both underground cables and overhead lines. Simulation models are implemented in both MATLAB/SIMULINK, and DigSilent/Power Factor software. The models allow detailed investigation of the different fault factors and grounding methods. Results are obtained to evaluate the impact of each grounding method on the SLG fault features. Isolated neutral, solid grounding, resistance grounding and Petersen coil (Arc suppression coil) grounding are compared for different fault locations, fault incidence angles, and fault resistances. Current and voltage waveforms, as well as symmetrical components are used to describe the fault case.

1. INTRODUCTION

The method of grounding has a small influence during normal operation of the system, but becomes important and effective when an earth fault occurs to an overhead line (OHL) or an underground cable (UGC). The selection of system grounding method requires deep analysis. The correct grounding solution may be obtained through a great amount of calculations and simulations of the network during fault. The different grounding methods, in common use are:

- a) Solidly or direct grounding (effective grounding).
- b) Unearthed or Isolated neutral (floating neutral point).
- c) High impedance (resistance) grounding.
- d) Low impedance (resistance) grounding.
- e) Resonant or Petersen Coil grounding (compensated grounding).

A fault on a power system is an abnormal condition that involves failure risks of power system equipment. Generally, two types of failures can occur. The first is an insulation failure that results in a short circuit fault. The second is a failure that results in an interruption of current flow. Short circuit faults can occur between phases, or between phases and earth, or both. When the system is grounded by a low resistance or directly (solidly) grounded, the fault current will be very large. The characteristics of earth-fault current depend on the method of neutral point grounding as shown in this paper.

Many researchers in the past few years discussed the correlation between different types of neutral grounding and earth-fault, including fault localization and detection in MV networks. Jordanian utility in general uses direct or through resistance grounding without considering the nature of the MV feeders and their different configurations.

In [1–4], the authors compared between different types of neutral grounding. The authors in [5–8] studied the system currents and voltages behavior during fault, for the different system parameters. Isolated neutral systems have small fault current levels. These currents depend generally on the capacitances between the phases and the ground. Many researchers developed protection algorithms for compensated networks with high shunt capacitive connections [9–13]. Voltages and currents have non-sinusoidal evolution during the fault occurrence and clearance periods because of a component called dead-beat or free component as discussed in [11]. Analysis of overvoltages generated by SLG faults in Petersen coil grounded MV networks is presented in [14]. The authors in [15] studied the impact of some neutral grounding methods on the fault characteristics in Al Ain distribution company in UAE. Some experimental fault cases were tested under different conditions on a distribution company in Czech republic with Petersen coil grounding. The findings are reported in [16]. Ref. [17] presents an analysis and comparison of earth fault characteristics in the medium voltage distribution networks (20 kV) with high impedance grounding. The results are based on

the evaluation of 476 real case data recordings, obtained from substations of distribution networks, during the observation period of 3 years. The study dealt with the clearing of earth faults, arcing fault characteristics, appearance of transients and magnitudes of fault resistances.

The paper presents fault simulation models implemented in MATLAB/SIMULINK, and DigSilent/Power Factory. The created models allow for detailed investigation of different factors including the method of grounding the neutral point. Grounding transformers, MV distribution lines, and their accurate parameters are included. In the studied Jordanian electrical power system, the neutral grounding is by resistance for both OHL's feeders and UGC's feeders irrespective of their lengths. The single line to ground (SLG) fault currents and voltages are compared for different fault locations, fault resistances, and grounding methods. This can help to select the most proper grounding system for a specific network.

2. SINGLE PHASE TO GROUND FAULT ANALYSIS

The following simplifications are normally made:

- All currents are considered to be zero before the occurrence of the fault.
- Shunt elements in the transformer model are neglected.
- Shunt capacitances of transmission lines in most cases are neglected, but it is considered in case of UGC's.

2.1. Resistance Earthed Networks

Figure 1 shows modeling of earth fault in a network with resistance earthed neutral for a fault at the end of the cable feeder.

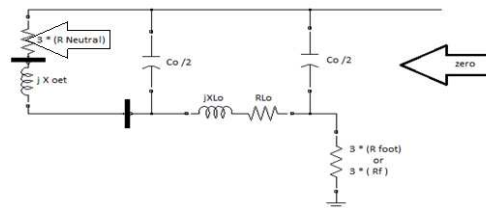


Figure 1: Zero sequence network of resistance earthed system.

The earth fault current in resistance earthed system is [2, 3]:

$$I_f = \frac{3E}{Z_1 + Z_2 + Z_0 + 3R_f} \tag{1}$$

where, E is the phase voltage, Z_1 is the positive sequence impedance, Z_2 is the negative sequence impedance, Z_0 is the zero sequence impedance. R_f is fault resistance and R_{foot} is footing resistance of the faulted tower.

Taking into account the capacitance of the specific faulted feeder only, I_f consists of resistive and reactive components as ($R_f = 0$):

$$I_f = I_R + jI_C = \frac{E}{R_n} + j3\omega C_0 E \tag{2}$$

where, R_n is the neutral grounding resistance.

The magnitude of the neutral displacement voltage will be:

$$V_{0n} = \frac{I_f}{\sqrt{\left(\frac{1}{R_n}\right)^2 + (3\omega C_0)^2}} \tag{3}$$

2.2. Compensated Earthed Networks

Figure 2 shows the modeling of earth fault in a network with resonant earthed neutral for a fault at the end of the cable feeder.

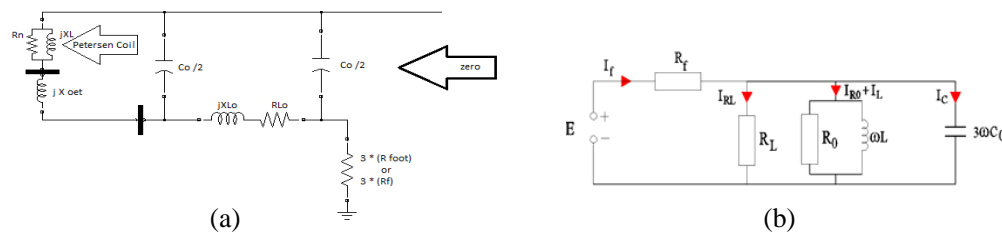


Figure 2: Model of a resonant-earthed neutral system, (a) zero sequence network, (b) Thevenin's equivalent circuit of the zero sequence network.

The solid earth fault current is determined by [2, 3]:

$$I_f = \left[\frac{R_L + R_0}{R_L R_0} \right] E + j \left[3\omega C_0 - \frac{1}{\omega L} \right] E \quad (4)$$

Coil tuning condition is achieved when:

$$3\omega C_0 - \frac{1}{\omega L} = 0 \quad (5)$$

In case of complete compensation, $3LC\omega^2 = 1$, the solid earth fault current will be:

$$I_f = \frac{R_L R_0}{R_L + R_0} E \quad (6)$$

The displacement of neutral point voltage will be:

$$V_{0n} = E \frac{Z_0}{Z_{0f}} \quad (7)$$

where,

$$R_e = \frac{R_L R_0}{R_L + R_0}, \text{ and } Z_{0f} = \frac{(R_e \cdot jX_0) + R_f(R_e + jX_0)}{R_e + jX_0}.$$

X_0 : Equivalent reactance of zero sequence network.

Z_0 : Equivalent impedance without fault resistance.

Z_{0f} : Equivalent impedance in the presence of fault resistance.

3. THE SYSTEM UNDER STUDY

A real system in Jordan (Tareq S/S) is used as a case study. The network is depicted in Figure 3 and consists of:

- A three 80 MVA three phase transformers 132/33 kV with YNd1 connection.
- 200 KVA three phase transformers 33/0.4 kV with ZNyn11 connection. This creates an artificial neutral point for grounding. The zero sequence impedance of this transformer is 38.8 Ω /phase (given by the manufacturer).
- Feeders, connected to the MV busbar, and made up of 7 UGCs, and 3 OHLs. The OHL is made up of ACSR (Aluminum Conductor Steel Reinforced) conductors with 150 mm² cross section area, while the UGC is made up of aluminum conductors with XLPE (Cross Linked Polyethylene) insulation, with 300 mm² cross section area.
- The existing grounding method is by a resistance of 19.05 ohm. This resistance is connected to a collecting point for the three neutral points of the zigzag transformers.

Simulation models of the system are constructed in both MATLAB/SIMULINK and DIGSILE-NT environments. Simulation results are presented and compared to the analytically calculated ones.

4. SIMULATION RESULTS

Investigation of SLG faults on "Safe way A" feeder (single circuit UGC feeder) for all different cases of neutral point grounding is presented. Digsilent program results are displayed by figures that show:

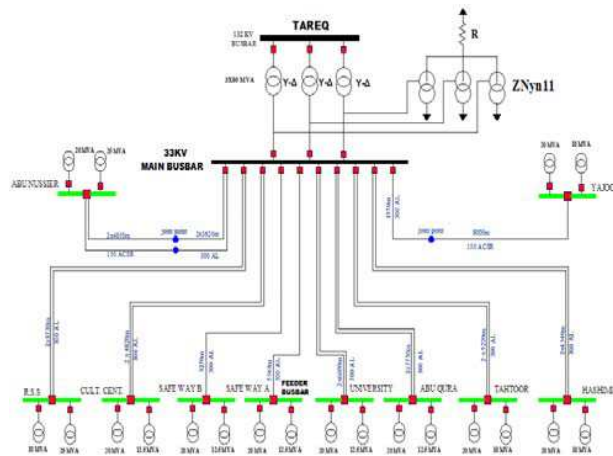
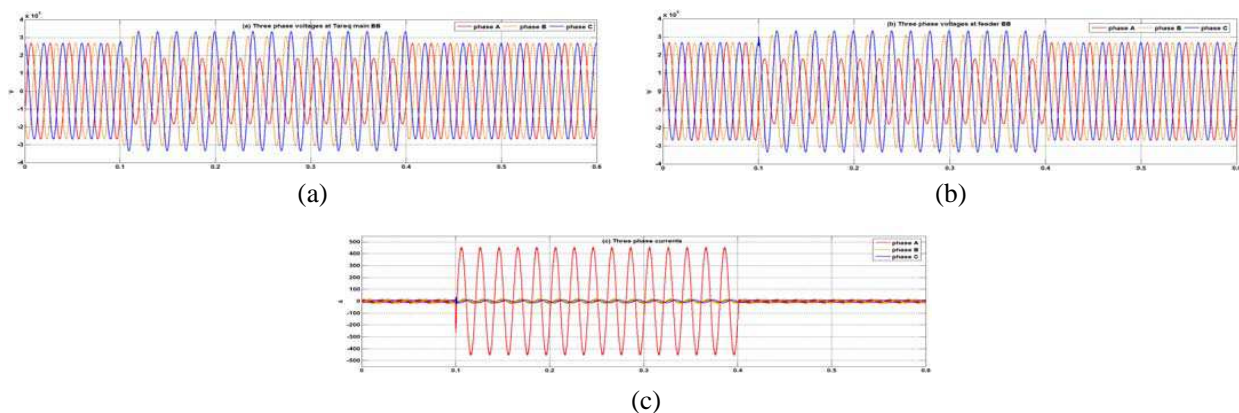


Figure 3: Single line diagram of case study system.

Figure 4: Fault at the end of the line (Safe way A), for low resistance grounded system, $R_f = 40 \Omega$, (a) three phase voltages at Tareq main BB, (b) three phase voltages at feeder BB, and (c) three phase currents.

- i Fault impedance in ohm (resistance R_f and reactance X_f).
- ii Feeder under consideration (i.e., the label of faulted feeder) for example, “Safe way A” feeder.
- iii Sequence voltages (labeled as 0-1-2 sequence voltages, U_0 , U_1 , and U_2) in kV with phase angles in degrees.
- iv Short circuit level in MVA (labeled as “Sk”).
- v Short circuit current (labeled as I_{kss}) in kA with phase angle in degrees.
- vi Sequence currents (labeled as 0-1-2 sequence currents, I_0 , I_1 , and I_2) in kA with phase angles in degrees.
- vii Example feeder line to ground voltages (labeled as A, B, C values at observation location) in kV with phase angle in degrees. It shows the statement “SHC on line: Safe way A” which means short circuit on the example feeder “Safe way A”.

4.1. Low Resistance Grounding

Assume an A-G fault at the end of the line (Safe way A) with $R_f = 40 \Omega$. The presence of R_f , in addition to the grounding resistance, causes an appreciable reduction in distortion of voltages and currents waveforms. The fault current and the phase voltages obtained by the two softwares are shown in Figures 4–6. The neutral displacement voltage is less than 6 kV as determined by both softwares.

4.2. High Resistance Grounding

For A-G fault at the end of the line (Safe way A) with $R_f = 40 \Omega$, simulation results are shown in Figures 7–9. The current flow in the neutral is limited, while the current at fault location is higher because of the contribution of capacitive currents. Neutral displacement voltage and neutral current curves at clearance time do not converge to zero value instantaneously because of the nine

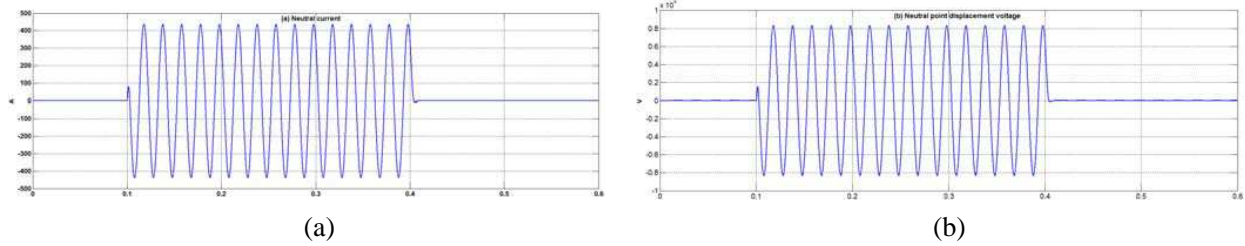


Figure 5: Fault at the end of the line (Safe way A), for low resistance grounded system, $R_f = 40 \Omega$, (a) neutral current and (b) neutral point displacement voltage.

Verification		Short-circuit calculation complete		Single phase to ground /	
Short-circuit duration	0.10 s	Fault impedance	Resistance, R_f	40.00 Ohm	
			Reactance, X_f	0.00 Ohm	
Short circuit location		0-1-2 Sequence voltages [kV] [deg]		shc	
safeway A		U1	19.41 -42.94	A	6.613 0.347 145.08
		U2	0.15 -147.90	B	0.000 0.000 0.00
		U0	5.99 116.79	C	0.000 0.000 0.00
				2kss	0.116 145.08
					0.116 145.08
					0.347 145.08
Grid: Tareq Feeders		System Stage: Tareq Feeders		Annex: / 2	
rtd.v. Line to Ground Voltages [kV] [deg]		0-1-2 Sequence Voltages [kV] [deg]		shc Currents [kA] [deg]	
Values at Observation Location				0-1-2 Sequence Currents [kA] [deg]	
shc on line: safeway A		A	13.88 -34.08	U1	19.41 -42.94
		B	21.13 -178.88	U2	0.15 -147.90
		C	21.46 86.18	U0	5.99 116.79

Figure 6: Digsilent outputs for low resistance grounded system, Fault is at the end of the line (Safe way A), $R_f = 40 \Omega$.

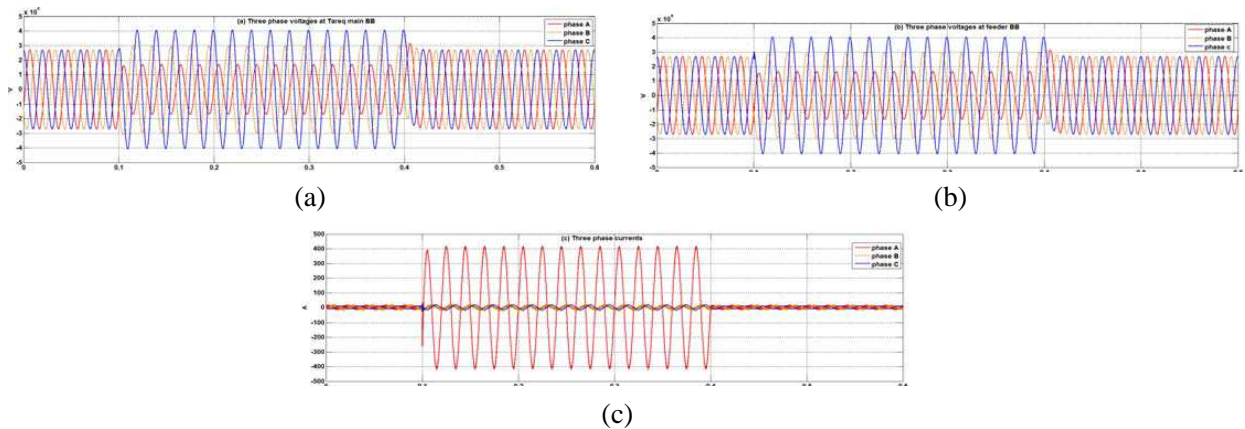


Figure 7: Fault at the end of the line (Safe way A), for high resistance grounded system, $R_f = 40 \Omega$, (a) three phase voltages at Tareq main BB, (b) three phase voltages at feeder BB, and (c) three phase currents.

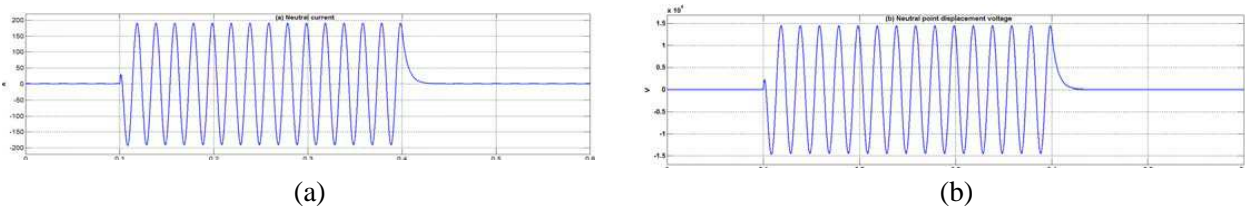


Figure 8: Fault at the end of the line (Safe way A), for high resistance grounded system, $R_f = 40 \Omega$, (a) neutral current and (b) neutral point displacement voltage.

healthy feeders affecting the response of currents and voltages. In case the healthy feeders are disconnected the neutral current converge to zero instantaneously. The location of the fault and the presence of R_f in addition to HRG explains why small fault current exists. The disturbances and distortion disappears because of R_f existence and the fault location is far away from the supply point. The figures show similar results for the two softwares.

verification		Single Phase to Ground /									
Short-circuit calculation complete											
Short-Circuit Duration		Fault Impedance									
Break Time		Resistance, Zf		0.00 ohm							
		Reactance, Xf		0.00 ohm							
Short circuit location		0-1-2 sequence voltages [kV] [deg]				I _{sk} [] []		I _{skss} [] []		0-1-2 sequence currents [] []	
safeway A		U1	19.43	-89.85	A	0.485	0.025	178.67	I1	0.008	178.67
		U2	0.02	-114.43	B	0.000	0.000	0.00	I2	0.008	178.67
		U0	19.46	110.12	C	0.000	0.000	0.00	I0	0.025	178.67
Values at observation location		rtd.v. Line to ground voltages [kV] [deg]		0-1-2 Sequence voltages [kV] [deg]		I _{sk} [MVA]		Currents [kA] [deg]		0-1-2 Sequence currents [kA] [deg]	
smc on line: safeway A		A	0.00	-46.30	U1	19.43	-89.85				
		B	31.89	140.12	U2	0.02	-114.43				
		C	31.71	80.16	U0	19.46	110.12				

Figure 12: Digsilent outputs for Petersen coil grounding system, Fault at the end of the line (Safe way A), $R_f = 0 \Omega$.

Table 1: MATLAB results for petersen coil grounding, fault at the end of the line (Safe way A), $R_F = 0 \Omega$.

Neutral Voltage	19432.20 Vrms -179.74°
Neutral Current	24.74 Arms 90.33°
Compensated Fault Current	472.73 Arms 89.41°

cable length), the zero sequence capacitance is approximately $0.28 \mu\text{F}/\text{km}$, the total capacitive impedance of 5.44 km cable X_{C0} is 2089.744Ω . The inductance of local compensation grounding coil is 2.2173 H, the resistive losses is about 2.4% with local coil resistance of 17.4146Ω . Neutral point displacement voltage reaches near phase to ground voltage, the results from Matlab program is 19.43 kV and 19.46 kV from Digsilent.

5. CONCLUSIONS

Fault calculation models are implemented in both MATLAB/SIMULINK, and DigSilent for a MV network in Jordan. The models enable the detailed investigation of the earth fault under different fault factors and methods of grounding the neutral point. For Low resistance neutral grounding systems, SLG fault current can be controlled by adjusting the value of the earthing resistance. The charging currents of line to ground capacitors (especially UGC) contribute to the fault current. Voltages at healthy phases are slightly higher than 80% of the line to line voltages and higher than voltage levels of solidly grounded networks. For high resistance neutral grounding systems, SLG fault current can be reduced to near load currents. Voltages of healthy phases may equal the line to line voltage, during fault. Protection schemes may malfunction. For isolated neutral systems, fault current is low and is determined mainly by charging capacitors in case of mostly UGC feeders. Voltages to ground at healthy phases reach and may exceed line to line voltages. For compensated neutral grounding (Petersen coil), charging capacitive current of healthy phases that flow through the neutral wire are greatly damped. Petersen coil can be adjusted to match MV network changes. The resistive part of Petersen coil determines the amount of the fault current through neutral. Maximum voltage of healthy phases can reach line to line voltage level. Traditional relaying schemes can not be effective in this case. Enhanced earth-fault relay designs are required if Petersen coil grounding is applied.

REFERENCES

1. Muhammad, T. A.-H., "Neutral ground resistor monitoring schemes," *IEEE International Symposium on Electrical Insulation*, Indianapolis, USA, Sep. 19–22, 2004.
2. Roberts, J., H. J. Altuve, and D. Hou, "Review of ground fault protection methods for grounded, ungrounded, and compensated distribution systems," Schweitzer Engineering Laboratories, 2001.
3. Welfonder, T. and V. Leitloff, "Location strategies and evaluation of detection algorithms for earth faults in compensated MV distribution systems," *IEEE Transactions on Power Delivery*, Vol. 15, No. 4, 2000.
4. Griffel, D., Y. Harmand, V. Leitloff, and J. Bergeal, "A new deal for safety and quality on MV networks," *IEEE Transactions on Power Delivery*, Vol. 12, No. 4, 1428–1433, 1997.

5. Abdel-Fattah, M., "A transient fault detection technique with varying fault detection window of earth modes in unearthed MV systems," *6th International Conference on Power Quality and Supply Reliability*, Estonia, 2008.
6. Statan, I., I. Proouc, and I. Dobra, "Contributions to the rational method of neutral grounding with MATLAB/SIMULINK," Technical University of Moldova, 2007.
7. Gross, E. T. B., "Sensitive fault protection for transmission lines and distribution feeders," *AIEE Transactions*, Vol. 60, 968–972, 1941.
8. Hunt, L. F. and J. H. Vivian, "Sensitive ground protection for radial distribution feeders," *AIEE Transactions*, Vol. 59, 84–90, 1940.
9. Zamora, I., A. J. Mazon, F. Antepara, M. Puhlinger, and J. R. Saenz, "Experiences of neutral resonant system implementation in gorliz substation," *CI RED 17th International Conference on Electricity Distribution*, Barcelona, May 12–15, 2003.
10. Van de Sandt, R., J. Lowen, J. Paetzold, and I. Erlich, "Neutral grounding in off-shore wind farm grids," *IEEE Bucharest Power Tech. Conference*, Romania, Jun. 28–Jul. 2, 2009.
11. Dumitru Toader, S. H., C. Blaj, and I. Cata, "Numerical simulation of single phase faults in medium voltage electrical networks," University of Timisoara, Romania, 2010.
12. GernotDruml, A. K. and O. Seifert, "A new directional transient relay for high ohmic earth faults," *CI RED 17th International Conference on Electricity Distribution*, Barcelona, May 12–15, 2003.
13. Henriksen, T. and A. Petteteig, "Detection of earth fault in a medium voltage distribution network," *International Conference on Power System Transients*, Lyon, France, Jun. 4–7, 2007.
14. Cerretti, A., F. M. Gatta, A. Geri, S. Lauria, M. Maccioni, and G. Valtorta, "Temporary overvoltages due to ground faults in MV networks," *IEEE PowerTech 2009*, 1–8, Bucharest, 2009.
15. Mariappan, V., A. B. S. M. Rayees, and M. AlDahmi, "Grounding system analysis to improve protection system performance in distribution networks," *12th IET International Conference on Developments in Power System Protection (DPSP 2014)*, 1–6, 2014.
16. Toman, P., J. Dvořák, J. Orságová, and S. Mišák, "Experimental analysis of electrical values during earth faults," *Electric Power Quality and Supply Reliability Conference (PQ)*, 185–190, 2010.
17. MattiLehtoneen, S., "Characteristics of earth faults in electrical distribution networks with high impedance grounding," *Electric Power Systems Research*, Vol. 44, No. 3, 155–161, Mar. 1998.

A Novel Ultrathin CdS/CdTe Solar Cell with Conversion Efficiency of 31.2% for Nano-area Application

M. Sabaghi¹, A. Majdabadi¹, S. Khosroabadi², and S. Marjani^{1,3}

¹Laser and Optics Research School

Nuclear Science and Technology Research Institute (NSTRI), Tehran, Iran

²Department of Electrical Engineering, Imam Reza International University, Mashhad, Iran

³Department of Electrical Engineering, Ferdowsi University of Mashhad, Mashhad, Iran

Abstract— Due to limited availability and the rising price, the layer thickness reduction of solar cells is an attractive prospect. In this paper, we investigated a thin high efficiency structure of CdTe solar cells for nano-area application. The proposed structure, achieved by rotating 90° in the base line structure, suggests high efficiency due to high current density. The proposed structure showed acceptable efficiency which is quite noteworthy in reducing the amount of material used and associated losses. The result showed a considerable improvement over the 15% efficiency of the reference sample. Under global AM 1.5 conditions, the designed cell had a V_{OC} of 866 mV, a J_{SC} of 74.84 mA/cm², and a FF of 48.2%, corresponding to a conversion efficiency of 31.2%.

1. INTRODUCTION

Third generation thin-film solar cells are the most promising field of photovoltaic solar cell research. They are much cheaper to manufacture (due to using simpler deposition processes), and require much less materials, as compared to the conventional single-crystal cells. Polycrystalline CdTe films have high optical absorption coefficient and are normally used in a CdS/CdTe heterojunction configuration. Because of its near ideal band gap of 1.45 eV and high optical absorption coefficient, CdTe has long been a leading material in thin film solar cell fabrication. The most important parameter that affects photon absorption is thickness of the CdTe layer [1, 2]. Reducing the CdTe absorber layer thickness is an attractive prospect due to limited availability and the rising price of Te with regards to very high volume Photovoltaic module manufacture in the future. *Another advantage is that overall material consumption will decrease along with module production costs.* CdS films are suitable as a window layer for CdS/CdTe solar cells. Thinner CdS films produce higher J_{SC} [3, 4]. The maximum theoretical efficiency reported for CdTe solar cells are 28–30% [5, 6]. The record cell efficiency of CdTe solar cells have been increased by only 1.5% during the last 17 years [7–11]. The maximum cell efficiencies of the CdTe solar cells were reported to be between 16% and 16.5% [12–15]. The NRELverified cell efficiency of 20.4% and a module efficiency of 14% were reported by First Solar [16]. Increasing the efficiency of the CdTe thin film solar cells is a current hot research topic. Simulation of CdTe thin film solar cells is an important strategy to test the viability and prediction of the effect of physical changes on the cell performance in the proposed structures. Now, the challenge facing the researchers and technologists is increasing the efficiency of CdS/CdTe solar cell and decreasing the gap between the actual efficiency and the theoretical limit. The goal of this paper is to explore a higher efficiency CdTe solar cell by introducing a new structure.

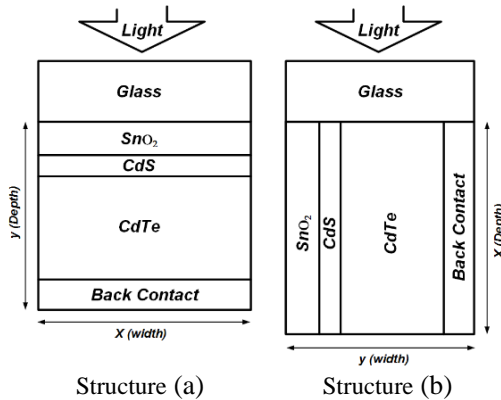
2. ANALYSIS OF CONVENTIONAL AND MODIFIED STRUCTURES

The mechanism of structures could be evaluated by numerical simulations enabling the design of new structures with better efficiency and stability. The starting point of this work was the baseline case as reported in [1]. In brief, the CdTe device model in the base line case consists of a 4 μ m-thick CdTe absorber layer, a 100-nm thick CdS window layer, and a 500-nm-thick SnO₂ buffer layer. Most of the important electronic parameters are listed in Table 1. The values have been chosen on the basis of theoretical considerations, experimental data and existing literature.

The back barrier in CdTe layer was low (0.3 eV). It is assumed that 5% of the incident light was reflected at the front contact. The electron lifetime of 0.5 ns was used in the CdTe absorber layer of the baseline case. Using the mentioned parameters, the baseline solar cell parameters were $V_{OC} = 0.865$ V, $J_{SC} = 25$ mA/cm², $FF = 73\%$, and $\eta = 157\%$. At the next step, this structure was modified by rotating 90° of the structure without dimension variation. Figure 1 illustrates the CdTe baseline case structure and the modified structures investigated in this study.

Table 1: Best cell parameters.

Layer Properties			
	CdS	SnO ₂	CdTe
Layer Width D [nm]	100	500	4000
Dielectric Constant ϵ/ϵ	10	9	9.4
Electron Mobility μ_e [cm ² /Vs]	100	100	32
Hole Mobility μ_h [cm ² /Vs]	25	25	4
Electron/Hole Density n, p [cm ⁻³]	$n: 10^{17}$	$n: 10^{18}$	$p: 2 \times 10^{14}$
Band Gap Energy E_g [eV]	2.4	3.6	1.5
Effective Density of States N_C [cm ⁻³]	2.2×10^{18}	2.2×10^{18}	8×10^{17}
Effective Density of States N_V [cm ⁻³]	1.8×10^{19}	1.8×10^{19}	1.8×10^{18}
Defect States			
	CdS	CdS	CdTe
Acceptor/Donor Defect Density N_{DG}, N_{AG} [cm ⁻³]	$A: 10^{17}$	$A: 10^{15}$	$D: 2 \times 10^{14}$
Defect Peak Energy E_A, E_D [eV]	midgap	midgap	midgap
Distribution Width W_G [eV]	0.1	0.1	0.1
Capture Cross Section σ_e [cm ²]	10^{-17}	10^{-15}	10^{-12}
Capture Cross Section σ_h [cm ²]	10^{-12}	10^{-12}	10^{-15}



Structure (a)

Structure (b)

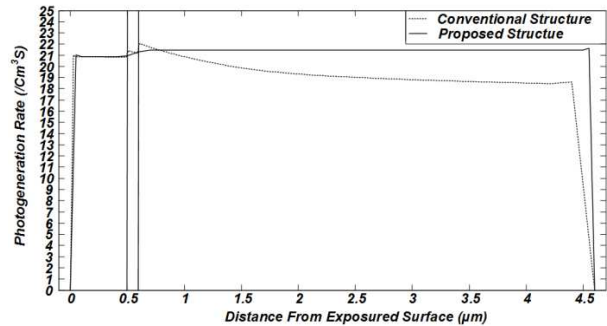


Figure 1: Structures of the CdTe solar cells: (a) baseline case structure and (b) modified cell structure for higher efficiency.

Figure 2: Photogeneration rate for the conventional and proposed structure.

The proposed structure has many advantages such as high photogeneration and low recombination rate. The J_{SC} of the cell can be improved by reducing the carrier recombination losses at the back contact or increasing the photogeneration rate in the absorber layer. Because the light enters to layers independently, the photogeneration rate is high in each layer. Figure 2 shows the comparison the photogeneration rate between conventional and proposed structure.

In addition, using less semiconductor material by thin cells is one of the main goals of today's solar cell research. Also, the thinning will reduce the recombination loss as well as lower production time and the energy need to produce solar cells. Consequently, all of these factors will decrease the production cost. Hence, it is possible to reduce the dimension of proposed structure considerably and achieve better base line results, simultaneously. Figure 3 shows the current-voltage and power-voltage curves for comparison with the base line case.

As it is shown in Figure 3, the conversion efficiency can be increased to 31.2% mostly due to improvement of J_{SC} compared to the base line case. Although FF is smaller than base line case because of the high difference between J_{SC} and maximum current of the cell the important parameters of the solar cell are much more than base line case. Figure 4 and Figure 5 show the characteristics of the proposed cell by decreasing the cell depth.

It is clear from Figure 4, the J_{SC} decreases and V_{OC} increases by increasing the depth. Therefore, cell has a lower FF . Figure 6 shows the cell efficiency and FF of the proposed structure as a function of depth.

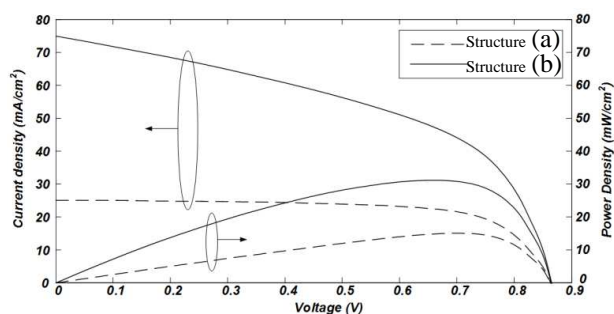


Figure 3: characteristics of the (a) baseline case structure and (b) modified cell structure for higher efficiency.

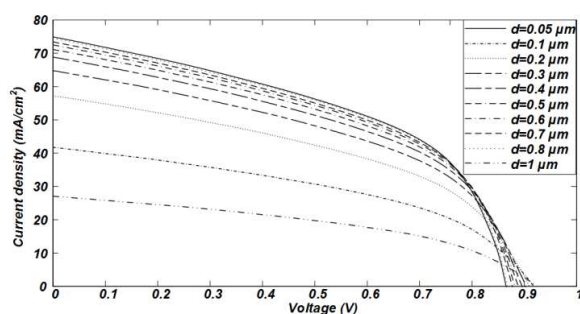


Figure 4: Light J - V curves of the cell with the lower depth (d).

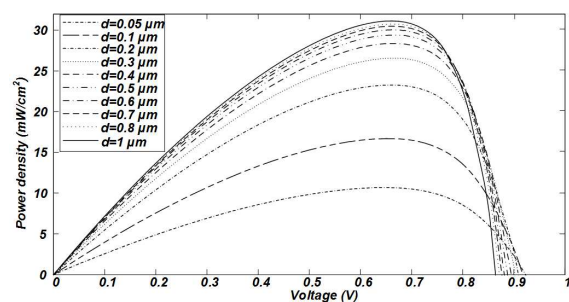


Figure 5: Power curves of the cell with the lower depth (d).

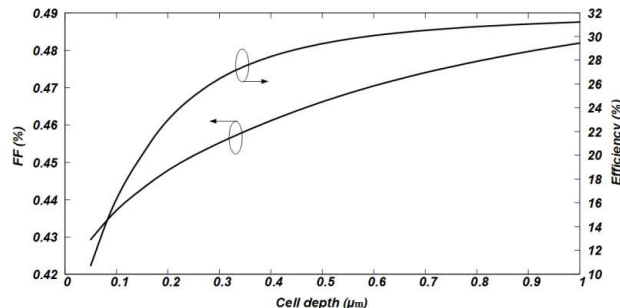


Figure 6: Efficiency and FF of the cell as a function of the cell depth.

Because of reducing the depth corresponding to a thinner cell, photogeneration rate decreases. As a result, the efficiency of the cell is decreased. It can be seen from Figure 5 by decreasing the depth up to 0.1, the cell efficiency is still better than base line case.

3. CONCLUSION

In this study, a base line structure is considered and a new structure is proposed which is achieved by rotating 90° in the base line structure. The result showed a considerable improvement over the 15% efficiency of the reference sample. The proposed structure showed acceptable efficiency which is quite noteworthy in reducing the amount of material used and associated losses. It was shown that $0.1 \mu\text{m}$ of CdTe absorber layer was sufficient to produce conversion efficiency over 15%. Under global AM 1.5 conditions, the designed cell had a V_{OC} of 866 mV, a J_{SC} of 74.84 mA/cm^2 , and a FF of 48.2%, corresponding to a conversion efficiency of 31.2%.

REFERENCES

1. Khosroabadi, S. and S. H. Keshmiri, "Design of a high efficiency ultrathin CdS/CdTe solar cell using back surface field and backside distributed Bragg reflector," *Opt. Express*, Vol. 22, A921–A929, 2014.
2. Khosroabadi, S., S. H. Keshmiri, and S. Marjani, "Design of a high efficiency Cds/Cdte solar cell with optimized step doping, film thickness, and carrier lifetime of the absorption laye," *Journal of the European Optical Society*, Vol. 9, 14052-1–14052-6, 2014.
3. Hana, J., C. Liaoa, T. Jianga, C. Spanheimerb, G. Haindlb, G. Fub, V. Krishnakumarb, K. Zhaoa, A. Kleinb, and W. Jaegermannb, "An optimized multilayer structure of CdS layer for CdTe solar cells application," *Journal of Alloys and Compounds*, Vol. 509, No. 17, 5285–5289, 2011.
4. Krishnakumar, L. V., J. Han, A. Klein, and W. Jaegermann, "CdTe thin film solar cells with reduced CdS film thickness," *Thin Solid Films*, Vol. 519, No. 7, 7138–7141, 2011.
5. Meyers, P. V. and S. P. Albright, "Photovoltaic materials, 'history'" *Progress in Photovoltaics: Research and Applications*, 161–168, 2000

6. Bonnet, D., "CdTe thin-film PV modules," *Practical Handbook of Photovoltaic: Fundamentals and Applications*, 333–366, Elsevier, Oxford, 2003.
7. Green, M. A., K. Emery, Y. Hishikawa, W. Warta, and E. D. Dunlop, "Solar cell efficiency tables (Version 38)," *Progress in Photovoltaics: Research and Applications*, Vol. 19, No. 5, 84–92, 2011.
8. Kosyachenko, L. A., A. I. Savchuk, and E. V. Grushko, "Dependence of efficiency of thin-film CdS/CdTe solar cell on parameters of absorber layer and barrier structure," *Thin Solid Films*, Vol. 517, No. 7, 2386–2391, 2009.
9. Britt, J. and C. Ferekides, "Thin film CdS/CdTe solar cell with 15.8% efficiency," *Applied Physics Letters*, Vol. 62, No. 22, 2851–2852, 1993.
10. Pena, J. L., O. Ares, V. Rejon, A. Rios-Flores, J. M. Camacho, N. Romeo, and A. Bosio, "A detailed study of the series resistance effect on CdS/CdTe solar cells with Cu/Mo back contact," *Thin Solid Films*, Vol. 520, No. 2, 680–683, 2011.
11. Colegrove, E., R. Banai, C. Blissett, C. Buurma, J. Ellsworth, M. Morley, S. Barnes, C. Gilmore, J. D. Bergeson, R. Dhere, M. Scott, T. Gessert, and S. Sivananthan, "High-efficiency polycrystalline CdS/CdTe solar cells on buffered commercial TCO-coated glass," *Journal of Electronic Materials*, Vol. 41, No. 10, 2833–2837, 2012.
12. Razykov, T. M., C. S. Ferekides, D. Morel, E. Stefanakos, H. S. Ullal, and H. M. Upadhyaya, "Solar photovoltaic electricity: Current status and future prospects," *Solar Energy*, Vol. 85, No. 8, 1580–1608, 2011.
13. Rios-Flores, A., O. Ares, J. M. Camacho, V. Rejon, and J. L. Pena, "Procedure to obtain higher than 14% efficient thin film CdS/CdTe solar cells activated with HCF₂Cl gas," *Solar Energy*, Vol. 86, No. 2, 780–785, 2012.
14. Kanevce, A. and T. A. Gessert, "Optimizing CdTe solar cell performance: Impact of variations in minority-carrier lifetime and carrier density profile," *IEEE Journal of Photovoltaics*, Vol. 1, No. 1, 99–103, 2011.
15. Wu, X., J. C. Keane, R. G. Dhere, C. DeHart, D. S. Albin, A. Duda, T. A. Gessert, S. Asher, D. H. Levi, and P. Sheldon, "16.5% efficient CdS/CdTe polycrystalline thin film solar cell," *Proc. 17th Conf. IEEE European Photovoltaic Solar Energy*, 995–1000, Munich, Germany, 2001.
16. First Solar Inc., 2014, <http://www.firstsolar.com/en/Innovation/Advanced-Thin-Film-Modules>.

High Gain Printed Monopole Arrays for Wireless Applications

M. Farran¹, S. Boscolo², D. Modotto¹, A. Locatelli¹,
A. D. Capobianco³, M. Midrio², and V. Ferrari¹

¹Dipartimento di Ingegneria dell'Informazione, Università degli Studi di Brescia, Italy

²Dipartimento di Ingegneria Elettrica, Gestionale e Meccanica, Università degli Studi di Udine, Italy

³Dipartimento di Ingegneria dell'Informazione, Università degli Studi di Padova, Italy

Abstract— In this work we discuss the design of planar arrays in which $N + 1$ parasitic monopoles, properly placed in a linear array of N active elements, allow a broadside radiation and a gain value close to that of a standard $2N + 1$ active element array. Parasitic metallic strips are placed symmetrically on both sides of each microstrip monopole and, in order to achieve the correct phase lag for a broadside pattern, meandered lines are inserted between the feeding microstrips and the active monopoles.

Linear arrays working in the wireless local area network (WLAN) band around 2.4 GHz and composed of 5×1 and 9×1 microstrip monopoles with their feeding network have been designed and fabricated on FR4 substrates. In order to obtain a unidirectional pattern, a metallic plane reflector is placed at a distance of about $\lambda/4$ from the array board: predicted gain (11 dB for 5×1 array and 15 dB for 9×1 array) and bandwidth (around 600 MHz) are larger than for conventional microstrip patch arrays having similar board dimensions.

1. INTRODUCTION

Antenna arrays are commonly used in wireless communication base stations which are nowadays facing the challenges of wider bandwidths and higher gains for an increased channel capacity. Compact arrays can be composed of printed antennas offering a large variety of designs, for instance: patch antennas [1], printed dipole antennas [2], printed monopole antennas and their variants (e.g., the inverted-F) [3, 4]. The disadvantage of patch antennas is their narrow bandwidth, which prevents their use in many applications. On the contrary, the design of printed monopoles is flexible and moderate to wide bandwidth (300 MHz to 1 GHz) impedance matching can be achieved [3, 4], therefore, microstrip monopoles have been widely adopted in wireless communication systems [5, 6]. According to the principles of Image Theory, the monopole and its mirror image with respect to the ground plane will form a dipole antenna [7]. However, the antenna is installed on a finite ground plane, whose size and shape can affect both the resonance frequency and the radiation pattern.

In this paper, we present two printed planar arrays of monopoles with their feeding networks; as can be seen in the drawings of Figure 1, these arrays are formed of N ($= 2$ and 4) active monopoles and $N + 1$ ($= 3$ and 5) parasitic monopoles. Only the active monopoles are fed directly, whereas the parasitic radiators are fed through the currents induced by the active monopoles and by the current passing across the ground plane, as there is no balun at the input port. To obtain a broadside pattern and maximize directivity it is necessary to properly choose magnitude and phase of the currents exciting each isotropic microstrip radiator. We numerically demonstrate that, by using meandered lines capable of delaying the currents feeding the active monopoles, a broadside radiation pattern can be obtained with a gain value close to that of a standard $2N + 1$ ($= 5$ and 9) active element array. The details of the antenna design and its radiation performance are described in the following sections.

2. ANTENNA ARRAY DESIGN

The array radiating elements are present on both faces of a standard FR4 substrate: the active elements are fabricated on the front of the substrate, whereas the parasitic elements are fabricated on the back of the same substrate. The proposed arrays are illustrated in Figure 1. The expected monopoles length is a quarter-wavelength, but this value must be tuned by numerical simulations since the resonance condition is influenced by the finite size of the ground plane (i.e., the large rectangular plane on the substrate back). As shown in Figure 1(a), the key concept of our design is to place symmetrically on both sides of each active monopole (at a distance of about $\lambda/4$) two parasitic metallic strips which are protrusions of the ground plane. The meandered lines are inserted between the feeding microstrip lines and the active monopoles and act as phase-delay lines for the current feeding the active monopoles. The microstrip network between the input

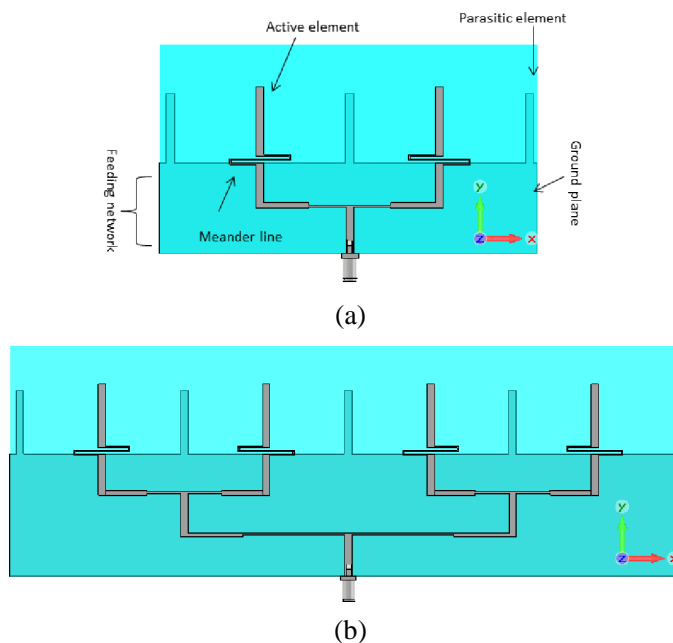


Figure 1: Drawing of the microstrip monopole arrays: (a) 5×1 array, (b) 9×1 array. The feeding network, the meanders and the active monopoles are on the substrate front face, whereas the ground plane and the parasitic elements are on the substrate back face.

port and the active elements allows for a wide bandwidth impedance matching. In the case of the 5×1 array (Figure 1(a)), the input 50-Ohm microstrip is split into two 100-Ohm lines, which are followed by 70-Ohm quarter wave transformers connected to the 50-Ohm microstrips feeding the meanders. Numerical simulations performed by means of CST Microwave Studio show that the current densities on the parasitic strips are mainly induced by the driven monopoles. In our design only an unbalanced waveguide like the microstrip is requested; this choice implies that some current passes across the ground plane and reaches the parasitic elements, but the same current is useful to achieve impedance matching on a wider band.

Each meandered delay line is composed of 5 segments with a width of 0.5 mm and a total length l that must compensate for the phase delay among the active monopoles and the parasitic ones; a long optimization procedure gave the value $l = 2.86$ cm.

CST simulations confirm that the $2N + 1$ radiators are fed in phase and it must be underlined that the currents flowing in the parasitic elements are less intense than the ones in the active monopoles. Without the presence of the meanders the relevant gain enhancement due to the array factor of $2N + 1$ isotropic elements cannot be observed, even by significantly changing the radiating elements separation or optimizing the feeding network.

A thorough numerical optimization has led to the geometrical dimensions of the final designs displayed in Figure 1: the substrate total area is 13.9×7.6 cm² for the 5×1 array and 27.1×9.2 cm² for the 9×1 array, the area occupied by each meander is 2.25×0.35 cm² and the driven and parasitic microstrips have a width of 2.9 mm.

3. RESULTS

Prototypes were milled on FR4 substrates (with thickness 1.58 mm, $\epsilon_r = 4.5$, $\tan \delta = 0.025$) and measured in anechoic chamber by using a two port Agilent N5230 PNA-L network analyzer. The simulated and measured reflection coefficients of the 5×1 and 9×1 arrays are shown in Figure 2(a) and 2(b), respectively. The 10 dB impedance matching bandwidth ranges from 2.2 GHz to 2.91 GHz for the 5×1 linear array, with a fractional bandwidth (FBW) of 0.28, and ranges from 2.2 GHz to 2.65 GHz (FBW = 0.17) for the 9×1 linear array. The simulated and measured return losses are in good agreement for the 5×1 linear array; considering the 9×1 linear array, we have almost the same -10 dB bandwidth, but the minima predicted by the numerical simulation are 15 dB smaller than the measured ones.

Figure 3(a) shows the calculated 3D radiation pattern of the 5×1 array; as expected from basic array theory, there are two main lobes (tilted by 10° with respect to the normal to the

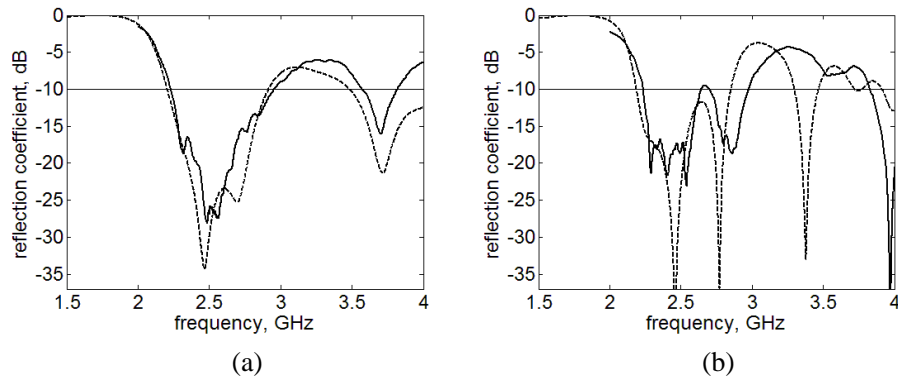


Figure 2: Computed (dashed lines) and measured (solid lines) reflection coefficients: (a) 5×1 array, (b) 9×1 array.

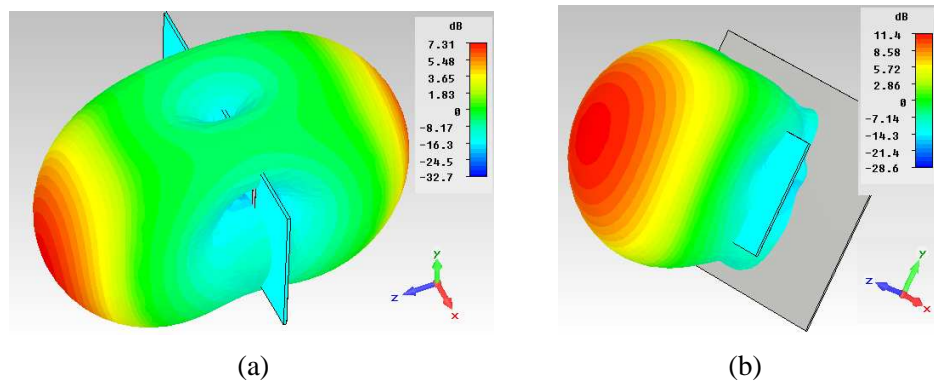


Figure 3: Radiation patterns of the 5×1 array at the frequency of 2.4 GHz: (a) plain array, (b) array with metallic plane reflector.

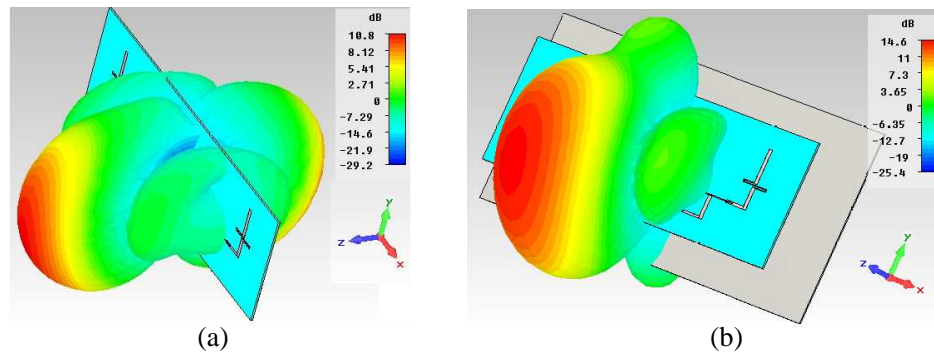


Figure 4: Radiation patterns of the 9×1 array at the frequency of 2.4 GHz: (a) plain array, (b) array with metallic plane reflector.

board) and the gain is 7.3 dB. In order to obtain a unidirectional pattern, a metallic plane reflector ($18 \times 12 \text{ cm}^2$) is placed at a distance of 3 cm from the array board and the resulting 3D pattern is shown in Figure 3(b); the main lobe is almost perpendicular to the board (the tilt is only 5° and the corresponding gain is 11.4 dB (the increase in gain is even larger than the 3 dB predicted by theory). The 3D radiation pattern of the 9×1 array exhibits a gain of 10.8 dB (see Figure 4(a)), which can be augmented up to 14.6 dB when a metallic plane reflector ($31 \times 12 \text{ cm}^2$) is placed at a distance of 3 cm (see Figure 4(b)). In the case of the 9×1 array, secondary lobes are present (with a side lobe level of -10 dB) and the main lobe is tilted of 20° irrespectively of the presence of the metal reflecting plane.

4. CONCLUSION

Two printed arrays with N active microstrip-fed element and $N + 1$ parasitic strips have been designed and characterized at 2.4 GHz: meanders are used to enforce a phase lag to the currents flowing in N of the radiating metallic strips and determine a broadside radiation. Simple fabrication techniques that are inexpensive can be employed to realize these structures and the feeding network is much more simple than those required by monopole arrays already reported in the literature [6]. The results of this study have shown that by adding $N + 1$ parasitic elements, we can obtain a broadside radiation gain value close to that one of a standard $2N + 1$ isotropic element array and the bandwidth is significantly larger (> 600 MHz) than the one of conventional microstrip patch arrays [8]. In spite of the compact board areas, gains of 11 dB and 15 dB are achieved with a metallic plane reflector placed at a distance of about $\lambda/4$. In order to verify the array performance, prototypes have been fabricated and are currently under test. The proposed antennas may be suitable candidates for WLAN point to point operations.

REFERENCES

1. Pozar, D. P., "Microstrip antennas," *Proceedings of the IEEE*, Vol. 80, 79–91, 1992.
2. Li, X., S. X. Gong, and Y. G. Yang, "Dual-band and wideband design of a printed dipole antenna integrated with dual-band balun," *Progress In Electromagnetics Research Letters*, Vol. 6, 165–174, 2009.
3. Soras, C., M. Karaboikis, G. Tsachtsiris, and V. Mikios, "Analysis and design of an inverted-F antenna printed on a PCMCIA card for the 2.4 GHz ISM card," *IEEE Antennas Propagat. Mag.*, Vol. 44, 37–44, 2002.
4. Coulibaly, Y., T. A. Denidni, L. Talbi, and A. R. Sebak, "A new single layer broadband CPW fed-printed monopole antenna for wireless application," *Canadian Conference on Electrical and Computer Engineering*, Vol. 3, 1541–1544, 2004.
5. Kuo, Y.-L. and K. L. Wong, "Double-T monopole antenna for 2.4/5.2 GHz dual-band WLAN operations," *IEEE Transactions on Antennas and Propagation*, Vol. 51, 2187–2192, 2003.
6. Ahmad, A. S., M. Thevenot, J. M. Flo'h, and M. Mantash, "High gain array of monopoles-coupled antennas for wireless applications," *International Journal of Antennas and Propagation*, Vol. 2012, Article ID 725745, 2012.
7. Balanis, C. A., *Antenna Theory: Analysis and Design*, 3rd Edition, Wiley, New York, USA, 2005.
8. Khraysat, Y. S. H., "Design of 4 elements rectangular microstrip patch antenna with high gain for 2.4 GHz applications," *Modern Applied Science*, Vol. 6, 68–74, 2012.

Technology Advances in GNSS High Precision Positioning Antennas

D. V. Tatarnikov

Topcon Positioning Systems, Russia

Abstract— Typical error of high precision positioning with the Global Navigation Satellite Systems (GNSS) is currently about $\pm 1 \dots 2$ cm in real time; multipath reflections from the Earth surface underlying the receiver antenna is the largest error source. Newly developed compact low-loss rover antennas and reference station antennas are presented. The developed antennas with cutoff pattern potentially bring the millimeter precision in “almost” real time to the realm of practice. With the antennas, precision achieved is estimated to be of 0.65 mm in rms sense given phase noise of the system smoothed out within a time interval of 1 minute span.

1. INTRODUCTION

Currently, typical error of high precision positioning with the Global Navigation Satellite Systems (GNSS) is of the order of $\pm 1 \dots 2$ cm in real time and of $1 \dots 2$ mm in post-processing. The technique is widely used in various areas of business and research. A high precision system processes a variety of the GNSS signals along with certain types of corrections [1]. However, even with the best open sky sites there remains a site-dependent error associated with the reflections of satellite signals from the earth surface underlying the user antenna. The reflections are referred to as multipath and are the major contribution to the total error of positioning. The way to mitigate the error is a proper shaping of the receiving antenna pattern.

From antenna technology standpoint the GNSS spectrum is a plurality of two sub-bands: the Lower GNSS band (1160–1300 MHz) and the Upper GNSS band (1540... 1610 MHz). The antennas are to receive right-hand circular polarized (RHCP) signals. One would mention that the increase of the antenna noise temperature largely contributes to malfunctioning the phase lock loops (PLL) of the receiver. This differentiates the high precision equipment from other branches of satellite positioning where the delay lock loop is of interest. Thus, the art of the antenna design is to provide with compact low loss antennas. An ideal antenna for high precision applications would have +3 dB gain for all the directions in top semi-sphere and 0 gain for the directions underneath. This is to mitigate the reflections. In practice, antenna gain roll-off from zenith to horizon of about 10... 15 dB is viewed as acceptable. Larger roll-offs normally are associated with the PLL malfunctioning, in particular in regards to low elevated satellites. The desire to approach the step-like pattern yet keeping antennas to practical size is one of the major directions in antenna developments. Last but not least, cost efficiency is a factor.

It is practical to characterize antennas by the down up ratio $DU(\theta^e) = F(-\theta^e)/F(\theta^e)$. Here $F(\pm\theta^e)$ is the antenna pattern reading for a certain angle θ^e above (below) the local horizon. Within the specular reflections model, the ratio gives the multipath error to positioning [1]. Typical plots approximated by linear trends are shown in Fig. 1. The curve 1 is for the so-called rovers, i.e., antennas for practical use in the field. This kind of behavior allows to achieve the precision in real time mentioned above. The curve 2 is for base stations. Here, mm-level precision in post-processing is achievable. Finally, the curve 3 is for “no-multipath” antenna which would be required for millimeter precision is real time. In regards to the latter one would mention that normally satellites below 10 degrees elevation are omitted during processing. This is due to a large degree of distortion of their signals by natural or human-made obstacles. Thus, “no multipath” antenna would have about 40 dB drop of the gain (cutoff) within ± 10 degrees angular sector.

This paper is an overview of results and perspectives of the developments done in Technology Center of Topcon Corp. in Moscow, Russia. Books [2, 3] could be recommended for a broader view of the GNSS receiving antenna technology.

2. PATCH ANTENNAS WITH ARTIFICIAL DIELECTRIC SUBSTRATES

Given an acceptable roll-off of the gain from zenith to horizon of above, a common patch antenna is to have a dielectric substrate with relative permittivity equal to about four [1]. Then, antenna Q -factor estimates [4] show that the required bandwidth claims for the substrate thickness to be of about 1 cm or more. Dense low-loss substrates of such thickness contribute to antenna weight increase and manufacturing complications. As an alternative, patch antennas with substrates made

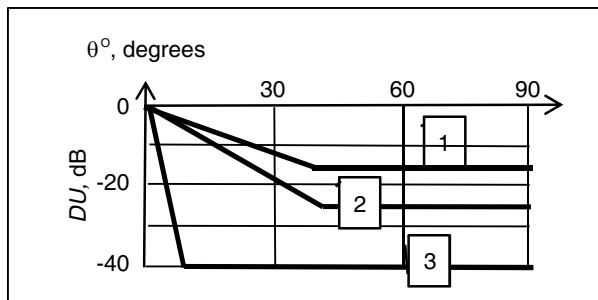


Figure 1: Down-up ratio versus satellite elevation.

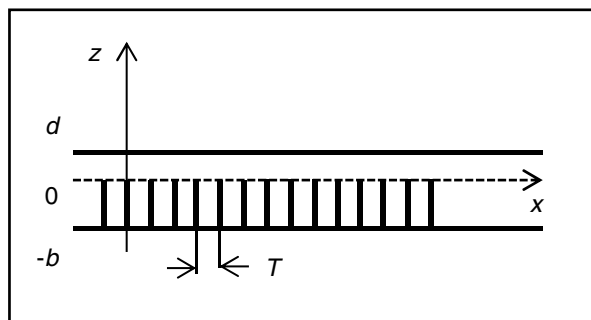


Figure 2: Parallel-plate waveguide filled with a structure of ribs.



Figure 3: Dual band patch antenna with comb substrates.

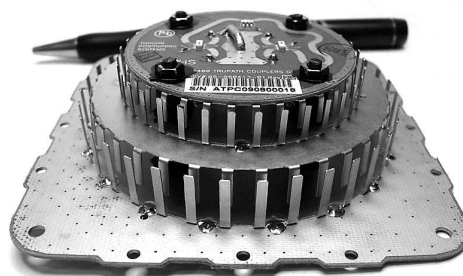


Figure 4: Dual band patch antenna with capacitive frame.

of light weight metal structures have been considered [5, 6]. Basics of the approach are illustrated as follows.

Consider a parallel-plate waveguide partially filled with the structure of metal ribs located at $-b < z < 0$ (Fig. 2). For $T \ll \lambda$, let the ribs form an averaged inductive surface impedance $Z_S = i\eta_0 t g(kd)$ (with k being a wavenumber, λ being a wavelength, η_0 being an intrinsic impedance, all of free space, and i being an imaginary unit). Then, for $b, d \ll \lambda$ the slowdown factor β of the wave propagating in x direction in the area $0 < z < d$ is $\beta = \sqrt{\epsilon_{eff}} = \sqrt{1 + b/d}$ [7]. Here ϵ_{eff} is equivalent effective dielectric permittivity. Thus, for small enough d a high ϵ_{eff} potentially could be actualized. For circular polarized antennas one is interested in a structure of thin pins rather than ribs. More accurate estimates [5] show that $\epsilon_{eff} \approx 4$ is achievable. Fig. 3 illustrates a dual-band patch antenna stack [8]. The antenna has been used for navigation of automated machines in agriculture and construction.

Further on, with TM_{10} cavity mode of a patch antenna, the electric field intensity in the area near the antenna center of symmetry is small. This suggests that pins of the central area could be removed. This has led to the patch stack design with substrates in the form of a capacitive frame [9]. The sample is shown in Fig. 4. The weight of this stack is 150 gram.

One would mention that the estimates [6] show that a capacitive frame potentially offers a slight bandwidth increase versus a regular dielectric. The way to estimate ϵ_{eff} is like follows. Consider a linear polarized squared patch antenna furnished with such a frame (Fig. 5). For a wave propagating in between a patch and a ground plane in the x -direction an equivalent longitudinal chain circuit of Fig. 6(a) holds. Here, the characteristic impedance $W = \eta_0 h/a$ is taken as that of the cut of a parallel-plate waveguide filled with air with width a equal to the patch size and height h equal to the substrate thickness. Let B_{C1} be the susceptance of capacitors per one period of the longitudinal structure 1 (Fig. 5) and β_1 be the equivalent slowdown factor of the structure. For $T \ll \lambda$ and not too big β_1 , for the chain of Fig. 6(a) the expression $\beta_1 = \sqrt{1 + (B_{C1}W/kT)}$ holds [10].

Next, consider an equivalent circuit of a patch antenna in the form of a quarter-wave stub (Fig. 6(b)). Here G_Σ is the admittance [4], B_{C2} is the total susceptance of transversal structure 2 of Fig. 5. It is assumed that the stub is filled with a homogeneous medium with slowdown factor

β_1 of above; thus, the characteristic impedance is $W_1 = \eta_0 h / (\beta_1 a)$. The resonant condition for the stub is $B_{C2} W_1 = ctg(k\beta_1 a/2)$. For the circular polarized antenna, the structures 1 and 2 are identical. Writing B_C for the susceptance of one capacitor one has $B_{C1} = 2B_C$, $B_{C2} = B_C a/T$. Let $\alpha = B_C \eta_0 h/T$ be the constitutive parameter of the substrate. Then, one has a system of two equations $\beta_1 = \sqrt{1 + (2\alpha/ka)}$; $\alpha = \beta_1 ctg(k\beta_1 a/2)$. The equations define the resonant size a as a function of α . Effective permittivity of the substrate ϵ_{eff} is then introduced by writing $\beta = \sqrt{\epsilon_{eff}} = \lambda/(2a)$. A convenient way to solve the equations could be seen in [1].

With some applications the Lower GNSS band narrows to 1215...1260 MHz. This is the so-called dual frequency L1/L2 functionality. Then, a compact concentric dual band patch antenna could be considered rather than a stack. The concentric antenna introduced by late 90-s employing ceramic substrate is shown in [1]. In Fig. 7 a version with a metal capacitive substrate is illustrated. The inner patch is for L1 band and the outer is for L2. The antenna has weight of 90 gram.

3. COMPACT MULTIPATH-PROTECTED ROVER ANTENNAS

The antennas are to meet the curve 1 of Fig. 1. For the purpose, a patch antenna onto a flat metal ground plane is the most common arrangement. Estimates [1] show that the minimal acceptable ground plane size is about half-the wavelength. With the ground plane of lesser size, the antenna multipath rejection capability degrades. To overcome the limit, an anti-antenna approach has been suggested [11]. The approach could be illustrated as follows. Consider a two-dimensional model in the form of two parallel magnetic line currents arranged into a stack with respect to the vertical z -axis such that $\vec{j}_{1,2}^m = U_{1,2} \delta(z \mp d) \vec{x}_0$. Here $U_{1,2}$ are magnitudes of voltages across the currents, $\delta(z \mp d)$ are the Dirac delta-functions, \vec{x}_0 is the unit vector of Cartesian frame, $d \ll \lambda$. If $U_2 = -U_1 \exp(-2ikd)$ then the pattern in the z - y plane is a cardioid with radiation downward suppressed. Now consider two patch antennas arranged in a vertical stack (see Fig. 8; the top antenna 1 has a ceramic substrate and the bottom antenna 2 has a comb metal substrate of above. A low-noise amplifier 3 is arranged atop the antenna 1). The top patch antenna is active

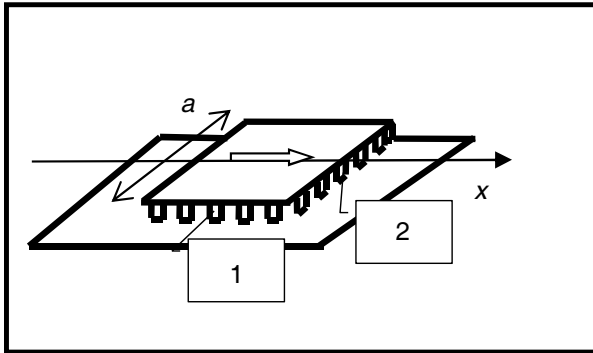


Figure 5: Linear polarized patch antenna with capacitive frame.

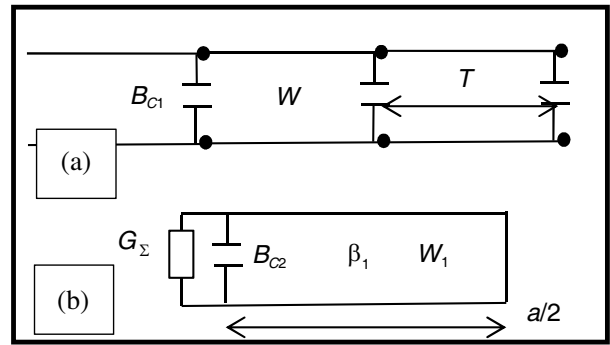


Figure 6: Longitudinal and transverse equivalent circuits.



Figure 7: Concentric L1/L2 antenna.

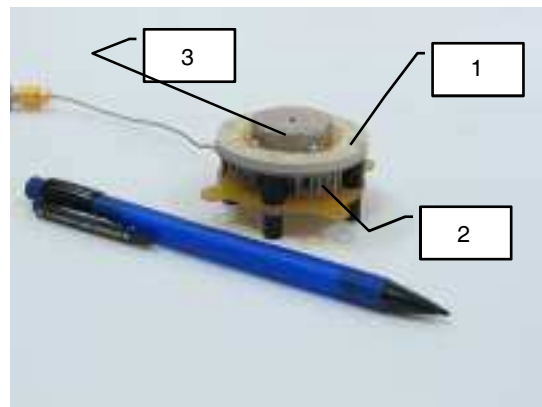


Figure 8: Implementation of anti-antenna concept.

and the bottom patch antenna is passive and tuned such that the just described relationship of voltages across the radiating slots of the two antennas holds. The bottom patch is called the anti-antenna [12]. The antenna stack does not require a ground plane. Compared to flat metal ground plane, size reduction in horizontal plane by a factor of $\sqrt{\epsilon_{eff}}$ is achieved. Here ϵ_{eff} is the effective permittivity of the substrate. The details and examples of dual band quadri-patch structures could be seen in [1, 12, 13]. The approach has been employed in a design of compact positioning units (sensors) [14]. As an example, the left panel in Fig. 9 illustrates an antenna stack and the anti-antenna arranged atop the housing with receiver electronics. Measured antenna patterns are shown at the right panel. With the design, the down-up ratio in nadir direction (at 180°) exceeds 15 dB in absolute value.

Another type of compact antennas not requiring a ground plane for multipath protection is helices. Helix antennas have been employed for satellite positioning since the beginning in late 1980-s (see [2, 15] and references therein). With compact designs, sufficient bandwidth is a topic for further developments. As an example of the newly done developments, Fig. 10(a) illustrates the dual-band quadrifilar helix antenna compatible with GPS, GLONASS, Galileo and BeiDou satellite systems. The type of the pattern achieved is illustrated at the right panel of the figure.

We complete this Section with the remark that by constructing a linear combination of spherical harmonics one is able to achieve a pattern of the kind of $\exp(-i\varphi)(dP_n^1(\cos\theta)/d\theta + P_n^1(\cos\theta)/\sin\theta)(\vec{\theta}_0 - i\vec{\varphi}_0)$. Here θ, φ are the zenith angle and azimuth, respectively, $\vec{\theta}_0, \vec{\varphi}_0$ are the unit vectors of a spherical coordinate frame, $P_n^1(\cos\theta)$ is the Legendre function of the n -th order. The pattern has only a RHCP component within the entire sphere thus with radiation downwards suppressed. This type of pattern could be achieved by a pair of magnetic m and electric e current rings coinciding with each other. In spherical coordinates, $\vec{j}^{e,m} = \vec{\varphi}_0 I^{e,m} \exp(-i\varphi) \delta(r-a) \delta(\theta - \pi/2) / r$ with the magnitudes obeying $I^m = i\eta_0 I^e$. With small enough a a perfect cardioid pattern is realized. An

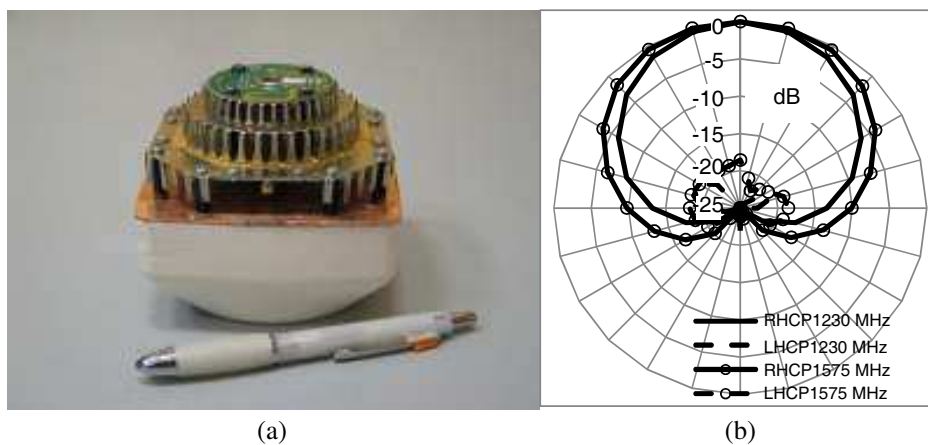


Figure 9: Integrated sensor of position.

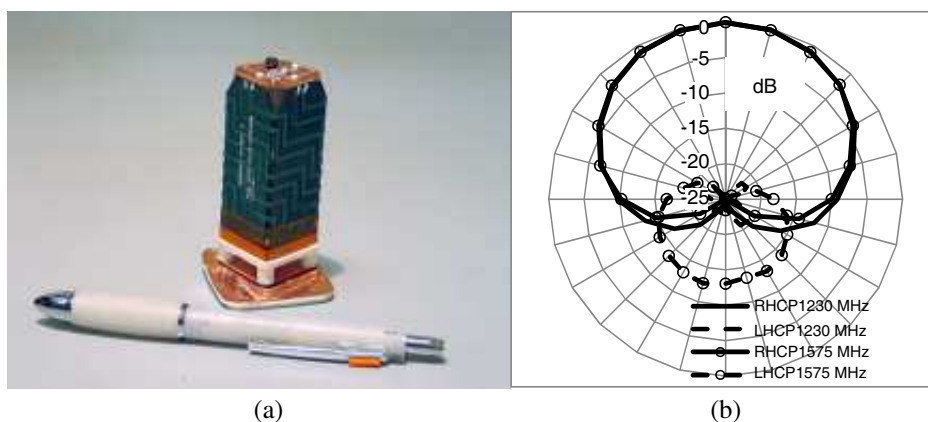


Figure 10: Dual band helix antenna.

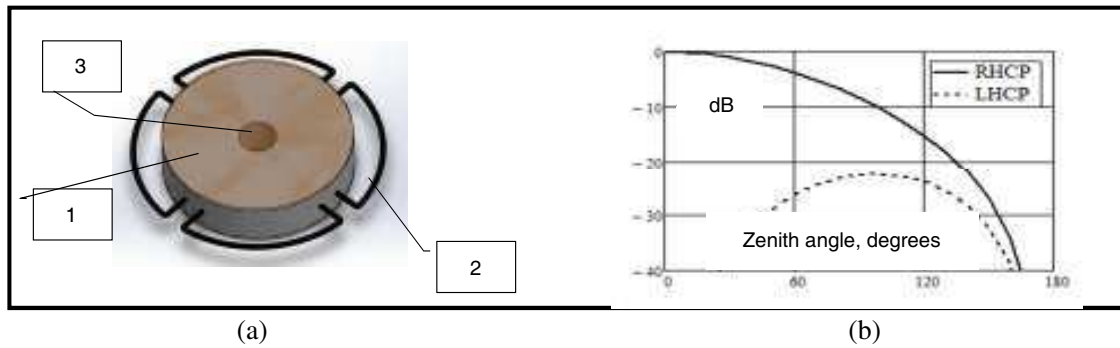


Figure 11: Symmetrical patch antenna combined with a loop antenna.

example of the respective structure is shown in Fig. 11(a). Here 1 is a symmetrical patch antenna, 2 is a wire loop antenna. Power combiner 3 is located at the center of the patch antenna. Calculations with the CST software have shown that at the distance between the patch and the loop of the order of hundredths of the wavelength, the two antennas are de-coupled due to geometrical and electrical symmetry. The calculated pattern is shown at the right panel of Fig. 11. Here, the cross-polarized (LHCP) component does not exceed -20 dB with the down-up ratio in nadir direction exceeding 40 dB in absolute value. The size of the structure is about $1/4$ of the wavelength.

4. REFERENCE STATION ANTENNAS

The antennas generally meet the curve 2 of Fig. 1. The most common example is a Choke Ring ground plane antenna serving for geodetic community for more than 20 years. See [16] for the basics of design and [1] for a photopicture and antenna patterns. The Choke Ring ground plane realizes a high capacitive impedance surface. However, a natural feature of such surfaces is antenna pattern narrowing. One would mention that with two dimensional approximation and large enough ground plane, an antenna pattern null in the direction grazing the ground plane is formed. This is well-known, details could be checked in [12]. Said narrowing affects the ability of the antenna to support tracking of low elevated satellites. With the goal of widening the pattern while not affecting the multipath rejection capabilities of an antenna, a non-planar pyramidal structure has been suggested [17]. The approach of [18, 19] could be illustrated as follows.

Consider two magnetic ring currents placed at a small distance from each other (Fig. 12(a)). The currents obey $\exp(-i\varphi)$ behavior versus azimuth, the magnitudes of the two currents are related such that to approach a cardioid pattern in the elevation plane. The currents are to model radiation of a circular polarized antenna arranged atop a ground plane. Let the ground plane (a dotted line in Fig. 12(a)) be of a spherical shape and realize a perfect magnetic conductor (PMC) boundary. Then, as discussed in [18], with small enough R the radiation pattern approaches that of the currents in free space. However, with R increases within a practically reasonable range, the antenna gain for low elevations stays almost unchanged while the radiation in the direction downwards decreases rapidly. This has served as a base for designing an antenna shown at the right panel of the figure. Here, a PMC surface is realized by a straight pins structure. The antenna has a larger gain in the directions of low elevated satellites versus a common Choke Ring ground plane while having the same multipath protection. Other details of the design could be checked in [1, 18]. The internal volume of the antenna is utilized to accommodate high- Q cavity filters for interference suppression.

Another type is the so-called field reference station antennas. The antennas are intended for practical applications in the field environment and are to provide with the precision competitive to those for the reference stations while having less weight and size. Potentials to control the radiation pattern by semi-transparent ground planes with complex grid impedance have been discussed in [20]. With antenna shown in Fig. 13(a) the semi-transparency is achieved by a slot loaded by a system of complex impedances. The radiating pattern of the antenna is illustrated in Fig. 13(a). Here the antenna gain roll-off from zenith to horizon is $10 \dots 13$ dB while the down/up ratio in nadir direction is -25 dB. One of the features of the field reference station antennas is decreased intensity of the near-fields in the region underneath. This is to reduce the errors in positioning associated with metal objects which normally appear with practical setups. In geodetic literature, the errors are referred to as near-field effects [21]. Fig. 13(c) illustrates the test setup with a metal disk

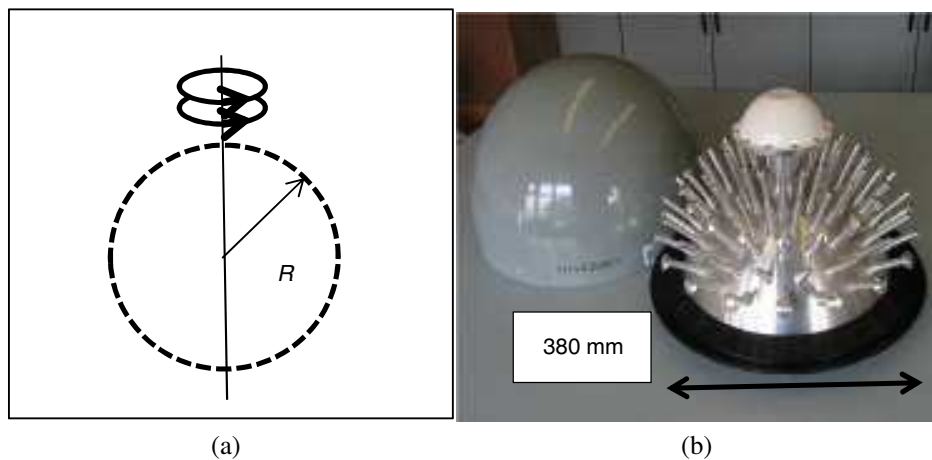


Figure 12: Reference station antenna with convex impedance ground plane.

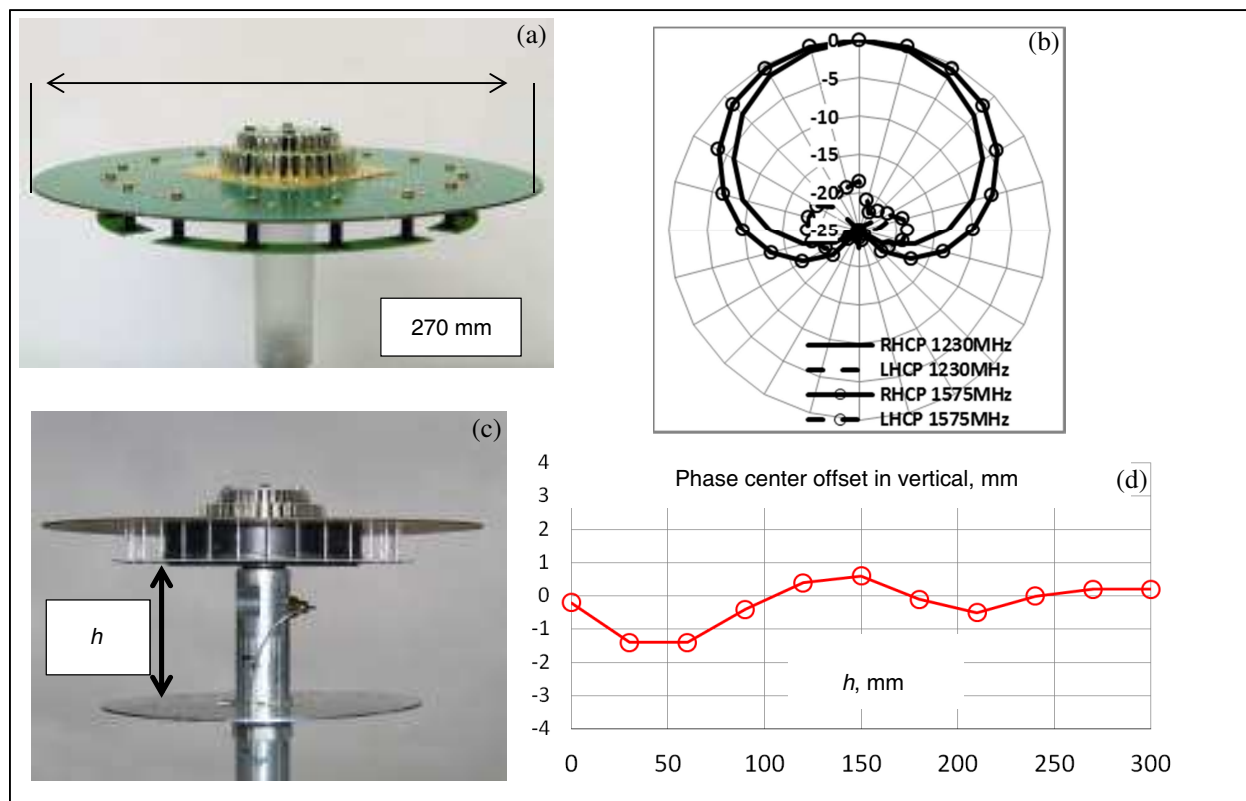


Figure 13: Field reference station antenna with semi-transparent ground plane.

underneath the antenna. Fig. 13(d) shows the measured extra offset of the phase center of the antenna versus distance to the disk. For the distance exceeding about a quarter of the wavelength, the extra offset does not exceed 1 mm.

5. POTENTIALS FOR MM-PRECISION OF POSITIONING IN REAL TIME

The respective antennas are to approach the curve 3 of Fig. 1. So far, a vertical array antenna has been presented in [22]. The antenna exceeds 2 meters in height and is intended as a ground base for unmanned aircraft landing. Reference station antenna with a capacitive impedance ground plane of 3 meters in diameter is presented in [1, 23]. With this antenna, the multipath error falls below phase noise of the system. Perspectives of employing the antenna for CORS reference stations of the International GNSS Service (IGS) are discussed in [24]. However, dimensions of the antennas of above are substantial in wavelength scale. Further developments in the direction [25] show

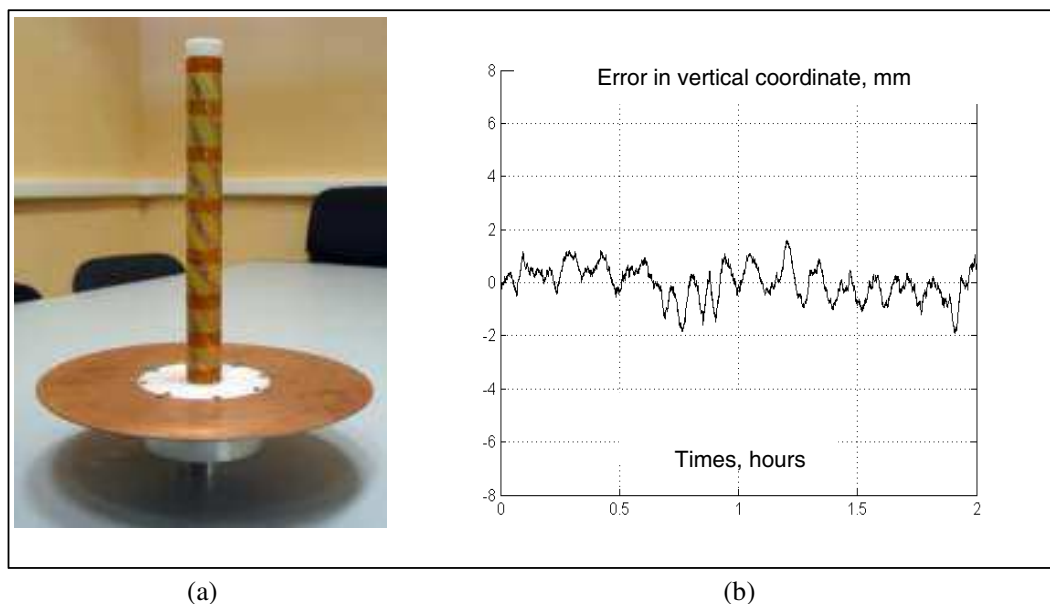


Figure 14: Travelling wave helix antenna with cutoff pattern.

that competitive performance could be achieved with travelling wave helix antennas of about 1.5 wavelength height. An antenna sample is shown at the left panel of Fig. 14. The right panel illustrates the remaining multipath error to positioning in real time, with the noise being smoothed by a moving window of 1 minute span. The rms of the error is estimated as of 0.65 mm. One would mention that with such antennas it is no longer multipath that is the major error contribution but rather the phase noise.

6. CONCLUSION

Different kinds of antennas for high precision positioning developed at Topcon Center of Technology have been discussed. Newly developed compact rover antennas, field reference station antennas and antennas with cutoff pattern are presented. One would mention that with high precision applications so far, the antenna noise factor is to be kept at minimal levels. The newly developed antennas with cutoff patterns of moderate size potentially bring the mm precision in “almost” real time into the realm of practice.

REFERENCES

1. Leick, A., L. Rapoport, and D. Tatarnikov, *GPS Satellite Surveying*, 4th Edition, Wiley, New York, 2015.
2. Rao, B. R., W. Kunysz, P. Fante, and K. McDonald, *GPS/GNSS Antennas*, Artech House, Norwood, 2013.
3. Chen, X., C. G. Parini, B. Collins, Y. Yao, and M. U. Rehman, *Antennas for Global Navigation Satellite Systems*, Wiley, New York, 2012.
4. Garg, R., P. Bhartia, I. Bahl, and A. Ittipiboon, *Microstrip Antenna Design Handbook*, Artech House, Norwood, 2001.
5. Tatarnikov, D., “Patch antennas with artificial dielectric substrates,” *Antennas*, Vol. 1, No. 128, 35–45, Radiotekhnika, Moscow, 2008 (in Russian).
6. Tatarnikov, D., “Enhanced bandwidth patch antennas with artificial dielectrics substrates for high precision satellite positioning,” *IWAT IEEE International Workshop on Antenna Technology, Small Antennas and Novel Metamaterials*, Santa-Monica, CA, Mar. 2009.
7. Silin, R. A. and V. P. Sazonov, *Slow-wave Structures*, National Lending Library for Science and Technology, Boston Spa Eng., 1971.
8. Tatarnikov, D., A. Astakhov, P. Shamatulsky, I. Soutiaguine, and A. Stepanenko, “Patch antenna with comb substrate,” U.S. Patent 7,710,324 B2, 2008.
9. Tatarnikov, D., A. Astakhov, A. Stepanenko, and P. Shamatulsky, “Patch antenna with capacitive elements,” U.S. Patent 8,446,322 B2, 2013.

10. Tretyakov, S., *Analytical Modeling in Applied Electromagnetics*, Artech House, Norwood, 2003.
11. Soutiaguine, I., D. Tatarnikov, A. Astakhov, V. Fillipov, and A. Stepanenko, "Antenna structures for reducing the effects of multipath radio signals," U.S. Patent 6,836,247 B2, 2004.
12. Tatarnikov, D., I. Soutiaguine, V. Filippov, A. Astakhov, A. Stepanenko, and P. Shamatulsky, "Multipath mitigation by conventional antennas with ground planes and passive vertical structures," *GPS Solutions*, Vol. 9, No. 3, 194–201, 2005.
13. Tatarnikov, D., A. Astakhov, and P. Shamatulsky, "Compact dual frequency RTK antennas," *Proc. of the 24-th Int. Tech. Meeting of the Institute of Navigation (ION GNSS 2011)*, 1179–1182, Sep. 20–23, 2011.
14. Tatarnikov, D., P. Shamatulsky, and A. Astakhov, "Compact multipath-resistant antenna system with integrated navigation receiver," U.S. Patent 8,842,045 B2, 2014.
15. Rabemanantsoa, J. and A. Sharaiha, "Size reduced multi-band printed quadrifilar helical antenna," *IEEE Trans. AP*, Vol. 59, No. 9, 3138–3143, 2011.
16. Tranquilla, J. M., J. P. Carr, and H. M. Al-Rizzo, "Analysis of a choke ring ground plane for multipath control in global positioning system (GPS) applications," *IEEE Trans. AP*, Vol. 42, No. 7, 905–911, 1994.
17. Kunysz, W., "A three dimensional choke ring ground plane antenna," *Proc. of the Institute of Navigation ION GNSS 2003*, 1883–1888, 2003.
18. Tatarnikov, D., A. Astakhov, and A. Stepanenko, "GNSS reference station antenna with convex impedance ground plane: Basics of design and performance characterization," *Proc. of the Int. Tech. Meeting of the Institute of Navigation ION ITM 2011*, 1240–1245, 2011.
19. Tatarnikov, D., A. Astakhov, and A. Stepanenko, "Broadband convex ground planes for multipath rejection," U.S. Patent 8,441,409 B2, 2013.
20. Tatarnikov, D., "Semi-transparent ground planes excited by magnetic line current," *IEEE Trans. AP*, Vol. 60, No. 6, 2843–2852, 2012.
21. Dilssner, F., G. Seeber, G. Wübbena, and M. Schmitz, "Impact of near-field effects on the GNSS position solution," *Proc. ION GNSS 2008*, 612–624, Institute of Navigation, 2008.
22. Lopez, A. R., "GPS landing system reference antenna," *IEEE Antennas and Propagation Magazine*, Vol. 52, No. 1, 105–113, 2010.
23. Tatarnikov, D. and A. Astakhov, "Large impedance ground plane antennas for MM-accuracy of GNSS positioning in real time," *PIERS Proceedings*, 1825–1829, Stockholm, Aug. 12–15, 2013.
24. Mader, G. L., A. Bilich, and D. Tatarnikov, "BigAnt: Engineering and experimental results," *IGS Workshop*, Pasadena, 2014.
25. Tatarnikov, D. and I. Chernetsky, "Travelling-wave antennas with semitransparent surfaces for forming a cutoff pattern," *PIERS Proceedings*, Prague, Czech Republic, accepted for presentation, 2015.

Travelling Wave Antennas with Semitransparent Surfaces for Forming a Cutoff Pattern

D. V. Tatarnikov and I. M. Chernetsky
Topcon Positioning Systems, Moscow, Russia

Abstract— Opportunities to achieve a cutoff pattern with the travelling wave antennas of moderate size are discussed. A qualitative model in the form of a parallel plate waveguide with semitransparent endings has been evaluated. A quadrifilar helix antenna with embedded reactances with the length of about 1.5 wavelength has been built. The antenna possesses a smooth pattern in the top semi-sphere with 20 dB drop of the gain (cutoff) while crossing the local horizon. Antenna functionality in applications to positioning with the Global Navigation Satellite Systems has been tested. RMS of positioning error is shown to be of 0.65 mm provided phase noise of the system smoothed out within 1 minute span.

1. INTRODUCTION

Antennas with a cutoff pattern are of special interest to various applications, in particular, to high-precision positioning with the Global Navigation Satellite Systems (GNSS). At the best open sky sites the ground reflections, referred to as multipath, are the largest error source. The multipath error is proportional [1] to antenna down-up ratio understood as $DU(\theta^e) = F(-\theta^e)/F(\theta^e)$. Here $F(\pm\theta^e)$ is the antenna pattern reading for a certain angle θ^e above (below) the local horizon. Currently, for practical antennas the DU readings are [1, 2] about $-5 \dots -7$ dB for 10 degrees getting down to $-15 \dots -25$ dB for directions close to the zenith. This sets up the best achievable positioning precision of $1 \dots 2$ cm in real time. For mm-level precision the figure of multipath suppression is 20 dB or better starting from low elevations [1, 3]. Thus, the antenna is to have a smooth pattern in top semi-sphere with a sharp drop (cutoff) while crossing the horizon. So far, a vertical array antenna exceeding 10 wavelengths has been presented in [4]. The antenna is intended as a reference for automated aircraft landing. In [5], a large impedance ground plane of 15 wavelengths in diameter is shown. With the latter, multipath error is shown to fall below the system noise resulting in 0.7 mm precision of positioning with the noise filtered out.

However, the antennas of above are substantial in the wavelength scale. The paper is to discuss opportunities and present results of realizing the cutoff pattern with antenna of moderate size. One is to note a coaxial leaky wave antenna presented in [6]. The antenna forms a dipole-type omnidirectional pattern typical for communication purposes. In what follows, in Section 2 a qualitative model of a parallel plate waveguide with the semitransparent endings is discussed. The model is to evaluate the opportunities of forming the cutoff pattern. Then, in Section 3, a quadrifilar helix antenna with embedded reactances is presented. Finally, in Section 3, the results of antenna field tests in regards to positioning are shown.

2. PARALLEL PLATE WAVEGUIDE WITH SEMITRANSSPARENT WALLS

The geometry under consideration is shown at the left panel of Figure 1. Here, a parallel plate waveguide is excited by a TEM wave travelling in positive z -direction. The waveguide width a is chosen such that all the higher order modes are evanescent. The waveguide plates end up with semitransparent segments of the length h shown by thick dashed lines. Semitransparency is understood such that the boundary conditions [7]

$$\begin{aligned} \vec{E}_\tau^+ &= \vec{E}_\tau^- = \vec{E}_\tau \\ \left[\vec{n}_0, \vec{H}_\tau^+ - \vec{H}_\tau^- \right] &= \vec{j}_S^e = \vec{E}_\tau / Z_g \end{aligned} \quad (1)$$

hold across each of the segments. In (1), $\vec{E}(\vec{H})_\tau^{+,-}$ are the tangential components of electric and magnetic field intensities at two sides of the segment, the unit normal vector \vec{n}_0 points from the “−” surface to the “+” one (see Figure 1), \vec{j}_S^e is the equivalent electric current surface density, brackets $[\]$ stand for the cross-product, Z_g is the parameter called grid impedance [7]. The impedance is assumed to be varying as a function of z . Thin sheet layers approximating the conditions (1) are

commonly known. For applications to travelling wave antennas see [6], applications to antenna ground planes could be checked in [8].

To model the radiation of the waveguide, a standard method of moments is applied. For the purpose, a perfectly conducting insert closing the waveguide at $z = 0$ is introduced. The distance L is large enough such that two conditions hold: a) it is only the TEM wave that contributes to the field intensities inside the waveguide at $z = 0$; b) electric currents flowing at the exterior of the waveguide in the domain $z < 0$ have decayed such that the currents contribution to the radiation pattern is negligible. To compensate for the insert, an equivalent magnetic current is introduced at both two sides of the insert. The magnetic current is shown by dotted lines at the left panel of the figure. In the domain $z < 0$ the fields inside the waveguide are the incident and the reflected TEM waves only; there are no electric currents at the exterior surfaces of the waveguide in the domain as mentioned.

In the domain $z > 0$, unknown electric surface currents are introduced. The currents are shown by thin dashed lines at the right panel of Figure 1. In the insert plane $z = +0$ the electric current surface density I is related to the magnetic current amplitude U such that $I = (2V - U)/(\eta_0 a)$. Here V is the incident wave voltage, η_0 is the intrinsic impedance of free space. To ensure continuity of the electric charge, two basic functions in the form of half-triangle with amplitudes I are introduced at $x = \pm a/2$; the rest of the waveguide walls are covered by triangle basic functions with amplitudes I_n . The problem is reduced to the system of linear algebraic equations with respect to I_n with the voltage U serving as a source. Matrix elements are evaluated numerically employing representations in spectral domain similar to [8].

With the calculations, the values of Z_g at the perfectly conducting surfaces were set up to zero. The profile $Z_g(z)$ at the semitransparent portion (thick dashed lines at the right panel of

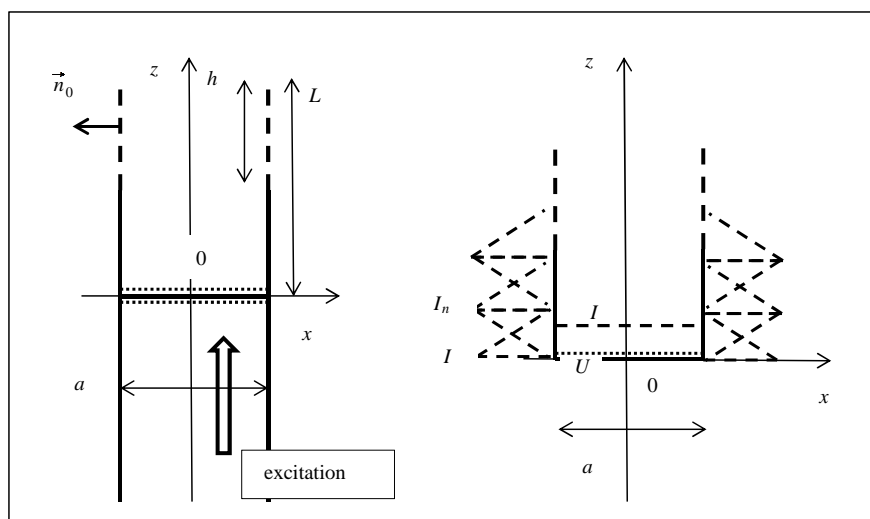


Figure 1: Geometry of the parallel plate waveguide with semitransparent endings and electric currents representation.

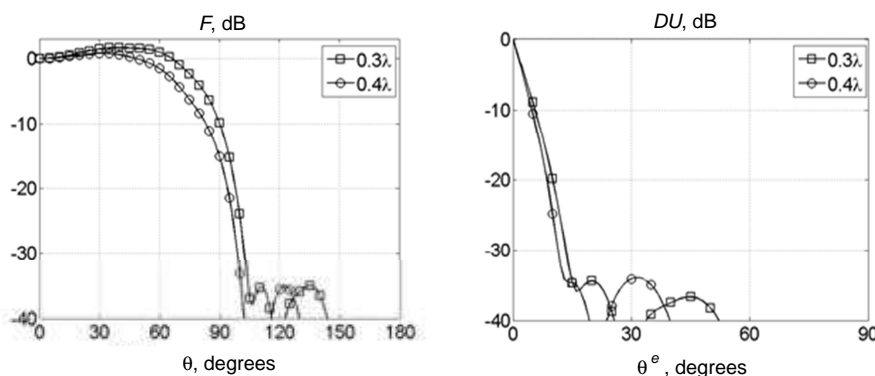


Figure 2: Calculated results for the parallel plate waveguide with semitransparent endings.

the figure) was optimized such that the cutoff radiation pattern would be achieved. The calculated results are shown at Figure 2 for the radiation pattern and down-up ratio at the left and right panels respectively. In the legend, the respective waveguide width a is shown in fractions of the wavelength. One may note that the down-up ratio exceeds 20 dB in absolute value starting from 10 degrees. It has been defined that h of about 1.5 wavelengths is sufficient. The reflection coefficient does not exceed 10^{-5} within the bandwidth of $\pm 10\%$.

3. QUADRIFILAR HELIX ANTENNA WITH EMBEDDED REACTANCES

For practical implementation, a quadrifilar helix antenna with embedded reactances has been synthesized. A general view of the antenna is shown at the left image of Figure 3. Antenna is intended for L1 GNSS band (1560...1610 MHz).

Measured antenna patterns for the θ th and the φ th linear polarized components and the down-up ratio in terms of total power are illustrated in Figure 4. As seen, antenna pattern roll-off from the zenith to 10 degrees elevation does not exceed 15 dB which is a typical practical figure for GNSS positioning antennas. The down-up ratio exceeds 20 dB in absolute value starting from 10 degrees.

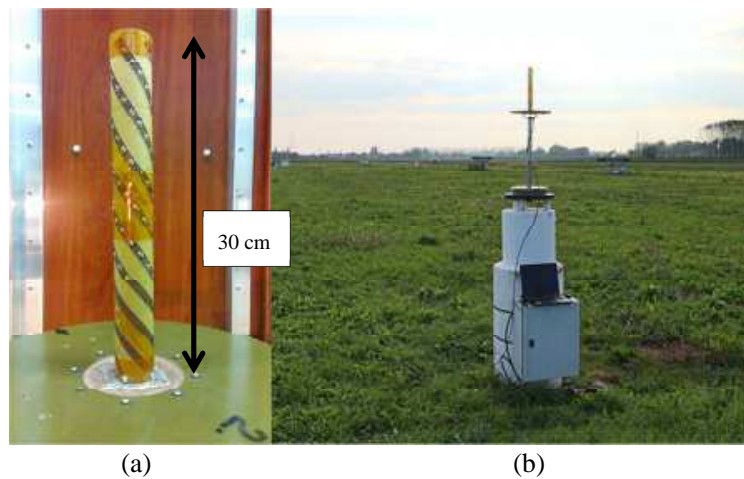


Figure 3: (a) General view of the helix antenna and (b) antenna installed at the test range.

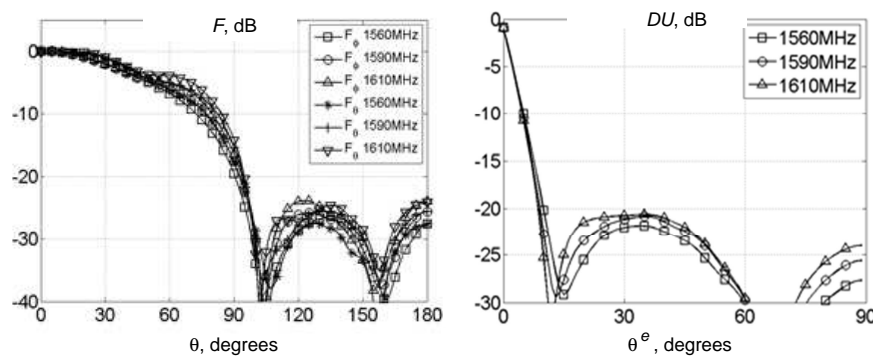


Figure 4: Measured antenna pattern for the helix antenna with embedded components and the down-up ratio.

4. FIELD TEST RESULTS

The antenna installed at the concrete pier of the test range is illustrated at the right panel of Figure 3. With differential positioning, the reference station antenna was of the same type. Real time error of positioning in the vertical coordinate is shown in Figure 5. For this data, the system noise has been smoothed within 1 minute time interval. As seen, the remaining error does not exceed ± 1.7 mm with RMS estimated as 0.65 mm. The result coincides with that reported in [5].

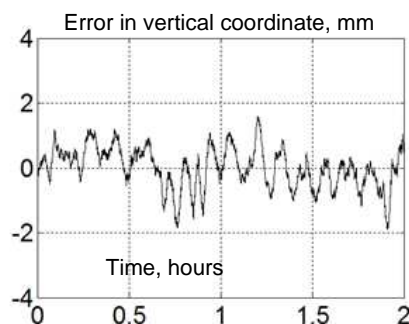


Figure 5: Real time error in vertical coordinate with the noise smoothed out within 1 minute span.

5. CONCLUSION

The results presented indicate that the cutoff pattern with about 20 dB drop of the gain while crossing the local horizon is achievable with travelling wave antennas of about 1.5 wavelengths size. With this kind of the pattern, it is no longer multipath but rather the system noise that is the largest error source in satellite positioning. Rms of positioning below 1 mm after smoothing the noise within about 1 minute span is shown. Thus, such kind of positioning in “almost” real time may become of practical interest.

REFERENCES

1. Leick, A., L. Rapoport, and D. Tatarnikov, *GPS Satellite Surveying*, 4th Edition, Wiley, New York, 2015.
2. Rao, B. R., W. Kunysz, P. Fante, and K. McDonald, *GPS/GNSS Antennas*, Artech House, Norwood, 2013.
3. Counselman, C. C., “Multipath-rejecting GPS antennas,” *Proceedings of the IEEE*, Vol. 87, No. 1, 86–91, 1999.
4. Lopez, A. R., “GPS landing system reference antenna,” *IEEE Antennas and Propagation Magazine*, Vol. 52, No. 1, 105–113, 2010.
5. Tatarnikov, D. and A. Astakhov, “Large impedance ground plane antennas for mm-accuracy of gnss positioning in real time,” *PIERS Proceedings*, 1825–1829, Stockholm, Sweden, 2013.
6. Attiya, A. M., “Omni-directional leaky-wave coaxial antenna,” *PIERS Proceedings*, 1830–1833, Stockholm, Sweden, Aug. 12–15, 2013.
7. Tretyakov, S., *Analytical Modeling in Applied Electromagnetics*, Artech House, Norwood, 2003.
8. Tatarnikov, D., “Semi-transparent ground planes excited by magnetic line current,” *IEEE Trans. Antennas and Propagation*, Vol. 60, No. 6, 2843–2852, 2012.

Parametric Analysis and Optimisation of a 8–18 GHz Quad-ridged Horn Antenna

Deniz Bolukbas^{1,2} and Ali Ziya Ozer²

¹Department of Electrical and Electronics Engineering, Okan University, Istanbul, Turkey

²Electromagnetic Design and Analysis Team, Figes A.S., Pendik, Tuzla, Turkey

Abstract— In this paper, parametric analysis and optimization of a 8–18 GHz ultra wide band (UWB) quad-ridged horn (QRH) antenna is presented. As an initial configuration a horn antenna is designed with boxed dimensions of $5.4 \times 5.4 \times 8$ cm as defined in [1]. The gain of the antenna varies between 10 dBi–13 dBi over the entire bandwidth. The co-polarization and cross polarization graphics are presented. It's expected that, the variation of physical dimensions affects the antenna parameters. To analyze these effects the parametric analysis simulations are performed with ANSYS HFSS software.

1. INTRODUCTION

Ultra wide band antennas with high gain are required to meet the requirements of today's telecommunication sector. Parabolic reflector antennas are probably the most widely used for this purpose in the microwave region. Horn antennas can be used as a feed and provide high gain, low VSWR, relatively wide bandwidth. To extend the maximum practical bandwidth of a horn, ridges are introduced in the flared part of the antenna. The radiation phenomenon is based on the wave impedance transition from waveguide line to the impedance of free space through ridges. One of the most preferred methods to increase the bandwidth and gain of horn antennas is to use double or quad ridges [2, 3].

In this paper, the parametric analysis and optimization of a QRH antenna is presented. The antenna is fed by from either one port or double port. At each analysis the fed type is described. Simulations are performed by ANSYS HFSS. HFSS offers multiple state-of-the-art solver technologies based on finite element, integral equation or advanced hybrid methods to solve a wide range of microwave applications. The QRH antenna is simulated by Finite Element Method, FEM.

The organization of this paper is as follows. Section 1 is introduction. In Section 2, the design parameters of the antenna are explained. A QRH is designed as defined in [1] as an initial configuration. The antenna is analyzed and the return loss, gain pattern, co-polarization and cross polarization of the antenna are given for the entire band width. The variations on physical dimensions of the antenna are implemented and the effects on antenna parameters are presented in Section 3. It has been observed that the dimension variation effects may differ for upper or lower frequencies. The conclusion is given at Section 4.

2. INITIAL CONFIGURATION QRH ANTENNA

A QRH antenna is designed based on the design explained in [1]. The dimensions of the antenna are described in Figure 1. The physical sizes of the antenna are given in Table 1. The horn fed by coaxial cable.

Table 1: The physical sizes of QRH antenna for initial configuration.

Parameter	Length (cm)	Parameter	Length (cm)
<i>A</i>	1.6	<i>L1</i>	4
<i>B</i>	1.6	<i>L2</i>	4
<i>A1</i>	5.6	<i>d1</i>	0.3
<i>B1</i>	5.6	<i>w</i>	0.14

The return loss value and gain of QRH antenna is presented in Figures 2(a) and 2(b) respectively. In 8–18 GHz frequency band, the gain varies between 10.67 to 12.37 dBi.

The gain pattern of the antenna is given at Figure 3(a) and *E*-field inside of the horn is given at Figure 3(b). The 3D beam pattern of QRH antenna at 8 GHz and 18 GHz are presented at Figures 3(c) and (d) respectively.

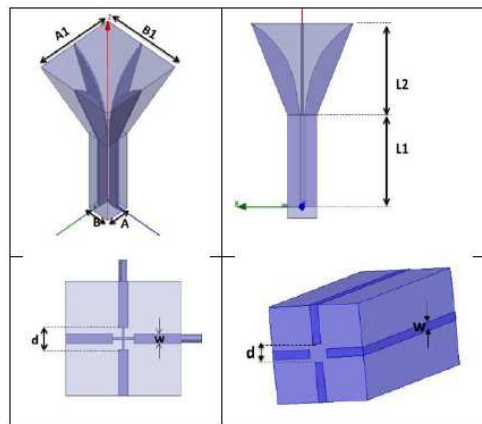


Figure 1: The description of horn antenna's dimensions.

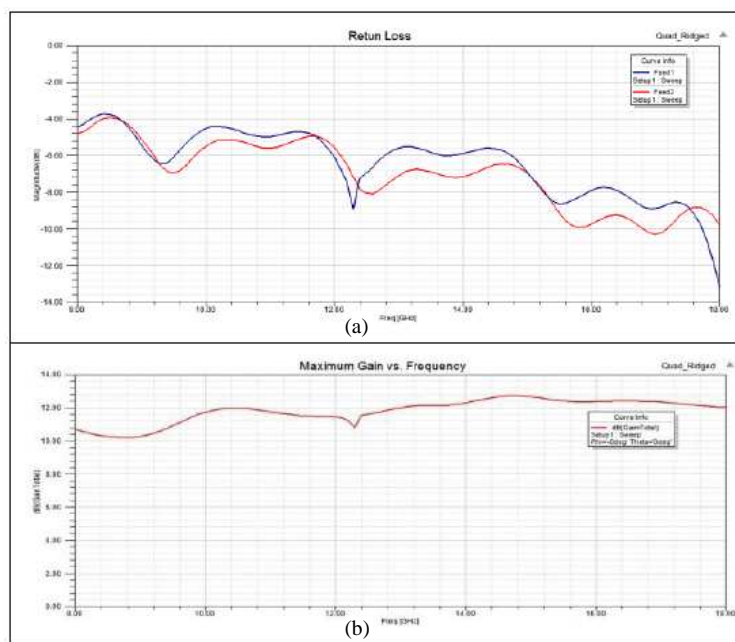


Figure 2: (a) Return loss. (b) The gain at 8–18 GHz.

The co-polarisation and cross polarization pattern are given at Figure 4(a) *E*-plane for 8 GHz, (b) *H*-plane for 8 GHz, (c) *E*-plane for 18 GHz and (d) *H*-plane for 18 GHz respectively.

3. PARAMETRIC ANALYSIS

For parametric analysis, the dimensions of the horn antenna is parametrised. As a first analysis, the outer dimensions *A1* and *B1* is selected to be equal and the values are given in Table 2.

Table 2: The parametric variation *A1* and *B1*.

Case 1	$A1 = B1 = 2.6$
Case 2	$A1 = B1 = 4.1$
Case 3	$A1 = B1 = 5.6$
Case 4	$A1 = B1 = 7.1$
Case 5	$A1 = B1 = 8.6$

The analysis are performed for five cases. The gain patterns for five cases are given for 8 GHz, and 18 GHz at Figures 5(a) and (b) respectively. The beamwidth and gain varies with parametric change of outer dimensions as presented at Figure 5.

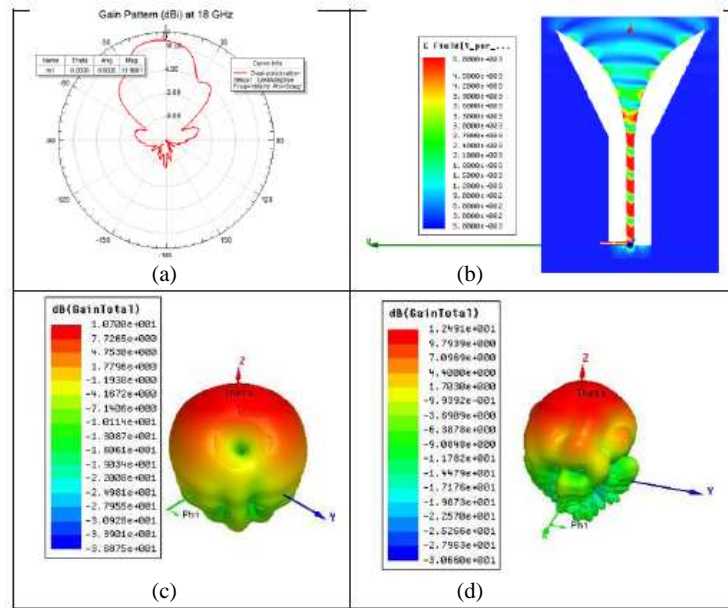


Figure 3: At 18 GHz (a) at 18 GHz, (b) *E*-field at 18 GHz, (c) 3D radiation pattern at 8 GHz, (d) 3D radiation pattern at 18 GHz.

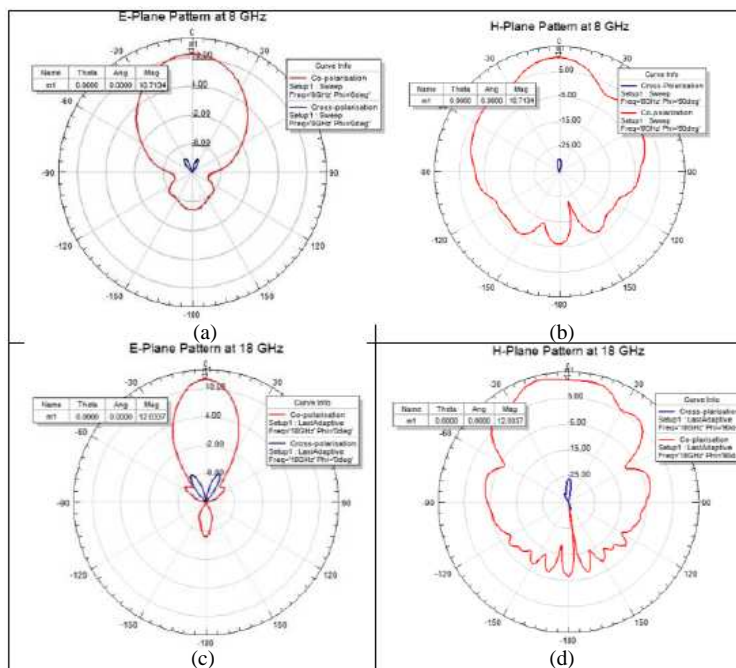


Figure 4: Co-polarisation and cross polarization pattern (a) *E*-plane for 8 GHz and (b) *H*-plane for 8 GHz and (c) *E*-plane for 18 GHz and (d) *H*-plane for 18 GHz.

The maximum gain for cases are simulated for entire band width. When the outer dimensions are increased it is observed that the gain decrease due to increasing beamwidth. The dimensions are varied from 2.6 cm to 8.6 cm. The numerical values of gain are presented at Table 3 and graphic is presented at Figure 6.

The advantage of this type of parametric analysis is mainly to find the optimal values for each parameter. At this parametrical analysis, it's observed that the gain is maximized for $A_1 = B_1 = 4.1$ cm. The parametrical sweep can be repeated with smaller steps to find the maximum gain while the outer dimensions vary from 4.1 cm to 5.6 cm.

This analysis is repeated while $A_1 = 5.6$ cm and constant, B_1 is varying from 2.6 cm to 8.6 cm. The numerical values of gain are presented at Table 4.

The graphic for gain vs frequency is presented at Figure 7.

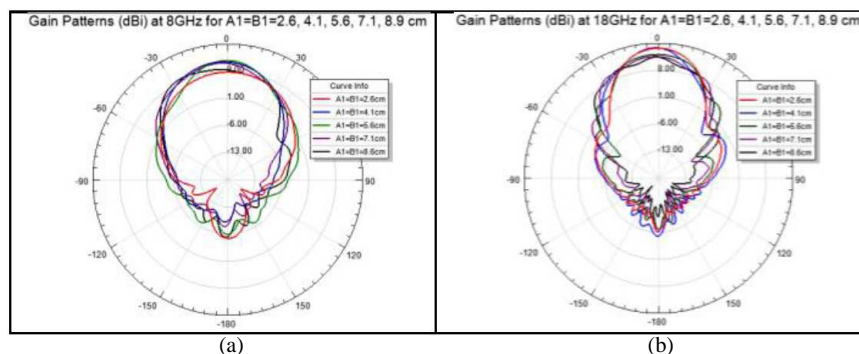


Figure 5: Gain pattern for (a) 8 GHz. (b) 18 GHz.

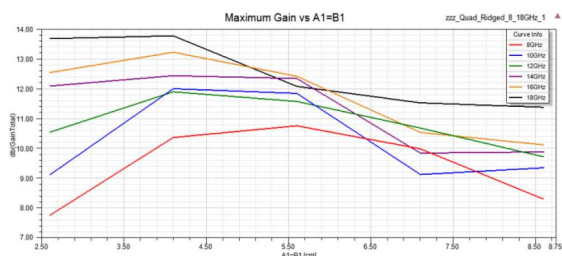


Figure 6: Gain pattern for varying dimensions.

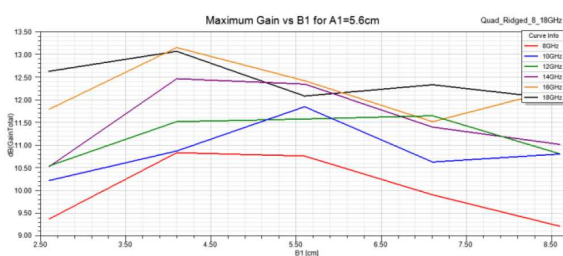


Figure 7: Gain pattern for varying $B1$ dimensions.

In this case to obtain the maximum gain, $B1$ can be selected around 5.6 cm, while $A1$ is constant.

The 3D Beam Pattern of antenna at 18 GHz is presented at Figure 8(a) for $B1 = 2.6$ cm and Figure 8(b) for $B1 = 8.6$ cm respectively. The 3D patterns indicate that beamwidth increases as $B1$ increases.

For the varying dimensions of $B1$ the E plane and H plane radiation patterns are presented at Figure 9 for 8 GHz and 18 GHz. It is also observed that beamwidths are increased as long as $B1$ increases.

The parametric analysis are performed also for d and w parameters as they were described at Figure 1.

The w parameter is selected to vary from 0.1 cm to 0.16 cm. This variation has almost no

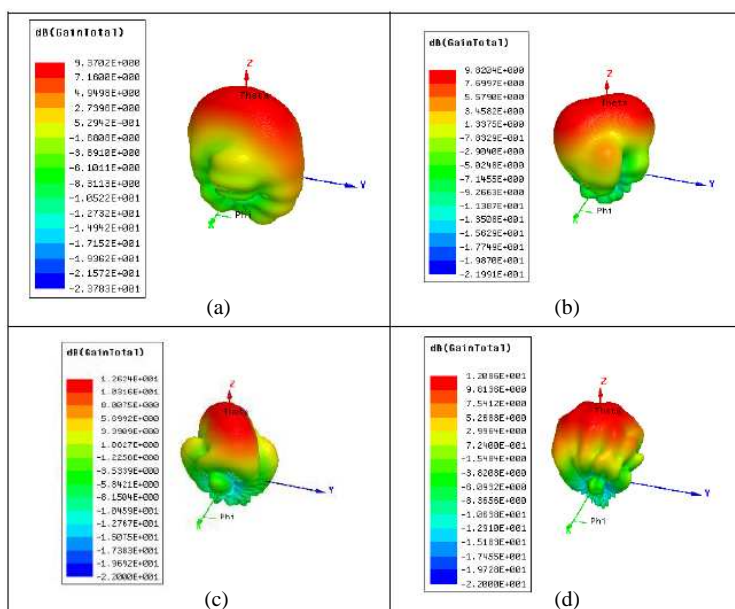


Figure 8: 3D beam pattern of antenna at 8 GHz. (a) $B1 = 2.6$ cm. (b) $B1 = 8.6$ cm and at 18 GHz. (c) $B1 = 18$ GHz. (d) $B1 = 8.6$ cm.

Table 3: Gain vs dimensions for $A1 = B1$.

	Freq [GHz]	A1=B1=2.6cm	A1=B1=4.1cm	A1=B1=5.6cm	A1=B1=7.1cm	A1=B1=8.6cm
1	8.00	7.76	10.37	10.76	9.99	8.30
2	10.00	9.11	12.00	11.84	9.13	9.35
3	12.00	10.54	11.90	11.57	10.68	9.72
4	14.00	12.09	12.44	12.34	9.84	9.88
5	16.00	12.54	13.22	12.42	10.54	10.12
6	18.00	13.68	13.77	12.08	11.53	11.38

Table 4: Gain vs dimensions for $A1 = 5.6$ cm.

	Freq [GHz]	B1=2.6cm	B1=4.1cm	B1=5.6cm	B1=7.1cm	B1=8.6cm
1	8.00	9.37	10.83	10.76	9.91	9.21
2	10.00	10.22	10.87	11.84	10.63	10.80
3	12.00	10.54	11.52	11.57	11.85	10.80
4	14.00	10.52	12.46	12.34	11.40	11.01
5	16.00	11.79	13.15	12.42	11.52	12.24
6	18.00	12.62	13.06	12.08	12.33	12.01

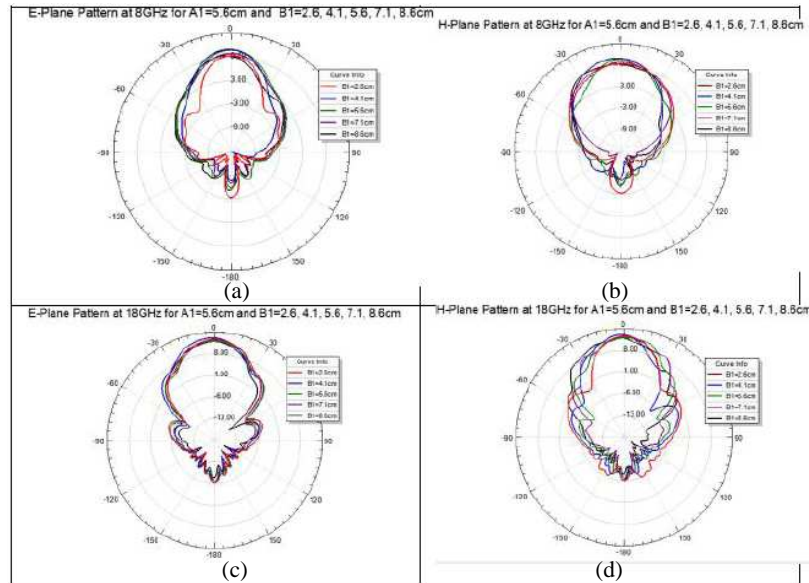


Figure 9: (a) E plane pattern at (b) H plane pattern at 8 GHz. (c) E plane pattern at 18 GHz. (d) H plane pattern at 18 GHz.

influence on gain at the entire bandwidth as can be seen at Figure 10.

With a similar approach, the parameter is selected to vary from 0.2 cm to 0.4 cm. The gain graphic shows that the optimum parameter of $d = 0.30$ cm as can be seen at Figure 11.

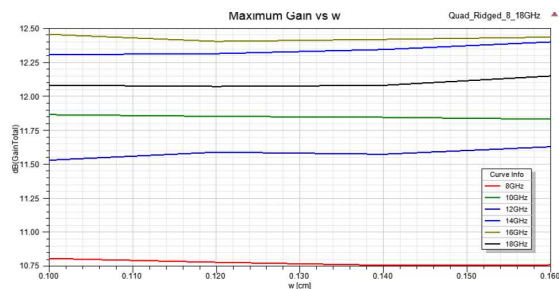


Figure 10: Gain vs w parameter.

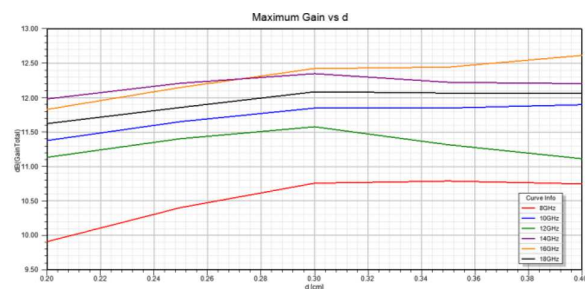


Figure 11: Gain vs d parameter.

4. CONCLUSION

In this paper, the quad ridged horn antenna design is performed, parametric analysis are simulated and the results are presented. The simulation tools are very useful for this kind of parametric analysis. With the help of such tools the best performance of the antenna can be achieved.

REFERENCES

1. Dehdasht-Heydari, R., H. R. Hassani, and A. R. Mallahzadeh, "Quad ridged horn antenna for UWB applications," *Progress In Electromagnetics Research*, Vol. 79, 23–38, 2008.
2. Mallahzadeh, A. R., A. A. Dastranj, and H. R. Hassani, "A novel dual-polarized double-ridged horn antenna for wideband applications," *Progress In Electromagnetics Research B*, Vol. 1, 67–80, 2008.
3. Mohamed, H. A., H. Elsadek, and E. A. Abdallah, "Quad ridged UWB TEM horn antenna for GPR applications," *2014 IEEE Radar Conference*, 0079, 0082, 19–23 May 2014.

Suppression of Light Scattering with ENZ-metamaterials

Alexander S. Shalin^{1,2,3}, Pavel A. Belov¹, and Yuri S. Kivshar^{1,4}

¹ITMO University, St. Petersburg 197101, Russia

²Kotel'nikov Institute of Radio Engineering and Electronics of RAS, Ulyanovsk 432011, Russia

³Ulyanovsk State University, Ulyanovsk 432017, Russia

⁴Nonlinear Physics Center, Australian National University, Canberra ACT 0200, Australia

Abstract— Cloaking devices enabling to hide objects from external observers have numerous potential applications but still face challenges in realization, especially in the visible spectral range. In particular, inherent losses and extreme parameters of metamaterials required for the cloaking are the limiting factors. Here, we propose and demonstrate numerically nearly perfect concealing of objects in ENZ-metamaterials (homogeneous and layered realizations) acting alignment-free scattering suppression covers. The suppression of visibility relies on the reconstruction of a plane wavefront after scattering of light by an object placed inside an anisotropic metamaterial with vanishing permittivity along one of the major crystallographic directions (uniaxial ENZ metamaterial). We also consider a realistic realization of the metamaterial as a metal-dielectric multilayer and demonstrate the cloaking in forward and backward directions with perfectly preserved wavefronts and less than 10% absolute intensity change.

1. INTRODUCTION

Numerous approaches for controlling electromagnetic characteristics have been developed and employed in antennas engineering for the enhancement of scattering cross-sections and radiation directivities [1]. While the main technological effort has been focused at the millimeter and radio frequencies ranges where majority of applications are, considerable interest at the optical frequencies has recently emerged. Optical antennas have been already found use in tailoring radiation properties of emitters, solar cells applications, and more [2].

Reduction of scattering cross-sections in a specifically designed material environment leads to reduced detectability of objects, and may, ultimately, result in their invisibility for an external observer. The concept of ‘cloaking’ was introduced in [3, 4] and gained remarkable attention due to continuous demand to achieve invisibility for radar waves [5] and visible light [6–8]. The general approaches for cloaking rely either on transformation optics concepts [3] or on conformal optical mapping of complex electromagnetic potentials [4]. While the former generally results in the requirements on strongly anisotropic electric and magnetic susceptibilities of a medium of a cloak, the latter approach requires a position-dependent refractive index variation but is restricted for two-dimensional geometries.

One of the main challenges in the development of practical cloaking devices is to minimize demands for permeability and anisotropy and reduce inherent material losses of required materials. The so-called ‘carpet cloak’ has been proposed and implemented to mitigate these factors by imposing certain geometrical restrictions and utilizing quasi-conformal mapping [9, 10]. Qualitatively different approach to cloaking utilizes epsilon-near-zero (ENZ) metamaterials to suppress a dipolar scattering of a concealed object [11]. While number of the ENZ metamaterial realizations exist in the radio frequency range [12, 13], in optics such an anisotropic response may be achieved through metal-dielectric layered structures [14], semiconductor heterostructures [15], or vertically aligned arrays of nanorods [16].

Here we demonstrate scattering suppression from an arbitrary (not necessarily subwavelength) sized objects placed inside a homogeneous ENZ-metamaterial and its layered metal-dielectric realization. Investigation of the exact numerical model, taking into account material losses and finite dimensions of the metamaterial, shows the possibility of nearly perfect cloaking of arbitrary shaped bodies with the minimal variations of the phase front of the transmitted/reflected optical wave and highly suppressed scattering. The proposed scheme does not require extreme electric and magnetic susceptibilities and can operate in an alignment-free manner. It is worth noting that the proposed approach is qualitatively different from other approaches when the incident light does not interact with a cloaked object being bended around by a material layer (e.g., [3, 5]) or when the scattered field is suppressed with another anti-parallel dipole [11]. Recently, similar scheme for scattering suppression in homogeneous ENZ metamaterial was proposed; however, no practical implementation was given [17].

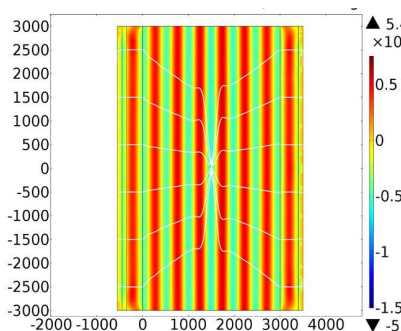


Figure 1: Electric field radiation by the dipole situated inside ENZ-metamaterial. Dipole is oriented along y -axis, wavelength — 540 nm, $\varepsilon_x = 0.004$, $\varepsilon_y = 1.23$. White lines — power flow.

2. HOMOGENEOUS METAMATERIALS

Let us firstly consider a radiating dipole situated inside a homogeneous epsilon-near-zero metamaterial. As the basic leading term in the multipolar decomposition of the scattered field is the dipole, the understanding of dipolar emission inside ENZ metamaterial will enable to analyze scattering from complex structures. Fig. 1 shows the results of electromagnetic modelling of dipolar emission inside the ENZ slab. As may be observed, the y -component (along the vanishing component of the effective permittivity tensor) shows remarkable structure of flat phase fronts, which is substantially different from the classical pattern. The dielectric tensor in this simulation was taken to be $\varepsilon_x = 0.004$, $\varepsilon_y = 1.23$. Consequently, the dipolar scattering from an embedded object supposed to provide similar flat type of fronts of scattered waves.

Figure 2 shows the result of scattering on 2 different objects, embedded in homogeneous ENZ metamaterial — (a) dielectric cylinder (b) cylinder made of perfect electric conductor (PEC). In both cases the distortion of the incident wave front is almost negligible and the y -component of the total electrical field outside the metamaterial is homogeneous. It means that the object, embedded within the metamaterial slab is invisible. It is worth noting the conceptual difference between cases (a) and (b). In the first case the field penetrates the object and obtains the phase lag, while in the second case the field at the interior of the object is identically zero. In both cases, however, the scattered field in the presence of the embedded object and without is the same, making it invisible for an observer, situated either in front or behind the structure. The key effect, responsible for the scattering suppression, is the flat phase fronts of the scattered field. Additional minor scattering takes place along the x axis and this radiation is going to infinity if the ideal ENZ material ($\varepsilon_x = 0$). Furthermore, the remarkable property to be considered is the overall size of the embedded objects — in both cases the cylinder's diameter is comparable to the wavelength of the excitation. The size of the object does not affect the scattering suppression characteristics.

3. METAL-DIELECTRIC MULTILAYERED METAMATERIALS

While the above discussion was based on ideal homogeneous metamaterial, its actual realization could have an impact on the device performance. Hereafter, layered realization was considered. The effective permittivity tensor of layered composites can be directly evaluated from their thickness, periodicity, and optical parameters of the constitutive materials [e.g., 18]. While this approach can predict optical properties of the composites made of low contrast positive epsilon layers, it faces severe challenges once negative permittivity (plasmonic metals) materials are involved. Optical properties of these multilayered composites determined by guided surface electromagnetic modes (surface plasmon polaritons) on metal-dielectric interfaces, and spatial dispersion effects become especially significant in the parameters range where the effective medium theory (EMT) predicts vanishing values of permittivity [18].

The parameters used for analysis of homogeneous structure were obtained with layered realization, while effective medium theory, developed at [18], was used in order to find proper geometrical arrangement of the layers. The metamaterial parameters with the Au layer thickness of $d_g = 20$ nm and air thickness of $d_a = 100$ nm were considered with dispersive Au [19] and nondispersive dielectric. It is worth noting, that layered system, based on practical possible realization, do have optical losses, which were neglected in the homogeneous realization.

Figure 3 shows the results for the scattering on a cylindrical object, placed inside layered meta-

material. The remarkable similarity between ideal homogeneous case and realistic system, could be observed. While the field inside the object obtained relatively curved shape, the total transmitted field maintain its flat nature. Direct calculations show that the minor difference in performance between ideal and layered cases is within the range of 5% in the amplitude. Consequently, layered realization could suppress the scattering exactly in the same way the homogeneous ENZ meta-material does. Our resent original paper provides detailed description of the phenomena and also addresses issues of strong spatial dispersion in metal-dielectric composites [20].

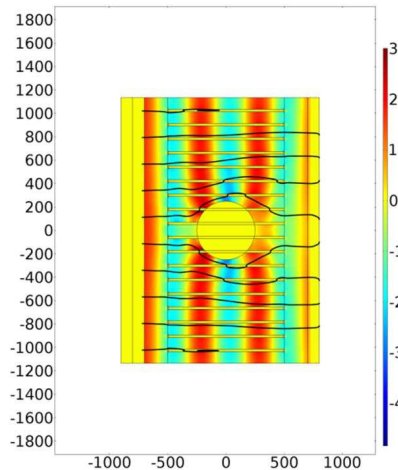


Figure 3: Electric field (y -component) distributions for the plane wave illuminating the multilayered cloak (a) with the 500 nm diameter PEC cylinder inside. Layers are 20 nm gold and 100 nm air. Black lines represent power flow.

4. CONCLUSION

We have shown that ENZ-metamaterials can perform as nearly-perfect scattering suppression devices for the objects of larger than wavelength sizes. The fundamental principle behind this new type of cloaking relies on the flat phase fronts of the scattered radiation. The scattering is controlled by the vanishing component of dielectric tensor along the propagation direction of the incident wave. In this case, the scattered field has flat phase fronts that do not distort the shape of the incident radiation. As the result, the transmitted field is only slightly attenuated with the wavefront maintaining its original profile, making the detection (almost always based on the amplitude and wavefront deformation observations) by a prying observer to be impossible. The same considerations are applicable for observation in reflection with the phased matched cloak (Figs. 2, 3). The proposed type of cloaking may find use not only in the conventional concealing applications but also serve as a platform for ‘cloaked detectors’ schemes [21] where bulk and alignment free cloaks may significantly reduce the complexity of the realization.

ACKNOWLEDGMENT

This work was partially supported by the Government of the Russian Federation (Grant 074-U01), Russian Fund for Basic Research (project #15-02-01344), and Australian Research Council. The calculation of field distributions has been supported by the Russian Science Foundation Grant No. 14-12-01227.

REFERENCES

1. Stutzman, W. L. and G. A. Thiele, *Antenna Theory and Design*, 3rd Edition, John Wiley & Sons, 2012.
2. Novotny, L. and N. van Hulst, “Antennas for light,” *Nature Photon.*, Vol. 5, 83–90, 2011.
3. Pendry, J. B., D. Schurig, and D. R. Smith, “Controlling electromagnetic fields,” *Science*, Vol. 312, 1780–1782, 2006.
4. Leonhardt, U., “Optical conformal mapping,” *Science*, Vol. 312, 1777–1780, 2006.
5. Schurig, D., J. J. Mock, B. J. Justice, S. A. Cummer, J. B. Pendry, A. F. Starr, and D. R. Smith, “Metamaterial electromagnetic cloak at microwave frequencies,” *Science*, Vol. 314, 977–980, 2006.

6. Valentine, J., J. Li, T. Zentgraf, G. Bartal, and X. Zhang, "An optical cloak made of dielectrics," *Nature Materials*, Vol. 8, 568–571, 2009.
7. Gabrielli, L. H., J. Cardenas, C. B. Poitras, and M. Lipson, "Silicon nanostructure cloak operating at optical frequencies," *Nature Photon.*, Vol. 3, 461–463, 2009.
8. Cai, W., U. K. Chettiar, A. V. Kildishev, and V. M. Shalaev, "Optical cloaking with metamaterials," *Nature Photon.*, Vol. 1, 224–227, 2007.
9. Li, J. and J. B. Pendry, "Hiding under the carpet: A new strategy for cloaking," *Phys. Rev. Lett.*, Vol. 101, 203901, 2008.
10. Landy, N. I. and W. J. Padilla, "Guiding light with conformal transformations," *Opt. Express*, Vol. 17, 14872, 2009.
11. Alu, A. and N. Engheta, "Achieving transparency with metamaterial and plasmonic coatings," *Phys. Rev. E*, Vol. 72, 16623, 2005.
12. Edwards, B., A. Al, M. E. Young, M. Silveirinha, and N. Engheta, "Experimental verification of ϵ -near-zero metamaterial coupling and energy squeezing using a microwave waveguide," *Phys. Rev. Lett.*, Vol. 100, 033903, 2008.
13. Liu, R., Q. Cheng, T. Hand, J. J. Mock, T. J. Cui, S. A. Cummer, and D. R. Smith, "Experimental demonstration of electromagnetic tunneling through an epsilon-near-zero metamaterial at microwave frequencies," *Phys. Rev. Lett.*, Vol. 100, 023903, 2008.
14. Jacob, Z., J. Y. Kim, G. V. Naik, A. Boltasseva, E. E. Narimanov, and V. M. Shalaev, "Engineering photonic density of states using metamaterials," *Appl. Phys. B*, Vol. 100, No. 1, 215–218, 2010.
15. Ginzburg, P. and M. Orenstein, "Nonmetallic left-handed material based on negative-positive anisotropy in low-dimensional quantum structures," *J. Appl. Phys.*, Vol. 103, 083105, 2008.
16. Ginzburg, P., F. J. Rodríguez Fortuño, G. A. Wurtz, W. Dickson, A. Murphy, F. Morgan, R. J. Pollard, I. Iorsh, A. Atrashchenko, P. A. Belov, Y. S. Kivshar, A. Nevet, G. Ankonina, M. Orenstein, and A. V. Zayats, "Manipulating polarization of light with ultrathin epsilon-near-zero metamaterials," *Opt. Express*, Vol. 21, 14907–14917, 2013.
17. Luo, J., W. Lu, Z. Hang, H. Chen, B. Hou, Y. Lai, and C. T. Chan, "Arbitrary control of electromagnetic flux in inhomogeneous anisotropic media with near-zero index," *Phys. Rev. Lett.*, Vol. 112, 073903, 2014.
18. Orlov, A., I. Iorsh, P. Belov, and Y. Kivshar, "Complex band structure of nanostructured metal-dielectric metamaterials," *Opt. Express*, Vol. 21, 1593–1598, 2013.
19. Palik, E. D., *Handbook of Optical Constants of Solids*, Academic Press, 1985.
20. Shalin, A. S., P. Ginzburg, A. A. Orlov, I. Iorsh, P. A. Belov, Y. S. Kivshar, and A. V. Zayats, "Scattering suppression from arbitrary objects in spatially dispersive layered metamaterials," *Phys. Rev. B*, Vol. 91, 125426, 2015.
21. Fan, P., U. Chettiar, L. Cao, F. Afshinmanesh, N. Engheta, and M. Brongersma, "An invisible metal semiconductor photodetector," *Nature Photon.*, Vol. 6, No. 6, 380–385, 2012.

THz Characterization of ITO Films on p-Si Substrates

E. R. Brown¹, W.-D. Zhang¹, H. Chen², and G. T. Mearini²

¹Department of Physics and Electrical Engineering
Wright State University, Dayton, OH 45435, USA

²Genvac Aerospace, Inc., 110 Alpha Park, Cleveland, OH 44143, USA

Abstract— This paper reports broadband THz free-space transmission measurements and modeling of indium-tin-oxide (ITO) thin films on p-doped Si substrates. Two such samples having ITO thickness of 50 and 100 nm, and DC sheet conductance 260 and 56 Ω/sq , respectively, were characterized between 0.2 and 1.2 THz using a frequency-domain spectrometer. The 50-nm-film sample displayed very flat transmittance over the 1-THz bandwidth, suggesting it is close to the critical THz sheet conductance that suppresses multi-pass interference and thereby achieves THz passive *equalization*. This is consistent with a simple transmission-line (TEM wave) model of the propagation. Also, the value of THz sheet conductance that best fits the transmittance data is roughly 50% higher than the dc value for both samples, suggesting that the ac conductivity is non-Drudian.

1. INTRODUCTION

Indium-tin oxide (ITO) has long been of interest as a transparent ohmic-contact (TOC) material for infrared detectors and other applications because of its unique optical properties and their variability by material composition [1–4]. In recent years ITO has migrated into the THz region along with interesting metamaterial-based component research also aimed at the TOC application [5–7]. Perhaps the most important study was made of ITO on semi-insulating GaAs where it was found that for a specific ITO thickness the internal reflections in a GaAs substrate can be suppressed, making the THz transmission flat with frequency [8]. A key feature of ITO in these applications is that its bulk conductivity is in the semi-metallic range, $\sigma \sim 10^4\text{--}10^5$ S/m, compared $\sigma > 10^7$ S/m for common (transition) metals, so that sheet resistances of around $\eta_o = 377 \Omega/\text{sq}$ can be obtained with film thicknesses of ~ 100 nm instead of the few-nm required of common transition metals. This makes the deposition more accurate and reproducible. However, the electrical properties of ITO depend on several material characteristics, such as the stoichiometry, and the effect of these on GHz-to-THz (RF) electrical conductivity is not yet well understood.

2. EXPERIMENTAL METHODS

For the present experiments, two ITO films having thickness 50 nm (#1) and 100 nm (#2) were deposited on p-silicon (CMOS-grade) substrates by reactive-ion-assisted, electron-beam evaporation with a stoichiometry of $\approx 10\%$ tin into indium oxide [9]. The thickness and bulk dc conductivity of the Si substrates were 393 μm and 6.0 S/m (16.7 $\Omega\text{-cm}$), respectively. The sheet resistance (conductance) of both ITO films was measured by the standard 4-point (Kelvin) dc probe technique and found to be 260 Ω/sq (3.85 mS/sq) and 56 Ω/sq (17.9 mS/sq) for films #1 and #2, respectively. Assuming uniform conduction through the films, these correspond to bulk conductivities of $\sigma_0 = 7.7 \times 10^4$ S/m for the 50-nm film, and $\sigma_0 = 1.79 \times 10^5$ S/m for the 100 nm film.

After fabrication the transmittance of a bare p-Si substrate (control sample) and the two ITO samples was measured from ≈ 200 to 1200 GHz using a diode-laser-driven photomixing spectrometer (Emcore PB7100). As described in detail previously [10], this instrument provides a combination of high resolution (~ 500 MHz), high dynamic range (~ 80 dB at 200 GHz; > 30 dB at 1.2 THz), and continuous tuning with no voids or laser mode-hops. The instrumental block diagram is shown in Figure 1 along with the location of the ITO-on-Si samples at the center point between the transmitter and receiver where the THz beam is almost perfectly collimated. For the control substrate and each of the ITO samples, three spectra are used to calculate the transmittance: (1) background spectrum $B(\nu)$ with all samples removed from the THz path, (2) noise floor $N(\nu)$ with the THz path in Figure 1 blocked by a metal plate, and (3) each of the three sample spectra $S_n(\nu)$. The individual transmittances $T_n(\nu)$ are then calculated as $T_n = [S_n(\nu) - N(\nu)]/[B(\nu) - N(\nu)]$.

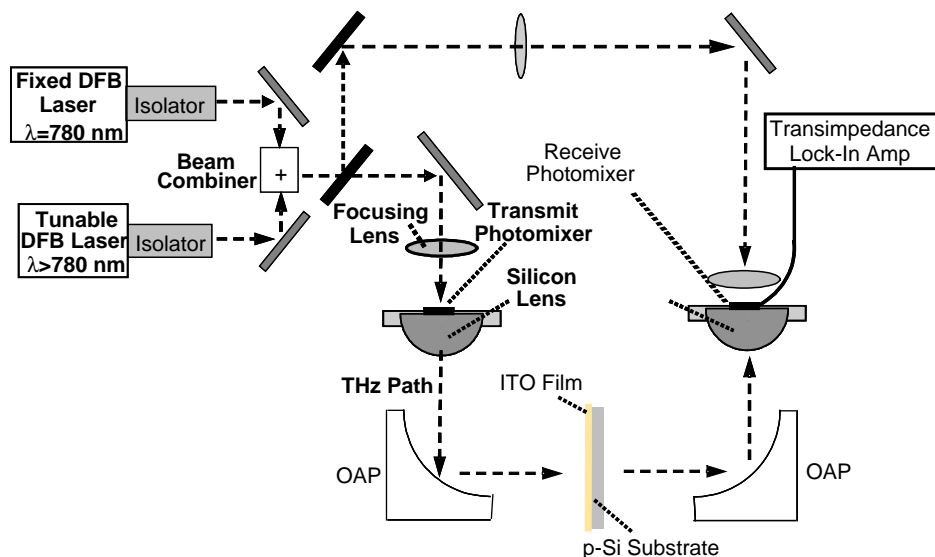


Figure 1: Instrumental block diagram for measuring ITO THz transmission vs frequency.

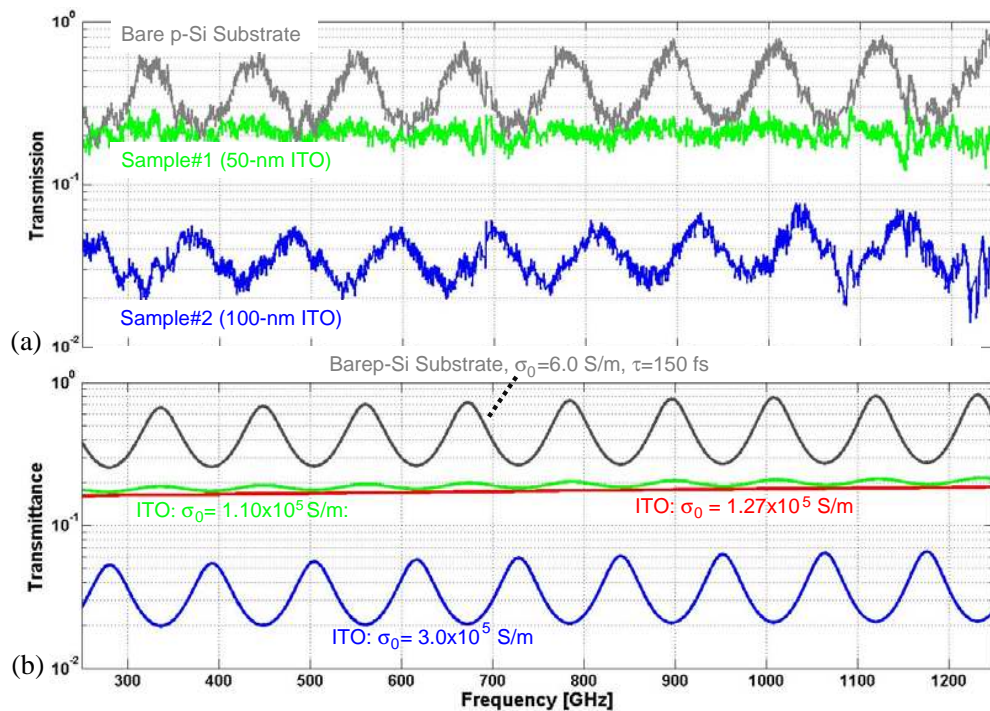


Figure 2: (a) Experimental THz transmittance for two ITO-on-Si substrates, and bare Si substrate. (b) Simulated THz transmittance for same samples as (a) plus a third ITO sample having the critical value of THz sheet conductance, which corresponds to a bulk conductivity, $\sigma = 1.27 \times 10^5$ S/m for the 50-nm-thick film. The slight upward trend in all curves is caused by the Drude-like behavior of the ac conductivity of the silicon.

3. EXPERIMENTAL RESULTS

Figure 2(a) shows the three transmittance spectra plotted on a logarithmic scale for comparative purposes. The Si control substrate shows the highest overall transmittance but also the strongest oscillation vs frequency of the three samples over the 1.0-THz bandwidth. This is caused primarily by the large real-part of dielectric function of silicon in the THz region ($\epsilon_r \approx 11.66$ [11]). The period of oscillation is very close to that expected for any lossless parallel-plate etalon, $\Delta\nu = c/(2nt) = 112$ GHz (for $n = 3.42$ and $t = 393$ μm). The oscillating transmittance is reminiscent of ideal dielectric-etalon optical behavior except that the low-frequency transmittance does not reach unity

at the peaks because of absorptive losses in the p-Si, presumably caused by the free holes. To better understand this we carried out numerical computations using a stratified-media, characteristic-matrix approach described in Ref. [12]. The absorptive losses in the p-Si can then be described by a complex dielectric function $\varepsilon(\omega) = \varepsilon_r \varepsilon_0 - j\sigma/\omega$ where σ is the electrical conductivity and ε_0 is the vacuum permittivity [13]. We applied the Drude model long-known to work well in crystalline semiconductors up to THz frequencies or higher at room temperature: $\sigma(\omega) = \sigma_0/(1 + j\omega\tau)$, where σ_0 is the dc bulk conductivity, τ is the momentum relaxation time, and the + sign assumes a counterclockwise rotating phasor, $e^{+j\omega t}$, convention for the propagating-wave time dependence. The simulated transmittance through the bare p-Si is plotted in Figure 2(b) for $\sigma_0 = 6.0$ S/m consistent with dc 4-point-probe measurements, and $\tau = 150$ fs is determined by iteration. It mimics the experimental in all respects, especially the period of oscillation.

We then characterized the two ITO films deposited on the separate but materially-equivalent p-Si substrates, and the experimental transmittance is plotted in Figure 2(a). The transmittance of the 50-nm-thick film occurs just below the valleys of the bare-Si substrate, and the transmittance of the 100-nm film is significantly lower, as expected from the much higher dc sheet conductance of the 100-nm film (56 Ω /sq) compared to the 50-nm film (260 Ω /sq). It was surprising, however, that the 50-nm-film transmittance displayed so much less oscillation than the 100-nm transmittance. It appears that the THz transmission is “equalized” over the entire 1 THz of bandwidth — similar in effect to what has been designed into broadband telephone circuits for nearly a century [14], including modern Digital Subscriber Line (DSL) technology. So we augmented the stratified-media simulation, now including the ITO film into the model and parameterizing it by a complex THz bulk conductivity $\varepsilon(\omega) = \varepsilon_r \varepsilon_0 - j\sigma_{\text{THz}}/\omega$. We assumed that $\varepsilon_r = 1.0$ and the THz conductivity σ is a constant — a reasonable assumption given that the momentum relaxation time of electrons is probably much less than $1/\omega$ across the experimental band equal because of the ceramic nature of the ITO. The silicon-substrate parameters were the same as discussed above. By iteration once again, we determined good-fit values of $\sigma_{\text{THz}} = 1.1 \times 10^5$ S/m in the 50-nm film, and $\sigma_{\text{THz}} = 3.0 \times 10^5$ S/m in the 100-nm film. The resulting transmittance curves in Figure 2(b) are in good agreement with the corresponding experimental spectra of 2(a). Interestingly, both of these σ_{THz} values are substantially higher than the corresponding dc values measured by 4-pt probing, the 50-nm-film value being 43% higher, and the 100-nm-film value being 68% higher. This suggests that the frequency-dependent conductivity of ITO is non-Drudian.

4. PHYSICAL BASIS AND DESIGN RULE

Now we address the physical basis for the 50-nm-ITO transmittance spectrum being more *equalized* than the 100-nm spectrum, and present a useful *design rule*. The clue is the 180° phase shift in the oscillating transmittance spectrum of Figure 2 in going from the bare-Si (or 50-nm-ITO) to the 100-nm ITO. A feature of any etalon structure that can cause such a phase shift is a sign change in the reflection coefficient at one of the interfaces. From the Fresnel equations, the interfacial transmission coefficients are generally real and positive. To explore this further we display in Figure 3(a) a transmission-line-model — a simplification of the stratified-media approach — which assumes the ITO film thickness is much less than the material wavelength, and that the propagation within the Si substrate can be represented as a TEM mode on a transmission line. The model predicts a transmittance that depends on the air-ITO-Si transmission coefficient (the ratio of the transmitted to incident electric fields) and the Si-air transmission coefficient, both of which are always positive and mostly independent of frequency. However, the oscillation in the overall transmittance arises from the subsequent reflection at the Si-ITO-air interface and the (“multi-pass”) interference it creates with the first pass of radiation through the substrate.

The transmission line model predicts a Si-ITO-air reflection coefficient of

$$\Gamma = (Z_{\perp} - Z_S) / (Z_{\perp} Z_S) \quad (1)$$

where Z_S is the substrate characteristic impedance [= $\eta_0/(\varepsilon_r)^{1/2}$], $Z_{\perp} = \eta_0 \cdot Z_{\text{ITO}}/(\eta_0 + Z_{\text{ITO}})$, Z_{ITO} is the ITO sheet impedance, and $\eta_0 = 377 \Omega$. Clearly, Γ changes sign at the critical value $Z_{\perp} = Z_S$ where Γ is also identically zero, and therefore multi-pass interference should be suppressed. This can be re-written as $Z_S = \eta_0 \cdot Z_{\text{ITO}}/(\eta_0 + Z_{\text{ITO}})$, or solving for the critical value:

$$Z_{\text{ITO},C} = Z_S \eta_0 / (\eta_0 - Z_S). \quad (2)$$

Neglecting the imaginary part of the dielectric function of Si, we have $\varepsilon_r = 11.66$ and get $Z_S = 110.4 \Omega$ /sq. Eq. (2) then yields a value $Z_{\text{ITO}} = 156.1 \Omega$ /sq, which corresponds to a bulk conduc-

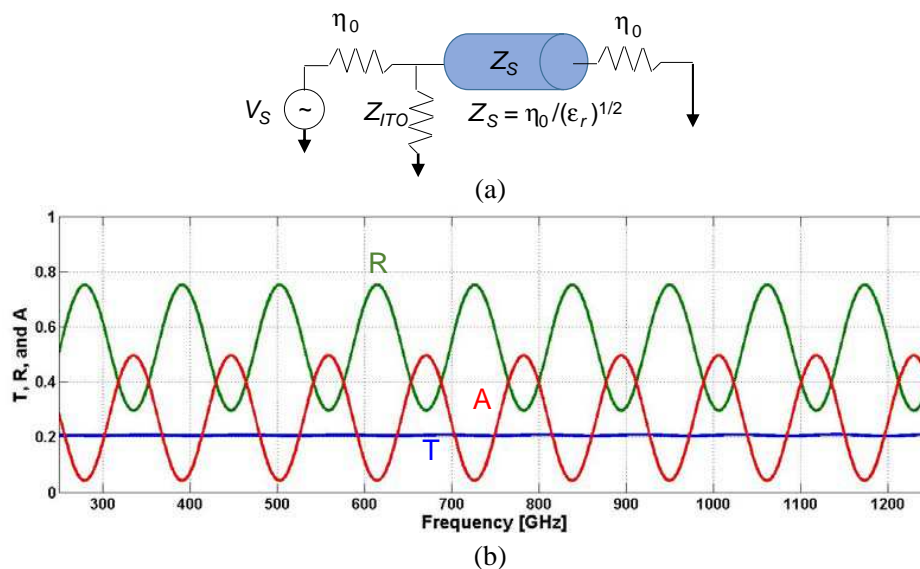


Figure 3: (a) Transmission-line equivalent circuit of the ITO-on-Si etalon. (b) Calculated values of transmittance T , reflectance R , and absorbance A for ITO film having the critical value of THz sheet conductance.

tivity of 1.28×10^5 S/m for the 50-nm-thick ITO film. Armed with this value, we repeated the stratified-medium computation for a fictitious ITO layer having these properties, and the results are shown in Figure 2(b). As predicted, the oscillations in the transmittance are almost totally suppressed, the small deviation being caused by the frequency-dependent dielectric function of Si through the Drude model. For Z_{ITO} greater than this critical value, $Z_{||}$ becomes greater than Z_S and Γ is positive according to (1). For Z_{ITO} less than this value, $Z_{||}$ is less than Z_S and Γ becomes negative.

5. DISCUSSION

Unfortunately, having the critical value of sheet impedance does not mean that standing waves are suppressed entirely, but only their effect on the forward transmittance T . To emphasize this, Figure 3(b) shows other straightforward results from the transmission-line model — the overall reflectance R and absorbance A — for the ITO-Si etalon. R is the fraction of incident power reflected back to the source, and A is the fraction absorbed, such that $T + R + A = 1$. In this case we artificially set the THz conductivity of the p-Si to zero so as not to confuse ITO absorption with Si bulk absorption. As expected, T is flat with frequency, but R and A both oscillate with the characteristic period $\Delta\nu = 112$ GHz. And they are 180° out of phase, meaning that at any frequency where the etalon displays maximum absorption, it also displays minimum reflection, and vice versa. This has implications for the use of ITO and other thin-film absorbers (e.g., graphene) in free-space-coupled THz quasi-optical components.

ACKNOWLEDGMENT

This material is based upon work supported by, or in part by, the US Army Research Laboratory and the US Army Research Office under contract number W911NF-11-1-0024.

REFERENCES

1. Hamberg, I. and C. G. Granqvist, "Transparent and infrared-reflecting indium-tin-oxide films: Quantitative modeling of the optical properties," *Appl. Optics*, Vol. 24, No. 12, 1815–1819, 1985.
2. Henry, J. and J. Livingstone, "ITO film analyses by FTIR," *Infrared Phys. Technol.*, Vol. 36, 779–784, 1995.
3. Tamada, M., H. Koshikawa, F. Hosoi, and T. Suwa, "FTIR reflection absorption spectroscopy for organic thin-film on ITO substrate," *Thin Solid Films*, Vol. 315, 40–43, 1998.
4. Brewer, S. H. and S. Franzen, "Optical properties of indium tin oxide and fluorine-doped tin oxide surfaces: Correlation of reflectivity, skin depth, and plasmon frequency with conductivity," *J. Alloys and Compounds*, Vol. 338, 73–79, 2002.

5. Yang, C.-S., C.-H. Chang, M.-H. Lin, P. Yu, O. Wada, and C.-L. Pan, “THz conductivities of indium-tin-oxide nanowhiskers as a graded-refractive-index structure,” *Opt. Express*, Vol. 20, Suppl. 4, 441–451, 2012.
6. Kim, J.-I., K. H. Ji, M. Jang, H. Yang, R. Choi, and J. K. Jeong, “Ti-doped indium tin oxide thin films for transparent field-effect transistors: Control of charge-carrier density and crystalline structure,” *ACS Appl. Materials and Interfaces*, Vol. 3, 2522–2528, 2011.
7. Yang, C.-S., C.-M. Chang, P.-H. Chen, P. Yu, and C.-L. Pan, “Broadband terahertz conductivity and optical transmission of indium-tin-oxide (ITO) nanomaterials,” *Opt. Express*, Vol. 21, No. 14, 16670–16682, 2013.
8. Kroll, J., J. Darmo, and K. Unterrainer, “Metallic wave-impedance matching layers for broadband terahertz optical systems,” *Opt. Express*, Vol. 15, 6552–6560, 2007.
9. Genvac Aerospace Inc., United States Patent# 6,153,271.
10. Demers, J. R., R. T. Logan, Jr., N. J. Bergeron, and E. R. Brown, “A coherent frequency-domain THz spectrometer with a signal-to-noise ratio 60 dB at 1 THz,” *Proc. SPIE Defense and Security*, Paper# 6949-8, Orlando, FL, Mar. 16–20, 2008.
11. Bolivar, P. H., M. Brucherseifer, J. G. Rvivas, R. Gonzalo, I. Ederra, A. L. Reynolds, M. Holker, and P. Mgt, *IEEE Trans. Microwave Theory and Tech.*, vol. 51, 1062–1066, 2003.
12. Born, M. and E. Wolf, *Principles of Optics*, 4th Edition, Pergammon, Oxford, 1970.
13. Ulaby, F. T., *Fundamentals of Applied Electromagnetics*, 2001 Media Edition, Eqn. 7.4, Prentice-Hall, Upper Saddle River, NJ, 2001.
14. Zobel, O. J., “Distortion correction in electrical circuits with constant resistance recurrent networks,” *Bell Systems Technical Journal*, Vol. 7, 438, 1928.

Coupled Resonator Mediated Transmission of Light through Sub-wavelength Holes for Multispectral Imaging Applications

W. R. Buchwald and K. C. Kerby-Patel
University of Massachusetts Boston, USA

Abstract— Using finite difference time domain techniques, the transmission of light through $6\ \mu\text{m}$ period arrays of sub-wavelength holes in optically thick metallic films is investigated. Over the wavelength range $2\ \mu\text{m}$ to $16\ \mu\text{m}$, it is observed that by centering an additional metallic element within the sub-wavelength hole, well defined resonance peaks are produced which are strongly dependent on resonator and hole dimensions but only weakly dependent on metal film thickness. Resonant line-width however, is found to be strongly dependent on metal film thickness. Thicker films produced the narrowest full-width half-max values, which were less than $1.0\ \mu\text{m}$. Such control of resonant wavelength and line-width, along with the size of the elements investigated and the $6\ \mu\text{m}$ array period used, suggests the fabrication of an optical filter with transmission properties that vary across the face of a focal plane array for use in multispectral imaging applications.

1. INTRODUCTION

The interaction of freely propagating electromagnetic waves with patterned metallic structures dates back to the invention of the optical diffraction grating. Investigations of those gratings led to the observation of Woods [1] anomalies and their explanation by Raether [2] as being caused by the excitation of surface plasmon oscillations. At longer wavelengths, the field of frequency selective surfaces as discussed by Munk [3] and finally the more recent extraordinary optical transmission (EOT) of light through sub-wavelength holes as observed by Ebbson [4], all rely on the excitation of some type of surface mode which has an in-plane or a near in-plane wave vector. In addition to the optical excitation of freely propagating modes with grazing angle wave vectors caused by grating or grating-like topologies, there are also the generation of surface plasmon polaritons with in-plane propagation vectors, which are governed by a dispersion relation of the form

$$k = \sqrt{\frac{\epsilon_d \epsilon(\omega)}{\epsilon_d + \epsilon(\omega)}} \quad (1)$$

where ϵ_d is the relative permittivity of the dielectric adjacent to the metallic element surface, $\epsilon(\omega)$ is the frequency dependent permittivity of the metal, k is the surface wave propagation vector, ω is the frequency of oscillation and c is the speed of light in vacuum [5]. Space prohibits a detailed discussion of this dispersion relation other than to address the salient characteristics pertinent to this work. In particular, $\epsilon(\omega)$ is in general complex and two branches of solutions will result, one of which always falls below the light line for the material. This surface plasmon polaritons branch deviates little from the light line at the longer wavelengths investigated for this work. Significantly, because the branch does fall below the light line, in general there is never enough incident energy available to directly excite a surface plasmon mode from a freely propagating field. Because of this, some means, such as a grating or a scattering event, is required to impart the transverse momentum required to excite the surface plasmon mode. Evanescent excitation of plasmon modes is also possible but not pertinent to this work [6].

This work utilizes finite difference time domain numeric methods to investigate the coupled resonator characteristics of arrays of holes in thick metal films. The particular topology investigated here places an additional metallic resonator within the hole. It is observed that the addition of the central resonator produces longer wavelength resonances controlled by the lateral dimensions of the hole and resonator. It is further observed that narrower resonant line widths result when the films are of a thickness comparable to the array period.

Although no closed form analytic predictive equations are presented, the ability to vary a relatively narrow band transmission by controlling lateral dimensions, suggests such a topology's use as a filter placed directly in front of a focal plane array. An array of similar sized elements would allow distinct narrow-band spectral lines to be allocated on a pixel by pixel basis while others pixels could be allocated for broadband image formation. Such a filter, operating in the long wave $7\ \mu\text{m}$

to 13 μm range, is suggested for use in multispectral imaging systems to allow for the determination of scene spectral content and in turn identification of pathogens or adverse chemical compounds in real time at video frame rates. Such a multispectral imaging system would impact cancer diagnosis and treatment as well as providing front line defense capability for homeland security applications.

2. FDTD SIMULATIONS

The basic metallic topology used for this work is shown in the Fig. 2(a). Fig. 1(b) shows the simulated, finite difference time domain (FDTD) transmission intensity through arrays of 3 μm and 4 μm holes, in a 2 μm thick Au plate, simulated over the 2 μm to 16 μm range without the addition of the central resonator. For all simulations, Drude theory was used to determine the frequency dependent permittivity using plasma and relaxation frequencies of 1.36×10^{16} (rad/s) and 4.05×10^{13} (rad/s) respectively. Periodic boundary conditions were used in the plane of the film and perfectly matched layers in the direction of incident plane wave propagation. This result of a strong transmission peak near the wavelength equal to the array period, (the arrow in the figure), is consistent with both experimental and simulated data obtained by other authors [7].

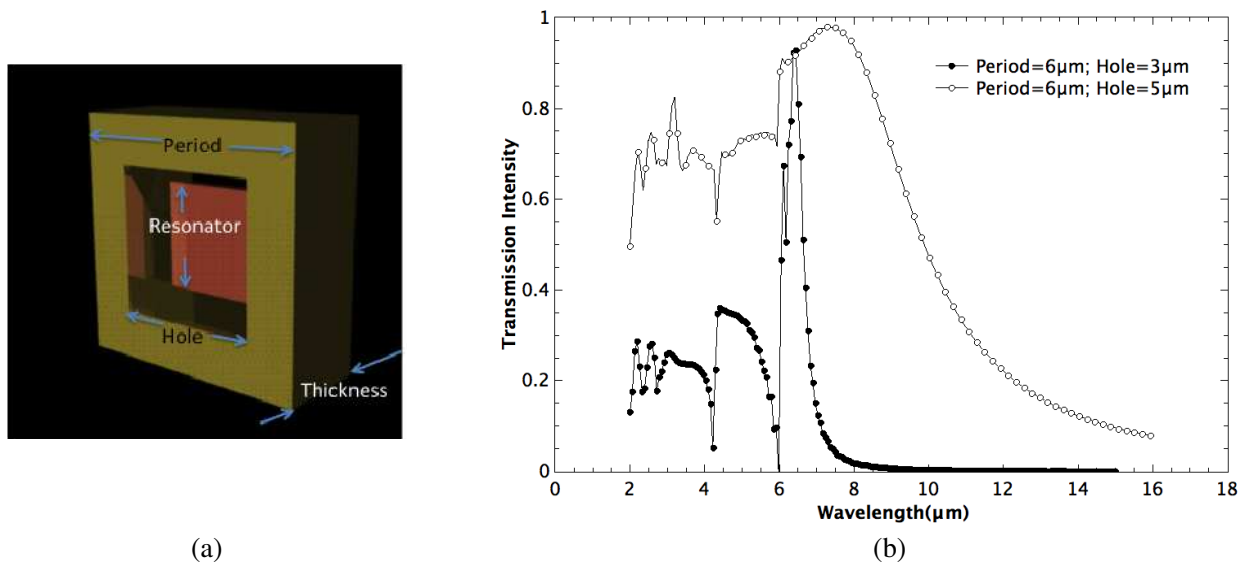


Figure 1: (a) Topology and nomenclature used in this work. (b) Simulated transmission through both a 3 μm and 4 μm hole in the 2 μm thick film. For this simulation no resonator was present. The arrow marks the wavelength equal to the array period and serves as the demarcation between guided and freely propagating fields interfering to the left at shorter wavelengths and plasmon related resonances to the right at longer wavelengths as described in the later sections of this work.

Figure 2 shows the transmission intensity when a 3.5 μm wide central resonator element is centered in the 4.0 μm hole and illustrates the effect of thickness on system response. When both central resonator and Au plate are thin (i.e., 0.1 μm), a very broad peak is seen at a wavelength of roughly 14 μm and the resonance at the array period wavelength is dramatically suppressed. When the plate thickness is increased to 2 μm while keeping the resonator thin and centered between the front and back plate surfaces, the resonant frequency shifts to a lower wavelength. More significantly, a dramatic reduction is observed in the resonance line width from 7 μm FWHM to less than 1 μm FWHM. When both the resonator and plate thicknesses are increased to 2 μm , the 14 μm resonance shifts to a slightly longer wavelength and additional narrow resonance peaks are seen at roughly 7 μm and below while still maintaining a relatively narrow line width. It is this narrowing of the resonant response which makes this topology suitable as a filter element. Interestingly, it was found that when the thin central resonator was aligned with either the front or back surface of the plate as opposed to being centered between the two surfaces, no reduction in line width was observed. This suggests that the spreading of the electric field over a larger area reduces loss, improving the resonator quality factor.

Figure 3 shows transmission intensity as a function of both 4 μm and 3 μm holes with 3.5 μm and 2.5 μm resonators respectively at array periods of both 6 μm and 7 μm . The arrows in the

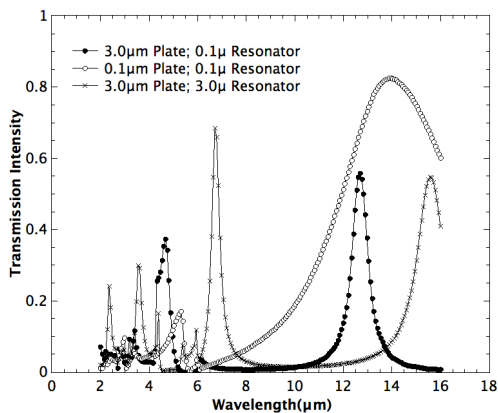


Figure 2: Array response as a function of plate and resonator thickness for a $4\ \mu\text{m}$ wide hole and a $3.5\ \mu\text{m}$ wide resonator.

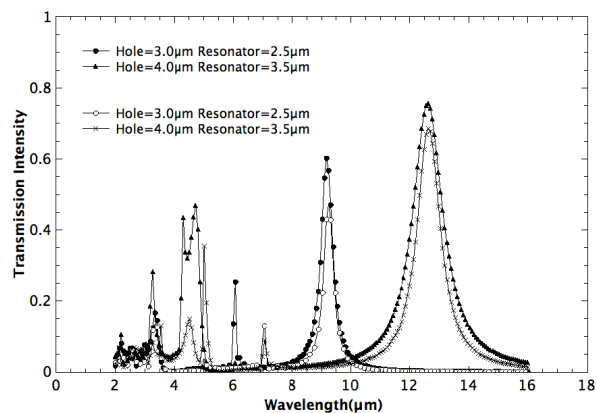


Figure 3: Transmission resonance of two different hole/resonator combinations as a function of array period. The arrows show the fundamental array period resonance for each period. No effect on resonance wavelength is observed to be a function of the array period for this system.

figure point to the resonance that correspond to each array period; no significant shift in resonance due to this change in period is observed. Figure 4 shows the effects of resonance wavelength for a fixed hole width of $3\ \mu\text{m}$ as a function of both resonator width and resonator thickness. This figure illustrates the typical tuning range that could be expected for this type of metallic filter element.

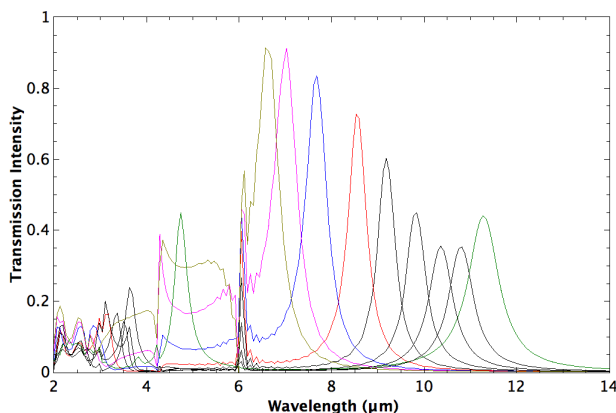


Figure 4: Resonance wavelengths for a $3\ \mu\text{m}$ wide hole in a $2\ \mu\text{m}$ thick Au film as the thickness and width of the initially $0.1\ \mu\text{m}$ thick, $2.5\ \mu\text{m}$ wide resonator is varied.

3. DISCUSSION

Although the predictive behavior of the loaded hole topology investigated here, in terms of any combination of hole width, array period, resonator dimension and film thickness is not immediately at hand, a few general observations are made regarding transmission through an array of holes without resonator loading.

It is generally assumed that the optical transmission of light through sub-wavelength holes is a plasmon-mediated process. Because plasmon modes require the addition of transverse momentum in order to be excited, either a scattering event, or a grating based topology is required. In this case, both the edges of the hole as well as the hole periodicity, effectively producing a grating topology, are available to provide the needed transverse momentum for plasmon mode generation. Once the plasmon modes are generated, standing waves will be resonantly established across the face of the film in order to satisfy the array periodicity of the system. Thus, the most fundamental mode will have a wavelength equal to the array period times the effective index [8]. At the wavelengths

investigated here, and from Equation (1), the effective index of a freely propagating plasmon mode is seen not to deviate substantially from unity. In addition, it has previously been shown that the guided plasmon mode available to this system, namely the 90° wedge mode, also has an effective index that does not substantially deviate from unity [9]. This implies that the fundamental resonant wavelength should be roughly equal to the array period, as has been observed in this work. Additional structure in the hole-only transmission case results from the holes acting as a grating and producing waves with propagation vectors at grazing angles.

Because the array period alone sets the fundamental resonant frequency it is the array periodicity that sets the minimum energy available to excite any plasmon mode.

In other words, there is enough energy available in the incident photons to excite those plasmon modes to the right of the wavelength equal to the array periodicity once the momentum matching condition is met. All those effects to the left of the fundamental array periodicity wavelength, stem from freely propagating field interactions, which have propagation vectors out of the plane of the film.

These freely propagating fields are above the cutoff frequency of the hole when acting as a waveguide, and allow free transmission of propagating fields through the hole when appropriate boundary conditions are met.

Once excited, plasmon modes carry energy from the incident side of the film to the exit side of the film and resonate with the geometric features there. These resonant interactions can be complex in nature, but once excited, produce transmission into the far field, similar to that produced by oscillating dipoles.

Qualitatively, the structure can be described as an effective impedance encountered by the plasmon mode currents. The gaps between resonator and screen present a capacitance that depends on the width of the gap, thicknesses of the screen and resonator, front-to-back position of the resonator, and the lateral dimensions of the hole and resonator. The path length around hole presents a resistance and inductance to plasmon mode current. The interaction of these two features produces a resonance at a larger wavelength than the fundamental mode of the holes-only structure. Increasing the inductance or capacitance by modifying the geometry will increase the resonant wavelength of the structure.

It is not clear at this point the best methodology to use to model the interactions of these weakly bound plasmon modes and their trajectories over the meta-surface topology, nor how to a priori predict the resonant condition. The reduction in line width due to film thickness does suggest however a lower loss and higher quality factor resonance is achieved by increasing the metal thickness of the plate and the resonator to values comparable to the array period.

4. CONCLUSION

A resonator-loaded hole in a metal film has been investigated using FDTD techniques. A dramatic reduction in transmission resonance line-width has been observed when the metal film thickness is increased to values on the order of the array period. This reduction in line width, along with the overall size of the arrays, suggests a potential application of such films as a narrow band filter for multispectral imaging applications, whereby each individual pixel of a focal plane array can be assigned a specific spectral line by placing a suitably designed array directly over each pixel of the focal plane imaging array.

REFERENCES

1. Wood, R. W., "On a remarkable case of uneven distribution of light in a diffraction grating spectrum," *Philos. Mag*, Vol. 4, 396, 1912.
2. Raether, B. A., *Surface Plasmons on Smooth and Rough Surfaces and on Gratings*, Springer-Verlag, Berlin, 1988.
3. Munk, H., *Frequency Selective Surfaces: Theory and Design*, John Wiley and Sons, 2000.
4. Ebbesen, T. W., H. J. Lezec, H. F. Ghaemi, T. Thio, and P. A. Wolf, "Extraordinary optical transmission through sub-wavelength hole arrays," *Nature*, Vol. 391, 667, 1998.
5. Maier, S. A., *Plasmonics: Fundamentals and Applications*, Springer, 2007.
6. Kretschmann, E. and H. Raether, "Radiative decay of non-radiative surface plasmons excited light," *Z. Naturforsch*, Vol. 23a, 2135, 1968.
7. Degiron, A., H. J. Lezec, W. L. Barnes, and T. W. Ebbesen, "Effects of hole depth on enhanced light transmission through sub-wavelength hole arrays," *Applied Physics Letters*, Vol. 81, 4327, 2002.

8. Mrejen, M., A. Israel, H. Taha, M. Palchan, and A. Laws, "Near-field characterization of extraordinary optical transmission in sub-wavelength aperture arrays," *Optics Express*, Vol. 15, 9129, 2007.
9. Pan, Z., J. Guo, R. Soref, W. Buchwald, and G. Sun, "Guided plasmon modes of triangular and inverted triangular cross-section silver nanoridges," *JOSE B*, Vol. 29, 950, 2012.

MM-wave-to-THz Modulation with Graphene-oxide-silicon Etalon Structures

W.-D. Zhang¹, P. H. Q. Pham², E. R. Brown¹, and P. J. Burke²

¹Department of Physics and Electrical Engineering
Wright State University, Dayton, OH 45435, USA

²Department of Electrical and Computer Engineering
University of California, Irvine 92697, USA

Abstract— This paper presents both numerical modeling and experimental demonstration of a MM-wave-to-THz amplitude modulator based on a graphene-oxide-silicon structure. The silicon substrate not only supports back gate bias but also acts as Fabry-Perot etalon resonant cavity for perpendicular-incident radiation. Graphene deposited on one surface of the etalon provides a tunable sheet conductance and etalon transmittance under gate bias. A 1.4-dB depth-of-modulation is measured with a 101 GHz setup, and modulation of 530 GHz radiation is also demonstrated. In all cases, the modulator behaves linearly with respect to gate bias and is easy to use because of its large aperture (~ 1 square cm) and transmission-mode operation.

1. INTRODUCTION

Millimeter-wave (MMW) and THz radiation have found application in medical imaging because their propagation characteristics can be used to sensitively detect the hydration level of targeted bio-tissues [1–3]. For the development of imaging systems, an amplitude modulator is a very useful component. The rough performance metrics of a practical modulator include ≥ 10 dB depth-of-modulation with at least 30 Hz of modulation bandwidth. One of the possible basis structures for a modulator is illustrated in Fig. 1(a). As a MMW-to-THz beam propagates through an etalon resonant cavity, its transmittance can be modified by a thin conducting film with tunable conductivity placed on either facet of the etalon. Of course, a conducting film also causes some absorption of the beam power.

In this paper, we report a realization of an amplitude modulator design with a graphene-oxide-silicon etalon structure [Fig. 1(b)]. The device consists of an oxide-pre-coated high-resistivity silicon substrate with a $\sim 1 \times 1$ -cm monolayer-thick graphene film deposited on top. The oxide is 90 nm thick. The structure is packaged into a graphene-channel field-effect transistor (GFET) with source and drain contacts deposited on the graphene, and a (back) gate contact on the opposite side of the silicon.

For perpendicular-incident radiation, the silicon slab functions as Fabry-Perot etalon. Its transmission spectrum displays resonant peaks located at integral multiples of $f_0 = c/2nL = 112$ GHz where $L = 392 \mu\text{m}$ is the silicon thickness, and $n = 3.41$ is its refractive index [4]. The graphene sheet provides tunable conductance by the back gate bias which shifts the energy of its Fermi level.

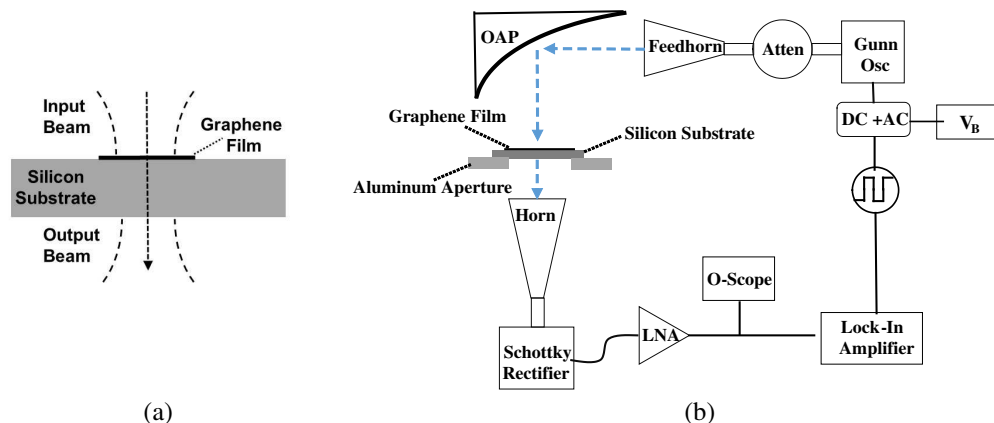


Figure 1: (a) Prototype amplitude modulator (graphene-oxide-silicon etalon). (b) 101 GHz modulation setup.

Then the overall transmission of perpendicular radiation is modified proportionally. For gate tuning, graphene has already been extensively studied as optical modulators during the past several years, first in the mid-infrared [5] and then in the THz region [6–8].

2. MODELING

The transmission matrix method [9] is applied to study the effect of graphene sheet conductance on transmittance of perpendicular radiation through the graphene-oxide-silicon etalon. This yields

$$T_e = \left| \frac{t_1 t_2 \exp\left(-j \frac{2\pi\sqrt{\varepsilon_s} L}{c}\right)}{1 + r_1 r_2 \exp\left(-j \frac{4\pi\sqrt{\varepsilon_s} L}{c}\right)} \right|^2 \quad (1)$$

where r_1 is the reflection coefficient at the air/Si interface, t_1 is the transmission coefficient at the air/Si interface, r_2 is the reflection coefficient at the Si/graphene interface, and t_2 is the transmission coefficient at graphene/air interface. These parameters are linked to the dielectric constants of silicon ε_s and graphene $\varepsilon_g = \text{Re}\{\varepsilon_g\} + j\text{Im}\{\varepsilon_g\}$ through [10]:

$$r_1 = \frac{1 - \sqrt{\varepsilon_s}}{1 + \sqrt{\varepsilon_s}}, \quad t_1 = \frac{2}{1 + \sqrt{\varepsilon_s}} \quad (2)$$

$$r_2 = \frac{\sqrt{\varepsilon_s} - (\sqrt{\varepsilon_g} + 1)}{\sqrt{\varepsilon_s} + (\sqrt{\varepsilon_g} + 1)}, \quad t_2 = \frac{2\sqrt{\varepsilon_s}}{\sqrt{\varepsilon_s} + (\sqrt{\varepsilon_g} + 1)}, \quad (3)$$

The transmittance T spectra for various sheet conductances are plotted in Fig. 2(a) and confirm that the strongest modulation occurs at the resonant frequencies of the etalon located at 112, 224, 336, 448, 560 GHz, etc.. The depth-of-modulation is defined here in terms of the ratio of the high transmittance T_{high} to the low transmittance T_{low} : $\text{DoM} = 10 * \log_{10}(T_{high}/T_{low})$, all of which depend on the graphene sheet conductance at the operating frequency. As observed in Fig. 2(a), at a peak of 112 GHz, the DoM is ≈ 5.0 dB if the sheet conductance is varied from 0.66 to 5.3 mS. In contrast, at a valley frequency such as 167 GHz, the DoM drops to ~ 1.0 dB given the same variation in sheet conductance. To see the modulation effect more directly, we plot in Fig. 2(b) the transmittance vs sheet conductance for various frequencies. Here we can see that at 112 GHz the transmittance drops from 0.8 to 0.08 (DoM = 10 dB) for a change of 0.6 to 13.6 mS. And for all frequencies, greater differential T occurs at smaller values of sheet conductance, especially in the range less than 4 mS. This is associated with the fact that the resonance quality factor Q increases rapidly in this range as displayed in Fig. 2(a) [11], which does not include the imaginary part of the graphene conductance. As an example, at the sheet conductance of 0.66 mS and at the 112-GHz peak [highest-DoM case considered in Fig. 2(a)], the Q is approximately 3.5.

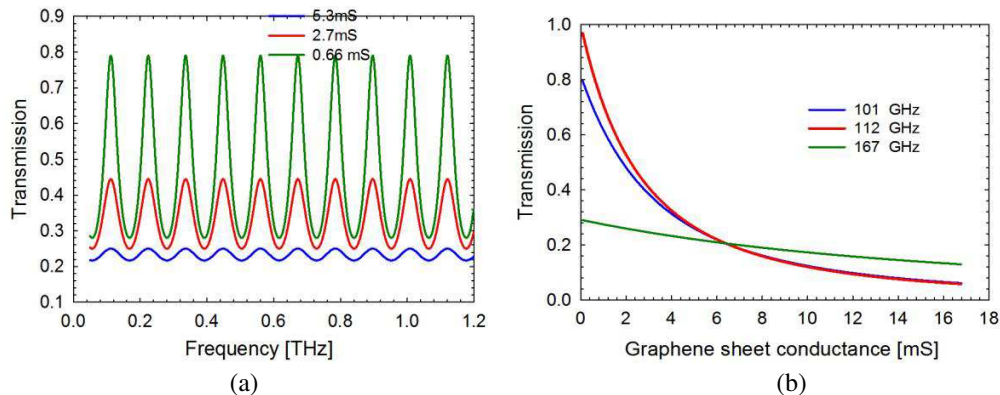


Figure 2: (a) The transmission at a sheet conductance vs. frequency. (b) The transmission at a single frequency vs. the graphene sheet conductance.

3. EXPERIMENTAL RESULTS

The graphene used in the present modulator structure was in the form of $\sim 1 \times 1$ cm films grown by CVD and then transferred from copper to silicon through a “fishing” procedure. Poly-methyl methacrylate (PMMA) was spun onto the graphene film on copper foil. The copper foil was then etched away using ammonium persulfate. Next the graphene deposited on PMMA was cleaned in DI water, and wettransferred onto a high-resistivity silicon substrate. Finally the PMMA was removed with acetone wash, and the graphene film was annealed in a hydrogen+argon atmosphere.

The first experimental setup includes a 101-GHz waveguide-mounted feedhorn-coupled Gunn-oscillator as the transmitter, and a waveguide-mounted feedhorn-coupled Schottky-rectifier as the receiver. The GFET structure was located at the focal plane of an off-axis paraboloid mirror located approximately half-way between the two [Fig. 1(b)]. The focused beam spot size is ≈ 5 mm, which is sufficiently matched to the large area of graphene. The bias to the Gunn-oscillator was square-wave amplitude modulated off-and-on with a MOSFET circuit. The detected signal from the Schottky rectifier was fed to a 1000x-gain low-noise voltage amplifier, and then demodulated with a lock-in amplifier synchronized to the square wave. The signal-to-noise ratio (SNR) was ~ 60 dB, which was determined by the average transmitted signal divided by its standard deviation over 600 sample points for the given modulation frequency (1 kHz) and lock-in amplifier integration time (0.3 ms).

The experimental results for the 101-GHz modulator are plotted in Fig. 3 where the best DoM was 1.4 dB — a 40% change. This occurred when the gate bias was varied from -4 V to $+34$ V. Simultaneously, the graphene sheet conductance (at a constant source-drain bias of 0.1 V) was monitored and changed from 1.6 mS to 0.4 mS. Beyond the gate bias of ~ 33 V, however, the sheet conductance decreased no further and took an upward (V-like) turn as it hit the Dirac point. Nevertheless, the experimental DoM is reasonably close to the theoretical value, which from Fig. 2(b) is $\approx 10 * \log_{10}(0.745/0.52)$, or 1.6-dB.

Similar measurements were conducted in a higher-frequency set-up having a 530 GHz transmitter

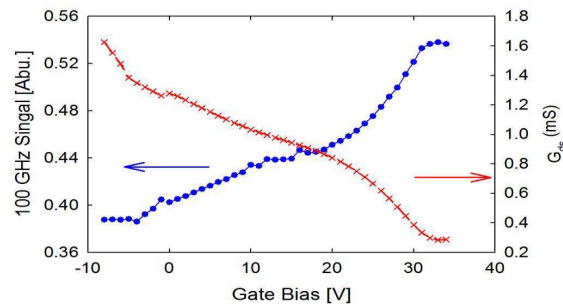


Figure 3: The measured modulation by gate bias at 101 GHz.

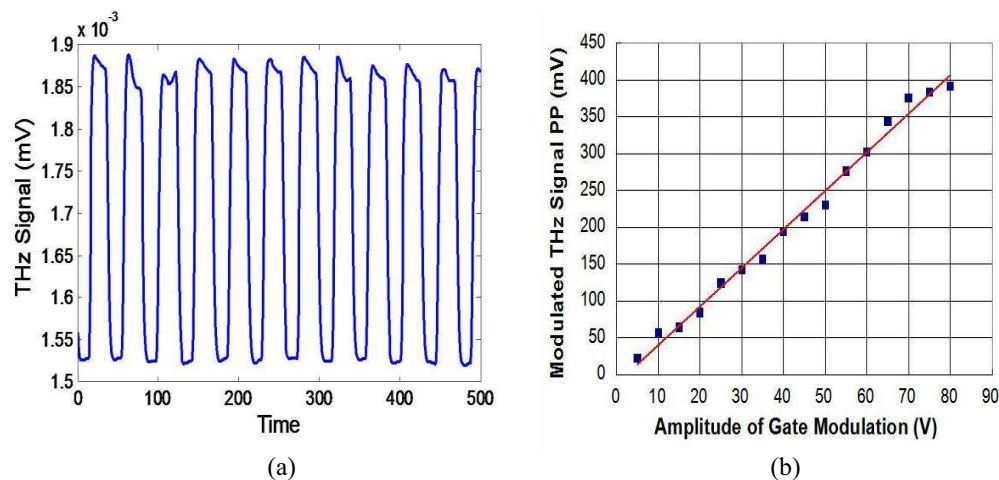


Figure 4: (a) The modulation of transmitted signal at 530 GHz. (b) The modulation amplitude as a function of gate bias.

and receiver. The transmitter consisted of a 11.0417 GHz source frequency multiplied 48x by a Schottky-diode varactor chain and coupled to free space through a diagonal feedhorn. The receiver was a low-noise Schottky-rectifier also coupled through a diagonal feedhorn and connected to a low-noise amplifier prior to lock-in demodulation. The modulation recorded with a 80 V square-wave gate bias is shown in Fig. 4(a) displaying pronounced modulation but with a DoM of only ≈ 0.8 dB. This is attributed partly to the fact that 530 GHz is 30 GHz far away from the nearest resonant peak in Fig. 2(a) at 560 GHz. Nevertheless, the modulation is still linear with gate bias as shown by the results plotted in Fig. 4(b).

4. CONCLUSIONS

We have modeled and demonstrated a voltage-controlled MMW-to-THz amplitude modulator based on a graphene-oxide-silicon etalon structure. The best measured experimental DoM was 1.4 dB at 101 GHz — less than the 10-dB goal generally applied to spatial modulators. However, analysis shows that the DoM could be enhanced by realizing greater transconductance change of the graphene film, and operating at a frequency having higher Q in the etalon. Thus there is room for improvement toward a practical MMW-to-THz amplitude modulator.

ACKNOWLEDGMENT

This material is based upon work supported by, or in part by, the U.S. Army Research Laboratory and the U.S. Army Research Office under contract number W911NF-11-1-0024.

REFERENCES

1. Gillian, C. W., B. Elizabeth, W. S. Stephen, and S. B. David, “Materials for phantoms for terahertz pulsed imaging,” *Phys. Med. Biol.*, Vol. 49, N363–N369, 2004.
2. Berry, E., et al., “Optical properties of tissue measured using terahertz pulsed imaging,” *Proc. SPIE*, Vol. 5030, 459–470, 2003.
3. Taylor, Z. D., et al., “Reflective terahertz imaging of porcine skin burns,” *Opt. Lett.*, Vol. 33, No. 11, 1258–1260, 2008.
4. Bolivar, P. H., M. Brucherseifer, J. G. Rvivas, R. Gonzalo, I. Ederra, A. L. Reynolds, M. Holker, and P. Mgt, *IEEE Transaction on Microwave Theory and Techniques*, Vol. 51, 1062–1066, 2003.
5. Liu, M., X. Yin, E. Ulin-Avila, B. Geng, T. Zentgraf, L. Ju, F. Wang, and X. Zhang, “A graphene-based broadband optical modulator,” *Nature*, Vol. 474, 64–67, 2011.
6. Sensale-Rodriguez, B., et al., “Broadband graphene terahertz modulators enabled by intraband transitions,” *Nat. Commun.*, Vol. 3, 780, 2012.
7. Rahm, M., J. Li, and W. J. Padila, “THz wave modulators: A brief review on different modulation techniques,” *J. Infrared Milli. Terahz Waves*, Vol. 34, 1–27, 2013.
8. Kakenov, N., et al., “Graphene-enabled electronically controlled terahertz spatial light modulator,” *Optics Letters*, Vol. 40, 1984–1987, 2015.
9. Born, M. and E. Wolf, *Principles of Optics: Electromagnetic Theory of Propagation, Interference and Diffraction of Light*, Cambridge University Press, 1993.
10. Falkovsky, L. A., *Physics-Uspekhi*, Vol. 51, 887–897, 2008.
11. We define Q in the usual way as $f_0/\Delta f_0$ where f_0 is the peak center frequency and Δf is its FWHM.

High Sensitive Ammonia Gas Sensor Based on Graphene Coated Microfiber

Xiaohui Sun^{1,2}, Qizhen Sun^{1,2}, Si Zhu¹,
Ye Yuan¹, Zhao Huang¹, Xin Liu¹, and Deming Liu^{1,2}

¹School of Optical and Electronic Information

Huazhong University of Science and Technology, Wuhan, Hubei 430074, China

²National Engineering Laboratory for Next Generation Internet Access System

Huazhong University of Science and Technology, Wuhan, Hubei 430074, China

Abstract— We report a sensitive all-fiber ammonia gas sensor based on graphene coated microfiber. Through light deposition and interaction with the evanescent field of the microfiber, the graphene can be effectively coated onto it. The absorbed ammonia gas molecules significantly influence the conductivity of the graphene, resulting in the increase of the refractive index, which makes the transmission optical power change with a sensitivity of 0.1352 dBm/100 ppm and high resolution of 0.74 ppm. The obtained results may have great potential applications in sensing fields with high sensitivity, fast response, easy fabrication and tunable ability.

1. INTRODUCTION

Ammonia is a kind of common poisonous gas in the atmosphere, mainly comes from the world of nature and artificiality. Being colorless and smelly, the ammonia gas may have irritation and corrosion effects to the human eyes and the upper respiratory tract mucous membrane. Therefore, ammonia gas sensor has been widely used in the fields of fire, agriculture, chemical industry, medicine, etc., including portable, pumping suction and fixed type, the detection principle of which mostly are electrochemical principle. However, miniaturized, high sensitivity and electrical magnetic immune ammonia gas sensors are badly in need of for severe environment.

In recent years there has been reported a variety of new methods for the detection of ammonia. Based on the Lambert-Beer's law, the traditional spectroscopy method is to detect the species and concentration according to the selective absorption to the spectra, which includes tunable diode laser absorption spectrum (TDLAS), non-dispersive infrared spectrum (NDIR) and Fourier transform infrared spectrum (FTIR) [1] etc.. Nevertheless, these methods need lots of additional circuit and measurement instrument with complex operations. D. Cheng [2] proposed to use the near-field technology to prepare the polyaniline nano-fiber sensor and obtained the sensitivity of 2.7% at 1×10^{-6} . In the meantime, the carbon nanotube sensor, prepared by using two-dimensional electrophoresis technology, has good linear response when the concentration is higher than 20×10^{-6} . Fazel Yavari [3] demonstrated a macro graphene foam-like three-dimensional network ammonia gas sensor comprised of few-layer graphene sheets with the sensitivity of 30% at 1000 ppm by detecting the electrical resistance. However, the sensor was susceptible to electromagnetic interference and the preparation process was complicated.

Micro/nano-fiber (MNF) [4] is a new type of optical waveguide with the diameter reaching to micron and nanometer level, featured with compact size, good flexibility, low loss, large evanescent field and ease of integration, which has a wide application in communication and sensor systems. Graphene [5] has monolayer thickness of 0.335 nm, which appears as single two-dimensional hexagonal lattice with high surface-to-volume ratio and excellent electronic-photon properties. It has been used as transparent conductive film, lithium ion battery, super capacitor, organic photovoltaic cell, electron field emitter, catalyst and gas sensor. Combining the advantages of MNF and graphene, we propose a passive and high sensitive ammonia gas sensor based on graphene coated microfiber (GCMNF), which is of easy fabrication, miniaturization, low cost and high sensitivity.

2. WORKING PRINCIPLE

Graphene has large specific surface area to increase the contact area between sensor and ammonia gas molecules, thus improving the sensitivity. Due to being similar to the P-type semiconductor, when the molecules absorbed on the surface of graphene, its impurity band will emerge near the Fermi level and change the electronic properties of graphene [6]. If the absorbed gas appears pull-electrical-effects [7], the holes will increase, making the electrical conductivity increase. On the

contrary, if the absorbed gas appears giving-electrical-effects, the redundant holes will be consumed, making the electrical conductivity decrease. Here ammonia gas molecule is the latter one, which makes the decreasing of the graphene electrical conductivity.

According to Ref. [8], the electrical conductivity and refractive index of graphene have the relationship of

$$\varepsilon_{eff} = 1 + i\sigma_c/\omega\varepsilon_0d \quad (1)$$

$$n = \sqrt{\varepsilon_{eff}} \quad (2)$$

Here σ_c is the electrical conductivity, d is the thickness of graphene, ε_{eff} is the effective permittivity, n is the refractive index of graphene. The real part of refractive index of graphene can be calculated as

$$n_{gr} = \left[\frac{-(\sigma_i - \omega\varepsilon_0d) + \sqrt{(\sigma_i - \omega\varepsilon_0d)^2 + \sigma_r^2}}{2\omega\varepsilon_0d} \right]^{\frac{1}{2}} \quad (3)$$

The simulation result is showed in Fig. 1, where the refractive index of graphene increases along with the increasing of the imaginary part of the electrical conductivity. According to the optical waveguide theory, the larger the refractive index of graphene, the larger of the n_{eff} [9]. Then the evanescent field increases as well as the transmission optical power in the core decreases along with the increasing of the n_{eff} . Based on the above analyses, the sensing of ammonia gas concentration can be achieved by measuring the variation of the transmitted optical power.

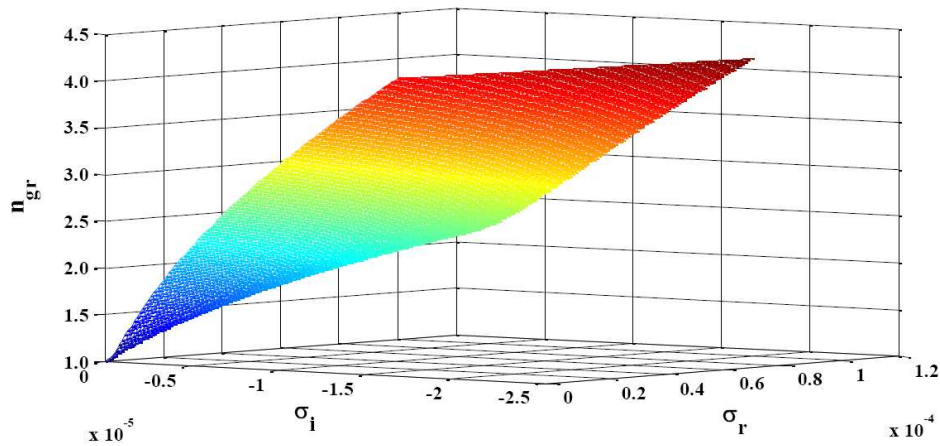


Figure 1: The real part of refractive index of graphene changes with the real and imagine parts of conductivity.

3. SYSTEM CONFIGURATION

The microfiber is bilaterally stretched from a standard single-mode-fiber (SMF) by using the flame-heating and taper-drawing technology. The microscope image of microfiber with the waist diameter of about 5 μm and the length of 10 mm is shown in Fig. 2(a). The graphene dispersion is confected by mixing 2 mg reduction of oxide graphene powder into 20 ml anhydrous ethanol with concentration of 0.1 mg/ml, and then the solution is dispersed by 80 w-59 kHz ultrasonic cleaner for 60 mins to make the graphene disperses in the ethanol uniformly, as depicted in Fig. 2(b). Then fix the two ends of the microfiber onto the three-dimensional alignment stages, and adjust the stage to make the whole microfiber dangling in the V groove. The whole deposition structure is shown in Fig. 2(c).

When 13 dBm of radiation from a broadband optical source is propagating in the microfiber, we drip several drops of graphene dispersion into the V groove, making the microfiber immersed in it. Based on the [10], the light injection from air into the dispersion thermally causes swirl and convection at the boundary, which helps to carry the graphene particles closer to the microfiber. Then, the optical tweezer effect can trap micro/nano-sized objects by the optical intensity diversion in the solution. The microfiber has large evanescent field, which causes the optical intensity diversion. The Lorentz force is applied onto the objects in the electromagnetic field and is stronger toward the higher optical intensity direction, thus tend to trap the graphene particles onto the microfiber.

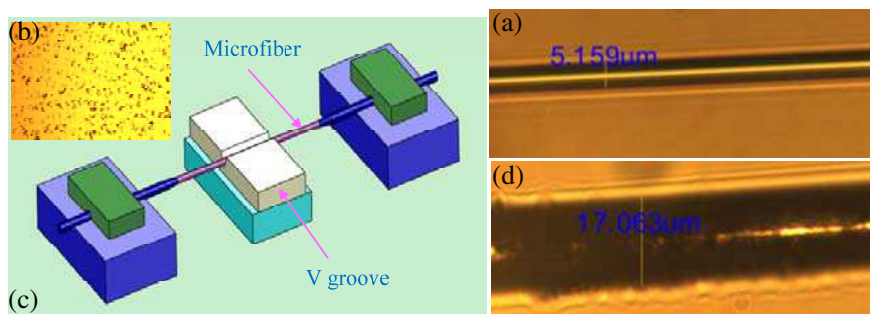


Figure 2: (a) Microscope image of bare microfiber, (b) microscope image of the graphene dispersion, (c) diagram of the deposition device, (d) microscope image of the graphene coated microfiber.

When dripping the graphene dispersion, the transmission loss increases first and then decreases gradually during the evaporation of ethanol. The optical power is collected by the optical power meter during the deposition process to measure the loss. Five minutes later, turn off the light source and wait for the ethanol to evaporate. When the power remains unchanged, it means that the ethanol is evaporated completely and the microfiber is well coated by graphene. Before and after the deposition, we both use alcohol and de-ionized water to clean the microfiber for 2 mins alternately to get rid of the dust and non-uniformly deposited graphene.

The graphene coated microfiber is clearly seen through the microscopy, as showing in Fig. 2(d). The thickness of the GCMNF is about 17.063 μm . It's a little thicker, maybe because of the high optical power leading to excess deposition, which may reduce the sensitivity of the GCMNF.

4. EXPERIMENT AND DISCUSSION

To evaluate the performance of the GCMNF for ammonia gas detection, we measured the transmission intensity of the GCMNF with ammonia gas concentration ranging from 0 to 500 ppm as shown in Fig. 3. The GCMNF was fixed into the gas chamber with the volume of about 1300 ml. The broadband light source was injected into the GCMNF and collected by the optical power meter. The catheter of the outlet was inserted into the beaker with water inside, in case of the ammonia leaking to the environment. 500 ppm of ammonia and nitrogen mixed gas as well as the pure nitrogen gas acted as the gas generators.

At first, we tested the stability of the broadband light source. The deviation of the output power of the light source was less than 0.001 dB in 20 mins, indicating that the light source was stable. Under the nitrogen atmosphere, enough NH_3 was injected into the chamber uniformly, which lasted for 200 s. To measure the reversibility of the system, inject N_2 instead of NH_3 and last for another 300 s. The pressure reducing valve was used to control the gas velocity and the power was detected every 30 s. We repeated the measurements for concentration rising and falling process and recorded the results to validate the repeatability of the gas sensor.

The experimental results are showing in Fig. 4. During the concentration of NH_3 increasing from 0 to 500 ppm, the transmission power decreases from -6.82 to -7.84 dBm the first time and -6.72 to -7.38 dBm the second time, respectively. Through the linear fitting, we obtain the sensitivity of 0.1352 dB/100 ppm. Since the resolution of the commercial optical power meter can be as high as

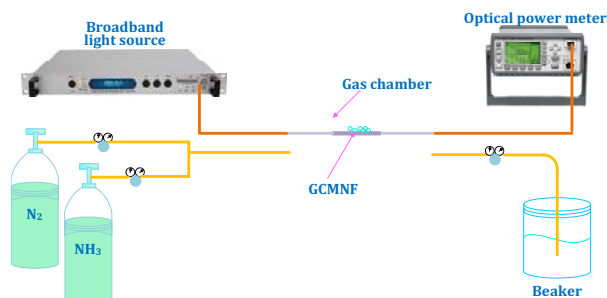


Figure 3: Schematic diagram of the ammonia gas sensor system.

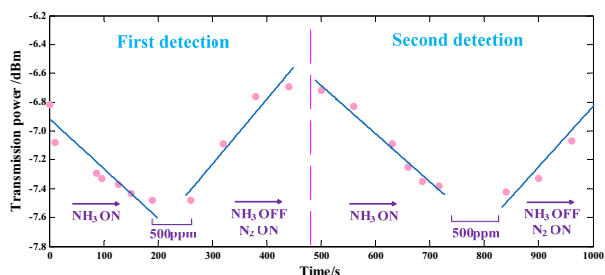


Figure 4: Transmission power changes with time.

0.001 dBm, the ammonia concentration resolution can reach to 0.74 ppm. When the concentration of NH_3 decreases from 500 to 0 ppm, the power is higher than the initial value, which may be result from the instability of the MNF.

The experiment errors mostly come from the following aspects, the air doesn't discharge completely and the NH_3 is discharged too quickly without full effect with the graphene. In addition, the MNF is unstable under the air impact, which also influences the transmission power.

It should be noted that the sensitivity can be improved by fabricating more uniform microfiber with small optical loss and appropriately adjusting the contact length between the graphene and MNF.

5. CONCLUSION

In conclusion, a sensitive all-fiber ammonia gas sensor based on the graphene coated microfiber is proposed and demonstrated. The absorption of the ammonia gas molecules have a strong influence on the refractive index of graphene, resulting in the transmission power change in microfiber with the sensitivity of 0.1352 dBm/100 ppm and high resolution of 0.74 ppm. In addition, the sensitivity is tunable by adjusting the coating thickness of graphene. Such a graphene coated microfiber with high sensitivity, fast response, easy fabrication, low cost and tunable ability would have great potential applications in environmental monitoring fields.

ACKNOWLEDGMENT

This work was supported by the National Natural Science Foundation of China (No. 61275004, No. 61290315), the European Commission's Marie Curie International Incoming fellowship (Grant No. 328263), the Natural Science Foundation of Hubei Province for Distinguished Young Scholars (No. 2014CFA036), and also partly supported by the National Key Scientific Instrument and Equipment Development Project of China (No. 2013YQ16048707).

REFERENCES

1. Zhang, Q., L. Wang, X. Yang, et al., "Monitoring procedures of ammonia released from live-stock farm," *Agro-Environment Science*, Vol. 26, No. B03, 309–312, 2007.
2. Chen, D., S. Lei, R. Wang, et al., "Dielectrophoresis carbon nanotube and conductive polyaniline nanofiber NH_3 gas sensor," *Analytical Chemistry*, Vol. 40, 2012.
3. Yavari, F., Z. Chen, A. V. Thomas, et al., "High sensitivity gas detection using a macroscopic three-dimensional graphene foam network," *Scientific Reports*, Vol. 1, 2011.
4. Tong, L., R. R. Gattass, J. B. Ashcom, et al., "Sub-wavelength diameter silica wires for low loss optical wave guiding," *Nature*, Vol. 426, No. 6968, 816–819, 2003.
5. Hanson, G. W., "Dyadic Green's functions and guided surface waves for a surface conductivity model of graphene," *Journal of Applied Physics*, Vol. 103, No. 6, 064302, 2008.
6. Zou, Y., "Theoretical study on gas sensing properties of functionalized graphene," Qufu Normal University, 2011.
7. Sun, F. and S. Xu, "Application of graphene material in gas-sensor," South China Normal University (Natural Science Edition), Vol. 45, No. 6, 92–98, 2013.
8. Simesek, E., "A closed-form approximate expression for the optical conductivity of graphene," *Optics Letters*, Vol. 38, No. 9, 1437–1439, 2013.
9. Yao, B., Y. Wu, Y. Cheng, et al., "All optical Mach Zehnder interferometric NH_3 gas sensor based on graphene/microfiber hybrid waveguide," *Sensors and Actuators B: Chemical*, Vol. 194, 142–148, 2014.
10. Kashiwagi, K. and S. Yamashita, "Deposition of carbon nanotubes around microfiber via evanescent light," *Optics Express*, Vol. 17, No. 20, 18364–18370, 2009.

High Resolution Demodulation Platform for Large Capacity Hybrid WDM/FDM Microstructures Sensing System Assisted by Tunable FP Filter

Fan Ai^{1,2}, Qizhen Sun^{1,2,3}, Jianwei Cheng^{1,2}, and Deming Liu^{1,2}

¹School of Optical and Electronic Information

Huazhong University of Science and Technology, Wuhan, Hubei 430074, China

²National Engineering Laboratory for Next Generation Internet Access System

Huazhong University of Science and Technology, Wuhan, Hubei 430074, China

³Aston Institute of Photonic Technologies, Aston University, Birmingham, B4 7ET, UK

Abstract— In this paper we proposed a demodulation scheme based on tunable FP filter for the WDM/FDM sensing system of the microstructure mentioned in the previous work. Simulation is done to prove the feasibility of demodulating the microstructure with the tunable FP filter. The experiments result showed high consistence with the simulation. And with the help of the high speed FPGA module and a high resolution AD/DA card, the system has achieved a very high resolution, up to 2.5 pm, and wavelength ranges 1520 nm to 1590 nm.

1. INTRODUCTION

Optical fiber sensors have many advantages over other sensing methods. It is immune to electromagnetic interference, chemical insert, and is quite small and weightless. In the previous work [1] in my laboratory, the microstructure based on two identical FBG has been proved to have very good sensing abilities and great potential for multiplex. The microstructure inherits the good advantage of high sensitivity low insertion loss from the FBG, but has greater capability than FBG. The capacity of the microstructure depends on the product of both wavelength channel and the frequency channel. To increase the capacity, we must expand the wavelength range of the demodulation system, and achieve a higher wavelength resolution.

There have been many demodulation schemes for spectrum sensing system. In general, two ways are typical in the demodulation of spectrum. One way is to use the diffraction gratings [2, 3]. Light is diffracted into different wavelength and then is collected by the CCD arrays. This way can achieve high demodulation speed and large wavelength bandwidth. But the wavelength resolution is limited by the number of the sensors in the CCD array. The other way is to construct the narrow band pass filter or take use of the tunable laser to get the data on different wavelength [4–7]. There is also a tradeoff between the resolution and the wavelength range.

In this paper, the tunable FP filter which has the bandwidth of 15 pm is selected. A spectrum demodulation system based on the tunable FP filter is introduced. The driving signal is produced by a high speed FPGA module and a DA module, signal from the PD is collected by the AD card. In this way we successfully demodulated the spectrum of the microstructure.

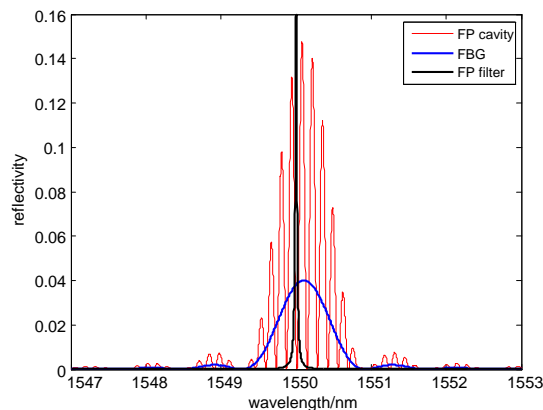


Figure 1: The typical spectrum of the FBG, microstructure and the FP tunable filter.

2. OPERATION PRINCIPLE AND SIMULATION

There have been many articles about the demodulation of FBG based on the FP filter. However the bandwidth of the FBG is about 2 nm typically, the bandwidth of the filter is about 50 pm. So when we use the FP filter to demodulate the FBG, the FP filter can be seen as a delta function. But when it comes to the FP cavity composed of the two identical FBG, the spectrum is very complex. The space of the fringe is very small. We cannot treat the FP filter as a delta function again.

Here is the reflection of the FBG.

$$r = \frac{\sinh^2(\sqrt{\kappa^2 - \bar{\sigma}^2}L)}{\cosh^2\left(\sqrt{\kappa^2 - \bar{\sigma}^2}L\right) - \frac{\bar{\sigma}^2}{\kappa^2}} \quad (1)$$

To simplify the result, we assume that the reflectivity of the FBG is quite low, then the reflection in spectrum of the microstructure can be expressed as:

$$R = 2r(1 + \cos(4\pi n_{eff}L_C/\lambda)) \quad (2)$$

L_c is the cavity length of the microstructure. The FP filter can be expressed as:

$$I_{FP} = 1/[1 + F \sin^2(\delta/2)] \quad (3)$$

$F = 4R/(1 - R)^2$, $\delta = 4\pi D/\lambda$, the bandwidth of the FP filter is decided by the reflectivity of the FP filter.

From the simulation results in Figure 1, the bandwidth of the FP filter and the fringe is in the same order of magnitude. And when we put the driving voltage on the FP filter, the cavity length D will change, so is the central wavelength of the filter. The demodulation result of the system will be calculated from:

$$I_{OUT}(\lambda) = \int_{\lambda_{min}}^{\lambda_{max}} R \times I_{FP} dD \quad (4)$$

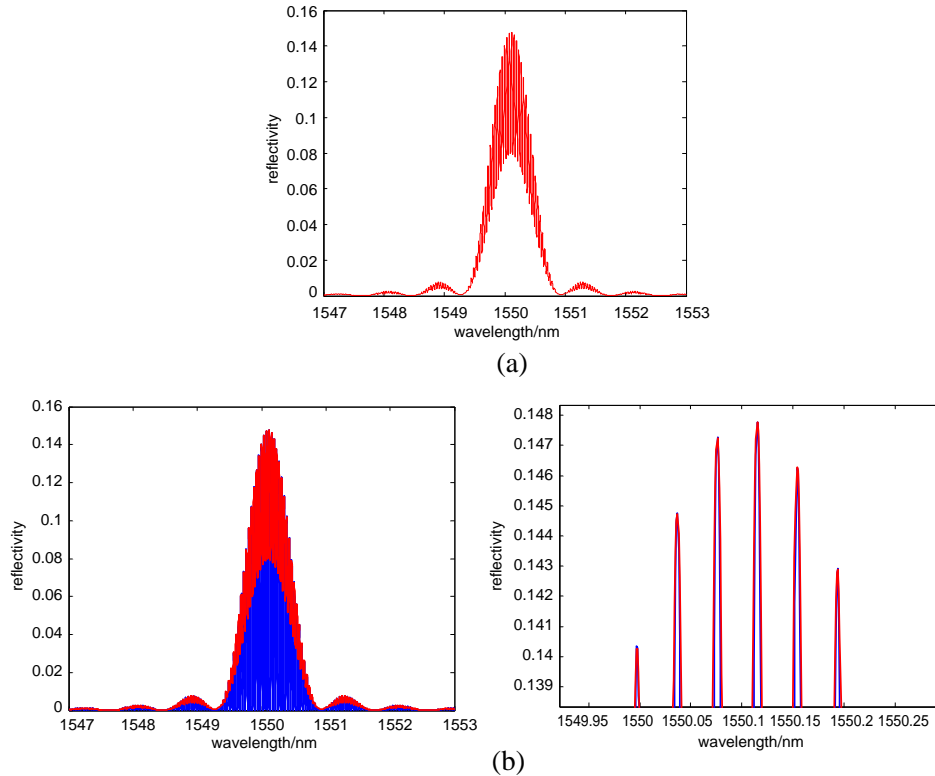


Figure 2: (a) The demodulated spectrum of the microstructure; (b) the comparison between the original spectrum and the demodulation result.

To get a better result, the bandwidth of the FP filter, we choose, is 16 pm, the cavity length of the microstructure is about 20 mm, the step change of the FP filter in wavelength is 1 pm. The simulation result of the demodulation result is shown in Figure 2.

From the results shown in Figure 2, the demodulation of the complex spectrum based on the tunable FP filter may cause some distortion but the peak of the fringe corresponds to the theoretical result correctly. The distortion is mainly decided by the density of the fringe, the bandwidth of the filter and the step of the driving voltage. Besides this the resolution of the demodulation system is just the step wavelength change of the tunable filter.

3. EXPERIMENTS SETUP

The schematic diagram is shown in Figure 3. The broadband light from the light source was transmitted to the microstructure through the circulator. The reflected light was then acquired by the photo detector. The driving signal was synchronized with the received signal by using one

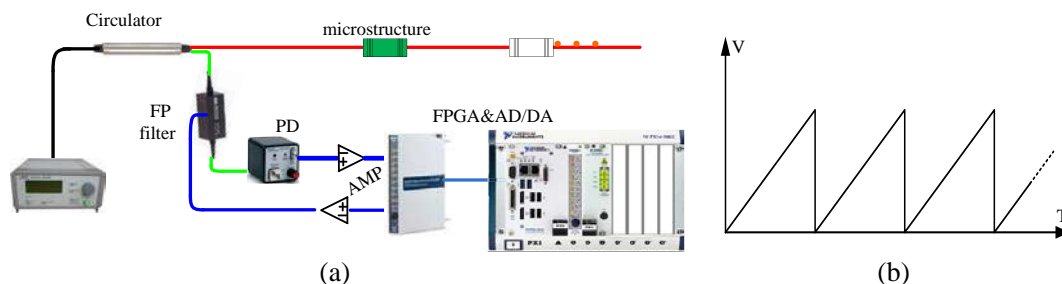


Figure 3: (a) Configuration of the system; (b) driving signal.

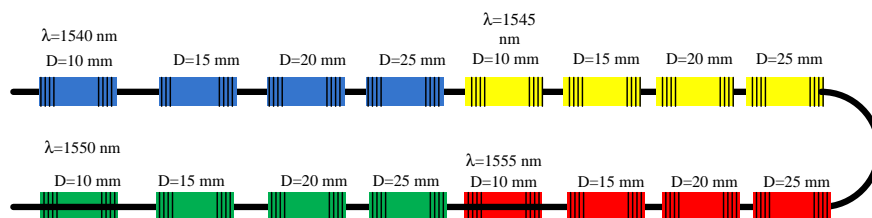


Figure 4: Schematic of the microstructure.

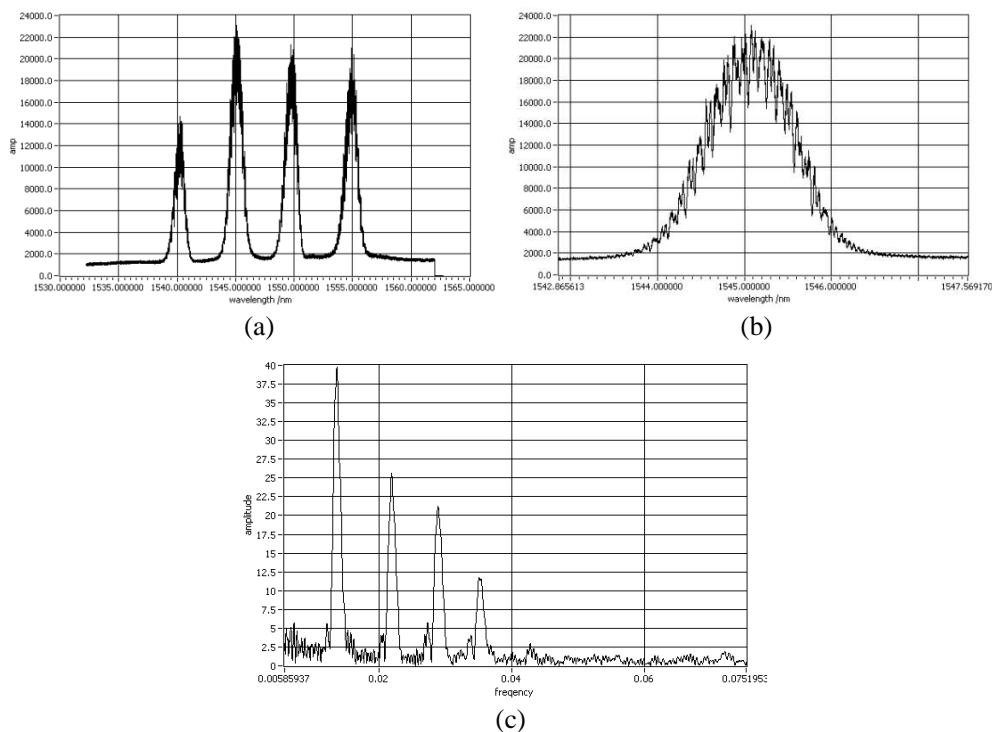


Figure 5: (a) The demodulation results; (b) one peak centered at the 1545 nm; (c) the frequency spectrum.

FPGA module. To ensure the repeatability of the detection, the driving signal is designed to be the sawtooth signal. And the data acquired from the photo detector is filtered and processed in the computer.

To test the demodulation result of the demodulation system, a sensing system of 16 microstructures containing 4 wavelengths and 4 frequencies is fabricated. The microstructure is shown in Figure 4.

4. RESULTS AND DISCUSSION

The demodulation results is shown in Figure 5. The wavelength ranges from 1532 nm to 1562 nm at the resolution of 2.5 pm. The driving frequency is 500 Hz. If we choose one peak to observe carefully, the demodulation results keep in high consistence with the simulation. After the fourier transmission, the four peak is very clear in the frequency spectrum. And due to the higher resolution, the system can double the capacity up to 2000.

5. CONCLUSION

The demodulation system based on the tunable FP filter can be used for the complex spectrum demodulation of the microstructure. The capacity and the demodulation speed of the microstructure sensing system will be greatly improved with the help of the system.

ACKNOWLEDGMENT

This work was supported by the National Key Scientific Instrument and Equipment Development Project of China (No. 2013YQ16048707) and the Fundamental Research Funds for Huazhong University of Science and technology (2011TS059).

REFERENCES

1. Li, X., Q. Sun, D. Liu, R. Liang, J. Zhang, J. Wo, P. P. Shum, and D. Liu, "Simultaneous wavelength and frequency encoded microstructure based quasi-distributed temperature sensor," *Opt. Express*, Vol. 20, 12076–12084, 2012.
2. Hu, Y., S. Chen, L. Zhang, and I. Bennion, "Multiplexing Bragg gratings combined wavelength and spatial division techniques with digital resolution enhancement," *Electron. Lett.*, Vol. 33, No. 23, 1973–1975, 1997.
3. Willsch, R., W. Ecke, and H. Bartelt, "Optical fiber grating sensor networks and their application in electric power facilities, aerospace and geotechnical engineering," *The 15th Optical Fiber Sensors Conference Technical Digest*, 49–54, Portland, OR, 2002.
4. Kersey, A. D., T. A. Berkoff, and W. W. Morey, "Multiplexed fiber Bragg grating strain-sensor system with a fiber Fabry-Perot wavelength filter," *Opt. Lett.*, Vol. 18, 1370–1372, 1993.
5. Kersey, A. D., T. A. Berkoff, and W. W. Morey, "High-resolution fibre-grating based strain sensor with interferometric wavelength-shift detection," *Electron. Lett.*, Vol. 28, No. 3, 236–238, 1992.
6. Volanthen, M., H. Geiger, M. G. Xu, and J. P. Dakin, "Simultaneous monitoring fibre gratings with a single acousto-optic tunable filter," *Electron. Lett.*, Vol. 32, 1228–1229, 1996.
7. Jung, J., Y. W. Lee, and B. Lee, "High-resolution interrogation technique for fiber Bragg grating strain sensor using long period grating pair and EDF," *The 14th International Conference on Optical Fiber Sensors (OFS-14)*, Venice, Italy, 2000.
8. Zhang, M., Q. Sun, Z. Wang, X. Li, H. Liu, and D. Liu, "A large capacity sensing network with identical weak fiber Bragg gratings multiplexing," *Optics Communications*, Vol. 285, Nos. 13–14, 3082–3087, Jun. 15, 2012.
9. Tan, Z., et al., "All-optical passive periodic sawtooth filter and its application to fast interrogation of fiber Bragg grating sensor array," *Optical Fiber Communication Conference*, Optical Society of America, 2012
10. Ning, Y. N., et al., "Bragg grating sensing instrument using a tunable Fabry-Perot filter to detect wavelength variations," *Measurement Science and Technology*, Vol. 9, No. 4, 599, 1998.

Diverging and Converging Beam Diffraction by a Wedge. Part II: Plane Wave Spectral Solutions and Complex Ray Solutions

M. Katsav¹, E. Heyman¹, and L. Klinkenbusch²

¹School of Electrical Engineering, Tel Aviv University, Tel Aviv 69978, Israel

²Institute of Electrical and Information Engineering, Christian-Albrechts-Universität zu Kiel
Kaiserstr. 2, Kiel D-24143, Germany

Abstract— In this present paper we present a novel solution for the diffraction of a converging beam. In that approach, the field of the incident converging beam is synthesized using the CS approach in conjunction with the plane wave spectral analysis, and the diffracted field is calculated using the appropriate integral representation expansion. The exact solution obtained via this spectral technique is then compared with an asymptotic solution obtained via CR tracing augmented with uniform complex ray diffraction. The CR solution includes also selection rules that delineate the CR lit and shadow zones for the diverging or converging beam cases. The overall goal of this research is the derivation of techniques for the analysis of 3D beam diffraction by a cone.

1. INTRODUCTION

The complex source (CS) method provides a canonical setting for the rigorous study of beam diffraction phenomena [1, 2]. In [3] we have used this approach for the analysis of two dimensional (2D) beam diffraction by a wedge as a function of the beam parameters: collimation, direction and displacement from the edge. However, as has been noted in [3], the straightforward CS formulation applies only for the case where the incident beam is diverging as it hits the edge, as schematized in Figure 1. In [4] we presented the novel solution that can be used for the case where the incident beam is converging (Figure 2). In this paper we extend this work by including the results of asymptotic complex ray tracing method augmented with uniform complex ray diffraction.

2. MODELING OF THE INCIDENT CONVERGING BEAM

We start with the conventional CS model in Figure 1 which, however, cannot be applied for the converging beam case of Figure 2. In this approach, the field is modeled as radiation from a point-source located at the complex coordinate point

$$\mathbf{r}_c = \mathbf{r}_0 + i\mathbf{b}, \quad \mathbf{r}_0 = (x_0, y_0) = (r_0, \phi_0), \quad \mathbf{b} = (x_b, y_b) = (b, \phi_b), \quad \mathbf{r}_c = (x_c, y_c) = (r_c, \phi_c) \quad (1)$$

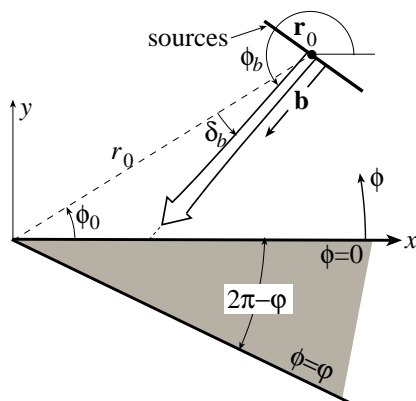


Figure 1: An incident diverging beam. A complex source beam (CSB; double arrow) emerges in the \mathbf{b} direction from the physical source distribution centered at \mathbf{r}_0 whose length is $2b$ (thick line). The waist of the resulting beam is also located on that line and its size $\sqrt{b/k} \ll b$.

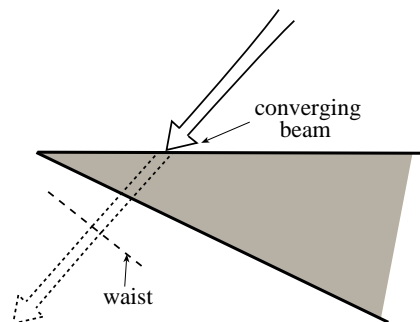


Figure 2: An incident converging beam. The beam propagates in the \mathbf{b} direction, converging to a waist at \mathbf{r}_0 , but it hits the wedge *before* it reaches that waist.

\mathbf{r}_0 and \mathbf{b} are real vectors expressed in (1) in cartesian and polar forms. In free space, the field due to the source in (1) is obtained by an analytic continuation of the 2D free space Green's function

$$G(\mathbf{r}, \mathbf{r}_c) = (i/4)H_0^{(1)}(ks), \quad s = \sqrt{(x - x_c)^2 + (y - y_c)^2}, \quad \text{Re } s \geq 0, \quad (2)$$

$H_0^{(1)}(ks)$ is the Hankel function of the first kind and zero order and s is the complex distance from \mathbf{r}_c to the real observation point \mathbf{r} .

As follows from the analysis above, the CS model in Figure 1 cannot describe the converging beam situation in Figure 2. In [4] this problem was circumvented by describing the incident converging beam as a plane wave integral, and then constructing the diffracted field due to these plane waves. The starting point is plane wave spectral representation of the solution in (2)

$$G(\mathbf{r}, \mathbf{r}_c) = \frac{i}{4\pi} \int_{\mathcal{C}^+} d\xi \zeta^{-1} e^{ik[\xi\eta \pm \zeta(\sigma - ib)]}, \quad \sigma \geq 0, \quad \zeta = \sqrt{1 - \xi^2} \quad \text{with} \quad \text{Im}\zeta \geq 0, \quad (3)$$

here (σ, η) are the beam coordinates centered at \mathbf{r}_0 such that σ is the coordinate *along* \mathbf{b} while η is the *transversal* coordinate. The integration contour \mathcal{C}^+ extends along and passes above and below the branch points at $\xi = \mp 1$, respectively. The plane wave representation of the converging beam is obtained by using the upper sign in (3) for all σ , namely [4]

$$u^i(\mathbf{r}; \mathbf{r}_c) = \frac{i}{4\pi} \int_{\mathcal{C}^+} \zeta^{-1} e^{ik[\xi\eta + \zeta(\sigma - ib)]} d\xi, \quad \sigma \geq 0, \quad (4)$$

\mathcal{C}^- is similar to \mathcal{C}^+ of (3) except that it passes below and above the branch points at $\xi = \mp 1$, respectively. $u^i(\mathbf{r}; \mathbf{r}_c)$ in (3) describes a beam propagating along the σ -axis from $-\infty$ to ∞ , having a waist at $\sigma = 0$ (i.e., at \mathbf{r}_0). It is convenient to put the integral in (4) in the form of an angular plane wave spectrum

$$u^i(\mathbf{r}; \mathbf{r}_c) = \frac{i}{4\pi} \int_{\mathcal{P}^\pm} d\alpha e^{-ikr \cos(\alpha - \phi)} \tilde{u}^i(\alpha; \mathbf{r}_c), \quad \tilde{u}^i(\alpha; \mathbf{r}_c) = e^{ikr_c \cos(\alpha - \phi_c)}, \quad (5)$$

where the Sommerfeld integration pathes \mathcal{P}^\pm extend from $-\pi/2 \pm \infty$ to $\pi/2 \mp \infty$, α is spectral angle measured from the σ -axis and \tilde{u}^i is the plane-wave spectrum. ϕ_c is complex angle defined via $\phi_c = \arctan(y_c/x_c)$. We note now that if $\phi_0 \approx \phi_b - \pi$ then (5) describes an incident diverging beam, as in Figure 1, whereas if $\phi_0 \approx \phi_b$ then (5) describes a converging incident beam as in Figure 2.

3. CONVERGING BEAM DIFFRACTION BY A WEDGE

Referring to Figure 1 we consider an acoustically soft wedge with faces at $\phi = 0$ and $\phi = \varphi$ (Figure 1). Considering an incident plane wave $e^{-ikr \cos(\phi - \alpha)}$ where α is direction of the plane wave arrival, the total field can be expressed as [1]

$$u_{\text{PW}}(\mathbf{r}; \alpha) = \frac{-1}{8\pi} \int_{\mathcal{I}} dw e^{ikr \cos w} D(\phi, \alpha; w), \quad (6)$$

where $D(\phi, \alpha; w)$ is spectral diffraction coefficient. The total field due to the incident wave in (5) is given [1, 3]

$$u(\mathbf{r}) = \frac{i}{4\pi} \int_{\mathcal{P}^\pm} d\alpha u_{\text{PW}}(\mathbf{r}; \alpha) \tilde{u}^i(\alpha) = \frac{i}{4\pi} \int_{\mathcal{P}^\pm} d\alpha \tilde{u}^i(\alpha) \frac{-1}{8\pi} \int_{\mathcal{I}} dw e^{ikr \cos w} D(\phi, \alpha; w), \quad (7)$$

where $\tilde{u}^i(\alpha; \mathbf{r}_0, \phi_b)$ is the spectrum of the incident beam as defined in (5). The spectral diffraction coefficient $D(\phi, \alpha; w)$ introduces the lattice of poles with 2φ periodicity: $w_p = \phi \pm \alpha \mp \pi + 2n\varphi$, with $n = 0, \pm 1, \pm 2, \dots$. Assuming that the incident beam hits the wedge as is shown Figure 2, the most relevant poles are given by $w_p = \phi \pm \alpha - \pi$. Depends on the observation angle ϕ , these poles move across the integration path as angle $\phi \pm \alpha$ increases through π and give rise to the geometrical part of the solution of (7), coincides with the field of direct and reflected complex rays $u^{\text{CR}}(\mathbf{r})$. Note that by extracting the contributions of these poles explicitly, the spectral integral in (6) may be regarded as the ‘‘diffracted field’’ $u_{\text{PW}}^d(\mathbf{r})$ associated with the incident plane wave. Therefore, following [3] we introduce the ‘‘diffracted field’’ associated with the incident beam

$$u^d(\mathbf{r}) = \frac{i}{4\pi} \int_{\mathcal{P}^\pm} d\alpha u_{\text{PW}}^d(\mathbf{r}; \alpha) \tilde{u}^i(\alpha) = \frac{i}{4\pi} \int_{\mathcal{P}^\pm} d\alpha \tilde{u}^i(\alpha) \frac{-1}{8\pi} \int_{\mathcal{I}^{\text{mod}}} dw e^{ikr \cos w} D(\phi, \alpha; w), \quad (8)$$

the integration path \mathcal{I}^{mod} extends along the imaginary w -axis [1, 3].

4. COMPLEX RAYS REPRESENTATION (CR)

In Reference [3], the complex ray representation of 2D beam diffraction by a wedge has been considered in the framework of the complex source (CS) approach. Here we extend this approach to the case of converging beam.

4.1. The Incident Field

The incident field of the converging beam can be treated by using complex geometrical optics. Thus the ingoing part of the incident converging beam is

$$u^i \sim i/4H_0^{(2)}(ks) \sim -\sqrt{\frac{1}{8\pi ks}} e^{-iks-i\pi/4}, \quad \text{Re } s > 0, \quad (9)$$

where s is the complex *distance* and given by (2). The corresponding complex rays are

$$\mathbf{r} = \mathbf{r}_c - s\mathring{\mathbf{s}}, \quad (10)$$

where $\mathring{\mathbf{s}} = (\mathring{s}_x, \mathring{s}_y)$ is the complex ray direction such that $\mathring{s} \cdot \mathring{s} = 1$. These rays emanate from the observation point \mathbf{r} and propagates toward the complex point \mathbf{r}_c . Beneath the waste \mathbf{r}_0 the ingoing beam field transforms into outgoing and is given by

$$u^i \sim i/4H_0^{(1)}(ks) \sim \sqrt{\frac{1}{8\pi ks}} e^{iks+i\pi/4}, \quad \text{Re } s > 0, \quad (11)$$

and the corresponding rays are expressed by

$$\mathbf{r} = \mathbf{r}_c + s\mathring{\mathbf{s}}. \quad (12)$$

In this case the rays emanate from the complex point \mathbf{r}_c and propagates toward the observation point \mathbf{r} .

4.2. The Field of the Direct Ray

To find the field scattered by a wedge, one needs the complex continuation of wedge geometry. This was done in [3] and we refer the reader to this work.

To find the field of the direct ray we calculate the distance $s(\mathbf{r})$ along the ray via (2) and then the ray direction $\mathring{\mathbf{s}}(\mathbf{r})$ via (10) for the real observation point lie above the waist or via (12) for the observation points lie beneath the waste. Using (10), (12) we find \mathbf{q}_j , the complex point where these rays intercept plane j defined above, and s_{q_j} , the distance from \mathbf{r}_c to \mathbf{q}_j . Note that s_{q_j} is found uniquely via (10)–(12) and that it does not involve a square root.

Selection rule 1: This ray is included in the field representation if \mathbf{q}_j does not belong to the complex extension of face j .

4.3. The Field of the Reflected Rays

In order to calculate the reflected complex rays it is convenient to consider the image points $\vec{\mathbf{r}}_{cj}$ of \mathbf{r}_c with respect to plane j . We introduce also the image point of the wais \mathbf{r}_{0j} . For the real observation points lie beneath the image waist \mathbf{r}_{0j} , the reflected rays have trajectories like to (10) $\mathbf{r} = \mathbf{r}_{cj} - s\mathring{\mathbf{s}}$. Next we calculate s with $\text{Re } s > 0$ and $\mathring{\mathbf{s}}$ in the same manner as described above for the incident ray. We also calculate the complex points $\bar{\mathbf{q}}_j$ where these rays intercept plane j , and the distances s_{q_j} from \mathbf{r}_{cj} to \mathbf{q}_j .

Selection rule 2.1: \vec{R}_j is included in the field representation only if \mathbf{r}_{qj} belongs to the complex extension of face j and also $0 < \text{Re}\{\bar{s}_{qj}\} < \text{Re}\{\bar{s}_j\}$.

For the real observation points lie above the image waist \mathbf{r}_{0j} , the reflected rays have trajectories like to (12) $\mathbf{r} = \mathbf{r}_{cj} + s\mathring{\mathbf{s}}$, we calculate the corresponding s with $\text{Re}\{s\} > 0$ and $\mathring{\mathbf{s}}$ in the same manner as described in above. We also calculate the complex points $\bar{\mathbf{q}}_j$ where the continuation of them intercept plane j , and the distances s_{q_j} from \mathbf{r}_{cj} to \mathbf{q}_j .

Selection rule 2.2: The ray is included in the field representation only if \mathbf{r}_{qj} belongs to the complex extension of face j .

The reflected field ψ^r is given by (9)–(11) with appropriate s multiplied by the boundary reflection coefficient.

5. COMPLEX RAYS DIFFRACTION

The edge diffracted field due to incident beam is given by (8). Here we derive the uniform representation for the (8). We start with evaluation the internal (dw) integral. The integral has two critical points: the saddle point $w_s = 0$ and the poles $w_p = \phi \pm \alpha - \pi$. Since the poles cannot cross the integration path we can evaluate it by applying the saddle-point technique which yields

$$u^d(\mathbf{r}) = \frac{i}{16\pi^2} \sqrt{\frac{2\pi}{ikr}} e^{ikr} \int_{\mathcal{P}^\pm} d\alpha e^{ikr_c \cos(\alpha - \phi_c')} D(\alpha, \phi). \quad (13)$$

The last integral has two saddle points $\alpha_s = \phi_c, \pi - \phi_c$ and the poles $\alpha_p = \pi \pm \phi$. In the case of diverging beam the integration path \mathcal{C}^+ can be deformed into SDP path through the saddle point $\alpha_s = \phi_c$ and in the case of converging beam the integration path \mathcal{C}^- can be deformed into SDP path through the saddle point $\pi - \phi_c$. The process of the uniform evaluation is based on the method outlined in [3]. The spectral diffraction coefficient $D(\alpha, \phi)$ is resolved in two terms: pole term and regular term

$$D(\alpha, \phi) = \frac{\mathcal{P}_p}{\alpha - \alpha_p} + \mathcal{R}_p(\alpha; \phi), \quad (14)$$

where $\mathcal{P}_p \equiv \lim_{w \rightarrow \alpha_p} (\alpha - \alpha_p) D(\alpha, \phi)$ and $\mathcal{R}_p(\alpha, \phi) = D(\alpha, \phi) - \frac{\mathcal{P}_p}{\alpha - \alpha_p}$. The pole term can be integrated analytically and the regular term can be evaluated asymptotically via the saddle point technique.

The analysis yields for diverging beam

$$u^d(\mathbf{r}) = \frac{\mathcal{P}_p}{16\pi} \sqrt{\frac{2\pi}{ikr}} e^{ik\chi_p} \operatorname{erfc}(-is_p) - \frac{\mathcal{R}_p(\phi_c, \phi)}{8\pi k \sqrt{rr_c}} e^{ik(r+r_c)}, \quad (15)$$

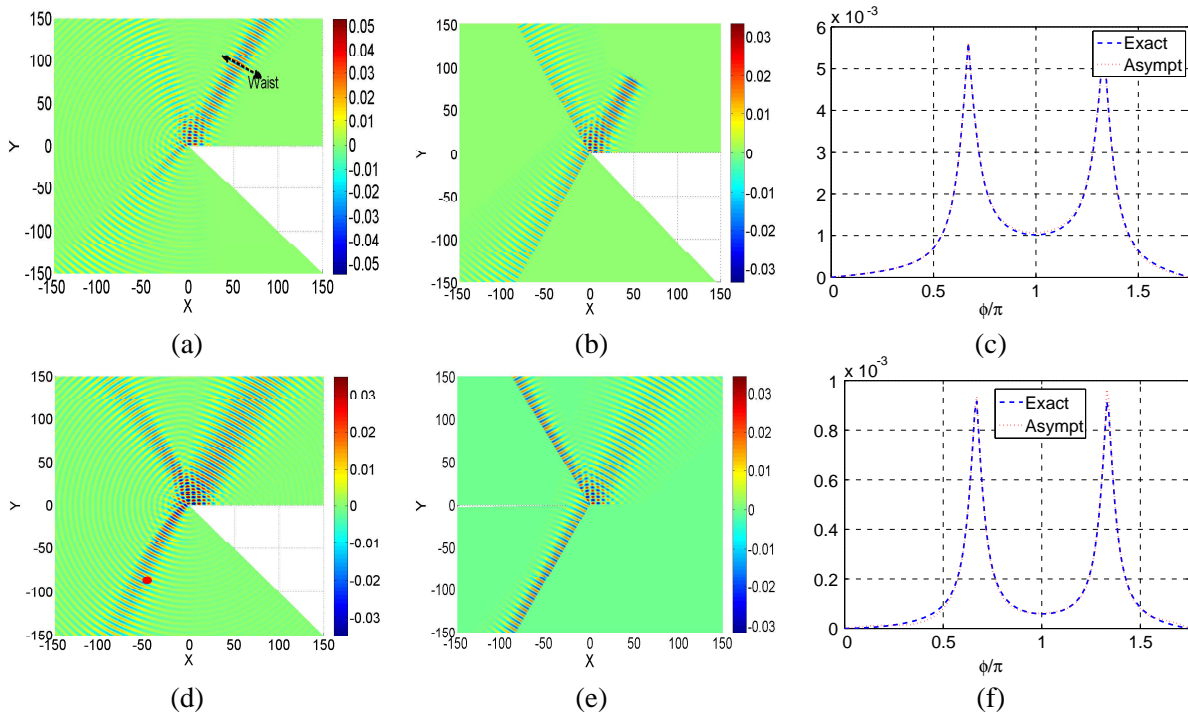


Figure 3: (a) The real part of the total field for the case of diverging beam calculated via (7). (b) The real part of the total field for the case of diverging beam calculated by CRT method. (c) The edge diffracted field for the case of diverging beam calculated at distance $r = 200$. The blue line represents the result obtained via the exact formulation (8) and the red line represents the results obtained via uniform asymptotic evaluation (15). Figures (d)–(f) likes to (a)–(c) but for the case of converging beam.

and for converging beam

$$u^d(\mathbf{r}) = \frac{\mathcal{P}_p}{16\pi} \sqrt{\frac{2\pi}{ikr}} e^{ik\chi_p} \operatorname{erfc}(-is_p) - \frac{\mathcal{R}_p(\pi - \phi_c, \phi)}{8\pi k \sqrt{rr_c}} e^{ik(r-r_c)}, \quad (16)$$

where χ_p is equals $\chi_p = -r_c \cos(\alpha_p - \phi_c)$ and s_p is given by $s_p = (\alpha_p - \phi_c) \sqrt{\frac{ikr_c}{2}}$ for diverging and $s_p = (\alpha_p - \pi + \phi_c) \sqrt{\frac{ikr_c}{2}}$ for converging beam.

6. NUMERICAL RESULTS

We consider diffraction by a 45° wedge (i.e., $\varphi = 1.75\pi$). The collimation length of the incident beam is $b = 80$ and its direction is $\phi_b = 240^\circ$. The units are set such that $k = 1$. We consider the case of the diverging beam with the waist location $(r_0, \phi_0) = (100, 60^\circ)$, and the case of converging beam with waist location $(r_0, \phi_0) = (100, 240^\circ)$. In Figure 3 we depict the total field, calculated via (7), the total field calculated by asymptotic CRT method and the edge diffracted field for the case of diverging beam Figures 3(a), (b), (c) and for the case of converging beam Figures 3(d), (e), (f).

7. CONCLUSION

We derived a new solution for the diffraction of a converging beam by a wedge. In that approach, the field of the incident converging beam is synthesized using the CS technique in conjunction with the plane wave spectral analysis, and the diffracted field is then calculated using the spectral techniques. The final result in (7) may be applied for both cases where the incident beam is either *diverging* or *converging* as it hits the wedge, as schematized in Figures 1 and 2, respectively. The validity of the new solution has been verified by applying it first to the *diverging* beam case where the solution is valid [3], (see Figures 3(a), (b), (c)) before applying it to the *converging* beam case (Figures 3(d), (e), (f)). The long term goal of this research is the derivation of scattering and diffraction coefficients for a beam impinging on a tip of a cone.

REFERENCES

1. Felsen, L. and N. Marcuvitz, *Radiation and Scattering of Waves*, Prentice-Hall, New Jersey, 1973.
2. Felsen, L. B., "Complex-source-point solutions of the field equations and their relation to the propagation and scattering of gaussian beams," *Symposia Matematica, Istituto Nazionale di Alta Matematica*, Vol. XVIII, 40–56, Academic Press, London, 1976.
3. Katsav, M., E. Heyman, and L. Klinkenbusch, "Complex-source beam diffraction by a wedge: Exact and complex rays solutions," *IEEE Trans. Antennas Propagat.*, Vol. 62, No. 7, 3731–3740, 2014.
4. Katsav, M., E. Heyman, and L. Klinkenbusch, "Converging beam diffraction by a wedge," *Proc. XXXI General Assembly of URSI*, Beijing, China, Aug. 2014.

Phase Behaviour of an Azimuthally Magnetized Two-layered Ferrite-dielectric Circular Waveguide

Mariana Nikolova Georgieva-Grosse¹ and Georgi Nikolov Georgiev²

¹Consulting and Researcher in Physics and Computer Sciences
Gerlingen D-70839, Germany

²Faculty of Mathematics and Informatics
University of Veliko Tirnovo "St. St. Cyril and Methodius", Veliko Tirnovo BG-5000, Bulgaria

Abstract— The areas of propagation in the $\bar{r}_0 - \bar{\beta}$ — phase plane, the $\bar{\beta}(\bar{r}_0)$ — phase characteristics and the lower and upper cut-off frequencies (the lower and upper normalized critical guide radii \bar{r}_{0cr} and $\bar{r}_{0en\pm}$, resp.) of the circular waveguide, containing a thick latching ferrite cylinder, magnetized azimuthally to remanence, surrounded by a thin dielectric toroid, are studied for the normal TE_{01} mode, assuming equal values of the relative permittivities of both strata, (\bar{r}_0 and $\bar{\beta}$ — the guide radius and phase constant, normalized with respect to the frequency and relative permittivity of anisotropic filling, “+” and “−” — subscripts, labeling quantities, relevant to positive, resp. negative direction of its magnetization). The principle outcome of the investigation is that the removal even of an insignificant part from the ferrite in the vicinity of the wall and its replacement by an isotropic medium changes substantially the phase behaviour of the configuration, compared to the case in which it fills in the whole transmission line, inspected earlier. This is visible for both signs of ferrite magnetization, but especially noticeable if its sign is positive (counter-clockwise). Besides, the alteration of the size of outer layer, of its permittivity, keeping that of the inner one the same and of the direction of magnetization of the ferrite load, are the most important factors that determine the position, boundaries, shape and dimensions of the region in the phase plane in which the wave might be sustained, as well as the distribution of its two kinds of cut-off frequencies (the critical radii).

1. INTRODUCTION

The circular waveguides, entirely or partially filled with ferrite of azimuthal magnetization are apt for the development of nonreciprocal digital phase shifters, operating in the normal TE_{01} mode, since they can provide differential phase shift when switching the remanent magnetization of their anisotropic load between its two stable states [1–8]. For certain combinations of parameters the multilayered ferrite-dielectric structures could afford an increased value of this important quantity [1–4, 8]. Due to the complexity of the tasks, however, still the phase behaviour of these configurations is not sufficiently clarified.

The purpose of this paper is the investigation of the phase behaviour of a two-layered geometry of the above type in which the anisotropic medium takes up its inner and the isotropic one — its outer region, using results of the recent solution of the propagation problem for the normal TE_{0n} modes in it [4]. To simplify the study, the discussion is confined to the TE_{01} mode solely. As earlier [4], the relative permittivities of both media are assumed equal. In addition, the relative size of the area, occupied by dielectric is small, compared to the one of the transmission line and the lower part of frequency band in which the wave could be sustained, is considered only.

2. FORMULATION OF THE PROBLEM

An infinitely long, uniform, lossless perfectly conducting circular waveguide of radius r_0 , loaded with a coaxially positioned latching ferrite cylinder of radius r_1 , magnetized azimuthally to remanence by an infinitely thin axial wire and a dielectric toroid of inner and outer radii r_1 and r_0 , resp., is considered. The ferrite has a Polder permeability tensor $\vec{\mu} = \mu_0[\mu_{ij}]$, $i, j = 1, 2, 3$, with nonzero components $\mu_{ii} = 1$ and $\mu_{13} = \mu_{31} = -j\alpha$, $\alpha = \gamma M_r / \omega$ ($-1 < \alpha < 1$), γ — gyromagnetic ratio, M_r — ferrite remanent magnetization, ω — angular frequency of the wave and a scalar permittivity $\varepsilon = \varepsilon_0\varepsilon_r$. The dielectric possesses a scalar permittivity and permeability $\varepsilon^d = \varepsilon_0\varepsilon_d$ and $\mu^d = \mu_0\mu_d$, resp., $\mu_d = 1$. It is accepted that $\varepsilon_r = \varepsilon_d$. The propagation of normal TE_{0n} modes with phase constant β is explored. Normalized quantities are introduced by the relations: $\bar{\beta} = \beta / (\beta_0\sqrt{\varepsilon_r})$, $\bar{r}_0 = \beta_0 r_0 \sqrt{\varepsilon_r}$ and $\bar{r}_1 = \beta_0 r_1 \sqrt{\varepsilon_r}$ with $\beta_0 = \omega\sqrt{\varepsilon_0\mu_0}$ [4–6].

3. PHASE BEHAVIOUR

Figures 1(a), (b) and 2(a), (b) depict the domain of transmission of the normal TE_{01} wave in the structure under study (portrayed by light green), magnetized in positive ($\alpha_+ > 0$) and negative ($\alpha_- < 0$) direction, resp., assuming anisotropic cylinder to waveguide radius ratio $\rho = 0.9$ and 0.95 , resp. ($\rho = \bar{r}_1/\bar{r}_0$, $0 < \rho < 1$). The corresponding normalized $\beta(\bar{r}_0)$ — phase characteristics with α as parameter are pictured here by solid and dashed lines, as well. The $\alpha = 0$ — solid curve (the lower border of the area in question for $\alpha_+ > 0$) dovetails to a geometry, wholly filled with dielectric of relative permittivity ε_r . In case of negative magnetization this boundary is composed of parts of the phase lines for small $\alpha_- < 0$. For upper limits of the areas inspected serve the En_{1-} - and En_{1+} -dotted envelopes (the sets of termination points of the $\beta(\bar{r}_0)$ — characteristics for higher frequencies) at which the propagation ceases. The appearance of the latter may be interpreted as

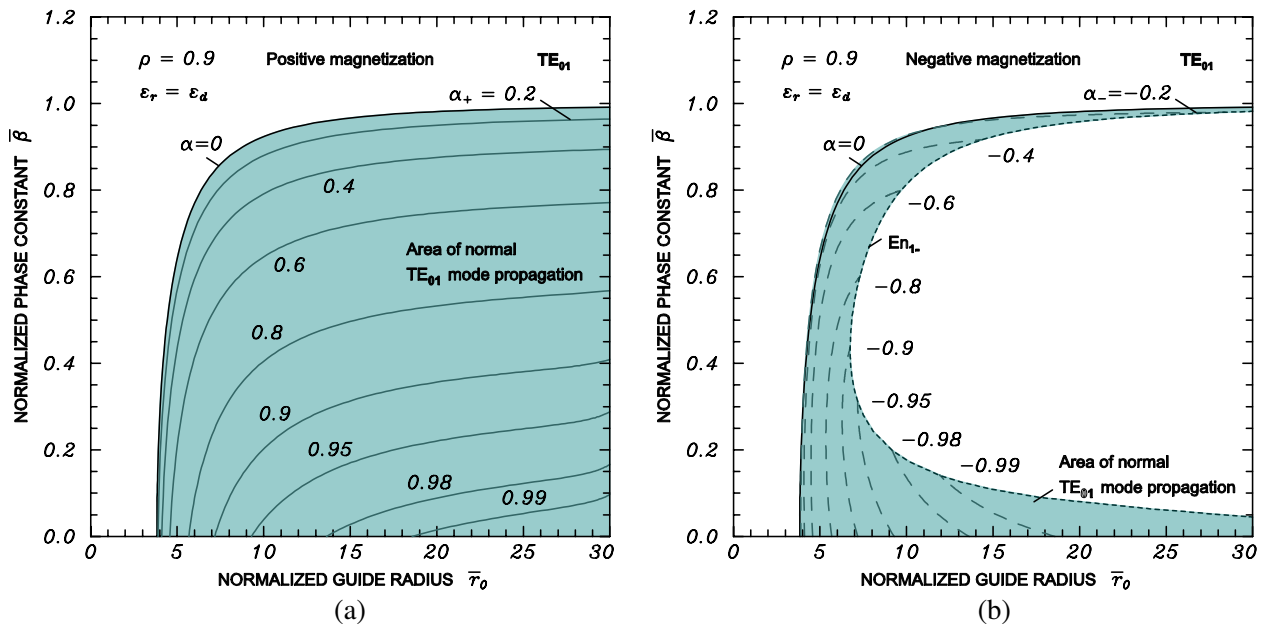


Figure 1: Area of transmission and phase characteristics of the ferrite-dielectric waveguide, magnetized azimuthally in: (a) positive and (b) negative direction for the normal TE_{01} mode in case $\rho = 0.9$.

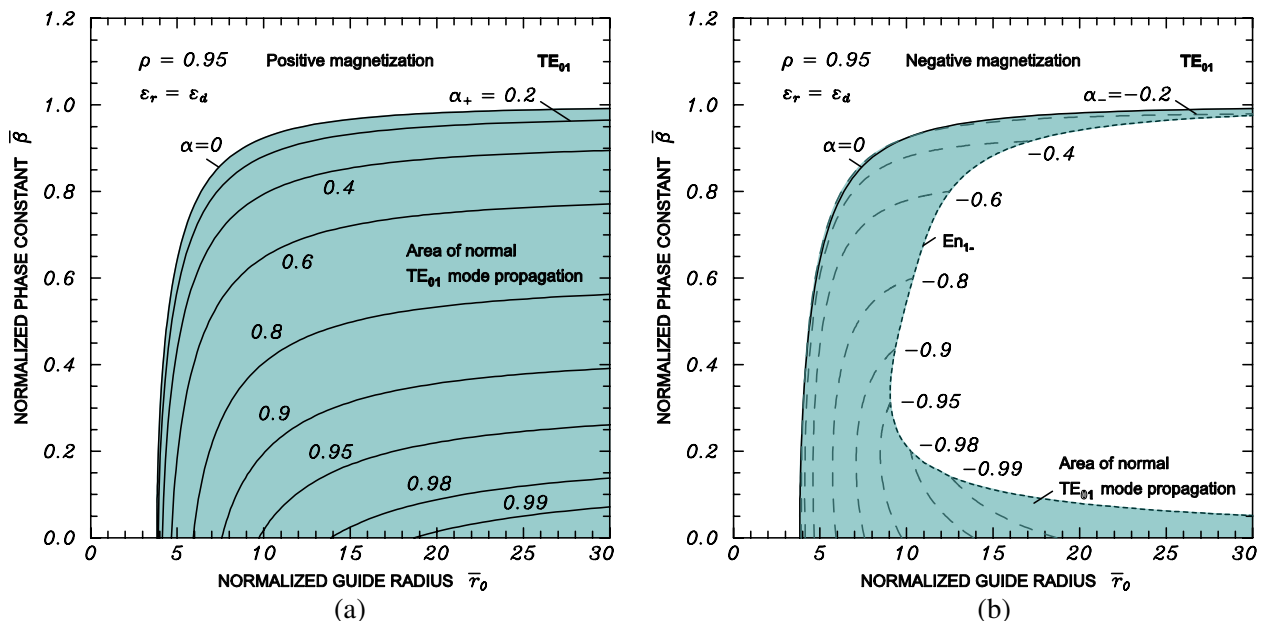


Figure 2: Area of transmission and phase characteristics of the ferrite-dielectric waveguide, magnetized azimuthally in: (a) positive and (b) negative direction for the normal TE_{01} mode in case $\rho = 0.95$.

a springing up of upper cut-off frequencies of the configuration. Accordingly, the conventional ones may be called lower cut-off frequencies.

The phase diagrams are plotted, employing the procedure, worked out earlier [4]. It uses the roots of the characteristic equation of the structure $\xi_{k_{\pm},n}^{(c)}(\bar{\varepsilon}, \rho, \alpha_{\pm})$ [4], derived in terms of complex Kummer confluent hypergeometric and the real Bessel and Neumann functions [9]. (k_{\pm} — imaginary part of the complex first parameter of Kummer function, $k_{\pm} = \alpha_{\pm}\bar{\beta}/(2\bar{\beta}_2)$, $\bar{\beta}_2 = \beta_2/(\beta_0\sqrt{\varepsilon_r})$, $\beta_2 = [\omega^2\varepsilon_0\mu_0\varepsilon_r(1 - \alpha^2) - \beta^2]^{1/2}$ — radial wavenumbers in the anisotropic medium [4]).

Table 1 lists the roots $\xi_{0,n}^{(c)}(\bar{\varepsilon}, \rho, \alpha_{\pm})$ ($k_{\pm} = 0$) of the equation mentioned and the lower cut-off frequencies of the configuration (the lower normalized critical guide radius) $\bar{r}_{0cr\pm} = \xi_{0,n}^{(c)}(\bar{\varepsilon}, \rho, \alpha_{\pm})/(2\sqrt{1 - \alpha_{\pm}^2})$ at which no propagation takes place ($\bar{\beta}_{cr\pm} = 0$) [10]. Table 2 presents the $L_1(c, n)$ and $\bar{L}_{3\pm}(c, \bar{\varepsilon}, \rho, \alpha_{\pm}, n)$ numbers and the upper cut-off frequencies of the waveguide (the upper normalized critical guide radii) $\bar{r}_{0en-} = L_1(c, n)/(|\alpha_{en-}|\sqrt{1 - \alpha_{en-}^2})$, resp. $\bar{r}_{0en\pm} = L_{3\pm}(c, \bar{\varepsilon}, \rho, \alpha_{en\pm}, n)/(|\alpha_{en\pm}|\sqrt{1 - \alpha_{en\pm}^2})$, pertinent to the case $\bar{\beta}_{en\pm} = \sqrt{1 - \alpha_{en\pm}^2}$, ($c = 3$, $\bar{\varepsilon} = \varepsilon_d/\varepsilon_r = 1$, $0 < \rho < 1$, $-1 < \alpha_- < 0$, $0 < \alpha_+ < 1$, $n = 1, 2, 3, \dots$, $|\alpha_-| \equiv |\alpha_+| \equiv |\alpha|$, $\bar{r}_{0cr-} \equiv \bar{r}_{0cr+} \equiv \bar{r}_{0cr}$, $\bar{r}_{0en-} \neq \bar{r}_{0en+}$) [4, 9]. All data correspond to normal TE_{01} mode ($n = 1$). The calculations are performed for $|\alpha| = 0.05(0.05)0.95$, on condition that $\rho = 1, 0.95$ and 0.9 . (For details on the definition and modeling of the various L numbers see Refs. [4, 7, 8, 10]. In some of them the notation $L(c, n)$ is advanced instead of $L_1(c, n)$.) The distribution of \bar{r}_{0cr} and $\bar{r}_{0en\pm}$ vs. $|\alpha|$ is presented in Figs. 3(a), (b) and 4(a), (b), resp. for the aforesaid numerical equivalents of ρ . The subscripts “cr” and “en \pm ” mark off quantities, relative to the lower and upper cut-off frequencies (to the En_{1-} - and En_{1+} -lines.) Note that the above expressions allow to write the equation of the envelopes $\bar{\beta}_{en-} = \bar{\beta}_{en-}(\bar{r}_{0en-})$, resp. $\bar{\beta}_{en\pm} = \bar{\beta}_{en\pm}(\bar{r}_{0en\pm})$ in parametric form [4]. The case $\rho = 1$ answers to waveguide, completely filled with ferrite in which there is only one envelope, relevant to negative ferrite magnetization — the En_{1-} -line of equation $\bar{\beta}_{en-} = \bar{\beta}_{en-}(\bar{r}_{0en-})$, see Ref. [3]).

Table 1: Values of the roots of the characteristic equation of the ferrite-dielectric structure $\xi_{0,n}^{(c)}(\rho)$ and of the lower cut-off frequencies \bar{r}_{0cr} for the TE_{01} mode in case $\varepsilon_d = \varepsilon_r$, $\rho = 1, 0.95$ and 0.9 as a function of $|\alpha|$.

ρ	$ \alpha $	0.05	0.10	0.15	0.20	0.25	0.30	0.35	0.40	0.45	0.50
1	$\xi_{0,n}^{(c)}(\rho)$	7.66341									
	\bar{r}_{0cr}	3.83650	3.85101	3.87555	3.91072	3.95737	4.01672	4.09043	4.18073	4.29069	4.42447
0.95	$\xi_{0,n}^{(c)}(\rho)$	7.66249	7.65969	7.65494	7.64810	7.63896	7.62725	7.61257	7.59439	7.57196	7.54427
	\bar{r}_{0cr}	3.83604	3.84914	3.87127	3.90290	3.94474	3.99777	4.06329	4.14308	4.23948	4.35569
0.9	$\xi_{0,n}^{(c)}(\rho)$	7.66167	7.65642	7.64753	7.63478	7.61785	7.59629	7.56951	7.53670	7.49681	7.44842
	\bar{r}_{0cr}	3.83563	3.84750	3.86752	3.89611	3.93384	3.98154	4.04031	4.11161	4.19741	4.30035
ρ	$ \alpha $	0.55	0.60	0.65	0.70	0.75	0.80	0.85	0.90	0.95	1.00
1	$\xi_{0,n}^{(c)}(\rho)$	7.66341									
	\bar{r}_{0cr}	4.58796	4.78963	5.04215	5.36546	5.79299	6.38618	7.27379	8.79054	12.27128	
0.95	$\xi_{0,n}^{(c)}(\rho)$	7.50991	7.46681	7.41192	7.34051	7.24492	7.11197	6.91715	6.61022	6.07361	
	\bar{r}_{0cr}	4.49607	4.66676	4.87669	5.13939	5.47665	5.92664	6.56547	7.58244	9.72556	
0.9	$\xi_{0,n}^{(c)}(\rho)$	7.38965	7.31793	7.22970	7.11992	6.98130	6.80295	6.56801	6.24916	5.79836	
	\bar{r}_{0cr}	4.42407	4.57371	4.75679	4.98494	5.27737	5.66913	6.23408	7.16828	9.28481	

Confronting the results obtained with the previous ones shows that:

i) The presence even of a slight non-uniformity in the anisotropic medium (of a thin dielectric toroid) in contact with the structure wall changes totally the phase behaviour of the waveguide compared to the case in which the ferrite occupies it entirely [3, 6]. For negative magnetization this is clearly visible juxtaposing Figs. 1(b) and 2(b) with Fig. 3 [6]. For positive magnetization it follows from Table 2, indicating the appearance of upper cut-off frequencies in case $\rho = 0.95$ and 0.9 , not observed when $\rho = 1$ (ferrite-filled waveguide). The upper limit of the propagation area (the envelope limit En_{1+}) however appears for values of \bar{r}_0 , lying out of the scale chosen (larger than 30).

Table 2: Values of the $L_1(c, n)$, $\bar{L}_{3-}(c, \bar{\varepsilon}, \rho, \alpha_-, n)$ and $\bar{L}_{3+}(c, \bar{\varepsilon}, \rho, \alpha_+, n)$ numbers and of the upper cut-off frequencies $\bar{\nu}_{0cr}$ for the TE_{01} mode in case $\varepsilon_d = \varepsilon_r$, $\rho = 1, 0.95$ and 0.9 as a function of $|\alpha|$.

ρ	$ \alpha $	0.05	0.10	0.15	0.20	0.25	0.30	0.35	0.40	0.45	0.50
1	L_1	6.59365									
	$\bar{\nu}_{0en-}$	132.03823	66.26872	44.46072	33.64810	27.23959	23.04009	20.11104	17.98567	16.40772	15.22739
0.95	L_{3-}	6.42086	6.41569	6.40685	6.39399	6.37658	6.35383	6.32463	6.28743	6.23994	6.17892
	$\bar{\nu}_{0en-}$	128.57799	64.48008	43.20110	32.62919	26.34280	22.20207	19.29052	17.15036	15.52755	14.26959
	L_{3+}	48.51598	48.37313	48.13345	47.79447	47.35258	46.80286	46.13881	45.35198	44.43147	43.36313
	$\bar{\nu}_{0en+}$	971.53477	486.16823	324.56174	243.90013	195.62215	163.54244	140.72614	123.70766	110.56376	100.14286
0.9	L_{3-}	5.64657	5.63076	5.60398	5.56557	5.51458	5.44973	5.36943	5.27170	5.15415	5.01401
	$\bar{\nu}_{0en-}$	114.36997	56.59123	37.78738	28.40167	22.78172	19.04291	16.37710	14.37973	12.82564	11.57937
	L_{3+}	24.58168	24.50957	24.38857	24.21741	23.99422	23.71647	23.38081	22.98291	22.51715	21.97626
	$\bar{\nu}_{0en+}$	492.24937	246.33049	164.45108	123.58393	99.12448	82.87204	71.31289	62.69103	56.03193	50.75199
ρ	$ \alpha $	0.55	0.60	0.65	0.70	0.75	0.80	0.85	0.90	0.95	1.00
1	L_1	6.59365									
	$\bar{\nu}_{0en-}$	14.35461	13.73678	13.34863	13.18995	13.29156	13.73678	14.72569	16.80764	22.22799	
0.95	L_{3-}	6.09947	5.99424	5.85188	5.65482	5.37652	4.97996	4.42183	3.66507	2.69066	
	$\bar{\nu}_{0en-}$	13.27875	12.48801	11.84695	11.31191	10.83804	10.37491	9.87533	9.34249	9.07055	
	L_{3+}	42.12844	40.70273	39.05234	37.12992	34.86577	32.15101	28.79961	24.44509	18.13731	
	$\bar{\nu}_{0en+}$	91.71505	84.79735	79.06017	74.27469	70.28279	66.98127	64.31854	62.31210	61.14304	
0.9	L_{3-}	4.84813	4.65297	4.42473	4.15939	3.85280	3.50075	3.09894	2.64290	2.12768	
	$\bar{\nu}_{0en-}$	10.55454	9.69369	8.95772	8.32044	7.76652	7.29322	6.92089	6.73692	7.17266	
	L_{3+}	21.35071	20.62784	19.79038	18.81409	17.66332	16.28255	14.57715	12.36132	9.15513	
	$\bar{\nu}_{0en+}$	46.48122	42.97466	40.06497	37.63570	35.60591	33.92198	32.55533	31.50978	30.86302	

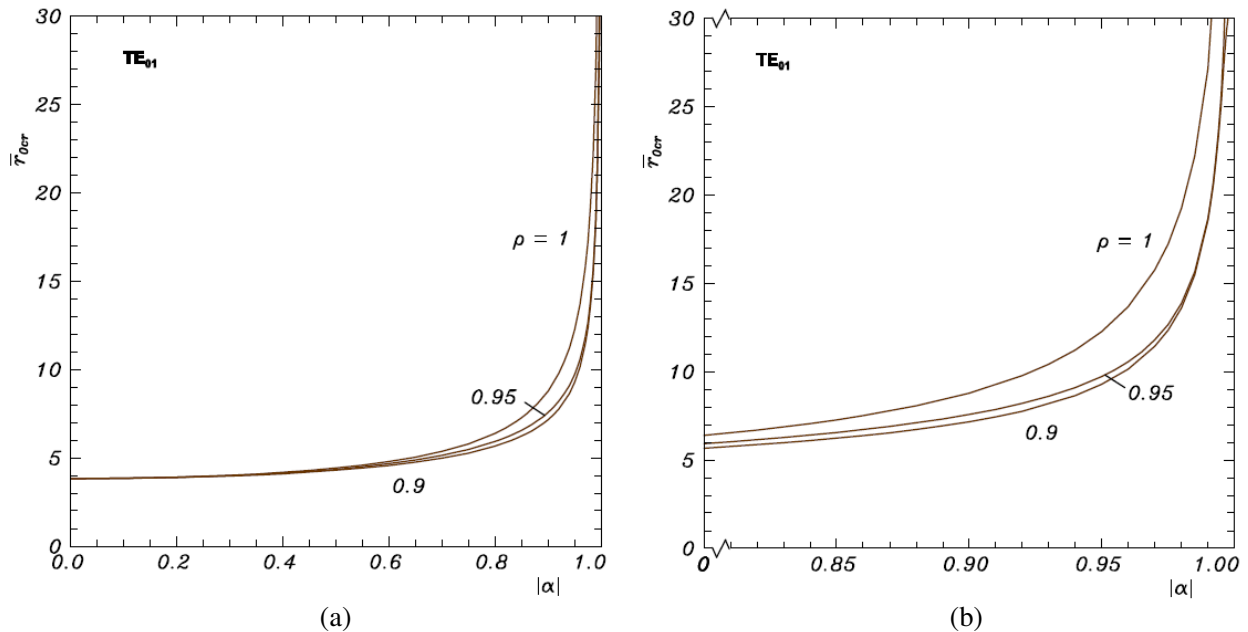


Figure 3: Dependence of the lower cut-off frequencies $\bar{\nu}_{0cr}$ of the ferrite-dielectric waveguide for the normal TE_{01} mode on $|\alpha|$ with ρ as parameter, assuming: (a) $|\alpha| = \langle 0 \div 1 \rangle$; (b) $|\alpha| = \langle 0.8 \div 1 \rangle$.

- ii) In view of the substantial influence of the value of $\varepsilon_d/\varepsilon_r$ — ratio on the phase portrait of a geometry, containing dielectric cylinder and ferrite toroid, established before [8], it might be expected that a similar dependence might be observed in the behaviour of the structure under study.
- iii) An insignificant variation of the parameter ρ (of the size of the area, taken by dielectric), keeping the $\varepsilon_d/\varepsilon_r$ — ratio constant, leads to a drastic deformation of phase curves, resp. of the

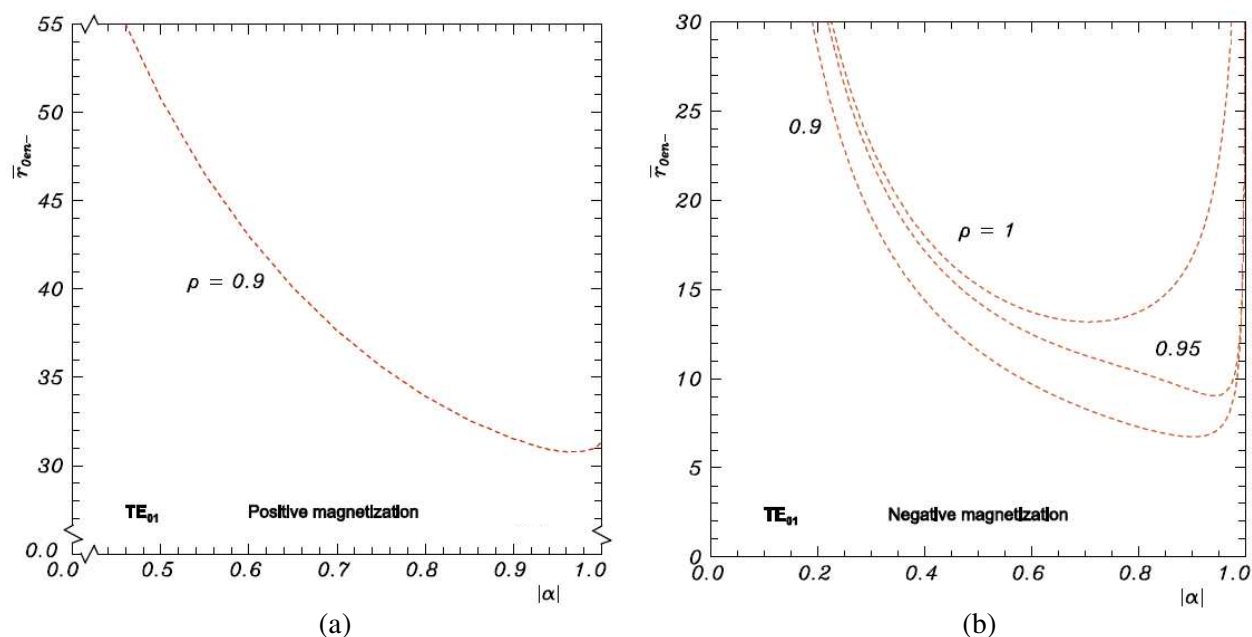


Figure 4: Dependence of the upper cut-off frequencies $\bar{\tau}_{0en+}$ and $\bar{\tau}_{0en-}$ of the ferrite-dielectric waveguide, magnetized azimuthally in: (a) positive and (b) negative direction for the normal TE_{01} mode on $|\alpha|$ with ρ as parameter.

region of transmission (cf. Figs. 1(a), (b) with Figs. 2(a), (b) for $\rho = 0.95$ and 0.9).

iv) A reversal of M_r , preserving ρ , the $\varepsilon_d/\varepsilon_r$ — ratio and $|\alpha|$ the same, entails an entire alteration of the position, limits, form and size of the domain of propagation.

v) The lower and upper cut-off frequencies for all ρ and $\varepsilon_d/\varepsilon_r$ — ratios change their places, if $|\alpha|$ is large (cf. Figs. 1(b) and 2(b) for negative magnetization and Tables 1 and 2 for both signs of M_r).

vi) The area in which the structure provides differential phase shift (may operate as a phase shifter) strongly depends on the dimension of the part of waveguide cross-section, taken by dielectric. In case it enlarges, the phase shift is afforded in a narrower frequency band.

4. CONCLUSION

The replacement of the outer part of the circular ferrite waveguide of azimuthal magnetization, propagating normal TE_n modes even by a thin dielectric toroid effects considerably its phase portrait. Envelope curves (resp. additional kind of cut-off frequencies) spring up at which the phase characteristics for both signs of magnetization terminate (the propagation stops). The dimensions of the area of wave propagation, of the frequency band in which differential phase shift is produced, are substantially influenced by the magnitude of dielectric insert.

ACKNOWLEDGMENT

We express our gratitude to our mother Trifonka Romanova Popnikolova and to our late father Nikola Georgiev Popnikolov for their self-denial and for their tremendous efforts to support all our undertakings.

REFERENCES

1. Clarricoats, P. J. B. and A. D. Olver, "Propagation in anisotropic radially stratified circular waveguides," *Electron. Lett.*, Vol. 2, 37–38, January 1966.
2. Baden-Fuller, A. J., *Ferrites at Microwave Frequencies*, IEE Electromagnetic Waves Series 23, Peter Peregrinus, London, UK, 1987.
3. Georgiev, G. N. and M. N. Georgieva-Grosse, "A new property of the complex Kummer function and its application to waveguide propagation," *IEEE Antennas Wireless Propagat. Lett.*, Vol. 2, 306–309, December 2003.
4. Georgiev, G. N. and M. N. Georgieva-Grosse, "Propagation in the circular waveguide, containing an azimuthally magnetized ferrite cylinder and a dielectric toroid," *Proc. 6th Europ.*

- Conf. Antennas Propagat. EuCAP 2012*, 5 pages, Prague, Czech Republic, article ID P-75, March 26–30, 2012.
5. Georgiev, G. N. and M. N. Georgieva-Grosse, “Advanced computational methods for analysis of the circular waveguide completely filled with azimuthally magnetized ferrite: Review of recent results,” *Proc. Fourteenth Int. Conf. Electromagn. Adv. Applicat. ICEAA '12*, 62–65, Cape Town, South Africa, September 2–7, 2012, (*Invited Paper* in the Special Session “Modern problems of mathematical and computational electromagnetics and their advanced applications,” organized by M. N. Georgieva-Grosse and G. N. Georgiev).
 6. Georgieva-Grosse, M. N. and G. N. Georgiev, “Advanced iterative methods for exact computation of the differential phase shift in the circular waveguide, completely filled with azimuthally magnetized ferrite: Review of recent results,” *Proc. Sixteenth Int. Conf. Electromagn. Adv. Applicat. ICEAA '14*, 1290–1293, Palm Beach, Aruba, August 3–8, 2014, (*Invited Paper* in the Special Session “Challenges in mathematical and computational electromagnetics and its applications,” organized by G. N. Georgiev and M. N. Georgieva-Grosse).
 7. Georgiev, G. N. and M. N. Georgieva-Grosse, “Circular waveguide, completely filled with azimuthally magnetized ferrite,” Chapter in *Wave Propagation*, 161–196, L. Rocha and G. Mateus (Eds.), Academy Publish, Cheyenne, Wyoming, USA, 2014.
 8. Georgieva-Grosse, M. N. and G. N. Georgiev, “Phase characteristics of the circular waveguide with an azimuthally magnetized ferrite cylinder and a dielectric toroid,” *Proc. 2015 IEEE AP-S Int. Symp. on Antennas Propagat. & URSI CNC/USNC Radio Science Meeting*, Vancouver, BC, Canada, July 19–25, 2015 (in print).
 9. Abramowitz, M. and I. Stegun, Eds., *Handbook of Mathematical Functions with Formulas, Graphs and Mathematical Tables*, Applied Mathematics Series 55, National Bureau of Standards, Washington, D.C., 1964.
 10. Georgiev, G. N. and M. N. Georgieva-Grosse, (*Invited Paper*), “Theory of the L numbers and its application to electromagnetism,” *Proc. 2015 URSI Atlantic Radio Science Conference URSI AT-RASC 2015*, Paper ID 1192(B20-4), Gran Canaria, Canary Islands, Spain, May 18–22, 2015.

A Nonlinear Boundary Condition for Continuum Models of Biomolecular Electrostatics

J. P. Bardhan¹, D. A. Tejani¹, N. S. Wieckowski¹,
A. Ramaswamy¹, and M. G. Knepley²

¹Northeastern University, Boston, MA, USA

²University of Chicago, Chicago, IL, USA

Abstract— Understanding the behavior of biomolecules such as proteins requires understanding the critical influence of the surrounding fluid (solvent) environment — water with mobile salt ions such as sodium. Unfortunately, for many studies, fully atomistic simulations of biomolecules, surrounded by thousands of water molecules and ions are too computationally slow. Continuum-solvent models based on macroscopic dielectric theory (e.g., the Poisson equation) are popular alternatives, but their simplicity fails to capture well-known phenomena of functional significance. For example, standard theories predict that electrostatic response is symmetric with respect to the sign of an atomic charge, even though response is in fact strongly asymmetric if the charge is near the biomolecule surface. In this work, we present an asymmetric continuum theory that captures the essential physical mechanism — the finite size of solvent atoms — using a nonlinear boundary condition (NLBC) at the dielectric interface between the biomolecule and solvent. Numerical calculations using boundary-integral methods demonstrate that the new NLBC model reproduces a wide range of results computed by more realistic, and expensive, all-atom molecular-dynamics (MD) simulations in explicit water. We discuss model extensions such as modeling dilute-electrolyte solvents with Debye-Huckel theory (the linearized Poisson-Boltzmann equation) and opportunities for the electromagnetics community to contribute to research in this important area of molecular nanoscience and engineering.

1. INTRODUCTION

Protein structure and function are determined in part by electrostatic interactions between the protein’s atomic charges and the surrounding biological fluid (solvent), a complex mixture of polar water molecules and dissolved charges such as sodium and potassium ions [1]. For over a century, biological scientists have modeled these interactions using macroscopic continuum models based on the Poisson-Boltzmann equation or Debye-Hückel theory [1, 2]. These popular mean-field theories assume that solvent molecules are infinitely small compared to the biomolecule solute [3, 4], a drastic simplification critical to enable pioneering theoretical studies using spherical and ellipsoidal models of protein shapes [5]. However, its justifications are increasingly questionable for atomistically detailed protein structures and predictions of binding affinities (binding free energies), which are of enormous value to understanding the molecular basis of disease and for designing improved therapeutic drugs.

In contrast, exponential growth in computing capabilities has enabled large-scale molecular-dynamics (MD) simulations that model the surrounding solvent in fully atomistic, explicit detail [6]. These calculations can provide far more realistic insights, but unfortunately require hundreds or thousands of times the computational resources that continuum models need. A rigorous statistical-mechanical argument establishes the connection between atomistic and continuum models [3, 7], creating an opportunity to develop more accurate continuum models by comparison to MD simulations, where new continuum theories can be tested against a wide array of challenging “computational experiments” which are unrealizable in real-world laboratories [8–11].

We have been advancing multiple approaches to improve continuum models [11–14]. One approach replaces the traditional model of the solvent as a macroscopic dielectric continuum (the familiar relation $D(r) = \epsilon(r)E(r)$), and instead models it as a nonlocal dielectric material [4, 15, 16], which limits short-range dielectric response using a convolution $D(r) = \int_{\text{solvent}} \epsilon(|r - r'|)E(r')dV'$. On the other hand, nonlocal models, and even many sophisticated nonlinear models, are still symmetric with respect to the sign of the protein charges. In reality, however, negative and positive charges near the solute surface produce substantially different responses. Asymmetry results from both water structure at the interface, and the fact that water hydrogens are much smaller than water oxygens [8, 9, 11, 17–20]. We have demonstrated, using atomistic MD calculations, that charge-sign asymmetries can be accurately reproduced if the electric potential is modeled as a piecewise-linear

plus constant (i.e., piecewise-affine) function of the charge [11]. The constant term in this model represents the interface potential induced by water structure around a completely uncharged version of the solute [21, 22], and the discontinuity in response coefficient occurs where the solute charge changes sign [11].

The few theories that directly address hydration asymmetry [19, 20, 23] are not actually Poisson models, but generalizations of the Born-ion problem (the spherically symmetric case of a sphere with a central charge). Recently we proposed the first successful asymmetric Poisson theory that can be solved for complex molecular geometries [14], by translating the existing models’ physical insights into a boundary-integral equation (BIE) formulation of the Poisson problem [24, 25]. This led to a modified BIE formulation in which we replaced the usual Maxwell boundary condition for the continuity of the normal flux with a nonlinear boundary condition (NLBC) [14]. Calculations showed that the new model successfully reproduces highly accurate MD calculations on a wide range of challenging test cases [10].

In the present paper, we improve the new NLBC model by ensuring that the potential outside the solute protein satisfies Gauss’s law sufficiently far from the solute. To demonstrate the new model, we have implemented a boundary-element method solver in MATLAB (all of the source code and data required to reproduce the figures in this paper are freely and publicly available online [26]). Calculations demonstrate that the improved model is more accurate for monovalent atomic ions, and illustrate that charge-sign hydration asymmetry effects are substantial for surface charges, with the magnitude of asymmetry decreasing rapidly for charges further from the solute — solvent interface. In particular, we predict that for surface charges in a sphere, the energetic difference between positive and negative charges does not depend strongly on the size of the sphere; this result implies that asymmetry is an essential piece of physics to include in models of molecular electrostatics. The next section describes the traditional, charge-sign symmetric continuum model, our modifications to incorporate asymmetric response, and a boundary-integral approach for solving the NLBC model. Section 3 describes a MATLAB implementation and presents computational results for single-atom ions as well as large spheres approximating full-sized proteins. The paper concludes in Section 4 with a summary and discussion.

2. THEORY

2.1. Symmetric Continuum Model and Boundary-integral Method

We consider a protein in an infinite dilute electrolyte solution. In the exterior region, which we label *I*, the potential obeys the linearized Poisson-Boltzmann equation $\nabla^2\varphi = \kappa^2\varphi$ where κ represents the inverse Debye screening length [1], and the dielectric constant is labeled ϵ_I (often taken to be 80, approximately that of bulk water). A thin shell of ion-free solvent separates the electrolyte solution from the protein. This region *II*, labeled the Stern or ion-exclusion layer, is a few Angstroms in width and simplistically models the finite size of the ions dissolved in the electrolyte. Here the potential obeys the Laplace equation and the dielectric constant is ϵ_{II} (usually $\epsilon_{II} = \epsilon_I$). The protein interior, labeled *III*, is a low-dielectric medium (ϵ_{III} is usually between 2 and 8) containing N discrete point charges, and the potential satisfies a Poisson equation $\nabla^2\varphi(r) = -\sum_{i=1}^N q_i\delta(r-r_i)$ where q_i and r_i specify the i th charge. The boundary a separates the protein region *III* and the Stern layer *II*, and the boundary b separates the Stern layer from the electrolyte solvent *I*. The potential is assumed to decay to zero suitably fast as $r \rightarrow \infty$, and the boundary conditions are

$$\varphi_{III}(\mathbf{r}_a) = \varphi_{II}(\mathbf{r}_a) \quad (1)$$

$$\epsilon_{III}\frac{\partial\varphi_{III}(\mathbf{r}_a)}{\partial n} = \epsilon_{II}\frac{\partial\varphi_{II}(\mathbf{r}_a)}{\partial n} \quad (2)$$

$$\varphi_{II}(\mathbf{r}_b) = \varphi_I(\mathbf{r}_b) \quad (3)$$

$$\epsilon_{II}\frac{\partial\varphi_{II}(\mathbf{r}_b)}{\partial n} = \epsilon_I\frac{\partial\varphi_I(\mathbf{r}_b)}{\partial n}. \quad (4)$$

The flux conditions Eqs. (2) and (4) are what we call the standard Maxwell boundary conditions (SMBC). By applying Green’s theorem in these three regions and taking suitable limits as the field point approaches each region’s bounding surface or surfaces, we obtain the coupled BIE

system [24, 27, 36]:

$$\begin{bmatrix} cccc \left(\frac{1}{2}I + K_{III,aa} \right) & -G_{III,aa} & 0 & 0 \\ \left(\frac{1}{2}I - K_{II,aa} \right) & +G_{II,aa} \frac{\epsilon_{III}}{\epsilon_{II}} & +K_{II,ab} & -G_{II,ab} \\ -K_{II,ba} & +G_{II,ba} \frac{\epsilon_{III}}{\epsilon_{II}} & \left(\frac{1}{2}I + K_{II,bb} \right) & -G_{II,bb} \\ 0 & 0 & \left(\frac{1}{2}I - K_{I,bb} \right) & +G_{I,bb} \frac{\epsilon_{II}}{\epsilon_I} \end{bmatrix} \begin{bmatrix} c\varphi_{III}(\mathbf{r}_a) \\ \frac{\partial \varphi_{III}}{\partial n}(\mathbf{r}_a) \\ \varphi_{II}(\mathbf{r}_b) \\ \frac{\partial \varphi_{II}}{\partial n}(\mathbf{r}_b) \end{bmatrix} = \begin{bmatrix} c \sum q_i G_{III} \\ 0 \\ 0 \\ 0 \end{bmatrix}, \quad (5)$$

where $G_{X,ij}$ and $K_{X,ij}$ represent the single- and double-layer boundary-integral operators associated with the Green's function of region X that map from a distribution on boundary j to the potential on boundary i .

2.2. Renormalized Nonlinear Boundary Condition Model

Our original work on the NLBC model employed only a single interface, the protein solvent — solute boundary a . For consistency, the regions it separates are still labeled III (solute) and II (solvent), and instead of Eq. (2) we have the nonlinear flux boundary condition

$$f(E_n(\mathbf{r}_a^-)) \frac{\partial \varphi_{III}(\mathbf{r}_a)}{\partial n} = (1 + f(E_n(\mathbf{r}_a^-))) \frac{\partial \varphi_{II}(\mathbf{r}_a)}{\partial n}, \quad (6)$$

where the field-dependent nonlinear function f is

$$f(E_n) = \frac{\epsilon_{III}}{\epsilon_{II} - \epsilon_{III}} - \alpha \tanh(\beta E_n - \gamma) - \alpha \tanh(-\gamma). \quad (7)$$

The first term of Eq. (7) represents the SMBC, and the last term ensures that the NLBC model recovers the standard model for weak electric fields, i.e., as $E_n \rightarrow 0$. As shown in our earlier work, the NLBC has only three free parameters α , β , and γ , which can be parameterized robustly against atomistic calculations. Numerical simulations using the NLBC model showed excellent agreement with atomistic results [14]. However, outside the solute, the potentials generated by this model fail to satisfy Gauss's law, as can be seen by considering a Born ion, i.e., a sphere with central charge. In particular, solutions satisfying SMBC automatically satisfy Gauss's law, whereas the NLBC cannot simultaneously satisfy Gauss's law and provide asymmetric response. This deficiency of central importance for problems involving multiple solute molecules, e.g., protein-drug binding; we propose to solve it by including a compensating charge distribution a few Angstroms away from the solute — solvent interface, at the Stern layer. This compensating charge ensures that Gauss's law is satisfied outside the second boundary. The modified boundary condition at b ensures that the model recovers the expected macroscopic dielectric behavior far from the protein surface, and is written

$$\left(-\frac{\sum q_i}{\epsilon_I} \right) \frac{\partial \varphi_{II}(\mathbf{r}_b)}{\partial n} = \left(\int_b \frac{\partial \varphi_{II}(\mathbf{r}_b)}{\partial n} dA \right) \frac{\partial \varphi_I(\mathbf{r}_b)}{\partial n}. \quad (8)$$

Defining s_1 and s_2 so that Eq. (8) can be written $s_1 \frac{\partial \varphi_{II}}{\partial n} = s_2 \frac{\partial \varphi_I}{\partial n}$, the system of coupled BIEs is

$$\begin{bmatrix} cccc \left(\frac{1}{2}I + K_{III,aa} \right) & -G_{III,aa} & 0 & 0 \\ \left(\frac{1}{2}I - K_{II,aa} \right) & +G_{II,aa} \frac{f}{1+f} & +K_{II,ab} & -G_{II,ab} \\ -K_{II,ba} & +G_{II,ba} \frac{f}{1+f} & \left(\frac{1}{2}I + K_{II,bb} \right) & -G_{II,bb} \\ 0 & 0 & \left(\frac{1}{2}I - K_{I,bb} \right) & +G_{I,bb} \frac{s_1}{s_2} \end{bmatrix} \begin{bmatrix} c\varphi_{III}(\mathbf{r}_a) \\ \frac{\partial \varphi_{III}}{\partial n}(\mathbf{r}_a) \\ \varphi_{II}(\mathbf{r}_b) \\ \frac{\partial \varphi_{II}}{\partial n}(\mathbf{r}_b) \end{bmatrix} = \begin{bmatrix} c \sum q_i G_{III} \\ 0 \\ 0 \\ 0 \end{bmatrix}. \quad (9)$$

Using Green's theorem again to determine the reaction potential $\varphi^{reac}(q)$ in the protein due to the solvent, the electrostatic charging free energy is then calculated as $\Delta G = \frac{1}{2}q^T \varphi^{reac}(q) + \varphi^{static} \sum q_i$, where we have modeled the static (interface) potential as a constant, see, e.g., [8, 11, 21] (following our previous work, we model $\varphi^{static} = 10.7$ kcal/mol/e). In contrast, the standard Poisson theory gives an energy $\Delta G = \frac{1}{2}q^T Lq$ where L is a symmetric negative definite operator.

3. COMPUTATIONAL RESULTS

3.1. Numerical Implementation

The full MATLAB code to reproduce the calculations and figures in this paper are freely available online at <http://www.bitbucket.org/jbardhan/piers15-code>. Our boundary-element method from

earlier work was extended from using only point-based discretizations of the relevant boundaries and unknown surface distributions, to use triangular boundary elements with piecewise-constant basis functions and centroid collocation. Following our earlier work, we use Picard iteration to solve the nonlinear BIE problem. Calculations on spherical molecules used the earlier point-based implementation for verification against earlier results. Calculations for ellipsoids used triangular meshes derived from the mesh obtained from MATLAB’s ellipsoid command, which takes as input the ellipsoid semi-axis lengths and a number n of subdivisions, and returns three $(n + 1)$ by $(n + 1)$ matrices (for the x , y , and z coordinates of the mesh vertices), which define planar quadrilaterals and triangles by subdividing the ellipsoid in angular coordinates (lines of latitude and longitude). By iterating over the quadrilaterals and subdividing, we obtain a triangular mesh suitable for our existing MATLAB implementation of the boundary-element method.

The ellipsoidal shape approximations are calculated using standard methods [28, 29]: the molecule, e.g., a protein, is defined as a set of atoms which are defined as spheres at specified locations and with specified radii, and with each possessing a single point charge at its center. The N atomic positions are represented by $\mathbf{r}_i = [x_i; y_i; z_i]$ and the radii are $[a_1, a_2, \dots, a_N]$. In order to estimate protein shape as an ellipsoid, we translate the molecule so its center of mass is at the origin, where the “mass” of the molecule is modeled as proportional to the sum of the atomic volumes, i.e., $M = \sum_{i=1}^N (a_i^3)$. The center of mass is defined as $\mathbf{r}_c = (M^{-1}) \sum_{i=1}^N (a_i^3)(\mathbf{r}_i)$, and so we translate the atoms according to $\mathbf{r}'_i = \mathbf{r}_i - \mathbf{r}_c$. Dropping the prime and referring only to the translated coordinates, the components of the molecule’s inertia tensor I are calculated as

$$I_{11} = \sum_{i=1} \left(m_i \left(y_i^2 + z_i^2 + \frac{2}{5} a_i^2 \right) \right) \quad (10)$$

$$I_{22} = \sum_{i=1} \left(m_i \left(x_i^2 + z_i^2 + \frac{2}{5} a_i^2 \right) \right) \quad (11)$$

$$I_{33} = \sum_{i=1} \left(m_i \left(x_i^2 + y_i^2 + \frac{2}{5} a_i^2 \right) \right) \quad (12)$$

$$I_{12} = \sum_{i=1} (m_i x_i y_i) \quad (13)$$

$$I_{13} = \sum_{i=1} (m_i x_i z_i) \quad (14)$$

$$I_{23} = \sum_{i=1} (m_i y_i z_i), \quad (15)$$

and by symmetry $I_{21} = I_{12}$, $I_{31} = I_{13}$, and $I_{32} = I_{23}$. The principal moments of inertia of the molecule are the eigenvalues of I . Choosing I_{xx} , I_{yy} , and I_{zz} such that $I_{xx} \leq I_{yy} \leq I_{zz}$, we find the semi-axes a , b , and c of an ellipsoid that has the same weight M and principal moments of inertia [28, 29]. This leads to $a = \sqrt{\frac{5}{2M}(-I_{xx} + I_{yy} + I_{zz})}$, $b = \sqrt{\frac{5}{2M}(I_{xx} - I_{yy} + I_{zz})}$, and $c = \sqrt{\frac{5}{2M}(I_{xx} + I_{yy} - I_{zz})}$. This ellipsoid is the simplest anisotropic approximation to the shape of the bio-molecule under consideration.

The results in Figure 1(a) represent continuum-model calculations of monovalent ions ($+1e$ and $-1e$ charges) as a function of ion radius. For comparison, reference data for biologically relevant ions obtained from all-atom molecular dynamics (MD) calculations [14] are plotted as symbols. The renormalized NLBC (thick curves) clearly fit the MD results better than the original NLBC model (thin curves), even though no new parameters have been introduced. The symmetric Poisson model is substantially incorrect; the most frequent approaches for ions involve adjusting atomic radii on an atom by atom basis, but this is not possible for multi-atom solutes [19, 20]. Figure 1(b) plots the deviations between the new NLBC model and a Poisson model that involves sign-symmetric dielectric response, but incorporates the static potential contribution: that is, the results plot the effects of asymmetry in the dielectric response at the molecule surface. The sample problems in this figure are a surface charge in a sphere of varying radius (1.5 Å from the surface), or a buried charge at its center. As expected, the buried charge experiences essentially symmetric response once it is more than a few Angstroms from the interface. In contrast, the surface charge experiences a surprisingly large asymmetry that is essentially constant even as the sphere radius increases. The

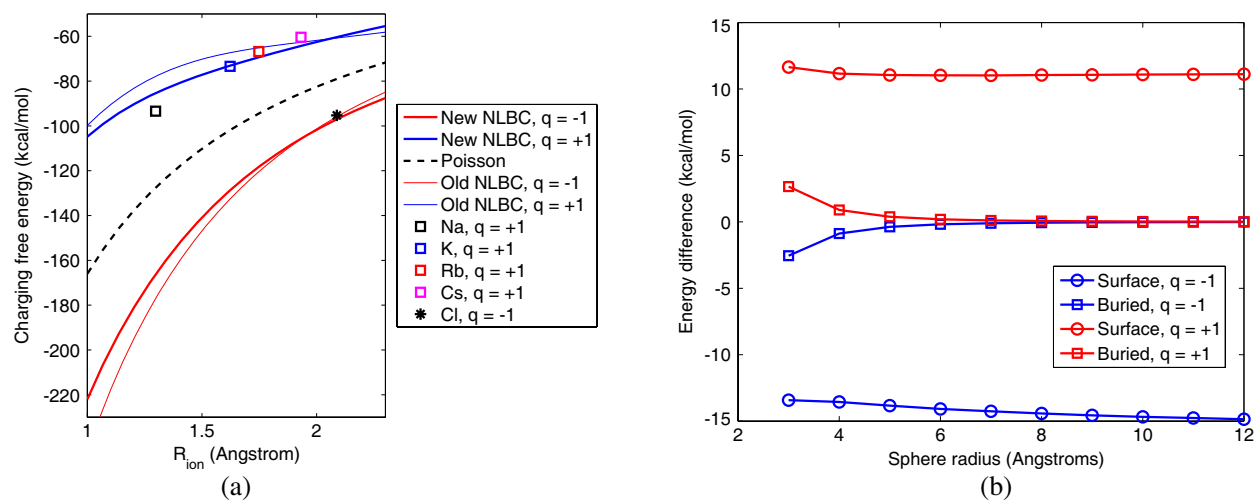


Figure 1: Charging free energies for single charges in spheres. (a) Common monovalent ions, calculated using all-atom molecular dynamics (symbols) [14], standard Poisson theory (black dashed line), the original NLBC model [14] (thin lines), and the new NLBC model presented in this work (thick lines). (b) Charging free energy for a single charge in a sphere, as a function of sphere radius, charge value, and charge location. Buried charges are situated at the sphere center; surface charges are located 1.5 Å from the sphere surface.

magnitude of this asymmetry is in line with previous MD calculations [11], and the persistence of this large deviation from standard models, even for protein-sized molecules, suggests that including accurate models of asymmetry should be a main goal in developing improved continuum theory.

4. DISCUSSION

In this work we have presented a continuum-electrostatic model for molecular solvation that models biologically important hydration asymmetry — a fundamentally non-continuum phenomenon — using an effective nonlinear boundary condition (NLBC). The NLBC replaces the traditional Maxwell boundary condition that enforces continuity of the electric flux at the interface, and the present model improves on our original work [14] by ensuring that Gauss’s law holds outside of the first shell of solvent molecules surrounding molecular solutes. The use of an effective boundary condition at the molecule — solvent interface represents a new frontier in biomolecular modeling, and was inspired by a long history of approximate boundary conditions in electromagnetic theory, e.g., [30] and rarefied gases [31, 32]. We hope that the present work will encourage experts in the electromagnetics community to contribute their insights and experience to support deeper understanding of molecular electrostatics, whether in improving models, analyzing their implications, or solving them numerically.

Our NLBC model is the first asymmetric theory that uses actual Poisson continuum theory, and in the simple case of a single ion, reproduces empirical and semi-empirical theories developed over decades of research into electrostatic asymmetry [17, 19, 20]. We note that the present model can treat dilute electrolyte solutions using the linearized Poisson-Boltzmann equation [1, 2] simply by modeling the Green’s function of the outermost region with the LPBE Green’s function $\frac{\exp(-\kappa|r-r'|)}{|r-r'|}$ instead of the $\frac{1}{|r-r'|}$ of the Laplace Green’s function. To demonstrate the new model’s accuracy, we have calculated the electrostatic charging free energies for single-atom ions and compared our results to more accurate, and much more computationally demanding, atomistic molecular dynamics calculations that include thousands of explicit water molecules. The results for ions in Figure 1 indicate that the new model exhibits substantially better accuracy than the original, and the enforcement of Gauss’s law is in fact even more important when modeling electrolyte solutions using the LPBE (results not shown). Calculations of amino-acid charging free energies, and the differences due to protonation or deprotonation, illustrate that the magnitude of asymmetric response decays rapidly with an atomic charge’s distance from the solute — solvent interface [8, 9, 11]. Our numerical calculations employed boundary-integral methods with simple model geometries, such as spheres for the monatomic ions and ellipsoids to model the amino acids. These ellipsoids represent simple shape approximations [28, 29] and we expect that they will be useful for fast approximate

calculations such as in implicit-solvent molecular dynamics [25, 33–35]. Calculations for atomistic models of large molecules such as proteins will require fast, parallel boundary-element method solvers [24, 36], and implementation of such software represents an area of ongoing work.

ACKNOWLEDGMENT

MGK was partially supported by the U.S. Department of Energy, Office of Science, Advanced Scientific Computing Research, under Contract DE-AC02-06CH11357, and also NSF Grant OCI-1147680. JPB has been supported in part by the National Institute of General Medical Sciences (NIGMS) of the National Institutes of Health (NIH) under award number R21GM102642.

REFERENCES

1. Sharp, K. A. and B. Honig, “Electrostatic interactions in macromolecules: Theory and applications,” *Annu. Rev. Biophys. Bio.*, Vol. 19, 301–332, 1990.
2. Bardhan, J. P., “Biomolecular electrostatics — I want your solvation (model),” *Computational Science and Discovery*, Vol. 5, 013001, 2012.
3. Beglov, D. and B. Roux, “Solvation of complex molecules in a polar liquid: An integral equation theory,” *J. Chem. Phys.*, Vol. 104, No. 21, 8678–8689, 1996.
4. Hildebrandt, A., R. Blossey, S. Rjasanow, O. Kohlbacher, and H.-P. Lenhof, “Novel formulation of nonlocal electrostatics,” *Phys. Rev. Lett.*, Vol. 93, 108104, 2004.
5. Kirkwood, J. G., “Theory of solutions of molecules containing widely separated charges with special application to zwitterions,” *J. Chem. Phys.*, Vol. 2, 351, 1934.
6. Phillips, J. C., R. Braun, W. Wang, J. Gumbart, E. Tajkhorshid, E. Villa, C. Chipot, R. D. Skeel, L. Kale, and K. Schulten, “Scalable molecular dynamics with NAMD,” *J. Comput. Chem.*, Vol. 26, 1781–1802, 2005.
7. Roux, B. and T. Simonson, “Implicit solvent models,” *Biophys. Chem.*, Vol. 78, 1–20, 1999.
8. Ashbaugh, H. S., “Convergence of molecular and macroscopic continuum descriptions of ion hydration,” *The Journal of Physical Chemistry B*, Vol. 104, No. 31, 7235–7238, 2000.
9. Rajamani, S., T. Ghosh, and S. Garde, “Size dependent ion hydration, its asymmetry, and convergence to macroscopic behavior,” *J. Chem. Phys.*, Vol. 120, 4457, 2004.
10. Mobley, D. L., K. A. Dill, and J. D. Chodera, “Treating entropy and conformational changes in implicit solvent simulations of small molecules,” *The Journal of Physical Chemistry B*, Vol. 112, 938–946, 2008.
11. Bardhan, J. P., P. Jungwirth, and L. Makowski, “Affine-response model of molecular solvation of ions: Accurate predictions of asymmetric charging free energies,” *J. Chem. Phys.*, Vol. 137, 124101, 2012.
12. Bardhan, J. P., “Nonlocal continuum electrostatic theory predicts surprisingly small energetic penalties for charge burial in proteins,” *J. Chem. Phys.*, Vol. 135, 104113, 2011.
13. Bardhan, J. P., “Gradient models in molecular biophysics: Progress, challenges, opportunities,” *Journal of Mechanical Behavior of Materials*, Vol. 22, 169–184, 2013.
14. Bardhan, J. P. and M. G. Knepley, “Modeling charge-sign asymmetric solvation free energies with nonlinear boundary conditions,” *J. Chem. Phys.*, Vol. 141, 131103, 2014.
15. Dogonadze, R. R. and A. A. Kornyshev, “Polar solvent structure in the theory of ionic solvation,” *J. Chem. Soc. Faraday Trans. 2*, Vol. 70, 1121–1132, 1974.
16. Fedorov, M. V. and A. A. Kornyshev, “Unravelling the solvent response to neutral and charged solutes,” *Molecular Physics*, Vol. 105, 1–16, 2007.
17. Latimer, W. M., K. S. Pitzer, and C. M. Slansky, “The free energy of hydration of gaseous ions, and the absolute potential of the normal calomel electrode,” *J. Chem. Phys.*, Vol. 7, 108–112, 1939.
18. Grossfield, A., “Dependence of ion hydration on the sign of the ion’s charge,” *J. Chem. Phys.*, Vol. 122, 024506, 2005.
19. Corbeil, C. R., T. Sulea, and E. O. Purisima, “Rapid prediction of solvation free energy. 2. The first-shell hydration (FiSH) continuum model,” *J. Chem. Theory Comput.*, Vol. 6, 1622–1637, 2010.
20. Mukhopadhyay, A., B. H. Aguilar, I. S. Tolokh, and A. V. Onufriev, “Introducing charge hydration asymmetry into the generalized born model,” *J. Chem. Theory Comput.*, Vol. 10, 1788–1794, 2014.

21. Cerutti, D. S., N. A. Baker, and J. A. McCammon, "Solvent reaction field potential inside an uncharged globular protein: A bridge between implicit and explicit solvent models?," *J. Chem. Phys.*, Vol. 127, 155101, 2007.
22. Kathmann, S. M., I-F. W. Kuo, C. J. Mundy, and G. K. Schenter, "Understanding the surface potential of water," *The Journal of Physical Chemistry B*, Vol. 115, 4369–4377, 2011.
23. Purisima, E. O. and T. Sulea, "Restoring charge asymmetry in continuum electrostatic calculations of hydration free energies," *The Journal of Physical Chemistry B*, Vol. 113, 8206–8209, 2009.
24. Altman, M. D., J. P. Bardhan, J. K. White, and B. Tidor, "Accurate solution of multi-region continuum electrostatic problems using the linearized poisson — Boltzmann equation and curved boundary elements," *J. Comput. Chem.*, Vol. 30, 132–153, 2009.
25. Bardhan, J. P., "Rapid bounds on electrostatic energies using diagonal approximations of boundary-integral equations," *Progress In Electromagnetics Research Symposium Abstracts*, 9, Cambridge, USA, Jul. 5–8, 2010.
26. Bardhan, J. P., D. Tejani, N. Wieckowski, A. Ramaswamy, and M. G. Knepley, "Public git repository containing all source code and data to reproduce the figures in this paper," <https://bitbucket.org/jbardhan/piers15-code>.
27. Yoon, B. J. and A. M. Lenhoff, "A boundary element method for molecular electrostatics with electrolyte effects," *J. Comput. Chem.*, Vol. 11, No. 9, 1080–1086, 1990.
28. Taylor, W. R., J. M. Thornton, and W. G. Turnell, "An ellipsoidal approximation of protein shape," *J. Mol. Graph.*, Vol. 1, 30–38, 1983.
29. Sigalov, G., A. Fenley, and A. Onufriev, "Analytical electrostatics for biomolecules: Beyond the generalized Born approximation," *J. Chem. Phys.*, Vol. 124, 124902, 2006.
30. Senior, T. B. A. and J. L. Volakis, "Approximate boundary conditions in electromagnetics," *IEEE*, London, 1995.
31. Maxwell, J. C., "On stresses in rarefied gases arising from inequalities of temperature," *Proceedings of the Royal Society of London*, Vol. 27, 304–308, 1878.
32. Von Smolan Smoluchowski, M., "Über wärmeleitung in verdünnten gasen," *Annalen der Physik*, Vol. 300, No. 1, 101–130, 1898.
33. Bardhan, J. P., "Interpreting the Coulomb-field approximation for generalized-Born electrostatics using boundary-integral equation theory," *J. Chem. Phys.*, Vol. 129, 144105, 2008.
34. Bardhan, J. P. and M. G. Knepley, "Mathematical analysis of the boundary-integral based electrostatics estimation approximation for molecular solvation: Exact results for spherical inclusions," *J. Chem. Phys.*, Vol. 135, 124107, 2011.
35. Bardhan, J. P. and M. G. Knepley, "Computational science and re-discovery: Open-source implementation of ellipsoidal harmonics for problems in potential theory," *Computational Science and Discovery*, Vol. 5, 014006, 2012.
36. Cooper, C. D., J. P. Bardhan, and L. A. Barba, "A biomolecular electrostatics solver using Python, GPUs and boundary elements that can handle solvent-filled cavities and Stern layers," *Comput. Phys. Commun.*, Vol. 185, 720–729, 2013.

Concerning the Circular- and Square-loop Antennas Mounted over a Ground Plane of Finite Extent

A. A. Ayorinde¹, S. A. Adekola^{1,2}, and A. Ike Mowete¹

¹Department of Electrical and Electronics Engineering
Faculty of Engineering, University of Lagos, Lagos, Nigeria

²Department of Electrical and Electronics Engineering
Niger Delta University, Wilberforce Island, Yenegoa, Nigeria

Abstract— As a natural sequel to an earlier presentation [1], which compared the performance features of equal perimeter circular- and square-loop antennas located over finite ground planes, this paper, using the same formulation, examines the same performance characteristics, but this time, with the antennas being of equal cross-sectional areas; and with loop heights varying between 0.05λ and 1.00λ at the operating (center) frequency of 1.25 GHz. Computational results for the antennas' input characteristics reveal that whereas they share virtually identical input resistance profiles, input reactance for the square loop has values that are in general, lower than those for the circular loop, for the entire range of 'height above ground plane' considered. Results for the E - and H -plane radiation field patterns indicate that when the loops are located at heights beyond 0.3λ above the finite ground plane, the front-lobes become distorted; an observation supported by the profiles of the forward directive gain, which display the 'notch filter response' behavior. Furthermore, the results suggest that acceptable front-to-back ratio performance can only be maintained if loop heights above the ground plane are kept below 0.3λ .

1. INTRODUCTION

The transformation of the characteristic bidirectional field pattern of a loop antenna radiating in free space to a unidirectional pattern is traditionally accomplished by backing the loop antenna with a large ground plane [6]. A typical example of an analytical technique employed for such structures is provided by the work of Shoamanesh and Shafai (1981) [5], in which the ground plane is considered as being essentially of infinite extent, (so that the image theory applies) and where analytical results reported a consequent gain enhancement for the antenna. The more practical problem for which the ground plane is of finite extent is more demanding because apart from the geometrical field and the reflected field that require evaluation, the diffracted fields due to the ground plane's edges must also be fully accounted for.

Previous notable works on the loop antenna located above a finite ground plane include that reported by Rojarajamont and Sekiguichi [2] who used an approximate current on the finite ground plane deduced from current due an infinite ground plane. Iwashige [3] employed the equivalent edge currents technique to evaluate the diffraction fields of a circular reflector, whereas Hejase et al. [4] utilized the Physical Optics (PO) method to determine the induced current on the square plate backing a circular loop antenna. In an earlier presentation, Ayorinde et al. [1] replaced the finite (solid) ground plane by grids constructed with thin wires, to address the radiation field problems of the circular-loop and square-loop antennas located above finite ground plane.

As an extension of that effort [1], this presentation examines the performance characteristics of circular- and square-loop antennas located over wire-grid ground planes of finite extent, with both loops characterized by equal cross-sectional areas. In addition to input impedance, far-zone fields and associated directive gain features; the front-to-back ratio (F/B) of the radiation intensity is also given consideration in this paper. And computational results suggest that for both loop antenna geometries of interest, an acceptable front-to-back ratio performance is sustainable when the antenna heights above the ground plane are less than 0.3λ at the operating frequency.

2. FORMULATION

Displayed in Figure 1(a) is a thin-wire circular loop antenna mounted at height h above a wire-grid ground plane while Figure 1(b) depicts a thin-wire square loop antenna at height h over a ground plane modeled by wire grids. It should be remarked that the above problem geometries are similar to the geometry studied in [1]. However, our interest here is when the cross-sectional area of the circular loop is equal to that of the square loop, that is, $[\pi a^2 = b^2]$, unlike in previous presentation [1], where the two loops have equal perimeter. Because the grids are constructed with

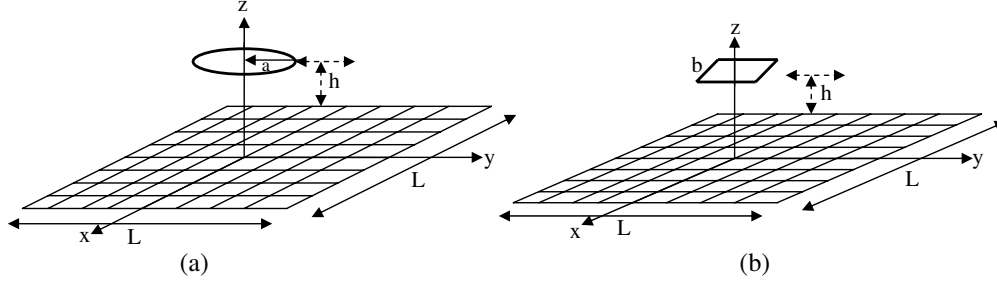


Figure 1: (a) A circular-loop antenna of radius a suspended at height h from a wire-grid ground plane. (b) A square loop antenna of side-length b at height h above a wire-grid ground plane.

both x -directed and y -directed wires, the total electric field at the far-zone is the superposition of the electric fields from the loop as well as the x -directed and y -directed wires. To avoid undue repetition, we rely substantially on the theory developed in [1], and therefore E_θ and E_φ components of the far-zone fields assume the following expressions:

$$E_\theta = E_{\ell\theta} + \sum_{n=1}^N E_{n\theta}^x + \sum_{n=1}^N E_{n\theta}^y \quad (1a)$$

and

$$E_\varphi = E_{\ell\varphi} + \sum_{n=1}^N E_{n\varphi}^x + \sum_{n=1}^N E_{n\varphi}^y \quad (1b)$$

where $E_{\ell\theta}$, $E_{n\theta}^x$ and $E_{n\theta}^y$ are the \hat{a}_θ -components of the electric fields due axial current distributions along the loop, n th x -directed wires and n th y -directed wires, respectively; while $E_{\ell\varphi}$, $E_{n\varphi}^x$ and $E_{n\varphi}^y$ are the \hat{a}_φ -components of the electric fields due to respective axial currents on the loop, n th x -directed and n th y -directed wires. The above electric field components can be calculated from:

$$E_{n\theta}^x = \frac{-j\omega\mu_0 e^{-jk_0 r} \cos\theta \cos\varphi}{4\pi r} \int_{-L/2}^{L/2} I(x') e^{jk_0 [x' \cos\varphi \sin\theta + (n-5)\frac{\lambda}{8} \sin\varphi \sin\theta]} dx' \quad (2a)$$

$$E_{n\theta}^y = \frac{-j\omega\mu_0 e^{-jk_0 r} \cos\theta \sin\varphi}{4\pi r} \int_{-L/2}^{L/2} I(y') e^{jk_0 [y' \sin\varphi \sin\theta + (n-5)\frac{\lambda}{8} \cos\varphi \sin\theta]} dy' \quad (2b)$$

$$E_{n\varphi}^x = \frac{j\omega\mu_0 e^{-jk_0 r} \sin\varphi}{4\pi r} \int_{-L/2}^{L/2} I(x') e^{jk_0 [x' \cos\varphi \sin\theta + (n-5)\frac{\lambda}{8} \sin\varphi \sin\theta]} dx' \quad (3a)$$

$$E_{n\varphi}^y = \frac{-j\omega\mu_0 e^{-jk_0 r} \cos\varphi}{4\pi r} \int_{-L/2}^{L/2} I(y') e^{jk_0 [y' \sin\varphi \sin\theta + (n-5)\frac{\lambda}{8} \cos\varphi \sin\theta]} dy' \quad (3b)$$

for circular loop $\ell = c$

$$E_{c\theta} = \frac{-j\omega\mu_0 a e^{-jk_0 r} \cos\theta}{4\pi r} \int_0^{2\pi} \sin(\varphi - \varphi') I(\varphi') e^{jk_0 [a \cos(\varphi - \varphi') \sin\theta + h \cos\theta]} d\varphi' \quad (4a)$$

$$E_{c\varphi} = \frac{-j\omega\mu_0 a e^{-jk_0 r}}{4\pi r} \int_0^{2\pi} \cos(\varphi - \varphi') I(\varphi') e^{jk_0 [a \cos(\varphi - \varphi') \sin\theta + h \cos\theta]} d\varphi' \quad (4b)$$

for square loop: $\ell = s$

$$\begin{aligned}
 E_{s\theta} = & \frac{-j\omega\mu_0 e^{-jk_0 r} \cos\theta \sin\varphi}{4\pi r} \int_{-b/2}^{b/2} I(y') e^{jk_0 [y' \sin\varphi \sin\theta - \frac{b}{2} \cos\varphi \sin\theta + h \cos\theta]} dy' \\
 & + \frac{-j\omega\mu_0 e^{-jk_0 r} \cos\theta \cos\varphi}{4\pi r} \int_{-b/2}^{b/2} I(x') e^{jk_0 [x' \cos\varphi \sin\theta - \frac{b}{2} \sin\varphi \sin\theta + h \cos\theta]} dx' \\
 & + \frac{-j\omega\mu_0 e^{-jk_0 r} \cos\theta \sin\varphi}{4\pi r} \int_{b/2}^{-b/2} I(y') e^{jk_0 [y' \sin\varphi \sin\theta + \frac{b}{2} \cos\varphi \sin\theta + h \cos\theta]} dy' \\
 & + \frac{-j\omega\mu_0 e^{-jk_0 r} \cos\theta \cos\varphi}{4\pi r} \int_{b/2}^{-b/2} I(x') e^{jk_0 [x' \cos\varphi \sin\theta + \frac{b}{2} \sin\varphi \sin\theta + h \cos\theta]} dx' \quad (5a)
 \end{aligned}$$

$$\begin{aligned}
 E_{s\varphi} = & \frac{-j\omega\mu_0 e^{-jk_0 r} \cos\varphi}{4\pi r} \int_{-b/2}^{b/2} I(y') e^{jk_0 [y' \sin\varphi \sin\theta - \frac{b}{2} \cos\varphi \sin\theta + h \cos\theta]} dy' \\
 & + \frac{j\omega\mu_0 e^{-jk_0 r} \sin\varphi}{4\pi r} \int_{b/2}^{-b/2} I(x') e^{jk_0 [x' \cos\varphi \sin\theta - \frac{b}{2} \sin\varphi \sin\theta + h \cos\theta]} dx' \\
 & + \frac{-j\omega\mu_0 e^{-jk_0 r} \cos\varphi}{4\pi r} \int_{b/2}^{-b/2} I(y') e^{jk_0 [y' \sin\varphi \sin\theta + \frac{b}{2} \cos\varphi \sin\theta + h \cos\theta]} dy' \\
 & + \frac{j\omega\mu_0 e^{-jk_0 r} \sin\varphi}{4\pi r} \int_{-b/2}^{b/2} I(x') e^{jk_0 [x' \cos\varphi \sin\theta + \frac{b}{2} \sin\varphi \sin\theta + h \cos\theta]} dx' \quad (5b)
 \end{aligned}$$

It may be remarked that the respective currents carried by the wire elements (including the loop) are determined using the method of moments. The front-to-back ratio (F/B), is calculated here using the standard formula:

$$F/B \text{ (dB)} = 10 \log_{10} \left[\frac{|E_\theta(\theta_f, \varphi_f)|^2 + |E_\varphi(\theta_f, \varphi_f)|^2}{|E_\theta(\theta_b, \varphi_b)|^2 + |E_\varphi(\theta_b, \varphi_b)|^2} \right] \quad (5c)$$

where (θ_f, φ_f) and (θ_b, φ_b) assume the respective values $(0^\circ, 0^\circ)$ and $(180^\circ, 0^\circ)$. Expressions utilized for other antenna parameters remain the same as those described elsewhere, [1]. Some computational results based on the above equations will now be presented.

3. COMPUTATIONAL RESULTS

Computational results are obtained based on the following values of parameters featuring in the above equations: a centre frequency of 1.25 GHz; square loop perimeter of 1λ which corresponds to 0.25λ side-length, radius of circular loop = 0.141λ ; the side-length of the square ground plane is 1λ , divided into eight equal segments; the loop height above the plane ranges from 0.05λ to 1.00λ ; wire radius = 0.001λ . The circular loop is excited at $\varphi = 0^\circ$ by a 1 V delta-gap source while the square loop is similarly excited at the corner ($x = 0.125\lambda$ and $y = -0.125\lambda$). The discussion of results begins with the input impedance.

3.1. Input Impedance

The calculated values of input resistance R_{in} and input reactance X_{in} of the circular- and square loop antennas at various antenna heights from 0.05λ to 1.00λ are plotted in Figure 2. It is worth

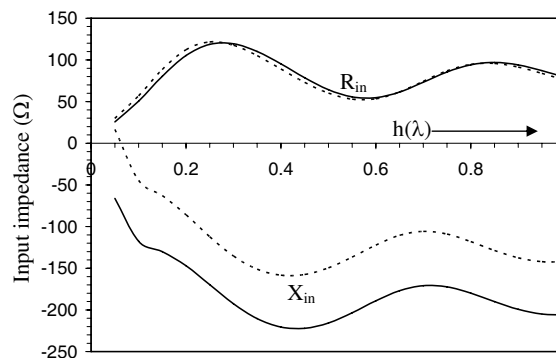


Figure 2: The input resistance R_{in} and input reactance X_{in} of the circular- and square-loop antennas versus the antenna height in wavelengths: —: circular loop; - - -: square loop.

reiterating that both loops are characterized by equal cross-sectional area. Evidently from the figure, one can see that both loops share virtually identical input resistance profiles, which vary in a sinusoidal fashion as the antenna height increases with the minimum R_{in} occurring at height 0.05λ . The variation of R_{in} from about $25\ \Omega$ to $125\ \Omega$ seems reasonable for some practical applications. On the other hand, there are marked differences in the input reactance X_{in} of circular loop and square loop even though the X_{in} profiles of both antenna appear similar. The square loop has input reactance values that are in general, lower than the input reactance of the circular loop for antenna height range $0.05\lambda \leq h \leq 1.00\lambda$ specified in this work. Remarkably, the square loop resonates at antenna height of 0.054λ while the circular loop does not, perhaps because of the corresponding lesser circumference of the circular loop which is 0.886λ .

3.2. Far-zone Electric Fields

Depicted in Figure 3 are the E_φ components of the radiated electric fields of the square- and circular-loop antennas superimposed on each other, on the E -plane ($\varphi = 0^\circ$) at various values of loop height. When the loops are at close proximity to the wire-grid ground plane (at $h = 0.05\lambda$), the major lobe is in the forward direction ($\theta = 0^\circ$), however, the back-lobe is appreciable which may be attributable to the strong interactions between the loops and the wire grids. As the antenna height increases, the magnitude of the back lobe decreases, and almost becomes negligible at loop height 0.30λ , with a well-defined major lobe in the forward direction. But at height 0.4λ , the direction of the major lobe shifts from the desired direction ($\theta = 0^\circ$) to a new direction $\theta = 35^\circ$, with a slight increase of the field component in the backward direction. Beyond $h = 0.40\lambda$, the patterns become more distorted and typified by side lobes as well as forward and backward lobes. It is noteworthy that at $h = 1.00\lambda$, the antenna patterns have no distinct well-formed lobes. To a large extent, the difference between the patterns of circular loop and square loop seems insignificant.

The E_θ components on the H -plane ($\varphi = 90^\circ$) of the radiated electric fields of the loop antennas at different loop heights from the wire-grid ground plane are graphically illustrated in Figure 4. As observed for the E_φ components above, the back lobe of the E_θ pattern at height 0.05λ is considerable due to aforementioned reason. However, as the antenna height increases, good reduction in the backlobe size is noted till the height is 0.30λ . Above loop height 0.30λ , the back-lobes begin to build up significantly as the loop height increases, although the back lobes at $h = 0.80\lambda$ are smaller than those at $h = 1.00\lambda$. It should be stated that at loop height 1.00λ , the E_θ patterns of both loops have degenerated into several lobes. Again, the E_θ patterns of both loops are somewhat indifferent.

From the features of E_θ and E_φ patterns in Figures 3 and 4, it is logical to limit the antenna height to a value less than 0.30λ .

3.3. Directive Gain and Front-to-Back Ratio (F/B)

To further illuminate the radiation characteristics of the circular- and square-loop antennas above a wire-grid plane of finite extent, the directive gain and front-to-back (F/B) of the radiation intensity of both loops are evaluated at several loop heights, and illustrated in the graphs displayed in Figures 5 and 6, respectively. It can be seen from Figure 5 that the forward directive gain G_d is maximum for both loops at height 0.05λ , and gradually decreases as the loop height increases. Worthy of note is the dip between heights 0.48λ and 0.57λ for both loops, and subsequent increase in G_d at height above 0.57λ . The G_d profiles in general exhibit the “notch filter response” behaviour

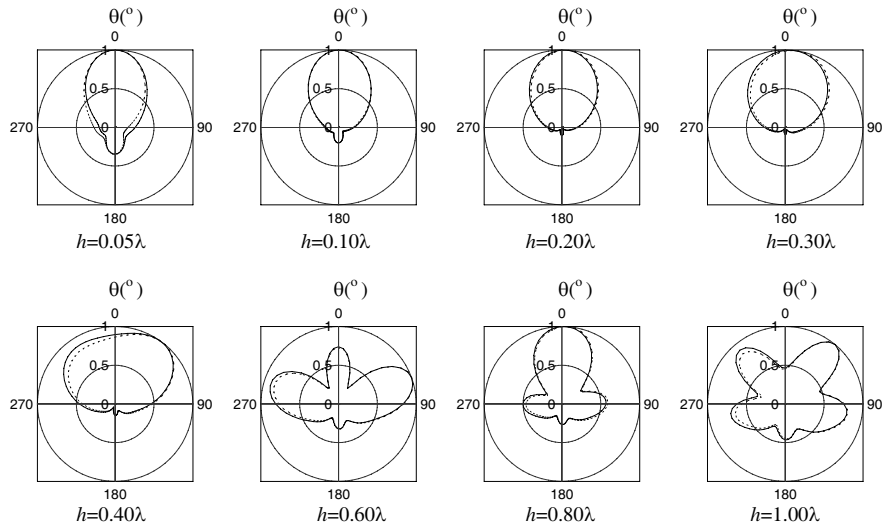


Figure 3: The E_φ components of the radiated fields on the E -plane ($\varphi = 0^\circ$) at various antenna heights: —: circular loop; - - -: square loop.

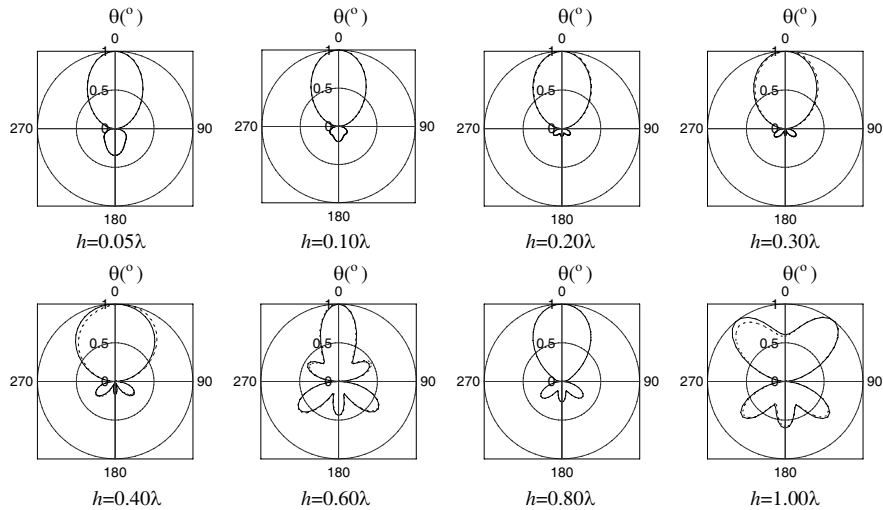


Figure 4: The E_θ components of the radiated fields on the H -plane ($\varphi = 90^\circ$) at different antenna heights: —: circular loop; - - -: square loop.

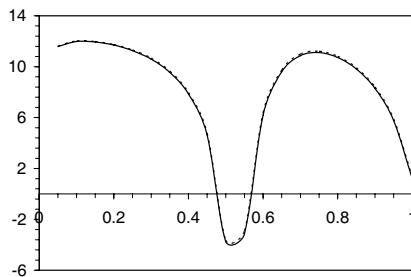


Figure 5: Forward directive gain G_d profiles of the circular- and square-loop antennas as a function of antenna height. —: circular loop; - - -: square loop.

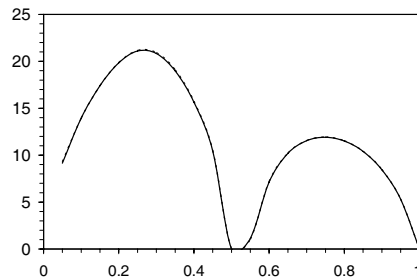


Figure 6: Variation of front-to-back ratio (F/B) of the radiation intensity of the circular- and square-loop antennas against the antenna height. —: circular loop; - - -: square .

which is consistent with the previous results of Hejase et al. [4] who employed the physical optics (PO) method to study similar problem.

The front-to-back ratio which gives a comparison between the radiation intensity in the forward

direction and backward direction, is shown in Figure 6 as a function of loop height. It is noted that the F/B is maximum at $h = 0.25\lambda$, which is in agreement with the E_θ and E_ϕ patterns. Lastly, the F/B profiles are the same for both loops, and they are in accordance with the G_d profiles.

4. CONCLUDING REMARKS

Using our previous formulation for loop antenna above ground plane of finite extent, modeled by wire grids, new results are obtained and reported here when the circular- and square-loop antennas have equal cross-sectional area, unlike in the prior presentation when the loops have equal perimeter of one wavelength. It is found that the loops have nearly identical input resistance profiles, whereas the input reactance values of the square loop are lower than those for the circular loop in the range of loop height specified. The radiation field patterns in the E - and H -planes suggest that the loop heights should be less than 0.3λ for well-defined major lobes in the forward direction, and negligible back-lobe. Finally, it is observed that the forward directive gain profile is identical to the “notch filter response” behavior.

REFERENCES

1. Ayorinde, A. A., S. A. Adekola, and A. I. Mowete, “Performance characteristics of loop antennas above a ground plane of finite extent,” *PIERS Proceedings*, 769–744, Taipei, March 25–28, 2013.
2. Rajarayamont, B. and T. Sekiguchi, “One-element loop antenna with finite reflector,” *Elect. & Comm. in Japan*, Vol. 59B, No. 5, 68–75, 1976.
3. Iwashige, J., “Analysis of loop antenna with circular reflector and its properties,” *Elect. & Comm. in Japan*, Vol. 63B, No. 11, 44–50, 1982.
4. Hejase, H., S. D. Gedney, and K. W. Whites, “Effect of a finite ground plane on radiated emissions from a circular loop antenna,” *IEEE Trans. Electromagnetic Comp.*, Vol. 36, No. 4, 364–371, 1994.
5. Shoamanesh, A. and L. Shafai, “Characteristics of circular loop antennas above a lossless ground plane,” *IEEE Trans. Ant. & Prop.*, Vol. 29, No. 3, 528–529, 1981.
6. Smith, G. S., “Loop antennas,” *Antenna Engineering Handbook*, Richard C. Johnson, Ed., 3rd Edition, Chapter 5, McGraw-Hill, 1984.
7. Harrington, R. F., “Matrix methods for field problems,” *Proc. IEEE*, Vol. 55, 136–149, 1967.

Electrical-optical Converter Using Electric-field-coupled Metamaterial Antennas on Electro-optic Modulator

Y. N. Wijayanto^{1,2}, A. Kanno¹, S. Nakajima¹, P. Daud²,
D. Mahmudin², and T. Kawanishi^{1,3}

¹National Institute of Information and Communication Technology (NICT), Japan

²Indonesian Institute of Sciences (LIPI), Indonesia

³Waseda University, Japan

Abstract— We propose an electrical-optical converter using electric-field-coupled metamaterial antennas on an electro-optic (EO) modulator for wireless millimeter-wave/terra-hertz applications. By wireless signal irradiation to the proposed device, strong millimeter-wave/terra-hertz electric field can be induced on the electric-field-coupled metamaterial antennas. The induced electric field can be used for optical modulation through EO effects when a lightwave propagates into an optical waveguide located under regions of the induced millimeter-wave/terra-hertz electric field. Analysis in millimeter-wave and optical modulation of the proposed device are discussed in detail for operational frequency of 100 GHz. Device experiment in fabrication and preliminary measurement are also reported.

1. INTRODUCTION

Radio-over-fiber (ROF) technology is promising for applications to broadband mobile communication, high-resolution imaging, low-induction electromagnetic compatibility measurement, and so on [1, 2]. By using the technology, microwave with high operational frequency for carrying large data size can be transferred through optical fibers with lightwave as a carrier. The required device in the ROF technology is a converter between electrical and optical signal signals. Electrical to optical converters for wireless radio-wave applications using microstrip antennas were proposed [3–6]. The microstrip antennas were fabricated on an electro-optic (EO) crystal such as LiTaO₃ or LiNbO₃. However, the antenna size has limitation due to very small size in operation to high frequency.

In order to improve the performance for high operational frequency in millimeter-wave or terra-hertz bands, an electrical-optical converters using metamaterial structure can be adopted. The device has small electrical size with compact structure. Interaction between capacitance and inductance of the metamaterial structure is considered to generate strong millimeter-wave/terra-hertz electric fields on the optical crystal for EO modulation. An EO modulator using metamaterial split ring resonator (SRR) for electrical-optical conversion was realized [7].

In this paper, we propose an electrical-optical converter using electric-field-coupled metamaterial antennas on an EO modulator for millimeter-wave/terra-hertz bands. The proposed device is composed of a straight optical waveguide and electric-field-coupled resonators on an EO crystal. Basically, the resonators consist of planar inductance and capacitance for generating strong millimeter-wave/terra-hertz electric field. EO modulation using the induced electric field can be obtained. Meandering-gaps are also adopted to compensate for EO modulation degradation due to transit time effects. Based on that, electrical-optical converter from wireless millimeter-wave/terra-hertz can be obtained. Additionally, the proposed device is easy in design and fabrication with planar structure. The device structure, analysis, and preliminary experiment results for 100 GHz operation frequency are discussed and reported.

2. DEVICE STRUCTURE

Figure 1 shows the basic structure of the proposed electrical-optical converter. Electric-field-coupled metamaterial antennas are fabricated on an EO crystal. A straight optical waveguide is fabricated on the EO crystal and located under the center gap of the electric-field-coupled metamaterial antennas as shown in Figure 1(b) for effective operation to electrical-optical conversion. The proposed device is composed in an array with large number single unit cell of the metamaterial antennas. It has small size as shown in Figure 1(a) with parts of capacitors and inductors. Polarization-reversed structures are required periodically to compensate for degradation of optical modulation due to transit-time effects. They can be realized by adopting meandering gap of the metamaterial antennas as shown typically in Figures 1(b) and (c). Additionally, a buffer layer is inserted between

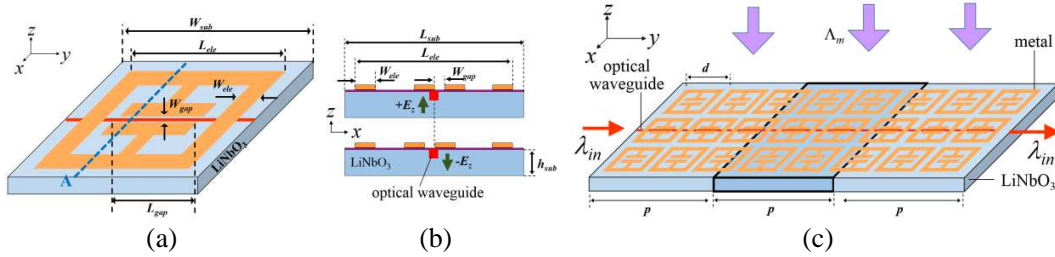


Figure 1: Structure of the proposed device: (a) a unit cell, (b) cross-sectional, and (c) whole views.

the EO crystal surface and the metal layer of the metamaterial antenna to minimize lightwave propagation loss.

When a wireless millimeter-wave signal is irradiated to the proposed device, millimeter-wave currents are induced on the electric-field-coupled metamaterial resonator. Millimeter-wave interaction of inductive and capacitive occurs on the proposed device. As a result, strong electric fields of the millimeter-wave are induced between them. The strong millimeter-wave electric field can be used for changing refractive index of an EO crystal due to the Pockel effects. Therefore, when lightwave propagates to an optical waveguide located close to region of the strong millimeter-wave electric field, optical phase modulation can be obtained. Based on the phenomena, the proposed device can be used for electrical to optical conversion by wireless millimeter-wave irradiation.

3. DEVICE ANALYSIS

The millimeter-wave resonator can be described qualitatively in terms of its equivalent circuit with a capacitor and two inductors [8]. The capacitor is connected in parallel to two loops, which provide inductance to the circuit and couples to the electric field. The electric-field-coupled circuit resonances due to electric field between capacitor and inductors.

The proposed device was analyzed in detail using electromagnetic analysis software. Table 1 shows the device parameters for millimeter-wave analysis. A single unit cell of the metamaterial resonator was calculated using periodic boundary condition.

The calculated millimeter-wave characteristics of the reflection (S_{11}) and transmission (S_{12}) for several variations of the parameters are shown in Figure 2. We can see that, operational frequency of the proposed device can be tuned by changing several variations of the designed parameters such as its substrate length in a unit cell, electrode length, and electrode width. The parameter changes contribute for values of capacitances and inductance in the metamaterial structure. The capacitance and inductance values are the main parameter for tuning the resonant frequency operation of the proposed device. Strong millimeter-wave electric field is induced across the gap as the capacitive circuit, it can be used for EO modulation. The designed metamaterial antennas were optimized for 100 GHz frequency operation.

Since the proposed device is an optical phase modulator, modulation efficiency can be used as a measure of the conversion efficiency of electrical-optical signals. The transit-time effect during

Table 1: Design parameters of the proposed device.

Parameter	Value
Operational frequency	~ 100 GHz
Substrate with z -cut LiNbO ₃ crystal	
• Thickness (h_{sub})	250 μm
Metal with gold material	
• Thickness	1.5 μm
Unit cell	
• Total size (L_{sub})	~ 250 μm
• Length of the metal (L_{ele})	~ 190 μm
• Width of the metal (W_{ele})	~ 30 μm
• Width of the center gap (W_{gap})	10 μm

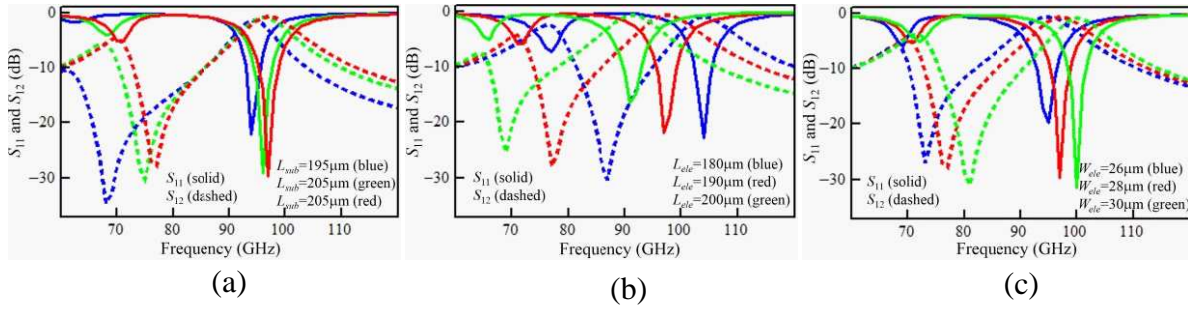


Figure 2: Calculated S₁₁ and S₁₂ characteristics of the proposed devices for variations of: (a) unit cell size (L_{sub}), (b) metal length (L_{ele}), and (c) metal width (W_{ele}).

interaction of the millimeter-wave and lightwave electric fields ($v_g t = y - y'$) is considered for the optical modulation [9]. The modulation efficiency of the proposed device corresponds to the sum of the integration of the millimeter-wave electric field observed by the lightwave. Optical modulation degradation due to the transit-time can be compensated for by polarization-inversed structure. The millimeter-wave and lightwave electric field interaction is periodically changed along the optical waveguide where the distance of the polarization-inversed structure as shown in Figure 1(c) can be expressed as,

$$p = \frac{2\pi}{k_m n_g} \quad (1)$$

where k_m is the wave number of the millimeter-wave in vacuum and n_g is the group index of the lightwave. In this propose device, polarization-inversed structure using simple meandering gap by controlling the position between the optical waveguide and gap edge as shown in Figure 1(b) is used to compensate for the optical modulation degradation.

4. DEVICE EXPERIMENT

The designed device was fabricated experimentally on a z -cut LiNbO₃ crystal a thickness of 250 μm . An optical waveguide for single mode operation in 1550 nm was fabricated on the crystal using titanium diffusion method. The titanium film was diffused with 11000°C for 10 hours. After that, silicon dioxide film layer with thickness of about 0.2 μm was deposited on the crystal. Planar metal electric-field-coupled metamaterial resonators were also fabricated on the crystal. The metal with a 1.5 μm -thick gold film were fabricated on the crystal using a thermal vapor deposition, standard photo-lithography, and lift-off technique. The optical waveguide was aligned precisely under one side of the gap edge for effective modulation since the z -cut LiNbO₃ crystal is used. A photograph of the fabricated device is shown in Figure 3. Additionally, the fabricated device was polished and cut using dicing machine at the end of the optical waveguide for lightwave coupling. Then, the fabricated device was coupled with optical fibers at the both sides of the optical waveguide ends as shown in Figure 3(c).

The optical waveguides in the fabricated device were coupled with optical fibers with measured insertion loss of about -8 dB. Basic operations of the fabricated device were also experimentally

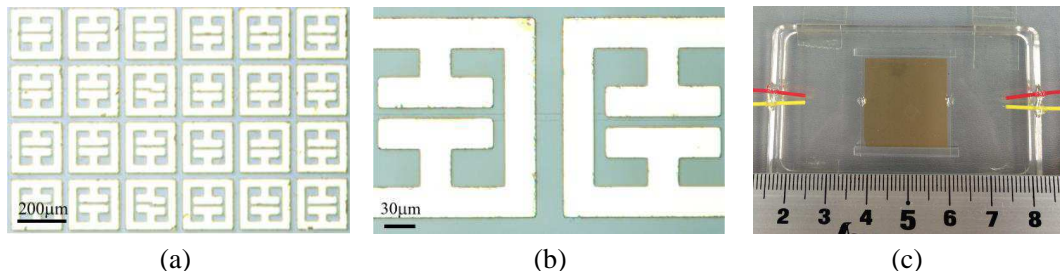


Figure 3: Photograph of the fabricated device, (a) metal resonator by microscope, (b) zoom-view for polarization-inversed structure, and (c) whole device view coupled with optical fibers ready for measurement.

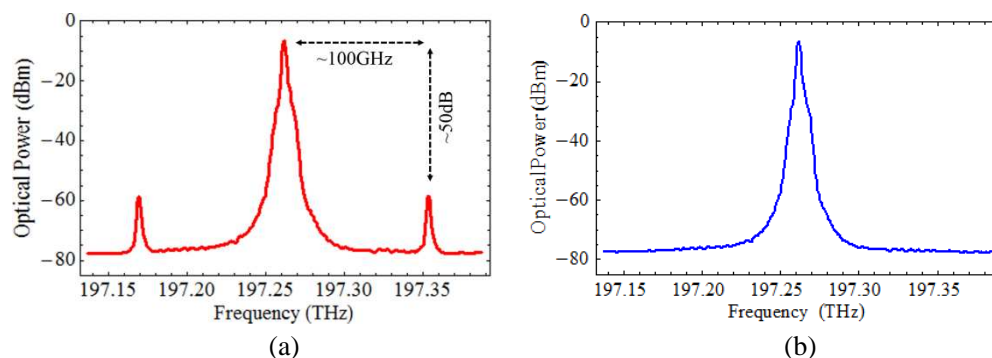


Figure 4: The measured optical spectra of the fabricate device by (a) irradiation and (b) no irradiation of millimeter-wave signals.

measured using simple measurement setup. 1.55 μm -wavelength light from laser was propagated and coupled to a light polarization controller, then connected to the fabricated device. 100 GHz-band millimeter-wave from generator was amplified and irradiated to the fabricated device. The output lightwave were measured using an optical spectrum analyzer. Typical of the measured output light spectra are shown in Figure 4 with and without millimeter-wave irradiation. We can see that clear optical sidebands can be obtained using the fabricated device by 100 GHz millimeter-wave irradiation. The power ratio between optical carrier and sidebands of about 50 dB were obtained using the fabricated device.

5. CONCLUSION

The electrical-optical converter using electric-field-coupled metamaterial antennas on an EO modulator was proposed for millimeter-wave/terra-hertz bands. The proposed device was analyzed and optimized for 100 GHz millimeter-wave bands. The optimized device was fabricated successfully. The fabricated device was measured also for its basic operation for electrical-optical conversion. Clear optical sidebands were obtained by irradiating 100 GHz millimeter-wave. Therefore, the basic operations of the proposed device for electrical-optical conversion were demonstrated successfully. The proposed device has a compact and simple structure, passive operation, and low millimeter-wave loss. Now, we are still attempting to measure the detail characteristics of the proposed device and investigate in further for promising applications.

ACKNOWLEDGMENT

Authors would like thanks to Prof. H. Murata from Osaka University Japan for his constructive comments and valuable advices during discussion and to Mr. A. A. Fathnan from Indonesian Institute of Sciences (LIPI) for his kind supports in calculation and analysis.

This research activity was conducted as part of the research project “R&D of High-Precision Imaging Technology Using 90 GHz Band Linear Cells,” funded by the Ministry of Internal Affairs and Communications, Japan.

REFERENCES

1. Chen, A. and E. Murphy, *Broadband Optical Modulators: Science, Technology, and Applications*, Taylor and Francis Group, CRC Press, North West, 2012.
2. Kanno, A., P. T. Dat, I. Hosako, T. Kawanishi, and H. Ogawa, “Radio-on-terahertz over fiber system for future mobile fronthauling,” *2014 IEEE Global Communications Conference (GLOBECOM)*, 2218–2222, 2014.
3. Murata, H., N. Kohmu, Y. N. Wijayanto, and Y. Okamura, “Integration of patch antenna on optical modulators,” *IEEE Photonics Society News*, Vol. 28, No. 2, E/O, Apr. 2014.
4. Wijayanto, Y. N., H. Murata, and Y. Okamura, “Electro-optic wireless millimeter-wave-light-wave signal converters using planar Yagi-Uda array antennas coupled to resonant electrodes,” *17-th Opto-Electronic Communications Conference*, 5E1-2, Busan, Korea, Jul. 2–6, 2012.
5. Wijayanto, Y. N., H. Murata, and Y. Okamura, “Wireless microwave-optical signal conversion in quasi-phase-matching electro-optic modulators using gap-embedded patch-antennas,” *IEICE Transactions on Electronics*, Vol. E96-C, No. 2, 212–219, 2013.

6. Wijayanto, Y. N., H. Murata, and Y. Okamura, “Electro-optic millimeter-wave-lightwave signal converters suspended to gap-embedded patch antennas on low- k dielectric materials,” *IEEE Journal of Selected Topics in Quantum Electronics*, Vol. 19, No. 6, Nov./Dec. 2013.
7. Murata, H., J. Nishioka, and Y. Okamura, “100 GHz-band electro-optic modulator using two-dimensional coupled-split-ring resonator array,” *19th Optoelectronics and Communications Conference (OECC) and the 39th Australian Conference on Optical Fibre Technology (ACOFT)*, 167–169, Engineers Australia, Barton, ACT, 2014.
8. Schurig, D., J. J. Mock, and D. R. Smith, “Electric-field coupled resonators for negative permittivity metamaterials,” *Appl. Phys. Lett.*, Vol. 88, Article No. 041109, 2006.
9. Yariv, A., *Quantum Electronics*, 3rd Edition, Wiley, New York, 1989.

Study of Change in Enzymatic Reaction under Radiowaves/Microwaves on Lactic Acid Dehydrogenase and Catalase at 2.1, 2.3 and 2.6 GHz

Sohni Jain¹, Vuk Vojisavljevic¹, and Elena Pirogova^{1,2}

¹School of Electrical and Computer Engineering, RMIT University, Melbourne, Australia

²Health Innovation Research Institute, RMIT University, Victoria, Australia

Abstract— There is an increasing need to study and evaluate the impact of weak radiofrequency (RF) radiation at the cellular and molecular levels because of the worldwide increase in use of wireless telecommunication devices, mainly mobile phones, which has resulted in increased human exposure to RF fields. This study aims to improve our understanding of impact of low power RF/MW radiation (4G mobile network frequencies) on enzymatic reactions. The selected enzymes play crucial roles in the biological processes. L-Lactic dehydrogenase (LDH) is extensively present in blood cells and heart muscles, and is a marker of common injuries and disease. Catalase enzyme can be found in all living organisms, it is important for protecting a cell from oxidative damage by reactive oxygen species (ROS). This *in vitro* study evaluates the effects of low power RF/MW on kinetics of LDH and Catalase enzymes irradiated at the frequencies of 2.1, 2.3, and 2.6 GHz and two powers of 17 and -10 dBm using the commercial Transverse Electro-Magnetic (TEM) cell. Furthermore, changes in biological activity of Catalase enzyme irradiated at the particular frequency and different powers were also evaluated. The comparative analysis of experimental findings reveal that MW exposures at the particular studied parameters can induce changes in the enzymes' kinetics, which in turn lead to modulation of rate of change in corresponding reactions these enzymes catalyse.

1. INTRODUCTION

In modern life, global population is continuously exposed to electromagnetic radiation emitted by mobile phones, computers, radars, smart meters and medical technology equipment etc.. In the last 10 years, use of mobile phone worldwide has increased by almost 200% resulting in 4.65 billion users in 2014. This rate is further increasing at approximately 5% annually [1]. Because mobile phone use is so widespread, public concerns about the possible health effects of RF exposures receive a lot of coverage in the media. Recent reports confirm that even weak RF/MW radiation can induce modulating effects on various biological systems [2, 4]. Intensive international research has found no conclusive or convincing evidence that mobile phones are damaging to health in the short or long term. However, in May 2011, IARC, which is a specialised agency of the World Health Organization, classified radiofrequency electromagnetic fields emitted from mobile phones, wireless devices, radio, television and radar as Group 2B or possibly carcinogenic to humans, based on an increased risk for glioma, a type of brain cancer [3]. Many national and international agencies have established safety guidelines for exposure to RF fields [4, 5]; however, concerns remain about the potential adverse health outcomes because of increasing RF field exposures, so the significance of investigating non-thermal effects at the molecular level cannot be underestimated. Radiation can affect the body in many ways, and the health effects may not become apparent for many years. These effects range from mild symptoms, such as skin reddening, to serious effects such as cancer and death. *In vitro* research shows that membrane structure and functionality can be altered upon exposures to RF fields [8]. *In vitro* studies also revealed that RF/ MW at the particular frequency and power induce changes in the enzyme's kinetics [9–13]. In addition, there are also other studies which have reported that the modulating effects of MW can also cause destruction at DNA level which resulted in the inhibition of cell proliferation [14, 15].

2. MATERIAL AND METHODS

2.1. Experimental Set-up

The commercial Transverse Electro-Magnetic (TEM) cell (No. TC-5062A UHF-TEM Cell) was used in this study to irradiate the selected example systems. TEM cell is an enclosed box made of a conductor material, with its dimensions varied depending on the operating frequency used. One end of the box is connected to signal generator from which external signal was applied to generate

Findings of latest research studies on the effects of low power MW radiation			
Study	Exposure	Frequency	Effect
J. Tang, et al., 2015 [16]	0.016 W/Kg	900 MHz	Impaired spatial memory and damages BBB permeability in rats
A. H. Eris, et al., 2015 [17]	608 mW/m ²	900 MHz	Retarder learning and deficit in special memory in rats.
H. J. Li, et al., 2015 [18]	5, 10, 20 mW/cm ²	2.856 GHz	Long-term, chronic MW exposure could induce dose dependent deficit of spatial learning and memory in rats
F. Aydogan, Unlu, 2015 [19]	0.4 W/Kg	2.1 GHz	Exposure to 2100 MHz RF radiation causes salivary gland damage to some extent and especially with longer exposure duration.

a predictable field inside the TEM Cell. The absorption coefficients of the analysed samples were measured using an Ocean Optics USB2000 spectrometer.

2.2. Model Proteins

In order to study the influence of RF/MW radiation on proteins *in vitro*, LDH [EC1.1.1.27] and Catalase [EC 1.11.1.6] were selected as model systems. LDH enzyme plays a central role in metabolic pathways of almost every cell. LDH catalyses the reversible reduction of Pyruvate to L-lactate using NADH as a co-enzyme. LDH activity is calculated from the rate of change in NADH absorbance at 340 nm. Catalase is responsible for decomposition of H₂O₂ to water and O₂. Catalase activity is calculated by measuring the total amount of H₂O₂ decomposed to form O₂. The reaction catalysed by Catalase enzyme is comparatively different from other enzymes as the rate of decomposition of H₂O₂ is proportional to the amount of Catalase present, whereas unlike other enzymatic reaction Catalase undergoes spontaneous decomposition during the reaction process.

2.3. Measurement Procedure for LDH

Tris HCl, 0.2 M, pH 7.3, 2.8 ml + 6.6 mM NADH, 0.1 ml + 30 mM Sodium Pyruvate were mixed and a final aliquot was prepared for each of the three test and three control sample. Amount of 0.1 ml of LDH solution was added to the cuvette and the absorption of the solution at 340 nm was recorded, and immediately after that the cuvettes were transferred to TEM cell for irradiation. After irradiation the cuvettes were removed from TEM cell and the absorbance was measured again at 340 nm. This procedure was repeated for both irradiated and control samples after every 5 minutes. The spectrophotometer was set to record the absorbance at every 2 s. The temperature was maintained at 25°C (Temperature Controller, Quantum Northwest, Inc.).

2.4. Measurement Procedure for Catalase Reagents

The Phosphate Buffer (50 mM Potassium Phosphate Buffer, pH 7.0 at 25°C) was prepared in a ultrapure ionized water using potassium phosphate, dibasic, trihydrate (Catalog Number P5504).

Hydrogen Peroxide Solution [0.036% (w/w)] was prepared in Phosphate Buffer using hydrogen peroxide (30% (w/w), Catalog Number H1009).

An initial Catalase solution of 10 mg/ml was prepared and immediately before use it was diluted to 100 units/ml in cold Phosphate Buffer. 1.45 ml of Hydrogen Peroxide Solution was pipetted into the test cuvettes, and 500 µl of previously prepared Catalase Solution were added in the cuvette. The activity of Catalase was measured with help of spectrophotometer and the absorbance values were recorded at 240 nm (A₂₄₀). Immediately after recording of absorption the cuvettes were placed inside the TEM cell for irradiation. Same procedure was repeated after 2 min, 7 minutes and 9 minutes and readings were recorded. During the experiment the temperature was maintained at 25°C.

In order to relate the rate of reaction, dissociation constant of hydrogen peroxide K was calculated using the following formula:

$$K = \frac{1}{t} \log \left(\frac{A}{A - x} \right)$$

where t is the time interval of second reading, 'A' is the amount H₂O₂ absorbed at the end of reaction and 'x' is the H₂O₂ absorbed at the time of second reading.

Both LDH and Catalase enzyme solutions were exposed at the selected frequencies of 2.1 GHz, 2.3 GHz and 2.6 GHz at two different powers of 17 dBm and -10 dBm.

3. RESULTS AND DISCUSSION

The experimental evaluation of catalytic activities in selected enzymes (Catalase and LDH) exposed to MW of different power and frequency range was conducted and the changes in rate of absorption (rate of reaction) of irradiated samples were compared with non-irradiated samples in order to understand the modulating effects of MW at different combination of frequency and power. The test samples were exposed to MW at 2.1 GHz, 2.3 GHz and 2.6 GHz at powers of -10 dBm and 17 dBm. In the second experiment, the test samples of Catalase were exposed at the frequency 2.6 GHz and different powers to understand the effect of changing power (power-dependence) at the particular frequency.

The results are presented in Figures 1, 2 and 3 respectively. Figure 1 clearly shows a consistent modulating effect of irradiation on dissociation constant K of H_2O_2 : a 20% increase at 2.1 GHz exposure, and a 25% decrease at 2.6 GHz exposure versus non-irradiated sample at 17 dBm. At the power of -10 dBm relative change in K value is inconsistent. As can be seen from Figure 1, at 2.1 and 2.3 GHz it increases by 70% as compared to non-irradiated sample but at 2.6 GHz it is

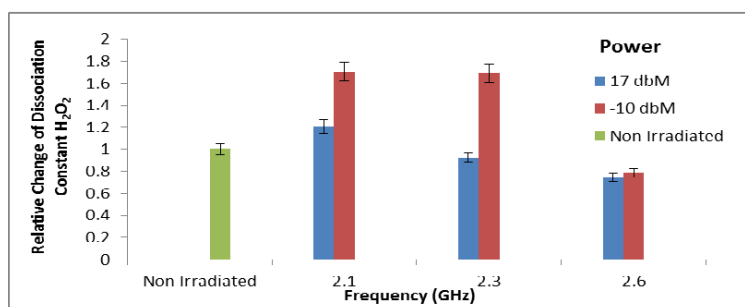


Figure 1: Relative change of Dissociation constant of H_2O_2 for irradiated vs. non-irradiated Catalase at the different frequencies.

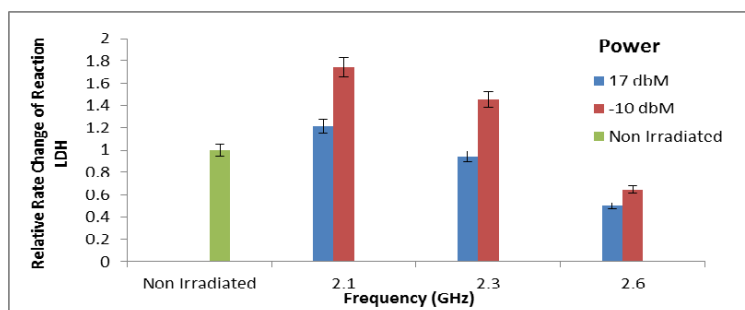


Figure 2: Relative change in rate of reaction of NADH for irradiated vs. non-irradiated LDH at the different frequencies.

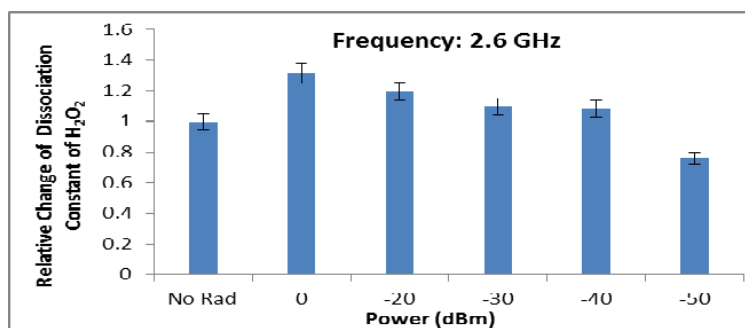


Figure 3: Relative change of Dissociation constant of H_2O_2 for irradiated vs. non-irradiated Catalase at 2.6 GHz and different powers.

reduced by 22%. However, 2.1 GHz exposures for both power levels induce maximum increase on dissociation constant K . At 2.6 GHz a decrease in activity for almost 25% is observed.

Figure 2 shows modulating effects of irradiation on LDH enzyme. Consistent decrease in rate of reaction at 17 dBm: a 21% increase at 2.1 GHz and almost 50% decrease at 2.6 GHz in comparison with non-irradiated sample were observed. Further at the power of -10 dBm under similar experimental conditions a steep change in rate of reaction was observed. At -10 dBm and 2.1 GHz reaction rate was increased by 75% and decreased by 35% at 2.6 GHz when compared to non-irradiated sample. Important to note, in both the enzymes the relative changes induced by exposures at -10 dBm and 2.3 GHz are not significant.

Finally, the effect of power on the activity of Catalase enzyme was investigated at the frequency of 2.6 GHz (Figure 3). The reason for studying the effects induced by exposures at 2.6 GHz is that this frequency is used as a carrier frequency by many telecommunication systems. To calculate the dissociation constant K , the same methodology was used as described above.

An interesting pattern is observed in relative change of dissociation constant, K , of H_2O_2 for irradiated versus non-irradiated samples. At 2.6 GHz and 0 dBm power, K value of the exposed sample was 32% higher than of non-irradiated sample. For -20 dBm the increase of almost 20% is recorded. For 30 dBm, an increase of 9% in K value is observed. Less significant increase is observed for -40 dBm. However, for -50 dBm, K was decreased by 25% compared to non-irradiated sample.

These findings confirmed our hypothesis that enzymatic activities can be changed by external exposures at low power MW irradiation, with the observed effects being power and frequency-dependant.

4. CONCLUSIONS

This study was aimed to test the hypothesis that the external low power MW radiation can affect catalytic activity of LDH and Catalase enzymes. Further to the analysis we also tested the relation and effect of frequency and power of applied irradiation on the enzyme reaction. The results obtained show that the MW radiation at selected frequencies and powers can produce modulating effects on the catalytic activity of selected enzymes by either increasing or decreasing the reaction rates.

Our second phase of experiment suggest that both frequency and power contribute separately for the modulating effects in the studied Catalase enzyme. The experimental findings highlight that even low power MW can induce modulating effects at the fixed frequency. However it requires further detailed investigation on a wide range of combinations of frequency and power to establish safe limits of MW exposures. Our findings reveal the significant relationship between the low power microwave exposures and catalytic activities in Catalase and LDH enzymes.

REFERENCES

1. Australian Communications and Media Authority (ACMA), Communications Report 2012–13, 2012.
2. World Health Organization (WHO), “Electromagnetic fields and public health: Mobile telephones and their base stations,” Jun. 2011, Available from: <http://www.who.int/mediacentre/factsheets/fs193/en>.
3. Volkow, N. D., D. Tomasi, G. J. Wang, et al., “Effects of cell phone radiofrequency signal exposure on brain glucose metabolism,” *JAMA*, Vol. 305, No. 8, 808–813, 2011.
4. ARPANSA Australian Radiation Protection and Nuclear Safety Agency “Maximum exposure levels to radiofrequency fields — 3 kHz to 300 GHz, Annex 3: Epidemiological studies of exposure to radiofrequencies and human health,” Sydney, 2008.
5. “ICNIRP guidelines for limiting exposure to time varying electric, magnetic and electromagnetic fields (up to 300 GHz), energy on human cardiovascular, reproductive, immune, and other systems: A review of the recent literature,” *Int. Journal of Hygiene and Environmental Health*, Vol. 211, Nos. 1–2, 1–29, 2003.
6. Istiaque, A., I. Taghrid, I. Cosic, and E. Pirogova, “Evaluation of the effects of extremely low frequency (ELF) pulsed electromagnetic fields (PEMF) on the bacterium *Staphylococcus aureus*,” *EPJ Nonlinear Biomedical Physics*, Vol. 1, No. 5, 1–17, 2013, Doi: 10.1140/epjnbp12.
7. Pirogova, E., I. Cosic, V. Vojisaljevic, and Q. Fang, “Use of infrared and visible light radiation as modulator of protein activity,” *Estonian Journal of Engineering*, Vol. 14, No. 2, 107–123, 2008.

8. Vojisavljevic, V., E. Pirogova, and I. Cosic, "The effect of electromagnetic radiation (550–850 nm) on L-Lactate dehydrogenase kinetics," *Intl. J. Radiation Biology*, Vol. 83, No. 4, 221–230, 2007.
9. Alshuhaim, H., V. Vojisavljevic, and E. Pirogova, "The effects of low power microwaves at 500 MHz and 900 MHz on yeast cells growth," *PIERS Proceedings*, 667–670, Taipei, Mar. 25–28, 2013.
10. Hamad, S. A., V. Vojisavljevic, and E. Pirogova, "Effects of low power microwaves at 1.8, 2.1, and 2.3 GHz on L-Lactic dehydrogenase and Glutathione peroxidase enzymes," *Journal of Electromagnetic Waves and Applications*, Vol. 28, No. 14, 1726–1735, 2014.
11. Phillips, J. L., O. Ivaschuk, T. Ishida-Jones, R. A. Jones, M. Campbell-Beachler, and W. Haggren, "DNA damage in Molt-4 T-lymphoblastoid cells exposed to cellular radiofrequency field in vitro," *Bioelectrochem. Bioenerg.*, Vol. 45, 103–110, 1998.
12. Diem, E., C. Schwarz, F. Adlkofer, O. Jahn, and H. RÄudiger, "Non-thermal DNA breakage by mobile-phone radiation (1800 MHz) in human-broblasts and in transformed GFSH-R17 ratgranulosa cells in vitro," *Mutat. Res.*, Vol. 583, 178–183, 2005.
13. Tang, J., Y. Zhang, L. Yang, Q. Chen, L. Tan, S. Zuo, H. F. Chen, and G. Zhu, "Exposure to 900 MHz electromagnetic fields activates the MKP-1/ERK pathway and causes blood-brain barrier damage and cognitive impairment in rats," *Brain Res.*, 2015, in Press.
14. Eris, A. H., H. S. Kiziltan, I. Meral, H. Genc, M. Trabzon, H. Seyithanoglu, B. Yagci, and O. Uysal, "Effect of short-term 900 MHz low level electromagnetic radiation exposure on blood serotonin and glutamate levels," *Bratisl. Lek. Listy.*, Vol. 116, No. 2, 101–103, 2015.
15. Li, H. J., R. Y. Peng, C. Z. Wang, S. M. Qiao, Z. Yong, Y. B. Gao, X. P. Xu, S. X. Wang, J. Dong, H. Y. Zuo, Z. Li, H. M. Zhou, L. F. Wang, and X. J. Hu, "Alterations of cognitive function and 5-HT system in rats after long term microwave exposure," *Physiol. Behav.*, Vol. 140, 236–246, 2015.
16. Aydogan, F., I. Unlu, E. Aydin, N. Yumusak, E. Devrim, E. E. Samim, E. Ozgur, V. Unsal, A. Tomruk, G. G. Ozturk, and N. Seyhan, "The effect of 2100 MHz radiofrequency radiation of a 3G mobile phone on the parotid gland of rats," *Am. J. Otolaryngol.*, Vol. 36, No. 1, 39–46, 2015.

Principles and Methods of EMF Safety Maintenance by Individual Protective Means

I. V. Bukhtiyarov, N. B. Rubtsova, S. Yu. Perov, O. V. Belaya, and T. A. Kravtsova
FSBSI “Research Institute of Occupational Health”, Moscow, Russian Federation

Abstract— According the electromagnetic safety principles one of way of this solution is protective mean use. There are 2 main kinds of protective means: collective and individual. Collective protective means in dependence of EMF frequency range decrease EMF value by means of EMF reflection or absorption. Individual protective means (protective suits) use as a rule in cases of static electric field, power frequency (50/60 Hz) electric field and radiofrequency (RF) EMF occupational exposure. The methods of these protective suits testing are developed in different countries. Great difficulties are connected with correct evaluation of RF EMF individual protective means protective characteristics. There is presented the method of RF EMF protective suit (PS) safety properties evaluation. Safety properties of modern PS are based on EMF reflection, which ensures shielding effect. PS is made of electro-conductive materials; all elements are connected to produce a “cover” around a human body, which allows reducing the EMF values to permissible levels. The testing of protective suit is carried out by special setup use. EMF is emitted by means of RF generator connected with antenna through amplifier. Special setup includes human body phantom (head, trunk and extremities) and measuring probe connected to personal computer by optic fiber. Phantom is placed in spatially homogeneous EMF for all body parts. EMF measurement is carried out in three control points (head, breast and groin) at fixed distances from RF EMF source in two phantom positions: in front and back to the RF EMF source (with and without PS). The results obtained by suggested approach allow determining PS protection level (in dB), and develop recommendations for construction upgrade. Furthermore, the obtained data of shielding effectiveness suggest that there is the relationship between protective properties and RF EMF values. Proposed method of PS shielding effectiveness evaluation can help analyze that relationship in future studies.

1. INTRODUCTION

High level electromagnetic field (EMF) human health protection is one of the major electromagnetic safety problems, occupational exposure especially. It is necessary in case of work near EMF sources like power transmission systems, cellular, satellite antennas, radars, radio and television transmitters and others. According the electromagnetic hygienic principles the worker protection is based on exposure time limits, safe distance from the EMF source and protective mean use. There are 2 main directions of protective means: collective and individual. Collective protective means in dependence of EMF frequency range decrease EMF value by means of EMF reflection or absorption.

There are some standards establishing the requirements to protective means in the Russian Federation. One of them establishes the requirements to static electric field protective means (GOST 12.4.123-83 Occupational safety standards system. “Means of static electricity protection. General technical requirements.”).

Two State standards provide the requirements for collective and individual protective means from power frequency (50 Hz) electric fields only.

50 Hz electric field protective means must meet the requirements:

- Stationary shielding devices — to requirements of GOST 12.4.154-85. Occupational safety standards system. “Screening devices for protection from power frequency fields. General technical requirements, basic parameters and dimensions”;
- Screening (conductive) suits — to requirements of GOST 12.4.172-87 Occupational safety standards system. “Individual screen set for protection from power frequency fields. General technical requirements and methods of control”.

In practice individual protective means (protective suits) are effective and convenient personal EMF protection in cases of maintenance and repair work on functioning equipment. It can be used when the others protection ways are impossible.

Protective suits (PS) are special protective clothing and used as a rule in cases of static electric field, power frequency (50/60 Hz) electric field (EF) and radiofrequency (RF) EMF occupational exposure.

Individual protective means from static electricity include: anti-electrostatic clothing, anti-electrostatic shoes, and safety devices anti-electrostatic (rings and bracelets), and hand protection means.

There are some special requirements for individual protective means. The typical PS consists from different constructive elements made of electrically conductive materials: coveralls (or jacket and pants), helmet with face shield, gloves and feet protective means (socks, boots and (or) shoes). All elements are electrically connected to produce a "cover" around a human body, which allows the EMF values decrease to permissible levels.

The modern shielding complete set for protection from power frequency electric fields represents the hi-tech product creating closed electrical spending space around of human body (individual "Faraday cage"), excepting penetration of electric field even very high intensity inside of screening spaces. Possessing high conductivity, complete sets shunt human body, excepting course through body displacement and pulse currents.

Conductive (screening) suits for bare-hand (hot-line) work besides protect user breath from dangerous air-ions formed as a result of air ionization under high voltage exposure. Shielding complete sets of the best world manufacturers combine high protective characteristics with demanded sanitary-and-hygienic parameters. Such complete sets are developed in Germany, USA, Japan, etc. Complete sets are widely applied today all over the world at repair and service of extremely high voltage (EHV) installations, in particular at carrying out of various kinds of works on energized transmission lines. In Russia application of individual shielding complete sets is obligatory at repair and service of the equipment in EHV installations zone of influence. Check of screening suit shielding properties is carried out by means of phantom of human body is developed. Phantoms were applied to determination of capacitive currents in human body, EF levels on human body surface on ground potential; values of capacitive and air-ion currents, EF intensity on body surface under hot-line works maintenance. Now phantoms are used for qualifying tests of screening suits in setup of FSBSI "Research Institute of Occupational Health". According to GOST 12.4.172-87, screening suit factor of shielding should not be less than 100.

There is the problem of RF EMF individual protective mean standardization and testing in the Russian Federation. New Standard: GOST 12.4.292-2013 Occupational safety standards system. "Shielding set for personal protection from radiofrequency electromagnetic field exposure. General technical requirements" was developed and introduced in 2014.

According this standard PS is for workers protection from RF EMF exposure in the frequency range from 10 kHz to 300 MHz by electrical component and in the frequency range from 300 MHz to 60 GHz by power density.

The main characteristic of PS that determines its' safety properties based on reflection or absorption energy, is the shielding effectiveness of whole PS. According the goal of adequate evaluation of RF EMF PS screening characteristics the research was directed to develop the correct RF EMF individual protective characteristics assessment method.

2. METHODS

The method of RF EMF protective suit (PS) safety properties assessment is tested. The aim of PS efficiency evaluation is to assess the shielding effectiveness at three points according to the most critical human body parts location: the head, chest and groin. Also it is rational to examine these points for PS design features and elements connection control.

The protective suit testing is carried out by special setup use (Fig. 1), which allows to measure RF EMF levels intensity without as well as with PS inside it's cavity and calculate the shielding effectiveness for the corresponding frequency.

Testing setup includes radioparent human body phantom (head, trunk and extremities), measuring probe connected to personal computer by optic fiber and RF EMF source (RF generator connected with antenna through amplifier). Phantom is placed in EMF spatially homogeneous for all body parts. EMF measurement are carried out at selected radiofrequency in three control points (head, breast and groin) at fixed distances from RF EMF source in two phantom positions: in front and back to the RF EMF source (with and without PS).

RF PS protective properties are determined by the EMF intensity attenuation degree and expressed by shielding factor (K_{SE}). K_{SE} is evaluated by electric field component in EMF frequency

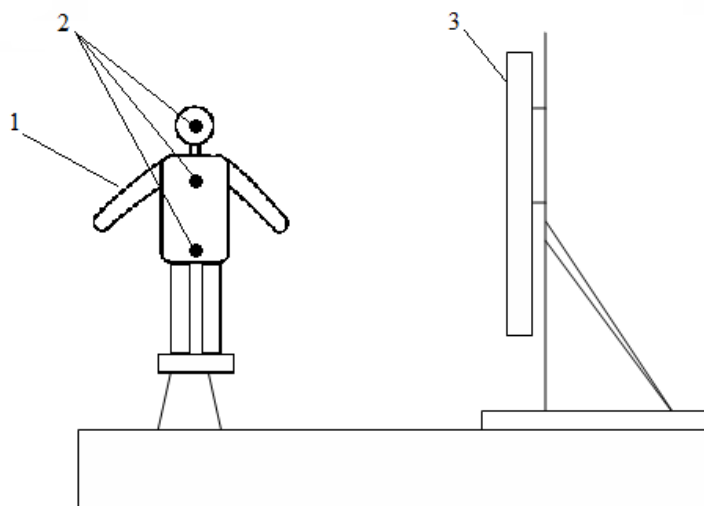


Figure 1: The setup for protective suit testing: 1 — human body phantom, 2 — control point, 3 — RF EMF source.

range from 10 kHz to 300 MHz (Eq. (1)) and by power density in EMF frequency range from 300 MHz to 300 GHz (Eq. (2)).

$$K_{SE} = 20 \log \frac{E_1}{E_2}, \quad (1)$$

where E_1 — RMS value of electric field strength of RF EMF without PS, E_2 — RMS value of electric field strength of RF EMF with PS.

$$K_{SE} = 10 \log \frac{PD_1}{PD_2}, \quad (2)$$

where PD_1 — RMS value of RF EMF power density without PS, PD_2 — RMS value of RF EMF power density with PS.

The shielding effectiveness testing results for 2 different PS models (Sample 1 and Sample 2) were evaluated by the RF EMF power density according Eq. (2) at frequencies: 900, 1800, 2100 and 2600 MHz. The measurements were carried at 3 control points and 2 phantom positions (back and front) during 6 minutes each one.

3. RESULTS

The results of suggested method testing in two different PS sample are presented in Fig. 2 and Fig. 3.

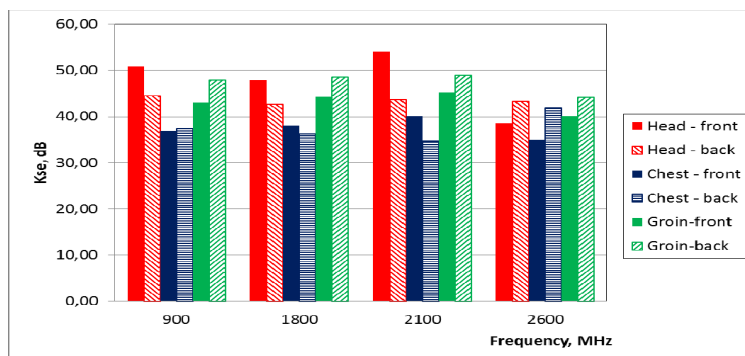


Figure 2: Frequency dependence of shielding effectiveness for PS Sample 1.

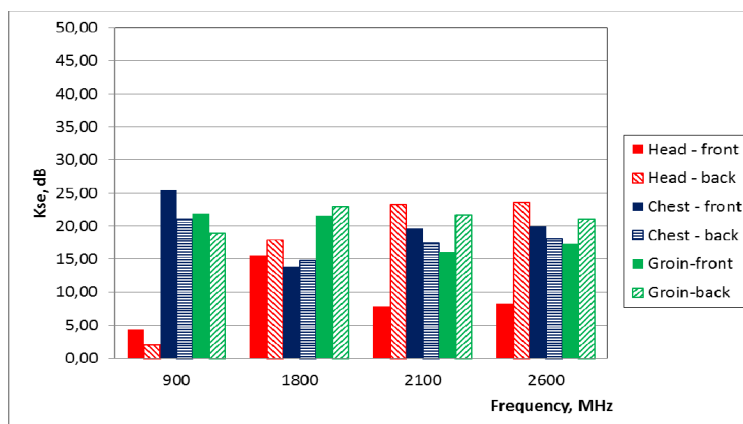


Figure 3: Frequency dependence of shielding effectiveness for PS Sample 2.

The shown diagrams allow to compare the protective properties of selected PS samples. According Technical Regulations of the Customs Union “Personal protective means safety” K_{SE} must be not less than 30 dB [1].

The results show that Sample 2 (Fig. 3) is not in compliance with requirements for RF PS because K_{SE} is less than 30 dB for all frequencies and testing points. The lowest K_{SE} values are obtained for head control point, which may be caused by helmet construction defects.

The Sample 1 (Fig. 2) provides the good RF EMF protection in considered frequency range, its’ K_{SE} is from 40 to 54 dB, and therefore corresponds to RF PS requirements.

4. CONCLUSION

Suggested method of RF EMF individual protective mean efficiency testing help to solve the problem of staff electromagnetic safety, and allows including this principle into standardized approach in Occupational safety standards system. Thus, we extend the system of individual protective means from EMF exposure (as human health risk factor) control.

The results obtained by suggested safety properties assessment testing method allows to determine PS RF EMF protection factor (in dB) and develop recommendations for construction upgrade. The shielding efficiency of PS material must be higher then protective suit, therefore the shielding effectiveness properties of material must be 30 dB at least, or higher.

Furthermore, the obtained data of shielding effectiveness suggest that there is the relationship between protective properties and RF EMF values. Proposed method of PS shielding effectiveness evaluation can help analyze those relationships in future studies.

REFERENCES

1. TR CU 019/2011 Technical Regulations of the Customs Union “Personal protective means safety”, (in Russian).

Experimental Study of Digital Enhanced Cordless Telecommunication Devices Electromagnetic Field Possible Hazard Health Effects

N. B. Rubtsova, S. Yu. Perov, O. V. Belaya, and E. V. Bogacheva
FSBSI “Research Institute of Occupational Health”, Moscow, Russian Federation

Abstract— Radiofrequency electromagnetic field (RF EMF) wireless personal telecommunication devices may be the reason of increased adverse human health effects. The most of recent studies analyze the possible health hazards of cellular phone EMF only. The goal of research was to investigate the Digital Enhanced Cordless Telecommunication (DECT) EMF biological effects to animal behavior and reproduction function. EMF exposure parameters: frequency 1890 MHz, continuous wave (CW), power density $250 \mu\text{W}/\text{cm}^2$ (exposure time 2 hours/day; 5 days/week; 4 weeks) and $500 \mu\text{W}/\text{cm}^2$ (3 hours/day; 5 days/week; 4 weeks). The objects: white rats male (330–350 and 200–220 g). Each exposed group had sham exposure. The evaluated parameters: weight (body, spleen, adrenal glands, testis), behavioral parameters (open field test), the function of reproduction system (epididymis sperm count, sperm osmotic resistance). Exposure value $500 \mu\text{W}/\text{cm}^2$: significant decrease of rats’ behavioral parameters after 5 days; decrease of behavioral parameters, sperm osmotic resistance, spleen and testis weights after 10 days; decrease of sperm osmotic resistance and body weight after 20 days. Exposure value $250 \mu\text{W}/\text{cm}^2$: significant decrease of rats’ sperm osmotic resistance after 20 days of exposure and 2 weeks after exposure, as well as significant decrease of adrenal glands weight and epididymis sperm count 2 weeks after exposure. There were carried out the simulation EMF exposure experiment. The simulation helps to find the dependency interrelation between power density, power exposure and specific absorption rates. The results showed that exposure to CW EMF at 1890 MHz with 500 and $250 \mu\text{W}/\text{cm}^2$ may lead to adverse health effects on reproductive system of male rats; and using of DECT devices may be evaluated as possible human health risk factor.

1. INTRODUCTION

Wireless personal telecommunications use a wide range of personal devices, which operate by transmitting and receiving the radiofrequency electromagnetic fields (RF EMF). The cordless telephones operate in 1880–1900 MHz frequency range according to the Digital Enhanced Cordless Telecommunication (DECT) standard. Such phones are popular personal portable devices used at workplace and home. There is increased number of recent studies analyzing the possible health hazards of wireless personal telecommunications EMF. The significant part of them focuses on potential EMF effects of cellular phones on nervous and reproductive systems to assess the adverse health effects on present and future generation. There are some scientific publications of experimental evidence DECT RF EMF biological effects [1, 2]. The goal of the research was to investigate DECT RF EMF (1890 MHz) acute and subacute exposure biological effects to animal behavior and reproduction function.

2. METHODS

There were carried out two series of experiment. Object of study: white rat males with body weight 330–350 g and 200–220 g (in different series of experiment respectively). The experiment groups of 12 animals were formed. Each exposed group had sham exposure group.

The animals were exposed to 1890 MHz EMF continuous wave (CW) with different power exposure parameters. In first series 24 exposed and 24 sham exposed rats were used. The animals were exposed to EMF with power density (PD) $500 \mu\text{W}/\text{cm}^2$ (exposure time 3 hours/day; 5 days/week; 4 weeks; power exposition, calculated as PD multiplication at the time result, was $1500 (\mu\text{W}/\text{cm}^2) \cdot \text{h}$). In second series 36 exposed and 36 sham exposed rats were used. The animals were exposed to EMF of power density $250 \mu\text{W}/\text{cm}^2$ (2 hours/day; 5 days/week; 4 weeks; the power exposition was $500 (\mu\text{W}/\text{cm}^2) \cdot \text{h}$).

The exposure system included sector antenna 739196 (KATHREIN WERKE KG, Germany), signal generator N5181A MXG (Agilent Technologies, USA) and amplifier HL-42W (Mini-Circuits, USA). The animals were placed into individual radio transparent containers with holes during experiment (exposure and sham exposure groups). Animal exposure area selection and exposure

parameters control were implemented by means of EMF measurement system DASY 52 NEO (SPEAG AG, Switzerland) and broadband EMF meter NARDA NBM-550 (Narda Safety Test Solutions, USA).

The behavioral parameters of animals were evaluated in open field test with hole reflex "entropy" parameter assessment after 1, 5, 10 and 20 days of exposure as well as 2 weeks after exposure.

The weight (body, spleen, adrenal glands, and testis) and the reproduction system parameters (epididymis sperm count, sperm osmotic resistance) were evaluated after 10 and 20 days of exposure as well as 2 weeks after exposure.

The statistical data processing was performed in STATISTICA 7.0 (StatSoft, USA) with U-test (Mann-Whitney).

Simulation of experiment was made by means of full wave 3D electromagnetic simulation software SEMCAD X14.8 (SPEAG AG, Switzerland) to specific absorption rate (SAR) parameters evaluation in each experiment series. The models calculated by the Finite-Difference Time-Domain method corresponded to the experimental EMF exposure conditions.

3. RESULTS

The data show significant decrease ($p < 0.01$) for 37% and 35% (relative to sham exposure group) behavioral parameter (hole reflex "entropy") of animals in group exposed to EMF with 1500 ($\mu\text{W}/\text{cm}^2$) · h power exposition (PD 500 $\mu\text{W}/\text{cm}^2$, 3h/day) after 5 and 10 days correspondingly. Subacute EMF exposure with 500 ($\mu\text{W}/\text{cm}^2$) · h power exposition (PD 250 $\mu\text{W}/\text{cm}^2$, 2 h/day) did not lead to any significant changes in animal behavior.

Different evaluated weight parameters of exposed and sham exposed animal groups data are presented in Table 1.

Table 1: Weight parameters data.

Power exposition	1500 ($\mu\text{W}/\text{cm}^2$) · h		500 ($\mu\text{W}/\text{cm}^2$) · h		
	10 days	20 days	10 days	20 days	2 weeks after exposure
Group	Days				
Body weight, g					
Exposed	339.58 ± 7.16	349.00 ± 3.93*	227.73 ± 4.28	257.08 ± 5.52	274.17 ± 8.14
Sham	366.25 ± 9.60	377.27 ± 12.07	240.00 ± 6.60	274.17 ± 7.41	296.82 ± 8.10
Spleen weight, g					
Exposed	0.72 ± 0.033**	0.84 ± 0.04	0.81 ± 0.04	0.82 ± 0.03	0.67 ± 0.04
Sham	0.94 ± 0.04	0.86 ± 0.05	0.79 ± 0.04	0.89 ± 0.06	0.74 ± 0.04
Adrenal glands weight, g					
Exposed	42.50 ± 3.05	47.27 ± 3.59	36.67 ± 2.25	39.17 ± 2.29	35.00 ± 1.95*
Sham	41.67 ± 3.22	47.27 ± 3.59	39.17 ± 1.93	42.50 ± 3.29	41.82 ± 1.82
Testis weight, g					
Exposed	2.49 ± 0.17**	2.44 ± 0.09	2.39 ± 0.14	2.79 ± 0.07	2.66 ± 0.08
Sham	3.14 ± 0.13	2.73 ± 0.17	2.64 ± 0.09	2.64 ± 0.12	2.83 ± 0.11
* $p < 0.05$; ** $p < 0.01$.					

The Table 1 shows:

- Significant decrease ($p < 0.05$) for 7% relative to sham exposed animals in body weight parameters of rats exposed by EMF with 1500 ($\mu\text{W}/\text{cm}^2$) · h power exposition after 20 days.
- No significant changes in body weight in group exposed by EMF with 500 ($\mu\text{W}/\text{cm}^2$) · h power exposition.
- Significant decrease ($p < 0.01$) for 23% relative to sham exposed group in spleen weight in group exposed by EMF with 1500 ($\mu\text{W}/\text{cm}^2$) · h power exposure after 10 days.
- No significant changes in adrenal glands weight with exception of decrease ($p < 0.05$) for 16% relative to sham in group exposed by EMF with 500 ($\mu\text{W}/\text{cm}^2$) · h power exposition after 2 weeks.

- Significant decrease ($p < 0.01$) for 21% relative to sham in testis weight in group exposed by EMF with $1500 (\mu\text{W}/\text{cm}^2) \cdot \text{h}$ power exposure after 10 days.
- No significant changes in testis weight in group exposed by EMF with $500 (\mu\text{W}/\text{cm}^2) \cdot \text{h}$ power exposition.

The study of reproductive function parameters shows: significant decrease ($p < 0.01$) for 16% (relative to sham exposure group) was observed in sperm osmotic resistance in group exposed by EMF with $1500 (\mu\text{W}/\text{cm}^2) \cdot \text{h}$ power exposition after 10 and 20 days of exposure. Also there were found sperm osmotic resistance significant decreases ($p < 0.05$) for 5% and 7% in group exposed by EMF with $500 (\mu\text{W}/\text{cm}^2) \cdot \text{h}$ power exposition after 20 days and 2 weeks after exposure respectively.

The epididymis sperm count decrease ($p < 0.05$) for 24% in group exposed by EMF with $500 (\mu\text{W}/\text{cm}^2) \cdot \text{h}$ power exposition 2 weeks after exposure.

Numerical simulation of experiment shows the small different mean SAR for both exposure series: 0.041 W/kg and 0.039 W/kg for first and second series respectively.

4. CONCLUSION

The data of experimental study show the effects of acute and subacute 1890 MHz EMF exposure to rat male behavioral parameters and reproductive system. Sperm osmotic resistance as a rat reproduction function estimated parameter was evident sensitive to EMF exposure. Significant decreases of this parameter were observed in groups exposed by EMF with $1500 (\mu\text{W}/\text{cm}^2) \cdot \text{h}$ power exposition as well as in groups exposed by EMF with $500 (\mu\text{W}/\text{cm}^2) \cdot \text{h}$ power exposition. The decrease of sperm osmotic resistance was more expressed under $1500 (\mu\text{W}/\text{cm}^2) \cdot \text{h}$ EMF power exposition than under $500 (\mu\text{W}/\text{cm}^2) \cdot \text{h}$ power exposition (the sperm osmotic resistance decreased during less period of high exposure ($500 \mu\text{W}/\text{cm}^2$) than lower ($250 \mu\text{W}/\text{cm}^2$)). These data support the concept of RF EMF cumulative efficiency.

The results showed that exposure to CW EMF at 1890 MHz with 500 and $250 \mu\text{W}/\text{cm}^2$ may lead to adverse health effects on reproductive system of male rats; and using of DECT devices may be evaluated as possible human health risk factor.

REFERENCES

1. Fragopoulou, A. F., A. Samara, M. H. Antonelou, A. Xanthopoulou, A. Papadopoulou, K. Vougas, E. Koutsogiannopoulou, E. Anastasiadou, D. J. Stravopodis, G. T. Tsangaris, and L. H. Margaritis, "Brain proteome response following whole body exposure of mice to mobile phone or wireless DECT base radiation," *Electromagn. Biol. Med.*, Vol. 31, No. 4, 250–274, 2012.
2. Manta, A. K., D. J. Stravopodis, I. S. Papassideri, and L. H. Margaritis, "Reactive oxygen species elevation and recovery in Drosophila bodies and ovaries following short-term and long-term exposure to DECT base EMF," *Electromag. Biol. Med.*, Vol. 33, No. 2, 118–131, 2014.

Geographical Distribution of Childhood Acute Leukaemia in the Metropolitan Area of Guadalajara, Mexico and Its Correlation with the Wireless and High Voltage Network

Leonardo Soto Sumuano^{1,2}, Carlos Ruiz Chavez³, Alberto Tlacuilo-Parra¹,
Roberto Garibaldi Covarrubias⁴, Hugo Romo Rubio^{4,5},
Mijail Suarez Arredondo¹, and Jesus Arriaga Dávila¹

¹Medical Research Division, UMAE Hospital de Pediatría CMNO, IMSS, Guadalajara, Mexico

²Information Systems Department, CUCEA, University of Guadalajara, Zapopan, Mexico

³Independent Consultant in Information Technologies, Guadalajara, Mexico

⁴Pediatric Hematology and Oncology Department

UMAE Hospital de Pediatría CMNO, IMSS, Guadalajara, Mexico

⁵Pediatric Hematology and Oncology Department

Nuevo Hospital Civil de Guadalajara, OPD, Guadalajara, Mexico

Abstract— This first study conducted by the University of Guadalajara, the Pediatric National Social Security Medical Center, the Hospital Civil de Guadalajara and the General Hospital of Guadalajara, shows the geographical and temporal distribution of 269 cases of children suffering from leukaemia in 6 municipalities in the metropolitan area of Guadalajara (2014). In Mexico, geographical information systems (GIS) have been rarely implemented to monitor spatial assessments of leukaemia. We present an analysis of the spatial distribution of acute leukaemia among children from 0 to 16 years of age in the metropolitan zone of Guadalajara, Mexico using individual case hospital data from the three main hospital facilities treating this population.

Methods: Using the approach of spatial epidemiology DBSCAN and 1-dist, cases of leukaemia obtained from the databases of hospitals resulted in “clusters” or groups of cases/100,000 inhabitants. Cancer cases were grouped according to an internationally recognized morphology.

Results: The results show the occurrence of 94 cases of leukaemia along the deployment path of high voltage electricity, or 36% of all reported cases are located less than 100 meters in distance from a distribution line and other results shows 24 cases/100,000 inhabitants for leukaemia (acute lymphoblastic leukaemia) LLA and 4.4 cases/100,000 inhabitants for leukaemia AML (acute myeloid leukaemia). These resulting measurements exceed international norms. The values are usually 3–5 cases/100,000 for LLA and 0.8 cases/100,000 for AML.

Conclusions: Although the etiology of most childhood leukaemias is unknown, there is a significant correlation between spatial disease cluster (with an unusually elevated disease incidence rate) and both the high voltage distribution network and the wireless communication network. Studies in the literature have focused on childhood leukaemia because of its relatively large incidence among children compared with other malignant disease, its apparent tendency to cluster, and the public concern over locally elevated leukaemia incidence.

1. INTRODUCTION

Undoubtedly the ability to generate electricity and distribute it for use in daily life has been one of the greatest inventions in the world. With this, humankind has taken a giant leap in its development and welfare Fig. 1. Carrying out these processes, however, has brought health risks; some risks are very obvious, such as the risk of being electrocuted. Other risks are not so obvious but still significant, such as the risk associated with non-ionizing radiation produced by the electromagnetic field that always accompanies electricity [12].

Non-ionizing radiation and its effects are not new; however it was not until a few years ago when discussions of this type of radiation became more intense as it was considered to have harmful effects on human health. It increased on one hand the risk to people who constantly use information technology devices, without control and without precaution, and on the other hand the risk to users and/or people living close (< 100 m) to high voltage power distribution lines generating very large electromagnetic fields at low frequencies [1, 12].

It has long been observed that scientists and experts have written about precautionary principles to be implemented among the population against non-ionizing radiation in the environment, but in many countries, including Mexico, people have ignored these precautions, giving greater importance

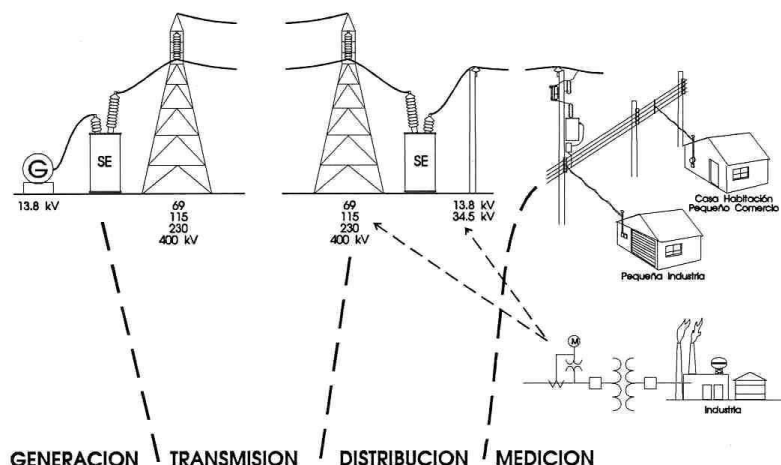


Figure 1: Process of production, transmission and distribution of electrical energy in Mexico.

to the benefits of “access”, “mobility”, “comfort” and “services”, putting the safety of their population at risk. On the other hand we must add that the modern services that telecommunications provides us are very profitable and are very necessary for the development of a country [2].

The World Health Organization (WHO) has already spoken in respect, supporting the recommendations of the International Commission on Non-Ionizing Radiation (ICNIRP International Commission on Non-Ionizing Radiation Protection, 2009; WHO, 2013) [3].

This paper shows the geographical distribution of cases of acute lymphoblastic leukaemia (ALL) and acute myeloid leukaemia (AML) and their relation to high voltage distribution lines in 6 municipalities of Greater Guadalajara.

2. BACKGROUND

Although we do not yet understand the causes, researchers have studied a number of possible explanations including genetic susceptibility, ionizing radiation, unusual patterns of exposure to infection, and non-ionizing radiation received from low frequency electromagnetic fields [4].

In some studies, it is said that about one child in every two thousand contracts leukaemia before the age of 15 years [5]; the equivalent study conducted in the Guadalajara Metropolitan Area found the number in this context to be five times higher [6]. This topic is very complex because although there is a great deal of research globally and a substantial amount of contributions concerning the process of how a child contracts acute leukaemia, we are still far from having causal conclusions about possible contaminants that could be the spark.

The rapid population increase in many cities in Mexico has created a disarray in the penetration of electricity services, lacking proper planning in distribution, resulting in dwellings that are literally situated below power lines. In addition, a lack of order in other services such as potable water distribution, and the mismanagement of organic waste in the population create the ideal stage for the appearance of disease, whether gastrointestinal or more serious, such as acute leukaemia [6].

Some studies report that 1.30% of cases of childhood leukaemia may be associated with power lines [6]. Other studies have shown that children living within a range of less than 200 meters of high-voltage lines have a risk as high as 70% of contracting leukaemia compared with children living beyond 600 meters [1]. In this study we obtained a geo-referenced census of acute leukaemia, resulting in a suprisingly large number of cases of leukaemia around certain residential areas. We obtained groupings of up to 16 cases of acute leukaemia in an area smaller than 10 square kilometers, with distances less than 1 kilometer between each case of leukaemia. Since 2001, the International Agency for Research on Cancer has classified extremely low frequency magnetic fields as “possibly carcinogenic”; as a result there are many studies trying to assess the risk factors [11].

The most important and striking part of this research was the large number of cases of leukaemia /inhabitants found in so little space. The source of information comes from three major hospitals in the city. On average, each hospital treats up to 80 cases per year of acute leukaemia in children younger than 14 years of age [5, 8].

3. METHODOLOGY

- I. For the first stage, a geo-referenced census of cases of lymphoblastic leukaemia and acute myeloid leukaemia was created for the first time in Mexico in the metropolitan area of Guadalajara, yielding a sample that represents 95% of all cases (Fig. 2).
- II. In the second stage, a study geo-referenced to the high voltage lines within the metropolitan area of Guadalajara was conducted (Fig. 3).
- III. The third stage was an analysis of cases of leukaemia near high voltage lines and a study of the associated pattern (Fig. 4).

Figure 2 shows a map of the Guadalajara metropolitan area and the geographic distribution of 268 (representing 95% of the total) cases of children suffering from any of two cases of acute leukaemia: 227 cases of acute lymphoblastic leukaemia and 42 cases of acute myeloid leukaemia. Using the concept of AGE^B¹ or Agglomeration Geographic Basic Statistics proposal for population studies, with support from the National Institute of Statistics, Geography and Informatics (INEGI) [4], the results showed 24 cases/100,000 for acute lymphoblastic leukaemia and 4.4 cases/100,000 for acute myeloid leukaemia. The comparison with global benchmarks indicates that there is a major problem, since the usual incidence of acute lymphoblastic leukaemia is 3–5 cases/100,000, and of acute myeloid leukaemia 0.8 cases/100,000.

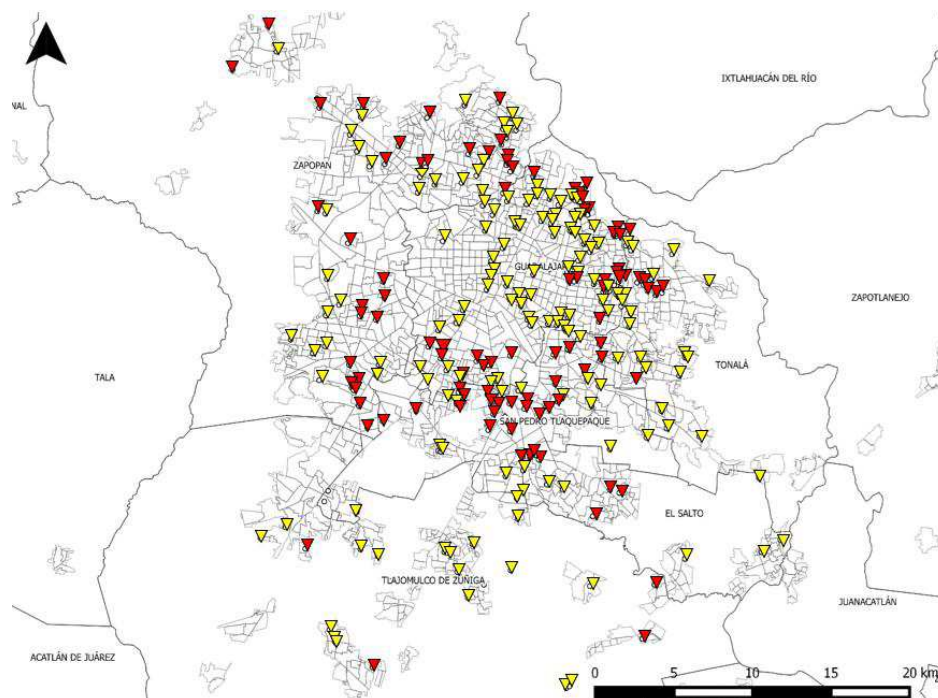


Figure 2: Cases of acute leukaemia in the population aged 0–14 years in the Guadalajara metropolitan area.

Figure 3 shows a map of Guadalajara and its metropolitan area, with corresponding routes of high voltage lines provided by the government enterprise Federal Telecommunications Commission (CFE). These routes show the high penetration of high voltage in the inner city. The characteristic of these lines is that they are unprotected elevated lines. The rapid pace of growth in the city of Guadalajara and its metropolitan area, along with extreme poverty generated in the last 20 years in the country, has led to the presence of many dwellings aside high voltage routes (closer than 30 meters). In marginalized areas such dwellings are literally adjacent to these lines (less than 15 meters). This is the reason why this study proposes to find a pattern among the high voltage routes and the number of cases of leukaemia in children under 14 years of age.

¹Agglomeration Geographic Basic Statistics (AGE^B). Branch municipalities or delegations that make up the country, first used in the Tenth General Census of Population and Housing, 1980 (INEGI) [4]. Its usefulness lies in allowing the formation of primary sampling units and the organization of statistical information. It has three main attributes: (a) it is easily recognizable in the field to be bounded by identifiable and enduring topographic features; (b) it is generally homogeneous in terms of geographical, economic and social characteristics; (c) the extension is such that it can be covered by a single person.

yielded 24 cases/100,000 for acute lymphoblastic leukaemia and 4.4 cases/100,000 inhabitants for acute myeloid leukaemia. The comparison with global benchmarks indicates that there is a major difference, since the usual incidence of acute lymphoblastic leukaemia is 3–5 cases/100,000, and of acute myeloid leukaemia 0.8 cases/100,000.

In the second stage the results show the occurrence of 94 cases of leukaemia along the deployment path of high voltage electricity, or 36% of all reported cases are located less than 100 meters in distance from a distribution line. In previous studies [10] conclusions were that living near a distribution line increased the risk of contracting a type of leukaemia by a factor of 3. In the present work only the two most frequent types of leukaemia were analyzed.

These results show that the investigation of cases of acute leukaemia in children and its relation to non-ionizing radiation, either low or high frequency, has just gotten off the ground. With future studies, it will be important to estimate the disease burden of this type of pollution.

5. CONCLUSIONS

While there is no proven cause and effect relationship of non-ionizing electromagnetic radiation from high voltage power sources at low frequency on human health, it is interesting to note a pattern associated with up to 30% of all cases of leukaemia and the deployment of high voltage power line; there is even a case in which 3 sources of high voltage power lines merge.

ACKNOWLEDGMENT

We thank the directors of the following hospitals, all located in the metropolitan Guadalajara area, for help in the use of their databases: the Decentralized Public Agency Civil Hospital, the Pediatric Hospital of the IMSS National Western Medical Center, and the General Hospital of Guadalajara.

REFERENCES

1. Milham, S. and E. M. Ossiander, "Historical evidence that residential electrification caused the emergence of the childhood leukaemia peak," *Medical Hypotheses*, 2001.
2. Soto Sumuano, L. and I. Cuiñas Gómez, "La contaminación electromagnética, reto para la sociedad del siglo XXI," *Trauco*, Guadalajara, México, 2010.
3. International Commission on Non Ionizing Radiation Protection, "ICNIRP statement on the "guidelines for limiting exposure to time-varying electric, magnetic, and electromagnetic fields (up to 300 GHz)," *Health Physics*, Vol. 97, No. 3, 257–258, 2009.
4. Instituto Nacional de Estadística y Geografía (INEGI), "Censo de población y vivienda," 2010, <http://inegi.org.mx/sistemas/mexicocifras>.
5. Fajardo-Gutierrez, et al., "Residencia cercana a Fuentes eléctricas de alta tensión y su asociación con leucemia en niños," *Boletín Médico del Hospital Infantil de México*, Vol. 50, No. 1, 32-8, 1993.
6. Soto, L., "Radiación electromagnética no ionizante en escuelas y hospitales de la Zona Metropolitana de Guadalajara, Trauco," *Guadalajara*, México, 2014.
7. Belson, M., B. Kingsley, and A. Holmes, "Risk factors for acute leukaemia in children: A review," *Environ Health Perspect*, Vol. 115, 138–145, 2007.
8. Perez-Saldivar, M. L., M. C. Ortega-Alvarez, A. Fajardo-Gutierrez, R. Bernaldez-Rios, M. L. Del Campo-Martinez, A. Medina-Sanson, and M. A. Palomo-Colli, "Father's occupational exposure to carcinogenic agents and childhood acute leukaemia: A new method to assess exposure (a case control study)," *BMC Cancer*, Vol. 8, 7, 2008.
9. Powell, R. M., "Biological effects from RF Radiation at low-intensity exposure, based on the Bioinitiative 2012 report, and the implications for smart meters and smart appliances," Retrieved from <http://marylandsmartmeterawareness.org>, 2013.
10. HESE-UK, "Power density: Radio frequency non-ionizing radiation," Working Document Retrieved from http://www.hese-project.org/hese-uk/en/niemr/power_density_effects.pdf, 2007.
11. World Health Organization, "The international EMF Project," Progress Report, June 2012–2013, Retrieved from http://www.who.int/peh-emf/publications/reports/IAC_2013_Progress_Report.pdf.
12. Rifai, A. B. and M. A. Hakami, "Health hazards of electromagnetic radiation," *Journal of Biosciences and Medicines*, Vol. 2, 1–12, 2014, <http://dx.doi.org/10.4236/jbm.2014.28001>.

Experimental Assessment of Influence Factors of Body Shadow Effect in Dosimetry Measurements in Indoor Enclosures

S. de Miguel-Bilbao¹, J. Roldán², J. Blas³, and V. Ramos¹

¹Health Institute Carlos III, Telemedicine and e-Health Research Unit, Madrid, Spain

²Health Institute Carlos III, National Center for Environmental Health, Madrid, Spain

³Department of Signal Theory, Communications and Telematic Engineering
University of Valladolid, Valladolid, Spain

Abstract— This study proposed a methodology of measurement to avoid the underestimation due to the presence of the wearer in the exposure data logged by bodyworn dosimeters. This uncertainty is defined as body shadow effect (BSE). The designed protocol isolates the treatment of the BSE from the uncertainty of the discontinuous transmission that is quantified by the duty factor. Simulations have been performed means of a software prediction tool in order to estimate the measured E -field levels with the designed experimental method. The validity of the proposed methodology has been checked through the comparison between the experimental and simulated results in terms of the cumulative distributions function (CDF).

1. INTRODUCTION

The use of wireless systems, such as WLAN spreading to a wide range of sectors, ranging from domestic households, to administrative as well as industrial and healthcare environments, with a broad and transverse application scope [1–3]. The number of personal devices that operate in the frequency band of 2.4 GHz is spreading in enclosed environments. Presently smartphones, tablets and laptops are equipped with a Wi-Fi interface that provides ubiquitous connectivity. Despite the benefits of this useful way of connection, some concern exists about the assessment of electromagnetic field (EMF) exposure of humans that use the emitting devices [4, 5].

Personal exposure meters (PEMs) are bodyworn devices for measuring exposure to EMF. The immediate proximity of the user underestimates EMF exposure levels in the registered data. This alteration is known as body shadow effect (BSE).

Regulations about the protection of human exposure to non-ionizing radiation provide thresholds to assure the health and protection of the human beings. These thresholds have been fixed taking into account unperturbed data provided by scientific studies, so these thresholds must be compared with objective and undisturbed data. The BSE has been studied by several authors, in some cases correction factors have been recommended to compensate the underestimation in the logged data by PEMs [6], but it is possible to avoid this effect, without a further treatment of data, through the design of a strict protocol of measure to avoid the influence of the wearer in the logged results.

This study describes the procedure of design of an experimental protocol of measurement of the E -field levels in indoor enclosures and dynamic conditions to avoid the influence of the BSE.

2. METHODS AND MATERIALS

In order to avoid the influence of the BSE it is necessary to know the position where the user has to wear the dosimeter in the realization of the experiment. Initial tests were required in order to know the position of the measuring device to avoid the influence of the wearer during the realization of the experiment. These preliminary measurements were performed in an indoor enclosure, in dynamic conditions with a real access point. The test was to measure the E -field levels with a dosimeter in different positions: completely non-line of sight (NLoS), and in line of sight (LoS) with the PEM situated one meter away from the user, and not in contact with the body.

The results obtained in this preliminary stage are summarized in Figure 1.

The obtained results match with similar works performed in outdoor and indoor conditions [6]: the position of the PEM situated 1 m away from the user is optimal to log reliable levels of exposure to E -field that are not affected by the underestimation caused by the influence of the human body.

After the analysis of the results shown in Figure 1, it is deducible the extreme low values logged by the PEMs under test. Between the 40% and the 60% of data are under the minimum value of the range of sensitivity of the dosimeter. Real Wi-Fi devices in general, and in particular the APs, do not transmit information continuously; it is depend on the traffic demand, the data rate, the

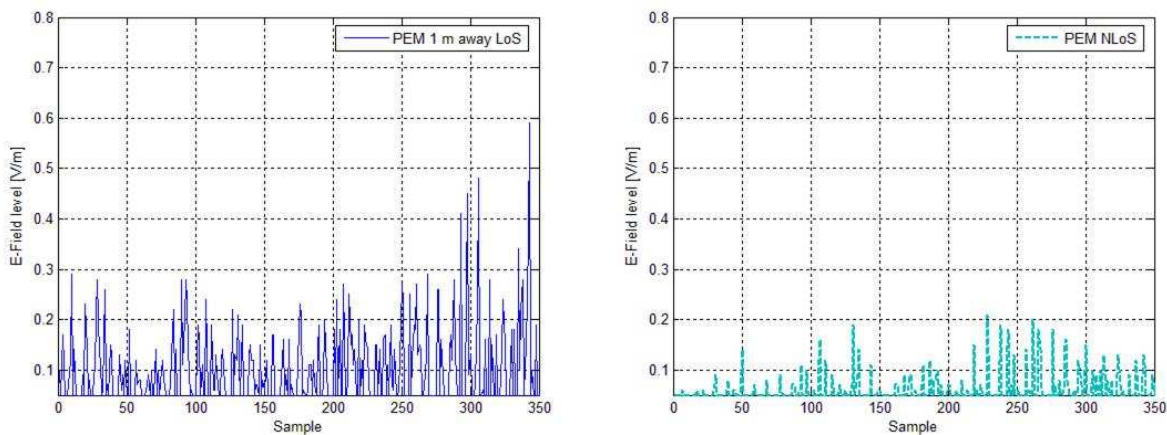


Figure 1: Results of PEMs worn in different positions: 1 m away in front of the body (LoS) and in the back (NLoS).

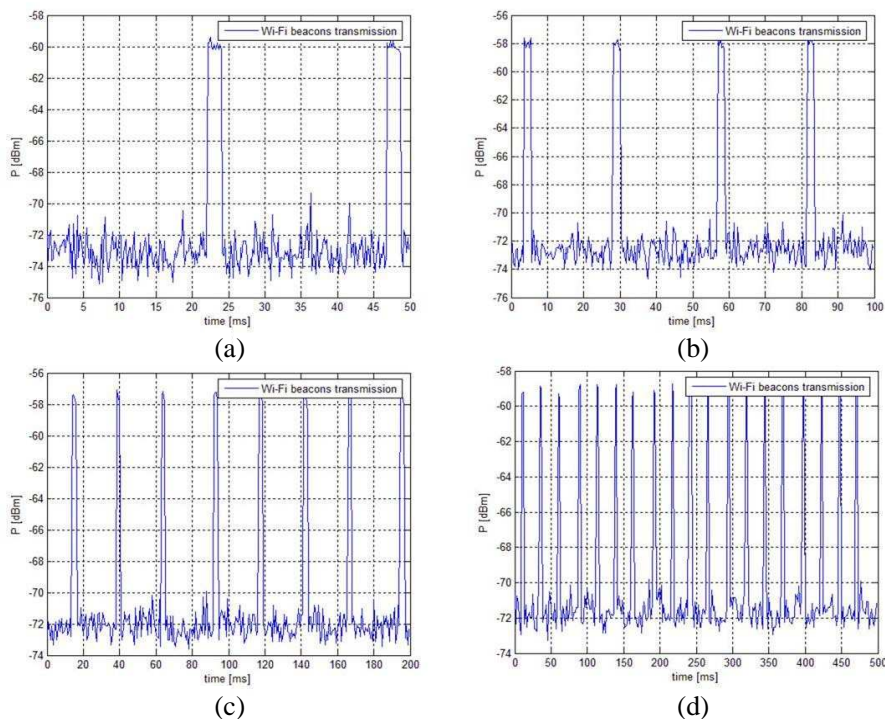


Figure 2: Single sweeps of beacon signal measured with a SA in zero span mode and different values of SWT: (a) 50 ms, (b) 100 ms, (c) 200 ms, (d) 500 ms.

quality of services (QoS), the protocol, the number of connected devices, etc.. When no devices are connected, the AP only transmits beacons, being the levels of E -field generated quite low.

It is possible to characterize the beacon transmission from the AP. Figure 2 illustrates singles sweeps taken with an spectrum analyzer (SA) in zero span mode, 1 MHz of resolution bandwidth (RBW), and a sweep time (SWT) from 50 ms to 500 ms. The period of the beacon transmission is 25 ms, and the value of the duty factor, or duty cycle (DC), is calculated following two procedures published in previous works. One of the methods proposes to calculate the duty factor in function of the number of samples above a mid-level called set point. In this case the duty factor is calculated with the following formula [7]:

$$DC = \frac{\text{number of samples} > \text{setpoint}}{\text{total number of samples}} \tag{1}$$

The second method calculates the DC with the theoretical definition: the ratio of active duration

t_{active} to total duration t_{total} of the WLAN transmission [8]:

$$T = 100 \times \frac{t_{active}}{t_{total}} \quad (2)$$

t_{active} is defined as the time that the signal is 5 dB above the signal noise equal to -72 dBm for the configuration settings. Figure 2 illustrates the transmission of the beacons with different SWT, the period of transmission of the beacons is 25 ms and the mean of t_{active} is about 3 ms.

The values of DC are estimated with both methods, and are shown in Table 1 in function of the SWT. For small values of SWT the values of DC are different. As the value of the sweep time increases the DC values obtained with both methods tend to converge.

Table 1: Results of the duty factor in function of the applied method and the sweep time.

Methods	Sweep time (ms)			
	50	100	200	500
Number of samples	0.1833	0.1400	0.1167	0.1400
Definition of duty factor	0.0800	0.0833	0.0967	0.1368

The DC obtained with both methods tends to converge when the number of samples is high. Approximating the results obtained for a sweep of 500 ms, the DC of the AP under test is about 14%, which justifies the high percent of non-detects in the results. To address the shadow effect in an isolated way, it is necessary to prevent the high number of non-detects by increasing the value of the DC. Therefore, it is intended to isolate the treatment of the shadow effect avoiding other uncertainties associated with using of PEMs. To achieve this purpose, experimental measurements have to be performed with a signal generator that transmits continuously and a biconical antenna.

The designed experimental protocol consists of the implementation of the measurements with a signal generator as radiation source, and with the measuring device situated 1 m away from the user to avoid the BSE. The designed protocol isolates the treatment of the BSE from the uncertainty of the discontinuous transmission. Simulations have been performed means of a software prediction tool in order to estimate the measured E -field levels obtained with the designed experimental method.

3. RESULTS

Figure 3(a) shows the experimental and simulated results. Both types of data vary in the same way in function of the distance from the radiation source.

In order to provide more exhaustive conclusions about the validity of the proposed methodology, the results have been compared in function of the p -value obtained with the Kolmogorov Smirnov

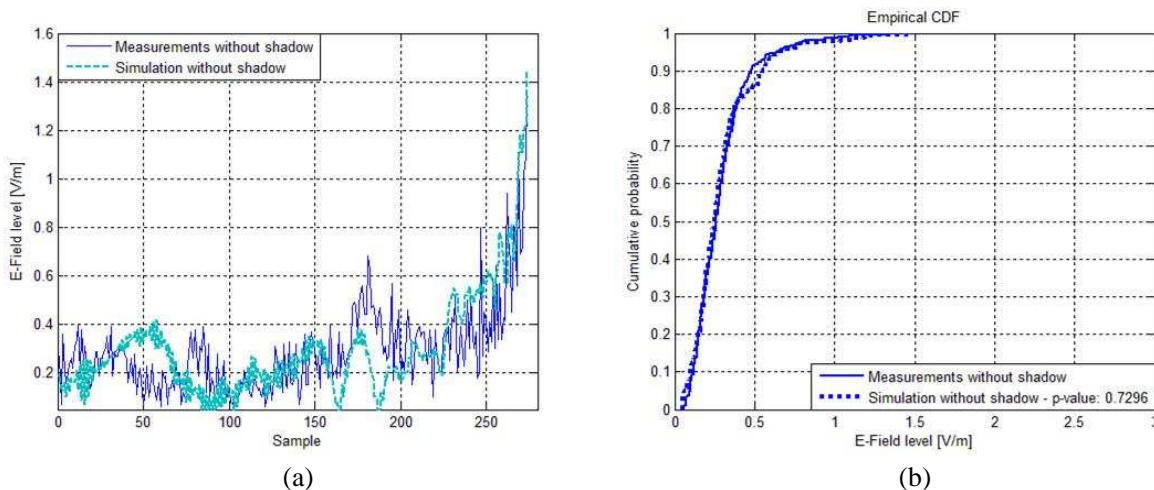


Figure 3: Comparison between experimental and simulated results, (a) in terms of E -field levels in V/m, (b) in terms of the CDFs.

test. The p -value is an indicator of the similarity between the cumulative distribution function (CDF) of the compared data. In this particular case the p -value is 0.7296, being a very acceptable result as it is shown in Figure 3(b) where the CDFs of the experimental and simulated results are compared.

4. CONCLUSION

This study has presented a methodology to evaluate the impact of Wi-Fi technology in terms of exposure to EMFs in indoor enclosures. The use of PEMs as measuring devices presents uncertainties that are necessary to avoid in order to obtain objective conclusions about exposure conditions. With this purpose requirements in the implementation of the experimental measurements have been fixed: the PEM has to be situated 1 m from the user to avoid the shadow effect, and in order to isolate the treatment of the BSE the radiation source must transmit continuously to avoid the non-detects. Taking into account these rules, evaluations of E -field levels have been made in an indoor enclosure by means of simulations and measurements. After comparing both types of data in terms of the variation of the E -field levels and in terms of the p -value, it is concluded that the designed experimental method avoids the non-detects and the underestimation by the shadow effect in the logged data, providing real, objective and non-disturbed data and conclusions about EMF exposure.

ACKNOWLEDGMENT

This work was supported by the project “Electromagnetic Characterization in Smart Environments of Healthcare, and their involvement in Personal, Occupational, and Environmental Health,” (PI14CIII/00056), and with the human resources of the project “Assessment of Exposure to Non-Ionizing Radiation from Wireless Communication Technologies and its Relation to the Health of Humans” (CA12/00038), both funding from Sub-Directorate-General for Research Assessment and Promotion (Health Institute Carlos III).

REFERENCES

1. Aguirre, E., P. Iturri López, L. Azpilicueta, S. de Miguel-Bilbao, V. Ramos, U. Garate, and F. Falcone, “Analysis of estimation of electromagnetic dosimetric values from non-ionizing radiofrequency fields in conventional road vehicle environments,” *Electromagn. Biol. and Med.*, Vol. 34, No. 1, 19–28, Mar. 2015.
2. Aguirre, E., J. Arpón, L. Azpilicueta, P. López, S. de Miguel, V. Ramos, and F. Falcone, “Estimation of electromagnetic dosimetric values from non-ionizing radiofrequency fields in an indoor commercial airplane environment,” *Electromagn. Biol. and Med.*, Vol. 33, No. 4, 252–263, 2014.
3. De Miguel-Bilbao, S., M. A. Martín, A. Pozo, V. Febles, J. A. Hernández, J. C. Fernández de Aldecoa, and V. Ramos, “Analysis of exposure to electromagnetic fields in a healthcare environment: Simulation and experimental study,” *Health Phys.*, Vol. 105, No. 5, S209–S222, 2013.
4. Lopez-Iturri, P., S. de Miguel-Bilbao, E. Aguirre, L. Azpilicueta, F. Falcone, and V. Ramos, “Estimation of radiofrequency power leakage from microwave ovens for dosimetric assessment at nonionizing radiation exposure levels,” accepted for publication in *Biomed. Res. Int.*, 2015.
5. De Miguel-Bilbao, S., E. Aguirre, P. Lopez-Iturri, L. Azpilicueta, J. Roldán, F. Falcone, and V. Ramos, “Evaluation of electromagnetic interference and exposure assessment from s-health solutions based on Wi-Fi devices,” accepted for publication in *Biomed. Res. Int.*, 2015.
6. De Miguel-Bilbao, S., J. García, V. Ramos, and J. Blas, “Assessment of human body influence on exposure measurements of electric field in indoor enclosures,” *Bioelectromagnetics*, Vol. 36, No. 2, 118–132, 2015.
7. Khalid, M., T. Mee, A. Peyman, D. Addison, C. Calderon, M. Maslanyj, and S. Man, “Exposure to radio frequency electromagnetic fields from wireless computer networks: Duty factors of Wi-Fi devices operating in schools,” *Progr. Biophys. Mol. Biol.*, Vol. 107, No. 3, 412–420, 2011.
8. Verloock, L., W. Joseph, G. Vermeeren, and L. Martens, “Procedure for assessment of general public exposure from WLAN in offices and in wireless sensor network testbed,” *Health Phys.*, Vol. 98, No. 4, 628–638, 2010.

A Perturbative Solution to Plane Wave Scattering from a Rough Dielectric Cylinder

Rahul Trivedi and Uday K. Khankhoje

Department of Electrical Engineering, Indian Institute of Technology Delhi, New Delhi, India

Abstract— In this paper, we present a perturbative second order closed form solution for the fields scattered from a stochastically rough, infinitely long dielectric cylinder. The electromagnetic boundary conditions at the surface of rough cylinder are perturbed to derive 0th, 1st and 2nd order boundary conditions that can be used to evaluate the scattered fields to the second order in the surface roughness. To validate our perturbative method, we compare it with a method of moments solution of the same problem - which, despite being valid for any arbitrary surface roughness, is computationally more expensive as compared to our analytical method. A region of validity is also estimated numerically, within which the perturbative solution accurately predicts the fields scattered from the rough cylinder. We report this region approximately as $h_0 < \lambda/25$ and $l > 5.84h_0$ for an exponentially correlated rough cylinder, where h_0 is the root mean square roughness, l is the correlation length and λ is the free space wavelength.

1. INTRODUCTION

Scattering from vegetation such as tree trunks, branches and leaves contributes significantly to radar scattering. At low microwave frequencies, branches and tree trunks can accurately be modelled as smooth cylinders for calculating their impact on the incident electromagnetic radiation [1, 2]. At higher frequencies, the surface roughness begins to play an increasingly important role and the cylinder can no longer be treated as smooth.

Numerical methods such as the method of moments or the finite element method allow us to accurately compute the fields scattered from cylinders with arbitrary roughness. However, their use is limited due to the large computational time involved. There have been many analytical studies that attempt to approximate the properties of rough cylinders, for instance treating the surface roughness as a periodic corrugation in a dielectric layer [3, 4] and modelling the scattered fields in the geometric optics approximation [5].

The small perturbation method (SPM) was originally developed to analytically model stochastically rough surfaces [6, 7]. The SPM has also been used to model rough conducting cylinders [8–10] and cylinders with impedance boundary conditions [11]. Although the SPM affords closed form expressions for the scattered fields, it breaks down as the surface roughness increases.

The analytical method developed in this paper is based on the perturbation of the boundary conditions at the surface of the rough cylinder. Several authors have used the SPM to model azimuthally rough conducting cylinders or rough cylinders with impedance surfaces, but there has been no previous report of a perturbative analysis of a rough *dielectric* cylinder with both azimuthally dependant and z dependant roughness. In contrast to the previous attempts to perturbatively analyse the scattering problem, which are based on an integral equation formulation, our approach, based on perturbing the boundary conditions at the cylinder surface, yields not only the scattered fields, but also the fields inside the cylinder. This makes it possible to extend our method to *finite* rough cylinders by using an approach similar to that used by Hulst [12] and Serker [13] in their treatment of finite smooth cylinders.

In Section 2 we derive the perturbed boundary conditions in the cylindrical coordinate system that can be used together with an appropriate eigen-expansion of the fields to obtain a second order solution to the scattering problem. In Section 3, we validate the perturbative method for an azimuthally rough exponentially correlated dielectric cylinder by comparing it with a method of moments based solution of the same problem. We also numerically derive a region of validity in terms of bounds on the root mean square roughness h_0 and the correlation length l of the rough surface within which the perturbative solution accurately captures the scattering properties of the rough cylinder.

2. THE PERTURBATIVE METHOD

The rough dielectric cylinder, shown in Fig. 1, can be mathematically represented by specifying a random process $h(\phi, z)$, which denotes the radial distance of a point on the cylinder surface at

azimuthal coordinate ϕ and z coordinate z from the mean smooth cylinder (with radius a). In this section, we derive a perturbed set of boundary conditions that can be used to derive a ‘‘Mie’’ like solution for scattering from this rough dielectric cylinder. The starting point of our analysis are the boundary conditions on the tangential components of the fields:

$$\mathbf{n} \times \Delta \mathbf{V} \Big|_{r=a+h} = 0 \text{ for } \mathbf{V} \equiv \mathbf{E} \text{ or } \mathbf{H} \quad (1)$$

where $\Delta \mathbf{V} \Big|_{r=a+h}$ is the discontinuity in \mathbf{V} across the cylinder surface and \mathbf{n} is a normal to the cylinder surface given by:

$$\mathbf{n} = \hat{r} - \left(\frac{1}{a+h} \right) \frac{\partial h}{\partial \phi} \hat{\phi} - \frac{\partial h}{\partial z} \hat{z} \quad (2)$$

Eq. (1) can be re-expressed in terms of the discontinuities in components of \mathbf{V} :

$$\Delta V_z \Big|_{r=a+h} = - \frac{\partial h}{\partial z} \Delta V_r \Big|_{r=a+h} \quad (3a)$$

$$(a+h) \Delta V_\phi \Big|_{r=a+h} = - \frac{\partial h}{\partial \phi} \Delta V_r \Big|_{r=a+h} \quad (3b)$$

Use of the Taylor series expansion along with Eq. (3) yields (to the second order in h or it's derivatives):

$$\Delta V_z \Big|_{r=a} + h \frac{\partial \Delta V_z}{\partial r} \Big|_{r=a} + \frac{h^2}{2} \frac{\partial^2 \Delta V_z}{\partial r^2} \Big|_{r=a} = - \frac{\partial h}{\partial z} \left(\Delta V_r \Big|_{r=a} + h \frac{\partial \Delta V_r}{\partial r} \Big|_{r=a} \right) \quad (4a)$$

$$\left(1 + \frac{h}{a} \right) \left(\Delta V_\phi \Big|_{r=a} + h \frac{\partial \Delta V_\phi}{\partial r} \Big|_{r=a} + \frac{h^2}{2} \frac{\partial^2 \Delta V_\phi}{\partial r^2} \Big|_{r=a} \right) = - \frac{1}{a} \frac{\partial h}{\partial \phi} \left(\Delta V_r \Big|_{r=a} + h \frac{\partial \Delta V_r}{\partial r} \Big|_{r=a} \right) \quad (4b)$$

To recast Eq. (4) into a more usable form, we expand the functions ΔV_p where $V \equiv E$ or H and $p \equiv r, \phi$ or z into a perturbation series:

$$\Delta V_p = \Delta V_p^{(0)} + \Delta V_p^{(1)} + \Delta V_p^{(2)} \dots \quad (5)$$

where $\Delta V_p^{(m)} \sim O(h^m)$. Clearly, $\Delta V_p^{(0)}$ corresponds to the solution of the scattering problem for a smooth cylinder. Eqs. (4) and (5) can then be used to derive the following equations in $\Delta V_p^{(m)}$:

1. *Zeroth Order Boundary Conditions:*

$$\Delta V_z^{(0)} \Big|_{r=a} = 0, \quad \Delta V_\phi^{(0)} \Big|_{r=a} = 0 \quad (6)$$

2. *First Order Boundary Conditions:*

$$\Delta V_z^{(1)} \Big|_{r=a} = -h \frac{\partial \Delta V_z^{(0)}}{\partial r} \Big|_{r=a} - \frac{\partial h}{\partial z} \Delta V_r^{(0)} \Big|_{r=a} \quad (7a)$$

$$\Delta V_\phi^{(1)} \Big|_{r=a} = -h \frac{\partial \Delta V_\phi^{(0)}}{\partial r} \Big|_{r=a} - \frac{1}{a} \frac{\partial h}{\partial \phi} \Delta V_r^{(0)} \Big|_{r=a} \quad (7b)$$

3. *Second Order Boundary Conditions:*

$$\Delta V_z^{(2)} \Big|_{r=a} = -h \frac{\partial \Delta V_z^{(1)}}{\partial r} \Big|_{r=a} - \frac{h^2}{2} \frac{\partial^2 \Delta V_z^{(0)}}{\partial r^2} \Big|_{r=a} - \frac{\partial h}{\partial z} \Delta V_r^{(1)} \Big|_{r=a} - h \frac{\partial h}{\partial z} \frac{\partial \Delta V_r^{(0)}}{\partial r} \Big|_{r=a} \quad (8a)$$

$$\begin{aligned} \Delta V_\phi^{(2)} \Big|_{r=a} &= -h \frac{\partial \Delta V_\phi^{(1)}}{\partial r} \Big|_{r=a} - \frac{h^2}{2} \frac{\partial^2 \Delta V_\phi^{(0)}}{\partial r^2} \Big|_{r=a} - \frac{1}{a} \frac{\partial h}{\partial \phi} \Delta V_r^{(1)} \Big|_{r=a} + \frac{h}{a^2} \frac{\partial h}{\partial \phi} \Delta V_r^{(0)} \Big|_{r=a} \\ &- \frac{h}{a} \frac{\partial h}{\partial \phi} \frac{\partial \Delta V_r^{(0)}}{\partial r} \Big|_{r=a} \end{aligned} \quad (8b)$$

In addition to the boundary conditions presented above, it is necessary to use an appropriate eigen-expansion of the scattered fields and the fields inside the cylinder so as to obtain a closed form expression for the scattered fields. Since the boundary conditions have been worked out in the cylindrical coordinates, an appropriate basis for representing the scattered fields would be the cylindrical wave basis. Once the scattered fields are known in terms of $h(\phi, z)$, it is a simple matter to evaluate the statistical properties of the scattered fields as a function of the statistical properties of the rough surface (i.e., the correlation function $R(\phi, z) = \overline{h(\Phi + \phi, Z + z)h(\Phi, Z)}$). For further details and derivations, please refer to the upcoming journal version of this paper [14].

3. RESULTS AND DISCUSSIONS

To validate our analytical approach, we compared the perturbative approach to a Method of Moment (MoM) solution of the same scattering problem. For simplicity, we assume an azimuthally rough cylinder (i.e., h is only a function of ϕ). Additionally, we also assume the cylinder surface to be exponentially correlated:

$$R(\phi) = \overline{h(\Phi + \phi)h(\Phi)} = h_0^2 \exp(-a|\phi|/l) \quad \forall \phi \in (-\pi, \pi) \quad (9)$$

where $h_0 = (\overline{h^2(\phi)})^{1/2}$ is the root-mean square (RMS) roughness and l is the correlation length of the surface. Additionally, note that $R(\phi)$ is periodic in ϕ with period 2π .

The perturbative solution derived in the previous section is valid if and only if $h(\phi, z)$ and its derivatives ($\partial h(\phi, z)/\partial \phi$ and $\partial h(\phi, z)/\partial z$) are small. Therefore, the perturbative solution is expected to deviate from the more accurate MoM analysis for large RMS roughness h_0 (resulting in large $h(\phi, z)$ per instance) and small correlation lengths l (resulting in larger derivatives of $h(\phi, z)$ per instance). By an exhaustive comparison between the perturbative solution and the MoM solution, we arrived at the following bounds on h_0 and l for a second order perturbative analysis to be reasonably accurate $-k_0 h_0 < 0.25$ and $k_0 l > 1.097$. A convenient measure of the derivative of $h(\phi, z)$ is the slope s defined by $s = h_0/l$. In terms of s , the perturbative solution was found to be accurate when $s < 5.84$. Fig. 2 shows the comparison between the ensemble average of the 2D scattering cross section calculated using the method of moments and the perturbative solution for $k_0 h_0 = 0.25$, $s = 0.019$ and $k_0 h_0 = 0.188$, $s = 5.84$ (these dimensions are just within the validity bounds stated above).

We emphasise that the perturbatively obtained expressions for the scattered fields are very simple to evaluate numerically. Within the region of validity, the perturbative solution is computationally far more efficient than any other numerical method which can be employed to solve the same problem. Also observe that our method directly gives the ensemble average of the scattered fields and derived quantities (such as the scattering cross section) in terms of the auto-correlation

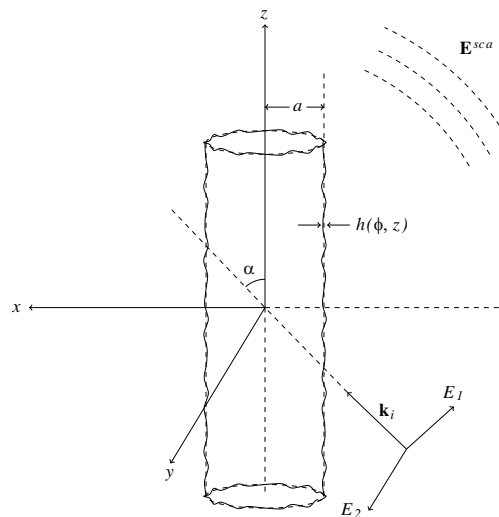


Figure 1: Schematic of the rough cylindrical scatterer with a stochastic roughness $h(\phi, z)$ and illuminated by a plane wave propagating with wavevector \mathbf{k}_i in the xz plane at an angle of α with the x axis. E_1 is the component of the electric field in the xz plane, while E_2 is the component along the y axis.

function of the surface roughness. A numerical analysis of the problem (such as using the method of moments or finite element method) can only yield the scattered fields for a particular *instance* of the rough cylinder, and the simulation would have to be repeated for a large number of instances to obtain the ensemble average of the fields and the derived quantities. For instance, in the MoM results shown in Fig. 2, we needed to calculate the scattering cross section for 100 instances of the rough cylinder to achieve convergence, and for each instance we had to solve a 600×600 dense matrix system to calculate the scattered fields.

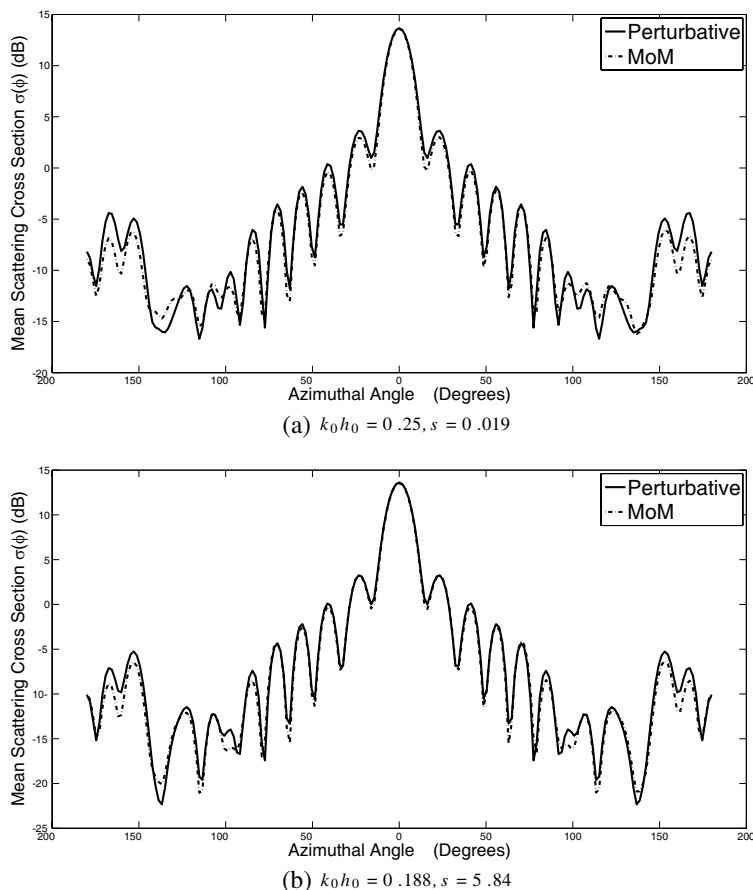


Figure 2: Variation of the mean scattering cross section ($\sigma(\phi)$) with ϕ calculated using the perturbative solution and Method of Moments. The MoM results were generated by averaging the scattering cross section calculated for 100 different instances of $h(\phi)$. In all calculations, the permittivity ϵ of the cylinder was assumed to be $2\epsilon_0$ and the radius a is taken to be $2\lambda_0$.

ACKNOWLEDGMENT

U K Khankhoje would like to acknowledge financial support from the INSPIRE Faculty Award (IFA-13 ENG-60) by the Department of Science and Technology, Government of India.

REFERENCES

1. Karam, M. and Fung, A., "Electromagnetic scattering from a layer of finite length, randomly oriented, dielectric, circular cylinders over a rough interface with application to vegetation," *Remote Sensing*, Vol. 9, No. 6, 1109–1134, 1986.
2. Chiu, T. and K. Sarabandi, "Electromagnetic scattering interaction between a dielectric cylinder and a slightly rough surface," *IEEE Transactions on Antennas and Propagation*, Vol. 47, No. 5, 902–913, 1999.
3. Lin, Y. C. and K. Sarabandi, "Electromagnetic scattering model for a tree trunk above a tilted ground plane," *IEEE Transactions on Geoscience and Remote Sensing*, Vol. 33, No. 4, 1063–1070, 1995.
4. Sarabandi, K. and F. T. Ulaby, "High frequency scattering from corrugated stratified cylinders," *IEEE Transactions on Antennas and Propagation*, Vol. 39, No. 4, 512–520, 1999.

5. El-Rouby, A. E. and F. T. Ulaby, “Mmw scattering by rough lossy dielectric cylinders and tree trunks,” *IEEE Transactions on Geoscience and Remote Sensing*, Vol. 40, No. 4, 351–378, 1951.
6. Rice, S. O., “Reflection of electromagnetic waves from slightly rough surfaces,” *Communications on Pure and Applied Mathematics*, Vol. 4, No. 2–3, 351–378, 1951.
7. Beckmann, P. and A. Spizzichino, *The Scattering of Electromagnetic Waves from Rough Surfaces*, Vol. 1, 511, Norwood, MA, Artech House, Inc., 1987.
8. Cabayan, H. and R. Murphy, “Scattering of electromagnetic waves by rough perfectly conducting circular cylinders,” *IEEE Transactions on Antennas and Propagation*, Vol. 21, No. 6, 893–895, 1973.
9. Eftimiu, C., “Electromagnetic scattering by rough conduction circular cylinders. i. angular corrugation,” *IEEE Transactions on Antennas and Propagation*, Vol. 36, No. 5, 651–658, 1988.
10. Eftimiu, C., “Electromagnetic scattering by rough conducting circular cylinders,” *Radio science*, Vol. 23, No. 5, 760–768, 1988.
11. Tong, T., “Scattering by a slightly rough cylinder and a cylinder with an impedance boundary condition,” *International Journal of Electronics Theoretical and Experimental*, Vol. 36, No. 6, 767–772, 1974.
12. Hulst, H. C. and H. van de Hulst, *Light Scattering by Small Particles*, Courier Dover Publications, 1957.
13. Serker, S., and A. Schneider, “Electromagnetic scattering from a dielectric cylinder of finite length,” *IEEE Transactions on Antennas and Propagation*, Vol. 36, No. 2, 303–307, 1988.
14. Trivedi, R. and U. K. Khankhoje, “A perturbative solution to plane wave scattering from a rough dielectric cylinder,” under revision.

Evaluation of the Angular Spectrum of Scattered High Frequency Radio Waves in the Anisotropic Collision Magnetized Ionospheric Plasma

G. V. Jandieri¹, Zh. M. Diasamidze², M. R. Diasamidze³, and I. Nemsadze⁴

¹Special Department, Georgian Technical University, Georgia

²Physics Department, Batumi Shota Rustaveli State University, Georgia

³Department of Exact and Natural Sciences, Batumi State Maritime Academy, Georgia

⁴Physics Department, Batumi Shota Rustaveli State University, Georgia

Abstract— Second-order statistical moments of scattered radiation in turbulent collision magnetized plasma. General dispersion equation is obtained at arbitrary angles of inclination of both external magnetic field and wave vector of an incident electromagnetic wave. Statistical characteristics of the phase fluctuations of scattered high frequency radio waves in the collision magnetized plasma caused by the electron density and external magnetic field fluctuations taking into account polarization coefficients for both ordinary and extraordinary waves are considered. The influence of collision frequency on the broadening and displacement of maximum of the angular spectrum is analyzed. Numerical calculations are carried out for the *F*-region of the ionosphere using experimental data.

1. INTRODUCTION

Investigation of statistical characteristics of small-amplitude electromagnetic waves propagating through a turbulent plasma slab is very important in many practical applications associated with both natural and laboratory plasmas [1]. It has been established that the energy loss due to the collisions between plasma particles can lead to a decrease in the amplitude of the electromagnetic waves and also to an appreciable distortion of the angular spectrum of radiation in the events of multiple scattering by random smooth inhomogeneities of the medium. In [2] it was shown that for a fixed collision frequency between plasma particles, the degree to which the absorption influences the angular spectrum of the scattered waves depends strongly on the propagation direction of the original incident wave with respect to the plasma boundary and also on the strength of an external magnetic field using the complex geometrical optics approximation. Broadening of the angular power spectrum of scattered electromagnetic waves in turbulent collision magnetized plasma for both power-law and anisotropic Gaussian correlation function of electron density fluctuations has been considered in [3] in complex ray (-optics) approximation.

In the present work, using the perturbation method, we calculate statistical characteristics of scattered electromagnetic waves in turbulent collision magnetized ionospheric plasma taking into account both electron density and external magnetic field fluctuations; and also polarization coefficients for both ordinary and extraordinary waves. General dispersion equation is obtained at arbitrary angles of inclination of both external magnetic field and wave vector of an incident electromagnetic wave. The influence of collision frequency on the broadening of the angular spectrum is analyzed. Numerical calculations were carried out for the *F*-region of the ionosphere using experimental data.

2. FORMULATION OF THE PROBLEM

At high frequency the effect of ions can be neglected. Maxwell's equations and equation of motion of the electron in collision plasma $ig\omega\mathbf{w} = (e/m)(\mathbf{E} + [\mathbf{w} \cdot \mathbf{H}_0]/c)$ lead to the wave equation for the electric field

$$\text{grad div } \mathbf{E} - \Delta \mathbf{E} - k_0^2 \mathbf{E} = -\frac{k_0^2 v g}{g^2 - u} \left\{ \mathbf{E} - \frac{i\sqrt{u}}{g} [\mathbf{E} \cdot \mathbf{m}] - \frac{u}{g^2} (\mathbf{E} \cdot \mathbf{m}) \mathbf{m} \right\}, \quad (1)$$

where \mathbf{w} is the velocity of electron, $g = 1 - is$, $s = \nu_{\text{eff}}/\omega$, $\nu_{\text{eff}} = \nu_{ei} + \nu_{en}$ is the effective collision frequency of electron with other plasma particles, $k_0 = \omega/c$, $u = \omega_H^2/\omega^2$ and $v = \omega_p^2/\omega^2$ are non-dimensional magneto-ionic parameters, $\omega_H = eH_0/mc$ and $\omega_p = 4\pi N e^2/m\omega^2$ are the electron gyrofrequency and plasma frequencies, respectively, N -electron density, e and m are the charge and

mass of an electron, $\mathbf{m} = \mathbf{H}_0/H_0$ is the unite vector along the direction of an external magnetic field locating in the yo z plane. Complex refractive index of the collisional magnetized plasma is

$$N^2 \equiv (n - i\kappa)^2 = 1 - \frac{2v(g - v)}{2g(g - v) - u_T \pm \sqrt{u_T^2 + 4u_L(g - v)^2}}, \quad (2)$$

where: $u_T = u \sin^2 \alpha$, $u_L = u \cos^2 \alpha$, α is the angle between vectors \mathbf{k} and \mathbf{H}_0 , upper sign corresponds to the ordinary wave, lower sign to the extraordinary wave; n is refractive index, κ is absorption index. Using perturbation method each parameter in the Equation (1) we submit as a sum of the mean value and small fluctuating terms: $\mathbf{E} = \langle \mathbf{E} \rangle + \mathbf{e}$, $\mathbf{H}_0 = \langle \mathbf{H}_0 \rangle + \mathbf{h}_0$, $N = \langle N \rangle + n$. The angular brackets indicate the statistical average. We assume that the mean values of electron density and magnetic field do not depend on coordinates. Fluctuating fields of scattered radio waves are random functions of the spatial coordinates and satisfy set of stochastic differential equation taking into account both electron density and external magnetic field fluctuations:

$$\left(\frac{\partial^2}{\partial x_i \partial x_j} - \Delta \delta_{ij} - k_0^2 \varepsilon_{ij} \right) e_j = j_i, \quad (3)$$

where the current density is $\mathbf{j}(\mathbf{r}) = -\frac{k_0^2 v_0 g}{g^2 - u_0} \{ -i \frac{\sqrt{u_0}}{g} [\langle \mathbf{E} \rangle \mathbf{h}'_0] - \frac{u_0}{g} (\langle \mathbf{E} \rangle \mathbf{m}) \mathbf{h}'_0 - \frac{u_0}{g^2} (\langle \mathbf{E} \rangle \mathbf{h}'_0) \mathbf{m} \} - \frac{k_0^2 v_0 g}{g^2 - u_0} \{ n' + \frac{2u_0}{g^2 - u_0} (\mathbf{m} \mathbf{h}'_0) \} \{ \langle \mathbf{E} \rangle - i \frac{\sqrt{u_0}}{g} [\langle \mathbf{E} \rangle \mathbf{m}] - \frac{u_0}{g^2} (\langle \mathbf{E} \rangle \mathbf{m}) \mathbf{m} \}$; where $\mathbf{h}'_0 = \mathbf{h}_0/|\langle \mathbf{H}_0 \rangle|$ and $n' = n/\langle N \rangle$ are external magnetic field and electron density fluctuations which are random functions of the spatial coordinates. Components of the dielectric permittivity for the collision plasma at $(1 \pm u_0) \gg s^2$, on the pole (vertical magnetic field $\alpha = 0^\circ$) are [1]:

$$\begin{aligned} \varepsilon_{xx} = \varepsilon_{yy} = \eta' - i s \tilde{\eta}'', \quad \varepsilon_{zz} = \varepsilon' - i s \tilde{\varepsilon}'', \quad \varepsilon_{xy} = s \tilde{\mu}' - i \mu'', \quad \eta' = 1 - \frac{v_0}{1 - u_0}, \quad \tilde{\eta}'' = \frac{v_0(1 + u_0)}{(1 - u_0)^2}, \\ \tilde{\mu}' = \frac{2 v_0 \sqrt{u_0}}{(1 - u_0)^2}, \quad \mu'' = \frac{v_0 \sqrt{u_0}}{1 - u_0}, \quad \varepsilon' = 1 - v_0, \quad \tilde{\varepsilon}'' = v_0. \end{aligned} \quad (4)$$

Index “zero” indicates the mean values of non-dimensional plasma parameters. Components of the wave vector in homogeneous medium are determined as:

$$k_x = k_0 N \sin \theta \sin \varphi \equiv k_0 \tau_1, \quad k_y = k_0 N \sin \theta \cos \varphi \equiv k_0 \tau_2, \quad k_z = k_0 N \cos \theta \equiv k_0 q, \quad \tau_1^2 + \tau_2^2 + q^2 = N^2,$$

where: θ is the angle between wave vector \mathbf{k} and z axis, φ is the angle between projection of vector \mathbf{k} on the xoy plane and x axis.

The dispersion relation in general case, at $\theta \neq 0$, $\varphi \neq 0$ and $\alpha \neq 0$ has the following form:

$$\Delta \equiv a_4 q^4 + a_3 q^3 + a_2 q^2 + a_1 q + a_0 = 0, \quad (5)$$

here: $a_4 = \varepsilon_{zz}$, $a_3 = 2 \tau_2 \varepsilon_{yz}$, $a_2 = \varepsilon_{yz}^2 - \varepsilon_{xz}^2 - \varepsilon_{zz}(\varepsilon_{xx} + \varepsilon_{yy}) + \tau_1^2(\varepsilon_{xx} + \varepsilon_{zz}) + \tau_2^2(\varepsilon_{yy} + \varepsilon_{zz})$, $a_1 = 2 \tau_2[\varepsilon_{yz}(\tau_1^2 + \tau_2^2) - \varepsilon_{xx}\varepsilon_{yz} - \varepsilon_{xy}\varepsilon_{xz}]$, $a_0 = (\tau_1^2 + \tau_2^2 - \varepsilon_{zz})(\tau_1^2\varepsilon_{xx} + \tau_2^2\varepsilon_{yy} - \varepsilon_{xx}\varepsilon_{yy} - \varepsilon_{xy}^2) + \varepsilon_{yz}^2(\tau_2^2 - \varepsilon_{xx}) - 2\varepsilon_{xy}\varepsilon_{xz}\varepsilon_{yz} + \varepsilon_{xz}^2(\varepsilon_{yy} - \tau_1^2)$.

We seek the solution set of Equation (3) by expansion of the Fourier integral over x and y coordinates using the boundary conditions: fluctuations are negligible below and above plasma layer. If the plane xoy coincides with the lower boundary of slab, at $z \geq L$ the waves propagating in the negative direction must be absent, and at $z \leq 0$ — in the positive direction. Snell's law gives: $\tau_1^2 + \tau_2^2 = N^2 \sin^2 \theta_0$, where θ_0 is an incident angle. Spectral components of the current density on the pole ($\alpha = 0^\circ$) substantially simplified:

$$\begin{aligned} \tilde{g}_y(\mathbf{x}, z) = \mp i k_0^2 \langle E_x \rangle [(D_1 + i s D_3) n' - (D_2 + i s D_4) h'_{0z}], \quad \tilde{g}_y(\mathbf{x}, z) = \pm i \tilde{g}_x(\mathbf{x}, z), \\ \tilde{g}_z(\mathbf{x}, z) = k_0^2 \langle E_x \rangle (F_1 + i s F_2) [h'_{0x}(\mathbf{x}, z) \pm i h'_{0y}(\mathbf{x}, z)], \end{aligned} \quad (6)$$

where: $D_1 = \frac{v_0}{1 - u_0}(1 \pm \sqrt{u_0})$, $D_2 = -\frac{v_0}{1 - u_0}[\pm \sqrt{u_0} + \frac{2u_0(1 \pm \sqrt{u_0})}{1 - u_0}]$, $D_3 = \frac{v_0}{(1 - u_0)^2}(1 \pm \sqrt{u_0})^2$, $D_4 = -\frac{2v_0}{(1 - u_0)^2}[\pm \sqrt{u_0} + \frac{u_0(3 + u_0 \pm 4\sqrt{u_0})}{1 - u_0}]$, $F_1 = \frac{v_0}{1 - u_0}(u_0 \pm \sqrt{u_0})$, $F_2 = \frac{v_0}{(1 - u_0)^2}[u_0(3 - u_0) \pm 2\sqrt{u_0}]$.

Hence, current density fluctuations in the xoy plane contain both electron density and external magnetic field fluctuations, while the z component — only magnetic field fluctuations.

We investigate statistical characteristics of scattered high frequency radio waves in the turbulent collisional magnetized plasma slab caused by electron density fluctuations if wave propagates along the external magnetic field z -axis ($\theta = \varphi = 0$). Taking into account that phase fluctuations φ_1 are determined by the expression $\varphi_1 = \text{Im}(e/\langle E_x \rangle)$, applying the residue theory for the poles of the Equation (5), for the y component of scattered radiation and arbitrary correlation function of the phased fluctuations $W_\varphi(\mathbf{r}_1, \mathbf{r}_2) = \langle \varphi_1(\mathbf{r}_1)\varphi_1^*(\mathbf{r}_2) \rangle$ at the observation points \mathbf{r}_1 and \mathbf{r}_2 caused by electron density fluctuations has the following form:

$$\begin{aligned} & \langle \varphi_1(x + \rho_x, y + \rho_y, L)\varphi_1^*(x, y, L) \rangle_{yD} \\ &= -D_1^2 k_0^2 L \int_{-\infty}^{\infty} dk_x \int_{-\infty}^{\infty} dk_y \int_{-\infty}^{\infty} d\rho_z \exp(ik_x \rho_x + ik_y \rho_y) W_n(k_x, k_y, \rho_z) \\ & \left(\frac{2}{\delta_2} (E_1 - s \cdot E_2) \left[\cos(k_{02} \rho_z) - \frac{\sin(2k_{02} L)}{2k_{02} L} \text{ch}(s \cdot \alpha_2 k_{02} \rho_z) \right] - \frac{1}{\delta_1} (E_3 + s \cdot E_4) \right. \\ & \cdot \left\{ \frac{\sin(p_2 k_0 L)}{p_2 k_0 L} \cos\left(\frac{p_1}{2} k_0 \rho_z\right) \text{ch}\left(s \cdot \frac{q_1}{2} k_0 \rho_z\right) - (J_1 + s \cdot J_2) \cos\left(\frac{p_2}{2} k_0 \rho_z\right) \text{ch}\left(s \cdot \frac{q_2}{2} k_0 \rho_z\right) \right. \\ & \left. \left. + (J_3 - s \cdot J_4) \sin\left(\frac{p_2}{2} k_0 \rho_z\right) \text{sh}\left(s \cdot \frac{q_2}{2} k_0 \rho_z\right) \right\} \right), \end{aligned} \quad (7)$$

where: $E_1 = \varepsilon' \mu'' - \frac{1}{k_0^2} [(\eta' - \mu'')k_x^2 + \varepsilon' k_y^2]$, $E_2 = \frac{G_2}{k_0^2} k_x k_y$, $E_3 = \frac{G_1}{k_0^2} k_x k_y$, $E_4 = \frac{1}{k_0^2} [(\eta' + \mu'')k_x^2 + \varepsilon' k_y^2]$, $G_1 = \tilde{\varepsilon}'' + \tilde{D}_3(\eta' + \mu'' - \varepsilon') - \frac{1}{2\varepsilon'^2}(\tilde{\eta}'' - \tilde{\mu}')$, $G_2 = \tilde{\varepsilon}'' + \tilde{D}_3(\eta' - \mu'' - \varepsilon') - \frac{1}{2\varepsilon'^2}(\tilde{\eta}'' + \tilde{\mu}')$, $\delta_1 = 4\mu'' \sqrt{\eta' + \mu''}$, $\delta_2 = 4\mu'' \sqrt{\eta' - \mu''}$, $p_1 = \sqrt{a + \sqrt{c}}$, $q_1 = \sqrt{c\alpha_2 - \sqrt{a}\alpha_1}$, $p_2 = \sqrt{a - \sqrt{c}}$, $q_2 = \sqrt{c\alpha_2 + \sqrt{a}\alpha_1}$, $\alpha_1 = b/2a$, $\alpha_2 = d/2c$, $k_{02} = k_0 \sqrt{c}$, $\tilde{D}_3 = \frac{1 \pm \sqrt{u_0}}{1 - u_0}$, $J_1 = \frac{\sin(p_1 k_0 L)}{p_1 k_0 L} \text{ch}(sq_1 k_0 L)$, $J_2 = \frac{q_1 \cos(p_1 k_0 L)}{p_1 k_0 L} \text{sh}(sq_1 k_0 L)$, $J_3 = \frac{\cos(p_1 k_0 L)}{p_1 k_0 L} \text{sh}(sq_1 k_0 L)$, $J_4 = \frac{q_1 \sin(p_1 k_0 L)}{p_1 k_0 L} \text{ch}(sq_1 k_0 L)$, ρ_x and ρ_y are distances between observation points spaced apart at small distances. Broadening of the angular power spectrum (APS) is determined as [4]: $\langle k_{x,y}^2 \rangle = -\partial^2 W_n / \partial \rho_{x,y}^2$.

3. NUMERICAL CALCULATIONS

Analytical and numerical calculations will be carried out for anisotropic Gaussian correlation function of electron density fluctuation [3].

$$W_n(k_x, k_y, \rho_z) = \frac{\langle N_1^2 \rangle}{4\pi} \frac{l_{\parallel}^2}{\chi \Gamma_0} \exp\left(-\frac{m^2}{l_{\parallel}^2} \rho_z^2 + in k_x \rho_z\right) \exp\left(-\frac{k_x^2 l_{\parallel}^2}{4\Gamma_0^2} - \frac{k_y^2 l_{\parallel}^2}{4\chi^2}\right), \quad (8)$$

where: $m^2 = \chi^2 / \Gamma_0^2$, $\Gamma_0^2 = \sin^2 \gamma_0 + \chi^2 \cos^2 \gamma_0$, $n = (\chi^2 - 1) \sin \gamma_0 \cos \gamma_0 / \Gamma_0^2$. The average shape of electron density irregularities has the form of elongate ellipsoid of rotation. The rotation axis is located in the plane of geomagnetic meridian. The ellipsoid is characterized with two parameters: the anisotropy factor for the irregularities equaling to the ratio of ellipsoid axes $\chi = l_{\parallel} / l_{\perp}$ (ratio of longitudinal and transverse linear scales of plasma irregularities with respect to the external magnetic field) and orientation equaling to the inclination angle γ_0 of the prolate irregularities with respect to the external magnetic field (sometimes with respect to horizon). Anisotropy of the shape of irregularities is connected with the difference of diffusion coefficients in the field align and field perpendicular directions. In the case $k_0 L < 1$ for nonmagnetic isotropic ($\chi = 1$) collisionless plasma ($s = 0$), at $\rho_x = \rho_y = 0$ we obtain the well-known formula for the variance of the phase fluctuations $W_{\varphi n} = \sqrt{\pi} \sigma_n^2 v_0^2 k_0^2 L l / 4$ [1].

The results of numerical calculations of the APS are illustrated in graphical form. The plots are constructed for an incident wave 3 MHz ($k_0 = 6.28 \cdot 10^{-2}$ m) using the following dimensionless parameters: $v_0 = 0.28$, $u_0 = 0.22$.

Figure 1 illustrates curves of the spectral width of scattered radio waves versus angle γ_0 for irregularities closely aligned along the magnetic field lines of the F -region in the principle plane. At fixed anisotropic factor $\chi = 13$, increasing characteristic linear scale of irregularities in the interval $l_{\parallel} = 1.1 \div 2.4$ km, angle of inclination is $\gamma_0 \approx 3^\circ$, and the width of the spectrum not

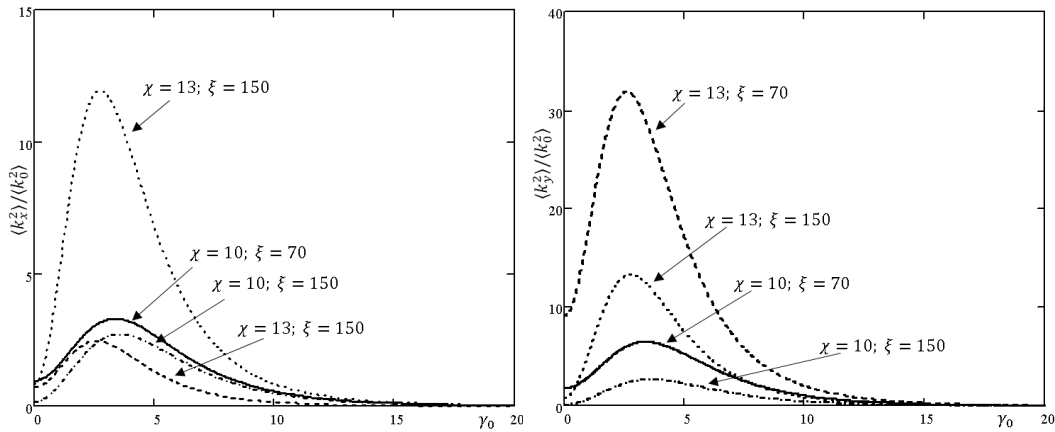


Figure 1: Plots of the spectral width of the APS in the principle and perpendicular planes as function of inclination angle of prolate irregularities γ_0 at different anisotropic parameter χ and ξ .

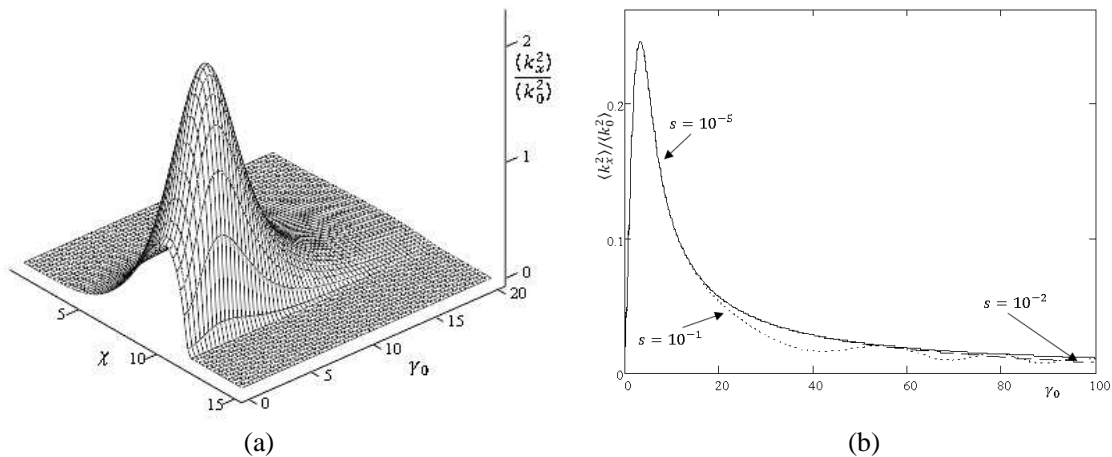


Figure 2: (a) 3-D picture of the spectral width of the APS in the principle plane versus anisotropy factor χ and angle of inclination γ_0 . (b) Dependence of the broadening of the APS as function of the parameter ξ in isotropic case $\chi = 1$ for different s .

varies. Decreasing parameter $\chi = 10$ maximum of the spectrum is at $l_{\parallel} \approx 1$ km and $\gamma_0 \approx 3.5^\circ$; for irregularities with $l_{\parallel} \approx 2.4$ km the width of the APS increases twice and the maximum displaced slightly, $\gamma_0 \approx 3^\circ$.

Figure 2(a) depicts 3D Figure of the APS of scattered electromagnetic waves in the principle plane having Gaussian form for anisotropic plasma irregularities; Figure 2(b) illustrates curves of broadening of the APS in isotropic case $\chi = 1$. Maximum of the spectrum is at $\xi = 3.4$ not depending on the collision frequency between plasma particles and corresponds to the characteristic spatial scale of irregularities of electron density fluctuations $l_{\parallel} = 50$ m.

Increasing parameter s up to $s = 10^{-1}$, tail of the spectrum oscillated and three minimums appear: $\xi_{\min}^{(1)} = 40.3$, $\xi_{\min}^{(2)} = 68.5$ and $\xi_{\min}^{(3)} = 89.4$ corresponding to the: $l_{\parallel}^{(1)} \approx 600$ m, $l_{\parallel}^{(2)} \approx 1.1$ km and $l_{\parallel}^{(3)} \approx 1.4$ km. The obtained results are in agreement with the observation data from earth satellites at an average height of 362 km [5].

4. CONCLUSIONS

Statistical characteristics of scattered radio waves are calculated in turbulent collision magnetized ionospheric plasma using the perturbation method. General dispersion equation is obtained in zero approximation at arbitrary angles of inclination of both external magnetic field and wave vector of an incident electromagnetic wave. Correlation function of the phase fluctuations of scattered electromagnetic waves is obtained for arbitrary correlation function of electron density fluctuations

taking into account polarization coefficients for both ordinary and extraordinary waves. The width of the APS substantially depends of the anisotropic factors characterizing field aligned irregularities, while location of maximum of the APS not substantially displaced. For isotropic irregularities three minimum appear in the APS allowing estimate characteristic linear scale of plasma irregularities. Numerical calculations for 3 MHz electromagnetic waves are in agreement with satellite observation data between heights of 153 and 617 km.

REFERENCES

1. Gershman, B. N., L. M. Erukhimov, and Y. Y. Yashin, *Wave Phenomena in the Ionosphere and Space Plasma*, Nauka, Moscow, 1979.
2. Jandieri, G. V., V. G. Gavrilenko, and A. A. Semerikov, "On the effect of absorption on multiple wave-scattering in a magnetized turbulent plasma," *Wave Random Media*, Vol. 9, 427–440, 1999.
3. Jandieri, G. V., A. Ishimaru, V. G. Jandieri, A. G. Khantadze, and Z. M. Diasamidze, "Model computations of angular power spectra for anisotropic absorptive turbulent magnetized plasma," *Progress In Electromagnetics Research*, Vol. 70, 307–328, 2007.
4. Jandieri, G. V., V. G. Gavrilenko, V. G. Jandieri, and A. V. Sorokin, "Some properties of the angular power distribution of electromagnetic waves multiply scattered in a collisional magnetized turbulent plasma," *Plasma Physics Report*, Vol. 31, No. 7, 604–615, 2005.
5. Chen, A. A. and G. S. Kent, "Determination of the orientation of ionospheric irregularities causing scintillation of signals from earth satellites," *J. Atm., Terr. Physics*, Vol. 34, 1411–1414, 1972.

Stochastic Geometry for Electromagnetic Scattering Modeling

Frédéric Gruy

Ecole Nationale Supérieure des Mines
158 Cours Fauriel, 42023 Saint-Etienne, Cedex 2, France

Abstract— The relationship between statistical distributions of geometrical parameters and scattering properties of particles has been underlined, particularly for optically soft particles. As the calculation of these distributions may be difficult, some simple rules for estimating them are presented in this paper. The method has been validated by the calculation of the scattering properties of a capsule shaped particle.

1. INTRODUCTION

Electromagnetic scattering by particles consisting in a homogeneous material has been studied a lot by numerically solving the Maxwell equations. Solutions depend on the morphology of the particles; this is revealed at the boundary conditions, i.e., the values of the physical quantities on the particle surface. In the case of a homogeneous material a relationship between the scattering properties, the optical indices of the material and the surface characteristics may be expected. The exact calculation of any shaped particle is possible by numerical methods [1]. However, the whole analysis needs a too large computational time if these exact methods are used for the calculation of the optical properties. Actually, the need of fast calculations is important for industrial applications, e.g., particle sizing and particle shape determination by means of optical methods, even if the accuracy is lower. Fitting the accuracy of the calculation with the accuracy of the measurement is sufficient. Thus simple and accurate expressions for the optical properties of particles or crystals are useful to solve inverse problems coming from such optical particle sizing techniques.

Moreover the use of relevant descriptors for the particle geometry can simplify the correspondence between optical and geometrical properties. In the past some optical approximations have been developed for the calculations for optically soft materials [2]. They include relations between the optical properties and the statistical distributions of geometrical parameters [3, 4]. Unfortunately, it appears that the analytical calculation of the statistical distributions can be very tedious even for simply shaped particles. The aim of this paper is to extract from the dedicated literature any information to evaluate the statistical distributions of any convex body and then calculate the scattering properties. The study of non convex particles, e.g., clusters, will be out of the scope of this paper.

2. RELATION BETWEEN SCATTERING PROPERTIES AND STATISTICAL DISTRIBUTIONS

The optical properties of a body depend on the relative refractive index m , i.e., the ratio between the refractive indices of the particle and the surrounding medium. Some scatterers dispersed in a liquid are characterized by a low optical contrast, i.e., $|m - 1| \ll 1$. In the past, two important analytical approximations [2] have been proposed for such particles: the Van de Hulst approximation, also known as anomalous diffraction (AD) approximation, for large particles and the Rayleigh-Debye-Gans (RDG) approximation for small particles. From a geometrical point of view, the AD approximation explicitly contains the $D_l(l)$ chord length distribution (CLD) of the scatterer. The chord length l is the distance between two points located on the body surface. RDG approximation considers the $D_P(r)$ distance distribution (DD) of scattering elements inside the scatterer. The distance r is the length between two any points inside the body. Now, we will focus our attention about the scattering of light by small and optically soft particles.

Within the RDG approximation, the differential scattering cross section per unit incident intensity (unpolarized light) is related to the amplitude form factor R . Considering that the object (scatterer) can randomly orientate, this optical property is thus obtained after calculating an average over all the object orientations (Equation (1)):

$$\langle C_{diff\ sca} \rangle = \frac{k^4 V^2}{4\pi^2} |m - 1|^2 \langle |R|^2 \rangle \frac{1 + \cos^2 \theta}{2} \quad (1)$$

with

$$\langle |R|^2 \rangle = \int_0^{l_{\max}} \frac{\sin(k_s r)}{k_s r} D_P(r) dr \quad (2)$$

\vec{k} , θ and \vec{k}_s ($k_s = 2k \sin(\theta/2)$) are the incident wave vector, the scattering angle and the scattering vector, respectively. V is the object volume.

Following the theory of stochastic geometry [3], there exists a relation between the two normalized distributions D_P and D_l for a convex particle:

$$D_P(r) = 12r^2 \int_r^{l_{\max}} D_l(l) (l-r) dl / \bar{l}^4 \quad (3)$$

l_{\max} is the maximum chord length of the particle.

By introducing Equation (3) into Equation (2), one express $\langle |R|^2 \rangle$ and the differential scattering cross section as a function of the CLD:

$$\langle |R|^2 \rangle = \frac{12}{\bar{l}^4 k_s^4} \left[2 - \int_0^{l_{\max}} (k_s l \sin(k_s l) + 2 \cos(k_s l)) D_l(l) dl \right] \quad (4)$$

Equation (4) shows that D_l is the relevant geometrical characteristic for the scattering cross section of optically soft particles. Equation (4) replaces the equation defining $\langle |R|^2 \rangle$ that is basically a sextuple integral. As a consequence, the use of CLD presents two advantages: simpler calculations and clear relationship between the particle morphology and the scattering properties.

Two ways can be used for calculating the CLD of a convex body: analytical calculation for the simplest shaped particles or Monte-Carlo Simulations (MCS). The MCS runs are carried out by generating unbiased random lines that cross the particle. The distance between the two points that intersect the body is calculated and recorded. The MC sampling distribution may be visually represented as the discrete probability histogram.

3. MATHEMATICAL PROPERTIES OF CLD

Statistical distributions have already been introduced by researchers in the field of the small angle scattering using X-rays (SAXS). Therefore we may compile the main results of the literature especially these ones concerning the SAXS theory. Moreover, additional properties have been discovered by the mathematicians.

We may consider the CLD of any convex body as the CLD of an equivalent spheroid or ellipsoid, i.e., a body with a smooth shape, modified by specific geometrical features. The latter ones are important for the shape of the CLD curve. They consist in flat faces as crystal facets, parallel (flat or curved) surfaces, parallel tangent planes, edges and corners. They correspond to discontinuities of the distribution density or its derivative.

We begin by investigating the effect of the curvature on CLD. For a convex body with a smooth surface the series expansion of CLD around $l = 0$ does not contain even terms. The first order term is an explicit function of the mean principal curvatures of the body [5, 6].

Chords intersect the surface at two points in a convex body; some chords are perpendicular to the tangent planes at the two end points and thus the latter ones are parallel. These chords are termed extremal chords. For instance, spheroids have two extremal chords: one for $l = 2a$ and the other for $l = 2b$, a and b being the semi-axes. A discontinuity of $dD_l(l)/dl$ will occur at these values. Wu and Schmidt [7] have investigated the properties of $D_l(l)$ when the chord is in the neighbourhood of an extremal chord. They give expressions for $D_l(l)$ around the extremal chord values denoted L . They show that $D_l(l)$ is continuous for $l = L$ whereas $dD_l(l)/dl$ is not.

Ciccariello [8–10] generalized the work of Wu and Schmidt: he considers the property of parallelism between some parts of body boundaries. He studied the case where the locus of the extremal chord ends is a surface. For instance, this surface is a sphere for $l = 2R$ if the particle is a sphere with radius R . One can show that $D_l(l)$ becomes discontinuous for this chord length value. If the parallelism occurs between two partial surfaces of the body, a discontinuity of $D_l(l)$ occurs at $l = L$, L being the distance between the two parallel surfaces. The contribution of the parallelism to $D_l(l)$ for $l \rightarrow L$ is given by Ciccariello.

The presence of edges leads to additional terms for $D_l(l)$ at $l = 0$. Ciccariello et al. [9,12] and Sobry et al. [11, 13] have shown that $D_l(0)$ is a simple function of the dihedral angle and of the edge length. All the edges contribute to $D_l(0)$. Edges (and corners) also contribute to $dD_l(l)/dl|_{l=0}$ [14]. However, it seems difficult to systemize this contribution.

4. CANONICAL EXPRESSION FOR CLD OF CONVEX PARTICLE

4.1. Principles

Singularities on the surface of a convex body play an important role about the CLD. They correspond to discontinuities of the distribution density and its derivatives. As seen in §3, the CLD discontinuities are slightly proportional to the extension (length or area) of the corresponding singularities. Each singularity is characterized by the values of the chord length and of the density (or its derivative) discontinuity. Generally, the contributions of these singularities are independent of each other and additive. The CLD of particles having a simple shape is not monotonous and show some features as discontinuities as well.

Moreover the integral geometry theory shows that the first order and fourth order CLD moments are related to the surface area S and the volume of the body:

$$\bar{l} = 4V/S \quad (5)$$

$$\bar{l}^4 = 12V^2/\pi S \quad (6)$$

Then we may establish the following rules for constructing the CLD:

- list the singularities (pairs of parallel tangent planes, pairs of parallel surfaces, edges),
- sort the singularities by increasing chord length values; quantify the corresponding discontinuity of density or of its derivative,
- interpolate the density between two singularities by means of polynomial functions,
- write the density $D_l(l)$ as a piecewise function,
- use the normalization condition for $D_l(l)$ and Equations (5)–(6) for calculating unknown polynomial coefficients in $D_l(l)$.

4.2. Illustration

One considers a capsule shaped particle. This one consists in two hemispheres with radius R and a circular cylinder with a radius R and length H . The capsule is a convex particle with one l -discontinuity for $l = 2R$ due to pairs of parallel surfaces and one $dD_l(l)/dl$ -discontinuity for $l = 2R + H$ due to one pair of parallel tangent planes. Following §4.1 we divide the l -range $[0; 2R + H]$ into several parts:

- $[0; 2R - \Delta l^-] D_1(l) = [(R + 3H/16) / (R^2(2R + H))] l$ see [5, 6]
- $[2R - \Delta l^-; 2R] D_2(l) = D_1(2R - \Delta l^-) + D_H(l) - D_H(2R - \Delta l^-)$

with $D_H(l) = -\frac{2H}{S} \ln |1 - \frac{l}{2R}|$ see [8–10]

- $[2R; 2R + \Delta l^+] D_3(l) = D_4(2R + \Delta l^+) + D_H(l) - D_H(2R + \Delta l^+)$
- $[2R + \Delta l^+; 2R + H] D_4(l) = F_D(l) + a_2(2R + H - l)^2 + a_3(2R + H - l)^3$

with $F_D(l) = \frac{4R(2R+H-l)}{H(2R+H)^2}$ see [7].

$l = 2R - \Delta l^-$ and $l = 2R + \Delta l^+$ are the length values for which the continuity of CLD function and its derivative is verified respectively:

$$\begin{aligned} D_1(2R - \Delta l^-) &= D_2(2R - \Delta l^-) & dD_1/dl &= dD_2/dl \\ D_3(2R + \Delta l^+) &= D_4(2R + \Delta l^+) & dD_3/dl &= dD_4/dl \end{aligned}$$

a_2 and a_3 are determined by using the normalization condition for $D_l(l)$ and the Equation (5) for the mean chord length value.

Figure 1 compares the CLD's issued from MCS and calculated by using the previous method. The agreement is good except the CLD part within the $[2R + \Delta l^+; 2R + H]$ range. In order to check the consequences of this deviation on the optical properties, we calculate the factor $\langle |R|^2 \rangle$ following Equation (4) for a capsule shaped particle with $R = 0.2 \mu\text{m}$ and $H = 0.4 \mu\text{m}$. Figure 2 represents the comparison between the $\langle |R|^2 \rangle$ factors using the two CLD calculations. The slight discrepancy between the two calculations of CLD does not lead to an significant deviation for $\langle |R|^2 \rangle$.

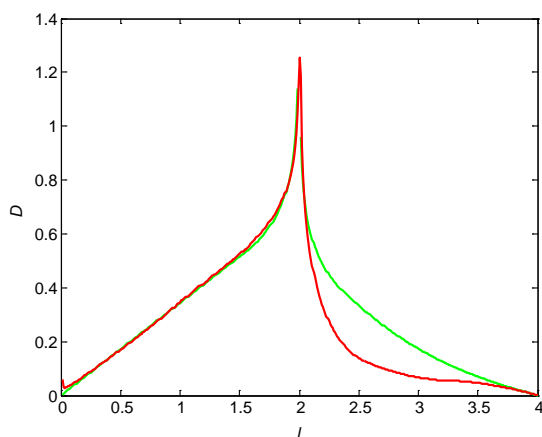


Figure 1: CLD for a capsule (hemisphere radius = 1, cylinder length = 2). red: MCS; green: our method.

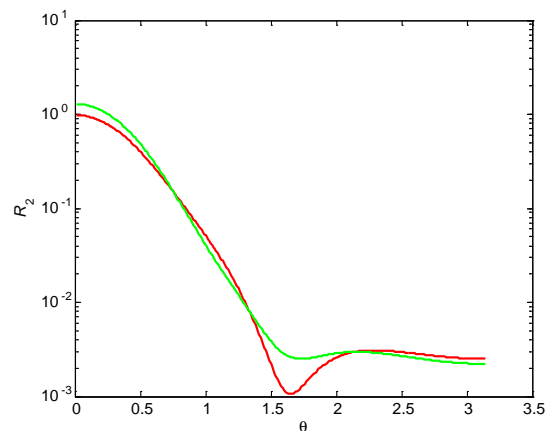


Figure 2: $\langle |R|^2 \rangle$ as a function of the scattering angle (rad) for a capsule ($R = 0.2 \mu\text{m}$, $H = 0.4 \mu\text{m}$). red: $D_l(l)$ from MCS; green: $D_l(l)$ from our method. $\lambda = 450 \text{ nm}$.

5. CONCLUSION

The methodology presented in this paper leads easily to an expression of the CLD that is needed for the scattering properties calculations. Improvements can be done by considering the interactions between singularities if any. This will be studied in the future.

REFERENCES

1. Kahnert, F. M., "Numerical methods in electromagnetic scattering theory," *J. Quant. Spectr. Rad. Transfer*, Vol. 79, 775–824, 2003.
2. Van de Hulst, H. C., *Light Scattering by Small Particles*, J. Wiley, New York, 1957.
3. Gille, W., *Particle and Particle Systems Characterization: Small-angle Scattering (SAS) Applications*, CRC Press, 2013.
4. Jacquier, S. and F. Gruy, "Application of scattering theories to the characterization of precipitation processes," *Light Scattering Reviews*, Vol. 5, 37–78, A. Kokhanovsky, Ed., Springer, 2010.
5. Kirste, R. and G. Porod, "Röntgenkleinwinkelstreuung an kolloiden systemen. Asymptotisches verhalten der streukurven," *Kolloid Zeitschrift & Zeitschrift für Polymere*, Vol. 184, 1–7, 1962.
6. Wu, H. and P. W. Schmidt, "Intersect distributions and small-angle X-ray scattering theory," *J. Appl. Cryst.*, Vol. 4, 224–231, 1971.
7. Wu, H. and P. W. Schmidt, "The relation between the particle shape and the outer part of the small-angle X-ray scattering curve," *J. Appl. Cryst.*, Vol. 7, 131–146, 1974.
8. Ciccariello, S., "Deviations from the Porod law due to parallel equidistant interfaces," *Acta Cryst.*, Vol. A41, 560–568, 1985.
9. Ciccariello, S. and A. Benedetti, "Parametrizations of scattering intensities and values of the angularities and of the interphase surfaces for three-component amorphous samples," *J. Appl. Cryst.*, Vol. 18, 219–229, 1985.
10. Ciccariello, S., "The leading asymptotic term of the small-angle intensities scattered by some idealized systems," *J. Appl. Cryst.*, Vol. 24, 509–515, 1991.
11. Sobry, R., J. Ledent, and F. Fontaine, "Application of an extended Porod law to the study of the ionic aggregates in telechelic ionomers," *J. Appl. Cryst.*, Vol. 24, 516–525, 1991.
12. Ciccariello, S., "Edge contributions to the Kirste-Porod formula: The truncated circular right cone case," *Acta Cryst.*, Vol. A49, 398–405, 1993.
13. Sobry, R., F. Fontaine, and J. Ledent, "Extension of Kirste-Porod's law in the case of angulous interfaces," *J. Appl. Cryst.*, Vol. 27, 482–491, 1994.
14. Ciccariello, S. and R. Sobry, "The vertex contribution to the Kirste-Porod term," *Acta Cryst.*, Vol. A51, 60–69, 1995.

A Study of Periodic Multilayered Structure in Fractional Dimension Space and Euclidian Space

M. J. Mughal¹ and Safiullah Khan²

¹COMSATS Institute of Information Technology, Islamabad, Pakistan

²Ghulam Ishaq Khan Institute of Engineering Sciences and Technology, Topi 23640, Pakistan

Abstract— In this paper, Transfer Matrix Method and modified Maxwell equations are used to find the general expressions for reflection and transmission coefficients of periodic multilayered structure. The structure is placed in D dimension space where D is integer for Euclidean space and non-integer for Fractional space. Characteristics of these structure are studied when an electromagnetic wave strikes on it at both normal and oblique incident angle. The final expressions are the function of frequency, dimension and incident angle. Numerical results for multilayered periodic strong chiral — strong chiral structure are presented. This study provides motivation to investigate the electromagnetic waves propagation in multilayered structures at fractional boundaries.

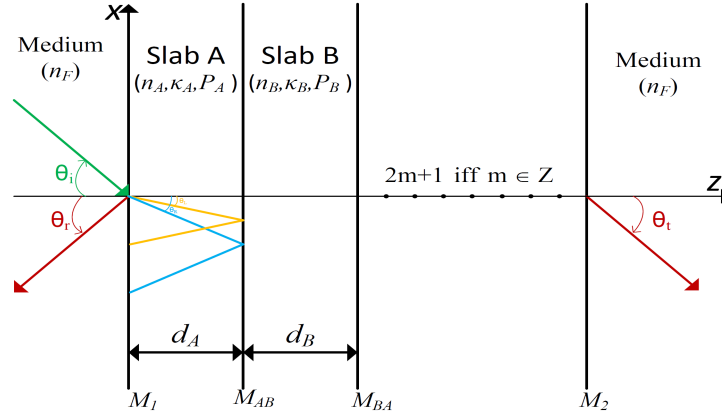
1. INTRODUCTION

Advances in the metamaterials (MTM) has significantly attracted the attention of researchers. Multilayered structures composed of composite materials are being widely used in applications such as antenna designing, lens designing, frequency selective surfaces etc. [1–3]. Since, metallic structures have losses associated with it, metamaterial structures are used to achieve desirable outcomes. Until recently, frequency, incident angle and constitutive parameters behaviour were studied but with the introduction of fractional calculus, effect of dimension can also be studied. Irregular surfaces, porous media, and complex structures can be modelled with fractional calculus [4]. In 1982, Mandelbrot introduced the concept of fractal for the first time [5]. Fractional calculus can be used to study the characteristics of homogenous models at fractal boundaries [6, 7]. It provides a way to introduce solutions of electromagnetic problems in fractional dimension space [8, 9]. In 1996, study of scalar wave equation was carried out using fractional integration and later analysis of source distributions which are equivalent to fractional dimension Dirac delta function [10, 11]. Therefore, a solution in D dimension space is required to understand the behaviour of the structures. Lately, solutions to plane wave, differential electromagnetic (EM) wave, cylindrical wave and spherical wave in D -dimension fractional space are developed in [4].

There are several types of metamaterials being used by researchers; single negative materials are those whose either permittivity or permeability is negative, double negative materials have both permittivity and permeability negative, materials whose image is non-superposable are called chiral materials. Chiral materials are further divided into chiral nihility and strong chiral materials; chiral nihility materials have permittivity ($\epsilon = 0$) and permeability ($\mu = 0$) equal to zero for certain range of frequencies and chirality is non-zero ($\kappa \neq 0$), when chirality to refractive index ratio is greater than unity the material is called strong chiral material (SC). In this paper SC–SC multilayered structure is placed in fractional space and euclidian space for study and analysis. In Section 2, model and formulation for n -layered periodic structure are discussed and expressions for reflected and transmitted fields are computed. In Section 3, numerical results for both the cases are presented and discussed followed by conclusion. Please note time dependency in this paper is taken as $e^{j\omega t}$ and is kept suppressed.

2. MODEL AND FORMULATION

A homogenous, non-dispersive periodic SC-SC multilayered structure is placed in D dimension space as shown in Figure 1. The width, refractive index, chirality and optical width of slab i are d_i , n_i , κ_i and $|n_i| d_i$, respectively where ($i = A, B$). The general incident, reflected and transmitted


 Figure 1: Five layered metamaterial structure placed in D dimension space.

fields in D ($2 \leq D \leq 3$) dimension are [4],

$$\mathbf{E}_i = [E_{i\parallel} (\hat{x} \cos \theta_i + \hat{z} \sin \theta_i) + E_{i\perp} \hat{y}] e^{-jk_F(-x \sin \theta_i)} (k_F z \cos \theta_i)^n \left[H_n^{(2)}(k_F z \cos \theta_i) \right], \quad (1)$$

$$\mathbf{H}_i = \frac{1}{\eta} [E_{i\parallel} \hat{y} - E_{i\perp} (\hat{x} \cos \theta_i + \hat{z} \sin \theta_i)] e^{-jk_F(-x \sin \theta_i)} (k_F z \cos \theta_i)^{nh} \left[H_{nh}^{(2)}(k_F z \cos \theta_i) \right], \quad (2)$$

$$\mathbf{E}_r = [E_{r\parallel} (\hat{x} \cos \theta_r - \hat{z} \sin \theta_r) + E_{r\perp} \hat{y}] e^{-jk_F(-x \sin \theta_r)} (k_F z \cos \theta_r)^n \left[H_n^{(1)}(k_F z \cos \theta_r) \right], \quad (3)$$

$$\mathbf{H}_r = \frac{1}{\eta} [-E_{r\parallel} \hat{y} + E_{r\perp} (\hat{x} \cos \theta_r - \hat{z} \sin \theta_r)] e^{-jk_F(-x \sin \theta_r)} (k_F z \cos \theta_r)^{nh} \left[H_{nh}^{(1)}(k_F z \cos \theta_r) \right], \quad (4)$$

$$\mathbf{E}_t = [E_{t\parallel} (\hat{x} \cos \theta_t + \hat{z} \sin \theta_t) + E_{t\perp} \hat{y}] e^{-jk_F(-x \sin \theta_t)} (k_F z \cos \theta_t)^n \left[H_n^{(2)}(k_F z \cos \theta_t) \right], \quad (5)$$

$$\mathbf{H}_t = \frac{1}{\eta} [E_{t\parallel} \hat{y} - E_{t\perp} (\hat{x} \cos \theta_t + \hat{z} \sin \theta_t)] e^{-jk_F(-x \sin \theta_t)} (k_F z \cos \theta_t)^{nh} \left[H_{nh}^{(2)}(k_F z \cos \theta_t) \right] \quad (6)$$

In the above equations subscript i , r , and t represent the incident, reflected and transmitted wave. Perpendicular and parallel component of the waves are represented by \perp and \parallel , respectively. Hankel function of the second kind and Hankel function of the first kind represents the forward travelling wave and backward travelling wave respectively and $n = \frac{|3-D|}{2}$ and $nh = \frac{|D-1|}{2}$ where D represents the dimension. Transfer Matrix Method (TMM) is applied on Equations (1)–(6) and electric and magnetic field expressions for strong chiral medium in [12], to compute field expressions on either side of the structure. The final expression is of the following form,

$$\begin{bmatrix} E_{i\parallel} \\ E_{i\perp} \\ E_{r\parallel} \\ E_{r\perp} \end{bmatrix} = [T] \begin{bmatrix} E_{t\parallel} \\ E_{t\perp} \end{bmatrix} \quad (7)$$

$$[T] = \begin{bmatrix} a_{11} & a_{12} \\ a_{21} & a_{22} \\ a_{31} & a_{32} \\ a_{41} & a_{42} \end{bmatrix} = [M_1][P_A][T_1]^m[M_2] \quad (8)$$

$$[T_1] = [M_{AB}][P_B][M_{BA}][P_A] \quad (9)$$

In Equations (8) and (9), $[P_A]$ and $[P_B]$ represents the propagation matrix, it includes the phase component of the wave. $[M_1]$, $[M_2]$, $[M_{AB}]$, and $[M_{BA}]$ represents matching matrix, it relates the fields on either side of the slab. All the propagation matrices and matching matrices are 4×4 except, $[M_2]$ whose size is 4×2 . Transfer matrix, $[T]$, relates the field on either side of the structure. The derived transfer matrix is for odd numbers of slabs. All the expressions computed are for D dimension (inserting integer value of D recovers classical results).

3. RESULTS

The expressions for reflected and transmitted fields are function of frequency (f), width (d), incident angle (θ_i), chirality (κ), and dimension (D). Figure 2 shows the reflectance and transmittance at oblique incidences for five layered structured composed of SC-SC alternating layers. It can be seen

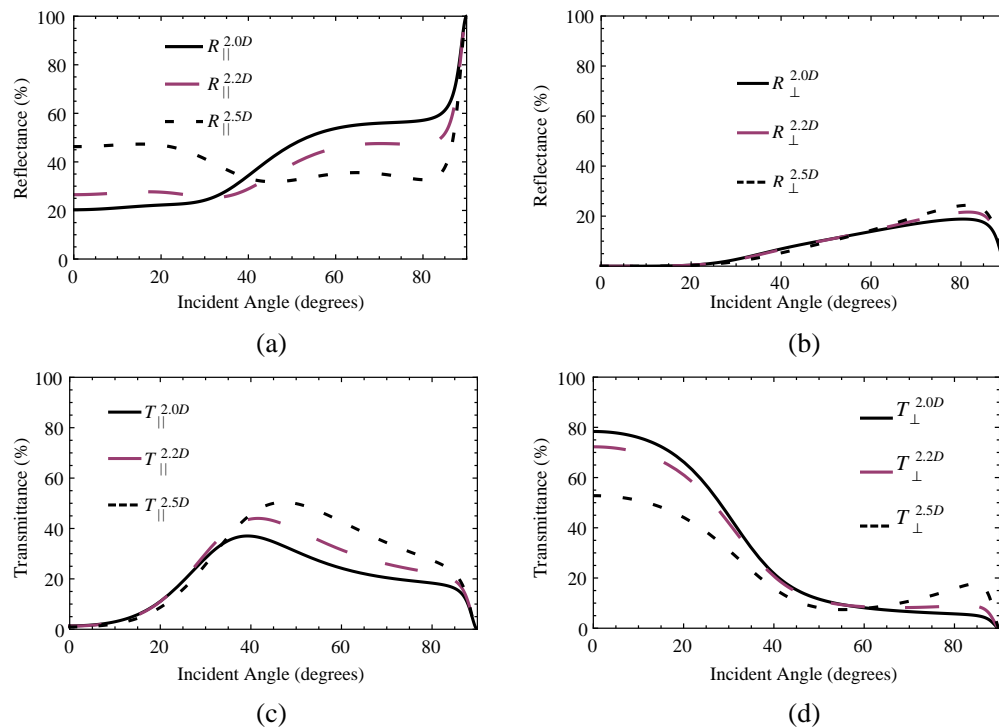


Figure 2: Reflectance and transmittance for five layered SC-SC structure. $n_A = 0.8$, $n_B = 0.6$, $\kappa_A = 1.2$, $\kappa_B = 1.0$, $|n_A|d_A = |n_B|d_B = \lambda_0/4$, $f/f_0 = 0.5$.

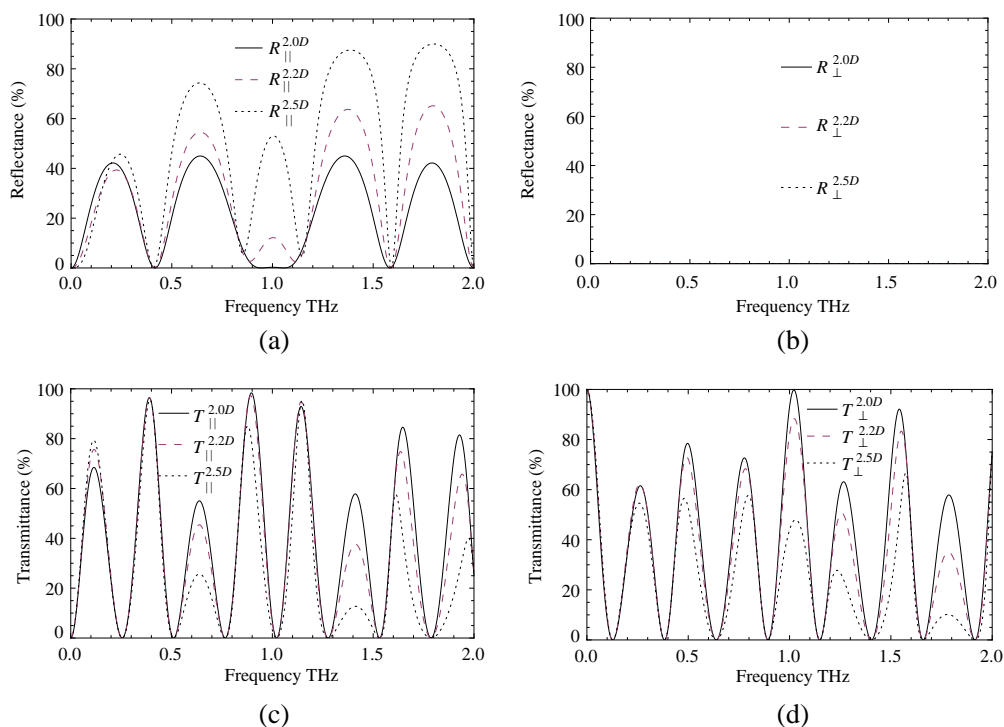


Figure 3: Reflectance and transmittance for five layered SC-SC structure. $n_A = 0.8$, $n_B = 0.6$, $\kappa_A = 1.2$, $\kappa_B = 1.0$, $|n_A|d_A = |n_B|d_B = \lambda_0/4$, $\theta_i = 0^\circ$.

in Figure 2(a), there is no significant power change in regions (0° – 30°) and (55° – 80°). Initially reflected power for $2.5D$ substrate is greater than $2.3D$ and $2.0D$ but after 40° , reflected power for $2.5D$ decreases and becomes lower than $2.3D$ and $2.0D$. Figure 2(b), shows that there is no significant difference in reflected power profile for perpendicular component of the wave. Figure 2(c), shows the transmitted power for parallel component of the wave. It can be seen that there is marginal difference of transmitted powers in (35° – 85°). The maximum transmitted power for $2.5D$ substrate structure is approximately 50% and it is 35% for $2.0D$ substrate. Figure 2(d), shows the transmitted power for the perpendicular component of the wave. At 0° transmitted power is approximately 78%, 72% and 53% for $2.0D$, $2.3D$ and $2.5D$ substrate, respectively. It means that polarization is rotated for the wave passing through all three types of substrate. Figure 3, shows the effect of frequency and dimension on the behavior of the five layered structure when a wave strike at normal incidence. It is seen in Figure 3(a) that the parallel component of the reflected power has bell-shaped windows for all substrates. At 1.0 THz, reflected power for $2.0D$, $2.3D$ and $2.5D$ are 0%, 10% and 55%, respectively. There is no perpendicular component of the reflected wave at 0° as shown in Figure 3(b), since only parallel component of the wave is incident. Figures 3(c) and 3(d), shows the behavior of transmitted component. Narrowbands with high transmitted power exists at regular intervals with power approximately equal to unity at 1.0 THz.

4. CONCLUSION

In the presented paper, the electromagnetic behavior of periodic multilayered structure when placed in fractional dimension space and integer dimension space is studied and discussed. Transfer Matrix Method is used to find the expressions for reflected and transmitted wave in D dimension space. These expressions are then numerically presented for analysis. All the numerical results satisfy the law of conservation of power. Inserting the integer value of D recovers the classical results. This study provides motivation to investigate the electromagnetic waves propagation in multilayered structures at fractional boundaries and waveguides filled with fractal media.

REFERENCES

1. Liu, C. H. and N. Behdad, "Tunneling and filtering characteristics of cascaded-negative metamaterial layers sandwiched by double-positive layers," *Journal of Applied Physics*, Vol. 111, 014906, 2012.
2. Sabah, C. and H. G. Roskos, "Design of a terahertz polarization rotator based on a periodic sequence of chiral-metamaterial and dielectric slabs," *Progress In Electromagnetics Research*, Vol. 124, 301–314, 2012.
3. Oraizi, H. and M. Afsahi, "Design of metamaterial multilayer structures as frequency selective surfaces," *Progress In Electromagnetics Research C*, Vol. 6, 115–126, 2009.
4. Zubair, M., M. J. Mughal, and Q. A. Naqvi, *Electromagnetic Fields and Waves in Fractional Dimensional Space*, 1st Edition, Springer, 2012.
5. Mandelbrot, B., *The Fractal Geometry of Nature*, Freeman, New York, 1982.
6. Hilfer, R., *Applications of Fractional Calculus in Physics*, World Scientific Publishing, 2000.
7. Sabatier, J., O. P. Agrawal, and J. A. Tenreiro Machado, *Advances in Fractional Calculus: Theoretical Developments and Applications in Physics and Engineering*, Springer, 2007.
8. Naqvi, Q. A. and A. A. Rizvi, "Fractional dual solutions and corresponding sources," *Progress In Electromagnetics Research*, Vol. 25, 223–238, 2000.
9. Lakhtakia, A., "A representation theorem involving fractional derivatives for linear homogeneous chiral media," *Microwave and Optical Technology Letters*, Vol. 28, No. 6, 385–386, 2001.
10. Engheta, N., "Use of fractional integration to propose some 'fractional' solutions for the scalar helmholtz equation," *Progress In Electromagnetics Research*, Vol. 12, 107–132, 1996.
11. Engheta, N., "On the role of fractional calculus in electromagnetic theory," *IEEE Antennas and Propagation Magazine*, Vol. 39, No. 4, 35–46, 1997.
12. Mughal, M. J., S. K. Marwat, N. Amin, and M. Omar, "Analysis of Periodic strong chiral-metamaterial structures as frequency selective surfaces and polarization rotators using transfer matrix method," *International Conference on Metamaterials and Photonic Crystals and Plasmonics*, 2014.

Electronic Counter-countermeasures in Bistatic Radars

Faran Awais Butt¹, Ijaz Haider Naqvi², and Madiha Jalil³

¹University of Management and Technology (UMT), Lahore, Pakistan

²Lahore University of Management Sciences (LUMS), Lahore, Pakistan

³University of Engineering and Technology (UET), Lahore, Pakistan

Abstract— Bistatic configuration of radars has become a topic of great interest for Electronic counter-countermeasures designers. The paper emphasized the need for bringing about a trend of employing bistatic radars in place of traditional monostatic radars which are no more useful under the hostile environment that is created by the electronic counter measures effect. It has been shown that noise and deception jamming can be countered using bistatic configuration of the radar system. Moreover, low observability of the target threat can also be dealt with using this configuration.

1. INTRODUCTION

Electronic counter measures and electronic counter-countermeasures are the two major types of electronic warfare that are always seem to be in competition with each other [1]. There has been a rapid increase in performance of both radar and electronic warfare since World War II [2]. Bi-static radars are gaining attention over the past decade because of its ECCM abilities [3]. Apart from the physical isolation of the system, most of the advantages of bi-static radar are because of the geometric properties of the system [4]. With the advancements in the ECM systems, there is a constant need to counter and hence nullify the effects of ECM and hence to make the radar capable of detection and localization of the target threat. Study of techniques in ECCM is promising [5]. Bistatic radar's history dates back to the earliest days of its invention [6]. Bistatic radar approach is not something which has to make a comeback in the radar technology, rather it has already a number of specialized applications in physics, wind measurements and by astronauts [7]. The important operation in passive bistatic processing is to keep apart the transmitter-to-receiver path and target-path (i.e., transmitter-to-target-to-receiver signals) [8]. Bistatic and multistatic radar configuration are promising areas of research which also require advances in many other areas as well [9]. There are a number of reasons which shows that the interests in multistatic configuration of radars will continue to grow [10, 11]. There is no doubt that a lot of research and development is in progress related to bistatic radars but still there are a lot of loopholes considering bistatic clutter [12]. MIMO radar which is more easily realized in bistatic configuration is a topic of great interest for radar designers interested in ECCM of radar systems. Nevertheless, considering this, there exist many engineering challenges that are needed to be addressed. Moreover, there has to be a better understanding of bistatic and multistatic radar cross section phenomenon [13]. MIMO radars have more degrees of freedom than typical monostatic radar. This enables improved angular resolution [14, 15], variable time energy management and improved parameter identification [16].

2. TRANSMIT POWER AND THE SIGNAL TO NOISE RATIO ANALYSIS

Figures 1 and 2 show the transmit power analysis of bistatic radar corresponding to max range product. For Fig. 1 baseline length has been set to 10km, the bistatic angle is 10 and RCS of the target is 20 dBsm whereas for Fig. 2, baseline length has been set to 2 km and the bistatic angle is 20 and RCS of the target is 10 dBsm. The figure shows if the RCS is reduced, greater transmitted power is required. Figures from 1 to 6 and 8 are drawn using [22].

Figures 3 and 4 show the signal to noise ratio analysis of bistatic radar corresponding to max range product. From these figures, it can be concluded that if the bistatic angle is increased, the corresponding SNR is reduced. The bistatic angle, i.e., positioning of transmitter and receiver has a big role to play in the overall working of the system.

3. RADAR CROSS SECTION ANALYSIS

The detection ability of the target is dependent upon a parameter which is the radar cross section. It describes the strength of the electromagnetic wave reflected from the target threat. RCS in terms

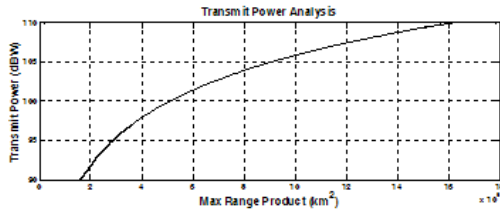


Figure 1: Transmit power analysis for Bistatic angle of 10 degrees and RCS of 20 dBsm.

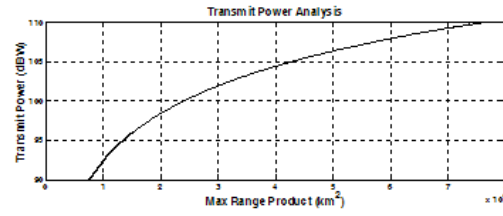


Figure 2: Transmit power analysis for Bistatic angle of 20 degrees and RCS of 10 dBsm.

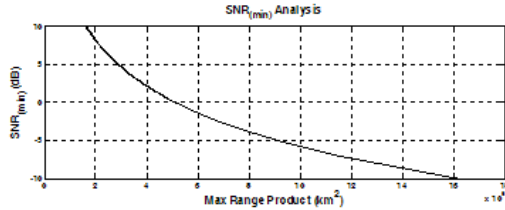


Figure 3: SNR analysis where angle is 10 and RCS of the target is 20 dBsm.

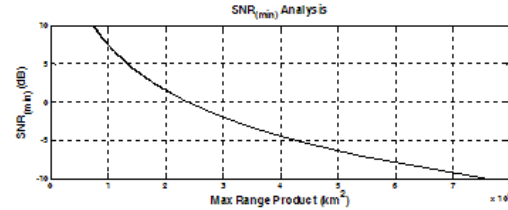


Figure 4: SNR analysis where angle is 20 and RCS of the target is 10 dBsm.

of electric field is given by [17].

$$\sigma = \lim_{r \rightarrow \infty} 4\pi r^2 \frac{|E_s|^2}{|E_I|^2} \quad (1)$$

Bistatic target RCS, denoted by σ_B is different from typical monostatic RCS. In the case of a small bistatic angle, the bistatic RCS is similar to the monostatic RCS: but, as the bistatic angle approaches 180° , the bistatic RCS becomes very large and can be approximated by [18].

$$\sigma_{B_{\max}} \approx \frac{4\pi A_t^2}{\lambda^2} \quad (2)$$

where λ is the wavelength and A_t is the target project area.

Power delivered to signal processor by the receiver's antenna is

$$P_R = \frac{P_t G_t G_r \lambda^2 \sigma_B}{(4\pi)^3 R_t^2 R_r^2 L_t L_r L_p} \quad (3)$$

The subscripts 't' and 'r' denote transmitter and receiver respectively. L_p is medium propagation losses and G is the gain of the antenna.

With a bistatic system, the energy is not scattered back directly but with an angle, β . The radar cross-section for scattering is dependent on this angle.

Bistatic radar range is written as

$$\sqrt{R_T R_R} = \left(\frac{P_t G_t G_r \sigma_B F_t^2 F_r^2 c^2}{(4\pi)^3 k T B D_2 L f^2} \right)^{1/4} \quad (4)$$

The subscripts 't' and 'r' denote transmitter and receiver respectively. σ_B is the bistatic radar cross-section. G is the gain of the antenna. F is the propagation factor. c is the velocity of light, k is Boltzmann's constant, T is the system noise temperature in K . DS is the signal-to-noise ratio required for detection, f is the frequency of the radar and L is the product of the losses.

Figure 5 shows the target RCS analysis of bistatic radar corresponding to max range product. The baseline length has been set to 10 km if the bistatic angle is set to 10° whereas, Fig. 6 shows the target RCS analysis of bistatic radar for the bistatic angle of 20° and baseline length has been set to 2 km. For a maximum range product of 4 km^2 , target RCS is 18 dBsm for Fig. 5 where as it is about 14 dBsm for the case where bistatic angle is greater, i.e., in Fig. 6. The beta angle is dependent upon the corresponding positioning of transmitter, receiver and the target. The liberty of deploying the transceiver system by taking into consideration the target threat gives an immense advantage to bistatic radar configuration as compared to the corresponding monostatic system.

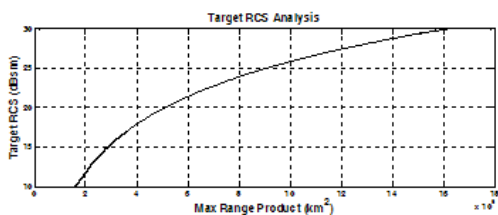


Figure 5: Target RCS analysis for Bistatic angle of 10° .

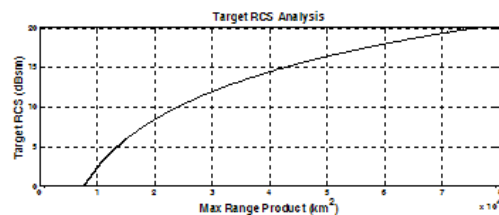


Figure 6: Target RCS analysis for Bistatic angle of 20° .

Low observable targets usually scatter in various directions where monostatic radar usually fails to detect. In such situations bistatic radar is far more probable for detecting such a target.

Figure 7 shows bistatic angle versus the radar cross section of a fuselage for an incidence angle of 30 degrees for radar's transmitted frequency of 2 GHz where, fuselage permittivity is 3.7 [23]. We can see that there is a range of angles where RCS is considerably greater and hence it would be easily detectable.

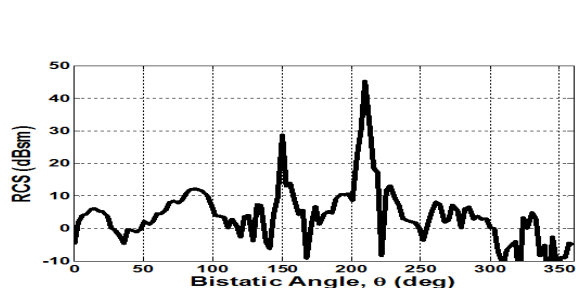


Figure 7: RCS vs. Bistatic angle.

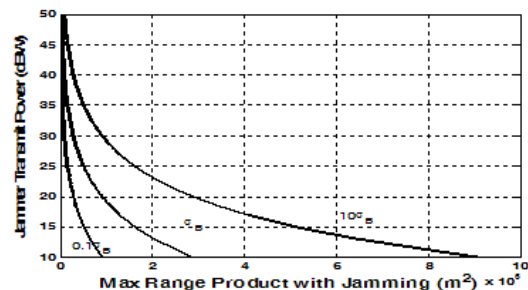


Figure 8: Jammer transmit power vs. max range product for jammer receiver range of 1 km.

The advancement in technology has enabled the radar designers to place the transmitter and receiver so much so that either of these can be even on ships or other carriers. The delocalization of transceiver system has enabled the designers to improve the detection abilities of the radar [19].

RCS reduction is achieved by shaping the target in a way that it does not scatter in the direction of transmitted signal. This shaping may reduce the RCS when looking at the front of a target using monostatic radar; however, it is often the case that the RF wave will scatter in a different direction, providing a large RCS in some “bistatic” direction [20].

A noise jammer typically radiates with a bandwidth that is wider than the radar receiver's. The effect is the raise in total power spectral density of the background noise in the receiver from N_0 to $N_0 + J_0$.

Where

$$J_0 = \frac{P_J G_J G_R F_J^2 \lambda^2}{(4\pi)^2 B_J R_J^2 L_J} \quad (5)$$

Under usual jamming conditions, jammers bandwidth is greater than receiver's noise bandwidth [21].

Figure 8 shows that as the RCS increases, jammer requires more transmit power for some value of maximum range product with jamming. Also, as the jammer receiver range is decreased, maximum range product is decreased for fixed values of jammer transmit power.

4. CONCLUSION

The paper has shown the advantages that the radar designers can exploit from a bistatic radar approach, courtesy of the geo placement of the distant receiver. Similarly bistatic approach allows simultaneous accomplishment of ECCM techniques which improves the probability of detection. Bistatic radars can also give the liberty to designers of employing MIMO functionality by making an intelligent transceiver system on both the sites. Low observable stealthy targets which scatter the incoming transmitted wave in various directions can be best dealt with if there is a corresponding

receiver or a transceiver system in best probable direction. Moreover for such targets, there is a range of aspect angles which can be exploited by using bistatic system. In addition to this, jammers which target the antenna sight of the radar for a typical monostatic system, no longer remains effective if there is a receiver at a distant sight.

REFERENCES

1. Butt, F. A. and M. Jalil, "An overview of electronic warfare in radar systems," *International Conference on Technological Advances in Electrical, Electronics and Computer Engineering (TAECE)*, IEEE, 2013.
2. Johnston, S. L., "World War 2 ECCM history," *IEEE Int. Radar Conf. Rec.*, 5.2–5.7, May 6–9, 1985.
3. Butt, F. A., I. H. Naqvi, and A. I. Najam, "Radar ECCM against deception jamming: A novel approach using bi-static and mono-static radars," *2012 15th International on Multitopic Conference (INMIC)*, IEEE, 2012.
4. Jackson, M. C., "The geometry of bi-static radar systems," *IEE Proceedings*, Vol. 133, Pt. F, No.7, Dec. 1986.
5. Guo, J. M., J. X. Li, and Q. Lv, "Survey on radar ECCM methods and trends in its development," *International Conference on Radar*, 2006.
6. Griffiths, H. D., "New directions in bistatic radar," *IEEE Radar Conference 2008, RADAR'08*, IEEE, 2008.
7. Willis, N. J. and H. D. Griffiths, eds., *Advances in Bistatic Radar*, SciTech Publishing Inc., Raleigh, NC, 2007, ISBN 1891121480.
8. Hack, D. E., et al., "Detection in passive MIMO radar networks," 1-1, 2014.
9. Griffiths, H., "Developments in bistatic and networked radar," *2011 IEEE CIE International Conference on Radar (Radar)*, Vol. 1, IEEE, 2011.
10. Willis, N. J. and H. D. Griffiths, eds., *Advances in Bistatic Radar*, SciTech Publishing Inc., Raleigh, NC, 2007, ISBN 1891121480.
11. Griffiths, H. D., "From a different perspective: Principles, practice and potential of bistatic radar," *Proc. International Conference RADAR 2003*, 1–7, Keynote Presentation, Adelaide, Australia, Sep. 3–5, 2003.
12. Griffiths, H. D., W. A. Al-Ashwal, K. D. Ward, R. J. A. Tough, C. J. Baker, and K. Woodbridge, "Measurement and modelling of bistatic radar seaclutter," *IET Radar Sonar and Navigation*, Vol. 4, No. 2, 280–292, Mar. 2010.
13. Haimovich, A. M., R. S. Blum, and L. J. Cimini, "MIMO radar with widely separated antennas," *Signal Processing Magazine*, Vol. 25.1, 116–129, IEEE, 2008.
14. Robey, F. C., S. Coutts, D. Weikle, J. C. McHarg, and K. Cuomo, "MIMO radar theory and experimental results," *38th Asilomar Conference on Signals, Systems and Computers*, 300–304, Nov. 2004.
15. Bekkerman, I. and J. Tabrikian, "Target detection and localization using MIMO radars and sonars," *IEEE Trans. Signal Processing*, Vol. 54, 3873–3883, Oct. 2006.
16. Xu, L., J. Li, and P. Stoica, "Adaptive techniques for MIMO radar," *14th IEEE Workshop Sensor Array and Multi-channel Processing*, 258–262, Waltham, MA, Jul. 2006.
17. Liu, Y., S.-X. Gong, and D.-M. Fu, "Theoretic study of antenna scattering," *ACTA Electronica Sinica*, Vol. 33, No. 9, Jun. 2004.
18. Mahafza, B. R., *Radar Systems Analysis and Design Using MATLAB*, CRC Press, 2000.
19. Kassem, M. J. B. and A. Khenchaf, "Bistatic mapping radar BISAR," *OCEANS 2003 Proceedings*, Vol. 5, IEEE, 2003.
20. *Principles of Modern Radar: Basic Principles*, SciTech Pub., 2010.
21. Willis, N. J., *Bistatic Radar*, SciTech Publishing, 2005.
22. Teo, C. L., "Bistatic radar system analysis and software development," *Naval Postgraduate School Monterey CA*, 2003.
23. Chatzigeorgiadis, F. and D. C. Jenn, "A MATLAB physical-optics RCS prediction code," *IEEE Antennas and Propagation Magazine*, Vol. 46.4, 137–139, 2004.

The Nonlinear Fiber-optic Channel: Modeling and Achievable Information Rate

E. Forestieri and M. Secondini

TeCIP Institute, Scuola Superiore Sant'Anna, Italy

Abstract— The problem of evaluating the channel capacity of a nonlinear fiber-optic system is reviewed. After properly defining the nonlinear fiber-optic channel, we consider a few alternative models and discuss their suitability for system design and performance evaluation. It is shown that using an accurate model can allow devising modulation and detection schemes providing higher robustness to nonlinear effects than those obtainable by simpler models.

1. INTRODUCTION

The evaluation of channel capacity in nonlinear fiber-optic systems is still an open issue. The main difficulty is due to the unavailability of an exact and mathematically tractable channel model. In fact, most of the results obtained so far either refer to highly simplified models or provide loose bounds to the capacity [1–15]. A useful and practical approach to lower bound the capacity is that of evaluating the achievable information rate for an arbitrarily fixed input distribution (modulation format) and a suboptimal decoder optimized for an approximate version of the channel (mismatched decoding). In this context, the capacity problem can be seen as a joint optimization of the achievable information rate over both the input distribution and the channel model [10, 15, 18]. It is thus clear that finding a good channel model for the optical fiber is the first step to design more efficient systems and derive tight bounds to the capacity.

According to the popular Gaussian noise (GN) model [19, 20], nonlinearity is simply modeled as additive white Gaussian noise: it cannot be compensated for, but it can be easily accounted for in the evaluation of channel capacity, leading to the conclusion that capacity vanishes at high powers. This result, however, is not supported by theory and is contradicted by some counter examples. Though it is now clear that the GN model has some limitations [15, 21, 22], it is still unclear whether these limitations are only of theoretical interest or do have a practical value.

The choice of the right model depends on the problem at hand: while numerical methods, such as the split-step Fourier method (SSFM) [23], are suitable for compensating deterministic nonlinearity through the digital backpropagation (DBP) technique [24], analytical approximations — based, for instance, on perturbation methods or Volterra series expansion — are more suitable for modeling stochastic effects such as signal noise-interaction and inter-channel nonlinearity [13, 25, 29]. Finally, an exact analytical model, accounting only for dispersion and nonlinearity, can be obtained by employing the inverse scattering (nonlinear Fourier) transform (IST) [30]. It is still unclear, however, whether this approach is competitive with the split-step Fourier method in terms of computational complexity and whether it can be used for modeling stochastic nonlinear effects.

By employing the aforementioned models, it is possible to show that the optimum modulation and detection strategies differ from those designed according to the GN model and typically used in fiber-optic systems. Therefore, in the second part of the paper, we consider different modulation and detection schemes aimed at providing higher robustness to nonlinear effects and investigate their actual advantage over GN-model-based strategies in terms of achievable information rate. Depending on the considered scenario, a non-negligible improvement is achieved. However, at high powers, the gap between lower and upper bounds to channel capacity remains large and does not allow to establish whether capacity is bounded or not. Possible directions for reducing the gap are finally discussed.

2. THE OPTICAL FIBER CHANNEL

In this section, we define the optical fiber channel and shortly discuss and compare different channel models available in the literature. We consider a generic multi-span optical fiber link, employing single-mode optical fibers and optical amplifiers exactly recovering the attenuation. Neglecting polarization effects (whose impact is shortly discussed at the end of this section) and accounting for attenuation/amplification, group velocity dispersion, Kerr nonlinearity, and amplified spontaneous emission (ASE) noise, the nonlinear evolution equation that governs the propagation of the

normalized complex envelope of the optical signal $u(z, t)$ through the optical fiber channel is

$$\frac{\partial u}{\partial z} = j \frac{\beta_2}{2} \frac{\partial^2 u}{\partial t^2} - ja(z) \gamma |u|^2 u + n(z, t) \quad (1)$$

where β_2 is the group-velocity-dispersion parameter, γ is the nonlinear coefficient, $a(z)$ accounts for variations of the average signal power along the link due to attenuation or amplification¹, and $n(z, t)$ is a forcing term that represents noise injected by optical amplifiers. The optical fiber channel can be considered as a waveform channel that, given the input waveform $u(0, t)$, produces the output waveform $u(z, t)$. In order to model and characterize the channel, it is customary to resort to a discrete-time channel model. This can be done by making some assumptions on the modulation and demodulation stages at the input and output of the channel, respectively. This assumptions usually corresponds to some constraints (e.g., bandwidth constraints) on the possible waveforms and have, therefore, an impact on the capacity of the resulting discrete-time channel.

We start by describing a single-user system (often referred to as single-channel system), in which only one user has access to the optical fiber. At the modulation stage, we assume that the input waveform $u(0, t)$ is strictly band-limited with low-pass bandwidth B , which is equivalent to say that the channel input can be represented by the sequence of symbols $\mathbf{x} = \{x_1, \dots, x_N\}$, which are mapped at rate $1/T = 2B$ onto the continuous waveform according to

$$u(0, t) = \sum_{k=1}^N x_k g(t - kT) \quad (2)$$

where $g(t) = \text{sinc}(2Bt)$. Because of the nonlinearity of (1), the bandwidth of the output waveform can be wider than B . Therefore, as opposed to the case of a linear channel, a demodulator with bandwidth B is not enough to provide, in general, a sufficient statistic. Nevertheless, in order to obtain a discrete-time representation of the output and a practical detection scheme, we assume that also the demodulator is band-limited, with a low-pass bandwidth ηB , where $\eta \geq 1$ is a parameter that accounts for a possible spectral broadening of the waveforms [31]. In principle, η can be set arbitrarily large to obtain a sufficient statistic. However, this is not practical and we will rather consider η as a technological constraint on the analog demodulator bandwidth that limits the achievable information rate on the channel. Thus, the received waveform $u(L, t)$ is filtered by a low-pass filter with transfer function $H(f) = \mathcal{F}\{h(t)\} = \text{rect}(f/(2\eta B))$ and sampled at rate $2\eta B$ to obtain the output samples $\mathbf{y} = \{y_1, \dots, y_{\eta N}\}$. The equivalent low-pass model of the system is represented in Fig. 1(a), where $G(f) = \mathcal{F}\{g(t)\}$.

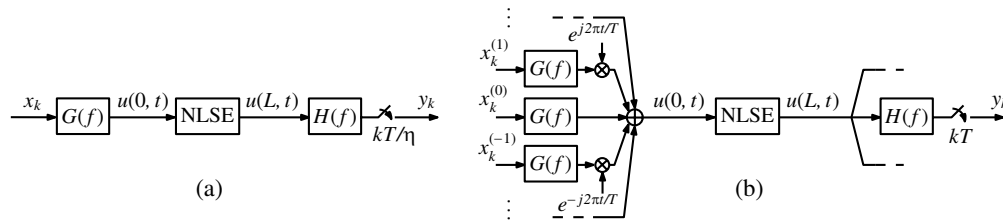


Figure 1: Equivalent low-pass system model: (a) single-user, (b) multi-user.

For the multi-user scenario, we consider WDM as the most practical (and widely employed) multiplexing technique. In this case, the input waveform is obtained by multiplexing different waveforms generated by different users according to (see Fig. 1(b))

$$u(0, t) = \sum_{\ell=-M}^M \sum_{k=1}^N x_k^{(\ell)} g(t - kT) e^{j2\pi \ell t/T} \quad (3)$$

where $\mathbf{x}^{(\ell)} = \{x_1^{(\ell)}, \dots, x_N^{(\ell)}\}$ is the sequence of symbols transmitted by user ℓ and $2M + 1$ is the number of users. We look at this system from the perspective of the central user ($\ell = 0$), assuming

¹For a link with K spans of same length D , it would be $a(z) = \sum_{k=0}^{K-1} e^{-\alpha(z-kD)} [u(z-kD) - u(z-kD-D)]$, where α is the attenuation parameter and $u(x)$ the unit-step function.

that the other users are out of his control and are a source of disturbance. In the sequel, by letting $\mathbf{x}^{(0)} = \mathbf{x}$, this scenario is formally described as in the single-user case, but replacing (2) with (3). Moreover, we set $\eta = 1$ since we assume that each user can demodulate only its “own” frequency band.

Equations (1)–(3) define the described channels only in an implicit way, as they do not provide an explicit expression of the output \mathbf{y} given the input \mathbf{x} . Such an explicit knowledge is fundamental when dealing with communication and information theory problems, such as system design or evaluation of performance and information theoretical limits. We distinguish between two different types of channel models: a deterministic model, which solves the propagation Equation (1) when all the involved quantities are deterministic; and a stochastic model, which provides the conditional distribution $p(\mathbf{y}|\mathbf{x})$ of the output given the input. Usually, the former is just a part of the latter. For instance, statistics of the stochastic model can be represented by collecting many random realizations obtained from the deterministic model; or a specific deterministic solution (e.g., noise free) can be part of the stochastic model when considering a perturbation approach. The deterministic model can be important even by itself, for instance to compensate for nonlinear effects through digital backpropagation.

Unfortunately, even in the deterministic case, Equation (1) cannot be exactly solved. However, it can be approximated with arbitrary accuracy by numerical methods. The SSFM is the most used one and allows to trade off between accuracy and complexity by selecting the step size. When neglecting the noise term, and assuming a constant power along the link (e.g., loss exactly compensated by distributed amplification), Equation (1) is exactly integrable by the IST method, which is the analogous of the Fourier transform for nonlinear systems. The optical waveform $u(z, t)$ is represented in the spectral domain by means of a set of scattering data, whose propagation is governed by a simple linear equation. While the propagation step is trivial, the operations of direct and inverse scattering (going from time domain to spectral domain and back) are quite involved compared to direct and inverse Fourier transform. Their numerical implementation poses many issues in terms of accuracy and complexity and is a subject of current research [32, 33]. Perturbation methods can also be used to solve (1) [13, 26–29]. Formally, an approximate (zeroth-order) solution is found by setting $\gamma = 0$ in (1), and then expressing the exact solution as a power series of γ , whose coefficients are evaluated by substituting the power series back into (1).

In the deterministic case, the most relevant issue is the required computational complexity to achieve a prescribed accuracy. As mentioned before, the SSFM is probably the most effective numerical approach in this sense. Perturbation methods and Volterra series provide explicit finite-order solutions, but have a limited accuracy (at a given order) and a higher computational complexity than SSFM when used to describe the whole link. Also the IST, so far, does not offer significant advantages over the SSFM in terms of computational complexity, even if more efficient algorithms are being developed. In terms of accuracy and complexity, the most promising approach seems to be that of combining perturbation methods with the SSFM approach to obtain an enhanced SSFM [34]: the idea is that of keeping the SSFM approach of dividing the fiber into many (dispersive and nonlinear) steps, but using perturbation methods to increase the accuracy of each step. In fact, through this approach, an experimental implementation of DBP with a reasonably low complexity (comparable to a conventional frequency-domain dispersion equalizer) has been demonstrated [35], showing that DBP is a feasible processing strategy.

3. ACHIEVABLE INFORMATION RATE

The evaluation of channel capacity [36], both for the single-user or multi-user scenario described in the previous section, is still an open issue, mainly because of the unavailability of an exact stochastic model $p(\mathbf{y}|\mathbf{x})$. In fact, even the information rate $I(\mathbf{X}; \mathbf{Y})$ for a given input distribution $p(\mathbf{x})$ is hard to evaluate without explicit knowledge of $p(\mathbf{y}|\mathbf{x})$. In this case, it is useful to resort to the concept of mismatched decoding and introduce the following auxiliary-channel lower bound [16–18]

$$\hat{I}(\mathbf{X}; \mathbf{Y}) \triangleq \lim_{N \rightarrow \infty} \frac{1}{N} E \left\{ \log \frac{q(\mathbf{y}|\mathbf{x})}{q_P(\mathbf{y})} \right\} \leq I(\mathbf{X}; \mathbf{Y}) \quad (4)$$

In (4), $q(\mathbf{y}|\mathbf{x})$ and $q_P(\mathbf{y})$ are, respectively, the conditional distribution for an arbitrary auxiliary channel and the output distribution obtained by connecting input (with distribution $p(\mathbf{x})$) to the same auxiliary channel. Expectation $E\{\cdot\}$, on the other hand, is taken with respect to the distribution $p(\mathbf{x})p(\mathbf{y}|\mathbf{x})$ of the real channel. The importance of the quantity defined in (4) is in its

properties, which hold for any real and auxiliary channel: it is a lower bound to $I(\mathbf{X}; \mathbf{Y})$ on the real channel; it is achievable by the maximum *a posteriori* probability (MAP) detector designed for the selected auxiliary channel; and it can be simply evaluated through simulations [17, 18] (the expectation with respect to $p(\mathbf{x})p(\mathbf{y}|\mathbf{x})$ can be computed by averaging over many realizations, without explicit knowledge of $p(\mathbf{y}|\mathbf{x})$). In the following, we will refer to (4) as the achievable information rate (AIR) for a given input distribution and mismatched decoder. According to this definition, it becomes clear what is the role of the approximated channel models introduced in the previous section: they provide the auxiliary-channel distribution $q(\mathbf{y}|\mathbf{x})$, which is sufficient to evaluate the corresponding AIR and to design a detector to achieve it. The actual information rate (and the optimum detector) is therefore obtained through a maximization of the AIR over all possible channel models. Finally, channel capacity is obtained as a maximization of the information rate over all possible input distributions $p(\mathbf{x})$ [36]. In the following, we will focus on the first maximization step (over channel models), assuming a fixed input distribution $p(\mathbf{x})$. This will provide us with different AIRs, corresponding to different lower bounds to the information rate (and, hence, to channel capacity). Moreover, in the multi-user scenario, we will assume that all users transmit with same input distribution and power (corresponding to behavioral model c in [37]).

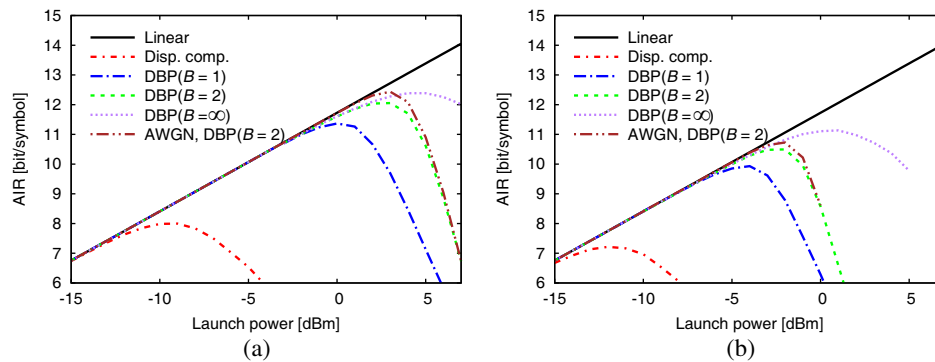


Figure 2: AIR for a single-channel system with different demodulation and detections: (a) standard fiber ($D = 17$ ps/nm/km); (b) low-dispersion fiber ($D = 2$ ps/nm/km).

For a single-user scenario, we consider an equivalent low-pass bandwidth $B = 25$ GHz, corresponding to an optical bandwidth of 50 GHz and a symbol rate of $1/T = 50$ GBd, and assume that the elements of \mathbf{x} are i.i.d. Gaussian symbols (the capacity-achieving distribution in the absence of nonlinear effects). The optical fiber link is a 1000 km dispersion-unmanaged link with ideal distributed amplification (the distributed gain exactly equals fiber loss, such that $a(z) = 1$, and the spontaneous emission factor is set to 1). The transmission fiber is a single-mode fiber with attenuation coefficient $\alpha = 0.2$ dB/km and nonlinear coefficient $\gamma = 1.27$ W⁻¹km⁻¹. Polarization effects are neglected, such that the propagation of the complex envelope is governed by (1). Two different values of the dispersion coefficients are considered: $D = 17$ ps/nm/km (a standard fiber) and $D = 2$ ps/nm/km (a low-dispersion fiber). Figs. 2(a) and (b) show the corresponding AIRs, obtained by using different receivers optimized for different approximated channel models. The first receiver is designed by completely neglecting nonlinear effects, i.e., assuming that the received signal is affected only by dispersion and AWGN. The output samples \mathbf{y} are obtained from the received waveform $u(L, t)$ by means of the demodulation scheme shown in Fig. 1, with $\eta = 1$ (which, in the absence of nonlinear effects, provides a sufficient statistic). After linear dispersion compensation, they are finally sent to a MAP detector optimized for the AWGN channel. The second receiver has the same demodulation bandwidth ($\eta = 1$) of the first one, but employs DBP² in place of linear dispersion compensation to compensate for deterministic nonlinear effects. After DBP (which employs

²The implementation of DBP requires setting some parameters which affect its numerical accuracy and complexity, namely, the number of steps along the propagation direction, the sampling rate, the number of samples in each processed block, and the number of overlapping samples — the last two parameters being required to employ the overlap-and-save algorithm to process long waveforms. Given the demodulation bandwidth, we consider the best possible implementation of DBP in terms of accuracy, without caring for complexity. Thus, all the aforementioned parameters are increased until no further accuracy improvements are observed. In particular, for what concerns sampling rate, though the signal after the demodulation filter is strictly band limited to a bandwidth ηB and completely represented by samples \mathbf{y} taken at rate η/T , the nonlinear processing of DBP may require a higher sampling rate to minimize numerical errors. Thus, digital resampling is employed to achieve the required sampling rate.

oversampling), samples are filtered again by an ideal rectangular filter of bandwidth B , resampled at symbol rate $1/T$, and sent to the MAP detector for the AWGN channel. The third receiver is similar to the second one, but with a wider demodulation bandwidth ($\eta = 2$) to account for spectral broadening during propagation. Finally, the fourth receiver assumes no bandwidth limitation in the demodulator (in practice, the demodulation bandwidth is increased until no further improvements of the AIR are observed). For comparison, we report also the AIR on the linear ($\gamma = 0$) channel (which is obtained with any of the previous receivers and equals the Shannon capacity of the AWGN channel) and the AIR for the third receiver ($\eta = 2$), when signal-noise interaction is artificially removed by injecting all the ASE noise at the receiver (after DBP). It can be observed that, depending on the approximated model considered to optimize the detector, different AIRs are obtained. The most relevant improvement is obtained by including DBP at the receiver (more than 3 bit/symbol for both dispersion values). Also doubling the bandwidth of the demodulator provides a relevant improvement (more than 1 bit/symbol). However, an additional increase of the bandwidth can provide only a marginal improvement, since the effect of signal-noise interaction becomes dominant. In order to address the problem of signal-noise interaction, a more accurate channel model should be considered, as done in [31] or [38], for instance. However, this would be irrelevant when neglecting spectral broadening ($\eta = 1$) and only slightly beneficial (as shown in the figures) when accounting for spectral broadening up to $\eta = 2$. Similar results are obtained for both dispersion values, though all the curves are shifted toward lower powers and lower AIRs when reducing dispersion. The problem of signal-noise interaction can be well addressed at zero dispersion [4]. In this case, nonlinearity is instantaneous and affects only the phase of the optical signal, while the amplitude, being unaltered, remains a reliable information carrier at any power. As a result, it can be demonstrated that channel capacity grows unbounded at zero dispersion [4], provided that an unlimited demodulator bandwidth is considered to account for a severe spectral broadening. It would be interesting (though, perhaps, not of practical value) to understand if a similar result can be extended also to the case of non-zero dispersion.

As a multi-user scenario, we consider exactly the same modulation, bandwidth, and link configurations considered in the single-user scenario, assuming that three users ($M = 1$) are present and transmit with same power and distribution. Fig. 3 shows the AIRs obtained (for the central user) by considering three different receivers optimized according to different approximated channel models. A standard ($D = 17$ ps/nm/km) and low-dispersion ($D = 2$ ps/nm/km) fiber are considered in Fig. 3(a) and (b), respectively. As in the first receiver is designed by completely neglecting nonlinear effects (i.e., assuming that the received signal is affected only by dispersion and AWGN) and the second receiver by replacing linear dispersion compensation with DBP. On the other hand, in this scenario, we do not consider wider demodulation bandwidths. Finally, the third receiver is optimized according to the FRLP model [13, 15] and is, therefore, capable of partially mitigating the effect of inter-channel nonlinearity. In particular, a Kalman equalization strategy is employed in [39], though similar results can be obtained through a simpler detection strategy when employing multi-carrier modulation [40]. In this case, compared to the single-user scenario, the channel seen by the central user is impaired also by inter-channel nonlinearity. As a result, the AIRs obtained by the first receiver (optimized for a linear channel) are slightly lower than in the single-user scenario. This is due to the fact that deterministic intra-channel nonlinearity and inter-channel nonlinearity

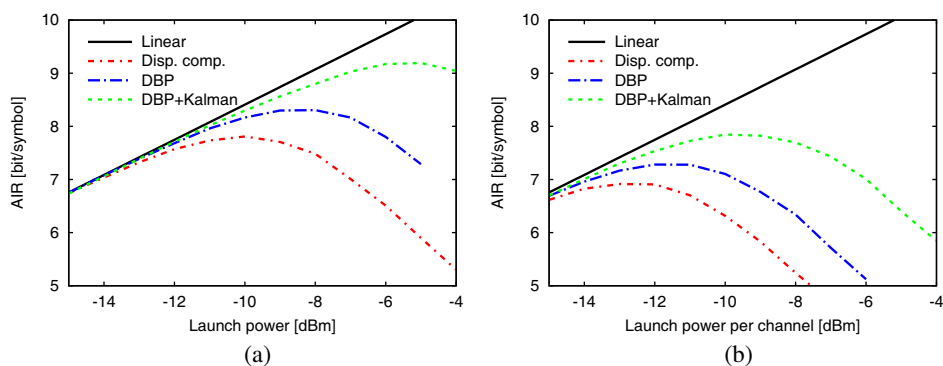


Figure 3: AIR for a WDM system with different demodulation and detections: (a) standard fiber ($D = 17$ ps/nm/km); (b) low-dispersion fiber ($D = 2$ ps/nm/km).

have a similar impact. On the other hand, the AIRs obtained by the second receiver (using DBP) are much lower as, in this case, inter-channel nonlinearity are dominant compared to spectral broadening and signal-noise interaction effects. In fact, only ~ 0.5 bit/symbol of AIR is gained by using DBP on the standard fiber and slightly less (~ 0.4 bit/symbol) on the low-dispersion fiber. On the other hand, a larger gain (an additional ~ 1 bit/symbol on the standard fiber and ~ 0.6 bit/symbol on the low-dispersion fiber) is obtained by designing the receiver according to a more accurate channel model that accounts also for inter-channel nonlinearity. It is worth noting that these gains are obtained by keeping the demodulator bandwidth limited to B , which is the practical constraint imposed for this scenario. In fact, higher gains could be obtained by performing DBP on a wider bandwidth (including the frequency bands assigned to the other users and, therefore, compensating also for inter-channel nonlinearity). In this case, signals from many users can be seen as originated and demodulated by a single super-user (constituting a super-channel, according to a common definition adopted in the literature), and the obtained results still hold, provided that B is the overall bandwidth of the super-user, while the remaining users are out of his control.

4. DISCUSSION AND CONCLUSION

The main message of this work is that an accurate modeling of the nonlinear optical fiber channel is fundamental to evaluate its capacity and design efficient communication systems that can approach such an ultimate theoretical limit. Even though simple models, such as the popular GN model, have proved accurate to predict the performance of conventional systems over the nonlinear optical fiber channel, they do not capture all the characteristics of the channel and are inadequate to study novel modulation and detection strategies that can deal with nonlinear effects and outperform conventional systems. In fact, by modeling nonlinear effects as AWGN, the GN model correctly predicts their impact on conventional systems, but also predicts that they cannot be compensated for or mitigated. On the other hand, we have shown that, by optimizing the receiver according to more accurate models, it is possible to outperform conventional systems and achieve higher information rates. A simple and well known example is that of DBP: even if deterministic intra-channel nonlinearity can be modeled as AWGN for what concerns its impact on conventional systems, it is easy to find out that it can be compensated for by employing a more accurate model (e.g., the SSFM for implementing DBP). In the same way, a proper model can help mitigating other nonlinear effects which, at first sight, might look like AWGN. This is the case, for instance, of inter-channel nonlinearity or signal-noise interaction.

The analysis and results presented in this work are based on some simplifying assumptions. First of all, single-polarization signals are considered and polarization effects are neglected. This is not realistic in practical systems and some care should be taken to extend the analysis to dual polarization systems (through the Manakov equation) and include polarization effects such as polarization mode dispersion. Nevertheless, the main message remains true and, in fact, some examples of DBP and mitigation of inter-channel nonlinearity and signal-noise interaction for dual polarization systems can be found also in the literature. Another important assumption is that of ideal distributed amplification. This is “less unrealistic”, as this scenario can be approached at will by employing Raman amplification and/or reducing amplifier spacing. Nevertheless, attenuation plays an important role in determining the dynamics of inter-channel nonlinearity and can significantly reduce the effectiveness of mitigation strategies [15, 29]. Finally, we have considered only three users (channels) in our multi-user scenario to speed up the simulations. This is, however, only a minor issue since the presence of other (more distant) channels has only a small additional impact on the information rate, especially when considering mitigation strategies, which become more effective on more distant channels [39].

The capacity problem remains open. In this work, we have addressed the problem from a receiver perspective, trying to maximize the achievable information rate for a given input modulation by acting on the detection strategy. Though there is still margin for improvement in this sense, we believe that more significant gains (and tighter lower bounds to capacity) can be achieved by removing the assumption of Gaussian i.i.d. input symbols and optimizing the input distribution.

ACKNOWLEDGMENT

This work was supported in part by the Italian Ministry for Education University and Research (MIUR) under the FIRB project COTONE

REFERENCES

1. Mitra P. P. and J. B. Stark, “Nonlinear limits to the information capacity of optical fiber communications,” *Nature*, Vol. 411, No. 6841, 1027–1030, 28 Jun. 2001.
2. Narimanov, E. E. and P. Mitra, “The channel capacity of a fiber optics communication system: Perturbation theory,” *J. Lightwave Technol.*, Vol. 20, No. 3, 530–537, Mar. 2002.
3. Ho, K.-P. and J. M. Kahn, “Channel capacity of WDM systems using constant-intensity modulation formats,” *Proc. Opt. Fiber Commun. (OFC)*, 731–733, paper ThGG85, 2002.
4. Turitsyn, K. S., S. A. Derevyanko, I. V. Yurkevich, and S. K. Turitsyn, “Information capacity of optical fiber channels with zero average dispersion,” *Phys. Rev. Lett.*, Vol. 91, No. 20, paper 203901, Nov. 2003.
5. Djordjevic, I., B. Vasic, M. Ivkovic, and I. Gabitov, “Achievable information rates for high-speed long-haul optical transmission,” *J. Lightwave Technol.*, Vol. 23, No. 11, 3755–3763, Nov. 2005.
6. Taghavi, M. H., G. C. Papen, and P. H. Siegel, “On the multiuser capacity of WDM in a nonlinear optical fiber: Coherent communication,” *IEEE Trans. Inform. Theory*, Vol. 52, No. 11, 5008–5022, Nov. 2006.
7. Tang, J., “A comparison study of the Shannon channel capacity of various nonlinear optical fibers,” *J. Lightwave Technol.*, Vol. 24, No. 5, 2070–2075, May 2006.
8. Essiambre, R.-J., G. Kramer, P. J. Winzer, G. J. Foschini, and B. Goebel, “Capacity limits of optical fiber networks,” *J. Lightwave Technol.*, Vol. 28, No. 4, 662–701, 15 Feb. 2010.
9. Ellis, A. D., Z. Jian, and D. Cotter, “Approaching the non-linear Shannon limit,” *J. Lightwave Technol.*, Vol. 28, No. 4, 423–433, Feb. 2010.
10. Djordjevic, I. B., “Ultimate information capacity of fiber-optic networks,” *Proc. SPIE*, 2010, Vol. 7621, No. 4, 7619–7621.
11. Bosco, G., P. Poggiolini, A. Carena, V. Curri, and F. Forghieri, “Analytical results on channel capacity in uncompensated optical links with coherent detection,” *Optics Express*, Vol. 19, No. 26, B438–B449, 16 Dec. 2011.
12. Mecozzi, A. and R.-J. Essiambre, “Nonlinear Shannon limit in pseudolinear coherent systems,” *J. Lightwave Technol.*, Vol. 30, No. 12, 2011–2024, 15 Jun. 2012.
13. Secondini, M. and E. Forestieri, “Analytical fiber-optic channel model in the presence of cross-phase modulation,” *IEEE Photon. Technol. Lett.*, Vol. 24, No. 22, 2016–2019, 15 Nov. 2012.
14. Serena, P., A. Bononi, and G. Colavolpe, “On the nonlinear capacity with memory of PS-QPSK and PDM-QPSK in WDM non-dispersion managed links,” *Proc. Europ. Conf. Optical Commun. (ECOC)*, paper We.2.C.1, 2012.
15. Secondini, M., E. Forestieri, and G. Prati, “Achievable information rate in nonlinear WDM fiber-optic systems with arbitrary modulation formats and dispersion maps,” *J. Lightwave Technol.*, Vol. 31, No. 23, 3839–3852, 2013.
16. Merhav, N., G. Kaplan, A. Lapidoth, and S. S. Shitz, “On information rates for mismatched decoders,” *IEEE Trans. Inform. Theory*, Vol. 40, No. 6, 1953–1967, Nov. 1994.
17. Pfister, H., J. B. Soriaga, and P. Siegel, “On the achievable information rates of finite state ISI channels,” *IEEE GLOBECOM’01*, Vol. 5, 2992–2996, 2001.
18. Arnold, D. M., H.-A. Loeliger, P. O. Vontobel, A. Kavvcic, and W. Zeng, “Simulation-based computation of information rates for channels with memory,” *IEEE Trans. Inform. Theory*, Vol. 52, No. 8, 3498–3508, Aug. 2006.
19. Poggiolini, P., “The GN model of non-linear propagation in uncompensated coherent optical systems,” *J. Lightwave Technol.*, Vol. 30, No. 24, 3857–3879, Dec. 2012.
20. Poggiolini, P., G. Bosco, A. Carena, V. Curri, Y. Jiang, and F. Forghieri, “The GN-model of fiber non-linear propagation and its applications,” *J. Lightwave Technol.*, Vol. 32, No. 4, 694–721, Feb. 2014.
21. Dar, R., M. Feder, A. Mecozzi, and M. Shtaif, “Properties of nonlinear noise in long, dispersion-uncompensated fiber links,” *Optics Express*, Vol. 21, No. 22, 25 685–25 699, Nov. 2013.
22. Agrell, E., A. Alvarado, G. Durisi, and M. Karlsson, “Capacity of a nonlinear optical channel with finite memory,” *J. Lightwave Technol.*, Vol. 32, No. 16, 2862–2876, Aug. 2014.
23. Taha, T. R. and M. J. Ablowitz, “Analytical and numerical aspects of certain nonlinear evolution equation, II, numerical, nonlinear Schroedinger equation,” *J. Computat. Phys.*, Vol. 5, 203–230, 1984.

24. Ip, E. and J. Kahn, "Compensation of dispersion and nonlinear impairments using digital backpropagation," *J. Lightwave Technol.*, Vol. 26, No. 20, 3416–3425, 2008.
25. Peddanarappagari, K. V. and M. Brandt-Pearce, "Volterra series transfer function of single-mode fibers," *J. Lightwave Technol.*, Vol. 15, 2232–2241, 1997.
26. Vannucci, A., P. Serena, and A. Bononi, "The RP method: a new tool for the iterative solution of the nonlinear Schrödinger equation," *J. Lightwave Technol.*, Vol. 20, No. 7, 1102–1112, Jul. 2002.
27. Song, H. and M. Brandt-Pearce, "A discrete-time polynomial model of single channel long-haul fiber-optic communication systems," *Proc. IEEE Int. Conf. Commun. (ICC)*, 1–6, 2011.
28. Secondini, M., E. Forestieri, and C. R. Menyuk, "A combined regular-logarithmic perturbation method for signal-noise interaction in amplified optical systems," *J. Lightwave Technol.*, Vol. 27, No. 16, 3358–3369, 15 Aug. 2009.
29. Dar, R., M. Feder, A. Mecozzi, and M. Shtaif, "Time varying ISI model for nonlinear interference noise," *Proc. Opt. Fiber Commun. (OFC)*, Mar. 2014.
30. Zakharov, V. E. and A. B. Shabat, "Exact theory of two-dimensional self-focusing and one-dimensional self-modulation of waves in nonlinear media," *Sov. Phys.-JETP*, Vol. 34, 62–69, 1972.
31. Marsella, D., M. Secondini, and E. Forestieri, "Maximum likelihood sequence detection for mitigating nonlinear effects," *J. Lightwave Technol.*, Vol. 32, No. 5, 908–916, Mar. 2014.
32. Wahls, S. and H. V. Poor, "Introducing the fast nonlinear Fourier transform," *Proc. IEEE Int. Conf. Acoust. Speech Signal Process. (ICASSP)*, 5780–5784, May 2013.
33. Wahls, S. and H. V. Poor, "Inverse nonlinear Fourier transforms via interpolation: The Ablowitz-Ladik case," *Proc. Int. Symp. Math Theory Networks Systems (MTNS)*, 1848–1855, Jul. 2014.
34. Secondini, M., D. Marsella, and E. Forestieri, "Enhanced split-step Fourier method for digital backpropagation," *Proc. Europ. Conf. Optical Commun. (ECOC)*, paper We.3.3.5., 2014.
35. Secondini, M., S. Rommel, F. Fresi, E. Forestieri, G. Meloni, and L. Potì, "Coherent 100G nonlinear compensation with single-step digital backpropagation," *Proc. Opt. Networks Design Model. (ONDM)*, 2015.
36. Cover, T. M. and J. A. Thomas, *Elements of Information Theory*, Wiley, New York, 1991.
37. Agrell, E. and M. Karlsson, "WDM channel capacity and its dependence on multichannel adaptation models," *Proc. Opt. Fiber Commun. (OFC)*, paper OTu3B.4, 2013.
38. Irukulapati, N., H. Wymeersch, P. Johannisson, and E. Agrell, "Stochastic digital backpropagation," *IEEE Trans. Commun.*, Vol. 62, No. 11, 3956–3968, Nov. 2014.
39. Secondini, M. and E. Forestieri, "On XPM mitigation in WDM fiber-optic systems," *IEEE Photon. Technol. Lett.*, Vol. 26, No. 22, 2252–2255, 2014.
40. Marsella, D., M. Secondini, E. Agrell, and E. Forestieri, "A simple strategy for mitigating XPM in nonlinear WDM optical systems," *Proc. Opt. Fiber Commun. Conf. (OFC)*, paper Th4D–3, 2015.

Flex-grid All-optical Interconnect Supporting Transparent Multi-hop Connection in Data Centers

Yuanyuan Hong¹, Xuezhi Hong², Sailing He^{1,3}, and Jiajia Chen³

¹Center for Optical and Electromagnetic Research
Zhejiang University, Hangzhou 310058, China

²ZJU-SCNU Joint Research Center of Photonics
South China Normal University, Guangzhou 510006, China

³School of Information and Communication Technology
KTH Royal Institute of Technology, Kista 16443, Sweden

Abstract— In this paper a novel flex-grid all-optical interconnect scheme is proposed for data center, where a transparent multi-hop connection can be realized by using optical bypass rather than going through optical-electric-optical conversions, enhancing energy efficiency for inter-rack communications. Moreover, elastic spectrum allocation is adopted in the proposed scheme to increase the resource utilization and scalability. Transmission performance evaluation has been carried out to verify the feasibility of the proposed scheme.

1. INTRODUCTION

With the rapid growth of new applications, such as cloud service, scientific computing, data analysis and large-scale social network service, the capacity demand for data center network is increasing explosively. Besides the network capacity, another challenging issue in the design and implementation of the data center is the power consumption. Therefore, interconnection scheme which can provide high capacity and low power consumption is of great importance to the data center.

Aiming at addressing the two challenges aforementioned, many optical interconnection schemes have been proposed, including the hybrid electronic/optical approaches, e.g., Helios [1] and c-Through [2], as well as purely optical switching based solutions, e.g., OSA [3]. Compared to the hybrid electronic/optical schemes, the purely optical switching paradigms are transparent to the optical signals (such as data rates, modulation formats) and can offer elastic spectrum allocation, leading to high spectrum efficiency in data center network [4]. The interconnection network in a large-scale data center typically consists of several tiers, e.g., edge, aggregation and core tiers. The aggregation/core tier is responsible for traffic flows among different racks as well as the ones from/to the Internet. Optical circuit switching schemes such as OSA can provide substantially higher bandwidth than electrical packet switching, and hence is considered in the core/aggregation tier. To realize non-blocking connection between any two racks and keep the optical switch matrix in a reasonable size, the multi-hop routing is employed [3], where the traffic passes several other racks until arriving at the destined rack. However, the existing optical circuit switching based schemes need to use O-E-O conversion at each hop for multi-hop connections [3, 5], which causes relatively low power efficiency and increases the complexity (and cost) of the interconnects at aggregation/core tier. In this regard, we enhance the optical circuit switching based interconnect architecture by offering transparent multi-hop connection. Moreover, the proposed scheme can easily adopt advanced modulation formats and flex-grid technology, which greatly enhances resource efficiency scalability [6]. An extensive assessment has been carried out for our proposed scheme, where the transmission performance of using different modulation formats and the baud rate has been validated by simulation. Besides, the impact of wavelength selective switch (WSS) transfer function on transmission performance has also been investigated.

2. FLEX-GRID ALL-OPTICAL INTERCONNECT OFFERING TRANSPARENT MULTI-HOP CONNECTIONS

The schematic diagram of the proposed scheme is shown in Fig. 1. In a top of the rack (ToR) switch which handles traffics from servers inside the rack, M bandwidth variable optical transceivers (BVTs) are employed to generate and detect optical signals with both varied baud rate and central frequency towards the core tier switch. Here M is the number of flows that one rack can communicate with the other racks simultaneously (i.e., the number of BVTs at the ToR). The ToR switches of different racks are connected via an optical switch matrix (OSM) which serves as the core tier

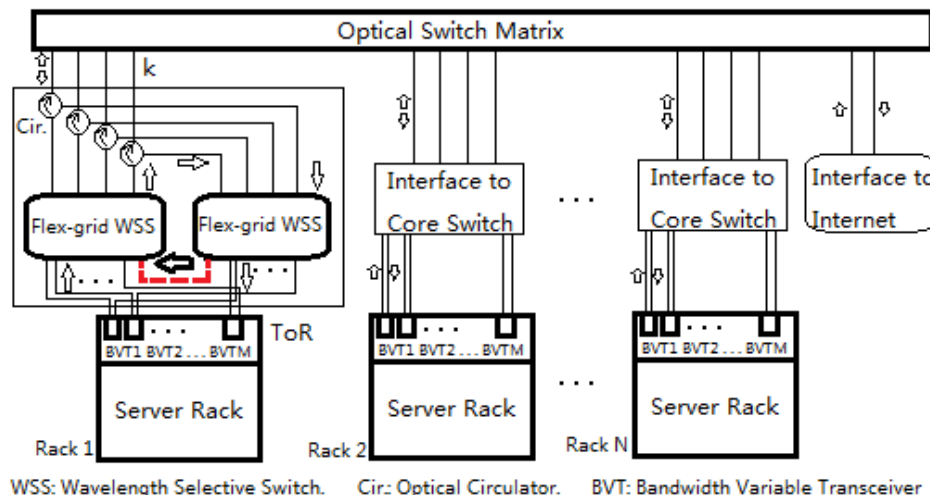


Figure 1: Proposed flex-grid all-optical interconnect supporting transparent multi-hop connections in data centers.

switch handling the communications among racks as well as the interfaces to the outside of the data center. Between the ToR switch (edge tier) and OSM (core tier) two $(M + 1) \times K$ flex-grid WSSs are employed. One is for the upstream direction (from edge tier to core tier) and the other is for the downstream direction. In the upstream, the traffic sent by M transceivers at ToR is combined into K groups and then transmitted to the OSM. In the downstream the traffic from the OSM are delivered to K input ports of WSS passing through an array of optical circulators. If the signals are not destined to this rack, they are conveyed to the input port of WSS for the upstream transmission (dashed red line in Fig. 1) and multiplexed with the signals generated by the connected rack. The multiplexed signals are rearranged into k groups for the next hop. The path computation typically is done by the controller where spectrum allocation and routing algorithm are employed. In such a way, the all-optical transparent connection can be established by bypassing the racks rather than sending back to the ToR with optical-electric-optical (O-E-O) conversion as in the multi-hop scheme (e.g., in [3]). Therefore, the all-optical connections can eliminate the power consumption caused by O-E-O conversion and reduce system complexity by avoiding extra transceivers at ToR for relay.

3. PERFORMANCE EVALUATION

In this section, performance evaluation has been carried out by using a professional simulation software VPI transmission Maker 9.1 [7] for communication system performance. We measure symbol error rate (SER) as a function of the received optical power and study on the impact of modulation formats, the number of hops, baud rate as well as WSS transfer function on transmission performance. In the simulation setup, we choose K as 4 which means each rack can communicate with other 4 racks through OSM simultaneously. The choice of K is based on the balance between the number of hops and the size of the OSM [3]. By changing the channel bandwidth and modulation format, the capacity of each WDM channel in the simulation can range from 10 Gb/s to 320 Gb/s, which is designed to meet the various capacity demands in the core tier for different applications [8].

3.1. Flex-grid All-optical Multi-hop Transmission Performance

As shown in Figs. 2 and 3, we investigate the transmission performance of the proposed scheme under different numbers of hops, modulation formats and baud rates by simulation. The Nyquist signaling is employed to realize a high spectrum efficiency system [9]. With Nyquist signaling the transmitted symbols are shaped by the raised-cosine pulses to demonstrate zero inter-symbol interference (ISI) property between consecutive symbols. Raised-cosine pulse shaping of Nyquist signaling brings higher spectrum efficiency at the expense of higher system complexity. For all the modulation formats listed in Fig. 2, the required received optical power increases for a certain level of symbol error ratio (SER) when the number of hops changes from 1 to 3. This can be attributed to the cascaded WSS filtering effect in the all-optical multi-hop connections. Larger inter-symbol interference (ISI) is induced with a larger number of hops. Table 1 and Table 2 show the optical

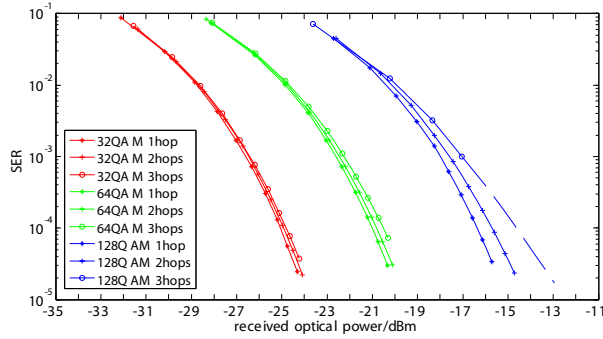


Figure 2: Results of SER versus received optical power in 1/2/3 hops and 32QAM/64QAM/128QAM cases with 40 Gbaud/s.

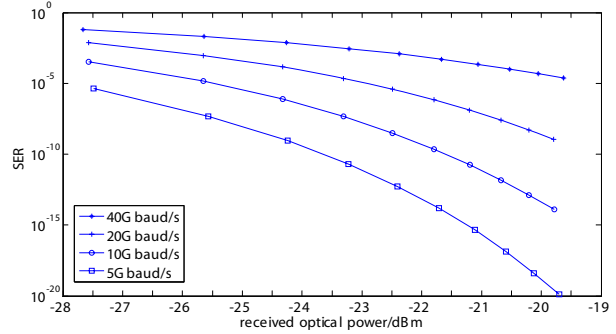


Figure 3: Results of SER versus received optical power for baud rate of 5 Gbaud/s, 10 Gbaud/s, 20 Gbaud/s, and 40 Gbaud/s corresponding to 30 Gbps, 60 Gbps, 120 Gbps and 240 Gbps when using 64QAM.

Table 1: Penalty of received optical power (dB) at $\text{SER} = 10^{-4}$ caused by using higher modulation format with the same number of hops.

	1 hop	2 hops	3 hops
32QAM vs. 64QAM/dB	4.10	4.15	4.30
64QAM vs. 128QAM/dB	4.65	5.05	5.85

Table 2: Penalty of received optical power (dB) at $\text{SER} = 10^{-4}$ caused by increasing the number of hops for the same modulation format.

	32QAM	64QAM	128QAM
1 hop vs. 2 hops/dB	0.15	0.20	0.60
2 hops vs. 3 hops/dB	0.15	0.30	1.10

power penalty at $\text{SER} = 10^{-4}$ caused by employing higher modulation formats and increasing number of hops, respectively, in both of which a larger optical power penalty is observed for higher modulation format when the number of hops increases. This can be explained by the fact that the signals with higher modulation format and passing more WSSs are more sensitive to ISI.

Flex-grid spectrum allocation can be employed in the proposed scheme. The connections having a spectral slot of 12.5 GHz, 25 GHz, 37.5 GHz, and 62.5 GHz corresponds to a baud rate of 5 Gbaud/s, 10 Gbaud/s, 20 Gbaud/s, and 40 Gbaud/s, respectively. Quadrature amplitude modulation (QAM) is used here. With different modulation format ranging from 4QAM to 256QAM and flexible channel bandwidth, various capacities are achieved (from 10 Gb/s to 320 Gb/s). The SER as a function of received optical power with different baud rate signals are presented in Fig. 3. It can be observed that the channel with higher baud rate has worse SER performance, where the influence of ISI is more severe.

3.2. Impact of WSS Transfer Function

In our scheme, the all-optical multi-hop connection highly relies on the WSS to realize optical bypass. The imperfection of the WSS passband causes ISI and thus lead to performance degradation to the system. Therefore, in this section we further study the impact of WSS passband profile on signal transmission performance. Today's commercial WSSs can have different transfer functions for passband [10]. The WSS considered here is assumed to have a super-Gaussian shape transfer function as $|H(f)|^2 = \exp(-(f - f_0/\Delta f)^{2n})$, wherein f is the optical frequency, f_0 is the center frequency of channel, Δf is the bandwidth and n is the order of filter [11]. We have run a set of simulation with WSSs having the same 3-dB bandwidth Δf but different orders of filter. The transfer function with the order of 4 (i.e., $n = 4$) is typical for early generation free-space single dimension MEMS mirror array based WSS, while the order of 6 (i.e., $n = 6$) represents the state-of-the-art WSS [12]. To show the impact of WSS passband profile on the all-optical multi-hop interconnection, we measure the SER as a function of received optical power with either a 4th or

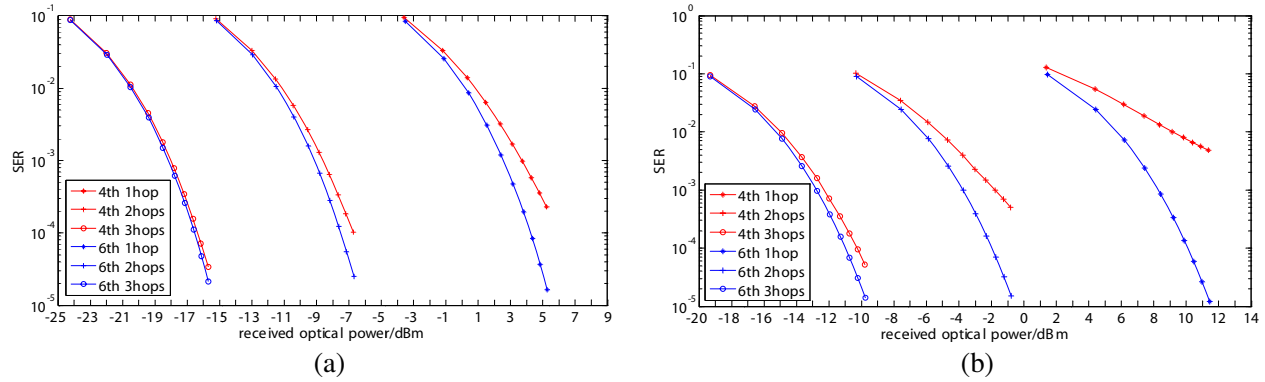


Figure 4: SER versus received optical power in 40 Gbaud/ssystem with a 4th and 6th super-Gaussian WSS under (a) 128QAM, and (b) 256QAM.

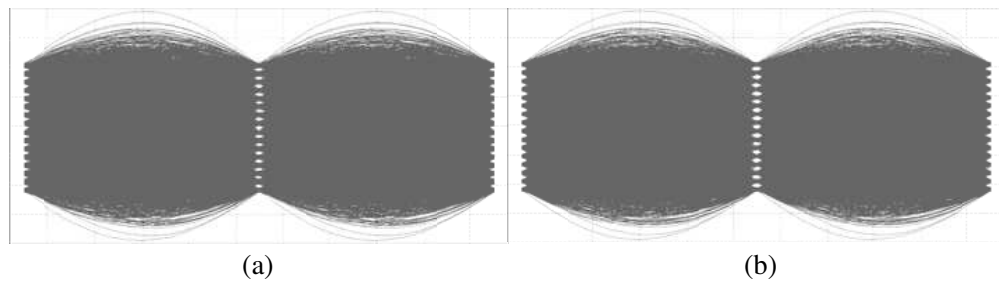


Figure 5: Eye diagram of 40 Gbaud/s 256QAM signal after 3 hops with a (a) 4th ($SER = 1.38e - 2$) or (b) with 6th ($SER = 9.54e - 4$) super-Gaussian WSS.

a 6th super-Gaussian WSS under various numbers of hops and modulation formats, as shown in Fig. 4.

According to Fig. 4, the system with 6th super-Gaussian WSS obviously outperforms the one with 4th super-Gaussian WSS in terms of SER under the same numbers of hops and modulation format. The reason is that the passband is more flat with a higher order super-Gaussian WSS [10] which causes less ISI to the Nyquist signal. The filtering induced ISI can be observed in the diagrams shown in Fig. 5. The performance gain by using the 6th super-Gaussian WSS increases with a larger number of hops. It is because by the cascading filtering effect of WSS for multiple hops. We also note that the performance of higher modulation format is more sensitive to the impact of the filter order. Therefore, in the cases with higher modulation formats and larger number of hops, WSS with the higher filter order (i.e., with higher passband flatness) is more preferable for the all-optical multi-hop connection.

4. CONCLUSION

A flex-grid all-optical interconnect scheme supporting transparent multi-hop connection for inter-rack communication is proposed. The transmission performance has been shown in terms of SER for various numbers of hops, modulation formats, baud rates and WSS transfer function. These simulation results verify that supporting up to 3 hops without any O-E-O conversion our scheme still could achieve acceptable SER performance by using WSSs. It is observed that the higher modulation format and larger number of hops will have negative impact on transmission performance, which could be an important factor to be considered in design of routing strategy. Moreover, the results also imply that a high filter order in WSS is recommended for system, particularly for the case with a relatively large number of hops and high modulation format.

ACKNOWLEDGMENT

The work described in this paper was carried out with the support by the National High Technology Research and Development Program (863) of China (No. 2012AA012201), the project titled “Enabling Scalable and Sustainable Data Center Networks” funded by Swedish Foundation of Strategic Research, the project titled “Towards Flexible and Energy-Efficient Data centre Networks” funded

by Swedish Research Council, and the China Postdoctoral Science Foundation (No. 2013M531868).

REFERENCES

1. Farrington, N., G. Porter, S. Radhakrishnan, H. H. Bazzaz, V. Sub-Ramanya, Y. Fainman, G. Papen, and A. Vahdat, “Helios: A hybrid electrical/optical switch architecture for modular data centers,” *Proceeding of ACM Special Interest Group on Data Communication*, 339–350, New Delhi, India, Aug. 2010.
2. Wang, G., D. G. Andersen, M. Kaminsky, K. Papagiannaki, T. S. Eugene Ng, M. A. Kozuch, and M. Ryan, “C-through: Part-time optics in data centers,” *Proceeding of ACM Special Interest Group on Data Communication*, 327–338, New Delhi, India, Aug. 2010.
3. Chen, K., A. Singla, A. Singh, K. Ramachandran, L. Xu, Y. Zhang, X. Wen, and Y. Chen, “OSA: An optical switching architecture for data center networks with unprecedented flexibility,” *T. Netw.*, Vol. 22, No. 2, 498–511, 2014.
4. Wen, K., X. Cai, Y. Yin, D. J. Geisler, R. Proietti, R. P. Scott, N. K. Fontaine, and S. J. B. Yoo, “Adaptive spectrum control and management in elastic optical networks,” *J. Sel. Area Comm.*, Vol. 31, No. 1, 39–48, 2013.
5. Liu, L., W. Peng, R. Casellas, T. Tsuritani, I. Morita, R. Martínez, R. Muñoz, and S. J. B. Yoo, “Design and performance evaluation of an open flow-based control plane for software defined elastic optical networks with direct detection optical OFDM (DDO-OFDM) transmission,” *Opt. Express*, Vol. 22, No. 1, 30–40, 2014.
6. Christodoulopoulos, K., I. Tomkos, and E. A. Varvarigos, “Elastic bandwidth allocation in flexible OFDM-based optical networks,” *J. Lightwave Technol.*, Vol. 29, No. 9, 1354–1366, 2011.
7. Garcia, M., H. Coll, D. Bri, and J. Lloret, “Software tools and simulators in the education of engineering of telecommunications,” *Proceeding of 5th WSEAS/IASME International Conference on Engineering Education and Research*, 337–342, Heraklion, Greece, Jul. 2008.
8. Mahimkar, A., A. Chiu, R. Doverspike, M. D. Feuer, P. Magill, E. Mavrogiorgis, J. Pastor, S. L. Woodward, and J. Yates, “Bandwidth on demand for inter-data center communication,” *Proceedings of the 10th ACM Workshop on Hot Topics in Networks*, Cambridge, MA, USA, Nov. 24, 2011.
9. Shi, J., J. Zhang, L. Tao, Y. Wang, Y. Wang, and N. Chi, “Characteristics of filtering effect for a polarization division multiplexed-quadrature phase shift keying signal with Nyquist and super-Nyquist spectrum efficiency employing various algorithms,” *Opt. Eng.*, Vol. 53, No. 7, 076109–076109, 2014.
10. “A performance comparison of WSS switch engine technologies,” JDSU white paper, http://www.jdsu.com/productliterature/wsscomp-wp-cms_ae.pdf.
11. Pulikkaseril, C., L. A. Stewart, M. A. F. Roelens, G. W. Baxter, S. Poole, and S. Frisken, “Spectral modeling of channel band shapes in wavelength selective switches,” *Opt. Express*, Vol. 19, No. 9, 8458–8470, 2011.
12. Marom, D. M., D. T. Neilson, D. S. Greywall, C. Pai, N. R. Basavanhally, V. A. Aksyuk, D. O. López, F. Pardo, M. E. Simon, Y. Low, P. Kolodner, and C. A. Bolle, “Wavelength-selective $1 \times k$ switches using free-space optics and MEMS micromirrors: Theory, design, and implementation,” *J. Lightwave Technol.*, Vol. 23, No. 4, 1620–1630, 2005.

Effective Lennard-Jones Parameters for CO₂-CO₂ Dispersion Interactions in Water and near Amorphous Silica-water Interfaces

P. Thiyam¹, O. I. Malyi², C. Persson^{1,2,3}, S. Y. Buhmann^{4,5},
D. F. Parsons⁶, and M. Boström²

¹Department of Materials Science and Engineering
Royal Institute of Technology, SE-100 44 Stockholm, Sweden

²Centre for Materials Science and Nanotechnology
University of Oslo, P. O. Box 1048, Blindern, NO-0316 Oslo, Norway

³Department of Physics, University of Oslo, P. O. Box 1048, Blindern, NO-0316 Oslo, Norway

⁴Physikalisches Institut, Albert-Ludwigs-Universität Freiburg
Hermann-Herder-Str. 3, 79104 Freiburg, Germany

⁵Freiburg Institute for Advanced Studies, Albert-Ludwigs-Universität Freiburg
Albertstraße 19, 79104 Freiburg, Germany

⁶School of Engineering and IT, Murdoch University, 90 South St, Murdoch, WA 6150, Australia

Abstract— Different models for effective polarizability in water and the corresponding dispersion forces between dissolved molecules are explored in bulk water and near interfaces. We demonstrate that the attractive part of the Lennard-Jones parameters, i.e., the van der Waals parameter C_6 ($U_{vdW} \approx -C_6/\rho^6$), is strongly modified when two carbon dioxide (CO₂) molecules are near an amorphous silica-water and near a vapor-water interface. Standard simulation parameters for near-surface modeling are based on intermolecular forces in bulk media.

1. INTRODUCTION

Tight rocks may provide most of the world's future fossil energy. New production methods that allow hydrocarbons to be produced directly from tight source rocks such as shale gas and shale oil systems have changed the world's energy outlook [1]. We are now at a stage where the technology for recovery has advanced beyond our scientific understanding of the underlying processes. This creates new opportunities for technological and scientific innovations. Much fundamental research focus on molecular physisorption/chemisorption and meso-scale transport processes in nanostructured shales. By understanding the underlying physical processes, the ultimate aim of such research is to realize a controlled conversion process of carbon dioxide (CO₂) to methane (CH₄) in model porous media and more generally in hydrofractured shale.

The fluctuation of the electromagnetic field in the vicinity of a molecule near a surface, or between surfaces, is different from that in free space giving rise to different interactions [2]. Using the formalism of Sambale et al. [4], we explore how the presence of interfaces influence intermolecular forces between a pair of CO₂ molecules. Traditional Lennard-Jones parameters are derived from intermolecular forces in bulk media. However, we show that the attractive part of the Lennard-Jones potential (i.e., the van der Waals attraction) changes near interfaces. It depends on the properties of the materials involved, the model of polarizability of the molecule used and the relative orientation of the molecules near the interface. The dispersion forces between dissolved CO₂ molecules are explored in bulk water and near amorphous silica-water and air-water interfaces using different models for effective polarizability, viz. the hardsphere model and Onsager's model [3].

In the next section, we first briefly describe the interaction of a single molecule in a medium with a surface. In Section 3, we discuss the theory of interaction of two molecules embedded in a medium near a surface. In Section 4, we briefly describe the two models of effective polarizability of the molecule in water. In Section 5, we explain the modeling of the dielectric functions of the background medium (water) and the surface of amorphous silica. We provide the van der Waals C_6 parameters for CO₂-CO₂ interaction in bulk water using different models of polarizability in Section 6. In Section 7, we present our main analysis and results. We end with a few conclusions in Section 8.

2. VAN DER WAALS ENERGY OF A SINGLE MOLECULE NEAR A WATER-SILICA INTERFACE

We explore the formalism due to Buhmann and co-workers for local field corrections when small carbon dioxide (CO₂) molecules are in a media [2–6]. The distance-dependent part of the retarded

van der Waals potential [2] of a polarizable molecule in water near an interface [4] is,

$$U(z) = k_B T \sum_{n=0}^{\infty} \frac{1}{2} \alpha_w(i\xi_n) \int_0^{\infty} \frac{dq q (f^p + f^s)}{\gamma_0}, \quad (1)$$

$$f^s = \xi_n^2 r_s \exp[-2\gamma_0 z]/c^2, \quad (2)$$

$$f^p = - \left(\frac{\xi_n^2}{c^2} + \frac{2q^2}{\epsilon_w} \right) r_p \exp[-2\gamma_0 z], \quad (3)$$

with the reflection coefficients of the interface,

$$\begin{aligned} r_s &= (\gamma_0 - \gamma_1)/(\gamma_0 + \gamma_1), \\ r_p &= (\epsilon\gamma_0 - \epsilon_w\gamma_1)/(\epsilon\gamma_0 + \epsilon_w\gamma_1), \quad \gamma_0 = \sqrt{q^2 + \epsilon_w\xi_n^2/c^2}, \\ \gamma_1 &= \sqrt{q^2 + \epsilon\xi_n^2/c^2}. \end{aligned} \quad (4)$$

Here ϵ_w and ϵ are the dielectric functions of water and the substrate respectively, and c is the velocity of light in vacuum. We define k_B as the Boltzmann constant and T is the temperature, and the prime indicates that the $n = 0$ term should be divided by 2. Furthermore $\alpha_w(i\xi_n)$ is the water-embedded molecular polarizability at the Matsubara frequencies $\xi_n = 2\pi k_B T n/\hbar$ [2, 7–9]. Here we consider systems at room temperature ($T = 300$ K).

3. EFFECT OF BACKGROUND MEDIA AND INTERFACES ON LONG-RANGE VAN DER WAALS FORCES

The presence of surfaces influences the van der Waals interaction between two molecules near an interface [5, 6]. At large CO₂-CO₂ separations the retarded van der Waals interaction between two molecules near a solid-water interface is

$$U_{vdW}(\bar{\rho}_a, \bar{\rho}_b) \approx -k_B T \sum_{n=0}^{\infty} \frac{1}{2} \alpha_w(i\xi_n)^2 \times \left\{ \left[\sum_{j=x,y,z} T_{jj}(\bar{\rho}_a, \bar{\rho}_b | i\xi_n)^2 \right] - 2T_{xz}(\bar{\rho}_a, \bar{\rho}_b | i\xi_n)^2 \right\}, \quad (5)$$

where $\bar{\rho}_{a,b}$ are the positions of the two molecules with respect to a fixed point at the interface, and the other factors are as described in the previous section. We study van der Waals interaction near amorphous silica-water interface and air-water interface. The susceptibility tensor element (T_{jj}) is a sum of contributions from bulk water susceptibility (T_{jj}^0), plus p (T_{jj}^{1p}) and s (T_{jj}^{1s}) interface corrections.

The susceptibility tensor elements for two polarizable particles near solid-air interfaces are well studied in the literature [10, 11]. Here we present the theory with arbitrary orientations for two CO₂ molecules in water near an amorphous silica-water interface. We consider only distances much larger than two radii where finite size effects can be neglected [12]. We consider the case when x is the distance between the two molecules parallel to the surface and z_a and z_b are the distances of atoms a and b from the surface.

We consider the general case where the two interacting CO₂ molecules are not situated in free space, but embedded in a water medium near a solid-water interface. The presence of the water medium modifies the van der Waals interaction in different ways: Firstly, the non-trivial refractive index of water $\tilde{n} = \tilde{n}(i\xi_n) = \sqrt{\epsilon_w(i\xi_n)}$ leads to a modified light propagation. As a result, the free-space susceptibility is replaced with its counterpart in a bulk water medium

$$\begin{aligned} T_{xx}^0 &= (A - Bx^2/d^2)e^{-\tilde{n}\xi_n d/c}/(\epsilon_w d^3), \\ T_{yy}^0 &= Ae^{-\tilde{n}\xi_n d/c}/(\epsilon_w d^3), \\ T_{zz}^0 &= [A - Bz_m^2/(d^2)]e^{-\tilde{n}\xi_n d/c}/(\epsilon_w d^3) \end{aligned} \quad (6)$$

with

$$\begin{aligned} A &= 1 + (d\tilde{n}\xi_n/c) + (d\tilde{n}\xi_n/c)^2, \\ B &= 3 + (3d\tilde{n}\xi_n/c) + (d\tilde{n}\xi_n/c)^2, \\ d &= \sqrt{x^2 + z_-^2}. \end{aligned} \quad (7)$$

Here, we define $z_+ = z_a + z_b$ and $z_- = z_a - z_b$ with the first being the distance between molecule a and the image of molecule b inside the surface and the second being distance between the two molecules.

The corresponding surface-induced corrections to the susceptibility matrix [10, 11] have contributions from p and s polarizations,

$$\begin{aligned} T_{xx}^{1s} &= \int_0^\infty dq (\xi_n^2/c^2) (q/\gamma_0) e^{-\gamma_0 z_+} r_s [J_0(qx) + J_2(qx)]/2, \\ T_{yy}^{1s} &= \int_0^\infty dq (\xi_n^2/c^2) (q/\gamma_0) e^{-\gamma_0 z_+} r_s [J_0(qx) - J_2(qx)]/2, \end{aligned} \quad (8)$$

$$\begin{aligned} T_{zz}^{1s} &= 0, \\ T_{xx}^{1p} &= - \int_0^\infty dq q \gamma_0 e^{-\gamma_0 z_+} r_p [J_0(qx) - J_2(qx)]/2, \\ T_{yy}^{1p} &= - \int_0^\infty dq q \gamma_0 e^{-\gamma_0 z_+} r_p [J_0(qx) + J_2(qx)]/2, \\ T_{zz}^{1p} &= - \int_0^\infty dq (q^3/\gamma_0) e^{-\gamma_0 z_+} r_p J_0(qx), \\ T_{xz(zx)}^{1p} &= \mp \int_0^\infty dq q^2 e^{-\gamma_0 z_+} r_p J_1(qx), \end{aligned} \quad (9)$$

with the reflection coefficients of the interface,

$$\begin{aligned} r_s &= (\gamma_0 - \gamma_1)/(\gamma_0 + \gamma_1), \\ r_p &= (\epsilon\gamma_0 - \epsilon_w\gamma_1)/(\epsilon\gamma_0 + \epsilon_w\gamma_1), \quad \gamma_0 = \sqrt{q^2 + \epsilon_w\xi_n^2/c^2}, \\ \gamma_1 &= \sqrt{q^2 + \epsilon\xi_n^2/c^2}. \end{aligned} \quad (10)$$

4. TWO MODELS FOR EFFECTIVE POLARIZABILITY OF MOLECULES IN WATER

The macroscopic electromagnetic field in a medium is different from the local field acting on a molecule. This can be accounted for via Onsager's real-cavity model [13]. Assuming that the molecule surrounded by a small spherical vacuum bubble, one can show [3] that local-field corrections lead to a replacement of the CO₂ free-space polarizability with their water-embedded counterparts

$$\alpha_w = \alpha \left(\frac{3\epsilon_w}{2\epsilon_w + 1} \right)^2 \quad (11)$$

where

$$\alpha(i\omega_n) = \alpha(0) \sum_j \frac{f_j}{1 + (\omega_n/\omega_j)^2}, \quad (12)$$

is replaced with the dynamic free-space polarizability obtained from ab initio calculations [14, 15]. The other model of polarizability of the molecule that we consider is the hardsphere model that treats the molecule as a homogeneous dielectric sphere of radius a . Its effective permittivity ϵ can be deduced from the free-space polarizability (12) via [16]

$$\alpha = a^3 \frac{\epsilon - 1}{\epsilon + 2}. \quad (13)$$

The excess polarizability of the homogeneous-sphere molecule in water is then [17]

$$\alpha_w = \epsilon_w a^3 \frac{\epsilon - \epsilon_w}{\epsilon + 2\epsilon_w}. \quad (14)$$

5. THE DIELECTRIC FUNCTIONS OF WATER AND AMORPHOUS SILICA

The dielectric function on the imaginary axis was obtained from the imaginary part of the function, and using the following version of the Kramers-Kronig dispersion relation

$$\varepsilon(i\xi) = 1 + \frac{2}{\pi} \int_0^{\infty} d\omega \frac{\omega \varepsilon_2(\omega)}{\omega^2 + \xi^2}. \quad (15)$$

This relation is the result of the analytical properties of the dielectric function [9]. In the integration we made a cubic spline interpolation of $\ln(\varepsilon_2(\omega))$ as a function of $\ln(\omega)$. The dielectric function of water [9] at room temperature ($T = 300K$) was based on the extensive experimental data found in Ref. [18].

The dielectric properties of amorphous silica were calculated using scissors-operator approximation ($\Delta=3.6$) for Perdew-Burke-Ernzerhof (PBE) density functional theory (DFT) calculations. The dielectric function on the imaginary frequency axis was determined from the Kramers-Kronig dispersion relation. The low-energy spectra are verified by calculating the static dielectric constants from the Born effective charges. The static dielectric constant was found to be 4.08 ± 0.11 . All calculations were carried out using the Vienna ab initio simulation package (VASP) with the Perdew-Burke-Ernzerhof (PBE) [19] functional. Projector augmented wave (PAW) pseudopotentials [20, 21] were used to model the effect of core electrons. The non-local parts of the pseudopotentials were treated in real and reciprocal space Born-Oppenheimer molecular dynamics (BOMD) and all other density functional theory (DFT) calculations, respectively. The cutoff energy for plane wave basis set was set to 400 and 300 eV for all static DFT and BOMD calculations, respectively. It should be noted that for BOMD, to make sure that the cutoff energy does not affect final energetics and electronic/optical properties, one of the amorphous samples was prepared using 400 eV as the cutoff energy (the calculations were performed for third annealing/quenching temperature protocol only, see below). To generate the amorphous structure, BOMD simulations with three different annealing/quenching temperature protocols were used. For all temperature protocols, atomic velocities were initialized at 5000 K using the Maxwell-Boltzmann distribution. Then, the system was melted and annealed for the period of 10 ps. The resulted system was quenched to 2500 K during the periods of 2.5 ps, 5 ps, and 10 ps for first, second, and third annealing/quenching temperature protocols, respectively. Then the systems were annealed for a period of 10 ps and finally were quenched to 1 K for a period of 30 ps. In all simulations, time step was set to 1 fs. It should be noted that the structure annealing was carried out using canonical ensemble BOMD (number of atoms, volume, and temperature was conserved). For all BOMD simulations, the system temperature was controlled using the Nosé thermostat [22–24]. The obtained structures were further fully optimized using quasi-Newton algorithm. Among four generated systems, the highest energy structure was not used for further calculations due to stabilisation of high energy local defects. The computed average band gaps for the amorphous structure was found to be 5.33 ± 0.01 eV.

6. CO₂ VAN DER WAALS PARAMETERS IN BULK WATER

The effective van der Waals parameter C_6 ($U_{vdW} \approx -C_6/\rho^6$) for the interaction of a pair of CO₂ molecules in bulk water is found to be -1.10×10^{-58} erg.cm⁶ for the Onsager's model of polarizability and -0.78×10^{-58} erg.cm⁶ for the hardsphere model of polarizability. We will show in the next section that this C_6 parameter is strongly modified in the presence of a surface. The C_3 coefficients for the interaction of a single CO₂ molecule with amorphous silica and air surfaces are given in Table 1.

Table 1: The C_3 values (the non-retarded van der Waals energy times z^3 in units of 10^{-37} erg.cm³) for CO₂-surface interaction for the hard sphere and Onsager's models near different interfaces. a-SiO₂ here refers to amorphous silica.

Interface	C_3 (Onsager)	C_3 (Hardsphere)
a-SiO ₂ -water	-4.43	-3.77
air-water	12.72	10.58

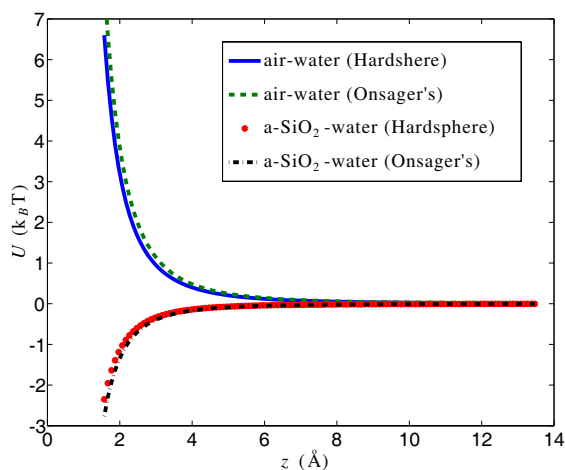


Figure 1: The non-retarded van der Waals energy in units of $k_B T$ of a CO_2 molecule near amorphous silica-water interface and near air-water interface for the hardsphere and Onsager's models of polarizability (at $T = 300$ K). Amorphous silica is written in short as a-SiO₂ in this figure and the following ones.

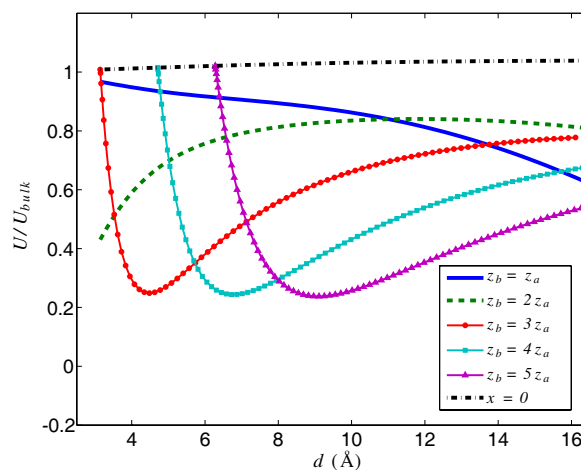


Figure 2: The ratio between the retarded van der Waals potential near an amorphous silica-water interface and the non-retarded van der Waals potential in bulk water of two CO_2 molecules with Onsager's model of polarizability (at $T = 300$ K). $z_a = 1.57 \text{ \AA}$.

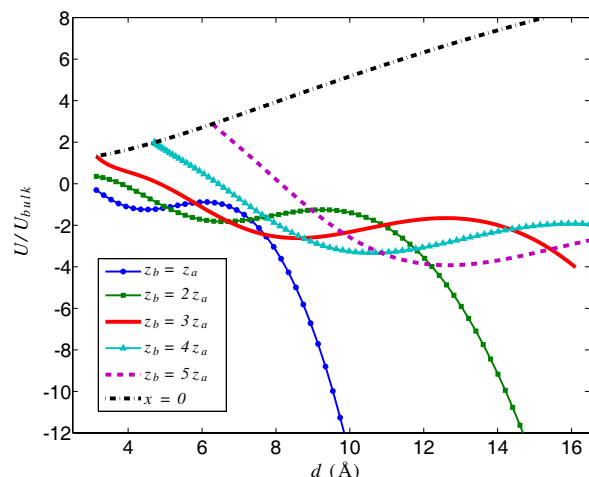


Figure 3: The ratio between the retarded van der Waals potential near an amorphous silica-water interface and the non-retarded van der Waals potential in bulk water of two CO_2 molecules with hardsphere model of polarizability (at $T = 300$ K). $z_a = 1.57 \text{ \AA}$.

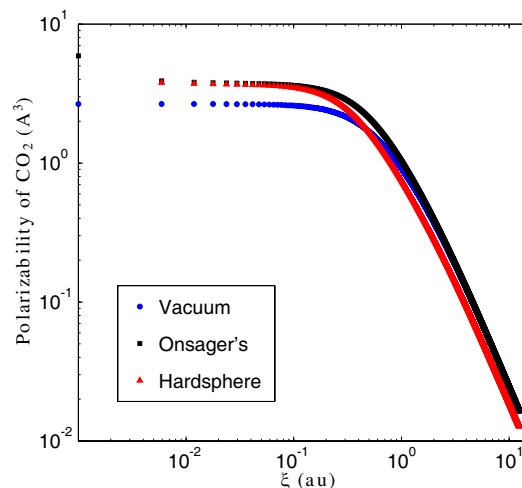


Figure 4: The polarizability of CO_2 in vacuum and the Onsager's and hardsphere models of polarizability of a CO_2 molecule in water in units of Å^3 . The polarizabilities are shown only at the room temperature Matsubara frequencies. The vacuum and Onsager's polarizability values for $\xi = 0$ are shown on the y -axis. The corresponding value for the hardsphere model at $\xi = 0$ is -129.83 \AA^3 .

7. SURFACE EFFECTS ON EFFECTIVE VAN DER WAALS PARAMETERS

In Fig. 1, we present the non-retarded van der Waals energy of a CO_2 molecule in water near amorphous silica and air surfaces as a function of molecule-surface separation distance. The two models of effective polarizability, namely the hardsphere and Onsager's models of polarizability behave very much the same for single molecule-surface interaction. In Fig. 2, we show the ratio of the retarded van der Waals potential U_{vdW} of two CO_2 molecules in water interacting near an amorphous silica surface at room temperature to the non-retarded van der Waals potential U_{bulk} of two CO_2 molecules interacting in bulk water in the absence of any surface. The first molecule is at the interface, i.e., z_a is fixed at a distance of one radius from the surface while the other molecule is placed at different positions in the medium ($z_b = z_a, 2z_a, 3z_a, 4z_a, 5z_a$). Varying x then

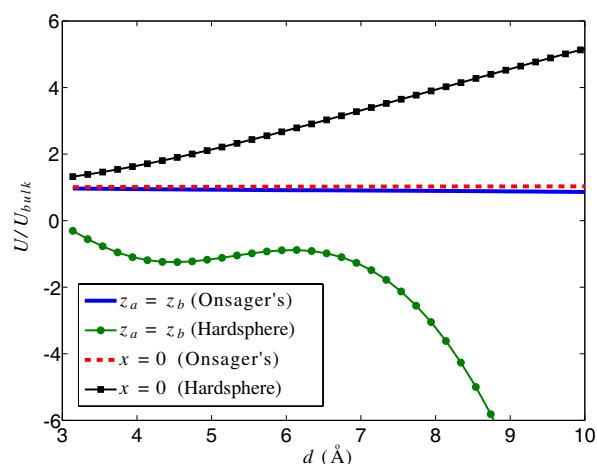


Figure 5: Comparisons of the ratio of interactions near an amorphous silica-water interface and in bulk water of two CO_2 molecules with the two different models of polarizability (at $T = 300$ K). The orientations considered here are for $z_a = z_b = 1.57$ Å and for $x = 0$.

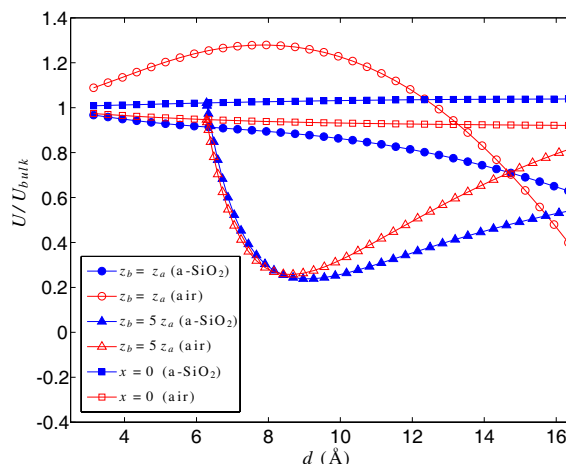


Figure 6: Comparisons of the ratio of interactions near an amorphous silica-water interface and near air-water interface of two CO_2 molecules with Onsager's model of polarizability (at $T = 300$ K) for three different types of orientations.

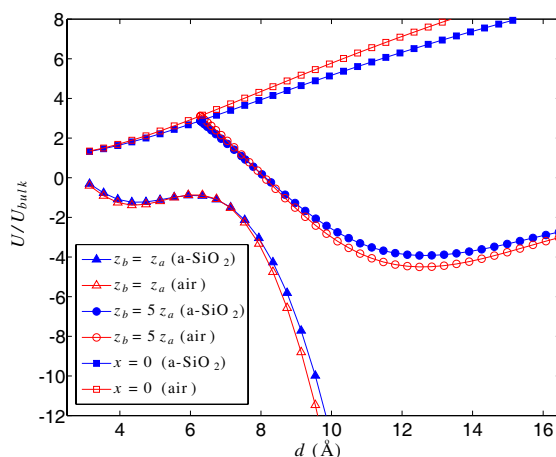


Figure 7: Comparisons of the ratio of interactions near an amorphous silica-water interface and near air-water interface of two CO_2 molecules with hard sphere model of polarizability (at $T = 300$ K) for three different types of orientations.

gives varying separation distances d between the two molecules. The model of polarizability of the molecules used is Onsager's model. In Fig. 3, we show similar plots but for the hardsphere model of polarizability. For both the hardsphere and Onsager's models of polarizability, we observe surface effects due to the presence of the amorphous silica surface. Depending on the orientation, we see that the ratio is larger or smaller than one. For the Onsager model of polarizability, the effect of the surface is minimum at the orientation $x = 0$, i.e., when the molecules are aligned perpendicular to the surface as shown by the very slight deviation from ratio 1 in Fig. 2 while in the hardsphere model, nothing conclusive can be said about which orientation is least or most affected by the surface. Another interesting observation is that the CO_2 molecules even repulse each other for the hardsphere model of polarizability (see Fig. 3) In this model, the polarizability of the molecule in the medium is the excess polarizability between the polarizability of the molecule and that of the medium. Since water is polar, its polarizability at zero frequency is large. The excess polarizability then becomes negative and the molecular sphere is essentially like a bubble. This is relevant at large distances where the zero-frequency contribution becomes dominant. At such retarded distances, the hardsphere molecule behaves like a void or bubble, and the repulsive force is analogous to negative gravity experienced by an air bubble rising in water. The hardsphere polarizability does not converge or converges very slowly to the free-space value for high frequencies.

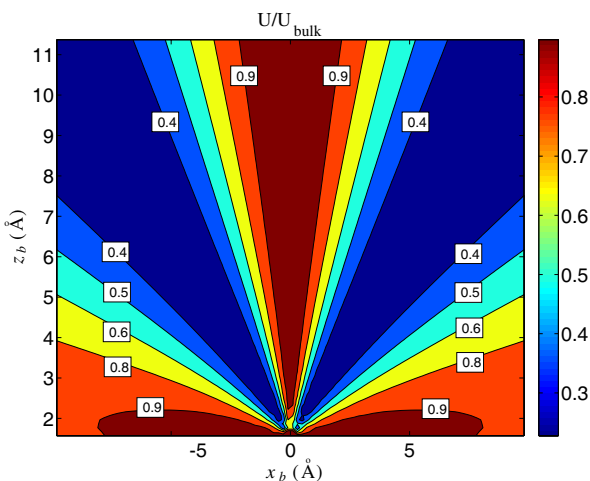


Figure 8: Contour plot showing the U/U_{bulk} ratio profile for Onsager's model of polarizability when z_a is fixed at one molecule radius from amorphous silica-water interface, i.e., $z_a = 1.57 \text{ \AA}$ while the second molecule continuously changes position.

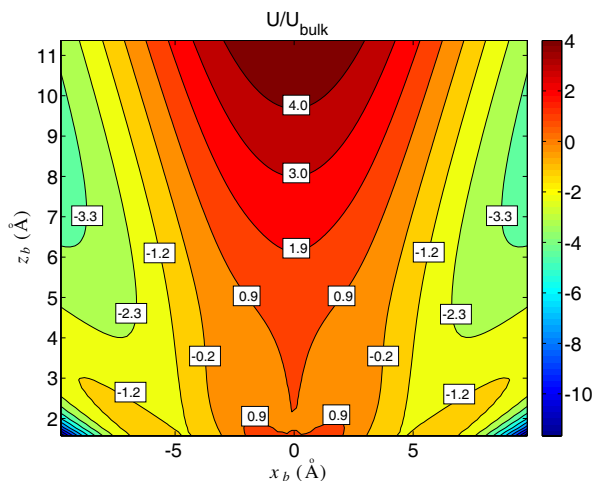


Figure 9: Contour plot showing the U/U_{bulk} ratio profile for the hardsphere model of polarizability when z_a is fixed at one molecule radius from amorphous silica-water interface, i.e., $z_a = 1.57 \text{ \AA}$ while the second molecule continuously changes position.

(see Fig. 4). In Fig. 4, we present the polarizability curve of CO_2 molecule in vacuum and the curves for the two models of polarizability of a CO_2 molecule in water for Matsubara frequencies at room temperature. In the Onsager model, the molecule has a strictly positive polarizability inside a vacuum bubble. The effect of the bubble is a moderate enhancement of the polarizability of upto 1.5 for infinite host-medium ϵ . For large frequencies and hence smaller ϵ , the factor converges to one and the polarizability then agrees with that in vacuum. Fig. 5 more clearly demonstrates the difference in behaviour of the ratio curves for the two models of polarizability shown here for two different types of orientation, namely, the $z_a - z_b = 0$ orientation in which the molecules are aligned parallel to the surface and $x = 0$ orientation in which the molecules are aligned perpendicular to the surface. To study the effects of different types of surfaces, we compare the interactions when the two CO_2 molecules are near an amorphous silica-water interface and near air-water interface for the orientations $x = 0$, $z_b = z_a$ and $z_b = 5z_a$ using Onsager's model and the hardsphere model in Figs. 6 and 7 respectively. Contour plots 8 and 9 show the ratio profile when the first molecule is fixed at the interface while the position of the second molecule is varied.

8. CONCLUSIONS

Lennard-Jones parameters for CO_2 - CO_2 interactions used in simulations on near-surface modeling are based on intermolecular forces in bulk media. We have demonstrated that such work based on CO_2 - CO_2 van der Waals interaction in bulk water may be misleading for simulations near interfaces. The van der Waals interaction may even turn repulsive near amorphous silica-water interfaces for the hardsphere model of polarizability in sharp contrast to the interaction in bulk media.

ACKNOWLEDGMENT

PT acknowledges support from the European Commission. MB, OM, and CP acknowledge support from the Research Council of Norway (Project: 221469). CP acknowledges support from the Swedish Research Council (Contract No. C0485101). We acknowledge access to high-performance computing resources via SNIC/SNAC and NOTUR. SYB gratefully acknowledges support by the German Research Council (grant BU 1803/3-1).

REFERENCES

1. Sapag, K., A. Vallone, A. García Blanco, and C. Solar, "Adsorption of methane in porous materials as the basis for the storage of natural gas," *Natural Gas*, Primoz Potocnik, Ed., 2010.
2. Mahanty, J. and B. W. Ninham, *Dispersion Forces*, Academic, London, 1976.
3. Sambale, A., S. Y. Buhmann, D.-G. Welsch, and M. S. Tomas, *Phys. Rev. A*, Vol. 75, 042109, 2007.

4. Sambale, A., D.-G. Welsch, Ho Trung Dung, and S. Y. Buhmann, *Phys. Rev. A*, Vol. 79, 022903, 2009.
5. Buhmann, S. Y., *Dispersion Forces I: Macroscopic Quantum Electrodynamics and Ground-State Casimir, Casimir–Polder and van der Waals Forces*, Springer, Heidelberg, 2012.
6. Buhmann, S. Y., *Dispersion Forces II: Many-Body Effects, Excited Atoms, Finite Temperature and Quantum Friction*, Springer, Heidelberg, 2012.
7. Lifshitz, E. M., *Zh. Eksp. Teor. Fiz.*, Vol. 29, 94, 1955.
8. Lifshitz, E. M., *Sov. Phys. JETP*, Vol. 2, 73, 1956.
9. Sernelius, B. E., *Surface Modes in Physics*, Wiley, Berlin, 2001.
10. Safari, H., S. Y. Buhmann, D.-G. Welsch, and H. T. Dung, *Phys. Rev. A*, Vol. 74, 042101, 2006.
11. Buhmann, S. Y., H. Safari, H. T. Dung, and D.-G. Welsch, *Optics and Spectroscopy*, Vol. 103, 374, 2007.
12. Thiyam, P., C. Persson, B. E. Sernelius, D. F. Parsons, A. Malthe-Sørensen, and M. Boström, *Phys. Rev. E*, in press, 2014.
13. Onsager, L., *J. Am. Chem. Soc.*, Vol. 58, 1486, 1936.
14. Parsons, D. F. and B. W. Ninham, *J. Phys. Chem. A*, Vol. 113, 1141, 2009.
15. Parsons, D. F. and B. W. Ninham, *Langmuir*, Vol. 26, 1816, 2010.
16. Jackson, J. D., *Classical Electrodynamics*, Wiley, New York, 1998.
17. Sambale, A., S. Y. Buhmann, and S. Scheel, *Phys. Rev. A*, Vol. 81, 012509, 2010.
18. Querry, M. R., D. M. Wieliczka, and D. J. Segelstein, *Handbook of Optical Constants of Solids II*, 1059, Academic Press, 1991.
19. Perdew, J. P., K. Burke, and M. Ernzerhof, *Phys. Rev. Lett.*, Vol. 77, 3865, 1996.
20. Kresse, G. and D. Joubert, *Phys. Rev. B*, Vol. 59, 1758, 1999.
21. Blöchl, P. E., *Phys. Rev. B*, Vol. 50, 17953, 1994.
22. Nosé, S., *Mol. Phys.*, Vol. 52, 255, 1984.
23. Hoover, W. G., *Physical Review A*, Vol. 31, 1695, 1985.
24. Nosé, S., *J. Chem. Phys.*, Vol. 81, 511, 1984.

The C-method as an Initial Value Problem: Application to Multilayer Gratings

Cihui Pan^{1,2,3}, Richard Dusséaux¹, and Nahid Emad^{2,3}

¹Laboratoire LATMOS, 11 Boulevard d'Alembert, Guyancourt 78280, France

²Laboratoire PRISM, 45 avenue des Etats-Unis, Versailles 78035, France

³Laboratoire Maison de la Simulation, Bâtiment 565, Gif-sur-Yvette Cedex 91191, France

Abstract— We study our approach of the C-method as an initial value problem for the efficient calculation of the N -dimensional scattering matrix of a grating. We apply this method to multilayer gratings with an arbitrary number of interfaces. The interfaces can have different functional form and amplitude and can be parallel or not.

For each interface separating two homogeneous media, we consider two horizontal planes above and below the interface, and define a coordinate system such that the interface and both horizontal planes correspond to coordinate surfaces. Inside the area delimited by the two horizontal planes, the Maxwell's equations lead to an initial value problem which can be solved with initial conditions satisfying the boundary conditions. Outside this area, the fields are represented by Rayleigh expansion. The scattering matrix between two consecutive media is obtained by using continuity relations between different components of fields on the horizontal planes.

We consider a $n + 1$ layer diffraction grating, thus there are n interfaces separating the layers. From the uppermost to downmost, these layers are composed of medium 1 to medium $n + 1$. Each medium has a constant optical index. Thus we can calculate the scattering matrix $S_{i,i+1}$ which associate the incoming and outgoing waves from medium i and $i + 1$. Then we collect all the scattering matrix of adjacent medium, $S_{i,i+1}$, $i = 1, \dots, n$ and obtain the global matrix $S_{1,n+1}$ by combination of elementary matrices $S_{i,i+1}$, $i = 1, \dots, n$.

The proposed method gives the efficiencies with a good accuracy. Experiments are performed on a three layer grating with interfaces described by Trigonometric functions. We also study the anomalies of coated dielectric gratings.

1. INTRODUCTION

The curvilinear coordinate method (C-method) is based on a covariant formulation of Maxwell's equations written in a coordinate system such that one of the coordinate surfaces coincide with the grating surface. It is a powerful theoretical tool for analyzing gratings [1, 2]. This method uses a new coordinate system such that the coordinates x and z are unchanged and y is replaced by $u = y - a(x)$ where $a(x)$ is the function describing the grating geometry. The new coordinate system enables us to express the problem as an eigenvalue problem which could be solved numerically. The covariant components of the electric and magnetic fields can be expanded as a linear combination of eigensolutions satisfying the outgoing wave condition. The boundary condition allows the diffraction amplitudes to be determined.

In this paper, we consider a new approach of the curvilinear coordinate method [3]. Instead of eigenproblem, this new approach translate the problem to an initial value problem which leads to the scattering matrix of a grating. We apply this method to multilayer gratings with an arbitrary number of interfaces. The interfaces can have different functional form and amplitude and can be parallel or not. For each interface separating two homogeneous media, we consider two horizontal planes above and below the interface, and define a coordinate system such that the interface and both horizontal planes correspond to coordinate surfaces. Inside the area delimited by the two horizontal planes, the Maxwell's equations lead to an initial value problem which can be solved with initial conditions satisfying the boundary conditions. Outside this area, the fields are represented by Rayleigh expansions. The scattering matrix between two consecutive media is obtained by using continuity relations between different components of fields on the horizontal planes. We consider a $n + 1$ layer diffraction grating, thus there are n interfaces separating the layers. From the uppermost to downmost, these layers are composed of medium 1 to medium $n + 1$. Each medium has a constant optical index. Thus we can calculate the scattering matrix $S_{i,i+2}$ which associate the incoming and outgoing waves from medium i and $i + 1$. Then we collect all the scattering matrix of adjacent medium, $S_{i,i+1}$, $i = 1, \dots, n$ and obtain the global matrix $S_{1,n+1}$ by combination of elementary matrices $S_{i,i+1}$, $i = 1, \dots, n$.

The article is structured as follows. In Section 2, we present the Maxwell's equations under the covariant form expressed in the new coordinate system which is adapted to the grating surface and horizontal planes. In Section 3, we introduce the concept of scattering matrix and how to form the global matrix $S_{1,n+1}$ from the local matrices $S_{i,i+1}$, $1 \leq i \leq n$. In Section 4, experiments are performed on a three layer grating with interfaces described by Trigonometric functions. We also study the anomalies of coated dielectric gratings. In Section 5, results and conclusions are given.

2. THE C-METHOD AS AN INITIAL VALUE PROBLEM

We consider a $n + 1$ layer diffraction grating. The interface is represented by a periodic cylindrical surface $y = a_i(x)$, $1 \leq i \leq n$. This surface separates the medium i from the medium $i + 1$. In Figure 1, two representative adjacent interfaces are shown. We consider separable layered grating, meaning that there exists a horizontal line $y = y_{i+1}$ separates the interface $y = a_i(x)$ and the interface $y = a_{i+1}(x)$ for each i . The interfaces in general have different functional forms and amplitudes, but there exists a value D such that D is the period of the function or a multiple of the period. The thickness h_i is measured between the middle lines of the two boundaries. The medium between the interface $y = a_i(x)$ and the interface $y = a_{i+1}(x)$ is homogeneous with optical index ν_i , impedance Z_i and wave number k .

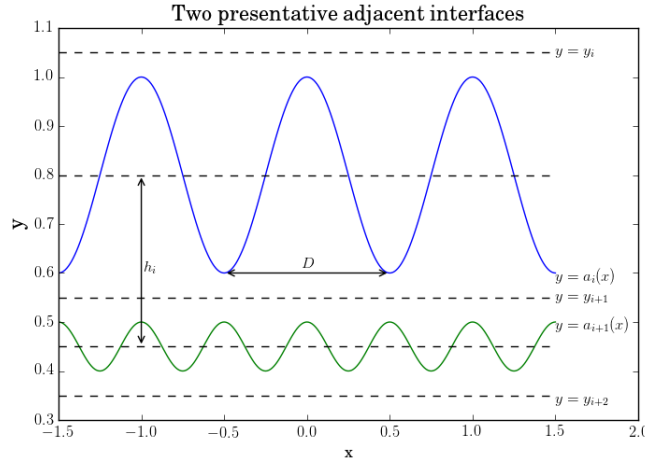


Figure 1: Notation for the description of a layered grating.

As the interfaces are separable, we can consider each interface separately and then combine to form the global matrix. For each interface $y = a_i(x)$, we consider the problem as in Figure 2.

Outside the region delimited by $y \leq y_i$ and $y \geq y_{i+1}$, under the Cartesian coordinates (x, y, z) , the field is represented by a linear combination of elementary plane waves, known as Rayleigh expansion:

$$\begin{cases} F_c^{(i)}(x, y) = \sum_n \left(c_n^{(i+)} \exp(-j\alpha_n x) \exp(-j\beta_n^{(i)} y) + c_n^{(i-)} \exp(-j\alpha_n x) \exp(j\beta_n^{(i)} y) \right) \\ G_c^{(i)}(x, y) = \sum_n \frac{\beta_n^{(i)}}{k^{(j)}} \left(c_n^{(i+)} \exp(-j\alpha_n x) \exp(-j\beta_n^{(i)} y) + c_n^{(i-)} \exp(-j\alpha_n x) \exp(j\beta_n^{(i)} y) \right) \end{cases} \quad (1)$$

The subscript c denotes the Cartesian components of electromagnetic field. In $E_{//}$ polarization, $F_c^{(i)}(x, y) = E_z^{(i)}(x, y)$, $G_c^{(i)} = Z^{(i)} H_z^{(i)}(x, y)$ and in $H_{//}$ polarization, $F_c^{(i)}(x, y) = Z^{(i)} H_z^{(i)}(x, y)$, $G_c^{(i)}(x, y) = -E_x^{(i)}(x, y)$. Superscripts (+) and (-) denotes a plane wave moving in direction along the z -axis and inverse the z -axis, respectively. The propagation coefficients of the n -th order diffraction are presented by α_n and $\beta_n^{(i)}$ with the relation

$$\alpha_n^2 + \left(\beta_n^{(i)} \right)^2 = k_i^2 \quad (2)$$

where $\text{Im}(\beta_n^{(i)}) < 0$ and $\alpha_n = k^{(1)} \sin \theta_0 + n \frac{2\pi}{D}$. The propagation coefficient $\beta_n^{(i)}$ defines the nature of the plane wave: a propagation wave if $\beta_n^{(i)}$ is real, and an evanescent wave if $\beta_n^{(i)}$ is imaginary.

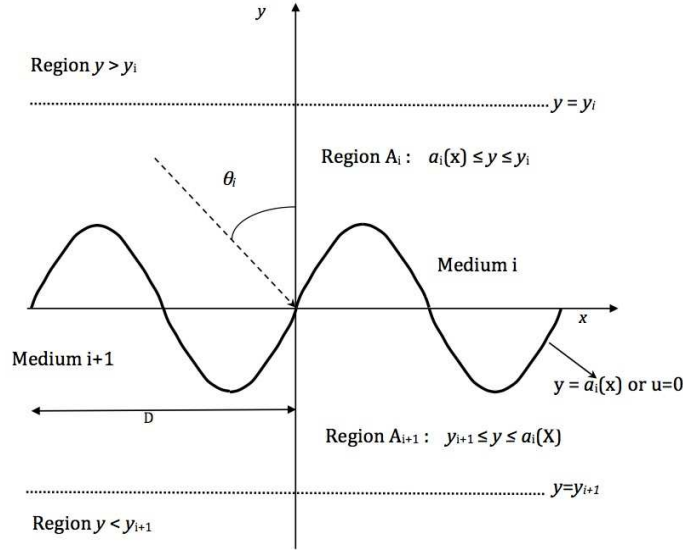


Figure 2: Notation for the description of interface $y = a_i(x)$, illuminated by a plane wave under the incidence θ_0 .

We define the local scattering matrix (S -matrix) to relate the amplitudes of outgoing plane waves $(c_n^{(i+)}, c_n^{((i+1)-)})$ to those of incoming waves $(c_n^{(i-)}, c_n^{((i+1)+)})$ such that

$$\begin{pmatrix} c_n^{(i+)} \\ c_n^{((i+1)-)} \end{pmatrix} = S_{i,i+1} \begin{pmatrix} c_n^{(i-)} \\ c_n^{((i+1)+)} \end{pmatrix} \quad (3)$$

here we use $c^{(m\pm)}$ to represent a vector containing the scattering amplitudes $c_n^{(m\pm)}$, $m = i, i + 1$.

Within the regions A_i and A_{i+1} defined by $a_i(x) \leq y \leq y_i$ and $y_{i+1} \leq y \leq a_i(x)$, we consider the non-orthogonal coordinate system defined as follows [3–5]:

$$\begin{cases} x' = x \\ u = y_m \frac{y - a_i(x)}{y_m - a_i(x)}, \quad m = i, i + 1 \\ z' = z \end{cases} \quad (4)$$

The grating surface $y = a_i(x)$ coincides with the coordinate surface $u = 0$ and the horizontal plane $y = y_m$ with $u = y_m$, $m = i, i + 1$. With the help of this non-orthogonal coordinate system, we manage to translate the problem to an initial value problem which can be solved numerically to obtain the local scattering matrix $S_{i,i+1}$ for all i . For more details, see [3].

We then combine the local scattering matrices to form the global scattering matrix $S_{1,n+1}$. In fact, if we have local scattering matrices $S_{p,q}$ and $S_{q,r}$ such that $p < q < r$, then we can obtain the scattering matrix $S_{p,r}$.

$$\begin{cases} \begin{pmatrix} c^{(p+)} \\ c^{(q-)} \end{pmatrix} = S_{p,q} \begin{pmatrix} c^{(p-)} \\ c^{(q+)} \end{pmatrix} = \begin{pmatrix} S_{p,q}^{(+)} & S_{p,q}^{(++)} \\ S_{p,q}^{(-)} & S_{p,q}^{(-+)} \end{pmatrix} \begin{pmatrix} c^{(p-)} \\ c^{(q+)} \end{pmatrix} \\ \begin{pmatrix} c^{(q+)} \\ c^{(r-)} \end{pmatrix} = S_{q,r} \begin{pmatrix} c^{(q-)} \\ c^{(r+)} \end{pmatrix} = \begin{pmatrix} S_{q,r}^{(+)} & S_{q,r}^{(++)} \\ S_{q,r}^{(-)} & S_{q,r}^{(-+)} \end{pmatrix} \begin{pmatrix} c^{(q-)} \\ c^{(r+)} \end{pmatrix} \end{cases} \quad (5)$$

Eliminating the vectors c^{q+} and c^{r-} , one glue the two scattering matrices to be one $S_{p,r}$:

$$S_{p,r} = \begin{pmatrix} S_{p,q}^{(+)} + S_{p,q}^{(++)}(I - S_{q,r}^{(+)}S_{p,q}^{(-)})^{-1}S_{q,r}^{(++)}S_{p,q}^{(-)} & S_{p,q}^{(++)}(I - S_{q,r}^{(+)}S_{p,q}^{(-)})^{-1}S_{q,r}^{(++)} \\ S_{q,r}^{(-)}(I - S_{p,q}^{(+)}S_{q,r}^{(-)})^{-1}S_{p,q}^{(-)} & S_{q,r}^{(-)} + S_{q,r}^{(-+)}(I - S_{p,q}^{(+)}S_{q,r}^{(-)})^{-1}S_{p,q}^{(+)}S_{q,r}^{(+)} \end{pmatrix} \quad (6)$$

So in this way, we glue $S_{1,2}$ and $S_{2,3}$ to get $S_{1,3}$, and then glue $S_{1,3}$ and $S_{3,4}$ to get $S_{1,4}$ and so on until we get the global matrix $S_{1,n+1}$. We can also explore the parallelism in this gluing

operation. For example, we can in the first step, obtain $S_{1,3}$, $S_{3,5}$, $S_{5,7}$... in parallel, and in the second step, obtain $S_{1,5}$, $S_{5,9}$, ... in parallel, and so on. This needs only $\mathcal{O}(\log(n))$ steps to get the global scattering matrix. Moreover, for the calculation of the local scattering matrix $S_{i,i+1}$, the proposed method in [3] leads to systems of first-order linear differential equations, the solution of which requires the choice of an iterative algorithm. The proposed method is based on numerical integrations with N independent initial vectors. The kernel of this computing process is the numerical integration. This approach is also particularly well adapted to large-scale parallel and distributed architectures. Indeed, in the context of a distributed system comprising a network of machines, each of the problems could be solved on a machine whose architecture can be single or multiple processors. The proposed new method has a significant degree of coarse grain parallelism and requires little communication. These features offer the possibility of reducing dramatically the computation time. It's an advantage compared with the conventional C-method which leads to eigenvalue problems and requires the use of global eigensolver like QR method. In order to improve the performances of the QR algorithm, we can parallelize it. Nevertheless, the exploitation of the parallelism of this algorithm is a delicate task. Indeed, in each of iteration of QR, only two rows and two columns of the matrix participate to computation imposing a parallel algorithm with a small degree of parallelism. The reduction in the computation time cannot be substantial.

3. NUMERICAL EXPERIMENTS

We perform an experiment in the article [6]. The grating considered is a sinusoidal defined by $a_1(x) = a_1 \cos(\frac{2\pi}{D}x)$, $a_2(x) = a_2 \cos(\frac{2\pi}{D}x)$. Figure 4 shows the efficiency curves under the polarization $E_{//}$, with the value of $\sin \theta_0$ varying from 0.24 to 0.38. With the same parameters as in that paper, Figure 3 is exactly the same as in the paper [6]. This can be used as a proof of the validity of our method. Moreover, we also performed more experiments to see how this figure changes when we change the amplitude of function $y = a_1(x)$ and the optical index ν_3 . Figure 4 shows how it is like when $a_1 = 0.01$ and Figure 5 shows the case when $\nu_3 = 1.5$, with other parameters fixed.

In Figure 3, the parameters of the corrugated waveguide is chosen in such a way that only one mode propagate if the interface were plane. We see from Figure 3 that in the vicinity of excitation of the guided wave the efficiency changes from 0 to 1. In Figure 4, the efficiency can not reach 0, it changes from a small value close to 0 to 1. In Figure 5, the efficiency can neither reach 0 nor 1. It can be observed that when a_1 varies from $0.02 \mu\text{m}$ to $0.01 \mu\text{m}$, the jump becomes steeper. One can also observe that the place of the jump moves towards the left direction. When we vary a_2 from $0.02 \mu\text{m}$ to $0.01 \mu\text{m}$, no similar phenomena can be observed. In fact, the curves seem almost stay the same.

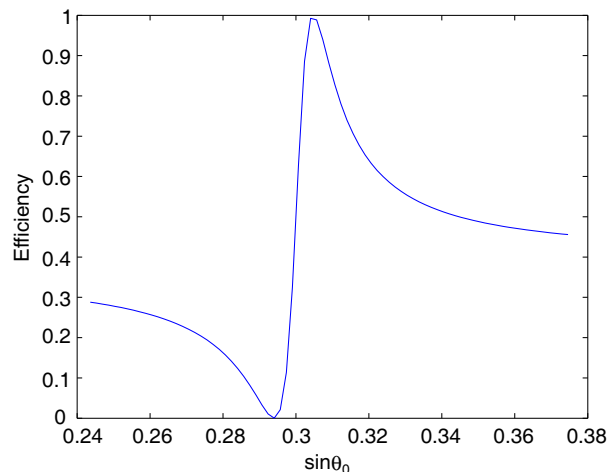


Figure 3: Diffraction efficiency of the zeroth reflected order of the sinusoidal grating. Parameters of the system are: $\nu_1 = \nu_3 = 1$, $\nu_2 = 2.3$, $h_1 = 0.19 \mu\text{m}$, $D = 0.37 \mu\text{m}$, $\lambda = 0.6328 \mu\text{m}$, $a_1 = a_2 = 0.02 \mu\text{m}$, for TE polarization.

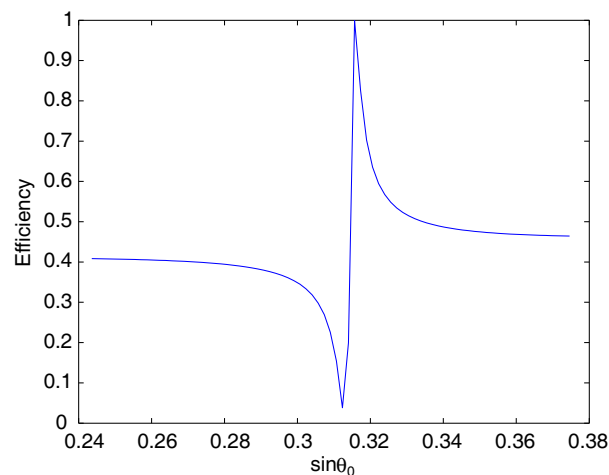


Figure 4: Diffraction efficiency of the zeroth reflected order of the sinusoidal grating. Parameters of the system are: $\nu_1 = \nu_3 = 1$, $4\nu_2 = 2.3$, $h_1 = 0.19 \mu\text{m}$, $D = 0.37 \mu\text{m}$, $\lambda = 0.6328 \mu\text{m}$, $a_1 = 0.01 \mu\text{m}$, $a_2 = 0.02 \mu\text{m}$, for TE polarization.

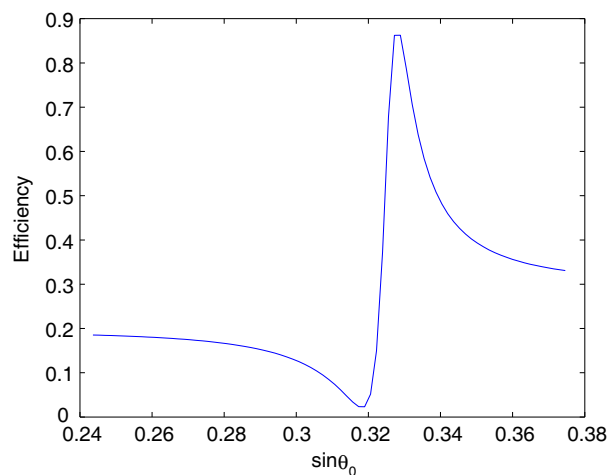


Figure 5: Diffraction efficiency of the zeroth reflected order of the sinusoidal grating. Parameters of the system are: $\nu_1 = 1$, $\nu_3 = 1.5$, $\nu_2 = 2.3$, $h_1 = 0.19 \mu\text{m}$, $D = 0.37 \mu\text{m}$, $\lambda = 0.6328 \mu\text{m}$, $a_1 = a_2 = 0.02 \mu\text{m}$, for TE polarization.

4. CONCLUSION

We studied our approach of the C-method as an initial value problem for the efficient calculation of the N -dimensional scattering matrix of a grating. We applied this method to multilayer gratings with an arbitrary number of interfaces. We have shown how to combine the local scattering matrix to obtain the global one. We have validate our method by comparison experiments results with that from published paper. The proposed method has very good accuracy as well as a natural of two level parallel property. This new version of C-method is an attractive alternative to analyze multilayered grating having parallel or non-parallel interfaces.

REFERENCES

1. Chandezon, J., G. Gaoult, and D. Maystre, "A new theoretical method for diffraction gratings and its numerical application," *J. Optics (Paris)*, Vol. 11, 235–241, 1980.
2. Li, L. and J. Chandezon, "Improvement of the coordinate transformation method for surface-relief gratings with sharp edges," *JOSA A*, Vol. 13, 2247–2255, 1996.
3. Pan, C., R. Dusséaux, Mandiaye Fall, and Nahid Emad, "Curvilinear coordinate method as an initial value problem: application to gratings," *JOSA A*, Vol. 32, No. 1, 143–149, 2015.
4. Dusséaux, R., P. Chambelin, and C. Faure, "Analysis of rectangular waveguide H -plane junctions in nonorthogonal coordinate system," *Progress In Electromagnetics Research*, Vol. 28, 205–229, 2000.
5. Afifi, S. and R. Dusséaux, "Statistical study of radiation loss from planar optical waveguides: The curvilinear coordinate method and the small perturbation method," *Journal of the Optical Society of America A, Optical Society of America*, Vol. 27, 1171–1184, 2010.
6. Popov, E., L. Mashev, and D. Maystre, "Theoretical study of the anomalies of coated dielectric gratings," *Optica Acta*, Vol. 33, No. 5, 607–619, 1986.

Efficient Numerical Solution for Time-domain Volume Integral Equations

J. Zhang and M. S. Tong

Department of Electronic Science and Technology
Tongji University, 4800 Cao'an Road, Shanghai 201804, China

Abstract— Electromagnetic (EM) analysis for inhomogeneous penetrable structures relies on the formulation of volume integral equations (VIEs) in integral equation approach and time-domain VIEs (TDVIEs) are required for transient interaction with the structures. The TDVIEs are usually solved by combining the method of moments (MoM) with well-designed basis function in spatial domain and a march-on-in-time (MOT) scheme in temporal domain. We propose a different approach in which the Nyström method is used in the spatial domain and the MoM with Laguerre basis and testing functions is employed in the temporal domain. The proposed approach can simplify the numerical implementation and fully solve the stability problem as in the traditional approach. A numerical example is presented to illustrate the approach and good results have been observed.

1. INTRODUCTION

Integral equation approach is widely used for solving electromagnetic (EM) problems. For inhomogeneous penetrable structures, the volume integral equations (VIEs) are indispensable, and furthermore the time-domain version (TDVIEs) should be applied when a transient interaction with the structures exists [1]. The TDVIEs are usually solved by combining the method of moments (MoM) with a well-designed basis function like the Schaubert-Wilton-Glisson (SWG) basis function [2] in spatial domain and a march-on-in-time (MOT) scheme in temporal domain [3]. The MoM requires conforming meshes in geometric discretization and also needs to perform two-fold integrations in evaluating matrix elements, resulting in certain inconvenience. On the other hand, the MOT has a well-known stability problem which has not been fully solved yet although various improvements were proposed [4].

In this work, we propose a different scheme to solve the TDVIEs for transient EM problems with penetrable objects. Unlike the conventional approach, the Nyström method is used in the spatial domain while the MoM with Laguerre basis and testing functions is employed in the temporal domain. The Nyström method uses a point-matching procedure to discretize integral equations and does not use any basis and testing functions so that the implementation can be simplified. Also, the method does not require conforming meshes and can endure low-quality meshes, leading to much convenience in geometric discretization [5]. In temporal domain, the expansion of Laguerre basis function can naturally enforce the causality and also the Galerkin's testing procedure can fully solve the numerical stability problem in a march-on-in-degree (MOD) manner [6]. Although the MOD may not be more efficient than the MOT, it is very suitable to solve transient problems [7]. Numerical examples for transient EM scattering by a dielectric cylinder are presented and the merits of proposed approach has been demonstrated.

2. TIME-DOMAIN VOLUME INTEGRAL EQUATIONS (TDVIES)

Consider the scattering of transient EM wave by a dielectric object with a volume V in the free space with a permittivity ϵ_0 and permeability μ_0 . The problem can be formulated by the TDVIEs which is reduced to a single electric-field TDVIE (EF-TDVIE) when the object is nonmagnetic. The EF-TDVIE states that the total electric field is equal to the summation of incident electric field and scattered electric field. The scattered electric field $\mathbf{E}^{sca}(\mathbf{r}, t)$ is related to the magnetic vector potential $\mathbf{A}(\mathbf{r}, t)$ and electric scalar potential $\Phi(\mathbf{r}, t)$ by

$$\mathbf{E}^{sca}(\mathbf{r}, t) = -\frac{\partial}{\partial t}\mathbf{A}(\mathbf{r}, t) - \nabla\Phi(\mathbf{r}, t) = -\frac{\mu_0}{4\pi} \int_V \frac{1}{R} \frac{\partial}{\partial t} \mathbf{J}(\mathbf{r}', \tau) dS' - \frac{1}{4\pi\epsilon_0} \nabla \int_V \frac{1}{R} q(\mathbf{r}', \tau). \quad (1)$$

where $\mathbf{J}(\mathbf{r}, t)$ and $q(\mathbf{r}', t)$ are the current density and charge density induced in the object, respectively, $R = |\mathbf{r} - \mathbf{r}'|$ is the distance between an observation point \mathbf{r} and a source point \mathbf{r}' , and

$\tau = t - R/c$ is the retarded time with c being the speed of light in free space. By using the continuity equation and introducing a new source vector $\mathbf{e}(\mathbf{r}, t)$ which is related to the charge density by $q(\mathbf{r}, t) = -\nabla \cdot \mathbf{e}(\mathbf{r}, t)$, we can write the EF-TDVIE as

$$\frac{\mu_0}{4\pi} \int_V \frac{1}{R} \frac{\partial^2 \mathbf{e}(\mathbf{r}', \tau)}{\partial t^2} dV' + \frac{1}{4\pi\epsilon_0} \int_V \nabla \nabla \left(\frac{1}{R} \right) \cdot \mathbf{e}(\mathbf{r}', \tau) dV' = \frac{\mathbf{e}(\mathbf{r}, t)}{[\epsilon_0 - \epsilon(\mathbf{r})]} + \mathbf{E}^{inc}(\mathbf{r}, t), \quad \mathbf{r} \in V. \quad (2)$$

3. NYSTRÖM-BASED SCHEME FOR SOLVING THE TDVIES

The dielectric object is discretized into N small tetrahedral elements and ΔV_n is the volume of the n th tetrahedron. The unknown source vector $\mathbf{e}(\mathbf{r}', t)$ can then be expanded as

$$\mathbf{e}(\mathbf{r}', t) = \sum_{n=1}^N e_n(t) \mathbf{e}_n(\mathbf{r}'). \quad (3)$$

If we apply the Nyström method in spatial domain, i.e., the integration over a small tetrahedron is replaced with a summation under a quadrature rule provided that the integrand is regular, then we have

$$\frac{\mathbf{e}(\mathbf{r}, t)}{[\epsilon_0 - \epsilon(\mathbf{r})]} + \mathbf{E}^{inc}(\mathbf{r}, t) = \frac{\mu_0}{4\pi} \sum_{n=1}^N \sum_{q=1}^Q \frac{w_{nq}}{R} \frac{\partial^2 e_n(\tau)}{\partial t^2} \mathbf{e}_n(\mathbf{r}'_{nq}) + \frac{1}{4\pi\epsilon_0} \sum_{n=1}^N \sum_{q=1}^Q w_{nq} \nabla \nabla \left(\frac{1}{R} \right) \cdot \mathbf{e}_n(\mathbf{r}'_{nq}) e_n(\tau) \quad (4)$$

where $\mathbf{e}_n(\mathbf{r}'_{nq}) = \mathbf{e}_{nq}$ is the value of unknown source vector at the q th quadrature point in the n th tetrahedron. If we choose the p th quadrature point in the m th tetrahedron as an observation point to perform a collocation procedure, then we have the following space-domain matrix equation

$$\frac{\mathbf{e}_{mp} e_m(t)}{[\epsilon(\mathbf{r}_{mp}) - \epsilon_0]} + \sum_{n=1}^N \sum_{q=1}^Q \left[\frac{\mu_0}{4\pi} \frac{\partial^2 e_n(\tau)}{\partial t^2} \mathbf{a}_{mpnq} + \frac{e_n(\tau)}{4\pi\epsilon_0} \mathbf{b}_{mpnq} \right] = \mathbf{E}^{inc}(\mathbf{r}_{mp}, t), \quad m=1, \dots, N; p=1, \dots, Q \quad (5)$$

where

$$\mathbf{a}_{mpnq} = \frac{w_{nq} \mu_0}{4\pi R_{mpnq}} \mathbf{e}_{nq}, \quad \mathbf{b}_{mpnq} = \frac{w_{nq}}{4\pi\epsilon_0} \nabla \nabla \left(\frac{1}{R} \right) \cdot \mathbf{e}_{nq}. \quad (6)$$

The above procedure could have a singularity problem which occurs when $m = n$ but we have developed a robust treatment technique [8].

In the temporal domain, we use the Laguerre function $\phi_j(t) = e^{-t/2} L_j(t)$ as a basis function to expand $e_n(t)$ [6]

$$e_n(t) = \sum_{j=0}^{\infty} e_{nj} \phi_j(st) \quad (7)$$

where s is the scaling factor to adjust the support of expansion. Substituting this expansion to Eq. (5) and using $\phi_i(st)$ as a testing function to test the equation, we can obtain

$$\begin{aligned} & \sum_{n=1}^N \sum_{q=1}^Q (0.25s^2 \mathbf{a}_{mpnq} + \mathbf{b}_{mpnq}) e_{nj} I_{ij}(sR_{mpnq}/c) \\ & - \sum_{n=1}^N \sum_{q=1}^Q \sum_{j=0}^{i-1} (0.25s^2 \mathbf{a}_{mpnq} + \mathbf{b}_{mpnq}) e_{nj} I_{ij}(sR_{mpnq}/c) \\ & - \sum_{n=1}^N \sum_{q=1}^Q \sum_{j=0}^i s^2 \mathbf{a}_{mpnq} \sum_{k=0}^{j-1} (j-k) e_{nk} I_{ij}(sR_{mpnq}/c) + \frac{\mathbf{e}_{mp} e_{mi}}{[\epsilon_0 - \epsilon(\mathbf{r}_{mp})]} + \mathbf{V}_{mpi} \end{aligned} \quad (8)$$

where $I_{ij}(sR_{mpnq}/c)$ and \mathbf{V}_{mpi} can be determined according to the appendix in [6]. Combining the space-domain and time-domain expansion coefficients together, we can solve the matrix equation with a march-on-in-degree (MOD) procedure.

4. NUMERICAL EXAMPLE

We consider the transient EM scattering by a dielectric cylinder to demonstrate the approach. The cylinder, which is centered at the origin of a rectangular coordinate system as shown in Fig. 1, has a height $h = 1.0$ m and a radius $a = 0.5$ m at its cross section. The relative permittivity of the cylinder is $\epsilon_r = 2.0$ and it is discretized into 886 tetrahedrons. A Gaussian plane wave is illuminating the scatterer along the $-z$ direction and the electric field is defined by

$$\mathbf{E}^{inc}(\mathbf{r}, t) = \hat{x} \frac{4e^{-\gamma^2}}{\sqrt{\pi T}}, \quad \gamma = \frac{4}{T}(ct - ct_0 + \mathbf{r} \cdot \hat{z}) \quad (9)$$

where T is the width of Gaussian impulse, and t_0 is the time delay denoting the time when the pulse peaks at the origin. We choose a Gaussian pulse with $T = 4.0$ lm (light meter) and $ct_0 = 6.0$ lm as an incident wave. Fig. 2 plots the solution of the θ -component of normalized far-zone scattered electric field observed along the backward direction. The result agrees well with the solution obtained from the inverse discrete Fourier transform (IDFT) of frequency-domain solution.

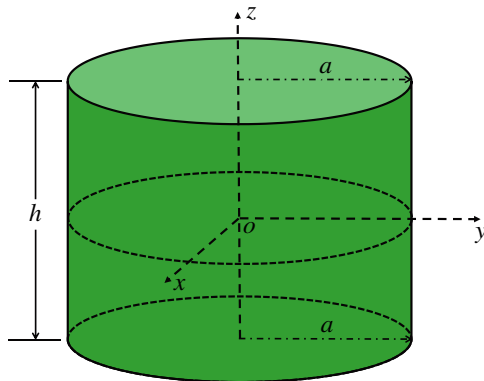


Figure 1: Geometry of a dielectric cylinder for transient scattering.

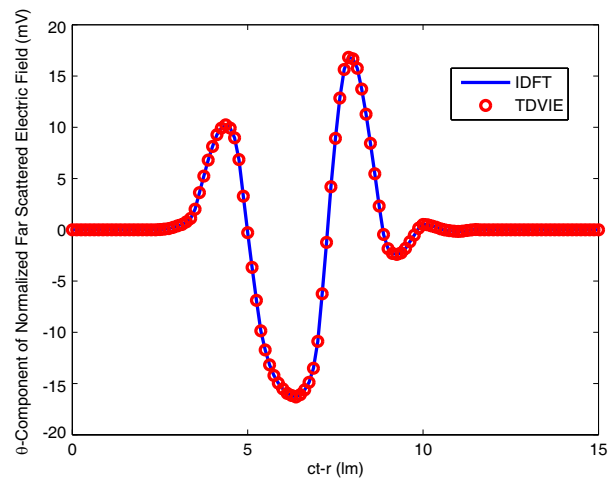


Figure 2: Solution of θ -component of normalized far-zone back-scattered electric field for transient scattering by a dielectric cylinder.

5. CONCLUSION

The TDVIEs are used to formulate the transient EM problems with penetrable objects. We propose a different scheme to solve the TDVIEs by combining the Nyström method in spatial domain and the MoM with the Laguerre basis and testing functions in temporal domain. The benefits of the scheme include the simple mechanism of implementation with allowance of using nonconforming and low-quality meshes in spatial domain, and also the natural satisfaction of causality with a full elimination of instability in temporal domain. A numerical example for transient EM scattering by a dielectric cylinder is presented and good results have been observed.

ACKNOWLEDGMENT

This work was supported by the International Collaboration Foundation for Science and Technology, Shanghai, China (Project No. 13520722600).

REFERENCES

1. Rao, S. M., *Time Domain Electromagnetics*, Academic Press, San Diego, 1999.
2. Schaubert, D. H., D. R. Wilton, and A. W. Glisson, "A tetrahedral modeling method for electromagnetic scattering by arbitrary shaped inhomogeneous dielectric bodies," *IEEE Trans. Antennas Propagat.*, Vol. 32, No. 1, 77–85, Jan. 1984.
3. Weile, D. S., G. Pisharody, N.-W. Chen, B. Shanker, and E. Michielssen, "A novel scheme for the solution of the time-domain integral equations of electromagnetics," *IEEE Trans. Antennas Propagat.*, Vol. 52, No. 1, 283–294, Jan. 2004.

4. Shi, Y. and J.-M. Jin, "A time-domain volume integral equation and its marching-on-in-degree solution for analysis of dispersive dielectric objects," *IEEE Trans. Antennas Propagat.*, Vol. 59, No. 3, 969–978, Mar. 2011.
5. Canino, L. S., J. J. Ottusch, M. A. Stalzer, J. L. Visher, and S. Wandzura, "Numerical solution of the Helmholtz equation in 2D and 3D using a high-order Nyström discretization," *J. Comput. Phys.*, Vol. 146, 627–663, 1998.
6. Jung, B. H., Y. S. Chung, and T. K. Sarkar, "Time-domain EFIE, MFIE, and CFIE formulations using Laguerre polynomials as temporal basis functions for the analysis of transient scattering from arbitrary shaped conducting structures," *Progress In Electromagnetics Research*, Vol. 39, 1–45, 2003.
7. Jung, B. H., Z. Ji, T. K. Sarkar, M. Salazar-Palma, and M. Yuan, "A comparison of marching-on in time method with marching-on in degree method for the TDIE solver," *Progress In Electromagnetics Research*, Vol. 70, 281–296, 2007.
8. Tong, M. S. and W. C. Chew, "Nyström method solution of volume integral equations for electromagnetic scattering by 3D penetrable objects," *IEEE Trans. Antennas Propagat.*, Vol. 58, No. 5, 1645–1652, May 2010.

Analysis of EM Emission Characteristics by Arbitrarily Oriented Microstrip Lines Based on TEM Cell Electric and Magnetic Coupling Fields

Jung-Yeol Park¹, Jin-A. Choi¹, Jae-Kyung Wee¹, In-Chae Song¹,
Boo-Gyoun Kim¹, Hyok Lee², and Seung-Real Ryu²

¹School of Electronics, Soongsil University, Korea

²Korea Automotive Technology Institute, Korea

Abstract— In this paper, we analyzed electromagnetic (EM) emission characteristics with arbitrarily oriented microstrip lines on a printed circuit board (PCB). The designed DUTs are based on line patterns between an integrated circuit (IC) and electronic parts on a PCB. These represent EM models of interconnect line, signal propagation, and IC itself. The method of lines (MoL) is used to calculate the coupling capacitance matrix between the microstrip lines and the transverse electromagnetic (TEM) cell. This matrix is also used to calculate self-inductance and coupling inductance. In order to apply this method to real system modules, a model library for coupling factors was built with variations of length and direction of microstrip lines. The comparison results between measurement and modeling shows good agreement below 200 MHz.

1. INTRODUCTION

The electromagnetic compatibility (EMC) problem of automotive ICs or high speed PCBs is caused by increase of RF interference between electronic systems at high operating frequency. In particular, the increasing complexity of PCB patterns aggravates the EM interference problem because the patterns act as antennas. Therefore the EM interference becomes a matter of concern in reliability of the system adopting automotive ICs or high speed PCBs. Various researches have been carried out about the conducted EM characteristics of PCB patterns or ICs.

It is known that coupling factors of microstrip lines mounted on a TEM Cell can be modeled by lumped circuit elements [1]. However further research on radiated EM characteristics is still needed although several measurement methods of electric and magnetic field coupling based on a TEM Cell were reported [2, 3]. In this paper, we designed some test PCB patterns for modeling and estimation of radiated EM interference. The radiated coupling factors between a TEM Cell and PCB patterns are calculated by using the MoL which is a very efficient method in comparison with other field solving methods. The accuracy of the model was evaluated through comparing simulated results of the MoL with measured results. Eventually, EM emission characteristics on the complex PCB patterns can be predicted by using the model library which is composed of the modeled parameters of PCB lines.

2. PCB PATTERN SET UP

The fabricated DUTs were designed with microstrip lines on PCB which were based on a real layout with an IC and interconnect lines as shown in Figure 1. In order to analyze the EM emission characteristics of a real PCB module designed patterns are categorized into three groups according to current direction on PCB, line direction, and IC modeling considering current flowing direction on an IC. In Group A, an IC is modeled in relation to capacitive and/or inductive effects according to current flowing direction on IC. Current is fed by a SMA connector mounted on the designed DUTs which are a two-direction type, a one-direction type, and a no-direction type as shown in Figure 1. The magnetic field effects of in-phase and out-of-phase signal direction on interconnects are evaluated with the DUTs in Group B which are designed with variations on current direction, interconnect line spacing, and line width. The DUTs in Group C are designed with variations on signal line directions and line lengths. The designed microstrip lines are fabricated on FR4 substrates with the thickness of 1.55 mm.

3. ANALYSIS PROCEDURE

The MoL which is considered as a special finite difference method is more effective in accuracy and simulation time than the regular finite difference method. The coupling capacitance between the microstrip line and the TEM Cell septum can be easily calculated by using quasi-static approach.

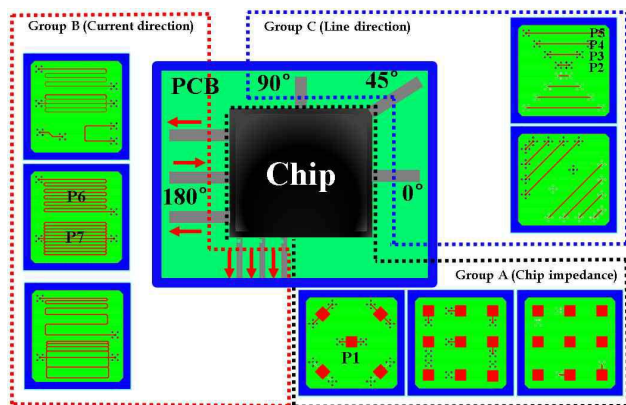


Figure 1: Examples of microstrip lines.

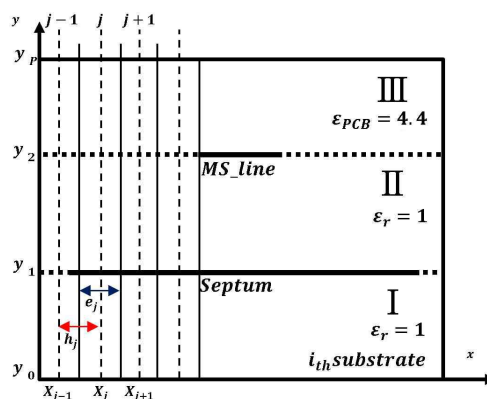
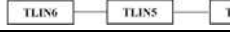


Figure 2: Cross section between TEM cell and microstrip line with finite ground planes [4].

Table 1: Coupling parameters for designed microstrip lines.

		P5 (70 mm)	P4 (50 mm)	P2 (30 mm)	According to direction		
Coupling Parameters	$C_{Coupling}$ [fF]	29.4	19.4	8.4	Fixed		
	$L_{Coupling}$ [pH]	135.8	81.7	30.2	$\cos(\alpha)L_{Coupling}$, where α =angle		
TEM Cell	Left Taper				$Z=39.8 \Omega$	$Z=61.3 \Omega$	$Z=49.4 \Omega$
	Central				C_1 [fF]	56.1	
	Right Taper				$Z=49.4 \Omega$	$Z=61.3 \Omega$	$Z=39.8 \Omega$

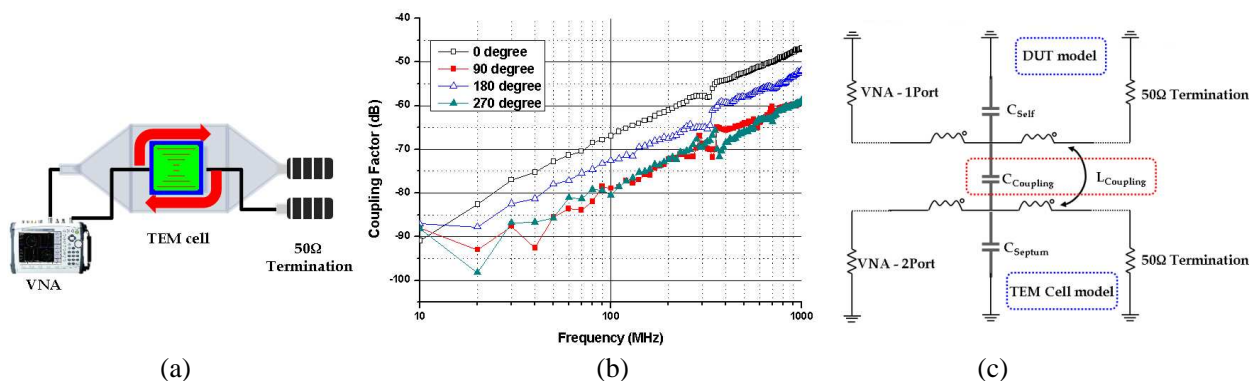


Figure 3: (a) Test environment, (b) coupling factors, and (c) model of coupling between the microstrip line and the TEM Cell septum.

The crosssection between the microstrip line and the TEM Cell in Figure 2 is used for coupling capacitance calculation [4].

The MoL simulation for the microstrip line can be directly expressed as the reduced capacitance matrix, and therefore does not need any manipulation [4]. By obtaining the reduced capacitance matrix for the given microstrip lines we can calculate the inductance matrix [5]. The TEM Cell model described in Table 1 is built by using generic TLIN transmission line models supported in Agilent ADS. The TLIN represents an ideal transmission line and is fully characterized by only two parameters such as characteristic impedance and electrical length. The each taper of the TEM Cell is divided into three sections to model change in characteristic impedance along the electrical length of the taper. Table 1 shows the extracted coupling parameters for the three microstrip lines with different line length in the direction of the DUT. This table is an example of a model library described in Section 4.

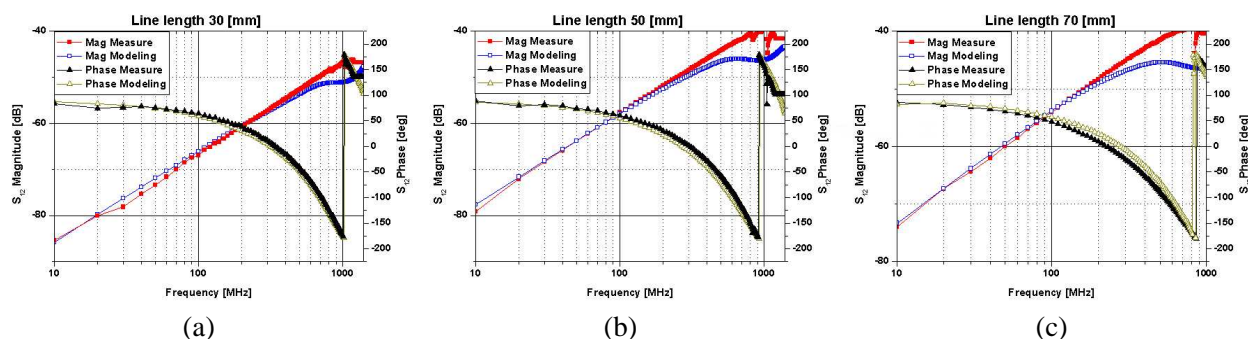


Figure 4: Measurements and modeling of the coupling for: (a) P3, (b) P4, and (c) P5.

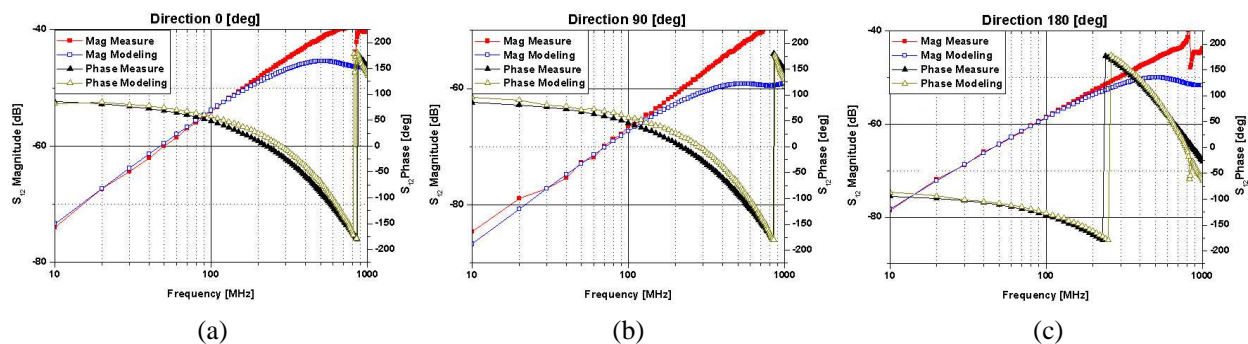


Figure 5: Measurements and modeling of the coupling for: (a) 0 degree, (b) 90 degree, and (c) 180 degree of P5.

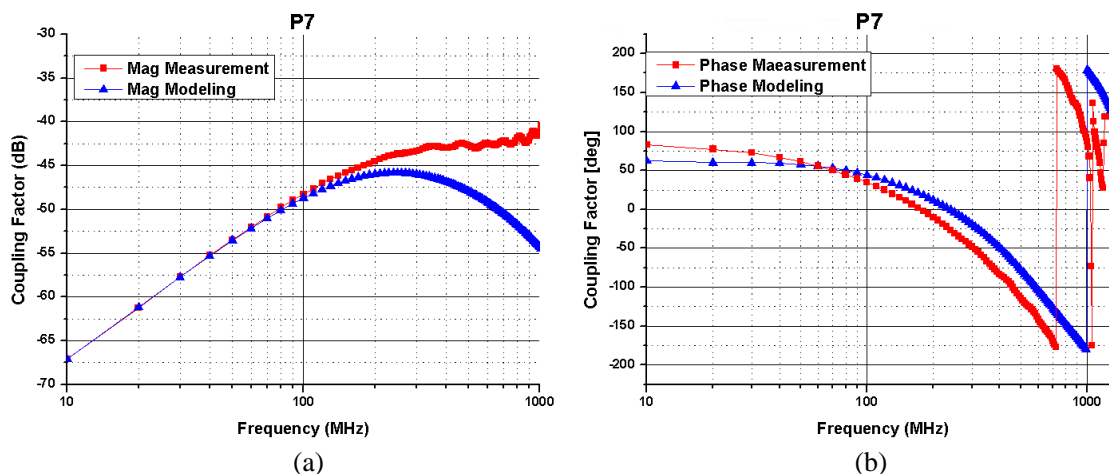


Figure 6: Comparison between measurement and modeling using a library for: (a) magnitude and (b) phase of P7.

4. SIMULATION AND MEASUREMENT RESULTS

Figure 3 shows the test environment, the plot of measured coupling factors according to direction of the DUT and the model of coupling between the microstrip line and the TEM Cell septum. The designed pattern on a 2-layer PCB was tested with the angle of direction of 0, 90, 180, and 270 degrees [6]. The measured results show that the coupling factor of the 0-degree case differs from that of the 180-degree case. Regardless of the direction of the DUT, the capacitive coupling always exists. In contrast, the inductive coupling between the TEM Cell septum and the DUT is minimized when the DUT is positioned perpendicularly with respect to the TEM Cell septum.

Figure 4 shows the comparison results between the measured coupling factors and the modeling parameters according to the microstrip line length. As shown in Figure 4, the phase of coupling factor shows good agreement between the measured and simulated results. However the magnitude of coupling factor is somewhat different at higher frequency. Figure 5 shows the results according to the angle of direction of the DUT. The comparison results of Figure 5 are similar to those of Figure 4. Therefore this modeling method based on a lumped element model can be applied to

system modules operated under 200 MHz.

In order to analyze coupling factors of group B designed according to current direction, the model library for coupling factors of microstrip lines is used. This library is created with variations of line direction and line length as shown in Table 1. As shown in Figure 6, the magnitude of the coupling factor shows good agreement between the measured and modeling results below 200 MHz. There is slight discrepancy in the phase of the coupling factor.

5. CONCLUSION

Using the MoL modeling technic, we analyzed coupling factors between the TEM Cell septum and the microstrip lines. In order to apply this method to real system modules, a model library for coupling factors was built with variations of length and direction of microstrip lines. The comparison results between measurement and modeling shows good agreement below 200 MHz. Therefore we can use this lumped element model to analyze EM emission characteristics of the system module with the operating frequency up to 200 MHz without other complicated EM tools.

ACKNOWLEDGMENT

This research was supported by a grant “High efficient heat rejection and supply technologies for zero emission vehicle (10035530)” from the Korea Evaluation Institute of Industrial Technology.

REFERENCES

1. Vanhee, F., J. Catrysse, R. Gillon, and G. Gielen, “Scalable equivalent circuit modelling of the E -field coupling to microstrips in the TEM cell,” *Proceedings EMC Europe 2008*, Hamburg, Germany, Sep. 2008.
2. “Integrated circuits measurement of electromagnetic emissions Part 2: Measurement of radiated emissions, TEM cell and wideband TEM cell method,” 1st Edition, IEC 61967-2, 2005.
3. “Integrated circuits — Measurement of electromagnetic immunity — Part 2: Measurement of radiated immunity, TEM cell and wideband TEM cell method,” 1st Edition, IEC 62132-2, 2010.
4. Zitouni, A., H. Bourdoucen, and T. N. Djoudi, “Quasi-static MoL-based approach for the analysis of multilayer transmission line structures,” *International Journal of Numerical Modelling: Electronic Networks, Devices and Fields*, Vol. 10, 209–216, 1997.
5. Wei, C., R. Barrington, J. Mautz, and T. Sarkar, “Multiconductor transmission lines in multilayered dielectric media,” *IEEE Trans. Microw. Theory Tech.*, Vol. 32, No. 4, 439–450, Apr. 1984.
6. Mandic, T., F. Vanhee, R. Gillon, J. Catrysse, and A. Baric, “Equivalent circuit model of the TEM cell electric and magnetic field coupling to microstrip lines,” *Proc. IEEE Int. Conf. Electron, Circuits, Syst.*, 247–250, Dec. 2009.

Algebraic Function Approximation for Eigenvalue Problem in Rectangular Waveguide Partially Filled with Transversely Magnetized Ferrite

Oguzhan Demiryurek¹ and Namik Yener²

¹Technical Education Faculty, Kocaeli University, Izmit, Kocaeli 41380, Turkey

²Technology Faculty, Kocaeli University, Izmit, Kocaeli 41380, Turkey

Abstract— In this work, a lossless and closed rectangular waveguide partially filled with a slab of transversely magnetized ferrite, without assuming vanishing of the derivative in the direction of the dc biasing field, has been analyzed using Method of Moment (MoM). Generally, there are basically three types of modes in the waveguide: propagating, evanescent and complex modes. To support evanescent mode, the waveguide must be bidirectional. But a rectangular waveguide filled with a slab of ferrite transversely magnetized is not bidirectional, if there exists no symmetry with respect to the rotation by π about an axis perpendicular to propagation direction. So such a waveguide does not support the evanescent waves. Propagation constant is complex or pure imaginary. Our waveguide is filled with a transversely magnetized gyrotropic medium and does not satisfy the condition of symmetry with respect to the rotation by π about an axis perpendicular to propagation direction. So it is not bidirectional and hence does not support evanescent modes. Results of the MoM are consistent with this situation. In a lossless and closed rectangular waveguide partially filled with a slab of transversely magnetized ferrite, Maxwell's equations, consisting of partial differential equations, are transformed into an infinite linear algebraic equation system by application of the Galerkin version of Moment method. As the result of algebraic operations, from the transmission line equations a quadratic eigenvalue problem is obtained whose eigenvalue corresponds to the propagation constant. The determinant of the coefficient matrix of the quadratic eigenvalue problem is a monic polynomial of the propagation constant whose coefficients are rational functions of the complex frequency. If the polynomial is set equal to zero and is multiplied by the common denominator of the coefficients, an algebraic equation is obtained. The roots of this equation are the propagation constants. In this work as the contribution, using algebraic function theory, the solution of the algebraic equation (propagation constant) for the waveguide filled with transversely magnetized ferrite medium, is expressed by means of a Puiseux series in the neighborhood of the algebraic branch point. Puiseux series coefficients are solved using transmission line equations and the propagation constant is computed from this series expansion. Puiseux series results are compared and found to conform with MoM results and the exact solution.

1. INTRODUCTION

Determination of waveguide propagation characteristics and modeling are very important issues for designing of microwave circuits. This is quite difficult for structures which have gyrotropic media such as magnetized ferrite as the filling medium. Analysis is usually performed by numerical techniques or using some simplifications. The exact dispersion relation for rectangular waveguide partially filled with a slab of ferrite transversely magnetized was obtained by assuming no dependence on the direction of the dc biasing field H_0 [1, 2]. The relevant structure was also examined by numerical methods such as the finite difference method [3], the spectral method [4]. Barziali and Gerosa have derived the dispersion relation with no restriction on the dependence along the direction of the dc magnetic field [5].

In this work, rectangular waveguide partially filled with a slab of transversely magnetized ferrite has been analyzed using the MoM. There is coupling between transverse and longitudinal field components, due to the bias direction of the ferrite slab hence transfer coefficient matrices are nonzero. It should be noted that the transfer coefficient matrices of the transmission line equations are zero in [6]. Therefore this study is distinguished from and more general than others [6–8] which also used the MoM.

The structure of a rectangular waveguide with transversely magnetized ferrite slab is shown in Figure 1. The permeability tensor for the ferrite slab magnetized transversely is given as follows [1],

$$[\mu] = \mu_0 \begin{bmatrix} \mu_r & 0 & -j\kappa \\ 0 & 1 & 0 \\ j\kappa & 0 & \mu_r \end{bmatrix}, \quad \mu_r = 1 + \frac{\omega_0\omega_m}{\omega_0^2 - \omega^2} \quad \text{ve} \quad \kappa = \frac{\omega\omega_m}{\omega_0^2 - \omega^2}. \quad (1)$$

Here, $\omega_0 = \gamma H_0$ Larmor resonance frequency, $\omega_m = \gamma(4\pi M_s)$, $\mu_0 = 4\pi \times 10^{-7}$ [H/m], $\gamma = 2.8$ [MHz/Oe] gyromagnetic ratio, H_0 [Oersted] dc magnetic biasing field, $4\pi M_s$ [Gauss] the saturation magnetization and ω operating frequency.

In Section 2, method used for examination of waveguide was taken up. In Section 3, Puiseux series results are compared with the MoM results and the exact solution.

2. METHOD

Fields of a closed, lossless, uniform waveguide filled with heterogeneous and/or anisotropic medium may be expanded as a Fourier series using eigenfunctions of waveguide filled with homogeneous and isotropic medium. Hence Maxwell's equations, consisting of partial differential equations, are transformed into an ordinary differential equation system which is called transmission line equations. In the inner product the test function used is set equal to basis function and this method is known as the Galerkin version of the MoM [9]. If the fields' dependence of the z direction is taken as $e^{-\gamma(p)z}$ and substituted in the ordinary differential equation system, a linear algebraic equation system is obtained [10]. This is as follows

$$-\gamma(p) \begin{bmatrix} v(p) \\ i(p) \end{bmatrix} = \begin{bmatrix} M(p) & -Z(p) \\ -Y(p) & N(p) \end{bmatrix} \begin{bmatrix} v(p) \\ i(p) \end{bmatrix}. \quad (2)$$

Here $p = \sigma + j\omega$ is the complex frequency, $Z(p)$, $Y(p)$, $M(p)$ and $N(p)$ are the series impedance, the shunt admittance, the voltage transfer coefficient and the current transfer coefficient matrices per unit length, respectively. These matrices are $2\mathbf{N} \times 2\mathbf{N}$ dimensional square matrices. Actually, they have infinite dimensions. But we use only finite truncations of these matrices in the approximation of the physical problem. \mathbf{N} denotes the number of empty waveguide mode functions used in Fourier series expansion. $2\mathbf{N} \times 1$ dimensional column vectors $v(p)$ and $i(p)$ are the transmission line voltages and currents. $Z(p)$ and $Y(p)$ are also Foster matrices [11]. The transfer coefficient matrices of $M(p) \neq 0$ and $N(p) \neq 0$ are not zero.

In (2), the eigenvalues of the coefficient matrix correspond to the propagation constants and can be calculated numerically. However numerical values do not allow us to have complete information about the behavior of the propagation constant. Using algebraic function theory, a functional approach can be brought about for the behavior of the propagation constant [6].

Assume that $Z^{-1}(p)$ and $Y^{-1}(p)$ are exists. If Equation (2) is arranged as in (3), a quadratic eigenvalue problem is obtained. Here, $\gamma_n(p)$ is n th eigenvalue and $v_n(p)$ is the eigenvector corresponding to $\gamma_n(p)$. In (3), all of expressions are functions of the complex frequency p . Therefore, for the sake of simplicity, p dependence has not been shown in (3). Here, \mathbf{I} denotes identity matrix.

$$[\gamma_n^2 \mathbf{I} + \gamma_n (M + ZNZ^{-1}) - ZY + ZNZ^{-1}M] v_n = 0 \quad (3)$$

In (3), we can write $Q(\gamma, p)v_n(p) = 0$. If $v_n(p) \neq 0$, $G(\gamma, p) = \det[Q(\gamma, p)]$ must be zero to ensure existence of a solution for (3). Determinant of $Q(\gamma, p)$ is a monic polynomial of $\gamma(p)$ whose coefficients are rational function of p . If this polynomial is set equal to zero and is multiplied by the common denominator of the coefficients

$$g(\gamma, p) = a_0(p)\gamma^{4\mathbf{N}}(p) + a_1(p)\gamma^{4\mathbf{N}-1}(p) + \dots + a_{4\mathbf{N}-1}(p)\gamma(p) + a_{4\mathbf{N}}(p) = 0 \quad (4)$$

i.e., an algebraic equation is obtained whose coefficients are entire rational functions of p . Roots of the algebraic equation correspond to the eigenvalues of (3) that is, propagation constants. These roots can be expressed using the series expansion about analytical and singular points. An algebraic equation can have only algebraic singularities [12]. These singularities can be poles or pole branch points which are zeros of $a_0(p)$ the coefficient of $\gamma^{4\mathbf{N}}(p)$ in (4) and branch points which are zeroes of the discriminant of (4).

In this work, solutions of propagation constant will be obtained about the algebraic branch point where the discriminant of $g(\gamma, p) = 0$ is equal to zero. Let $j\omega_B$ be an algebraic branch point on the $p = j\omega$ axis. At this point, $\gamma_n(j\omega)$ have two multiple roots and $\gamma_n(j\omega_B)$ is finite. n th eigenvalue $\gamma_n(j\omega)$ can be modeled by a Puiseux series expansion without negative power terms in the neighborhood of $j\omega_B$.

$$\gamma_n(j\omega) = \gamma_n(j\omega_B) + A_1 \sqrt{j\omega - j\omega_B} + A_2 (j\omega - j\omega_B) + \dots + A_m (j\omega - j\omega_B)^{m/2} + \dots \quad (5)$$

It is necessary to calculate the unknown coefficients of the series expansion, in order to determine the propagation constant numerically. A_1 in (5) was calculated through using various approximations for the derivatives of implicit function $G(\gamma, p)$.

2.1. Determination of A_1

An analytical expression will be obtained to determine A_1 in (5) using the results of expression of the eigenvalue equation in (3). Let $n = 1$ in (5). $\gamma_1(p)$ is second order multiple root at $p = j\omega_B$. Equation (5) can be arranged as follows.

$$\gamma_1(p) = \gamma_1(j\omega_B) + A_1 p' + A_2 (p')^2 + \dots + A_m (p')^m + \dots \quad (6)$$

Here $p' = \sqrt{p - j\omega_B}$. If Equation (6) is differentiated with respect to p' at $p' = 0$, the coefficient A_1 is obtained by,

$$A_1 = \left. \frac{d\gamma(p)}{dp'} \right|_{p'=0} = \left[-\frac{G_p}{G_\gamma} 2p' \right]_{\substack{p=j\omega_B \\ \gamma=\gamma_1(j\omega_B)}} \quad (7)$$

G_p and G_γ are derivatives of $G(\gamma, p)$ with respect to p and γ , respectively. G_γ will be vanish, when $p = j\omega_B$. In this case, we can express G_γ approximately in the neighborhood of $p = j\omega_B$.

$$G_\gamma = 2 [\gamma_1(p) - \gamma_1(j\omega_B)] E \quad (8)$$

Here $E = [\gamma_1(j\omega_B) - \gamma_3(j\omega_B)] [\gamma_1(j\omega_B) - \gamma_4(j\omega_B)] \dots [\gamma_1(j\omega_B) - \gamma_{4N}(j\omega_B)]$. From (6)

$$\gamma_1(p) - \gamma_1(j\omega_B) = A_1 p' + A_2 (p')^2 + \dots + A_m (p')^m + \dots \quad (9)$$

can be written. Using (7), (8) and (9) one has,

$$A_1 = \sqrt{-\frac{G_p}{E}} \quad (10)$$

G_p is equal to $G(\gamma, p)$ differentiated with respect to p it is found by employing standard formulae for the derivative of a determinant: $G_p = \text{trace}\{Adj[Q(\gamma, p)]\partial Q(\gamma, p)/\partial p\}$. Here, Adj denotes the adjugate matrix.

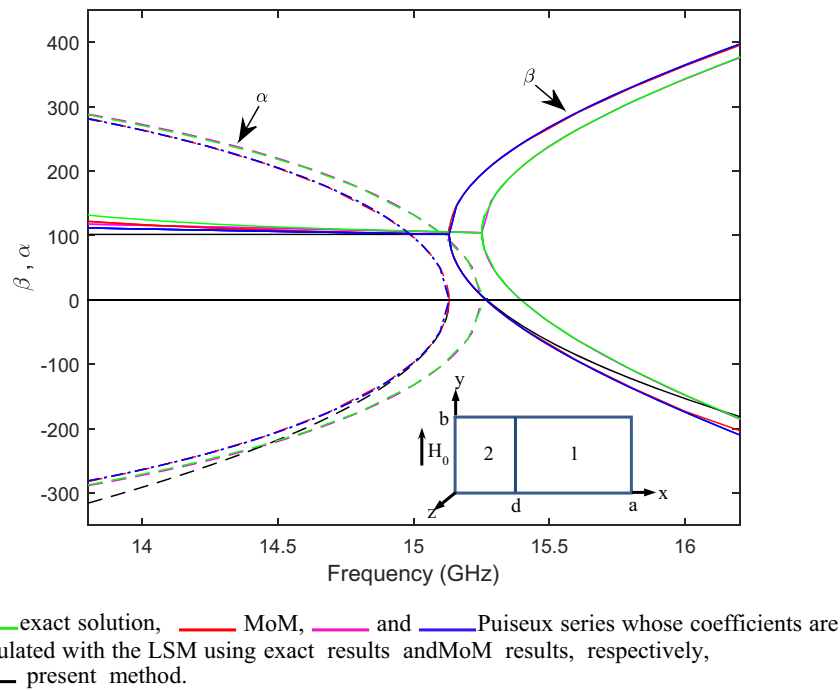


Figure 1: Phase coefficient (solid line) and attenuation constant (dashed line). Inset: cross-section of the rectangular waveguide partially filled with transversely magnetized ferrite. First region: (vacuum) ϵ_0, μ_0 , second region (ferrite): $\epsilon_f, [\mu]$.

Table 1: Coefficients of Puiseux series computed by analytical and the least squares.

Coefficients	Analytical	LSM (used MoM results)	LSM (used exact results)
$\gamma(j\omega_B)$	$j101.66413$	$j101.66413$	$j104.2164$
A_1	$-2.4397 \times 10^{-3} (1 + j)$	$-2.41842 \times 10^{-3} (1 + j)$	$-2.39622 \times 10^{-3} (1 + j)$
A_2	-	-1.17966×10^{-9}	-1.462739×10^{-9}
A_3	-	$-2.9394 \times 10^{-14} (1 - j)$	$-2.86085 \times 10^{-14} (1 - j)$

3. NUMERICAL EXAMPLE

The parameter values of the rectangular waveguide partially filled with transversely magnetized ferrite are as follows: $4\pi M_s = 2000$ Gauss, $H_0 = 500$ Oersted, $a = 10$ mm, $b = 12.5$ mm, $d = 2$ mm, $\varepsilon_f/\varepsilon = 12.6$. In Figure 1, the results of Puiseux series method were compared with the results of the exact solution and the MoM in the neighborhood of the algebraic branch point.

Coefficient A_1 in the Puiseux series in (5), was calculated analytically as explained in Section 2.1. Puiseux series coefficients were also obtained using the least square method (LSM) in [13]. While this calculation was made, the results of the MoM and exact solution were used. The coefficients are shown in Table 1.

On the frequency axis backward wave is converted into evanescent mode in bidirectional waveguide. However, in Figure 1, there exists a transition from the backward wave to the forward wave at ω_C , i.e., evanescent mode is absent. To support the evanescent mode, waveguide must be bidirectional [14]. Our waveguide's structure does not support the symmetry condition in [14], therefore it is not bidirectional. The propagation constant computations using MoM also confirm this.

4. CONCLUSION

Eigenvalues were expressed by Puiseux series in the neighborhood of the algebraic branch point with the help of algebraic function theory. An analytical method is developed to calculate Puiseux series coefficients using the results of expression of the MoM for structures which can be represented by (2). These coefficients are also computed with the LSM using the results of exact solution and the MoM. The calculated coefficients are seen Table 1 to be consistent with each other. This confirms the validity of developed method.

As it seen in Figure 1, between the results of Puiseux series, exact solution and the MoM, a very close agreement has been achieved. This provides us with a capability to investigate the propagation problem about singular points in waveguide by algebraic function theory.

REFERENCES

1. Pozar, D. M., *Microwave Engineering*, John Wiley & Sons, 2009.
2. Button, K. and B. Lax, "Theory of ferrites in rectangular waveguides," *IRE Transactions on Antennas and Propagation*, Vol. 4, 531–537, 1956.
3. Al-Barqawi, H., N. Dib, and M. Khodier, "A two-dimensional full-wave finite-difference frequency-domain analysis of ferrite loaded structures," *International Journal of Infrared and Millimeter Waves*, Vol. 29, 443–456, 2008.
4. Agalakov, A., S. Raevskii, and A. Titarenko, "A spectral method for calculation of rectangular shielded waveguides with an arbitrary anisotropic filling," *Journal of Communications Technology and Electronics*, Vol. 58, 498–508, 2013.
5. Barzilai, G. and G. Gerosa, "Modes in rectangular guides partially filled with transversely magnetized ferrite," *IRE Transactions on Antennas and Propagation*, Vol. 7, 471–474, 1959.
6. Yener, N., "Algebraic function approximation in eigenvalue problems of lossless metallic waveguides: Examples," *Journal of Electromagnetic Waves and Applications*, Vol. 20, No. 6, 731–745, 2006.
7. Yener, N., "A novel computational method for group velocity in metallic waveguides," *Applied Mathematics and Computation*, Vol. 153, 855–863, 2004.
8. Kelebekler, E. and N. Yener, "Backward wave modes of partially plasma column loaded cylindrical waveguide," *PIERS Proceedings*, 1084–1088, Marrakesh, Morocco, Mar. 20–23, 2011.
9. Harrington, R. F., *Field Computation by Moment Methods*, Oxford University Press, USA, 1993.

10. Schelkunoff, S., “Generalized Telegraphist’s equations for waveguides,” *Bell Syst. Tech. J.*, Vol. 31, 784–801, 1952.
11. Noble, D. F., “Circuit properties of dispersive coupled transmission lines and waveguides,” Ph.D., Electrical Engineering, Cornell University, 1971.
12. Knopp, K., *Theory of Functions*, Dover Publications, Mineola, NY, 1996.
13. Demiryurek, O. and N. Yener, “Determination of eigenvalues of closed lossless waveguides using the least squares optimization technique,” *PIERS Proceedings*, 450–454, Xi’an, China, Mar. 22–26, 2010.
14. Mrozowski, M., *Guided Electromagnetic Waves: Properties and Analysis*, Prentice-Hall of India, 2008.

The Transmittance of Electromagnetic Waves and Field Correlations in Multilayered Microspheres with Quasi-periodic Structures

M. Nájera-Villeda and G. Burlak

Centro de Investigación en Ingeniería y Ciencias Aplicadas
Universidad Autónoma del Estado de Morelos, Cuernavaca, Mor., México

Abstract— By means of the matrix transfer approach and the Green's function technique, the electromagnetic properties of the spectra transmission of coated microspheres with a multi-layer, the numerical quasi-periodic sequences from Cantor set and Pascal triangle structures are numerically studied.

The quasi-periodic structures allow to obtain the optical band intervals in the radiation field spectra. The location of the light in disordered systems offers a range of applications in the opto-electronics industry.

1. INTRODUCTION

In the following numerical investigation was working with Si and SiO₂ as two elementary layers the objective is to highlight the properties of electromagnetic oscillations in multi-layer micro-spheres quasi-periodic the cantor sequence set, Pascal triangle and Green's functions with control parameter (γ), numerical algorithms and numerical simulations, transmittance spectrum, peaks (resonances) narrow-dependent parameters (γ) and spherical harmonic numbers (m), calculations of frequencies obtained with a radial field distribution [1–3].

2. THE GENERALIZED CANTOR SET

The well-known set Cantor is created by repeatedly removing the open central third of a set of line segments. One can build various generalizations of the assembly by, for example, cutting the segments into a different number of intervals or choosing another scaling factor. In this work, a cell is constructed by replacing Cantor several times (not cleaned) of the third center of a stack assembly material layer if materials using both Si and SiO₂. The generalized radially set Cantor can be constructed from a stack for homogeneous iterations subsequent. In standard Cantor established the central fragment is eliminated in iterations leading to a “dust” fractal Cantor. However, in this paper we replace (rather than delete) fragment of the SiO₂ layer, while fragment is replaced by Si layer. This allows the construction of a solid spherical quasi-periodic stack with the generic properties of Pascal or a Cantor fractal patterns. For such fractal scale dimensionless factor γ that becomes a control parameter and takes values between 0 and 2.

2.1. The generalized Pascal Triangle

Advances in manufacturing technologies nano-structures and micro-spheres are given the possibility of studying multi-layer systems with all kinds of arrangements, which can lead to a lot of photonic and optoelectronic applications. In a micro-sphere such, only the narrow resonance spectrum (natural frequencies) can be seen as peaks in the frequency spectrum of the radiation. Therefore, it is of great interest to investigate how these characteristics are modified in a cell with a quasi-periodic spherical structure. In this paper, we investigate the optical properties of a micro-sphere layer with a dielectric stack, wherein the optical layers are built following of the Pascal or Cantor sequences.

2.2. Green Functions

The range of different structured constructs has promised a variety of physical phenomena of another unexpected way among which the experimental realization of a negative refractive index has been one of the main advantages. A typical meta-material combines continuous metal films with nanos-trip magnetic resonator that ultimately produce a negative index material. The film can be formed with a mixture of dielectric (for example, Si y SiO₂), forming a semi-metal film. These structures are fabricated using techniques preparing the meta-material structure in the optical range is even an advanced task. In recent experiments have shown that incorporation of the material gain in the meta-material makes it possible to produce an extremely low loss and an active-index. Optical negative index meta-materials (NIM) that is not limited by the inherent loss in the metal

component. In this experiment NIM optic network structure is approximately periodicity. The mechanism of compensation of losses in the sample is simple to understand. When excited by a pump pulse with sufficiently high power, a population inversion is formed within molecules. This provides a boost pulse suitably delayed probe whose wavelength coincides with the wavelength of stimulated emission molecules. Working with quasi-periodic structures: Set of Cantor and Pascal's triangle; applying the Green's function, SiO₂ that is used as a gain medium when applying in the nucleus nano-emitter or any part of the area surrounded by different layers. This allows a pulse of the electromagnetic wave handled properly.

The films can be formed with a mixture of dielectrics, in this case Si and SiO₂ can form a semi-metal films.

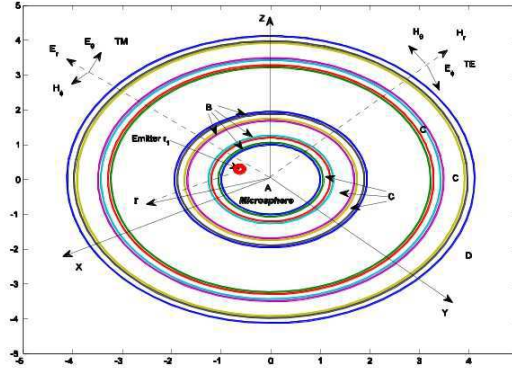


Figure 1: Micro-sphere multi-layer system with quasi-periodic structure added by a source of radiation (red circle).

In the following table the results of the simulation method used for calculation for the first two experiments 400 and 500 THz given by (E) in (A) angle type 0.5 and 0.9, (B) shows lens exposure or nanoesimor in this case 0.5, (C) Number of layers, 12, (D) maximum layer growth is handled with 4, (F) numbers of points in the 3D image (G) Type of angles, (H) the wall height of the outer layer 0.5, (I) the wall height of the inner layer.

Table 1: The parameters used in each spherical stack of quasi-periodic system.

	A	B	C	D	E	F	G	H	I
1	0.9	0.5	12	4	400	50			0.7
2	0.9	0.5	12	4	400	50			0.9
3	0.9	0.5	12	4	400	50			1.0
4	0.9	0.5	12	4	400	50			1.3
5	0.5	0.5	12	4	500	50	0.5	0.5	2.0
6	0.5	0.5	12	4	500	50	0.5	0.5	1.9
7	0.5	0.5	12	4	500	50	0.5	0.5	1.8
8	0.5	0.5	12	4	500	50	0.5	0.5	1.7

3. BASIC EQUATIONS

The quasiperiodic systems may be considered appropriate models to describe the transition of the periodic structure for perfect random structure. The spatial scale of the nanoemitter objects ($\sim 1\text{--}100\text{ nm}$) is at least one order of magnitude smaller than the spatial scale of microspheres ($\sim 10^3\text{--}10^4\text{ nm}$). Therefore in the coated microsphere (Fig. 2), we can represent the nanoemitter structure as a point source placed at \mathbf{r}' and having a dipole moment \mathbf{d}_0 . It is well known that the solution of the wave equation for the radiated electromagnetic field \mathbf{E} due to a general source $\mathbf{J}(\mathbf{r}')$ is

$$E_\theta = \frac{1}{kr\varepsilon} \frac{\partial^2 \Pi(\rho, \theta, \varphi)}{\partial r \partial \theta}, \quad H_\varphi = \frac{i}{r} \frac{\partial \Pi(\rho, \theta, \varphi)}{\partial \theta} \sqrt{\frac{\epsilon_0}{\mu_0}}. \quad (1)$$

$$\mathbf{E}(\mathbf{r}, \mathbf{r}', \omega) = -\mathbf{p}_0 \mathbf{G}(\mathbf{r}, \mathbf{r}', \omega) \tag{2}$$

$$\mathbf{G}(\mathbf{r}, \mathbf{r}', \omega) = \mathbf{G}^V(r, r', \omega) \delta_{fs} + \mathbf{G}^{(fs)}(\mathbf{r}, \mathbf{r}', \omega) \tag{3}$$

$$\mathbf{G}^V(\mathbf{r}, \mathbf{r}', \omega) = \frac{\hat{r}\hat{r}}{k_s^2} \delta(r - r') + \frac{ik_s}{4\pi} \sum_{q=e, n=1}^{\infty} \sum_{m=0}^n C_{nm} \mathbf{G}_{q, nm}^V(\mathbf{r}, \mathbf{r}', \omega) \tag{4}$$

In the following image the distribution of magnetic and electric field is displayed. The structure depends on the parameters inserted in each range, we study the dependence of Green's function with respect to range, resulting from simulations without changing the parameter range (which is no more than a parameter set cantor) in the following figure you can see the sum given by Nmax12, RM4 = Rmax with a value of 4, $f = Atom.f$ (frequency 400 Thz) for different types of exposure source 0.7, 0.9, 1.0 and 1.3 with a range of 1.0 and in third dimension.

4. NUMERICAL SIMULATION PERFORMED FOR CANTOR SET WITH GREEN FUNCTION

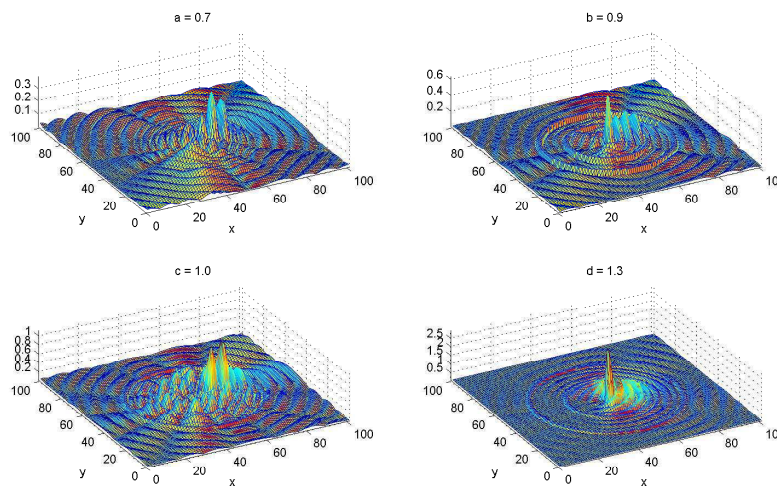


Figure 2: Parte distribution imaginary 3D Green's function for Cantor multilayers with layers Si and SiO₂ for parameters indicated in the Table 1.

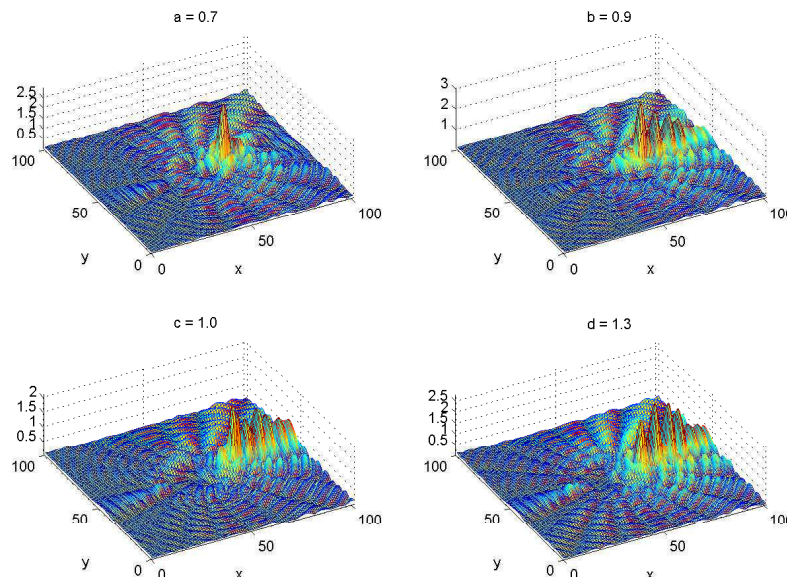


Figure 3: Parte distribution imaginary 3D Green's function for triangle Pascal multilayers with layers Si and SiO₂.

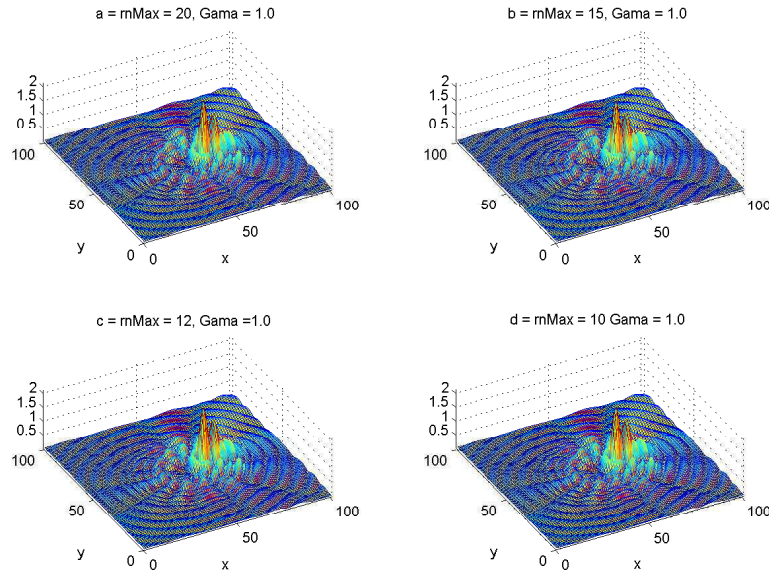


Figure 4: Simulation analysis of the Cantor set and function Green TM&TE. Here a distinct change in the sum of 20, 15, 12 and 10 and the exposure source is 1.5 working with TM&TE.

5. CONCLUSION

In this paper we have numerically studied the electromagnetic properties (narrow peak positions) of the transmission spectra for microspheres coated by a multilayered stack with the generalized Cantor and Pascal structures. As opposed to the standard Cantor system with removed $\gamma/3$ [$\gamma = 1$] sections the generalized solid stack with alternating Si/SiO₂ layers (in place of empty Cantor section) for such fractal pattern with general values of γ it is considered. It is found that the variations of parameter γ significantly affects the structure of the optical spectra. The waves phase interference in such a fractal pattern leads to creation of extremely narrow frequency peaks assisted by the progressively decreased radially inhomogeneous defects. Such peaks can be used in modern optoelectronics, e.g., for construction narrow optical filters.

ACKNOWLEDGMENT

This work was partially supported by CONACyT (Mexico) grants No. 169496 and No. 168104.

REFERENCES

1. Burlak, G., A. Diaz-de-Anda, and M. Najera, "The field confinement, narrow transmission resonances and Green function of a multilayered microsphere with metamaterial defects," *Microspheres: Technologies, Applications and Role in Drug Delivery Systems*, Nova Science Publishers, 2014.
2. Li, L.-W., P.-S. Kooi, and M.-S. Leong, "Electromagnetic dyadic Greens' function in spherically multilayered media," *IEEE Transactions on Microwave Theory and Techniques*, Vol. 42, No. 12, 1994.
3. Burlak, G. and A. Diaz-de-Anda, "The confinement of electromagnetic radiation of nanoemitters in a multilayered microsphere with left-handed layers," *JEMAA*, Vol. 2, 654–663, 2010.
4. Braginsky, V. B., M. L. Gorodetsky, and V. S. Ilchenko, "Quality-factor and nonlinear properties of optical whispering-gallery modes," *Phys. Lett. A*, Vol. 137, 393–399, 1989.
5. Xiao, Z. Y. and Z. H. Wang, "Super narrow bandpass filter using fractal cantor structures," *Int. J. Infrared. Milli.*, Vol. 25, 1315–1323, 2004.

Evaluation of Power Transistors Figure of Merit for Hard Switching Commutation Mode through Experimental Analysis

Michal Frivaldsky, Pavol Spanik, Boris Kozacek, and Marek Piri
 Faculty of Electrical Engineering, Department of Mechatronics and Electronics
 University of Zilina, Univerzitna 1, Zilina 010 26, Slovak Republic

Abstract— Nowadays demand for efficiency and high density of electronic device is high. Therefore, great emphasis is placed on the properties of electronic components such as diodes, transistors, transformers and more. Hence the scientific discipline was created Figure of Merit (FOM) which is dealing with this issue.

The proposed article deals about the analysis of FOM of several power MOSFETs, whereby main parameters are taken into consideration for calculation purposes. In order to verify faithfulness of FOM the experimental measurements for determination of switching as well as conduction losses of selected transistors are performed. Because experimental analysis represents time-consuming process for evaluation of transistor switching performance, the various FOM methodologies are being described taking into account main parameters for the FOM evaluation (transistor parasitics, gate charge, switching frequency, parameters of target application, e.g., voltage — current ratings). Comparisons between the amount of transistor's losses and its FOM indicator are provided.

1. INTRODUCTION

The development of switched mode power supplies significantly moved forward. Requested parameters of switched mode power supplies (SMPS) are reduction of the size and reduction of power losses (increase of efficiency). In this article we decided to analyze several methods of FOM for the power MOSFET transistors. These methods are:

- Switching FOM.
- Conduction FOM.
- Detailed FOM.
- Johnson FOM.

FOM is numeric value representing power parameter of components and other important factors, which affect this parameter. If we want to work with FOM method it's very important to know internal parasitic parameters. MOSFET transistors, through unipolar structure, belong to the fastest power semiconductor component. Dynamic parameters are limited by internal parasitic components [1–4]. The values of these parameters are given in components datasheets and are dependent on the internal structure of MOSFET and on its technology (manufacture). Selected transistors for FOM evaluation as well as experimental analysis of hard-switching commutation mode are CoolMOS IPW60R165CP, CoolMOS, SPP20N60C3 and MOSFET IRF840. The last mentioned device represents older technology of MOSFET transistors, whereby CoolMOS transistors exhibits currently best in class performance for power applications (for example solar inverters, renewable energy, telecom/servers, front-end converters etc...).

2. FOM FOR MOSFET TRANSISTORS

2.1. Switching FOM

Switching FOM is used to evaluate switching behaviour/performance. Next formula is valid for calculation:

$$\text{FoM}_{SW} = R_{DS(ON)} * Q_{GD}, \quad (1)$$

where

- Q_{GD} is main parameter of turn-on loss.
- $R_{DS(ON)}$ represents conduction losses, when transistor is in on-state.

Some manufactures indicates the value of Q_{SW} or Q_{GS2} . In this case we can find more accurate value of FOM_{SW} (2).

$$FOM_{SW} = R_{DS(ON)} * (Q_{GD} + Q_{GS}), \quad (2)$$

where

- Q_{SW} is representing sum of turn-on loss (related with $Q_{GD} + Q_{GS}$).
- Q_{GS} is gate charge between threshold voltage and Miller plateau.

2.2. Conduction FOM_{CON}

This is a traditional MOSFET FOM and determines rectified power loss. FOM_{CON} (3) represents the conduction losses and power losses of the transistor's gate electrode.

$$FOM_{CON} = (R_{DS(ON)} * Q_G) \quad (3)$$

For soft switching technique Q_{GD} is negligible and therefore we would like to reduce $R_{DS(ON)}$ in order to improve efficiency. On the other side, with reduction of $R_{DS(ON)}$, Q_G loss increases. There exist also better method which utilizes parameters Q_{OSS} (Output charge) and Q_{RR} (Reverse recovery charge) together with Q_G for evaluation of power loss. In most cases, switching performance is mostly missing; therefore combination with Q_{SS} is sometimes omitted in which conditions have no standards too. The eGaN transistors are Q_{RR} and Q_{OSS} negligibly small as compared to silicon MOSFETs [5].

2.3. Detailed FoM

If it is necessary to evaluate the performance of the transistor in terms of more precise choice, then more detailed information are needed where effect of turn-on, turn-off, conduction loss and loss due to gate excitation of transistor are considered (4).

$$P_{loss} = \frac{U_{in} \cdot I_o}{2} \cdot \frac{(Q_{GD} + Q_{GS}) \cdot R_G}{(U_{GS} - U_{PLT})} \cdot f_{SW} + \frac{U_{in} \cdot I_o}{2} \cdot \frac{(Q_{GD} + Q_{GS}) \cdot R_G}{U_{PLT}} \cdot f_{SW} + I_o^2 R_{DS(ON)} \frac{U_o}{U_{IN}} + Q_G U_{GS} f_{SW}, \quad (4)$$

where

- U_{PLT} is leading voltage of gate drive,
- I_o is nominal value of current taken from datasheet,
- f_{SW} is nominal switching frequency.

Furthermore, it is necessary to adopt new value namely excitation losses in gate circuit K_{GS} (5).

$$K_{GS}(U_{DR}) = 1 + \frac{U_{DR}}{U_{PLT} - U_{TH}} \cdot \frac{2U_{PLT}(U_{DR} - U_{PLT})}{U_{IN} I_o R_G}, \quad (5)$$

where U_{DR} is value of excitation voltage and U_{TH} is threshold voltage. After that it is possible to calculate FOM parameter for hard switching commutation mode (6). In the following equation consideration of the losses of individual components is accepted [6–9].

$$FOM = (Q_{GD} \cdot + K_{GS} Q_{GS}) \cdot R_{DS(ON)} \quad (6)$$

2.4. Johnson FoM

This method is for broadband gap devices like GaN transistors. Present type of transistor has desired properties for high power application such as size of band gap and thermal conductivity. Johnson value represents high frequency power of wide-energy devices and is proportional to saturation time and to the critical value of the electric field as shown in the following Formula (7).

$$FOM_{johnson} = \frac{v_{sat} E_{BD}}{2\pi}, \quad (7)$$

where

- v_{sat} represents speed of saturation.
- E_{BD} is the electric field which initiates the ionization.

However the value of FOM is not to be easily experimentally verified, because both parameters v_{sat} and E_{BD} are intrinsic properties of the components. On the other side it is possible to find these parameters by the simulation. These values can be coupled to the microwave measurements. In general the cut-off frequency f_t is associated with an effective speed of saturation, which can be calculated by Equation (8).

$$f_T = \frac{v_{sat}}{2\pi L_G}, \quad (8)$$

where

- L_G is effective length of gate.

Based on experimental analysis, it can be determined that the gate field varies almost linearly across the effective length of the gate. Visible change mainly occurs mostly at the end of turn-off interval. Since potential losses occur in the space between gate electrode and contacts we can write the equation for the breakdown voltage [6–9].

$$V_{BD} = \alpha \frac{E_{BD} L_G}{2}, \quad (9)$$

where

- α is an adjustable parameter which is associated with the voltage drop across the gate to the rated voltage of the device.

Therefore, we can rewrite the FOM within the experimentally determined parameters with the use of following Equation (10).

$$\text{FOM}_{\text{Johnson}} = \frac{1}{2\pi} (2\pi L_G f_T) \frac{2V_{BD}}{\alpha L_G} = \frac{2}{\alpha} f_T V_{BD} \quad (10)$$

The parameter α can be extracted directly from the measurement or simulation using the Formula (10) and the calculation of the breakdown voltage as integral field over the channel on which the first impact ionization occurs.

3. EVALUATION OF FOM OF SELECTED TRANSISTORS

Determination of FOM parameter of selected transistors was done with the use of methodology A — switching FoM (2), where effect of Miller capacitance is also considered. Conduction FoM has been evaluated with the use of (3), where Q_{RR} was also accepted. The results of calculations are shown in Table 1. As can be seen, the lowest value of switching and conduction FOM parameter is for IPW60R165CP transistor (the lower the value is the better performance of transistor may be achieved).

Table 1: Figure of merit for methodology A and B.

	FOM_{SW}	FOM_{CON}
IPW60R165CP	3,31	6,97
SPP20N60C3	8,36	18,62
IRF840	24,65	39,61

Table 2: The circuit and transistor parameters for FoM evaluation based on methodology C.

	U_{TH} [V]	U_{DR} [V]	U_{PLT} [V]	I_O [A]	U_{IN} [V]	R_G [Ω]
IPW60R165CP	3	15	5	variable	400	1.9
SPP20N60C3	3	15	5.5	variable	400	0.54
IRF840	4	15	5	variable	400	9.1

Table 3: Parametrical evaluation of figure of merit for hard switching based on methodology C.

$U_{in} = 400 \text{ V}$	IPW60R165CP		SPA20N60C3		IRF840	
$I \text{ [A]}$	K_{GS}	FOM	K_{GS}	FOM	K_{GS}	FOM
1	1.99	4.63	3.90	14.43	1.41	27.10
2	1.49	3.97	2.45	11.39	1.21	25.88
3	1.33	3.74	1.97	10.38	1.14	25.47
4	1.25	3.63	1.73	9.88	1.10	25.26
5	1.20	3.57	1.58	9.57	1.08	25.14
6	1.16	3.52	1.48	9.37	1.07	25.06
7	1.14	3.49	1.41	9.23	1.06	25.00
8	1.12	3.47	1.36	9.12	1.05	24.96
9	1.11	3.45	1.32	9.03	1.05	24.92
10	1.10	3.43	1.29	8.97	1.04	24.90

On the other side, if we need to evaluate selection of transistor more complexly, then it is necessary to consider also gate drive loss K_{GS} (5). This part becomes very important when very-high frequency operation is considered. Input values for calculation of detailed FoM as well as for calculation of K_{GS} listed in Table 2. Consequently the evaluation of FOM was made parametrically, i.e., in dependency on the parameters that are influencing hard-switching commutation mode in the most manners (switching frequency, load current). It must be said, that all FOMs have been computed for main circuit variables, at which experimental measurements were provided (Table 3).

As can be seen, the value of FoM from Table 2 is higher compared to FoM_{SW} , because losses from gate drive are taken into account too.

As can be seen from previous results IPW60R165CP is showing best performance, when complex and simple FOM has been calculated. When we look more in detail on the results from Table 3 it can be seen that IPW60R165CP is showing relatively small difference in the value of FOM, when change of transistor current is being considered. This can be explained in the way that internal capacitive parasitic components together with circuit and transistor parameters results in suitable value. IRF840 shows the best value of K_{GS} . However, internal parasitic components are decreasing qualitative indicator of this part markedly, thus utilization for high-end systems won't be a good choice.

Let's see if these results would also be confirmed after experimental analysis of hard-switching commutation mode.

4. EXPERIMENTAL ANALYSIS OF HARD-SWITCHING COMMUTATION MODE

The experimental analysis served for the analysis of dynamic properties during hard-switching of selected power transistors, whose selected type for analysis are CoolMOS IPW60R165CP, CoolMOS, SPP20N60C3 and MOSFET IRF840. The experimental analysis for FOM evaluation has been realized at these parameters:

$$- U_{DC} = 400 \text{ V.}$$

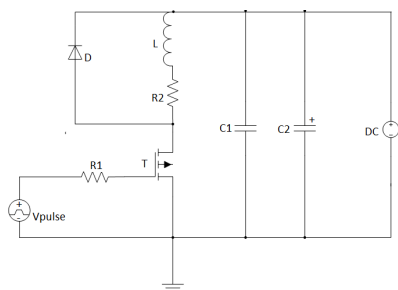


Figure 1: Principal schematic for experimental analysis of hard-switching.

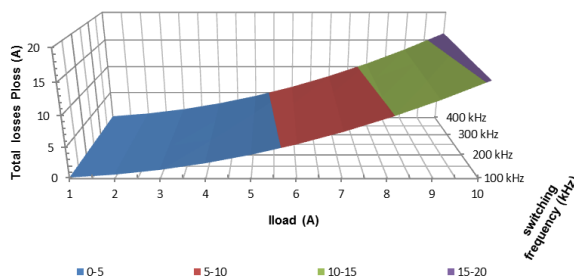


Figure 2: Principal schematic for experimental analysis of hard-switching.

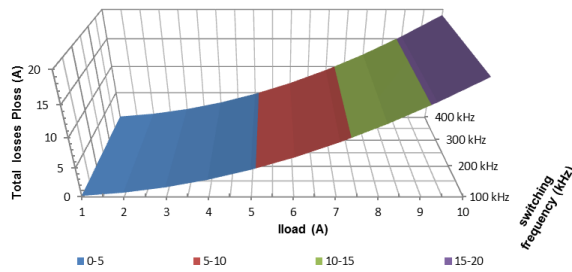


Figure 3: Principal schematic for experimental analysis of hard-switching.

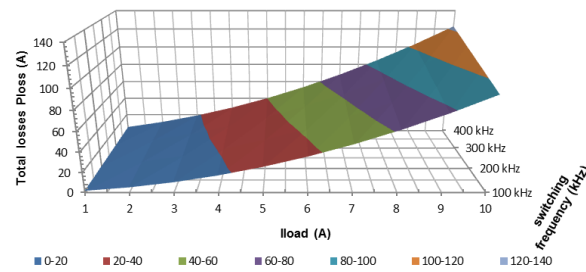


Figure 4: Principal schematic for experimental analysis of hard-switching.

- $I_{load} = 1\text{--}10\text{ A}$.
- $f_{sw} = 100\text{--}400\text{ kHz}$.

Principal schematic for the analysis is shown on Figure 1. The experimental analysis as well as FOM evaluation was made parametrically, i.e., in dependency on the parameters that are influencing hard-switching commutation mode in the most manners (switching frequency, load current).

Figure 2 to Figure 4 are showing results from parametrical experimental analysis of switching performance of transistor (evaluation of transistor's switching power losses) in dependency on transistor's current and switching frequency. Each transistor was investigated separately with the use of universal testing device and automatic switching loss evaluation algorithm, whereby each part of power loss has been evaluated independently, i.e., turn-on loss, conduction loss and turn-off loss [11–17].

Experimental measurements show that IPW60R165CP is achieving best switching performance in the whole investigated range of variables. Based on these results, it can be said that evaluation of FOM gives credible information about the quality of transistor performance for target application. Also, in order to improve qualitative indicators of modern SMPS, detailed FOM evaluation, where circuit parameters are being considered, gives proper information that can be sufficient during selection of proper power transistor structure.

Because the research and development process must be continuously accelerated (due to market requirements), the FOM methodology seems to be very valuable and perspective procedure for transistors quality evaluation.

5. CONCLUSION

The main aim of this paper was confirmation of FOM methodologies for the evaluation of the quality of power transistors from “efficiency” point of view. For this purpose the parametrical evaluation of detailed FOM was provided for several generations of MOSFET transistors. The confirmation of FOM results was provided in the way of experimental analysis of switching power losses during hard switching commutation mode. The measurements for each transistor were evaluated separately and switching losses in dependency on transistor's current and on switching frequency were calculated. The value of FOM is a power merit of devices, whose value indicates quality of semiconductor device. The lower this value is, the better the performance shall be. After comparisons between results of experimental analysis and results from FOM calculation, it can be said, that FOM methodologies presents very perspective solution for the selection of proper power device for selected power application.

In future works, we would like to focus on the evaluation of FOM parameter for soft-switching commutation modes (zero-voltage switching, zero-current switching) as well as on determination of FOM for various power devices (diodes — SiC, GaN transistors etc...). Consequently the quality indicator of proper semiconductor structures, will be verified during operation of target application system (e.g., SMPS for distributed systems), where system efficiency will be the most important merit.

ACKNOWLEDGMENT

The authors wish to thank to Slovak grant agency VEGA for project No. 1/0558/14 — Research of methodology for optimization of lifetime of critical components in perspective electronic appliances through the use of system level simulation.

REFERENCES

1. Deboy, G., N. Marz, J. P. Stengl, H. A. S. H. Strack, J. A. T. J. Tihanyi, and H. A. W. H. Weber, "A new generation of high voltage MOSFETs breaks the limit line of silicon," *International Electron Devices Meeting, IEDM '98, Technical Digest*, 683–685, 1998.
2. Hudgins, J. L., G. S. Simin, et al., "An assessment of wide bandgap semiconductors for power devices," *IEEE Transactions on Power Electronics*, Vol. 18, No. 3, May 2003.
3. Lu, B., W. Dong, Q. Zhao, and F. C. Lee, "Performance evaluation of CoolMOS/sup/spltrade// and SiC diode for single-phase power factor correction applications," *Eighteenth Annual IEEE Applied Power Electronics Conference and Exposition, APEC' 03*, Vol. 2, 651–657, 2003.
4. Baliga, B. J., "Power semiconductor device figure of merit for high frequency applications," *IEEE Electron Device Lett.*, Vol. 10, 455–457, 1989.
5. Johnson, A., "Physical limitations on frequency and power parameters of transistors," *RCA Review*, Vol. 26, 163–177, 1965.
6. Kim, I., S. Matsumoto, T. Sakai, and T. Yachi, "New power device figure of merit for high-frequency applications," *Proc. Power Semiconductor Devices and ICs*, 309–314, 1995.
7. Brown, J. and G. Moxey, "Power MOSFET basics: Understanding MOSFET characteristics associated with the figure of merit," *Vishay Siliconix*, Sep. 8, 2003.
8. Strydom, J., "eGaN(tm) — Silicon power shoot-out: Part 1, Comparing figure of merit (FOM)," EPC, Sep. 1, 2010.
9. Frivaldsky, M., "Topologická optimalizácia LLC Meniča," Univerzita of Zilina, 2013.
10. Frivaldský, M., P. Drgoňa, and P. Špánik, "Experimental analysis and optimization of key parameters of ZVS mode and its application in the proposed LLC converter designed for distributed power system application," *Electrical Power and Energy Systems*, Vol. 47, 448–456, 2013, ISSN: 0142-0615.
11. Frivaldský, M., P. Drgoňa, and P. Špánik, "Hard switching process optimization for selected transistor suited for high power and high frequency operation," *Journal of Energy and Power Engineering*, Vol. 4, No. 12, 2010, ISSN: 1934-8975.
12. Špánik, P., M. Frivaldský, P. Drgoňa, and J. Kandráč, "Efficiency increase of switched mode power supply trough optimization of transistor's commutation mode," *Elektronika IR Elektrotechnika*, Vol. 105, No. 9, 49–52, 2010, ISSN: 1392-1215.
13. Kindl, V., T. Kavalir, R. Pechanek, B. Skala, and J. Sobra, "Key construction aspects of resonant wireless low power transfer system," *ELEKTRO 2014*, 303–306, May 19–20, 2014.
14. Brandstetter, P., P. Chlebis, and P. Palacky, "Application of RBF network in rotor time constant adaptation," *Elektronika IR Elektrotechnika*, Vol. 113, No. 7, 21–26, 2011.
15. Grman, L., M. Hrasko, and J. Kuchta, "Single phase PWM rectifier in traction application," *Journal of Electrical Engineering-Elektrotechnicky Casopis*, Vol. 62, No. 4, 206–212, Aug. 2011.
16. Ferkova, Z., M. Franka, and J. Kuchta, "Electromagnetic design of ironless permanent magnet synchronous linear motor," *International Symposium on Power Electronics, Electrical Drives, Automation and Motion (SPEEDAM)*, 721–726, Italy, Jun. 11–13, 2008.
17. Kovacova, I. and D. Kovac, "Inductive coupling of power converter's EMC," *Acta Polytechnica Hungarica*, Vol. 6, No. 2, 41–53, 2009.

Improvement of Standard EM Fields Distribution in 4-port TEM Cell with Slit-structured Septum

Sung Woong Choi, Sang Bong Jeon, and Heung Mook Kim

Broadcasting & Telecommunications Media Research Lab.

Electronics and Telecommunications Research Institute

161 Gajeong-ro, Yuseong-gu, Daejeon 305-700, Republic of Korea

Abstract— This paper proposes a method of reducing the unwanted electromagnetic field component in the 4-port transverse electromagnetic cell with two internal septa, which is used for electromagnetic compatibility emission and immunity test. Adopting slit structure in the internal septa, 4-port transverse electromagnetic cell provide the improved standard EM field distribution inside the usable test volume.

1. INTRODUCTION

In recent years, as many kinds of electronic devices are present EM (electromagnetic) fields generated from these electronic devices may not only cause problems in the human body, but also affect the electronic devices to induce a malfunction and failure. Therefore, the EMC (electromagnetic compatibility) studies are actively ongoing so that radiation of undesired EM fields can be suppressed below a regulation value and a normal operation can be done in an EM field environment with a constant regulation value. Standard EM field generators such as transverse electromagnetic (TEM) cell and Gigahertz Transverse Electromagnetic (GTEM) cell are widely used in these EMC

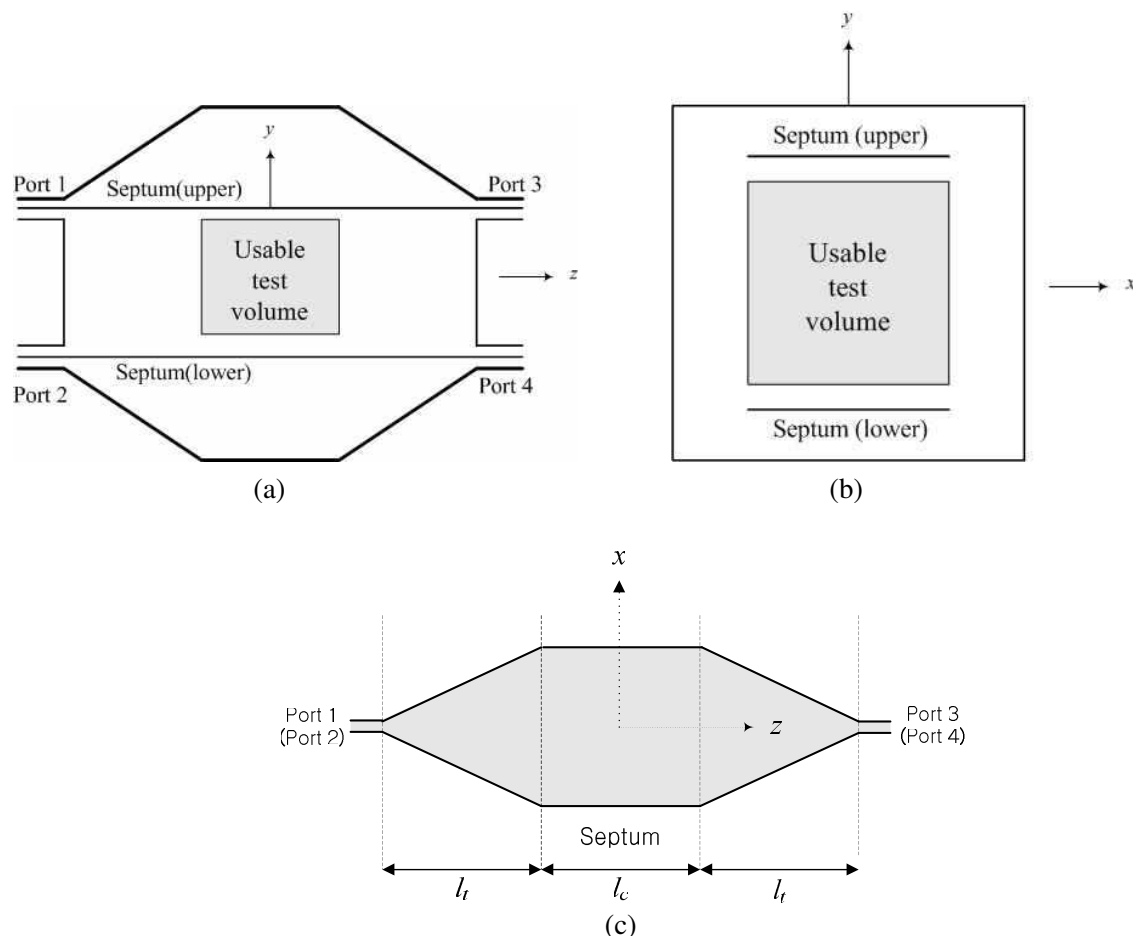


Figure 1: Geometry of 4-port TEM cell with two septa. (a) Side view, (b) cross-section view, (c) top view of septum.

field, but have a difficulty in reducing unwanted field components. That is, because the unwanted field components may occur highly in a direction corresponding to the traveling direction of the EM field, there is a problem when generating a near field mode as well as the TEM mode.

In this paper, we propose a method of reducing the unwanted EM field component in the 4-port TEM cell with two internal septa, which is used for EMC test. Adopting slit structure in the internal septa, 4-port TEM cell provide the improved standard EM field distribution inside the usable test volume. The reduction of the field component propagating the unwanted direction is shown without changing of wanted field component through EM simulation.

2. PERFORMANCE AND SIMULATION RESULT

The geometry of 4-port TEM cell with two septa is shown in Fig. 1. The 4-port TEM cell generates the standard EM field wave between two parallel septa connected to four ports at each end. Outer wall consists of the perfect conductor with zero potential.

Figure 2 shows the top view of the proposed septum in the 4-port TEM cell with one and 3 slits respectively; in Fig. 2(a), the width (w_x) of the slit is changing and in Fig. 2(b) the $w_x = 300$ mm and $w_{z_space} = 10$ mm in the septum with 3 slits.

Figure 3 and Fig. 4 are the graphs illustrating an intended and unintended electric field intensity of 4-port TEM cell with proposed slit-structured septum, respectively. Referring to Fig. 3, there is shown an electric field E_y intensity in a y -axis direction depending on the magnitude of frequency. In this case, since E_y in the y -axis is an intended electric field, it is preferred that a component of the E_y remains unchanged if possible irrespective of the presence or absent of the slits. Referring to Fig. 4, there is shown an electric field E_z intensity in a z -axis direction depending on the magnitude of frequency. In this case, since E_z in the z -axis is an unintended electric field, it is preferred that a component of E_z is needed to remove if any slit is present. As shown from Fig. 4, when a case of noslit where none of slits is formed is compared with a case of 1 slit ($w_x = 400$ mm) where one slit with a length of 400 mm is formed, the component of E_z of these cases exhibits a difference of about 4.1 dBV/m with as a base of 0.15 GHz. Further, it can be observed that a case where

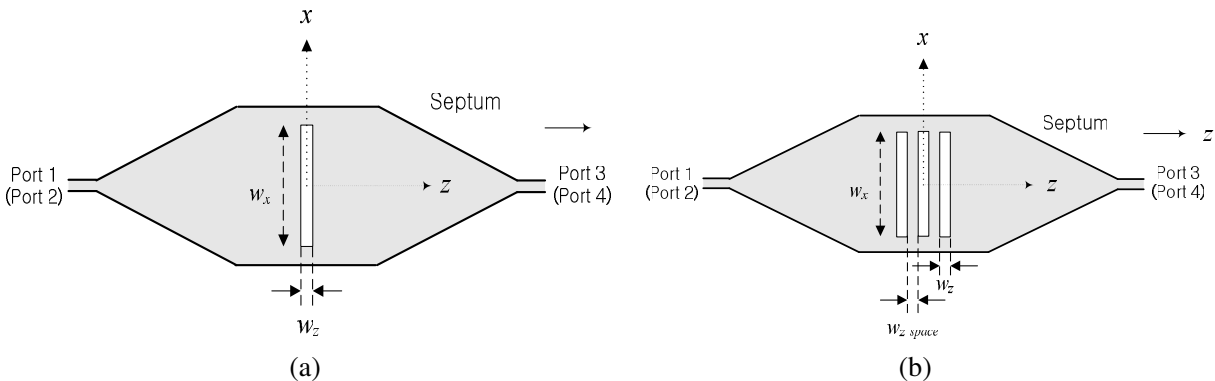


Figure 2: Top view of the proposed slit-structured septum. (a) 1 slit. (b) 3 slits.

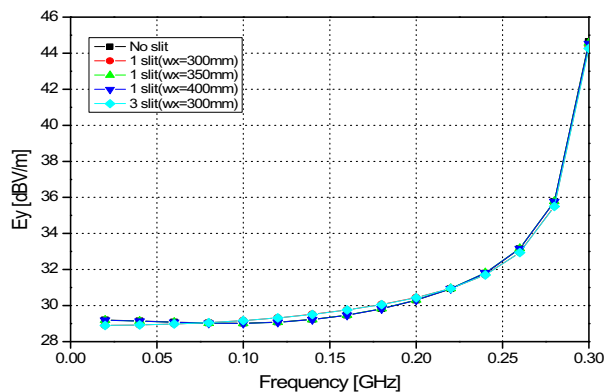


Figure 3: E_y intensity according to frequency.

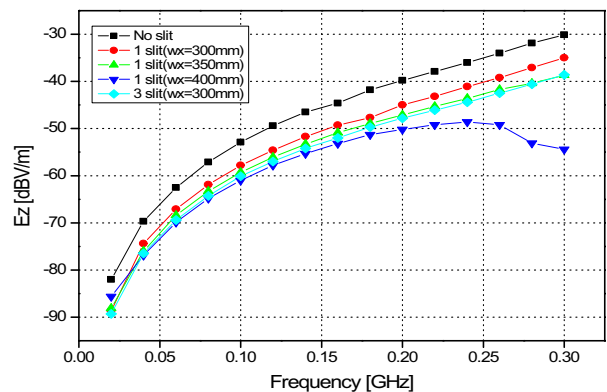


Figure 4: E_z intensity according to frequency.

even any one of the slits is formed is lower than a case where of noslit in the component of E_z . In addition, it can be also known that when the slits are the same in their lengths, the more the number of the slits is, the more the components of the unintended electric fields are removed.

As such, the amount of reduction in the electric field when the magnitude of frequency is changed differently is listed in a Table 1 as below.

Table 1: Reduction amount of E_z according to frequency.

Structure of slit		Frequency					
		100 MHz		150 MHz		200 MHz	
		E_z (dBV/m)	Reduction amount (dB)	E_z (dBV/m)	Reduction amount (dB)	E_z (dBV/m)	Reduction amount (dB)
No slit		-56.4	-	-48.9	-	-43.3	-
1 slit	$w_x = 300$	-58.2	1.8	-50.8	1.9	-45.4	2.1
	$w_x = 350$	-59.3	2.9	-52.2	3.3	-47.1	3.8
	$w_x = 400$	-61.0	4.6	-54.2	5.3	-50.2	6.9
3 slit	$w_x = 300$	-60.1	3.7	-53.0	4.1	-47.8	4.5

3. CONCLUSION

In this paper, a method of reducing the unwanted EM field component in the 4-port TEM cell was proposed. As described above, it is possible to reduce the component traveling in an unnecessary direction that occur in a TEM cell having two septa used as a standard EM wave field generator, which is one of the drawbacks of the TEM cell. Therefore, by applying the proposed slit structure, there is an effect on the improvement of Standard EM Fields distribution in the 4-port TEM cell.

ACKNOWLEDGMENT

This work was supported by the ICT R&D program of MSIP/IITP. [14-000-02-002, Development of Service and Transmission Technology for Convergent Realistic Broadcast].

REFERENCES

1. Crawford, M. L., "Generation of standard EM fields using TEM transmission cells," *IEEE Trans. Electromagn. Compat.*, Vol. 16, No. 4, 189–195, Nov. 1974.
2. Hansen, D., P. Wilson, D. Konigstein, and H. Schaer, "A broadband alternative EMC test chamber based on a TEM-cell anechoic-chamber hybrid concept," *Proceedings of the 1989 International Symposium on Electronic Compatibility*, 133–137, Sep. 1989.
3. Yun, J. H., H. J. Lee, and H. J. Hwang, "Straight coupled transmission-line cell for generating standard electromagnetic fields," *IEEE Trans. Electromagn. Compat.*, Vol. 44, No. 4, 515–521, Nov. 2002.
4. Jeon, S. B., J. H. Yun, and S. K. Park, "On the new design of a 4-port TEM waveguide with a higher cutoff-frequency and wider test volume," *ETRI Journal*, Feb. 2012.

A Short Note on the Optimization of Halbach Arrays Used as Magnetic Springs

D. Månsson

Royal Institute of Technology KTH, Sweden

Abstract— Modern neodymium magnets are today widely used for a wide variety of purposes and some commercial types have an adhesive force of approximately 100 kg even though the dimensions are only $5 * 5 * 2.5$ cm. Therefore the idea of using permanent magnets as springs isn't uncommon. Here, the specific magnetization scheme often described as a “Halbach array” is analyzed in the use as elements of a magnetic spring. The Halbach array has (ideally) a one sided flux and here both analytical methods using Maxwell's stress tensor and numerical simulations using FEMM are applied to calculate the restorative force created for two such opposing magnetic structures. This vertical force is highly dependent upon the dimensions of the structures and the magnetization wavelengths in the materials. Thus, varying these parameters will greatly affect the characteristics of the magnetic spring (e.g., spring stiffness, maximum restorative force etc.). Different applications will require different physical dimensions and magnetization wavelengths in the material.

1. INTRODUCTION

Halbach arrays are magnetic structures with special magnetic schemes with rotating (as function of position along the array) direction of magnetization. They were first described in 1973 by J. C. Mallinson [1] but later rediscovered and further explained by K. Halbach in 1981 [2]. The particular magnetization leads to a structure having (ideally) a one sided flux (i.e., the magnetic field is concentrated to the enhancing side and the field strength is (ideally) zero on the opposing, cancellation side of the structure). This constitutes however not a magnetic monopole. Halbach arrays were originally envisioned to be used for more accurate reading and writing information on magnetic tapes (see [1]) but are today used in such diverse application as free-electron lasers (as “wiguers”), magnetic levitation of high-speed trains, magnetic bearings and in brushless motors.

Here, Halbach arrays are analyzed in the use of elements in a magnetic spring. A magnetic spring is most easily formed by having two magnets with the same poles facing each other (e.g., “south-south”). However, using two simple “bar magnets” is not an optimal usage of magnetic material as much of the fields, and thus potential energy, “produced” isn't involved in the formation of the force between the two structures, (i.e., the fields that are not formed in the gap between the two magnets are not involved in the creation of the force). However, this not true if Halbach arrays are used as they will have almost all of their produced magnetic fields in the gap between the two structures.

Halbach arrays, where originally described as a continuous change of the direction of magnetization [1] and later as a segmented array of individual small magnets [2]. However, it can be seen (e.g., [3]) that decreasing the width of the individual magnets in a discretized array and, thus, the difference in the direction of magnetization between two subsequent magnets (i.e., increasing the discretization of the array) will have the shape of the magnetic field formed to converge to that formed by a continuous array. (The difference in magnetization direction, between two subsequent magnets, that is required to approximate a discretized Halbach array with a continuous is roughly 20° [3].) Therefore we can, if the discretization is enough, use the calculations for the magnetic field from a continuous Halbach array to describe the force created between two discretized Halbach array. (For a discretized Halbach array, internal forces are created between the individual magnets, but as has been seen [3] these are not of great concern as the forces are not large enough that available adhesive glue types can't hold the individual magnets in place.)

As will be described below, if Halbach arrays are used in a magnetic spring then the behavior of the spring is greatly affected by physical dimensions and the magnetization wavelength of the Halbach arrays.

2. RESTORATIVE FORCE

Here, the analytical calculation of the restorative force created follows $\mathbf{M} \rightarrow \mathbf{B} \rightarrow \mathbf{T} \rightarrow \mathbf{F}$, i.e., the magnetizations in the material (for the two Halbach arrays) give the total field created in the gap

between them. From this field Maxwell's stress tensor, on one of the two arrays, can be calculated and, thus, the force created between them.

We utilize two Halbach arrays, one above the other, both of dimensions α ("width" along \hat{x}), β ("height" along \hat{y}) and γ ("depth" along \hat{z}) and magnetization wavelength λ . Here, continuous arrays are used for the analyses but, as discussed above, these can be approximated by discretized arrays. Assume, for now, that the upper array is situated (this will be shifted later) so the top surface is at $y = 0$ and bottom surface at $y = -\beta$. The upper Halbach array is given the magnetization

$$\mathbf{M} = M_0 (\hat{\mathbf{x}} \sin kx + \hat{\mathbf{y}} \cos kx) \quad (1)$$

Here, k is the wavenumber ($k = \frac{2\pi}{\lambda}$) and λ is the magnetization wavelength in the material. From \mathbf{M} the magnetic flux density, \mathbf{B} , can be obtained via $\mathbf{B} = \mu_0(\mathbf{H} + \mathbf{M})$ and since $\nabla \cdot \mathbf{B} = 0$

$$\nabla \cdot \mathbf{H} = -\nabla \cdot \mathbf{M} \quad (2)$$

In addition, as permanent magnets only have bound magnetic currents ($\mathbf{J}_{free} = 0$) $\nabla \times \mathbf{H} = 0$. We can therefore describe the magnetic field with the magnetic scalar potential alone $\mathbf{H} = -\nabla\phi$ [4] and we get

$$\nabla \cdot \mathbf{M} = \nabla \cdot \nabla\phi = \nabla^2\phi \quad (3)$$

This can be solved [5] using the magnetization and necessary boundary conditions for the structure. From this scalar potential the magnetic field around the Halbach array can be obtained, through $\mathbf{H} = -\nabla\phi$. The magnetic field on the enhancing side of the upper array (i.e., below it) then becomes

$$\mathbf{H}_1 = M_0 \left(1 - e^{k\beta}\right) e^{ky} [\hat{\mathbf{x}} \sin(kx) - \hat{\mathbf{y}} \cos(kx)] \quad (4)$$

where, M_0 is the maximum magnetization in the material which is related to the residual magnetism via $M_0 = \frac{B_r}{\mu_0\mu_r}$ [6]. In the same way, the lower Halbach array is given the magnetization (assume, as above, top surface at $y = 0$ and bottom surface at $y = -\beta$)

$$\mathbf{M} = M_0 (\hat{\mathbf{x}} \sin kx - \hat{\mathbf{y}} \cos kx) \quad (5)$$

which creates an enhanced magnetic field, above the lower array, of

$$\mathbf{H}_2 = -M_0 \left(1 - e^{-k\beta}\right) e^{-ky} [\hat{\mathbf{x}} \sin(kx) + \hat{\mathbf{y}} \cos(kx)] \quad (6)$$

Having the top surface of the lower Halbach array at $y = 0$ and shifting the upper array upward a distance h (and adjusting for the shift in coordinate system for the upper array, i.e., change y to $y - (h + \beta)$ in \mathbf{H}_1) the total magnetic field ($\mathbf{H}_{tot} = \mathbf{H}_1 + \mathbf{H}_2$) in the gap becomes

$$\begin{aligned} \mathbf{H}_{tot} = M_0 \sin(kx) & \left[(1 - e^{k\beta}) e^{k(y-(h+\beta))} - (1 - e^{-k\beta}) e^{-ky} \right] \hat{\mathbf{x}} \\ & - M_0 \cos(kx) \left[(1 - e^{k\beta}) e^{k(y-(h+\beta))} + (1 - e^{-k\beta}) e^{-ky} \right] \hat{\mathbf{y}} \end{aligned} \quad (7)$$

To calculate the restorative force created when the two Halbach arrays are moved together we assume that the lower array is fixed and investigate the restorative force formed when the upper array is moved downward, i.e., h decreases. (As we have chosen opposing magnetizations, e.g., "South-South", this force will be directed upward on the upper array.) If we assume permanent magnets that move "slow" and don't induce electric fields (through $\nabla \times \mathbf{E} = -d\mathbf{B}/dt$) of any significance (see [3] for the justification of this) we form Maxwell's stress tensor (MST) using [4]

$$T_{ij} = \frac{1}{\mu_0} \left(B_i B_j - \frac{1}{2} \delta_{ij} B^2 \right) \quad (8)$$

The force now becomes

$$\mathbf{F} = \oint_S \mathbb{T} \cdot d\mathbf{a} \quad (9)$$

For the situation investigated here, we are primarily interested in the vertical component of the restorative force (as any displacement in the \hat{x} or \hat{z} direction can be handled by surrounding

fixtures). We form the tensor for the lower, fixed, array and it was seen (see [7]) that this situation can, with good accuracy, be approximated with

$$F_y = \oint_S (\mathbb{T} \cdot d\mathbf{a})_y \approx \int_{top} T_{yy,top} da_{top} = \gamma \int_{x=0}^{\alpha} T_{yy,top} dx \quad (10)$$

Thus, the complicated surface integral can be reduced to a line integral on the top surface of this array. Using (8) the tensor becomes (in the gap)

$$T_{yy,top} = \frac{1}{\mu_0} \left(B_y B_y - \frac{1}{2} (B_x^2 + B_y^2) \right) = \frac{1}{2\mu_0} (B_y^2 - B_x^2) \quad (11)$$

Using (7) (along with $\mathbf{B} = \mu_0 \mathbf{H}$ and $M_0 = \frac{B_r}{\mu_0 \mu_r}$) $T_{yy,top}$ becomes at the top surface of the lower array (i.e., $y = 0$)

$$\begin{aligned} T_{yy,top} &= \frac{B_r^2}{2\mu_0 \mu_r^2} (\cos^2(kx)\theta - \sin^2(kx)\psi) \\ \theta &= \left((1 - e^{k\beta}) e^{k(-h-\beta)} + (1 - e^{-k\beta}) \right)^2 \\ \psi &= \left((1 - e^{k\beta}) e^{k(-h-\beta)} - (1 - e^{-k\beta}) \right)^2 \end{aligned} \quad (12)$$

The line integral (10) can then easily be calculated using *Wolfram Alpha* [8]

$$\begin{aligned} F_y &= \gamma \frac{B_r^2}{2\mu_0 \mu_r^2} \int_{x=0}^{\alpha} (\cos^2(kx)\theta - \sin^2(kx)\psi) dx \\ &= \begin{bmatrix} c_1 = \theta - \psi \\ c_2 = \theta + \psi \end{bmatrix} = \gamma \frac{B_r^2}{2\mu_0 \mu_r^2} \frac{1}{4k} (2k\alpha c_1 + c_2 \sin(2k\alpha)) \\ &= \gamma \frac{B_r^2}{2\mu_0 \mu_r^2} \left(\frac{\alpha c_1}{2} + \frac{\lambda}{8\pi} c_2 \sin \left(\frac{4\pi\alpha}{\lambda} \right) \right) \end{aligned} \quad (13)$$

FEMM (“Finite Element Method Magnetics”) is a numerical simulation software that has been shown to be accurate (see [3] or [9] for more information) and we can investigate the force formed in the situation and compare it with the analytical results (see Figure 1). As we can see, the analytical and simulated results results agree well.

3. OBSERVATIONS

As can be seen from Figure 1 the magnetization wavelength in the material greatly affects the behavior of the magnetic spring. For instance, decreasing the wavelength (compared to the widths, α , of the arrays, i.e., λ/α) will increase the maximum restorative force (very short gap distances) but will reduce this force for larger distances. Comparing to a normal mechanical spring for which the restorative force can be described with, e.g., $\mathbf{F} = -kx'\hat{\mathbf{x}}$ the behavior can be understood with having a spring stiffness, k , that isn't constant (although mechanical springs are only approximately constant). In addition, as can be seen in Figure 2, changing the height (i.e., β) of the two arrays also changes the characteristics of the force in a non-linear way that is dependent on the value of the factor λ/α . For instance, a magnetization wavelength of $\lambda/\alpha = 0.25$ will, quite quickly, increase the maximal restorative force when increasing β whereas larger λ/α will not. This is important as one can falsely be lead to believe that adding more magnetic material will linearly increase the restorative force (which is not true). Looking at the characteristics of the forces shown in the figures we can translate this to a spring stiffness that is dependent upon the magnetization wavelength, dimensions as well as the gap distance. Thus, this imagined spring stiffness is hardly linear, i.e., $k = k(\lambda/\alpha, \beta, h)$.

In addition, a normal mechanical spring that is disturbed from its relaxed state will (barring mechanical deformation) try to restore the spring to its natural, relaxed, state (i.e., form). For the magnetic spring investigated here this isn't so. If compressed, for the here given magnetizations, the restorative force will act to separate the two Halbach arrays but if pulled apart no restorative force acts on the two arrays to pull them back together again. (If the magnetization is changed as to have a situation of “North-south”, then the two Halbach arrays will try to come together instead). The situation can be likened to having the natural, relaxed, state of an infinite gap distance.

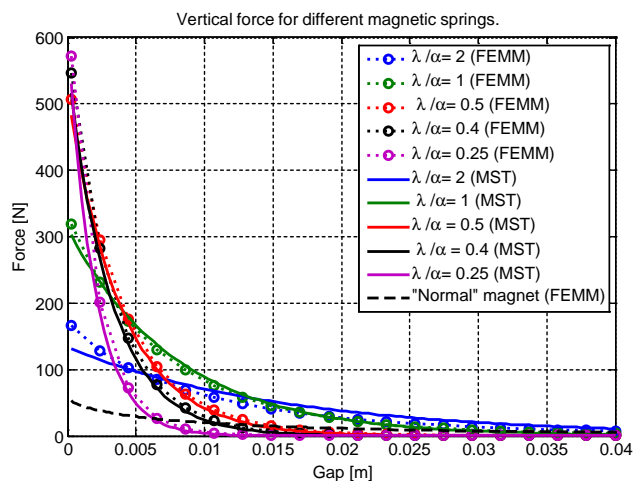


Figure 1: The vertical restorative force created (on the upper array) using two opposing Halbach arrays for cases of different wavelengths, λ (in relation to the width, α , of the Halbach arrays). The dimensions are here $\alpha = 5$ cm, $\beta = 1$ cm, $\gamma = 1$ cm and material with B_r , of approximately 1.3 T and $\mu_r = 1.5$. The results are acquired both using numerical simulations (FEMM) and Maxwell’s stress tensor (13). Both methods agree very well. Notice the much lower force (i.e., at most a factor of 10) created between two normal magnets of the same dimensions and maximum magnetization (M_0). The small differences, between the MST and FEMM results, in some cases, are due to the approximations made in order to acquire a simple analytical expression. (As explained in [7], the case where $\lambda/\alpha = 2$, the magnetic structures can’t be considered to be a Halbach array anymore).

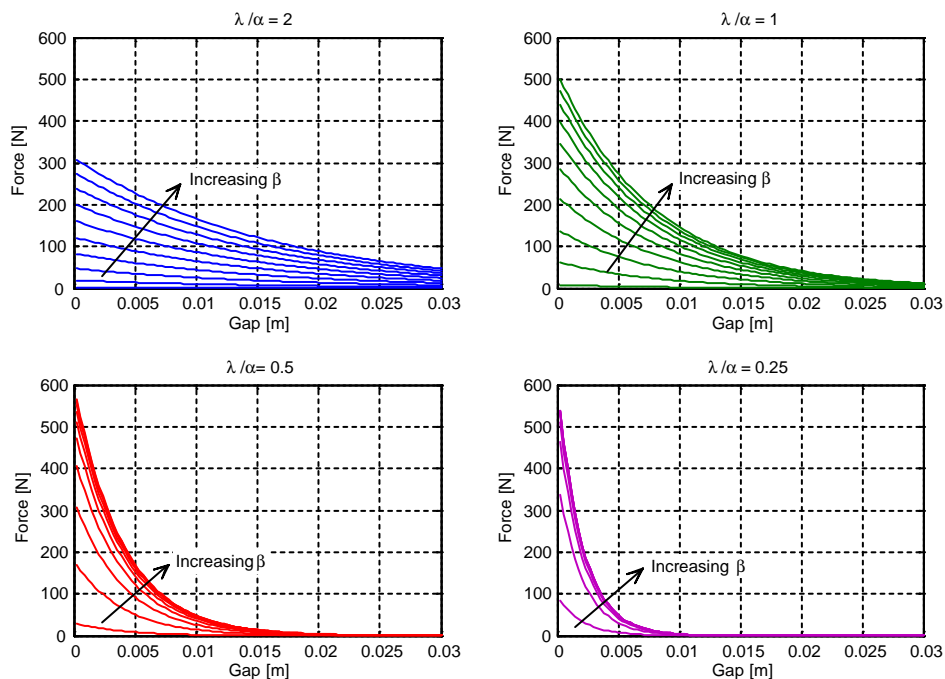


Figure 2: Using (13) the restorative force (on the upper array) is calculated for β having ten equally spaced values between $\beta = 0.1$ cm and $\beta = 2$ cm. As can be seen, for different λ/α , the change in β affects the vertical force differently. The color scheme is the same as for the cases in Figure 1.

Furthermore, using two “normal” magnets of equal dimensions and maximum magnetization (M_0) will result in a much smaller restorative force that is, however, much more linear with the gap distance compared to using Halbach arrays. Thus, for different applications that require different characteristics the dimensions and magnetization wavelengths can be adapted to suit this.

4. CONCLUSION

Using two Halbach arrays with opposing magnetizations will form a magnetic spring. The characteristics of the restorative force for this magnetic spring will be highly non-linear and dependent on the magnetization wavelength and actual dimensions of the Halbach arrays. Different configurations (i.e., dimensions and magnetization wavelengths) can be made to fit different applications.

ACKNOWLEDGMENT

This work was made possible through funding from the STandUP for Energy collaboration.

REFERENCES

1. Mallinson, J. C., “One-sided fluxes — A magnetic curiosity?,” *IEEE Trans. Magnetics*, Vol. 9, 678–682, 1973.
2. Halbach, K., “Physical and optical properties of rare earth cobalt magnets,” *Nuclear Instruments and Methods in Physics Research*, Vol. 187, 109–117, Aug. 1981.
3. Månsson, D., “On the suitability of using halbach arrays as potential energy storage media,” *Progress In Electromagnetics Research B*, Vol. 58, 151–166, 2014.
4. Griffiths, D. J., *Introduction to Electrodynamics*, 3rd Edition, Prentice-Hall Inc., Upper Saddle River, 1999.
5. Shute, H. A., J. C. Mallinson, D. T. Wilton, and D. J. Mapps, “One-sided fluxes in planar, cylindrical, and spherical magnetized structures,” *IEEE Trans. Magnetics*, Vol. 36, No. 2, Mar. 2000.
6. Ofori-Tenkorang, J. and J. H. ILang, “A comparative analysis of torque production in halbach and conventional surface-mounted permanent-magnet synchronous motors,” *IEEE Industry Applications Conference*, Orlando, USA, Oct. 8–12, 1995.
7. Månsson, D., “On the optimization of Halbach arrays as energy storage media,” *Progress In Electromagnetics Research B*, Vol. 62, 277–288, 2015.
8. WolframAlpha, Available at: <http://www.wolframalpha.com/>.
9. “Finite element method magnetics,” available: <http://www.femm.info/>.

Propagation of EM Fields through a Rotating Circular Hollow Dielectric Cylinder: Numerical Simulation in 2Ds

Mingtsu Ho, Hui-Hung Lin, and Tsaoan Chang

Graduate School of Opto-Mechatronics and Materials, WuFeng University, Taiwan

Abstract— The propagation of electromagnetic (EM) fields through a rotating circular hollow lossless dielectric cylinder has been numerically simulated in two dimensions and the numerical results were presented in this paper. The method of characteristics (MOC) is used to numerically solve the time-domain Maxwell equations. The passing center swing back grids (PCSBG) technique was devised and introduced in collaboration of MOC in a modified O-type grid system. The PCSBG scheme resolves the difficulty of the distortion of grid cells caused by the rotational movement of the object. There are two types of cylinder were used in this work. They are made of dielectric and impedance matching materials, illuminated by Gaussian EM pulses as the excitation sources, and may either be at rest or rotate at extremely high angular frequencies for better observation of its effects on the EM fields. The presented computational results, demonstrated in a side-by-side manner for clear comparisons, are the electric field distribution over the whole numerical domain and the EM fields sampled at the center of cylinder.

1. INTRODUCTION

The purpose of the present study is to numerically simulate the propagation of EM pulse through a rotating circular hollow dielectric cylinder and observe the effects of the rotating vessel on the EM fields. The MOC approach is used to solve the time-domain Maxwell equations in conjunction with the PCSBG technique in the modified O-type grid system. The former is for the difficulty of grid deformation caused by the rotating object while the latter for the satisfaction the requirement of minimum number of points representing the highest frequency content of interest. MOC has been reported to produce compatible results when compared with either that of finite-difference time-domain (FDTD) [1] where infinite long PEC strip was illuminated Gaussian EM pulse or theoretical values [2, 3] where a perfect surface was traveling and/or vibrating. Especially, in the Reference [3], the perfect surface was traveling at extremely high velocity, 90% of the light speed. In addition, MOC provides reasonable trends on the following cases: the effects of medium conductivity on the propagation of EM pulse onto conducting dielectric half space [4] and the propagation of EM pulse through lossless non-uniform dielectric slab [5]. To overcome the difficulty stemmed from the rotating cylinder, thanks to the nature of MOC positioning all the field components in center of the grid cell, the PCSBG technique was proposed in coalition with MOC [6, 7]. MOC with the aid of PCSBG was demonstrated to yield reasonable computational results in the scattered EM fields from rotating circular cylinder under the illumination of Gaussian EM pulse [8].

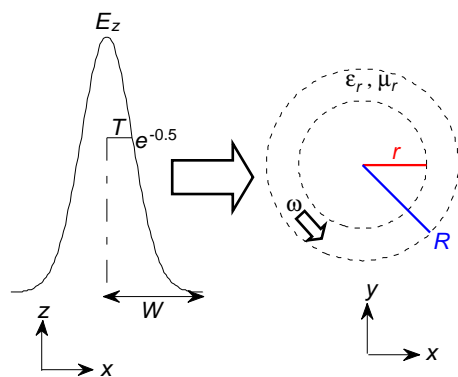


Figure 1: Definition of problem.

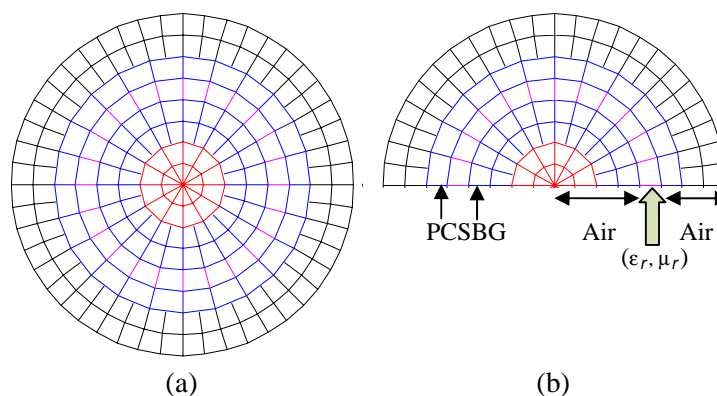


Figure 2: Modified O-type grid system.

2. THE PROBLEM AND THE PASSING CENTER SWING BACK GRIDS

The schematic diagram in Figure 1 depicts the definition of problem. The electric field intensity has a Gaussian profile with a peak value of unity, a width of $T = 0.2$ ns measured from the center

to the point of value of $e^{-0.5}$, and a cut-off level at 100 dB for practical reasons. The hollow cylinder is characterized by two radii r and R , the relative permittivity (ϵ_r) and permeability (μ_r), and the angular velocity ω (counter-clockwise). The EM scattering problems require a minimum quantity on the grid density. A regular O-type grid fails to meet such standard in long radius regions. The modified O-type grid was proposed to settle the situation and a simplified version of which is given in Figure 2(a) where the grid number circumferentially is doubled from zone to zone. Figure 2(b) illustrates the two passing center swing back grids (PCSBGs) layers as well as the definition of the materials that hollow cylinder is made of by giving ϵ_r and μ_r . Note that both PCSBG layers are portions of air inside and outside of the cylinder and that during the process only grids representing the rotating hollow cylinder and the two PCSBG layers are dynamic while the rest of grids stationary.

Figure 3(a) displays the situation without any treatment two layers of grids immediately adjacent to cylinder's boundaries are badly twisted and suffer from deformation as the hollow cylinder rotates, in which a black arrow indicates the direction of rotation. In Figures 3(b) and 3(c) a dark bold line inside the hollow cylinder and two arrows in PCSBGs are used as indicators. PCSBG is proposed to manipulate all skew grid lines to swing backward by one grid as in Figure 3(c) and then resume the rotation. With the aid of PCSBGs, MOC overcomes the difficulty caused by the rotating object.

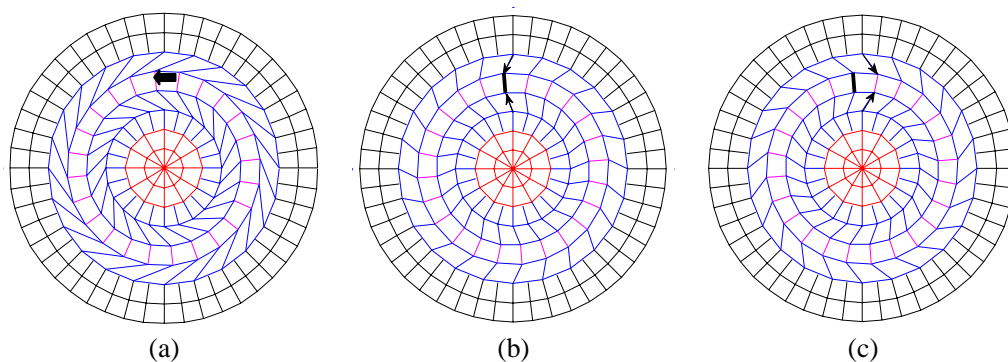


Figure 3: PCSBG in a modified grid: (a) without swing back grids; (b) grid lines pass the center point and are set to swing back; (c) after the swing back rotation continues.

3. THE PROBLEM SET UP

The present problem is featured by a circular hollow dielectric cylinder rotating at extremely high angular frequency which is impractical for the purpose of clear demonstrations the effects of rotating hollow cylinder (either $\epsilon_r = 4$, $\mu_r = 1$ or $\epsilon_r = \mu_r = 2$) on the propagation of the EM fields. The dimensions of the numerical model are: $r = 36$ mm, $R = 60$ mm, and domain boundary is 500 mm. The angular frequency ω is set based on the span of time of the Gaussian envelop, i.e., $2W$ in Figure 1. For a pulse width $T = 0.2$ ns, $2W$ is about 1.92 ns with a cut-off level of 100 dB. If the cylinder rotates one tenth of one cycle within $2W$, the instantaneous velocity of any point on the outer surface of the cylinder is about 6.54% of light speed.

The grid density in the unit of points per meter is 250 uniformly in radial direction and ranges from 210 to 680 in circumferential direction (the origin not included). The whole computational domain is composed of three sections. There are three zones in each section: inside (16, 32, 64), interior (64, 128, 256), and exterior (256, 512, 1024) of the hollow cylinder. The three numbers given within parentheses are the grid numbers in each layer from zone to zone. In total, numbers of layer and grid are 144 and 88000, respectively.

4. NUMERICAL RESULTS

Figure 4 illustrates the electric field intensity (E_z) distribution plots for hollow cylinder of $\epsilon_r = 4$ and $\mu_r = 1$, respectively sampled at 1.033 and 1.833 ns for three different angular frequencies of 0.1 and 0.5. Similar set of plots is given in Figure 5 for cylinder made of impedance matching material ($\epsilon_r = \mu_r = 2$). A number is given below each plot to indicate the angle degrees that the cylinder rotates at the sampling time. It is obvious that the reflected EM fields can be observed in the second and third rows of Figure 4 while they are undetectable in Figure 5 since the latter

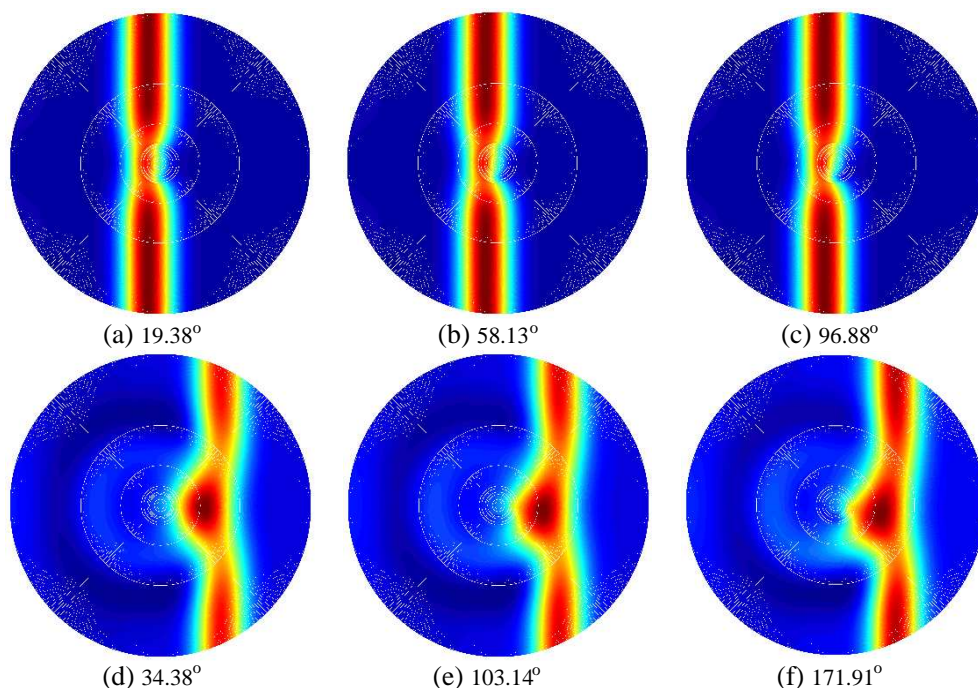


Figure 4: Electric field (E_z) distributions for cylinder ($\epsilon_r = 4$, $\mu_r = 1$) rotating at three different angular frequencies of (a), (d) 0.1, (b), (e) 0.3, and (c), (f) 0.5 sampled at (a), (b) (c) 1.033 and (d), (e) (f) 1.833 ns.

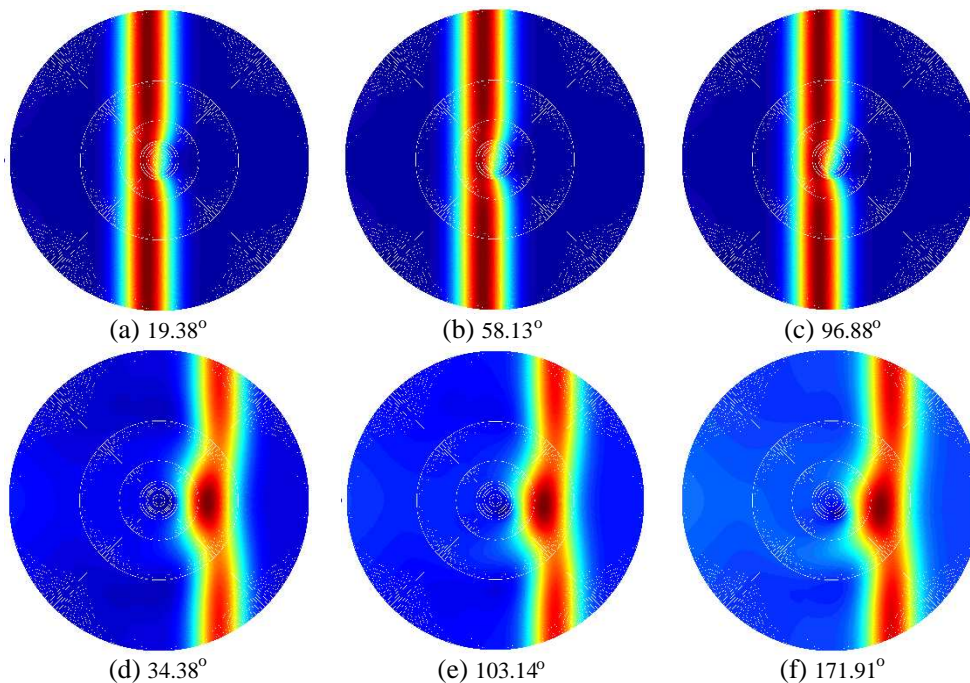


Figure 5: Electric field (E_z) distributions of cylinder ($\epsilon_r = \mu_r = 2$) rotating at three different angular frequencies of (a), (d) 0.1, (b), (e) 0.3, and (c), (f) 0.5 sampled at (a), (b) (c) 1.033 and (d), (e) (f) 1.833 ns.

is made of impedance matching material. The effects of the rotating hollow cylinder on the EM fields is noticeable, as speed increases the fields are dragged towards lower right for the following reasons: EM fields propagate at slower speed interior of cylinder than in air, and consequently stay in hollow cylinder for a longer time; the EM fields in the lower portion of cylinder propagate in the same direction as the cylinder while the upper opposite, which is getting more perceptible as speed increases.

There is no magnetic field component (solid lines) along the x -axis passing the cylinder center as

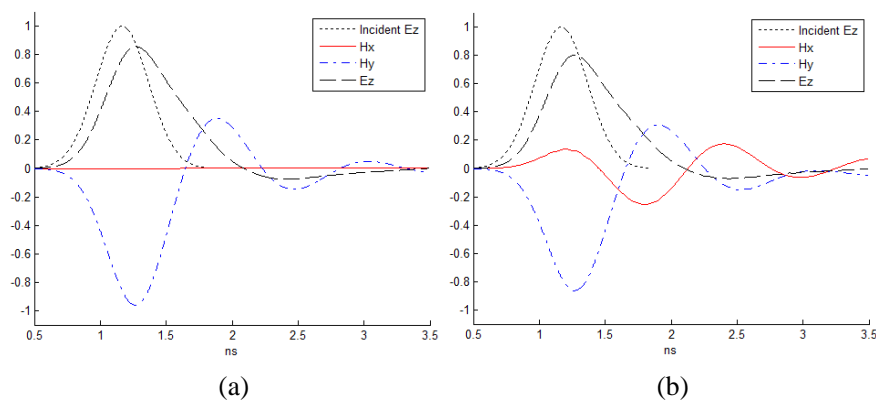


Figure 6: EM fields recorded at the cylinder ($\varepsilon_r = 4$, $\mu_r = 1$) center: (a) $\omega = 0$, (b) $\omega = 0.3$.

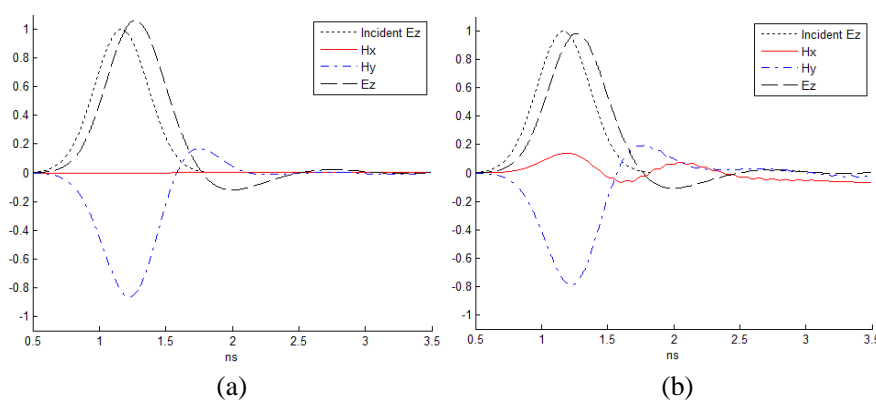


Figure 7: EM fields recorded at the cylinder ($\varepsilon_r = \mu_r = 2$) center: (a) $\omega = 0$, (b) $\omega = 0.3$.

in Figures 6(a) and 7(a). In both sets of graphs the incident electric field components (dotted lines) are given as a reference. Given in Figures 6(b) and 7(b), it is apparent that x -components of the magnetic fields (H_x) are no longer null in magnitude due to the rotation of the hollow cylinder and fluctuate with greater magnitudes in the dielectric cylinder than that in the impedance matching one. The larger level of fluctuation is originated from the facts that EM fields seem to be trapped interior of the dielectric vessel due to slower in speed and multiple reflection/transmission between interfaces while in the impedance matching vessel such phenomena are barely detectable.

5. CONCLUSION

In this paper, it has been shown that the method of characteristics integrating with the passing center swing back grids technique and solving the time-domain Maxwell equations in the modified O-type grid system, which not only overcame the difficulty of grid distortion due to the rotation of the object of interest but also met the criterion of minimum grid points within the shortest wavelength content. Furthermore, it produced computational outcomes bearing feasible trends of how the rotation of hollow cylinder affects the EM fields by demonstrating the field distribution over the numerical domain and the EM fields sampled at the cylinder center.

REFERENCES

1. Donohoe, J. P., J. H. Beggs, and M. Ho, "Comparison of finite-difference time-domain results for scattered EM fields: Yee algorithm vs. a characteristic based algorithm," *27th IEEE Southeastern Symposium on System Theory*, March 1995.
2. Ho, M., "Scattering of EM waves from traveling and/or vibrating perfect surface: Numerical simulation," *IEEE Transactions on Antennas and Propagation*, Vol. 54, No. 1, 152–156, January 2006.
3. Ho, M., "EM scattering from PEC plane moving at extremely high speed: Simulation in one dimension," *Journal of Applied Science and Engineering (JASE)*, Vol. 17, No. 4, 429–436, December 2014.

4. Ho, M. and F.-S. Lai, "Effects of medium conductivity on electromagnetic pulse propagation onto dielectric half space: One-dimensional simulation using characteristic-based method," *Journal of ElectroMagnetic Waves and Applications*, Vol. 21, No. 13, 1773–1785, 2007.
5. Ho, M., F.-S. Lai, S.-W. Tan, and P.-W. Chen, "Numerical simulation of propagation of EM pulse through lossless non-uniform dielectric slab using characteristic-based method," *Progress In Electromagnetics Research*, Vol. 81, 197–212, 2008.
6. Ho, M., "Simulation of scattered fields from rotating cylinder in 2D: Under illumination of TE and TM Gaussian pulses," *PIERS Proceedings*, 1646–1651, Moscow, Russia, August 18–21, 2009.
7. Ho, M., "Numerically solving scattered electromagnetic fields from rotating objects using passing center swing back grid technique: A proposal," *Journal of ElectroMagnetic Waves and Applications*, Vol. 23, No. 23, 389–394, 2009.
8. Ho, M., "Simulation of scattered EM fields from rotating cylinder using passing center swing back grids technique in two dimensions," *Progress In Electromagnetics Research*, Vol. 92, 79–90, 2009.

Rapid High-accuracy Modeling Simulation Method for Full Trajectory of the Ballistic Missile

Jianhua Wu, Gang Li, Jian Chen, Shiyong Xu, and Zengping Chen

Science and Technology on Automatic Target Recognition Laboratory

National University of Defense Technology, Changsha, China

Abstract— In view of the existing problems of trajectory model for ballistic missile, a method for full trajectory model of a ballistic missile over a rotating, ellipsoid earth has been developed. The method is based on the theory of minimal energy. The error of flight range is calculated with the method of Bessel's geodetic inverse solution and fourth-order Runge-Kutta, and then corrected by dichotomy iteration. The process is repeated until the ballistic missile impacts the target location within a predefined miss distance tolerance. Simulation results show that both the speed of ballistic generation and confidence get a noticeable rise with the established trajectory model in this paper.

1. INTRODUCTION

A ballistic trajectory is the path of an object that is dropped, thrown, served, launched. In the extraction technology for ballistic targets, establish ballistic trajectory model is the first step. One of the earliest studies of trajectory prediction and determination was conducted by Johann Heinrich Lambert. A method for the determination of the ballistic trajectory was developed with only giving the launch position and impact point over a spherical model [1]. A practical analytical approximation of projectile trajectories in 2D and 3D roughly based on linear drag model was introduced [2]. The ballistic missile trajectory based on elliptic trajectory theory and 4D external trajectory model was predicted [3]. B. Xiao [4] researched a method of energy ballistic orbit, based on the theory of two-body orbit trajectory, but without considering the characteristics of different flight phases for missile, F. Zhang [5] firstly obtained terminal ballistic parameters without considering the earth rotation, then corrected the terminal velocity by iteration to reduce the affection of the earth rotation. In many existing methods, the characteristics of different flight phases, the affection of the earth rotation and the low speed of ballistic generation are often ignored, and other contributions rely on a prior information. According to these researches, an iterative optimization method is proposed to establish a full ballistic trajectory model in this paper. Firstly, ballistic parameters at burnout point are initially estimated according to the theories of minimal energy trajectory and elliptic trajectory. Secondly, dynamic differential equations and missile airframe state vector are established. Finally, the error of flight range is calculated with the method of Bessel's geodetic inverse solution and fourth-order Runge-Kutta, and corrected by dichotomy iteration until the ballistic missile impacts the target location within a predefined miss distance tolerance. It turns out that the method can markedly decrease the iterations, speed up ballistic generation and improve the accuracy of the result. Moreover, the trajectory model established in this paper has been used in a signature extraction system for missile herd targets, and has shown good performance.

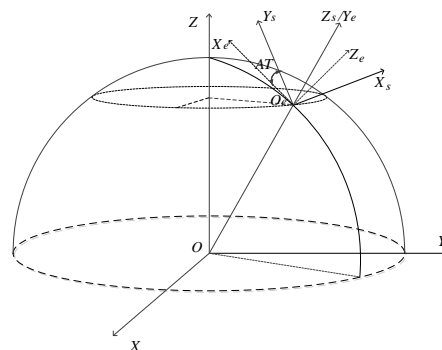


Figure 1: Coordinate system definition.

2. COORDINATE TRANSFORMATION

According to the flight dynamics, the mathematics model which describes targets motion principles would be highly simplified if choosing suitable reference system. The coordinate systems used in establishing kinematic equations for missile are Launch frame (X_e, Y_e, Z_e), East-North-Up (ENU) frame (X_s, Y_s, Z_s) and Earth-Centered-Inertial (ECI) frame (X, Y, Z), A_T is azimuth. Figure 1 depicts the three coordinate systems. As depicted in Figure 1, the transformation from an ENU position vector to an ECI position vector is given by the following vector-matrix operation

$$\mathbf{r}_{eci} = C_e^s \mathbf{r}_{enu} \quad (1)$$

the elements of the transformation matrix C_e^s are given by

$$C_e^s = \begin{bmatrix} -\sin j_0 & \cos j_0 & 0 \\ -\sin w_0 \cos j_0 & \sin w_0 \sin j_0 & \cos w_0 \\ \cos w_0 \cos j_0 & \cos w_0 \sin j_0 & \sin w_0 \end{bmatrix} \quad (2)$$

Here w_0 is the longitude, and j_0 is the latitude.

3. MINIMAL ENERGY TRAJECTORY MODEL

A method to determine the trajectory of a ballistic missile over a rotating, ellipsoid earth is developed with only giving the launch position, impact position, range angle in free-flight phase and geocentric distance at burnout point. Initial ballistic parameters at burnout point are estimated according to the theories of minimal energy trajectory and elliptic trajectory. In order to simplify the complexity of model, particle dynamic equations in flight and missile airframe state vector are established. Finally, The error of flight range is calculated with the method of Bessel's geodetic inverse solution and fourth-order Runge-Kutta, and corrected by dichotomy iteration. The process is repeated until the ballistic missile impacts the target location within a predefined miss distance tolerance.

3.1. Ballistic Parameters

The exact mathematical relationship among range angle in free-flight phase β_e , energy parameter γ_k and optimum ballistic angle θ_k are given by the following equation

$$\sin \frac{\beta_e}{2} = \frac{\gamma_k}{2e} \sin 2\theta_k \quad (3)$$

$$e = \sqrt{1 + \gamma_k(\gamma_k - 2) \cos^2 \theta_k} \quad (4)$$

where e is ellipse eccentricity. The relationship between γ_k and θ_k is deduced and the optimum θ_k is obtained if β_e is given by the method of maximum-minimum. γ_k is determined by r_k and V_k , the equation is as follow

$$\gamma_k = \frac{r_k V_k^2}{u} \quad (5)$$

r_k is the geocentric distance from burnout point to the earth's center, and V_k is the missile speed in this point. If r_k is given, the argument of γ_k is determined by V_k , and when θ_k is optimal, γ_k is minimal, V_k would also be minimal, similarly, the energy cost in full missile flight would also be minimum.

3.2. Boost Phase Trajectory Model

Dynamic and kinematic model for missile in boost flight phase is established in ECI coordinate system after analyzing the forces of missile in the phase, and the roles of missile are decided by propulsion, gravity, aerodynamic resistance, Coriolis and centripetal. A standard ellipsoid model of the earth is established and corrected by the second harmonic, dynamic equations in this flight phase are as follows

$$\dot{\mathbf{p}} = \mathbf{v} \quad \dot{\mathbf{v}} = \mathbf{a}_p + \mathbf{a}_D + \mathbf{a}_G + \mathbf{a}_{cor} + \mathbf{a}_{cen} \quad (6)$$

Here \mathbf{a}_p is propulsion acceleration, the direction is linear in velocity. $a_D = \frac{C_D(v(t))S\rho(h(t))v^2(t)}{2m(t)}$ is aerodynamic resistance acceleration, the direction is opposite to velocity, $C_D(v)$ is resistance

coefficient, $\rho(h)$ is air density. \mathbf{a}_G is gravity acceleration, \mathbf{a}_{cor} is Coriolis acceleration, and kinematic \mathbf{a}_{cen} is centripetal acceleration. Kinematic equations for missile are as follows:

$$\begin{cases} \dot{\mathbf{v}}_x = (a_p - a_D - a_{cen}) \frac{\mathbf{v}_x}{v_0} - \frac{u}{r_0^3} \left(\mathbf{p}_x + \frac{C_e}{r_0^2} \left(1 - 5 \left(\frac{p_z}{r_0} \right)^2 \right) \mathbf{p}_x \right) - a_{cor} \frac{\mathbf{p}_x}{r_0} \\ \dot{\mathbf{v}}_y = (a_p - a_D - a_{cen}) \frac{\mathbf{v}_y}{v_0} - \frac{u}{r_0^3} \left(\mathbf{p}_y + \frac{C_e}{r_0^2} \left(1 - 5 \left(\frac{p_z}{r_0} \right)^2 \right) \mathbf{p}_y \right) - a_{cor} \frac{\mathbf{p}_y}{r_0} \\ \dot{\mathbf{v}}_z = (a_p - a_D - a_{cen}) \frac{\mathbf{v}_z}{v_0} - \frac{u}{r_0^3} \left(\mathbf{p}_z + \frac{C_e}{r_0^2} \left(1 - 5 \left(\frac{p_z}{r_0} \right)^2 \right) \mathbf{p}_z \right) - a_{cor} \frac{\mathbf{p}_z}{r_0} \end{cases} \quad (7)$$

where, $r_0 = \sqrt{p_x^2 + p_y^2 + p_z^2}$ is the scalar distance from missile to the center of the earth, $v_0 = \sqrt{v_x^2 + v_y^2 + v_z^2}$ is the scalar velocity or speed of the missile, $C_e = \frac{3J_2R^2}{2}$ and J_2 is the second harmonic.

3.3. Post-boost Phase Trajectory Model

3.3.1. Dynamic and Kinematic Model in Post-boost Phase

Dynamic and kinematic model for missile in post-boost flight phase is established in ECI coordinate system, comparing to the forces of missile in boost phase, there is no propulsion, dynamic equations are as follows

$$\dot{\mathbf{p}} = \mathbf{v} \quad \dot{\mathbf{v}} = \mathbf{a}_D + \mathbf{a}_G + \mathbf{a}_{cor} + \mathbf{a}_{cen} \quad (8)$$

Kinematic equations for missile are as follows:

$$\begin{cases} \dot{\mathbf{v}}_x = (-a_D - a_{cen}) \frac{\mathbf{v}_x}{v_0} - \frac{u}{r_0^3} \left(\mathbf{p}_x + \frac{C_e}{r_0^2} \left(1 - 5 \left(\frac{p_z}{r_0} \right)^2 \right) \mathbf{p}_x \right) - a_{cor} \frac{\mathbf{p}_x}{r_0} \\ \dot{\mathbf{v}}_y = (-a_D - a_{cen}) \frac{\mathbf{v}_y}{v_0} - \frac{u}{r_0^3} \left(\mathbf{p}_y + \frac{C_e}{r_0^2} \left(1 - 5 \left(\frac{p_z}{r_0} \right)^2 \right) \mathbf{p}_y \right) - a_{cor} \frac{\mathbf{p}_y}{r_0} \\ \dot{\mathbf{v}}_z = (-a_D - a_{cen}) \frac{\mathbf{v}_z}{v_0} - \frac{u}{r_0^3} \left(\mathbf{p}_z + \frac{C_e}{r_0^2} \left(1 - 5 \left(\frac{p_z}{r_0} \right)^2 \right) \mathbf{p}_z \right) - a_{cor} \frac{\mathbf{p}_z}{r_0} \end{cases} \quad (9)$$

The missile airframe state vector is comprised of 6 elements that define the missile position and velocity. This state vector is written as

$$\mathbf{X} = (\mathbf{p}_x, \mathbf{p}_y, \mathbf{p}_z, \mathbf{v}_x, \mathbf{v}_y, \mathbf{v}_z) \quad (10)$$

Aiming to the problem of no solution to these nonlinear differential equations, the method of fourth-order Runge-Kutta is applied to numerical integration in this paper, fourth-order Runge-Kutta equations is written as

$$\begin{aligned} \mathbf{X}_{i+1} &= \mathbf{X}_i + \frac{h}{6} (X_{1i} + 2X_{2i} + 2X_{3i} + X_{4i}) \\ \begin{cases} X_{1i} = f_i(t, \mathbf{X}_i) \\ X_{2i} = f_i(t + \frac{h}{2}, \mathbf{X}_i + \frac{h}{2}X_{1i}) \\ X_{3i} = f_i(t + \frac{h}{2}, \mathbf{X}_i + \frac{h}{2}X_{2i}) \\ X_{4i} = f_i(t + h, \mathbf{X}_i + hX_{3i}) \end{cases} \end{aligned} \quad (11)$$

where h is the integration step. Simulations show that fourth-order Runge-Kutta is highly accurate than higher-order Runge-Kutta.

3.3.2. Dichotomy Iteration

The following expression is to determine whether the simulation results within a predefined miss distance tolerance

$$\Delta s = |S_T - S_P| < \varepsilon \quad (12)$$

S_T is geodetic distance, called theoretical flight range, which is estimated by the method of Bessel's geodetic inverse solution. The main idea of the method is that two points on the ellipsoid are

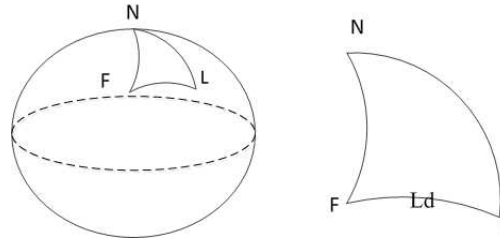


Figure 2: Bessel projection operation.

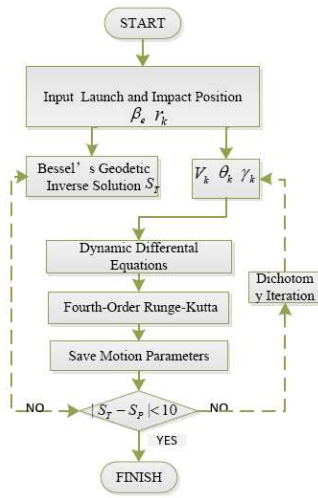


Figure 3: Simulation order of operation.

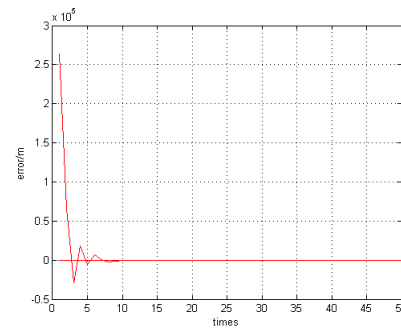


Figure 4: The range error vs. iteration time.

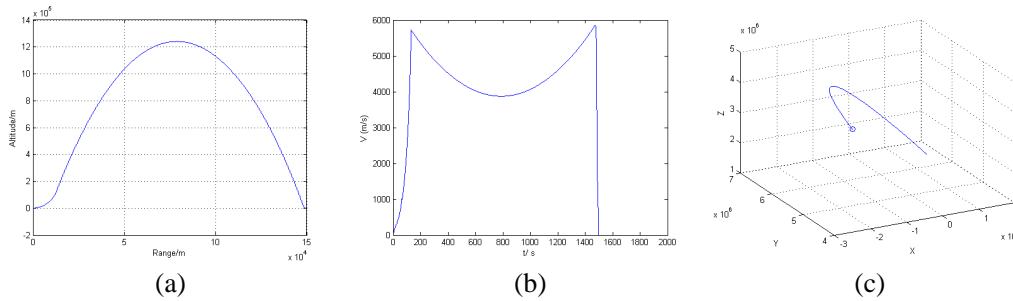


Figure 5: Ballistic missile trajectory. (a) Altitude vs. range. (b) velocity vs. time. (c) Minimal energy trajectory.

projected onto a secondary sphere based on the conditions of Bessel ellipsoid projection, then calculated by solving a spherical triangle. Figure 2 shows the procedure of Bessel projection. S_T is written as

$$S = A\sigma + (B'' + C''y) \sin \sigma \tag{13}$$

σ and y are calculated by the geodetic longitude and geodetic latitude at launch point and impact point, all the coefficients in Eq. (13) are calculated with Krasophuskii ellipsoid elements. S_P is practical flight range which is integrated by the method of fourth-order Runge-Kutta in the procedure of missile trajectory simulation.

The steps of dichotomy iteration and error correction can be summarized as follows:

- 1) Calculate S_T by Eq. (13) without considering the earth rotation in first iteration.
- 2) Generate the ballistic trajectory according to the dynamic and kinematic model established in this paper, save S_P and the flight time T in trajectory generation, calculate Δs .
- 3) Repeat first step, calculate S_T with taking into account the angle caused by the affection of the earth rotation in step 2). Then repeat second step, using the method of dichotomy iteration to correct Δs by adjusting the terminal velocity scalar, the whole process is repeated until the ballistic

missile impacts the target location within a predefined miss distance tolerance ε , $\varepsilon = 10$.

Figure 3 shows the algorithm of the whole trajectory simulation program.

4. SIMULATION

The simulation results in the paper show that the flight range error is 0.03684 m with 15 iteration times by the method of dichotomy iteration, Figure 4 shows the change of range error with iteration times.

Figure 5 shows the altitude and velocity of missile in whole flight and the full ballistic trajectory in 3D.

5. CONCLUSION

Large quantities of missile flight data is demanded in the technology of signature extraction for missile herd targets, rapid and highly accurate trajectory generation has important practical significance. In the paper, a method for full ballistic trajectory model of a ballistic missile over a rotating, ellipsoid earth is developed, and the ballistic trajectory generation is highly accelerated by iterative optimization. Simulation results show that the method has a high degree of confidence. A logical upgrade to the simulation is that improving the method of iteration to correct the error exactly from two points (range and azimuth). The idea will decrease the iteration times and improve simulation confidence, finally contribute to a more accurate trajectory, especially for long flight time missile.

ACKNOWLEDGMENT

This work was supported by Hunan province innovation foundation for postgraduate (CX2014B020), and National University of Defense Technology innovation foundation for excellent postgraduate (B140405).

REFERENCES

1. Harlin, W. J. and D. A. Cicci, "Ballistic missile trajectory prediction using a state transition matrix," *Applied Mathematics and Computation*, Vol. 188, 1832–1847, 2008.
2. De Carpentier, G. J. P., "Analytical ballistic trajectories with approximately linear drag," *International Journal of Computer Games Technology*, Vol. 2014, ID 463489, 2014.
3. Liu, Y. J., S. D. Qiao, J. C. Huang, "A method of impact point prediction of ballistic missile," *Journal of Ballistics*, Vol. 24, No. 1, 22–26, 2012.
4. Xiao B. and P. C. Guo, "Solution and simulation of limited energy trajectory for ballistic missile system simulation technology," *System Simulation Technology*, Vol. 5, No. 1, 12–17, 2009.
5. Zhang, F., K. S. Tian, and M. L. Xi, "The ballistic Missile tracking method using dynamic model," *IEEE CIE International Conference*, Vol. 1, 789–794, 2011.
6. Li, X. R. and V. P. Jilkov, "Survey of maneuvering target tracking. Part II: Motion models of ballistic and space targets," *IEEE Trans. on Aerosp. Electron. Syst.*, Vol. 46, No. 1, 96–119, 2010.

Electromagnetic Forces in the Complex-octonion Curved Space

Zi-Hua Weng

School of Physics and Mechanical & Electrical Engineering
Xiamen University, Xiamen 361005, China

Abstract— J. C. Maxwell applied the quaternion analysis to describe the electromagnetic theory. While A. Einstein depicted the gravitational theory by means of the tensor analysis and curved Four-spacetime. At present the scholars research the electromagnetic and gravitational features, making use of the complex-quaternion/octonion curved space. It is capable of defining the parallel translation and covariant derivative of the complex-octonion curved space, by means of the orthogonality of two complex octonions, depicting simultaneously the electromagnetic and gravitational features in the complex-octonion curved space. The study reveals that the connection coefficient and curvature of the complex-octonion curved space have an influence on the field strength and field source of the electromagnetic and gravitational fields, impacting the angular momentum, torque, and force, especially the electromagnetic force in the curved space.

1. INTRODUCTION

In order to define the component of one physics quantity in the curve coordinate system, it is necessary to introduce the tangent-frame component of one point in the curved space in the paper. Apparently the tangent frame belongs to the affine frame. In general the tangent-frame components are neither same length, nor perpendicular to each other. For the pseudo-Riemann space [1] in the General Theory of Relativity, the tangent-frame component may be the vector or the scalar. In the quaternion or octonion curved space, the tangent-frame component may be the quaternion or octonion respectively.

For the gravitational and electromagnetic theories in the curved space, not all affine frames are suitable to be chosen as the curve coordinate system. And it is essential to demarcate and filter out the appropriate affine frames farther. When we study the physics quantity and relevant features in the curved space, it is proper to stipulate to choose the orthogonal affine frame (or the orthogonal curve coordinate system), for the sake of reducing the correlative mathematical difficulty. Subsequently the physics quantity in the orthogonal affine frame can be transformed into that in one orthogonal and unitary affine frame, in order to draw a comparison between the physics quantity in the flat space with that in the tangent space of the curved space.

According to this arrangement, the gravitational and electromagnetic theories can be extended from the flat space into the curved space. Firstly, transform the gravitational and electromagnetic theories in the flat space into that under the orthogonal and unitary affine frame of the tangent space in the curved space; Secondly, transform the gravitational and electromagnetic theories in the orthogonal and unitary affine frame into that in the orthogonal affine frame; Thirdly, in the orthogonal affine frame, study the influence of the curved space on the force and so forth in the gravitational and electromagnetic fields.

2. COMPLEX-OCTONION CURVED SPACE

In the complex-quaternion flat space, the complex-quaternion radius vector is $\mathbb{R}_g(ih^0, h^1, h^2, h^3)$, with the basis vector being \mathbf{i}_i . Meanwhile, in the complex- S -quaternion flat space [2], the complex- S -quaternion radius vector is $\mathbb{R}_e(iH^0, H^1, H^2, H^3)$, with the basis vector being \mathbf{I}_i . In the complex-octonion flat space, two radius vectors, $\mathbb{R}_g(ih^0, h^1, h^2, h^3)$ and $\mathbb{R}_e(iH^0, H^1, H^2, H^3)$, can be combined together to become one complex-octonion radius vector,

$$\mathbb{R}(h^r) = \mathbb{R}_g + k_{eg}\mathbb{R}_e = ih^0\mathbf{i}_0 + h^p\mathbf{i}_p + ih^4\mathbf{i}_4 + h^{4+p}\mathbf{i}_{4+p}, \quad (1)$$

where $h^{j+4} = k_{eg}H^j$, and $\mathbf{i}_{j+4} = \mathbf{I}_j$. $\mathbf{i}_0^2 = 1$, and $\mathbf{i}_f^2 = -1$. $\mathbf{i}_r^2 = \mathbf{i}_r \circ \mathbf{i}_r$, for each subscript r . $\mathbb{R}_g = ih^0\mathbf{i}_0 + h^p\mathbf{i}_p$. $\mathbb{R}_e = iH^0\mathbf{I}_0 + H^p\mathbf{I}_p$. \circ is the octonion multiplication. h^i and H^i are all real. $r, s, t, u = 0, 1, 2, 3, 4, 5, 6, 7$. $f = 1, 2, 3, 4, 5, 6, 7$.

According to the multiplication of octonion, the norm S is written as, $S^2 = \mathbb{R} \circ \mathbb{R}^*$. The differential, dS , of the norm is able to be chosen as the arc length of the complex-octonion (rather than the real-octonion) curved space. Obviously, in case the contribution of \mathbb{R}_e can be neglected,

this norm will accord with the requirement of space-time interval in the physics. Herein $*$ is the octonion conjugate.

In the complex-quaternion curved space for the gravitational field, the complex-quaternion radius vector is, $\mathbb{R}_g(iu^0, u^1, u^2, u^3)$, with the tangent-frame quaternion being \mathbf{e}_i . In the complex- S -quaternion curved space for the electromagnetic field, the complex- S -quaternion radius vector is, $\mathbb{R}_e(iU^0, U^1, U^2, U^3)$, with the tangent-frame S -quaternion being \mathbf{E}_i . In the tangent space of complex-octonion curved space, the complex-octonion radius vector is, $\mathbb{R}(u^r) = \mathbb{R}_g(iu^0, u^1, u^2, u^3) + k_{eg}\mathbb{R}_e(iU^0, U^1, U^2, U^3)$. Making use of the transforming, $u^{j+4} = k_{eg}U^j$ and $\mathbf{e}_{j+4} = \mathbf{E}_j$, the complex-octonion radius vector can be written as, $\mathbb{R}(u^r) = iu^0\mathbf{e}_0 + u^p\mathbf{e}_p + iu^4\mathbf{e}_4 + u^{4+p}\mathbf{e}_{4+p}$.

In the orthogonal and nonunitary affine frame, the metric of complex-octonion curved space is,

$$dR^2 = d\mathbb{R}^* \circ d\mathbb{R} = g_{rs} du^r du^s, \tag{2}$$

where the metric coefficient is, $g_{rs} = \mathbf{e}_r^* \circ \mathbf{e}_s$. The orthogonal tangent-frame octonion is, $\mathbf{e}_r = \partial\mathbb{R}/\partial u^r$. \mathbf{e}_0 is the scalar part, while \mathbf{e}_f is the component of vector part. \mathbf{e}_r^2 is real and nonunitary. $\mathbf{e}_r^2 = \mathbf{e}_r \circ \mathbf{e}_r$, for each subscript r . $u^0 = v_0 t$, v_0 is the speed of light, and t is the time. u^i and U^i are all real.

However, in the complex-octonion curved space, what the paper will be involved in is, the mathematical manipulation between the quaternion operator (rather than the octonion operator) in the complex quaternion space, with the physics quantity of electromagnetic field in the S -complex quaternion space. So that the discussion of the space-time interval in the paper will be constrained to deal only with the component of the complex-quaternion radius vector, \mathbb{R}_g .

In one complex octonion space, when the product of two complex octonions, $\mathbb{G}(ig^0, g^f)$ and $\mathbb{Q}(iq^0, q^f)$, is equal to zero, that is, $\mathbb{G}^* \circ \mathbb{Q} = 0$, two octonions, \mathbb{G} and \mathbb{Q} , are perpendicular to each other. This definition is called as the octonion orthogonality. Therefore it is able to define one parallel translation in the complex-octonion curved space, including the quaternion parallel translation in the complex-quaternion curved space. Herein g^r and q^s are all real.

In the complex-octonion curved space, the complex-octonion physics quantity \mathbb{A}_1 , in the tangent space \mathbb{T}_1 of one point \mathbb{M}_1 on the complex-octonion manifold, can be disassembled in the tangent space \mathbb{T}_2 of the point \mathbb{M}_2 near \mathbb{M}_1 . According to the definition of octonion orthogonality, \mathbb{A}_1 can be separated into the projection component \mathbb{A}_2 in \mathbb{T}_2 , and the orthogonal component \mathbb{G}_2 perpendicular to \mathbb{T}_2 . While \mathbb{A}_2 is named for the parallel translation from \mathbb{A}_1 . And this definition is called as the octonion parallel translation. Especially, when the scalar parts of \mathbb{A}_1 and of \mathbb{A}_2 are all null, \mathbb{A}_1 and \mathbb{A}_2 both will be degenerated into the vectors. Further the orthogonality of octonion is reduced to that of vector, and the octonion parallel translation to the Levi-Civita parallel translation. When the complex octonion is reduced to the complex quaternion, the orthogonality of octonion is degenerated into that of quaternion, and the octonion parallel translation into the quaternion parallel translation (Table 1).

For the first-rank contravariant tensor $Y^s(\mathbb{Q})$ of one point \mathbb{Q} in the complex-octonion curved space, the component of octonion covariant derivation with respect to the coordinate u^t is,

$$\nabla_t Y^s = \partial Y^s / \partial u^t + \Gamma_{rt}^s Y^r, \tag{3}$$

Table 1: Comparison of major characteristics in some flat and curved spaces.

Term	pseudo-Euclidean space	pseudo-Riemann space	Quaternion space	Octonion space
tangent space	vector space	vector space	quaternion space	octonion space
orthogonality	vector	vector	quaternion	octonion
parallel translation	normal	Levi-Civita	quaternion	octonion
tangent frame	vector/scalar	vector/scalar	quaternion	octonion
metric	scalar product among vectors and scalars	scalar product among vectors and scalars	scalar product of quaternions	scalar product of octonions
connection coefficient	Γ_{jk}^i	Γ_{jk}^i	Γ_{jk}^i	Γ_{rt}^s
covariant derivation	$\partial_k A^i$	$\nabla_k A^i$	$\nabla_k A^i$	$\nabla_t A^s$

where Γ_{rt}^s is the connection coefficient. $g^{us} = (g_{us})^{-1}$, and $\Gamma_{rt}^s = (1/2)g^{us}(\partial g_{ru}/\partial u^t + \partial g_{ut}/\partial u^r - \partial g_{tr}/\partial u^u)$. Y^s is real.

3. ELECTROMAGNETIC FIELD EQUATIONS

In the complex-octonion curved space, the electromagnetic potential had been transformed from the orthogonal and unitary rectangular coordinate system (flat space) to the orthogonal and nonunitary affine frame (tangent space). From the integrating function of field potential, \mathbb{X} , the octonion field potential, $\mathbb{A} = \mathbb{A}_g + k_{eg}\mathbb{A}_e$, is defined as,

$$\mathbb{A} = i\Box^\times \circ \mathbb{X}, \tag{4}$$

where $\mathbb{A} = i\Box^\times \circ \mathbb{X} + i\Box^\times \otimes \mathbb{X}$. $\mathbb{X} = \mathbb{X}_g + k_{eg}\mathbb{X}_e$. The gravitational potential, $\mathbb{A}_g(a^0, a^1, a^2, a^3)$, is defined from the integrating function of gravitational potential, \mathbb{X}_g , that is, $\mathbb{A}_g = i\Box^\times \circ \mathbb{X}_g$. $\mathbb{A}_g = i\Box^\times \circ \mathbb{X}_g + i\Box^\times \otimes \mathbb{X}_g$. $i\Box^\times \circ \mathbb{X}_g$ and $i\Box^\times \otimes \mathbb{X}_g$ denote respectively the scalar and vector parts of \mathbb{A}_g . $\Box a^i = i\mathbf{e}_0 \nabla_0 a^i + \delta^{pq}\mathbf{e}_p \nabla_q a^i$. $\nabla a^i = \delta^{pq}\mathbf{e}_p \nabla_q a^i$. $\mathbf{e}^i = g^{ij}\mathbf{e}_j$. $\mathbb{X}_g = x^j \mathbf{e}_j$. The gauge equation is chosen as, $\nabla \times (x^p \mathbf{e}_p) = 0$. $\mathbb{A}_g = ia + \mathbf{a}$. $a = a^0 \mathbf{e}_0$, and $\mathbf{a} = a^p \mathbf{e}_p$. The integrating function, \mathbb{X}_e , of electromagnetic potential is one S -quaternion physics quantity, and $\mathbb{X}_e = X^j \mathbf{E}_j$. The electromagnetic potential is $\mathbb{A}_e(iA^0, A^1, A^2, A^3) = i\Box^\times \circ \mathbb{X}$. $\mathbb{A}_e = i\Box^\times \circ \mathbb{X}_e + i\Box^\times \otimes \mathbb{X}_e$. $i\Box^\times \circ \mathbb{X}_e$ and $i\Box^\times \otimes \mathbb{X}_e$ denote respectively the scalar and vector parts of \mathbb{A}_e . The gauge equation is chosen as, $\nabla \times (X^p \mathbf{E}_p) = 0$. $\mathbb{A}_e = i\mathbf{A}_Q + \mathbf{A}$. $\mathbf{A}_Q = A^0 \mathbf{E}_0$, and $\mathbf{A} = A^p \mathbf{E}_p$. Apparently, in the affine frame (Table 2), the electromagnetic potential includes not only the physics quantity (in the complex- S -quaternion curved space) but also the spatial parameter of curved space (in the complex-quaternion curved space). \times is the complex conjugate. a^i and A^i are all real.

The octonion field strength, $\mathbb{F} = \mathbb{F}_g + k_{eg}\mathbb{F}_e$, is defined as,

$$\mathbb{F} = \Box \circ \mathbb{A}, \tag{5}$$

where $\mathbb{F} = \Box \circ \mathbb{A} + \Box \otimes \mathbb{A}$. The gravitational strength, $\mathbb{F}_g(f^0, f^1, f^2, f^3)$, is defined as, $\mathbb{F}_g = \Box \circ \mathbb{A}_g$. $\mathbb{F}_g = \Box \circ \mathbb{A}_g + \Box \otimes \mathbb{A}_g$. The scalar part of \mathbb{F}_g is, $\Box \circ \mathbb{A}_g = if^0 \mathbf{e}_0$, and the vector part of \mathbb{F}_g is, $\Box \otimes \mathbb{A}_g = f^p \mathbf{e}_p$. The gauge equation of gravitational potential is chosen as, $f^0 = 0$. The vector part of gravitational strength can be separated into two components, $f^p \mathbf{e}_p = i\mathbf{g}/v_0 + \mathbf{b}$. One component, $\mathbf{g}/v_0 = (\mathbf{e}_0 \nabla_0) \circ \mathbf{a} + \nabla \circ a$, is relevant to the acceleration, while the other, $\mathbf{b} = \nabla \times \mathbf{a}$, is associated in the precession angular velocity [3]. The electromagnetic strength is, $\mathbb{F}_e(iF^0, F^1, F^2, F^3) = \Box \circ \mathbb{A}_e$. $\mathbb{F}_e = \Box \circ \mathbb{A}_e + \Box \otimes \mathbb{A}_e$. The scalar part of \mathbb{F}_e is, $\Box \circ \mathbb{A}_e = iF^0 \mathbf{E}_0$, and the vector part of \mathbb{F}_e is, $\Box \otimes \mathbb{A}_e = F^p \mathbf{E}_p$. The gauge equation of electromagnetic potential is chosen as, $F^0 = 0$. The vector part of electromagnetic strength can be separated into two components, $F^p \mathbf{E}_p = i\mathbf{E}/v_0 + \mathbf{B}$. One component, $\mathbf{E}/v_0 = (\mathbf{e}_0 \nabla_0) \circ \mathbf{A} + \nabla \circ A$, is the electric field intensity, while the other, $\mathbf{B} = \nabla \times \mathbf{A}$, is the magnetic flux density. f^0 and F^0 are real, and f^p and F^p are the complex numbers.

The octonion field source, $\mu\mathbb{S} = \mu_g\mathbb{S}_g + k_{eg}\mu_e\mathbb{S}_e$, is defined as follows,

$$-\mu\mathbb{S} = -(\mu_g\mathbb{S}_g + k_{eg}\mu_e\mathbb{S}_e - i\mathbb{F}^* \circ \mathbb{F}/v_0) = (\Box + i\mathbb{F}/v_0)^* \circ \mathbb{F}, \tag{6}$$

where $-\mu_g\mathbb{S}_g = \Box^* \circ \mathbb{F}_g$, and $-\mu_e\mathbb{S}_e = \Box^* \circ \mathbb{F}_e$. $-\mu_g\mathbb{S}_g = \Box^* \circ \mathbb{F}_g + \Box^* \otimes \mathbb{F}_g$, while $-\mu_e\mathbb{S}_e = \Box^* \circ \mathbb{F}_e + \Box^* \otimes \mathbb{F}_e$. The scalar part of \mathbb{S}_g is, $-\Box^* \circ \mathbb{F}_g/\mu_g = is^0 \mathbf{e}_0$, which is associated in the mass density. And the vector part of \mathbb{S}_g is, $-\Box^* \otimes \mathbb{F}_g/\mu_g = is^p \mathbf{e}_p$, which is relevant to the density

Table 2: The multiplication of the operator and the physics quantity in the complex-octonion curved space.

definition	expression meaning
$\nabla \cdot (\mathbf{e}_p a^p)$	$(\mathbf{e}_1 \cdot \mathbf{e}_1) \nabla_1 a^1 + (\mathbf{e}_2 \cdot \mathbf{e}_2) \nabla_2 a^2 + (\mathbf{e}_3 \cdot \mathbf{e}_3) \nabla_3 a^3$
$\nabla \times (\mathbf{e}_p a^p)$	$(\mathbf{e}_2 \times \mathbf{e}_3)(\nabla_2 a^3 - \nabla_3 a^2) + (\mathbf{e}_3 \times \mathbf{e}_1)(\nabla_3 a^1 - \nabla_1 a^3) + (\mathbf{e}_1 \times \mathbf{e}_2)(\nabla_1 a^2 - \nabla_2 a^1)$
$\nabla \circ (\mathbf{e}_0 a^0)$	$(\mathbf{e}_1 \circ \mathbf{e}_0) \nabla_1 a^0 + (\mathbf{e}_2 \circ \mathbf{e}_0) \nabla_2 a^0 + (\mathbf{e}_3 \circ \mathbf{e}_0) \nabla_3 a^0$
$(\mathbf{e}_0 \nabla_0) \circ (\mathbf{e}_p a^p)$	$(\mathbf{e}_0 \circ \mathbf{e}_1) \nabla_0 a^1 + (\mathbf{e}_0 \circ \mathbf{e}_2) \nabla_0 a^2 + (\mathbf{e}_0 \circ \mathbf{e}_3) \nabla_0 a^3$
$\nabla \cdot (\mathbf{E}_p A^p)$	$(\mathbf{e}_1 \cdot \mathbf{E}_1) \nabla_1 A^1 + (\mathbf{e}_2 \cdot \mathbf{E}_2) \nabla_2 A^2 + (\mathbf{e}_3 \cdot \mathbf{E}_3) \nabla_3 A^3$
$\nabla \times (\mathbf{E}_p A^p)$	$(\mathbf{e}_2 \times \mathbf{E}_3)(\nabla_2 A^3 - \nabla_3 A^2) + (\mathbf{e}_3 \times \mathbf{E}_1)(\nabla_3 A^1 - \nabla_1 A^3) + (\mathbf{e}_1 \times \mathbf{E}_2)(\nabla_1 A^2 - \nabla_2 A^1)$
$\nabla \circ (\mathbf{E}_0 A^0)$	$(\mathbf{e}_1 \circ \mathbf{E}_0) \nabla_1 A^0 + (\mathbf{e}_2 \circ \mathbf{E}_0) \nabla_2 A^0 + (\mathbf{e}_3 \circ \mathbf{E}_0) \nabla_3 A^0$
$(\mathbf{e}_0 \nabla_0) \circ (\mathbf{E}_p A^p)$	$(\mathbf{e}_0 \circ \mathbf{E}_1) \nabla_0 A^1 + (\mathbf{e}_0 \circ \mathbf{E}_2) \nabla_0 A^2 + (\mathbf{e}_0 \circ \mathbf{E}_3) \nabla_0 A^3$

of linear momentum. The electromagnetic source is $\mathbb{S}_e(iS^0, S^1, S^2, S^3)$. The scalar part of \mathbb{S}_e is, $-\square^* \odot \mathbb{F}_e/\mu_e = iS^0 \mathbf{E}_0$, and is associated in the density of electric charge. And the vector part of \mathbb{S}_e is, $-\square^* \otimes \mathbb{F}_e/\mu_e = S^p \mathbf{E}_p$, and is relevant to the density of electric current. μ , μ_g , and μ_e are the coefficients.

4. OCTONION ANGULAR MOMENTUM

In the complex-octonion curved space, the octonion linear momentum, $\mathbb{P}(p^i, P^i) = \mathbb{P}_g + k_{eg} \mathbb{P}_e$, is defined from the octonion field source,

$$\mathbb{P} = \mu \mathbb{S} / \mu_g, \quad (7)$$

where the component of the octonion linear momentum, \mathbb{P} , in the complex quaternion space is, $\mathbb{P}_g = \{\mu_g \mathbb{S}_g - (i\mathbb{F}/v_0)^* \circ \mathbb{F}\} / \mu_g = p^0 \mathbf{e}_0 + p^q \mathbf{e}_q$. And the component of the octonion linear momentum, \mathbb{P} , in the complex S -quaternion space is, $\mathbb{P}_e = \mu_e \mathbb{S}_e / \mu_g = P^0 \mathbf{E}_0 + P^q \mathbf{E}_q$. p^i and P^i are all real.

Subsequently, in the complex-octonion curved space, the octonion angular momentum, $\mathbb{L}(l^i, L^i) = \mathbb{L}_g + k_{eg} \mathbb{L}_e$, can be defined from the octonion linear momentum and radius vector,

$$\mathbb{L} = (\mathbb{R} + k_{rx} \mathbb{X})^\times \circ \mathbb{P}, \quad (8)$$

where $\mathbb{L} = (\mathbb{R} + k_{rx} \mathbb{X})^\times \odot \mathbb{P} + (\mathbb{R} + k_{rx} \mathbb{X})^\times \otimes \mathbb{P}$. The component of the octonion angular momentum, \mathbb{L} , in the complex quaternion space is, $\mathbb{L}_g = (\mathbb{R}_g + k_{rx} \mathbb{X}_g)^\times \circ \mathbb{P}_g + k_{eg}^2 (\mathbb{R}_e + k_{rx} \mathbb{X}_e)^\times \circ \mathbb{P}_e = l^0 \mathbf{e}_0 + l^q \mathbf{e}_q$. And the component of the octonion angular momentum, \mathbb{L} , in the complex S -quaternion space is, $\mathbb{L}_e = (\mathbb{R}_g + k_{rx} \mathbb{X}_g)^\times \circ \mathbb{P}_e + (\mathbb{R}_e + k_{rx} \mathbb{X}_e)^\times \circ \mathbb{P}_g = L^0 \mathbf{E}_0 + L^q \mathbf{E}_q$. l^i and L^i are all real.

5. OCTONION FORCE

In the complex-octonion curved space, the octonion torque, $\mathbb{W}(w^i, W^i) = \mathbb{W}_g + k_{eg} \mathbb{W}_e$, is defined from the octonion linear momentum,

$$\mathbb{W} = -v_0 (\square + i\mathbb{F}/v_0) \circ \mathbb{L}, \quad (9)$$

where $\mathbb{W} = v_0 (\square + i\mathbb{F}/v_0) \odot \mathbb{L} + v_0 (\square + i\mathbb{F}/v_0) \otimes \mathbb{L}$. The component of the octonion torque, \mathbb{W} , in the complex quaternion space is, $\mathbb{W}_g = -(i\mathbb{F}_g \circ \mathbb{L}_g + ik_{eg}^2 \mathbb{F}_e \circ \mathbb{L}_e + v_0 \square \circ \mathbb{L}_g) = w^0 \mathbf{e}_0 + w^q \mathbf{e}_q$. And the component of the octonion torque, \mathbb{W} , in the complex S -quaternion space is, $\mathbb{W}_e = -(i\mathbb{F}_g \circ \mathbb{L}_e + i\mathbb{F}_e \circ \mathbb{L}_g + v_0 \square \circ \mathbb{L}_e) = W^0 \mathbf{E}_0 + W^q \mathbf{E}_q$. w^i and W^i are all real.

In the complex-octonion curved space, the octonion force, $\mathbb{N}(n^i, N^i) = \mathbb{N}_g + k_{eg} \mathbb{N}_e$, is defined from the octonion torque,

$$\mathbb{N} = -(\square + i\mathbb{F}/v_0) \circ \mathbb{W}, \quad (10)$$

where $\mathbb{N} = (\square + i\mathbb{F}/v_0) \odot \mathbb{W} + (\square + i\mathbb{F}/v_0) \otimes \mathbb{W}$. The component of the octonion force, \mathbb{N} , in the complex quaternion space is, $\mathbb{N}_g = -(i\mathbb{F}_g \circ \mathbb{W}_g/v_0 + ik_{eg}^2 \mathbb{F}_e \circ \mathbb{W}_e/v_0 + \square \circ \mathbb{W}_g) = n^0 \mathbf{e}_0 + n^q \mathbf{e}_q$. And the component of the octonion force, \mathbb{N} , in the complex S -quaternion space is, $\mathbb{N}_e = -(i\mathbb{F}_g \circ \mathbb{W}_e/v_0 + i\mathbb{F}_e \circ \mathbb{W}_g/v_0 + \square \circ \mathbb{W}_e) = N^0 \mathbf{E}_0 + N^q \mathbf{E}_q$. n^i and N^i are all real.

In the above, the term, $(\square + i\mathbb{F}/v_0) \odot \mathbb{W} = n^0 \mathbf{e}_0$, denotes the scalar part of the octonion force, \mathbb{N} . While the term, $(\square + i\mathbb{F}/v_0) \otimes \mathbb{W} = n^q \mathbf{e}_q + k_{eg} (N^0 \mathbf{E}_0 + N^q \mathbf{E}_q)$, indicates the vector part of the octonion force, \mathbb{N} . The real part of the term, $n^0 \mathbf{e}_0$, is relevant to the mass continuity equation. While the real part of the term, $N^0 \mathbf{E}_0$, is associated with the current continuity equation. For the term, $n^q \mathbf{e}_q$, its imaginary part is connected with the force, and corresponded with the linear acceleration. And that its real part is corresponded with the precession angular velocity.

In the complex-octonion curved space, the imaginary part of $(n^p \mathbf{e}_p)/2$ is the force density, in the gravitational and electromagnetic fields, that is,

$$\mathbf{f} = \text{Im} \{(n^p \mathbf{e}_p)/2\}, \quad (11)$$

where the force density \mathbf{f} includes the inertial force, gravitational force, electromagnetic force, energy gradient force, and additional force term caused by curved space. The additional force term is relevant to the connection coefficient and curvature and so forth of the curved space.

The electromagnetic force, $\mathbf{F}_e = -\mathbf{B} \times (S^q \mathbf{E}_q) + \mathbf{E} \circ (S^0 \mathbf{E}_0)/v_0$, in the curved space is,

$$\mathbf{F}_e = -(B^2 S^3 - B^3 S^2) \mathbf{E}_2 \circ \mathbf{E}_3 - (B^3 S^1 - B^1 S^3) \mathbf{E}_3 \circ \mathbf{E}_1 \quad (12)$$

$$- (B^1 S^2 - B^2 S^1) \mathbf{E}_1 \circ \mathbf{E}_2 + (S^0 E^p / v_0) \mathbf{E}_p \circ \mathbf{E}_0, \quad (13)$$

where the product, $\mathbf{E}_i \circ \mathbf{E}_j$, belongs to the complex-quaternion curved space, according to the multiplication of octonion.

When the octonion field potential is chosen as the first-rank tensor in the complex-octonion curved space, the octonion linear momentum, angular momentum, and torque will be involved in the some spatial parameters of the complex-octonion curved space (Table 3). It means that the curved space has an influence on the octonion force, including the force, the mass continuity equation, and the current continuity equation.

Table 3: Some definitions of the physics quantity relevant to the gravitational and electromagnetic fields in the complex-octonion curved space.

physics quantity	definition
radius vector	$\mathbb{R} = \mathbb{R}_g + k_{eg}\mathbb{R}_e$
integral function	$\mathbb{X} = \mathbb{X}_g + k_{eg}\mathbb{X}_e$
field potential	$\mathbb{A} = i\mathbb{Q}^\times \circ \mathbb{X}$
field strength	$\mathbb{F} = \mathbb{Q} \circ \mathbb{A}$
field source	$\mu\mathbb{S} = -(i\mathbb{F}/v_0 + \mathbb{Q})^* \circ \mathbb{F}$
linear momentum	$\mathbb{P} = \mu\mathbb{S}/\mu_g$
angular momentum	$\mathbb{L} = (\mathbb{R} + k_{rx}\mathbb{X})^\times \circ \mathbb{P}$
octonion torque	$\mathbb{W} = -v_0(i\mathbb{F}/v_0 + \mathbb{Q}) \circ \mathbb{L}$
octonion force	$\mathbb{N} = -(i\mathbb{F}/v_0 + \mathbb{Q}) \circ \mathbb{W}$

6. CONCLUSIONS

In the complex-octonion curved space, from the definitions of octonion orthogonality, parallel translation, and covariant derivative, it is able to inference the octonion field potential, field strength, field source, linear momentum, angular momentum, torque, and force and so on in the gravitational and electromagnetic fields. The force consists of the inertial force, gravitational force, electromagnetic force, energy gradient, and additional force term caused by the complex-octonion curved space. The connection coefficient and curvature of the complex-octonion curved space may impact the additional force term. The study reveals that one may appraise the deviation amplitude of the complex-octonion curved space departure from its flat space, by means of the measurements of the field potential, field strength, and force and so forth.

It should be noted that the paper discussed only some simple cases about the influences of the complex-octonion curved space on the field potential, field strength, and force and so forth. However it clearly states that the connection coefficient, curvature and other spatial parameters of the curved space exert an influence on the physics features of gravitational and electromagnetic fields. In the following study, it is going to explore the impact of the force, in the strong gravitational and electromagnetic fields, on the movement statues of one charged objective in the complex-octonion curved space. Moreover, it may intend to describe the gravitational and electromagnetic theories with some generalized frames, and then transform the field theories into that in the orthogonal affine frame by means of the appropriate transformation.

ACKNOWLEDGMENT

This project was supported partially by the National Natural Science Foundation of China under grant number 60677039.

REFERENCES

1. Chanyal, B. C., P. S. Bisht, and O. P. S. Negi, "Octonionic non-Abelian Gauge theory," *International Journal of Theoretical Physics*, Vol. 52, No. 10, 3522–3533, 2013.
2. Weng, Z.-H., "Field equations in the complex quaternion spaces," *Advances in Mathematical Physics*, Vol. 2014, 450262, 6 pages, 2014.
3. Weng, Z.-H., "Angular momentum and torque described with the complex octonion," *AIP Advances*, Vol. 4, No. 8, 087103, 16 pages, 2014.

Electromagnetic Force on Charged Objects with the Angular Velocity

Zi-Hua Weng

School of Physics and Mechanical & Electrical Engineering
Xiamen University, Xiamen 361005, China

Abstract— The paper studies the influence of angular velocity on the electromagnetic force for one rotational charged object. In the complex octonion space, the radius vector and the integrating function of field potential can be combined together to become one compounding radius vector. The latter may be considered as the ‘radius vector’ in the complex-octonion compounding space (one function space). The complex-octonion compounding space will be regarded as the extension of one complex-octonion compounding field. In the complex-octonion compounding field, the angular velocity will impact the compounding field strength, field source and linear momentum and so on. The study reveals that the angular velocity has a direct influence on the compounding angular momentum, compounding torque, and compounding force and so forth, including the compounding force term exerting on the rotational charged object.

1. INTRODUCTION

The quaternion was applied by J. C. Maxwell to research the electromagnetic theory. Nowadays some scholars studied the electromagnetic and gravitational fields by means of the complex quaternion. The complex quaternion space for gravitational fields and that for electromagnetic fields can be combined together to become one complex octonion space. As a result the physics feature of two fields can be described simultaneously with the complex octonion [1], including the force in the presence of the gravitational field, electromagnetic field, and angular velocity.

In the complex octonion space, the radius vector and the integrating function of field potential are able to be combined together to become the compounding radius vector, which may be considered as the ‘radius vector’ in the compounding space (or one function space). In the physics, the space is the extension of the field [2]. Similarly the compounding space will be regarded as the extension of the compounding field. By analogy the field and space should be generalized to the compounding field and compounding space respectively. Further it is fit for studying the impact of the angular velocity on the field strength and field source and so on, from the compounding field and compounding space.

Making use of the complex octonion, the paper claims that there are some kinds of equilibrium states in these two fields. The field potential and velocity ratio both will impact the field strength, field source, and equilibrium state. So the variation of field potential may alter the force or torque. This inference may figure out the physical phenomenon relevant to the over-speed movement of stars on the fringe of a galaxy [3], although this uncertainty remains as puzzling as ever.

2. GRAVITATIONAL SOURCE

In the complex quaternion space for the gravitational field, the basis vector is $\mathbb{H}_g = (\mathbf{i}_0, \mathbf{i}_1, \mathbf{i}_2, \mathbf{i}_3)$, and the radius vector is $\mathbb{R}_g = ir_0\mathbf{i}_0 + \Sigma r_j\mathbf{i}_j$. The radius vector can be combined with the physical quantity, $\mathbb{X}_g = ix_0\mathbf{i}_0 + \Sigma x_j\mathbf{i}_j$, to become the compounding radius vector,

$$\bar{\mathbb{R}}_g = \mathbb{R}_g + k_{rx}\mathbb{X}_g, \quad (1)$$

where $\bar{\mathbb{R}}_g = i\bar{r}_0 + \bar{\mathbf{r}} = i\bar{r}_0\mathbf{i}_0 + \Sigma\bar{r}_j\mathbf{i}_j$. \mathbb{X}_g is the integrating function of complex-quaternion gravitational potential, $\mathbb{A}_g = ia_0\mathbf{i}_0 + \Sigma a_j\mathbf{i}_j$. i is the imaginary unit. $r_0 = v_0t$; v_0 is the speed of light; t denotes the time. \bar{r}_k, r_k, a_k , and x_k are all real. $k_{rx} = 1/v_0$. $\mathbf{i}_0 = 1$. $j = 1, 2, 3$; $k = 0, 1, 2, 3$.

In the mathematics, $\bar{\mathbb{R}}_g$ may be considered as one ‘radius vector’ in the compounding space of complex quaternions, which is one kind of function space with the quaternion basis vector \mathbb{H}_g . Further the \mathbb{A}_g and complex-quaternion velocity ratio, $\mathbb{T}_g = it_0\mathbf{i}_0 + \Sigma t_j\mathbf{i}_j$, will combine together to become the complex-quaternion compounding velocity ratio,

$$\bar{\mathbb{T}}_g = \mathbb{T}_g + k_{rx}\mathbb{A}_g, \quad (2)$$

where $\mathbb{T}_g = i\Box^\times \circ \mathbb{R}_g$; $\mathbb{A}_g = i\Box^\times \circ \mathbb{X}_g$; $\bar{\mathbb{T}}_g = i\Box^\times \circ \bar{\mathbb{R}}_g = i\bar{t}_0\mathbf{i}_0 + \Sigma\bar{t}_j\mathbf{i}_j$. $\Box = i\mathbf{i}_0\partial_0 + \Sigma\mathbf{i}_j\partial_j$, with $\nabla = \Sigma\mathbf{i}_j\partial_j$, and $\partial_k = \partial/\partial r_k$. The symbol \circ denotes the octonion multiplication. \times denotes the complex conjugate. \bar{t}_k , a_k , and t_k are all real.

Similarly, in this complex-quaternion compounding space, the complex-quaternion compounding gravitational potential is defined as,

$$\bar{\mathbb{A}}_g = \mathbb{A}_g + K_{rx}\mathbb{T}_g, \tag{3}$$

where $\bar{\mathbb{A}}_g = i\Box^\times \circ \bar{\mathbb{X}}_g = i\bar{a}_0\mathbf{i}_0 + \Sigma\bar{a}_j\mathbf{i}_j$. $\bar{\mathbb{X}}_g = \mathbb{X}_g + K_{rx}\mathbb{R}_g$. $K_{rx} = 1/k_{rx}$. \bar{a}_k is real.

Further the complex-quaternion compounding gravitational strength, $\bar{\mathbb{F}}_g = \bar{f}_0\mathbf{i}_0 + \Sigma\bar{f}_j\mathbf{i}_j$, is defined from the above,

$$\bar{\mathbb{F}}_g = \Box \circ \bar{\mathbb{A}}_g = \mathbb{F}_g + K_{rx}\mathbb{Y}_g, \tag{4}$$

where the curl of velocity ratio is, $\mathbb{Y}_g = \Box \circ \mathbb{T}_g = iy_0\mathbf{i}_0 + \Sigma y_j\mathbf{i}_j$. The gravitational strength is, $\mathbb{F}_g = \Box \circ \mathbb{A}_g = if_0\mathbf{i}_0 + \Sigma f_j\mathbf{i}_j$. In the gravitational field, φ is the scalar potential, while \mathbf{a} is the vectorial potential. The gauge equation is, $-\bar{f}_0 = \partial_0\bar{a}_0 - \nabla \cdot \bar{\mathbf{a}} = 0$. $a_0 = \varphi/v_0$ is the scalar. $\mathbf{a} = \Sigma(a_j\mathbf{i}_j)$, $\bar{\mathbf{a}} = \Sigma(\bar{a}_j\mathbf{i}_j)$. f_k , \bar{f}_k , and y_k are all real.

In the complex-quaternion compounding space, the complex-quaternion compounding field source $\bar{\mathbb{S}}$ is defined from the above,

$$(i\bar{\mathbb{F}}_g/v_0 + \Box)^* \circ \bar{\mathbb{F}}_g = -\mu\bar{\mathbb{S}} = -\mu_g\bar{\mathbb{S}}_g + i\bar{\mathbb{F}}_g^* \circ \bar{\mathbb{F}}_g/v_0, \tag{5}$$

where μ and μ_g are the constants. The complex-quaternion compounding gravitational source is, $\bar{\mathbb{S}}_g = i\bar{s}_0\mathbf{i}_0 + \Sigma\bar{s}_j\mathbf{i}_j$. $\bar{\mathbb{S}}_g = \mathbb{S}_g + K_{rx}\mathbb{Z}_g$. $\mu_g\mathbb{S}_g = -\Box^* \circ \mathbb{F}_g$, and $\mu_g\mathbb{Z}_g = -\Box^* \circ \mathbb{Y}_g$. $\bar{\mathbb{F}}_g^* \circ \bar{\mathbb{F}}_g/(2\mu_g)$ is one energy term in the gravitational field. $*$ denotes the octonion conjugate. For one single mass particle, there is, $\bar{\mathbb{S}}_g = m\bar{\mathbb{V}}_g$, with m being the density of inertial mass. $\bar{\mathbb{V}}_g = \partial\bar{\mathbb{R}}_g/\partial t = i\bar{v}_0\mathbf{i}_0 + \Sigma\bar{v}_j\mathbf{i}_j$. \bar{s}_k and \bar{v}_k are all real. $\mu_g < 0$.

3. ELECTROMAGNETIC SOURCE

The complex octonion space \mathbb{E} is able to be separated into two orthogonal subspaces, the complex quaternion space \mathbb{H}_g and the complex S -quaternion space, $\mathbb{H}_e = (\mathbf{I}_0, \mathbf{I}_1, \mathbf{I}_2, \mathbf{I}_3)$. The \mathbb{H}_g is propitious to describe the gravitational field, while the \mathbb{H}_e is fit for depicting the electromagnetic field, with $\mathbb{H}_e = \mathbb{H}_g \circ \mathbf{I}_0$. In the complex octonion space, the basis vector $\mathbb{O} = (\mathbf{i}_0, \mathbf{i}_1, \mathbf{i}_2, \mathbf{i}_3, \mathbf{I}_0, \mathbf{I}_1, \mathbf{I}_2, \mathbf{I}_3)$.

In the complex S -quaternion space for electromagnetic fields, the radius vector is $\mathbb{R}_e = iR_0\mathbf{I}_0 + \Sigma R_j\mathbf{I}_j$, with the basis vector being \mathbb{H}_e . And the \mathbb{R}_e can be combined with the physical quantity, $\mathbb{X}_e = iX_0\mathbf{I}_0 + \Sigma X_j\mathbf{I}_j$, to become the compounding radius vector,

$$\bar{\mathbb{R}}_e = \mathbb{R}_e + k_{rx}\mathbb{X}_e, \tag{6}$$

where $\bar{\mathbb{R}}_e = i\bar{R}_0 + \bar{\mathbf{R}} = i\bar{R}_0\mathbf{I}_0 + \Sigma\bar{R}_j\mathbf{I}_j$. \mathbb{X}_e is the integrating function of complex-quaternion electromagnetic potential, $\mathbb{A}_e = iA_0\mathbf{I}_0 + \Sigma A_j\mathbf{I}_j$. R_k , \bar{R}_k , A_k , and X_k are all real.

In the octonion space for the gravitational and electromagnetic fields, the $\bar{\mathbb{R}}_e$ and $\bar{\mathbb{R}}_g$ can be combined together to become the compounding radius vector,

$$\bar{\mathbb{R}} = \bar{\mathbb{R}}_g + k_{eg}\bar{\mathbb{R}}_e = \mathbb{R} + k_{rx}\mathbb{X}, \tag{7}$$

where $\mathbb{X} = \mathbb{X}_g + k_{eg}\mathbb{X}_e$, and $\mathbb{R} = \mathbb{R}_g + k_{eg}\mathbb{R}_e$. k_{eg} is the coefficient, with $k_{eg}^2 = \mu_g/\mu_e$.

In the mathematics, $\bar{\mathbb{R}}$ can be considered as the ‘radius vector’ in the complex-octonion compounding space (or function space) with the basis vector \mathbb{O} . In the complex-octonion compounding space, the complex-octonion velocity, $\mathbb{T} = \mathbb{T}_g + k_{eg}\mathbb{T}_e$, is combined with the complex-octonion potential, $\mathbb{A} = \mathbb{A}_g + k_{eg}\mathbb{A}_e$, to become the complex-octonion compounding velocity,

$$\bar{\mathbb{T}} = \bar{\mathbb{T}}_g + k_{eg}\bar{\mathbb{T}}_e = \mathbb{T} + k_{rx}\mathbb{A}, \tag{8}$$

where $\mathbb{T} = i\Box^\times \circ \mathbb{R}$. $\bar{\mathbb{T}} = i\Box^\times \circ \bar{\mathbb{R}}$. $\mathbb{A} = i\Box^\times \circ \mathbb{X}$. $\mathbb{T}_e = i\Box^\times \circ \mathbb{R}_e = iT_0\mathbf{I}_0 + \Sigma T_j\mathbf{I}_j$. $\bar{\mathbb{T}}_e = \mathbb{T}_e + k_{rx}\mathbb{A}_e$. $\bar{\mathbb{T}}_e = i\Box^\times \circ \bar{\mathbb{R}}_e = i\bar{T}_0\mathbf{I}_0 + \Sigma\bar{T}_j\mathbf{I}_j$. $\mathbb{A}_e = i\Box^\times \circ \mathbb{X}_e = iA_0\mathbf{I}_0 + \Sigma A_j\mathbf{I}_j$. T_k , \bar{T}_k , and A_k are all real.

In the complex-octonion compounding space, the complex-octonion compounding electromagnetic potential, $\bar{\mathbb{A}}$, is defined as,

$$\bar{\mathbb{A}} = \bar{\mathbb{A}}_g + k_{eg}\bar{\mathbb{A}}_e = \mathbb{A} + K_{rx}\mathbb{T}, \tag{9}$$

where $\bar{\mathbb{A}}_e = i\bar{\square} \times \bar{\mathbb{X}}_e = i\bar{A}_0\mathbf{I}_0 + \Sigma\bar{A}_j\mathbf{I}_j$, $\bar{\mathbb{A}} = i\bar{\square} \times \bar{\mathbb{X}}$, $\bar{\mathbb{X}} = \bar{\mathbb{X}}_g + k_{eg}\bar{\mathbb{X}}_e$, \bar{A}_k is real.

Similarly the complex-octonion compounding electromagnetic strength, $\bar{\mathbb{F}} = \bar{\mathbb{F}}_g + k_{eg}\bar{\mathbb{F}}_e$, is defined from the compounding potential $\bar{\mathbb{A}}$,

$$\bar{\mathbb{F}} = \bar{\square} \circ \bar{\mathbb{A}} = \mathbb{F} + K_{rx}\mathbb{Y}, \quad (10)$$

where $\mathbb{F}_e = \square \circ \mathbb{A}_e = iF_0\mathbf{I}_0 + \Sigma F_j\mathbf{I}_j$; $\bar{\mathbb{F}}_e = \bar{\square} \circ \bar{\mathbb{A}}_e = i\bar{F}_0\mathbf{I}_0 + \Sigma\bar{F}_j\mathbf{I}_j$; $\mathbb{F} = \square \circ \mathbb{A} = \mathbb{F}_g + k_{eg}\mathbb{F}_e$. $\mathbb{Y} = \square \circ \mathbb{T}$. $\mathbb{Y}_e = \square \circ \mathbb{T}_e = iY_0\mathbf{I}_0 + \Sigma Y_j\mathbf{I}_j$. In the electromagnetic field, ϕ is the scalar potential, $\mathbf{A} = \Sigma A_j\mathbf{I}_j$ is the vectorial potential. $\mathbf{A}_0 = A_0\mathbf{I}_0$, with $A_0 = \phi/v_0$. $\bar{\mathbf{A}}_0 = \bar{A}_0\mathbf{I}_0$, $\bar{\mathbf{A}} = \Sigma\bar{A}_j\mathbf{I}_j$. The gauge equation is $-\bar{\mathbb{F}}_0 = \partial_0\bar{\mathbf{A}}_0 - \nabla \cdot \bar{\mathbf{A}} = 0$. Y_k , F_k , and \bar{F}_k are all real.

In the complex-octonion compounding space, the complex-octonion compounding field source $\bar{\mathbb{S}}$ is defined from the $\bar{\mathbb{F}}$,

$$(i\bar{\mathbb{F}}/v_0 + \bar{\square})^* \circ \bar{\mathbb{F}} = -\mu\bar{\mathbb{S}} = -(\mu_g\bar{\mathbb{S}}_g + k_{eg}\mu_e\bar{\mathbb{S}}_e) + i\bar{\mathbb{F}}^* \circ \bar{\mathbb{F}}/v_0, \quad (11)$$

where μ_e is the constant, with $\mu_e > 0$. $\bar{\mathbb{S}}_e = i\bar{S}_0\mathbf{I}_0 + \Sigma\bar{S}_j\mathbf{I}_j$. $\bar{\mathbb{S}}_e = \mathbb{S}_e + K_{rx}\mathbb{Z}_e$. $\mu_e\mathbb{S}_e = -\bar{\square}^* \circ \mathbb{F}_e$, and $\mu_e\mathbb{Z}_e = -\bar{\square}^* \circ \mathbb{Y}_e$. $\bar{\mathbb{F}}^* \circ \bar{\mathbb{F}}/\mu_g = \bar{\mathbb{F}}_g^* \circ \bar{\mathbb{F}}_g/\mu_g + \bar{\mathbb{F}}_e^* \circ \bar{\mathbb{F}}_e/\mu_e$. $\bar{\mathbb{F}}_e^* \circ \bar{\mathbb{F}}_e/(2\mu_e)$ is one energy term in the electromagnetic field, and is different to the electromagnetic field energy. For a single charged particle, $\bar{\mathbb{S}}_e = q\bar{\mathbb{V}}_e$. q is the density of electric charge. $\bar{\mathbb{V}}_e = \partial\bar{\mathbb{R}}_e/\partial t = i\bar{V}_0\mathbf{I}_0 + \Sigma\bar{V}_j\mathbf{I}_j$. \bar{V}_k and \bar{S}_k are all real.

4. ANGULAR MOMENTUM

In the complex-octonion compounding space, the linear momentum density, $\bar{\mathbb{P}} = \bar{\mathbb{P}}_g + k_{eg}\bar{\mathbb{P}}_e$, is defined as

$$\bar{\mathbb{P}} = \mu\bar{\mathbb{S}}/\mu_g, \quad (12)$$

where $\bar{\mathbb{P}}_g = i\bar{p}_0 + \bar{\mathbf{p}} = i\bar{p}_0\mathbf{i}_0 + \Sigma\bar{p}_j\mathbf{i}_j$. $\bar{p}_0 = \hat{m}\bar{v}_0$, $\bar{p}_j = m\bar{v}_j$; $\hat{m} = m + \Delta m$, with \hat{m} being the density of gravitational mass. $\bar{\mathbb{P}}_e = i\bar{P}_0 + \bar{\mathbf{P}} = i\bar{P}_0\mathbf{I}_0 + \Sigma\bar{P}_j\mathbf{I}_j$. $\bar{P}_0 = M\bar{V}_0$, and $\bar{P}_j = M\bar{V}_j$; $M = q\mu_e/\mu_g$. $\Delta m = -\bar{\mathbb{F}}^* \circ \bar{\mathbb{F}}/(\bar{v}_0v_0\mu_g)$. \bar{P}_k and \bar{p}_k are all real.

In the above the linear momentum $\bar{\mathbb{P}}$ consists of a few terms, including the linear momentum term $\bar{\mathbb{S}}_g$ of one mass object, the term $k_{eg}\mu_e\bar{\mathbb{S}}_e/\mu_g$ of one charged particle, the term $\bar{\mathbb{F}}_g^* \circ \bar{\mathbb{F}}_g/(\mu_gv_0)$ of gravitational fields, and the term $\bar{\mathbb{F}}_e^* \circ \bar{\mathbb{F}}_e/(\mu_ev_0)$ of electromagnetic fields.

From the definition of complex-quaternion velocity ratio \mathbb{T}_g , one can find its relation with the velocity, $\mathbb{V}_g = \partial\mathbb{R}_g/\partial t$. Sometimes the physics quantity $(v_0\mathbb{T}_g)$ possesses the same vectorial part with \mathbb{V}_g , but their scalar parts are different. In the case, there are, $v_0t_j = v_j$, and $v_0t_0 \neq v_0$. Herein $\mathbb{V}_g = iv_0\mathbf{i}_0 + \Sigma v_j\mathbf{i}_j$. v_k is real.

In the complex-octonion compounding space for the electromagnetic and gravitational fields, the complex-octonion angular momentum, $\bar{\mathbb{L}} = \bar{\mathbb{L}}_g + k_{eg}\bar{\mathbb{L}}_e$, can be defined from the complex-octonion compounding radius vector $\bar{\mathbb{R}}$ and linear momentum $\bar{\mathbb{P}}$. That is,

$$\bar{\mathbb{L}} = \bar{\mathbb{R}} \times \bar{\mathbb{P}}, \quad (13)$$

where $\bar{\mathbb{L}}_g = \bar{L}_{10} + i\bar{\mathbf{L}}_1 + \bar{\mathbf{L}}_1$; $\bar{\mathbf{L}}_1 = \Sigma\bar{L}_{1j}^i\mathbf{i}_j$, $\bar{\mathbf{L}}_1 = \Sigma\bar{L}_{1j}\mathbf{i}_j$. $\bar{\mathbb{L}}_e = \bar{L}_{20} + i\bar{\mathbf{L}}_2 + \bar{\mathbf{L}}_2$. $\bar{\mathbf{L}}_2^i = \Sigma\bar{L}_{2j}^i\mathbf{I}_j$, $\bar{\mathbf{L}}_2 = \Sigma\bar{L}_{2j}\mathbf{I}_j$, $\bar{\mathbf{L}}_{20} = \bar{L}_{20}\mathbf{I}_0$. $\bar{\mathbf{L}}_1$ covers the angular momentum. $\bar{\mathbf{L}}_2$ consists of the magnetic dipole momentum. $\bar{\mathbf{L}}_2^i$ includes the electric dipole momentum. And $\bar{\mathbf{L}}_{20}$ may contains the spin magnetic momentum. \bar{L}_{1k} , \bar{L}_{1j}^i , \bar{L}_{2k} , and \bar{L}_{2j}^i are all real.

5. OCTONION TORQUE

In the complex-octonion compounding space for the electromagnetic and gravitational fields, the complex-octonion torque, $\bar{\mathbb{W}} = \bar{\mathbb{W}}_g + k_{eg}\bar{\mathbb{W}}_e$, is defined from $\bar{\mathbb{L}}$ and $\bar{\mathbb{F}}$,

$$\bar{\mathbb{W}} = -v_0(i\bar{\mathbb{F}}/v_0 + \bar{\square}) \circ \bar{\mathbb{L}}, \quad (14)$$

where $\bar{\mathbb{W}}_g = i\bar{W}_{10}^i + \bar{W}_{10} + i\bar{\mathbf{W}}_1 + \bar{\mathbf{W}}_1$. $\bar{\mathbf{W}}_1^i = \Sigma\bar{W}_{1j}^i\mathbf{i}_j$, $\bar{\mathbf{W}}_1 = \Sigma\bar{W}_{1j}\mathbf{i}_j$. \bar{W}_{10}^i is the compounding energy density, and $\bar{\mathbf{W}}_1^i$ is the compounding torque density. $\bar{\mathbb{W}}_e = i\bar{W}_{20}^i + \bar{W}_{20} + i\bar{\mathbf{W}}_2 + \bar{\mathbf{W}}_2$. $\bar{\mathbf{W}}_2^i = \Sigma\bar{W}_{2j}^i\mathbf{I}_j$, $\bar{\mathbf{W}}_2 = \Sigma\bar{W}_{2j}\mathbf{I}_j$. \bar{W}_{1k} , \bar{W}_{1k}^i , \bar{W}_{2k} , and \bar{W}_{2k}^i are all real.

The compounding energy includes the proper energy, kinetic energy, work, gravitational potential energy, electromagnetic potential energy, gravitational field energy, and electromagnetic field energy and so on. The compounding energy density can be expressed as,

$$\begin{aligned}\bar{W}_{10}^i &= \left(\bar{\mathbf{g}} \cdot \bar{\mathbf{L}}_1^i / v_0 - \bar{\mathbf{b}} \cdot \bar{\mathbf{L}}_1 \right) - v_0 \left(\partial_0 \bar{L}_{10} + \nabla \cdot \bar{\mathbf{L}}_1^i \right) + k_{eg}^2 \left(\bar{\mathbf{E}} \cdot \bar{\mathbf{L}}_2^i / v_0 - \bar{\mathbf{B}} \cdot \bar{\mathbf{L}}_2 \right) \\ &\approx - \{ v_0 \bar{p}_0 (\bar{v}_0 / v_0) + \bar{v}_0 \bar{p}_0 (\nabla \cdot \bar{\mathbf{r}}) \} - \{ v_0 (\partial_0 \bar{\mathbf{r}}) \cdot \bar{\mathbf{p}} + v_0 \bar{\mathbf{r}} \cdot \partial_0 \bar{\mathbf{p}} \} \\ &\quad - \{ (\bar{p}_0 \bar{a}_0 + \bar{\mathbf{a}} \cdot \bar{\mathbf{p}}) + k_{eg}^2 (\bar{\mathbf{A}}_0 \circ \bar{\mathbf{P}}_0 + \bar{\mathbf{A}} \cdot \bar{\mathbf{P}}) \} \\ &\quad + k_{eg}^2 \{ (\bar{\mathbf{E}} / v_0) \cdot (\bar{\mathbf{r}} \circ \bar{\mathbf{P}}_0) - \bar{\mathbf{B}} \cdot (\bar{\mathbf{r}} \times \bar{\mathbf{P}}) \} + \{ (\bar{\mathbf{g}} / v_0) \cdot (\bar{p}_0 \bar{\mathbf{r}}) - \bar{\mathbf{b}} \cdot \bar{\mathbf{L}}_1 \},\end{aligned}\quad (15)$$

where the gauge conditions for the compounding field potential are chosen as, $\nabla \times \bar{\mathbf{x}} = 0$, and $\nabla \times \bar{\mathbf{X}} = 0$. The gravitational potential is, $\bar{\mathbb{A}}_g = i\bar{a}_0 + \bar{\mathbf{a}}$, with $\bar{a}_0 = \partial_0 \bar{x}_0 + \nabla \cdot \bar{\mathbf{x}}$, and $\bar{\mathbf{a}} = \partial_0 \bar{\mathbf{x}} - \nabla \bar{x}_0$. The electromagnetic potential is, $\bar{\mathbb{A}}_e = i\bar{\mathbf{A}}_0 + \bar{\mathbf{A}}$, with $\bar{\mathbf{A}}_0 = \partial_0 \bar{\mathbf{X}}_0 + \nabla \cdot \bar{\mathbf{X}}$, and $\bar{\mathbf{A}} = \partial_0 \bar{\mathbf{X}} - \nabla \circ \bar{\mathbf{X}}_0$. The gravitational strength is, $\bar{\mathbf{f}} = i\bar{\mathbf{g}} / v_0 + \bar{\mathbf{b}}$, with $\bar{f}_0 = 0$. The gravitational acceleration is, $\bar{\mathbf{g}} / v_0 = \partial_0 \bar{\mathbf{a}} + \nabla \bar{a}_0$. The other component is, $\bar{\mathbf{b}} = \nabla \times \bar{\mathbf{a}}$. The electromagnetic strength is, $\bar{\mathbf{F}} = i\bar{\mathbf{E}} / v_0 + \bar{\mathbf{B}}$, with $\bar{\mathbf{F}}_0 = 0$. The electric field intensity is, $\bar{\mathbf{E}} / v_0 = \partial_0 \bar{\mathbf{A}} + \nabla \circ \bar{\mathbf{A}}_0$, and the magnetic flux density is, $\bar{\mathbf{B}} = \nabla \times \bar{\mathbf{A}}$. $\bar{\mathbf{F}} = \Sigma(\bar{F}_j \mathbf{I}_j)$. $\bar{\mathbf{B}} = \Sigma(\bar{B}_j \mathbf{I}_j)$. $\bar{\mathbf{E}} = \Sigma(\bar{E}_j \mathbf{I}_j)$. $\bar{\mathbf{f}} = \Sigma(\bar{f}_j \mathbf{i}_j)$. $\bar{\mathbf{g}} = \Sigma(\bar{g}_j \mathbf{i}_j)$. $\bar{\mathbf{b}} = \Sigma(\bar{b}_j \mathbf{i}_j)$. \bar{B}_j , \bar{E}_j , \bar{g}_j , and \bar{b}_j are all real. \bar{F}_j and \bar{f}_j are all complex.

In a similar way, the compounding torque density can be expressed as

$$\begin{aligned}\bar{\mathbf{W}}_1^i &= \left(\bar{\mathbf{g}} \times \bar{\mathbf{L}}_1^i / v_0 - \bar{L}_{10} \bar{\mathbf{b}} - \bar{\mathbf{b}} \times \bar{\mathbf{L}}_1 \right) - v_0 \left(\partial_0 \bar{\mathbf{L}}_1 + \nabla \times \bar{\mathbf{L}}_1^i \right) + k_{eg}^2 \left(\bar{\mathbf{E}} \times \bar{\mathbf{L}}_2^i / v_0 - \bar{\mathbf{B}} \circ \bar{\mathbf{L}}_{20} - \bar{\mathbf{B}} \times \bar{\mathbf{L}}_2 \right) \\ &\approx \bar{p}_0 \bar{\mathbf{g}} \times \bar{\mathbf{r}} / v_0 + k_{eg}^2 \{ \bar{\mathbf{E}} \times (\bar{\mathbf{r}} \circ \bar{\mathbf{P}}_0) / v_0 - \bar{\mathbf{B}} \times (\bar{\mathbf{r}} \times \bar{\mathbf{P}}) \} - v_0 \bar{\mathbf{r}} \times \partial_0 \bar{\mathbf{p}} - (\bar{\mathbf{r}} \cdot \bar{\mathbf{p}}) \bar{\mathbf{b}} - \bar{\mathbf{b}} \times (\bar{\mathbf{r}} \times \bar{\mathbf{p}}) + \bar{\mathbf{a}} \times \bar{\mathbf{p}},\end{aligned}\quad (16)$$

where the compounding torque consists of a few terms, including the torque terms caused by the gravity, inertial force, Lorentz force, and other force terms and so forth.

6. OCTONION FORCE

In the complex-octonion compounding space for the gravitational and electromagnetic fields, the compounding force is able to encompass various force terms, including the inertial force, the gravity, the electromagnetic force, the gradient of energy, and the interacting force between the dipole moment with the magnetic strength and so on.

In the complex-octonion compounding space, the octonion force, $\bar{\mathbf{N}} = \bar{\mathbf{N}}_g + k_{eg} \bar{\mathbf{N}}_e$, is defined from $\bar{\mathbf{W}}$ and $\bar{\mathbf{F}}$,

$$\bar{\mathbf{N}} = -(i\bar{\mathbf{F}} / v_0 + \square) \circ \bar{\mathbf{W}},\quad (17)$$

where $\bar{\mathbf{N}}_g = i\bar{N}_{10}^i + \bar{N}_{10} + i\bar{\mathbf{N}}_1^i + \bar{\mathbf{N}}_1$. $\bar{N}_{10}^i = \Sigma \bar{N}_{1j}^i \mathbf{i}_j$, $\bar{\mathbf{N}}_1 = \Sigma \bar{N}_{1j} \mathbf{i}_j$. The scalar part \bar{N}_{10} is the compounding power, and the vectorial part $\bar{\mathbf{N}}_1^i$ is the compounding force. $\bar{\mathbf{N}}_e = i\bar{N}_{20}^i + \bar{N}_{20} + i\bar{\mathbf{N}}_2^i + \bar{\mathbf{N}}_2$. $\bar{N}_{20}^i = \Sigma \bar{N}_{2j}^i \mathbf{I}_j$, $\bar{\mathbf{N}}_2 = \Sigma \bar{N}_{2j} \mathbf{I}_j$. \bar{N}_{1k} , \bar{N}_{1k}^i , \bar{N}_{2k} , and \bar{N}_{2k}^i are all real.

In case the compounding field strength is relatively weak, the compounding power density

$$\bar{N}_{10} = (\partial_0 \bar{W}_{10}^i - \nabla \cdot \bar{\mathbf{W}}_1) + \left(\bar{\mathbf{g}} \cdot \bar{\mathbf{W}}_1 / v_0 + \bar{\mathbf{b}} \cdot \bar{\mathbf{W}}_1^i \right) / v_0 + k_{eg}^2 \left(\bar{\mathbf{E}} \cdot \bar{\mathbf{W}}_2 / v_0 + \bar{\mathbf{B}} \cdot \bar{\mathbf{W}}_2^i \right) / v_0,\quad (18)$$

can be written approximately as,

$$\begin{aligned}\bar{N}_{10} / k_p &\approx \partial_0 (\bar{p}_0 \bar{v}_0) - \nabla \cdot (\bar{v}_0 \bar{\mathbf{p}}) + L_{10} (\bar{\mathbf{b}} \cdot \bar{\mathbf{b}} - \bar{\mathbf{g}} \cdot \bar{\mathbf{g}} / v_0^2) / (v_0 k_p) \\ &\quad + k_{eg}^2 \bar{L}_{10} (\bar{\mathbf{B}} \cdot \bar{\mathbf{B}} - \bar{\mathbf{E}} \cdot \bar{\mathbf{E}} / v_0^2) / (v_0 k_p) + k_{eg}^2 \bar{\mathbf{E}} \cdot \bar{\mathbf{P}} / v_0 + \bar{\mathbf{g}} \cdot \bar{\mathbf{p}} / v_0,\end{aligned}\quad (19)$$

where $k_p = (k - 1)$ is the coefficient, with k being the dimension of compounding vector $\bar{\mathbf{r}}$.

When the compounding field strength is comparative weak, the compounding force

$$\begin{aligned}\bar{\mathbf{N}}_1^i &= \left(\bar{W}_{10}^i \bar{\mathbf{g}} / v_0 + \bar{\mathbf{g}} \times \bar{\mathbf{W}}_1^i / v_0 - \bar{W}_{10} \bar{\mathbf{b}} - \bar{\mathbf{b}} \times \bar{\mathbf{W}}_1 \right) / v_0 - \left(\partial_0 \bar{\mathbf{W}}_1 + \nabla \bar{W}_{10}^i + \nabla \times \bar{\mathbf{W}}_1^i \right) \\ &\quad + k_{eg}^2 \left(\bar{\mathbf{E}} \circ \bar{\mathbf{W}}_{20}^i / v_0 + \bar{\mathbf{E}} \times \bar{\mathbf{W}}_2^i / v_0 - \bar{\mathbf{B}} \circ \bar{\mathbf{W}}_{20} - \bar{\mathbf{B}} \times \bar{\mathbf{W}}_2 \right) / v_0,\end{aligned}\quad (20)$$

can be written approximately as,

$$\begin{aligned} \bar{\mathbf{N}}_1^i/k_p \approx & -\partial_0(\bar{\mathbf{p}}\bar{v}_0) + \bar{p}_0\bar{\mathbf{g}}/v_0 + \bar{L}_{10}(\bar{\mathbf{g}} \times \bar{\mathbf{b}} + k_{eg}^2\bar{\mathbf{E}} \times \bar{\mathbf{B}}) / (v_0^2 k_p) \\ & -\bar{\mathbf{b}} \times \bar{\mathbf{p}} - \nabla(\bar{p}_0\bar{v}_0) + k_{eg}^2(\bar{\mathbf{E}} \circ \bar{\mathbf{P}}_0/v_0 - \bar{\mathbf{B}} \times \bar{\mathbf{P}}), \end{aligned} \quad (21)$$

where $(\bar{p}_0\bar{\mathbf{g}}/v_0)$ is the gravity. $\partial_0(-\bar{v}_0\bar{\mathbf{p}})$ is the inertial force. $\{k_{eg}^2(\bar{\mathbf{E}} \circ \bar{\mathbf{P}}_0/v_0 - \bar{\mathbf{B}} \times \bar{\mathbf{P}})\}$ covers the electromagnetic force. $\nabla(\bar{p}_0\bar{v}_0)$ is the energy gradient.

7. CONCLUSIONS AND DISCUSSIONS

According to the viewpoint of function space, the radius vector and velocity ratio can be combined together to become one ‘radius vector’ in the compounding space. And the compounding space is able to be considered as the extension of one compounding field, according to the relationship between the field with the space. In the compounding space, there are several kinds of equilibrium states, although the torque and force both may not be equal to zero. This means that the velocity ratio will impact the angular momentum, torque, and force and so forth. Therefore the physics feature of the rotational charged object should depart from the deduction deriving from the Newton’s law of gravitation and the classical Coulomb’s law.

In the complex-octonion space for electromagnetic and gravitational fields, when the torque $\mathbf{W}_1^i = 0$ and the force $\mathbf{N}_1^i = 0$, the neutral/charged object stays on one equilibrium state. Similarly in the complex-octonion compounding space, when $\bar{\mathbf{W}}_1^i = 0$ and $\bar{\mathbf{N}}_1^i = 0$, the rotational neutral/charged object stays on one kind of ‘equilibrium state’, although there may be $\mathbf{W}_1^i \neq 0$ and $\mathbf{N}_1^i \neq 0$. And it is correspondent with $\bar{\mathbf{f}} = 0$ (that is, the weightlessness state), while $\mathbf{f} \neq 0$. It may be able to be applied to figure out the stable over-speed movement of the rotational stars on the fringe of a galaxy. Also it may be used to explain the stable over-speed movement of the rotational charged objects.

In some special situations, the above equations in the complex-octonion compounding space will be reduced to the simple cases in the complex-octonion space. When \mathbb{T} , \mathbb{Y} , and \mathbb{Z} are all approximate to zero, $\bar{\mathbb{A}}$, $\bar{\mathbb{F}}$, and $\bar{\mathbb{S}}$ will be degenerated into \mathbb{A} , \mathbb{F} , and \mathbb{S} respectively, further the physics quantities $\bar{\mathbb{L}}$, $\bar{\mathbb{W}}$, and $\bar{\mathbb{N}}$ will be degenerated into \mathbb{L} , \mathbb{W} , and \mathbb{N} respectively.

It should be noted that the study for the influence of angular velocity on the electromagnetic force of rotational charged objects examined only some simple cases. Despite its preliminary characteristics, this study can clearly indicate that the angular velocity should impact the equilibrium state and electromagnetic force and so forth. For the future studies, the research will focus on the investigation about the equilibrium state of rotational charged objects.

ACKNOWLEDGMENT

This project was supported partially by the National Natural Science Foundation of China under grant number 60677039.

REFERENCES

1. Weng, Z.-H., “Field equations in the complex quaternion spaces,” *Advances in Mathematical Physics*, Vol. 2014, 450262, 6 Pages, 2014.
2. Weng, Z.-H., “Angular momentum and torque described with the complex octonion,” *AIP Advances*, Vol. 4, No. 8, 087103, 16 Pages, 2014.
3. Zwicky, F., “On the masses of nebulae and of clusters of nebulae,” *Astrophysical Journal*, Vol. 86, No. 3, 217–246, 1937.

Power Spectrum Method for the Processing of the DNA in the Genome Sequencing

M. Valla, E. Gescheidtova, and P. Fiala

Department of Theoretical and Experimental Electrical Engineering, DTEEE, FEKT
Brno University of Technology, Brno, Czech Republic

Abstract— The fractal systems are broadly found throughout the nature, generally in any scale. For each dimension (1D, 2D ...) in any structures and in any mathematical algorithms or in any object (sequence, line, square) its dimension can be calculated. These dimensions are specific parameters for description of the DNA sequence characters ACGT strings. Generally a first step consists in the converting of a one-dimensional sequence into the image. In the second step, the method for calculating the dimensions for all scales is selected. For the calculations of the above mentioned dimensions the Power Spectrum (PS) method has been proposed and examined. The Power Spectrum method provides universal calculation of dimension and it allows to obtain the resulting multifractal coefficient. The multifractal coefficient represents the means rate of approximation to ideal power spectrum. It has to be emphasized that the multifractal coefficient is independent of any scale to be chosen. Moreover, the multifractal coefficient serves as an advanced parameter for mathematical description of analyzed specific sequence of the deoxyribonucleic acid (DNA) or the whole genome. The conversion of the sequence into the image as the first step of the pre-processing can be used also for the alternative imaging and the description of sequence and it is possible to choose another method for the processing and analyzing a fractal image (for example Box Counting method). In the paper, the method for the processing of the DNA in the genome sequencing, the Power Spectrum method, will be introduced. The results of the Power Spectrum methods will be presented also.

1. INTRODUCTION

Theory of fractal originated on basis of observation of natural structures. Application of this knowledge for DNA analysis leads to additional insight to genome. Term fractal is derived from Latin *fractus*, which means fraction. Fractals are geometrical shapes, which have non integer dimension and are similar for each other. Self-similarity is phenomenon, which occurs in case, when structure looks identical at whatever magnification. Mathematically, this phenomenon is called invariance against change of scale factor. For each object, its dimension can be calculated. There are many algorithms for calculation of this magnitude. For calculating itself, PS method (Power Spectrum method) was chosen. PS provides more possibilities of analysis at the cost of moderate increasing of calculating demands (for example optional possibilities of local segmentation). Our aim consisted in application of theory of fractals for analysis of images obtained from sequence of DNA code. Image output can be also presented as multidimensional transformation and record of genomic signal (from linear entry in line to planar in figure). All algorithms were developed in environment of matrix laboratory MATLAB.

Bovine virus diarrhea (BVD) is chosen, it is disease of animals, namely cattle. Are analyzed in three versions of the virus genome. Complete genome is downloaded from the NCBI public database.

Description of sequence “Bovine foam virus complete genome” is given by locus ID NC 001831 and length 12 002 bp. Metadata sequence — “A” base is represented by 302% (3 619 nucleotides), “C” base by 226% (2 717 nucleotides), “G” base by 22,8% (2 735 nucleotides) and “T” base by 244% (2 931 nucleotides).

Description of sequence “Bovine immunodeficiency virus complete genome” is given by locus ID NC 001413 and length 8 482 bp. Metadata sequence — “A” base is represented by 318% (6 699 nucleotides), “C” base by 212% (1 798 nucleotides), “G” base by 23,8% (2 017 nucleotides) and “T” base by 232% (1 968 nucleotides).

Description of sequence “Bovine leukaemia virus complete genome” is given by locus ID NC 001414 and length 8 419 bp. Metadata sequence — “A” base is represented by 22,0% (1 850 nucleotides), “C” base by 33,1% (2 790 nucleotides), “G” base by 21,0% (1 770 nucleotides) and “T” base by 23,9% (2 009 nucleotides). Bovine virus is closely related to human T — lymphotropic virus type HTLV-I.

2. METHODS

Processing of DNA chains is done in two steps, each step is one method used. The first method converts a linear chain DNA into an image (Chaos Game) and for converting the second image into a spectral region (Power Spectrum).

2.1. Chaos Game Representation of DNA

Linear record for DNA sequence (for example AGGCTGGAATGC) must be transformed into figure by following procedure. Square with four apexes — A, C, G, T (opposite pairs A-C and G-T) — and initial point, which is situated at the centre of square, are defined.

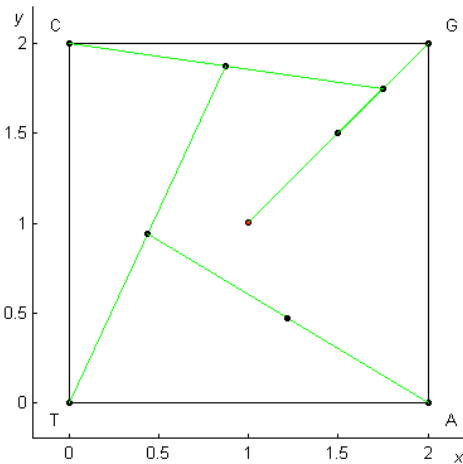


Figure 1: Initiation of attractor designed from first four nucleotides of sequence GCTA.

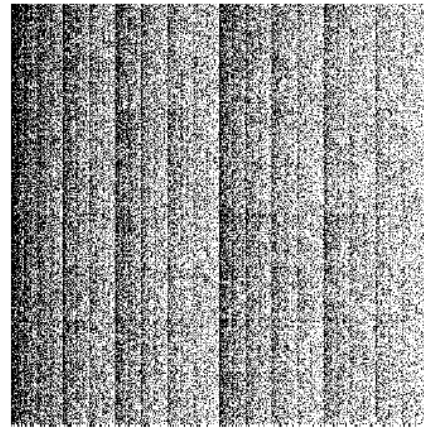


Figure 2: Chaos Game representation of DNA codes of sequence NG_013224 (ID NCBI database).

Square is filled by points by modified method *Chaos game* (description of method: initial point is connected with apex, which is given by character at given position in sequence and at one half of distinct between initial point and apex, point is projected; new point is initial for new interaction — new connection of point with next square apex is given by subsequent character of sequence; schematic demonstration first four steps methods in Figure 1).

2.2. Power Spectrum Method

Power Spectrum represents method of image evaluation by calculation of its power spectrum. Calculation is based on Fourier transformation (obtaining of real and imaginary part of image, marking $F(k_i)$), which is subsequently exponentiated; result is power spectrum P_i expressed by formula (1) [1],

$$P_i = |F(k_i)|^2 = \left(\sqrt{\text{Re}(F(k_i))^2 + \text{Im}(F(k_i))^2} \right)^2 = \text{Re}(F(k_i))^2 + \text{Im}(F(k_i))^2 \quad (1)$$

where $\text{Re}(F(k_i))^2$ is real part of frequency spectrum, $\text{Im}(F(k_i))^2$ is imaginary part of frequency spectrum and k_i is dimensional frequency at i th value. In addition, model of ideal power spectrum \hat{P}_i must be considered.

\hat{P}_i is obtained as model of one-dimensional fractal system (2)

$$\hat{P}_i = c \cdot \frac{1}{|k_i|^\beta} = c \cdot |k_i|^{-\beta}, \quad (2)$$

where c is constant of power spectrum and β is exponent related to fractal dimension D . Aim of this method is in determination of constant β , from which dimension is calculated. Calculation of constant β is realised in accordance with formula (3):

$$\beta = \frac{N \sum_{i=1}^N (\ln P_i) (\ln |k_i|) - \left(\sum_{i=1}^N \ln |k_i| \right) \left(\sum_{i=1}^N \ln P_i \right)}{\left(\sum_{i=1}^N \ln |k_i| \right)^2 - N \sum_{i=1}^N (\ln |k_i|)^2}, \quad (3)$$

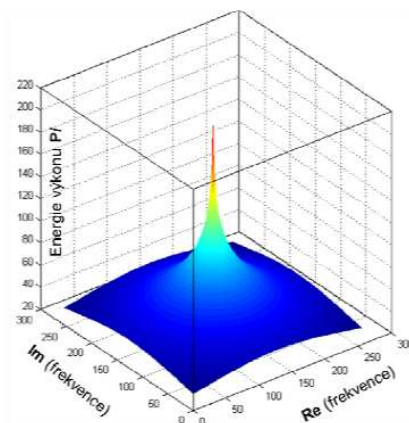


Figure 3: Ideal fractal \hat{P}_i power spectrum of DNA image.

where N indicates number of samples of spectrum.

Subsequently, calculation of PS multifractal coefficient dimension MCD is easy and is represented by formula (4):

$$MCD_{PS} = \frac{5 - \beta}{2} \tag{4}$$

Whole detailed deduction is described in [1], or also with example and figures of individual steps of calculation in [2].

3. RESULTS

Bovine virus is closely related to human T — lymphotropic virus type HTLV-I.

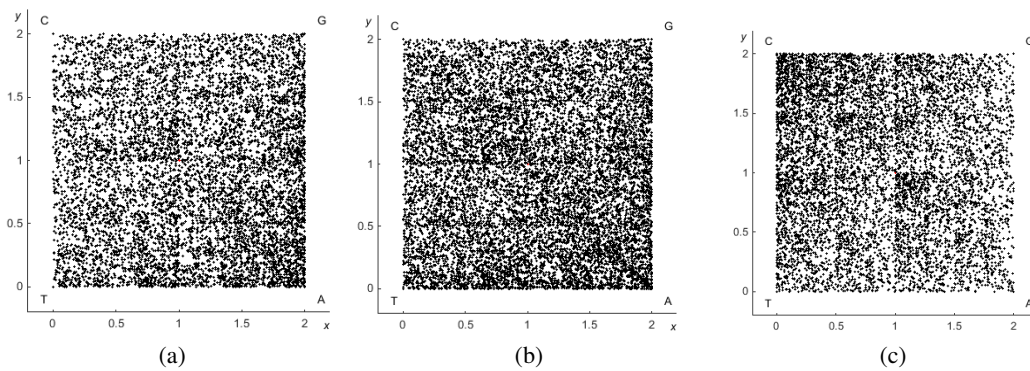


Figure 4: Chaos game representation of image of sequence Bovine foamy virus. (a) Bovine immunodeficiency virus. (b) Bovine leukaemia virus (c).

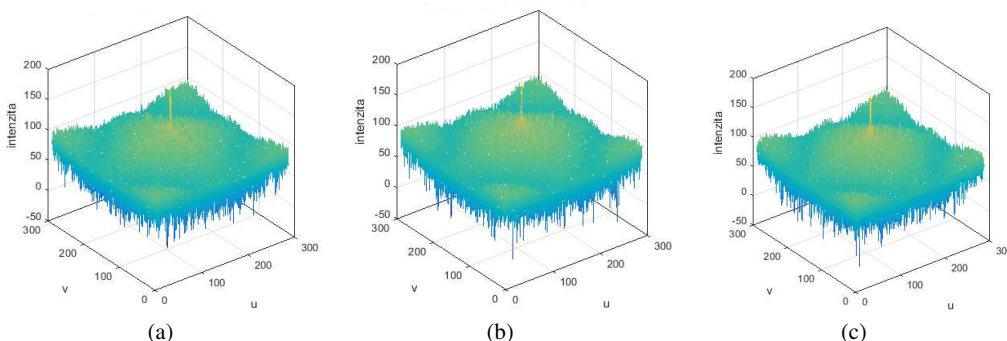


Figure 5: Power spectrum of image of sequence Bovine foamy virus. (a) Bovine immunodeficiency virus. (b) Bovine leukaemia virus (c).

Table 1: Resulting multifractal coefficients model sequences calculated by PS method.

<i>Name</i>	<i>ID sequence</i>	<i>MCD_{PS} [-]</i>
Bovine leukaemia virus	NC 001414	1,813
Bovine immunodeficiency virus	NC 001413	1,818
Bovine foamy virus	NC 001831	1,880

4. CONCLUSIONS

PS method provides universal calculation of dimension and obtains resulting multifractal coefficient MCD. Multifractal coefficient, it means rate of approximation to ideal power spectrum, serves as parameter for mathematical description of analysed sequence. Conversion of sequence to image can be used also for alternative imaging and description of sequence. Fractal coefficient can be used for parameterization and mutual comparing of DNA sequences.

ACKNOWLEDGMENT

Research described in this paper was financed by the by the project of Czech Science Foundation 15-08803S and National Sustainability Program under grant LO1401. For the research, infrastructure of the SIX Center was used.

REFERENCES

1. Turner, J. T., *Fractal Geometry in Digital Imaging*, ISBN 0-12-703970-8, Academic Press, Leicester, 1998.
2. Berthelsen, C. L., "Fractal analysis of DNA sequence data," 160, The University of Utah, 1993.

Lorentz-like Transformations for the Velocity and Acceleration

Zi-Hua Weng

School of Physics and Mechanical & Electrical Engineering
Xiamen University, Xiamen 361005, China

Abstract— Making use of the orthogonal transformation in the complex quaternion coordinate system, it is able to deduce directly invariants relevant to the radius vector and velocity, drawing out the Lorentz transformation and so forth, without the help of introducing the basic postulate. When the coordinate system transforms orthogonally from one to the other, the scalar part of and norm of one complex quaternion physical quantity will remain invariable respectively. Therefore the coordinate transformation between two three-dimensional coordinate systems, in the presence of relative movement, is equivalent to the orthogonal transformation between two complex quaternion coordinate systems. The above means that the paper is able to derive the Galilean and Lorentz transformations and so on for the radius vector, velocity, and acceleration. Especially it is not necessary to introduce additionally the invariant or basic postulate into the complex quaternion space, to deduce the coordinate transformations.

1. INTRODUCTION

In 1873 J. C. Maxwell was the first to apply the quaternion to describe the electromagnetic theory. This method spirits up subsequent scholars to adopt the complex quaternion to depict various aspects of electromagnetic fields, including Maxwell's equations, transmission of electromagnetic wave [1], force [2], and Lorentz transformation [3] and so on. In recent years some scholars applied the complex quaternion [4] to depict the Lorentz transformation and Special Theory of Relativity. M. M. Acevedo etc. figured out the Lorentz transformation [5] and so on by means of the quaternion. On the basis of the group of Lorentz transformation, I. Abonyi etc. constructed one pair of relativistic vectors and skew-symmetric tensors, representing a relativistic quaternion formulation of Maxwell's electrodynamics [6]. M. T. Teli investigated the quaternion representation of Lorentz transformation [7].

Analyzing the above researches reveals that all of these existing studies started off with some invariants (the space-time interval, or the speed of light), to deduce the Lorentz transformation and so forth. In other words, these existing studies possess the same distinguishing feature: they had to import additionally the invariant for deducing the coordinate transformation. However the paper is able to deduce some invariants, from the orthogonal transformation (or the rotational transform) of the complex quaternion coordinate system, inferring the Lorentz transformation and so forth. Obviously in the complex quaternion space, it is not necessary to introduce additionally the invariant to be the basic postulate for the Special Theory of Relativity.

In the physics, there is the relative movement between two three-dimensional coordinate systems, although the times in these two coordinate systems are different to each other. In the mathematics, this relative movement between two three-dimensional coordinate systems is equivalent to the orthogonal transformation between two quaternion coordinate systems. In the orthogonal transformation of quaternion coordinate system, the scalar remains invariable.

Making use of the above equivalency, the paper is capable of inferring invariants, related with the relative movement between two three-dimensional coordinate systems, including the scalar part of radius vector, norm of radius vector, scalar part of velocity, and norm of velocity. Further from the combination of these invariants, one can deduce the Galilean and Lorentz transformations and so on. That is, the paper can direct infer the invariant and Lorentz transformation, from the property of complex quaternion space. It is not necessary to introduce additionally the invariant, related with the coordinate transformation, into the complex quaternion space.

2. RADIUS VECTOR AND VELOCITY

In the complex quaternion space, there are two coordinate systems, $\mathbb{H}(ir_0, r_k)$ and $\mathbb{H}'(ir'_0, r'_k)$. In the complex quaternion coordinate system \mathbb{H} , the complex quaternion radius vector is, $\mathbb{R}(r_j) = ir_0\mathbf{i}_0 + \sum r_k\mathbf{i}_k$, the complex quaternion velocity is, $\mathbb{V}(v_j) = iv_0\mathbf{i}_0 + \sum v_k\mathbf{i}_k$. In the complex quaternion coordinate system \mathbb{H}' , the complex quaternion radius vector is, $\mathbb{R}'(r'_j) = ir'_0\mathbf{i}'_0 + \sum r'_k\mathbf{i}'_k$, the complex

quaternion velocity is, $\mathbb{V}'(v'_j) = iv'_0\mathbf{i}'_0 + \Sigma v'_k\mathbf{i}'_k$. Herein r_j and r'_j are all real. i is the imaginary unit. $\mathbf{i}_0 = 1$, $\mathbf{i}_k^2 = -1$. $\mathbf{i}'_0 = 1$, $\mathbf{i}'_k{}^2 = -1$. $j = 0, 1, 2, 3$. $k = 1, 2, 3$.

Sometimes the complex quaternion coordinate system can be considered as the three-dimensional coordinate system with the time t . The paper will concentrate on the studying of one special case in the following context. There is the relative movement along one coordinate axis between two three-dimensional vector parts, $\mathbb{H}(r_k)$ and $\mathbb{H}'(r'_k)$, in the complex quaternion coordinate systems. According to the mathematical viewpoint, this relative movement is equivalent to the orthogonal transformation between two complex quaternion coordinate systems, $\mathbb{H}(ir_0, r_k)$ and $\mathbb{H}'(ir'_0, r'_k)$.

When the complex quaternion coordinate system orthogonally transforms from $\mathbb{H}(ir_0, r_k)$ to $\mathbb{H}'(ir'_0, r'_k)$, the scalar part of and norm of one complex quaternion physics quantity will remain invariant respectively. Making use of the scalar part of radius vector and of velocity, as well as the norm of radius vector and of velocity, it is able to deduce some invariants in the complex quaternion coordinate system for the radius vector and velocity. Further from a few different combinations of these invariants, the paper is capable of inferring some coordinate transformations.

2.1. Galilean Transformation

From the complex quaternion radius vector and velocity, it is capable of deducing one coordinate transformation, which is able to be degenerated into the Galilean transformation. In the complex quaternion coordinate transformation, according to the physical property, which the scalar part of radius vector and of velocity remain invariant respectively, there are,

$$r'_0 = r_0, \quad v'_0 = v_0, \quad (1)$$

where $r_0 = r_{00} + v_0t$, $r'_0 = r'_{00} + v'_0t'$. t and t' are respectively the time interval in \mathbb{H} and \mathbb{H}' . r_{00} and r'_{00} are initial values. $v_1 = \partial r_1 / \partial t$, $v'_1 = \partial r'_1 / \partial t'$.

The above consists of two invariants in the complex quaternion space, and the coordinate transformation can be derived from these two invariants. When two coordinate systems possess one relative movement along the direction, $r_1\mathbf{i}_1$, with the relative speed, v_1 , the coordinate transformation is,

$$r'_0 = r_0, \quad r'_1 = r_1 - r_0v_1/v_0, \quad r'_2 = r_2, \quad r'_3 = r_3. \quad (2)$$

Choosing the initial values, $r_{00} = 0$ and $r'_{00} = 0$, the above is degenerated into the Galilean transformation in the Classical Mechanics as follows,

$$r'_0 = r_0, \quad r'_1 = r_1 - v_1t, \quad r'_2 = r_2, \quad r'_3 = r_3. \quad (3)$$

2.2. Lorentz Transformation

From the norm of complex quaternion radius vector and the complex quaternion velocity, it is able to infer one coordinate transformation, which may be reduced into the Lorentz transformation. The norm of complex quaternion radius vector is,

$$S_R = \mathbb{R} \circ \mathbb{R}^* = -r_0^2 + \Sigma r_k^2, \quad (4)$$

where $*$ denotes the quaternion conjugate, and \circ is the quaternion multiplication.

In a similar way, in the complex quaternion coordinate systems \mathbb{H}' , the norm of complex quaternion radius vector is, $S'_R = \mathbb{R}' \circ \mathbb{R}'^* = -r'^2_0 + \Sigma r'^2_k$.

In the complex quaternion coordinate transformation, according to the physical property, which the norm of radius vector and the scalar part of velocity remain invariant respectively, there are,

$$S'_R = S_R, \quad v'_0 = v_0. \quad (5)$$

The above covers two invariants in the complex quaternion space, and the coordinate transformation can be derived from these two invariants. The deduction of coordinate transformation is similar to that of the pseudo-orthogonal transformation in the Minkowski space.

When two coordinate systems possess one relative movement along the direction, $r_1\mathbf{i}_1$, with the relative speed, v_1 , the coordinate transformation is,

$$r'_1 = (r_1 - r_0v_1/v_0) / (1 - v_1^2/v_0^2)^{1/2}, \quad r'_2 = r_2, \quad (6)$$

$$r'_0 = (r_0 - r_1v_1/v_0) / (1 - v_1^2/v_0^2)^{1/2}, \quad r'_3 = r_3. \quad (7)$$

Choosing the initial values, r_{00} and r'_{00} , to be all zero, the above is reduced into the Lorentz transformation in the Special Theory of Relativity,

$$r'_1 = (r_1 - v_1 t) / (1 - v_1^2/v_0^2)^{1/2}, \quad r'_2 = r_2, \quad (8)$$

$$t' = (t - r_1 v_1/v_0^2) / (1 - v_1^2/v_0^2)^{1/2}, \quad r'_3 = r_3. \quad (9)$$

The above is fit for the situation that the relative speed v_1 is comparative fast. When $v_0^2 \gg v_1^2$, the Lorentz transformation will be degenerated into the Galilean transformation.

Obviously in the mathematics, the Lorentz transformation can be considered as the combination of two parts of coordinate transformations. a) The first step. By means of the property of orthogonal transformation, the coordinate system transforms from $\mathbb{H}(ir_0, r_k)$ into $\mathbb{H}'(ir'_0, r'_k)$, and this part of coordinate transformation possesses the initial values. b) The second step. Making use of the property of parallel-movement transformation, two coordinate systems, $\mathbb{H}(ir_0, r_k)$ and $\mathbb{H}'(ir'_0, r'_k)$, are transformed into two new ones, $\mathbb{H}(it, r_k)$ and $\mathbb{H}'(it', r'_k)$, and this part of coordinate transformation possesses a part of initial values.

3. VELOCITY AND ACCELERATION

In the complex quaternion coordinate system $\mathbb{H}(iv_0, v_k)$, the complex quaternion acceleration is, $\mathbb{D}(d_j) = id_0\mathbf{i}_0 + \Sigma d_k\mathbf{i}_k$. In the complex quaternion coordinate system $\mathbb{H}'(iv'_0, v'_k)$, the complex quaternion acceleration is, $\mathbb{D}'(d'_j) = id'_0\mathbf{i}'_0 + \Sigma d'_k\mathbf{i}'_k$. Making use of the scalar part of velocity and of acceleration, and the norm of velocity and of acceleration, it is able to deduce the coordinate transformation and invariants, in the complex quaternion coordinate system for the velocity and acceleration. In other words, substituting the velocity and acceleration for the radius vector and velocity respectively in the above context, the paper is capable of inferring the Lorentz-like transformation and so forth for the velocity. Herein d_j and d'_j are all real.

3.1. Galilean-like Transformation

From the complex quaternion velocity and acceleration, it is able to deduce one coordinate transformation. In the complex quaternion coordinate transformation, according to the physical property, that the scalar parts of velocity and of acceleration remain invariable respectively, there are,

$$v'_0 = v_0, \quad d'_0 = d_0, \quad (10)$$

where $v_0 = v_{00} + d_0 t$, $v'_0 = v'_{00} + d'_0 t'$. v_{00} and v'_{00} are initial values. $d_1 = \partial v_1 / \partial t$, $d'_1 = \partial v'_1 / \partial t'$.

The above consists of two invariants in the complex quaternion space, and the coordinate transformation can be derived from these two invariants. This transformation is similar to the Galilean transformation. When two coordinate systems possess one relative movement along the direction, $v_1\mathbf{i}_1$, with the relative acceleration, d_1 , the coordinate transformation is,

$$v'_0 = v_0, \quad v'_1 = v_1 - v_0 d_1 / d_0, \quad v'_2 = v_2, \quad v'_3 = v_3. \quad (11)$$

Under the influence of the scalar part d_0 of acceleration, the scalar part v_0 of velocity may be varying. This is similar to the case of the scalar part r_0 of radius vector. That is, under the influence of the scalar part v_0 of velocity, the scalar part r_0 of radius vector may be varying. However for each time t , the scalar part v_0 of velocity remains invariant in the orthogonal transformation. Of course the scalar part v_0 of velocity may be altered for the different time t .

3.2. Lorentz-like Transformation

From the norm of complex quaternion velocity and the complex quaternion acceleration, it is able to infer one coordinate transformation. In the complex quaternion coordinate systems \mathbb{H} , the norm of complex quaternion velocity is, $S_V = \mathbb{V} \circ \mathbb{V}^* = -v_0^2 + \Sigma v_k^2$. And in the complex quaternion coordinate systems \mathbb{H}' , the norm of complex quaternion velocity is, $S'_V = \mathbb{V}' \circ \mathbb{V}'^* = -v'^2_0 + \Sigma v'^2_k$. In the complex quaternion coordinate transformation, according to the physical property, which the norm of velocity and the scalar part of acceleration remain invariable respectively, there are,

$$S'_V = S_V, \quad d'_0 = d_0. \quad (12)$$

The above covers two invariants in the complex quaternion space, and the coordinate transformation can be deduced from two invariants. This transformation is similar to the Lorentz

transformation. When two coordinate systems possess one relative movement along the direction, $v_1\mathbf{i}_1$, with the relative acceleration, d_1 , the coordinate transformation is,

$$v'_1 = (v_1 - v_0 d_1 / d_0) / (1 - d_1^2 / d_0^2)^{1/2}, \quad v'_2 = v_2, \quad (13)$$

$$v'_0 = (v_0 - v_1 d_1 / d_0) / (1 - d_1^2 / d_0^2)^{1/2}, \quad v'_3 = v_3. \quad (14)$$

The above is fit for the situation that the relative acceleration d_1 is comparative high. When $d_0^2 \gg d_1^2$, the above will be degenerated into the Galilean-like transformation.

In the complex quaternion space, one invariant (or basic postulate), applied by the Galilean and Lorentz transformations, is that the speed of light is invariable. And this basic postulate is applied in the Classical Mechanics and Special Theory of Relativity. However the above applies one different invariant (or basic postulate), that is, the speed of light is variable.

At one interface between two different optical media (such as, the gas and liquid), the speed of light is variable obviously. In the local bulky region of this interface, the transmitted light will vary gradually its speed from one value to the other. If the thickness of this interface is large enough, the variation of the speed of light should be in evidence. Modifying the thickness of interface between the gas and liquid, the observer may be able to measure, d_0 , which is the derivative of the speed of light with respect to the time t .

Obviously the paper spreads the application range of coordinate transformations in the complex quaternion space. In the paper, the application range of coordinate transformations was extended from the Galilean and Lorentz transformations in the vacuum, into the Lorentz-like transformation in the waveguide.

4. RADIUS VECTOR, VELOCITY, AND ACCELERATION

In the complex quaternion coordinate system, making use of not only the scalar part of radius vector, velocity, and acceleration, but also the norm of radius vector, velocity, and acceleration, it is able to deduce some invariants in the complex quaternion coordinate system for radius vector and velocity. Further from a few different combinations of these invariants, the paper is capable of inferring one coordinate transformation as follows.

From the norm of complex quaternion radius vector and of complex quaternion velocity, and the complex quaternion acceleration, it is able to deduce one coordinate transformation. In the complex quaternion coordinate transformation, according to the physical property, the norm of radius vector, the norm of velocity, and the scalar part of acceleration remain invariable respectively, there are,

$$S'_R = S_R, \quad S'_V = S_V, \quad d'_0 = d_0. \quad (15)$$

The above involves three invariants in the complex quaternion space, and the coordinate transformation can be derived from these three invariants. a) From the invariants, Eq. (12), it is capable of inferring the first part of coordinate transformation. When two coordinate systems possess one relative movement along the direction, $v_1\mathbf{i}_1$, with the relative acceleration, d_1 , and the coordinate transformations are, Eqs. (13) and (14); b) From the invariants,

$$S'_R = S_R, \quad (16)$$

it is able to draw out the second part of coordinate transformation. When two coordinate systems possess one relative movement along the direction, $r_1\mathbf{i}_1$, with the relative speed, v_1 , the Lorentz transformation is,

$$r'_1 = (r_1 - r_0 v_1 / v_0) / (1 - v_1^2 / v_0^2)^{1/2}, \quad r'_2 = r_2, \quad (17)$$

$$r'_0 = (r_0 - r_1 v_1 / v_0) / (1 - v_1^2 / v_0^2)^{1/2}, \quad r'_3 = r_3, \quad (18)$$

where v_0 and v'_0 are all constant, however $v'_0 \neq v_0$.

Plugging the ratio (v'_0 / v_0) , from Eqs. (13) and (14), into the above is able to conclude the relation formulae between the times, T and T' . $T = r_0 / v_0$, and $T' = r'_0 / v'_0$. Obviously the time t and the velocity v_0 both are changeable. The above is fit for the situation, in which the relative speed v_1 and relative acceleration d_1 both are comparative high.

5. DISCUSSIONS

In the complex quaternion space, when the coordinate system transforms orthogonally, the scalar is invariable. This scalar includes the scalar part of and norm of one complex quaternion physics quantity.

According to the above property, it is able to deduce various coordinate transformations of the complex quaternion physics quantity. In the coordinate system for the radius vector and velocity, one infers the Galilean and Lorentz transformations for the complex quaternion radius vector. In the coordinate system for the velocity and acceleration, the paper concludes the Galilean-like and Lorentz-like transformations for the complex quaternion vector. Obviously in the coordinate system for the radius vector, velocity, and acceleration, the combinatorial coordinate transformation is comparative complicated.

It should be noted that the investigation for the coordinate transformations has examined only some simple cases in the complex quaternion space. Despite its preliminary characteristics, this study can clearly indicate that some invariants and the Lorentz transformation for the radius vector and so on can be derived from the orthogonal transformation of the complex quaternion system, revealing the influence of velocity on the radius vector. Meanwhile making use of the orthogonal transformation of complex quaternion system, the paper is capable of deducing the Galilean-like and Lorentz-like transformations and so on for the velocity and acceleration, uncovering the influence of acceleration on the velocity. In the following study, the research will concentrate on only the investigations and applications of the Lorentz-like transformation for the velocity and so on.

ACKNOWLEDGMENT

This project was supported partially by the National Natural Science Foundation of China under grant number 60677039.

REFERENCES

1. Edmonds, J. D., "Quaternion wave equations in curved space-time," *International Journal of Theoretical Physics*, Vol. 10, No. 2, 115–122, 1974.
2. Weng, Z.-H., "Angular momentum and torque described with the complex octonion," *AIP Advances*, Vol. 4, No. 8, 087103, 16 Pages, 2014.
3. Nakamura, T. K., "Lorentz transform of black body radiation temperature," *Europhysics Letters*, Vol. 88, No. 2, 20004, 4 Pages, 2009.
4. Grusky, S. M., K. V. Khmelnytskaya, and V. V. Kravchenko, "On a quaternionic Maxwell equation for the time-dependent electromagnetic field in a chiral medium," *Journal of Physics A: Mathematical and General*, Vol. 37, No. 16, 4641–4647, 2004.
5. Acevedo, M. M., J. López-Bonilla, and M. Sánchez-Meraz, "Quaternions, Maxwell equations and lorentz transformations," *Apeiron*, Vol. 12, No. 4, 371–384, 2005.
6. Abonyi, I., J. F. Bito, and J. K. Tar., "A quaternion representation of the Lorentz group for classical physical applications," *Journal of Physics A: Mathematical and General*, Vol. 24, No. 14, 3245–3254, 1991.
7. Teli, M. T., "Quaternionic form of unified Lorentz transformations," *Physics Letters A*, Vol. 75, No. 6, 460–462, 1980.

Realization of a Compact High Speed Mass Storage System

Haishan Tian, Wenge Chang, and Xiangyang Li

College of Electronic Science and Engineering

National University of Defense Technology, Deya Street 109, Changsha 410073, China

Abstract— Conventional on-board storage systems are often weighty, large and high power consumption, which can't meet the requirement of the miniature airborne synthetic aperture radar (SAR) system. A new data storage system, integrated with SAR signal processor, is presented in this paper. The compact flash (CF) card and the FPGA are used as storage medium and the host respectively, in the data storage system. However, the major problem of high speed data storage is the irregular write response time due to the internal overhead in the card and frequently cluster switching involving retrieving and updating of cluster connection information. Two methods are presented in this paper to solve the problem. The first one is that the DDR3 flashes connecting with the DSP are iteratively used as the buffer of the SAR data. Another method is that all the available clusters are pre-allocated at once when the files are created. To verify our proposal, the prototype data storage system is implemented on a signal processing board and a CF card with the capacity of 128 GB. The added size, weight, and power consumption for the data storage are really small. Moreover, the data writing rate is over 100 MB/s. As a consequence, the system achieves our goal successfully in that storage system of the miniature SAR is compact, high speed and large capacity.

1. INTRODUCTION

There is a growing interest in lightweight cost-effective synthetic aperture radar (SAR) with the fast image generation capacity and even small enough to be mounted on a miniature aerial vehicles (AVs). This demands for the compact SAR components. With ongoing bandwidth growing of the beat spectrum of the SAR, the compact storage system with the capacity of the high speed mass storage is acute needed in some applications where the bandwidth of the data links is limited.

At present, the hard magnetic disk, solid-state disk, flash and CompactFlash (CF) card are the usual mediums for the data storage [1]. The CF card is the most suitable medium for the data storage of the SAR data due to its high data transfer rate, small dimension, large capacity, easily be upgraded, shock resistance and other features [2]. Based on the CF card, this paper addresses the design of the high speed mass storage. It should be mentioned that the prototype of the storage system is a real-time SAR imaging processor which includes ADC, FPGA, DSP, and CF card, as shown in Figure 5. The SanDisk Extreme Pro CF card with the capacity of 128 GB is the high speed storage medium; the Xilinx Virtex-6 XC6VLX75T type FPGA is used as the host of the CF card; the TI TMS320C6678 DSP is used for signal processing. The data storage system can achieve the data transfer rate of 100 MB/s.

2. SYSTEM DESIGN

As the capacity of the CF card increases up to 128 GB, the FAT file system, which has simple architecture and a higher compatibility with other systems, is needed to manage the storage effectively [4, 5]. The FAT file system contains four major parts: Master Boot Record (MBR), Dos Boot Record (DBR), File Allocation Table (FAT) and DATA region. These four parts contain the boot codes, system parameters, data cluster interconnection information, and data of the files, respectively.

There are two obstacles for the demand of the high speed of the data storage. The first one is the internal overhead, such as the operation of erasing the content of the sectors is needed before the sectors write operation of the CF card. The time of such implicit operation is relatively long and can't be predicted precisely. Another obstacle is the frequently cluster switching that the data writing of a new cluster needs a series of operations, such as retrieving and updating of cluster connection information in FAT, which produce irregular response times, especially for the data writing with large size. Follows are implementation architecture of the data storage and relatively methods to overcome these two obstacles.

2.1. Data Flow

The article addresses the data flow of the data storage/signal processing integrated system, as shown in Figure 1. The FPGA fetches the raw data from the A/D converter and preprocesses these data to generate the base band data (preprocessed data), the sample rate of which is much lower than that of the raw data. Then the preprocessed data is feed to the DSP. For the image data storage, the DSP generates the resulting image data and sends the imaging data to the DDR3 flashes connecting with DSP. For the preprocessed data storage, the DSP doesn't process the received data and just sends these data to the DDR3 flashes. Finally, the SAR data is read from the DDR3 flashes by the DSP and sent back to the FPGA when the SAR data could be wrote into the CF card by the FPGA.

To meet the demand of high data transfer rate, the SRIO interface between the FPGA and the DSP, and the DDR3 interface between the DSP and the DDR3 flashes, are used for data transfer. The bandwidth of the SRIO is 5 Gbps and the DDR3 can reach the data transfer rate over 10 GB/S, which are all much faster than the maximum data writing rate (150 MB/s now) of the CF card. In order to solve the problem of the mismatch of the data rate between the SRIO and the CF card, two FIFOs in the FPGA are added as the buffers of the SAR data.

2.2. Implementation Architecture

Based on the flow chart of data storage/signal processing integrated system in Figure 1, the data storage contains two types of process. The first process consists of data transfer that SAR data is transferred from the DDR3 flashes to the FPGA, and the data reading/writing of the CF card. Another process is control logic, whose primary function is controlling the flow of the first process. As a consequence, the implementation of the data storage could be divided into two channels. The first one is the data channel that is made up of the data transfer unit and the CF card read/write unit which has six subunits: the DBR and MBR read unit, FAT read unit, FAT write unit, FDT read unit, FDT write unit, and data write unit. Figure 2 illustrates the implementation architecture of the data storage. To get the SAR data, the data transfer unit transfers the SAR data (preprocessed or imaging data) from the DDR3 flashes to the FPGA. Finally, the six subunits of the CF card read/write unit implement parameters searching, the cluster connection retrieving and updating, the file directory retrieving and updating, and the data writing to the CF card, respectively. The schematic of the FPGA implementation for the data transfer unit and the CF card read/write unit are shown in Figure 3 and Figure 4, respectively.

In the control channel, there are five sub-controllers: the data transfer controller, DBR and MBR read controller, FAT read/write controller, FDT read/write controller and data write controller. The first sub-controller controls the operations of the data transfer. The other sub-controllers form the file system controller, which controls the CF card read/write operation to store data in the form of FAT32 file system.

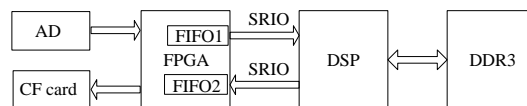


Figure 1: The data flow of the storage system.

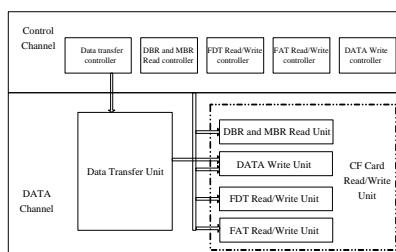


Figure 2: The FPGA implementation architecture of the data storage.

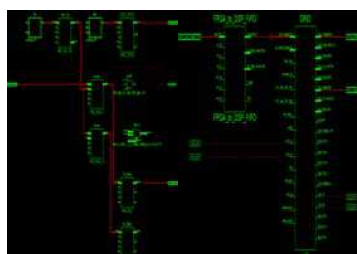


Figure 3: The schematic of the implementation about data transfer unit.

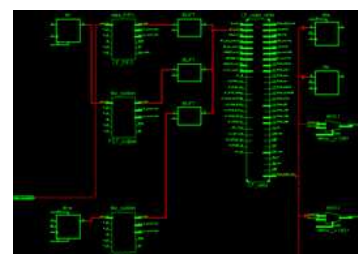


Figure 4: The schematic of FPGA implementation about CF card read/write unit.

2.3. High Speed Design

For the first obstacle for the high speed data storage, the long and unpredictable write preparing time is a vital problem. The preparation time is not fixed, usually within 700 μs , but occasionally abnormal time can reach 60 μs . Assume the data transfer rate is 80 MB/s, the data buffer with capacity of at least 4.8 MB is required. However, the capacity of 4.8 MB is much larger than that of the memory in the XC6VLX75T FPGA, with the RAMs of 700 KB. The way to expand the memory of the FPGA, at first glance, is that the large capacity buffer, such as the Static RAM [6], FIFO and Dynamic RAM, connects with the FPGA. But the complexity, size and power consumption of data storage system will be increased. As the matter of fact, the buffer already exists: the DDR3 Flashes with very large capacity has been connected with the DSP, as shown in Figure 1. If this large capacity memory can be used as the FPGA's buffer, whatever the design and the implementation of the storage would be very compact. Fortunately, the answer is positive. As we noticed in Figure 1, the FPGA is connected with the DSP via SRIO. The buffer to the DSP is completely transparent for the FPGA through the SRIO interface. In other words, the FPGA can access the buffer of the DSP.

For the second obstacle of the high speed data storage that the FAT32 file system requires frequently retrieving and updating of the cluster connection and the file directory, the procedure is so complex that it may influence the stability of system and take relatively long time as well. In this paper, the method called file system pre-allocation is adopted to reduce the switching overhead in the FAT file system operation. Firstly, all data is stored orderly in the DATA region of CF card, which makes the cluster connections ordinal in the FAT as well. Secondly, the size and name of files are constrained in a certain rule, which can make it possible that omitting the operation of information retrieving in the FAT and FDT, because the cluster connection information of all files is clear according to rule. Thirdly, all available clusters are pre-allocated in the FAT according to the rules we made once the storage procedure starts. So the file can be written without further operation of cluster allocation.

3. EXPERIMENT

To evaluate the performance of data storage system, we have implemented the data storage system in the prototype of the SAR real-time processor, as shown in Figure 5. Yellow marked parts are the key devices of the data storage system: CF card, FPGA, DDR3 Flashes and DSP. The added size for the data storage is quite small, about 60 mm \times 41 mm \times 2 mm and the added weight is no more than 70 grams.

The capacity, speed and power consumption are the key parameters of storage system. Obviously, the capacity of storage system equals that of CF card, about 128 GB. Based on the flow chart of the data storage/signal processing integrated system, the data transfer rate of the SRIO interface and the DDR3 interface, and data writing rate of the CF card are three restriction factors for the speed of the CF card. As a consequence, their data rates needed to be tested on the data storage system.

The data rates of the SRIO and DDR3 interface are all independent of the data transfer direction. In the test of the data transfer rate of the SRIO interface, the data with different count is generated by the FPGA and transferred to the DSP through the SRIO interface. The DSP measures the time and validates the correctness of the data. The result of the DSP indicates all transferred data is

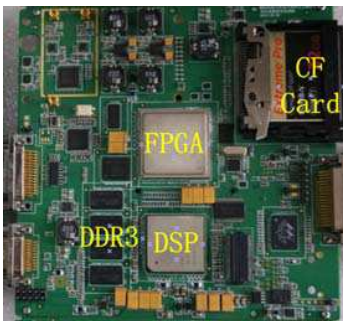


Figure 5: Hardware platform of data storage system.

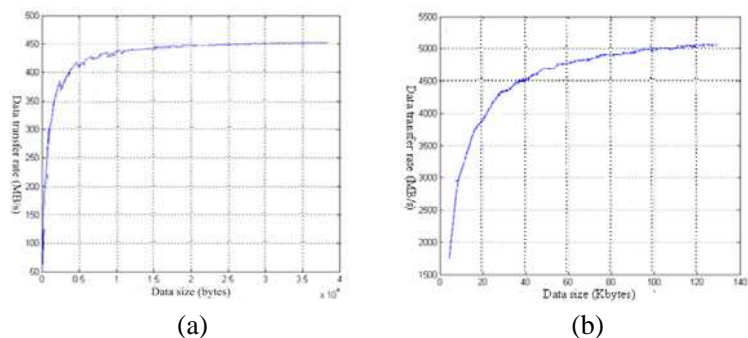


Figure 6: Data transfer rate of SRIO and DDR3 interface. (a) Data transfer rate of SRIO. (b) Data transfer rate of DDR3.

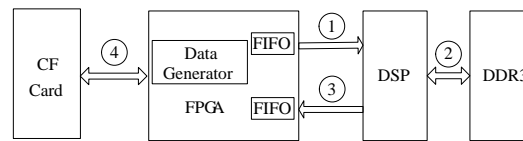


Figure 7: Flow chart of experiment.

correct. The data transfer data rate reaches about 452 MB/s when the data count is 32 KB and keeps steadily as the count of data increases, as shown in Figure 6(a).

For test of the data transfer rate of the DDR3 interface, the DSP generates the data with different count and sends the data to the DDR3 flashes, and measures the transfer time. Then the data stored in the DDR3 is read by the computer through the DSP emulator and validated by the computer. The result indicates the data is all correct. Figure 6(b) shows the data transfer rate of the DDR3, which reaches about 5032 MB/s when the data count is 120 KB and keeps steadily as the count of data increases.

Figure 7 illustrates the flow chart of the speed test of the data storage system. The data with the capacity of 8 GB generated by the FPGA in the sustained rate of 100 MB/s and sent to the DSP through the SPIO interface. The DSP fetches the data and sends them into the DDR3 Flashes. Then the data in the DDR3 is read by the DSP and transferred to the FIFO of the FPGA when the CF card starts to store the data. Finally the data is written to the CF card. The data in the CF card is read and validated by the Computer. The result indicates that the data stored in the CF card is same as that of the data generator in the FPGA. So the maximum transfer rate of storage system is more than 100 MB/s.

The total power consumption of the data storage/signal processing system is about 18 W and the power for implementing the function of signal processing is more than 16.8 W in the temperature of 18°C. As a consequence, the add power consumption for the data storage is no more than 1.2 W.

4. CONCLUSION

The design of data storage system with high speed and large capacity is presented and implemented in the prototype of SAR real-time processor in this paper. The CF card is used as the basic medium and the FPGA is as its host in the storage system. The DDR3 flashes connecting with the DSP are used to make up the disadvantage of the CF card, of which the write response time is irregular. The method of file system pre-allocation is presented to solve the switching overhead problem of FAT32 file system. According to the experimental test of storage system, the system achieves our goal successfully in that storage system of the miniature SAR is compact, high speed and large capacity.

It is pointed that the storage system can also be easily modified to be a SAR data re-player where the preprocessed SAR data stored in the CF card is read by the FPGA and then transferred to the DSP to generate the imaging data. This function is very useful for the test of the SAR imaging algorithm. Moreover, CF card with higher data writing rate and larger capacity can be used in this system without modifying any hardware. In other words, this storage system could be upgraded in future.

REFERENCES

1. Qiao, L. and H. Xu, "Realization of high speed mass storage data record card with CF card and SDRAM," *IEEE International Instrumentation and Measurement Technology Conference*, 1363–1366, Texas, United States, May 2010.
2. Li, L. and Y. Yang, "The application of CF card in the system of real-time processing on high-volume data," *2nd International Conference on Information Engineering and Computer Science (ICIECS)*, 1062–1065, Wuhan, China, Dec. 2010.
3. Compact Flash Association, CF+ and Compact Flash Specification Revision 4.1, 2007.
4. Choi, M., H. Park, and J. Jeon, "Design and implementation of a FAT file system for reduced cluster switching overhead," *2nd International Conference on Multimedia and Ubiquitous Engineering*, 355–360, Busan, Korea, Apr. 2008.
5. Park, S. and S.-Y. Ohm, "New techniques for real-time FAT file system in mobile multimedia devices," *IEEE Transactions on Consumer Electronics*, Vol. 52, No. 1, 1–9, 2006.
6. Deng, L., H. Zhao, and Y. Yang, "Realization of high-speed and big-capability data recorder," *11th International Conference on Electronic Measurement & Instruments (ICEMI)*, 1062–1065, Harbin, China, Aug. 2013.

Analyzing Five-layer Planar Optical Waveguides with Kerr-type Nonlinear Metamaterial Guiding Films

Yaw-Dong Wu, Ming-Hsiung Cheng, and Tien-Tsorng Shih

Department of Electronic Engineering
National Kaohsiung University of Applied Sciences, Kaohsiung, Taiwan

Abstract— In this paper, we proposed a method to analyze the electric field distributions of the five-layer planar optical waveguide structure with nonlinear metamaterial guiding films. The proposed nonlinear metamaterial planar optical waveguide is composed of two different kinds of media. One is the Kerr-type nonlinear metamaterial in the guiding films, and the other is the linear double-positive medium (DPS) in the interaction layer, in the cladding and in the substrate. We have derived the transcendental equations of the proposed five-layer planar optical nonlinear metamaterial waveguide structure. The propagation characteristics of the transverse electric (TE) waves were investigated analytically and numerically in the this structure. The analytical and numerical results show excellent agreement. The simulation results are helpful to figure out the propagation situation of the TE polarized waves in the five-layer nonlinear metamaterial waveguide structure. The transverse magnetic (TM) polarized waves can also be predicted by the similar process. It can also be very useful for designing a planar nonlinear metamaterial waveguide devices.

1. INTRODUCTION

Recently, a great number of papers are presented and investigated in the metamaterial. The metamaterial is a new type of artificial materials as well as so-called the left-handed medium (LHM). The metamaterial exhibits simultaneously negative dielectric permittivity and magnetic permeability [1–3]. In the past, most of papers have been concerned with linear metamaterial in wave propagation, applications, and components [4–12]. The kerr-type nonlinear medium has a phenomenon of optical solitons. From the theoretical investigation of spatial optical solitons, the applications of the kerr-type nonlinear medium have been proposed [13, 14]. Zharov et al. [15] have analyzed the nonlinear properties of left-handed metamaterials in two-dimensional periodic structure created by arrays of wires and split-ring resonators. Shadrivov et al. [16] have studied both linear and nonlinear surface waves at the interface between a left-handed medium and a conventional medium. Here we investigate the electric field distributions of the five-layer planar optical waveguide structure with the kerr-type nonlinear metamaterial guiding films. The propagation characteristics of the TE waves were investigated analytically and numerically. The analytical and numerical results show excellent agreement.

2. ANALYSES AND NUMERICAL RESULTS

In this section, the modal theory was used to drive the TE-polarized field for the five-layer planar optical waveguide with the kerr-type nonlinear metamaterial guiding films, as shown in Fig. 1. We consider the TE waves propagating along the z -direction. The wave equation can be reduced to as follows.

$$\frac{\partial^2 E_y}{\partial z^2} + \frac{\partial^2 E_y}{\partial x^2} + \frac{\partial^2 E_y}{\partial y^2} = \frac{n_j}{c^2} \frac{\partial^2 E_y}{\partial t^2}, \quad j = f, c, s, i \quad (1)$$

In Eq. (1) the electric field in each layer can be expressed as:

$$E_y(x, z, t) = E_j(x) \exp[j(\omega t - \beta k_0 z)], \quad j = f, c, s, i \quad (2)$$

where β is the effective refractive index, ω is the angular frequency, and k_0 is the wave number in the free space. For the Kerr-type nonlinear metamaterial, the square of the refractive index n_f^2 can be expressed as:

$$n_f^2 = \mu_f \varepsilon_f + \alpha |E(x)|^2 \quad (3)$$

where $\mu_f \varepsilon_f$ is the square of the linear refractive index of the nonlinear metamaterial and α is the nonlinear coefficient. By substituting Eq. (2) into the wave equation Eq. (1), considering the case

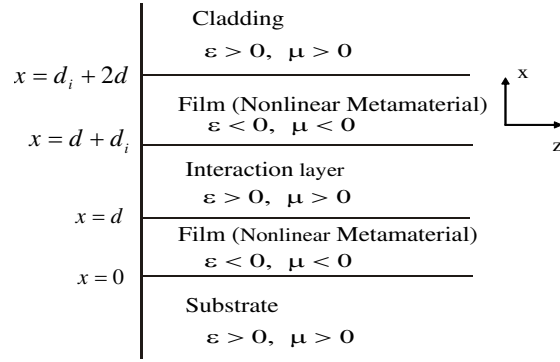


Figure 1: The structure of five-layer planar optical waveguide with nonlinear metamaterial film.

$\beta < \varepsilon_f \mu_f$ and matching the boundary conditions, the transverse electric fields in each layer can be written as:

$$E_y(x) = E_c \exp\{-P_c[x - (2d + w)]\} \quad 2d + w < x \quad (4)$$

$$E_y(x) = b \cdot cn\{A[x - (d + w) + x_0] | B\} \quad d + w < x < 2d + w \quad (5)$$

$$E_y(x) = E_i \{\exp[-P_i(x - d)] + \exp\{P_i[x - (d + w)]\}\} \quad d < x < d + w \quad (6)$$

$$E_y(x) = b \cdot cn\{A[x + x_0] | B\} \quad 0 < x < d \quad (7)$$

$$E_y(x) = E_s \exp[P_s x] \quad x < 0 \quad (8)$$

where

$$A = \left[(a^2 + b^2) \left(\frac{\alpha_2 k_0^2}{2} \right) \right]^{1/2}, \quad B = \frac{b^2}{a^2 + b^2}, \quad a^2 = \frac{\sqrt{H^4 + 2\alpha_2 k_0^2 K} + H^2}{\alpha_2 k_0^2}$$

$$b^2 = \frac{\sqrt{H^4 + 2\alpha_2 k_0^2 K} - H^2}{\alpha_2 k_0^2}, \quad H^2 = k_0^2 (n_2^2 - \beta^2), \quad P^2 = k_0^2 (\beta^2 - n_1^2) \quad j = c, i, s \quad (9)$$

The parameters E_s and E_d are the values of the electric field at the lower (at $x = 0$) and upper (at $x = w + 2d$) boundaries of the film, respectively. K and x_0 are the first and the second constant of integration. The cn is a specific Jacobian elliptic function. For simplicity, the modulus B is omitted in the following discussions. On the other hand, the first integration can be expressed as follows:

$$K = k_0^2 E_s^2 \left(\left(\frac{\mu_f}{\mu_s} \right)^2 (\beta^2 - \varepsilon_s \mu_s) - (\varepsilon_f \mu_f - \beta^2) + \frac{\alpha E_s^2}{2} \right)$$

$$= k_0^2 E_c^2 \left(\left(\frac{\mu_f}{\mu_c} \right)^2 (\beta^2 - \varepsilon_c \mu_c) - (\varepsilon_f \mu_f - \beta^2) + \frac{\alpha E_c^2}{2} \right) \quad (10)$$

By the matching boundary condition, the transcendental equation can be expressed as:

$$\frac{E_d P \mu_f}{\mu_i} = \left\{ A \cdot [E_{i1} \exp(-Rw) + E_{i2}] \cdot sn[Ad] dn[Ad] \cdot \left\{ 1 - B \cdot \left[1 - \left(\frac{E_{i1} \exp(-Rw) + E_{i2}}{b} \right)^2 \right] \right\} \right.$$

$$- A \cdot [E_{i1} \exp(-Rw) + E_{i2}] \cdot B_4 \cdot sn[A_4 d] cn^2[Ad] dn[Ad] \left[1 - \left(\frac{E_{i1} \exp(-Rw) + E_{i2}}{b} \right)^2 \right]$$

$$+ \left\{ cn[Ad] dn^2[Ad] - \left[\frac{E_{i1} \exp(-Rw) + E_{i2}}{b} \right]^2 \cdot B_4 \cdot sn^2[Ad] cn[Ad] \right\}$$

$$\cdot R \cdot [E_{i1} \exp(-Rw) - E_{i2}] \frac{\mu_f}{\mu_i} / P \cdot \left\{ 1 - B \cdot sn^2[Ad] \cdot \left[1 - \left(\frac{E_{i1} \exp(-Rw) + E_{i2}}{b} \right)^2 \right] \right\}^2 \quad (11)$$

where sn and dn are the Jacobian elliptic functions. Eq. (11) can be solved numerically. on the other hand, for the case $\epsilon_f \mu_f < \beta$, we only have to replace A, B, a, b , and x_0 in Eq. (9) with A', B', a', b' , and x'_0 , and get these equations with similar representations. When constants β and E_0 are determined, all the other constants, K, A, a, b, B , and E_d are also determined.

We used the formulae derived in the preceding section to calculate the transverse electric field functions in the five-layer planar optical waveguides with the kerr-type nonlinear metamaterial guiding films. We use numerical examples to presented some simulation results. The numerical results are shown from the Figs. 2–6. Figure 2 shows the curve of the transcendental equation in nonlinear metamaterial waveguide with constant: $\mu_f = -2, d_f = 3 \mu\text{m}, d_i = 3 \mu\text{m}, \epsilon_f \mu_f = 1.57, \epsilon_s \mu_s = \epsilon_c \mu_c = 1.55, \alpha = 6.3786 \mu\text{m}^2/\text{V}^2$, and $\lambda = 1.3 \mu\text{m}$. As the results shown in Figs. 2–6, the electric field distributions for several points as shown in the Fig. 2.

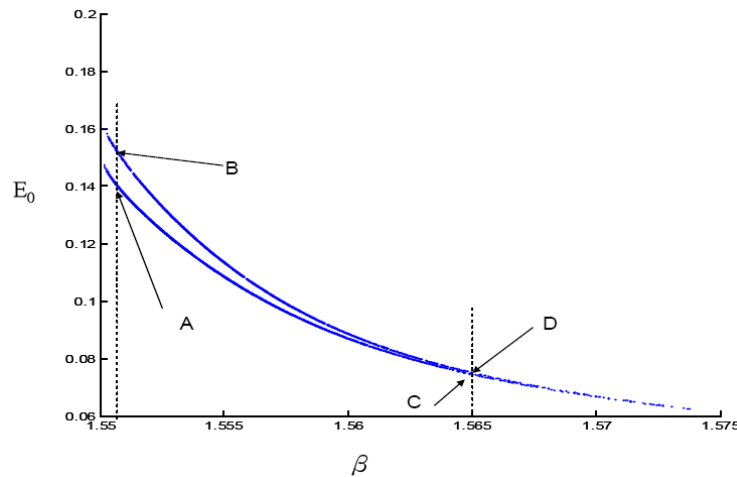


Figure 2: Dispersion curve of the five-layer waveguide with kerr-type nonlinear metamaterial guiding film.

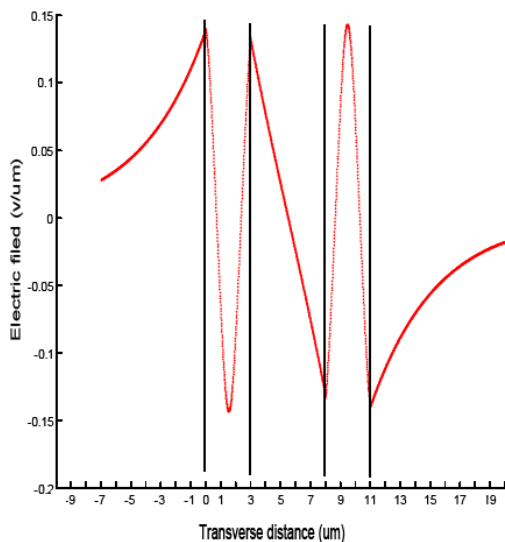


Figure 3: The electric field distributions with respect to A point in the Fig. 2.

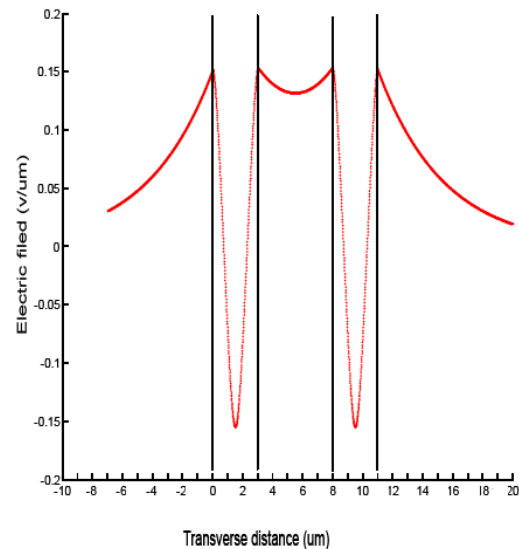


Figure 4: The electric field distributions with respect to B point in the Fig. 2

3. CONCLUSION

In this paper, we have analyzed the transverse electric field of each layer in five-layer planar optical waveguide with the kerr-type nonlinear metamaterial guiding films. The transcendental equation

can be depicted by the value of the boundary electric field and the effective refraction index. We also show the evolutions of the electric field with different effective refraction index. The similar process can be used to predict the propagation characteristics of TM waves in this structure. The simulation result is also helpful to figure out the propagation situation of the TE polarized waves.

ACKNOWLEDGMENT

This work was partly supported by Taiwan's National Science Council under Grants NSC-103-2221-E-151-004.

REFERENCES

1. Veselago, V. G., "The electrodynamics of substances with simultaneously negative values of ϵ and μ ," *Sov. Phys. Usp.*, Vol. 10, 509–514, 1968.
2. Shelby, R. A., D. R. Smith, and S. Schultz, *Science*, Vol. 292, 77–79, 2001.
3. Ziolkowski, R. W. and E. Heyman, "Wave propagation in media having negative permittivity and permeability," *Phys. Rev. E*, Vol. 64, 056625, 2001.
4. Manapati, M. B. and R. S. Kshetrimayum, "SAR reduction in human head from mobile phone radiation using single negative metamaterials," *Journal of Electromagnetic Waves and Applications*, Vol. 23, No. 10, 1385–1395, 2009.
5. Hwang, R.-B., H.-W. Liu, and C.-Y. Chin, "A metamaterial-based E -plane horn antenna," *Progress In Electromagnetics Research*, Vol. 93, 275–289, 2009.
6. Huang, M. D. and S. Y. Tan, "Efficient electrically small prolate spheroidal antennas coated with a shell of double-negative metamaterials," *Progress In Electromagnetics Research*, Vol. 82, 241–255, 2008.
7. Si, L.-M. and X. Lv, "CPW-FED multi-band omni-directional planar microstrip antenna using composite metamaterial resonators for wireless communications," *Progress In Electromagnetics Research*, Vol. 83, 133–146, 2008.
8. Al-Naib, I. A. I., C. Jansen, and M. Koch, "Single metal layer CPW metamaterial band-pass filter," *Progress In Electromagnetics Research Letters*, Vol. 17, 153–161, 2010.
9. Ziolkowski, R. W. and E. Heyman, "Wave propagation in media having negative permittivity and permeability," *Phys. Rev. E*, Vol. 64, 056625, 2001.
10. Milonni, P. W. and G. J. Maclay, "Quantized-field description of light negative-index media," *Opt. Commun.*, Vol. 228, 161–165, 2003.
11. Mirza, I. O., J. N. Sabas, S. Shi, and D. W. Prather, "Experimental demonstration of metamaterial based phase modulation," *Progress In Electromagnetics Research*, Vol. 93, 1–12, 2009.
12. Sabah, C. and S. Uckun, "Multilayer system of Lorentz/drude type metamaterials with dielectric slabs and its application to electromagnetic filters," *Progress In Electromagnetics Research*, Vol. 91, 349–364, 2009.
13. Sukhorukov, A. A., Y. S. Kivshar, H. S. Eisenberg, and Y. Silberberg, "Spatial Optical Solitons in Waveguide Arrays," *IEEE Journal of Quantum Electron*, Vol. 39, No. 1, 31–50, 2003.
14. Johansson, M., A. A. Sukhorukov, and Y. S. Kivshar, "Discrete reduced-symmetry solitons and second band vortices in two dimensional nonlinear waveguide arrays," *Physical Review: E*, Vol. 80, No. 4, 046604–046619, 2009.
15. Zharov, A. A., I. V. Shadrivov, and Y. S. Kivshar, "Nonlinear properties of left-handed metamaterials," *Phys. Rev. Lett.*, Vol. 91, 037401-1, 2003.
16. Shadrivov, I. V., A. A. Sukhorukov, Y. S. Kivshar, A. A. Zharov, A. D. Boardman, and P. Egan, "Nonlinear surface waves in left-handed materials," *Phys. Rev. E*, Vol. 69, 016617, 2004.

Permittivity of Thin Quantum Dot Film with Local Field Effects

M. N. Anokhin, A. A. Tishchenko, and M. N. Strikhanov
National Research Nuclear University “MEPhI”, Moscow, Russia

Abstract— It is known that electronic properties of a quantum dot (QD) depend on its size and shape. Spectrum of emission light of a QD is changed by tuning their core diameter. For example, the cadmium selenite (CdSe) QDs emit blue light when the diameter of the core is 2 nm and emit red light when it is 7 nm [1]. Because of it QDs have a good potential for using in different light emitting devices including organic light emitting diodes (OLEDs). For example, QDs gives a good opportunity for design white OLEDs etc..

1. INTRODUCTION

QD films have a lot of applications in optoelectronic devices because of their unique properties of QD. Such as size- and shape-tunable optical and electronic properties (e.g., the band gap in a QD proportional to its size). QDs are bright and photostable and can show a very high photoluminescence quantum efficiency (around 90%) [2, 3]. So QD films are very perspective for using in different kinds of electronic and optoelectronic device applications [4]. For example, light emitting diodes (QD-LEDs), field-effect transistors (FETs) and photodetectors.

2. DIELECTRIC PROPERTIES OF THIN QUANTUM DOT FILM

Let us consider a thin film of the amorphous substance $2b$ wide. It is composed of N uniformly located spherically symmetric QDs. Let all the QDs be anisotropic and have polarizability $\alpha_{ij}(\omega)$:

$$\alpha_{ij}(\omega) = \alpha_{\perp}(\omega) (\delta_{ij} - e_i e_j) + \alpha_{\parallel}(\omega) e_i e_j. \quad (1)$$

We work in the dipole approximation as a QD diameter is considerably smaller than the wave-length of light:

$$\mathbf{j}^{mic}(\mathbf{r}, \omega) = (-i\omega) \sum_b \mathbf{d}(\mathbf{R}_b, \omega) \delta(\mathbf{r} - \mathbf{R}_b), \quad (2)$$

where $\mathbf{d}(\mathbf{R}_b, \omega)$ is the moment dipolaire of the b -th molecule, $b = \overline{1, N}$, N is the total number of molecules of the substance.

Let put in vacuum a source creating the field \mathbf{E}_0 . Linearity of Maxwell's equations allows us to obtain the Fourier transform of the solution of Maxwell's equations in a medium as sum of an external field (which has not yet interacted with any of the molecules) and a sum of all the secondary fields created by all the molecules [5]:

$$E_i^{mic}(\mathbf{r}, \omega) = E_i^0(\mathbf{r}, \omega) + \frac{1}{2\pi^2} \int d^3l S_{ij}(\mathbf{l}, \omega) \alpha_{jk}(\omega) \sum_b E_k^{mic}(\mathbf{R}_b, \omega) \exp\{-i\mathbf{l}(\mathbf{R}_b - \mathbf{r})\}, \quad (3)$$

where

$$S_{ij}(\mathbf{l}, \omega) = \frac{(\omega/c)^2 \delta_{ij} - l_i l_j}{l^2 - (\omega/c)^2 - i0}. \quad (4)$$

Averaging (3) over the location of other QDs we find the local field E_i^{loc} :

$$E_i^{loc}(\mathbf{R}_a, \omega) = E_i^0(\mathbf{R}_a, \omega) + \frac{1}{2\pi^2} \int d^3l S_{ij}(\mathbf{l}, \omega) \alpha_{jk}(\omega) \int d^3R_{ba} N w(\mathbf{R}_{ba}) E_k^{loc}(\mathbf{R}_a + \mathbf{R}_{ba}, \omega) \exp\{-i\mathbf{l}\mathbf{R}_{ba}\}, \quad (5)$$

where $w(\mathbf{R}_{ba})$ is the probability density of finding the b -th molecule at the distance $\mathbf{R}_{ba} = \mathbf{R}_b - \mathbf{R}_a$ ($k = \overline{1, N-1}$):

$$w(\mathbf{R}) = \frac{1}{V} [1 - f(\mathbf{R})], \quad (6)$$

where $f(\mathbf{R})$ is the radial distribution function, that in fact describes the structure of film.

Averaging over the coordinates of all the QDs of the substance we obtain the macroscopic field:

$$E_i(\mathbf{R}, \omega) = E_i^0(\mathbf{R}, \omega) + \frac{1}{2\pi^2} \int d^3 R' S_{ij}(-\mathbf{R}', \omega) P_j(\mathbf{R} + \mathbf{R}', \omega), \quad (7)$$

where

$$S_{ij}(-\mathbf{R}', \omega) = \int d^3 q S_{ij}(\mathbf{q}, \omega) \exp\{-i\mathbf{q}\mathbf{R}'\}, \quad (8)$$

$$P_j(\mathbf{R}, \omega) = n\alpha_{jk}(\omega) E_k^{loc}(\mathbf{R}, \omega), \quad (9)$$

where n is the number density:

$$n = \frac{N}{V} \quad (10)$$

Now we can obtain a relation between the macroscopic field \mathbf{E} and the local field \mathbf{E}^{loc} :

$$E_i(\mathbf{R}, \omega) = E_i^0(\mathbf{R}, \omega) + \frac{1}{2\pi^2} \int d^3 R' S_{ij}(-\mathbf{R}', \omega) P_j(\mathbf{R} + \mathbf{R}', \omega). \quad (11)$$

We write this equation in the coordinates (\mathbf{q}, z, ω) :

$$E_i(\mathbf{q}, z, \omega) = E_i^{loc}(\mathbf{q}, z, \omega) + 4\pi n \int \frac{d^2 R'}{(2\pi)^3} \int_{-b-Z}^{b-Z} dZ' \exp\{i\mathbf{q}\mathbf{R}'\} f(\mathbf{R}') S_{ij}(-\mathbf{R}', \omega) \alpha_{jk}(\omega) E_k^{loc}(\mathbf{q}, z, \omega). \quad (12)$$

Equation which connects the Fourier transforms of the local and macroscopic fields [6]:

$$t_{ik}(\mathbf{q}, \omega) E_k^{loc}(\mathbf{q}, \omega) = E_i(\mathbf{q}, \omega), \quad (13)$$

where

$$t_{ik}(\mathbf{q}, \omega) = \delta_{ik} + 4\pi n \int \frac{d^2 R'}{(2\pi)^3} \int_{-b-Z}^{b-Z} dZ' \exp\{i\mathbf{q}\mathbf{R}'\} f(\mathbf{R}') S_{ij}(-\mathbf{R}', \omega) \alpha_{jk}(\omega). \quad (14)$$

Taking into account that:

$$4\pi P_i(\mathbf{q}, z, \omega) = [\varepsilon_{ij}(\mathbf{q}, z, \omega) - \delta_{ij}] E_j(\mathbf{q}, z, \omega). \quad (15)$$

And using Eq. (9) and Eq. (13) we obtain the dielectric permittivity:

$$\varepsilon_{ik}(\mathbf{q}, z, \omega) = \delta_{ik} + 4\pi n \alpha_{ij}(\omega) t_{jk}^{-1}(\mathbf{q}, z, \omega). \quad (16)$$

In the long-wave approximation:

$$n^{-1/3} \ll q^{-1} \ll c/\omega. \quad (17)$$

$$\varepsilon_{ik}(z, \omega) = \varepsilon_{\perp}(z, \omega) (\delta_{ik} - e_i e_k) + \varepsilon_{\parallel}(z, \omega) e_i e_k, \quad (18)$$

where

$$\varepsilon_{\perp}(z, \omega) = \frac{1 + 4\pi n \alpha_{\perp}(\omega) (2/3 - c(z))}{1 - 4\pi n \alpha_{\perp}(\omega) (1/3 + c(z))}, \quad (19)$$

$$\varepsilon_{\parallel}(z, \omega) = \frac{1 + 4\pi n \alpha_{\parallel}(\omega) (2/3 - c(z))}{1 - 4\pi n \alpha_{\parallel}(\omega) (1/3 + c(z))},$$

$$c(z) = \int d^3 l \int_{Z-b}^{Z+b} \frac{dZ'}{2\pi} \exp\{il_z Z'\} f(\mathbf{l}_{\perp}, -Z'). \quad (20)$$

The radial distribution function $f(\mathbf{R})$ is defined as:

$$f(\mathbf{R}) = n(\mathbf{R})/n, \quad (21)$$

where $n(\mathbf{R})$ is the local number density, that determines number of QDs $dN(\mathbf{R})$ in the differential of volume dV on the distance \mathbf{R} from the fixed QD:

$$n(\mathbf{R}) = \frac{dN(\mathbf{R})}{dV} \quad (22)$$

Function $f(\mathbf{R})$ can be found experimentally. For example, using x-ray diffraction [7].

3. DISCUSSION

In this work we study a natural variation of dielectric properties of a very thin film consisting of QDs, with thickness in some QD diameters. For such thin film usually used macroelectrodynamical approach does not work, which needs improving of existing techniques. We manage to obtain the generalized Clausius-Mossotti relation for dielectric permittivity of thin film from the first principles with help of the local field theory [5–7]. The distinctive feature of the local field theory is that it permits to take into account interaction between the QDs, and to express the results through the properties of single QD and radial function of distribution, characterizing their mutual disposition. In article [5] such method was developed for an amorphous substance occupying a half-space. Here we develop this technique for the case of very thin layer using dipole approximation assuming that a QD diameter is considerably smaller than the wave-length of light. We obtain the conditions when resonance lines for system of interacting QDs are shifted in comparison with the resonance lines of a single QD, which is defined by local field effects.

REFERENCES

1. Uddin, A. and C. C. Teo, “Fabrication of high efficient organic/CdSe quantum dots hybrid OLEDs by spin-coating method,” *Proc. SPIE 8622, Organic Photonic Materials and Devices XV*, 86220X, Mar. 6, 2013.
2. Flory, F., Y. J. Chen, C. C. Lee, L. Escoubas, J. J. Simon, P. Torchio, J. Le Rouzo, S. Vedraïne, H. Derbal-Habak, J. Ackermann, I. Shupyk, and Y. Didane, “Optical properties of dielectric thin films including quantum dots,” *Applied Optics*, Vol. 50, No. 9, C129–C134, 2011.
3. Jauffred, L., A. C. Richardson, and L. B. Oddershede, “Three-dimensional optical control of individual quantum dots,” *Nano Letters*, Vol. 8, No. 10, 3376–3380, 2008.
4. Korala, L., Z. Wang, Y. Liu, S. Maldonado, and S. L. Brock, “Uniform thin films of CdSe and CdSe(ZnS) core(shell) quantum dots by sol-gel assembly: Enabling photoelectrochemical characterization and electronic applications,” *ACS Nano*, Vol. 7, No. 2, 1215–1223, 2013.
5. Anokhin, M. N., A. A. Tishchenko, M. I. Ryazanov, and M. N. Strikhanov, “Permittivity of anisotropic dielectric near surface with local field effects,” *J. Phys.: Conf. Ser.*, Vol. 541, 012023, 2014.
6. Ryazanov, M. I. and A. A. Tishchenko, “Clausius-Mossotti-type relation for planar monolayers,” *JETP*, Vol. 103, 539, 2006.
7. Ryazanov, M. I., “The effect of the natural variation in the polarization of a near-surface layer onelectromagnetic surface waves,” *JETP*, Vol. 83, 529, 1996.

New Design of All-optical Flip-flop Device Based on Multimode Interference Photonic Crystal Waveguides

Yaw-Dong Wu, Jui-Hong Hsu, Hsiu-Chuan Huang, and Tien-Tsorng Shih

Department of Electronic Engineering
National Kaohsiung University of Applied Sciences, Kaohsiung, Taiwan

Abstract— In this paper, we proposed an all-optical flip-flop device based on the multimode interference (MMI) with photonic crystal (PC) waveguides. The proposed all-optical logic gate was numerically studied by the finite-difference time-domain method (FDTD). In recent years, the photonic crystal is a very popular topic due to photonic band gaps (PBGs) which were known to exist in the periodically modulated dielectric materials. We try to combine the MMI principle and photonic crystal waveguide to design a whole new all-optical RS flip-flop device based on the MMI PC waveguide structures. By introducing a point defect rod both in the control ports, we can make outgoing field propagating in the output waveguide or not. The intensity profiles show snapshots optioned at different times. This numerical results show that the proposed PC waveguide structure could really function as an all-optical RS flip-flop logic gate. Note that if we have an RS flip-flop, we can realize various much complex logic processing based on it.

1. INTRODUCTION

Since photonic band gaps (PBGs) were known to exist in periodically modulated dielectric materials [1, 2], which are the so-called photonic crystals (PCs), a large number of studies have been devoted to revealing their unique properties [3]. These artificial sub-micro structures provide flexible controls of light by breaking periodicity and by introducing defects. Recently, well-established fabrication technologies and advanced numerical methods have enabled the sophisticated engineering of PCs dispersion characteristics [4, 5]. In devices based on PBG, well-known lightwave behaviors, such as directional coupling and resonance effect in cavities, have been exploited as well as in conventional optical devices based on total internal reflection (TIR), and their characteristics have been thoroughly investigated in many papers [6, 7]. Compared with those in conventional TIR devices, the well-known behaviors of lightwave in PBG devices are observed in much smaller operating regions, due to the PCs ability to interact with light on a wavelength scale. For instance, the directional coupling between adjacent line-defect waveguides occurs within a few wavelengths [8, 9]. This strong interaction with light in PBG devices is expected to usher in an era of ultra-compact lightwave circuits that operate with much improved functionalities. While such lightwave behaviors have been successfully adopted into PBG devices, they are assumed to take place in structures that ensure single-mode operation for the robust performance of devices. Hence, few studies in the available literatures focus primarily on discussing PCs line-defect waveguides (PCWs) that support multi-mode operation. Furthermore, researches on self-imaging phenomena that might be observed in multi-mode PCWs, to our knowledge, have not been reported so far. In this paper, we observe the propagation of lightwaves in multi-mode PCWs to determine if self-imaging phenomena occur and, if so, to confirm that they can be utilized to control lightwaves in an ultra-compact structure. To demonstrate self-imaging phenomena in multi-mode PCWs, a numerical computation is performed with the finite-difference time-domain (FDTD) method. Asakawa's group proposed a different type of flip-flop operation using symmetric Mach-Zehnder switches implemented in PCs [10]. It has been proposed that all-optical flip-flops can be realized by using two nonlinear etalons with appropriate

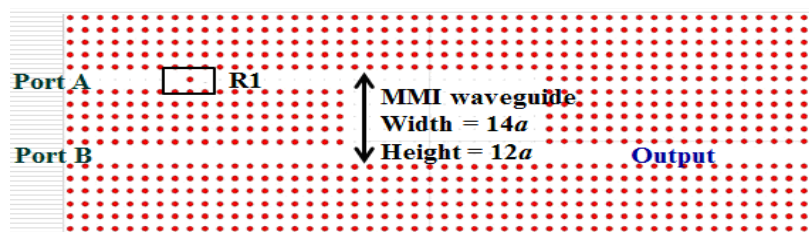


Figure 1: All-optical switch consisting MMI waveguide (width = $12a$, and height = $14a$).

cross-feedback [11, 12], but this proposal is unsuitable for on-chip integration. Notomi's group proposed a different design using two PCs nanocavities in [13]. In this paper, we proposed an all-optical flip-flop device based on the MMI with PC waveguide structure. This numerical results show that the proposed PC waveguide structure could really function as an all-optical RS flip-flop logic gate.

2. ANALYSES AND NUMERICAL RESULTS

We consider a MMI PC all-optical switch composed of dielectric rods in air with a square array and a lattice constant a , as shown in Figure 1. The radius and the refractive index of the rods are $r = 0.18a$ and $n = 3.6(\text{Si})$, respectively. The proposed structure is composed two input ports, the MMI waveguide, and the output port. In this proposed structure, the signal port B will always on. By properly changing the radius of the defect rod $R1$, the state of the output port will be changed. Figure 2 shows the transmission efficiency of the output port for different $R1$ ($0.08a \sim 0.38a$). When $R1$ is $0.31a$, the control power will affect the MMI waveguide to turn off the output, due to the phase difference is 180° of the control port and signal port. Now we know the point defect effectiveness in this kind of structure, and then we will design a RS flip-flop. We introduce a point defect both in the CR and CS control ports, as shown in Figure 3. The radius and the refractive

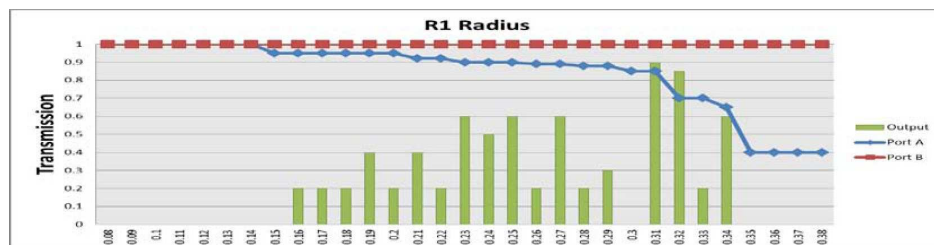


Figure 2: The output chart of $R1$ radius in the control port and output transmission power.

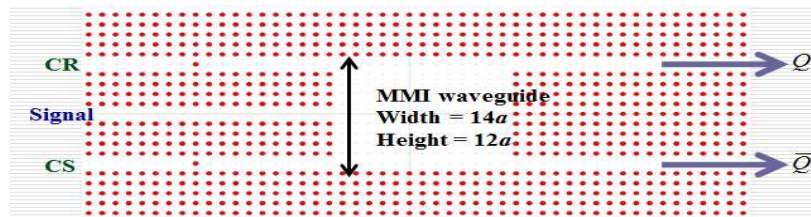


Figure 3: The proposed all-optical flip-flop based on the MMI PC waveguide structure.

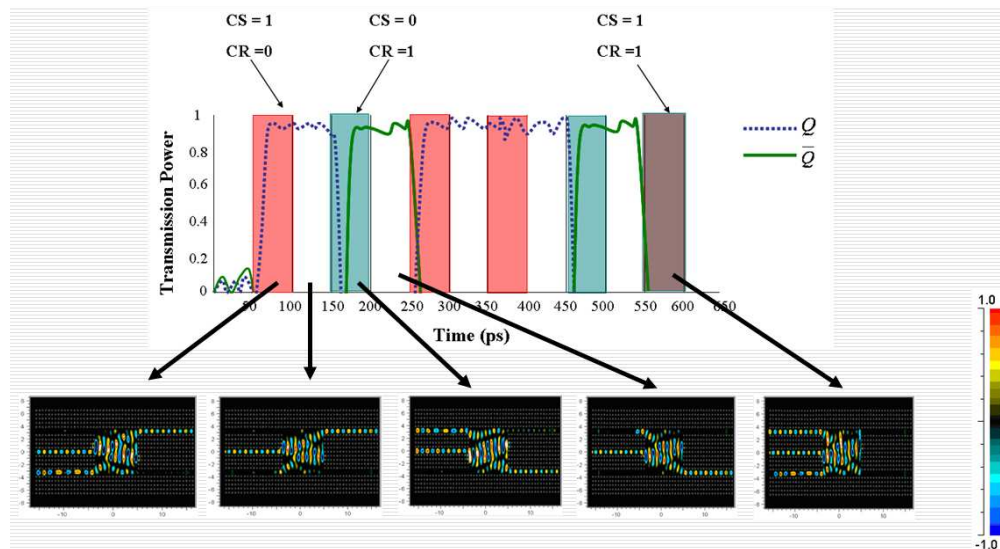


Figure 4: Time sequence of three inputs (single, control set, and control reset), and two outputs (Q , and \bar{Q}). The bottom plots are snapshots of intensity profiles of the RS flip flop device.

index of the rods are $r = 0.18a$, and $n = 3.6$. The radius of the point defect $R1 = 0.31a$ in the control R (CR) and control S (CS) waveguide.

By changing the states of two control ports (CS and CR), the states of the output port will also be changed. In this simulation, the incident wave with wavelength $\lambda = 1.55 \mu\text{m}$ is launched as a signal. Here, we assume the boolean values “0” and “1” corresponding to the absent of the output field or not. For the case 1, when the states of CS and CR are “1” and “0”, respectively, the output Q is “1” and \bar{Q} is “0”. If the control set is turned off in the next timing, the output port will remain the same state. For the case 2, when CS is “0” and CR is “1”, the output Q is “0” and \bar{Q} is “1”. If the control reset is turned off in the next timing, the output result was not be changed. For the case 3, when CS is “1” and CR is “1”, the output Q is “0” and \bar{Q} is “0”. All of the numerical results are shown in Figure 4.

3. CONCLUSIONS

We propose a new design of an all-optical RS flip-flop based on the MMI PCW. By introducing a point defect rod both in the control ports, we can make outgoing field propagating in the output waveguide or not. The intensity profiles show snapshots optioned at different times. This numerical results show that the proposed PC waveguide structure could really function as an all-optical RS flip-flop logic gate. Note that if we have an RS flip-flop, we can realize various much complex logic processing based on it.

ACKNOWLEDGMENT

This work was partly supported by Taiwan’s National Science Council under Grants NSC-103-2221-E-151-004.

REFERENCES

1. Chutinan, A., M. Okano, and S. Noda, “Wider bandwidth with high transmission through waveguide bends in two-dimensional photonic crystal slabs,” *Appl. Phys. Lett.*, Vol. 80, 1698–1700, 2002.
2. Talneau, A., L. L. Gouezigou, N. Bouadma, M. Kafesaki, C. M. Soukoulis, and M. Agio, “Photonic-crystal ultrashort bends with improved transmission and low reflection at $1.55 \mu\text{m}$,” *Appl. Phys. Lett.*, Vol. 80, 547–549, 2002.
3. Yariv, A., Y. Xu, R. K. Lee, and A. Scherer, “Coupled-resonator optical waveguide: A proposal and analysis,” *Opt. Lett.*, Vol. 24, 711–713, 1999.
4. Olivier, S., C. Smith, M. Rattier, H. Benisty, C. Weisbuch, T. Krauss, R. Houdré, and U. Oesterlé, “Miniband transmission in a photonic crystal coupled-resonator optical waveguide,” *Opt. Lett.*, Vol. 26, 1019–1021, 2001.
5. Kim, W. J., W. Kuang, and J. D. O’Brien, “Dispersion characteristics of photonic crystal coupled resonator optical waveguides,” *Opt. Lett.*, Vol. 11, 3431–3437, 2003.
6. Johnson, S. G., S. Fan, P. R. Villeneuve, and J. D. Joannopoulos, “Guided modes in photonic crystal slabs,” *Phys. Rev. B*, Vol. 60, 5751–5758, 1999.
7. Noda, S., A. Chutinan, and M. Imada, “Trapping and emission of photons by a single defect in a photonic bandgap structure,” *Nature*, Vol. 407, 608–610, 2000.
8. Kim, S., I. Park, and H. Lim, “Proposal for ideal 3-dB splitters-combiners in photonic crystals,” *Opt. Lett.*, Vol. 30, 257–259, 2005.
9. Saavedra, C. E. and Y. Zheng, “Ring-hybrid microwave voltage-variable attenuator using HFET transistors,” *IEEE Trans. Micro. Theory Tech.*, Vol. 53, 2430–2434, 2005.
10. Niemi, T., L. H. Frandsen, K. K. Hede, A. Harpøth, P. I. Borel, and M. Kristensen, “Wavelength-division demultiplexing using photonic crystal waveguides,” *IEEE Photonic Technol. Lett.*, Vol. 18, 226–228, 2006.
11. Halevi, P., A. A. Krokhin, and J. Arriaga, “Photonic crystals as optical components,” *Appl. Phys. Lett.*, Vol. 75, 2725–2727, 1999.
12. Chen, C. C., H. D. Chien, and P. G. Luan, “Photonic crystal beam splitters,” *Appl. Opt.*, Vol. 43, 6188–6190, 2004.
13. Shinya, A., S. Mitsugi, E. Kuramochi, and M. Notomi, “Ultrasmall multi-port channel drop filter in two dimensional photonic crystal on silicon-on-insulator substrate,” *Opt. Express*, Vol. 14, 12394–12400, 2006.

Ultrashort Pulse Generation in Tapered Photonic Crystal Fiber at 400 nm

A. Manimegalai^{1,5}, E. Gunasundari¹, Abdosllam M. Abobaker², K. Senthilnathan¹,
S. Sivabalan³, K. Nakkeeran⁴, and P. Ramesh Babu¹

¹Photonics, Nuclear and Medical Physics Division, School of Advanced Sciences
VIT University, Vellore 632 014, India

²Department of Communications Engineering, College of Electronic Technology, Bani Walid, Libya

³School of Electrical Engineering, VIT University, Vellore 632 014, India

⁴School of Engineering, University of Aberdeen, Aberdeen AB24 3UE, UK

⁵Department of Electronics and Communication Engineering, GTEC, Vellore 632 102, India

Abstract— In this paper, we design hexagonal and octagonal TPCFs wherein dispersion and nonlinearity vary exponentially at 400 nm wavelength according to the self-similar analysis. By exploiting these optical properties, we demonstrate the effective pulse compression schemes at 400 nm wavelength.

1. INTRODUCTION

The generation of ultrashort pulses at shorter wavelength near 450 nm is especially preferred in satellite sensors, ophthalmology in optical coherence tomography system, optical imaging, etc [1]. However, it is difficult to produce such a shortest pulse at near visible wavelength even from the best available laser sources. Of late, the generation of desired pulse width of ultrashort pulses is quite possible through pulse compression technique with the advent of photonic crystal fiber (PCF) where the anomalous dispersion can also be obtained at visible regime [2]. Achieving single mode and high dispersion near the visible wavelength turns out to be a challenging task in the generation of ultrashort pulses using PCF. In general, there are two proven ways to enhance the nonlinearity and dispersion values in PCFs. First, one can modify the design of PCF with large air hole size leading to high nonlinearity and large dispersion. However, this usually results in switching over to multimode propagation owing to larger values of air hole size. Second, the nonsilica technology such as SF₆, TF10, CS₂, nitrobenzene, and so on, enhances the nonlinearity and eventually requires relatively less input energy [3]. In general, the tapering is done by reducing the pitch and diameter. Fiber tapering provides a convenient way to reduce the mode-field diameter of fibers, thereby allowing for a better pulse compression [4]. We, thus, emphasize that the tapered PCFs (TPCFs) are very much suitable for effective pulse compression when compared to conventional PCFs. In this paper, we design hexagonal and octagonal TPCFs wherein group velocity dispersion (GVD) and nonlinearity vary exponentially at 400 nm wavelength in line with the self-similar analysis. By exploiting these optical properties, we demonstrate the effective pulse compression schemes at 400 nm wavelength.

2. DESIGN OF THE PROPOSED TPCF

The proposed geometric hexagonal and octagonal tapered structures consist of five rings of air holes. TPCFs can be designed by simultaneous reduction of their geometrical parameters, namely, air-hole diameter, d , and pitch, Λ . While tapering the PCF, we decrease the value of the pitch as per self-similar condition [5].

$$\Lambda(z) = \Lambda_0 \exp(-\sigma z), \quad (1)$$

where Λ is the pitch, if σ is the decay rate and z is the propagation distance.

The geometrical structures of the proposed hexagonal and octagonal TPCFs are shown in Fig. 1(a). Here pitch is kept at 7 μm .

3. OPTICAL PROPERTIES

In this section, we describe an important linear effect called. It is known that the dispersion does depend on both operating wavelength and the physical parameters such as core diameter and pitch. The value of GVD is determined from the second derivative of the computed n_{eff}

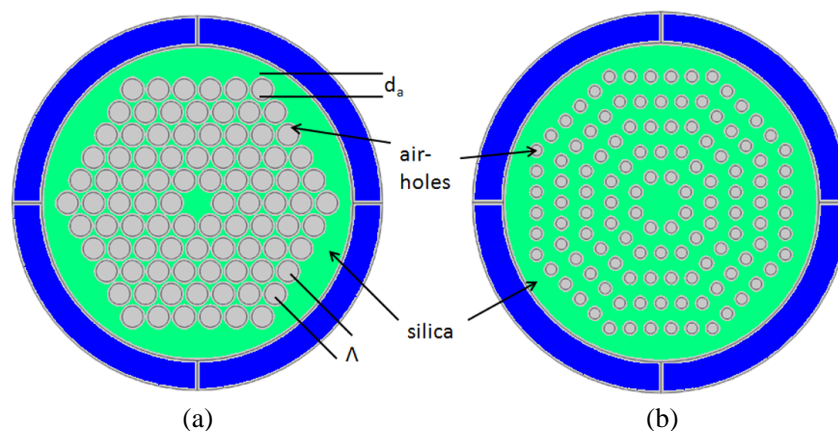


Figure 1: Geometrical structure of (a) hexagonal and (b) octagonal TPCFs when $\Lambda = 7 \mu\text{m}$.

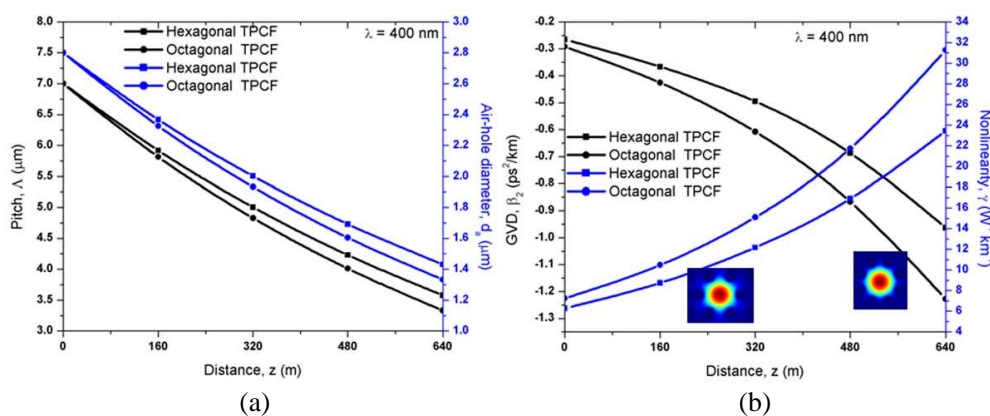


Figure 2: (a) Pitch and air-hole diameter with respect to distance at 400 nm wavelength and (b) variations of GVD and nonlinearity for the proposed hexagonal and octagonal TPCF at 400 nm wavelength.

using finite element method [6]. It is clear that the proposed tapered PCFs exhibit anomalous dispersion varying exponentially based on self similar condition at 400 nm wavelength. To compute the effective nonlinearity, we first calculate the effective area, A_{eff} . From the numerical results, we find that the effective area decreases and hence the effective nonlinearity increases exponentially as shown in Fig. 2(b).

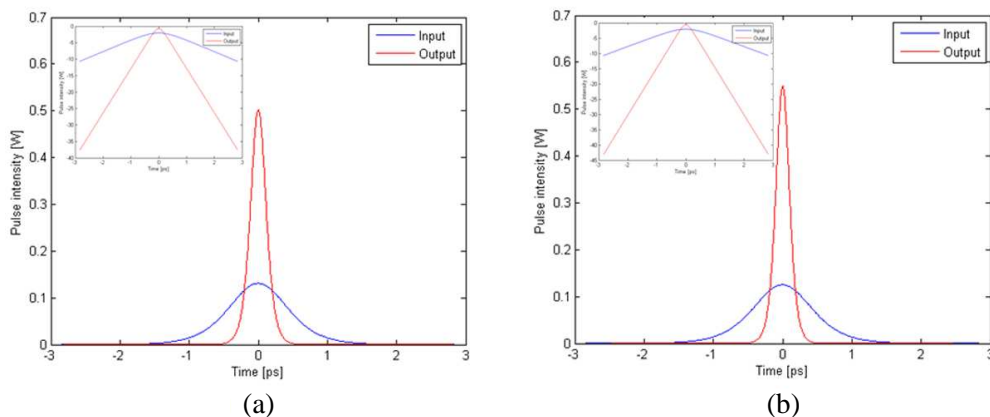


Figure 3: The calculated output pulse profiles through self-similar analysis of the proposed (a) hexagonal and (b) octagonal TPCFs at 400 nm wavelength with their log plots.

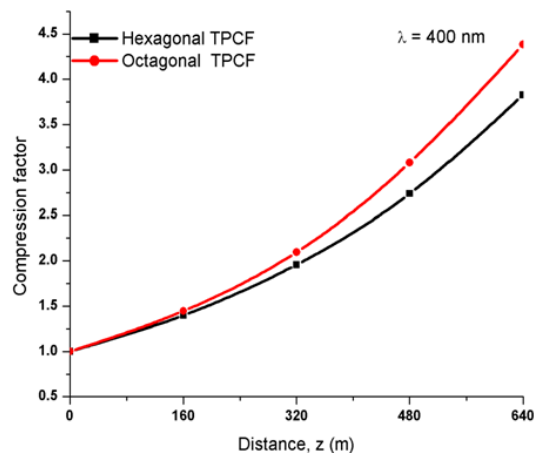


Figure 4: Compression factor of self similar pulse compression for tapered PCF at 400 nm.

4. SELF SIMILAR PULSE COMPRESSION

Self-similar pulses are preferred since the linear chirp facilitates efficient pulse compression. A self-similar analysis has been utilized to study linearly chirped pulses in optical fiber and fiber amplifiers. It is obvious that length of the TPCF is a significant factor for a compact self similar pulse compressor [7]. We choose the fiber length in such a way that it is always lesser than the chirp length in order to ensure that the chirp does not contribute to the spectrum of the compressed pulses. The calculated output pulse profiles through self-similar analysis of the proposed (a) hexagonal and (b) octagonal TPCFs at 400 nm wavelength are shown in Fig. 3.

Note that the initial full width at half-maximum (FWHM) intensity of the pulse is $1.76T_0$. Here FWHM is kept as 1 ps. It is obvious that length of the TPCF is a significant factor for a compact self similar pulse compressor [8]. We choose the fiber length in such a way that it is always lesser than the chirp length in order to ensure that the chirp does not contribute to the spectrum of the compressed pulses.

5. CONCLUSION

We have been able to generate the self-similar ultrashort pulses at 400 nm wavelength using both hexagonal and octagonal tapered photonic crystal fibers. We strongly envisage that the proposed TPCFs at 400 nm wavelength would find useful in satellite sensors, ophthalmology, optical imaging, etc..

ACKNOWLEDGMENT

KSN wishes to thank CSIR [No. 03(1264)/12/EMR-II] and DST [No. SR/FTP/PS-66/2009], Government of India, for the financial support through the sponsored projects. SS wishes to thank DST [No. SR/S2/LOP-0014/2012], Government of India, for the financial support through the sponsored project.

REFERENCES

1. Kudlinski, A., M. Lelek, B. Barviau, L. Audry, and A. Mussot, "Efficient blue conversion from a 1064 nm microchip laser in long photonic crystal fiber tapers for fluorescence microscopy," *Opt. Lett.*, Vol. 18, No. 16, 2010.
2. Moores, J. D., "Nonlinear compression of chirped solitary waves with and without phase modulation," *Opt. Lett.*, Vol. 21, No. 8, 555–557, 1996.
3. Varshney, S. K., K. Sasaki, K. Saitoh, and M. Koshiya, "Design and simulation of 1310 nm and 1480 nm single-mode photonic crystal fiber Raman lasers," *Optics Express*, Vol. 16, No. 2, 549–559, 2008.
4. Nguyen, H. C., B. T. Kuhlmeiy, E. C. Magi, M. J. Steel, P. Domachuk, C. L. Smith, and B. J. Eggleton, "Tapered photonic crystal fibers: Properties, characterization and applications," *Appl. Phys. B*, Vol. 81, Nos. 2–3, 377–387, 2005.

5. Raja, V. J., K. Senthilnathan, K. Porsezian, and K. Nakkeeran, "Efficient pulse compression using tapered photonic crystal fiber at 850 nm," *IEEE J. Quantum Electronics*, Vol. 46, No. 12, 1795–1802, 2010.
6. Comsol Multiphysics 3.4, 2008, Online Available: www.comsol.com.
7. Li, Q., K. Senthilnathan, K. Nakkeeran, and P. K. A. Wai, "Nearly chirp and pedestal-free pulse compression in nonlinear fiber Bragg gratings," *J. Opt. Soc. Am. B*, Vol. 26, No. 3, 432–443, 2009.
8. Li, F., et al., "Highly coherent supercontinuum generation with picoseconds pulses by using self-similar compression," *Optics Express*, Vol. 22, 27339–27354, 2014.

A Method of ISAR Sequences Quality Assessment for Aerospace Target

Gang Li, Qingkai Hou, Shiyu Xu, and Zengping Chen

Science and Technology on Automatic Target Recognition Laboratory
National University of Defense Technology, Changsha, China

Abstract— In this paper, the traditional ISAR image quality evaluation standard and its limitation is analyzed. An ISAR quality evaluation method of aerospace targets is presented, combining with ISAR imaging mechanism and the structural characteristics of aerospace targets, referencing the standard of optical image quality evaluation. Beyond some current commonly used indications, a new indication based on the power spectrum is adopted in this method. The simulation data and real data show the validity of the algorithm.

1. INTRODUCTION

Inverse synthetic aperture radar (ISAR) can generate 2D image for a non-cooperative moving target [1], and be used for military and civilian purpose. In practice, the effect of ISAR imaging is affected by many factors; some quality problem is existed in the ISAR image, such as blur, deformation, tailing, ghost copy etc. [2]. So it is necessary to evaluate the image quality by some corresponding parameters. In addition, the research on that how to choose the high quality image from the mass result, has important significance to realize image interpretation and obtain the target information. The techniques for SAR image quality assessment have been developed in recent years, and already formed a commercial product, but the research on ISAR image is still poor.

In the traditional method, image entropy and contrast is adopted to evaluate ISAR image quality, however, this method is only suitable for comparing the image quality from the same measurement data in different processing algorithm. It still has no viable standard on that how to evaluate the ISAR images in different measurement periods.

This paper analyzes the traditional ISAR image quality evaluation standard and its limitation in Section 2. ISAR imaging mechanism and the structural characteristics of aerospace targets is analyzed in Section 3. Referencing the standard of optical image quality evaluation, an ISAR quality evaluation method of aerospace targets is presented in Section 4. Beyond some current commonly used indications, a new indication based on the power spectrum is adopted in this method. Experimental results and performance analysis are reported in Section 5, followed by conclusion in Section 6.

2. TRADITIONAL STANDARD OF ISAR IMAGE QUALITY ASSESSMENT

Objective image quality measures have been developed to quantitatively estimate the perceived image quality. There are three types of objective image quality measures: full-reference (FR), reduced-reference (RR), and no-reference (NR), which have full, partial, and no access to a reference (distortion-free) image, respectively [3]. ISAR image quality assessment belongs to NR.

Currently, image entropy and contrast is adopted as two indications, when evaluating the ISAR images. Image entropy is used to characterize the image clarity. It is defined by:

$$Entropy = - \sum_{m=1}^M \sum_{n=1}^N \frac{|I(m, n)|^2}{S} \ln \frac{|I(m, n)|^2}{S} \quad (1)$$

When $S = \sum_{m=1}^M \sum_{n=1}^N |I(m, n)|^2$, M denotes the number of HRRPs and N is the number of range bins in HRRP. Figure 1 shows ISAR images with different entropy.

ISAR image contrast is defined by the ratio between the standard deviation and mean value of image intensity, which can be expressed as

$$C = \frac{\sqrt{E \left((I^2(m, n) - E(I^2(m, n)))^2 \right)}}{E(I^2(m, n))} \quad (2)$$

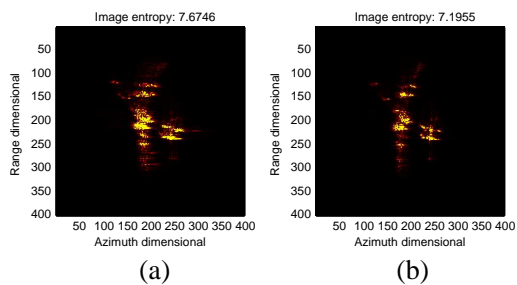


Figure 1: ISAR images with different entropy.

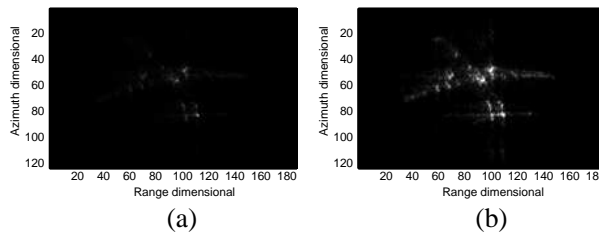


Figure 2: ISAR images with different contrast. (a) Original image. (b) Enhanced image.

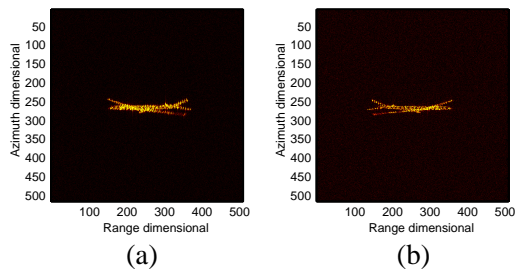


Figure 3: ISAR imaging results of Simulate data.

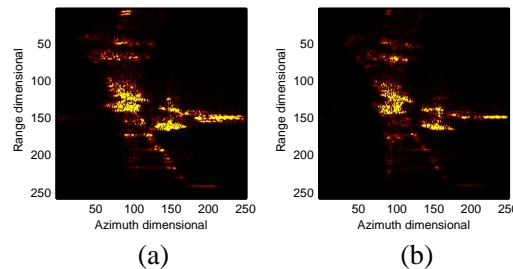


Figure 4: ISAR images with defocus blur.

Table 1: Entropy and contrast of ISAR images shown in Figure 3.

	Entropy	Contrast		Entropy	Contrast
Figure 3(a)	8.1045	11.5667	Figure 3(b)	8.9662	11.1414

Image contrast has an important effect on image segmentation, target region extraction and target classification. Many factors may cause low image contrast. Sidelobe and coherent speckle increases the energy of background, disrupts the original outline structure of target, and thus reduces the contrast of target and background. Some ISAR images' dynamic range is small, resulting in the low contrast. The higher the ISAR image contrast, the clearer the image, more conducive to the extraction and classification of target. Figure 2 shows a group of ISAR images. The original image is shown in Figure 2(a). Figure 2(b) shows the enhancement result. It is obvious that the enhanced image highlights the target brightness, suppresses background noise, and improves image quality.

Entropy and contrast, can reflect the quality of ISAR, but need to point out that it is effective for comparing the ISAR images generated by the same measuring data under different processing algorithms; in other cases, it is not always reliable. Figure 3 shows two different ISAR imaging results. The contrast and entropy of them is shown in Table 1. From the entropy and contrast, the quality of Figure 3(a) is better; this is obviously inconsistent with the actual visual effects. It still has no viable standard on that how to evaluate the ISAR images in different measurement periods.

3. AEROSPACE COMPLEX TARGET ISAR IMAGE CHARACTERISTICS ANALYSIS

In the ISAR imaging process, there are many factors lead to blurred images, such as sidelobe enhancement, noise, ghost, defocusing etc.. Among them, the defocusing is one of the important factors that cause ISAR images blur.

For aerospace object, the motion parameters and the state is usually unknown. The existence of complex motion during the flight, such as maneuver, transfer etc., make the error in translational motion compensation, nonlinear correction, and cross-range scaling, is difficult to avoid. And the scattering centers of aerospace target is more intensive; even a high-resolution, it is difficult to avoid migration through resolution cells (MTRC). All these will lead to ISAR images focusing not well and generate blur image. As shown in Figure 4. Blur will lead to a decline in ability of target recognition of ISAR image, therefore need quantitative evaluation of blur degree.

The blur parameters assessment method based on the blur image spectrum diagram, which is

presented in [4], has been widely researched and applied. The method which adopts the image edge along the direction of motion as a motion blur measure is indicated in [4–6]. Experiments show that the motion blur evaluation algorithms cannot be directly used in defocus blur degree evaluation of ISAR image, this is because the low signal-to-noise ratio (SNR) of ISAR image. ISAR has the similar imaging mechanism with SAR. According to the characteristic of SAR images, literature [7] proposed a new method using truncated spectrum of SAR images and average edge width of salient image areas after med-value filtering with big windows to evaluate the defocusing blur of SAR images. Because the quality, it is difficult to extract the edge of ISAR images, so the method of literature [7] is not applicable to ISAR images.

High frequency part of ISAR image can represent the image detail. For the image which exist defocusing blur, the high frequency part damage is serious, and the high frequency power spectrum will be lower, so we can consider using high frequency component of the power spectrum of image as a measurement of its blur degree.

4. ISAR IMAGE QUALITY ASSESSMENT

4.1. Image Power spectrum

In order to carry on the spectrum analysis, image can be transform to the frequency domain. The two-dimensional spectrum of ISAR image is written as $F(u, v)$, then the power spectrum $P(u, v)$ can be obtained by

$$P(u, v) = \frac{|F(u, v)|^2}{M \times N} \quad (3)$$

where (u, v) is the frequency coordinate in two-dimensional space; and $M \times N$ is the size of image.

4.2. ISAR Image Quality Assessment Based on Wavelet Power Spectrum

Usually, when the image is blurred, the high frequency components will be lost, and the high frequency power spectrum of image will change with the change of the high frequency components, so we can use the change of the high frequency power spectrum to describe blurred image quality.

High frequency component often presents the edge of the image and the image contour, therefore we do the processing for image through the wavelet decomposition. First using the ISAR image wavelet transform to extract the approximate image cA , and three high frequency sub images $cHcV$, cD that correspond to horizontal, vertical and diagonal, respectively. Because ISAR image defocus will lead to the change of the high frequency components, so we take the ratio between high frequency components and low frequency components, as the evaluation indexes. The higher the ratio is, the worse the image. Here the power spectrum of cI , cH , cV , cD , are written as cI_PS , cH_PS , cV_PS , cD_PS , respectively, which can be obtained according to (3). The evaluation indexes $InPs$ is defined as

$$InPs = \frac{3 * mean2(cI_PS)}{mean2(cH_PS) + mean2(cV_PS) + mean2(cD_PS)} \quad (4)$$

In the application process, it is found that the effect of proposed method is not very good, when the image in the sequence has a large change. This is because, with the changes of the pose, the shape and size of the object appeared in the image is also different. If the background region is too large, the mean of power spectrum will be reduced, which will affect the evaluation results. To exclude this effect, the method this paper adopts, is to intercept the target region; and only do the analysis for the power spectrum of target region.

5. EXPERIMENT RESULT AND ANALYSIS

In this section, we present two numerical examples to demonstrate the performance of the proposed approach. All the algorithms in this section run on Matlab 2010a. The operating system is

Table 2: Parameters of radar system.

Parameter	Setting value	Parameter	Setting value
Carrier frequency	10 GHz	Bandwidth	1 GHz
Original azimuth	45°	Original pitch	45°
Echo number	512	Sampling number	512

Microsoft Windows XP Professional SP3 and processor is Pentium Dual-Core 2.7 GHz \times 2 CPU. The computer memory is 2 GB of system RAM.

5.1. Simulation ISAR Sequences

In the simulated experiment, the parameters of the radar system are listed in Table 2. The model we choose in this paper is Boeing 737-800. Figure 5 shows the simulation ISAR sequences of the Boeing 737-800. The phase disturbance, which appends in the simulated experiment, satisfies $(b) > (d) > (c) > (a)$.

Figure 6 shows the target region which is extracted in this paper. Without loss of generality, here we present the assessment result using the proposed method and traditional evaluation index. The assessment result is shown in Table 3.

Table 3 indicates that the assessment result of proposed method satisfies $(b) < (d) < (c) < (a)$; this is consistent with the actual situation.

5.2. Real ISAR Sequences

In the experiment, the real data provided by Science and Technology on Automatic Target Recognition Laboratory (ATR) of China was used. The data were collected by ATR's experimental ground-based imaging radar. The target was a flying airplane of Boeing 737-800. The carrier frequency was $f_c = 10$ GHz, and the bandwidth was $B = 1$ GHz. Figure 7 shows the real ISAR

Table 3: The assessment result of simulation ISAR result.

	(a)	(b)	(c)	(d)
Image entropy	7.891	8.547	9.311	9.310
Image contrast	2.957	1.356	1.796	1.879
Mean gradient	0.0248	0.0253	0.0371	0.0365
InPS (original image)	6.654	11.484	9.574	9.840
Proposed method InPS (target region)	6.664	11.941	10.225	10.831

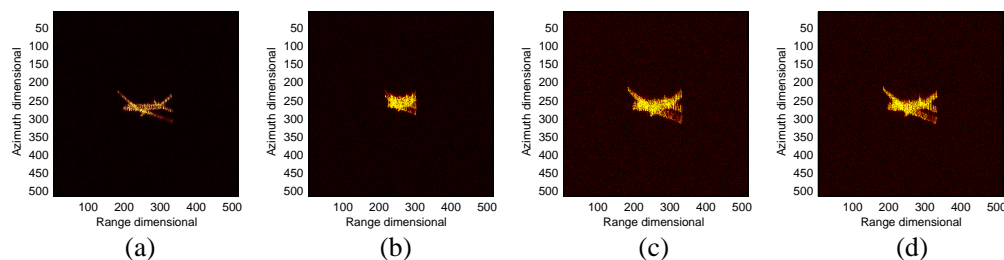


Figure 5: Simulation ISAR sequence.

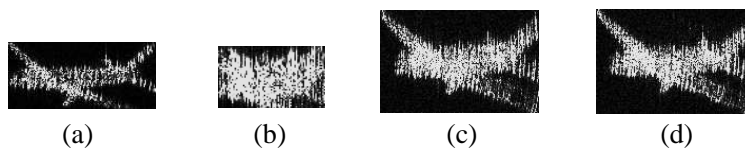


Figure 6: The target region.

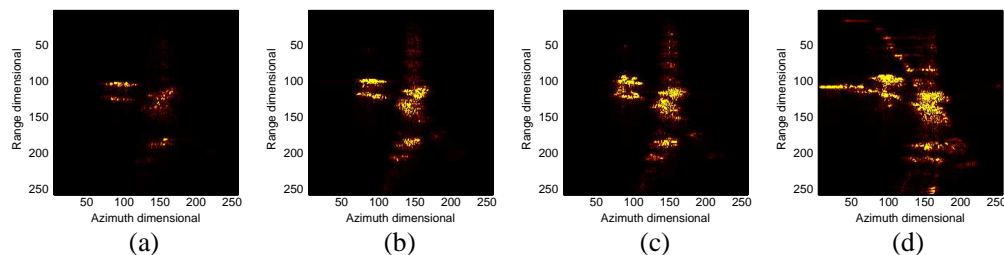


Figure 7: Real ISAR sequence.

Table 4: The assessment result of real ISAR result.

	(a)	(b)	(c)	(d)
Image entropy	5.988	7.043	7.252	7.814
Image contrast	8.607	5.194	5.227	5.348
Mean gradient	0.0361	0.0683	0.0740	0.0948
InPS(original image)	7.335	8.945	9.755	11.930
Proposed method InPS (target region)	7.977	8.914	9.744	11.983

sequences of the Boeing 737-800. The result of quality assessment is shown in Table 4.

Table 4 indicates that the assessment result of proposed method satisfies $(d) < (c) < (b) < (a)$; this is consistent with the subjective assessment result.

6. CONCLUSION

This paper analyzes the traditional ISAR image quality evaluation standard and its limitation. An ISAR quality evaluation method of aerospace targets is presented. Beyond some current commonly used indications, a new indication based on the power spectrum is adopted in this method. The simulation data and real data show the validity of the algorithm.

ACKNOWLEDGMENT

This work was supported by the National Natural Science Foundation of China (Grant No. 61471373).

REFERENCES

1. Chen, C. C. and H. C. Andrews, "Target-motion-induced radar imaging," *IEEE Trans. on Aerosp. Electron. Syst.*, Vol. 16, No. 1, 2–14, 1980.
2. Wong, S. K., G. Duff, and E. Riseborough, "Distortion in the inverse synthetic aperture radar (ISAR) images of a target with time-varying perturbed motion," *IEE Proc. — Radar Sonar Navig.*, Vol. 150, No. 4, 221–227, 2003.
3. Ji, H. and C. Liu, "Motion blur identification from image gradients," *IEEE Conference on Computer Vision and Pattern Recognition*, 1–8, Anchorage, AK, 2008.
4. Narvekar, N. D. and L. J. Karam, "A no-reference image blur metric based on the cumulative probability of blur detection (CPBD)," *IEEE Trans. on Image Processing*, Vol. 20, No. 9, 2678–2683, 2011.
5. Ferzli, R. and L. J. Karam, "A no-reference objective image sharpness metric based on the notion of just noticeable blur (JNB)," *IEEE Trans. on Image Processing*, Vol. 18, No. 4, 717–728, 2009.
6. Elder, J. H. and S. W. Zucker, "Local scale control for edge detection and blur estimation," *IEEE Trans. on Pattern Analysis and Machine Intelligence*, Vol. 20, No. 7, 699–716, 1998.
7. Zhang, H., "Research on the SAR image quality assessment," National University of Defense Technology, Changsha, 2012.

Compensation for System Distortion Using Low Signal-to-noise-ratio Echo from Spherical Satellite

Jianzhi Lin, Weixing Li, Weihua Wang, Gang Li, and Zengping Chen

Science and Technology on Automatic Target Recognition Laboratory
National University of Defense Technology, Changsha 410073, China

Abstract— Compensation for amplitude and phase distortion in inverse synthetic aperture radar (ISAR) system is important for the system performance. People cannot help but take an active radar calibrator on a tower as an external test target to measure the distortion and carry out the compensation though it includes extraneous components and induces additional distortion. So a new method for distortion compensation is presented, which is based on the low signal-to-noise-ratio (SNR) echo from a spherical satellite. The technique of pulse compression based on matched filtering is used and then the target region is extracted and inverse matched filtering is applied to achieve the high SNR echo. Thus the amplitude and phase error coefficients can be calculated, which results in excellent compensation for the system distortion. Experimental results based on real radar data show the effectiveness of the proposed method. Comparison results with other scheme are also presented to prove the superiority of our approach.

1. INTRODUCTION

Inverse synthetic aperture radar (ISAR) has a rapid development all over the world, owing to its high resolution and the ability to extract target information such as structure, motion state, and other target identifying characteristics in all-weather and night and day circumstances [1]. In order to achieve the high-range resolution, ISAR system operates over large bandwidths, which brings in the issue of distortion. The non-ideal components comprising the system are not able to keep linear amplitude and phase characteristics across the bandwidth [2]. The generated waveform may undergo distortion in the transmitter, antenna, propagation medium [3, 4], and the receiver and so on. Thus the actual transmitted and received signal deviates from the ideal signal, which results in the bad performance of the signal-to-noise-ratio (SNR) and major lobe and side lobe.

There are two types of techniques to measure the amplitude and phase distortions in the system: closed loop and the employment of an external test target [2]. The former including pre-distortion technique [5–7] excludes antenna and propagation medium, leading to limited results. The latter uses the complete system and is better. The type of the test target may be a corner reflector, a metallic ball towed by a balloon, an active radar calibrator (ARC) on a tower, or a spherical satellite. However, the reflector suffers from high level of clutter. The metallic ball is difficult to carry out daily in practice. The current approach is to use the ARC. But the ARC includes optic transceivers, fibre-optic delay line, and amplifiers, inducing additional distortion [2]. Although it is best to take the spherical satellite as the test target, it is unpractical because the SNR is too low.

In this paper, we analyse the reason why the low SNR signal received from the satellite fails to compensate for the distortion. Then we utilize pulse compression technique based on matched filtering (MF) to find the target region and then take inverse MF on the region to get high SNR signal. Thus we can achieve the distortion coefficients and compensate for the system distortion. Experiments based on real radar data show that the results are better than that by the ARC.

2. THEORY STUDY AND PROPOSED METHOD

2.1. Theory of Compensation for System Distortion

Compensation for distortion in a system using stretch processing in pulse compression is complicated [8, 9]. But it is much simpler in a system using matched-filter correlation processing in pulse compression, because the system can be treated as a series of linear wideband sub-systems such as a transmitter, an antenna, a receiver and so on.

Let $F_{\text{ideal}}(f)$ represent the spectrum of the ideal transmitted signal $f_{\text{ideal}}(t)$. Denote $F_{\text{actual}}(f)$ as the spectrum of the actual received signal $f_{\text{actual}}(t)$ from the test point target. As for the linear system, the transmission characteristic can be obtained as follows:

$$H(f) = \frac{F_{\text{actual}}(f)}{F_{\text{ideal}}(f)} \quad (1)$$

A physical system will exhibit nonlinear frequency responses that can be described by a Fourier series expansion as follows [10]:

$$H(f) = \left[a_0 + \sum_{n=1}^{\infty} a_n \cos(2\pi c_n f) \right] \cdot \exp \left[-j2\pi b_0 f - j \sum_{m=1}^{\infty} b_m \sin(2\pi d_m f) \right] \quad (2)$$

which represents the system distortion. Thus (1) also represents the amplitude and phase error coefficients of the signal across its frequency band. And with the distortion coefficients we can compensate the radar returns as follows [2]:

$$F_{\text{comp}}(f) = \frac{F_{\text{target}}(f)}{H(f)} = F_{\text{target}}(f) \cdot \frac{F_{\text{ideal}}(f)}{F_{\text{actual}}(f)} \quad (3)$$

where $F_{\text{comp}}(f)$ is the compensated spectrum and $F_{\text{target}}(f)$ is the distorted spectrum of the real target. Thus, the compensated signal $f_{\text{comp}}(t)$ can be obtained by the inverse Fourier transform of $F_{\text{comp}}(f)$.

Specially, if the real target is just the test point target, then (3) would become:

$$F_{\text{comp}}(f) = F_{\text{ideal}}(f) \quad (4)$$

Hence, the compensated spectrum of the test point target is the ideal spectrum of the signal that is aimed to be transmitted. Thus, after the compensation we can obtain the undistorted signal.

2.2. Method for Compensation in Low SNR Condition

From the scheme described above, we can see that the key issue is the validity of the distortion coefficients in (1). However, the above scheme does not take into account noise. In practice, the signal from the target includes noise. Hence, (1) should be rewritten as:

$$H(f) = \frac{F_{\text{actual}}(f) - F_{\text{noise}}(f)}{F_{\text{ideal}}(f)} \quad (5)$$

where $F_{\text{noise}}(f)$ is the noise spectrum.

In high SNR condition, $F_{\text{noise}}(f)$ is much smaller than $F_{\text{actual}}(f)$, so it can be passed over and the coefficients calculated by (1) are effective. Whereas, in low SNR condition, $F_{\text{noise}}(f)$ is as much as $F_{\text{actual}}(f)$, so it must be taken into account and the coefficients calculated by (1) are ineffective.

According to (2), the phase characteristic of the real system is probably linear though it somewhat departs from the ideal linear. However, the phase characteristic calculated by (1) is far from linear in low SNR condition. Fig. 1 shows the situation. Fig. 1(a) shows the phase characteristic calculated by (1) based on the signal received from the ARC in high SNR condition while Fig. 1(b) from the spherical satellite in low SNR condition. We can see that the former is approximately linear while the latter is completely nonlinear. Hence the latter cannot exactly represent the characteristic of the system and is ineffective.

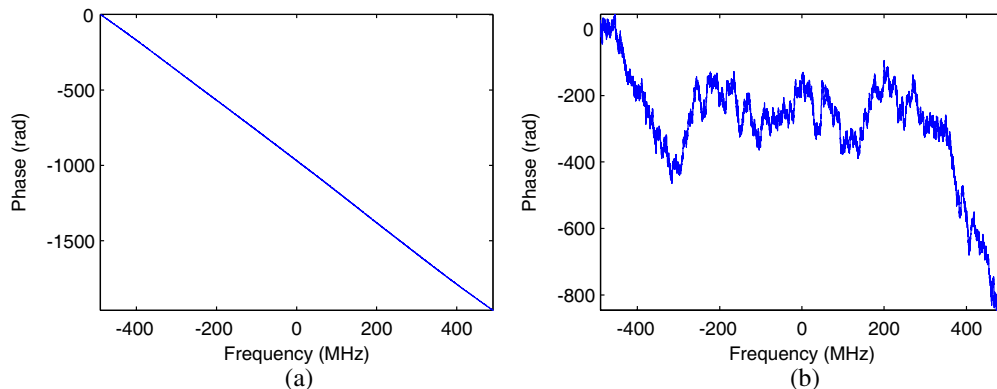


Figure 1: Phase characteristic calculated by (1) based on the echo from: (a) ARC in high SNR condition, and (b) satellite in low SNR condition.

Our method is to improve the SNR. It is well known that the signal power can be increased BT (B is the bandwidth and T is the pulse width) times by using pulse compression technique for the linear frequency modulation waveform. The quantity BT is referred to as the time-bandwidth product. As the ISAR system utilizes frequency modulation, the time-bandwidth product can be much greater than unity. Hence, the target region can be quickly found after pulse compression and then the SNR can be increased by inverse dealing. The concrete steps are as follows:

- Step 1.** Take the spherical satellite as the test target and get the received discrete-time signal $f_{\text{actual}}(t_n)$, which is low SNR.
- Step 2.** Take MF on $f_{\text{actual}}(t_n)$ and get the high-resolution range profile (HRRP) $f_{\text{actualM}}(t_n)$.
- Step 3.** Find and extract the target region $f'_{\text{actualM}}(t_n)$.
- Step 4.** Take inverse MF on $f'_{\text{actualM}}(t_n)$ and get $f'_{\text{actual}}(t_n)$, which is high SNR.
- Step 5.** Calculate the distortion coefficients: obtain the spectrum $F'_{\text{actual}}(f_n)$ of $f'_{\text{actual}}(t_n)$; construct the ideal transmitted signal $f_{\text{ideal}}(t_n)$ and get its spectrum $F_{\text{ideal}}(f_n)$; the ratio of the two spectra produces the transmission characteristic $H(f_n) = A(f_n) \cdot \exp[jP(f_n)]$, where $A(f_n)$ is the amplitude-frequency response and $P(f_n)$ is the phase-frequency response.
- Step 6.** Implement the least squares curve fitting on $P(f_n)$ to get the linear phase-frequency response $P'(f_n)$. Let $\Delta P(f_n) = P(f_n) - P'(f_n)$, which represents the departure between the actual phase response of the system and the ideal linear one. The coefficients used for compensation can then also be $\Delta H(f_n) = A(f_n) \cdot \exp[j\Delta P(f_n)]$.
- Step 7.** Take the Fourier transform on the received signal $f_{\text{target}}(t_n)$ from the real target to get $F_{\text{target}}(f_n)$ and divide it by the coefficients $H(f_n)$ or $\Delta H(f_n)$ to obtain the compensated spectrum $F_{\text{comp}}(f_n)$. After the inverse Fourier transform the compensated signal $f_{\text{comp}}(t_n)$ is achieved.

Steps 1 to 5 are enough for obtaining the distortion coefficients. Step 6 is for calculating the departure between the actual and ideal phase responses. A flowchart for better understanding of the proposed method is given in Fig. 2. After the compensation, we can carry out MF, motion compensation, and the range-Doppler method to get a clear image of the target.

The phase characteristic based on the above signal received from the spherical satellite in low SNR condition after processing is shown in Fig. 3, which is approximately linear now. Thus, the effective distortion coefficients can also be achieved in low SNR condition with the proposed method.

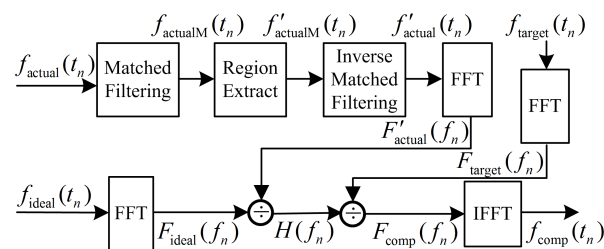


Figure 2: Flowchart of the proposed method.

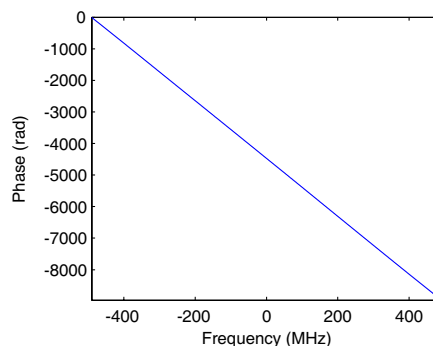


Figure 3: Phase characteristic based on the echo from satellite in low SNR condition after processing.

3. EXPERIMENT

The experiments are carried out on the basis of some ISAR system under field conditions in China. We take an ARC and a spherical satellite as the external test targets one at a time on the same day. And a non-point target is also observed.

In order to demonstrate the effectiveness of the distortion coefficients calculated by the proposed method, we calculate the phase errors $\Delta P(f_n)$ based on the received signals from both the ARC and the satellite as shown in Fig. 4(a). The comparison of amplitude responses $A(f_n)$ is shown in Fig. 4(b). We can see the phase errors $\Delta P(f_n)$ are almost the same and the amplitude responses

$A(f_n)$ are similar. Thus the distortion coefficients extracted from the satellite echo are probably equivalent to those extracted from the ARC echo. As a result, the distortion coefficients calculated by the presented method are effective and can be used to compensate for the system distortion.

In order to see the compensation effect, we use the above two distortion coefficients to compensate some other echo from the spherical satellite and then apply MF to get the HRRP. The results are shown in Fig. 5. Due to the system distortion, the HRRP does not seem like a point target, and the SNR, the range resolution, and the time side lobe performance are significantly degraded before compensation. And the compensation is the solution. Furthermore, compensation by the spherical satellite is better than that by the ARC. This is because the ARC includes extraneous components, which induce additional distortion.

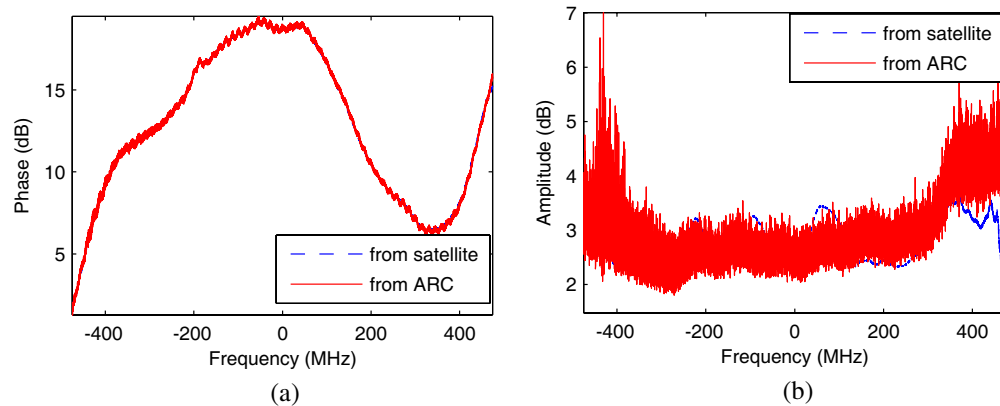


Figure 4: Comparisons of distortion coefficients extracted from satellite echo and ARC echo: (a) phase errors $\Delta P(f_n)$, and (b) amplitude responses $A(f_n)$.

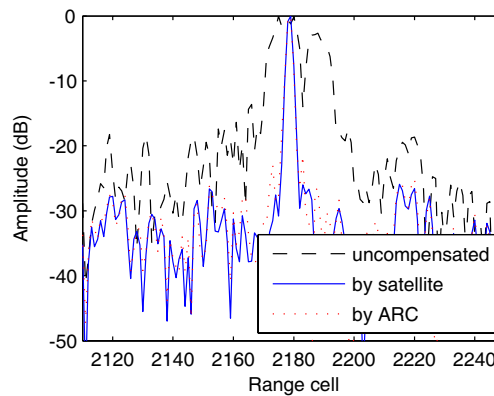


Figure 5: Comparison of the compensation results.

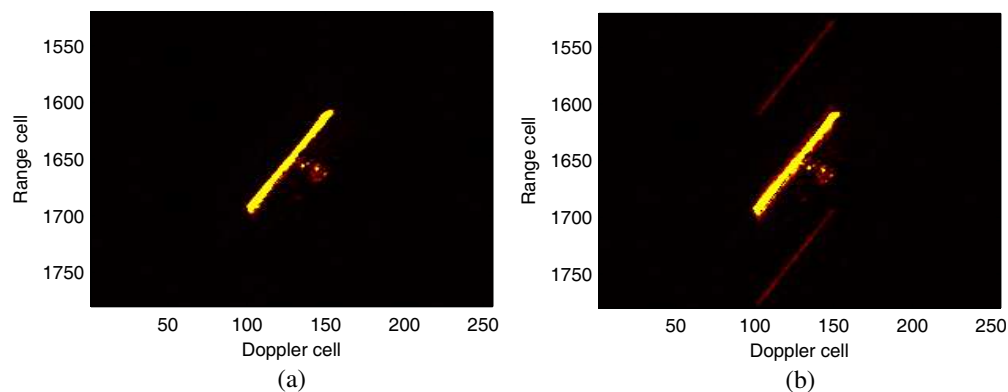


Figure 6: ISAR imaging results of non-point target after compensation: (a) by satellite, and (b) by ARC.

Compensation for the non-point target is presented to prove the effectiveness and the superiority of our method in Fig. 6, where ISAR imaging results are shown. Fig. 6(a) is the result after compensation by the satellite while Fig. 6(b) by the ARC. Comparing the two figures, we can see that the former has a clearer image of the target than the latter. And the latter has two virtual images symmetrically beside the target image, owing to the additional distortion of the ARC.

4. CONCLUSION

In the absence of any method for compensating for the system distortion, the system performance will be badly degraded. Theoretically speaking, the spherical satellite is the best external test target. But in practice, the SNR is too low. In this paper, we solve the problem based on MF and inverse MF techniques. Experiments using real radar data have verified the effectiveness and the superiority of our method. Yet, it should be mentioned that this study only focuses on the system distortion compensation, and thus compensation for target motion errors needs to be further studied for better imaging results.

REFERENCES

1. Zhang, B., Y. Pi, and X. Yang, "Terahertz imaging radar with aperture synthetic techniques for object detection," *Proceedings of ICCW-2013*, 921–925, Budapest, Hung, 2013.
2. Tait, P., *Introduction to Radar Target Recognition*, The Institution of Engineering and Technology, London, 2009.
3. Chandra, M., "Tropospheric-propagation induced distortion of wideband signals," *Proceedings of EuCAP-2013*, 2531–2531, Gothenburg, Swed., 2013.
4. Chen, C., Z. Ding, and C. Wang, "The analysis of dispersive distortions on linear polarization radar signal," *Proceedings of 2013 IET International Radar Conference*, 1–5, Xi'an, China, 2013.
5. Swaminathan, J. N. and P. Kumar, "Design and linearization of solid state power amplifier using pre-distortion technique," *Proceedings of ICCCI-2013*, 1–3, Coimbatore, India, 2013.
6. Kim, S. and N. Myung, "Wideband linear frequency modulated waveform compensation using system predistortion and phase coefficients extraction method," *IEEE Microw. Compon. Lett.*, Vol. 17, No. 11, 808–810, 2007.
7. Grimm, M., M. Allen, J. Marttila, et al., "Joint mitigation of nonlinear RF and baseband distortions in wideband direct-conversion receivers," *IEEE Trans. Microw. Theory Techn.*, Vol. 62, No. 1, 166–182, 2014.
8. Witt, J. and W. Nel, "Range Doppler dynamic range considerations for Dechirp on receive radar," *Proceedings of EuRAD-2008*, 136–139, Amsterdam, Neth., 2008.
9. Krichene, H., E. Brawley, K. Lauritzen, et al., "Time sidelobe correction of hardware errors in stretch processing," *IEEE Trans. Aerosp. Electron. Syst.*, Vol. 48, No. 1, 637–647, 2012.
10. Wheeler, H. A., "The interpretation of amplitude and phase distortion in terms of paired echoes," *Proceedings of the I.R.E.*, Vol. 27, No. 6, 359–384, 1939.

Enhanced Efficiency of Second Harmonic Generation with Twelve-fold Photonic Quasi-crystal Fiber in Telecommunication Band

Ritapa Bhattacharjee¹, Abdosllam M. Abobaker², K. Senthilnathan¹, S. Sivabalan³,
K. Nakkeeran⁴, and P. Ramesh Babu¹

¹Photonics, Nuclear and Medical Physics Division

School of Advanced Sciences, VIT University, Vellore, Tamil Nadu 63214, India

²Department of Communications Engineering, College of Electronic Technology, Bani Walid, Libya

³School of Electrical Engineering, VIT University, Vellore, Tamil Nadu 63214, India

⁴University of Aberdeen, Fraser Noble Building, Aberdeen AB24 3UE, UK

Abstract— We design an index guided silica core photonic quasi-crystal fiber of twelve-fold symmetry for enhancing the efficiency of second harmonic generation by using the fundamental input wavelength of 1.55 μm in the telecommunication band. With the available poling technology, we optimize the pitch of the photonic quasi-crystal fiber at 7 μm and report a relative efficiency of second harmonic generation as 38.22%W⁻¹cm⁻² when the overlap area is 2.74 μm^2 and phase-mismatch factor is 0.102 μm^{-1} .

1. INTRODUCTION

Second harmonic generation (SHG) in telecom band is reported by many recent works which are helpful for the characterization of ultrashort pulses [1]. Enhancing the efficiency of SHG using photonic crystal fibers (PCFs) is also reported [2]. We recently analyzed the role of photonic quasi-crystal fibers in enhancing the efficiency and bandwidth of SHG [3, 4]. PQF, unlike PCF, has no translational symmetry. The lattice of cladding holes in PQF follows only rotational or mirror symmetry [5]. This structural modification in PQF helps in bringing the desired properties such as low confinement loss, endlessly single mode nature etc to a larger degree. Moreover, the circular nature of air hole distribution in the cladding of PQF increases the tight confinement of light in the core and hence increases the possibility of decreasing overlap area between fundamental and second harmonic. The quasi periodic arrangement of holes in the cladding does highly influence the modal confinement as well as the intensity distribution of both the fundamental and second harmonic fields inside the core. As a result, the two most important aspects of second harmonic generation, namely, phase mismatch factor and overlap area related to the efficiency of second harmonic generation get highly affected. Moreover, these two quantities must be as minimum as possible for enhancing the efficiency of second harmonic generation. Hence, in this study, we emphasize on minimizing these two factors with proper choice of geometrical parameters of the PQF. In [3, 4], we have used 1.06 μm wavelength as input fundamental wavelength for SHG. Owing to the importance of SHG in telecommunication band, in this work, we analyze the efficiency of SHG from 1.55 μm fundamental wavelength with twelve-fold photonic quasi-crystal fiber (PQF).

2. SHG THEORY

The efficiency of second harmonic generation is expressed as,

$$\eta = \frac{P_{2\omega}}{P_{\omega}} = P_{\omega} l^2 \frac{(d_{eff})^2}{A_{ovl}} \text{sinc}^2 \left(\frac{\Delta\beta l}{2} \right) \frac{8\pi^2}{\lambda_f^2 n_f^2 n_{sh} \epsilon_0 c} \quad (1)$$

Here P_{ω} is the fundamental power, $P_{2\omega}$ is the second harmonic power l is the length of the fiber, $d_{eff} (= \chi^{(2)}/2\pi)$ is the non-linearity factor associated with second order susceptibility, $\chi^{(2)}$ [2–4]. A_{ovl} is the overlap area of interaction between fundamental and second harmonic waves and the same is given by, $A_{ovl} = 1/I_{ovl}^2 = |\iint E_{sh}^* E_f^2 dx dy|^{-2}$ where I_{ovl} is the overlap integral factor and E_f and E_{sh} are the normalized electric field intensities of fundamental and second harmonic waves, respectively. $\Delta\beta$ is the phase mismatch factor between fundamental and second harmonic, λ_f is the fundamental wavelength, n_f and n_{sh} are the refractive indices of fundamental and second harmonic waves, respectively and c is the velocity of light. For a poled fiber, the quasi-phase matching (QPM)

technique is essential for the required phase-matching between fundamental and second harmonic. For an ideal QPM of 1st order, the phase mismatch factor is, $\Delta\beta = \Delta\beta' - l_{qpm} = 0$, where $\Delta\beta' = 2\beta_1 - \beta_2$, is the wave-vector mismatch between fundamental (β_1) and second harmonic (β_2) wave-vectors, respectively and $l_{qpm} (=2\pi/\Delta\beta')$ is the QPM grating period. Longer QPM period helps in easier fabrication process in terms of altering the poling voltage over a sample periodically.

3. PQF DESIGN

The design of the twelve-fold PQF is shown in Fig. 1(a). In Fig. 1(a), the gray region signifies silica while the white holes represent air holes. Here we use Penrose type tiling with square and thin and thick types of rhombi for arrangement of air hole unit cells in the cladding [4, 5]. Here the lattice constant or pitch, Λ , is varied from 1 to 15 μm for the analysis. The upper limit of pitch is considered for low effective mode area and lower limit of pitch is considered for tight confinement of modes of both fundamental and second harmonic. The relative air hole diameter, d/Λ , is fixed at 0.5 by considering single mode propagation requirement [5]. Also we already reported the best overlap area can be achieved by PQF is at relative hole diameter 0.5 [3, 4]. Figs. 1(b) and (c) show the tight modal confinement of fundamental and second harmonic, respectively, for a pitch of 7 μm and a fiber length of 10 cm. From Figs. 1(b) and (c), we observe that the modal distribution of second harmonic approaches that of the fundamental. This can highly reduce the overlap area of SHG. Also due to the presence of 12 air holes in the first ring of the cladding, both the fundamental and second harmonic modes are tightly confined to the core and also become circular.

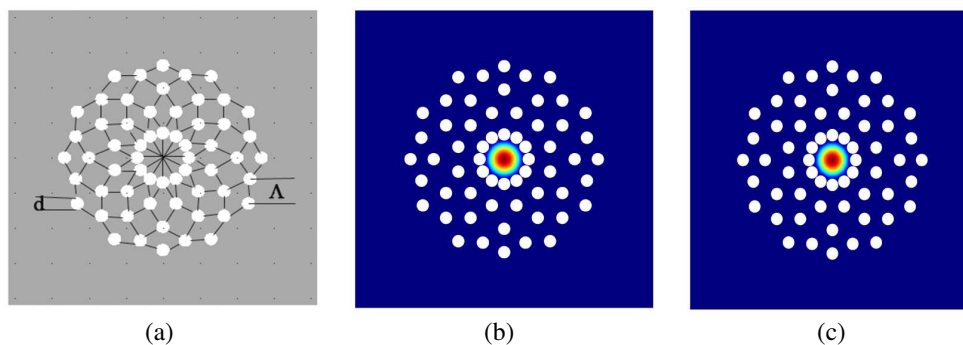


Figure 1: (a) The geometrical structure of the proposed PQF, (b) confinement of fundamental mode, (c) confinement of second harmonic mode.

4. SHG ANALYSIS

The Fig. 2 shows the variation of phase mismatch factor and overlap area with respect to pitch. Here we observe that, when pitch increases, the phase-mismatch factor decreases but the overlap area increases. Here we consider the quasi-phase matching (QPM) of first order for phase matching between fundamental and second harmonic. Hence the efficiency of SHG gets affected mainly with

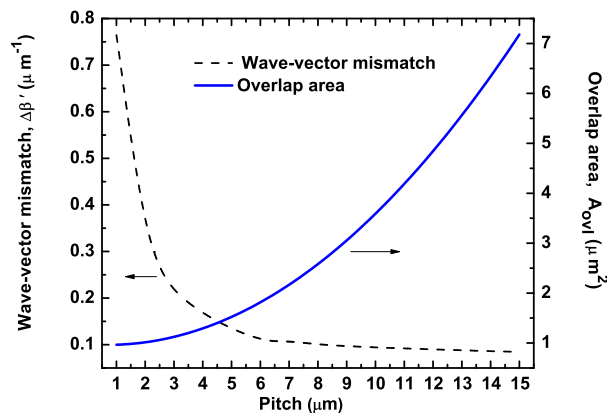


Figure 2: Variation of phase-mismatch factor and overlap area with respect to pitch.

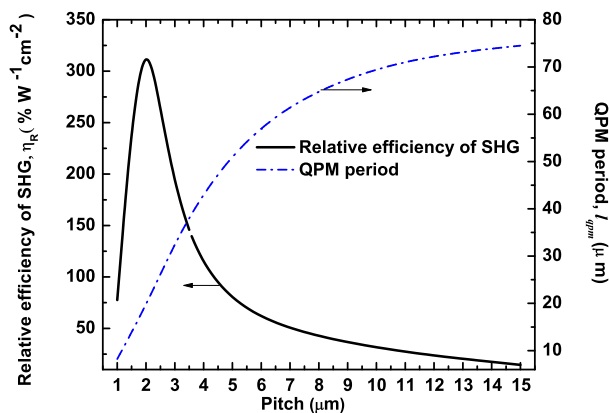


Figure 3: Variation of relative efficiency and QPM period with pitch.

the variation in overlap lap area. We point out that lowering the wave-vector mismatch parameter helps to get high QPM length and thus poling process becomes easier.

Having computed all the hitherto discussed physical parameters, we compute the relative efficiency (η_R) of SHG which is defined as, $\eta_R = \frac{\eta}{P_o L^2}$.

The Fig. 3 shows the variation of relative efficiency of SHG as well as the QPM length with variation of pitch. Here we find the efficiency increases with decrease in pitch where as the QPM length increases with increase in pitch.

In order to meet the poling requirements in PCF, we optimize the pitch value to be $7\ \mu\text{m}$ and all the results presented in this work reflect for this pitch [6]. Hence at this pitch we report a relative efficiency of $38.22\%W^{-1}\text{cm}^{-2}$ where the QPM period is of $61.59\ \mu\text{m}$. In Table 1, we compare the SHG efficiency and QPM length with already reported values of PCF in [2].

Table 1: Comparison of relative efficiency and QPM length between proposed PQF and PCF reported in [2]

Medium	η_R ($\%W^{-1}\text{cm}^{-2}$)	QPM length μm
PCF [2]	3.71	29.10
proposed PQF	33.22	61.59

In Table 1, we find that the proposed PQF exhibits a very high relative efficiency as well as QPM length when compared with the PCF reported in [2].

5. CONCLUSION

We have designed the twelve-fold PQF for enhancing the efficiency of second harmonic generation of $1.55\ \mu\text{m}$ of telecommunication band. For an optimum pitch of $7\ \mu\text{m}$, we report a relative efficiency of $38.22\%W^{-1}\text{cm}^{-2}$. We are enormously optimistic that with development of poling technique, the efficiency at the lower pitches of the twelve-fold PQF can also be obtained. In future, this work may be extended for higher harmonic generation of $1.55\ \mu\text{m}$.

ACKNOWLEDGMENT

KSN wishes to thank CSIR [No. 03(1264)/12/EMR-II] and DST (No. SR/FTP/PS-66/ 2009), the government of India, for the financial support through the project. SS wishes to thank DST (No. SR/S2/LOP-0014/2012), the government of India, for the financial support through the project.

REFERENCES

1. Yang, S.-D., S.-D. Yang, A. M. Weiner, K. R. Parameswaran, and M. M. Fejer, "400-photon-per-pulse ultrashort pulse autocorrelation measurement with aperiodically poled lithium niobate waveguides at $1.55\ \mu\text{m}$," *Opt. Lett.*, Vol. 29, No. 17, 2070–2072, 2004.
2. Bache, M., H. Nielsen, J. Lsggaard, and O. Bang, "Tuning quadratic nonlinear photonic crystal fibers for zero group velocity mismatch," *Opt. Lett.*, Vol. 31, 1612–1614, 2006.
3. Bhattacharjee, R., K. Senthilnathan, S. Sivabalan, and P. Ramesh Babu, "Exploring a photonic quasi-crystal fiber for enhancing the efficiency of second harmonic generation: Modeling and analysis," *Opt. Mater.*, Vol. 35, 2132–2137, 2013.
4. Bhattacharjee, R., K. Senthilnathan, S. Sivabalan, and P. Ramesh Babu, "Designing photonic quasi-crystal fibers of various folds: Onto optimization of efficiency and bandwidth of second harmonic generation," *App. Opt.*, Vol. 53, 2899–2905, 2014.
5. Kim, S., C. Kee, and J. Lee, "Novel optical properties of six-fold symmetric photonic quasicrystal fibers," *Opt. Express*, Vol. 15, 13221–13227, 2007.
6. Faccio, D., A. Busacca, W. Belardi, V. Pruneri, P. G. Kazansky, T. M. Monro, D. J. Richardson, B. Grappe, M. Cooper, and C. N. Pannell, "Demonstration of thermal poling in holey fibres," *Electron. Lett.*, Vol. 37, 107–108, 2001.

Few-cycle Pulse Generation Using Solid-core Photonic Quasi-crystal Fiber

K. Senthilnathan¹, M. S. Aruna Gandhi¹, S. Sivabalan², P. Ramesh Babu¹,
Abdosllam M. Abobaker³, and K. Nakkeeran⁴

¹Photonics, Nuclear and Medical Physics Division, School of Advanced Sciences
VIT University, Vellore 632 014, India

²School of Electrical Engineering, VIT University, Vellore 632 014, India

³Department of Communications Engineering, College of Electronic Technology, Bani Walid, Libya

⁴School of Engineering, Fraser Noble Building, University of Aberdeen, Aberdeen AB24 3UE, UK

Abstract— In recent years, the generation of few cycle pulses has been of great scientific and technological interest. In this line, the microstructured optical fibers have been playing a vital role since the desired optical properties can easily be engineered by adjusting the geometrical parameters. The recent results reveal that the quasicrystals exhibit several interesting photonic properties over periodic crystals. A solid core photonic quasi-crystal fiber (SC-PQF) is a novel microstructured fiber with quasi periodicity in structure and has a long range order with aperiodic arrangement in its cladding region. The structure of the cladding region consists of air holes of diameter d and pitch, Λ , with five rings of air holes. In the central region, the air hole is removed and the resulting solid silica core acts as a defect and gives rise to the propagation of guided modes. The photonic quasi-crystal fiber provides very large nonlinearity and sufficiently low dispersion that could be exploited for generating single cycle pulses. We look for the hitherto mentioned optical properties in the proposed SC-PQF by carefully optimizing the geometrical parameters namely, core diameter and the pitch. Eventually, with the proposed fiber, we study both dispersion and nonlinearity for a range of wavelengths from 0.6 to 1.1 μm and demonstrate sufficiently low dispersion ($-1.9478 \text{ ps}^2/\text{m}$) with zero confinement loss and enhanced nonlinearity ($\gamma = 578 \text{ W}^{-1}\text{m}^{-1}$) for a wavelength of 0.85 μm . The soliton effect compression of the femtosecond pulses in the proposed SC-PQF at 0.85 μm wavelength is numerically studied. A 15 fs pulse compressed down to 4 fs results in nearly 1.4 cycles of pulse generation.

1. INTRODUCTION

The search for the attosecond laser pulses is at the lead of the research in the laser physics. Pulses in the attosecond range may give rise to the development of attoelectronics, making it possible to study the dynamics and to control electronic processes in biology, chemistry, and solid-state physics, in the same way femtosecond laser technology led to femtochemistry [1–3]. Soliton effect pulse compression and propagation has been experimentally studied in the temporal domain in fibers [4], fiber Bragg gratings [5], photonic nanowires [6] and photonic crystal fibers [7–10]. In recent years, the generation of few and single cycle pulses in highly nonlinear photonic crystal fibers (PCFs) has been numerically studied [11, 12]. These few cycle pulses are generated by the mode-locked lasers and fiber-based pulse compression techniques. This fiber-based pulse compression technique is smartly used with the play of the dispersion and nonlinearity. In the fiber based lasers, mainly, there are two important pulse compression processes, namely, adiabatic pulse compression and soliton effect pulse compression. In the adiabatic pulse compression, the compressed pulses suffer from pedestals that arise because of the energy distribution in the wings of the intense output pulse [13]. More recently, the study of the higher order soliton effect pulse compression in a waveguide has been carried out [14].

In this work, we design a SC-PQF that exhibits very less confinement loss for a wide range of wavelengths. Besides, we also compute the enhanced optical properties, namely, low group velocity dispersion and high nonlinearity. These optical properties may be exploited for generating few-cycle pulses as well as supercontinuum [15–20].

2. GEOMETRIC DESIGN OF SC-PQF

Figure 1 shows the geometric structure of the proposed SC-PQF using finite element method with nine rings of air holes in its cladding region. The perfectly matched layer is designed for calculating the confinement loss of the proposed SC-PQF. This SC-PQF design has the basis of Stampfli quasicrystal structure [21, 22]. This type of quasicrystal structure has the repetition of the

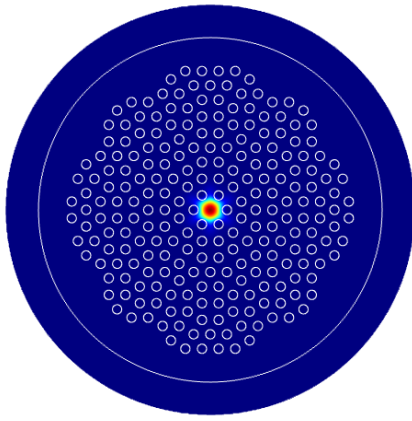


Figure 1: Fundamental mode of the proposed SC-PQF for 0.85 μm .

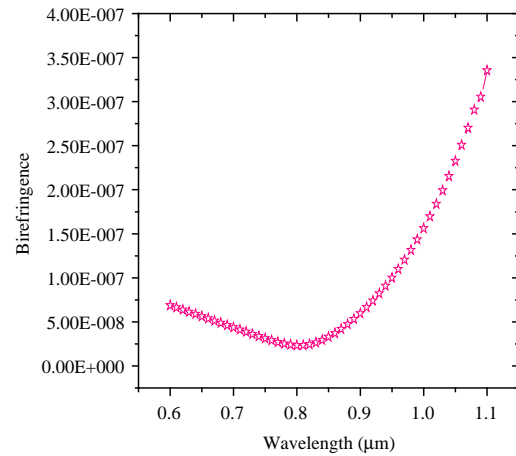


Figure 2: Birefringence of the proposed SC-PQF for 0.6 to 1.1 μm .

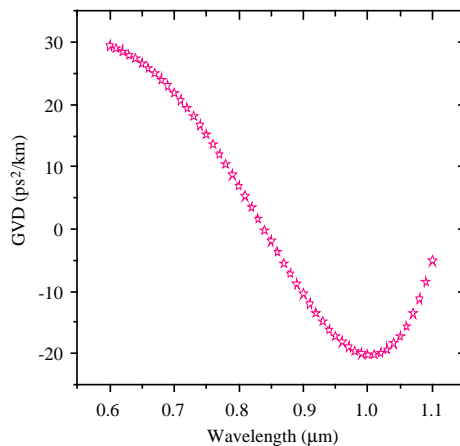


Figure 3: Group velocity dispersion as a function of wavelength.

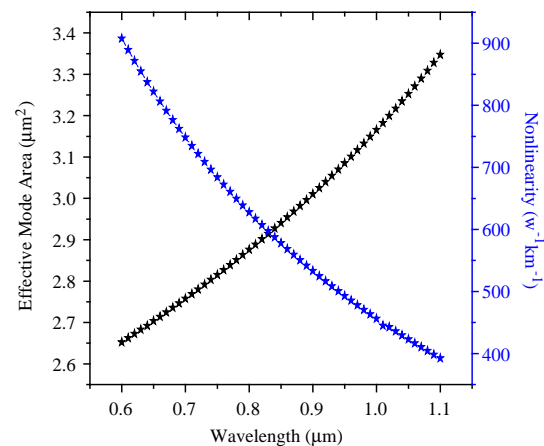


Figure 4: Effective mode area and nonlinearity as a function of wavelength.

square and the triangle arrangement of air holes in its cladding region. We calculate the effective refractive index (n_{eff}) of the fundamental mode for the proposed design and the same, is used to compute the dispersion from 0.6 to 1.1 μm wavelength.

3. OPTICAL PROPERTIES OF SC-PQF

In this section, we explore the various waveguiding properties of the proposed SC-PQF such as birefringence, group velocity dispersion, confinement loss, effective mode field area and nonlinearity.

Figure 2 describes the birefringence, B , of the proposed fiber and the same is determined by the difference between the effective indices of two orthogonal polarization modes. Initially the birefringence decreases from 0.6 μm to till 0.8 μm and above 0.8 μm wavelength, the birefringence gradually increases upto 1.1 μm . This is due to a relatively large effective refractive index difference between x and y polarization components for higher wavelengths. The birefringence observed for 0.85 μm wavelength is 3.27882×10^{-8} .

Figure 3 explains second order dispersion for a range of wavelengths from 0.6 to 1.1 μm . We have been able to achieve a low GVD ($-1.9478 \text{ ps}^2/\text{km}$) at 0.85 μm wavelength. These properties are crucial for the requirements of the few-cycle pulse generation. For the proposed SC-PQF, we calculate the confinement loss using the imaginary part of the effective refractive index of the fundamental mode with the perfectly matched layer.

Next, we compute the effective mode field area and nonlinearity by calculating the fundamental mode field area as shown in the Figure 4. We obtain a nonlinearity of $578 \text{ W}^{-1}\text{km}^{-1}$ at 850 nm wavelength. Here, the nonlinearity decreases as the wavelength increases. This is due to the fact that the mode confinement is tight at lower wavelengths and it becomes less as the wavelength increases.

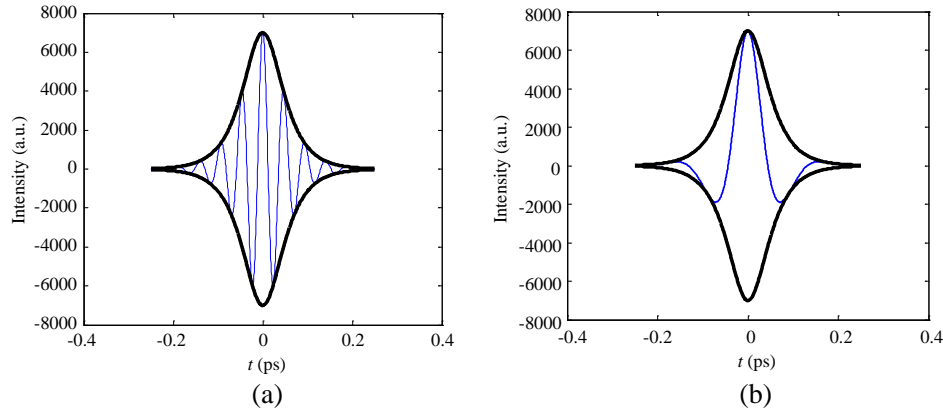


Figure 5: (a) & (b) Represent the input pulses and output pulses with number of oscillations for the proposed SC-PQF at $0.85 \mu\text{m}$.

4. PULSE COMPRESSION USING SC-PQF

In this work, we present a higher-order pulse compression with high nonlinear effects in the proposed SC-PQF. The evolution of the pulses inside the proposed SC-PQF is governed by the higher-order nonlinear Schrodinger equation (HNLSE) which includes the effects of anomalous GVD, self-phase modulation, self-steeping and stimulated Raman scattering. We adopt the usual split-step Fourier method to solve the HNLSE numerically. The generalized form of the HNLSE for the propagation of femtosecond pulses in an optical fiber is written in the form [23],

$$\frac{\partial A}{\partial z} + \frac{i\beta_2}{2} \frac{\partial^2 A}{\partial T^2} - \frac{i\beta_3}{6} \frac{\partial^3 A}{\partial T^3} = i\gamma \left[|A|^2 A + \frac{i}{\omega_0} \frac{\partial}{\partial T} (|A|^2 A) - T_R A \frac{\partial |A|^2}{\partial T} \right],$$

where A is the field envelope, T is the physical time in the retarded frame, z is the physical distance, β_2 is the second-order dispersion, β_3 is the third-order dispersion, γ is the nonlinear coefficient and T_R is the response time of the Raman effect. We consider the propagation of N th order soliton whose envelope field is chirp-free hyperbolic secant pulse given as,

$$A(o, T) = \sqrt{P_0} \operatorname{sech} \left(\frac{T}{T_0} \right),$$

where P_0 is the peak power and T_0 is the input soliton duration. A chirp-free hyperbolic secant pulse $A(o, T)$ is launched into the fiber with $\beta_2 = -1.9478 \text{ ps}^2/\text{km}$, $\gamma = 578 \text{ W}^{-1}\text{km}^{-1}$, $T_R = 3 \text{ fs}$. The full width at half maximum (FWHM) of the initial pulse is 15 fs. Here the pulse compression is achieved by choosing the fiber length suitably so that the initial pulse undergoes the required temporal narrowing. In the present work, as is evident from the Figure 7, we demonstrate a compression of an input pulse of width 15 fs to less than 4 fs which consists of 1.4 cycles, using a SC-PQF of core diameter at an operating wavelength of $0.85 \mu\text{m}$.

Figure 5(a) explains the number of oscillations of the input pulses. We take input pulse width of 15 fs with 5.34 cycles. Figure 5(b) represents the output pulse which consists of 1.4 cycles with less than 4 fs for the proposed SC-PQF at $0.85 \mu\text{m}$.

5. CONCLUSION

The waveguiding properties of a SC-PQF with a solid-core have been investigated. It has been found that the proposed SC-PQF exhibits the desired optical properties over a wide range of wavelengths from 0.6 to $1.1 \mu\text{m}$.

Further, we have been able to achieve sufficiently low dispersion ($\beta_2 = -1.9478 \text{ ps}^2/\text{m}$) with zero confinement loss and enhanced nonlinearity ($\gamma = 578 \text{ W}^{-1}\text{m}^{-1}$) for a wavelength of $0.85 \mu\text{m}$. The soliton effect compression of the femtosecond pulses in the proposed SC-PQF at $0.85 \mu\text{m}$ wavelength has also been numerically studied. The crux of the work lies in a 15 fs pulse having been compressed to 4 fs encompassing 1.4 cycles of pulse generation. We are of the opinion that the proposed structure would turn out to be an appropriate candidate for the supercontinuum generation.

ACKNOWLEDGMENT

KSN wishes to thank CSIR [No. 03(1264)/12/EMR-11] for the financial support through the project. SS wishes to thank DST [No. SR/S2/LOP-0014/2012], Government of India, for the financial support through the project.

REFERENCES

1. Corkum, P. B., *Nature*, Vol. 403, 845–846, London, 2000.
2. Porras, M. A., F. Salazar-Bloise, and L. Vazquez, *Opt. Lett.*, Vol. 26, 376–378, 2001.
3. Papadogiannis, N. A., B. Witzel, C. Kalpouzos, and D. Charalambidis, *Phys. Rev. Lett.*, Vol. 83, 4289–4292, 1999.
4. Mollenauer, L. F., R. H. Stolen, and J. P. Gordon, “Experimental observation of picosecond pulse narrowing and solitons in optical fibers,” *Phys. Rev. Lett.*, Vol. 45, 1095, 1980.
5. Eggleton, B., R. Slusher, M. de Sterke, P. Krug, and J. Sipe, “Bragg grating solitons,” *Phys. Rev. Lett.*, Vol. 76, 1627, 1996.
6. Foster, M., A. Gaeta, Q. Cao, and R. Trebino, “Soliton-effect compression of supercontinuum to few-cycle durations in photonic nanowires,” *Opt. Express*, Vol. 13, 6848, 2005.
7. Ouzounov, D. G., F. R. Ahmad, D. Müller, N. Venkataraman, M. T. Gallagher, M. G. Thomas, J. Silcox, K. W. Koch, and A. L. Gaeta, “Generation of megawatt optical solitons in hollow-core photonic band-gap fibers,” *Science*, Vol. 301, 1702, 2003.
8. Gerôme, F., K. Cook, A. K. George, W. J. Wadsworth, and J. Knight, “Delivery of sub-100 fs pulses through 8 m of hollow-core fiber using soliton compression,” *Opt. Express*, Vol. 15, 7126, 2007.
9. Dudley, J. M. and J. R. Taylor, “Ten years of nonlinear optics in photonic crystal fibre,” *Nature Photonics*, Vol. 3, 85, 2009.
10. Amorim, A. A., M. V. Tognetti, P. Oliveira, J. L. Silva, L. M. Bernardo, F. X. Kärtner, and H. M. Crespo, “Sub-two-cycle pulses by soliton self-compression in highly nonlinear photonic crystal fibers,” *Opt. Lett.*, Vol. 34, 3851, 2009.
11. Amorim, A. A., et al., “Sub-two-cycle pulses by soliton self-compression in highly nonlinear photonic crystal fibers,” *Opt. Lett.*, Vol. 34, 3851–3853, 2009.
12. Voronin, A. A. and A. M. Zheltikov, “Solitons evolving toward few- and single-cycle pulses in photonic-crystal fibers,” *Laser Phys.*, Vol. 18, 12, 2008.
13. Vasantha Jayakantha Raja, R., K. Senthilnathan, K. Porsezian, and K. Nakkeeran, “Efficient pulse compression using tapered photonic crystal fiber at 850 nm,” *IEEE J. Quantum Electron.*, Vol. 46, 1795–1803, 2010.
14. Foster, M., A. Gaeta, Q. Cao, and R. Trebino, “Soliton-effect compression of supercontinuum to few-cycle durations in photonic nanowires,” *Opt. Express*, Vol. 13, 6848–6855, 2005.
15. Peccianti, M., et al., “Subpicosecond optical pulse compression via an integrated nonlinear chirper,” *Opt. Express*, Vol. 18, 7625–7633, 2010.
16. Mollenauer, L. F., R. H. Stolen, J. P. Gordon, and W. J. Tomlinson, “Extreme picosecond pulse narrowing by means of soliton effect in single-mode optical fibers,” *Opt. Lett.*, Vol. 8, 289–291, 1983.
17. Shverdin, M. Y., D. R. Walker, D. D. Yavuz, G. Y. Yin, and S. E. Harris, “Generation of a single-cycle optical pulse,” *Phys. Rev. Lett.*, Vol. 94, 033904, 2005.
18. Liao, M., et al., “Tellurite microstructure fibers with small hexagonal core for supercontinuum generation,” *Opt. Express*, Vol. 17, 12174–12182, 2009.
19. Dudley, J. M. and J. R. Taylor, “Ten years of nonlinear optics in photonic crystal fibre,” *Nature Photon.*, Vol. 3, 85–90, 2009.
20. Merghem, K., et al., “Short pulse generation using a passively mode locked single InGaAsP/InP quantum well laser,” *Opt. Express*, Vol. 16, 10675–10683, 2008.
21. Sivabalan, S. and J. P. Raina, “Large pitch photonic quasi-crystal fiber amplifier,” *IEEE Photon. J.*, Vol. 4, No. 3, 943–951, 2012.
22. Sivabalan, S. and J. P. Raina, “High normal dispersion and large mode area photonic quasi-crystal fiber stretcher,” *IEEE Photon. Technol. Lett.*, Vol. 23, No. 16, 1139–1141, 2011.
23. Agrawal, G. P., *Nonlinear Fiber Optics*, 4th Edition, Academic, 2009.

Overcoming Bandwidth Limitation of LED by Using Multilevel Differential PAM in VLC

S. H. Yang, D. H. Kwon, and S. K. Han

Department of Electrical and Electronic Engineering, Yonsei University
50 Yonsei-ro, Seodaemun-Gu, Seoul, Korea

Abstract— We propose a novel modulation and de-modulation method to reduce the complexity of transmitter and receiver which is named multilevel differential pulse amplitude modulation (MD-PAM). The proposed modulation scheme transmits different PAM signals with same amplitude and unit time delay using different multiple LED chips. Optical signals from each LED chips are superposed during through the optical wireless channel and directly detected at the single optical receiver. Received signal is demodulated using signal power difference which is changed by light intensity. As a result, we experimentally confirmed that 100-Mbit/s transmission was possible using two LED chips which have 25 MHz modulation bandwidth, respectively.

1. INTRODUCTION

Commercial white light-emitting diodes (LEDs) have the great advantage to become the main device for indoor and outdoor illumination and already used for lighting source of numerous devices due to their energy efficiency, eco-friendly, and small size than previously light sources like as incandescent, uorescent light, and so on. LEDs also provide a cost-effective solution for transmitters of optical wireless communication systems [1–5]. In the infrared range, such systems provide wireless local-area-network connectivity in the order of several Mbps and above, in both line of sight and the diffuse regime. It is also possible to modulate the visible light emitted by lighting LEDs, hence providing illumination and wireless connectivity, simultaneously. These systems are usually referred to as optical wireless visible light communication (OWVLC) systems. However, narrow modulation bandwidth of commercial white LED is limitation of OWVLC. Modulation bandwidth of commercial white LED is limited about several MHz by characteristics of device. Therefore, using a simple modulation format which is non-return-zero on-off-keying (NRZ-OOK), the data rate reaches only to several Mbps. Thus, several studies have been carried out to overcome the intrinsic bandwidth limitation of LED. First of all, for the white lighting, most devices for illumination use a blue LED which illuminates a layer of yellow phosphor. These two colors are mixing and creating a white light. However, modulation bandwidth is typically lower than 3 MHz by slow time constant of the yellow phosphor material, thus optical blue filtering techniques have been reported to improve the modulation bandwidth [4, 5]. However, blue filtering also removes a large portion of the signal power, depending on the color spectrum emitted from the LED package, thus optical power loss is additionally occurred. Secondly, to enlarge modulation bandwidth and compensate the channel response, electrical pre-, post-equalizer circuits are adopted. The characteristic of pre- and post-equalizer have high pass filter (HPF). Thus, power loss is occurred and additional electric amplifier is required to compensate the power loss. Thirdly, to obtain the additional optical wireless channel, wavelength division multiplexing (WDM) based on RGB LED and optical color filter at receiver or polarization division multiplexing (PDM) based on polarizer is researched [6, 7]. However, proposed methods are also loss of optical power is occurred according to color filtering or polarization filtering. Fourthly, high-speed wireless connectivity is implemented using spectrally efficient modulation methods: quadrature-amplitude-modulation (QAM) with orthogonal frequency division multiplexing (OFDM) or discrete multi-tone (DMT) with water-filling algorithms [8, 9]. The transmission capacity can be increased significantly, because spectral efficiency is maximized. However, these modulation methods need additional digital signal processing such as fast Fourier transform (FFT) and inverse fast Fourier transform (IFFT), thus hardware and computational complexity of transmitter and receiver is increasing. In addition, modulated signals have a high peak-to-average power ratio (PAPR). Such a high PAPR necessitates the linear devices to have large dynamic range which is difficult to accommodate because light source can saturate and clip the peak at the high values. Thus, a RF devices and lighting source with nonlinear characteristics will cause undesired distortion. In addition, peaking the LED increased its temperature, which in turn leads to undesired color shift and reduced LED lifetime. Last, spatial modulation (SM) is introduced [10, 11]. Generally, SM is required different channel gain or transmitted signal power

is required. One of the special form of the GM is generalized space shift keying (GSSK). In this case, with an array of N_t LEDs, GSSK can send N_t bits/symbol. However, it is required different channel gain with 2^{N_t-1} levels. Thus, additional time synchronization between different LEDs are required. Another method is superposed pulse amplitude modulation (SPAM). The SPAM is using characteristics of optical wireless channel. Superposed different signals from different LEDs are detected single receiver. The modulation order is also N_t bit/symbols, however it is also required different intensity ranges of $V, 2V, 4V, 2^{N_t-1}V$ to obtain 2^N -SPAM. Thus, nonlinearity of device can be occurred where high signal power required LED.

In this paper, we propose a novel modulation and de-modulation format to reduce the complexity of transmitter and receiver which is named multilevel differential pulse amplitude modulation (MD-PAM). The proposed modulation scheme transmits different PAM signals with same amplitude and unit time delay using multiple LED chips, respectively. Optical signals from every LED chips are linearly accumulated during through the optical wireless channel and directly detected at the single optical receiver. Received signal is demodulated using received signal power difference which is changed by light intensity. As a result, we experimentally confirmed that 100-Mbit/s transmission was possible using LED which has 25 MHz modulation bandwidth.

2. OPTICAL WIRELESS CHANNEL CHARACTERISTICS

Generally, OWVLC use intensity modulation and direct detection (IM/DD) which is traditional modulation method using optical wired and wireless communication system. The single LED produces an instantaneous optical power waveform which is expressed X and it was always positive values with average transmitted power can be describe as

$$P_t = \lim_{x \rightarrow 0} \frac{1}{2T} \int_{-T}^T X(t) dt \quad (1)$$

where T is time period of transmitted optical signal. The produced electrical power which is converted from optical receiver is decided by response to all light incident on its effective area. For now we assume an ideal channel H_0 , and we represent the light as

$$P_{opt} = h_0 X(t) + P_{amb} \quad (2)$$

where $H_0 X(t)$ is the light intensity from single LED and P_{amb} is and unwanted light component from all other light sources and it can include LEDs. The optical receiver converts this light into a current and it can be changed received signal power PRF. Random nature of photo-electronic interactions within the optical receiver, the additional noised component $N(t)$ is generated. This noise component is random and distribution pattern is same with Poisson distribution. Thus, current and its variance are proportional to the total irradiance. The received signal power PRF can be describe as two different terms: a positive signal composed by P_t and P_{amb} , and noise component which is zero-mean fluctuation, or shot noise and it can be describe as

$$P_{RF} = R(H_0 X(t) + P_{amb}) + N(t) \quad (3)$$

where R is the responsivity of the used optical receiver including effective area. The additional noise component including shot noise is appropriate to model $N(t)$ as white and Gaussian distribution. Thus, we can expect that if different LEDs generate optical signals which component is P_{amb} , received optical and electrical signals are linearly accumulated.

3. EXPERIMENTS AND RESULTS

The modulation bandwidth of the commercial white LEDs is not over the 10 MHz and it was the intrinsic characteristics of the LED. Fig. 1 shows the frequency response of electrical-optical-electrical system using white LED (OSRAM LE UW S2W). The 3 dB bandwidth of used avalanche photodiode (APD) is 100 MHz which obtain data-sheet from HAMAMATSU, thus bandwidth limitation is caused by used LED. From Fig. 1, the 3 dB bandwidth of the used LED is approximately 1.5 MHz, so the expected data rate cannot over the 10 Mbps when using NRZ-OOK. In this experiment, the modulation bandwidth can be enhanced up to 25 MHz by using a pre-equalizer.

Multiple optical signal transmitting is enabled in the optical wireless channel and superposed light intensity can be detected at the receiver part. The operation principle of proposed modulation format is shown in Fig. 2. The generated pseudorandom binary sequence (PRBS) signals are

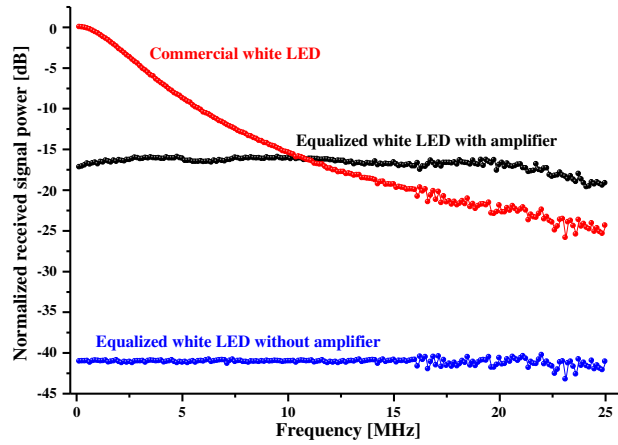


Figure 1: Frequency response of used commercial white LED.

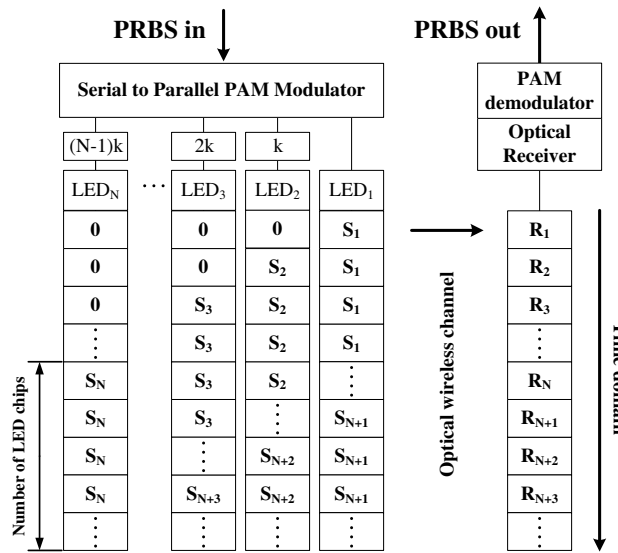


Figure 2: Block diagram of proposed MD-PAM algorithms.

modulated using PAM modulator and distributed in parallel to N different LED chips. When wanted total transmission rate is PRBS, the symbol period of transmitted signal when modulation format is M-PAM is τ which can be calculated by $\log_2 M = PRBS \cdot \tau$. The distributed and modulated signal at each LED chip can be described as

$$S_i[N(t-1) + i + k] = MPAM[N(t-1) + i], \quad 0 \leq k < N \quad \text{and} \quad 0 < i \leq N \quad (4)$$

where S_i is a transmitted signal at the i th LED chip, t is a unit time, and k is an arbitrary constant. The required modulation bandwidth of proposed system of each LED chip is decreases by $PRBS = \log_2 M$; thus, the bandwidth limitation of the LED can be overcome and frequency efficiency at the view of LED is 2 bits/Hz. The received optical intensity $R(t)$ becomes then linearly superposed while passing through the optical wireless channel. The received signal power variation for unit time is determined by a single LED device, thus, the demodulated signal $D(t)$ can be obtained by

$$D(t) = \begin{cases} R(t) & \text{if } t = 1 \\ R(t) - R(t-1) & \text{if } 1 < t \leq N \end{cases} \quad (5)$$

during first symbol duration. However, after first duration, demodulation method is slightly different because received signal is affected by previous symbol when received optical power difference is zero. Thus, demodulation method can be describe as

$$D(t) = R(t) - R(t-1) + D(t-N) \quad (6)$$

The random bits were generated by offline process and the generated 4-PAM signals are distributed to different two port of an arbitrary waveform generator (AWG). The electrical signals are transmitted to each LED chip using bias-tee. The time delay between different two channels is given by digital signal process. After the pre-equalizer the signal is transferred to each LED chip. The light intensity of a single LED device was changed by the 4-PAM signal and the superposed optical signals are detected by APD. The generated electrical signals were captured by a mixed signal oscilloscope. After synchronization, the received signals were demodulated.

The BER measurements have been done for the signal performance evaluation. When 100 Mbps PRBS signals are generated, the assigned symbol rate per single LED chip is 25 MSymbol/s according to proposed modulation method. The received eye-diagram of the single LED is shown in Fig. 3(a). When the Ch1 and Ch2 transmitted at the same time, received signals are accumulated and it is shown Fig. 3(b). Demodulation is possible using distinguishable levels and threshold values. After demodulation, BER 10^{-3} is achieved which is FEC limitation.

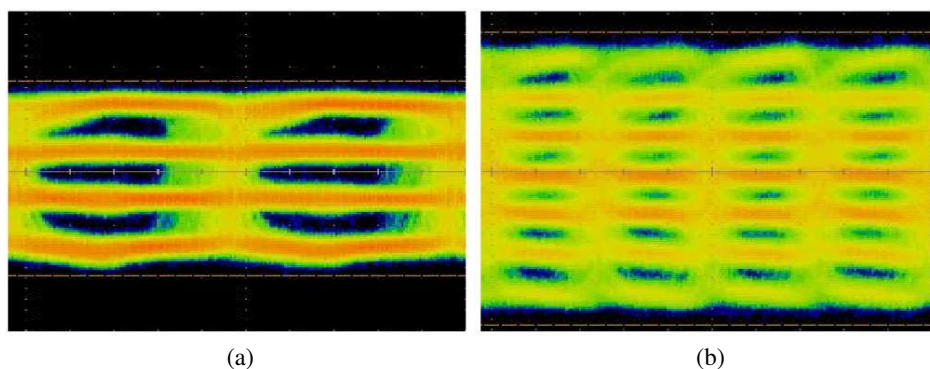


Figure 3: Eye-diagram of received signal (a) single LED only, (b) two different LEDs, simultaneously.

4. CONCLUSIONS

We propose and experimentally demonstrate the MDPAM with white LEDs based OWVLC. A commercial white LED with a modulation bandwidth of 1.5 MHz was used for the lighting source. The experiment is performed using a single LED light source which is composed of four chips for the transmission distance of 0.8 m. Two LED chips are separately modulated using MPAM and accumulated light is detected by a single APD. We achieved BER 10^{-3} for 100-Mbit/s. In addition, proposed system expect that the transmission rate can be linearly increased as we increase the number of LEDs. Thus, the possible transmission data rate can be extremely increased even using a low frequency response LED transmitter.

ACKNOWLEDGMENT

This work was supported by the National Research Foundation of Korea (NRF) grant funded by the Korea government (MSIP) (No. 2013R1A2A2A01008341).

REFERENCES

1. Gancarz, J., H. Elgala, and T. D. D. Little, "Fundamental analysis for visible-light communication system using LED lights," *IEEE Trans. Consum. Electron.*, Vol. 51, No. 12, 34–41, 2013.
2. Komine, T. and M. Nakagawa, "Fundamental analysis for visible-light communication system using LED lights," *IEEE Trans. Consum. Electron.*, Vol. 50, No. 1, 100–107, 2004.
3. Tanaka, Y., T. Komine, S. Haruyama, and M. Nakagawa, "Indoor Visible communication utilizing plural white LEDs as lighting," *Proceedings of 12th IEEE PIMRC*, F81–F85, 2001.
4. Le-Minh, H., D. O'Brien, G. Faulkner, L. Zeng, K. Lee, D. Jung, and Y. Oh, "High-speed visible light communications using multiple-resonant equalization," *IEEE Photon. Technol. Lett.*, Vol. 20, No. 14, 1243–1245, 2008.
5. Li, H., X. Chen, B. Huang, D. Tang, and H. Chen, "High bandwidth visible light communications based on a post-equalization circuit," *IEEE Photon. Technol. Lett.*, Vol. 26, No. 2, 119–122, 2014.

6. Cossu, G., A. M. Khalid, P. Choudhury, R. Corsini, and E. Ciaramella, "3.4 Gbit/s visible optical wireless transmission based on RGB LED," *Opt. Express*, Vol. 20, No. 26, B501–B506, 2012.
7. Wang, Y., C. Yang, Y. Wang, and N. Chi, "Gigabit polarization division multiplexing in visible light communication," *Opt. Letters*, Vol. 39, No. 7, 1823–1826, 2014.
8. Vucic, J., C. Kottke, S. Nerreter, K. D. Langer, and J. W. Walewski, "513 Mbit/s visible light communications link based on DMT-modulation of a white LED," *J. Lightwave Technol.*, Vol. 28, No. 24, 3512–3518, 2010.
9. Jung, S., S. Jung, and S. Han, "I/Q channel separated baseband OFDM optical transmission using orthogonal polarizations in IM/DD system," *J. Lightwave Technol.*, Vol. 32, No. 13, 2392–2398, 2014.
10. Popoola, W. O. and H. Haas, "Demonstration of the merit and limitation of generalised space shift keying for indoor visible light communications," *J. Lightw. Technol.*, Vol. 32, No. 10, 1960–1965, 2014.
11. Li, J. F., Z. T. Huang, R. Q. Zhang, F. X. Zeng, M. Jiang, and Y. F. Ji, "Superposed pulse amplitude modulation for visible light communication," *Opt. Express*, Vol. 21, No. 25, 31006–31011, 2013

Compact Waveguide Load with Thin Film Resistor

Manseok Uhm, Hongyeal Lee, Changsoo Kwak, Sohyeon Yun, and Inbok Yom

Satellite & Wireless RF Technology Section, Electronics and Telecommunications Research Institute, Korea

Abstract— In this paper, we present a compact rectangular waveguide load using tantalum nitride (TaN) thin film resistor (TFR) as an absorber for Ka band applications. The TFR having good temperature coefficient and stable performances is attached on an alumina substrate. It can be easily attached to an end wall of a waveguide for connecting an adjacent waveguide flange. To achieve good impedance matching over a wide frequency range, we put TFR with stepped shape at the center of waveguide. It is designed with an alumina substrate with TaN TFR. The actual size of the 5 mil alumina substrate with sheet resistance of $100 \Omega/\text{sq}$ is $3.5 \text{ mm} \times 9.0 \text{ mm}$. Verification of the design results has been carried out by fabrication and measurement of the waveguide load. Return loss above 20.0 dB has been obtained over frequency range of 4.0 GHz in the Ka band.

1. INTRODUCTION

Due to excellent electrical performances such as low insertion loss, high return loss and high power handling capacity, waveguide components are widely adopted for microwave communication systems in spite of a relatively larger volume than microstrip or coaxial components. Waveguide loads are needed for directional couplers used for test set-up and hybrid waveguide couplers to obtain high output power by combining parallel multiple power amplifiers with solid-state devices [1, 2]. Especially, a compact waveguide load is required to develop compact SSPA using hybrid couplers (branch coupler or magic-tee combiner) with matched loads.

Since absorbing material in the waveguide attenuates input RF signal, the shape and the place of absorber depend on electrical performances of loads. In general, gradual increase of absorber makes good impedance matching over a wide bandwidth. The absorber is located at the center of a waveguide where the electric field intensity is the greatest [3].

We proposed a compact rectangular waveguide load using a thin film resistor (TFR) as an absorber. It works by placing a resistor in the center of the waveguide. To make good impedance matching over wide frequency range, we put thin film resistor with stepped shape. Tantalum nitride (TaN) TFR with good temperature coefficient and stable performances is produced on an alumina substrate that shows suitable accuracy of dimension [4]. We designed a compact waveguide load with TaN thin film resistor for Ka band applications. The resistivity is $100 \Omega/\text{sq}$ and the height of substrate is 5 mil. The proposed matching termination can be easily attached at the end wall of a waveguide. Thus it can be easily connected to the waveguide flange of a component. Several samples for WR 28 standard waveguide were fabricated and measured to confirm the reproducibility. The actual size of the alumina substrate is $3.5 \text{ mm} \times 9.0 \text{ mm}$. We confirmed that all the results agreed excellently. The measured return loss above 20.0 dB has been obtained over the frequency range 26.5 GHz to 30.5 GHz.

2. DESIGN AND ANALYSIS

2.1. Design of Compact Waveguide Load

Figure 1 shows the structure of the waveguide load with TFR attached on the dielectric substrate in this work. The substrate with TFR is located in the center of waveguide. The substrate which can be easily mounted on the end wall of the waveguide plays a role of supporting the TFR. In order to design the waveguide load, the effect of the dielectric substrate must be considered because the substrate affects the total resistivity.

We choose TaN material and alumina substrate, since the TaN TFR has good temperature coefficient and stable performances, and an alumina substrate shows suitable accuracy of dimension. The impedance matching characteristics depend on the length and the shape of the TFR with the sheet resistance. An easy way to implement a compact waveguide load is to use gradual increasing the width of the film resistor to get good return loss over a wide frequency range. We used multiple sections instead of tapering to avoid sharp edge where the strong electric field occurs. A three-stepped TFR is obtained by compromising between the length of a TFR and return loss. The compact waveguide load with TaN thin film resistor is designed as shown in Figure 2. The

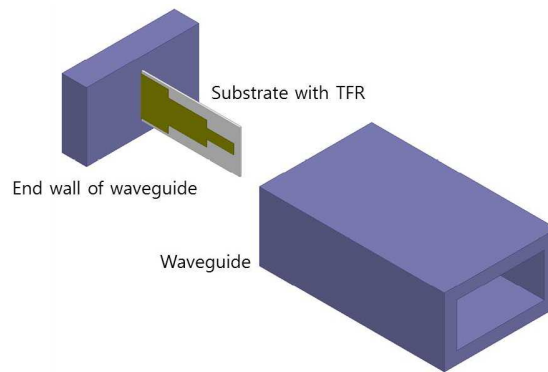


Figure 1: Structure of the proposed waveguide load with thin film resistor.

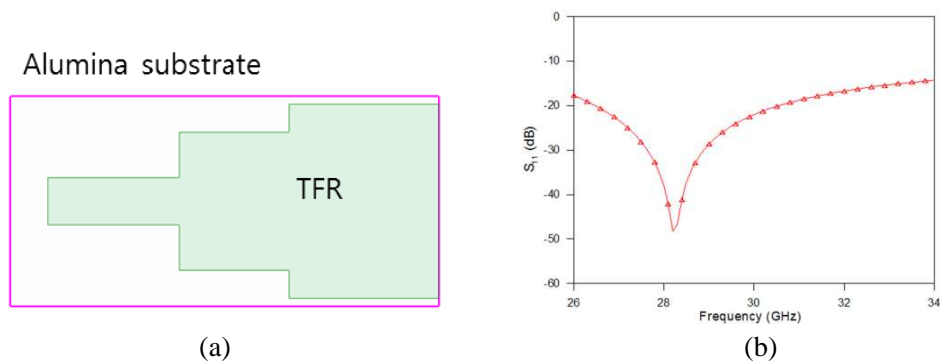


Figure 2: (a) The layout of TFR on the alumina substrate. (b) Return loss of the designed waveguide load.

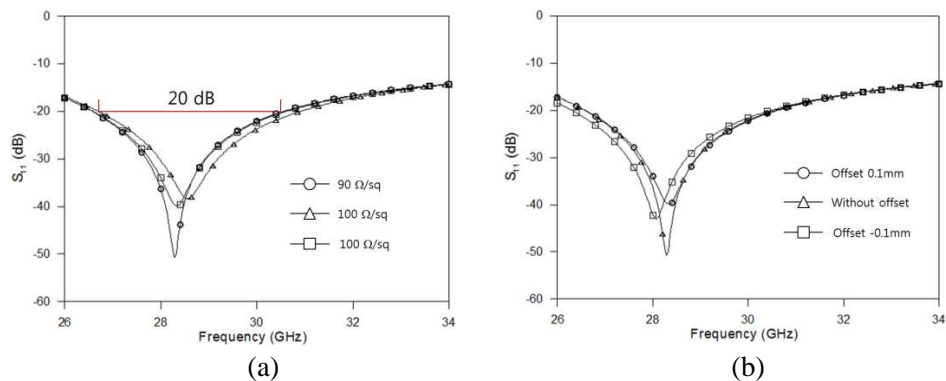


Figure 3: (a) Return loss according to the variation of $\pm 10\%$ sheet resistance. (b) Return loss according to the variation of $\pm 0.1\text{mm}$ offset.

resistivity is $100\ \Omega/\text{sq}$ and the height of substrate is 5 mil. The actual size of the alumina substrate is $3.5\ \text{mm} \times 9.0\ \text{mm}$.

2.2. Sensitivity Analysis

In particular, frequency characteristics may deteriorate due to fabrication error at higher frequency band such as millimeter band. Thus a waveguide load having wideband characteristics while being easily fabricated and assembled is required. Sensitivity analysis is performed according to the fabrication and assembling tolerance such as the variation of sheet resistance and dimension error. Figure 3(a) shows the return loss with respect to the variation of sheet resistance. The sheet resistance can be varied due to fabrication error and variation of temperature. Return loss above 20 dB is maintained over 3.8 GHz range within the variation of $\pm 10\%$ sheet resistance. While assembling alumina substrate with TFR on the end wall of waveguide, the position of longitudinal direction will be changed due to human errors. Figure 3(b) shows the return loss according to the change of position such as $\pm 0.1\ \text{mm}$ offset. Note that the proposed load has stable return loss

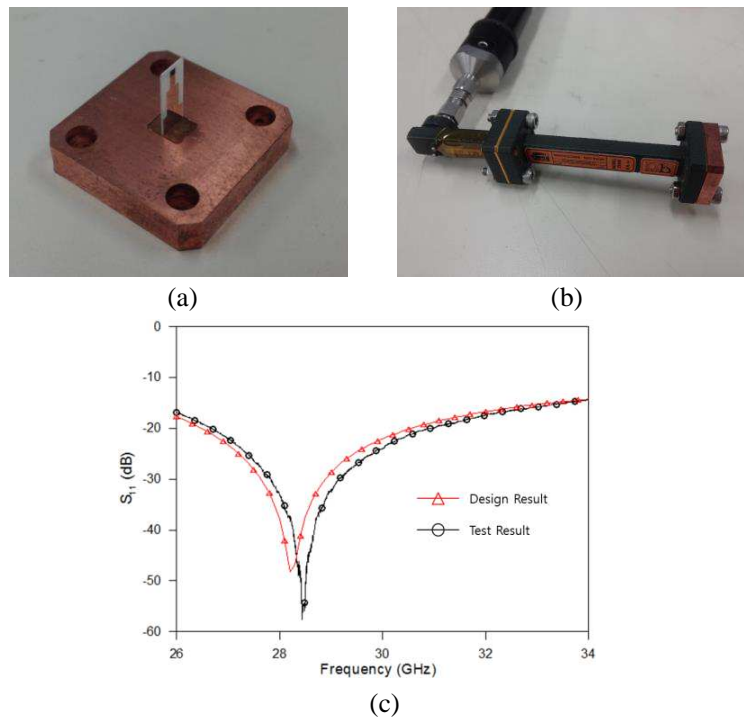


Figure 4: (a) Fabricated compact waveguide load. (b) Rectangular waveguide connected with the fabricated load. (c) Design and test results.

characteristics during variation of resistance and dimension error.

3. FABRICATION & MEASUREMENT

Several samples for WR 28 standard waveguide were fabricated and measured to confirm the reproducibility. Figure 4(a) shows the fabricated compact waveguide load composed of an end-wall and an alumina substrate with TFR. As shown in Figure 4(b), the compact load can be easily connected with the standard flange of a rectangular waveguide line. Figure 4(c) shows the simulated and measured results of the designed load. We confirmed that all the results agreed excellently. The measured results have proved the design results, as shown in Figure 4(c). Return loss above 20.0 dB has been obtained over 4.0 GHz of bandwidth in the Ka band.

4. CONCLUSION

In this paper, a compact waveguide load composed of a dielectric substrate with TFR has been proposed. This compact load can be easily fabricated and connected to the waveguide lines. The fabricated load has return loss above 20 dB over the frequency range 26.8 GHz to 30.8 GHz. It can be applied to a waveguide termination for hybrid combiners. For high power applications, the thermal analysis can be followed in the near future.

ACKNOWLEDGMENT

This work was supported by the ICT R&D program of MSIP/IITP. [B0101-15-0141, Development of Flexible Payload Technologies for Next Satellite Broadcasting and Communications].

REFERENCES

1. Vaden, K. R., "Computer aided design of Ka-band waveguide power combining architectures for interplanetary spacecraft," Tech. Memo. NASA/TM 2006-214108, NASA, Cleve-Land, OH, Feb. 2006.
2. Zhao, L., J. Xu, L. Wang, and M.-Y. Wang, "A novel Ka-band solid-state power combining amplifier," *Progress In Electromagnetics Research C*, Vol. 23, 161–173, 2011.
3. Uher, J., J. Bornemann, and U. Rosenberg, *Waveguide Components for Antenna Feed Systems: Theory and CAD*, Artech House, Norwood, MA, 1993.

4. Bozorg-Grayeli, E., Z. Li, M. Asheghi, G. Delgado, A. Pokrovsky, M. Panzer, D. Wack, and K. E. Goodson, "High temperature thermal properties of thin tantalum nitride films," *Applied Physics Letters*, Vol. 99, 261906-1–261906-3, 2011.

Channel Equilibration in Wideband Digital Array Radar Test-bed

Weixing Li, Jianzhi Lin, Weihua Wang, Biao Tian, and Zengping Chen

Science and Technology on Automatic Target Recognition Laboratory
National University of Defense Technology, Changsha, China

Abstract— In actual digital array radar (DAR) systems, analog components will cause frequency-dependent amplitude and phase mismatch among receive channels. This paper demonstrates the design and implement of the channel equilibration subsystem of an 8-element DAR test-bed. An ultra-wideband waveform generator is designed for generating various calibration signals and the pre-distortion algorithm is presented to compensate for the reconstruction errors. In the receive channels, an improved inverse Fourier Transform algorithm for filter design is investigated in detail based on analysis of real receive channels. The processing results of measured data show the high performance of channel equilibration algorithms.

1. INTRODUCTION

Wideband Digital array radar (DAR) is widely used in space surveillance, for it meets the requirements for multi-functions and multi-beams simultaneously while providing large dynamic range, resistance to interferes and flexible control [1–3]. In actual systems, analog components such as feed lines, amplifiers, band-pass filters and ADCs will cause the distortion of frequency responses of each channel as well as amplitude and phase mismatch between receive channels, which will severely degrades the performances of the array.

Active calibration algorithms are widely researched and applied to compensate for channel mismatch. Lars Pettersson in Swedish Defense Research Agency designed a 15 tap equalizing FIR filter in a 12 channel S-band digital beam-forming antennas, and the cancellation ration was improved from -29 dB to -75 dB [4]. In the 96-element, L-band DAR prototype established by the Office of Naval Research, receive data were fed into a 20-tap, 16 bit complex FIR for equalization [5]. Wang Fang proposed a modified equilibration algorithm making use of Fourier Transform, which had excellent real-time performance [6]. Zhang Yue improved the filter-design algorithm by linear-fitting and designed the equilibration filter for a DAR test-bed with the bandwidth of 200 MHz [7]. As the simultaneous bandwidth of DAR test-bed has reached up to 500 MHz nowadays, the fundamental challenge in channel equilibration is the design of high quality wideband waveform generator as well as the realization of equilibration algorithms on FPGA-based processors [8, 9].

This paper focuses on channel equilibration of an 8-element L/S band DAR test-bed. In Section 2, a flexible wideband waveform generator is designed. Pre-distortion method according to working mode of DAC is implemented to improve the quality of waveforms. In Section 3, the inverse Fourier Transform algorithm is studied based on analysis of measured data, and then the equilibration filter is realized by FFT. In Section 4, experiments are carried out in the anechoic chamber, and some results are demonstrated in detail. Conclusions are drawn in Section 5.

2. WIDEBAND WAVEFORM GENERATION AND CALIBRATION

2.1. Design of Wideband Waveform Generator

Channel equilibration module in the DAR test-bed is illustrated in Figure 1. The equilibration algorithms are carried out in three steps. Firstly, wideband calibration signals are generated by the waveform generator according to the command of control computer. Then the signals are injected into each digital module through calibration network that is composed of a power divider and a coupler. Secondly, the calibration data are received by digital modules and transmitted to the control computer through optical fiber links, and the frequency responses are obtained. Thirdly, design the equilibration filters and send the coefficients to digital module for measured data equilibration.

The wideband waveform generator is composed of a FPGA carrier board and digital-to-analog convertor (DAC) card. The carrier board is a VPX product equipped with two Xilinx Virtex chips XC6VSX315T. The high-speed wideband DAC is integrated on a FPGA Mezzanine Card (FMC), which can be plugged into the FPGA carrier board. It is a single-channel, 12 bits DAC with the highest sampling rate of 3 Gsps. By setting the chip to work in different modes, it is capable of generating analog waveforms from 0 GHz to 6 GHz. When the DAR test-bed works in calibration

mode, FPGA receives commands from the controller, and produces desired waveforms by direct digital synthesis (DDS). The low-speed baseband digital data are sent to the DAC to generate high-frequency analog waveforms.

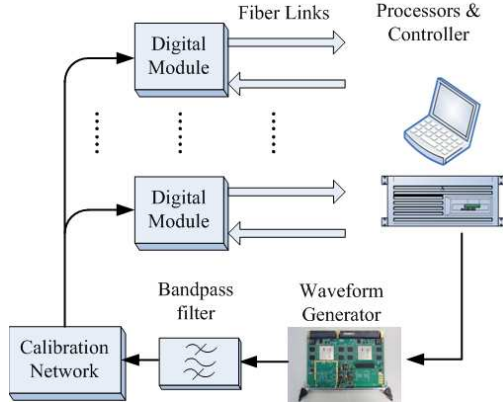


Figure 1: Block of channel equilibration subsystem.



Figure 2: High-speed wideband DAC card.

2.2. Pre-distortion Algorithm for Waveform Generation

The DAC integrates a sample-and-hold to reconstruct waveforms from baseband data. However, it is impossible to realize an impulse function in actual components. Therefore reconstruction errors are introduced, leading to deterioration of analog waveforms.

Suppose the desired signal is $s(t)$, the sampling rate is T_s and the baseband data can be expressed as $s(nT_s)$, So the reconstruction function is $s_r(t) = \sum_{n=-\infty}^{\infty} s(nT_s)q(t - nT_s)$, where $q(t)$ is the reconstruction factor. The Fourier Transform of $s_r(t)$ is as follows:

$$S_r(\omega) = \sum_{n=-\infty}^{\infty} s(nT_s) \int_{-\infty}^{+\infty} q(t - nT_s) e^{-j\omega t} dt = Q(\omega) \left(\sum_{n=-\infty}^{\infty} \int_{-\infty}^{+\infty} s(t) e^{-jnT_s\omega} dt \right) = Q(\omega) \tilde{S}(\omega) \quad (1)$$

where $\tilde{S}(\omega) = \int_{-\infty}^{+\infty} s(t) \cdot \left(\sum_{n=-\infty}^{\infty} \delta(t - nT_s) \right) e^{-j\omega t} dt = \frac{1}{T_s} \sum_{n=-\infty}^{\infty} S(\omega - n\frac{2\pi}{T_s})$ and $S(\omega)$ is Fourier Transform of the desired signal. It is clear that $\tilde{S}(\omega)$ is the extension of $S(\omega)$ by the period of $\frac{2\pi}{T_s}$.

It can be concluded from Equation (1) that the output waveform is the combination of extension of the desired signal and the modulation function $Q(\omega)$. The distortion resulting from the modulation can be calibrated by pre-distortion method. That means imposing the inverse filter of $Q(\omega)$ on baseband data to compensate for the distortion.

Taking the DAC in Figure 2 as an example, The Fourier Transform of reconstruction factor is:

$$Q(\omega) = T_s \cdot e^{-j\frac{T_s}{2}\omega} \cdot \sin\left(\frac{T_s}{4}\omega\right) \cdot \text{sinc}\left(\frac{T_s}{4}\omega\right) \quad (2)$$

Then the pre-distortion function is obtained:

$$P(\omega) = \frac{1}{T_s} \cdot e^{-j\frac{T_s}{2}\omega} \cdot \frac{1}{\sin(\frac{T_s}{4}\omega) \cdot \text{sinc}(\frac{T_s}{4}\omega)} \quad \frac{2\pi}{T_s} < |\omega| < \frac{3\pi}{T_s} \quad (3)$$

In this paper, the baseband data of the LFM signal (the bandwidth is 500 MHz, and the center frequency is 2.7 GHz) is generated by the FPGA. After pre-distortion processing, the calibrated data is sent to DAC. The analog waveforms are shown in Figure 3. After calibration, the ripple is reduced and the quality is improved significantly.

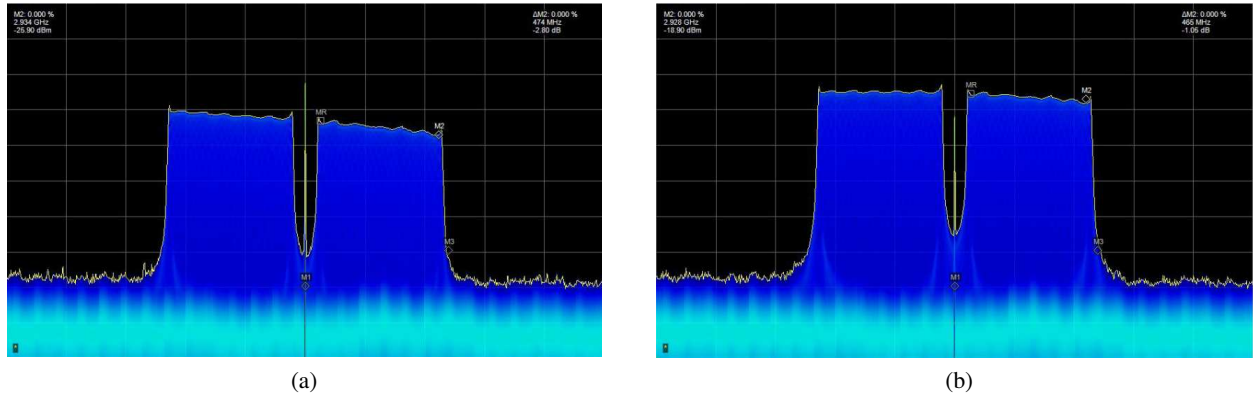


Figure 3: Spectrum of 2.45-2.95 GHz LFM signal. (a) before calibration. (b) after calibration.

3. FREQUENCY DOMAIN EQUILIBRATION ALGORITHM

3.1. Improved Inverse Fourier Transform Algorithm

In actual DAR system, equilibration filters are usually added into the receive channels to compensate for channel mismatch. Reference [7] has proposed an improved inverse Fourier Transform algorithm to design the equilibration filters and applied it in a DAR prototype with the bandwidth of 200 MHz successfully. Since the instantaneous bandwidth of the DAR test-bed has increased to 500 MHz, this paper makes further study on the algorithm with the help of measured data.

Suppose there are channels in the system, the frequency response of reference channel and i th channel is $S_{ref}(k)$ and $S_i(k)$ respectively. The desired response of i th equilibration filter is:

$$H_{di}(k) = \frac{S_{ref}(k)}{S_i(k)} \quad i = 1, 2, \dots, M \quad k = 0, 1, \dots, K-1 \quad (4)$$

Suppose the complex coefficients of the i th equilibration filter is $h_i(n) \quad n = 0, 1, \dots, N-1$, then the discrete frequency response is:

$$H_i(k) = \sum_{n=0}^{N-1} h_i(n) e^{-j\omega n} \Big|_{\omega = \frac{2\pi}{M}k} \quad (5)$$

According to the Least-Square criterion, when the mean square error between $H_{di}(k)$ and $H_i(k)$ reaches the minimum value, the optimum $h_i(n)$ can be obtained taking account of the Parsval theorem as follows:

$$\min_h E_i = \min_h \sum_{k=0}^{K-1} |H_{id}(k) - H_i(k)|^2 = \min_h \sum_{n=0}^{K-1} |h_{id}(n) - h_i(n)|^2 \quad (6)$$

In Equation (6), $h_i(n)$ is the coefficients of equilibration filter, and it only has N values, so it can be expressed as:

$$\min_h E_i = \min_h \sum_{n=0}^P |h_{id}(n)|^2 + \sum_{n=P+1}^{P+N} |h_{id}(n) - h_i(n)|^2 + \sum_{n=P+N+1}^{K-1} |h_{id}(n)|^2 \quad (7)$$

The optimum values of $h_i(n)$ can be obtained that by choosing the P maximum values of $h_{id}(n)$.

However, in practical circumstance, the traditional inverse Fourier Transform method is sensitive to the out-band noise. A more practical method is to poly-fit the out-band frequency response, that is, replace the desired response in Equation (6) by Equation (8):

$$H_{di}(k) = \begin{cases} \frac{S_{ref}(k)}{S_i(k)} & \frac{K}{2}(1 - \frac{2B}{f_s}) \leq k \leq \frac{K}{2}(1 + \frac{2B}{f_s}) \\ a + b \cdot k & \text{others} \end{cases} \quad (8)$$

where a and b are the coefficients which are determined by poly-fit of the in-band data.

Taking the first channel as an example, the measured frequency response is shown in Figure 4(a). The in-band response changes slowly while the out-band response changes dramatically and discontinuously. Figure 4(b) demonstrates the modified desired response and the frequency responses of equilibration filters with 40, 80, 160 taps. It can be learned that a 160-tap complex filter is needed to approach the frequency response of the channel with the bandwidth of 500 MHz.

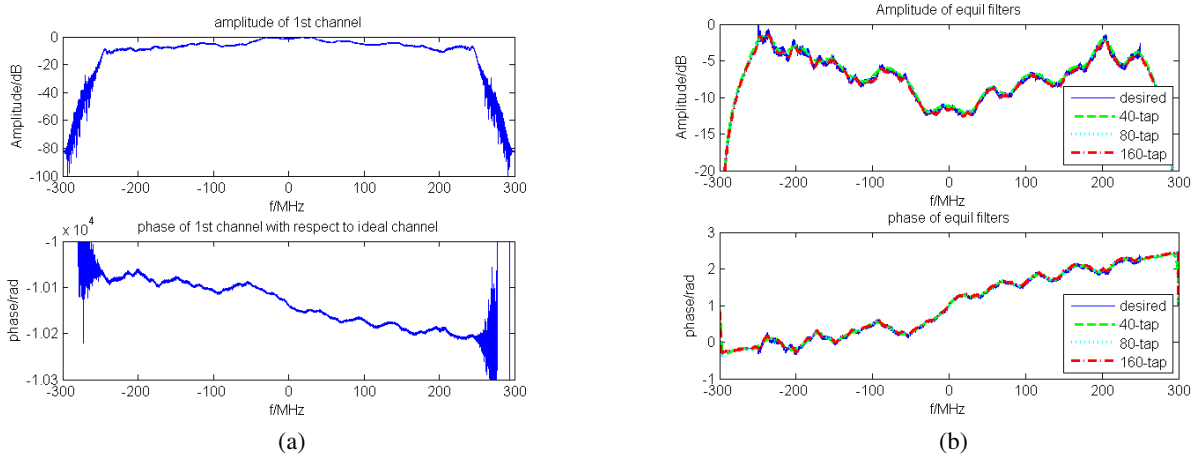


Figure 4: Measured channel responses and equilibration filter. (a) Response of the first channel. (b) Responses of equilibration filters with different taps.

3.2. Realization of Channel Equilibration in FPGA

In conventional method, channel equilibration is realized by complex FIR filter. However, as the bandwidth increases, the taps of equilibration filters becomes so high that it is unaffordable for FPGA. In order to realize equilibration in actual systems, FFT based on Overlap addition method is applied to simplify the implementation and the requirements for hardware.

Suppose the receive data is $x(n)$, the equilibration filter is $h(n)$, and $x(n)$ can be divided into a series of segments:

$$x_i(n) = \begin{cases} x(n) & iN_2 \leq n \leq (i+1)N_2 - 1 \\ 0 & \text{others} \end{cases} \quad (9)$$

Then the equilibration output is:

$$y(n) = x(n) * h(n) = \sum_{i=-\infty}^{\infty} x_i(n) * h(n) \quad (10)$$

The length of $x_i(n)$ and $h(n)$ is N_2 and N respectively, so convolution can be realized by FFT:

$$y(n) = \sum_{i=-\infty}^{\infty} IFFT(FFT(x_i(n), L) \cdot FFT(h(n), L)) \quad (11)$$

Where $L = N + N_2 - 1 = 2^M$.

4. EXPERIMENTAL RESULTS

To demonstrate the performance and effectiveness of the channel equilibration algorithms, experiments are carried out in an anechoic chamber by the DAR test-bed. When power on, the test-bed works in calibration mode. The high-quality LFM signal with the bandwidth of 500 MHz and center frequency of 2.7 GHz is generated by the wideband waveform generator.

The equilibration filters are designed using improved inverse Fourier Transform algorithm and their coefficients are sent to digital module. The measured data are captured and equilibrated by the filters, and the results are demonstrated in Figure 5(a). After equilibration, the amplitude ripple is decreased significantly, and the phase linearity is improved effectively.

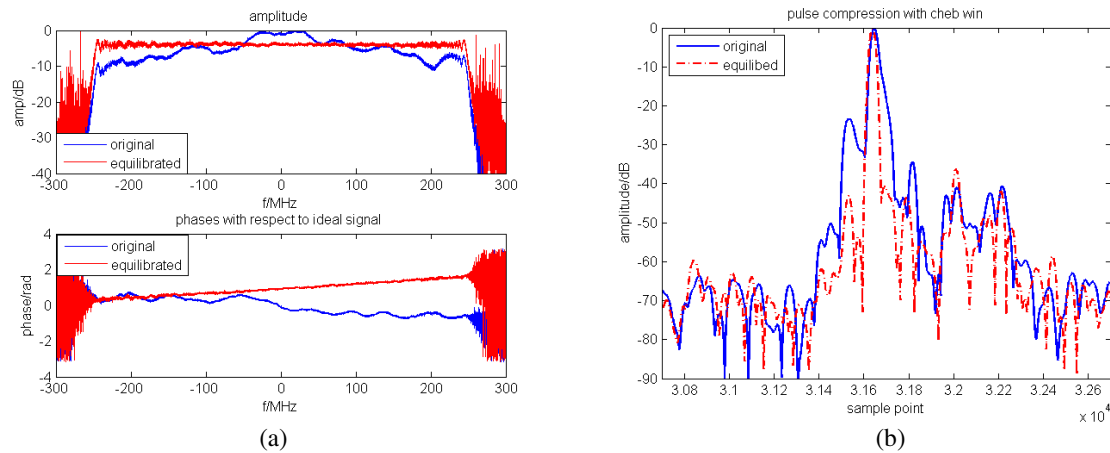


Figure 5: Processing results of measured data. Solid: before equilibration. Dash: after equilibration. (a) Frequency domain responses. (b) Pulse compression.

The compare of pulse compression before and after channel equilibration are illustrated in Figure 5(b). After equilibration, the main lobe becomes narrower and the side lobes are suppressed, leading to an increase in system resolution and dynamic range.

The convolution of equilibration filters and measured data are realized by FFT based on overlap addition. Taking a 160-tap equilibration filter as an example, the FFT method only need only 58 DSP slices in FPGA, while the FIR filter method need 480. So the FFT method is feasible to realize in wideband DAR systems.

5. CONCLUSION

This paper demonstrates the design and implement of channel equilibration subsystem in wideband DAR test-bed. The wideband waveform generator is capable of generating various wideband waveforms by DDS. An effective structure of improved inverse Fourier Transform algorithm is presented, which is feasible to realize in FPGA. Experiments are carried out by an 8-element wideband DAR test-bed. The expected results have shown the effectiveness and high performance of the channel calibration module.

REFERENCES

1. Mir, H. S. and L. Albasha, "Low-cost high-performance digital radar test bed," *IEEE Transactions on Instrumentation and Measurement*, Vol. 62, No. 1, 221–229, 2013.
2. Lu, Q. and W. Xuegang, "A new Wideband Digital Array Radar (WB-DAR) experiment system," *2014 IEEE Region 10 Symposium*, 440–445, 2014.
3. Li, T. and X. Wang. "Development of wideband digital array radar," *International Computer Conference on Wavelet Active Media Technology and Information Processing, Region 10 Symposium*, 286–289, 2013.
4. Pettersson, L., "Experiences using DOA methods with a small digital beamforming antenna," *IEEE International Symposium on Phased Array Systems and Technology*, 164–169, 2003.
5. Cantrell, B., J. de Graaf, and F. Willwerth, "Development of a digital array radar (DAR)," *IEEE Aerospace and Electronic Systems Magazine*, Vol. 17, No. 3, 22–27, 2002.
6. Wang, F., Y. Fu, B. Meng, and L. Chen, "Performance analysis and improvement of the equalization algorithm based on fourier transform for radar channel," *EIACTA Electronic Sinica*, Vol. 34, No. 9, 1677–1680, 2006.
7. Zhang, Y., Q. Bao, and J. Yang, "Design and implementation of channel equalization method for wideband digital array radar," *Signal Processing*, Vol. 26, No. 3, 453–457, 2010.
8. Saville, M. A., K. Monroe, and C. Allen, "Processing-based tuner gain correction in a wideband multi-channel receiver," *2010 IEEE Radar Conference*, 1106–1110, 2010.
9. Kim, S.-Y. and N.-H. Myung, "Wideband linear frequency modulated waveform compensation using system predistortion and phase coefficients extraction method," *IEEE Microwave and Wireless Components Letters*, Vol. 17, No. 11, 808–810, 2007.

An Ultra Low-power and Low-noise VCO Using Transformer Coupled Dual LC Tanks Topology

Tzu-Yun Chou, Kuan-Hsiu Chien, and Hwann-Kaeo Chiou

Department of Electrical Engineering, National Central University, Jhongli City, Taoyuan, Taiwan

Abstract— A K-band low power voltage-controlled oscillator (VCO) using transformer coupled dual LC tanks is implemented in a 90-nm CMOS process. The use of transformer provides tight coupling factor between two LC tanks that improves the phase noise performance by increasing the output signal swing and waveform symmetry of the VCO. In addition, taking advantage of the tight-coupling transformer, the inductor layout is properly designed to obtain a high Q-factor and a die area comparable to single-inductor VCO. The VCO core dissipates very small DC power of 1.61 mW from a 0.7-V supply due to the benefit of tight-coupled transformer. The measured phase noise is -97.61 dBc/Hz at 1-MHz offset from 23.99 GHz oscillation frequency.

1. INTRODUCTION

Fully integrated voltage controlled oscillators play an important role in RF transceivers. Over the past few years, the development of low-cost and low-power RF integrated circuits for wireless communication have attracted great attention. Numerous VCO topologies constructed in CMOS technology have been developed to achieve the performance of low power consumption, low phase noise and high operation frequency [1–5]. Work [1] proposed an asymmetrical current-reused oscillator that used only one pair of NMOS and PMOS transistors to achieve low DC power of 1 mW. However, as compared to conventional complementary cross-coupled CMOS counterpart, the differential outputs of the mentioned oscillator exhibit unbalanced output power level. Even though low-voltage operation can save the power consumption of the circuits, low-voltage operation may limit the output signal swing which in turn reduces the signal-to-noise ratio and degrades system performance [2]. The cross-coupled LC VCO has attracted much interest due to its easy implementation and reliable start-up condition [3, 4]. However, it limits in terms of reducing phase noise owing to the fact that the output swing of the VCOs is constrained. oscillation frequency of 24 GHz is -97.61 dBc/Hz. With only a power dissipation of 1.61 mW, the proposed VCO has an excellent FOM of -183.14 dBc/Hz.

In this work, the authors propose a transformer-based VCO for high frequency application that adopts the strength of magnetic coupling between two LC tanks to obtain large oscillation amplitude and achieve low phase noise under low supply voltage.

2. CIRCUIT DESIGN

By using the proposed transformer, a coupled dual LC tanks VCO is fabricated in a 90-nm CMOS technology. Fig. 1 shows the schematic of the proposed VCO. It consists of a transformer-based resonator that includes two identical LC tanks coupled by the transformer. The cross-coupled transistors (M_1) with the size of $8\ \mu\text{m}/90\ \text{nm}$ provide an effective negative resistance for the VCO core to compensate the resistive loss in the LC-tanks. The fine-tuned varactors C_{var} ($7 \sim 10.3$ fF) are used for frequency tuning. L_p and L_s are the self-inductances of each coil of the transformer. L_p incorporating with C_{var} acts as the primary LC tank, while L_s and MIM capacitor C_2 (27.4 fF) form the secondary LC tank. The secondary LC tank is DC isolated from the primary one, thus it does not consume DC power from the primary LC tank. Accordingly, compared to the conventional topology, this core power consumption can be significantly reduced. The drain voltage could swing above the supply voltage by using the proposed transformer. Effectively, the oscillation amplitude is enhanced, and the supply voltage can be reduced for the same phase noise with lower power consumption or for better phase noise with the same power consumption. By using the transformer equivalent T-model, the input admittance of transformer is shown in (1).

$$Y_{in} = \frac{1 + s^2 L_S C_2}{s^3 C_2 [L_S L_P - M^2] + s L_P} \quad (1)$$

Figure 2(a) shows the equivalent circuit model I of the VCO which consists of the input admittance of the transformer in parallel with the varactors. Fig. 2(b) depicts the small-signal model of

the VCO. The oscillation frequency ω_0 can be derived as (2).

$$\omega_0 = \sqrt{\frac{A + \sqrt{A^2 - 8C_{var}C_2(L_P L_S - M^2)}}{2C_{var}C_2[L_P L_S - M^2]}} \quad (2)$$

where $A = L_P C_{var} + 2C_2 L_S$, $M = k\sqrt{L_P L_S}$ is the mutual inductance, and k represents of the coupling factor between L_P and L_S .

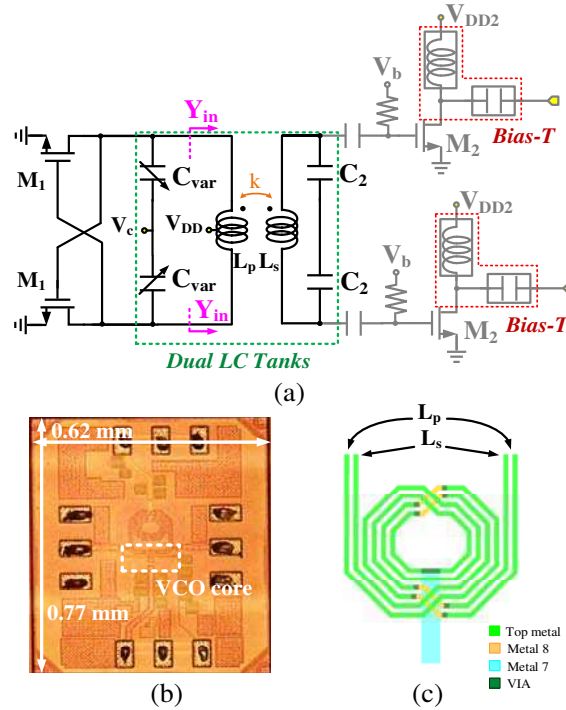


Figure 1: The proposed low-power K-band CMOS VCO. (a) Schematic of the proposed VCO. (b) Chip photograph of the proposed VCO. (c) Top view of transformer.

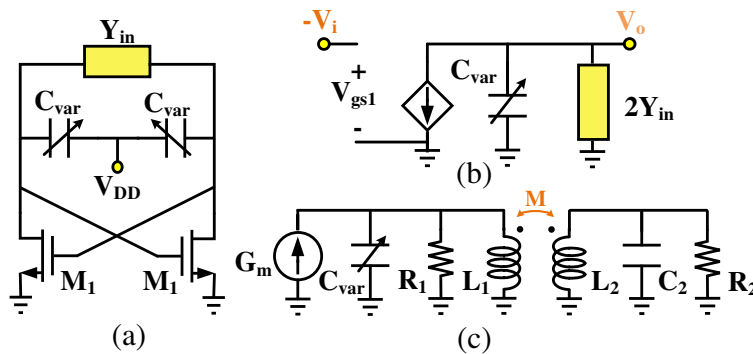


Figure 2: The proposed VCO equivalent circuit with admittance. (a) Equivalent circuit model I of the proposed VCO. (b) Small-signal model of the proposed VCO. (c) Equivalent circuit model of the proposed VCO.

On-chip transformer design: The implementation of the transformer is the major challenge to facilitate the strong coupling required for two coils and the connections with the varactors. The planar transformer is realized by the turn ratio 1 : 1 transformer as shown in Fig. 1(c). The transformer consists of a three-turn primary coil (L_P) and secondary coil (L_S), which wound together in a common-centric configuration. The outer dimension of the transformer is $113 \mu\text{m}$, and the metal width of each coil is $3 \mu\text{m}$. The extracted self-inductances of the primary coil L_P and the secondary coil L_S are 946.6 and 760.8 pH at 24 GHz, respectively. The electromagnetic simulation

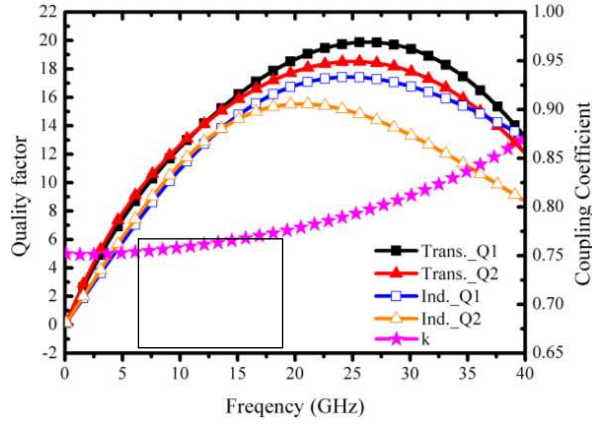


Figure 3: The quality factors and coupling coefficients of transformer and single inductor.

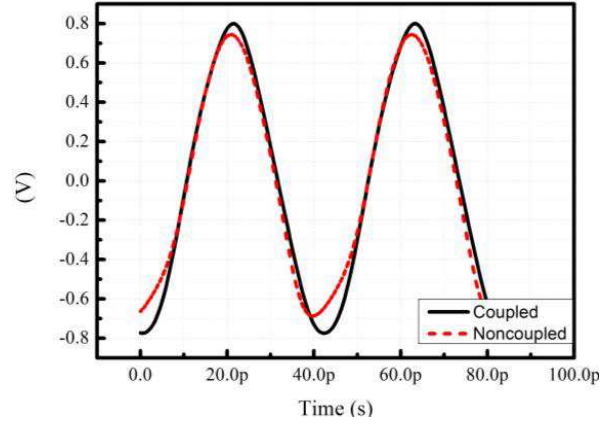


Figure 4: The output voltage waveforms of the coupled and non-coupled VCOs.

results using ADS Momentum are shown in Fig. 3, where the coupling coefficient of the transformer k is 0.79 at 24 GHz. k represents the transformer coupling factor between two LC tanks. Works [4] and [5] conclude that the tighter coupling factor, the higher quality factor. Fig. 3 shows the quality factor (Q) of the self-inductances of the transformer and single inductor. The quality factors of the proposed transformer are higher than that of the single inductor.

Fig. 4 shows the output voltage waveforms of the coupled and non-coupled VCOs. Work [6] suggests that the oscillator with symmetric waveform will have better phase noise performance. As noted, the waveform of the coupled VCO has larger swing and better symmetric waveform than those of the non-coupled one. Thus, the proposed VCO yields better phase noise than conventional one. In transformer model, the turn ratio between primary and secondary coils can be derived as (3).

$$n = \sqrt{\frac{L_s}{L_p}} = \frac{V_2}{V_1} = \frac{I_1}{I_2} \quad V_2 = V_1 \sqrt{\frac{L_1}{L_2}} \quad (3)$$

Figure 2(c) shows the equivalent model for the transformer of Fig. 1(a), where the port voltages of the tight-coupled lossy transformer V_1 and V_2 have the following relations as (4)–(5).

$$V_1(j\omega) = \frac{G_m j\omega}{(\omega_{o1}^2 - \omega^2) + j\omega \left(\frac{\omega_{o1}}{Q_1}\right)} \Bigg|_{\omega=\omega_{o1}} = \frac{G_m Q_1}{\omega_{o1}} \quad (4)$$

$$V_2 = \frac{k}{M} \frac{G_m Q_1 L_1}{\omega_{o1}} = \frac{k}{M} G_m Q_1 \sqrt{L_1^3 C_{var}} \quad (5)$$

where $G_m = -g_m/2$, and $Q_1 = R_1 \sqrt{C_{var}/L_1}$.

At parallel resonance, the voltage is at a maximum and the impedance is also at a maximum. Hence, it can be derived that V_2 is maximum when the resonant frequency at $\omega_{o1} = \omega_{o2}$.

3. MEASUREMENTS

Measurement Results: The proposed VCO is implemented in a 90-nm CMOS technology. The transformer provides strong coupling between the two LC tanks. The Q values of L_p and L_s are 18.5 and 19.7. Fig. 1(b) shows the micrograph of the VCO with a chip size of $0.77 \times 0.62 \text{ mm}^2$, including the pads. The phase noise is measured by an Agilent E5052B signal source analyzer. The VCO operates at a power supply of 0.7 V and consumes a current of 2.3 mA. The measured output power is -7.16 dBm . Fig. 5 shows the measured and simulated phase noise at 24 GHz, where the measured phase noise at 1 MHz and 10 MHz offset frequency are -97.61 and -123.6 dBc/Hz . As seen, the phase noise of the transformer coupled VCO obtains a 15-dB improvement compared to the non-coupled inductor VCO. The measured tuning range is from 23.6 to 24 GHz when the tuning voltage V_c changes from 0 to 0.7 V.

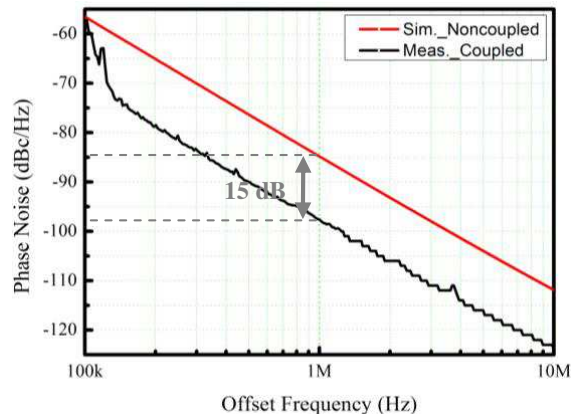


Figure 5: Measured (transformer coupled VCO) and simulated (non-coupled VCO) phase noise.

4. CONCLUSION

A novel dual LC tanks VCO has been proposed to obtain low power operation using the strength of magnetic coupling in the transformer. The proposed design also makes certain symmetry properties exist in the waveform of the oscillation which improves the phase noise noticeably. The proposed VCO has successfully demonstrated in good performance based on a 90-nm CMOS process. The measured phase noise at 1-MHz offset frequency from the oscillation frequency of 24 GHz is -97.61 dBc/Hz. With only a power dissipation of 1.61 mW, the proposed VCO has an excellent FOM of -183.14 dBc/Hz.

ACKNOWLEDGMENT

This work was supported in part by the Ministry of Science and Technology, Taiwan, R. O. C. under Contract MOST 101-2221-E-008-073-MY3. National Chip Implementation Center (CIC) of National Applied Research Laboratories, Taiwan, R. O. C., is also acknowledged for chip fabrication.

REFERENCES

1. Yun, S. J., S. B. Shin, H. C. Choi, and S. G. Lee, "A 1 mW current-reuse CMOS differential LC-VCO with low phase noise," *2005 Int. Solid-State Circuits Conf.*, Vol. 1, 540–616, 2005.
2. Kwok, K. C. and H. C. Luong, "Ultra-low-voltage high-performance CMOS VCOs using transformer feedback," *2005 IEEE J. Solid-State Circuits*, Vol. 40, No. 3, 652–660, 2005.
3. Liu, S. L., K. H. Chen, T. Chang, and A. Chin, "A low-power K-band CMOS VCO with four-coil transformer feedback," *IEEE Micro. Wireless. Compon. Lett.*, Vol. 20, No. 8, 459–461, 2010.
4. Zou, Q., K. Ma, K. S. Yeo, and W. M. Lim, "Design of a Ku-band low-phase-noise VCO using the dual LC tanks," *IEEE Trans. on Circuits and Systems II: Express Briefs*, Vol. 59, No. 5, 262–266., May 2012
5. Safarian, Z. and H. Hashemi, "Wideband multi-mode CMOS VCO design using coupled inductors," *IEEE Trans. on Circuits and Systems I: Regular Papers*, Vol. 56, 1830–1843, 2009.
6. Hajimiri, A. and T. H. Lee, "A general theory of phase noise in electrical oscillators," *IEEE J. Solid-State Circuits*, Vol. 33, 179–194, 1998.

A Reconfigurable Bandpass to Bandstop Filter Using PIN Diodes Based on the Square Ring Resonator

Salman Arain, Muhammad Ali Babar Abbassi, Symeon Nikolaou, and Photos Vryonides
Department of Electrical Engineering, Frederick University, Cyprus

Abstract— This paper presents a reconfigurable, bandpass to bandstop switchable filter, based on the square ring resonator topology with two tuning stubs, which control the filter's response. In the proposed design, switching between the bandpass and bandstop response is achieved by strategically placing two PIN diodes, at locations where the diodes do not affect the resonating response of the overall design. Skyworks SMP1345-079LF RF PIN diodes are used in order to allow switching between bandpass to bandstop responses. The operating frequency of the filter is at 2.4 GHz. The -3 dB bandwidth for the bandpass filter ranges from 1.9 GHz to 3.2 GHz, with an average insertion loss of 0.8 dB. For the bandstop filter the loss is 0.3 dB and the -10 dB rejection bandwidth is from 2.2 GHz to 2.7 GHz. DC bias lines of $\lambda/4$ overall length are integrated with radial matching stubs, to ensure compact overall size of the circuit. The key advantage of this type of filter is the efficient switching ability between the two different operational states, the bandpass and bandstop. The proposed filter is simulated on a commercially available, low cost Roger 4003C substrate having $\epsilon_r = 3.55$ and $\tan \delta = 0.0027$ and substrate thickness 0.813 mm. The proposed filter can be a good candidate for transceivers operating in strong interference environments, for reconfigurable radios, or for alternating transmission and reception schemes, in the highly congested, 2.4 GHz frequency band.

1. INTRODUCTION

Microwave filters are of paramount importance when dealing with RF communication systems. Modern day developments in this area have led to the necessity for compact, multipurpose and efficient designs. Under this prism, electronically switchable filters are gaining wide interest from both researchers and developers. Microwave filters are designed keeping in mind both structure compactness and easiness in their switching ability among alternative operational modes. Using commercially available PIN diodes, filters can be designed to switch between different geometric shapes with different resonating frequencies which result in eventually reconfigurable structures.

The microstrip square ring resonator, has been widely used for the development of microwave filters due to its compact size, low radiation loss and high Q factor [1]. Nowadays, emerging wireless communication systems require multiband, multifunctional and switchable capabilities. Under these circumstances a single filter cannot meet the requirements for all operating bands while the use of multiple filters occupies larger surface area with higher design cost [2]. To solve this problem, reconfigurable filters [3] are required. Bandpass and bandstop filters are two of the most commonly encountered components for any communication system. Bandpass filters are used to pass a specific band of frequencies while bandstop filters are required to suppress specific band of frequencies [4]. A compact and low insertion loss, square ring resonator, bandpass filter, has been presented in [5]. Several bandpass filters with switchable bandwidth based on the square ring resonator using PIN diodes have been presented in the past [6–8]. Recently reconfigurable filters from bandpass to bandstop filters were reported [9] based on varactor diodes by using odd and even degenerate modes. In [10, 11] reconfigurable bandpass to bandstop filters with controllable poles were presented. Although these reported reconfigurable bandpass to bandstop filters show additional features, they are more complex in terms of design and they have considerably larger size, when compared with the suggested filter topology.

In this paper, a simple, compact and low cost design is presented, based on a square ring resonator with two tuning open stubs capable of switching between bandpass and bandstop response around the center frequency of 2.4 GHz. The transition from bandpass to bandstop response is achieved using electronic switching, i.e., by using a DC voltage source to forward or reversely bias two PIN diodes.

2. PROPOSED RECONFIGURABLE BANDPASS-BANDSTOP FILTER DESIGN

It is well known that several modes can be supported by the ring resonator and can be excited if desired, depending on the perturbation and coupling methods. In addition resonance occurs when

standing waves are set up along the ring something that happens when the circumference of the ring is an integer multiple of the guided wavelength. To understand the basic phenomena underlying the operation of the ring, it is useful to first understand its field configuration for the different modes which are described in detail in [1]. In the absence of any discontinuity a maximum field point occurs at the point where the feed line excites the resonator. It is also worth noting that this point is independent of the position of the feed line that extracts microwave power. This is very important from the standpoint of mode suppression. As it can be seen in Figure 1 the output feed line is placed to an angle of 270 degrees where there is a field minimum for first and third modes. As a result, since there is odd-mode excitation and the output feed line is coupled to a position where there is a minimum electric field the ring circuit provides a stopband and exhibits bandstop characteristic.

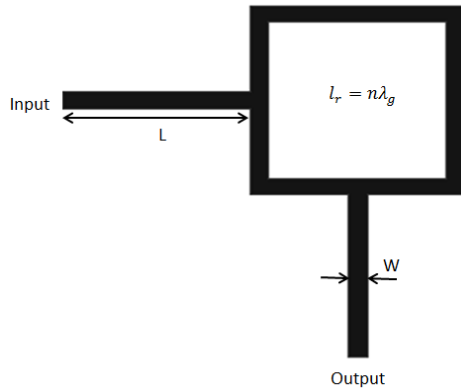


Figure 1: Bandstop filter based on ring resonator.

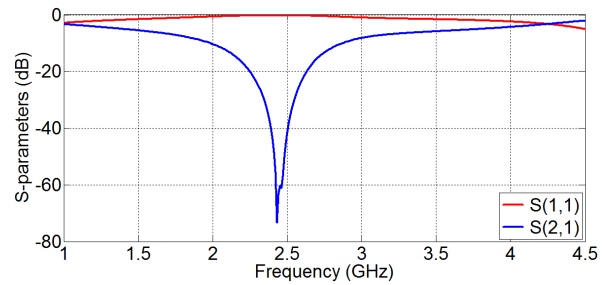


Figure 2: Simulated S -parameters for the bandstop filter (From Figure 1).

L is the common length of both feed lines and W is their width. The lengths and widths of the two feed lines are kept the same to avoid multiple mode generation. The circumference of the ring resonator is given by $l_r = n\lambda_g$, where n is the mode number and λ_g is the guided wavelength. The guided wave length is given in Equation (1).

$$\lambda_g = \frac{c}{f\sqrt{\epsilon_r}} \quad (1)$$

where c is the speed of light, f is the operating frequency and ϵ_r is the relative dielectric constant. With $L = 18$ mm and $W = 1.8$ mm, the full wave simulated S -parameters are displayed in Figure 2. As it can be seen the filter provides a -20 dB band rejection from 2.3 to 2.6 GHz, while the resonance frequency is set at 2.4 GHz.

A reconfigurable bandpass to bandstop filter using a microstrip square loop resonator is proposed in Figure 3, in which the square ring is used as the resonator and two microstrip tuning stubs are used as the perturbation elements. The bandpass filter is developed from the bandstop filter that was introduced earlier in Figure 1. The proposed reconfigurable bandpass-bandstop ring resonator filter, as shown in Figure 3, is very similar to the traditional dual-mode ring resonator filters with stub-loaded perturbation elements.

Two tuning open stubs having length $\lambda/4$ at 2.4 GHz, placed at the centre of either side of the ring resonator and in orthogonal to each other orientation are used to achieve a wide passband response with a steep roll-off frequency characteristic. By changing the lengths of these two tuning stubs, the frequency response of the ring circuit is varied. Two attenuation poles are thus created and form a wide passband filter response. This approach can be interpreted as using two stopbands induced by two tuning stubs in conjunction with the wide passband. The effect of the addition of the two tuning stubs is a steeper roll-off frequency response, and wider passband zone.

In this work the filter was simulated using cost effective Roger 4003C substrate having $\epsilon_r = 3.55$, $\tan \delta = 0.0027$ with a substrate thickness of 0.813 mm. The Skyworks SMP1345-079LF PIN diode switches are incorporated in order to realize the switchable design from bandpass to bandstop filter. As can be observed from the schematic in Figure 3, the PIN diodes are located directly on the square ring and they electrically connect and disconnect the open stubs with lengths $S1$ and $S2$ respectively. The overall inner ring size is 17.2 mm \times 17.2 mm. For the circuit simulations the PIN

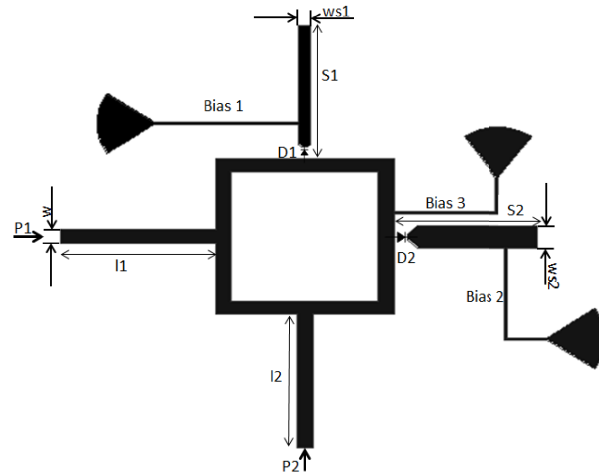


Figure 3: Proposed design for reconfigurable bandpass-bandstop filter.

diodes are replaced with either $3\ \Omega$ resistors, or $0.15\ \text{pF}$ capacitors [12] for the ON and OFF state of the PIN diodes respectively. Once DC bias voltage is applied directly on the radial stubs of the bias lines named Bias1 and Bias3 with a forward current of 10 mA the two PIN diodes are turned ON. Hence, open stubs $S1$ and $S2$ become connected with the ring, resulting in the wideband passband filter response of Figure 4. When the PIN diodes are simultaneously reverse biased, the tuning stubs are disconnected which in return produces a bandstop response as shown in Figure 5.

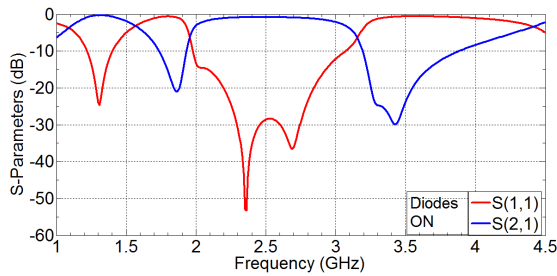


Figure 4: S -parameters of bandpass filter (ON State).

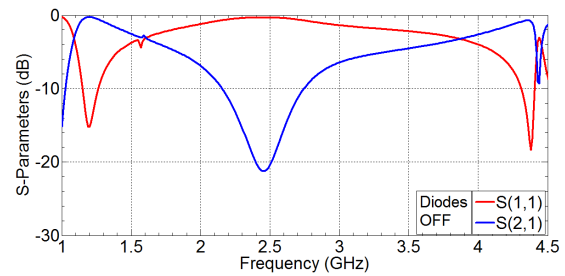


Figure 5: S -parameters of bandstop filter (OFF State)

High impedance DC bias lines of $110\ \Omega$ characteristic impedance are integrated with radial stubs for biasing the diodes. The angle, positions and dimensions of the radial stubs directly affect the S parameter responses therefore they are optimized using parametric simulations. The angle of the radial stubs is chosen to be 70 degrees after optimization. The complete list of filter parameters is given in Table 1.

Table 1: Filter parameters

Symbol	Value (mm)
$l1$ (Input line)	18
$l2$ (Output line)	18
w (Width of input/output line)	1.8
$S1$ (Length of stub 1)	17.8
$S2$ (Length of stub 2)	16.8
$ws1$ (Length of stub 1)	1.4
$ws2$ (Length of stub 2)	3

3. SIMULATION RESULTS AND DISCUSSION

The reconfigurable filter simulations have been carried out using a full wave simulator. When both diodes are simultaneously forward biased, a bandpass filter response is achieved having $-3\ \text{dB}$

passband zone from 1.9 GHz to 3.2 GHz with an average insertion loss of around 0.8 dB in the passband zone while having a return loss below -30 dB for the larger part of the passband zone. The presence of the two tuning stubs cause two attenuation poles at 1.85 GHz with -22 dB rejection, at 3.4 GHz with -30 dB rejection. The simulated S -parameters for bandpass response, are presented in Figure 4.

When the diodes are reversed biased, a bandstop filter response is achieved with a -10 dB bandwidth that ranges from 2.2 GHz to 2.7 GHz with a rejection level greater than 20 dB and with an average loss of 0.3 dB. The simulated S -parameters are shown in Figure 5.

4. CONCLUSION

A simple to fabricate, low cost, reconfigurable, bandpass to bandstop filter is proposed based on the square ring resonator. The design consists of two tuning stubs and two PIN diodes as switching elements. By switching the PIN diodes ON and OFF a reconfigurable bandpass-bandstop filter is achieved. The reconfigurable filter was designed with a center frequency at 2.4 GHz having a passband zone ranging from 1.9 GHz to 3.2 GHz and -10 dB rejection band ranging from 2.2 GHz to 2.7 GHz. In bandpass mode the filter had less than 1 dB of insertion loss with a fractional bandwidth of 54%. The overall filter design can be fabricated on a 57 mm \times 57 mm size board. The proposed reconfigurable filter can be a good candidate for high interference systems and for alternating transmission and reception schemes, in the highly congested 2.4 GHz frequency band.

REFERENCES

1. Chang, K. and L.-H. Hsieh, *Microwave Ring Circuits and Related Structures*, John Wiley & Sons, 2004.
2. Matthaei, G. L., L. Young, E. M. T. Jones, G. Matthaei, and L. Young, *Microwave Filters, Impedance Matching Networks and Coupling Structures*, Artech House, 1964.
3. Karim, M. F., A.-Q. Liu, A. Alphones, and A. Yu, "A reconfigurable micromachined switching filter using periodic structures," *IEEE Transactions on Microwave Theory and Techniques*, Vol. 55, No. 6, 1154–1162, June 2007.
4. Shen, J., G. Hong, and M. J. Lancaster, *Microstrip Filters for RF/Microwave Applications*, John Wiley & Sons, 2004.
5. Hsieh, L.-H. and K. Chang, "Compact, low insertion-loss, sharp-rejection, and wide-band microstrip bandpass filters," *IEEE Transactions on Microwave Theory and Techniques*, Vol. 51, No. 4, 1241–1246, April 2003.
6. Karim, M. F., A.Q. Liu, A. Alphones, and A. B. Yu, "A novel reconfigurable filter using periodic structures," *Microwave Symposium Digest, 2006. IEEE MTT-S International*, 943–946, IEEE, 2006.
7. Vryonides, P., S. Nikolaou, S. Kim, and M. M. Tentzeris, "Reconfigurable dual-mode bandpass filter with switchable bandwidth using pin diodes," *International Journal of Microwave and Wireless Technologies*, 1–6, 2014.
8. Kim, C. H. and K. Chang, "Ring resonator bandpass filter with switchable bandwidth using stepped-impedance stubs," *IEEE Transactions on Microwave Theory and Techniques*, Vol. 58, No. 12, 3936–3944, December 2010.
9. Chen, Y.-M., S.-F. Chang, C.-Y. Chou, and K.-H. Liu, "A reconfigurable bandpass-bandstop filter based on varactor-loaded closed-ring resonators [technical committee]," *Microwave Magazine, IEEE*, Vol 10, No.1, 138–140, June 2009.
10. Cho, Y.-H. and G. M. Rebeiz, "Two-and four-pole tunable 0.7–1.1-ghz bandpass-to-bandstop filters with bandwidth control," *IEEE Transactions on Microwave Theory and Techniques*, Vol. 62, No.3, 457–63, March 2014.
11. Cho, Y.-H. and G. M. Rebeiz, "0.7–1.0-ghz reconfigurable bandpass-to-bandstop filter with selectable 2-and 4-pole responses," *IEEE Transactions on Microwave Theory and Techniques*, Vol. 62, No. 11, November 2014.
12. Skyworks Inc., www.skyworksinc.com, Diode Data sheet (SMP1345-079LF), Accessed on March 2014.

Power Electronics for an Energy Harvesting Concept Applied to Magnetic Resonance Tomography

L. Middelstaedt¹, S. Foerster², R. Doebbelin¹, and A. Lindemann¹

¹Otto-von-Guericke-University Magdeburg, Germany

²formerly Otto-von-Guericke-University Magdeburg, Germany

Abstract— In this paper the possibility of utilizing magnetic fields of magnetic resonant imaging (MRI) scanners for energy harvesting is investigated. The magnetic energy is converted into electric energy supplying small sensor systems that can be used for interventional medical applications within an MRI scanner. Suitable magnetic field components for energy harvesting are analyzed and a corresponding inductor design is discussed. Accordingly, a power electronic circuit is developed and successfully tested within an MRI scanner wirelessly powered by an inductor.

1. INTRODUCTION

Concerning the power supply of small power electronic applications for devices used in the interventional medical field in magnetic resonance tomography (MRT), e.g., for wireless power supply of small sensors and electronics in catheters, this paper investigates the approach of energy harvesting inside the MRI scanner. While in [1] basic investigations on energy harvesting in MRT were carried out by measuring the DC output power for one setup, this paper investigates and evaluates the induction coil design in more detail by determining the induced voltage and the self resonances of the inductors. Additionally, the time variant magnetic RF field and the gradient field are compared in terms of induced voltage depending on the induction coil placement relative to the isocenter, which is the geometrical center of the magnet where the static magnetic field and the RF field are the strongest and homogenous.

2. ANALYSIS OF MAGNETIC FIELDS IN MRT

In order to supply an electronic circuit using energy harvesting within an MRI scanner, suitable magnetic fields need to be defined and analyzed.

2.1. Magnetic Fields in MRT

Within magnetic resonance tomography (MRT) applications magnetic fields of different orientations, magnitudes and frequencies are generated in order to produce images of different body tissues. The three main magnetic fields that need to be distinguished are [2–4]:

- B_0 : strong static, uniform magnetic field in z direction.
- B_1 : high frequency excitation field (≈ 123 MHz for $B_0 = 2.89$ T according to Larmor frequency [5]) rotating in the xy plane and having the highest amplitude in the isocenter.
- B_G : gradient field with x , y , and z components with location-depending characteristics.

Figure 1 shows the corresponding geometry definitions. Considering the magnetic fields and according to Faraday's Law, the B_1 and B_G fields can be utilized to convert portions of the magnetic energy into electric energy, as stated in [1] as well.

2.2. Field Simulation

To investigate the induction behavior of inductor with different geometries excited by the B_1 field, a numerical field simulation model was created in EMPIRE XCcelTM. B_1 is homogenous and rotates in the xy plane with a frequency of approximately 123 MHz. To create a magnetic field with these characteristics in EMPIRE XCcelTM four electromagnetic (EM) waves are superimposed, so that the electric field components cancel out and the resulting homogenous H field is rotating in the xy plane. Therefore, the amplitudes of the electric components \vec{E} of the four EM waves have to be equal. Two contrary polarized EM waves having opposite direction of propagation \vec{k} with

$$\vec{k} = \vec{E} \times \vec{H} \quad (1)$$

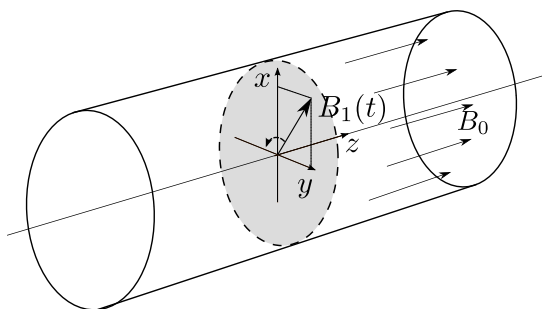


Figure 1: Definition of axes within an MRI scanner and corresponding magnetic fields.

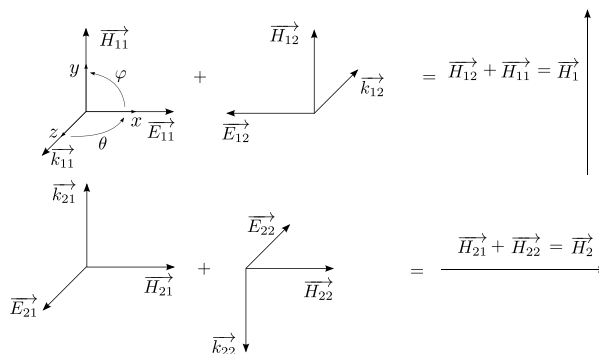


Figure 2: Orientation of two pairs of electromagnetic waves, resulting in two homogenous H fields.

are added and result in one homogenous H field with an orientation as shown in Figure 2. Adding the two homogenous H fields \vec{H}_1 and \vec{H}_2 rotated relatively to each other geometrically and electrically by 90° results in a single circularly polarized homogenous H field. To realize a 90° phase shift between \vec{H}_1 and \vec{H}_2 for ≈ 123 MHz a time delay of 2.0316 ns needs to be applied.

With the model of B_1 the induction characteristic of different geometries can be analyzed and compared. It is important, that the defined simulation geometry is smaller than the wave length of the B_1 field. For larger geometries the superposition of the four EM waves does not result in one circularly polarized homogenous H field.

3. LAYOUT AND DESIGN OF PROTOTYPE

3.1. Inductor Design

For the inductor design different considerations need to be taken into account, i.e., the orientation, frequency and strength of the exciting magnetic field. As already mentioned, the frequency of the B_1 field equals ≈ 123 MHz and it rotates in the xy plane at the location of the isocenter. Here, the field strength is the highest and depends on the sequence of the MRT that is applied. However, the absolute amplitude of B_1 is small and hence a large number of turns might be plausible. Contrary, a large number of turns increases the effect of capacitive coupling between turns and therefore decreases the first resonant frequency of the inductor [6]. Only below the first resonant frequency, the inductor behaves strongly inductive. For higher frequencies the parasitic capacitive component may become dominant and hence the induced output voltage decreases. An optimization is reached, when the first resonant frequency is slightly above the excitation frequency.

Additionally, the inductor can be optimized by maximizing the effective area, that is exposed to the magnetic field. Since the direction of excitation varies between the x and y axes it is desired to design the winding in a way, that the inductor is excited by the B_1 field from both components considering that the area which is orthogonal to the varying field represents the effective area of the inductor. While in literature inductors with different coils for each orientation [4] or a Figure 8 coil with one orientation [7] are described, this paper proposes an approach that uses only one coil with tilted turns wound around an acrylic glass tube. The turns are arranged with a 45° angle (see Figure 3).

In Figure 4 different orientations are displayed. For orientation 1 and orientation 2 the inductor



Figure 3: Prototype induction coil with 100 turns on cylindrical acrylic tube.

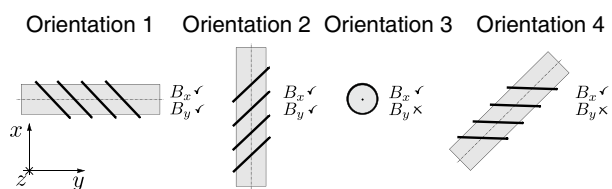


Figure 4: Orientation of winding setup on an acrylic glass tube concerning exciting B field components.

is excited by the x and y component of the exciting B_1 field. For the other orientations only the excitation by B_x is given. However, for orientation 3 the x -excitation is possible only because of the tilted turns. For orientation 4 the tilted turns lead to an elliptic area, which is larger than a circular area. Thus, the increased effective area leads to an increased inductance and therefore increased induced voltage.

3.2. Power Electronic Circuit Design

The inductor is used as a wireless AC voltage source. In order to supply small power electronic applications like sensors a low DC voltage is needed. Hence, the input voltage needs to be converted using a power electronic circuit. In the first stage the input voltage is rectified with diodes and buffered using a capacitor. Due to the fluctuation of buffered voltage a DC-DC converter with charging management is used in the second stage, to achieve a constant output voltage. The block diagram of the circuit is shown in Figure 5. The circuit charges an output buffer capacitor and supplies an LED with an ohmic resistance in series.

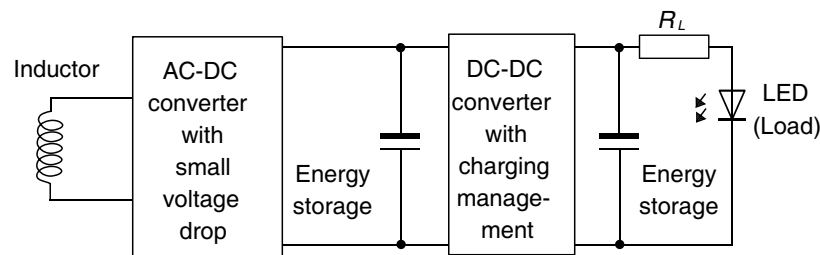


Figure 5: Block diagram of the power electronic circuit supplying an LED [8].

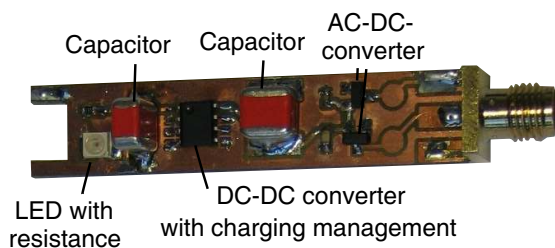


Figure 6: Assembled circuit board with electronic elements.

Figure 7: Prototype with inductor and circuit board.

For the use in MRT applications, e.g., for interventional medical use, the circuit needs to fulfill different requirements. Next to a small size, the voltage drop over the circuit elements needs to be as small as possible to ensure a high efficiency. Furthermore, the imaging process of the MRT should not be affected, requiring the circuit elements to be of non-magnetic material. Widely used electronic elements with nickel alloys for solder connections can not be applied. Elements with a copper-tin-zinc alloy serve as a substitute. Different suppliers, e.g., Maxim or Texas Instruments, have developed highly integrated circuits for energy harvesting applications, that offer a DC-DC converter with additional charging management and different protection and charging controls combined in a minimized package of only approximately 9 mm^2 . The prototype uses such an IC that is soldered onto a circuit board (see Figure 6). The board was slid into the inductor in order to reduce size and create a compact device as displayed in Figure 7. An SMA socket is used to connect a measurement cable with the device to measure the induced voltage.

4. RESULTS

The induction characteristics of two inductors with different numbers of turns were compared. For inductor 1 100 turns were applied, whereas inductor 2 has only six turns. The impedance characteristic at the exciting frequency of $\approx 123 \text{ MHz}$ is of higher importance. At 500 kHz the inductance of inductor 1 is approximately 400 times larger than of inductor 2. Contrary, at $\approx 123 \text{ MHz}$ both inductors show an impedance value in the same order of magnitude, as can be seen from Table 1. The phase angles show, that the parasitic capacitances of inductor 1 have a major

Table 1: Impedance characteristic of inductors at ≈ 123 MHz.

	Z	φ
Inductor 1	200Ω	-70°
Inductor 2	450Ω	87°

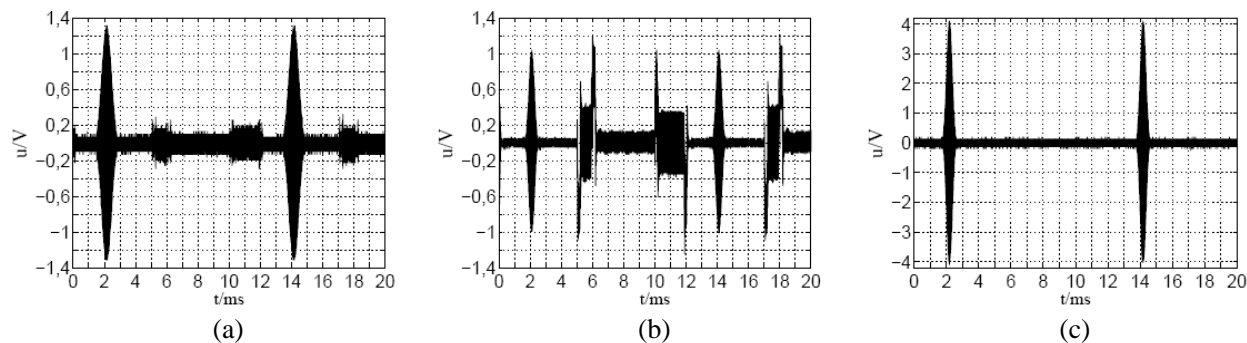


Figure 8: Induced voltage for different inductors at different positions. (a) Inductor 1 at isocenter, (b) inductor 1 outside of isocenter, (c) inductor 2 at isocenter.

influence and the impedance characteristic is not inductive any more. On the other hand, inductor 2 still shows a mostly inductive behavior.

Accordingly, the induced voltages differ. In Figure 8 the oscillograms of the induced voltages for both inductors are shown, while the voltage of inductor 1 was measured at different positions in relation to the isocenter. The periodicity of the three measurements is the same. At 2 ms and 14 ms the B_1 field induces a voltage. At 5 ms, 10 ms, and 18 ms the gradient field B_G shows its influence. Inductor 1 was placed at the isocenter as well as approximately 20 cm outside of it. Since B_1 is the strongest here, the corresponding induced voltage is the highest with 1.4 V and oscillates with ≈ 123 MHz. The voltages induced by B_G are negligible. Placing the inductor 1 outside of the isocenter leads to a reduction of the induced voltage related to B_1 but increases the induced voltages related to B_G considerably (see Figure 8(b)). In Figure 8(c) inductor 2 was placed at the isocenter and B_1 induces large voltages of 4 V. In this case the reduced number of turns and thus an increased first resonant frequency leads to clearly improved induction characteristic.

This proves, that voltages with sufficient amplitudes are induced at the isocenter as well as outside of it. Not only B_1 but also B_G contribute to the harvesting concept, depending on the position.

Finally, inductor 2 was connected to the power electronic circuit and placed inside the MRI scanner. The magnetic fields lead to an induced voltage that powered the LED wirelessly, which therefore luminates.

5. CONCLUSION

An energy harvesting concept was presented for supplying small low power electronic devices wirelessly for medical applications in an MRI scanner using its magnetic fields. A fundamental simulation was parametrized to model the B_1 field, so that the inductance characteristic of different inductor designs can be simulated and compared.

Then different aspects if the inductor designs were discussed. For an optimized layout a small number of turns is important so that the first resonant frequency of the inductor is higher than the characteristic frequency of the B_1 field. Furthermore, the orientation of the turns is important. An elliptic design was presented, allowing a good induction characteristic independent from the inductors orientation in the magnetic field.

A power electronic circuit was developed, that is able to supply a load consisting of an output buffer capacitance and an LED with resistance. Finally, the prototype was successfully tested within an MRI scanner.

ACKNOWLEDGMENT

The authors would like to thank the State of Sachsen-Anhalt and the German Federal Ministry for Education and Research (BMBF) for supporting our work within the framework of the project Forschungscampus STIMULATE.

REFERENCES

1. Hoefflin, J., E. Fischer, J. Hennig, and J. G. Korvink, "Energy harvesting towards autonomous MRI detection," *Proc. Intl. Soc. Mag. Reson. Med.*, Vol. 21, 2013.
2. Bernstein, M., K. King, and X. Zhou, *Handbook of MRI Pulse Sequences*, Elsevier, 2004.
3. Kuperman, V., *Magnetic Resonance Imaging: Physical Principles and Applications*, Academic Press, 2000.
4. Sun, T., X. Xie, and Z. Wang, *Wireless Power Transfer for Medical Microsystems*, Springer Science+Business Media, New York, 2013.
5. Reiser, M., W. Semmler, and H. Hricak, *Magnetic Resonance Tomography*, Springer-Verlag, Berlin, Heidelberg, 2008.
6. Middelstadt, L., S. Skibin, R. Dobbelin, and A. Lindemann, "Analytical determination of the first resonant frequency of differential mode chokes by detailed analysis of parasitic capacitances," *2014 16th European Conference on Power Electronics and Applications (EPE'14-ECCE Europe)*, 1–10, Aug. 2014.
7. Hoefflin, J., E. Fischer, J. Hennig, and J. G. Korvink, "Energy harvesting with a Figure 8 coil towards energy autonomous MRI detection," *54th Experimental Nuclear Magnetic Resonance Conference*, Apr. 2013.
8. Middelstaedt, L., S. Foerster, and A. Lindemann, "Energy harvesting im MRT," *IGIC, Conference on Image-guided Interventions, Magdeburg*, 2014.

Fast Time-domain Imaging for One-stationary Bistatic Forward-looking SAR

Hongtu Xie, Daoxiang An, Xiaotao Huang, and Zhimin Zhou

College of Electronic Science and Engineering
National University of Defense Technology, Changsha, Hunan 410073, China

Abstract— In this paper, a fast time-domain imaging method called the fast backprojection algorithm (FBPA) is proposed for the one-stationary bistatic forward-looking synthetic aperture radar (OSBFSAR). First, the backprojection (BP) algorithm of the OSBFSAR is introduced. Then, the FBPA of the OSBFSAR based on the subaperture BP imaging is provided, and the sampling requirements of the polar subimage grid are derived from the bandwidth angle. Finally, the implementation of the proposed FBPA is discussed. Simulation results are shown to prove the validity of the proposed algorithm.

1. INTRODUCTION

One-stationary bistatic forward-looking synthetic aperture radar (OSBFSAR) [1] is a special bistatic SAR (BSAR) [2] system with a stationary radar fixed on the top of a high tower or mountain, working in the forward-looking mode [1]. It not only inherits the advantages of the BSAR, such as reducing vulnerability for military application and improving the detectability of stealth targets, but also carries out the high-resolution scene imaging in the forward direction [3]. However, its larger bistatic angle and synthetic aperture may induce the complicated range-azimuth coupling of echo data, which may increase the difficulty of the high-resolution imaging for the OSBFSAR [3].

Reconstructing the BSAR scene is performed by the BSAR imaging algorithms, divided into two classes: the frequency-domain algorithm and time-domain algorithm. The frequency-domain algorithms usually aim to minimize processing time, but it may lead to a number of limitations such as integration time, motion error, approximate processing, etc., which constrains its application. In contrast, the time-domain algorithms don't face to these limitations, but they require a high computational load. Time-domain backprojection algorithm (BPA) is considered as a linear transformation from the echo data into the SAR image, thus it can be applied directly to the OSBFSAR imaging [4]. To reduce the computational load, the fast implementation of the BPA has been used for the strip-map BSAR imaging, i.e., the fast backprojection algorithm (FBPA) and fast factorized backprojection algorithm (FFBPA) [5]. However, the FBPA has not been either mentioned or investigated for the OSBFSAR imaging in the earlier publications.

The aim of this paper is to present the FBPA to process the OSBFSAR echo data based on [5]. Note that its availability is also used to the FFBPA since the processing principles of the FBPA and FFBPA are the same. Section 2 introduces the BPA for the OSBFSAR. Section 3 describes the proposed FBPA for the OSBFSAR imaging in detail. Section 4 proves its validity based on the simulation results. Section 5 gives the conclusion.

2. BPA FOR OSBFSAR

Figure 1 shows the imaging geometry of the OSBFSAR. Moving radar moves along the straight line l_M parallel to the Y -axis direction at the speed V_M , with the position $\mathbf{r}_M(\eta) = (0, y_M(\eta), z_M)$ at the slow time η . The position of the stationary radar B is $\mathbf{r}_S = (x_S, 0, z_S)$. Assume that the scene is always illuminated by the stationary radar, and the moving radar operates in the forward-looking spotlight mode. P is an arbitrary scattering target in the scene, with the position \mathbf{r}_P . The ranges from the moving and stationary radars to the target P at η are $R_M(\eta, \mathbf{r}_P)$ and $R_S(\mathbf{r}_P)$, respectively. Thus, the traveling distance of a radar pulse radiated from the moving radar impinging on the target P , and then reflected to the stationary radar at η is

$$R(\eta, \mathbf{r}_P) = R_M(\eta, \mathbf{r}_P) + R_S(\mathbf{r}_P) = |\mathbf{r}_P - \mathbf{r}_M(\eta)| + |\mathbf{r}_P - \mathbf{r}_S|. \quad (1)$$

Provided that the transmitted signal is $p(\tau)$, after the demodulation and range compression, the received signal of the target P becomes

$$s_{rc}(\tau, \eta) = \sigma_p \cdot p_{rc} [B(\tau - R(\eta, \mathbf{r}_P)/c_0)]. \quad (2)$$

4. SIMULATION RESULTS

Simulation results are shown in this section to compare the performances of the proposed FBPA and BPA. The simulation parameters are shown in Table 1. The moving radar position at $\eta = 0$ is (0, 0, 500) m. Nine scattering targets labeled as $A \sim I$ are located in the scene (100 m \times 100 m, range \times azimuth), and the scene center position is (0 m, 0 m, 0 m), which are shown in Fig. 4(a). Both range and azimuth intervals of all scattering targets are 30 m, and the RCS of all scattering targets is assumed to be 1 m² for simplification.

Table 1: Simulation parameters of the OSBFSAR system.

Center frequency	Signal bandwidth	Sampling frequency	Pulse duration	PRF	Moving radar altitude (speed)	Stationary radar position
500 MHz	200 MHz	240 MHz	1 μ s	100 Hz	200 m (45 m/s)	(-500, 0, 50) m

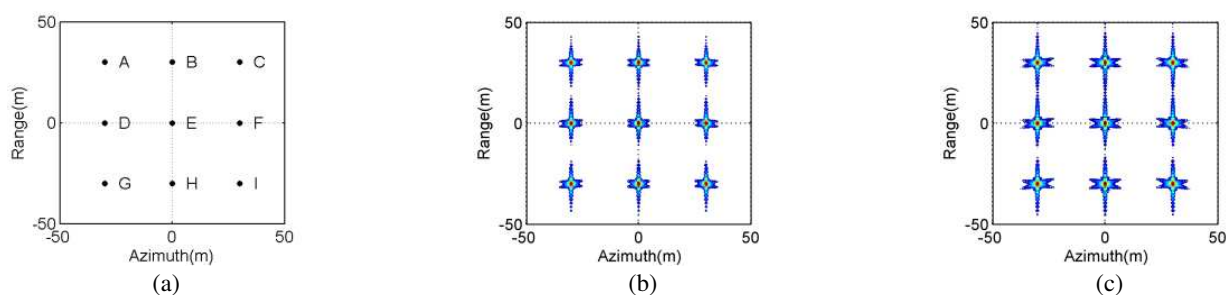


Figure 4: Imaging results obtained by the different algorithms. (a) Targets distribution; (b) BPA; (c) FBPA.

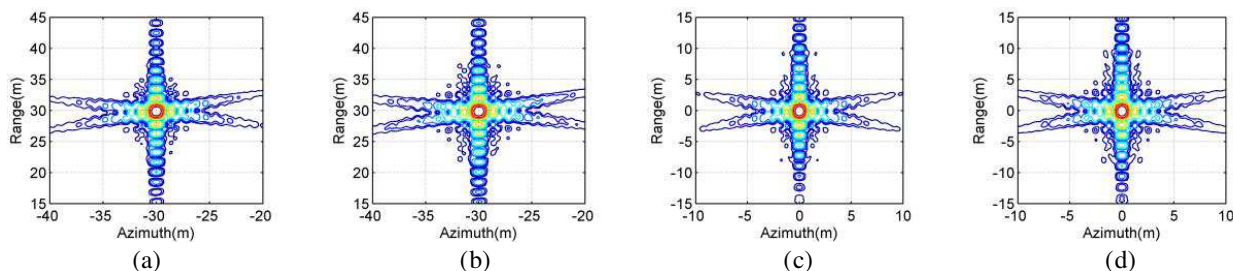


Figure 5: Imaging results of targets A and E. (a) Imaging result of the target A extracted from Fig. 4(b); (b) Imaging result of the target A extracted from Fig. 4(c); (c) Imaging result of the target E extracted from Fig. 4(b); Imaging result of the target E extracted from Fig. 4(c).

Table 2: Measured parameters of the targets A and E.

Algorithms	Target A				Target E			
	Resolution (m)		PSLR (dB)		Resolution (m)		PSLR (dB)	
	Range	Azimuth	Range	Azimuth	Range	Azimuth	Range	Azimuth
BPA	1.282	0.814	-13.26	-13.30	1.358	0.732	-12.97	-13.40
FBPA	1.288	0.821	-13.27	-13.29	1.360	0.734	-12.95	-13.42

Figures 4(b) and 4(c) give the scene imaging results obtained by different algorithms. From Figs. 4(b) and 4(c), it is seen that all scattering targets are focused well. Fig. 5 give the contours of the imaging results of the targets A and E, which are extracted from Figs. 4(b) and 4(c). It is shown that the focusing performance of the targets A and E by the proposed FBPA is very similar to that by the BPA. The measured parameters of the targets A and E are calculated and listed in

Table 2. From Table 2, it is seen that the measured parameters of the targets A and E focused by the two algorithms are almost identical. The processing time of two algorithms is also measured, which is 107.2 s and 10.4 s for the BPA and proposed FBPA, respectively.

5. CONCLUSION

This paper presents a FBPA to focus the OSBFSAR echo data. This method reconstructs a SAR scene in the ground plane instead of the slant-range plane. First, the BPA of the OSBFSAR is introduced. Then, the FBPA of the OSBFSAR based on the subaperture BP imaging is provided, and then the sampling requirements of the polar subimage grid are derived from the bandwidth angle. Finally, the implementation of the proposed FBPA is discussed. This method can keep the accuracy and robust of the BPA but with a reduced computational load. The simulation results prove its validity.

ACKNOWLEDGMENT

This work was supported by the National Natural Science Foundation of China: Research on the key techniques of low frequency ultra wideband synthetic aperture radar interferometry (61201329) and Research Project of National University of Defense Technology (JC14-04-02).

REFERENCES

1. Espeter, T., I. Walterscheid, J. Klare, A. R. Brenner, and J. H. G. Ender, "Bistatic forward-looking SAR: Results of a spaceborne-airborne experiment," *IEEE Trans. Geosci. Remote Sens. Lett.*, Vol. 8, No. 4, 765–768, 2011.
2. Xie, H. T., D. X. An, X. T. Huang, and Z. M. Zhou, "Fast time-domain imaging in elliptical polar coordinate for general bistatic VHF/UHF ultra-wideband SAR with arbitrary motion," *IEEE J. Sel. Topics Appl. Earth Observ.*, Vol. 8, No. 2, 879–895, Feb. 2015.
3. Zhang, H. R., Y. Wang, and J. W. Li, "New application of parameter-adjusting polar format algorithm in spotlight forward-looking bistatic SAR processing," *Proc. APSAR*, 384–387, Tsukuba, Japan, 2013.
4. Xie, H. T., D. X. An, X. T. Huang, X. Y. Li, and Z. M. Zhou, "Fast factorised backprojection algorithm in elliptical polar coordinate for one-stationary bistatic very high frequency ultrahigh frequency ultra wideband synthetic aperture radar with arbitrary motion," *IET Radar Sonar Navig.*, Vol. 8, No. 8, 946–956, Oct. 2014.
5. Vu, V. T., T. K. Sjögren, and M. I. Pettersson, "Fast time-domain algorithms for UWB bistatic SAR processing," *IEEE Trans. Aerosp. Electron. Syst.*, Vol. 49, No. 3, 1982–1994, 2013

Rapid Echo Simulation for One-stationary Bistatic SAR Based on FFT and Subaperture Processing

Hongtu Xie, Daoxiang An, Xiaotao Huang, and Zhimin Zhou

College of Electronic Science and Engineering, National University of Defense Technology
Changsha, Hunan 410073, China

Abstract— In this study, a rapid echo simulation method based on fast Fourier transform (FFT) and subaperture processing for the one-stationary bistatic synthetic aperture radar (OSBSAR) is presented. First, the OSBSAR geometry is built in elliptical polar coordinate, and then the scene is divided into several equidistant elliptical rings. Based on the equivalent scatterer model, the approximate SAR system transfer function is derived, thus each pulse echo is calculated by the convolution of the transmitted signal and transfer function using the FFT. To further improve the simulation efficiency, the subaperture and subscene processing are used. The transfer function for the same subaperture pulses is calculated by the weighted sum of all the subscene equivalent scattering coefficient in the same equidistant elliptical ring using the FFT. Implementation of the proposed method is discussed. Simulation results are given to prove its validity.

1. INTRODUCTION

One-stationary bistatic synthetic aperture radar (OSBSAR) [1] is a special bistatic SAR (BSAR) system [2], with a stationary radar fixed on the top of a high tower or mountain. It inherits the BSAR advantages, such as greater anti-jamming ability, reducing military vulnerability, getting additional information and flexibility of the system design. Therefore, it has gained wide attention in both military and civilian fields [3].

Echo simulation is important in the SAR research, such as the system design, algorithms test and so on [4]. In general, the echo simulation contains the scene simulation and rapid echo generation. The simulation of the BSAR scene scattering characteristic was studied in [5]. In this paper, we only focus on the rapid generation of the OSBSAR echo, which means that we start with a reflectivity map as an input.

Echo simulation methods main include the time-domain method, two dimensional FFT (2DFFT) method and imaging inverse processing (IMIP) method. Time-domain method simulates echo data pulse by pulse and target by target (TBT) according to the SAR geometry. It can simulate the accuracy echo because of no approximation, but with the huge computational load. 2DFFT method [6] and IMIP method [7] has the high simulation efficiency but with some approximate processing in the echo simulator. To improve the simulation efficiency but with the high simulation precision, a subaperture based echo simulation method for monostatic SAR is given in [8], which may be extend for the BSAR echo simulation.

This paper explores a rapid echo simulation (RES) method for OSBSAR based on [8]. Section 2 introduces the echo simulation based on equivalent scatterer. Section 3 describes the proposed RES method for OSBSAR in detail Section 4 proves its validity based on the simulation results. Section 5 gives the conclusion.

2. ECHO SIMULATION BASED ON EQUIVALENT SCATTERER

OSBSAR geometry is shown in Fig. 1. Moving radar moves parallel to Y axis direction, with the position $(0, y_M(\eta), z_M)$ at the slow time η . Stationary radar is located at $(x_S, 0, z_S)$. The scene is composed of several targets distributed on rectangle grids. Scene grid size is $M \times N$ (range \times azimuth), and the range and azimuth spacing between adjacent grids are Δx and Δy , respectively. x_{\min} is the minimum ground range of the scene, and its azimuth center line is the X axis. Assume that the moving and stationary radars of OSBSAR are perfectly synchronized. The bistatic range from the moving and stationary radars to the grid (m, n) at η is

$$\begin{aligned} R(\eta, m, n) &= R_M(\eta, m, n) + R_S(\eta, m, n) \\ &= \sqrt{(x_{\min} + m\Delta x)^2 + (y_M(\eta) - (n - N/2)\Delta y)^2 + z_M^2} \\ &\quad + \sqrt{(x_S - (x_{\min} + m\Delta x))^2 + ((n - N/2)\Delta y)^2 + z_S^2}, \quad 1 \leq m \leq M, \quad 1 \leq n \leq N \quad (1) \end{aligned}$$

Supposed that the transmitted signal is $p(\tau) = w_r(\tau) \exp(j2\pi f_c \tau + j\pi\gamma\tau^2)$. τ is the fast time, γ is the chirp rate, $w_r(\cdot)$ is the range envelope, c is the speed of light, f_c is the center frequency. Thus the scene echo is

$$s(\tau, \eta) = \sum_{m=1}^M \sum_{n=1}^N \sigma_{mn} w_r[\tau - R(\eta, m, n)/c] \cdot \exp \left[-j2\pi f_c R(\eta, m, n)/c + j\pi\gamma (\tau - R(\eta, m, n)/c)^2 \right] \quad (2)$$

where σ_{mn} is the scattering coefficient of the grid (m, n) .

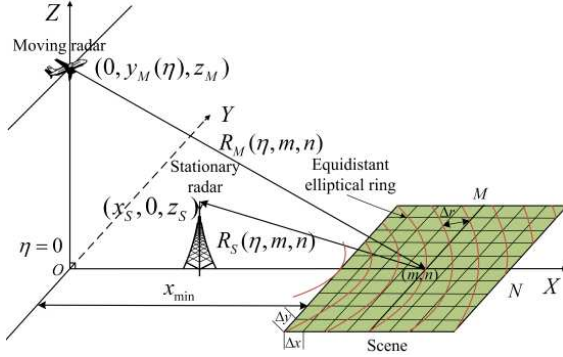


Figure 1: Imaging geometry of the OSBSAR.

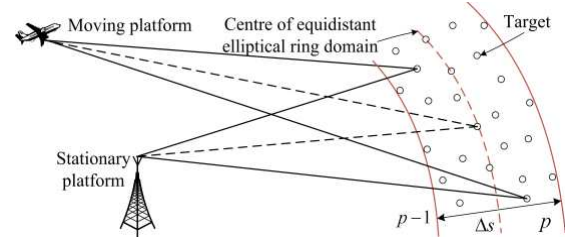


Figure 2: Target distribution between two adjacent equidistant elliptical rings.

To improve the speed, the fast echo simulation based on the equivalent scatterer is first introduced. Basic idea is to divide the scene into several equidistant elliptical rings, and the targets in scene are considered as distributing in the equidistant elliptical rings. The scattering coefficient of targets in the same equidistant elliptical ring is substituted by that of an equivalent scatterer. Assume that Δs is the interval between the adjacent elliptical rings. $R_{\min}(\eta)$ and $R_{\max}(\eta)$ are minimum and maximum ranges from the moving and stationary radars to the scene. The number of equidistant elliptical rings is

$$N_p(\eta) = \text{round}((R_{\max}(\eta) - R_{\min}(\eta))/\Delta s) + 1 \quad (3)$$

The target distribution between two adjacent equidistant elliptical rings is shown in Fig. 2. $p-1$ and p are two adjacent equidistant elliptical rings, and the bistatic ranges from them to the radars are $R_{\min}(\eta) + (p-1)\Delta s$ and $R_{\min}(\eta) + p\Delta s$, respectively. The spacing between the $(p-1)$ -th and p -th equidistant elliptical rings is the p -th equidistant elliptical ring domain. The dashed ring is its center, and the bistatic range from it to the radars is

$$R(\eta, p) = R_{\min}(\eta) + (p-1/2)\Delta s \quad (4)$$

To calculate targets' scattering coefficients in the center of the equidistant elliptical ring domain, the bistatic ranges from the radars to all targets in this domain is replaced by the bistatic range from the radars to its center. So, an equivalent scatterer is substituted for all targets in this domain, whose scattering coefficient is

$$\sigma(\eta, p) = \sum_{i=1}^{I_p} \sigma_i \exp[-j2\pi f_c \Delta R_i(\eta, p)/c] \quad (5)$$

I_p is the number of targets in the p -th equidistant elliptical ring domain, σ_i is the i -th target's scattering coefficient. $\Delta R_i(\eta, p)$ is the difference between the bistatic range from the i -th target to the radars and bistatic range from the center of the p -th equidistant elliptical ring domain to the radars, then we have

$$\Delta R_i(\eta, p) = R_i(\eta) - (R_{\min}(\eta) + (p-1/2)\Delta s) \quad (6)$$

Based on the equivalent scatterer, the scene echo is rewritten as

$$s(\tau, \eta) = \sum_{p=1}^{N_p(\eta)} \sigma(\eta, p) \exp[-j2\pi f_c R(\eta, p)/c] \cdot w_r[\tau - R(\eta, p)/c] \exp \left[j\pi\gamma (\tau - R(\eta, p)/c)^2 \right] \quad (7)$$

We can find that the latter two items in (7) are only related to τ . So, the scene echo can be rewritten as

$$s(\tau, \eta) = w_r(\tau) \exp(j\pi\gamma\tau^2) \otimes_{\tau} \sum_{p=1}^{N_p(\eta)} \sigma(\eta, p) \exp[-j2\pi f_c R(\eta, p)/c] \cdot \delta[\tau - R(\eta, p)/c] \quad (8)$$

\otimes_{τ} is the convolution versus τ . It is well known that the convolution can be performed by the FFT.

3. RES FOR OSBSAR

To further improve the simulation speed, the subaperture and subscene processing is used. First, the system transfer function for the same subaperture pulses is calculated by the weighted sum of all the subscenes equivalent scattering coefficient in the same equidistant elliptical ring domain, and then the subaperture pulse echo is simulated by the convolution of the transmitted signal and system transfer function using the FFT.

3.1. Geometry in Elliptical Polar Coordinate

Geometry in elliptical polar coordinate is shown in Fig. 3. A_{η_c} is the moving radar position at the aperture center time η_c , and A_{η} is the moving radar position at η . B is the stationary radar position. The position of the arbitrary scene grid (m, n) is $(x_m, y_n, 0)$. The range between the grid (m, n) and A_{η_c} is r_M , and r_S is the range from the grid (m, n) to B . Let ρ be the bistatic range of the grid (m, n) and θ be the angle between r_M and Y axis positive direction at η_c , respectively. $\Delta\theta$ is the angular sampling spacing of the scene. So the elliptical polar coordinates of the grid (m, n) are defined as follow

$$\begin{cases} \rho = r_M + r_S = R_M(\eta_c, m, n) + R_S(\eta_c, m, n) \\ \theta = \arccos((y_n - y_M(\eta_c))/r_M), \theta \in [(\pi - \Theta)/2, (\pi + \Theta)/2] \end{cases} \quad (9)$$

Θ is the moving radar beam width. As shown in [1], r_M and r_S can be expressed as a function of (ρ, θ) .

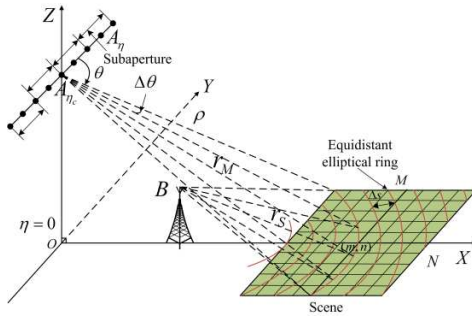


Figure 3: Geometry in elliptical polar coordinate.

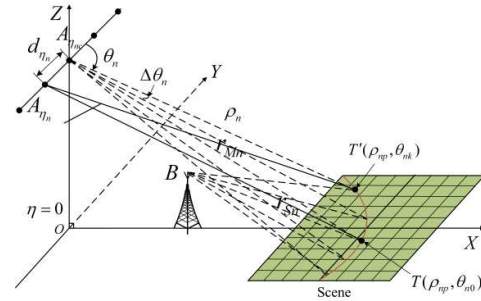


Figure 4: Subaperture processing in the echo simulation.

In Fig. 3, the scene is divided into several elliptical polar subscenes, and the targets in scene is considered as distributing in the elliptical polar subscenes. $R(\eta, \rho_p, \theta_k)$ is the bistatic range from the A_{η} and B to the k -th elliptical polar subscene in the p -th equidistant elliptical ring domain. Thus, the scene echo is given by

$$s(\tau, \eta) = w_r(\tau) \exp(j\pi\gamma\tau^2) \otimes_{\tau} \sum_{p=1}^{N_p(\eta)} \sum_{k=1}^{N_k(\eta)} \sigma(\eta, \rho_p, \theta_k) \cdot \exp[-j2\pi f_c R(\eta, \rho_p, \theta_k)/c] \cdot \delta[\tau - R(\eta, \rho_p, \theta_k)/c] \quad (10)$$

where $N_k(\eta)$ is the number of the elliptical polar subscenes in the p -th equidistant elliptical ring domain at η . $\sigma(\eta, \rho_p, \theta_k)$ is the scattering coefficient of the k -th elliptical polar subscene in this domain, which is

$$\sigma(\eta, \rho_p, \theta_k) = \sum_{i=1}^{I_{p,k}} \sigma_i \exp[-j2\pi f_c (R_i(\eta) - R(\eta, \rho_p, \theta_k))/c] \quad (11)$$

$I_{p,k}$ is the number of targets in the k -th elliptical subscene in the p -th equidistant elliptical ring domain.

3.2. Subaperture Processing

Radar pulses are split into several groups, i.e., subapertures (See Fig. 3). Each subaperture contains the same number of radar pulses. Assume that the subaperture time is very short, so all pulses in the same subaperture is considered as sharing the same scene scope [8]. Subaperture processing in the echo simulation is shown in Fig. 4. Suppose that η_{nc} is the n -th subaperture center time, $A_{\eta_{nc}}$ is the radar position of the central pulse at η_{nc} , A_{η_n} is the radar current position at η_n . The elliptical polar coordinates (ρ_n, θ_n) are defined similar to (ρ, θ) in Fig. 3. $\Delta\theta_n$ is the scene angular sampling spacing. d_{η_n} is the length of $\overline{A_{\eta_{nc}}A_{\eta_n}}$. $T'(\rho_{np}, \theta_{nk})$ and $T(\rho_{np}, \theta_{n0})$ are two elliptical subscenes in the p -th equidistant elliptical ring domain, and $\theta_{nk} = \theta_{n0} + k\Delta\theta_n$. Considering the central pulse position $A_{\eta_{nc}}$, the range $R(\eta, \rho_p, \theta_k)$ in (10) is the same for all elliptical subscenes in the p -th equidistant elliptical ring domain. Thus, (10) can become

$$s(\tau, \eta_{nc}) = w_r(\tau) \exp(j\pi\gamma\tau^2) \otimes_{\tau} \sum_{p=1}^{N_p(\eta_{nc})} \sum_{k=-N_k(\eta_{nc})/2}^{N_k(\eta_{nc})/2} \sigma(\eta_{nc}, \rho_{np}, \theta_{nk}) \cdot \exp[-j2\pi f_c R(\eta_{nc}, \rho_{np})/c] \cdot \delta[\tau - R(\eta_{nc}, \rho_{np})/c] \quad (12)$$

$R(\eta_{nc}, \rho_{np})$ is the bistatic range from radars $A_{\eta_{nc}}$ and B to the p -th elliptical ring domain. As considering other pulse position A_{η_n} , the bistatic range $R(\eta_n, \rho_{np}, \theta_{nk})$ is different from the bistatic range $R(\eta_{nc}, \rho_{np})$. But $R(\eta_n, \rho_{np}, \theta_{nk})$ can be computed from $R(\eta_{nc}, \rho_{np})$. Thus, we have

$$R(\eta_n, \rho_{np}, \theta_{nk}) = |A_{n\eta}T'| + |BT'| = (|A_{nc}T'| + |BT'|) + [(|A_{n\eta}T'| + |BT'|) - (|A_{n\eta}T| + |BT|)] + (|A_{n\eta}T| - |A_{nc}T|) = R(\eta_{nc}, \rho_{np}) + \Delta R_1 + \Delta R_2 \quad (13)$$

From (13), we can find that the ranges $R(\eta_{nc}, \rho_{np})$ and ΔR_2 is independent of k . Thus, (10) can be written as

$$s(\tau, \eta_n) = w_r(\tau) \exp(j\pi\gamma\tau^2) \otimes_{\tau} \sum_{p=1}^{N_p(\eta_{nc})} \sum_{k=-N_k(\eta_{nc})/2}^{N_k(\eta_{nc})/2} \sigma(\eta_n, \rho_{np}, \theta_{nk}) \cdot \exp[-j2\pi f_c (R(\eta_{nc}, \rho_{np}) + \Delta R_1 + \Delta R_2)/c] \cdot \delta[\tau - R(\eta_n, \rho_{np}, \theta_{nk})/c] \quad (14)$$

Provided that the subaperture time is very short, it is reasonable that scattering coefficient $\sigma(\eta_n, \rho_{np}, \theta_{nk})$ can be approximately substituted by $\sigma(\eta_{nc}, \rho_{np}, \theta_{nk})$. Further assume that the radar beam width is not very wide, so $\delta[\tau - 2R(\eta_n, \rho_{np}, \theta_{nk})/c]$ and $\delta[\tau - 2R(\eta_n, \rho_{np}, \theta_{n0})/c]$ are almost identical. Therefore, (14) becomes

$$s(\tau, \eta_n) \approx w_r(\tau) \exp(j\pi\gamma\tau^2) \otimes_{\tau} \sum_{p=1}^{N_p(\eta_{nc})} \{\sigma(\eta_n, \rho_{np}) \cdot \exp[-j2\pi f_c (R(\eta_{nc}, \rho_{np}) + \Delta R_2)/c] \cdot \delta[\tau - R(\eta_n, \rho_{np}, \theta_{n0})/c]\} \quad (15)$$

$\sigma(\eta_n, \rho_{np})$ is the scattering coefficient of the p -th equidistant elliptical ring domain at the position A_{η_n} , i.e.,

$$\sigma(\eta_n, \rho_{np}) = \sum_{k=-N_k(\eta_{nc})/2}^{N_k(\eta_{nc})/2} \sigma(\eta_{nc}, \rho_{np}, \theta_{nk}) \cdot \exp[-j2\pi f_c \Delta R_1/c] \quad (16)$$

r_{Mnp} is the range from the central pulse position $A_{\eta_{nc}}$ to the elliptical subscene $T(\rho_{np}, \theta_{n0})$, and the range from the stationary radar to the elliptical subscene $T(\rho_{np}, \theta_{n0})$ is r_{Snp} . r'_{Mnp} is the range from the current pulse position A_{η_n} to the elliptical subscene $T'(\rho_{np}, \theta_{nk})$, and the range from the stationary radar to the elliptical subscene $T'(\rho_{np}, \theta_{nk})$ is r'_{Snp} . Thus, we have

$$|A_{n\eta}T| + |BT| = \sqrt{r_{Mnp}^2 + d_{\eta_n}^2 + 2r_{Mnp}d_{\eta_n} \cos(\theta_{n0})} + r_{Snp} \approx r_{Mnp} + r_{Snp} + d_{\eta_n} \cos(\theta_{n0}) \quad (17)$$

In a similar way, the range $|A_{n\eta}T'| + |BT'|$ is approximated as

$$|A_{n\eta}T'| + |BT'| \approx r'_{Mnp} + r'_{Snp} + d_{\eta_n} \cos(\theta_{n0} + k\Delta\theta_n) \quad (18)$$

Then, the range difference ΔR_1 can be calculated by

$$\Delta R_1 \approx r'_{Mnp} + r'_{Snp} + d_{\eta_n} \cos(\theta_{n0} + k\Delta\theta_n) - (r_{Mnp} + r_{Snp} + d_{\eta_n} \cos(\theta_{n0})) \quad (19)$$

Under the assumption that radar beam width is not very wide, then $k\Delta\theta_n$ is usually small enough. Thus, $\cos(\theta_{n0} + k\Delta\theta_n) - \cos(\theta_{n0}) \approx -k\Delta\theta_n \sin(\theta_{n0})$ is reasonable. Besides $r_{Mnp} + r_{Snp} = r'_{Mnp} + r'_{Snp}$, then (19) is approximated as

$$\Delta R_1 \approx -d_{\eta_n} k\Delta\theta_n \sin(\theta_{n0}) \quad (20)$$

Therefore, (16) can be written as

$$\sigma(\eta_n, \rho_{np}) = \sum_{k=-N_k(\eta_{nc})/2}^{N_k(\eta_{nc})/2} \sigma(\eta_{nc}, \rho_{np}, \theta_{nk}) \cdot \exp [j2\pi f_c d_{\eta_n} k\Delta\theta_n \sin(\theta_{n0})/c] \quad (21)$$

If the scene angular sampling spacing is meet

$$\Delta\theta_n = c/(f_c d_{L_n} \sin(\theta_{n0})) \quad (22)$$

d_{L_n} is the range from the central pulse position $A_{\eta_{nc}}$ to edge pulse position, then (21) becomes

$$\sigma(\eta_n, \rho_{np}) = \sum_{k=-N_k(\eta_{nc})/2}^{N_k(\eta_{nc})/2} \sigma(\eta_{nc}, \rho_{np}, \theta_{nk}) \cdot \exp [j2\pi k d_{\eta_n} / d_{L_n}] \quad (23)$$

The size of the n -th subaperture is $2L_n$, and its index is $l_n = -L_n \cdots L_n$, then the discrete expression of (23) is

$$\sigma(l_n, \rho_{np}) = \sum_{k=-N_k(\eta_{nc})/2}^{N_k(\eta_{nc})/2} \sigma(\eta_{nc}, \rho_{np}, \theta_{nk}) \cdot \exp [j2\pi k W_{l_n}] \quad (24)$$

$W_{l_n} = d_{l_n} / d_{L_n} = l_n / L_n$, and d_{l_n} is the value of d_{η_n} at the l_n radar pulse position. Compared with the formula of the FFT, it is seen that (24) can be calculated by the FFT. The scene echo for the n -th subaperture is

$$s(\tau, \eta_n) \approx w_r(\tau) \exp(j\pi\gamma\tau^2) \otimes_{\tau} \sum_{p=1}^{N_p(\eta_{nc})} \{ \text{FFT} [\sigma(\eta_{nc}, \rho_{np}, \theta_{nk})] \cdot \exp [-j2\pi f_c (R(\eta_{nc}, \rho_{np}) + \Delta R_2)/c] \cdot \delta [\tau - R(\eta_n, \rho_{np}, \theta_{n0})/c] \} \quad (25)$$

Similarly, (25) can be performed by the FFT operation.

3.3. Implementation

According to the proposed RMS method, its implementation is given as follows:

(1) Set the simulation parameters and scene scattering coefficients; (2) Generate the transmitted signal and compute its FFT; (3) Divide the moving radar synthetic aperture into several subapertures; (4) Start the subaperture processing, separate the scene into several equidistant elliptical ring domain and elliptical subscenes; (5) Calculate the equivalent scattering coefficients of the elliptical subscenes at the subaperture central pulse. Based on this elliptical subscene scattering coefficients, calculate the equidistant elliptical rings' scattering coefficients for all the subaperture pulses using the FFT; (6) Calculate the system impulse response function and its FFT for all subaperture pulses; (7) Multiply the results of (2) and (6), and then transform their product into the time-domain using the IFFT and the obtain the subaperture pulse echo; (8) In terms of the subaperture order, repeat (4)–(7), and then the scene echo can be generated.

4. SIMULATION RESULTS

Simulation results are shown to verify the validity of the proposed RES method. Echo simulated by the TBT method is used as the referenced echo. To prove its correctness by the evaluation of imaging results, echoes simulated by different simulation methods are processed by the backprojection algorithm (BPA).

Simulation parameters are shown in Table 1. 81 scattering targets are located in the scene ($200\text{ m} \times 200\text{ m}$, range \times azimuth), and are arranged in 9 rows and 9 columns. Range and azimuth spacing between the adjacent scattering targets are 20.98 m and 22.44 m. Central target position is (1100 m, 0 m, 0 m). Scattering coefficients of all targets are assumed to be 1, and effects of the jamming, noise and multipath aren't considered.

Table 1: Simulation parameters of the OSBSAR system.

Center frequency	Signal bandwidth	Sampling frequency	Pulse duration	PRF	Azimuth beam width	Moving radar altitude (speed)	Stationary radar position
500 MHz	200 MHz	240 MHz	1 μs	100 Hz	10.2°	100 m(45 m/s)	(400, 0, 10) m

Figure 5 shows echoes simulated by the TBT and proposed RES methods. It is seen that the amplitude and phase of simulated echoes are very similar. Simulated echoes in Fig. 5 are processed by the BPA, and imaging results are shown in Fig. 6. It is found that the imaging results in Figs. 6(b) and 6(d) are very similar to that shown in Figs. 6(a) and 6(c), but their focusing qualities are slightly degraded due to the approximations in echo simulation. Processing time of the TBT and proposed RES methods are 20067.3 s and 1425.4 s, respectively. Compared with the TBT method, the simulation efficiency of the proposed method is improved about 14.1 times.

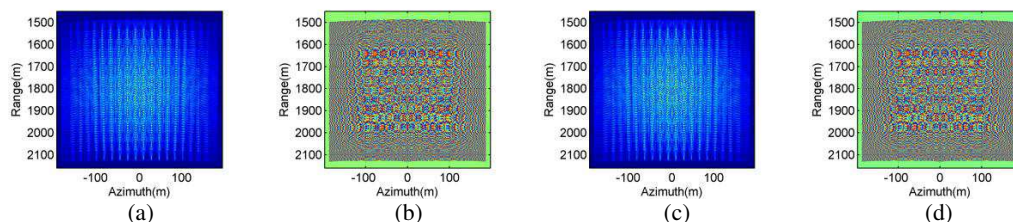


Figure 5: Scene echoes including 81 scattering targets. (a), (b) Amplitude and phase of the scene echo simulated by the TBT method; (c), (d) Amplitude and phase of the scene echo simulated by the proposed RES method.

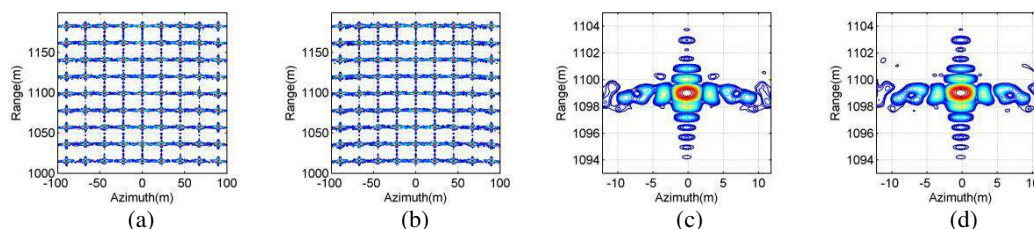


Figure 6: Imaging results. (a) Imaging result of the echo in Figs. 5(a)–(b); (b) Imaging result of the echo in Figs. 5(c)–(d); (c) Imaging result of the central target in Fig. 6(a); (d) Imaging result of the central target in Fig. 6(b).

5. CONCLUSION

This paper presents a rapid echo simulation method based on FFT and subaperture processing for OS-BSAR. The equivalent scatterer, subaperture processing and FFT operation can achieve great efficiency improvement in the OSBSAR echo simulation. The proposed RES method is verified by

the simulation results, which has enriched the echo simulation method and will provide reliable echo source for the further OS-BSAR research.

ACKNOWLEDGMENT

This work was supported by the National Natural Science Foundation of China: Research on the key techniques of low frequency ultra wideband synthetic aperture radar interferometry (61201329) and Research Project of National University of Defense Technology (JC14-04-02).

REFERENCES

1. Xie, H. T., D. X. An, X. T. Huang, X. Y. Li, and Z. M. Zhou, "Fast factorised backprojection algorithm in elliptical polar coordinate for one-stationary bistatic very high frequency ultrahigh frequency ultra wideband synthetic aperture radar with arbitrary motion," *IET Radar Sonar Navig.*, Vol. 8, No. 8, 946–956, Oct. 2014.
2. Xie, H. T., D. X. An, X. T. Huang, and Z. M. Zhou, "Fast time-domain imaging in elliptical polar coordinate for general bistatic VHF/UHF ultra-wideband SAR with arbitrary motion," *IEEE J. Sel. Topics Appl. Earth Observ.*, Vol. 8, No. 2, 879–895, Feb. 2015.
3. Henke, D., A. Barmettler, and E. Meier, "Bistatic experiment with the UWB-CARABAS sensor-first results and prospects of future applications," *Proc. IGARSS*, Capetown, South Africa, Jul. 2009, 234–237.
4. Franceschetti, G., M. Migliaccio, D. Riccio, and G. Schirinzi, "SARAS: A synthetic aperture radar (SAR) raw signal simulator," *IEEE Trans. Geosci. Remote Sens.*, Vol. 30, No. 1, 110–123, Jan. 1992.
5. Zhang, M., Y. W. Zhao, Y. Zhao, and H. Chen, "A bistatic synthetic aperture radar imagery simulation of maritime scene using the extended nonlinear chirp scaling algorithm," *IEEE Trans. Aerosp. Electron. Syst.*, Vol. 49, No. 3, 760–776, Jul. 2013.
6. Franceschetti, G., A. Iodice, A. Natale, and D. Riccio, "Bistatic SAR simulation time and frequency domain approaches," *Proc. DSP*, 1–7, Corfu, Greece, 2011.
7. Qiu, X. L., D. H. Hu, L. J. Zhou, and C. B. Ding, "A bistatic SAR raw data simulator based on inverse ω -k algorithm," *IEEE Trans. Geosci. Remote Sens.*, Vol. 48, No. 3, 1540–1547, Mar. 2010.
8. Wen, L. and T. Zeng, "A sub-aperture based SAR raw signal generation method," *Proc. IET International Radar Conference*, 89–92, Guilin, China, Jan. 2009.

Shielding and Mitigations of the Magnetic Fields Generated by the Underground Power Cables

N. İl, S. Ozen, M. Çakir, and H. F. Carlak

Electrical & Electronics Engineering, Akdeniz University, Antalya 07058, Turkey

Abstract— In urban areas, especially in city centres, underground power cable usage in power distribution lines has been increasing dramatically. In this study, shielding the source and shielding the underground power cable raceway are investigated. In order to mitigate the magnetic field caused by underground power cables, two different shield topologies, the flat plate and the reverse-U shape shielding screens, are examined theoretically and practically on currently used cable raceways. The most appropriate shielding type is investigated.

1. INTRODUCTION

In recent years, increasing energy demand results in more loading in power transmission lines and correspondingly more magnetic field occurrence around transmission lines. These excessive magnetic fields can cause harmful effects on human health. These fields can also lead to deteriorating effects on the sensitive electronic equipment due to the electromagnetic interference. Therefore, investigation of the magnetic field that occurs around the underground cable lines used in the energy distribution network has become an important research topic. There are number of design options that would mitigate the magnetic field. However, magnetic field management can be basically classified into two main categories; which are shielding the subject and shielding the source. High voltage power line magnetic fields can occur at the top of the underground cable channels in city centers, playgrounds near the substations, on sidewalks, at business centers and many other vital areas which have energy demands. According to the studies, although the harmful effects of electromagnetic fields over human health are not totally confirmed, the results are sufficient to make the people worry, and hence, some of the countries have published safety standards for electromagnetic fields [1–4]. Measurement results are evaluated according to the limits of international standards or national standards according to the limit values which are considered as not to be damaging to the human health [5, 6].

In this study, the magnetic field levels on the underground power cable channels were measured and the behaviors to reduce the magnetic field of the different shielding materials were evaluated. The results are evaluated in the light of safety limits and recent studies maintained in this regard, and the optimal screen type for cable channels have investigated.

2. THE THEORY OF SHIELDING AND SHIELDING MATERIALS

Electric field shielding effectiveness (SE_E) and the magnetic field shielding effectiveness (SE_M) of a plate shield are obtained by the following equations.

$$SE_E = 20 \log_{10} \left| \frac{\hat{E}^{inc}}{\hat{E}^{tran}} \right|, \text{ (dB)} \quad (1)$$

$$SE_M = 20 \log_{10} \left| \frac{\hat{H}^{inc}}{\hat{H}^{tran}} \right|, \text{ (dB)} \quad (2)$$

where, \hat{E} is the electric field intensity (V/m), \hat{H} is the magnetic field intensity (A/m), *inc* is the incident wave, *tran* is the transmitted wave, and SE is the function of frequency. In shielding, the attenuation of electromagnetic waves from the air/conductive surface and with regard to the interaction enters the screen conductor takes place in three stages. These are: Reflection Losses (R_{dB}), Absorption Losses (A_{dB}) and Multiple Reflections (M_{dB}). The priority phase of the shielding is a reflection. To reflect wave with shielding, shielding is required to have load carriers (electrons and holes) which interact to each other. As a result, the shielding must be electrically conductive.

The Shielding Effectiveness of (dB) is denoted by the following expression:

$$SE_{dB} = R_{dB} + A_{dB} + M_{dB} \quad (3)$$

$$SE_{dB} \approx \underbrace{20 \log_{10} \left| \frac{\eta_0}{4\eta} \right|}_{R_{dB}} + \underbrace{20 \log_{10} e^{t/\delta}}_{A_{dB}} + \underbrace{20 \log_{10} \left| 1 - e^{-2t/\delta} e^{-j2t/\delta} \right|}_{M_{dB}} \quad (4)$$

E/H ratio varies depending on the characteristics of the source in the near field region. If the source has high current and low voltage character, the magnetic field is dominant in the near field region and the ratio of $E/H < 377\Omega$. Whenever getting farther from this region, H decreases by $1/r^3$ and E decreases by $1/r^2$ ratio. On the other hand, if the source has high voltage and low current character, the electric field is dominant in the near field region and the ratio of $E/H > 377\Omega$. Whenever getting farther from this region, H decreases by $1/r^2$ and E decreases by $1/r^3$ ratio. In the near field, the wave impedances of E and H fields are expressed as;

$$\eta_E = \frac{\eta_0 \lambda_0}{2\pi r} \gg \eta_0 \quad \text{and} \quad \eta_H = \frac{\eta_0 2\pi r}{\lambda_0} \ll \eta_0 \quad (5)$$

The electrical properties of some materials used in shielding are given in Table 1. The effect of the thickness of the shielding material versus shielding effectiveness is shown in Figure 1.

Table 1: Electrical properties of some shielding materials.

Material	Resistivity (ρ) (Ωm)	Conductivity (σ) (Siemens/m)	Magnetic Permeability (μ_r)	Skin Depth (m)		
				Frequency 50 Hz	Frequency 60 Hz	Frequency 100 Hz
Aluminum	2.82×10^{-8}	3.5×10^7	1	0.012	0.01	0.008
Copper	1.68×10^{-8}	5.58×10^7	1	0.0092	0.0084	0.0065
Iron	9.58×10^{-8}	1.04×10^7	500	0.0031	0.0028	0.0022
Steel	1.61×10^{-7}	6.21×10^6	100	0.0029	0.0026	0.0020

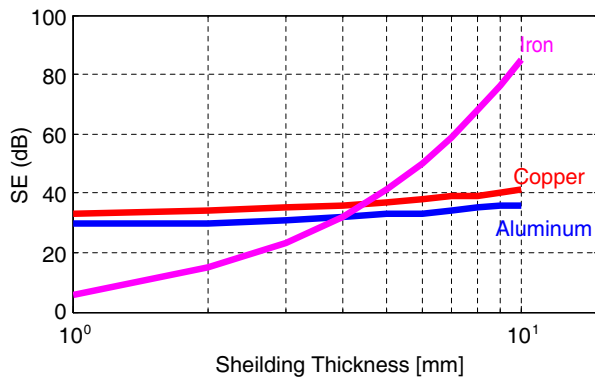


Figure 1: Shielding effectiveness versus material thickness for iron, copper and aluminum materials.



Figure 2: Measurement in the high voltage channel with reversed U galvanized shielding.

3. MAGNETIC FIELD MITIGATIONS OF UNDERGROUND POWER CABLES

In this study, 2 mm thick galvanized flat sheet, 2 mm thick flat iron plate, and 2 mm thick reversed U-shaped galvanized sheet (see Fig. 2) is used in the cable channels measurements as an electromagnetic field shielding material. Three-axis Hioki FT3470 brand magnetic field measurement device was used in the magnetic field measurements. This device is capable of RMS measurements in the range of 2 micro Tesla–2 mT, 0.5 mG–20 Gauss, 0.040 A/m–1592 A/m within 250 ms time periods with $\pm 3.5\%$ accuracy in the X, Y, Z -axis. Frequency range is from 10 Hz to 400 kHz.

The cable channel included HV cables has 80 cm depth and 66 cm width. There are 3 piece of $1 \times 240/25 \text{ mm}^2$ cross sectional XLPE cable for R, S, T phases. Line voltage of the plant is

31.5 kV. During the measurement, the load was recorded as 400 kW ($pf = 0.97$) and the current was observed as approximately 7.55 A. Shielding material thickness of 2 mm flat iron sheet and 2 mm reversed U galvanized sheet was used for the electromagnetic field measurements in the HV cable channel. For each shielding material, measurements were taken with 20 cm intervals from the vertical plane of the cable channel through the central axis of the ground level and the values were recorded. The measurement results are shown in Table 2.

Table 2: Magnetic field measurements in the HV cable channel.

HEIGHT	Usage of Uncovered Channel (μT)	Usage of Reversed U Type Galvanized Sheet (μT)	Usage of 2 mm thick Flat Iron Plate (μT)
0 cm	0.462	0.387	0.263
20 cm	0.385	0.332	0.227
40 cm	0.282	0.248	0.181
60 cm	0.181	0.164	0.129
80 cm	0.157	0.145	0.117
100 cm	0.134	0.125	0.11

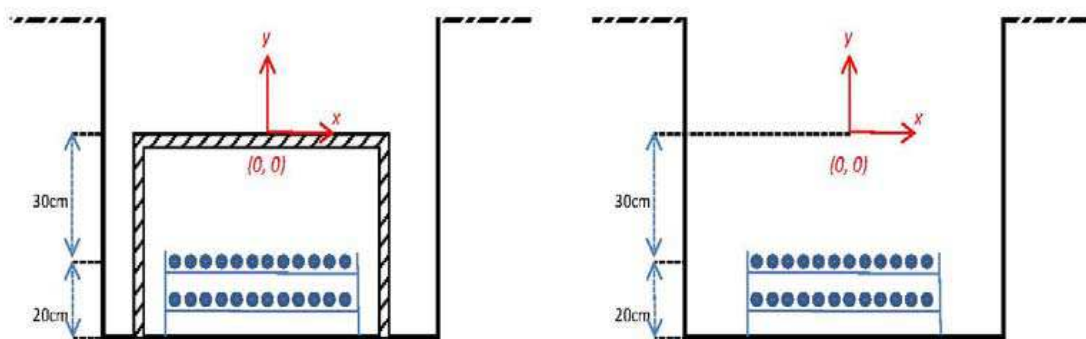


Figure 3: Representation of LV cable channel.

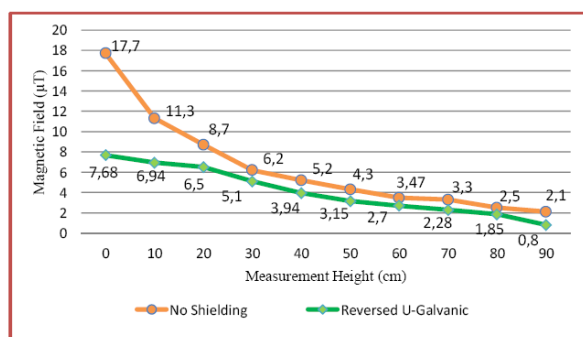


Figure 4: Comparison of LV measurement results.

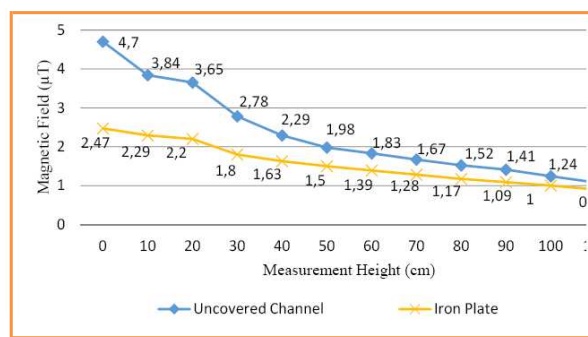


Figure 5: Shielding effect of iron sheet in the LV cable channel.

While the cable channel is uncovered and the top of the channel is covered with galvanized and iron sheets, the measurements of the magnetic field were carried out. Since multiple cable arrangement has been used, the current value was not measured separately for each cable channel. The LV output of the facility has been installed as balanced and approximately 38 kW load existed in each phase during the measurements.

For each shielding material, measurements were acquired at the central axis of the cable channel from ground level through 10 cm intervals at a vertical plane and the values were recorded. While the change of the shielding effectiveness of reversed-U galvanized in the LV power channel is shown in Fig. 4, the shielding effectiveness of the iron plate is shown in Fig. 5.

It is concluded that, better shielding efficiency is achieved when closed shields are used. On the other hand, in case of the flat plate shield usage, the efficiency depends on the electrical properties and the thickness of the material.

4. CONCLUSION

When measurements and the research findings which are obtained with established mechanisms with different shielding materials in the LV and HV cable channels are analyzed, the results denoted that “the shielding materials used and the distance between the source of the electromagnetic wave and the shielding material directly affects the shielding effectiveness”. The measurement results made with different shielding materials showed that when the iron plate is used as the magnetic field shielding material, the highest shielding effectiveness is reached. U-typed screen displays are more effective than plain plate shaped. Accepted magnetic field limits should be revised, and in the light of recent research, regulations all over the world should be updated by reducing the general trend under the 0.3–0.4 μT level. While facilities and power transmission lines are being designed, the magnetic field calculation of the cable channels and their panels should be carried out. The analysis of power losses that occur in the screen materials for the lines to be screened, it is recommended as a further study subjects that can be done in this field.

ACKNOWLEDGMENT

This study was supported by Akdeniz University, Scientific Research Projects Supporting Unit (BAPYB).

REFERENCES

1. Ozen, S., S. Helhel, and O. H. Colak, “Electromagnetic field measurements of radio transmitters in urban area and exposure analysis,” *Microwave and Optical Technology Letters*, Vol. 49, No. 7, 1572–1578, 2007.
2. Sergeant, P. and S. Koroglu, “Electromagnetic losses in magnetic shields for buried high voltage cables,” *Progress In Electromagnetic Research*, Vol. 115, 441–460, 2011.
3. Del Pino Lopez, J. C., P. Cruz Romero, and P. Dular, “Parametric analysis of magnetic field mitigation shielding for underground power cables,” *Renewable Energy and Power Quality Journal*, No. 5, 1–8, 2007.
4. Ozen, S., “Low-frequency transient electric and magnetic fields coupling to child body,” *Radiation Protection Dosimetry*, Vol. 128, No. 1, 62–67, 2008.
5. Cerezci, O., Z. Kartal, K. Pala, and A. Turkkan, “Elektromanyetik Alan ve Sağlık Etkileri,” *Ozsan Matbaacılık*, 132, 2012.
6. Ozen, S., S. Helhel, G. Kahya, M. Cakir, and S. Yalcin, “Evaluations of occupational exposure and magnetic field levels at hospital environments,” *Pamukkale Univ. Muh. Bilim. Derg.*, Vol. 20, No. 8, 300–303, 2014, DOI: 10.5505/pajes.2014.82905.

Occupational Exposure Assessment of Power Frequency Magnetic Field in 154/31.5 kV Electric Power Substation in Turkey

S. Ozen, S. Helhel, and H. F. Carlak

Electrical & Electronics Engineering Department, Akdeniz University, Antalya 07058, Turkey

Abstract— The survey of magnetic field measurements from the 154/31.5 kV substation in the city of Antalya have been proposed for an occupational exposure assessment. The magnetic field measurements are carried out from a substation equipment; including all transformers, circuit breakers, feeders and buses, under the in-coming and out-going power lines and operator tables surrounding the substation. The magnetic field is measured as 0.46 μT at the minimum loaded season and 1.34 μT at maximum loaded season over the operator desk. Workers are exposed to 0.3 μT and even more magnetic field for eight hours period per day. In switchgear regions, the maximum magnetic field measurement is 20 μT at the minimum loaded season and may reach up to 65 μT . Outdoor magnetic field values at the circuit breaker region may approach to 45 μT depending on operator heights.

1. INTRODUCTION

The effects of exposure to power frequency electromagnetic fields take the attention of the public as an important topic. These 50-Hz field exposures raise the question of what kind of effects these may have on human health. Some epidemiological studies have found weak associations between the exposure to power-frequency EMFs and some forms of cancer, such as leukemia; while other studies have failed to find such associations. Accordingly, the risk of the adverse health effects is getting higher [1, 2]. The scientific evidence suggesting that ELF-EMF exposures pose any health risk is not sufficient. The strongest evidence for health effects comes from associations observed in human populations with two forms of cancer: childhood leukemia and chronic lymphocytic leukemia in occupationally exposed adults. While the support from individual studies is not adequate, the epidemiological studies demonstrate for some methods of measuring exposure, a fairly consistent pattern of a small, increased risk with increasing exposure that is somewhat weaker for chronic lymphocytic leukemia than for childhood leukemia. Scientists [3–6] observed an increased leukemia risk for children in one or more exposure group, and the risks of adult cancer based on residential exposure to ELF-EMF have been evaluated in a number of studies. Of great concern are the findings of an Auckland university study detailing very high magnetic fields beneath lines in Auckland with significant effects on occupants [6]. This paper presents the results of measurements of the power frequency magnetic fields on a 154/31.5 kV substation in Turkey. A real time measurements were carried out in substations, since the actual magnetic field exposure to occupants is important.

2. DESCRIPTION OF THE SUBSTATION AND MEASUREMENTS

The substation is situated in a residential area about 10 km west side of city of Antalya. Figure 1 depicts part of the substation and Figure 2 shows the simple layout of the substation. There are two 154 kV incoming lines and two outgoing lines, and twelve 31.5 kV outgoing lines. Tables 1 and 2 depict the power and current load details of feeders loading at the time of measurement recorded.

Magnetic fields in the substation was measured by using a commercially available magnetic field meter, ELT-400 Exposure Level Tester, Narda Safety Test Solutions, and Wandel & Golterman, Germany. Figure 3 depicts the magnetic field variations throughout the control room of the substation. The location of the peak magnetic fields obtained in the control room is the location where AC-DC power unit is present, and magnetic field value reaches up to 4 μT for the substation. For three-control room, operator desks read between 0.33 μT and 1.1 μT . Figure 4(a) represents the magnetic field measurements taken in front of the cells and from the back of the cells. In the switchgear region of substation, measured magnetic field value goes up to 20 μT at both front and

Table 1: 154/31.6 kV Substation loads during the measurements of 31.6 kV lines.

Feeder No.	1	2	3	4	5	6	7	8	9	10	11	12
Amp.	94	265	35	70	1.9	7.8	14	25.5	220	177	117	176.8

Table 2: The measured magnetic field different locations in the open areas of the substation.

Measurement Locations	Magnetic field (μT)
31.5 kV side of TR-A	4.7
31.5 kV side of TR-B (2 m from TR-B)	7.4
In front of the circuit breaker (SF6)	8.8
Under the 154 kV busbar for TR-B input	3.95
Under the 154 kV busbar for TR-A input	6.5

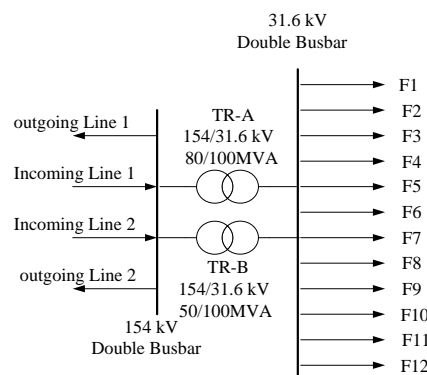


Figure 1: Open areas of the substation.

Figure 2: Simple plan layout of the substation.

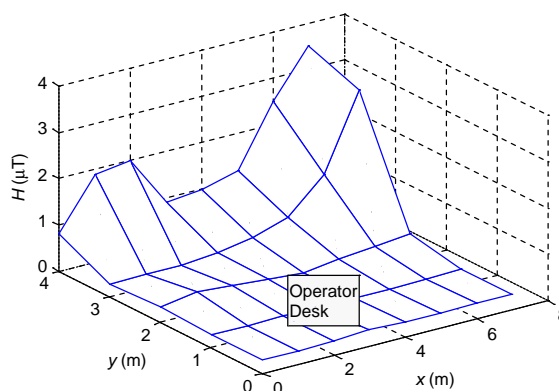


Figure 3: Magnetic field variation for the operator office and daily working room.

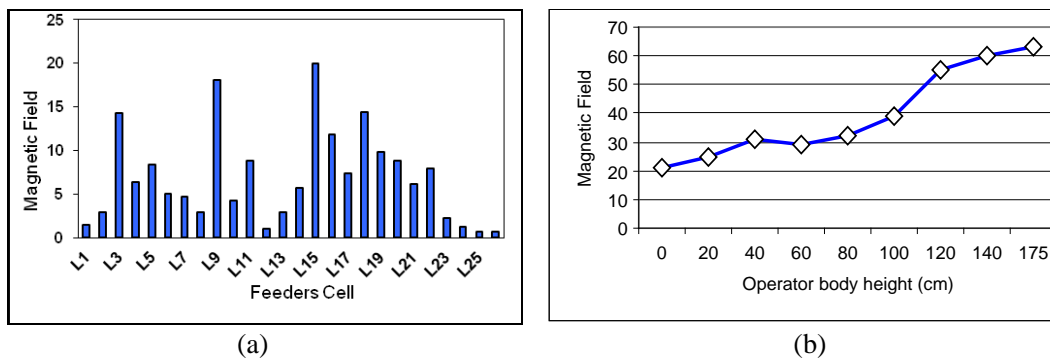


Figure 4: (a) Magnetic field (μT) values at operators working locations. (b) Represents the magnetic field variations over the operator body height while standing in front of 31.5 kV command panel of TR-B.

backside of the related cell. These values are valid at one of the measurement dates. Figure 4(b) shows magnetic field variation over the operator body height while standing in front of 31.5 kV command panel for TR-B. As demonstrated at Figure 4(b), the longitudinal magnetic field varies

between 20 μT and 62 μT at the substation.

3. INDUCED ELECTRIC FIELD AND CURRENT DENSITY

The interaction of time varying electric fields with the human body results in the flow of electric charge (current), the polarization of bound charge (for motion of electric dipoles), and reorientation of electric dipoles already present in tissue. The relative magnitudes of these different effects depend on the electrical properties of the body — that is, electrical conductivity and permittivity. Electric conductivity and permittivity vary with the type of body tissue and depend on the frequency of the applied field. Electric fields to the body induce a surface charge on the body; this results in induced currents in the body, the distribution of which depends on exposure conditions, size and shape of the body, and the position of the body in the field [7, 8]. To determine the current density that is induced inside human body standing different locations at substation. The human body is simulated as prolate spheroid [9]. According to Faraday's law, a changing external magnetic field produces an internal electric field inside the body. Thus, the internal induced electric field components can be expressed by the following equations:

$$\vec{E}_x = j\omega \left(\frac{zB_y}{2} - \frac{b^2yB_z}{a^2 + b^2} \right) \quad (1)$$

$$\vec{E}_y = j\omega \left(\frac{a^2}{a^2 + b^2} \right) (xB_z - zB_x) \quad (2)$$

$$\vec{E}_z = j\omega \left(\frac{b^2yB_x}{a^2 + b^2} - \frac{xB_y}{2} \right) \quad (3)$$

where B_x , B_y , and B_z are the three components of the external magnetic field and ω is the angular frequency the external magnetic field. Total electric field \vec{E} induced inside the body can be expressed by $E = (E_x^2 + E_y^2 + E_z^2)^{1/2}$, and the current density \vec{J} induced inside the body by the internal field can be determined as $\vec{J} = \sigma\vec{E}$. Where σ is the electric conductivity of the body tissue (S/m). Since we are dealing with the biological body and considering the ELF magnetic field, we have $\sigma \gg \omega\epsilon$ (ϵ ; permittivity of the body), and hence the displacement current component can be neglected [10–12]. The second-order magnetic field due to the current induced inside the model is also neglected. For this reason, the magnetic field inside the body can be regarded as a uniform. Here, the frequency of external magnetic field is 50 Hz and the conductivity of the body is 0.2 S/m [13]. Table 3 summarizes the maximum induced electric fields and current densities at different operation locations in the substation corresponding to the average magnetic field values resulted from the measurements in the substations.

Table 3: Maximum induced electric fields and current densities for different locations in the substation.

Measurement Locations	Magnetic field (μT)	$J(\mu\text{A}/\text{m}^2)$
Operator desktop	0.35	1.517
In front of 31.5 kV Command panel for main bar	40	173.416
31.5 kV side of TR-A	4.7	20.376
31.5 kV side of TR-B (2m from TR-B)	7.4	32.082
In front of the circuit breaker (SF6)	8.8	38.15
Under the 154 kV bus bar for TR-B input	3.95	17.124
Under the 154 kV bus bar for TR-A	6.5	28.18

A location that the occupants are working under the maximum average magnetic field was chosen for the data collection. Occupants' desks are reading an induced current density of 1.517 $\mu\text{A}/\text{m}^2$.

4. CONCLUSION

There are four occupants staying 8 hours of shift. Operator desks at substation read a lowest magnetic field of 0.35 μT at minimum loaded season and reached up to 1.1 μT at maximum loaded season that means operators exposed to a magnetic field of 0.35 μT and more by eight hours a day during a year. In switchgear regions, the maximum magnetic field reading is 20 μT at minimum

loaded season and reached up to $65 \mu\text{T}$. Outdoor magnetic field measurement at circuit breaker region goes up to $40 \mu\text{T}$ with respect to operator heights. Instead these values are in the limit of International Radiation Protection Association, results given by open literature say that those values are unfortunately in the risk region [1–9]. That's why, employer should force scientists to find a way of decreasing magnetic flux density for such working or living places. For the chosen substations, under the normal load conditions, a maximum magnetic field of $40 \mu\text{T}$ is measured at 31.5 kV main bus and in the substation. For this magnetic field strength, the maximum internal induced current density is about $173.4 \mu\text{A}/\text{m}^2$. For this type of work places, epidemiological and biological studies should be taken into account for a low level magnetic field strength.

ACKNOWLEDGMENT

This study was supported by Akdeniz University, Scientific Research Projects Supporting Unit (BAPYB).

REFERENCES

1. Wong, P. S. and A. Sartre, "Simultaneous AC and DC magnetic field measurement in the residential area; implication for resonance theories of the biological effects," *IEEE Transactions on Power Delivery*, Vol. 10, No. 4, 1995.
2. Hamza, A. H., S. A. Mahmoud, N. M. Abdel-Gawad, and S. M. Ghania, "Evaluation of magnetic induction inside humans at high voltage substations," *Electric Power Systems Research*, Vol. 74, 231–237, 2005.
3. Feychting, M. and A. Ahlbom, "Magnetic fields and cancer in children residing near Swedish high-voltage power lines," *American Journal of Epidemiology*, Vol. 138, 467–481, 1993.
4. Olsen, J. H., A. Nielsen, and G. Schulgen, "Residence near high voltage facilities and risk of cancer in children," *British Medical Journal*, Vol. 307, 891–895, 1993.
5. Verkasalo, P. K., E. Pukkala, M. Y. Hongisto, J. E. Valjus, P. J. Jarvinen, K. V. Heikkila, and M. Koskenvuo, "Risk of cancer in Finnish children living close to power lines," *British Medical Journal*, Vol. 307, 895–898, 1993.
6. Smart, R., "Health effects of high voltage transmission lines: A survey of the medical literature," Dec. 2004.
7. Özen, Ş., "Low-frequency transient electric and magnetic fields coupling to child body," *Radiation Protection Dosimetry*, Vol. 128, 62–67, 2008.
8. ICNIRP Guidelines, "Guidelines for limiting exposure to time varying electric, magnetic, and electromagnetic fields (up to 300 GHz)," 1998.
9. Deford, J. F. and O. P. Gandhi, "Impedance method to calculate currents induced in biological bodies exposed to quasi-static electromagnetic fields," *IEEE Trans. Electromagnetic Compat.*, Vol. 27, No. 3, 168–173, 1985.
10. Xi, W., M. A. Shutly, and O. P. Gandhi, "Induced electric currents in models of man and rodents from 60 Hz magnetic fields," *IEEE Trans. Biomed. Eng.*, Vol. 41, 1018–1023, 1994.
11. Ozen, S. and S. Helhel, "Analysis of induced current to child body caused by 50 Hz EM waves," *URSI 2006*, 180–182, Ankara, Sep. 6–8, 2006.
12. Özen, Ş., "Evaluation and measurement of magnetic field exposure at a typical high voltage substation and its power lines," *Radiation Protection Dosimetry*, Vol. 128, 198–205, 2008.
13. International Non-Ionizing Radiation Committee of the International Radiation Protection Association, "Interim guidelines on limits of exposure to 50/60 Hz electric and magnetic fields," *Health Phys.*, Vol. 58, 13–122, 1990.

Effect of Renewable Energy Sources to the Stability of the Low Voltage Distribution Networks

Z. Szabo^{1,3}, F. Zezulka^{2,3}, Z. Roubal^{1,3}, P. Marcon^{1,3}, O. Sajdl^{2,3}, and I. Vesely^{2,3}

¹FEEC, Department of Theoretical and Experimental Electrical Engineering
Brno University of Technology, Technicka 12, Brno, Czech Republic

²FEEC, Department of Control and Instrumentation

Brno University of Technology, Technicka 12, Brno, Czech Republic

³FEEC, Centre for Research and Utilization of Renewable Energy

Brno University of Technology, Technicka 12, Brno, Czech Republic

Abstract— The paper describes the recent development in the area of renewable energy sources (RES). Shows the situations in countries supporting a great growth of RES, particularly in photovoltaic energy what leads to the big problems. The modelling of situation shows that in a very near future there will be a big overflow of electrical energy production in the low voltage networks (LVN). It would evoke necessity to transfer energy into higher voltage networks. However it's not possible, because of the protection systems of high voltage networks (HVN) are developed for the opposite flow of energy. The traditional power engineering industry assumes centralized energy sources (power plants), and delivers electrical energy into consumers via very high voltage networks (transition networks VHN), high voltage networks (HVN) into LVN. In the low voltage networks the energy is totally consumed. Because of the existing protection systems in the HVN, and the recent energy distributors and producers correspond with this traditional conception, is necessary to consume all energy from RES in the low voltage networks where it was produced. Our contribution deals with this phenomenon and offers some part solution of the problem.

1. INTRODUCTION

Recent development in the area of RES shows, that situation in countries supporting a great growth of RES, particularly photovoltaic leads to big problems. Modelling studies shows that, in a very near future there will be a big overflow of electrical energy production in the networks of NN (low voltage networks). It would evoke necessity to transfer energy into higher voltage networks. However it will not be possible while protection systems of high voltage networks are developed for the opposite flow of energy. The traditional power engineering industry assumes that centralized energy sources (power plants) deliver electrical energy into consumers via very high voltage networks (transition networks VVN), high voltage networks (transition networks VN) into low voltage networks (NN). In low voltage networks is the energy totally consumed. Because the existing protection systems, the recent short-time task for energy distributors and producers, corresponding this traditional conception, is to consume all energy from RES in low voltage networks where it was produced.

2. STATE OF THE ART

On the Fig. 1 is shown a typical star topology of an energy network. The energy, produced in power plants is transformed from 6 to 30 kV typically to 115 kV or 230 kV (VVN). Let us assume an energy network, i.e., from smaller power plants. The energy from turbines will be transformed to the high voltage 115 kV phase AC transmission network. In the Fig. 1 there are shown several lines of the VVN (very high voltage network). Each of the lines goes into a transform station (DTS GROUP) and is transformed and distributed into several (e.g., ten) high voltage lines (22 kV AC). These lines (i.e., outsides VN distribution lines) go to single localities and there are transformed to 400 V AC of the low voltage distribution lines NN. These NN distribution lines goes to single consumers (households, schools, institutions, SMEs), i.e., to OMs.

In the recent time situation in the single OMs as well as in the whole NN network can be more complicated in the past. The task for electrical energy distribution in the past was to deliver enough energy in a high quality (voltage and frequency) to consumers. Next tasks in a near future will be specified as how and where to spend surplus energy which will be produced in NN networks by non-stable distributed photovoltaic (FV) [7], wind power plants and etc. [10]. Simulation which goes from information of installed and contract promised power from RES shows, that power and

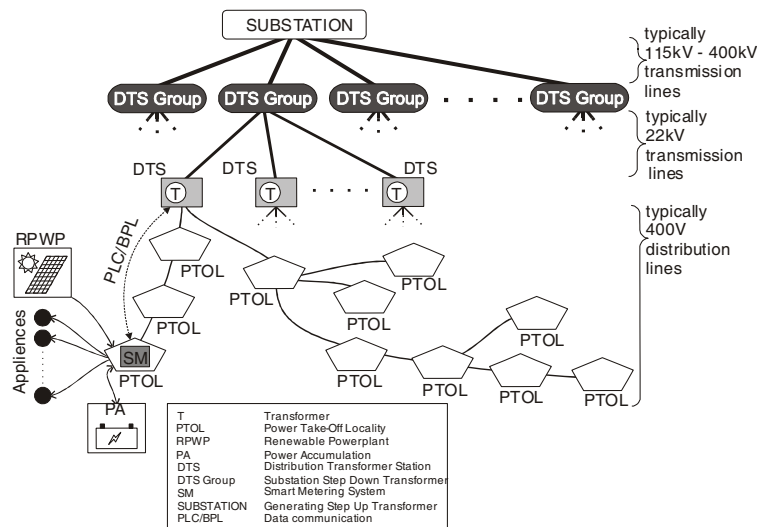


Figure 1: Topology of electrical networks.

energy volume from RES will be greater than consumed power and energy in the existing NN framework [9].

Therefore distributors and producers of electrical energy have to solve the problem where and how to spend so much energy in the framework of the NN network where it was produced or in the all NN networks behind one transformer 22 kV/400 V AC. In emergency case would be still acceptable to spend an surplus of the energy volume in the framework of more than one NN network. The contribution deals with possibilities how to influence energy consumption in NN networks by a smart control combining operator control as well as individual control from OMs. At present only an operator control from a central operator level is realized in so called two tariff system. Authors assumed that individual control of energy consumption in the NN network's framework, combined with still existing two tariff system could be an important mean for stability of electrical grids with RES.

Solution of the problem has several aspects. The first one is a data acquisition and prediction of the possible development of energy loss or energy surplus in the NN network framework behind one DTS 22 kV/400 V. It will depend much on a weather forecast in the area concerned. Second aspect consists in an equipment of any OM, i.e., monitoring and measurement instrumentation to measure OM's own energy consumption [5]. The last aspect consists in creation a motivation mechanism to motivate OMs to cooperate with central operator station to stabilize the NN grid. Authors assume the dynamic tariff of energy will be the most motivation mechanism.

3. SUBJECT OF THE PROBLEM

Contribution deals mostly with technical aspects of the problem of the stability NN grids with important quotient of energy from renewable energy sources. As it was already said, central operator stations as well as OMs have to be equipped by instrumentation for energy monitoring, individual as well as centralized appliances control (switch on-switch off) and by prediction of time development of energy prices.

Such prerequisites to stabilize NN networks is named "smart metering system" and its possible solution named smart-energo system is specified in next chapters.

3.1. Smart Metering and Control System [1, 2]

In the Fig. 2 is shown the complete project conception of the system for monitoring, planning and energy saving with stabilization of a grid with important ratio of renewable energy sources [3, 8]. The concept of the system goes out from the fact that households are equipped mostly by one or three phase electrical installation with one central distributor. There are current protectors and energy meters. Next the electrical installation is split into more light and socket's networks, which are protected by one or three phase protectors. From the electricity meter the electrical installation is user available. The system smart-energo uses two types of energy monitors [6].

The first one is the SM1 (Smart Meter 1) [4] and it makes monitoring of the whole energy consumption of the flat or house (households) or the whole energy consumption of a small energy

consumer (SMS, institutions, offices, etc.). The SM1 is situated at the distributor behind the energy meter and monitors the whole energy consumption in one or three phases. The second element [4] of the system smart-energo is the SM2. It is an element for energy consumption monitoring of an electrical appliance that is connected in one socket. The SM2 can be realized as a special wall socket (with additional measuring sensors, processing electronic and communication interfaces). A communication of SM2 is done by WLS or via power line. In this epoch when households are not totally equipped by internet we decided to realize SM2 in these two options. The SM2 can be realized on demand as a pass-through module or as a special wall socket with embedded SM2 functionality additionally to the standard power functions of the socket.

One new option of the system smart-energo for internet based monitoring (PDA, netbook, notebook, PC, tablet) is its total distribution. That means, data of energy consumption are written in local memories of each SM2s and because of the fact, that SM2s are developed by WIFI interface, data can be observed directly in PDAs, netbooks, notebooks, tablets, PCs in WLS intranet of the households or enterprises, institutions etc. System would enable a distance monitoring by users via internet in a near future. As shown in the Fig. 2, SM1s are equipped by internet interface (Ethernet, GPRS and other interfaces). The world first internet based system which is equipped by such a service is Google energy monitoring system. Users have access to individual user's database with historical data of their individual energy consumption from anywhere.

The recommended PWL (Power Line) option for SM2 (recommended by energy distribution firms for this temporary time period) enables direct translation data from SM2s to the SM1 without WLS (Wireless) interfaces in SM2s via power lines connecting any wall socket for energy purposes. The price for such a solution is not cheaper in general and authors believe on a final solution in the WLS option. The block diagram of the SM2 is described in the Fig. 4.

3.2. SM1 Module for Monitoring of the Whole Energy Consumption of a User

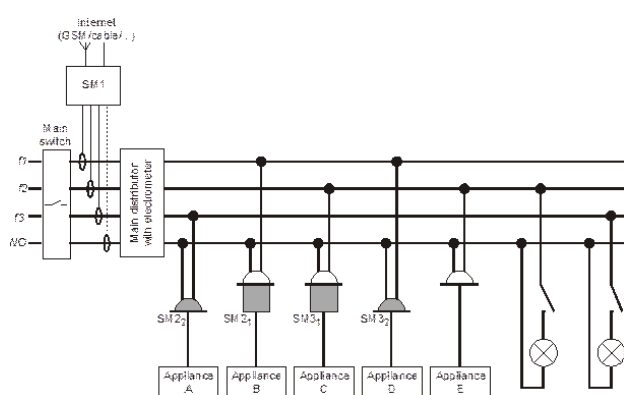


Figure 2: Complete project conception.

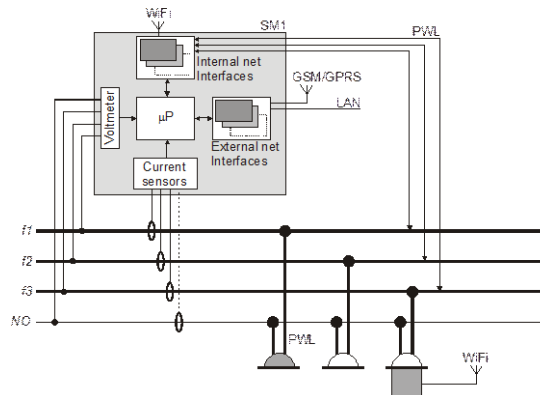


Figure 3: Block diagram of SM1.

This module (Fig. 3) is intended to be situated and installed in energy distributors of households or in central energy distributors of smaller energy consumers. The SM1 is only one device for a consumer. The SM1 will monitor the total energy consumption continuously over the all day, week, and years. Module is supplied directly from a power line. Module SM1 is connected to a power lines directly in the main distributor via current measuring transformer and enables to measure the total current and power of individual smaller energy consumer. The installation of SM1 is as simple as possible to motivate consumers to accept it. System is equipped by a simple display for visual monitoring and indication of the function.

As mentioned above the SM1 will collect data from SM2s and send them to the user or to the database of a provider via internet.

3.3. SM3 Module for Monitoring And Distance Control

The principal block diagram of the module SM3 [4] is in the Fig. 5. This diagram is very similar to the SM2's diagram, but its function is smarter. By means of energy breaker (just in the power socket) the electric current into the socket is switched on and switched off. These actions are controlled by an embedded microcontroller. The SM3 is controlled by individual user (from the central SM1 and/or intranet/internet) and/or central control station of the smart grid system. Communication of the SM3 in the household framework is via WLS and/or PWL and no direct

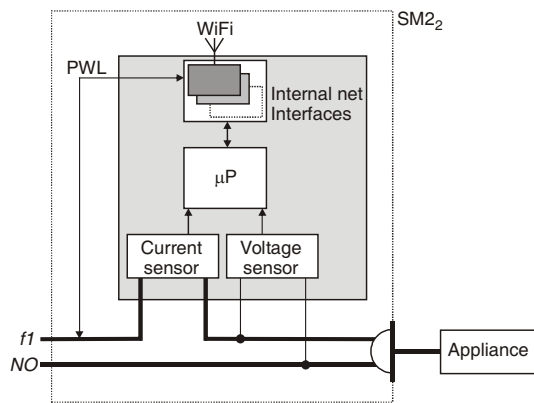


Figure 4: Block diagram of SM2.

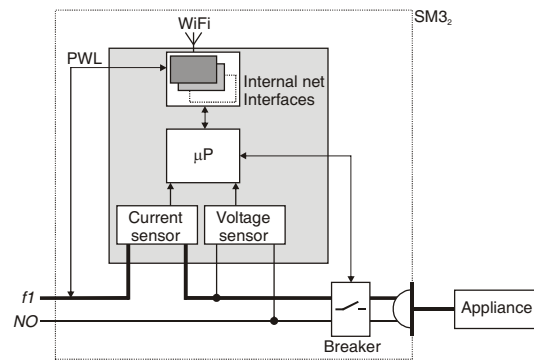


Figure 5: Block diagram of SM3.

connection of SM3 towards central control station of the smart grid and towards direct internet based access of user is planned. The basic higher level communication of the smart-energo system via internet is possible from the SM1 module only.

Thanks to the module SM3 the smart-energo system realizes an important step from a pure smart metering system towards smart-grid functionality. Its future enhancements, an individual user could influence an individual energy consumption according the lower or higher tariff for energy and in the same moment to contribute to the stabilization of the grid with important share (ratio) of renewable energy sources. A new generation of the SM3 should take into account also appliances equipped by an embedded individual control systems which don't enable switching by simple connection/disconnection of the power line in the socket.

4. SW FOR DATA PROCESSING AND CONTROL

The measured data from the SM1 and individual SM2s will be stored in individual data storages of SMs with defined size. Historical data will be stored in the central database of the smart grid/smart metering system for marketing and management as well as for research purposes.

Another important function of the SW will be information about the dynamical tariff of costs for energy. The tariff is proposed to correspond with excess or lack of energy in the smart grids. And the excess or lack of energy should dynamically depend on the weather situation in area of PV and wind farms. The smart-energo system expects to utilize precise weather forecasts from internet sources (Nordic servers and others).

Next generation of the system will be equipped by more sophisticate SW with advisory functions to help users to economize their energy consumption according adaptive and learning algorithms.

5. CONCLUSION

Contribution deals with the idea of NN network stability by a combination of an operator and a lot of individual smart control systems in OMs. The system is intended for NN distribution networks with important deal of RESs. Presented system smart-energo contributes to NN grids stability by means of individual control based on economical behaviour of many small energy consumers. System is modular and enables not only monitoring but will more and more enable an individual control of bigger electrical appliances in households and by smaller energy consumers in order to save money for electrical energy. By proposed dynamical tariff for energy, smart-energo will contribute to a better stabilization of grids with great ratio of renewable energy sources by following mechanism: price for energy unit will dynamically correspond to excess or lack of energy from renewable sources (PV and wind farms).

There are described block diagrams of smart-energo hardware elements SM1, SM2 and SM3 and their functions specification in the contribution, as well as the basic specification of an user's SW. The smart-energo system is conceived to utilize internet weather forecast services to predict an excess or a lack of energy from renewable energy sources to plan strategy for energy consumption by households and by smaller energy consumers.

ACKNOWLEDGMENT

This work was supported by Operational Program Research and Development for Innovations; project CVVOZE — Center for Research and Utilization of Renewable Energy Sources no. of contract CZ.1.05/2.1.00/01.0014 and Brno University of Technology. Part of the work was carried out with the support of core facilities of CEITEC — Central European Institute of Technology under CEITEC — open access project, ID number LM2011020, funded by the Ministry of Education, Youth and Sports of the Czech Republic under the activity “Projects of major infrastructures for research, development and innovations”. This work was supported also by the project “TA02010864 — Research and development of motorized ventilation for the human protection against chemical agents, dust and biological agents” and project “TA03020907-REVYT-Recuperation of the lift loss energy for the lift idle consumption” granted by Technology Agency of the Czech Republic (TA ČR). Part of the work was supported by project “FR-TI4/642-MISE-Employment of Modern Intelligent MEMS Sensors for Buildings Automation and Security” granted by Ministry of Industry and Trade of Czech Republic (MPO).

REFERENCES

1. Zezulka F., O. Sajdl, Z. Bradac, and J. Sembera, “Experimental smart grid,” *Proceedings of 11th IFAC/IEEE International Conference PDES 2012*, Brno, IFAC-PapersOnLine/Elsevier, 2012, ISBN: 978-3-902823-21-2.
2. Veselý, I., F. Zezulka, O. Sajdl, and J. Šembera, “Problems of energy saving in electrical experimental network/ smart grid in advanced batteries accumulators and fuel cells,” *13th ABAF Book of Proceedings*, 1–8, 2012, ISBN: 978-80-214-4610-6.
3. Zezulka, F., O. Sajdl, J. Šembera, and I. Veselý, “System for measurement, prediction and energy save,” *Annals of DAAAM for 2011 & Proceedings*, 1387–1388, Vienna AT, DAAAM International Vienna, TU Wien, 2011, ISBN978-3-901509-73-5.
4. Zezulka, F., Z. Bradac, O. Sajdl, and J. Sembera, “SMART — NERGO,” *System for Measurement, Prediction and Energy Save*, Project proposal in TACR 2012, Brno university of Technology, July 2012.
5. Machacek, Z., R. Slaby, R. Hercik, and J. Koziorek, “Advanced system for consumption meters with recognition of video camera signal,” *Elektronika Ir Elektrotechnika*, Vol. 18, No. 10, 57–60, 2012, ISSN 1392-1215.
6. Kocian, J., M. Tutsch, S. Ozana, and J. Koziorek, “Modeling and simulation of controlled systems and technologies in industrial control,” *Proceedings of the 4th International Conference on Advanced Computer Theory and Engineering, ICACTE 2011*, 213–217, ASME Press, New York, 2011, 859933, ISBN 978-0-7918-5993-3.
7. Tutsch, M., P. Vojcinak, J. Koziorek, and M. Skrepek, “Using automated evaluation of efficiency for photovoltaic power plant,” *In Proceedings of the 16th IEEE Symposium on Emerging Technologies and Factory Automation, ETFA 2011*, 1–4, September 5–9, 2011, Toulouse, France, E-ISBN: 978-1-4577-0016-3, Print ISBN: 978-1-4577-0017-0, ISSN: 1946-0740.
8. Slanina, Z. and V. Srovnal, “Embedded linux scheduler monitoring,” *12th IEEE International Conference on Emerging Technologies and Factory Automation*, 2007, ISBN: 978-1-4244-0826-9.
9. Kocian, J., J. Koziorek, M. Pokorny, “Implementation of fuzzy logic control based on PLC,” *Proceedings of IEEE International Conference on Emerging Technologies and Factory Automation, ETFA 2011*, Paper 2325, 8 pages, Toulouse, France, September 5–9, 2011, ISBN 978-1-4577-0016-3.
10. Koziorek, J. and Z. Slanina, “Control system for the prototype of hydrogen powered car,” *WSEAS Transactions on Systems*, Vol. 4, No. 12, 2454–2459, 2005, ISSN 1109-2777.

Sensor Design and Data Transfer in a Smart Grid

Z. Roubal^{1,3}, P. Marcon^{1,3}, Z. Szabo^{1,3},
O. Saidl^{2,3}, I. Vesely^{2,3}, and F. Zezulka^{2,3}

¹Department of Theoretical and Experimental Electrical Engineering, Brno University of Technology
Technicka 12, Brno 612 00, Czech Republic

²Department of Control and Instrumentation, Brno University of Technology
Technicka 12, Brno 612 00, Czech Republic

³Centre for Research and Utilization of Renewable Energy
Technicka 12, Brno 612 00, Czech Republic

Abstract— This paper discusses the sensing of physical variables used in smart grid power modeling. In the applied distant power sources, we measured the interdependence between physical variables such as lighting (in the photovoltaic power plant) and water level (in the hydroelectric power plant). The data were transferred via a DA4 datalogger, which used the GPRS; the data represented physical variables stored in an SQL database. In our 24V smart grid, the power obtained from a power source was measured. In the hydroelectric power plants was problem with non-harmonic voltage and current generated turbine. The module designed for accurate power measurement included an analog multiplier, and it was powered — together with the datalogger — by a small photovoltaic panel. Functionally, the module was directly connected with a cable to a PC hosting the Compact Rio program. The last of the renewable energy sources utilized was a battery-powered, self-charging wind power plant.

1. INTRODUCTION

The distant power source experiments were performed using an experimental energy network (E.E.N.) formed within the Centre for Research and Utilization of Renewable Energy (CRURE). The obtained energy was measured on the spot, directly or indirectly, and transmitted via a DA4 datalogger and the GPRS to an SQL database. The values accumulated in the database were subsequently processed by CompactRIO and employed during the laboratory simulation. For correct modeling of the performance, we placed sensors in the given locations and measured the power transfer characteristics of the applied renewable sources [1].

2. CONFIGURATION

Small power plants utilizing renewable energy sources are connected to a grid. Some of these plants are shown at the Laboratory of Automation, Brno University of Technology, where the E.E.N. is located. A PV panel and a small wind power plant are situated on the roof of the building; the hydropower plant, however, is located elsewhere for practical reasons. A hydrogen fuel cell will be connected to the smart grid in the nearest future. The electric energy produced by these remote sources is materialized and connected into the E.E.N. by means of RES (Remote Energy Sources) boxes, see the Appendix. Each RES box is controlled by the CompactRIO and LabView control systems according to the information provided by the GPRS wireless data logger situated near the remote source to measure its power P_i .

The resources supplying the E.E.N. are a wind and a water turbines, a fuel cell, solar panels, and possibly other renewable elements (such as a gas turbine). Each of these items supplies approximately 200–500 W peak to the E.E.N. Given the simplicity of the physical realization, the safety experiments, and the low cost, the E.E.N. works with 24 V DC.

The authors are convinced that this simplification is acceptable for most variants of the control algorithm in the smart grid design methodology. In this context, one of the objectives is to develop a strategy for switching and controlling the amount of energy supplied by the varied energy sources. Within the development of such a strategy, it will be necessary to consider consumption fluctuations and stochastic changes in the wind, sunshine, and partly also the water flow. The designed E.E.N. is equipped with a number of batteries for each individual power source; however, the introduction of centralized battery storage is proposed. Although the storage of electric energy in the form of hydrogen does not seem to be a promising approach, a hydrogen fuel cell (FC) (one metal-hydride container as a form of hydrogen storage) will be integrated into the E.E.N. in order to materialize a source of peak energy.

Personal computers physically connected via simple DC/AC converters without the need for strict adherence to the phasing and frequency constituted an important portion (appliance) of the E.E.N. Other appliances so connected to the E.E.N. included heaters, car battery charges, and also electrolyzers (EL) as a backup to store the energy produced by overgeneration. The energy consumption is controlled by the CompactRIO/LabView control systems and the Control Block (CB2), see the Appendix. At this point, the researchers simplified their situation: to switch and control the sources into a common energy grid, the CB2 controls the current (and power) only because the E.E.N. is a DC grid. The authors assume that the optimal control strategy, developed for the DC E.E.N., will be adequate to that commonly developed for a three-phase AC grid, where the resources are connected and synchronized at the same frequency and phasing. The reason for such assumption consists in the fact that the control of each energy source frequency and its proper phasing is a standard question and a standard technical solution of each AC energy source. These features do not correspond with the higher strategic algorithms of distribution, production, consumption, and optimality (the time optimum, and the energy and fuel optimal real time control) of the grids in general. Hence, such strategic algorithms to be developed, simulated, and evaluated in experiments with the E.E.N. will be appropriate for any other smart grid.

3. MONITORING

Two solar panels with the total power of 360 Wp were installed on the roof of the central laboratory building; these devices supply the experimental Smart Grid. The solar panels are manufactured by Solartec, which also delivers the battery charging regulator.

The applied four lead-acid batteries exhibit the total capacity of 120 Ah. They are connected in parallel and provide the total voltage of 12 V when charged. If the solar panel voltage is higher than that of the batteries, the regulator will initiate the charging cycle. The regulator includes overvoltage protection; if the batteries are fully charged, the cycle is terminated. The device is shown in Fig. 1.

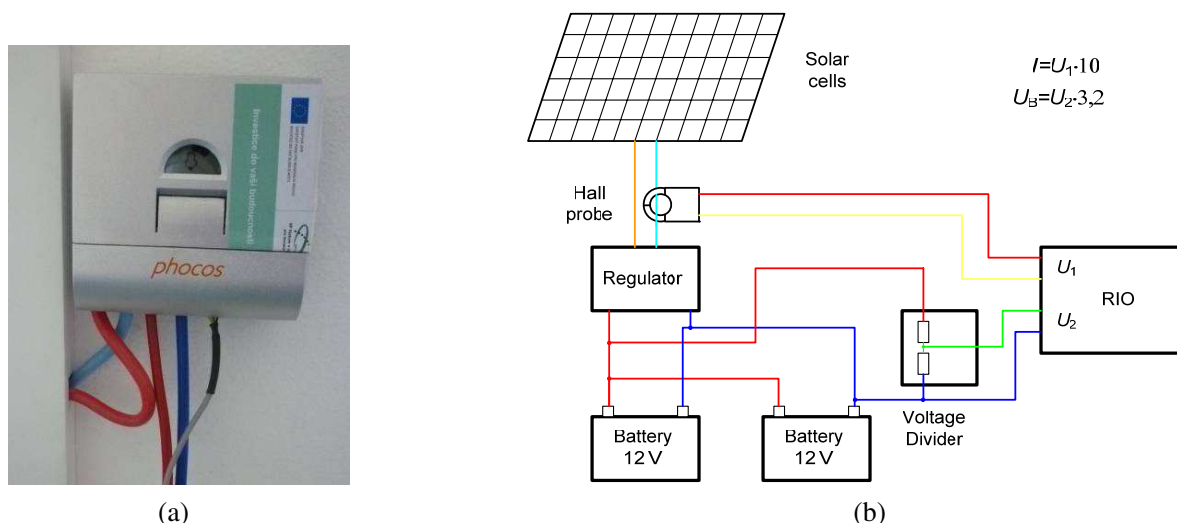


Figure 1: (a) The battery charging regulator of the solar power plant, (b) the solar cell system: power measurement.

Generally, the regulator facilitates the recording of the charging current and battery voltage from the USB interface. However, the value of the current did not correspond to reality, and we had to create a module to measure the current at the input and the voltage at the output of the regulator. The related block diagram is indicated in Fig. 1(b).

In the previous phases of solar cell modeling [2], the solar power plant source and the supplied power values were measured in remote laboratories; in the current system, the power station is connected directly to the grid, and this arrangement enabled us to find the transfer function between the power and the lighting. The solar cells with the applied photometer are shown in Fig. 2.

Figure 3(a) indicates the dependence of both values (LUX Solar) in winter, on the morning of 15 March 2014. The main problem we had to face was the cloudy weather and low angle of the solar rays illuminating the cells. The transfer function is linear, and it is shown in Fig. 3(b).



Figure 2: The solar cells and the (a) photometer and (b) detailed.

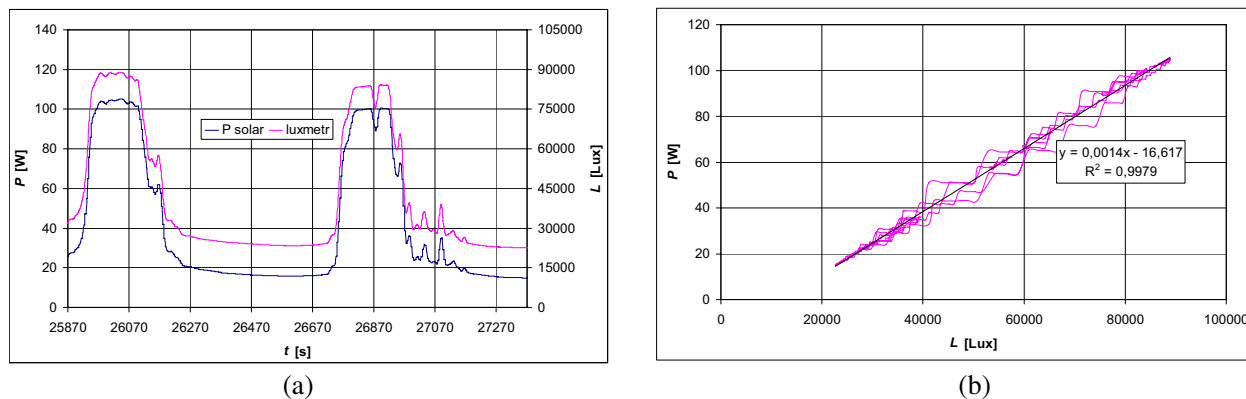


Figure 3: The relationship between (a) the lighting and the power provided by the solar cells lant, (b) the transfer function between solar power and lighting.

4. HYDROPOWER MONITORING

To enable on-line monitoring of the voltage in the battery positioned in the research laboratory, we used a DA4 datalogger placed in a telephone pillar. This datalogger included a SIM card, which sent the data to a CRURE server via the T-Mobile GSM network operator [3]. From this server, the data were resent to the central system server of the provider. This CRURE-based system allowed us to observe the electrical variables in a solar panel. The acquired information was used to simulate the solar panels in the experimental smart grid. We utilized the power supply of 80 V/50 A controlled through Labview. In the measuring intervals, we established the water level and the voltage of the datalogger supplied from a small solar panel. Thus, it was possible to model the behavior of a solar panel in the smart grid. The selected time interval was chosen as a compromise between the real (simulated) hydropower plant and the cost of the data transfer. The sensing of this variable was realized by means of an auxiliary CIO unit with 10 V analog voltage inputs.

Figure 4 shows the general structure of the hydropower plant. The main part of the station is a hydroelectric turbine, which generates energy in the form of an electric field. The energy produced by the turbine is fed to a regulator, which should keep the harmonic network voltage at 230 V and maintain the frequency of 50 Hz. It is possible to connect a load (and also a charger) to the

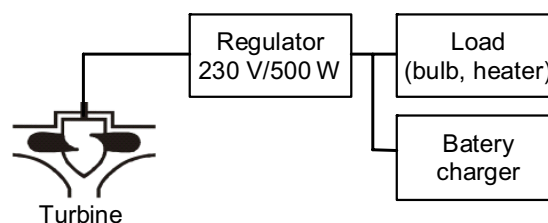


Figure 4: A block diagram of the hydroelectric unit.

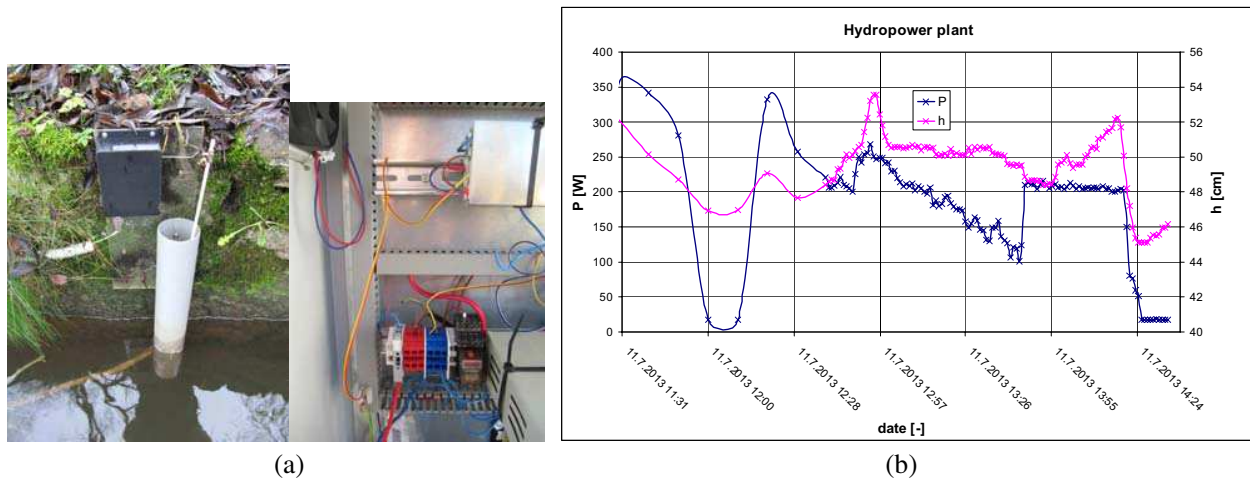


Figure 5: (a) The water level sensors and the measurement module and (b) the three-hour record turbine output power.

output of the regulator. The function of the charger is to charge the 12 V battery of the datalogger transmitting to an SQL server the data related to the water level and the current output power value.

The measurement was performed at the small hydroelectric station. Our aim was to determine the conversion characteristics between the water level in the weir and the corresponding actual output power. The switchboard cabinet comprising the hydropower plant regulator and a load was completed with a water level measuring module, a power meter, and a voltmeter for the non-harmonic waveform. Fig. 6 right shows the three-hour record of the turbine output power; the decrease power is depend leaves and water turbulence.

5. CONCLUSIONS

The paper presents the output power characteristics of a photovoltaic and a hydroelectric power plants; these characteristics can be suitably utilized in the modeling of an E.E.N.. The power units can be connected directly to the grid loads via a regulator; alternatively, the energy can be stored in batteries. Data loggers are located in the stations to transmit the measured output power data to an SQL server. In the future, the data could be used to support the entire process of modeling the E.E.N. functions.

ACKNOWLEDGMENT

This research work has been carried out in the Centre for Research and Utilization of Renewable Energy (CVVOZE). Authors gratefully acknowledge financial support from the Ministry of Education, Youth and Sports of the Czech Republic under NPU I programme (project No. LO1210).

REFERENCES

1. Hidayatullah, N. A., B. Stojcevski, and A. Kalam, "Analysis of distributed generation systems," *Technologies and Future Motivators Influencing Change in Electricity Sector, Smart Grid and Renewable Energy*, Vol. 1, 216–229, 2011.
2. Zzulka, F., Z. Bradac, Z. Szabo, Z. Roubal, and P. Marcon, "Design and functional description of an experimental smart grid," *Proceedings of International Conference Engineering, Technologies and System, TECHSYS*, Technical University of Sofia, Bulgaria, 2013.
3. Vesely, I., F. Zzulka, J. Sembera, and Sajdl, "Problems of energy saving in electrical experimental network/smart grid," *13th ABAF Book of Proceedings Advanced Batteries Accumulators and Fuel Cells*, 1–8, 2012.

Low-complexity Design of an 8×8 Modulation Configurable K -best MIMO Detector

Muh-Tian Shiue and Syu-Siang Long

Department of Electrical Engineering, National Central University, Zhongli 32001, Taiwan

Abstract— In this paper, a low complexity 8×8 MIMO detector supporting QPSK, 16-QAM, and 64-QAM is presented. A breadth-first type known as distributed K -best (DKB) algorithm is applied in the design. Compared with the conventional K -best algorithm, the DKB reduces the number of visited nodes at each layer from $K\sqrt{M}$ to $2K - 1$, where K and M are the quantity of candidates and constellation size, respectively. To further reduce power consumption, a shift multiplier which simply operates bits shifting and additions is proposed to replace the conventional multiplier. In addition, the proposed multi-stage circuit architecture only requires K clock cycles to find the best K candidates, and the sorting circuits for the conventional K -best can be avoided in our design. The proposed 8×8 MIMO detector has been implemented by a 90-nm CMOS technology with a core area of $0.99 \times 0.99 \text{ mm}^2$. The average power consumption is about 17.2 mW at 74 MHz and 1 V supply voltage.

1. INTRODUCTION

Multiple-input multiple-output (MIMO) technologies have become a trend in the recent communication standards to enhance the channel capacity and signal reliability. From standpoint of improving bandwidth efficiency, *Spatial multiplexing* is the most studied MIMO technique, which can effectively increase the data throughput within a limited bandwidth. Let us consider a spatial multiplexing MIMO system with N_t transmitter antenna and N_r receiver antenna. The real-valued baseband equivalent model can be written as:

$$\mathbf{Y} = \mathbf{H}\mathbf{s} + \mathbf{n}. \quad (1)$$

In (1), $\mathbf{s} = [\Re\{s_1 s_2 \dots s_{N_t}\} \Im\{s_1 s_2 \dots s_{N_t}\}]^T$ is the transmitted symbol vector. For each element s_i is independently chosen from M -QAM constellation set Ω and transmitted by i th antenna, where $\Re\{\cdot\}$, $\Im\{\cdot\}$ and $[\cdot]^T$ imply taking real and imaginary part of a signal and transposing of a matrix; $\mathbf{Y} = [\Re\{y_1 y_2 \dots y_{N_r}\} \Im\{y_1 y_2 \dots y_{N_r}\}]^T$ is the received symbol vector by N_r antennas; \mathbf{H} denotes the real-valued channel matrix of size $2N_r \times 2N_t$, whose entries are identically independent distributed (i.i.d) zero-mean Gaussian random variables; and $\mathbf{n} = [n_1 n_2 \dots n_{2N_r}]^T$ is a white Gaussian noise vector with variance $\frac{\sigma^2}{2}$. The optimum solution for (1) is called maximum-likelihood (ML) decoding, which finds out the most likely symbol vector $\hat{\mathbf{s}}$ according to minimum-distance criterion as follows:

$$\hat{\mathbf{s}} = \arg \min_{\mathbf{s} \in \Omega^{2N_t}} \|\mathbf{Y} - \mathbf{H}\mathbf{s}\|^2. \quad (2)$$

The ML decoder should exhaustively compute \sqrt{M}^{2N_t} possible symbol vectors to determine one $\hat{\mathbf{s}}$. Its complexity grows exponentially with the number of antenna and constellation order. Thus, such ML decoder is not feasible for hardware implementation.

Consequently, some simplified recursive searching algorithms have been developed for practical realization. According to the searching direction, these approaches can be classified into two categories, the *depth-first* type and *breadth-first* type [1]. Compared with depth-first algorithm, K -best belonged to the breadth-first algorithm is suitable for a high throughput MIMO detector design. Because K -best owns forward tree-searching path and regular path pruning rule, it can be implemented in a paralleled pipelined fashion. Several researches have investigated the MIMO detection based on K -best algorithm [1–4]. However, most of these published studies only provide 4×4 antenna configuration and cannot support multiple modulation schemes.

To transforming ML decoding into tree-branch searching, thanks to QR decomposition, i.e., $\mathbf{H} = \mathbf{Q}\mathbf{R}$, where \mathbf{R} and \mathbf{Q} are upper triangle matrix and unitary matrices, respectively. By applying \mathbf{Q}^H at both left and right sides of (1), results in $\hat{\mathbf{Y}} = \mathbf{Q}^H\mathbf{Y} = \mathbf{R}\mathbf{s} + \mathbf{Q}^H\mathbf{n} = \mathbf{R}\mathbf{s} + \mathbf{w}$.

Since \mathbf{R} is an upper triangular matrix, (2) can be re written in recursive form by above formula:

$$\hat{\mathbf{s}} = \arg \min_{\mathbf{s} \in \Omega^{2N_t}} \sum_{i=1}^{2N_r} \underbrace{\left| \tilde{y}_i - \sum_{j=i}^{2N_t} R_{ij} s_j \right|^2}_{i\text{th layer PED: } e_i(\mathbf{s}^{(i)})} . \quad (3)$$

The tree-searching process starts from layer- $2N_t$ down to layer-1 and calculates accumulated *partial Euclidean distance* (PED): $T_i(\mathbf{s}^{(i)}) = T_{i+1}(\mathbf{s}^{(i+1)}) + e_i(\mathbf{s}^{(i)})$ at i th layer to find the best path which owns minimum PED in (3).

The conventional K -best scheme can concurrently expand and sort the children nodes to find the candidates. However, the best K candidates of DKB scheme are one by one sequentially listed in \mathbf{K}_i within K clock cycles. Owing to this feature, the DKB can avoid the complicated sorting circuit and only requires a minimum finder circuit to select the child in \mathbf{L}_i which has minimum PED. It should be noted that the number of visited nodes at each layer is $2K - 1$, which is independent of the constellation size M . Therefore, the DKB is more suitable to apply to expand to high-order constellation modulations. The total number of visited nodes for DKB is $\sqrt{M} + (2N_t - 1)(2K - 1)$. Compared to the conventional K -best algorithm, the DKB scheme is a efficient procedure to choose the best K candidates.

In this paper, the 8×8 MIMO detector which can flexibly support various modulation schemes, such as QPSK, 16-QAM and 64-QAM, is presented. Besides, the proposed detector also supports unequal modulation, i.e., different spatial streams can apply unequal modulation schemes. In our design, we adopt a modified K -best algorithm with lower computational complexity to save power consumption. In addition, a novel shift multiplier (SM) is proposed to simplify the multiplication complexity.

2. ARCHITECTURE AND CIRCUIT DESIGN

The architecture of the proposed multi-stage 8×8 MIMO detector is depicted in Fig. 1. The DKB building block consists of a *first child unit* (FCU), a *next child unit* (NCU) and register banks. The register banks are used to store the PEDs, the contender list \mathbf{L}_i and the K -best candidate list \mathbf{K}_i at i -th layer. According to the K -best candidates result \mathbf{K}_{i+1} from the previous layer, in the first, the FCU finds out the corresponding K FCs and stores them into the contender register. Their PEDs are also stored into the PED register. As all the K PEDs have been computed by the FCU, the NCU will find the minimum PED index and select the corresponding FC into the K -best candidate register \mathbf{K}_i . Meanwhile, the NCU enumerates its best sibling node as the next child (NC). Then the selected FC in contender register \mathbf{L}_i is replaced by this NC and the PED register is also updated with this NC PED. In each cycle, the FCU and NCU can determine one FC and NC, respectively. Therefore, each DKB stage completes the best K candidates and delivers them to the next pipelined stage within K clock cycles. An advantage of this DKB pipeline architecture is that the K -value can be configured flexibly due to its regular hardware manner.

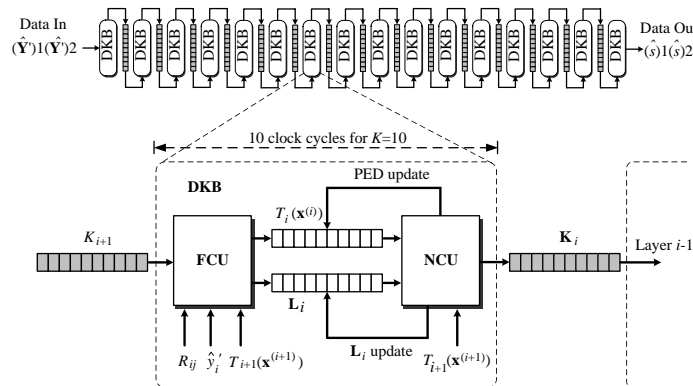


Figure 1: Circuit architecture of the proposed multi-stage 8×8 MIMO detector.

2.1. Shift Multiplier

From (3), it can be seen that the multiplication of R_{ij} and s_j play the most complicated roles in the PED computation. In order to simplify the multiplication complexity, we propose a *shift multiplier* (SM) approach which can reduce the area and critical path delay of the multiplication significantly. In convention, $s_j \in \Omega = \{-\sqrt{M} + 1, \dots, -1, 1, \dots, \sqrt{M} + 1\}$ is an odd number set in the real-valued axis, and $R_{ij}s_j$ requires a real multiplier. The SM approach uses a new signal set $\Omega' = \{-\sqrt{M}, \dots, -2, 0, \dots, \sqrt{M}\}$ instead of Ω by left shifting the original axis by one. The new signal set Ω' is represented in Fig. 2(a). In the case of 16-QAM, each value of new signal set is power of two, i.e., $\Omega' = \{-4, -2, 0, 4\}$.

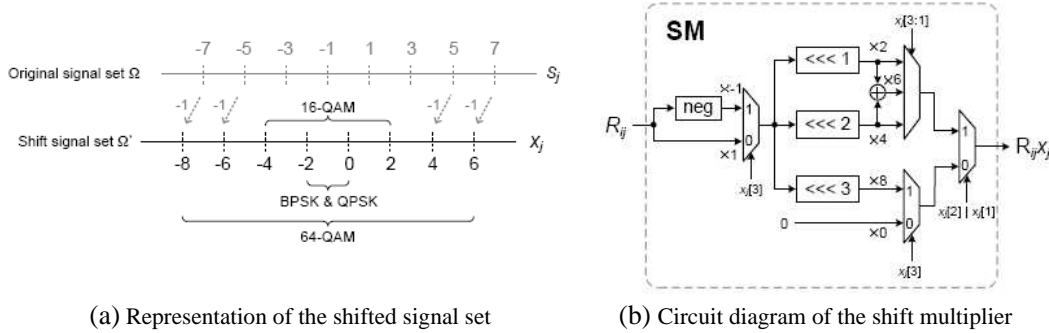


Figure 2: (a) Representation of the shifted axis. (b) Hardware implementation of the shift multiplier.

Therefore, R_{ij} multiplied by the shifted signal can be implemented by the proposed SM circuit. The received signal vector $\hat{\mathbf{Y}}$ can be represented by:

$$\hat{\mathbf{Y}} = \mathbf{R}(\mathbf{s} - \mathbf{e}) + \mathbf{R}\mathbf{e} + \mathbf{w}, \quad (4)$$

where $\mathbf{e} = [1 \ 1 \ \dots \ 1]^T$ is a $2N_t \times 1$ all one vector. Let $\mathbf{x} = \mathbf{s} - \mathbf{e}$ be the new shifted signal vector in set Ω' . Then (4) can be rewritten as:

$$\hat{\mathbf{Y}}' = \hat{\mathbf{Y}} - \mathbf{R}\mathbf{e} = \mathbf{R}\mathbf{x} + \mathbf{w}. \quad (5)$$

The decoding process of (5) is identical to the (2) except the new shifted signal \mathbf{x} and the new received vector $\hat{\mathbf{Y}}'$

Since our design supports multiple modulation schemes from QPSK to 64-QAM, the new maximum range of signal set $x_j \in \Omega' = \{-8, -6, -4, -2, 0, 2, 4\}$ should be considered. R_{ij} multiplied by values $(\pm 2, \pm 4, 8)$ is realized by only shift operation. The computation of $\pm 6R_{ij}$ can also be easily implemented by $(\pm 2R_{ij}, \pm 4R_{ij})$ with summation. The block diagram of the proposed SM circuit is depicted in Fig. 2(b). The “neg” block denotes the sign inversion operation.

2.2. FCU and Configurable NCU

For each parent node in \mathbf{K}_{i+1} , the FCU of the i -th layer is used to find the FC with the smallest PED. Eq. (3) shows that the FC of a parent node in \mathbf{K}_{i+1} is the one which has the minimum distance increment $|e_i(\mathbf{x}^{(i)})|^2$, i.e.,

$$x_{i,\text{FC}} = \arg \min_{x_i \in \Omega'} \left| \underbrace{\hat{y}'_i - \sum_{j=i+1}^{2N_i} R_{ij}x_j - R_{ii}x_i}_{\text{center } C_i(\mathbf{x}^{(i)})} \right|^2, \quad (6)$$

where $C_i(\mathbf{x}^{(i)})$ is referred to as *center*. Thus the FC can be found by quantizing $C_i(\mathbf{x}^{(i)})/R_{ii}$ to the nearest constellation signal in Ω' .

When the FC is decided, the NC that belongs the same parent node can be enumerated based on zigzag principle. The zigzag operation of 1D SE-enumeration for 16-QAM is given in Fig. 3(a).

The l -th enumeration of NC can be expressed as follow:

$$\begin{aligned} \text{NC}(l+1) &= \text{NC}(l) + d(l) \times \mu(l) \\ \mu(l+1) &= \mu(l) + 2 \\ d(l+1) &= \begin{cases} -d(l), & \text{if BoundFlag} = 0 \\ d(l), & \text{if BoundFlag} = 1, \end{cases} \end{aligned} \quad (7)$$

where l starts at zero and $\text{NC}(0)=\text{FC}$; $d(l)$ denotes right or left enumerative direction, and $d(0) = +1$ or -1 depends on the center falling on right or left side of the FC; μ is the enumerative step-size and $\mu(0) = 2$. The step-size is accumulated by two after each enumeration. Since there are K FC candidates that may enumerate their NCs, we need to record three current statuses of the K NCs for the next enumeration. The three status are enumeration direction, step-size and NC value. The enumeration circuit diagrams are shown in Fig. 3(b). In each clock cycle, the step-size with “MinIdx” is accumulated by two and change direction by multiplying (± 1). The the MinIdx -th NC can be enumerated according to (7).

2.3. Chip Implementation and Comparison

The proposed 8×8 MIMO detector is implemented in 90-nm CMOS technology. The core area of this chip is $0.99 \times 0.99 \text{ mm}^2$ and the power consumption is 17.2 mW operating at 74 MHz and 1 V supply voltage. The throughput of this design is given by $\Phi = (N_t \log_2 M) f_{\text{clk}} / K$, where f_{clk} is the clock frequency. Since our design supports two K -value configurations, i.e., $K = 5, 10$, this

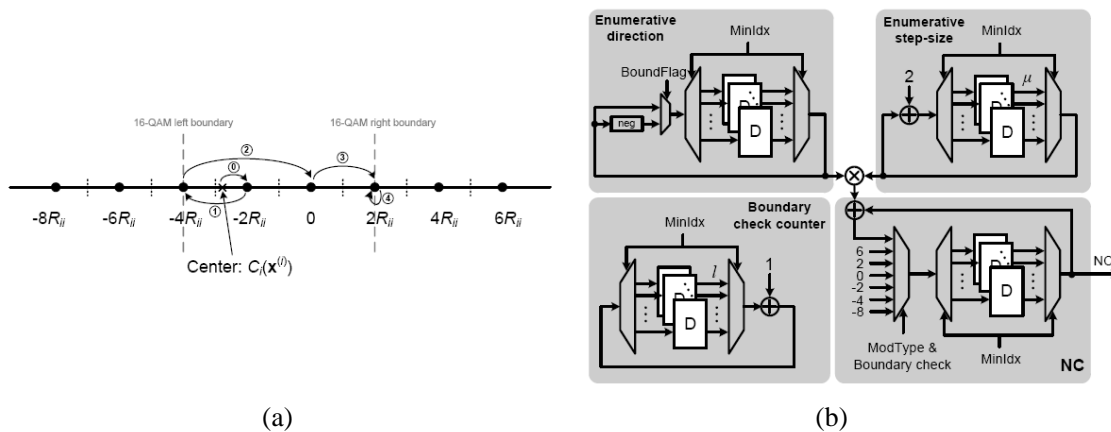


Figure 3: (a)Representation of the 1D SE-enumeration for 16-QAM. (b) Circuit diagram of the configurable NC enumeration.

Table 1: Chip comparison of the MIMO detectors.

Reference design	JSAC' 06 [1] IC1	JSSC' 05 [6]	TVLSI 07 [4]	ISSCC' 09 [7]	JSSC' 10 [8]	This work	
Antenna	4×4	4×4	4×4	4×4	$N_t = 2 - 8$ $N_r = 2 - 8$	8×8	
Modulation	16-QAM	16-QAM	64-QAM	64-QAM	QPSK 16-QAM 64-QAM	QPSK 16-QAM 64-QAM	
Algorithm	K-best	Depth-first	K-best	DKB	MBF-FD	DKB	
Model (Real/Complex)	Real	Complex	Complex	Real	Complex	Real	
Output type	Hard	Hard	Soft	Hard	Soft	Hard	
Technology	0.35 μm	0.25 μm	0.13 μm	0.13 μm	0.13 μm	0.09 μm	
Gate count	91 K	117 K	280 K	114 K	350 K	323 K	
Area (mm^2)	5.76	N/A	2.38	2.31	1.77	0.98	
Max. clock rate	100 MHz	51 MHz	270 MHz	282 MHz	198 MHz	74 MHz	
Max. throughput (Mbps)	53.5	73.5	8.57	675	429 (88, 64-QAM)	$K=5$ 710	$K=10$ 355
Power (mW)	626	360	94	135	74.8	17.15	17.2
Normalized power (pJ/bit)	384 (7.28%)	282 (5.35%)	5273 (100%)	82 (1.55%)	71 (1.35%)	24 (0.46%)	49 (0.92%)

chip can provide a maximum throughput at 710 Mbps. Table 1 lists the performance comparison between this chip and other MIMO detector ICs. To eliminate the process factor, the normalized power is formulated as

$$P_{\text{norm}} = \text{power} \times \left(\frac{1.0}{V_{\text{dd}}} \right) \times \left(\frac{0.09}{\text{Tech}} \right) \times \left(\frac{1}{\text{Throughput}} \right).$$

From Table 1, our design consumes less power and has high power efficiency than other listed ICs.

3. CONCLUSION

In this paper, we have presented a low-complexity design of 8×8 modulation configurable MIMO detector. From the algorithmic aspect, the DKB scheme provides efficient candidate searching procedure. In terms of hardware design, the new signal set Ω' allows the SM to replace the conventional complicated multiplier. Furthermore, multiple modulation schemes from QPSK to 64-QAM are flexibly supported in our design. This chip is implemented in 90-nm CMOS technology and achieve significant improvement in power consumption by low complexity hardware design.

ACKNOWLEDGMENT

The authors would like to thank Chip Implementation Center of National Applied Research Laboratories (CIC/NARL) for providing chip design service. This work was supported by Ministry of Science and Technology, Taiwan, under Grant 103-2220-E-008-004.

REFERENCES

1. Guo, Z. and P. Nilsson, "Algorithm and implementation of the K -best sphere decoding for MIMO detection," *IEEE J. SEL. AREAS COMMUN.*, Vol. 24, No. 3, 491–503, 2006.
2. Wenk, M., M. Zellweger, A. Burg, N. Felber, and W. Fichtner, " K -best MIMO detection VLSI architectures achieving up to 424 Mbps," *Proc. of ISCAS*, 1151–1154, 2006.
3. Shabany, M. and P. G. Gulak, "Scalable VLSI architecture for K -best lattice decoders," *Proc. of ISCAS*, 940–943, 2008.
4. Chen, S., T. Zhang, and Y. Xin, "Relaxed K -best MIMO signal detector design and VLSI implementation," *IEEE Trans. on Very Large Scale Integr. (VLSI) system*, Vol. 15, No. 3, 328–337, Mar. 2007.
5. Shabany, M., K. Su, and P. G. Gulak, "A pipelined scalable high-throughput implementation of a near-ML K -best complex lattice decoders," *Proc. of ICASSP*, 3173–3176, 2008.
6. Burg, A., M. Borgmann, M. Wenk, M. Zellweger, W. Fichtner, and H. Bolcskei, "VLSI implementation of MIMO detection using the sphere decoding algorithm," *IEEE J. Solid-State Circuits*, Vol. 40, 1566–1577, 2005.
7. Shabany, M. and P. G. Gulak, "A 0.13 μm CMOS 655 Mb/s 4×4 64-QAM K -best MIMO detector," *Proc. of IEEE Int. Solid-State Circuits Conf. (ISSCC)*, 256–257, 2009.
8. Liao, C.-H., T.-P. Wang, and T.-D. Chiueh, "A 74.8 mW soft-output detector IC for 8×8 spatial-multiplexing MIMO communications," *IEEE J. Solid-State Circuits*, Vol. 45, No. 2, 411–421, 2010.

Analysis and Construction of Static Inverter with Multi-windings Transformer for High Power Voltage Source

J. M. Grochowalski and Z. Frąckiewicz

Faculty of Electrical Engineering, West Pomeranian University of Technology, Szczecin, Poland

Abstract— High power static voltage inverters found their application in a power conversion for isolated power grids, especially in the shipbuilding and the maritime industry. Most of the problems related to the design of such inverters are that very often nominal power of such devices is comparable to nominal power of its load. In this contribution a design of such voltage source, its computer simulations and experimental results are shown.

1. INTRODUCTION

Ships and shipping industry is a big part of global economy. Without shipping international trade, import/export of raw materials or goods would be not possible. Global trade has permitted a variety of resources to be widely accessible.

At December 2010 world fleet of propelled sea-going merchant ships of no less than 100 GT includes 104 304 ships with an average age of 22 years and cargo carrying fleet in 2011 is 55 138 ships of an average age 19 years [1].

For shipyards or ports located in the city area it is important to reduce the impact of the activity of such facilities on the local community. To reduce pollution and noise generated by an on board generators or in case of technical reasons (vessel is under a maintenance in shipyard, and it cannot use its own on board power generator) shipyards or ports owners can install an on-shore power supply [2].

Additionally this solution gives economical savings — power from the local electrical network is cheaper than generated by diesel generators, particularly when the oil prices continuously growth.

The problem arises, when the ship's electrical network standard is different from the local electrical grid — it cannot only be used transformers to change voltage level, but it also it is needed to change the frequency.

To do this a converter is necessary, which transforms electrical energy from local network to the required by the ship network. One type of converters is the power inverter, which is a power electronics device that converts energy from local grid to the ship's electrical network.

2. REQUIREMENTS FOR THE VESSEL'S ELECTRICAL POWER SUPPLY

A voltage source which is used to supply ship's internal electrical network need to meet specific characteristic imposed by the country of registration of the vessel laws. This regulations describes minimal requirements for the electrical generators, if it should be used as a power supply for ship's electrical network. This requirements also relates to an auxiliary power supply such as the on-shore power supply.

Vessels, according to its type, registered in Poland has to follow rules presented in the *Rules for the Classification and Construction of Sea-going Ships, Rules for the Classification and Construction of Small Sea-going Ships, Rules for the Classification and Construction of High Speed Craft or Rules for the Classification and Construction of Inland Waterways Vessels* of the *Polski Rejestr Statków*.

Requirements for main source of electric power for Sea-going Ships are presented in Part *VIII. Electrical Installations and Control Systems*. Table 1 shows main requirements for ship's electrical power supply [3].

As it is stated above there are two main problems associated with the design of electrical power supply — maintain voltage in specific range with low voltage deviation (low harmonics distortion) and withstand overload and short-circuit currents. This has to be kept in mind while designing such devices.

3. HIGH POWER VOLTAGE SOURCE SYSTEM

The voltage source proposed in this paper consist of two main parts: a Voltage Source Inverter (VSI) controlled by a microcontroller and a multi-winding transformer. A block diagram of this device is shown in Figure 1.

Table 1: Main requirements for ship’s electrical power supply (A.C. system).

No.	Type of Requirement	Overview of Requirement
1	Overcurrent	A.C. system — 50% for 120 s Withstand three-fold rated current for 2 s
2	Short Circuit	Peak value of short-circuit current less than fifteen-fold rated current
3	Voltage Changes	Voltage in maintained within $\pm 3.5\%$ at rated load
4	Voltage in Load Changes	85%–120% of the nominal voltage for maximum 1.5 s
5	Voltage Deviation	Less than 5% — voltage instantaneous value to the first harmonic:

The multi-winding transformer is a three phase transformer with the one winding with N turns of coil per phase on the primary side and the two windings with N_1 and N_2 turns of coil per phase on the secondary side. The schematic of the transformer is shown in Figure 2.

The main elements of the Voltage Source Inverter (VSI) are switching devices. For small to medium power systems (up to 100 kVA) it is possible to use IGBT modules. With high working frequency (about 10 kHz) and output filters it is easy to generate sufficient output voltage with very low distortions [4].

The problem arises for high power systems (over 1 000 kVA). In that case none transistors can be used. Instead thyristors are used. Working frequency is lower — about 1 kHz and less for higher powers.

The Voltage Source Inverter (VSI) presented in this paper is a three phase inverter with thyristors as a switching device [5]. The output phase voltage is a square wave, with working frequency 50 Hz and conducting angle between 120 to 180 degrees. Figure 3 shows an example of VSI output phase voltage.

With low working frequency of the VSI the transformer parameters like number of turns of the coil in secondary windings and connections of those windings was optimized to minimize the Voltage Deviation and the Total Harmonic Distortion (THD) in output voltage. The Voltage Deviation mentioned in the part 2 of this contribution is measured according to this equation:

$$u_w = \frac{\Delta U_m}{\sqrt{2}U_1} \cdot 100\% \tag{1}$$

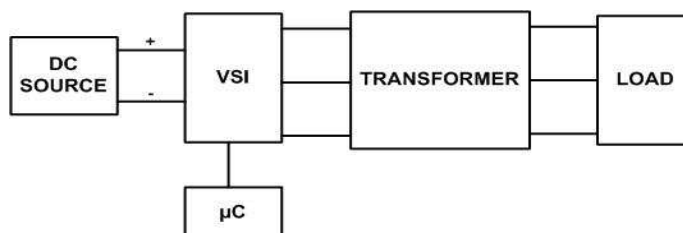


Figure 1: Block diagram of the proposed high power voltage source.

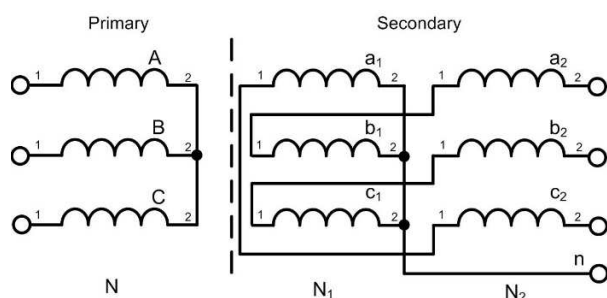


Figure 2: Schematic of the multi-winding transformer.

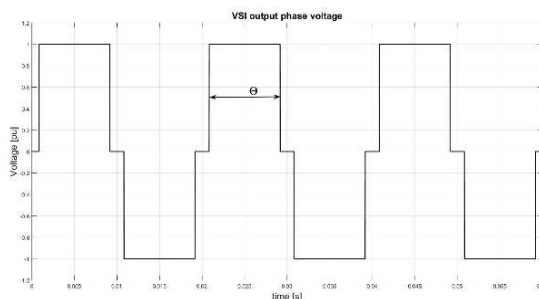


Figure 3: The VSI output phase voltage. Frequency $f = 50$ Hz, conducting angle $\Theta = 150^\circ$.

where:

ΔU_m — the maximum value of the distorted voltage,
 U_1 — the first harmonic effective value of voltage,
 and THD according to this equation:

$$K = \frac{1}{U_N} \sqrt{\sum_{v=2}^n U_v^2} \cdot 100\% \quad (2)$$

where:

U_N — effective value of the network voltage (RMS),
 U_v — effective value of voltage of v -number harmonic,
 n — number of higher harmonic.

4. COMPUTER SIMULATIONS

The proposed High Power Voltage Source with multiple configurations of the transformer was simulated in MATLAB. Additionally it was optimized for the minimal THD and minimal Voltage Distortion in the output voltage in MATLAB. All simulations was made with this parameters:

- High Power Voltage Source VSI — 3-phase, output frequency 50 Hz, square wave, output phase voltage 230 V (RMS), variable conducting angle,
- High Power Voltage Source Transformer — 3-phase, power $S_N = 1\,000$ kVA, input/output phase voltage 230 V/230 V (RMS), $U_K = 6\%$, $I_{0\%} = 1.3\%$, $P_0 = 2\,000$ W, $P_N = 10\,500$ W, variable N_1 and N_2 ,
- Load — 3-phase, resistive, 750 kW.

Figure 4 shows output voltage waveforms for different transformer configuration (primary winding connected in a wye and delta) with a first harmonic compound and calculated parameters (THD, Voltage Deviation, etc.).

5. EXPERIMENTAL RESULTS

The experimental system was build and tested according to simulation results. It consisted of a DC voltage source, a VSI controlled by microcontroller (ARM7) and an output multi-winding

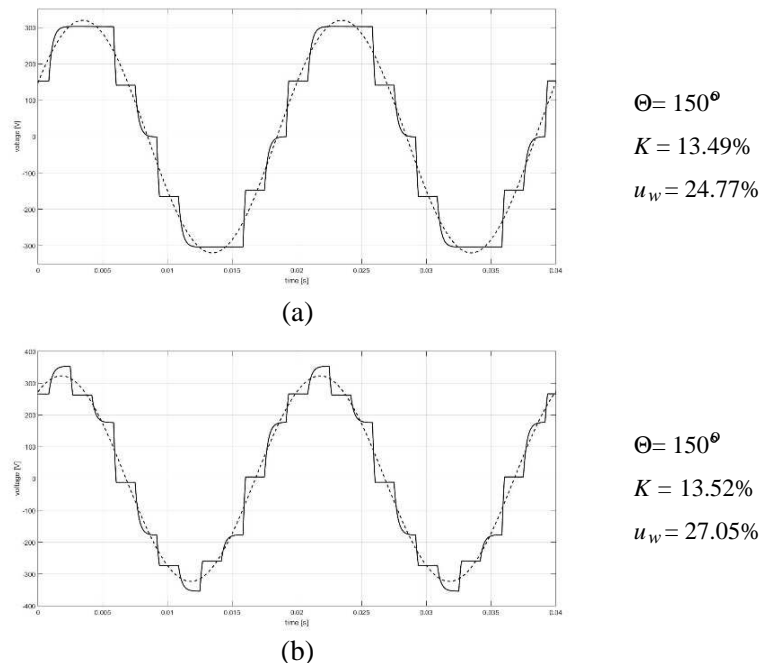


Figure 4: The output voltage waveform (solid) and first harmonic (dashed) for different configurations of the transformer: (a) primary winding connected in wye, (b) primary winding connected in delta.

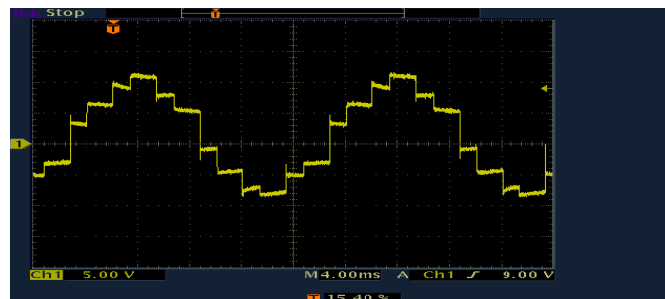


Figure 5: The photo of the experimental setup.



(a)

$\Theta=150^\circ$
 $K=19.46\%$
 $u_w=42.56\%$



(b)

$\Theta=150^\circ$
 $K=19.24\%$
 $u_w=45.37\%$

Figure 6: The output voltage waveform on the load for different configurations of transformer: (a) primary winding connected in wye, (b) primary winding connected in delta.

transformer. A load was wye connected three resistors. Figure 5 shows photo of the experimental setup and the Figure 6 phase voltage across the load.

The differences between the simulation and experimental results are mainly caused by a simplification in the theoretical model used in simulations (i.e., excluding a non-linearity of the transformer, ideal switching devices and a non-inductive load).

6. CONCLUSION

A concept of the high power static voltage source, which could be used as an external power source for ship's internal electrical network, was proposed in this contribution. After theoretical study, computer simulations and optimization, experimental model was created. In particular, the properties of the system in frequency domain were studied in order to minimize THD and Voltage Distortion level.

It is our opinion that the concept proposed is promising and we expect in the future to get further improvements, despite the actual system did not meet successfully all imposed by the law requirements.

REFERENCES

1. International Shipping Facts and Figures — Information Resources on Trade, Safety, Security, Environment, Maritime Knowledge Centre, Mar. 2, 2012, <http://www.imo.org/>.
2. “An effective solution for port emissions reduction,” ABB webpage, <http://www.abb.com/>.
3. “Rules for classification and construction of sea-going ships. Part VIII, Electrical installations and control systems,” Polski Rejestr Statków, Apr. 2015.
4. Lettl, J. and R. Dolecek, “EMC increasing of PWM rectifier in comparison with classical rectifier,” *Radioengineering*, Vol. 17, No. 4, Dec. 2008.
5. Frąckowiak, L., *Energoelektronika, Część 2*, Wydawnictwo Politechniki Poznańskiej, Poznań, 2000 r.

Modelling and Analysis of an Electro-optical System with an Off-quadrature Biased Modulator

D. M. S. Morais¹, J. Panasiewicz^{1,2}, and G. M. Pacheco¹

¹Aeronautics Technical Institute, Brazil

²National Institute for Space Research, Brazil

Abstract— This paper describes the behavior of a microwave external modulation link composed of: optical and radio frequency sources, Mach-Zehnder modulator (MZ), optical fiber and photodetector. The electro-optical circuit modulates the RF signals and transmits them to the detector through the optical fiber. The main contribution of this paper lies on the different approach to the system analysis; we consider an off-quadrature biased MZM.

By extending the mathematical model found in the literature for the case of different bias voltages, we compute a few performance parameters of the system like Gain and SFDR. For computing those parameters we use a custom made program written in the MATLAB environment.

In addition to the system's characterization and insights on its off-quadrature operation, another contribution of this article is the model validation. We assembled the electro-optical circuit and measured some performance parameters for different values of bias voltages. By comparing the experimental results with the theoretical ones, we validated the model. Finally, we also consider the applications for microwave signals distribution by optical fiber links.

1. INTRODUCTION

The low attenuation inherent to optical fibers, its immunity to electromagnetic interference and its physical dimensions [1] are factors that contributed to the widespread utilization of this propagation channel in a variety of communication systems in high frequencies.

Analog optical links are the basis of many applications in microwave photonics, such as: signal processing, telecommunications, networking, radars and other systems; being them military or commercial. This variety of applications stimulates research on the field of high capacity optical links. Some examples of related topics are the development of systems that operate at wavelengths in which the fiber attenuation is low [2], the chromatic dispersion of optical sources is reduced [3] and the performance of photodetectors is optimized [1].

In this paper, we present metrics such as Gain and Spurious Free Dynamic Range (SFDR) of an analog optical link based on a Mach-Zehnder (MZ) external modulation scheme. Starting with an on quadrature modulation the gain and SFDR are considered in the sense of link gain control without change the laser source power, the radio frequency modulation power or the MZ modulator. Instead those changes it is considered an off quadrature link operation and the corresponding effect on the SFDR.

2. ANALOG FIBER OPTIC LINK

The optical link is composed of three stages: modulation, transmission and photodetection [3, 4]. As illustrated in Figure 1, the analog signal is applied to a MZ optical modulator that controls the intensity of a carrier generated by a laser. The MZ output is transmitted through a low-loss optical fiber and detected by a high-speed photodetector.

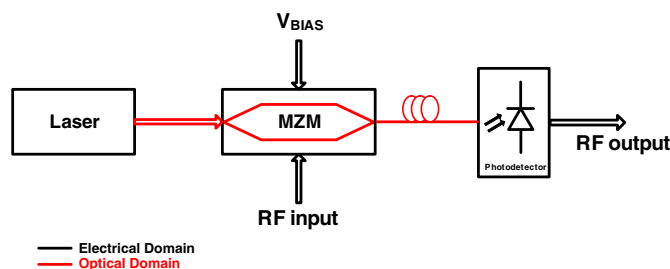


Figure 1: Optical link.

Based on models of this optical link [5, 6], we calculate the total gain of the optical power (g_{Tme}) as a function of the MZM slope efficiency (s_{mz}) with general bias (V_{DC}):

$$s_{mz} = \sqrt{\frac{R_S}{P_{RF}}} \left(\frac{T_{mz} P_{CW}}{2} \right) \left[\sin \left(\frac{\pi (V_{DC} + \sqrt{P_{RF} R_S})}{V_\pi} \right) \right] \quad (1)$$

$$g_{Tme} = \frac{4 \cdot S_{mz}^2 \cdot r_d^2 \cdot R_{mz}^2 \cdot T_F^2}{\left[(R_s + R_{mz})^2 + (\omega \cdot C_{mz} \cdot R_s \cdot R_{mz})^2 \right] \cdot \left[1 + 4 \cdot (\omega \cdot C_D \cdot R_L)^2 \right]} \quad (2)$$

$$G_T = 10 \cdot \log(g_{Tme}) \quad (3)$$

where: R_s (modulation source resistance), ω (angular velocity of the RF signal), C_D (photodetector junction capacitance), R_L (laser resistance), r_d (optical receptor responsivity), C_{MZ} (MZM capacitance), P_{CW} (optical power of the laser), T_{MZ} (optical transmission coefficient of the MZM), T_F (optical transmission coefficient between the modulation and detection devices), R_{mz} (resistance of the MZM) $e V_\pi$ (half-wavelength voltage). On the Table 1 it is shown the values for the parameters used together the Equations (1), (2) and (3).

Using custom made MATLAB software we obtained the MZ transfer function for any V_{dc} bias voltage value.

In Table 1, we present the values of the parameters used to obtain the optical link gain according to the equations above.

Table 1: Values of the parameters.

$R_{mz} = 43 \Omega$	$k = 1.38 \times 10^{-23} \text{ J/K}$	$R_s = R_L = 50 \Omega$	$f = 1 \text{ GHz}$	$V_\pi = 2.92 \text{ V}$
$C_{mz} = 8.33 \text{ pF}$	$P_{RF} = 0 \text{ dBm}$	$T_{mz} = 0.3$	$r_D = 1$	$\Delta f = 5 \text{ GHz}$
$C_D = 0.3 \text{ pF}$	$V_{DC} = 0.73 \text{ V}$	$T_F = 0.3$	$P_{CW} = 10 \text{ mW} - 15 \text{ mW}$	$T = 293 \text{ K}$

3. RESULTS AND DISCUSSIONS

The theoretical results are obtained as mentioned before from a custom-made program in MATLAB, which is based on the generalized equations mentioned in Section 2. For validating the routines we considered the optical link showed in Figure 1. After the measurements we obtained the following results for V_{DC} equal to 0 V: $P_{cw} = 10 \text{ mW}$, $G_T = -34 \text{ dBm}$ and $\text{SFDR} = 84 \text{ dB} \cdot \text{Hz}^{2/3}$.

Figure 2 shows the output optical link for the above parameters with V_{DC} equal to 0 V as mentioned.

Figure 3 shows the SFDR obtained with MATLAB routine to $V_{DC} = 0 \text{ V}$.

Figure 4 shows the output optical link for the above parameters with V_{DC} equal to 0.73 V.

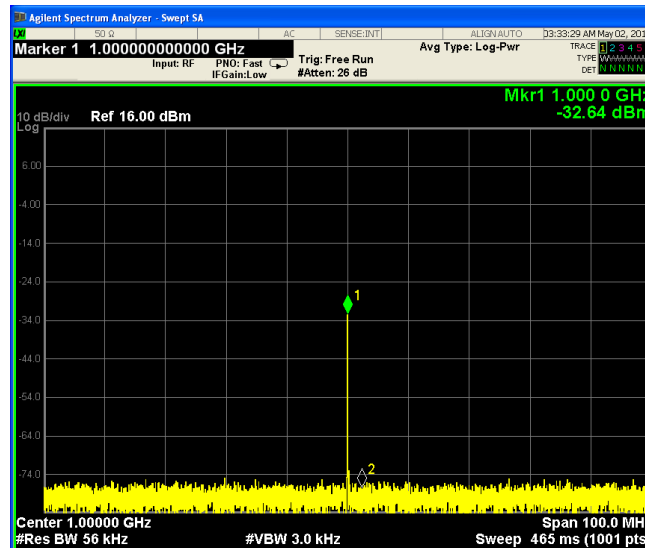


Figure 2: Optical link output for $P_{CW} = 10 \text{ mW}$ and $V_{DC} = 0 \text{ V}$.

Figure 5 shows the SFDR obtained with MATLAB routine to $V_{DC} = 0.73$ V.

As we can see the G_T is a function of V_{DC} . The role characteristics of the optical link as gain and SFDR, for example, depend on V_{DC} .

The optical link characteristics controlled by the V_{DC} , enable the adjustment the link output

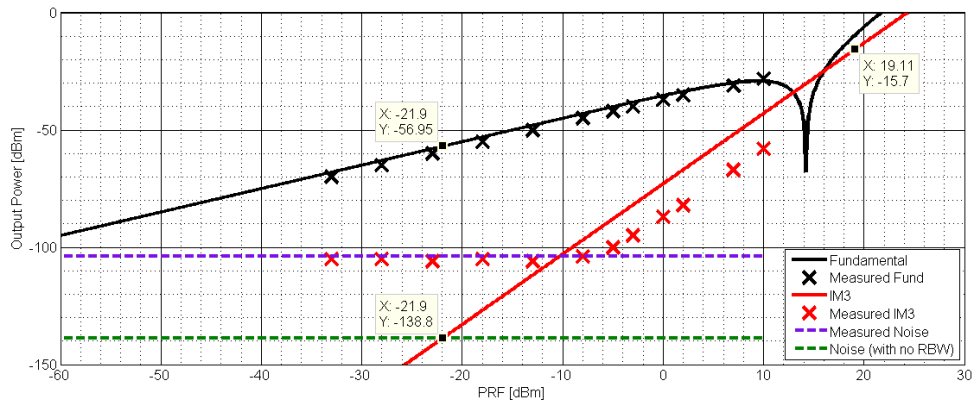


Figure 3: SFDR with $V_{DC} = 0$ V.

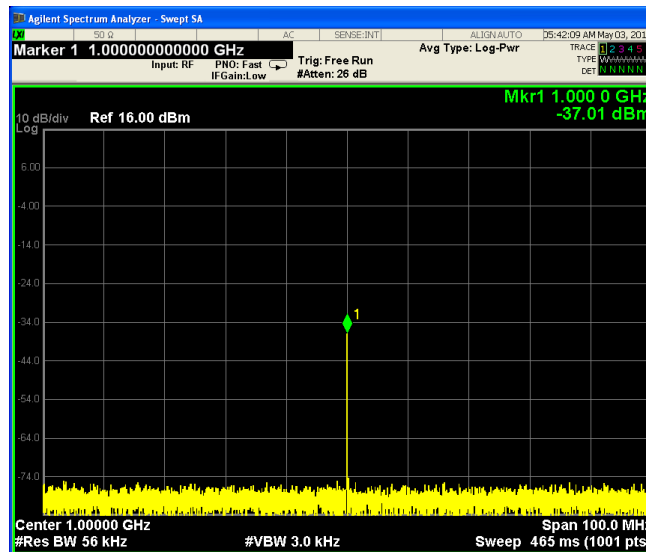


Figure 4: Optical link output for $P_{CW} = 10$ mW and $V_{DC} = 0.73$ V

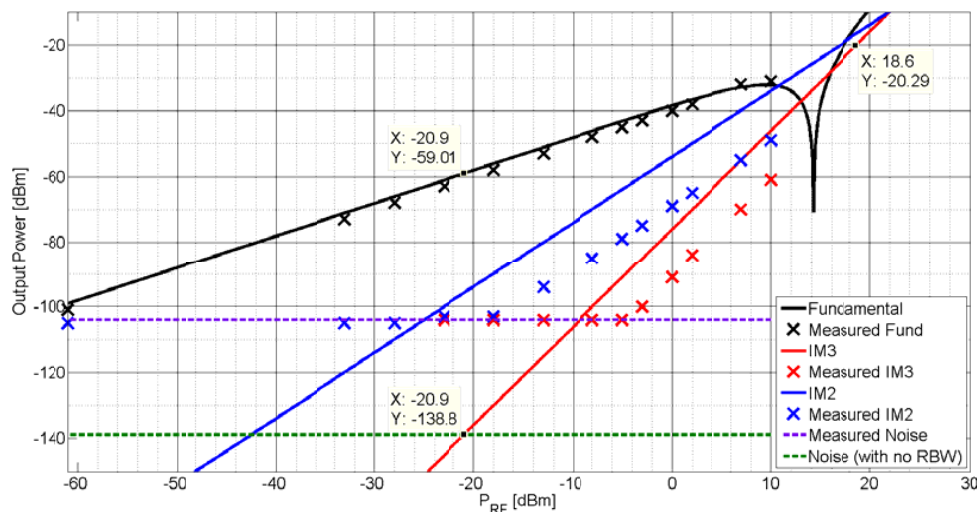


Figure 5: SFDR with $V_{DC} = 0.73$ V.

characteristics without changing the parameters from Table 1. It is not necessary to change the laser source, the modulator or the photodetector.

For validating the model we investigate the optical link at different operation points.

As before, we obtained the following results for V_{DC} equal to 0.73 V: $P_{cw} = 10$ mW, $G_T = -37$ dBm and SFDR = $86 \text{ dB}\cdot\text{Hz}^{2/3}$.

4. FINAL REMARKS

To summarize the article, we first introduced a generalized theoretical model for the analog link and then we validated the model by comparing experimental data with the equivalent values from the mathematical model (obtained from the MATLAB program or by simple algebra, depending on the case). The general results agree with the analysis based on the custom-made MATLAB routine. The authors are going to investigate more detailed optical link characteristics in the sense of RF input bandwidth and power. Such analysis will enable an electronic optical link control.

On a final remark, we emphasize the importance of the subject. Transmitting microwave signals through optical fibers can benefit many applications, ranging from transmission and distribution to high frequency reception systems. Its low attenuation and immunity to electromagnetic interference are the characteristics that stand out when dealing with long-range transmissions of signals, e.g., radars and mobile telephony. For this reason, modeling and assessing the characteristics of analog electro-optical links is increasingly important.

REFERENCES

1. Iezekiel, S., *Microwave Photonics: Devices and Applications*, John Wiley & Sons, Chichester, 2009.
2. Bailey, D. and E. Wright, *Practical Fiber Optics*, 1st Edition, Newness Press, 2003.
3. Cox, C. H., *Analog Optical Links: Theory and Practice*, Cambridge University Press, 2004.
4. Cox, III, C. H. and E. I. Ackerman, "Microwave photonics: Past, present and future," *Microwave Photonics Conference*, 9–11, Sep.–Oct. 2008.
5. Ackerman, E. I. and C. H. Cox, III, "RF fiber-optic link performance," *IEEE Microwave Magazine*, 50–58, Dec. 2001.
6. Chang, W. S. C., *RF Photonics Technology in Optical Fiber Links*, Cambridge University Press, 2002.

Studies on the Photoluminescence of a Novel Europium (III) Complex in Solution

Meng Shi¹, Xinxin Meng¹, Fufang Su¹, Zongbao Li⁴, and Xiaobo Xing^{2,3}

¹Shandong Provincial Key Laboratory of Laser Polarization and Information Technology
Qufu 273165, China

²Centre for Optical and Electromagnetic Research
South China Normal University, Guangzhou 510006, China

³Education Ministry's Key Laboratory of Laser Life Science & Institute of Laser Life Science
College of Biophotonics, South China Normal University, Guangzhou 510631, China

⁴Department of Physics and Electronic Science, Tongren University, Guizhou 554300, China

Abstract— The novel ternary europium(III) complex is synthesized. The photophysical sensitization process involves an energy transfer from functional hemicyanine (aminostyrylpyridinium) cation. The sensitization mechanism follows the Förster, which is significantly different from the Dexter, the most commonly used energy transfer mechanism from ligand. When the complex is dissolved in a variety of solvents (acetone, dimethylformamide, ethanol and acetonitrile), a remarkable solvent effect is observed. The emission intensity of europium(III) complex in acetonitrile is much stronger than that in other solvents. The solvent effect on the photophysical properties is studied. The result indicates that the solvent influences the emission intensity by aid of many factors not only polarity.

1. INTRODUCTION

Lanthanide ions and their coordination complexes have been attracting considerable attention owing to their unique optical properties, such as large Stokes shifts, high color purity and long luminescence lifetimes [1, 2], which gives rise to many potential applications, including biological imaging [3, 4] and medical diagnostics [5, 6]. In recent years combining the advantages of both lanthanide and two-photon scanning microscopy, two-photon sensitized luminescence of lanthanide complexes attracts great attention, which is in favor of less-harmful labeling and deep-penetrating bioimaging applications. For one- and two-photon absorption induced luminescence of lanthanide complexes, the sensitization by the so-called antenna effect is frequently used to overcome the low molar absorption coefficient of the Laporte forbidden $f-f$ transitions ($\epsilon < 1 \text{ L mol}^{-1} \text{ cm}^{-1}$). The most popular sensitization of lanthanide luminescence is via an energy transfer from the triplet excited state of ligand [7–9], and the energy transfer follows Dexter mechanism [10].

Recently, the sensitization from charge transfer (CT) excited state of organic chromophore provides an alternative process resulting in a red-shift of the excitation wavelength [11, 12]. This process due to the design of antenna with donor-acceptor charge transfer transitions. Therefore, a novel europium(III) complex $[\text{Eu}(\text{tta})_4 \cdot \text{DEASPI}]$ is synthesized by using *trans*-4-[*p*-(*NN*-Diethylamino)styryl]-*N*-methyl-pyridinium (DEASPI) as counterion to combine with a europium (III)-thenoyltrifluoroacetato(*tta*) moiety. The spectra of $\text{Eu}(\text{tta})_4 \cdot \text{DEASPI}$ also demonstrate that the sensitization is through CT states of DEASPI and follows the Förster mechanism.

The europium(III) complexes as luminescent probe are extensively applied in the aqueous solution, the solvent effect on the luminescence properties of complexes has to be taken into consideration [13–15]. However, the solvent effect on energy transfer via CT excited states in lanthanide complex has rarely been reported. In this manuscript, the study of the solvent effect on the photophysical properties of $\text{Eu}(\text{tta})_4 \cdot \text{DEASPI}$ is provided. It will be helpful for the synthesis and application of europium complexes.

2. EXPERIMENTAL

2.1. Syntheses and Structures of the Molecules

Nuclear magnetic resonance spectra were measured on a FX-90Q NMR spectrometer. Element analyses were performed on a Perkin 2400(II) autoanalyser. The melting points and decomposition temperatures were measured on Perkin Elmer DTA 1700 differential thermal analyzer and on a Perkin Elmer TGS-2 thermogravimetric analyzer at a heating rate of $20^\circ\text{C min}^{-1}$ under nitrogen atmosphere, respectively.

Synthesis of 4-methyl-N-methyl-pyridinium iodide (A): Using a three-neck flask fitted with a stirrer, thermometer, and condenser, 4-picoline (1 equiv) and methyl iodide (1.1 equiv) were mixed in toluene. The solution was stirred at room temperature for 4 h and then refluxed for 30 min. After cooling, the solution was filtered and the solid was washed with ethyl ether. The pale yellow solid was dried under vacuum, yield 21.2 g (90%). ^1H NMR (DMSO-*ds*) δ 2.56 (s, 3 H), 4.20 (s, 3 H), 7.0 (d, 2 H), 8.90 (d, 2 H) ppm.

Synthesis of trans-4-[p-(N,N-Diethylamino)styryl]-N-methylpyridinium iodide (B): A mixture of A (1 equiv) and 4-(N,N-dimethylamino)-benzaldehyde (1 equiv) in dried ethanol was treated with piperidine and was refluxed for 4 h. The resulting suspension was cooled. The precipitate was filtered off. Yield (82%) and T_d 264.7°C. Purified by column chromatography on silica gel using ethanol as eluent. ^1H NMR (DMSO-*d*₆) δ : 8.67 (2 H, d, J 6.84 Hz), 8.04 (2 H, d, J 6.84 Hz), 7.91 (1 H, d, J 15.61 Hz), 7.58 (2 H, d, J 8.79 Hz), 7.12 (1 H, d, J 15.63 Hz), 6.75 (2 H, d, J 8.80 Hz), 4.18 (3 H, s), 3.43 (4 H, q, 6.84), 1.13 (6 H, 6.84). Anal. calcd for C₁₈H₂₃N₂I: C 54.83, H 5.88, N 7.10, I 32.19; found: C 54.94, H 5.92, N 7.06, I 32.08.

Synthesis of trans-4-[p-(N,N-Diethylamino)styryl]-N-methylpyridinium tetrakis(α -thenoyltrifluoroacetato) europium(III): to a mixture of B (1 equiv) and of HTTA (4 equiv) neutralized with aqueous ethanol-NaOH solution (4 equiv) was added dropwise of aqueous Eu(NO₃)₃ (1 equiv) under constant stirring. The resulting precipitate was filtered off. A nearly saturated solution of the precipitate in 95% ethanol was allowed to evaporate slowly, and after 24 h red powder was obtained. Anal. calcd for C₅₀H₄₃N₂F₁₂O₈S₄Eu: C 45.91, H 3.31, N 2.14, Eu 11.62; found: C 45.34, H 3.52, N 2.46, Eu, 11.24.

The formula of Eu(tta)₄·DEASPI used in this work is trans-4-[p-(N,N-Diethylamino)styryl]-N-methyl-pyridinium tetrakis (α -thenoyltrifluoroacetato) europium(III). The anion Eu(tta)₄[−] is balanced in charge by the pyridine-cation DEASPI, which is close to europium ion through Coulombic interaction. The three-dimensional structure of Eu(tta)₄·DEASPI is shown in Scheme 1. The anion Eu(tta)₄[−] whose eight ligand conjugated structure is formed by Eu³⁺ and the oxygen atoms of the four α -thenoyltrifluoroacetato (HTTA). The cation DEASPI is used as one- and two-photon sensitizer for europium ion.

2.2. Methods and Instruments

The UV-vis absorption spectra were recorded by a UV-Vis-NIR scanning spectrophotometer (Shimadzu, model UV-3101PC). The fluorescent spectra were measured by a fluorescence spectrophotometer (Hitachi, model F-4500). The quantum-yield was measured by the standard comparison method [16], using Rhodamine 6G as the reference standard.

For the measurement of transient behavior, the excitation source is an OPA pumped by the third harmonic of a mode-locked Nd : YAG laser (Continuum, PY61C-10) with a repetition rate of 10 Hz. The tunable range of this OPA is from 760 to 1090 nm. An optical multi-channels analyzer was used as the recorder. The ultrafast laser beam passed firstly through a couple of Nicol's prisms, which were used as an attenuator to obtain a tunable excitation intensity. The laser beam was focused into the sample by a lens of $f = 5$ cm. The fluorescence was collected by a telescope system at the perpendicular direction of the pump beam. Before the input slit of optical multi-channels analyzer, a HA30 filter was inserted for cut off the excitation laser.

The TPA cross section δ was determined by comparing its TPA induced up-conversion fluorescence to that of Rhodamine 6G according to Eq. (1) [17]:

$$\delta = \delta_{cal} \frac{F n c_{cal} \phi_{cal}}{F_{cal} n_{cal} c \phi} \quad (1)$$

where, ϕ is the fluorescence quantum yield, c is the concentration, n is the refractive index, and F is the intensity of up-converted fluorescence. The cal subscript refers to the standard reference solution.

3. RESULTS

The UV-vis absorption spectra of DEASPI (in solid) and Eu(tta)₄·DEASPI (in dash) in acetonitrile at the concentration of 1×10^{-5} mol L^{−1} are shown in Fig. 1. In the absorption spectrum of Eu(tta)₄·DEASPI, two absorption bands around 340 nm and 485 nm are observed. Among them, the ultraviolet absorption band is attributed to tta [18], and the blue one results from DEASPI. In the spectral range of 600–900 nm, there is no intrinsic linear absorption for the two molecules.

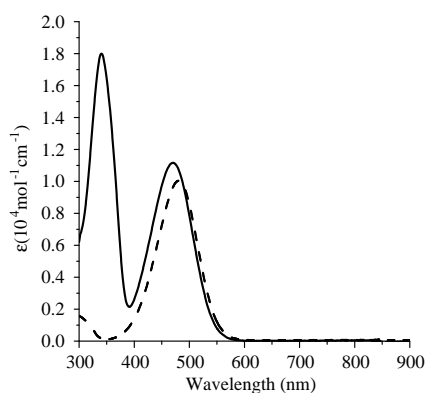


Figure 1: The UV-vis absorption spectra of $\text{Eu}(\text{tta})_4 \cdot \text{DEASPI}$ (in solid) and DEASPI (in dash) in acetonitrile ($1 \times 10^{-5} \text{ mol L}^{-1}$).

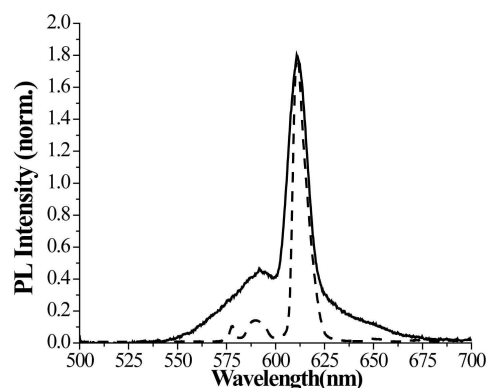


Figure 2: Fluorescent emission spectra of $\text{Eu}(\text{tta})_4 \cdot \text{DEASPI}$, solid line: $\lambda_{ex} = 485 \text{ nm}$; dashed line: $\lambda_{ex} = 340 \text{ nm}$.

The fluorescent spectra of $\text{Eu}(\text{tta})_4 \cdot \text{DEASPI}$ under 485 nm excitation are measured (as shown in Fig. 2). In the fluorescent spectra of $\text{Eu}(\text{tta})_4 \cdot \text{DEASPI}$ (dashed line for $\lambda_{ex} = 340 \text{ nm}$, solid line for $\lambda_{ex} = 485 \text{ nm}$), the distinct emission peak of 611 nm corresponds to the hypersensitive transition ${}^5\text{D}_0 \rightarrow {}^7\text{F}_2$ of Eu^{3+} [19]. Under 340 nm excitation, there are only emission peaks of Eu^{3+} in the emission spectrum. Under 485 nm excitation, the emission spectrum of $\text{Eu}(\text{tta})_4 \cdot \text{DEASPI}$ consists of not only emission band of DEASPI but also the characteristic emission peak ${}^5\text{D}_0 \rightarrow {}^7\text{F}_2$ of Eu^{3+} . 485 nm corresponding to the absorption peak of DEASPI, therefore, it can be concluded that the fluorescence of Eu^{3+} in $\text{Eu}(\text{tta})_4 \cdot \text{DEASPI}$ under 485 nm excitation is sensitized by CT states of DEASPI rather than $f-f$ transitions of $\text{Eu}(\text{III})$.

$\text{Eu}(\text{tta})_4 \cdot \text{DEASPI}$ is dissolved in acetone, DMF, ethanol and acetonitrile, respectively. The complex exhibits effective europium(III) luminescence in acetonitrile, however in other solutions the fluorescence intensity decreases obviously. For dissolved in different solvents, the emission intensity of $\text{Eu}(\text{tta})_4 \cdot \text{DEASPI}$ is in the order of acetonitrile > DMF > acetone > ethanol. This ordering is not in accordance with polarity of solvent, indicate that solvent influence the fluorescence not only by polarity. Furthermore, the emission peak of DEASPI shift with different solvents, indicate that the solvent influence the CT states of DEASPI. Detailed analysis of solvent effect is provided in following Discussion.

4. DISCUSSION

DEASPI is a stilbene-type chromophore with high thermal stability and photostability, and it has donor- π -bridge-acceptor (D- π -A) character [20]. The D- π -A structure is a typical charge-transfer structure. In DEASPI, the nitrogen of the pyridinium group loses an electron and makes the group prone to attract electrons from the amino group on another end of the DEASPI. i.e., pyridinium group plays as an acceptor and the amino group plays as a donor. The inherent electrical dipole moment appears in DEASPI. A solvent cage is formed when solvent molecules cover the outermost layer of DEASPI, which increases the geometrical distance between the cation and anion. The electronegativity in DMF and acetone is stronger than acetonitrile, which gives rise to more prominent solvent cage effect and decreases the fluorescence.

In addition, it is well known that ‘hypersensitive transitions’ is a unique property for lanthanide ions, which is very sensitive to the surrounding environment. These transitions are described by the term ‘pseudo-quadrupole transitions’, they obey the selection rule $|\Delta J| \leq 2$, $|\Delta L| \leq 2$, $\Delta S = 0$ [21]. According to Binnemans [22], the hypersensitive transitions are evidently influenced by Judd-Ofelt intensity parameter Ω_2 , which is determined by the asymmetry of the coordination environment of the lanthanide ion. Our previous study indicates that the increase of the asymmetry leads to the enhancement of hypersensitive transitions [23]. In this manuscript, the hypersensitive transition ${}^5\text{D}_0 \rightarrow {}^7\text{F}_2$ (612 nm) was significantly affected by the solution medium. It is because $\text{Eu}(\text{III})$ can provide nine coordination bonds, there are unsaturated for $\text{Eu}(\text{III})$ in $\text{Eu}(\text{tta})_4 \cdot \text{DEASPI}$, as illustrated in Fig. 3. In this case, solvent molecules can take part in the coordination to the Eu^{3+} , such as water molecule can take part in the coordination to the Eu^{3+} ions [24]. Compared with other organic solutions, acetonitrile provides more asymmetry of the coordination environment of

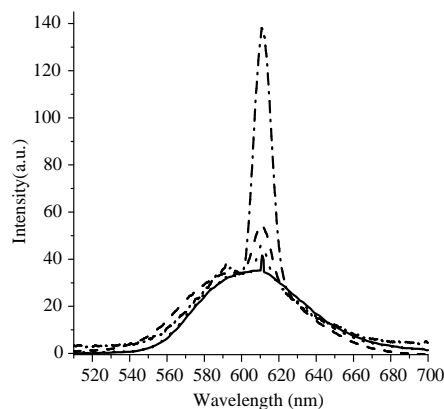


Figure 3: The emission spectra of $\text{Eu}(\text{tta})_4\cdot\text{DEASPI}$ in acetone (in dot), DMF (in dash), ethanol (in solid) and acetonitrile (in dash-dot) at 485 nm excitation.

Eu(III) ion. Therefore, the emission intensity of transition ${}^5\text{D}\rightarrow{}^7\text{F}_2$ is much higher than in other solutions.

5. CONCLUSION

In conclusion, the prominent solvent effect on the optical properties of $\text{Eu}(\text{tta})_4\cdot\text{DEASPI}$ is analyzed: Firstly, the formation of solvent cage changes the geometrical distance between the donor and the acceptor; Secondly, the solvent molecules take part in the coordination environment of Eu(III) ion, which changes the emission intensity of hypersensitive transition ${}^5\text{D}\rightarrow{}^7\text{F}_2$. All of factors lead to the solvent effect is remarkable in this kind of europium complex.

ACKNOWLEDGMENT

We thank Grants-in-Aids from the National Science Funds of China (Nos. 11104162, 11274200, 61177077), the Shandong Province Young and Middle-Aged Scientists Research Awards Fund (No. 2011BSB01110), the Guangdong Natural Science Foundation (2013B090500123, 2014A030313-432).

REFERENCES

1. Bünzli, J.-C. G. and C. Piguet, *Chemical Society Reviews*, Vol. 34, 1048–1077, 2005.
2. Vereb, G., E. Jares-Erijman, P. R. Selvin, and T. M. Jovin, *Biophysical Journal*, Vol. 74, 2210–2222, 1998.
3. Qian, G., Z. Zhong, M. Luo, D. B. Yu, Z. Q. Zhang, Z. Y. Wang, and D. G. Ma, *Advanced Materials*, Vol. 21, 111–116, 2009.
4. Sun, P. P., J. P. Duan, J. J. Lih, and C. H. Cheng, *Advanced Functional Materials*, Vol. 13, 683–691, 2003.
5. Yam, V. W. W., K. K. W. Lo, W. K. M. Fung, and C. R. Wang, *Coordination Chemistry Reviews*, Vol. 171, 17–41, 1998.
6. Tsukube, H., S. Shinoda, and H. Tamiaki, *Coordination Chemistry Reviews*, Vol. 226, 227–234, 2002.
7. Fu, L. M., X. F. Wen, X. C. Ai, Y. Sun, Y. S. Wu, J. P. Zhang, and Y. Wang, *Angewandte Chemie — International Edition*, Vol. 117, 757–760, 2005.
8. Werts, M. H. V., N. Nerambourg, D. Pelegry, Y. L. Grand, and M. Blanchard-Desce, *Photochemical & Photobiological Sciences*, Vol. 4, 531–538, 2005.
9. Lis, S. and G. Pawlicki, *Journal of Luminescence*, Vol. 130, 832–838, 2010.
10. Dexter, D. L., *Journal of Chemical Physics*, Vol. 21, 836–850, 1953.
11. D'Aléo, A., A. Picot, A. Beeby, J. A. G. Williams, B. L. Guennic, C. Andraud, and O. Maury, *Inorganic Chemistry*, Vol. 47, 10258–10268, 2008.
12. D'Aléo, A., F. Pontillart, L. Ouahab, C. Andraud, and O. Maury, *Coordination Chemistry Reviews*, Vol. 256, 1604–1620, 2012.
13. Ke, W. L., S. L. Wei, and Y. T. Min, *Spectrochimica Acta Part A: Molecular and Biomolecular Spectroscopy*, Vol. 66, 590–593, 2007.

14. Ansari, A. A., N. Singh, A. F. Khan, S. P. Singh, and K. Iftikhar, *Journal of Luminescence*, Vol. 127, 446–452, 2007.
15. Wielgus, M., J. Michalska, M. Samoc, and K. Bartkowiak, *Dyes and Pigments*, Vol. 113, 426–434, 2015.
16. Demas, J. N. and G. A. Crosby, *Journal of Chemical Physics*, Vol. 75, 991–1024, 1971.
17. Xu, C. and W. W. Webb, *Journal of the Optical Society of America B — Optical Physics*, Vol. 13, 481–491, 1996.
18. Shavaleev, N. M., S. J. A. Pope, Z. R. Bell, S. Faulkner, M. D. Ward, *Dalton Transactions*, 808–814, 2003.
19. Pavithran, R., N. S. S. S. Kumar Biju, M. L. P. Reddy, S. A. Junior, and R. O. Freire, *Inorganic Chemistry*, Vol. 45, 2184–2192, 2006.
20. Wang, H. Z., H. Lei, Z. C. Wei, F. L. Zhao, X. G. Zheng, N. S. Xu, X. M. Wang, Y. Ren, Y. P. Tian, Q. Fang, and M. H. Jiang, *Chemical Physics Letters*, Vol. 324, 349–353, 2000.
21. Peacock, R. D., *Structure and Bonding*, Vol. 22, 83, Berlin, 1975.
22. Binnemans, K., K. V. Herck, and C. G. Walrand, *Chemical Physics Letters*, Vol. 266, 297, 1997.
23. Shi, M., M. Pan, F. F. Su, F. Q. Wu, P. G. Han, and D. Z. Hao, *Journal of Luminescence*, Vol. 132, 398–402, 2012.
24. Tang, Q., S. X. Liu, D. D. Liang, F. J. Ma, G. J. Ren, F. Wei, Y. Yang, and C. C. Li, *Journal of Solid State Chemistry*, Vol. 190, 85–91, 2012.

Metamaterial Terahertz Bandpass Filters: A Comparison between Metallic and Graphene-based Structures

M. Bana Kermani¹, M. Khodaei¹, A. Nasiri², and H. Baghban¹

¹School of Engineering-Emerging Technologies, University of Tabriz
Tabriz 51666-14761, Iran

²Department of Engineering, University College of Nabi Akram, Tabriz 51385-1488, Iran

Abstract— Metamaterial-based optoelectronic devices including Terahertz filters play a definitive role in advancement of THz technology. In this article we present a design procedure to obtain voltage-dependent carrier density control in a GaN-based heterostructure with a Schottky gate configuration which serves as the substrate for a THz bandpass filter (BPF). The introduced structure consists of a cross shaped metallic layer on the AlGaIn/GaN heterostructures. Then, we investigate tuning of transmission properties and the tunability of the filter. An overall tunability of about 103 GHz in the resonance frequency was obtained by varying the applied voltage from -8 V to 2 V . Also, a plasmonic metamaterial based on the graphene cross-shaped structure is studied and a comparison has been performed between the optical properties of graphene-based cross-shaped structure and the original structure.

1. INTRODUCTION

Among different THz passive devices, THz wave band pass filters with multi frequency operations are crucial elements to enhance the efficiency in applications such as astronomy, terahertz signal processing, imaging, communications, and biomedical and chemical sensors [1, 2]. On the other hand, the exciting possibilities of artificially designed metamaterials with sub-wavelength scale, customizable electromagnetic (EM) properties and ability to control them at unit cell level, make them promising candidate for development of versatile THz components [3, 4]. However, due to the resonant nature of metamaterials, their operation has been confined to a narrow spectral range. The performance of metamaterial-based THz wave BPFs could be extended tremendously if their response is dynamically tuned. In this article we mainly focus on the active tuning of the filtering characteristics of metallic and graphene based structures.

2. RESULTS AND DISCUSSION

The considered metallic structure consists of a cross shaped metallic layer on the AlGaIn/GaN heterostructures as illustrated in Figure 1. The transmission properties of the designed structure at different bias voltages have been depicted in Figure 2.

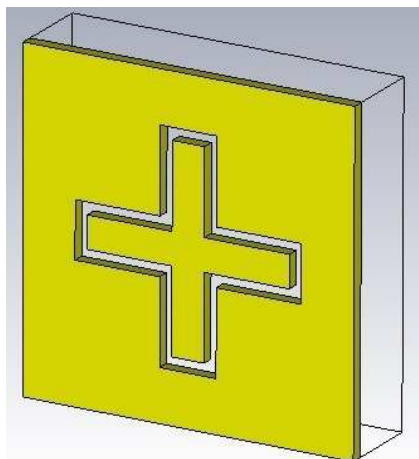


Figure 1: Cross-shaped THz BPF considered for study.

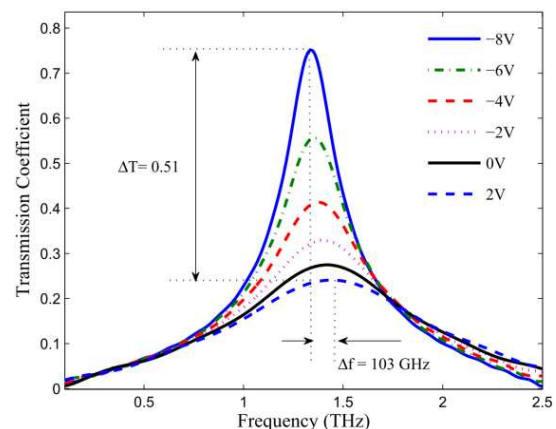


Figure 2: Transmission characteristics of the THz-BPF as a function of applied bias voltage.

To explore the active tuning of this structure, we have reduced the thickness of metal parts to $0.2 \mu\text{m}$ and the metallic part has been embedded on an $\text{Al}_x\text{Ga}_{1-x}\text{N}/\text{GaN}$ heterostructures with relative thickness of 20 nm and $0.35 \mu\text{m}$ for $\text{Al}_x\text{Ga}_{1-x}\text{N}$ and GaN layers, respectively as the substrate. In order to enable voltage-controlled conductivity of the substrate, metallic parts are electrically connected with $1 \mu\text{m}$ wide metallic (copper) connections which make the structure sensitive to polarization of THz wave. All simulations have been done for normal incidence. The array and substrate effectively form a Schottky diode, where dielectric properties of the substrate can be controlled by controlling the carrier density via applied gate voltage. An electric signal affects the high-frequency conductivity as well as the dielectric constant of the substrate in critical areas near the designed meta-molecules and thus, affects their resonant response. A self-consistent Schrödinger-Poisson approach has been utilized to obtain the energy subbands and the Fermi level in which the voltage-dependent sheet carrier density for $\text{Al}_x\text{Ga}_{1-x}\text{N}/\text{GaN}$ structure has been included through

$$N_s = \frac{\varepsilon(x)}{e(d_d + d_i)} \left(V_a - V_{th} - \frac{E_f(x)}{e} \right) \quad (1)$$

where $\varepsilon(x)$ is the dielectric constant, E_f is the Fermi level, d_d and d_i are doped and undoped AlGaN thickness, and V_a and V_{th} stand for applied voltage and threshold voltage respectively, given by

$$V_{th}(x) = \phi^b(x) - \Delta E(x) - \frac{eN_d d_d^2}{2\varepsilon(x)} - \frac{\sigma(x)}{\varepsilon(x)} (d_d + d_i) \quad (2)$$

The threshold voltage depends on the conduction band discontinuity between $\text{Al}_x\text{Ga}_{1-x}\text{N}/\text{GaN}$ denoted by $\Delta E(x)$, ϕ^b as the Schottky barrier at metal/ AlGaN interface, dopant concentration, N_d , and the polarization induced charge density, $\sigma(x)$, at $\text{Al}_x\text{Ga}_{1-x}\text{N}/\text{GaN}$ interface. Depending on the dopant concentration and Al mole fraction and consequently, the Fermi level, one may assume several confined energy levels, n , to obtain the total sheet carrier concentration inside the well through

$$N_s = \sum_{n=1}^{n=n_0} \frac{mk_b T}{\pi \hbar^2} \ln(1 + \exp((E_f - E_n)/k_b T)) \quad (3)$$

Plasma frequency of the (2DEG) can be then defined by $\omega_p = (N_s e^2 / \varepsilon_0 m^*)^{0.5}$ where $m^* = 0.22 m$ is the effective electron mass in GaN and m is the free-electron mass.

As illustrated in Figure 2, an overall tunability of about 103 GHz in the resonance frequency was obtained by varying the applied voltage from -8 V to 2 V .

It is noteworthy to mention that graphene-based THz filters are more flexible to achieving tunability, and the continuous forms of graphene can be transferred to a flat substrate and the carrier concentration of each layer in a graphene-based multi-layer filter can be dynamically tuned.

The surface conductivity of graphene that contains the effect of interband and intraband transitions has been calculated through the local limit of random-phase approximation (RPA). The surface conductivity depends on the temperature, the intrinsic carrier relaxation time, τ , and the

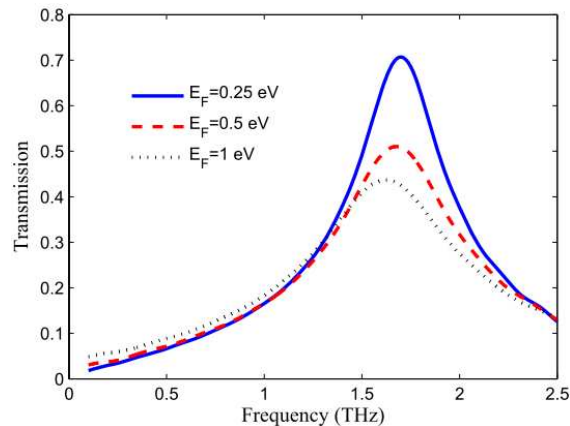


Figure 3: Transmission characteristics of the THz-BPF based on graphene as a function of Fermi energy.

Fermi level (which depends on the external bias voltage). Obtained results show considerable resonance strength and dynamically controllable feature.

Figure 3 shows the obtained transmission characteristics for the graphene-based THz filter which has the same structure as the metallic (copper) filter designed in this study. Beside the resonance shift which arises from the difference in the dielectric function of the copper and graphene at THz frequencies, a similar behavior is seen in graphene-based filter with varying the Fermi energy. As it is clear from Figure 3, increasing the voltage-induced Fermi energy increases the electron density and consequently, shorts the gap in the structure resulting in the reduced transmission of the structure.

The surface conductivity of graphene that contains interband and intraband transitions can be calculated through [5]

$$\sigma_s(\omega) = \frac{2e^2 k_b T}{\pi \hbar^2} \frac{i}{\omega + i\tau^{-1}} \log \left[2 \cosh \left(\frac{E_F}{2k_b T} \right) \right] + \frac{e^2}{4\hbar} \left[H \left(\frac{\omega}{2} \right) + \frac{4i\omega}{\pi} \int_0^\infty \frac{H(\varepsilon) - H(\varepsilon/2)}{\omega^2 - 4\varepsilon^2} d\varepsilon \right], \quad (4)$$

where

$$H(\varepsilon) = \frac{\sinh(\hbar\varepsilon/k_b T)}{\cosh(E_F/k_b T) + \cosh(\hbar\varepsilon/k_b T)}, \quad (5)$$

Here, T is the temperature and E_F is the Fermi energy.

REFERENCES

1. McGovern, W. R., P. R. Swinehart, E. L. Hogue, D. R. Daughton, and J. V. DeLombard, "Formation of chromate conversion coatings on Al-Cu-Mg intermetallic compounds and alloys," *SPIE Defense, Security, and Sensing*, 838506, 2012.
2. Piesiewicz, R., T. Kleine-Ostmann, N. Krumbholz, D. Mittleman, M. Koch, J. Schoebel, et al., "Short-range ultra-broadband terahertz communications: Concepts and perspectives," *IEEE Antennas and Propagation*, Vol. 49, 24, 2007.
3. Withayachumnankul, W. and D. Abbott, "Metamaterials in the terahertz regime," *IEEE J. Photon.*, Vol. 1, 99–118, 2009
4. Chiang, Y. J., C. S. Yang, Y. H. Yang, C. Pan, and T. J. Yen, "An ultrabroad terahertz bandpass filter based on multiple-resonance excitation of a composite metamaterial," *Applied Physics Letters*, Vol. 99, 191909, 2011.
5. Wang, J., W. Lu, X. Li, X. Gu, and Z. Dong, "Plasmonic metamaterial based on the complementary split ring resonators using graphene," *J. Phy. D: Appl. Phys.*, Vol. 47, 325102, 2014.

Some Effects of Specific Interest on the Brain of Children with Autism Spectrum Disorder (ASD): A Functional Near-infrared Spectroscopy Study

Huilin Zhu^{1*}, Yuebo Fan³, Xinge Li^{1,2}, Dan Huang³, Huan Guo², and Sailing He^{1,4}

¹Centre for Optical and Electromagnetic Research, South China Academy of Advanced Optoelectronics
South China Normal University (SCNU), Guangzhou 510006, China

²School of Psychology, South China Normal University (SCNU), Guangzhou 510631, China

³Guangzhou Rehabilitation and Research Center for Children with ASD, Guangzhou 510540, China

⁴Department of Electromagnetic Engineering, Royal Institute of Technology, Stockholm 10044, Sweden

Abstract— Autism spectrum disorder (ASD) is a neuro-developmental disorder, characterized by two major domains: impairments in the social cognition and communication as well as restricted, repetitive, stereotyped interests and behaviors. In this study, functional near-infrared spectroscopy (fNIRS) was applied to investigate the atypical activation pattern of language areas (bilateral inferior frontal gyrus and bilateral temporal cortex) and uncover the impact of a specific interest on the brain function of children with ASD. We employed a listening comprehension task to stimulate the language areas of 2 ASD boys (A1 and A2) who had strong interests in the experiment material (“Lightning McQueen”) and another 2 ASD boys (A3 and A4) who were matched with A1 and A2 respectively by age, intelligence quotient, language ability and the severity of symptoms. Our results showed that, during the task, the picture of “Lightning McQueen”, but not the words of “The little red car”, elicited stronger activation in the bilateral inferior frontal gyrus and temporal cortex of A1 and A2 than A3 and A4. These results could facilitate our understanding of language development of ASD and reconsider the role of specific interests (especially visual stimuli) played in the brain functional development of ASD.

1. INTRODUCTION

Functional near infrared spectroscopy (fNIRS) is an emerging non-invasive optical method for neuroimaging, which is increasingly applied to study infants, children, adolescents, adults and clinical populations, with the purpose of revealing typical and atypical developmental patterns of the brain [1]. Autism spectrum disorder (ASD) is a neurodevelopmental disorder, characterized by impaired social cognition and communication, rigid, repetitive, and stereotyped patterns of behavior and interests. Previous studies have demonstrated that adults and adolescents with ASD exhibited atypical activation and connectivity pattern in the language area of the brain [2, 3], including the bilateral inferior frontal gyrus (IFG) and temporal cortex (TC), which suggested the disrupted developmental pattern of language regions of ASD. However, IFG and TC were not only responsible for language processing but also contributed to social perception and cognition [4, 5]. Hence, in this study, we used fNIRS to measure the hemodynamic responses of IFG and TC when ASD children were performing a listening comprehension task and investigate how a specific interest in the task, as a social cognition component, could influence the activation pattern of IFG and TC. We hypothesized that a specific interest would improve the malfunction of language areas of children with ASD.

2. MATERIALS AND METHODS

2.1. Participants and Experiment Protocol

Participants were 4 children from 7 to 9 years of age who were diagnosed as ASD. All of the participants were boys and right-handed. During the listening comprehension task, children were asked to listen to a list of sentences and then answered the questions with two different types of promptings (pictures or words). There were 4 trials in each block and 2 blocks in the experiment. One block included the prompting of pictures of “Lightning McQueen” and another block included the prompting of words of “The little red car”. All the trials in each block and all the blocks were presented by e-prime 2.0 randomly. The experiment protocol was approved by the Institutional Review Board of Guangzhou Rehabilitation and Research Center for Children with ASD.

*Corresponding author: Huilin Zhu (huilin.zhu@coer-scnu.org).

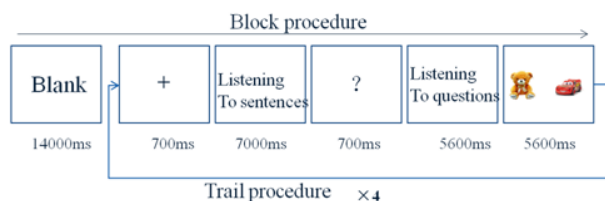


Figure 1: The block procedure (with the prompting of pictures).

Among the 4 children, 2 children with ASD (A1 and A2) showed strong interests in a cartoon character named “Lightning McQueen” which was one of the materials used in the experiment. A1 was preoccupied by “Lightning McQueen” and its relevant movies, games and pictures, whereas A2 was a car expert who knew “Lightning McQueen” very well, but his interest also extended to other cars, especially to red racing cars. Therefore, we compared the brain performances of A1 and A2 with another 2 ASD boys (A3 and A4) who were match with A1 and A2 respectively in age, intelligence quotient, language ability and the severity of symptoms.

2.2. NIRS Measurements

Measurements were performed with a fNIRS system (FOIRE-3000, Shimadzu Corporation, Kyoto, Japan) working at three wavelengths, 780 nm, 805 nm and 830 nm with a sampling rate of 14.286 Hz (time resolution = 70 ms). The distance between the emitter and detector was fixed at 3 cm. The measured brain regions and channel configurations were shown in Figure 2.

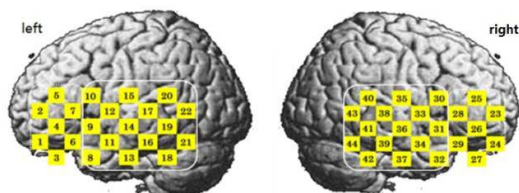


Figure 2: Channel configurations in IFG and TC. There were 14 channels (left hemisphere: from Channel 1 to Channel 7, right hemisphere: from Channel 23 to Channel 29) covering IFG and 30 channels (left hemisphere: from Channel 8 to Channel 22, right hemisphere: from Channel 30 to Channel 44) covering TC. We used international 10-10 system to locate: Channel 4 and 26 were located in F7 and F8; Channel 9 and 31 were located in the FT7 and FT8.

2.3. Data Analysis

Only HbO data was included in analysis. We used NIRS-SPM [6] to preprocess and statistically analysis the data and define the spatial correlates underlying the different conditions. For each participant, the raw time course data were preprocessed to remove sources of noises and artifacts by the hemodynamic response function (hrf) and wavelet-MDL detrending algorithm (wavelet-MDL). Then, we performed a general linear model (GLM) to test the effect of different promptings by convolving the task with the hemodynamic response function (without time or dispersion derivatives) and computing parameter estimates (beta values of the GLM as the weights). The F contrasts were calculated for one-way comparison: promptings (pictures and words) at each channel. To control for false positives caused by multiple comparisons, all p values were corrected by false discovery rate. The significant channels were mapped onto the corresponding location of the cortex.

3. RESULTS

We analyzed and compared the brain activation (HbO) between A1 and A3, as well as between A2 and A4, who were matched in pairs with age, intelligence quotient, language ability and the severity of ASD symptoms respectively. Compared to A3 and A4, A1 and A2 were very interested in “Lightning McQueen”. As the statistical parametric mapping shown in Figure 3, A1 and A2 showed significant stronger activation in the bilateral IFC and bilateral TC than A3 and A4 when performing the listening comprehension task under the prompting of the pictures (with visual stimuli of “Lightning McQueen”). In particular, for A1 who was preoccupied by “Lightning McQueen”, there

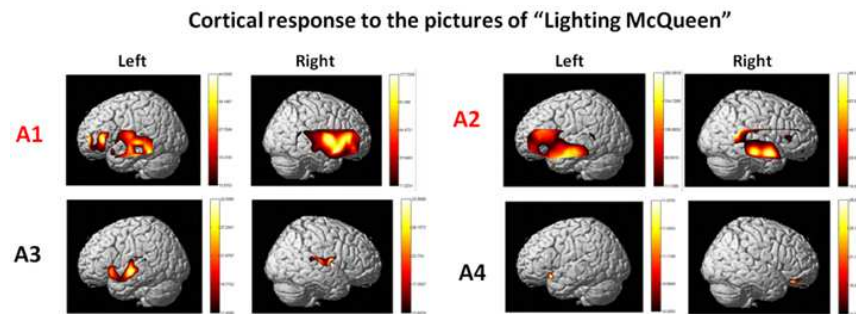


Figure 3: The statistical parametric mapping of all the children with ASD. The regions with color were statistically significant channels by general linear model analysis ($P_{FDR} < 0.05$). There were obvious activation of IFG and TC to experiment condition with the pictures of “Lightning McQueen” in A1 and A2 but not in A3 and A4.

was more activation in the bilateral IFG and bilateral TC to the pictures of “Lightning McQueen” than A3.

4. DISCUSSION

In the present study, we employed fNIRS to detect the activation pattern in IFG and TC under listening comprehension task and reveal the effect of a specific interest on brain function of children with ASD. Previous studies have demonstrated the language areas, such as Broca’s area (left IFG) and Wernicke’s area (left superior TC) were significantly less activated in adolescents and adults with ASD underlying language and communication defects. However, we observed that 2 children with ASD, named A1 and A2, who were very interested in one of the materials in the experiment (“Lightning McQueen”), exhibited pronouncedly stronger activation in the bilateral IFG and bilateral TC than A3 and A4 children, who did not show any interests in the experiment stimuli. In line with another study with functional magnetic resonance imaging [7], our results implicated that a specific interest may play an important role in the functional development of brain language areas of children with ASD. Furthermore, the visual preference of participants with ASD was also observed in our results. Previous fMRI studies have indicated that participants with ASD prefer to use visual coding strategy rather than verbal coding strategy during language processing [8]. We found that, although A1 had a restricted interest in the pictures of “Lightning McQueen” whereas A3 had extended interests in both the pictures of “Lightning McQueen” and the words of “The little car”, they consistently exhibited stronger activation in the bilateral IFG and bilateral TC to the pictures of “Lightning McQueen” than to the words of “The little car”, which suggested that there was enhanced visual processing in domains such as language in ASD.

5. CONCLUSION

In summary, by using fNIRS to investigate how a specific interest could affect the atypical brain function of language areas of children with ASD, we mainly found, 2 ASD children showed pronounced stronger activation in the bilateral inferior frontal gyrus and temporal cortex in response to their favorite cartoon character than matched ASD children. Our results implied that specific interests in visual stimuli, like some pictures of favorite cartoon character, could have a positive effect on improving the atypical brain function of children with ASD underlying social cognition and language impairments. Additionally, our study also suggests that fNIRS is a feasible and effective technique to monitor the brain activity of awoken children with autism spectrum disorder.

ACKNOWLEDGMENT

This work was supported by Guangdong Innovative Research Team Program (No. 2010 01D0104799 318), the Natural Science Foundation of Guangdong province (2014A030310502).

REFERENCES

1. Vanderwert, R. E. and C. A. Nelson, “The use of near-infrared spectroscopy in the study of typical and atypical development,” *NeuroImage*, Vol. 85, 264–271, 2014.

2. Zhu, H., Y. Fan, H. Guo, D. Huang, and S. He, “Reduced interhemispheric functional connectivity of children with autism spectrum disorder: Evidence from functional near infrared spectroscopy studies,” *Biomedical Optics Express*, Vol. 5, 1262–1274, 2014.
3. Tesink, C. M., J. K. Buitelaar, K. M. Petersson, R. J. van der Gaag, J. P. Teunisse, and P. Hagoort, “Neural correlates of language comprehension in autism spectrum disorders: When language conflicts with world knowledge,” *Neuropsychologia*, Vol. 49, 1095–1104, 2011.
4. Rizzolatti, G. and L. Craighero, “The mirror-neuron system,” *Annual Review of Neuroscience*, Vol. 27, 169–192, 2004.
5. Frith, U. and C. D. Frith, “Development and neurophysiology of mentalizing,” *Philosophical Transactions of the Royal Society of London. Series B: Biological Sciences*, Vol. 358, 459–473, 2003.
6. Tak, S., S. J. Yoon, J. Jang, K. Yoo, Y. Jeong, and J. C. Ye, “Quantitative analysis of hemodynamic and metabolic changes in subcortical vascular dementia using simultaneous near-infrared spectroscopy and fMRI measurements,” *Neuroimage*, Vol. 55, 176–184, 2011.
7. Grelotti, D. J., A. J. Klin, I. Gauthier, P. Skudlarski, D. J. Cohen, J. C. Gore, and R. T. Schultz, “fMRI activation of the fusiform gyrus and amygdala to cartoon characters but not to faces in a boy with autism,” *Neuropsychologia*, Vol. 43, 373–385, 2005.
8. Kana, R. K., T. A. Keller, V. L. Cherkassky, N. J. Minshew, and M. A. Just, “Sentence comprehension in autism: Thinking in pictures with decreased functional connectivity,” *Brain*, Vol. 129, 2484–2493, 2006.

Broadband Cross Polarization Converter Formed by Twisted F-shaped Chiral Metamaterial

D. K. Sharma and S. K. Pathak

Microwave and ECE Diagnostic Division, Institute for Plasma Research, India

Abstract— A broadband cross polarization converter (CPC), formed from a Twisted-F Shaped Chiral Metamaterial (TFSCM), having high optical activity is reported in this work. The proposed structure supports high polarization conversion efficiency which is demonstrated numerically. The enhanced optical activity is observed which exhibits the presence of cross coupling phenomena between magnetic fields and is explained on the basis of surface current distribution.

1. INTRODUCTION

Metamaterials are tailored composite man-made materials made up of sub-wavelength size building blocks. It possessed different properties from their constituent materials. Those properties are produced mainly due to geometry of unit cell structure. By properly designing these structure one can achieve unique properties such as negative refractive index, extreme permittivity or permeability values, and negative magnetic permeability which are beyond from natural available materials. This unique property leads to new solutions and possibilities in various applications from information processing and telecommunication to sensing, imaging and security [1]. Specially the property of negative refractive index have possibility to produce the light of high resolution without any diffraction limits that will leads to new possibilities in data storage devices, imaging and lithography [1]. As well as the property of backward wave propagation (phase and group velocity are anti-parallel) can be used in variety of telecommunication devices such as transmission lines, waveguides, antenna, filters etc. [1].

A very interesting category of metamaterial is Chiral metamaterial. Now days it attracted much attention in controlling light polarization. It exhibits high value of optical activity (polarization rotation of linear polarized wave) and circular dichroism (left- and right-handed circularly polarized light absorption difference) that will highly exceeds these phenomena [2–4]. Another unique capability of Chiral metamaterial is in achieving, negative refraction through alternative Chiral route. It provides negative refractive index for circular polarized light.

In this work we present, Twisted-F Shaped Chiral Metamaterial (TFSCM) structure which supports high cross-polarization efficiency due to presence of large optical activity.

2. TFSCM DESIGN AND OPTICAL ACTIVITY

In Fig. 1(a), geometry of unit cell of TFSCM is shown. It consists of Chiral metallic pattern printed on both side of dielectric spacer. FR-4 substrate of 1 mm thick used as dielectric spacer having dielectric constant and loss-tangent respectively is 4.3 and 0.025. On front and back side of dielectric spacer, metallic pattern of F-shaped is printed and rotated opposite by 25° along the direction of electromagnetic wave propagation.

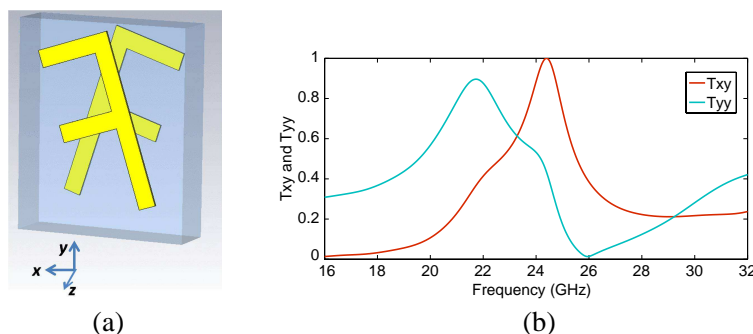


Figure 1. (a) Unit cell of TFSCM structure. F-shaped metallic inclusions are printed on both side of FR-4 dielectric substrate. (b) Cross (T_{xy}) and co-polarization (T_{yy}) transmission coefficients of the TFSCM.

To understand the optical behavior of TFSCM, we perform numerical simulations of the structure. For that purpose we used, Finite Integration Technique/Method based CST Microwave Studio (Computer Simulation Technology GmbH, Darmstadt, Germany) software. In simulation, periodic boundary is applied in x and y directions and absorbing boundary is applied in z direction. At one side of the structure, linearly polarized EM wave is incident having electric field in y -direction. On other side of the structure, transmitted electric field is measured in x and y directions. Further the value of electric field is used in order to calculate, cross (T_{xy}) and co-polarization (T_{yy}) transmission coefficients as per Equations (1) and (2) [2].

$$T_{xy} = E_x^t / E_y^i \quad (1)$$

$$T_{yy} = E_y^t / E_y^i \quad (2)$$

Here E_y^i is incident electric field in y direction, E_y^t is transmitted electric field in y direction and E_x^t is transmitted electric field in x direction. In Fig. 1(b), the numerical simulation results of T_{xy} and T_{yy} are presented. It is observed that regime of cross-polarization is found in frequency range 23.26 to 29.25 GHz. Other distinct features of TFSCM seen in Fig. 1 are (i) The regime of maximum cross-polarization also have non-zero value of co-polarization (e.g., co-polarization transmission level at 24.4 GHz is $T_{yy} = 0.43$). (ii) Regime of cross polarization also consists frequency points where transmission amplitude of co-polarization is almost zero (e.g., cross and co-polarization amplitude level respectively at 25.95 GHz are $T_{xy} = 0.013$ and $T_{yy} = 0.39$).

The proposed design supports high transmission level of cross polarization conversion (T_{xy}) which is a sign of large optical activity. To derive the full picture of optical activity of the proposed structure one need to analyse transmission level of circular polarized wave. This information is

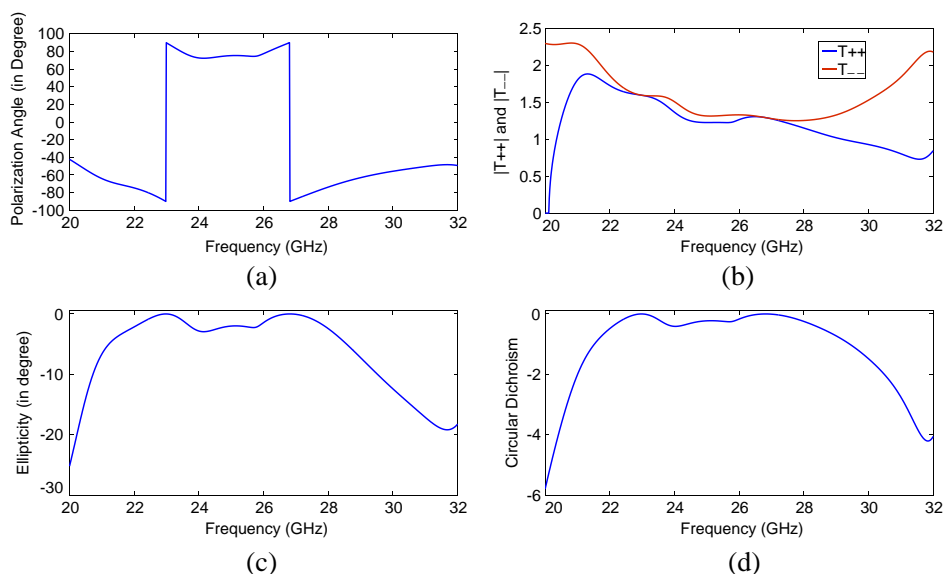


Figure 2. (a) Polarization rotation angle. (b) Right handed and left handed circular polarization coefficients. (c) Ellipticity. (d) Circular dichroism.

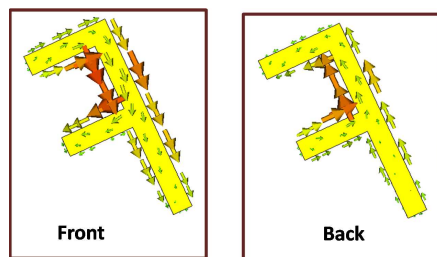


Figure 3.

directly obtained from transmission data of linearly polarized wave by Equations (3) and (4) [1].

$$T_{++} = 1/2((T_{xx} + T_{yy}) + i(T_{xy} + T_{yx})) \quad (3)$$

$$T_{--} = 1/2((T_{xx} + T_{yy}) - i(T_{xy} + T_{yx})) \quad (4)$$

Here T_{--} and T_{++} respectively are left and right handed circular polarization coefficients. Ellipticity (η), Polarization rotation angle (θ) and Circular Dichroism (CD) are also used in order to characterize optical activity of the structure. The value of those parameters are calculated from the transmission levels of LCP (T_{--}) and RCP (T_{++}) by Equations (5), (6) and (7).

$$\theta = 1/2[\arg(T_{++}) - \arg(T_{--})] \quad (5)$$

$$\eta = 1/2 \tan^{-1}[(|T_{++}| - |T_{--}|)/(|T_{++}| + |T_{--}|)] \quad (6)$$

$$CD = |T_{++}|^2 - |T_{--}|^2 \quad (7)$$

The polarization rotation angle is plotted in Fig. 2(a). It is observed that the value of polarization rotation angle is sustain around 90° for spectrum 23 to 26.8 GHz. In this spectrum y -polarized beam is converted to x -polarized beam. In identifying, pure optical activity the Ellipticity is a prime indicator. The Chiral metamaterial should possess pure optical activity for CPC design. For that the value of Ellipticity should be minimum. The Ellipticity is a measure of degree of circular/elliptical polarized wave and its low level describes the maintaining linearly polarized state at output. It is observed from Fig. 2(c) that the structure supports pure optical activity for a wide frequency spectrum 23.12 to 29.15 GHz. From Figs. 2(b) and (d) this can be confirmed, where Fig. 2(b) dictates that for corresponding spectrum (22.98 and 26.82 GHz) transmission levels of LCP and RCP are almost same and Fig. 2(d) shows that at frequency of 22.98 and 26.82 GHz Ellipticity become almost zero which is a desirable feature of an ideal CPC design.

In order to describe the mechanism of cross polarization and strong optical activity of TFSCM. We analyse the surface current distribution on twisted F-shaped structure. In Fig. 3, simulation results of surface current distribution is shown at 23.12 GHz. It is observed that magnetic dipoles are excited on top and bottom layer by incident EM wave and arrange anti-symmetrically due to anti-parallel flow of current in top and bottom metal plates. The coupling in between pair of magnetic dipoles leads to cross polarization transmission and strong optical activity.

3. CONCLUSION

In this paper, we have presented a new geometry of Chiral metamaterial and explore its optical activity numerically. Simulation results show that TFSCM supports cross-polarization characteristics over a wide frequency spectrum.

REFERENCES

1. Kenanakis, G., R. Zhao, A. Stavriniadis, G. Konstantinidis, N. Katsarakis, M. Kafesaki, C. M. Soukoulis, and E. N. Economou, "Flexible chiral metamaterials in the terahertz regime: A comparative study of various designs," *Optics Express*, Vol. 2, 1702, 2012.
2. Rajkumar, R, N. Yogesh, and V. Subramanian, "Cross polarization converter formed by rotated-arm-square chiral metamaterial," *Journal of Applied Physics*, Vol. 114, 224506, 2013.
3. Li, Z, K. B. Alici, E. Colak, and E. Ozbay, "Complementary chiral metamaterials with giant optical activity and negative refractive index," *Applied Physics Letters*, Vol. 98, 161907, 2011.
4. Ye, Y. and S. He, "90° polarization rotator using a bilayered chiral metamaterial with giant optical activity," *Applied Physics Letters*, Vol. 96, 203501, 2010.

Effect of Frequent Degree of Deceiving on the Prefrontal Cortical Response to Deception: A Functional Near-infrared Spectroscopy (fNIRS) Study

Fang Li^{1,2}, Huilin Zhu^{1*}, Shijing Wu¹, Qianqian Gao^{1,2},
Ziqiang Hu^{1,2}, Jie Xu¹, Guixiong Xu¹, and Sailing He^{1,3}

¹Centre for Optical and Electromagnetic Research
South China Academy of Advanced Optoelectronics South China Normal University (SCNU)
Guangzhou 510006, China

²School of Psychology, South China Normal University (SCNU), Guangzhou 510631, China

³Department of Electromagnetic Engineering, Royal Institute of Technology, Stockholm 10044, Sweden

Abstract— Functional near-infrared spectroscopy (fNIRS) is an emerging brain-imaging technique which has been used to various areas. Previous studies have indicated that frequent deceiving would make deceiving easier. In this study, fNIRS was used to explore the effect of frequent degree of deceiving on the prefrontal cortical response to deception. Self-related questions were used in the experiment. The results showed different patterns of neural activation between non-frequent deceiving and frequent deceiving. In Channel 11 (in the left prefrontal cortex), non-frequent deceiving led to a greater neural activation than telling the truth, while this pattern did not appear in frequent deceiving. Our finding suggested that fNIRS has ability to detect deception under different situations.

1. INTRODUCTION

Functional near-infrared spectroscopy (fNIRS) is a new brain-imaging technique which can measure the neural activities of the cortical regions of the brain [1]. It can simultaneously assess the concentration changes of oxy hemoglobin (HbO), deoxy hemoglobin (Hb) and total hemoglobin (HbT) [2], which are the three indicators of cerebral metabolism. In recent years, fNIRS has been widely used because of its non-invasiveness, low cost, excellent temporal resolution and reasonable spatial resolution [3–5].

Deception is a common behavior in the social circumstances. In real life, deceiving requires more effort in contrast to telling truth [6]. Recent fNIRS studies have consistently revealed that deceiving could cause greater neural activation than telling truth in the prefrontal cortex [7, 8]. However, many other factors can affect the brain activities of deceiving, such as the frequent degree of deceiving. Verschuere et al. found that frequent deceiving could make deceiving easier, in other words, people needed not put too much effort to deceive when they deceived frequently [9]. In agree with this finding, other fMRI studies confirmed that deceiving more could decrease the neural activation during deceptions [10, 11].

In the present study, we firstly used fNIRS to investigate the effect of the frequent degree of deceiving on the neural activities of the deception. In order to increase the ecological validity of this study, we used self-related questions in the experiment because self-related questions are more meaningful to the participants. Furthermore, previous studies provided evidence that self-related deception could lead to greater neural activation than non self-related deception [12, 13]. Therefore, we inferred that self-related deception was more sensitive to the frequent degree of deception.

2. METHODS

2.1. Participants and Protocol

12 college students participated in this study. They were all right-handed and had no neurological or psychiatric diseases.

Before the experiment, each participant was required to fill out a questionnaire which contained 64 self-related questions (for example, “Do you have a younger male cousin?”). Then each participant was told to complete two conditions: baseline condition and task condition. In the baseline condition, participants were required to tell the truth all the time when asked self-related questions; In the task condition, participants were required to make skillful deception. They could decide by

*Corresponding author: Huilin Zhu (huilin.zhu@coer-scnu.org).

their own whether or not to deceive in a given question. Each condition had 32 questions, which were the same as the questionnaire. 32 questions in one condition were set in a random order.

2.2. Experimental Setup

42 channels of an fNIRS system (FOIRE-3000, Shimadzu Corporation, Kyoto, Japan) with three wavelengths (780 nm, 805 nm, and 830 nm) were used. The parameters of concentration changes of oxygenated hemoglobin (HbO), deoxygenated hemoglobin (HB) and total hemoglobin (HbT) were measured. These three parameters were determined with the modified Beer-Lambert law. The international 10-10 system [14] was used to localize the different areas of the prefrontal cortex (PFC) (Fig. 1).

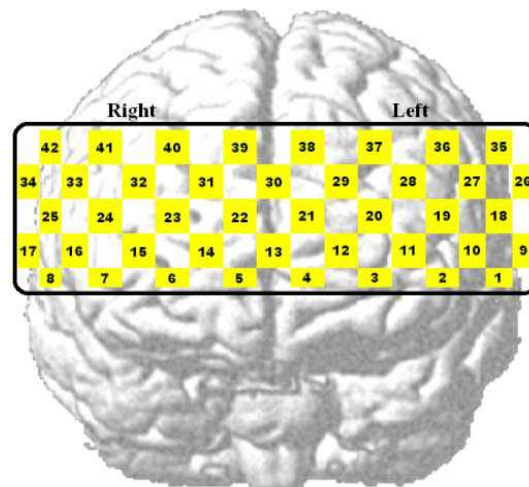


Figure 1: 42 channels covering the prefrontal cortex of the brain.

2.3. Data Analysis

By using the NIRS-SPM [15], the hemodynamic response function filter and a wavelet-MDL (minimum description length) detrending algorithm were used to remove physical noise and artifacts. In this study, only the data of change in HbO was selected because HbO signal was most sensitive to neural activation.

To explore the effect of the frequent degree of deceiving on the neural activities of the deception, several steps were performed: Firstly, the number of deceiving in the task condition was calculated for each participant. Then all the participants were ranked according to the number of deceiving from high to low. The top 50% of the participants were divided into frequent deceiving group, and other half were divided into non-frequent deceiving group. Secondly, the truth-telling trials in the baseline condition and the deceiving trials were selected for further analysis. The truth-telling trials were defined as the trials in which the answers of self-related questions were consistent with the questionnaire, and the deceiving trials were defined as the trials in which the answers of self-related questions were not consistent with the questionnaire. Thirdly, truth-telling trials in the baseline condition and deceiving trials in the task condition were averaged channel by channel for each participant. At last, 2 (truth-telling vs. deceiving) \times 2 (frequent deceiving vs. non-frequent deceiving) repeated measurement analysis of variance was performed.

For depicting HbO activation maps of different groups, the HbO data of truth-telling trials and deceiving trials were averaged across the participants respectively in each group, then the HbO data of “deceiving trials *minus* truth-telling trials” of the two groups were calculated.

3. RESULT

HbO activation maps were shown in Fig. 2. Greater HbO activation was observed in the case of deceiving (whether non-frequent deceiving or frequent deceiving) as compared to the case of telling the truth. In addition, different HbO activation patterns were shown in non-frequent deceiving and frequent deceiving.

The statistical analysis showed that the main effects of trial type were significant ($p < 0.05$) in channels 36 and 42. In these two channels, deceiving trials during deception led to significant increase in HbO than truth-telling trials in the baseline. The results also showed that the main

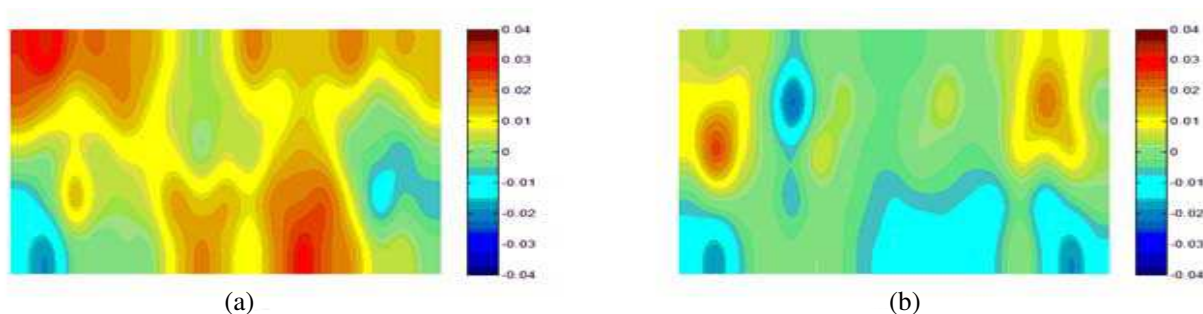


Figure 2: HbO activation maps of two groups. (a) The brain response to “deceiving trials *minus* truth-telling trials” of non-frequent deceiving group. (b) The brain response to “deceiving trials *minus* truth-telling trials” of frequent deceiving group.

effects of group were significant ($p < 0.05$) in Channel 30, 38 and 39. In these three channels, the non-frequent deceiving group showed significant increase in HbO than frequent deceiving group. In particular, the results indicated that the interaction effect of trial type and group was significant ($p < 0.05$) in channel 11. Simple effect analysis showed that the left prefrontal area of non-frequent deceiving group showed significant increase in HbO in deceiving trials during deception than truth-telling trials in the baseline, whereas the comparison between the deceiving trials and truth-telling trials in the frequent deceiving group was not statistically significant (Fig. 3).

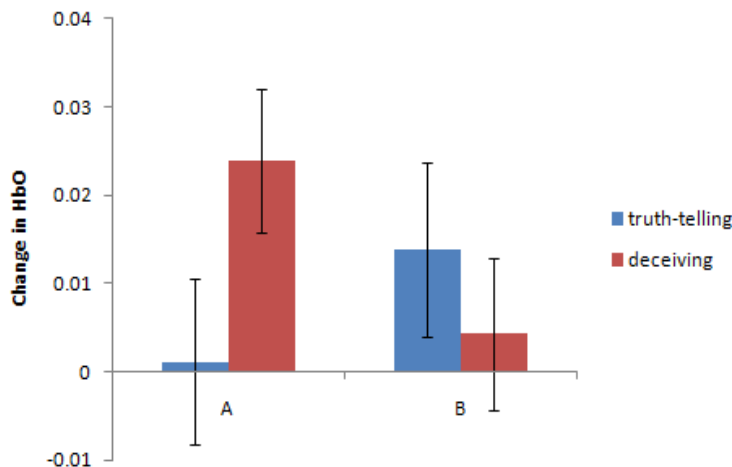


Figure 3: Change in HbO in channel 11 of two groups. A represents non-frequent deceiving group, and B represents frequent deceiving group.

4. DISCUSSION

Recently, fNIRS has been increasingly used in various areas. In this study, we utilized fNIRS to explore the effect of frequent degree of deceiving on the neural activities of deception. We used self-related questions in this experiment.

In this study, we have found that in general deceiving led increased HbO in the prefrontal cortex of the brain than telling truth. This result was in accordance with previous study [12, 13], indicating that when people made self-related deception, they also needed more cognitive effort than telling the truth. Specially, our study showed that when participants deceived, non-frequent deceiving group exhibited greater neural activation in channel 11 in the left prefrontal cortex. However, this pattern did not appear in the frequent deceiving group. This result was in line with previous fMRI studies [10, 11], suggesting that frequent deceiving would make deceiving easier so that people no longer need to put much effort in it [9]. In addition, the function of the prefrontal cortex was related to inhibiting and task switching [16]. Thus frequent deceiving participants did not need too many cognitive resources to inhibit the truth and produce a new response. The present study demonstrated that fNIRS could distinguish the neural response between non-frequent deceiving

and frequent deceiving, which implied that fNIRS could be used to detect deception under different situations.

5. CONCLUSION

In summary, we have used fNIRS to examine the effect of frequent degree of deceiving on the prefrontal cortical response to deception. Our findings have shown that non-frequent deceiving and frequent deceiving could cause different prefrontal cortical responses. In the left prefrontal cortex, non-frequent deceiving would lead to greater neural activation than telling the truth, while frequent deceiving would not have such a pattern. These results suggested that fNIRS has the ability to detect deception under different situations.

ACKNOWLEDGMENT

This work was supported by Guangdong Innovative Research Team Program (No. 2010 01D0104799 318), the Natural Science Foundation of Guangdong province (2014A030310502).

REFERENCES

1. Leff, D. R., F. Orihuela-Espina, C. E. Elwell, et al., "Assessment of the cerebral cortex during motor task behaviours in adults: A systematic review of functional near infrared spectroscopy (fNIRS) studies," *Neuroimage*, Vol. 54, No. 4, 2922–2936, 2011.
2. Pouliot, P., T. P. Y. Tran, V. Birca, et al., "Hemodynamic changes during posterior epilepsies: An EEG-fNIRS study," *Epilepsy Research*, Vol. 108, No. 5, 883–890, 2014.
3. Elwell, C., "Shedding light on brain development," *NIR News*, Vol. 25, No. 8, 25–27, 2014.
4. Gálvez-Cerón, A., E. Serrano, J. Bartolomé, et al., "Predicting seasonal and spatial variations in diet quality of Pyrenean chamois (*Rupicapra pyrenaica pyrenaica*) using near infrared reflectance spectroscopy," *European Journal of Wildlife Research*, Vol. 59, No. 1, 115–121, 2013.
5. Zhu, H., Y. Fan, H. Guo, et al., "Reduced interhemispheric functional connectivity of children with autism spectrum disorder: Evidence from functional near infrared spectroscopy studies," *Biomedical Optics Express*, Vol. 5, No. 4, 1262–1274, 2014.
6. Vartanian, O., P. J. Kwantes, D. R. Mandel, et al., "Right inferior frontal gyrus activation as a neural marker of successful lying," *Frontiers in Human Neuroscience*, Vol. 7, 616, 2013.
7. Sai, L., X. Zhou, X. P. Ding, et al., "Detecting concealed information using functional near-infrared spectroscopy," *Brain Topography*, Vol. 27, No. 5, 652–662, 2014.
8. Ding, X. P., X. Gao, G. Fu, et al., "Neural correlates of spontaneous deception: A functional near-infrared spectroscopy (fNIRS) study," *Neuropsychologia*, Vol. 51, No. 4, 704–712, 2013.
9. Verschuere, B., A. Spruyt, E. H. Meijer, et al., "The ease of lying," *Consciousness and Cognition*, Vol. 20, No. 3, 908–911, 2011.
10. Greene, J. D. and J. M. Paxton, "Patterns of neural activity associated with honest and dishonest moral decisions," *Proceedings of the National Academy of Sciences*, Vol. 106, No. 30, 12506–12511, 2009.
11. Jiang, W., H. Liu, J. Liao, et al., "A functional MRI study of deception among offenders with antisocial personality disorders," *Neuroscience*, Vol. 244, 90–98, 2013.
12. Marchewka, A., K. Jednorog, M. Falkiewicz, et al., "Sex, lies and fMRI — Gender differences in neural basis of deception," *PloS One*, Vol. 7, No. 8, e43076, 2012.
13. Ganis, G., R. R. Morris, and S. M. Kosslyn, "Neural processes underlying self-and other-related lies: An individual difference approach using fMRI," *Social Neuroscience*, Vol. 4, No. 6, 539–553, 2009.
14. Koessler, L., L. Maillard, A. Benhadid, et al., "Automated cortical projection of EEG sensors: Anatomical correlation via the international 10-10 system," *Neuroimage*, Vol. 46, No. 1, 64–72, 2009.
15. Tak, S., S. J. Yoon, J. Jang, et al., "Quantitative analysis of hemodynamic and metabolic changes in subcortical vascular dementia using simultaneous near-infrared spectroscopy and fMRI measurements," *Neuroimage*, Vol. 55, No. 1, 176–184, 2011.
16. Ding, X. P., L. Sai, G. Fu, et al., "Neural correlates of second-order verbal deception: A functional near-infrared spectroscopy (fNIRS) study," *Neuroimage*, Vol. 87, 505–514, 2014.

Light Moves Macro-objects

D. E. Lucchetta¹, F. Simoni¹, L. Nucara^{2,3}, and R. Castagna¹

¹Dipartimento SIMAU, Università Politecnica delle Marche, Via Brecce Bianche, Ancona 60131, Italy

²The BioRobotics Institute, Scuola Superiore Sant'Anna
Viale Rinaldo Piaggio 34, Pontedera, PI 56025, Italy

³Center for Micro-BioRobotics@SSSA, Istituto Italiano di Tecnologia
Viale Rinaldo Piaggio 34, Pontedera, PI 56025, Italy

Abstract— Photons energy can be conventionally converted into mechanical work through a series of energy expensive steps. It has been shown how some of these steps can be bypassed obtaining a direct conversion of photons energy into mechanical work. The most common way consists of using light in the visible or near infrared to move small objects floating on fluid surfaces exploiting the Marangoni effect. In this work we use a low power visible light source to induce a thermal surface tension gradient thus moving a floating object on a fluid surface. By real time tracking of the object trajectory we can determine some physical properties related to the floating object and to the supporting fluid. Moreover from the experimental data fitting we can evaluate the applied driving force due to light irradiation and object heating. In addition we show how even transparent object can be moved by light when the supporting fluid is properly doped.

In order to study the light induced motion of small objects on fluids [1–5] we performed a series of experiments by using an experimental setup based on an Argon Ion cw laser impinging on a small cork disc floating on three different fluids: water, ethanol and a solution of ethanol and an azo-dye whose absorption spectrum is centered around the blue wavelength of $\lambda = 476.5$ nm used to irradiate the cork. Fig. 1 shows the steps of the irradiation process at different time intervals when a small cork disk, whose diameter is 5 mm thickness 2 mm and mass $m = 0.058$ g, floats on ethanol. As it is shown in Fig. 1(a), at the beginning of irradiation the cork disc is partially heated by light in order to induce the thermal gradient necessary to its motion. Indeed, with a uniform irradiation the object will not move along any particular direction because a thermal gradient cannot be established. After 1.5 seconds of irradiation (corresponding to Fig. 1(b)), the object motion starts along the direction defined by the induced gradient. The effect of irradiation becomes negligible when the object moves outside the light beam; after that a deceleration process occurs until the motion stops in about 6 seconds from the beginning of the irradiation. A typical object's displacement vs. time is shown in Fig. 2.

The object motion along the x direction can be described by the following equation:

$$\left(\frac{d^2x}{dt^2}\right) + \frac{D}{m} \left(\frac{dx}{dt}\right)^2 - \frac{\langle F \rangle}{m} = 0 \quad (1)$$

where $\langle F \rangle$ is the average force due to light irradiation and D is defined by $D = 1/2\rho SC_D$, being ρ the density of the solution, S the displaced area and C_D the drag coefficient. When the heating effect prevails on the dissipative term the object velocity increases until a maximum value is reached. At this location the acceleration is zero and there is an equilibrium between the two forces. After that the motion slows down and stops. By neglecting the driving force when the object is out of the light beam we can drop this term for the second part of motion and write:

$$\left(\frac{d^2x}{dt^2}\right) + \frac{D}{m} \left(\frac{dx}{dt}\right)^2 = 0 \quad (2)$$

Which can be easily solved and gives:

$$x = x_0 + \frac{m}{D} \ln \left(1 + \frac{Dv_0}{m} (t - t_0) \right) \quad (3)$$

Equation (3) can be successfully used to fit the experimental data concerning the deceleration process. As an example in Fig. 2 it is reported as dashed line the data fit made by using $D =$

0.04 g/cm and $v = 0.5$ cm/s. Once D is known the drag coefficient or the density of the solution can be easily calculated. Also the value of D derived from the experimental data fit can be used in Eq. (1) to determine the average value of F_l by fitting the first part of the curve using the solution of Eq. (1):

$$x = x_0 + \frac{m}{D} \log \left(\cosh \left(\sqrt{\frac{\langle F_l \rangle D}{m}} (t - t_0) \right) \right) \quad (4)$$

The fit reported in the inset of Fig. 2 allows evaluating $\langle F_l \rangle = 0.5$ mN. This value is compatible with an induced temperature gradient of about 1.5°C , see Fig. 3, measured when the cork sample is replaced by a PT100 resistance temperature detector.

As can be seen from the Fig. 3, after the start of irradiation the temperature change in ethanol reaches quickly the maximum value of $\Delta T = 1.5^\circ\text{C}$ where as in other fluids such as water it takes

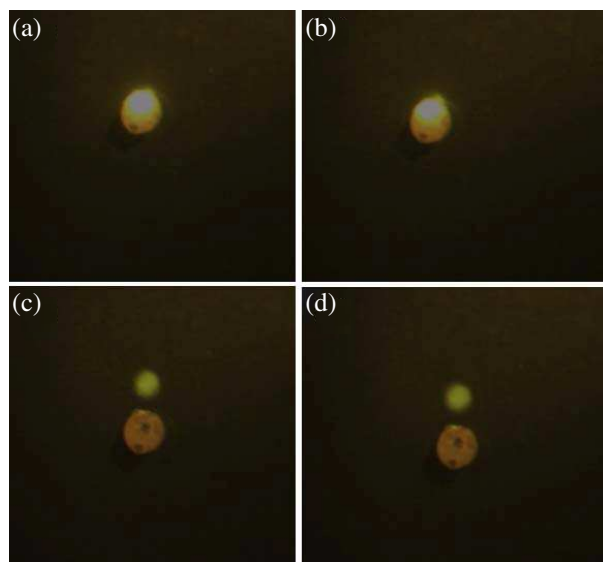


Figure 1: Position of a cork disc floating on ethanol after (a) 1.0, (b) 1.5, (c) 5.0 and (d) 6.0 seconds from the start of laser irradiation (power $P = 300$ mW, $\lambda = 476.5$ nm, spot diameter $d = 3$ mm).

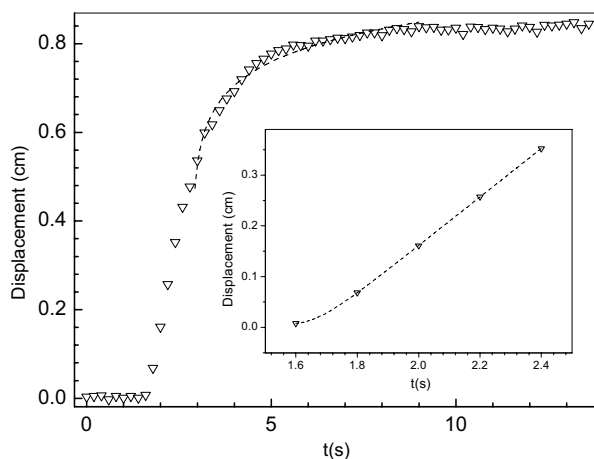


Figure 2: Typical object's displacement vs time. The dashed line represents the data fit of the deceleration process using $D = 0.04$ and $v = 0.5$ cm/s. The inset shows the data fit related to the initial part of motion using Eq. (4).

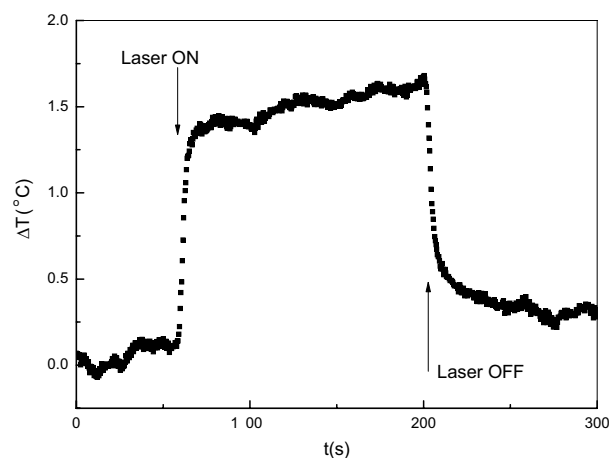


Figure 3: Induced temperature change in ethanol as function of the irradiation time measured using a PT100 thermocouple placed near the upper liquid surfaces. The irradiation power is 300 mW at $\lambda = 476.5$ nm.

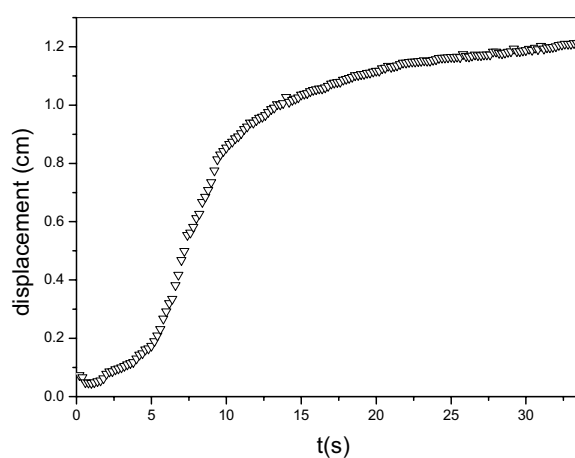


Figure 4: Sample displacement in ethanol doped with an azo-dye. The laser spot is 2 mm far from the cork disc.

a much longer time to get a comparable change. These results can be explained taking into account the different specific heat capacities of the two fluids. How this different physical behavior reflects on the motion of the floating object is still under investigation. It is worth remarking how by doping the ethanol with a proper azo-dye able to absorb part of the irradiated energy the object can be slowly moved even in a no contact mode. Acting this way transparent objects can be moved on floating liquids as shown in the preliminary results in Fig. 4.

REFERENCES

1. Marangoni, C., “Sul principio della viscosità superficiale dei liquidi stabili,” *Il Nuovo Cimento*, Ser. 2, 5/6, 239–273, 1872.
2. Okawa, D., S. J. Pastine, A. Zettl, and J. M. J. Fréchet, “Surface tension mediated conversion of light to work,” *J. Am. Chem. Soc.*, Vol. 131, 5396–5398, 2009.
3. Florea, L., K. Wagner, P. Wagner, G. G. Wallace, F. Benito-Lopez, D. L. Officer, and D. Diamond, “Photo-chemopropulsion-light-stimulated movement of microdroplets,” *Adv. Mat.*, Vol. 19, 7339–7345, 2014.
4. Diguët, A., R.-M. Guillemic, N. Magome, A. Saint-Jalmes, Y. Chen, K. Yoshikawa, and D. Baigl, “Photomanipulation of a droplet by the chromocapillary effect,” *Angew. Chem. Int. Ed.*, Vol. 48, 9281–9284, 2009.
5. Diguët, A., et al., “Photomanipulation of a droplet by the chromocapillary effect,” *Angew. Chem. Int. Ed.*, Vol. 48, 9281–9284, 2009.

Fabrication of a Nanoscale Plasmonic Fishnet Structure for the Enhancement of Absorption in Thin Film Solar Cells

Sayan Seal, Vinay Budhraja, Liming Ji, and Vasundara V. Varadan

Department of Electrical Engineering, University of Arkansas, USA

Abstract— Incorporating plasmonic structures in the back spacer layer of thin film solar cells (TFSC's) is an efficient way to increase the yield. The plasmonic fishnet structure is one such geometry using which this effect can be realized. Numerical simulations have shown the ability of these structures to bring about an enhancement in the short circuit current density of TFSCs at specific wavelengths. We show that light absorption in the a-Si absorber layer is enhanced by a factor of 10.6 at the design wavelength of 690 nm due to the presence of the fishnet structure. Furthermore, the total absorption over all wavelengths was increased by a factor of 3.2. The short circuit current density of the TFSC was increased by 30% as a result of including the fishnet.

This paper presents the fabrication process of the fishnet structure. A fishnet structure made of silver was fabricated using a combination of electron beam lithography and thermal evaporation. A complete TFSC was fabricated using PECVD to deposit a-Si on the fishnet structure. In effect, the fishnet was placed in the back spacer layer preventing shadowing effects. The final structure optically resembled a TFSC in all respects except that there were no doped layers. The fishnet structure is essentially a mesh of linewidth 100 nm, and a thickness of 20 nm.

1. INTRODUCTION

Solar cells are among the most widely researched form of renewables in the world today. What makes solar cells and renewables in general, attractive is the fact that it is a one-time investment. However, there is also good reason why solar cells are not preferred over fossil fuel based solutions despite their obvious advantages. The reason is that the efficiency of solar cells does not compare to conventional energy sources. Hence the cost per watt of solar cell technology is far from competitive as it stands today. One plausible option to reduce the cost per watt figure is to use less material for the active region of the solar cell. In fact, the cost of silicon (Si), the most prevalent material used in wafer solar cells today, constitutes a majority of the cost of production [1, 2].

However, reducing the amount of material in the active region would automatically reduce efficiency further — this is because the probability of absorption of an incoming photon reduces drastically as the volume of material decreases. If a suitable method can be devised to ensure that the absorption within a smaller volume of material is comparable to that within a comparatively thicker wafer, the overall production costs may be greatly reduced. Thin Film Solar Cells (TFSCs) offer such a solution. Instead of expensive crystalline Si wafers, these cells use cheap, vapor-deposited amorphous Si (a-Si) as the active material. The principle of making this thin layer of a-Si (usually only a fraction of the wafer thickness of wafer-based cells) appear optically comparable to a Si wafer is simple to understand. Multiple reflections are induced within the thin film, so that the effective path length of an incoming photon is increased within the active material. This is achieved by scattering the incoming light (photons) at the back surface of the active layer, giving rise to diffuse reflections and enhancing the optical path of the photon within the absorber layer.

Several solutions for achieving this back-surface scattering have been offered in the form of nanodomes [3, 4], blazed gratings [5], and incorporating plasmonic nanoparticles in the spacer layers [6–8]. Of the aforementioned solutions, the embedding of nanoparticles to achieve enhanced scattering has been the subject of greatest interest and debate. To begin with, they are easy to process, and offer significant increase on absorption with a minimal increase in volume.

However, plasmonic nanoparticles do offer advantages with one major drawback — they resonate only at specific frequencies dictated by the size and distribution of nanoparticles. A better solution would be one that has all the benefits offered by a plasmonic back-surface design, but without the frequency limitation. The plasmonic fishnet structure proposed by Ji and Varadan [9] offers precisely that. A metallic fishnet at the back spacer layer of a TFSC was predicted to cause an enhancement in the useful absorption within the active layer. It must be noted that the entire enhancement in absorption as a result of employing plasmonic structures does not necessarily translate to the generation of an EHP which will lead to subsequent increase in the current output from the cell. A large percentage of the absorbed energy is dissipated as loss in the nanoparticles.

It was demonstrated that for a plasmonic fishnet structure, the loss in the fishnet was negligible, and most of the scattered radiation was absorbed by the active region of the solar cell.

However, the fishnet TFSC was a theoretical concept. Despite its advantages, the major barrier standing in the way of this theory becoming a commercial solar cell was the fabrication process for the super fine metallic fishnet. The subject of this paper is the design of a reliable and repeatable process for the fabrication of a metallic fishnet, designed to resonate around a wavelength of 700 nm.

2. MATERIALS AND METHODS

Figure 1 shows a schematic that outlines the various steps required to fabricate a fishnet solar cell. The inset figure shows a schematic of the complete TFSC structure. The design of the fishnet corresponded to a plasmonic resonance at 700 nm, since the goal was to optimize the absorption in this wavelength range. This is because the absorption of a-Si, the material of choice for the active region of the cell, has very low absorption near this wavelength. The line width of the optimized fishnet was 100 nm, spaced 600 nm apart, and 20 nm thick.

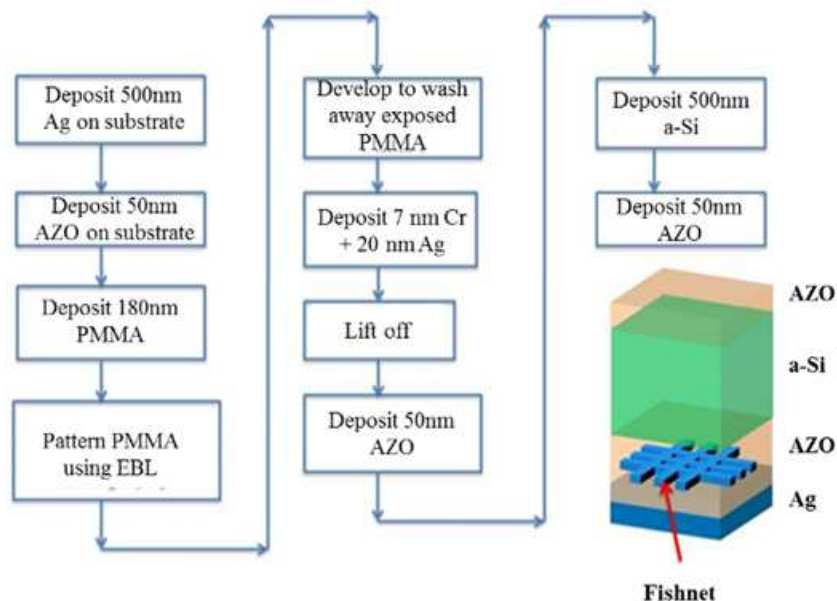


Figure 1: Schematic showing the fabrication process for the fishnet thin film solar cell.

The most involved step in the fabrication process is Electron Beam Lithography — the process that allows us to literally draw the fishnet pattern onto a substrate. The JBX 550ZD system from JEOL was used for this purpose. Obtaining a successful pattern is a combination of the resist thickness, electron dose and development time. Prior to lithography, the substrate was coated with an electron beam sensitive resist, Poly-Methyl-Methacrylate (PMMA). Ideally the resist layer should be made as thin as possible. This would allow us to use a smaller electron dose and enable us to write patterns with very small line widths, but thick enough so that the lift-off process would not be inhibited. After this step, the sample has to be dipped in acetone to dissolve the remaining PMMA, thus getting rid of the metal layer above the PMMA, as if we “lift off” the metal. The resist thickness was chosen to be around 180 nm for this design. The spin speed was chosen as 4000 rpm from the spin speed curves for 4% PMMA provided by MicroChem.

The thickness of the resist layer was measured to be around 180 nm averaged over ten measurements across randomly chosen points on the sample surface. Once the proper resist thickness was determined, the Electron Beam Lithography (EBL) process followed. The principle of EBL is in similar to photolithography in many respects. The surface of the substrate was spin coated with an electron sensitive resist. A controlled electron beam then engraved the pattern onto this resist. No mask was required like in photolithography.

The number of electrons incident on the resist per square cm is defined as the dose. It is measured in $\mu\text{C}/\text{cm}^2$. This dose was optimized for this particular design. For the fishnet structure was varied from $500 \mu\text{C}/\text{cm}^2$ to $800 \mu\text{C}/\text{cm}^2$. The best results were obtained for a dose of $800 \mu\text{C}/\text{cm}^2$. After the writing process was completed, the sample was developed using a solution of MIBK : IPA (1 : 3).

The final development time for a 1 mm \times 1 mm fishnet pattern was 25 seconds. After development there was a fishnet shaped groove in the PMMA layer. The sample was washed using IPA for 30 seconds to remove any residual developer within the grooves and the sample was blown dry using nitrogen. Following this, the resist was baked at 100°C on a hot plate for 60 seconds. This rid the sample surface of moisture or organic residues, and made the PMMA columns structurally more rigid.

The next step was to evaporate metal onto the grooves to obtain a metallic fishnet structure on the substrate. The sample was loaded onto a thermal evaporator. According to design specifications, the thickness of the fishnet should be 20 nm, but it was found that thin films of silver had issues adhering to the AZO surface. So a 7 nm layer of chromium was used below the silver layer to promote adhesion. Once evaporation was completed a lift off had to be performed, followed by the deposition of the final layers of a-Si and AZO.

3. RESULTS AND DISCUSSIONS

The theoretically optimized design for the silver fishnet structure had a linewidth of 100 nm. Fig. 2 shows the result obtained in the first trial. A dose of 1000 $\mu\text{C}/\text{cm}^2$ was used initially and the fishnet was patterned on a 180 nm thick layer of resist. The development time was varied between 35 seconds and 30 seconds.

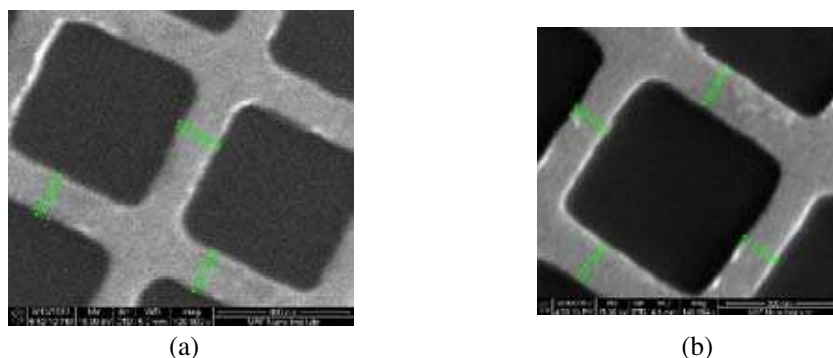


Figure 2: Optimization of development time. (a) Development time = 35 seconds. (b) Development time = 30 seconds.

A development time of 35 seconds worked best giving a linewidth of 115 nm. However the linewidth was not uniform over the entire pattern and varied between 108 nm to 123 nm. 30 seconds gave narrower linewidths overall, but regions around the corners showed signs of underdevelopment. The linewidth obtained was still around 115 nm, but there was much more consistency in the linewidth than before.

A dose optimization was performed next to get close to a 100 nm line width. Keeping the development time constant at 30 seconds, the dose was changed from 500 $\mu\text{C}/\text{cm}^2$ to 800 $\mu\text{C}/\text{cm}^2$ in steps of 100 $\mu\text{C}/\text{cm}^2$. From the results [Fig. 3], it can be observed that a dose of 800 $\mu\text{C}/\text{cm}^2$ gave an average linewidth of about 105 nm. Using a dose smaller than this resulted in underexposure.

It was expected that using a marginally shorter development time could give us a perfect 100 nm linewidth. The best results were obtained using a development time of 25 seconds [Fig. 4]. The

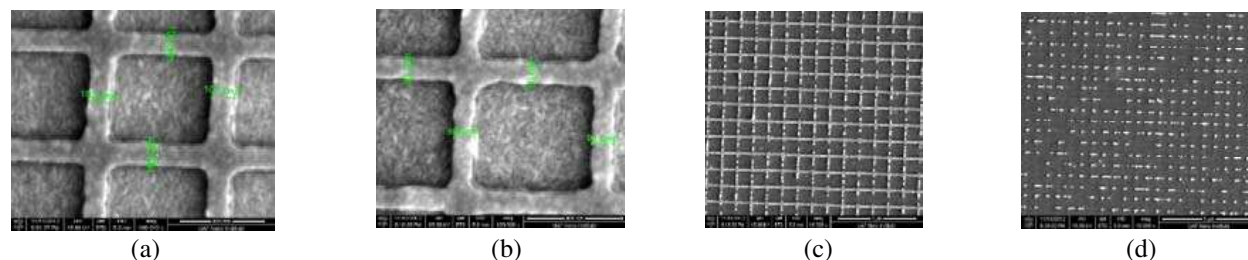


Figure 3: Final dose optimization step at: (a) Dose = 800 $\mu\text{C}/\text{cm}^2$; (b) Dose = 700 $\mu\text{C}/\text{cm}^2$; (c) Dose = 600 $\mu\text{C}/\text{cm}^2$; (d) Dose = 500 $\mu\text{C}/\text{cm}^2$.

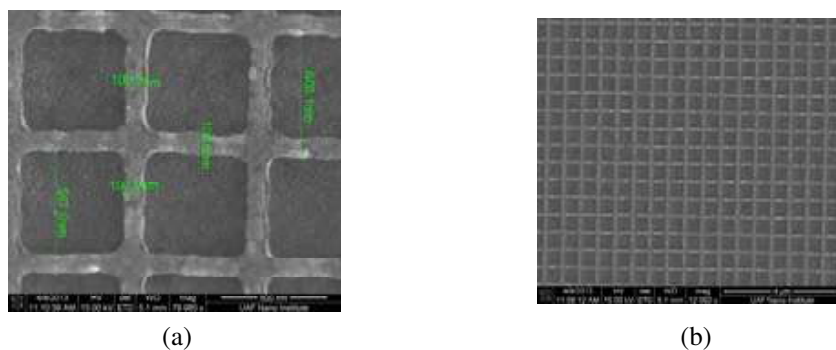


Figure 4: 100 nm linewidth pattern using a dose of $800 \mu\text{C}/\text{cm}^2$, design linewidth of 85 nm, and develop time of 25 seconds. (a) Linewidth = 100 nm. (b) Pattern uniform over whole area.

linewidth was found to be uniformly 100 nm at the center of the pattern as well as the corners, with proper lift off across the entire patterned area. Also a consistent pitch size of 598 nm was obtained.

The above recipe was repeated on at least eight fishnets to make sure that a repeatable and reliable fabrication process was developed. The SEM showed the same 100 nm linewidth for all samples that were fabricated using the above recipe. Following the fabrication of the fishnet, the rest of the steps in Fig. 1 had to be completed to obtain a complete thin film solar cell structure. 50 nm of AZO was deposited using DC sputtering, followed by 500 nm a-Si using PECVD. The 50 nm AZO front spacer was deposited using DC sputtering as well. Thus the fabricated structure optically resembled a thin film solar cell in all respects. Fig. 5 shows that the absorption increased by a factor of $12.8\times$ at the design wavelength of 700 nm as a result of including the fishnet.

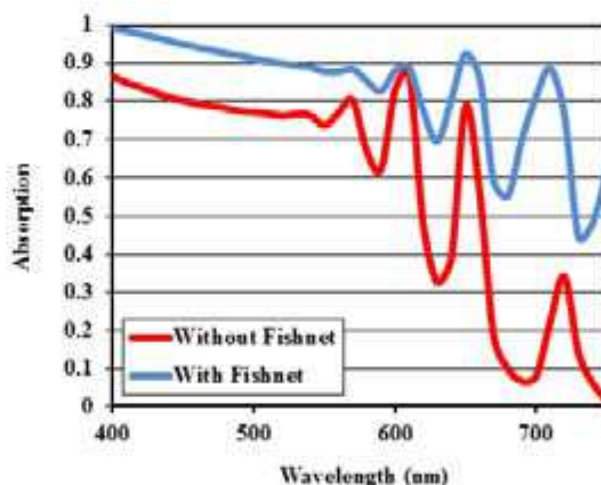


Figure 5: Experimental results showing a $12.8\times$ enhancement in the absorption.

4. CONCLUSIONS

A reliable and repeatable process for the fabrication of a fishnet TFSC was established. The process allows for a clean pattern, tailored to meet the specifications of the solar cell. The key to the successful fabrication of this structure involved an appropriate combination of resist thickness, exposure dose, and development time. Measurements taken on the fabricated cell showed a $12.8\times$ increase in the absorption of the solar cell, which predicted a 30% increase in the J_{SC} .

ACKNOWLEDGMENT

The authors acknowledge the research support provided by the National Science Foundation under EPS-1003970. We also acknowledge the collaboration with Dr. J. Cui, University of Arkansas at Little Rock, for AZO deposition.

REFERENCES

1. Mints, P. and J. Donnelly, "Photovoltaic manufacturer shipments, capacity and competitive analysis 2010/2011," *Navigant Solar Services Program*, Palo Alto, CA, 2011.
2. Goodrich, A., T. James, and M. Woodhouse, "Solar PV manufacturing cost analysis: U.S. competitiveness in a global industry," available on NREL website: <http://www.nrel.gov/docs/fy12osti/53938.pdf>.
3. Zhu, J., C. M. Hsu, Z. Yu, S. Fan, and Y. Cui, "Nanodome solar cells with efficient light management and self-cleaning," *Nano Lett.*, Vol. 10, 1979–1984, 2010.
4. Nam, W. J., L. Ji, T. L. Benanti, V. V. Varadan, S. Wagner, Q. Wang, W. Nemeth, D. Neidich, and S. J. Fonash, "Incorporation of a light and carrier collection management nanoelement array into superstrate a-Si:H solar cells," *Appl. Phys. Lett.*, Vol. 99, No. 073113, 2011.
5. Heine, C. and R. H. Morf, "Submicrometer gratings for solar energy applications," *Applied Optics*, Vol. 34, No. 14, 2476–2482, 1995.
6. Ferry, V. E., M. A. Verschuuren, H. B. T. Li, E. Verhagen, R. J. Walters, R. E. I. Schropp, H. A. Atwater, and A. Polman, "Light trapping in ultrathin plasmonic solar cells," *Optics Express*, Vol. 18, No. S2, A237–A245, 2010.
7. Ferry, V. E., L. A. Sweatlock, D. Pacifici, and H. A. Atwater, "Plasmonic nanostructure design for efficient light coupling into solar cells," *Nano Lett.*, Vol. 8, No. 12, 4391–4397, 2008.
8. Bhattacharya, J., N. Chakravarty, S. Pattnaik, W. Dennis Slafer, R. Biswas, and V. L. Dalal, "A photonic-plasmonic structure for enhancing light absorption in thin filmsolar cells," *Appl. Phys. Lett.*, Vol. 99, 131114, 2011, doi: 10.1063/1.3641469.
9. Ji, L. and V. V. Varadan, "Fishnet metastructure for efficiency enhancement of a thin film solar cell," *Journal of Applied Physics*, Vol. 110, 043114, 2011.

Spontaneous Formation of Square Optical Vortex Lattice in a Transverse Section of Broad-area Laser

A. A. Krents^{1,2}, A. V. Pakhomov^{1,2}, D. A. Anchikov¹, and N. E. Molevich^{1,2}

¹Samara State Aerospace University, Samara 443086, Russia

²Lebedev Physical Institute, Samara 443011, Russia

Abstract— The square vortex lattice is studied using the full Maxwell-Bloch system. Properties and conditions of formation stationary and nonstationary lattices are investigated. The frequency of vortex oscillations and necessary conditions for these oscillations are obtained.

1. INTRODUCTION

The paper studies the spontaneous formation of square optical vortex lattice (SVL) in broad-area lasers theoretically. The possible motion of vortices is also studied. The nonlinear interaction of numerous transverse modes in broad-area lasers can lead to the spontaneous formation of complex spatiotemporal optical structures including the SVL. The SVL is experimentally observed in the Nd:YVO₄ laser [1–3], in a broad-area CO₂ laser operating at a single longitudinal mode [4], in the solid-state laser with optical pumping on a chip LiNdP₄O₁₂[5], in a Na₂ laser [6], in the vertical cavity surface emitting laser [7].

2. BASIC EQUATIONS

We studied the formation of SVL both analytically and numerically using the full Maxwell-Bloch model:

$$dE/dt = \sigma(P - E) + ia\Delta E; dP/dt = -(1 + i\delta)P + DE; dD/dt = -\gamma[D - r + 0.5(E^*P + EP^*)], \quad (1)$$

where Δ is the transverse two-dimensional Laplace operator, E , P are, respectively, the dimensionless electric field and polarization amplitudes, D is the dimensionless population inversion. σ , γ are the dimensionless electric field and inversion decay rates, respectively, r is the pump parameter, δ is the detuning.

3. TRAVELLING WAVE SOLUTION

The simplest solution of Equations (1) is travelling wave solution [8]:

$$E = E_0 \exp(i\vec{k}\vec{r} - i\Omega t), P = P_0 \exp(i\vec{k}\vec{r} - i\Omega t), D = D_0, \quad (2)$$

where $E_0 = \sqrt{r - D_0}$, $P_0 = \frac{(\sigma + i(-\Omega + ak^2))}{\sigma} E_0$, $\Omega = \frac{\delta\sigma + ak^2}{\sigma + 1}$, $D_0 = 1 + \left(\frac{\delta - ak^2}{\sigma + 1}\right)^2$.

Here, \vec{k} is the transverse component of radiation wave vector. In case $\delta \leq 0$, the most attracting solution is the steady-state solution (travelling wave with $k = 0$), which corresponds to the radiation along the optical axis of the resonator. If $\delta > 0$, the travelling wave with $k = \sqrt{\frac{\delta}{a}} \equiv k_0$ is the most attracting solution, which corresponds to the radiation with some small angle to the optical axis. In this paper, we consider the case $\delta > 0$. Then, solution (2) has the form:

$$E = P = \sqrt{r - 1} \exp(i\vec{k}_0\vec{r} - i\delta t), \quad D = 1 \quad (3)$$

4. SQUARE VORTEX LATTICE SOLUTION

Transverse plane (x, y) is isotropic. The direction of vector \vec{k}_0 is arbitrary. A solution in form of superposition of traveling waves of form (3) is possible. In broad-area lasers, the square vortex lattice is observed as a result of four waves nonlinear interaction. Let us find the solution of Equation (1)

in the form of superposition of four waves:

$$E(t, r) = \sum_{j=1}^4 E_j(t) \exp\left(i\left(\vec{k}_j \vec{r} - \delta t\right)\right), \quad P(t, r) = \sum_{j=1}^4 P_j(t) \exp\left(i\left(\vec{k}_j \vec{r} - \delta t\right)\right), \quad (4)$$

$$D(t, r) = D_0 + \sum_{j=1}^4 d_{j,j}(t) \exp\left(2i\vec{k}_j \vec{r}\right) + \sum_{j=1}^4 d_{j,j+1}(t) \exp\left(i\left(\vec{k}_j + \vec{k}_{j+1}\right) \vec{r}\right),$$

where $\vec{k}_1 \uparrow \downarrow \vec{k}_2$, $\vec{k}_3 \uparrow \downarrow \vec{k}_4$, $\vec{k}_1 \perp \vec{k}_3$, $j = 1, 2, 3, 4, 1, 2, \dots$

After substituting (4) in original system (1) and taking into account only the lowest-order harmonics, original system (1) is reduced to the system of ordinary differential equations describing interaction of four waves:

$$\begin{aligned} \partial_t E_j &= \sigma (P_j - E_j) \\ \partial_t P_j &= -P_j + D_0 E_j + E_{j+1} d_{j,j} + E_{j+2} d_{j,j+3} + E_{j+3} d_{j,j+1} \\ \partial_t D_0 &= -\gamma \left[D_0 - r + \frac{1}{2} \sum_{j=1}^4 (E_j^* P_j + E_j P_j^*) \right] \\ \partial_t d_{j,j} &= -\gamma \left[d_{j,j} + \frac{1}{2} (E_j^* P_{j+2} + E_{j+2} P_j^*) \right] \\ \partial_t d_{j,j+1} &= -\gamma \left[d_{j,j+1} + \frac{1}{2} (E_j P_{j+3}^* + E_{j+1} P_{j+2}^* + E_{j+2}^* P_{j+1} + E_{j+3}^* P_j) \right] \end{aligned} \quad (5)$$

System (5) has several equilibrium points. Each equilibrium point matches different spatiotemporal structures: single travelling wave, standing wave or SVL. The SVL solution has a form:

$$|E_j|^2 = |P_j|^2 = \frac{r-1}{5}, \quad D_0 = 1 + \frac{r-1}{5}, \quad d_{j,j} = \frac{1-r}{5} \exp(i(\phi_j - \phi_{j+2})), \quad d_{j,j+1} = 0 \quad (6)$$

$$(\phi_1 + \phi_3) - (\phi_2 + \phi_4) = \pi \quad (7)$$

The SVL is the result of interference of four travelling waves with the phase condition (7). The SVL consists of first order optical vortices. Moreover, the SVL solution is stable for the pump parameter r near the threshold value $r \geq r_{th}$. Distance between neighboring vortices could be founded:

$$\lambda_{SVL} = \pi \sqrt{a/\delta} \quad (8)$$

5. NUMERICAL SIMULATION

For numerical simulation of Equation (1), we used the split step Fourier method. Random initial conditions were used. For $\delta > 0$, the nonstationary process of SVL formation was observed beginning with the appearance of numerous random vortices. In sufficiently long time, they occupy the stationary positions and form the ordered structure — SVL (Figs. 1(a), (b)). Relation (8) is in a good agreement with our numerical results. For $r \approx r_{th}$, the SVL is stationary. In the far field, we obtain four bright spots corresponding to four travelling waves (Fig. 1(c)).

The SVL becomes unstable with increase of $r > r_{cr}$. The critical value of pump $r = r_{cr}$ depends on parameters of model (1). In this case, the motion of vortices around equilibrium points is observed (Figs. 2(a), (b)). In the far field, we obtain eight bright spots (Fig. 2(c)).

The radius R of the vortex trajectory depends on the pump value $R \sim \sqrt{r - r_{cr}}$. This type of stability loss is close to the supercritical Hopf bifurcation.

6. ANALYTICAL DESCRIPTION OF OSCILLATIONS IN VORTEX LATTICE

Eight bright spots in the far field (Fig. 2(c)) correspond to two square vortex lattices. As we can see in Fig. 2(c), the secondary SVL have a wavenumber $k = \sqrt{2}k_0$. Using relations (2) and (4), we can find the secondary SVL solution in the analogous form. Superposition of two SVL with different wave numbers $k = k_0$ and $k = \sqrt{2}k_0$ and appropriate different frequencies gives the oscillating SVL. A frequency of these oscillations was calculated from (2):

$$\omega = \delta / (\sigma + 1) \quad (9)$$

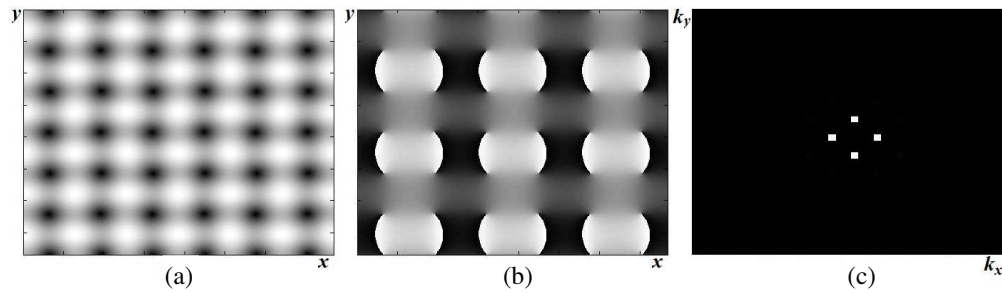


Figure 1: Stationary square vortex lattice: (a) intensity distribution, (b) phase distribution and (c) far field. Here, x , y are transverse coordinates and k_x , k_y are appropriate wave numbers.

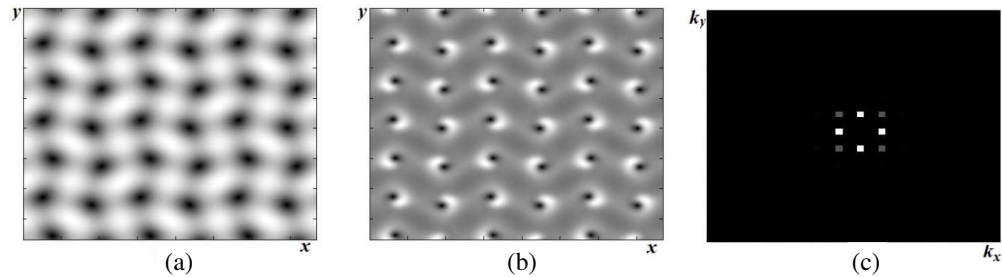


Figure 2: Stationary square vortex lattice: (a) intensity distribution, (b) $|P(x, y)|$ and (c) far field.

This formula is in a very good agreement with our numerical results. Also from (2) we obtained the necessary condition for the existence of these two square vortex lattices: $r \geq 1 + \omega^2$. The vortex motion is observed only if this condition is satisfied.

7. CONCLUSION

We studied the formation of SVL both analytically and numerically using the full Maxwell-Bloch model. The single travelling wave solution was investigated. Interaction of four travelling waves was investigated as well. The square vortex lattice solution was obtained analytically. A distance between neighboring vortices were found analytically. The split step Fourier method was used for numerical simulation of Maxwell-Bloch equations. Formation of SVL was observed numerically. For $r \approx r_{th}$, the SVL is stationary. The SVL becomes unstable with increase of $r > r_{cr}$. In this case, the motion of vortices around equilibrium points is observed. In the far field, we obtain eight bright spots. Eight bright spots in the far field correspond to two square vortex lattices. This simple idea allows us to calculate the frequency of vortex oscillations. Also we obtained the necessary condition for the existence of these two square vortex lattices.

ACKNOWLEDGMENT

The study was supported in part by the Ministry of education and science of Russia under Competitiveness Enhancement Program of SSAU for 2013-2020 years and by State assignment to educational and research institutions under projects 1451, GR 114091840046, by RFBR under grant 14-02-31419 mol_a.

REFERENCES

1. Chen, Y. F. and Y. Lan, "Spontaneous transverse pattern formation in a microchip laser excited by a doughnut pump profile," *Appl. Phys. B.*, Vol. 75, 453–456, 2002.
2. Chen, Y. F. and Y. Lan, "Formation of optical vortex lattices in solid-state microchip lasers: Spontaneous transverse mode locking," *Physical Review A.*, Vol. 64, 063807, 2001.
3. Chen, Y. F. and Y. Lan, "Transverse pattern formation of optical vortices in a microchip laser with a large Fresnel number," *Physical Review A*, Vol. 65, 013802, 2001.
4. Louvergneaux, E., D. Hennequin, D. Dangoisse, and P. Glorieux "Transverse mode competition in a CO₂ laser," *Physical Review A*, Vol. 53, 4435–4438, 1996.
5. Otsuka, K. and S. Chu, "Generation of vortex array beams from a thin-slice solid-state laser with shaped wide-aperture laser-diode pumping," *Optics Letters*, Vol. 34, 10–12, 2009.

6. Brambilla, M., F. Battipede, L. A. Lugiato, V. Penna, F. Prati, C. Tamm, and C. O. Weiss, "Transverse laser patterns I. Phase singularity crystals," *Physical Review A*, Vol. 43, 5090–5113, 1991.
7. Scheuer, J. and M. Orenstein, "Optical vortices crystals spontaneous generation in nonlinear semiconductor microcavities," *Science*, Vol. 285, 230–233, 1999.
8. Jacobsen, K., J. V. Moloney, A. C. Newell, and R. Indik, "Space-time dynamics of wide-gain-section lasers," *Physical Review A*, Vol. 45, 2076–2086, 1992.

Thin Film Dielectric Gradient Optical Structures for Space Photonics

O. Volpian¹, A. Kuzmichev², G. Ermakov¹, Yu. Obod¹, N. Silin³, and S. Shkatula¹

¹Scientific-Manufacturing Enterprise “Fotron-Auto Ltd.”, Moscow, Russia

²National Technical University “Kiev Polytechnical Institute”, Kiev, Ukraine

³Far Eastern Federal University, Vladivostok, Russia

Abstract— Characteristics, technological aspects and test results of thin film dielectric gradient optical structures for space and aviation photonics are considered. The perspectives of pulse magnetron sputtering for manufacturing optical structures are shown. The gradient and nanogradient refraction index profiles provide wide-band and wide-angle working spectral characteristics of the systems and their stability against power laser radiation and space environmental factors.

1. INTRODUCTION

Photonics plays an important role in space and aviation technology. It includes devices for optical and laser navigation, detection of objects by their emission, reflection, transmission, or absorption and then their location, tracking, and recognition, etc.. The basis for many devices is interference structures (IS). They typically present themselves as dielectric optical coatings from alternating layers of materials with high n_h and low n_l refractive indexes n . The high level of complexity of tasks solved with space and aviation photonics brings new higher requirements to IS; as an example of such requirements one can point out requirements to spectral characteristics of IS: superwide working wavelength band (e.g., $\lambda = 0.5 \dots 5.0 \mu\text{m}$), simultaneous operation on multiple wavelengths, wide viewing angle, deep modulation of amplitude characteristics (e.g., $R_1 > 99.9\%$, $R_2 < 0.1\%$, and so on, here R is reflectance), high spectral resolution (e.g., $\Delta\lambda_{0.5} < 2 \text{ nm}$ at transmission $T_{0.5} > 0.8$), low optical losses ($1 - T - R < 5 \cdot 10^{-5}$).

The huge challenge is to ensure resistance and spectral characteristics stability of IS over a long time period (up to tens years) against action of space environment factors, including intermittent high-intensity heating and deep cooling, UV radiation, and against factors related to the functioning of spacecraft, in particular, laser radiation with high power density ($W > 10^9 \text{ W/cm}^2$) and plasma. Authors' experience in the design and manufacture of precision optical coatings and lasers assumes that these problems can be solved by use of thin film dielectric optical structures with gradient profiles of refractive indexes n instead of the conventional multilayer IS with an abrupt stepwise changes of the refractive index n_h/n_l and n_l/n_h at the layer boundaries in going from one layer to another [1, 2]. The latter negatively affects mechanical and thermal stability and laser damage resistance. The gradient optical structures have been shown to satisfy the above mentioned requirements to spectral characteristics and provide obtaining different kinds of filters, mirrors, high-contrast polarizers, phase converters and antireflection coatings. However we should know what is resistance of these structure to action of space environmental factors and laser radiation. Therefore, design, technological aspects and test results of thin film dielectric gradient and nanogradient optical structures for space and aviation photonics are considered in the paper.

2. DESIGN OF GRADIENT OPTICAL STRUCTURES

If the permittivity $\varepsilon = \varepsilon(z)$ and, accordingly, the refractive index $n = n(z)$ continuously, gradually distributed by a certain law along the normal axis (thickness) \mathbf{z} of a thin film dielectric optical structure, the latter is called as gradient one with longitudinal $1D_z$ gradient [1], while optics comprising such structure is called as gradient optics. If change of ε or n occurs on the thickness less than 100 nm, such structure is called as nanogradient one. The use of various refractive index profiles $n(z)$ (linear, quadratic, sinusoidal-like, polynomial of fifth degree and others) can improve the amplitude-spectre, angle, polarization, phase characteristics; in particularly, very wide working spectrum band and wide operation angle may be provided. For example, Figure 1 depicts the gradient profile $n(z)$, leading to excellent characteristics of hyperwide-band (0.5–5 μm) gradient antireflection coating for sapphire optical elements at incident angles of 0° , 10° and 25° . Note, the given profile $n(z)$ has not very complex shape.

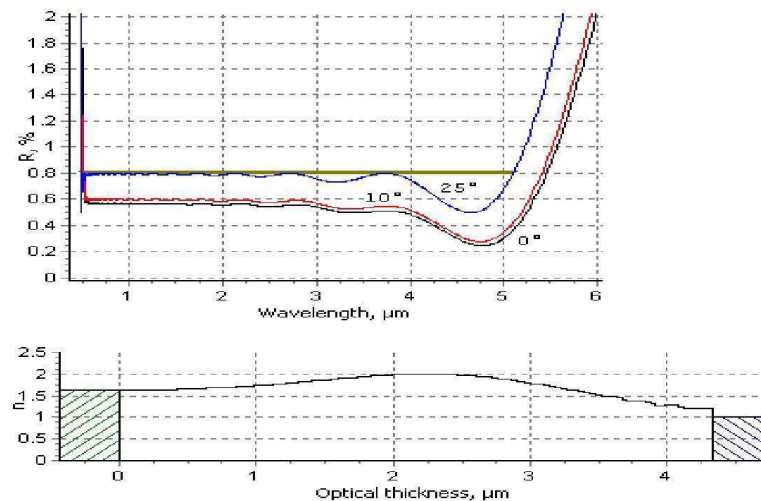


Figure 1: Antireflection feature of the gradient coating at three values of incident angles (upper plot) and its refractive index profile $n(z)$ (lower plot).

For the design of gradient optical structures a new method of analytical and numerical synthesis for given spectrum characteristics has been developed. It is based on a combination of two algorithms: analytical one, using Fourier analysis to determine the gradient construction, and a heuristic algorithm of its searching to solve the problem of optimization. On the basis of the new synthesis method an engineering program for computer simulation of thin film gradient optical structures has been developed.

3. TECHNOLOGICAL ASPECTS OF MANUFACTURING GRADIENT COATINGS

There are different approaches to deposition of thin film dielectric gradient structures. Among them one can point out some known methods: glancing-angle deposition with electron beam evaporation of source materials and plasma-enhanced chemical vapor deposition from gas precursors [3]. The more preferable technique, to our best knowledge, is based on ion sputtering of source materials (targets), especially, ion sputtering in a magnetron discharge allowing deposition of precision optical structures [1–5]. The magnetron discharge is a low pressure gas discharge in crossed electric and magnetic fields where cathode serves as a sputtered target.

Therefore, an automatic two-magnetron sputtering system with computer control and monitoring *in situ* has been developed [1] and successfully employed for obtaining various thin film gradient optical structures with filtering, reflection or antireflection properties. Figure 2 depicts the diagram of magnetron set-up for deposition of longitudinal 1D_z gradient coatings. Magnetrons sputter different materials (M1 — Si; M2 — metals: Nb, Ta, Ti) in atmosphere of reactive gas mixture Ar + O₂. Coordinates X_1 , X_2 and X_3 , algorithm of substrate movement over the magnetrons, and sputtering power of each magnetron determine composition of material deposited on the substrate. The deposited material composition in turn determines the current value of $n(z)$. Ar is used as a sputtering gas. O₂ is used for oxide synthesis from deposited Si and metal on the substrate surface. Oxygen is chemically activated in magnetron discharge plasma as well as in activator A and due to UV laser radiation directed towards the substrate. The mid-frequency pulse mode of magnetron operation is used [1]. The monitoring *in situ* system (spectrovisor) allows to test optically the deposit directly during the fabrication process and to make corrections of operation parameters if it is necessary.

4. TESTING GRADIENT OPTICAL STRUCTURES

Testing the fabricated thin film optical structures was carried out to confirm their comprehensive long time period resistance to intense laser and other kinds of radiation, thermomechanical action (cyclic temperature changes) and other aerospace factors (including vacuum). It was accepted the quick and cheapest way to evaluate the properties of optical structures is acceleration of testing by forcing degradation processes. The accelerated testing was carried out in laboratory conditions simulating the real space situation with use of the method of planning multifactor experiments and

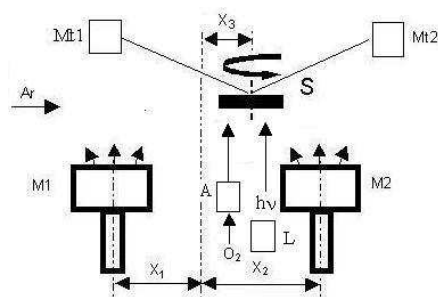


Figure 2: Two-magnetron sputtering system for deposition of thin film gradient structures. A — gas activator (O_2); Ar — sputtering gas; L — UV laser; M1, M2 — magnetron sputters; Mt1, Mt2 — optical parts for monitoring the structures *in situ*; S — rotating the substrate; arrows indicate the direction of sputtered atoms movement.

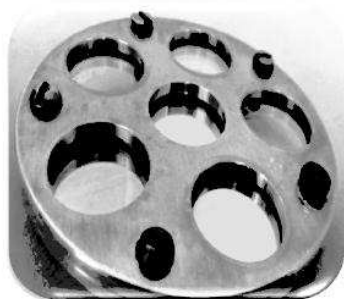


Figure 3: Photograph of specimens with gradient thin film optical structures (disposed on the holder) after thermocycling test.



Figure 4: The fiber optic device with the capsule for fixing the tested specimen inside of the heating-cooling chamber.

models describing the resource dependency on influencing factors.

Consider an example of testing results. The fabricated optical structures are resistant to laser radiation with power density $W > 10^9 \text{ W/cm}^2$ for $\lambda = 1.064 \text{ nm}$, $\tau = 10 \text{ ns}$ and physical thickness of thin film optical structures less than $2 \mu\text{m}$. When the thickness was up to $5 \mu\text{m}$, the structures were resistant to the combined effect of space factors — the combination of thermal cycling ($\Delta t^\circ = -60/+70^\circ\text{C}$, 100 cycles) with UV exposure at power density $W > 100 \text{ W/cm}^2$ for $\lambda = 300 \text{ nm}$.

The quick test on thermomechanical stability of the gradient structures has been developed and performed. To determine the time resource, 3500 cycles of heating and cooling with the coefficient of load increasing $C_{in} =$ were carried out. One cycle included heating up to $+180^\circ\text{C}$ with 5 minutes exposure and cooling down to -190°C (by immersion into liquid nitrogen) with 1 minute exposure. Therefore every cycle created two thermal stocks ($-$ & $+$) for specimens. Thin film adhesion measurements were carried out after every 500 cycles of heating/cooling by the method of “Scotch tape”. Figure 3 shows the appearance of the specimens with thin film structures after 3500 exposure cycles. The 7 years resource on thermomechanical stability of thin film gradient optical structures fabricated with magnetron sputtering has been confirmed. It should be noted that the confirmed resource meets world standards on reliability for optical devices. A number of the manufactured gradient structures showed the resource of 10–15 years that is above the world average.

It was also necessary to test the stability of optical structures during continuously varying operating conditions (*in situ*). For this, we developed a device with a separate specimen’s capsule connected with optic fiber to a microspectrophotometer (Figure 4). The capsule is disposed in a heating-cooling chamber (Figure 4) then the device provides measuring spectral characteristics *in situ*. The tests were conducted with the developed nanogradient interference narrow-band filter with hyperwide barrier zone. Their procedure, for the instance, was as follows: the specimen was placed in the capsule. The microspectrophotometer was calibrated. At the beginning, the transmission spectrum was measured at $+20^\circ\text{C}$. Then the capsule was cooled to temperature of -30°C , maintained 20 minutes for establishment of the temperature and the transmission spectrum was determined. After this, the capsule was heated up to $+45^\circ\text{C}$, held-on for 20 minutes and the spectrum was measured. Then the capsule was heated up to $+70^\circ\text{C}$, held-on for 20 minutes and

the transmission spectrum was determined again.

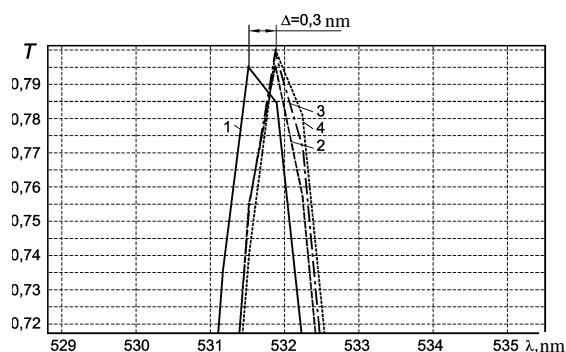


Figure 5: Transmission characteristics of the nanogradient filter when exposed to heat and cold; the sample temperature: 1 — $+20^{\circ}\text{C}$, 2 — -30°C , 3 — $+45^{\circ}\text{C}$, 4 — $+70^{\circ}\text{C}$.

Figure 5 shows the measured *in situ* transmission spectra of a filter at the beginning (the left curve) and during the test. It is seen that the shift Δ of the developed nanogradient interference narrow-band filter characteristics is small ($\Delta \approx 0.3\text{ nm}$) in the given temperature range that provides stable work of optical structures, manufactured by pulse magnetron sputtering, in aviation and space photonic devices.

5. CONCLUSION

The gradient structures with different refraction index profiles (simple “one-periodical”, multi-periodical, rugate-like, with apodization, etc.) with excellent properties, including gradient optical metamaterials [5] for devices based on transformation optics, have been produced. As an example of efficient applications of the developed and manufactured gradient optical structures one can point out their success application in laser ranging and location devices (the increase of energy efficiency by 30–40%). The experiments showed the gradient and nanogradient refraction index profiles provide wide-band or narrow-band and wide-angle working spectral characteristics (antireflective and others) in the visible and near IR field of the manufactured full-dielectric low-loss coatings and their stability against high-power laser radiation, thermal, mechanical and space environmental factors. The perspectives of mid-frequency pulse magnetron sputtering technology of thin film dielectric gradient optical structures for space photonics are confirmed.

ACKNOWLEDGMENT

The work was financially supported by the Ministry of Education and Science of the Russian Federation (Agreement with Fotron-Auto, Ltd. No. 14.579.21.0066) and the Far Eastern Federal University (project No. 14-08-2/3-20_u).

REFERENCES

1. Volpian, O. D., A. I. Kuzmichev, and Yu. A. Obod, “Technological aspects of obtaining gradient optical metamaterial,” *PIERS Proceedings*, 277–281, Moscow, Russia, Aug. 19–23, 2012.
2. Shvartsburg, A. B., Y. A. Obod, A. I. Kuzmichev, O. D. Volpian, and Y. N. Parkhomenko, “Nanogradient all-dielectric FIM: Technology of fabrication and the first experiments,” *Opt. Mat. Exp.*, Vol. 4, 2250–2261, 2014.
3. Volpian, O. D. and A. I. Kuzmichev, “Nanogradient optical coating,” *Russ. J. Gen. Chem.*, Vol. 83, 2182–2194, 2013.
4. Bartzsch, H., S. Lange, P. Frach, and K. Goedicke, “Graded refractive index layer systems for antireflective coatings and rugate filters deposited by reactive pulse magnetron sputtering,” *Surf. Coat. Tech.*, Vol. 180, 616–620, 2004.
5. Volpian, O. D. and A. I. Kuzmichev, “Negative refraction of waves. Introduction into physics and technology of electromagnetic metamaterials,” *Avers*, Kiev, 2012 (in Russian).

3-D Microwave Scanner for Biomedical Applications: A Preliminary Prototype

A. Cuccaro¹, A. Brancaccio¹, B. Basile², M. J. Ammann³, R. Solimene¹, and G. Ruvio³

¹Seconda Università di Napoli, Via Roma 29, Aversa, CE 81031, Italy

²B. & B. Sas, Strada Fienile 1, Casalnuovo di Napoli, NA 80013, Italy

³Dublin Institute of Technology, Kevin Street, Dublin 8, Ireland

Abstract— This paper introduces the prototype of a scanning system operating in the microwave range 0.5–4 GHz with strong potential for biomedical applications such as breast cancer detection or to assess shape-discontinuity in bones. A fully automated scanner was designed to reduce mechanical uncertainties and data acquisition time. Accurate positioning and synchronization with data acquisition enables a rigorous proof-of-concept for the microwave imaging procedure. The system can remotely control two printed antipodal Vivaldi antennas that scan a phantom across a set of positions arranged in cylindrical coordinates. For antenna miniaturization and improved coupling, the antennas and their interface and the phantom are immersed in a coupling medium that presents electric properties similar to adipose tissue. The system performs automatically both the antenna positioning and data acquisition and post-processing. In the current version the reflection coefficients are measured by a Vector Network Analyzer (VNA). But the integration of dedicated chipboard attached to each antenna to replace the VNA and speed up data acquisition is on process. Without any difficult *a priori* antenna characterization, the system is to detect, in the phantom, enclosed regions with distinctive dielectric contrast.

1. INTRODUCTION

Microwave medical imaging was presented as one of the most promising emerging imaging modalities of the last two decades. Although the most targeted application has been breast cancer imaging [1, 2], other biomedical diagnostic areas have also been proposed [3, 4]. Based fundamentally on the dielectric contrast between tissues, microwave medical imaging offers a low-cost, non-ionising and non-invasive method. From a practical perspective, the imaging process involves illuminating the tissue of interest with a wideband radar pulse and recording the reflected (and sometimes transmitted) signals from any dielectric boundaries present within the tissue. Several different mechanisms for combining these signals to create an image have been proposed. These algorithms can be divided into two broad categories: those that seek to identify the presence and location of significant dielectric scatterers in the tissue; and those whose aim is to reconstruct the entire dielectric profile of the tissue under examination.

Besides, the choice of the most suitable imaging procedure, a very important role is played by the RF system and in particular by the antennas. Ultra-wideband (UWB) antennas have been largely used for microwave medical imaging as they can offer a very large operating band, stable radiation properties, and compact dimensions [5, 6]. In order to fully assess the achievable performance of a near-field microwave detection system, the presence of the antenna must be taken into account.

In this paper, we present a preliminary prototype of 3-D microwave scanner for medical applications. After a brief description of its functional parts, results are shown for the following scenarios: a metal scatterer in homogeneous background; skin-fat-muscle-bone phantom. Images are reconstructed by using three different methods: an interferometric version of the Multiple Signal Classification (MUSIC) algorithm [7], non-coherent migration [8] which is a particular version of beamforming, and the standard wideband MUSIC technique [9].

2. 3-D MICROWAVE SCANNER

The 3-D scanner here presented is meant to extend the investigation which was carried out in [7] in a more controlled environment. The prototype is made of the following parts:

- Two printed antipodal Vivaldi antennas that can be manoeuvred to adjust their height and distance from the phantom;
- A turntable that rotates the phantom with an accuracy of $\pm 1^\circ$;
- A tank that contains the measuring setup immersed in a coupling medium with permittivity equal to 12;

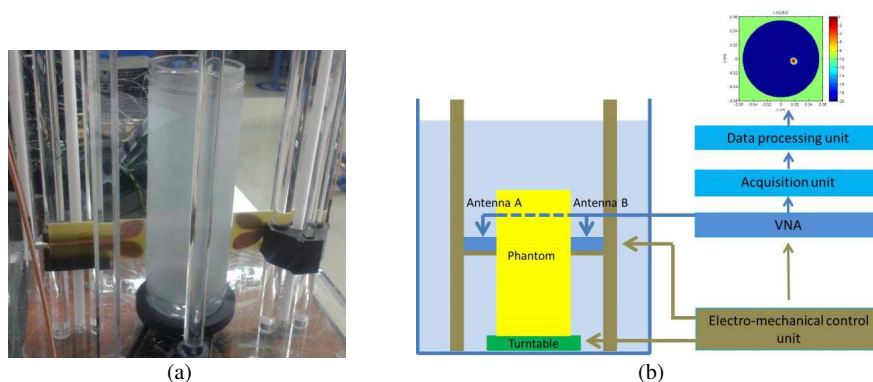


Figure 1: (a) Detail of the scanner; (b) Functioning blocks of the scanner.

- A VNA to measure the S-parameters at terminals of the antennas;
- An acquisition unit to synchronize the antenna/phantom positioning with the data acquisition;
- A data processing unit to generate reconstructed images from the measured datasets.

The system records S_{11} and S_{22} of the antennas sampled across 801 equally sparse points in the frequency range 0.5–4 GHz.

The coupling medium was obtained with a mixture of a 50% kerosene-50% safflower oil solution and de-ionised water in the proportion of 80% and 20%, respectively, as in [7].

Although the measurements carried out in this investigation are based on a set of cylindrical positions of scanning position, the 3-D scanner can be adjusted for semi-spherical layouts as well.

3. RESULTS

The scanner was preliminary assessed for a very simple homogeneous scenario with the investigation imaged area totally filled with the coupling medium and an 8-mm thick cylindrical metal bar used as target. This test was performed in order to estimate the delocalization error due to the mismatch of the equivalent permittivity used by the algorithm to generate the image from the actual permittivity of the coupling medium. 10° rotations in 36 equally spaced measurements were taken at the same antenna height corresponding to 10° sectors.

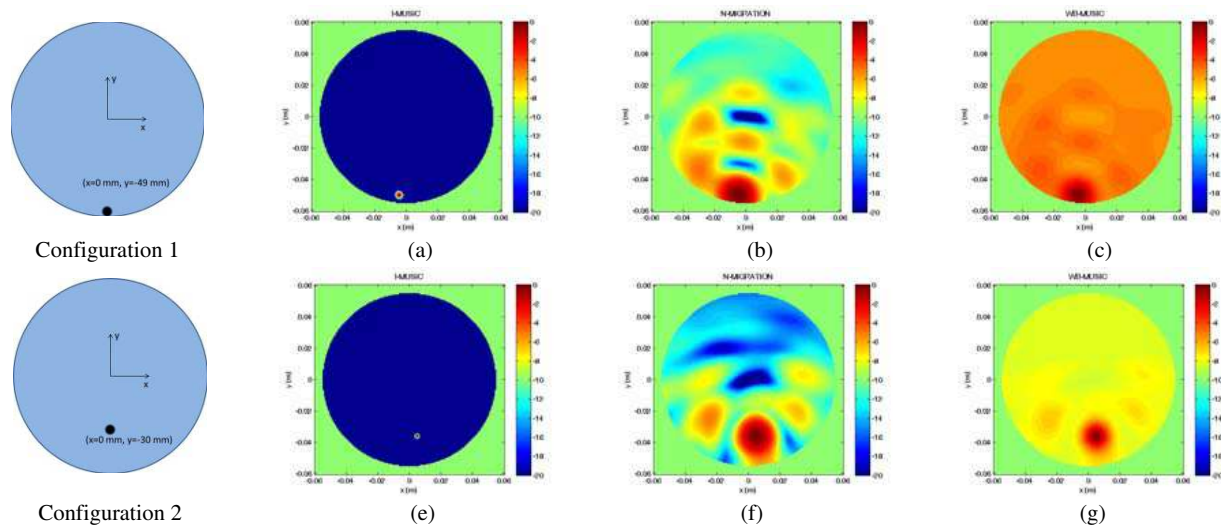


Figure 2: Image reconstructions in homogeneous scenario. (a), (e) I-MUSIC; (b), (f) non-coherent migration; (c), (g) wideband MUSIC.

A delocalization error occurs in the range of 1 mm for the configuration 1 and 5.9 mm for the configuration 2, respectively. Delocalization of the target in the reconstructed image is due to the losses of the coupling medium that are not taken into account in the Green's function of the imaging algorithms [10].

Finally a realistic phantom that mimics a cow's leg was prepared by using a bovine metacarpal bone section with muscle tissue attached and wrapped into pork fat and turkey skin for easier workability. The phantom has an overall diameter of approximately 100 mm and the length of 250 mm with the bone-section of an approximate diameter of 28 mm. Three slices spaced 10 mm were considered for the screening with 36 scans per each slice.

The dielectric properties of the corresponding human tissues in the phantom are listed in Table 1 at the centre frequency of 1.75 GHz [11–13].

Table 1: Dielectric properties of corresponding human tissues in phantom at 2.75 GHz.

	Conductivity [S/m]	Relative permittivity
Bone cortical	0.45429	11.207
Marrow	0.10877	5.2644
Muscle	1.9515	52.363
Fat	0.11809	5.2492
Skin	1.7802	42.442

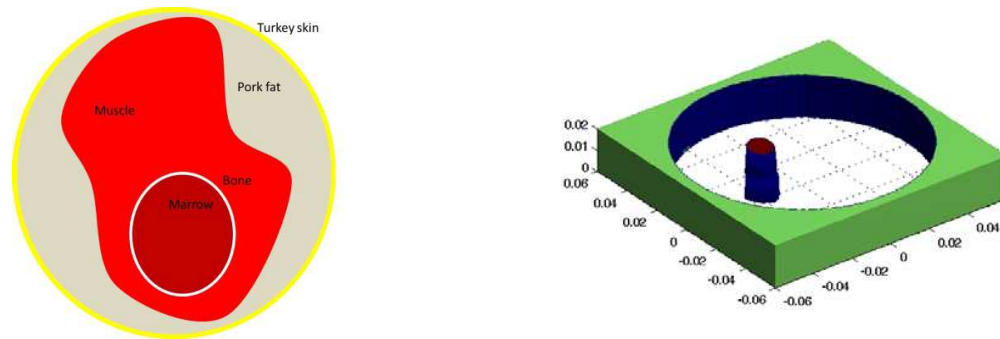


Figure 3: Sketch of the phantom cross-section. 3-D reconstruction performed with Non-coherent migration.

4. CONCLUSIONS

The prototyped 3-D scanner here presented showed significant potential in microwave medical imaging. An estimation of the delocalization error was achieved by using a metallic bar of diameter equal to 8 mm as a target in three different configurations. The measured reflection coefficients were processed with three linear non-coherent methods: an interferometric version of the Multiple Signal Classification (MUSIC) algorithm, non-coherent migration, and the standard wideband MUSIC technique. Reconstructions showed a delocalization error which is equal to 1 mm for the configuration 1 and 5.9 mm for the configuration 2, respectively.

From experimental results carried out on a multi-layer phantom including skin, fat, muscle and bone, successful reconstruction were achieved of the bone section. The phantom was scanned across three equally spaced slices to obtain a 3-D bone image reconstruction.

REFERENCES

1. Nikolova, N. K., "Microwave imaging for breast cancer," *IEEE Microwave Magazine*, Vol. 12, No. 7, 78–94, 2011.
2. Fear, E. C., P. M. Meaney, and M. A. Stuchly, "Microwaves for breast cancer detection?," *IEEE Potentials*, 12–18, Feb./Mar. 2003.
3. Fhager, A. and M. Persson, "A microwave measurement system for stroke detection," *7th Loughborough Antennas and Propagation Conference, LAPC 2011*, Loughborough, 14–15 Nov. 2011.
4. Tian, Z., P. M. Meaney, M. J. Pallone, S. Geimer, and K. D. Paulsen, "Microwave tomographic imaging for osteoporosis screening: A pilot clinical study," *Conf. Proc. IEEE Eng. Med. Biol. Soc.*, 1218–1221, 2010.

5. Jafari, H. M., M. J. Deen, S. Hranilovic, and N. K. Nikolova, "A study of ultrawideband antennas for near-field imaging," —it *IEEE Trans. Antennas Propag.*, Vol. 55, No. 4, 1184–1188, 2007.
6. Flores-Tapia, D. and S. Pistorius, "Real time breast microwave radar image reconstruction using circular holography: A study of experimental feasibility," *Med. Phys.*, Vol. 38, 5420–5431, 2011.
7. Ruvio, G., R. Solimene, A. Cuccaro, D. Gaetano, J. E. Browne, and M. J. Ammann, "Breast cancer detection using interferometric MUSIC: Experimental and numerical assessment," *Medical Physics*, Vol. 41, No. 10, 103101/1–11, 2014.
8. Ahmad, F. and M. G. Amin, "Non-coherent approach to through-the-wall radar localization," *IEEE Trans. Aerosp. Electron. Syst.*, Vol. 42, No. 4, 1405–1419, 2006.
9. Yavuz, M. E. and F. L. Teixeira, "On the sensitivity of time-reversal imaging techniques to model perturbations," *IEEE Trans. Antennas Propag.*, Vol. 56, 834–843, 2008.
10. Solimene, R., G. Ruvio, A. Dell'Aversano, A. Cuccaro, M. J. Ammann, and R. Pierri, "Detecting point-like sources of unknown frequency spectra," *Progress In Electromagnetics Research*, Vol. B, No. 50, 347–364, 2013.
11. Gabriel, C., "Compilation of the dielectric properties of body tissues at RF and microwave frequencies," *Report N.AL/OE-TR- 1996-0037, Occupational and Environmental Health Directorate, Radiofrequency Radiation Division*, Brooks Air Force Base, Texas, USA, June 1996.
12. Gabriel, C., S. Gabriel and E. Corthout, "The dielectric properties of biological tissues: I. Literature survey," *Phys. Med. Biol.*, Vol. 41, 2231–2249, 1996.
13. Gabriel, S., R. W. Lau, and C. Gabriel, "The dielectric properties of biological tissues: II. Measurements in the frequency range 10 Hz to 20 GHz," *Phys. Med. Biol.*, Vol. 41, 2251–2269, 1996.

UWB Waveguide Breast Tumor Detection System Based on Delay and Sum Reconstruction Algorithm

Ondrej Fiser, Ilja Merunka, and Jan Vrba

Department of Electromagnetic Field, Faculty of Electrical Engineering
Czech Technical University in Prague, Czech Republic

Abstract— The purpose of this contribution is breast malignant tumor detection through the confocal delay and sum reconstruction algorithm. The tumor signal is extracted from background and used for reconstruction. For higher accuracy the scattered signal from all four UWB waveguide antennas, which are located around the breast, were used.

1. INTRODUCTION

Breast cancer is one of the major diseases among women. Unfortunately, over 2000 of affected women die from breast cancer in the Czech Republic. The chances of survival for the patient are dependent on disease stage when cancer is captured. Therefore, it is necessary to diagnose this disease as soon as possible. Currently for breast cancer detection mammography is utilized. For this examination ionizing X-Rays are used. X-Rays increases likelihood of the built up of cancer which is a risk for healthy patients. It is therefore necessary to develop new methods for tumor detection. To the most promising method developing in laboratories we can count microwave tomography and confocal microwave imaging.

2. ANTENNA SYSTEM CONFIGURATION

For imaging purposes the UWB double-ridged horn antenna intended for medical imaging was adopted from [1]. Total four antennas are placed equidistantly around a breast model (see Figure 1). The whole antenna system is immersed in canola oil.

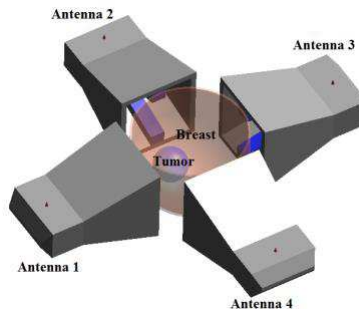


Figure 1: Used numerical model with breast with tumor and four UWB antennas.

3. NUMERICAL BREAST PHANTOM

A simple circular homogeneous breast phantom (100 mm in diameter) with a thin skin layer (2 mm thick) was used. This used breast phantom is based on a phantom published in [2]. In this phantom a spherical tumor of diameter 20 mm at various positions was inserted. The values of relative permittivity and conductivity of fat, skin and malignant tumor tissue are listed in Table 1.

Table 1: Dielectric properties of tissues in numerical phantom (adopted from [3]).

Material	Relative permittivity ε [-]	Conductivity σ [S/m]
Fat	9	0.4
Skin	35.7	3.17
Tumor	50	4
Canola Oil	3	0.04

4. IMAGE RECONSTRUCTION ALGORITHM

Time signals needed for reconstruction were obtained from numerical simulations in FDTD electromagnetic field simulator SEMCAD X Aletsch 14.8 [4]. The reconstruction algorithm for delay and sum was implemented. The transmitting antenna sends a RF pulse through the breast model. Transmitted signal is a Gaussian pulse of central frequency 4.5 GHz and bandwidth 8 GHz (see Figure 2).

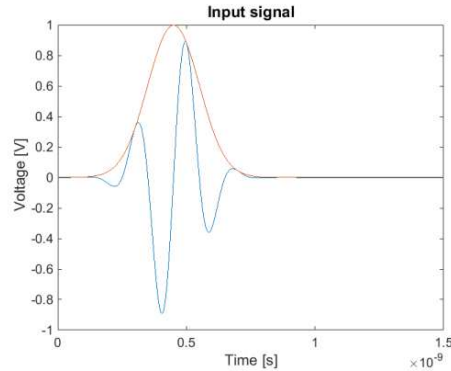


Figure 2: Transmitted Gaussian pulse with bandwidth 8 GHz.

The place of the change in dielectric parameters of material (canola oil X skin X fat X tumor) scatters the incident wave. The scattered wave can be received in all antennas which are placed around the breast. The method consists of two phases. In the first phase a scan of scattered field of breast without the tumor is performed. In the second phase (e.g., after 1 year in next medical examination) second scan will be made. For all signals Hilbert transformation is applied and prepared signals with/without tumor are subtracted from each other. Obtained differential signals are reflections from changes, which occurred (e.g., from tumor). From the knowledge of the average velocity wave propagation in the breast and from measured time difference between peak of the transmitted signal (from transmitting antenna) and received signal peak. Then the distance of the reflections from each antenna is found (assumed tumor position). The velocity of propagating wave (v) is calculated according to the Equation (1).

$$v = \frac{\sqrt{2}}{\sqrt{\varepsilon \cdot \mu}} \cdot \frac{1}{\left(\sqrt{1 + \left(\frac{\sigma}{\omega \cdot \varepsilon} \right)^2} \right) + 1} \quad (1)$$

where c is speed of light [$\text{m}\cdot\text{s}^{-1}$], ε is permittivity [$\text{F}\cdot\text{m}^{-1}$], μ is permeability [$\text{H}\cdot\text{m}^{-1}$], σ is conductivity [$\text{S}\cdot\text{m}^{-1}$] and ω is angular velocity [$\text{rad}\cdot\text{s}^{-1}$].

Position of the wave diffuser is on the circle with the center in the antenna power probe. The power intensity for each position in the breast is the sum of power intensity from each receiving antenna. For tumor localization the distance must be measured even from other antennas. Then it is possible to calculate intersections of the circles defining the distance of the tumor from each antenna. For high accuracy it is good to use all antennas as transmitters sequentially. In the case of uncertain tumor position (in case that peak appears more than once in signal) we can rotate the whole antenna system by 45 degrees and thus increases the localization accuracy. Used method seems to be very promising for breast tumor detection. Its disadvantage is the need to dispose signals from the breast at a time when the tumor did not occur.

5. RECONSTRUCTION RESULTS

We tested the algorithm for 20 mm diameter tumor that was inserted in the numerical breast phantom. For better algorithm evaluation we investigate two different tumor positions. The first tumor position is on the main axes in front of the antenna 1. For the second tumor position we rotate the whole breast by 45 degrees. Thus we deflect tumor which now does not lie on one of main axes passing center of antennas.

5.1. First Position

In the Figure 3(a) is the tumor position in the breast (tumor center $x = 30, y = 50$) and Figure 3(b) shows the reconstruction results. The black circle indicates the real tumor position in our numerical model which is shown in the Figure 3(a). The highest signal intensity indicates the predicted tumor position. The biggest intensity of received signal (reflection) is on the left side of the tumor. This is caused because antenna 1 is nearest to the tumor and therefore has the strongest signal. Used hemispherical numerical model has larger diameter, so we get small response from more distant antennas (e.g., antenna 3). According to the reconstruction results it is possible to estimate the position of the tumor relatively accurate. It is worse with the size and shape determination.

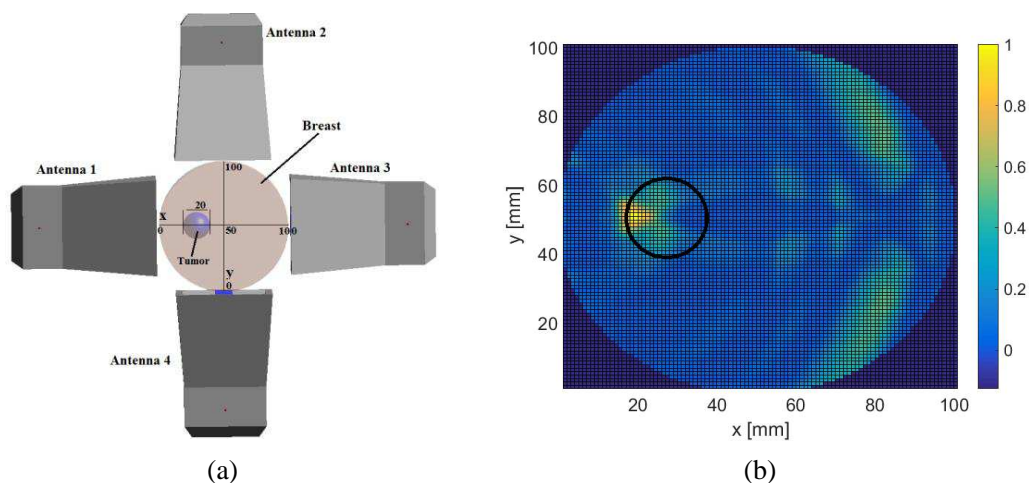


Figure 3: (a) Numerical model with tumor and (b) reconstructed 2D cross section.

5.2. Second Position

In the Figure 4(a) the second tumor position is shown. The breast was turned by 45 degrees against the position 1. The position of the tumor is $x = 35$ mm and $y = 70$ mm. Therefore the tumor is not on any of major axis that passes through the center of waveguide antenna. Used waveguide antennas have the highest intensity of electric field in the center of aperture. That's why the reflected signal has lower intensity and therefore is in the Figure 4(b) lower contrast. Even though the tumor imposition outside the main axis can be also detect with relative high accuracy. According to the Figure 4(b) it is clear that the tumor image is less contrast than in the position 1.

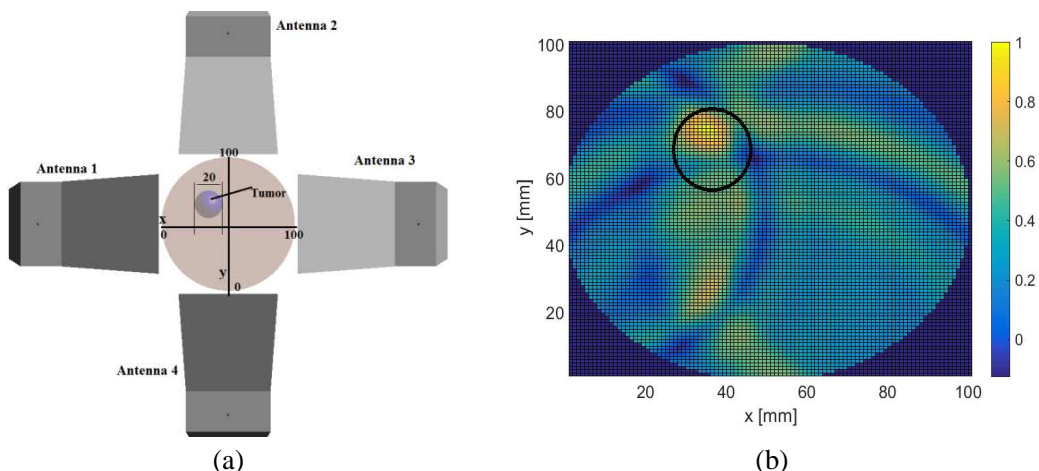


Figure 4: (a) Numerical model with tumor and (b) reconstructed 2D cross section.

6. CONCLUSION

In this contribution the delay and sum algorithm was implemented for tumor detection in simple heterogeneous numerical breast phantom. The reconstructed tumor position was reconstructed from the acquired time signals. For successful detection of tumor position it was necessary to obtain time signals when the tumor was not present. In the case used for reconstruction only signals obtained from transmitting antennas (which were also receivers) the reconstruction with multiple tumor positions was obtained. Major improvements of reconstruction images brought signals obtained from side antennas from transmitting antenna point of view. These signal intensities are normally by about one order lower in magnitude. So it was necessary to normalize these signals and properly sum them with other signals. In this contribution the tumor detection is discussed. We examine the reconstruction algorithm by 2 tumor positions. The obtained results seem to be very promising. Another important step for future work is finding the right way how to normalize the acquired signal and how to compensate the attenuated signal.

ACKNOWLEDGMENT

This study was supported by the COST Action TD1301: “Development of a European-based Collaborative Network to Accelerate Technological and as well as by the Student Grant System of the Czech Technical University in Prague by student’s project SGS 2014, with number SGS14/189/OHK3/3T/13: “Interactions of EM field with biological systems and theirs applications in medicine.”.

REFERENCES

1. Latif, S., S. Pistorius, and L. Shafai, “A double-ridged horn antenna design in canola oil for medical imaging,” *2013 International Conference on Advances in Electrical Engineering (ICAEE)*, 421–424, 2013.
2. Davis, S., H. Tandradinata, S. Hagness, and B. Van Veen, “Ultrawideband microwave breast cancer detection: A detection-theoretic approach using the generalized likelihood ratio test,” *IEEE Transactions on Biomedical Engineering*, Vol. 52, No. 7, 1237–1250, 2005.
3. Li, X. and S. Hagness, “A confocal microwave imaging algorithm for breast cancer detection,” *IEEE Microwave and Wireless Components*, 130–132, 2001.
4. SPEAG AG, SEMCAD X Reference Guide, Online Available: <http://download.speag.com/releases/semcad/1485/documentation/SEMCAD-X-Manual.pdf>.

Axiomatics of the Blondel-Park Transformation

G. F. Crosta¹ and G. Chen²

¹University of Milan Bicocca, Italy

²Texas A & M University, USA

Abstract— The doubly-fed induction generator (*DFIG*) is a key constituent of energy conversion plants. The control of a *DFIG* is a challenge, whenever the primary energy supply (e.g., the wind velocity field) is characterised by intermittency. The mathematical model and control of a *DFIG* rely on the BLONDEL-PARK transformation, which is known to simplify the governing equations. The distinctive feature of this contribution consists of showing how the BLONDEL-PARK transformation derives from a set of conditions to be met by a group. Such a group is shown to exist and to continuously depend on one parameter. The uniqueness of its infinitesimal generator is also shown. As an application, the well-known electric torque theorem is proved in a simple way, which relies on a “product of matrices” formula. The latter, in turn, is a by-product of the axiomatic deduction of the BLONDEL-PARK transformation.

1. INTRODUCTION

The equations which describe the ideal doubly-fed induction generator (*DFIG*) have been studied for more than a century. Interest in the electric machine equations has obviously been motivated by the need to understand and improve the conversion from mechanical to electrical work as well as controlling the plant. Control is needed to face uncertainty in the primary energy supply (e.g., intermittency of the wind velocity field in front of a wind turbine) as well as in the electric load. In turn, the design of a control algorithm benefits from knowledge of the abstract properties of the plant model equations. Said equations, and the related changes of variables, center on two matrices, the rotor-to-stator mutual inductance matrix, $\mathbf{L}_{sr}[\cdot]$, and the BLONDEL [1]-PARK [2] transformation matrix, $\mathbf{K}[\cdot]$. In the past, two pieces of work addressed the ideal *DFIG* from the points of view of dynamical systems [3] and, to some extent, group theory [4]. The presentation herewith differs from previous ones, because it aims at deriving the BLONDEL-PARK transformation from first principles, i.e., basic requirements which formalise some physical properties.

2. PROPERTIES REQUIRED OF A FRAME TRANSFORMATION

Without providing too many details, electric currents, magnetic flux linkages and voltages of an induction machine form 3-vectors which are usually represented in the $\{abc\}$ stator and rotor frames. For example, the stator currents form a vector

$$\vec{j}_{\{abc\}s} = \begin{bmatrix} j_{as} \\ j_{bs} \\ j_{cs} \end{bmatrix} \in \mathbb{R}^3,$$

the components of which are functions of time $t \in \mathfrak{T}$. Similar notations and representations hold for other electric quantities. In order to remove redundancy sitting in $\{abc\}$ frames, another frame, called $\{dq0\}$, is introduced, where only two components of a vector shall matter, the direct one, d , and the quadrature component, q .

DEF. 1. (The $dq0$ frame.) Let $\{dq0\}$ denote a reference frame for electric quantities of axes d and q , subject to the following specifications, *d.1*) to *d.3*).

d.1) Representations of any given electric variable with respect to the *direct*, a.k.a. d , axis and the stator a axis (as) shall be given by the same function evaluated at arguments which differ by the phase angle β_s . Similarly, the difference in phase angles of variables pertaining to the rotor ar axis shall be β_r . The relation of the two angles to θ_r is

$$\beta_s = \beta_r + \theta_r. \quad (1)$$

d.2) The *quadrature* axis, a.k.a. q , shall be orthogonal to d in the $L^2([0, 2\pi])$ sense: if $\zeta_d[\cdot]$ and $\zeta_q[\cdot]$ are the d - and q -components of a (generally complex-valued) signal which depend on an angle, η , then

$$\oint \zeta_d[\eta]^* \zeta_q[\eta] d\eta = 0, \quad (2)$$

where $\oint \equiv \int_0^{2\pi}$.

d.3) The third entry of a vector in the $\{dq0\}$ frame shall represent a zero sequence, e.g.,

$$j_a + j_b + j_c = 0, \quad \forall t \in \mathfrak{T}. \quad (3)$$

In abstract terms, the sought for relation between $\{abc\}$ and $\{dq0\}$ is formalised as follows.

PBM. 1. (The $\{abc\}$ to $\{dq0\}$ transformation problem.) Find a transformation which maps vectors (electric quantities) from the $\{abc\}$ s and, respectively, the $\{abc\}r$ frames to the $\{dq0\}$ frame, as specified by DEF. 1 and

K.1) is invertible and linear,

K.2) conserves instantaneous electric power,

K.3) has the same functional form for both stator and rotor quantities,

K.4) depends at most on one real parameter (an “electric angle”) and is of class \mathcal{C}^1 at least with respect to that parameter.

K.5) The parameter may be different for stator as compared to rotor quantities.

K.6) Transformed flux linkages are magnetically decoupled. (Diagonalisation.)

3. THE TRANSFORMATION GROUP

There is a solution to PBM. 1 and the solution procedure is constructive.

THM. 1. (Existence and representation of the one parameter group.)

T1.1) (representation) The sought for transformations form one-parameter groups of operators

$$\mathbf{K}[\eta] = \mathbf{K}_0 \cdot e^{\eta \mathbf{F}}. \quad (4)$$

T1.2) (left multipliers) Possible \mathbf{K}_0 's ($\equiv \mathbf{K}[0]$) are [only two are shown for reasons of space]

$$\mathbf{K}_0^{(a)} = \sqrt{\frac{2}{3}} \begin{bmatrix} 1 & -\frac{1}{2} & -\frac{1}{2} \\ 0 & \frac{\sqrt{3}}{2} & -\frac{\sqrt{3}}{2} \\ \frac{1}{\sqrt{2}} & \frac{1}{\sqrt{2}} & \frac{1}{\sqrt{2}} \end{bmatrix}, \quad \mathbf{K}_0^{(b)} = \sqrt{\frac{2}{3}} \begin{bmatrix} 1 & -\frac{1}{2} & -\frac{1}{2} \\ 0 & -\frac{\sqrt{3}}{2} & \frac{\sqrt{3}}{2} \\ -\frac{1}{\sqrt{2}} & -\frac{1}{\sqrt{2}} & -\frac{1}{\sqrt{2}} \end{bmatrix}. \quad (5)$$

T1.3) (infinitesimal generator) The matrix \mathbf{F} in Eq. (4) is unique and reads

$$\mathbf{F} = \frac{1}{\sqrt{3}} \begin{bmatrix} 0 & 1 & -1 \\ -1 & 0 & 1 \\ 1 & -1 & 0 \end{bmatrix}. \quad (6)$$

REM. The algebra of \mathbf{F} is of independent interest: the left zero divisors of \mathbf{F} and recurrent formulas for its powers are also derived, which have not been provided before.

REM. Eventually, THM. 1 leads to a streamlined proof of the electric torque theorem. In fact, this is made possible by a formula for the product of the BLONDEL-PARK transformation matrices (Eq. (4)) with the θ_r derivative of the mutual inductance matrix: $\mathbf{K}[\theta] \cdot \left(\frac{\partial \mathbf{L}_{sr}}{\partial \theta_r}\right)[\theta_r] \cdot \mathbf{K}[\beta]^{-1} = \frac{3}{2} \mathbf{A}_3$. No details can be worked out herewith for reasons of space.

4. CONCLUSION

The above results support the relevance of group theory in the modeling of electric machines and of *DGIGs* in particular. The axiomatic deduction, from PBM. 1 to THM. 1, of the BLONDEL-PARK transformation stated as existence of a one-parameter, continuous and differentiable group of transformations does not seem to have been addressed before and is the distinctive feature of this contribution.

ACKNOWLEDGMENT

G. F. Crosta gratefully acknowledges the financial support of the home University's *Fondo di Ateneo per la ricerca*, from 2010 onwards and the research agreement between the home University and *Digicom Co.*, GALLARATE, IT.

G. Chen and G. F. Crosta gratefully acknowledge the partial support by the *Texas NORMAN HACKMAN Advanced Research Program Grant #010366-0149-2009* from the *Texas Higher Education Coordinating Board*.

REFERENCES

1. Blondel, A., *Synchronous Motor and Converters — Part III*, McGraw-Hill, New York, 1913.
2. Park, R. H., “Two-reaction theory of synchronous machines — Part I,” *AIEE Trans.*, Vol. 48, No. 2, 716–730, 1929.
3. Willems, J. L., “A system theory approach to unified electric machine analysis,” *Int. Journ. Control*, Vol. 15, No. 3, 401–418, 1972.
4. Liu, X. Z., G. C. Verghese, J. H. Lang, and M. K. Önder, “Generalizing the BLONDEL-PARK transformation of electrical machines: Necessary and sufficient conditions,” *IEEE Trans. Circuits and Systems*, Vol. 36, No. 8, 1058–1067, 1989.